GENERAL LINEAR ACOUSTICS [20]

(Continued)

CONTENTS—*Continued from preceding page*

CONTENTS—*Continued from preceding page*

CONTENTS—*Continued from preceding page*

ACOUSTICAL NEWS—USA

Elaine Moran
Acoustical Society of America, Suite 1NO1, 2 Huntington Quadrangle, Melville, NY 11747-4502

Editor's Note: *Readers of this Journal are encouraged to submit news items on awards, appointments, and other activities about themselves or their colleagues. Deadline dates for news items and notices are 2 months prior to publication.*

Announcement of the 2003 Election

In accordance with the provisions of the bylaws, the following Nominating Committee was appointed to prepare a slate for the election to take place on 18 April 2003:

Katherine S. Harris, *Chair*   Victor W. Sparrow
Laurel H. Carney   Maureen Stone
James F. Lynch

The bylaws of the Society require that the Executive Director publish in the *Journal* at least 90 days prior to the election date an announcement of the election and the Nominating Committee's nominations for the offices to be filled. Additional candidates for these offices may be provided by any Member or Fellow in good standing by letter received by the Executive Director not less than 60 days prior to the election date and the name of any eligible candidate so proposed by 20 Members or Fellows shall be entered on the ballot.

Biographical information about the candidates and statements of objectives of the candidates for President-Elect and Vice President-Elect will be mailed with the ballots.

CHARLES E. SCHMID
Executive Director

The Nominating Committee has submitted the following slate:

FOR PRESIDENT-ELECT
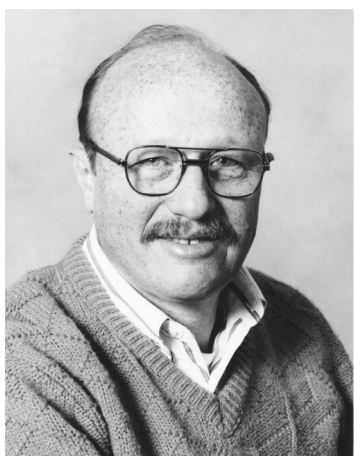
William A. Kuperman

Janet M. Weisenberger

FOR VICE PRESIDENT-ELECT
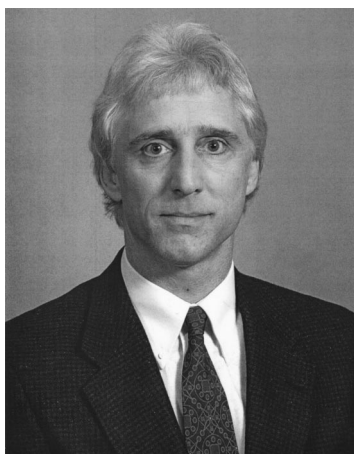
Mark F. Hamilton

Donna L. Neff

FOR MEMBERS OF THE EXECUTIVE COUNCIL

Yves H. Berthelot

Bennett M. Brooks
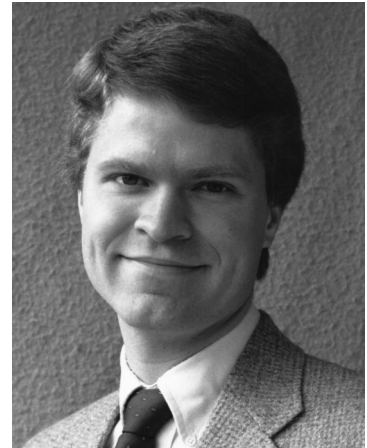
E. Carr Everbach
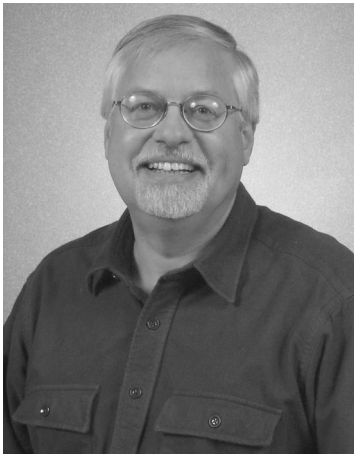
George V. Frisk

Mardi C. Hastings
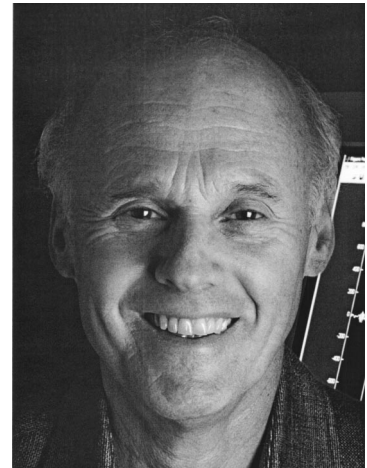
Joseph M. Perkell

Meena Agarwal selected recipient of the 2002 Stetson Scholarship

ASA member Meena Agarwal was selected the recipient of the 2002–03 Raymond H. Stetson Scholarship in Phonetics and Speech Production. Ms. Agarwal is a graduate student in the Department of Communication Disorders at Bowling Green State University in Bowling Green, Ohio. She received BS and MS degrees from the University of Bombay, India. Ms. Agarwal's current work includes projects that clarify important roles the false vocal folds might have in voice production and the effects of the false vocal folds on the translaryngeal airflow resistance. Her master's thesis was on "Aerodynamic analysis of voice in pubertal and post pubertal age groups."

The Stetson Scholarship, which was established in 1998, honors the memory of Professor Raymond H. Stetson, a pioneer investigator in phonetics and speech science. Its purpose is to facilitate the research efforts of promising graduate students and postgraduates. The Scholarship includes a $3000 stipend for one academic year. Past recipients have been Roger Steeve (1999), Elizabeth K. Johnson (2000), and Jeffery Jones (2001).

Applications for the award are due in March each year. For further information about the award, please contact the Acoustical Society of America, Suite 1NO1, 2 Huntington Quadrangle, Melville, NY 11747-4502; Tel.: 516-576-2360; Fax: 516-576-2377; E-mail: asa@aip.org; Web: http://asa.aip.org. Application information can also be found on the ASA Home Page at ⟨http://asa.aip.org/fellowships.html⟩.

David T. Bradley selected recipient of the 2002 ASA Minority Fellowship

ASA member David T. Bradley has been selected the recipient of the 2002–03 Minority Fellowship. Mr. Bradley is a graduate student in the Architectural Engineering Program at the University of Nebraska in Omaha, Nebraska. He received a BS from Grinnell College. Mr. Bradley's research interest is in the field of performance space acoustic design.

The Minority Fellowship was established in 1992 with the goal of supporting minority students in their pursuit of graduate level degrees in acoustics. The Fellowship includes a $13 000 stipend for one academic year plus $1000 in travel support to attend an ASA meeting. Past recipients have been Brian Scott (1993), J. Sean Allen (1997), Guillermo E. Aldana (1999), and Vernecia Sharae' McKay (2001). The next award will be available for the 2003–04 academic year. The fellowship may be renewed for one additional year.

For further information about the Fellowship, please contact the Acoustical Society of America, Suite 1NO1, 2 Huntington Quadrangle, Melville, NY 11747-4502; Tel.: 516-576-2360; Fax: 516-576-2377; E-mail: asa@aip.org; Web: http://asa.aip.org. Application information can also be found on the ASA Home Page at ⟨http://asa.aip.org/fellowships.html⟩.

USA Meetings Calendar

Listed below is a summary of meetings related to acoustics to be held in the U.S. in the near future. The month/year notation refers to the issue in which a complete meeting announcement appeared.

2003

13–15 March	American Auditory Society Annual Meeting, Scottsdale, AZ [American Auditory Society, 352 Sundial Ridge Cir., Dammeron Valley, UT 84783; Tel.: 435-574-0062; Fax: 435-574-0063; E-mail: amaudsoc@aol.com; WWW: www.amauditorysoc.org].
28 April–2 May	145th Meeting of the Acoustical Society of America, Nashville, TN [Acoustical Society of America, Suite 1NO1, 2 Huntington Quadrangle, Melville, NY 11747-4502; Tel.: 516-576-2360; Fax: 516-576-2377; E-mail: asa@aip.org; WWW: asa.aip.org].
5–8 May	SAE Noise & Vibration Conference & Exhibition, Traverse City, MI [P. Kreh, SAE International, 755 W. Big Beaver Rd., Suite 1600, Troy, MI 48084; Fax: 724-776-1830; WWW: http://www.sae.org].
23–25 June	NOISE-CON 2003, Cleveland, OH [INCE Business Office, Iowa State Univ., 212 Marston Hall, Ames, IA 50011-2153; Fax: 515-294-3528; E-mail: ibo@ince.org].
5–8 Oct.	IEEE International Ultrasonics Symposium, Honolulu, HI [W. D. O'Brien, Jr., Bioacoustics Research Lab., Univ. of Illinois, Urbana, IL 61801-2991; Fax: 217-244-0105; WWW: www.ieee-uffc.org].
10–14 Nov.	146th Meeting of the Acoustical Society of America, Austin, TX [Acoustical Society of America, Suite 1NO1, 2 Huntington Quadrangle, Melville, NY 11747-4502; Tel.: 516-576-2360; Fax: 516-576-2377; E-mail: asa@aip.org; WWW: asa.aip.org].

2004

24–28 May	75th Anniversary Meeting (147th Meeting) of the Acoustical Society of America, New York, NY [Acoustical Society of America, Suite 1NO1, 2 Huntington Quadrangle, Melville, NY 11747-4502; Tel.: 516-576-2360; Fax: 516-576-2377; E-mail: asa@aip.org; WWW: asa.aip.org].
3–7 Aug.	8th International Conference of Music Perception and Cognition, Evanston, IL [School of Music, Northwestern Univ., Evanston, IL 60201; WWW: www.icmpc.org/conferences.html].
15–19 Nov.	148th Meeting of the Acoustical Society of America, San Diego, CA [Acoustical Society of America, Suite 1NO1, 2 Huntington Quadrangle, Melville, NY 11747-4502; Tel.: 516-576-2360; Fax: 516-576-2377; E-mail: asa@aip.org; WWW: asa.aip.org].

Errata

There were errors in the article ''F. V. Hunt Postdoctoral Fellowship awarded to Constantine Coussios'' [J. Acoust. Soc. Am. **112**, 1 (2002)]. The correct spelling of the fellowship recipient's first name is Constantin. The title of his dissertation was ''Monitoring of Hemolysis by Acoustic Scattering.'' Also, because the photo was cropped for spacing purpose, it was not possible to show the book that Dr. Coussios was holding, which was *Sound and Sources of Sound* by A. P. Dowling and J. E. Ffowcs Williams. The editor extends her apologies to Dr. Coussios for these errors.

Cumulative Indexes to the *Journal of the Acoustical Society of America*

Ordering information: Orders must be paid by check or money order in U.S. funds drawn on a U.S. bank or by Mastercard, Visa, or American Express credit cards. Send orders to Circulation and Fulfillment Division, American Institute of Physics, Suite 1NO1, 2 Huntington Quadrangle, Melville, NY 11747-4502; Tel.: 516-576-2270. Non-U.S. orders add $11 per index.

Some indexes are out of print as noted below.

Volumes 1−10, 1929−1938: JASA and Contemporary Literature, 1937–1939. Classified by subject and indexed by author. Pp. 131. Price: ASA members $5; Nonmembers $10.

Volumes 11−20, 1939−1948: JASA, Contemporary Literature, and Patents. Classified by subject and indexed by author and inventor. Pp. 395. Out of Print.

Volumes 21−30, 1949−1958: JASA, Contemporary Literature, and Patents. Classified by subject and indexed by author and inventor. Pp. 952. Price: ASA members $20; Nonmembers $75.

Volumes 31−35, 1959−1963: JASA, Contemporary Literature, and Patents. Classified by subject and indexed by author and inventor. Pp. 1140. Price: ASA members $20; Nonmembers $90.

Volumes 36−44, 1964−1968: JASA and Patents. Classified by subject and indexed by author and inventor. Pp. 485. Out of Print.

Volumes 36−44, 1964−1968: Contemporary Literature. Classified by subject and indexed by author. Pp. 1060. Out of Print.

Volumes 45−54, 1969−1973: JASA and Patents. Classified by subject and indexed by author and inventor. Pp. 540. Price: $20 (paperbound); ASA members $25 (clothbound); Nonmembers $60 (clothbound).

Volumes 55−64, 1974−1978: JASA and Patents. Classified by subject and indexed by author and inventor. Pp. 816. Price: $20 (paperbound); ASA members $25 (clothbound); Nonmembers $60 (clothbound).

Volumes 65−74, 1979−1983: JASA and Patents. Classified by subject and indexed by author and inventor. Pp. 624. Price: ASA members $25 (paperbound); Nonmembers $75 (clothbound).

Volumes 75−84, 1984−1988: JASA and Patents. Classified by subject and indexed by author and inventor. Pp. 625. Price: ASA members $30 (paperbound); Nonmembers $80 (clothbound).

Volumes 85−94, 1989−1993: JASA and Patents. Classified by subject and indexed by author and inventor. Pp. 736. Price: ASA members $30 (paperbound); Nonmembers $80 (clothbound).

Volumes 95−104, 1994−1998: JASA and Patents. Classified by subject and indexed by author and inventor. Pp. 632. Price: ASA members $40 (paperbound); Nonmembers $90 (clothbound).

ACOUSTICAL NEWS—INTERNATIONAL

Walter G. Mayer
Physics Department, Georgetown University, Washington, DC 20057

ASA Scholarships for Students in the Former Soviet Union

A few years ago the *Society* established the Committee on Commonwealth of Independent States/Eastern Union (CSI/EU) which was to award a number of ASA Scholarships to doctoral students in the Former Soviet Union. After about two years of scholarship awards, 22 students have submitted abstracts of their research work to the Committee.

The titles of the abstracts, names, affiliations, and e-mail addresses of the authors are listed below. The text of individual abstracts can be obtained by contacting the scholarship recipients directly.

Ultrasonic method of increasing of wood density and shaping of the wood items. Feodor F. Legusha, St. Petersburg State Marine Technical University, St. Petersburg, 198262 Russia. (legusha@smtu.ru)

Influence of effects of rib-stiffening on vibration of plates. Nikita Dementyev, Department of Hydrophysics, St. Petersburg State Marine Technical University, St. Petersburg, Russia. (nickdem@mail.ru)

Development of a method of estimation of low-frequency hydroacoustic fields scattered from thin-walled elastic shells having internal saturation. Stanislav Yavorski, Department of Ship and Industrial Acoustics, Krylov Shipbuilding Research Institute, St. Petersburg, Russia. (syavorsky@mail.ru)

Acoustical investigation of the shear viscoelastic properties of liquids. Bair B. Damdinov, Buryat Scientific Center of the Russian Academy of Sciences, Ulan-Ude, 670047 Russia. (bdamd@ofpsrv.bsc.buryatia.ru)

Stimulation of acoustic horizontal polarization waves by developing fissures in main pipelines. Denis Zlobin, Izhevsk University, Izhevsk, 426011 Russia. (denis2@udm.net)

Investigation of rock elastic properties in the Kola super deep borehole. O. Golovataya, Geological Institute, Kola Science Center of the Russian Academy of Sciences, Apatity, Murmansk region, 184200 Russia. (gorich@geoksc.apatity.ru)

Nonlinear effects in intense acoustic waves containing shock in media with a frequency-dependent law of absorption. Svetlana S. Kashcheeva, Department of Acoustics, Physics Faculty, Moscow State University, Moscow, 119899 Russia. (svetak@acs366bphys.msu.su)

Supersonic jet noise and the influence of instability waves on the noise. Victor Kasyanov, Aero-Hydrodynamics Institute, Moscow region, 140180 Russia. (vkopiev@mx.iki.rssi.ru)

Statistical characteristics of acoustic signals in marine environments and the signal-to-noise ratio at linear equidistant acoustical antennas. Alexsey Kulakov, Technical University of Radiotechnics, Electronics and Automation, Moscow, 117454 Russia. (bvp@akin.ru)

Engineering design parametric echo sounder for bottom profiling. Aleksandr Kutsenko, Taganrog University, Taganrog, 347900 Russia. (fep@tsure.ru)

The analysis and design of ultrasonic electro-acoustical transformers and instruments for surgery. Andrey Lobachev, Bauman State Technical University, Moscow, 107005 Russia. (fep@tsure.ru)

A new approach to the continuous recognition of speech. Ivan Lysyuk, Moscow Institute of Physics and Technology, Moscow region, 141700 Russia. (vns@iitp.ru)

Measurement of acoustic power at cavitation. Igor M. Margulis, Andreyev Acoustics Institute, Shvernik Street 4, Moscow, Russia. (margulis@mtu-net.ru)

Bubble cloud oscillation in a compressible viscous liquid. Elvira Sh. Nasibullayeva, Institute of Mechanics, Ufa Branch of the Russian Academy of Sciences, Karl Marx Street 12, Ufa, 450000 Russia. (elvira@anrb.ru)

The propagation of nonlinear stochastic waves in non-dispersive media. Galina Pasmanik, Nizhny Novgorod State University, Nizhny Novgorod, 603600 Russia. (nikvas@rf.unn.runnet.ru)

Laser opto-acoustic diagnostics of heterogeneous media. Ivan M. Pelivanov, Department of Acoustics, Physics Faculty, Moscow State University, Moscow, 119899 Russia. (nikvas@rf.unn.runnet.ru)

Sound radiation into liquid undergoing cavitation. Grigory Romanenko, Department of Acoustics, Physics Faculty, Moscow State University, Moscow, 119899 Russia. (andreev@acs366b.phys.msu.su)

Some aspects of sound characteristics of first year old infants. Alla Samokischuk, St. Petersburg State University, St. Petersburg, Russia. (allaspw@mail.ru)

Polydisperse bubble cluster dynamics in shock wave cavitation. Georgii N. Sankin, Lavrentyev Institute of Hydrodynamics, Novosibirsk, 630090 Russia. (georgiisankin@yahoo.com)

Experimental investigation of the enhancement of efficiency of thermal and mechanical effects of powerful focused ultrasound beams on biological tissue-like media due to their nonlinearity. Tatiana Sinilo, Department of Acoustics, Physics Faculty, Moscow State University, Moscow, 119899 Russia. (tanya@acs366b.phys.msu.su)

Nonlinear resonances and their manifestation in the acoustics of bubble media. Ekaterina Sosedko, Pacific Ocean Institute, Vladivostok, 690002 Russia. (s_kat@mail.ru)

Modeling of heating of biological tissue by high intensity focused ultrasound using transducers of different geometry. Elena A. Filonenko, Department of Acoustics, Physics Faculty, Moscow State University, Moscow, 119899 Russia. (lenafilko@yahoo.co.uk)

International Meetings Calendar

Below are announcements of meetings and conferences to be held abroad. Entries preceded by an * are new or updated listings.

December 2002

9–13   **International Symposium on Musical Acoustics (ISMA Mexico City)**, Mexico City, Mexico. (Fax: +52 55 5601 3210; Web: www.unam.mx/enmusica/ismamexico.html)

11–13   **International Conference on Sonar-Sensors & Systems (ICONS2002)**, Cochin (Kerala), India. (Fax: +91 484 424858; e-mail: root@drnpol.drdo.com)

19–21   **3rd WSEAS International Conference on Acoustics, Music, Speech and Language Processing**, Tenerife, Canary Islands, Spain. (Web: www.wseas.org/conferences/2002/tenerife/icamsl/)

January 2003

9–10   **Calibration and Measurement in Underwater Acoustics**, Teddington, Middlesex, UK. (Fax: +44 208 943 6217; Web: www.ioa.org.uk/meetings/calibration_2002.html)

March 2003

17–20   **German Acoustical Society Meeting (DAGA2003)**, Aachen, Germany. (Fax: +49 441 798 3698; e-mail: dega@aku-physik.uni-oldenburg.de)

18–20   **Spring Meeting of the Acoustical Society of Japan**, Tokyo, Japan. (Fax: +81 3 5256 1022; Web: wwwsoc.nii.ac.jp/asj/index-e.html)

24–26   **27th International Acoustical Imaging Symposium**, Saarbrücken, Germany. (Fax: +49 6819302 5903; Web: www.izfp.fhg.de)

April 2003
6–10   **IEEE International Conference on Acoustics, Speech, and Signal Processing**, Hong Kong, Hong Kong. (Web: www.en.polyu.edu.hk/%7Ecassp03)

7–9   **WESPAC8**, Melbourne, Australia. (Web: www.wespac8.com)

May 2003
19–21   **5th European Conference on Noise Control (Euronoise 2003)**, Naples, Italy. (Fax: +39 81 239 0364; Web: www.euronoise2003.it)

June 2003
8–13   **XVIII International Evoked Response Audiometry Study Group Symposium**, Puerto de la Cruz, Tenerife, Spain. (Web: www.ierasg-2003.org)

16–18   **Acoustics 2003—Modeling & Experimental Measurements**, Cadiz, Spain. (Fax: +44 238 029 2853; Web: www.wessex.ac.uk/conference/2003/acoustics/index.html)

29–3   **8th Conference on Noise as a Public Health Problem**, Amsterdam-Rotterdam, The Netherlands. (Fax: +31 24 360 1159; e-mail: office.nw@prompt.nl)

July 2003
7–11   **10th International Congress on Sound and Vibration**, Stockholm, Sweden. (Fax: +46 88 661 9125; Web: www.congex.com/icsv10)

14–16   **8th International Conference on Recent Advances in Structural Dynamics**, Southampton, UK. (Web: www.isvr.soton.ac.uk/sd2003)

August 2003
6–9   **Stockholm Music Acoustics Conference 2003 (SMAC03)**, Stockholm, Sweden. (Web: www.speech.kth.se/music/smac03)

25–27   **Inter-Noise 2003**, Jeju Island, Korea. (Fax: +82 42 869 8220; Web: www.icjeju.co.kr)

September 2003
1–4   **Eurospeech 2003**, Geneva, Switzerland. (Web: www.symporg.ch/eurospeech2003)

7–10   **World Congress on Ultrasonics**, Paris, France. (Fax: +33 1 46 33 56 73; Web: www.sfa.asso.fr/wcu2003)

16–19   ***Autumn Meeting of the Acoustical Society of Japan**, Nagoya, Japan. (Fax: +81 3 5256 1022; Web: wwwsoc.nii.ac.jp/asj/index-e.html)

23–25   ***2nd International Symposium on Fan Noise**, Senlis, France. (CETIAT, B.P.2042, 69603 Villeurbanne, France; Fax: +33 4 72 44 49 99; Web: www.fannoise2003.org)

October 2003
15–17   **34th Spanish Congress on Acoustics**, Bilbao, Spain. (Fax: +34 91 411 7651; Web: www.ia.csic.es/sea/index.html)

December 2003
10–12   **(New Dates)*3rd International Workshop on Models and Analysis of Vocal Emissions for Biomedical Applications**, Firenze, Italy. (Fax: +39 55 479 6767; Web: www.maveba.org)

March 2004
17–19   ***Spring Meeting of the Acoustical Society of Japan**, Atsugi, Japan. (Fax: +81 3 5256 1022; Web: wwwsoc.nii.ac.jp/asj/index-e.html)

22–26   **Joint Congress of the French and German Acoustical Societies (SFA-DEGA)**, Strasbourg, France. (Fax: +49 441 798 3698; e-mail: sfa4@wanadoo.fr)

April 2004
5–9   **18th International Congress on Acoustics (ICA2004)**, Kyoto, Japan. (Web: www.ica2004.or.jp)

August 2004
23–27   **2004 IEEE International Ultrasonics, Ferroelectrics, and Frequency Control 50th Anniversary Conference**, Montreal, Canada. (Fax: +1 978 927 4099; Web: http://www.ieee-uffc.org/index2-asp)

24–27   ***Inter-noise 2004**, Prague, Czech Republic. (I-INCE, Herrick Laboratories, Purdue University, West Lafayette, Indiana, USA; Fax: +1 765 494 0787; Web: www.i-ince.org)

September 2004
13–17   **4th Iberoamerican Congress on Acoustics, 4th Iberian Congress on Acoustics, 35th Spanish Congress on Acoustics**, Guimarães, Portugal. (Fax: +351 21 844 3028; e-mail: dsilva@lnec.pt)

BOOK REVIEWS

P. L. Marston

Physics Department, Washington State University, Pullman, Washington 99164

These reviews of books and other forms of information express the opinions of the individual reviewers and are not necessarily endorsed by the Editorial Board of this Journal.

Editorial Policy: *If there is a negative review, the author of the book will be given a chance to respond to the review in this section of the Journal and the reviewer will be allowed to respond to the author's comments. [See "Book Reviews Editor's Note," J. Acoust. Soc. Am.* **81***, 1651 (May 1987).]*

Acoustics for Audiologists

Peter Haughton

Academic Press, New York, 2002.
456 pp. Price: $79.95 (hardcover) ISBN: 0123329221.

It is essential for an audiologist to have a working knowledge of acoustics, but many beginning students struggle to understand the fundamental physical concepts that form the basis for their work. Peter Haughton's text succeeds in covering almost all of the underlying principles of acoustics necessary to understand the scientific bases of audiometric calibration, sound measurement, middle ear impedance measures, and room acoustics. The book is thorough without being intimidating. Math skills in algebra and trigonometry are necessary, but calculus is not used in the explanations. Haughton goes well beyond the level of the introductory text by Speaks (1999), and is much better suited for use in the classroom than the recent book by Vilchur (2000), which bears the same title.

This book consists of ten chapters and two appendices. There are questions and exercises at the end of Chaps. 2–9 that could be used as homework assignments. Some exercises marked as "practical" often require a hands-on activity such as building a pendulum or performing calculations based on spreadsheet examples. Chapter 1, entitled "The Basics," introduces concepts from classical mechanics that are essential to the understanding of acoustics: moving bodies, mass, momentum, force, work, energy, and power. Electrical quantities such as current, voltage, resistance, inductance, and capacitance are introduced since they will be useful in dealing with transducers in Chap. 8. Properties of materials such as density and specific gravity, elasticity, and viscosity are also presented. The final section deals with properties of gases. Amazingly, this presentation occupies only 26 pages in the book.

Chapter 2 introduces "Vibrations." Terms such as frequency, period, cycle, and amplitude are defined. Forced and free vibration are described. The description of simple harmonic motion and sinusoidal waveforms features several differential equations, but they are never identified as such! Instead, $\ddot{y}$ and $\dot{y}$ are identified simply as the particle acceleration and velocity, respectively. Energy relationships in free and forced vibration are discussed, leading to a presentation of resonance. The chapter ends with a presentation of root-mean-square values.

Chapter 3 is titled "Sound Waves." A unique "twist" of terminology leads the author to describe the displacement, velocity, and acceleration of "sound particles" instead of the more commonly used "air molecules." Wave motion due to sound is described and concepts such as plane progressive waves are introduced. The relations among frequency, velocity, and wavelength are presented. The often-confusing concepts of "group velocity" and "phase velocity" are introduced and explained. Particle displacement and velocity, sound pressure, and energy for sinusoidal sound waves are then discussed and illustrated with numerical examples. Sound intensity and energy density are covered next. The final part of the chapter presents the effects produced by combining sound waves: interference, standing waves, beats, diffraction, refraction, and reflection.

Chapter 4, "Sources of Sound," begins with a presentation of the concept of the point source and the resulting spherical wavefront, which leads naturally to the inverse-square law. Double sources, infinite baffles, and circular pistons are described before the section headed "Practical Sources." The practical sources described are tuning forks, loudspeakers, and audiometric and hearing aid headphones. The final device discussed is the audiometric bone vibrator.

Chapter 5 introduces "Nonsinusoidal Waveforms." The concept of the Fourier transform is introduced and the relationship between waveform properties and spectral properties is described. Initially, the waveforms are assumed to be continuous for discussions of signals and noise, filters, the speech spectrum, and periodic signals. Then the concept of sampling is introduced with the appropriate discussion of aliasing. This leads to a presentation of the discrete Fourier transform and its relationship to the Fourier series and the fast Fourier transform (FFT). The omission of a discussion of the Nyquist rate, and its importance in aliasing, flaws an otherwise excellent presentation of this often-difficult material. The remainder of Chap. 5 presents signal averaging, system linearity and distortion, and modulation. The importance of these signal-processing techniques is related to audiology in almost every discussion.

Chapter 6 is titled "Measuring Sound." The mathematical bases for the decibel calculations are given in Appendix A. After an introduction to the calculation of the dB, the chapter presents "other decibel scales" such as *Hearing Level, Sensation Level, Masking Level, Hearing Threshold Level,* and *Uncomfortable Loudness Level*. Then a thorough discussion of microphones and their calibration is presented. Next, sound level meters are described in some detail. The A, B, and C weighting scales are discussed, followed by a presentation of the temporal characteristics of sound level meters. Applications such as combined sound levels and measuring noise exposure are described at the end of the chapter, as are the measurement of subjective qualities of loudness and pitch.

The seventh chapter covers impedance. The initial presentation is of the general concept of impedance and the representation of impedance in vector and complex number forms. Very thorough presentations of mechanical and acoustical impedance concepts are followed by a discussion of the clinical measurement of tympanometry and the acoustic impedance of the human ear. The relationship between impedance and admittance is presented in enough detail to help the novice understand this important relationship.

Chapter 8 brings us calibration and testing of audiometric equipment. It begins with a discussion of "Standards." Calibration of circumaural and insert earphones is presented with enough detail that the attentive student should be able to carry out these calibrations after mastering this section. Sound-field calibration and calibration for speech audiometry are presented next. Discussions of calibrating the calibrators and problems in standardizing audiometric zero round out this thorough, but very practical, chapter.

The brief ninth chapter covers audiometric test rooms and, in the process, presents concepts essential to understanding room acoustics: reverberation and background noise. Given the recent interest in classroom acoustics, this chapter is very applicable to audiological practice.

The tenth chapter provides a very brief overview of the electroacoustic characteristics of hearing aids. This is intentional on the part of the author. He notes that this topic is covered in a number of recent works, which he presents in a suggested reading list at the end of the chapter. However, essential concepts such as gain, frequency response, and nonlinear input–output characteristics are presented. Harmonic and intermodulation distortion products and their role in hearing aid testing are also introduced.

The two appendices are titled "Supplementary Mathematics" and "Working with Decibels." They present a thorough review of the algebra and trigonometry essential to understanding the concepts presented in the

text. The decibel appendix has four sets of exercises to illustrate each topic (with answers given at the end of the appendix).

Throughout the text, the writing style is clear and nonthreatening. It does not read like a traditional calculus or physics text; however, it is not written in the "Isn't science wonderful!" vein. The serious graduate student in an audiology program should be able to master most of the concepts presented here. Given the exercises included with eight of the ten chapters, a creative instructor should be able to devise appropriate laboratory experiences to supplement the text material. For audiologists already in professional practice, this text offers the chance to reinforce their knowledge of this important area. Despite the implied narrow focus of the title, anyone engaged in hearing research may find this book of use in understanding basic issues of calibration and sound measurement.

LAWRENCE L. FETH
Ohio State University
Speech & Hearing Science
Columbus, Ohio 43210-1372

Shallow Water Acoustics

Boris G. Katsnelson and Valery G. Petnikov

Springer-Praxis Publishing, Chichester, UK, 2001.
267 pp. Price: $129.00 (hardcover) ISBN: 1-85233-184.4.

Due to both civilian and military applications and concerns, the emphasis in ocean acoustics research has shifted markedly in the past decade towards shallow water (the coastal region from the continental shelf break shoreward). Anti-submarine warfare in the "littoral" (a currently popular U.S. Navy misnomer for shallow water), anthropogenic noise pollution, marine mammal studies, and underwater communications are just a few of the many reasons that people are interested in the acoustic properties of shallow water. Moreover, this interest seems to be intensifying, and so the time has become ripe for textbooks and monographs which can provide shallow water practitioners with an overview of this unique area of interest. Until rather recently, shallow water acoustics was merely treated as a chapter or two in textbooks that treated all of ocean acoustics as a whole. This was unfortunate, in that the shallow water environment has unique oceanographic, geologic, biologic, and even chemical properties, which merit a fuller, dedicated description. In 1997, this situation began to change. The Beijing International Conference Proceedings Monograph *Shallow Water Acoustics* by Zhang and Zhou[1] provided a rather comprehensive collection of modern research articles in the area. More germane to this review, Katsnelson and Petnikov also published the initial Russian language version of *Shallow Water Acoustics*, Akustika Melkogo Morya[2] in that year. The English language monograph that we are reviewing here is in fact an extension of that 1977 Russian book. Before turning to that monograph, it would be worth noting that recently, three more books have been either published or are in advanced development, which have strong components of shallow water acoustics. The first is *Ocean Acoustic Interference Phenomena and Signal Processing*, a topical collection of articles edited by William Kuperman and Gerald D'Spain.[3] The second is the upcoming proceedings of the NATO SACLANT Centre Conference on Ocean Acoustic Variability, which will be published by Kluwer soon after the October 2002 conference.[4] The third is a volume on "Scattering of Sound by Ocean Internal Waves," being produced by the U.S. Office of Naval Research, which should be completed in the 2003 timeframe.[5] These collections should add greatly to the current library of shallow water acoustics works—however, it should be noted that the book under review is the only real *textbook* devoted solely to the topic, and so holds a unique place both in the current and near-future literature.

Turning to Katsnelson's and Petnikov's *Shallow Water Acoustics*, I will begin with a few general observations, before turning to a detailed look at the text. To begin with, the title of this book really should be "Low-frequency shallow water acoustics," as it deals almost exclusively with the 25–1000-Hz frequency band, above the seismic regime and below the ray theory regime, in which the shallow seas act as an acoustic modal wave-

guide. This is explained immediately in the book, but is not apparent in the title. Second, this book is an improved version of the earlier Russian work, adding chapters on the ambient noise field in shallow water and diffraction of acoustic waves by localized inhomogeneities in shallow water. Both these topics are timely and interesting. A small disappointment, noted by the authors, is that the book only describes work published up to about 2000, and so omits some of the newer developments in shallow water acoustics. A third observation concerns that this book is, and what it is not. This book is a survey text intended for underwater acousticians who have a general background in ocean acoustics and want to learn more about shallow water acoustics. It treats both theory and experiment on an even footing, keeping a nice overall balance. Also, this book is an excellent introduction to the extensive Russian literature on shallow water acoustics, and the Russian approach to the problems of shallow water acoustics, which has some interesting differences with the American and European approaches. In treating what the book is not, it is not a textbook for beginners, despite the fact that it derives most of its theoretical results from first principles. The many approximations discussed in the book demand a degree of physical insight from the reader that is not to be expected from those who are entirely new to ocean acoustics. Nor is this book a comprehensive review of all the research that has been done in shallow water acoustics. The authors stuck with the theme of a survey volume which will give the reader quantitatively based overview, even though they certainly had the credentials to pursue a thorough review. But this is again a matter of style and choice. One should take this book on the terms it is offered, or disappointment will ensue.

Let us now examine the text itself, on a chapter-by-chapter basis. In Chap. 1, the book begins by defining shallow water acoustics as the variant of the "waveguide problem" in which the normal mode representation of the acoustic field most naturally provides the theoretical backbone. Though ray theory, parabolic equation, and other propagation models are used in the text, the mode picture always stands in the forefront. Immediately after that definition, the chapter describes the acoustic properties of coastal sediments (the bottom boundary) and the water column (the waveguide volume and surface boundary). Though quite brief, and concentrated mostly on the acoustic properties of the medium, this section gives adequate environmental background about the physical waveguide to enable a reader to perform useful calculations in a wide variety of coastal environments. Chapter 1 ends with a brief theoretical description of the sound field due to point sources, which organizationally should be the beginning section of Chap. 2.

In Chap. 2, the authors provide the basic theory needed to describe the shallow water acoustic waveguide. The standard treatment of a point acoustic source in a layered waveguide, including attenuation, is presented in Sec. 2.1, showing the mode poles and the branch line integral one needs to evaluate in general. In Sec. 2.2, this theory is then focused on the specific case of the "Pekeris waveguide," i.e., an isovelocity water column overlying an isovelocity half-space bottom.[6] This canonical case provides indispensable insights for understanding shallow water acoustics, and indeed one would be hard pressed to write a book on shallow water acoustics without including this classic case study. Section 2.3 presents somewhat more novel material, discussing the theory and properties of the modal attenuation coefficients using a simple physical picture that combines rays, modes, and reflection coefficients with beam displacement. This picture quickly provides useful analytic forms of the attenuation as a function of the waveguide properties, acoustic frequency, and modal index. These, in turn, are used to infer the long-range modal composition and average intensity of the acoustic field, among other things. This section is a good example of the "useful physical approximations" approach that the authors repeatedly turn to in the book, which is one of the books' main attractions. Section 2.4 completes the discussion of the basics of range-independent waveguides by including the effects of bottom layering.

Chapter 3, entitled "Approximate methods in shallow water acoustics," covers a range of diverse methods, very loosely organized by having some degree of approximation inherent in them. Section 3.1 briefly examines first-order perturbation theory methods in the modal context, with applications to calculating the modal attenuation coefficient and finding perturbations to the soundspeed profile. The next section of Chap. 3 covers coupled and adiabatic mode theory, using a simple first-order form of the coupled equations that makes the physical interpretation of the solutions rather transparent. The criterion for adiabacity is also discussed in a physically insightful form. Section 3.3 delves into the "horizontal rays and ver-

tical modes'' three-dimensional field theory popularized in the USA by Weinberg and Burridge,[7] but with the added sophistication of the trajectory perturbation forms developed by Kravtsov.[8] This latter material is quite useful and elegant, and perhaps not so well known to US and European investigators. Section 3.4 describes an approximate solution to the coupled mode equations in an expansion called ''generalized modes.'' Again, this particular topic might be new to some readers. Section 3.4 treats the average and fluctuating components of the range-dependent acoustic field, noting as justification that ''as one moves away from the source, the sound field pattern becomes less regular, taking on a rather blurred structure, which may appear random, despite the fact that this pattern is completely deterministic.'' Two simple examples of waveguides with variable bathymetry are used to illustrate the results of this section.

Chapter 4 treats a subject of great current interest, the nature of the acoustic field in a shallow water waveguide containing random inhomogeneities. As expected, the initial discussion in the chapter centers around the types of random inhomogeneities one sees in shallow water, including internal waves, ocean thermohaline microstructure, bottom roughness, and surface roughness. One notable omission to this list is subbottom random structure, which is also of interest and importance to modern shallow water studies. Since waveguide range dependence couples modes, the coupled normal mode picture is revisited in Sec. 4.2, only this time with the random medium properties built in. The stochastic coupled mode equations are derived which give the mean (coherent) component of the acoustic field and its attenuation due to scattering. In the next section, the coupled intensity equations are derived which give the fluctuating (incoherent) component of the acoustic field, completing the theoretical picture. In the case of close coupling (or equivalently, small angle scattering), the coupled mode picture can be simplified into a diffusion equation, which provides analytical and semi-analytical solutions and average decay laws. This theory is shown in Sec. 4.4. In Sec. 4.5, two examples are constructed to illustrate the theory of the preceding sections. These are the Pekeris waveguide, but with random inhomogeneities included, and the irregular bottom waveguide. Finally, the depth dependence of the intensity is examined for the case of a point source in shallow water with random inhomogeneities. A useful, albeit too brief, discussion of the transition of the waveguide behavior from deterministic to random is included in this last section.

In Chap. 5, the emphasis turns to experimental techniques in shallow water. Following a simple introduction to the spreading and attenuation losses that largely determine the ranges one is constrained to in measuring the acoustic field in shallow water, the book proceeds to a discussion of various methods of filtering normal modes experimentally. After quickly reviewing the standard broadband mode filtration techniques of travel time dispersion and matched array processing, the book looks in Sec. 5.3 at a somewhat less usual way of separating the modes—with a moving CW source, using the fact that different modes have different wavenumber perturbations due to motional effects. The characteristics of explosive charges are treated next, giving some nice practical insights into their range of usefulness. The chapter then turns to shallow water experiments along stationary acoustic tracks, a subject of great personal interest to this reviewer. Both the Russian ''source ship-to-receiver ship'' style experiments (which in recent years used two modern quieted research ships, the R/V *Akademic Iofee* and R/V *Akademic Sergei Vavilov*, upon which I first met the authors) and autonomous and telemetered moored experiments are discussed in some detail. Details of array element localization are also discussed.

The stage having been set by Chap. 5, the authors then embark on one of the meatiest chapters of the book, devoted to ''acoustic monitoring,'' which is the Russian phrase for determining the properties of the ocean and seabed acoustically. Starting from an example of predicted and measured transmission loss along a 300-km track in the Barents Sea, the authors show how well (or poorly) one can fit the average and fluctuating components of the acoustic field versus range, even with a very basic fluid bottom model. After a brief digression into numerical modeling issues, the authors then hone in on which physical parameters most affect acoustic transmissions and our estimates of them. Unsurprisingly, medium attenuation in the bottom (which can be due to inelastic, viscous, or scattering effects) is immediately singled out as the least well known quantity, and so a sizeable section of the chapter (Sec. 6.1) is devoted to its practical measurement. The next section, 6.2, concentrates on water column volume scattering effects. Two tidal effects are singled out for examination here—the barotropic tidal effect of the water depth variation and the baroclinic tidal effect of the internal tides,

particularly the nonlinear internal tides, which have been a topic of great research interest lately. The next sections of the chapter discuss experimental measurements and simple analyses of the amplitude and phase fluctuations of CW acoustic signals, the ''beam wander'' of a phased array, and a waveguide dispersion effects in shallow water. The reader may initially wonder what the connection is between these physical effects and waveguide monitoring. About midway through Sec. 6.3 this connection is made via the ''classical tomography'' problem,[9] showing that due to waveguide dispersion and scattering, deep water and shallow water measurement techniques are not always simply transportable. This sets up the next section, 6.4, on the uses of matched field processing and other inversion techniques in shallow water, including variants of classical tomography. In this section, a rather general recipe is given for performing acoustic monitoring/inversion (labeled ''matched field tomography''), along with various examples. The last section of this chapter deals with using the frequency dependence of the sound interference pattern to monitor the ocean medium. In this section, the device of ''phase dislocations'' (points where, due to the interference of the normal modes, the amplitude is zero and the phase indeterminate) is used to extract medium properties, specifically by using a broadband stationary experiment. This is another example of a technique that is not so well known to Western scientists, but commonly used by Russian researchers.

In Chap. 7, the noise field in shallow water is treated. Though many noise source mechanisms are available to consider, the authors choose to concentrate on near-surface sources (physically surface waves) modeled as a distribution of dipoles. As this example shows many of the salient characteristics of shallow water noise, no matter what the source, it is a reasonable one to consider. In Secs. 7.1 and 7.2, the general properties of the noise intensity distribution are derived, as well as the correlation properties of the field. The well-known Kuperman–Ingenito results[10] are displayed as a centerpiece of this analysis. In Sec. 7.3, the authors consider the competition between the discrete and continuous modal spectrum contributions to the noise field, as a function of frequency and waveguide parameters. In Sec. 7.4, the comparison between the deep and shallow water noise fields is discussed, displaying how the shallow bottom is the arbiter of this difference. In Sec. 7.5, the directionality of the noise field is considered. The authors nicely show the transition from the simplest physical view, where the noise directionality is the directionality of the source distribution, modulo the cosine of the vertical angle, to a more sophisticated model, where the sound is also redistributed by angle-dependent absorption in the bottom and scattering by random inhomogeneities. In the final section of Chap. 7, the authors treat the depth dependence of the noise field intensity due to the vertical sound speed profile.

Chapter 8 is the final technical chapter of the book, entitled ''Diffraction of acoustic waves on localized inhomogeneities in shallow water sound channels.'' In this chapter, the scattering by an ''extended discrete object'' (e.g., a submarine) in a waveguide is addressed, using the free space scattering properties of the object and the acoustic modal characteristics of the waveguide. The output of a fixed source-receiver ''tripwire'' range to such a disturbance is then calculated, showing a concrete usage of this formalism. This formalism is then extended to soft spheroids in a waveguide, an approximation apropos to marine mammal monitoring.

Chapter 9, the Conclusions, presents a brief summary of the results of the previous chapters, only from a more philosophical viewpoint than a technical one.

At this point, let me return to the overview of the book. Having finished the book, I found that I was very gratified by what I had read, but was also left wishing that the authors would have included more topics and examples. Numerical modeling, the combination of various measurement techniques to constrain the ocean description, time-reversed techniques, waveguide invariants, array coherence measurements, and many other topics that are part of shallow water acoustics should eventually be treated in such a text. As a complement to the authors, I would hope that they consider this as an impetus to start a ''Volume II—Continuing Topics in Shallow Water Acoustics'' text, as their physical insight and presentation in this volume made it a pleasure to read. But, this minor drawback aside, I would heartily recommend this book to any researcher or graduate student working in shallow water acoustics. It presents an overview of a very active field from a fresh viewpoint, and with a fine feel for the basic physics of the medium. It is a book that is well worth the rather high price that Springer-Praxis charges, and I would encourage you to add it to your bookshelf.

[1] R. Zhang and J. X. Zhou (eds.), *Shallow Water Acoustics* (China Ocean, Beijing, 1997).

[2] B. G. Katsnelson and V. G. Petnikov, *Akoustika Melkogo Morya* (Nauka, Moscow, 1997).

[3] W. A. Kuperman and G. L. D'Spain (eds.), ''Ocean Acoustic Interference Phenomena and Signal Processing,'' AIP Conference Proceedings 621, San Francisco, CA (AIP, Melville, NY, 2001).

[4] SACLANT conference, ''Impact of environmental variability on acoustic predictions and sonar performance,'' La Spezia, Italy, September 2002.

[5] *Sound Propagation Through Ocean Internal Waves*, a book currently being produced under ONR auspices.

[6] C. L. Pekeris, ''Theory of propagation of explosive sound in shallow water,'' Geol. Soc. Am. Mem. **27**, 1–117 (1948).

[7] R. Burridge and G. Weinberg, ''Horizontal rays and vertical modes,'' in *Wave Propagation and Underwater Acoustics*, edited by J. B. Keller and J. S. Papadakis (Springer-Verlag, New York, 1977), pp. 86–150.

[8] Yu. A. Kravtsov and Yu. I. Orlov, *Geometrical Optics of Inhomogeneous Media* (Springer-Verlag, New York, 1990).

[9] W. H. Munk and C. Wunsch, ''Ocean acoustic tomography: a scheme for large scale monitoring,'' Deep-Sea Res., Part A **26**, 123–161 (1979).

[10] W. A. Kuperman and F. Ingenito, ''Spatial correlation of surface generated noise in a stratified ocean,'' J. Acoust. Soc. Am. **67**, 1988–1996 (1980).

JAMES F. LYNCH
Woods Hole Oceanographic Institution
Woods Hole, Massachusetts 02543

OBITUARIES

Daniel L. Johnson • 1936–2002
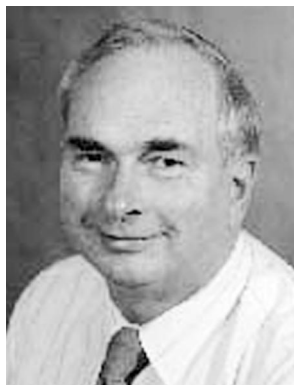
Daniel L. Johnson, a Fellow of the Acoustical Society of America and the Society's Standards Director, died suddenly and unexpectedly at his home in Provo, Utah, on 2 May 2002.

Daniel Johnson was born on 24 January 1936 in Manistee, Michigan. His father was in the military and throughout Dan's childhood the family moved as often as two or three times a year. His longest stay in any one town was a three-year period spent in Anchorage, Alaska. After earning the B.S. degree in Engineering at the United States Military Academy at West Point (1958), he was commissioned a 2nd Lieutenant in the US Air Force. During a distinguished Air Force career which lasted 26 years, Johnson received many medals and awards, including the Air Force Commendation Medal in both 1962 and 1966, and the Bronze Star in 1968 (while serving in Vietnam).

Johnson continued his higher education while serving with the Air Force. In 1960, he received a Master of Science degree from the University of Michigan in Aeronautical Engineering and Instrumentation Engineering. In 1971, he received a Ph.D. in Aerospace Engineering from the University of Colorado. Shortly thereafter, he was assigned to the Aerospace Medical Research Laboratory at Wright–Patterson, and became associated with Henning von Gierke, Director of the Biodynamics and Bionics Division, and Charles Nixon, Chief of the Biological Acoustics Branch. This was the beginning of a distinguished career in acoustics, marked by a lifelong dedication to studying the effects of noise on hearing.

During his long tenure at Wright–Patterson, Dr. Johnson carried out studies with the Fels Research Institute to understand the effects of recreational, environmental, and occupational noise on human auditory development. He did important pioneering research on the auditory and physiological effects of infrasound. He worked with the National Institute for Occupational Safety and Health to develop methods for calculating the effectiveness of hearing protectors, leading to the proof of the efficacy of muff-type hearing protection for very high-level impulse noise. Other research defined the effects of long-duration (greater than 24 hours) noise on temporary threshold shift growth and recovery and developed mathematical models for predicting permanent threshold shifts due to continuous noise exposure and for calculating corrections to account for the influences of intermittency and impulsive sounds. This work, which explained the cause and effect relationships for noise-induced hearing loss, was recognized with his being the first recipient of the Air Force's Harry G. Armstrong Award for Scientific Excellence. He also received the Force Systems Command Award for Scientific Achievement (1974), the Air Force Meritorious Service Medal (1974), and the Air Force Systems Command Award for Scientific Achievement (1977).

While at Wright–Patterson Air Force Base, he was assigned to work with the Environmental Protection Agency's (EPA) Office of Noise Abatement and Control to develop recommendations for national guidelines on noise levels and criteria for protecting people from noise-induced hearing loss. This work led to development of national and international standards on the measurement and assessment of noise exposure in industry and the military. This was a particularly thorny issue and the entire process spanned 18 years to achieve consensus among all the International Standards Organization (ISO) member countries and numerous experts involved. This achievement was possible in part because of Johnson's unique ability to conciliate differences while staying true to his goal. One of his most noteworthy characteristics—and one that helped him throughout his involvement in standards activities—was his happy and optimistic outlook. Johnson never ceased to believe that reasonable people could work together and reach a consensus.

In 1984, when he retired from the Air Force, Colonel Johnson was awarded the Legion of Merit, the second-highest noncombat award given by the Air Force. Dr. Johnson then became Chief Scientist at Larson Davis, where he provided technical oversight for the development of a large variety of acoustic and laboratory instruments. He continued and expanded his role with scientific and professional organizations. Because of his unbiased insight and scientific acumen, Johnson was asked to serve first as an advisor and then as a member on the National Academy of Science/National Research Council Committee on Hearing, Bioacoustics and Biomechanics (CHABA). He served on CHABA Working Groups that studied hazardous exposure limits to both intermittent as well as steady state noise, that evaluated human responses to impulsive noise (especially sonic booms), and that developed guidelines for evaluating the environmental impact of noise.

In 1989, Johnson became Director of EG&G's Biophysics Operations at Kirkland Air Force Base in Albuquerque. There, he led the largest ever U.S. government funded research project on the effects of blast noise on hearing. Working with Dr. Jim Patterson and the U.S. Army Aeromedical Research Laboratory, Johnson and his colleagues studied the human auditory effects of exposure to free field blast over-pressures. He was instrumental in developing a unique facility for producing high level blast over-pressures and for designing a research protocol to enable his team to safely study the effects of impulsive sounds on humans. This research documented previously unknown interactions between blast over-pressures and hearing protector performance. Utilizing these results, Johnson and Patterson proposed new criteria for protecting humans from high-level impulse noises.

In 1998 Dr. Johnson became President of Interactive Acoustics, Inc., in Provo, Utah, where he continued to work on hearing protection issues.

Dr. Johnson often expressed the belief that scientific knowledge could be implemented for public health and safety through standards, and this motivated extensive participation in activities related to standards. From 1997 until the time of his death, he was ASA Standards Director and Chair of the Acoustical Society of America Committee on Standards (ASACOS), which oversees the entire ASA Standards program. He served as Vice Chair of ASACOS from 1993 to 1997 and filled other ASACOS roles for a decade before that. Other contributions to ASA Standards included service as: Vice Chair (1984–1986) and Chair (1986–1990) of Standards Committee S1 Acoustics; Chair (1990–1995) of Standards Committee S12 Noise; Chair of Working Group, S3/WG62, Effects of Impulse Noise on Hearing; and Chair of Working Group, S3/WG58, Hearing Conservation Criteria. He was also a member of many other standards working groups of the Acoustical Society, the Committee on Hearing and Bioacoustics (CHABA), the American Society for Testing of Materials (ASTM), and the Society of Automotive Engineers (SAE).

Dr. Johnson became a member of the Acoustical Society in 1973 and was elected a Fellow in 1978. He was a long-time member of the Technical Committee on Noise (1979–2002) and served as its Chair from 1991 to 1994. He also served on the Membership Committee from 1996 to 2002. Johnson served on the editorial boards of *Noise Control Engineering* (1980–1983), *Journal of Low Frequency Noise and Vibration* (1982–1989) and *Journal of Occupational Hearing Loss* (1998–2002). At the time of his death he was serving on the Board of Directors of the National Hearing Conservation Association (NHCA), which in 1999 presented him with its highest honor, the ''Outstanding Hearing Conservationist'' award.

Johnson married Dorothy Chandler in 1963 and they had six children: Romer D. Johnson, Olin M. Johnson, Daniela D. Johnson Bennion, Wenona J. Johnson Lenberg, Conrad C. Johnson, and Garrett H. Johnson. At the time of his death, he had eleven grandchildren.

Dan enjoyed life fully and he was curious about everything. He looked forward to his regular basketball games and enjoyed many outdoor activities including hunting and skiing, especially when he shared these outings with his children. He was always ready for a game of bridge. His colleagues in ASA will remember his cheerful demeanor, his outlandish ties, and, most importantly, his many scientific contributions to the Acoustical Society and to society at large.

MARK R. STEPHENSON
SUSAN BLAESER

REVIEWS OF ACOUSTICAL PATENTS

Lloyd Rice
11222 Flatiron Drive, Lafayette, Colorado 80026

The purpose of these acoustical patent reviews is to provide enough information for a Journal reader to decide whether to seek more information from the patent itself. Any opinions expressed here are those of reviewers as individuals and are not legal opinions. Printed copies of United States Patents may be ordered at $3.00 each from the Commissioner of Patents and Trademarks, Washington, DC 20231. Patents are available via the Internet at http://www.uspto.gov.

Reviewers for this issue:

GEORGE L. AUGSPURGER, *Perception, Incorporated, Box 39536, Los Angeles, California 90039*
MARK KAHRS, *Department of Electrical Engineering, University of Pittsburgh, Pittsburgh, Pennsylvania 15261*
DAVID PREVES, *Micro-Tech Hearing Instruments, 3500 Holly Lane No., Suite 10, Plymouth, Minnesota 55447*
DANIEL R. RAICHEL, *2727 Moore Lane, Fort Collins, Colorado 80526*
KEVIN P. SHEPHERD, *Mail Stop 463, NASA Langley Research Center, Hampton, Virginia 23681*
WILLIAM THOMPSON, JR., *Pennsylvania State University, University Park, Pennsylvania 16802*
ROBERT C. WAAG, *Department of Electrical and Computer Engineering, Univ. of Rochester, Rochester, New York 14627*

6,386,755

43.28.Vd ACOUSTIC PYROMETER

Dean E. Draxton *et al.*, assignors to Combustion Specialists, Incorporated
14 May 2002 (Class 374/117); filed 5 January 2000

In a coal-fired boiler, pendant tubes **38** may occupy a space more than 50 ft across. Slag accumulates on the tubes and must be removed periodically using blasts of steam. However, the cleaning process introduces additional corrosion and should be performed no more often than necessary. For various technical reasons discussed in the patent, accurate measurements of
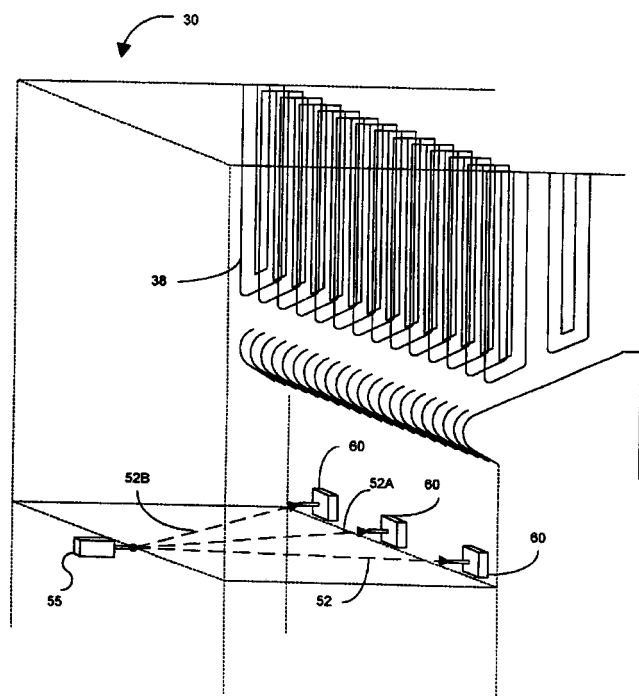
gas temperature can facilitate more efficient operation of the boiler and also determine when cleaning is required. The invention includes a generator of pulsed acoustic signals **55** and one or more receivers **60**. A signal processing system filters out background noise and then calculates temperature as a function of transit time.—GLA

5,822,272

43.30.Gv CONCENTRIC FLUID ACOUSTIC TRANSPONDER

Donald E. Ream, Jr., assignor to the United States of America as represented by the Secretary of the Navy
13 October 1998 (Class 367/2); filed 13 August 1997

A passive acoustic transponder consists of two concentric thin-walled spherical shells. The region interior to the inner sphere and the annular region between them are each filled with different refracting fluids. Through the choice of these fluids, the sphere sizes, the shell materials, and wall thicknesses, it is possible to realize transponders with a wide variety of frequency responses and target strengths.—WT

5,877,460

43.30.Jx DEVICE FOR TALKING UNDERWATER

Ritchie C. Stachowski, Moraga, California
2 March 1999 (Class 181/127); filed 16 September 1997

A more or less horn-shaped structure made of a rigid plastic has a smaller open end with an elastomeric mouth fitting for forming a water-tight seal around a user's mouth while the larger end is sealed with a thin diaphragm, which could be the same material as the rest of the horn. The sides of the horn's body contain one-way blow valves for releasing the user's exhausted air in the form of small bubbles. When one speaks, while underwater, the thin diaphragm is set into vibrations which reradiate the sounds into the water. The small released air bubbles allegedly do not radiate much interfering noise.—WT

6,366,534

43.30.Lz UNDERWATER HIGH ENERGY ACOUSTIC COMMUNICATIONS DEVICE

Robert Woodall and Felipe Garcia, assignors to the United States of America as represented by the Secretary of the Navy
2 April 2002 (Class 367/145); filed 2 April 2001

Two metal spherical shells are held in concentric spaced-apart positions by a large number of radially oriented springs. The space interior to both spheres may be filled with pressurized gas or liquid. The inner surface of the outer sphere supports many explosive devices consisting of a squib, a

radially oriented tube, and a projectile such as a small metal sphere. Firing signals from a micro-controller detonate selected sets of the squibs in pre-programmed sequences thereby launching the projectiles to strike the inner sphere. The resulting vibrations of this shell subsequently radiate high-level, broadband, acoustic signals into the surrounding acoustic medium. An aux-iliary hydrophone on the assembly allows a remote source to communicate with the micro-controller, thereby varying the firing signals to produce a coded acoustic signal.—WT

6,396,770

43.30.Nb STEERABLE THERMOACOUSTIC ARRAY

Charles A. Carey *et al.*, assignors to BAE Systems Information and Electronic Systems Integration Incorporated
28 May 2002 (Class 367/141); filed 28 June 1982

To provide communication between an airplane and a submerged sub-marine (or some other submerged hydrophone system), a modulated laser beam (or particle beam) is radiated from the airplane towards the surface of the ocean and moved across that surface at a speed equal to the speed of sound in water divided by the sine of the incident angle. The beam of energy incrementally heats the water causing thermal expansion or explosive va-porization, either of which effects create a sound wave in the water.—WT

6,377,514

43.30.Tg ACOUSTIC LENS-BASED SWIMMER'S SONAR

Thomas E. Linnenbrink *et al.*, assignors to Q-Dot, Incorporated
23 April 2002 (Class 367/11); filed 6 April 2000

A hand-held diver's ultrasonic imaging system consists of a two-dimensional grid array of identical acoustical video converter elements. Each of these elements consists of a set of polymethylpentene acoustic lenses, a multi-element focal plane transducer array fashioned from 1–3 composite piezoceramic, and associated electronics to drive a VGA display mounted in the diver's mask in C-scan format. The transducer array is used in both transmit and receive modes. The whole sonar unit, with the excep-tion of the battery pack strapped to the swimmer, is housed in a cylindrical can 6.7 in. in diameter by 15 in. long.—WT

6,377,515

43.30.Vh SYNCHRONIZED SONAR

Robert W. Healey, assignor to Brunswick Corporation
23 April 2002 (Class 367/88); filed 4 August 2000

An electronic control system is described which can interconnect a number of closely spaced identical sonars, such as fish-finders or depth-finders, and allow them to be energized simultaneously so that all of the units are listening for the echo at the same time. This will presumably reduce cross-unit interference. Alternatively, the many sonars are electroni-cally interconnected and energized in a predetermined temporal manner, designed so that again the sonars do not interfere with each other.—WT

6,349,791

43.30.Wi SUBMARINE BOW DOME ACOUSTIC SENSOR ASSEMBLY

Daniel M. Glenning and Bruce E. Sandman, assignors to the United States of America as represented by the Secretary of the Navy
26 February 2002 (Class 181/140); filed 3 April 2000

A submarine bow dome acoustic sensor comprises an acoustically transparent outer hull **10** and an inner pressure hull **12** that define a free-flooded compartment **14**. Within this compartment, an acoustic panel **16**, which may be planar (as shown) or hemispherical, with an optically reflect-ing surface **20**, is mounted on acoustically isolating supports **18**. The panel is fashioned of a relatively stiff plastic or aluminum. A laser scanner **22** (or possibly a number of such scanners), also mounted in the free-flooded com-partment **14**, casts a laser beam **24** onto the surface **20**. This beam (or
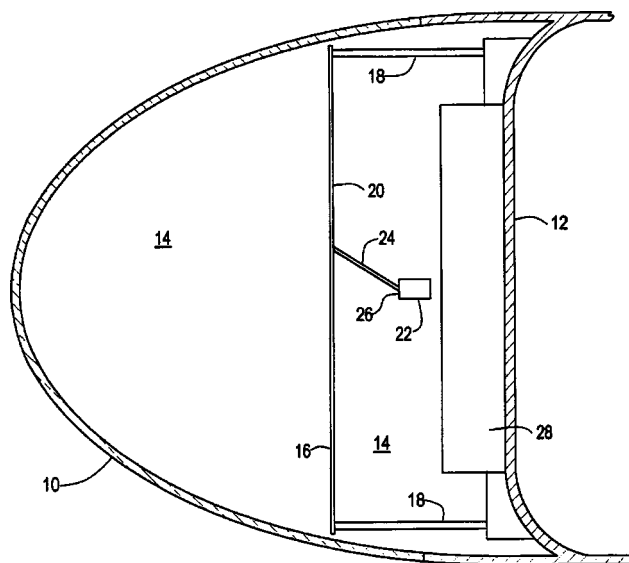
beams) can be moved rapidly over portions of surface **20**. Sensor **26**, which may be mounted on each scanner housing as indicated, receives the reflec-tions of the laser beam **24** from panel surface **20**. Doppler shifts of these reflected light waves, because of vibrations of panel **16** caused by a noise generating or reflecting object in the surrounding acoustic medium, provide information for the calculation of the location and speed of that object. An array of acoustic sources **28** permits an active mode of operation of this vibrometer-sensor system.—WT

6,370,084

43.30.Xm ACOUSTIC VECTOR SENSOR

Benjamin A. Cray, assignor to the United States of America as represented by the Secretary of the Navy
9 April 2002 (Class 367/141); filed 25 July 2001

An acoustic vector sensor is realized by encasing a commercially available tri-axial accelerometer within a sphere of syntactic foam of suffi-cient size to render the whole structure neutrally buoyant. This, in turn, is surrounded by a thin spherical shell of viscoelastic rubber which is acous-tically transparent yet isolates the accelerometer from structure-borne sound that may enter through any attachment points.—WT

5,822,271

43.30.Yj SUBMARINE PORTABLE VERY LOW FREQUENCY ACOUSTIC AUGMENTATION SYSTEM

Richard M. Ead and Robert L. Pendleton, assignors to the United States of America as represented by the Secretary of the Navy
13 October 1998 (Class 367/1); filed 1 April 1998

To augment the acoustic signature of a submarine or to duplicate the signatures of other submarines for training purposes, a mobile target very-low-frequency projector is suitably mounted within a dedicated torpedo shell which is then positioned within the flooded torpedo tube of any submarine. Control and power are provided from the submarine to the device. The device operates wholly within the torpedo tube and does not need to be launched.—WT

5,859,812

43.30.Yj SELF POWERED UNDERWATER ACOUSTIC ARRAY

Michael J. Sullivan *et al.*, assignors to the United States of America as represented by the Secretary of the Navy
12 January 1999 (Class 367/130); filed 14 October 1997

A housing, to which a line array of sensors is attached, contains a shrouded impeller and a shielded electric generator. As the assembly is towed through the water, enough electric power is generated locally to supply the needs of the sensor electronics without having to plumb electric power down from the tow ship. This significantly reduces the size of the towing cable and electromagnetic interference problems associated with high power levels on long cables. Data transmission from the sensors back to the tow ship is via a fiber optic cable in the tow cable.—WT

5,878,000

43.30.Yj ISOLATED SENSING DEVICE HAVING AN ISOLATION HOUSING

Neil J. Dubois, assignor to the United States of America as represented by the Secretary of the Navy
2 March 1999 (Class 367/188); filed 1 October 1997

A "windscreen" to isolate a hydrophone from flow noise consists of a more or less cylindrically shaped two-part housing made of an acoustically transparent material such as PVC. The base part of the housing is permanently attached to the host structure, e.g., a naval vessel. The cap portion of the housing features a number of holes to allow for free-flooding of the interior and for gas bubbles to escape, as well as containing a number of resilient elements, such as rubber bands, to suspend and vibration isolate the hydrophone within that free-flooded but sealed cavity.—WT

6,370,085

43.30.Yj EXTENDABLE HULL-MOUNTED SONAR SYSTEM

Jonathan Finkle *et al.*, assignors to the United States of America as represented by the Secretary of the Navy
9 April 2002 (Class 367/173); filed 3 August 2001

A system is described to deploy one or more arrays of sonar transducers (and other sensors) away from the hull of a submarine while it is in motion thereby increasing their effective aperture. This is accomplished via a set of support arms that extend radially outward from an attachment point

at the bow of the hull much like the ribs of an umbrella. These arms are positioned in an approximately equispaced circumferential arrangement around the hull. The transducers, either sources or receivers, can be mounted on these arms, or extend between the arms, or be located between the arms and the hull on auxiliary supports, or there could be towed line arrays attached to the ends of the arms. This system of arms and transducer arrays folds into longitudinal grooves on the hull during high-speed transit of the submarine to reduce self-noise.—WT

6,377,516

43.30.Yj ULTRASONIC TRANSDUCER WITH LOW CAVITATION

John Whiteside and Craig Mehan, assignors to Garmin Corporation
23 April 2002 (Class 367/173); filed 8 December 2000

An ultrasonic sonar transducer, such as used with a depth-finder or fish-finder system, is described. The sonar includes a conventional transducer element **12** in housing **14** designed for mounting on a ship's hull. The bottom face **34** of the housing is curved such that no major portion of it is
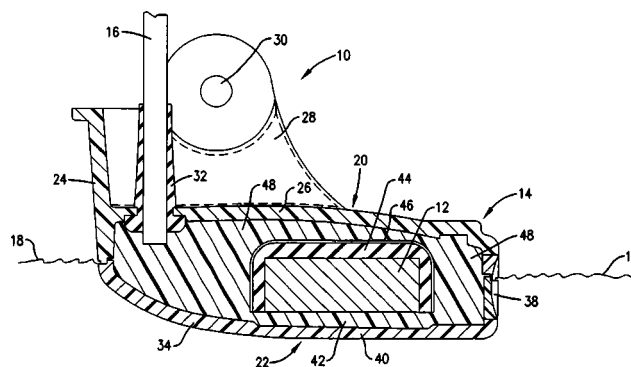
parallel to the active face of the transducer element **12**. The front end of the housing is raised relative to the rear, creating a positive angle of attack relative to the direction of water flow. This produces a pressure gradient over the bottom face which promotes laminar flow, thereby reducing the noise associated with turbulence and cavitation.—WT

6,404,701

43.30.Yj ENCAPSULATED VOLUMETRIC ACOUSTIC ARRAY IN THE SHAPE OF A TOWED BODY

Thomas R. Stottlemyer, assignor to the United States of America as represented by the Secretary of the Navy
11 June 2002 (Class 367/20); filed 16 July 2001

The central, cylindrical portion of a towed underwater body is envisioned to contain a set of electroacoustic transducers encapsulated in a solid casting of polyurethane which both prevents water intrusion into the transducer elements and allegedly increases the cavitation threshold, thereby allowing the array of transducers to be driven to a greater acoustic intensity.—WT

6,400,645

43.30.Yj SONOBUOY APPARATUS

Bruce W. Travor, assignor to the United States of America as represented by the Secretary of the Navy
4 June 2002 (Class 367/4); filed 11 October 2001

A sonobuoy apparatus, sized to fit into a standard canister, includes a set of telescopic arms **34** which elongate as the weighted canister **20** and weighted acoustic projector unit **40** both fall downward. Hinge arrangements **36** at the upper ends of each of the telescopic arms cause the arms to
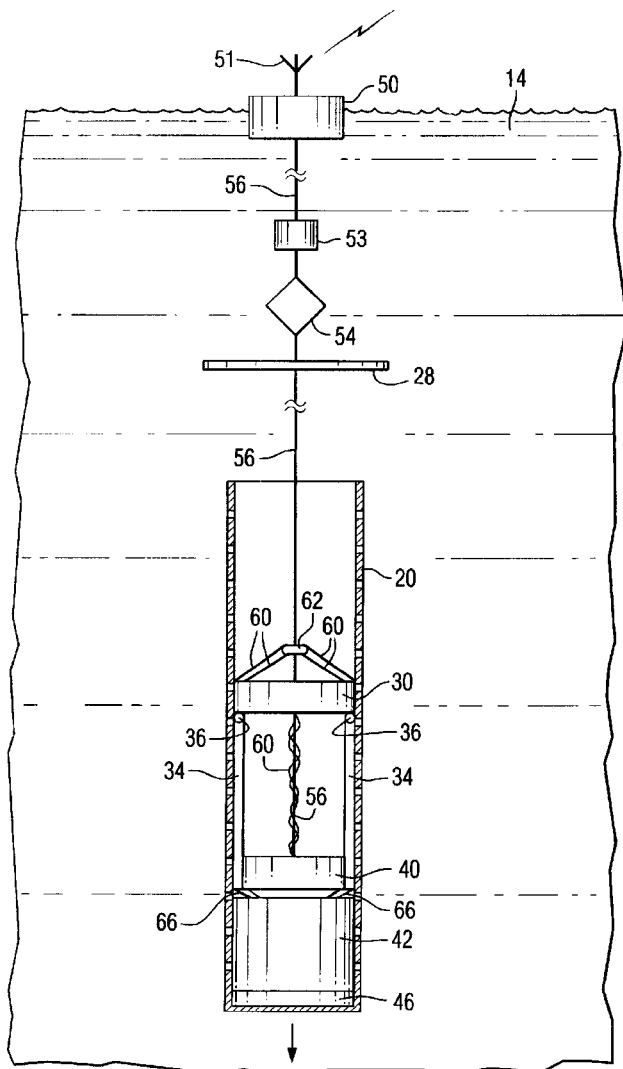
rotate to a near-horizontal orientation after the canister falls away. These deployed arms support hydrophones (not shown) at various positions along the arms and also along tension lines stretched between the arms at their outer ends. Surface flotation unit **50** houses the transmitter/receiver equipment and antenna **51** while **28** damps vertical motion of the assembly.—WT

5,884,650

43.35.Ei SUPPRESSING CAVITATION IN A HYDRAULIC COMPONENT

Anthony A. Ruffa, assignor to the United States of America as represented by the Secretary of the Navy
23 March 1999 (Class 137/13); filed 26 February 1997

It is suggested that the cavitation threshold in some flow region can be raised through the use of an acoustic transducer that radiates an acoustic

field into the flow region thereby increasing the ambient pressure. There is no discussion of what happens during the half of the cycle in which that radiated acoustic pressure field subtracts from the ambient pressure.—WT

6,396,484

43.35.Pt ADAPTIVE FREQUENCY TOUCHSCREEN CONTROLLER USING INTERMEDIATE-FREQUENCY SIGNAL PROCESSING

Robert Adler et al., assignors to Elo Touchsystems, Incorporated
28 May 2002 (Class 345/177); filed 29 September 1999

This controller is intended for an acoustic touchscreen in which acoustic or ultrasonic waves are generated and directionally propagated across the touchscreen surface utilizing the phenomena of surface acoustic waves. The controller can either utilize look-up tables to achieve the desired output frequency or it can use a multi-step process in which it first determines the frequency requirements of the touchscreen and then adjusts the burst frequency characteristics, the receiver circuit center frequency, or both, in accordance with the touchscreen requirements. In one embodiment, the adaptive controller compensates for global mismatch errors through a digital multiplier that modifies the output of a crystal reference oscillator. In another embodiment, a digital signal processor provides corrections based on stored values that compensate for both global and local signal variations.—DRR

5,900,533

43.35.Sx SYSTEM AND METHOD FOR ISOTOPE RATIO ANALYSIS AND GAS DETECTION BY PHOTOACOUSTICS

Mau-Song Chou, assignor to TRW Incorporated
4 May 1999 (Class 73/24.01); filed 3 August 1995

The system includes a tunable laser that is directed into a sample at energy levels sufficient to generate detectable acoustic emissions. A microphone detects these emissions for processing and analysis.—WT

6,404,536

43.35.Sx POLARIZATION INDEPENDENT TUNABLE ACOUSTO-OPTICAL FILTER AND THE METHOD OF THE SAME

Eric Gung-Hwa Lean et al., assignors to Industrial Technology Research Institute
11 June 2002 (Class 359/308); filed in Taiwan, Province of China 30 December 2000

In this filter, input light is diffracted into two light beams, one affected by acoustic waves and the other not. A polarization beam displacer/combiner is employed to separate the input light beam into two orthogonal beams. Several acousto-optical polarized rotators are used to rotate the polarization of a particular light wavelength by 90 degrees. The two beams are properly combined to form orthogonal beams.—DRR

6,391,020

43.35.Ty PHOTODISRUPTIVE LASER NUCLEATION AND ULTRASONICALLY-DRIVEN CAVITATION OF TISSUES AND MATERIALS

Ron Kurtz et al., assignors to The Regents of the University of Michigan
21 May 2002 (Class 606/2); filed 6 October 1999

This apparatus creates a cavitation nucleus in a target material by focusing optical radiation, in the form of a short pulse laser beam, at a
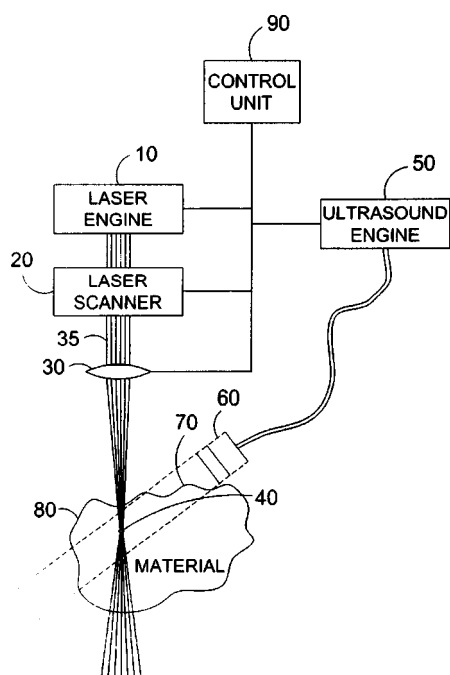
portion of the material and then causing mechanical disruption in another portion of the materials adjacent to the cavitation nucleus by subjecting the cavitation nucleus to ultrasound waves.—DRR

6,392,540

43.35.Ty NON-AUDITORY SOUND DETECTION SYSTEM

Mary E. Brown, Rochester, New York
21 May 2002 (Class 340/540); filed 4 May 2000

This is a device for converting sound into nonaudiory signals to alert a user to the presence of a predetermined sound. The system consists of a main control unit and a transceiver. The transceiver is used to transmit an activation signal upon receiving the predetermined sound. A remote assembly contains an attachment device which can be worn by the user and can generate a nonauditory signal (such as a flash of light).—DRR

6,390,979

43.35.Yb NONINVASIVE TRANSCRANIAL DOPPLER ULTRASOUND COMPUTERIZED MENTAL PERFORMANCE TESTING SYSTEM

Philip Chidi Njemanze, Owerri IMO, Nigeria
21 May 2002 (Class 600/438); filed 24 August 2001

The device purports to determine the mental performance capacity of a human subject for performing a given task by measuring the subject's baseline blood flow velocity in cerebral arteries using a transcranial Doppler ultrasound instrument. Two probes are placed on the temples and the laterality index for both arteries is calculated. A computer is used to present mental tasks on a monitor while simultaneously monitoring in real-time the mean blood flow velocity during each stage of the task. The acquired data is processed to yield mental performance indices that may be relayed via cellular telephony to a remote computer or mission control.—DRR

6,390,982

43.35.Yb ULTRASONIC GUIDANCE OF TARGET STRUCTURES FOR MEDICAL PROCEDURES

Frank M. Bova, Gainesville, Florida *et al.*
21 May 2002 (Class 600/443); filed 21 July 2000

The system described in this patent combines an ultrasound probe with both passive and active infrared tracking systems to provide a real time image display of the entire region of interest. This is done without probe movement. Real time tracking of the target region permits physiological
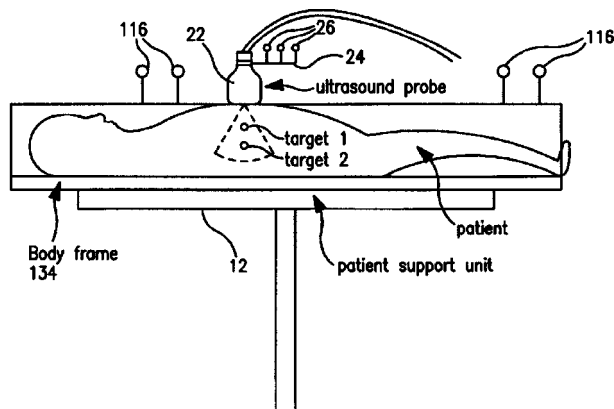
gating and probe placement during image acquisition so that all external displacements introduced by the probe can be monitored during the time of treatment. The system may be used in the surgical arena for image guidance during radiation therapy and surgery.—DRR

6,390,983

43.35.Yb METHOD AND APPARATUS FOR AUTOMATIC MUTING OF DOPPLER NOISE INDUCED BY ULTRASOUND PROBE MOTION

Larry Y. L. Mo and Dean W. Brouwer, assignors to GE Medical Systems Global Technology Company, LLC
21 May 2002 (Class 600/453); filed 7 September 2000

The device monitors the blood vessel wall signal input to a spectral Doppler processor to check for clutter induced by probe motion. The clutter is typically of higher frequency than that due to normal vessel wall motion. Threshold logic is applied to check for energy within a frequency band greater than the normal wall signal frequencies. If significant energy above some ''rattle'' threshold is detected for a predefined time interval, the Doppler audio is automatically muted. This can be effected at one or more points within the Doppler audio signal path in a conventional scanner. If the rattling clutter is no longer detected, the Doppler audio is reactivated or ramped up smoothly.—DRR

6,398,732

43.35.Yb ACOUSTIC BORDER DETECTION USING POWER MODULATION

George A. Brock-Fisher and David M. Prater, assignors to Koninklijke Philips Electronics, N.V.
4 June 2002 (Class 600/443); filed 11 February 2000

The described method entails the control of an ultrasound system to identify a boundary between a tissue region and a blood-filled region that lies within a region of interest (ROI). A contrast agent is initially administered to the ROI and then ultrasound beams are transmitted at different power levels into the ROI. Signal returns from the beams are processed to determine a phase difference. It is claimed that under certain circumstances a phase change in echo returns occurs at the boundary between tissue and

blood-containing contrast agent. Detection of the phase change provides for precise identification of the boundary on the basis of the time interval in which the phase change is detected.—DRR

6,398,736

43.35.Yb PARAMETRIC IMAGING ULTRASOUND CATHETER

James B. Seward, assignor to Mayo Foundation for Medical Education and Research
4 June 2002 (Class 600/466); filed 20 October 1999

The subject device provides parametric images of a surrounding in-sonated environment. Parametric imaging is defined as the imaging of quantifiable ''parameters'' for visible two-, three-, four-, or nonvisible, higher-dimensional, temporal physiological events. Visible motion is a fourth-dimensional event and includes surrogate features of cardiac muscular contraction, wall motion, valve leaflet motion, etc. Nonvisible motion is a higher-dimensional event that encompasses slow nonvisible occurrences (e.g., remodeling, transformation, aging, healing, etc.) or fast nonvisible events (i.e., heat, electricity, strain, compliance, perfusion, etc.). An ultrasound catheter with parametric imaging capability can obtain dynamic digital or digitized information from the surrounding environment and display information features or quanta as static or dynamic geometric figures from which discrete or gross quantifiable information can be obtained.—DRR

5,756,898

43.35.Zc PASSIVE ACOUSTIC METHOD OF MEASURING THE EFFECTIVE INTERNAL DIAMETER OF A PIPE CONTAINING FLOWING FLUIDS

Victor Diatschenko et al., assignors to Texaco Incorporated
26 May 1998 (Class 73/592); filed 27 June 1994

A change in the internal diameter of a pipe, whether it is decreased because of the accumulation of nonflowing material or increased because of corrosion or erosion, is detected by observing a shift in the characteristic frequency of the pipe. The measuring system is entirely passive in that it requires only that vibrations of the pipe be excited by the noise generated by the flow within the pipe. Furthermore, because the diameter measurement is not based on acoustic signal transit time, the present system is not dependent on the assumption of uniform flow conditions within the pipe.—WT

6,371,095

43.35.Zc ULTRASOUND WHISTLES FOR INTERNAL COMBUSTION ENGINE

Walter E. Sacarto, Denver, Colorado
16 April 2002 (Class 123/590); filed 21 August 2000

Ultrasonic whistles are proposed to improve the mixing of air and fuel prior to ignition in an internal combustion engine. They may be placed in a cylinder head, around a valve stem, or in a carburetor. Various whistle designs are described.—KPS

6,402,769

43.38.Ar TORSIONAL ULTRASOUND HANDPIECE

Mikhail Boukhny, assignor to Alcon Universal Limited
11 June 2002 (Class 606/169); filed 21 January 2000

This handpiece design features a set of piezoelectric elements constructed of segments capable of both longitudinal and torsional motion. An appropriate ultrasound driver drives the set of elements at their respective resonant frequencies to produce longitudinal and torsional oscillations.—DRR

6,332,029

43.38.Bs ACOUSTIC DEVICE

Henry Firouz Azima et al., assignors to New Transducers Limited
18 December 2001 (Class 381/152); filed in the United Kingdom 2 September 1995

This is another in a long line of recent NXT patents. This particular issue delineates 48 pages of examples of vibratory panels in ceilings, easels, pianos, vending machines, and more. The patent does not discuss any of the more substantive issues such as shaker placement, panel construction, etc. These are discussed in British Patent 235008 (or European Patent 1068770).—MK

6,399,870

43.38.Bs MUSICAL INSTRUMENTS INCORPORATING LOUDSPEAKERS

Henry Azima et al., assignors to New Transducers Limited
4 June 2002 (Class 84/744); filed in the United Kingdom 2 September 1995

This is another NXT patent. Place a vibration panel on the back of an electronic musical instrument. Evidently, they forgot to include this application in their application compendium (United States Patent 6,332,029, reviewed above).—MK

5,898,642

43.38.Fx SONAR ANTENNA

Jean-Marie Wagner, assignor to Etat Francais represente par le Delegue General pour l'Armement
27 April 1999 (Class 367/158); filed in France 28 September 1995

Normally a planar array of Tonpilz-type sonar transducers is realized by first making individual transducers and then bonding or otherwise attaching them in a grid arrangement to an acoustically transparent elastomeric material layer which constitutes the acoustic window. Here it is proposed to first bond to the acoustic window layer a continuous layer of material of the size and shape that represents the ensemble of head masses of the entire array. The head mass layer has a set of predrilled and tapped holes corresponding to the positions of the stress bolts of the set of Tonpilz transducers. Then the head mass layer is cut into a series of orthogonal grooves (groove depths equal to head mass layer thickness and spacings equal to head mass dimensions) to produce a grid arrangement of individual head masses. The remainder of each of the Tonpilz transducers is then assembled onto these separate but spatially arranged head masses in standard fashion.—WT

6,386,041

43.38.Fx STEP COUNTING DEVICE INCORPORATING VIBRATION DETECTING MECHANISM

David Yang, Taipei, Taiwan, Province of China
14 May 2002 (Class 73/651); filed 1 February 2000

Those who choose walking for excercise often use a pedometer to keep track of the distance covered, or more accurately the number of steps taken. The invention is a small, self-contained step-counting device that can be attached to shoes or clothing. A piezoelectric transducer detects vibrations which are then analyzed, counted, and displayed.—GLA

6,362,726

43.38.Ja SOUNDER DEVICE WHICH DEFLECTS SOUND AWAY FROM A HOUSING

Kieron Chapman, assignor to Fulleon Limited
26 March 2002 (Class 340/384.7); filed in the European Patent Office 27 February 1997

An acoustical alarm device comprises a base member **1** for mounting against a ceiling **2** (the figure is drawn inverted) that supports a sounder plate **1a** which is generally of concave shape. The transducer **7** and its housing **4** are displaced from the sounder plate by a series of spacers **9** creating gap **8**. Sound radiated by **7** is reflected off the sounder plate **1a**
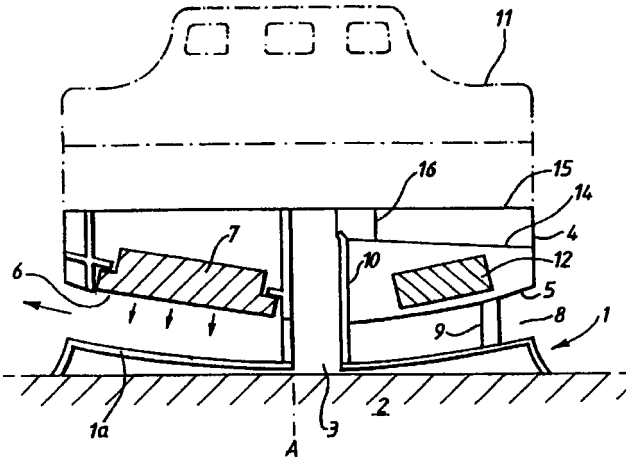
outwardly through gap **8**. Central channel **3** permits the routing of electrical cables to auxiliary detectors and/or lights indicated schematically by dashed lines **11**. Tag **12** indicates an electronics module mounted within housing **4**. An alleged advantage of this design is that both the transducer module and the electronics module can be encapsulated simultaneously as opposed to prior art designs that required separate encapsulations.—WT

6,377,696

43.38.Ja LOUDSPEAKER SYSTEMS

Stuart Michael Nevill, assignor to B & W Loudspeakers Limited
23 April 2002 (Class 381/345); filed in the United Kingdom 2 May 1997

The intent, as in some transmission line loudspeaker designs, is to completely absorb rear radiation from speaker **2′** without introducing acoustic resonances or excessive cone damping. Those readers familiar with
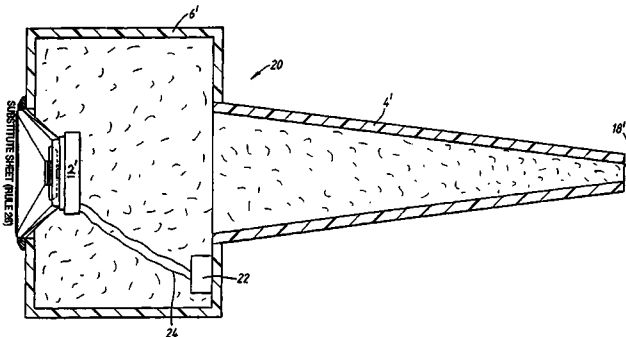
1970s speaker systems will find that the patent document—text, illustrations, and claims—almost perfectly describes the Webb transmission line system featured in "Audio Amateur Loudspeaker Projects, 1970–1979."—GLA

6,381,334

43.38.Ja SERIES-CONFIGURED CROSSOVER NETWORK FOR ELECTRO-ACOUSTIC LOUDSPEAKERS

Eric Alexander, South Ogden, Utah
30 April 2002 (Class 381/99); filed 23 February 1999

With resistive loads, series and parallel frequency dividing networks perform equally well. With reactive loudspeaker loads, the series network has the annoying property of altering the high-frequency filter in response to the woofer's changing impedance. Prior art also includes at least one
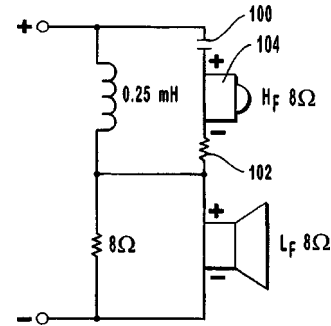
speaker-level constant-voltage network in which a relatively high impedance tweeter was bridged across the inductor of a second-order low-pass section. The patent describes a number of configurations that seem to make use of a little of each.—GLA

6,381,337

43.38.Ja SOUND REPRODUCTION DEVICE OR MICROPHONE

Marc Adam Greenberg, assignor to Floating Sounds Limited
30 April 2002 (Class 381/345); filed in the United Kingdom 9 December 1995

From time to time inventors come up with the idea of pumping air in and out of a balloon to reproduce sound. In this case, however, the surface of
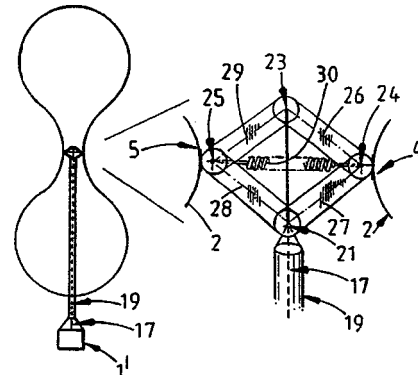
an inflatable balloon is mechanically driven at two or more points. The configuration can also be used as a microphone.—GLA

6,384,550

43.38.Ja SPEAKER AND DRIVE DEVICE THEREFOR

Hideaki Miyakawa *et al.*, assignors to Canon Kabushiki Kaisha
7 May 2002 (Class 318/116); filed in Japan 6 September 1994

One might guess that this circuit is intended to drive a digital loudspeaker. Not quite. It drives a supersonic vibration wave motor, which in
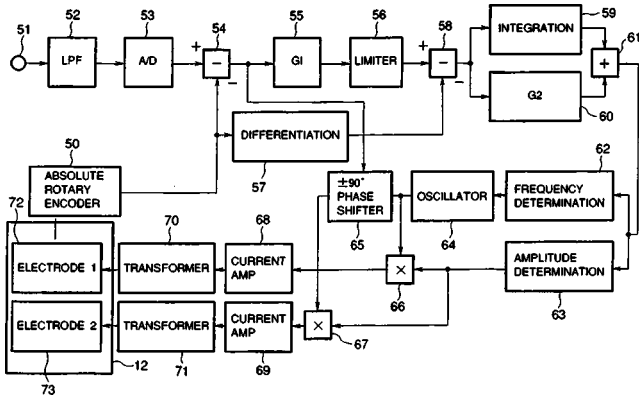
turn drives a loudspeaker cone. The patent teaches us that since such a wave motor has relatively high mass and substantial friction, "...no resonance phenomenon takes place." Moreover, since the wave motor generates no back emf, it follows that "...no group delay phenomenon takes place." The concept of minimum-phase response seems to have eluded the four inventors.—GLA

6,385,324

43.38.Ja BROADBAND LOUDSPEAKER

Karl Heinz Köppen, assignor to Sorus Audio AG
7 May 2002 (Class 381/336); filed in Germany 17 March 1997

It is certainly not unusual to see loudspeakers mounted on convex spherical surfaces. The novel feature of this design is 45-degree rear deflec-

tion plane **9**. We are told that reflected waves must pass several times through internal damping material and, as a result, axial standing waves cannot develop.—GLA
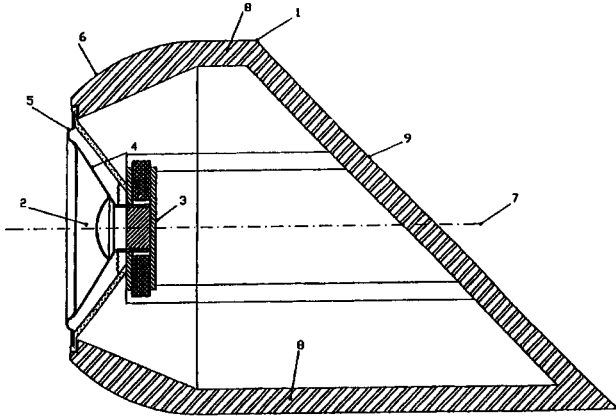
6,389,144

43.38.Ja SOUND FIELD EQUALIZING APPARATUS FOR SPEAKER SYSTEM

Deog Jin Lee, assignor to LG Electronics Incorporated
14 May 2002 (Class 381/340); filed in the Republic of Korea 29 July 1997

In the 1940s, Altec-Lansing patented a loudspeaker design in which a
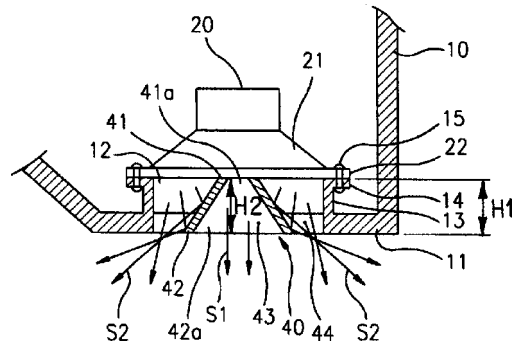
little multicell horn was mounted in front of a loudspeaker. This invention eliminates the cells.—GLA

6,389,146

43.38.Ja ACOUSTICALLY ASYMMETRIC BANDPASS LOUDSPEAKER WITH MULTIPLE ACOUSTIC FILTERS

James J. Croft III, assignor to American Technology Corporation
14 May 2002 (Class 381/345); filed 17 February 2000

In 1994, the bandpass configuration shown was thoroughly analyzed and documented by JBL in an unpublished research project. However, the patent includes one variant in which sealed chamber **21** is quite large and
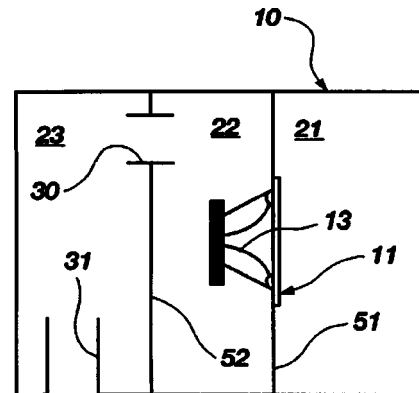
uncontrolled, such as the trunk cavity of an automobile. Another variant includes an internal acoustic notch filter. Neither of these specific geometries was anticipated by the JBL study.—GLA

6,389,140

43.38.Kb CERAMIC PIEZOELECTRIC TYPE MICROPHONE

Jose Wei, Hsin Tien City, Taipei, Taiwan, Province of China
14 May 2002 (Class 381/173); filed 30 November 1999

This patent describes a contact (throat) microphone in which high-density foam is used to conduct mechanical vibrations from the user's skin to a piezoelectric transducer. With proper selection of the foam material and its thickness, the patent asserts that improved high-frequency fidelity can be achieved and background noise suppressed.—GLA

6,363,156

43.38.Lc INTEGRATED COMMUNICATION SYSTEM FOR A VEHICLE

Timothy S. Roddy, assignor to Lear Automotive Dearborn, Incorporated
26 March 2002 (Class 381/86); filed 18 November 1998

Microphones are distributed within the passenger compartment of a van so that passengers in the rear can communicate with those in the front. Furthermore, each passenger is also able to operate an on-board cell phone and control the vehicle's sound system. A digital signal processor is used to reduce unwanted microphone signals and feedback.—KPS

6,377,862

43.38.Md METHOD FOR PROCESSING AND REPRODUCING AUDIO SIGNAL

Hidetoshi Naruki and Shoji Ueno, assignors to Victor Company of Japan, Limited
23 April 2002 (Class 700/94); filed in Japan 19 February 1997

A DVD has sufficient space to consider the addition of other information about the stored tracks, specifically data concerning playback parameters such as equalization and reverb.—MK

6,378,010

43.38.Md SYSTEM AND METHOD FOR PROCESSING COMPRESSED AUDIO DATA

David Burks, assignor to Hewlett-Packard Company
23 April 2002 (Class 710/68); filed 10 August 1999

Filed in 1999, this patent proposes a very simple computer architecture for a DSP system that compresses audio data on a CD-ROM. Even in 1989, this would have been starkly obvious.—MK

6,392,133

43.38.Md AUTOMATIC SOUNDTRACK GENERATOR

Alain Georges, assignor to dBtech SARL
21 May 2002 (Class 84/609); filed 17 October 2000

This conceptual patent uses two pages and three claims to propose mixing an external audio track with an existing video track. Owing to the brevity, nothing close to real is described.—MK

6,392,576

43.38.Md MULTIPLIERLESS INTERPOLATOR FOR A DELTA-SIGMA DIGITAL TO ANALOG CONVERTER

Gerald Wilson and Robert S. Green, assignors to Sonic Innovations, Incorporated
21 May 2002 (Class 341/143); filed 21 August 2001

Delta sigma converters use oversampling to achieve high SNR. However, there is a tradeoff between the oversampling rate and the processing speed required in the DSP circuitry. The inventors propose using interpolation and decimation combined with a zero-order hold and a lattice filter design. The lattice filter implementation is noteworthy for using shifts and adds to avoid multiplication. The patent writing is clear and concise.—MK

6,393,401

43.38.Md PICTURE DISPLAY DEVICE WITH ASSOCIATED AUDIO MESSAGE

Alan R. Loudermilk and Wayne D. Jung, assignors to LJ Laboratories, L.L.C.
21 May 2002 (Class 704/272); filed 6 December 2001

In 2002, a "talking picture" has a different interpretation from the 1930s. Here, the inventors propose adding a sound storage chip that can be activated by a switch on the picture frame. They also propose other systems that show the same sense of originality.—MK

6,385,320

43.38.Vk SURROUND SIGNAL PROCESSING APPARATUS AND METHOD

Tae-Hyun Lee, assignor to Daewoo Electronics Company, Limited
7 May 2002 (Class 381/17); filed in the Republic of Korea 19 December 1997

Several earlier patents describe methods of producing virtual surround sound sources from a single pair of loudspeakers. Using head-related transfer functions, the circuitry shown is intended to create two rear virtual sound
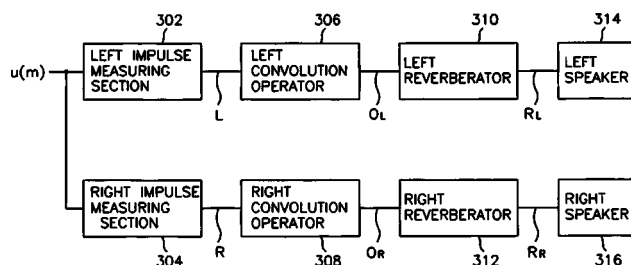
images in addition to the two real front sound images. At the same time, reverberation is added to simulate a more spacious sonic environment.—GLA

6,360,844

43.50.Gf AIRCRAFT ENGINE ACOUSTIC LINER AND METHOD OF MAKING THE SAME

William H. Hogeboom and Gerald W. Bielak, assignors to The Boeing Company
26 March 2002 (Class 181/213); filed 2 April 2001

An acoustic liner for use in the nacelle of an aircraft engine consists of alternating sections of absorptive liner and low-resistance liner. The latter serves to scatter low-mode-order noise into higher modes that are more readily absorbed. The low-resistance liner is composed of a perforated sheet, having percent open area of at least 15%, a honeycomb layer, and an impervious backing sheet. Methods of manufacture to achieve varying cavity depths in the honeycomb layer are described, thus enabling absorption over a broad frequency range. Applications to circular inlets as well as to splitters in the aft engine duct are described.—KPS

6,364,054

43.50.Gf HIGH PERFORMANCE MUFFLER

John Bubulka et al., assignors to Midas International Corporation
2 April 2002 (Class 181/264); filed 27 January 2000

This patent describes a muffler intended for use with high-performance automobiles that creates a "deep throaty high performance sound." The cross section is rectangular with the width being two and one-half times
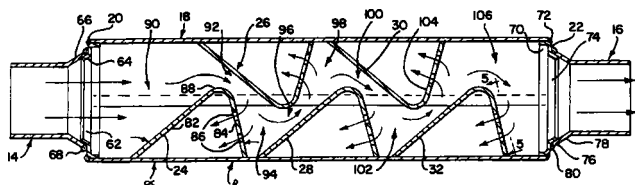
greater than the height. Arranged along the length are deflector plates, such as **24**. These plates are perforated and form a series of chambers and a sinuous path for the exhaust gases.—KPS

6,367,580

43.50.Gf SOUND ADJUSTABLE TAIL PIPE STRUCTURE

Ming-Tien Chang, assignor to Liang Fei Industry Company, Limited
9 April 2002 (Class 181/241); filed 11 July 2000

A muffler tail pipe is adjustable, so that the same muffler can be used on a range of different cars and engines. The alignment of **23** and **24** can be
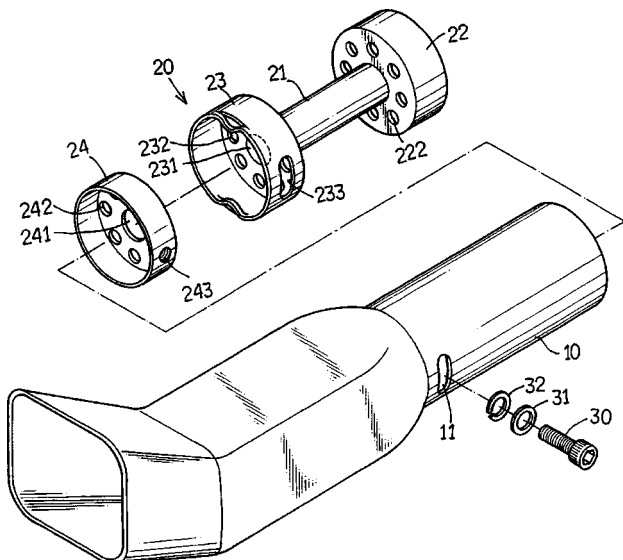
altered by means of the arrangement using the oblong slot **11**, thus adjusting the airflow through the tail pipe.—KPS

6,404,152

43.50.Gf MOTOR CONTROL DEVICE

Takashi Kobayashi *et al.*, assignors to Hitachi, Limited
11 June 2002 (Class 318/254); filed in Japan 29 May 1998

The device is essentially a feed-back system that reduces undesired sound caused by ring oscillations in the radial direction of the stator inside an electric motor. The electromagnetic force drift is measured to provide corrective coefficients to the activation current.—DRR

6,394,655

43.50.Ki METHOD AND APPARATUS FOR INFLUENCING BACKGROUND NOISE OF MACHINES HAVING ROTATING PARTS

Jürgen Schnur and Silvia Tomaschko, assignors to DaimlerChrysler AG
28 May 2002 (Class 384/247); filed in Germany 13 June 1998

This method of reducing the perceptible vibrations of rotating parts entails the monitoring of mounting conditions between a shaft bearing and a rotating part. By varying the mounting conditions, the transfer function is varied, particularly for vibrations between the rotating part and the shaft bearing or a component in contact with the shaft bearing. A radial adjustment unit containing piezoelectric elements varies the mounting conditions. The transfer function of the vibrations is thereby varied.—DRR

6,360,607

43.50.Lj SOUND DETECTOR DEVICE

Francois Charette *et al.*, assignors to Ford Global Technologies, Incorporated
26 March 2002 (Class 73/587); filed 9 August 1999

A device aimed at detecting and locating squeaks and rattles in an automobile consists of a pair of microphones **50** connected to headphones **68**. A mechanism is provided which allows the operator to vary the separa-

tion distance between the microphones. This capability, along with the selection of center frequency and bandwidth, allows the operator to efficiently locate the source of sounds in a vehicle.—KPS
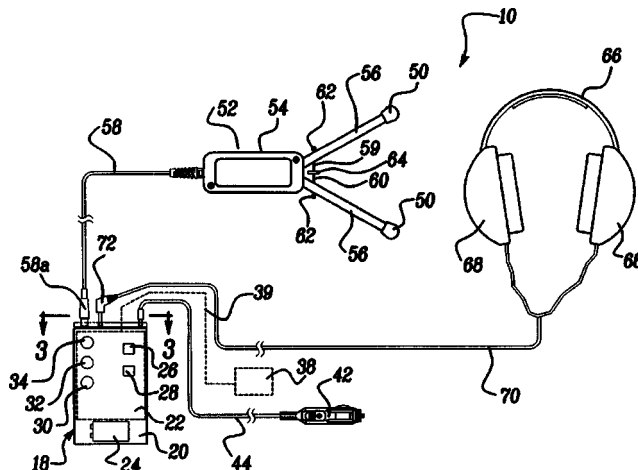
6,363,984

43.50.Lj TIRE TREAD PITCH SEQUENCING FOR REDUCED NOISE

Christopher D. Morgan, assignor to Kumho & Company, Incorporated
2 April 2002 (Class 152/209.2); filed 25 October 1999

A tread design is proposed in which repeated pitches of three different lengths are arranged around the circumference of a tire in order to reduce rolling tire noise. One hundred different pitch sequences are defined, all of which claim reduced noise.—KPS

6,399,868

43.55.Lb SOUND EFFECT GENERATOR AND AUDIO SYSTEM

Makoto Yamato and Tony Williams, assignors to Roland Corporation
4 June 2002 (Class 84/701); filed 28 September 2000

Given a two-channel (stereo) input, the question is how to produce a five-channel output. The Roland unit uses an unspecified multichannel re-

guide into soft tissue, such as the tip of a finger, thereby producing a photoacoustic interaction. The resulting acoustic signal is detected by a transducer and analyzed to provide the desired parametric reading.—DRR
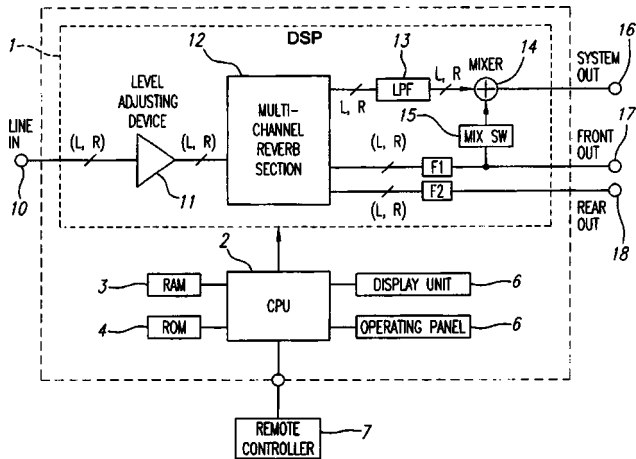
verb **12** followed by a low-pass filter to create ''presence'' for the center (surround) channel. While low frequencies do add ''presence,'' they do not make a soundfield or even close (contrary to claims of the patent).—MK

6,386,037

43.58.Gn VOID DETECTOR FOR BURIED PIPELINES AND CONDUITS USING ACOUSTIC RESONANCE

William F. Kepler and Fred A. Travers, assignors to the United States of America as represented by the Secretary of the Interior
14 May 2002 (Class 73/579); filed 6 June 2001

This void detection device is a little robotic car that can move through buried conduit. Power and telemetry signals pass through umbilical cord **28**. An acoustic exciter **12** repeatedly taps the wall of the conduit and the re-

sulting acoustic waves are detected by sensor **18**. If a hidden void **V** is encountered, the acoustic signal changes. External circuitry analyzes the frequency response signals in comparison with a baseline response obtained from a known good area of conduit.—GLA
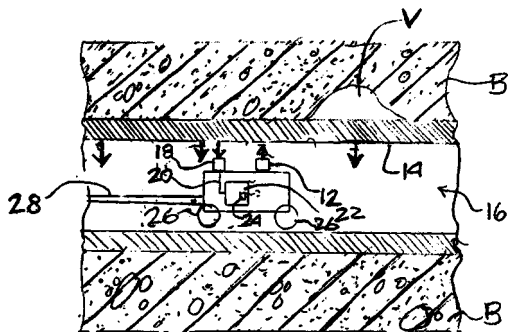
6,403,944

43.58.Kr SYSTEM FOR MEASURING A BIOLOGICAL PARAMETER BY MEANS OF PHOTOACOUSTIC INTERACTION

Hugh Alexander MacKenzie and John Matthew Lindberg, assignors to Abbott Laboratories
11 June 2002 (Class 250/214.1); filed in the United Kingdom 7 March 1997

This is a system intended to measure a biological parameter such as blood glucose. The system operates by directing laser pulses from a light

6,390,014

43.58.Wc ACOUSTIC SIGNALING DEVICE FOR CULINARY-USE VESSELS, IN PARTICULAR FOR KETTLES

Tiziano Ghidini, assignor to Frabosk Casalinghi, S.P.A.
21 May 2002 (Class 116/150); filed in the European Patent Office 24 September 1999

True tea aficianados know that black teas demand 100 °C water. Therefore, many tea kettles feature whistles to alert the brewer that the water has
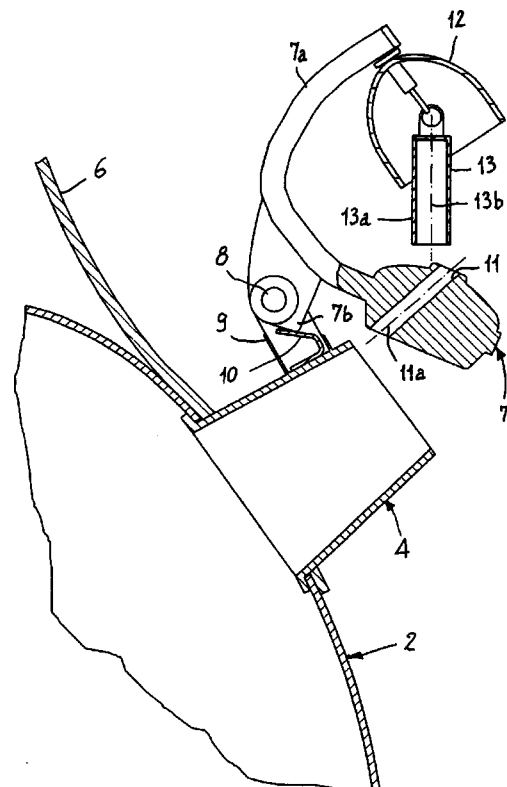
reached boiling. This patent claims that whistles are subject to clogging due to calcium deposits and therefore proposes a steam driven ''clanger.''—MK

6,394,874

43.58.Wc APPARATUS AND METHOD OF USE FOR SOUND-GENERATING FINGER PUPPET

Takao Kubo and Todd Miller Lustgarten, assignors to Hasbro, Incorporated
28 May 2002 (Class 446/327); filed 4 February 2000

Sound generator chips can show up anywhere, including finger puppets. The finger can close a switch that activates a battery powered micro-

processor **24** that outputs to a (very) small speaker **25**. When will infrared communication for all five fingers be patented?—MK
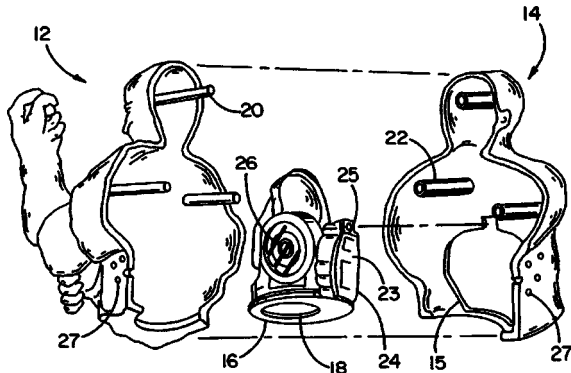
6,394,875

43.58.Wc BICYCLE MOUNTED NOISE-MAKING DEVICE

Terry Smith, Tustin, California
28 May 2002 (Class 446/404); filed 31 March 2000

Using a clothespin to attach a playing card to a bicycle's rear forks doesn't make the bike sound like a motorcycle. So, if you add a pipe and a horn, you can imitate various motorcycle sounds. The inventors claim "The flexible contact is designed to be easily replaceable, even by a child."—MK

6,400,275

43.58.Wc AUDITORY CUES FOR NOTIFICATION OF DEVICE ACTIVITY

Michael C. Albers, assignor to Sun Microsystems, Incorporated
4 June 2002 (Class 340/635); filed 23 June 1999

Many devices, like toasters, lack necessary and sufficient displays. So, when attaching such devices to a computer network, why not use audible tones to indicate the connection status? This obvious concept is the total sum of this patent.—MK

6,402,580

43.58.Wc NEARLY HEADLESS NICK NOISEMAKER CANDY TOY

Thomas J. Coleman, Abingdon, Virginia *et al.*
11 June 2002 (Class 446/72); filed 11 April 2001

Harry Potter fans know Nearly Headless Nick. The inventors know they can reuse their earlier patent (United States Patent 5,855,500) to create a rattle with a skeleton head.—MK

6,337,999

43.60.−c OVERSAMPLED DIFFERENTIAL CLIPPER

Robert A. Orban, assignor to Orban, Incorporated
8 January 2002 (Class 700/94); filed 18 December 1998

Clipping or compression of audio waveforms is a necessity in any system with a fixed dynamic range. However, clipping introduces new harmonics that can alias down to baseband. The inventor, who has been working on audio processors for many years, proposes to oversample and then
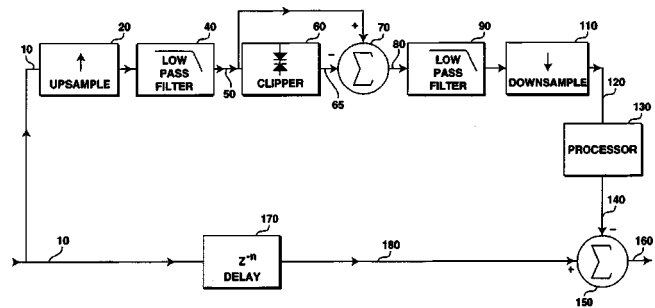
clip. Further, the "clippings" are filtered and then downsampled, "processed" (e.g., filtered), and subtracted from the delayed input. The patent writing is succinct and clear.—MK

6,402,782

43.64.Yp ARTIFICIAL EAR AND AUDITORY CANAL SYSTEM AND MEANS OF MANUFACTURING THE SAME

Alastair Sibbald and George Derek Warner, assignors to Central Research Laboratories, Limited
11 June 2002 (Class 623/10); filed in the United Kingdom 15 May 1997

This device is a laminated artificial pinna having a concha, fossa, and auditory canal. The auditory canal is constructed and arranged with respect to the concha so the center of the entrance of the auditory canal is 15 to 20
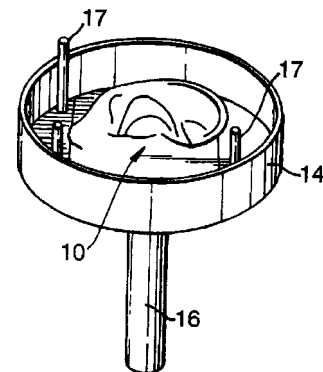
mm from the rear wall of the concha and 9 to 15 mm from the concha floor and the alignment of the turning point of the entrance of the auditory canal is substantially horizontal.—DRR

6,390,971

43.66.Ts METHOD AND APPARATUS FOR A PROGRAMMABLE IMPLANTABLE HEARING AID

Theodore P. Adams *et al.*, assignors to St. Croix Medical, Incorporated
21 May 2002 (Class 600/25); filed 4 February 2000

A completely implanted middle ear hearing aid is adjusted by the physician or wearer remotely via infrared, ultrasonic, or rf wireless means. The programmer-transmitter sends encoded acoustic signals to the implant that may be in the form of pulse code modulation telemetry. Post-fitting adjustments that can be made by the wearer during use without the need for surgery include volume control, frequency response, and device on-off.—DAP

6,393,130

43.66.Ts DEFORMABLE, MULTI-MATERIAL HEARING AID HOUSING

Paul R. Stonikas and Robert S. Yoest, assignors to Beltone Electronics Corporation
21 May 2002 (Class 381/322); filed 16 July 1999

A manufacturing method is described for a compliant hearing aid in which the multi-material housing deforms in response to ear canal shape changes as the hearing aid wearer moves his or her jaw. Temporary deformation of the soft shell is also used during manufacture to slide components through constricted channels in the internal cavity of the housing. Afterward, remaining spaces inside the shell are filled in with a curable material.—DAP

6,402,682

43.66.Ts HEARING AID

Patrik Johansson, assignor to Nobel Biocare AB
11 June 2002 (Class 600/25); filed in Sweden 11 April 1997

A detachable electronics module is mounted externally in the mastoid bone where it can be accessed for battery replacement and servicing. Amplified sound is conveyed from the module through the skin into the middle ear cavity via a surgically implanted tube. The result is that the natural movement of the eardrum caused by sounds from the outside is enhanced by amplified sounds impinging on the middle ear side of the eardrum. The advantage of this approach is amplification while leaving the ear canal open,
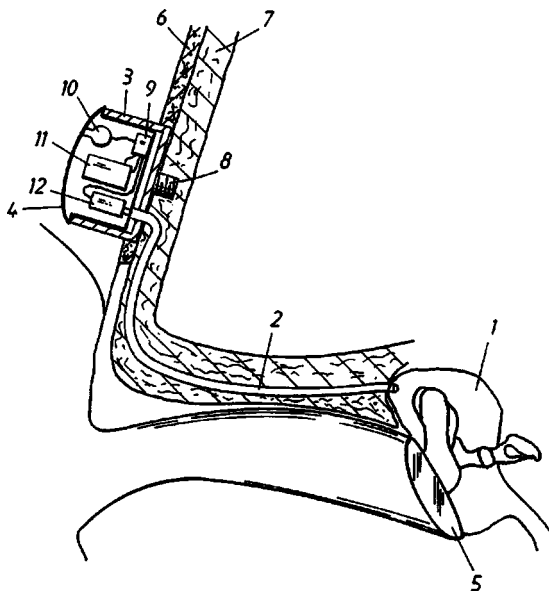
which eliminates occlusion problems inherent with conventional air conduction hearing aids.—DAP

6,404,895

43.66.Ts METHOD FOR FEEDBACK RECOGNITION IN A HEARING AID AND A HEARING AID OPERATING ACCORDING TO THE METHOD

Tom Weidner, assignor to Siemens Audiologische Technik GmbH
11 June 2002 (Class 381/318); filed in Germany 4 February 1999

Acoustic feedback is recognized by monitoring the hearing aid output signal level while attenuating a frequency band in the signal transmission path between the hearing aid receiver and microphone in which the feedback could occur. When feedback is present in a monitored frequency band, the signal level is reduced by the attenuation more than would be expected
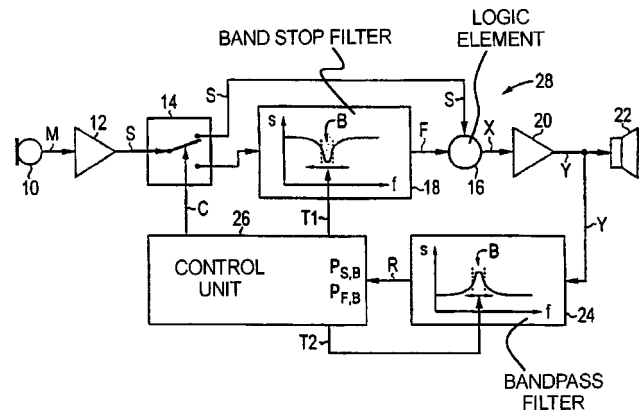
without feedback. While detecting whether feedback is present, the microphone output can be switched between no attenuation and attenuation in a particular frequency band, causing the duration of the attenuation to be varied so that this scheme can be implemented continuously in multiple frequency bands in which feedback is likely to occur.—DAP

6,366,883

43.72.Ja CONCATENATION OF SPEECH SEGMENTS BY USE OF A SPEECH SYNTHESIZER

Nick Campbell and Andrew Hunt, assignors to ATR Interpreting Telecommunications
2 April 2002 (Class 704/260); filed in Japan 15 May 1996

This speech synthesizer stores multiple versions of each phoneme for synthesis use. As the training speech is analyzed, multiple allophones of each phoneme are stored, along with feature information to be used for indexing and a weighting value based on the number of similar units already stored and the degree of similarity of the new unit to the stored units. During synthesis, a feature search locates the stored phoneme most suitable for use in constructing the output utterance.—DLR

6,366,884

43.72.Ja METHOD AND APPARATUS FOR IMPROVED DURATION MODELING OF PHONEMES

Jerome R. Bellegarda and Kim Silverman, assignors to Apple Computer, Incorporated
2 April 2002 (Class 704/266); filed 8 November 1999

This speech synthesis system uses a sum-of-products model to scale and average the durations of phonemes extracted from the training speech data. Minimum and maximum durations of the training phonemes and the number and position of the phonemes in the utterance form the basis of a

nonexponential, root sinusoidal transformation used to model phoneme durations in the synthesis output.—DLR

6,366,887

43.72.Ja SIGNAL TRANSFORMATION FOR AURAL CLASSIFICATION

William J. Zehner and R. Lee Thompson, assignors to the United States of America as represented by the Secretary of the Navy
2 April 2002 (Class 704/278); filed 12 January 1998

Certain auditory tasks, such as listening to sonar echoes, depend on the ability of the human listener to classify or categorize the signal in some meaningful way. This patent proposes a method of altering the signal so as to make it sound more speechlike and so easier for the perceptual system to make quick judgments of similarity or signal class. Certain temporal and spectral patterns are detected and their amplitudes and spectra are mapped to produce more speechlike amplitudes, spectra, and redundancy patterns.—DLR

6,366,885

43.72.Lc SPEECH DRIVEN LIP SYNTHESIS USING VISEME BASED HIDDEN MARKOV MODELS

Sankar Basu *et al.*, assignors to International Business Machines Corporation
2 April 2002 (Class 704/270); filed 27 August 1999

Video and audio speech data is analyzed to train either a hidden Markov model or a neural network in order to generate video frames with lip motions synchronized to a supplied audio sound track. During the training phase, audio and video data streams are simultaneously processed to determine a suitable phoneme classification. Video frames are selected directly according to cepstral feature similarities. There is a brief mention without further elaboration of a video smoothing process which would occur during the synthesis reconstruction.—DLR

6,363,348

43.72.Ne USER MODEL-IMPROVEMENT-DATA-DRIVEN SELECTION AND UPDATE OF USER-ORIENTED RECOGNITION MODEL OF A GIVEN TYPE FOR WORD RECOGNITION AT NETWORK SERVER

Stefan Besling and Eric Thelen, assignors to U.S. Philips Corporation
26 March 2002 (Class 704/270.1); filed in the European Patent Office 20 October 1997

Pattern recognition is enabled for a wide range of subjects and for many clients by selecting a recognition model from several recognition models of the same type using an adaptation profile to cover commonly used sequences and specific areas of interest. Selection is further enhanced by using the model improvement data provided by acoustic training with a few sentences from the user. Only one basic model, for a given type, and a number of much smaller adaptation models need be stored. Cited advantages include not having to store a specific model for each user, reusing recognition models for many users, and a reduced amount of training required for each user.—DAP

6,370,504

43.72.Ne SPEECH RECOGNITION ON MPEG/AUDIO ENCODED FILES

Gregory L. Zick and Lawrence Yapp, assignors to University of Washington
9 April 2002 (Class 704/251); filed 22 May 1998

For use in automatic video indexing applications, a technique is described capable of recognizing continuously spoken words in compressed MPEG/audio. Decompression of the MPEG/audio file and creation of an
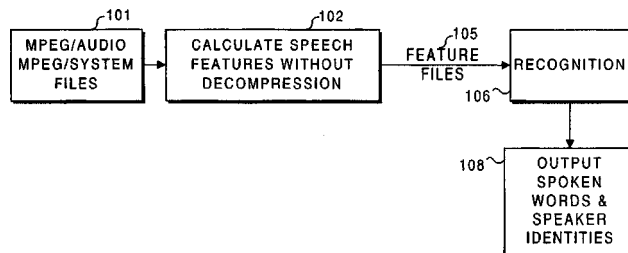
intermediate file are not required because training and feature recognition are performed based on the extracted subbands of the files using a hidden Markov model as a speech recognizer.—DAP

6,374,219

43.72.Ne SYSTEM FOR USING SILENCE IN SPEECH RECOGNITION

Li Jiang, assignor to Microsoft Corporation
16 April 2002 (Class 704/255); filed 20 February 1998

To date, speech recognition systems have treated silence as a special word in the lexicon. However, in an isolated speech recognition system, taking into account transitions from silence to other words and the reverse is computationally intensive. In this patent, a feature extraction module first divides words into codewords representing phonemes. Possible words are
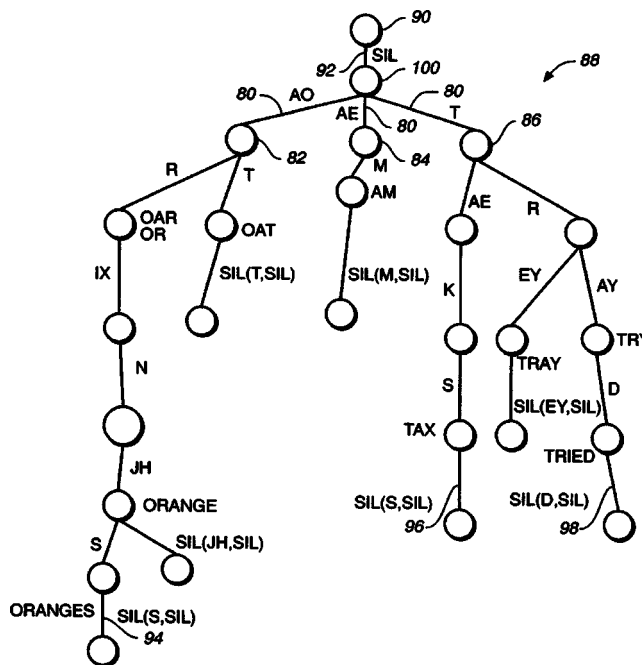
provided as a prefix tree including several phoneme branches connected at nodes (e.g., "Orange" in the figure). Several phoneme branches are bracketed by at least one input silence branch and at least one output silence branch. Optionally, several silence branches are provided in the prefix tree that represent context-dependent silence periods.—DAP

6,374,222

43.72.Ne METHOD OF MEMORY MANAGEMENT IN SPEECH RECOGNITION

Yu-Hung Kao, assignor to Texas Instruments Incorporated
16 April 2002 (Class 704/256); filed 16 July 1999

Speech recognition involves expanding a search tree according to the size of the vocabulary, frequently resulting in very large storage requirements. To reduce the search space and to speed up the search involved in comparing the input speech to speech models, slots with bad scores are removed from the storage space while expanding the search tree. These memory spaces are later replaced with slots that have better scores and are more likely to match the input speech. There are three levels of hidden Markov model (HMM) utilization when a speech frame enters: all the possible words in the sentence HMM are expanded by expanding their individual phone sequence in the lexicon HMM which requires, in turn, expanding their phonetic HMMs that contain acoustic observations.—DAP

6,403,870

43.75.Bc APPARATUS AND METHOD FOR CREATING MELODY INCORPORATING PLURAL MOTIFS

Eiichrio Aoki, assignor to Yahama Corporation
11 June 2002 (Class 84/609); filed in Japan 18 July 2000

Automatic composition has been attempted by various musicians since the creation of the digital computer. As usual with Yamaha patents, many critical details such as motive variation are not detailed (and are barely mentioned). The inventor seems totally unaware of the large body of work on using generative grammars for analysis and composition (e.g., Lerdahl and Jackendoff).—MK

6,392,137

43.75.Gh POLYPHONIC GUITAR PICKUP FOR SENSING STRING VIBRATIONS IN TWO MUTUALLY PERPENDICULAR PLANES

Osman K. Isvan, assignor to Gibson Guitar Corporation
21 May 2002 (Class 84/726); filed 27 April 2000

Since Fender's original patent in 1961, electric guitar manufacturers use magnetic pickups for ferromagnetic strings. It is well known that vibrating strings exhibit both horizontal and vertical modes, so more than 20 years
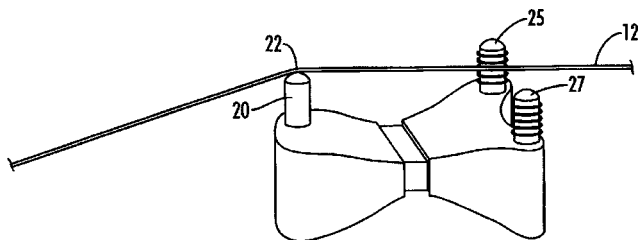
ago separate transducers for each mode were proposed. Here, the use of two sensors **25** and **27** is proposed. These are fed to an RMS scaler and mixer.—MK

6,380,468

43.75.Hi DRUM HAVING SHELL CONSISTING OF MORE THAN ONE KIND OF VIBRATORY ELEMENT ARRANGED IN PARALLEL WITH RESPECT TO SKIN

Fumihiro Shigenaga, assignor to Yamaha Corporation
30 April 2002 (Class 84/411 R); filed in Japan 30 September 1999

Drum materials affect the timbre of the hit as a factor of the material properties. So if the drum body is replaced with a composite, drummers are unhappy. The inventor proposes (in broken English: ''The difference in propagation sheep resulted in sound quality'') insertion of metal rods or bars in the shell to increase propagation speed.—MK

6,376,759

43.75.Mn ELECTRONIC KEYBOARD INSTRUMENT

Satoshi Suzuki, assignor to Yamaha Corporation
23 April 2002 (Class 84/615); filed in Japan 24 March 1999

A keyboard instrument has limited expressiveness—the action is fixed, the pitches fixed, etc. How can this be made more flexible so that keyboard performers can use their training and technique to control a synthesizer? The

MUSICAL EXPRESSIONS	SENSORS AND SWITCHES OF KEYBOARD					CONTROLS FOR ACTUALIZATION OF PERFORMANCE TECHNIQUES ON KEYBOARD	CONTROL FACTORS IN MUSICAL EXPRESSIONS
	TOUCH-HI	VELOCITY ON / KEY STROKE	HAMMER PRESSURE	KEY DEPRESSION	VELOCITY OFF / LEFT/RIGHT KEY		
TENUTO						EG CONTROL WITH KEY STROKE, TONE VOLUME (DECAY: HAMMER PRESSURE, SUSTAIN: KEY PRESSURE)	
MARCATO		●	●	●		SAME ABOVE	EG
STACCATO	●		●			KEY OFF BY TOUCH OFF	EG
SLUR			●			SUCCEED EG OF PRECEDING KEY BY SLUR PEDAL	EG
LEGATO		●	●	●		SUSTAIN KEY ON FURTHER LONGER THAN TENUTO	EG
PORTAMENTO	●					TOUCH TARGET SURFACE OF KEY AFTER KEY-ON	CONTINUOUS VARIATIONS OF PITCHES ONLY
GLISSANDO	●					SAME ABOVE	SEQUENTIAL VARIATIONS OF PITCHES ONLY
VIBRATO				●		VARIATIONS IN LEFT/RIGHT PRESSURES AFTER KEY ON	PITCH
TREMOLO						DEPRESSION OF KEY	ACCENT, REITERATION OF SAME NOTE
KOBUSI (OR REITERATION)	●					SMALL VARIATIONS IN PORTAMENTO	CONTINUOUS VARIATIONS OF PITCHES
CRESCENDO				●		CHANGE TONE VOLUME BY KEY DEPRESSION	TONE VOLUME CONTROL
DECRESCENDO		●		●		REVERSE TO CRESCENDO	TONE VOLUME CONTROL
TONE COLOR VARIATIONS				●		FILTER CONTROL BY KEY DEPRESSION	FILTER, EFF CONTROLS
REVERBERATION		●			●	CONTROL RELEASE RATE BY KEY-OFF VELOCITY	RR
RAPID PERFORMANCE IN PPP		●				TONE-GENERATION CONTROL BY STROKE POSITION	TONE VOLUME, TONE COLOR CONTROLS

answer presented here depends on (1) more pedals with pressure and velocity sensors and (2) a complex finite state machine that guides the instrument modes.—MK

6,380,469

43.75.Mn KEYBOARD MUSICAL INSTRUMENT EQUIPPED WITH KEY ACTUATORS ACCURATELY CONTROLLING KEY MOTION

Haruki Uehara, assignor to Yamaha Corporation
30 April 2002 (Class 84/439); filed in Japan 21 June 2000

Yet another Disklavier™ patent, this time it's devoted just to the key mechanism. As shown, the solenoids **240**, **241**, operated by controller **230**,
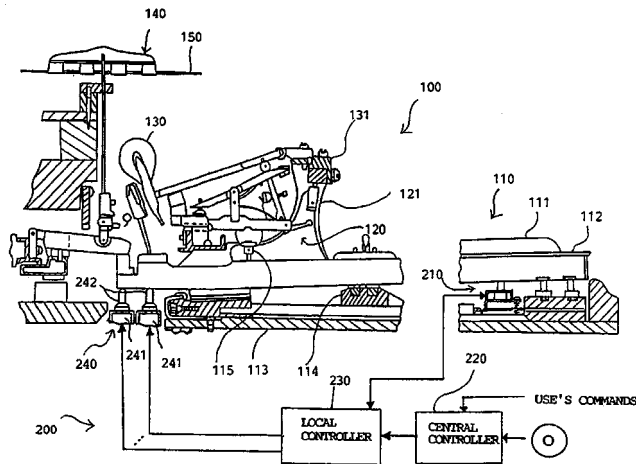
can actuate key **112**, which will control action **120** and hammer **130**. The controller can also sense key motions via sensors **210**.—MK

6,392,136

43.75.Mn MUSICAL TONE GENERATION STRUCTURE OF ELECTRONIC MUSICAL INSTRUMENT

Masao Kondo *et al.*, assignors to Yamaha Corporation
21 May 2002 (Class 84/718); filed in Japan 19 June 2000

In a computer-controlled piano like the Disklavier™, the strings can be damped so that no sound is audible. If so, then the electronics can generate
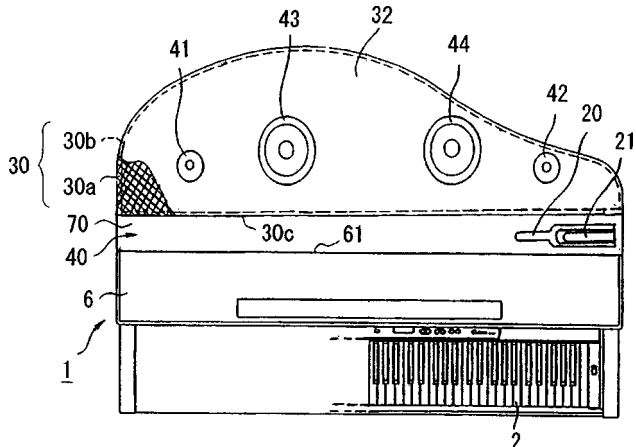
the sound, but now the problem is how to make it "originate" from the piano. The solution is to use a set of loudspeakers in the lid. Uprights need not apply.—MK

6,403,872

43.75.Mn KEYBOARD MUSICAL INSTRUMENT FAITHFULLY REPRODUCING ORIGINAL PERFORMANCE WITHOUT COMPLICATED TUNING AND MUSIC DATA GENERATING SYSTEM INCORPORATED THEREIN

Shigeru Muramatsu *et al.*, assignors to Yamaha Corporation
11 June 2002 (Class 84/724); filed in Japan 16 December 1999

This is yet another Disklavier™ patent, this time focusing on the hammer/string interface. Eleven different embodiments are disclosed.—MK

6,380,470

43.75.St TRAINING SYSTEM FOR MUSIC PERFORMANCE, KEYBOARD MUSICAL INSTRUMENT EQUIPPED THEREWITH AND TRAINING KEYBOARD

Yuji Fujiwara *et al.*, assignors to Yamaha Corporation
30 April 2002 (Class 84/470 R); filed in Japan 13 April 1999

The principle behind this invention is simply this: a MIDI stream with on/off events can light up LEDs on the tops of the keys. Among the embodiments is a ten-key keyboard reminiscent of Englebart's chord-set. The English in the patent is almost unbearable, e.g., "The reason why the beginners feel hard is that optical indicators are too many to quickly search them for the radiation."—MK

6,392,132

43.75.St MUSICAL SCORE DISPLAY FOR MUSICAL PERFORMANCE APPARATUS

Haruki Uehara, assignor to Yamaha Corporation
21 May 2002 (Class 84/477 R); filed in Japan 21 June 2000

Essentially, this is an automatic page turner for a piano player. Using an automatic speech recognition system, the performer speaks a command and the display changes accordingly. However, good human page turners are silent and use automatic nod recognition.—MK

6,390,923

43.75.Wx MUSIC PLAYING GAME APPARATUS, PERFORMANCE GUIDING IMAGE DISPLAY METHOD, AND READABLE STORAGE MEDIUM STORING PERFORMANCE GUIDING IMAGE FORMING PROGRAM

Kensuke Yoshitomi *et al.*, assignors to Konami Corporation
21 May 2002 (Class 463/43); filed in Japan 1 November 1999

Continuing the tradition of arcade contest of man versus machine, this patent compares human performance on an artificial drum or guitar against a known template. This is reminiscent of United States Patent 6,342,665 [reviewed in J. Acoust. Soc. Am. **112**(3), 803 (2002)].—MK

6,392,135

43.75.Wx MUSICAL SOUND MODIFICATION APPARATUS AND METHOD

Toru Kitayama, assignor to Yamaha Corporation
21 May 2002 (Class 84/622); filed in Japan 7 July 1999

This could have been an interesting and educational patent. But it lacks specificity and the translation of Japanese to English is poor including "truck" for "track," "memorized" for "stored," and so forth. The patent concerns the reuse of acoustic data by a MIDI stream digital instrument. The
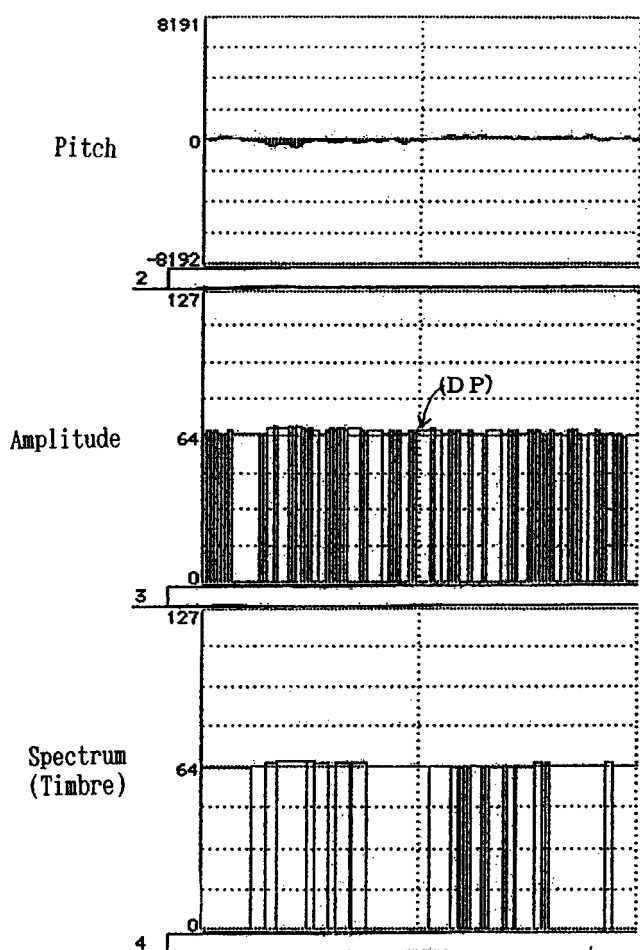
acoustic data is analyzed into amplitude and frequency, with the frequency mistakenly called ''timbre.'' The signal is also analyzed for attack, sustain, decay, and release by unknown and undisclosed methods. After being stored, these parameters can be recombined to make new sounds. If your only tool is a MIDI hammer, then you see all instruments as MIDI nails.—MK

6,403,871

43.75.Wx TONE GENERATION METHOD BASED ON COMBINATION OF WAVE PARTS AND TONE-GENERATING-DATA RECORDING METHOD AND APPARATUS

> **Masahiro Shimizu and Hideo Suzuki, assignors to Yamaha Corporation**
> **11 June 2002 (Class 84/622); filed in Japan 27 September 1999**

Essentially, this patents the user interface for a waveform editor. Each waveform has the following time domain representations: waveform, pitch, amplitude, ''spectral template,'' and ''time template.'' These names are completely arbitrary since Yamaha says nothing about how these ''templates'' are created from acoustic sounds. Further, they say nothing about how to resynthesize notes from this representation. Perhaps this will become clear in a later patent.—MK

6,390,995

43.80.Gx METHOD FOR USING ACOUSTIC SHOCK WAVES IN THE TREATMENT OF MEDICAL CONDITIONS

> **John A. Ogden and John F. Warlick, assignors to Healthtronics Surgical Services, Incorporated**
> **21 May 2002 (Class 601/2); filed 25 June 1999**

The idea of this method, intended for medical treatment of a variety of pathological conditions associated with osseous or musculoskeletal environments, is to apply a sufficient number of acoustic shock waves to the site of a pathological condition to generate micro-disruptions, nonosseous tissue stimulation, increased vascularization, and circulation and induction of growth factors to induce or accelerate a body's healing processes and responses.—DRR

6,402,965

43.80.Gx SHIP BALLAST WATER ULTRASONIC TREATMENT

> **Patrick K. Sullivan *et al.*, assignors to Oceanit Laboratories, Incorporated**
> **11 June 2002 (Class 210/748); filed 13 July 2000**

A ship's ballast water is pumped through intake and outtake manifolds which are internally lined with piezoelectric material to create long continuous electroacoustic transducers within these pipes. The high-intensity sound fields created by these transducers can potentially destroy micro-organisms, algae, diatoms, veligers, fish larvae, and plankton, thus preventing the introduction of nonindigenous species into new and unwelcome environments.—WT

6,396,402

43.80.Ka METHOD FOR DETECTING, RECORDING AND DETERRING THE TAPPING AND EXCAVATING ACTIVITIES OF WOODPECKERS

> **Robert Paul Berger and Alexander Leslie McIlraith, assignors to Myrica Systems Incorporated**
> **28 May 2002 (Class 340/573.2); filed 12 March 2001**

The device, which consists of a housing with mounting flanges for direct attachment to a utility pole or the like, can receive vibrations resulting from woodpeckers' activities. A transducer attached to the mounting wall of the housing converts the vibrations into signals. A circuit compares the vibrations with a long-term average and emits an output in response to detection above a threshold. The outputs are counted and, if the number within a predetermined time exceeds a preset minimum, a sound transmitter is actuated to emit a deterrent sound. A memory contains various deterrent sounds, including those usually made by predators, to discourage the woodpeckers. The power source consists of a solar cell charging a battery.—DRR

6,379,304

43.80.Qf ULTRASOUND SCAN CONVERSION WITH SPATIAL DITHERING

> **Jeffrey M. Gilbert *et al.*, assignors to TeraTech Corporation**
> **30 April 2002 (Class 600/447); filed 23 November 1999**

This scan conversion accepts lines of ultrasonic b-scan echoes in a polar format and produces data in a Cartesion format by using either software or hardware in a computer that is connected to an ultrasonic scan head. Ultrasonic echo, positional, and other data are sent from the scan head to the computer. The conversion uses spatial dithering to approximate pixel values that fall between two input data points.—RCW

6,398,734

43.80.Qf ULTRASONIC SENSORS FOR MONITORING THE CONDITION OF FLOW THROUGH A CARDIAC VALVE

George E. Cimochowski and George W. Keilman, assignors to VascuSense, Incorporated
4 June 2002 (Class 600/454); filed 12 August 1999

A parameter indicative of the condition of a cardiac valve is established by monitoring blood flow and/or velocity in a vessel that is coupled to the cardiac valve or in a chamber adjacent to an artificial heart valve. One or more ultrasonic transducers are supplied either in a cuff or a wall arrangement deployed about a cardiac vessel to monitor the parameter with respect to a natural or artificial valve. Transient or Doppler measurements are made using an appropriate number of transducers to determine either blood volumetric flow or velocity. Various implantable electronic circuits enable a transducer to be driven and to receive an ultrasonic signal indicative of the status of the blood flow and thus, the condition of the heart valve. A radio frequency coil coupled to an external power supply and monitoring console conveys power to the ultrasonic transducers and receives the blood flow data signals.—DRR

6,405,069

43.80.Qf TIME-RESOLVED OPTOACOUSTIC METHOD AND SYSTEM FOR NONINVASIVE MONITORING OF GLUCOSE

Alexander A. Oraevsky and Alexander A. Karabutov, assignors to Board of Regents, the University of Texas System
11 June 2002 (Class 600/407); filed 6 October 1999

A wideband optoacoustic transducer measures the spatial in-depth profile of optically-induced acoustic pressure transients in tissues in order to
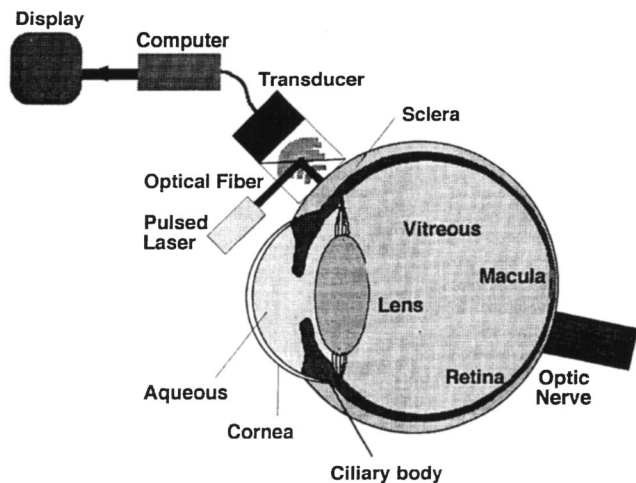
determine the laser-induced profile of absorbed optical distribution. This type of technique can be applied to monitor glucose concentration in various human or nonhuman tissues, cell cultures, solutions, or emulsions.—DRR

6,379,306

43.80.Qf ULTRASOUND COLOR FLOW DISPLAY OPTIMIZATION BY ADJUSTING DYNAMIC RANGE INCLUDING REMOTE SERVICES OVER A NETWORK

Michael J. Washburn *et al.*, assignors to General Electric Company
30 April 2002 (Class 600/454); filed 27 December 1999

Values corresponding to color flow signals from an ultrasonic Doppler imaging instrument are stored in a memory. A dynamic range compression scheme based on an analysis of the signals in the memory is used to determine a second set of values that are stored and used for display locally as well as at a remote facility via communication over a network.—RCW

6,394,955

43.80.Sh DEVICE ATTACHABLE TO A THERAPEUTIC HEAD FOR ADJUSTABLY HOLDING AN ULTRASOUND TRANSDUCER, AND THERAPEUTIC HEAD IN COMBINATION WITH SUCH A DEVICE

Lucas Perlitz, assignor to Siemens Aktiengesellschaft
28 May 2002 (Class 600/439); filed in Germany 1 February 1999

The device provides adjustability in holding an ultrasonic transducer and it can be attached at a therapeutic head that emits acoustic waves converging into a focus. The device has at least one element that can be swiveled about an axis. The ultrasonic transducer is at least indirectly attachable at the element such that its acoustic axis, as well as the swivel axis when the device is attached, proceed substantially through the focus of the therapeutic head.—DRR

6,394,956

43.80.Sh RF ABLATION AND ULTRASOUND CATHETER FOR CROSSING CHRONIC TOTAL OCCLUSIONS

Chandru V. Chandrasekaran *et al.*, assignors to Scimed Life Systems, Incorporated
28 May 2002 (Class 600/439); filed 29 February 2000

This catheter combines an ultrasound transducer and a rf ablation electrode. The ultrasound transducer transmits into and receives echos from a blood vessel. The echo signals are processed and used to produce an image of the tissue surrounding the catheter. A driveshaft rotates the transducer to

yield a 360-degree view of the vessel wall. At the distal end of the driveshaft is an electrode that is coupled to a rf generator delivering rf energy for ablating occluding material inside the vessel.—DRR

6,398,753

43.80.Sh ULTRASOUND ENHANCEMENT OF PERCUTANEOUS DRUG ABSORPTION

David H. McDaniel, Virginia Beach, Virginia
4 June 2002 (Class 604/22); filed 9 October 1998

This is a system for enhancing and improving the transcutaneous delivery of topical chemicals or drugs. A disposable container contains a substantially sterile unit dose of an active agent adapted for a single use in a medical instrument. The unit dose is formulated to enhance transport of the active agent through mammalian skin when the active agent is applied to skin that is exposed to light and/or ultrasound.—DRR

6,384,516

43.80.Vj HEX PACKED TWO DIMENSIONAL ULTRASONIC TRANSDUCER ARRAYS

John Douglas Fraser, assignor to ATL Ultrasound, Incorporated
7 May 2002 (Class 310/334); filed 21 January 2000

These transducer arrays are comprised of elements closely packed in a
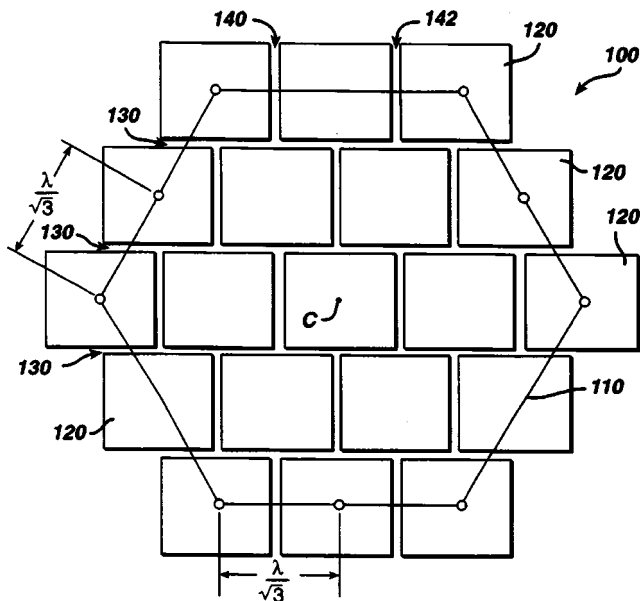
hexagonal configuration such as shown in the figure.—RCW

6,390,981

43.80.Vj ULTRASONIC SPATIAL COMPOUNDING WITH CURVED ARRAY SCANHEADS

James R. Jago, assignor to Koninklijke Philips Electronics N.V.
21 May 2002 (Class 600/443); filed 23 May 2000

Spatial compounding is accomplished by beam steering that depends on both the curvature of the array and electronic phasing in ways advanta-

geous for beamforming and image registration coefficients, uniformity in sampling, reduction of speckle, and achievement of a large compounded area.—RCW

6,390,984

43.80.Vj METHOD AND APPARATUS FOR LOCKING SAMPLE VOLUME ONTO MOVING VESSEL IN PULSED DOPPLER ULTRASOUND IMAGING

Lihong Pan *et al.*, assignors to GE Medical Systems Global Technology Company, LLC
21 May 2002 (Class 600/453); filed 14 September 2000

A gate selecting a volume for Doppler analysis is locked onto the selected vessel by using pattern matching in images from successive frames processed in the space domain or the Fourier domain to determine how much a vessel in the image has translated and rotated from one frame to the next.—RCW

6,394,967

43.80.Vj METHOD AND APPARATUS FOR DISPLAYING LUNG SOUNDS AND PERFORMING DIAGNOSIS BASED ON LUNG SOUND ANALYSIS

Raymond L. H. Murphy, Wellesley, Massachusetts
28 May 2002 (Class 600/586); filed 30 October 2000

This lung sound diagnostic system contains a plurality of transducers that may be placed at various sites around the patient's chest. The microphones are coupled to signal processing circuitry and A/D converters that supply digitized data to a computer system. A program in the computer collects and organizes the data and formats the data into a combinatorial
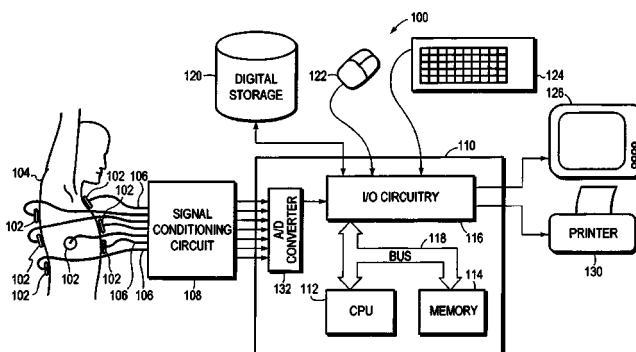
display that can be shown on a monitor screen or printed out. The system may also include application programs for detecting and classifying abnormal sounds. An analysis program can compare selected criteria corresponding to the detected abnormal sounds with predefined thresholds in order to provide a likely diagnosis.—DRR

6,396,931

43.80.Vj ELECTRONIC STETHOSCOPE WITH DIAGNOSTIC CAPABILITY

Cicero H. Malilay, Los Angeles, California
28 May 2002 (Class 381/67); filed 8 March 1999

This stethoscope is a self-contained, hand-held, electronic unit that includes a built-in chestpiece, speaker, and visual monitor. It includes a memory containing prerecorded heart and lung sounds along with a brief description of the malady producing the sounds so that a technician may compare the actual sounds with the prerecorded sounds and obtain a suggested diagnosis on the monitor.—DRR

6,398,731

43.80.Vj METHOD FOR RECORDING ULTRASOUND IMAGES OF MOVING OBJECTS

Bernard M. Mumm *et al.*, assignors to Tomtec Imaging Systems GmbH
4 June 2002 (Class 600/437); filed in Germany 25 July 1997

Images of a moving object are acquired with a moving transducer. Based on the amount of object movement, images are either not acquired or not processed. Images not processed are omitted when the images are assembled and displayed.—RCW

6,398,733

43.80.Vj MEDICAL ULTRASONIC IMAGING SYSTEM WITH ADAPTIVE MULTI-DIMENSIONAL BACK-END MAPPING

Constantine Simopoulos *et al.*, assignors to Acuson Corporation
4 June 2002 (Class 600/443); filed 24 April 2000

This back-end mapping uses beamformed signals after detection. The processing consists of logarithmic compression followed by a mapping based on the system noise level and a target display value of soft-tissue echoes. The mapping includes gain and dynamic range.—RCW

6,398,735

43.80.Vj DETECTING A RELATIVE LEVEL OF AN ULTRASOUND IMAGING CONTRAST AGENT

David W. Clark, assignor to Koninklijke Philips Electronics N.V.
4 June 2002 (Class 600/458); filed 7 March 2000

The relative level of an ultrasound contrast agent is detected by determining a level from ultrasonic echoes produced in a region with contrast agent present, determining a level of echoes from the region after destruction of the contrast agent, and forming the ratio of the two levels.—RCW

Wave impedances of drill strings and other periodic media

Douglas S. Drumheller

Geothermal Research Department, Sandia National Laboratory, P.O. Box 5800, Albuquerque,
New Mexico 87185-1033

It is commonly known that wave reflections are caused by abrupt spatial variations in the physical parameter called *wave impedance*. When a material contains a spatially periodic distribution of wave impedances some very interesting and complex wave propagation phenomena will occur. Two examples of such periodic structures immediately come to mind: the first is a sandwiched structure of two types of plates, say for example, identical layers of thin steel plates interspersed with identical thick aluminum plates; and the second is a large number of identical long thin pipes that are connected from end to end with identical short heavy threaded couplings. The pipe assembly is our primary concern here because it represents the drill string, used worldwide to drill for natural energy resources. We want to understand how waves propagate through drill strings because we want to use them as a means of communication. But while the second structure is our primary concern, it is the study of the first structure, composed of layers, that is the truly historical problem and the source of much of our understanding of this rich set of wave physics. Traditionally, wave propagation in periodic media has been studied as an eigenvalue problem. The eigenvalues themselves yield information about phase velocities, group velocities, passbands, and stopbands. Most often the analysis has stopped there and the eigenvectors have been ignored. Here we turn our attention to the eigenvectors, using them to evaluate the impedance of the periodic structure with particular emphasis on the periodic drill string. As you might expect the impedance of the drill string is a complex number, which is evaluated from a very complicated expression. However, we have discovered that the impedance at two physical locations along the length of each piece of drill pipe in the drill string always reduces to a real number. This is immensely important because it allows us to match the impedance of the drill string to our communication devices. We show how this leads to the effective design of repeaters, noise cancelers, wave terminators, and quarter-wave transformers for a drill-string communication system. © *2002 Acoustical Society of America.*
[DOI: 10.1121/1.1513365]

PACS numbers: 43.20.Bi, 43.20.El, 43.20.Mv, 43.60.Bf [DEC]

I. INTRODUCTION

Over recent years we have developed a communication system that uses extensional stress waves in hollow steel drill pipe to carry encoded data (for example, see Drumheller[1]). Drill pipe is of course used to drill for natural gas and oil as well as other natural resources such as geothermal energy stored in hot subterranean fluids. The devices we are developing will be used to transmit data back to the surface from instruments housed in the drill string near the bit. Other so-called "down-hole" communication systems are already employed by drilling companies because drillers would like to know where they are heading. They would also like to know some of the formation characteristics. For example, is oil present?

Obviously it is also possible to establish a communication link with a data cable stretched down the hollow interior of the drill pipe, but the cable deployment interrupts the drilling process. As a result it is not economical. The commonly used alternative is to transmit the data as a sequence of pressure pulses in the well mud. This is a very slow method of communication, and unless data compression methods are employed the data-transmission rate is less than 1 baud. Also it doesn't always work especially if gas is injected into the mud. That is becoming a more common practice called under-balanced drilling.

Our "acoustical telemetry system," which really uses extensional stress waves, bypasses many of these problems. A 10-W transmitter can easily communicate at 10 to 100 baud even without employing data compression methods. But it has range limitations. We know this method can be used to communicate over distances in excess of 10 000 feet, but drilling projects are getting deeper. Some projects are reaching beyond 25 000 feet. The answer to this problem is to use repeaters. From the standpoint of compatability with standard drilling processes, this is possible because the repeater would be totally contained within the wall of the drill pipe, and it would only require small amounts of electrical energy ($\leqslant 100$ mW) that are available from modest sized battery packs.

The crux of the successful design of a repeater is to reduce what is often called *injection loss*. This term describes the following problem. Suppose a wave propagates along the drill string where it encounters a repeater. Unless the repeater is carefully designed some of the energy of this incident wave will be reflected back into the drill pipe. The remainder of the signal will then be injected into the repeater in a weakened state that is more difficult to detect. Likewise, after we

measure this signal we can use a phased array of transducers within the repeater to relay the message in a specified direction, but as that wave tries to leave the repeater a portion of it will also be reflected; that is, the repeater will be unable to inject all of its energy back into the drill pipe. The injection losses suffered by waves trying to get into and out of the repeater can be significant. As a penalty for ignoring this issue we might actually have to double the number of repeaters in the system.

II. ANALYSIS OF IMPEDANCE

We can solve the injection-loss problem by matching the wave impedance of the repeater to that of the drill pipe. Indeed as we shall see the impedance of the repeater is easily characterized as that of a uniform thick-walled cylinder, which is the product of the mass density, sound speed, and cross-sectional area of the cylinder wall. In terms of the usual electrical analogy for these systems, the repeater impedance is a real number and therefore purely resistive. (See p. 9 of Kino.[2])

In contrast the computation of the impedance of the drill pipe is far more difficult because it is a periodic structure. It is composed of individual 30-ft joints of hollow tubing threaded together with relatively massive connections called tool joints. In fact the impedances of the tool joints are about five times greater than the impedances of the tubes. This forms a one-dimensional periodic structure of hollow cylinders connected in a straight line along their respective central axes. The array exhibits classical characteristics that are similar to those of an electrical comb filter. This array has already been studied in detail as a classical eigenvalue problem in Drumheller[3] and Barnes and Kirkwood.[4] (You should note an important difference in these works. Barnes and Kirkwood mistakenly use the longitudinal velocity in their calculations rather than the bar velocity.) Indeed, we typically prefer to communicate with a carrier frequency of either 635 Hz, which is the center of the third passband, or 920 Hz, which is the center of the fourth passband. Next we examine the eigenvectors associated with this eigenvalue solution. They yield the solution for the impedance of the drill string. In general, we shall find that this impedance is a complex number meaning the drill string has a reactive impedance that cannot be matched to the purely resistive impedance of the repeater. (As we shall see a purely resistive impedance means the force and velocity of the material are in phase while the presence of any reactive component will place this quantities out of phase.) However, at particular points along the length of the drill string, its impedance is also purely resistive and therefore it is possible to match the impedance of the repeater to that of the drill string at these locations. (This is a particularly attractive approach because as we have said the wave impedance is proportional to the cross-sectional area of the cylindrical wall, and that parameter is easily adjusted during the design and actual fabrication of the repeater.)

It is important to notice that the drill-string problem is a special case of a larger class of problems. Léon Brillouin wrote a classical text about these solutions in 1946.[5] Indeed the phenomena exhibited by the drill string is often called
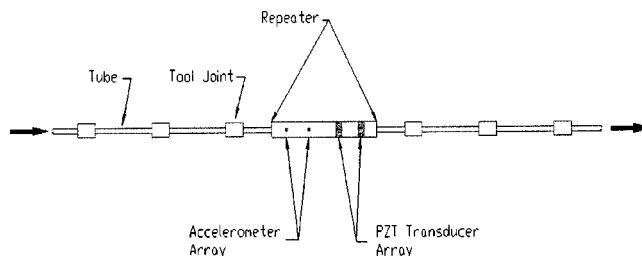
FIG. 1. A repeater mounted in a drill string.

Brillouin scattering, and it's a special case of what he calls the ''one-dimensional mechanical lattice.'' In his book he says, ''The one-dimensional mechanical lattice is an academic rather than a practical problem, and the only important instance of one-dimensional structures is found in electric lines....'' We shall see that on this one minor point, Brillouin was wrong. The injection loss problem gives us an opportunity to apply relatively abstract wave physics to an extremely important commercial application.

A. The repeater

Repeaters can be constructed by placing a pair of accelerometers and a pair of piezoelectric PZT transmitters into a steel housing. (See Fig. 1.) We use the accelerometers to measure weak waves approaching from the left. After interpreting the data in this signal we use the PZT transducers to broadcast a much stronger message signal to the right. (As an alternate approach we could use the amplified accelerometer signal to drive the PZT transmitters directly. We call this a *wave amplifier*. It is discussed in the Appendix; however, as we shall see this device is inherently unstable in our application.) The virtue of using PZT transmitters is that relative to other devices such as magnetostrictive terfenol, they are inexpensive, energy efficient, easy to construct, and simple to power. But most importantly they can be formed into continuous rings that surround the central core of the repeater housing. In this way the impedance of the PZT stack can be very closely matched to that of its steel housing. Indeed we have designed systems in which the wave impedances of the different repeater elements are so closely matched that it is reasonable to model all of them as a single homogeneous hollow-circular cylinder. (See Drumheller.[6,7]) Thus to solve the injection-loss problem we need only match the impedance of this hollow cylinder to that of the drill pipe. We shall see that the simplest way of doing this is to adjust the cross-sectional area of the cylinderical wall of the repeater housing.

Determination of the impedance of this hollow cylinder is straight forward. Consider the following relationships:

$$F/A = E \frac{\partial u}{\partial x}, \quad \frac{\partial F}{\partial x} = \rho A a, \tag{1}$$

where F is the axial force (positive in tension) acting on the cross-sectional area A of the cylindrical wall. The cylinder has a mass density of ρ and a Young's modulus of E. In terms of the position x and time t, the axial motion of the cylinder is described by its material displacement u, material velocity $v \equiv \partial u/\partial t$, and material acceleration $a \equiv \partial^2 u/\partial t^2$.

Douglas S. Drumheller: Wave impedances of drill strings

The first expression in Eqs. (1) is Hooke's law for the axial deformation of the cylinder, and the second expression is Newton's second law of motion. We can combine these two equations to obtain the following wave equation:

$$\frac{\partial^2 u}{\partial t^2} = c^2 \frac{\partial^2 u}{\partial x^2}, \tag{2}$$

where

$$c = \sqrt{\frac{E}{\rho}} \tag{3}$$

is the speed of sound for an extensional wave propagating in a bar. As an example, for steel $c = 5.13$ km/s. If the characteristic wavelength of the propagating wave is long in comparison to the outside diameter of the cylinder, Hooke's law accurately represents the extensional motion produced by the wave. A typical outside diameter for the steel drill-string components in a well is 6 inches. Waves with frequencies below 8 kHz have wavelengths that are more than four times this diameter, and they are accurately modeled by this wave equation.

The well-known d'Alembert solution to the wave equation is

$$u(x,t) = f(x - ct) + g(x + ct), \tag{4}$$

where $f(\cdot)$ and $g(\cdot)$ are arbitrary functions of the special combinations $x \pm ct$ of time and position. (See p. 105 of Drumheller.[8]) From the d'Alembert solution we obtain the equally well-known result for simple waves,

$$F = \mp zv. \tag{5}$$

Here the $-$ and $+$ signs are used, respectively, for simple waves traveling either in the positive-x or negative-x directions, and

$$z \equiv \rho c A \tag{6}$$

is the wave impedance of the cylinder. The wave impedance z is the key to the injection-loss problem because it relates the force F to the material velocity v. These two variables are continuous across the interfaces between the different cylindrical elements of our one-dimensional drill string. As with the traditional solutions for waves in infinite media, the amplitudes of the reflected and transmitted waves at these interfaces are solely determined by the wave impedances of the two cylinders adjacent to each interface. *If the impedance remains constant across an interface, there is no reflection and hence there is no injection loss.*

You will notice that the cross-sectional area A of the cylindrical wall appears in the expression for the wave impedance. Thus even if two adjoining cylinders are made from the same material, a wave reflection will occur if they have different wall areas. We see that it is also possible that the intersection of two cylinders of different material will not produce a reflection provided their wall areas are adjusted to make their impedances equal.

The wave impedance z of a cylinder is a real number. In the nomenclature of common electrical analogies for linear wave problems, we say that this impedance is purely resistive. Because we are interested in wave reflections at the
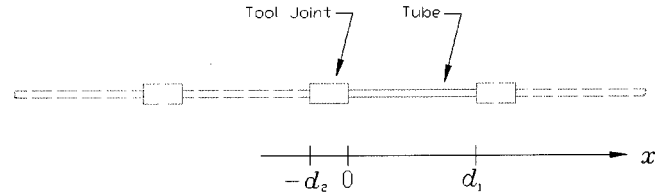
FIG. 2. The coordinate system for drill pipe.

interface between the cylinder representing the repeater and the drill pipe assembly, we shall now turn our attention to evaluating the impedance of the drill pipe. For it we find a far more complicated situation.

B. The drill pipe

While we seem to be concerned about the relative impedances of the repeater and the drill string, we do not seem to be worried about the changes in impedance between the tubes and tool joints in the drill string itself. However, that is not true. Indeed, the hundreds of tool-joint connections in a typical drill string cause a complex set of wave reflections that form the comb filter effect we mentioned earlier. This forces us to broadcast narrow-band signals that fall within the frequency boundaries of the passbands of this periodic structure. Indeed we already know that the frequency characteristics of the periodic drill string are analyzed as an eigenvalue problem. (See Ref. 3.) Here we shall learn that the solution to the injection loss problem is found in the eigenvectors of the same analysis. While we shall briefly review the equations that form the matrix components of this analysis, you should refer to Ref. 3 for more details.

Consider any adjacent pair of cylinders of the drill string; that is, a cylinder that represents a tool joint and a neighboring cylinder that represents a tube. They are illustrated with solid lines in Fig. 2. Notice their common interface is located at $x = 0$. In the tool joint $x < 0$, and in the tube $x > 0$. The length, cross-sectional wall area, mass density, and speed of sound of each cylinder are d_s, a_s, ρ_s, and c_s where $s = 1,2$ denotes the tube and tool joint, respectively. Each of these cylinders is represented by a wave equation similar to Eq. (2). We shall examine the following time-harmonic solutions for the force and the material velocity in each cylinder:

$$F_s(x,t) = \mathcal{F}_s(x,\omega) \exp(i\omega t), \tag{7}$$

$$v_s(x,t) = \mathcal{V}_s(x,\omega) \exp(i\omega t), \tag{8}$$

in which

$$\mathcal{F}_s(x,\omega) = A_s \exp(-iK_s m) + B_s \exp(iK_s m), \tag{9}$$

$$z_s \mathcal{V}_s(x,\omega) = A_s \exp(-iK_s m) - B_s \exp(iK_s m), \tag{10}$$

and

$$z_s = \rho_s c_s a_s, \tag{11}$$

$$K_s = \omega / z_s, \tag{12}$$

$$m = \begin{cases} \rho_2 a_2 x, & x \leq 0, \\ \rho_1 a_1 x, & x > 0. \end{cases} \tag{13}$$

Here A_s and B_s are arbitrary constants, ω is the circular frequency, and $i^2 = -1$. Two sets of conditions are applied to these solutions. The first set of conditions requires that the force and material velocity are continuous at $x=0$. The second set of conditions arises from the Floquet theorem (see Brillouin,[5] p. 173) which says that the solutions must have the following form:

$$\mathcal{F}_s(x,\omega) = f_s(m,\omega)\exp(-ikmd/r), \tag{14}$$

$$z_s \mathcal{V}_s(x,\omega) = g_s(m,\omega)\exp(-ikmd/r), \tag{15}$$

where k is the complex wave number and

$$r = r_1 + r_2, \tag{16}$$

$$d = d_1 + d_2, \tag{17}$$

$$r_s = \rho_s a_s d_s. \tag{18}$$

Each set of functions $f_s(x,\omega)$ and $g_s(x,\omega)$ must form a periodic field of period d. In Ref. 3 we show how these conditions lead to the two requirements of continuity

$$f_2(0,\omega) = f_1(0,\omega), \tag{19}$$

$$(1/z_2)g_2(0,\omega) = (1/z_1)g_1(0,\omega), \tag{20}$$

and the two requirements of periodicity

$$f_2(-d_2,\omega) = f_1(d_1,\omega), \tag{21}$$

$$(1/z_2)g_2(-d_2,\omega) = (1/z_1)g_1(d_1,\omega). \tag{22}$$

Taken together these four conditions form the following eigenvalue problem:

$$[C_{ij}]\begin{bmatrix} A_1/z_1 \\ B_1/z_1 \\ -A_2/z_2 \\ -B_2/z_2 \end{bmatrix} = \begin{bmatrix} 0 \\ 0 \\ 0 \\ 0 \end{bmatrix}, \tag{23}$$

where

$$[C_{ij}] = \begin{bmatrix} z_1 & z_1 & z_2 & z_2 \\ 1 & -1 & 1 & -1 \\ z_1 e^{\alpha_1 r_1} & z_1 e^{\beta_1 r_1} & z_2 e^{-\alpha_2 r_2} & z_2 e^{-\beta_2 r_2} \\ e^{\alpha_1 r_1} & -e^{\beta_1 r_1} & e^{-\alpha_2 r_2} & -e^{-\beta_2 r_2} \end{bmatrix}, \tag{24}$$

and

$$\alpha_s = i(kd/r - K_s), \tag{25}$$

$$\beta_s = i(kd/r + K_s). \tag{26}$$

Equations (23) completely characterize the behavior of the drill pipe within the context of our wave theory. [This eigenvalue formulation for the drill string problem is nearly identical to the formulation for longitudinal stress waves propagating normal to layers of a periodically layered medium. (See p. 120 in Bedford and Drumheller.[9]) Two changes are required to obtain the formulation for layered media. First normalize the cross-sectional wall areas. ($A_s = 1$.) Then replace the expression for the bar velocity, $c_s = \sqrt{E_s/\rho_s}$ by the longitudinal velocity $c_s = \sqrt{(\lambda_s + 2\mu_s)/\rho_s}$ where λ_s and μ_s are the Lamé material constants of the layer. As a consequence all of the results that we will obtain for the drill string

TABLE I. Properties of steel drill pipe, $\rho = 7.89$ Mg/m^3 and $c = 5.13$ km/s.

Component	d_s (m)	A_s (mm^2)	z_s (Mg/s)
Tube ($s=1$)	8.84	3400	138
Tool joint ($s=2$)	0.61	16 000	649

apply equally well to the layered medium. However, from a practical standpoint one significant difference does exist. The wave impedance of the drill string is easily modified by alteration of the cross-sectional wall area, but the same cannot be said for the layered medium. Here the wave impedance is limited to the discrete values associated with available materials.]

We now face the following task. For any real value of the circular frequency ω, we must evaluate the complex wave number k and the four constants, A_1, A_2, B_1, and B_2. To do this we first assume a value of the circular frequency. Then for a nontrivial solution of Eqs. (23) to exist, the determinant of $[C_{ij}]$ must be zero. Evaluation of this determinant yields the following characteristic equation:

$$\cos kd = \cos(\omega d_1/c_1)\cos(\omega d_2/c_2) - \tfrac{1}{2}(z_1/z_2$$
$$+ z_2/z_1)\sin(\omega d_1/c_1)\sin(\omega d_2/c_2). \tag{27}$$

We use this transcendental equation to evaluate the eigenvalue k. We find that over certain regions of ω, k has real values. These frequency regions are called passbands. Over the remaining values of ω that lie between the passbands, k has complex values. These regions are called stopbands.

Consider a typical drill string whose properties are listed in Table I. By using Eq. (27) we calculate the passbands and stopbands of this drill string. (See Fig. 3.) The shaded regions are the stopbands, and the clear areas between them are the passbands. Both the passbands and the stopbands are numbered in sequence from the left. For example, 600 Hz falls in passband 3, and 500 Hz falls in stopband 2. We shall only illustrate the solutions within each passband where two quantities are shown. The phase velocity $c_p \equiv \omega/k$ is illustrated as a dashed line, and the group velocity $c_g \equiv d\omega/dk$ is illustrated as a solid line. Notice that the group velocity drops to zero at the edges of the passbands. This means that
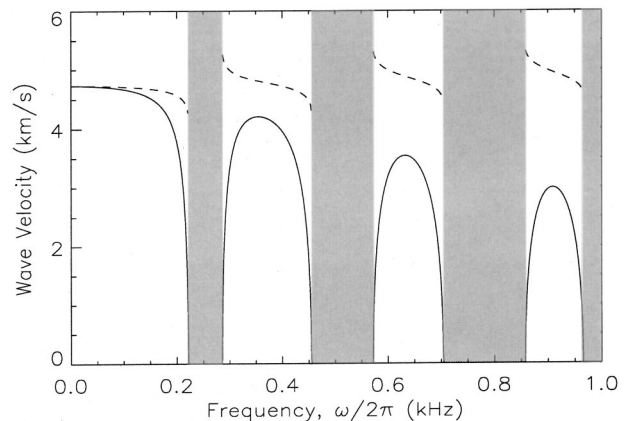
FIG. 3. Passbands and stopbands of drill pipe. The group velocity (—) and the phase velocity (- - -) are illustrated only within the passbands.

Douglas S. Drumheller: Wave impedances of drill strings
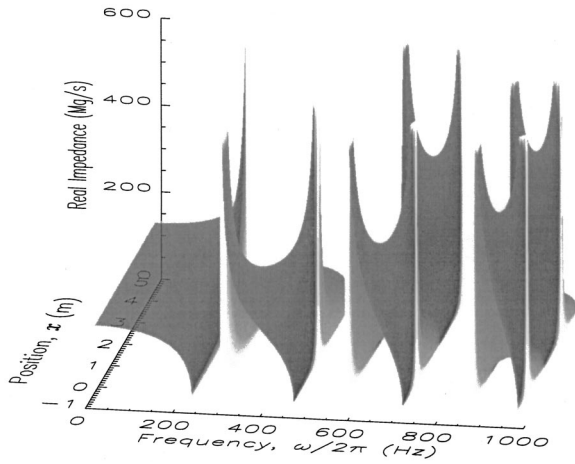
FIG. 4. Real part of the wave impedance of drill pipe.

standing waves develop at these frequencies. Indeed we know that communication is only possible in the central portions of the passbands.

Our previous knowledge about this telemetry problem is contained within the eigenvalue analysis that we have just described. By using this analysis we have identified the carrier frequencies that will successfully propagate long distances through drill pipe. However, to analyze the injection-loss problem we must proceed one step further to the evaluation of the four components A_1, A_2, B_1, and B_2 of the eigenvector. This of course is a routine algebraic exercise; however, the real issue here will be the interpretation and practical use of the results.

The components of the eigenvector can only be evaluated to within a common arbitrary constant, η. The solutions are

$$A_1 = \eta z_1 \cof(C_{11}), \tag{28}$$

$$B_1 = \eta z_1 \cof(C_{12}), \tag{29}$$

$$A_2 = -\eta z_2 \cof(C_{13}), \tag{30}$$

$$B_2 = -\eta z_2 \cof(C_{14}), \tag{31}$$

where $\cof(C_{ij})$ represents the cofactor of the matrix element C_{ij}. While the solutions for F_s and v_s can only be determined to within an arbitrary constant, the impedance $z(x,\omega) = F_s/v_s$ can be determined exactly by substitution of the results from Eqs. (28) through (31) into Eqs. (14) and (15).

By following this procedure we are able to evaluate the impedance of the drill string described in Table I. (See Fig. 4.) This is a plot of a three-dimensional surface that represents the real part of this impedance function. The vertical axis is $\mathrm{Real}[z(x,\omega)]$. Position x and frequency ω are the horizontal axes. We have only plotted $\mathrm{Real}[z(x,\omega)]$ between $-d_2/2 \leq x \leq d_1/2$ because it is symmetric about both $x = -d_2/2$ and $d_1/2$. The illustrated frequency range includes the first four passbands of the drill string. Notice that $\mathrm{Real}[z(x,\omega)] > 0$ in the passbands. It is actually negative in the stopbands, but it does not appear so here because we have clipped the plotted values of impedance to lie between 0 and 600 Mg/s. Within the passbands, the shading of the surface represents the phase angle $\varphi(x,\omega)$ of the impedance,

$$\varphi \equiv \tan^{-1}[\mathrm{Imaginary}(z)/\mathrm{Real}(z)]. \tag{32}$$

The ridge lines of the saddles as well as the lines $x = -d_2/2$ and $d_1/2$ correspond to locations where $\varphi = 0$. The lighter regions correspond to $\varphi > 0$ and the darker regions correspond to $\varphi < 0$.

In Fig. 5 we present a detailed illustration of the phase angle φ for just the third passband. As before we plot the results for one-half of a tube and tool joint. Here the function $\varphi(x,\omega)$ is plotted as a shaded surface with the vertical axis representing φ. In this case the shading is due to a light source and does not correspond to any variable from the analysis. Contours of constant phase angle are projected to a plane above this surface and labeled in nonuniformly spaced levels of $(-60, -45, 0, 45, 60)$ degrees. The dashed line $x = 0$ represents the interface between the tool joint and tube. Within the passband $-\pi/2 \leq \varphi \leq \pi/2$. The phase angle is antisymmetric about the midpoints of the tool joint and tube. Thus in this passband as well as all others, $\varphi(-d_2/2, \omega) = \varphi(d_1/2, \omega) = 0$ and the impedance is always
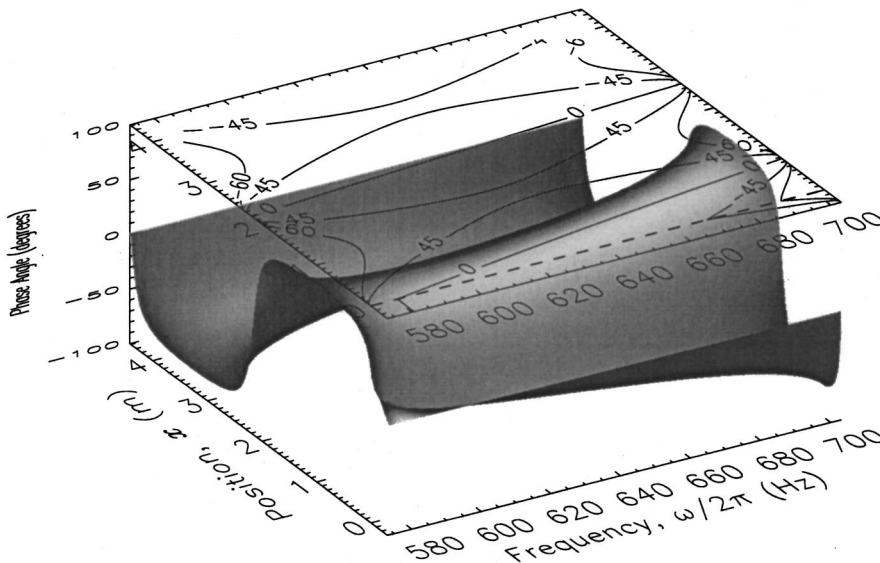
FIG. 5. Phase angles of the wave impedance in the third passband of drill pipe.
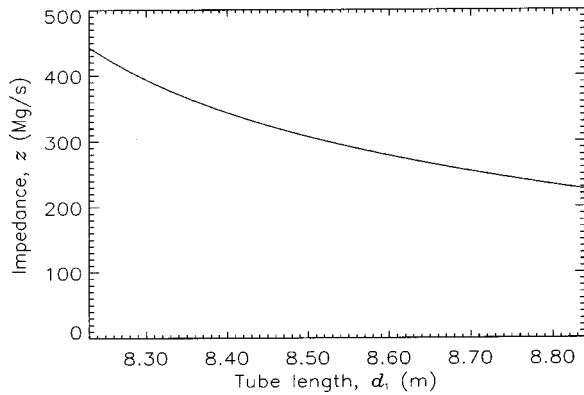
FIG. 6. The effect of tube length on the impedance at the midpoint of a tool joint for a frequency of 635 Hz.

FIG. 7. Midpoint impedance of tubes (—) and tool joints (- - -).

real at these locations. Furthermore, these are the only two physical locations where Imaginary(z) is zero for all frequencies. Because of this fact, at these particular points it is possible to match the impedance of the drill string to that of a uniform cylinder of constant diameter. *These are the points at which we can connect our repeater.*

C. Variable pipe length

Actual drill strings are often assembled from individual pipes that exhibit significant variations in length. While some "30-ft" pipe is manufactured with length tolerances under an inch, other pipe may vary by as much as 3 ft. Our impedance analysis offers us some interesting insights into the effects of such aperiodicity. We note that the shoulders of the individual screw couplings of the drill pipes are located near the midpoints of the assembled tool joints, and unscrewing a particular tool joint essentially breaks it in half. Indeed we find that different length pipes have different impedances at this location. For a frequency of 635 Hz we show how the impedance at the midpoint of the tool joint changes with tube length. (See Fig. 6.) Much of this change results from a shift in the location of the passband as we alter the tube length. Thus while 635 Hz is at the center of the third passband for the longer tubes, it is off center for the shorter tubes. Clearly, an impedance mismatch will occur when drill pipes of different lengths are connected together. One way of reducing the effects of numerous mismatches in a long drill string is to rearrange the individual drill pipes according to length. This moderates strong reflections by producing a "smooth gradient" in the impedance. Such an idea was actually tested in the field. (See Drumheller[10] as well as Drumheller and Knudsen.[11]) The effect of reordering the pipes was significant and reduced the apparent wave attenuation in the drill string by more than 50% in some passbands.

D. Repeater-drill pipe interface

Suppose we must detect and repeat a communication signal that is broadcast in the third passband of the drill string. At an appropriate location we break the drill string apart and insert a repeater into it. Our goal is to choose a location that allows us to match the impedance of the repeater to that of the drill string. This will minimize or possibly even eliminate injection loss.
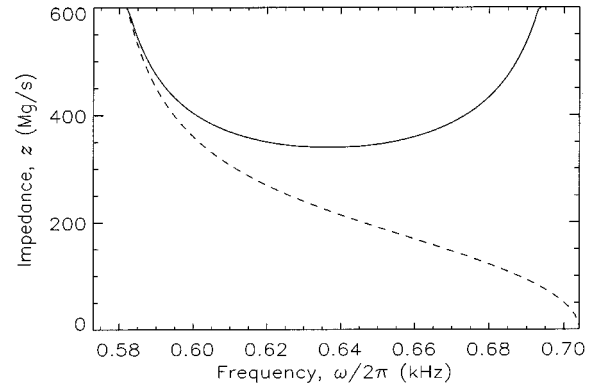
The impedance of the repeater is a real number. Thus we must select a location on the drill string where its impedance is also real. That occurs at the midpoints of each tube and tool joint of the drill string. In Fig. 7 we illustrate the impedance of the drill string over the third passband. The dashed line is the impedance at the midpoint of the tool joint, and the solid line is the impedance at the midpoint of the tube. If the impedance values in this plot are divided by the quantity ρc then we obtain a plot of area. You will note that this is not the physical cross-sectional area of the drillstring wall at either of these midpoints. To make this distinction clear we will call this area the *acoustic cross-section*, $\mathcal{A}$ of the drillstring. (The uniform cylinder is a degenerate case in which the value of the physical cross section of the cylindrical wall is equal to the acoustic cross section; that is, $\mathcal{A}=A$. In our examples all of the system components are constructed from steel. Thus the same value of ρc applies to every component and as you shall see our objective will be to match the acoustic cross sections of neigboring components.)

For any given frequency you will notice that the impedance of the drill string and consequently the acoustic cross section is always greater at the midpoint of the tube. Choosing this location will allow the repeater to have a larger cross-sectional wall area. For example, consider the impedance at the midpoint of the tube, which is 348 Mg/s. From Eq. (6) the acoustic cross section at this point is

$$\mathcal{A}=z/\rho c=3.48\times10^5/(7890\times5130)$$

$$=0.0086 \text{ m}^2=13.2 \text{ in}^2. \tag{33}$$

Moreover, suppose the repeater case is also constructed of steel. Then to eliminate injection loss the cross-sectional wall area of the repeater must be equal to this value of the acoustic cross section. Indeed we shall find that this impedance match will work over most frequencies in the central portion of the third passband. If instead the repeater is attached to the midpoint of a tool joint where the impedance is approximately 220 Mg/s, then it must be matched to the acoustic cross section at that point

$$\mathcal{A}=z/\rho c=2.2\times10^5/(7890\times5130)$$

$$=5435 \text{ mm}^2=8.42 \text{ in}^2. \tag{34}$$

Douglas S. Drumheller: Wave impedances of drill strings

Either placement with correspondingly matched acoustic cross sections will allow for an equally satisfactory exchange of wave energy between the drill string and the repeater. However, if we attach the repeater to the midpoint of a tube we will have a greater volume in which to house the components. We could also increase the cross section of the repeater by constructing it from alternative materials with smaller values of ρc such as aluminum or titanium.

III. TRANSIENT WAVE ANALYSIS

So far we have restricted much of our analysis of the repeater and the drill pipe to the behavior of time-harmonic waves. However, we have another analysis tool that has proven to be extremely important to the development of this technology. It is a simple algorithm for the computation of the transient response of stress waves in this one-dimensional geometry. (See Drumheller.[12]) This algorithm is based upon the method of characteristics, and indeed, as we have previously demonstrated, it provides analytical solutions to certain classes of problems. Moreover, these solutions have proven to be reliable predictors of wave behavior not only in a controlled laboratory setting, but also in actual field test applications. (See Refs. 10 and 11.) Here we shall apply this analysis to a hypothetical repeater design to demonstrate the practical effectiveness of our method for reducing injection losses.

A. Transducer isolation

In Fig. 1 we illustrate a repeater mounted in a drillstring. Signals in the form of propagating stress waves approach the repeater along the drill pipe from the left. The job of the repeater is to detect the messages in these relatively weak incoming signals and rebroadcast them as high-amplitude stress waves that continue to propagate along the drill pipe to the right. (There is no preferred method for encoding the data on the stress wave. That aspect of the repeater design is similar to most communication systems wherein the rate of transmission of data is limited by the bandwidth of the transmission path, which in this case is approximately one-half of the width of the passband or passbands used to carry the signal.) As we have already noted one crucial issue for the successful operation of the repeater is injection loss. However, a second crucial issue now presents itself. *Can we spatially isolate the processes of detection and rebroadcast so that both processes might occur simultaneously and at the same frequency, or will the feedback from the strong outgoing signal mask the weak incoming message*? We shall see that this new issue of isolation also depends directly upon reduction of injection loss.

As before we shall assume that the repeater operates over a range of frequencies that lie within the central half of the third passband. The center of this band is at $f = 635$ Hz. The repeater itself has two PZT transmitters. Let the wavelength of f be λ. The distance between PZT transmitters is $\lambda/4$, where

$$\lambda/4 = c/(4f) = 5130/(4 \times 635) = 2 \text{ m.} \qquad (35)$$

To the left of the transmitter array are two accelerometers that are also spaced $\lambda/4$ apart. As we show in the Appendix,
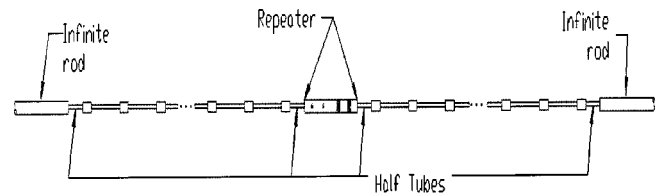
FIG. 8. A repeater mounted in a drill string with infinite boundary conditions.

we can use the $\lambda/4$ spacing of the accelerometers and the transmitters to operate both of them as phased arrays that only detect and rebroadcast waves that propagate to the right. The impedances of all of the transducer elements as well as the surrounding casing are adjusted to the results of Eq. (33).

Suppose for a moment that the repeater is infinitely long. In particular suppose the two PZT transmitters are spaced $\lambda/4$ apart within an infinitely long rod, in which all the components have identical impedances. From the symmetry of this geometry it is clear that if either transmitter is driven alone with a signal of frequency f, it will emit extensional waves of equal stress amplitudes in both directions. Indeed, given the design constraints of the drilling system, we have not found a practical transducer design in the technical or patent literature that does not exhibit this symmetry property. However, as we show in the Appendix, a simple electrical circuit can be employed to drive both transmitters in such a way as to emit wave energy in only one direction. We shall see that this type of phased array is effective for controlling the direction of the emitted wave energy not only at the frequency f to which it is *tuned*, but also over the entire communication band. Indeed, it has been our experience in practice that the ratios of the energy broadcast in each direction can be controlled to greater than 30 dB over this entire range of frequencies.[13]

We can also operate the accelerometers as a phased array. In the Appendix we discuss an array that only senses waves that propagate to the right. Again it is our experience in practice that the signal outputs produced by left-traveling and right-traveling waves also differ by more than 30 dB. When the accelerometer and transmitter arrays are combined as a repeater in an infinitely long rod, feedback isolation can be as high as the combined directional sensitivities of the transmitter and accelerometer arrays, which in this case is 60 dB. However, we emphasize that up to this point this degree of isolation has only been achievable in long uniform rods where there are no injection losses.

Let us now return to the finite-length repeater. We shall place it into the middle of a drill string in order to test its transient response. (See Fig. 8.) To each end of the repeater we attach half-length tubes. Their purpose of course is to place the repeater at the midpoint of a tube of the drill string and thereby reduce the injection losses. To each of these half tubes we attach 25 standard sections of drill pipe. Another half-length tube followed by a rod with an impedance equal to that of the repeater is then added to each end. Infinite boundary conditions are specified at both ends of the problem. (The outer half tubes and the bounding rods are not necessary to the function of the repeater. They are just a

J. Acoust. Soc. Am., Vol. 112, No. 6, December 2002

Douglas S. Drumheller: Wave impedances of drill strings   2533

FIG. 9. The $x-t$ diagram of the isolation test.

FIG. 10. The velocity histories for the isolation test. The dotted line is the integrate output of the accelerometer array, and the solid line is the material velocity v in drill string near $x \approx 580$ m.
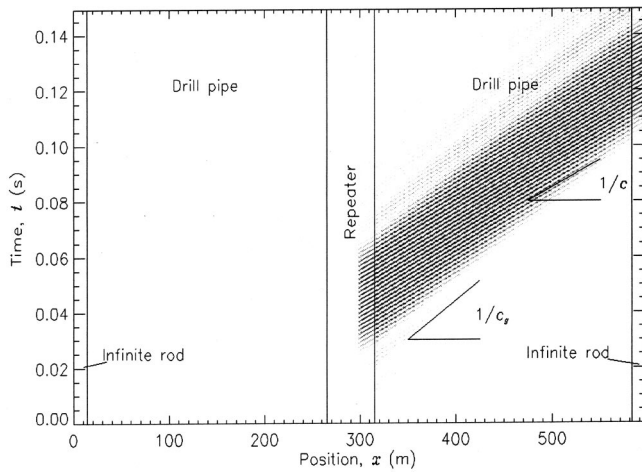
convient method to more clearly illustrate the function of the repeater by allowing the broadcast wave to exit the problem geometry. For a discussion of infinite boundary conditions see Drumheller.[3])

Our object now is to demonstrate that very good isolation is also possible in the finite-length repeater. This occurs for two reasons.

(1) *In this simple one-dimensional system the phased array of transmitters is very effective in controlling the direction of extensional waves.*
(2) *With our method of impedance matching the repeater to the drill string, we virtually eliminate reflections at the repeater-drill string interface.*

To test the isolation let's assume that no incoming waves are approaching the repeater from the left. Now, we drive the transmitter array and broadcast a signal to the right. In the absence of an incoming wave whatever signal we produce in the accelerometer array will be an indication of the degree of isolation. For purposes of comparison we shall also monitor the history of the material velocity v at two other locations. Both locations are at midpoints of full-length tubes in the drill string. The first midpoint-velocity measurement is directly to the right of the repeater at $x \approx 320$ m, and the second is adjacent to the right boundary rod at $x \approx 580$ m. (See Fig. 9.) We shall drive the transmitter array with two types of voltage signals—a signal of constant frequency and a burst composed primarily of 20 sine waves. We shall consider the burst input first.

We could drive the transducer array with a voltage signal consisting of a sequence of 20 sine waves of frequency $f = 647$ Hz. However, this finite sequence of sine waves actually has too broad a range of frequency components for our proposes. So instead let's pass this signal through a filter to produce another signal that primarily contains frequencies between 620 and 660 Hz. Then we apply this filtered signal to the transmitter array. The results of this calculation are contained in Fig. 9 as an $x-t$ diagram that illustrates the computed material velocity $v(x,t)$ of the drill string and repeater over all spatial points x (horizontal axis) and for every time t (vertical axis). The vertical solid lines indicate the
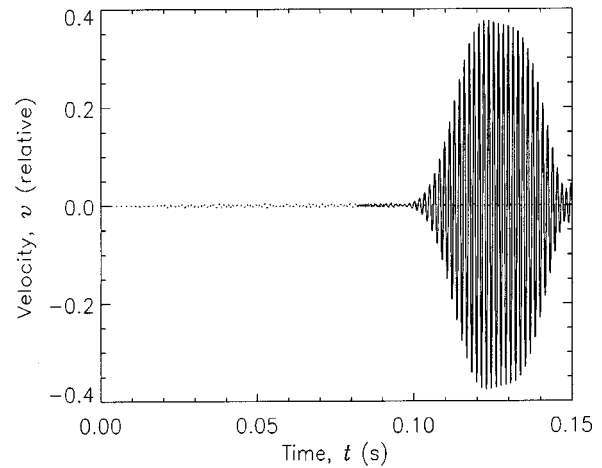
locations of the major interfaces between the drill pipe, repeater, and the bounding infinite rods. (Notice that the repeater is quite long. We have lengthened the repeater to improve the clarity of the $x-t$ diagram. Physical lengths of actual repeaters can easily be reduced to 5 m or less.) At each particular point (x,t) the material velocity $v(x,t)$ is represented as a shade of gray. To improve the clarity of the reproduction of this image, only negative values of v are plotted with $v \geqslant 0$ being white. The transmitter array broadcasts a wave to the right. This wave appears as a broad positive sloping stripe. The absence of a negative sloping stripe on the left is an indication of the directional characteristics of the transmitter array. You will notice that the signal on the right successfully leaves the repeater, travels through the 25 sections of drill pipe, enters the infinite rod on the right, and then exits the computation. The complex pattern within the stripe is an excellent illustration of the physical concepts of phase and group velocity. The slope of this stripe is equal to the inverse of the group velocity $1/c_g$. In the central portion of the third passband of the drill string, $c_g \approx 3.5$ km/s. Within the stripe you can see finer characteristic lines. These lines have slopes that are equal to the inverse of the phase velocity $1/c_p$, where $c_p \approx 5$ km/s.

To quantify the isolation between the accelerometers and the transmitters, we compare the output of the accelerometer array, which is located near $x \approx 280$ m to that of the midpoint-velocity measurement near $x \approx 580$ m. Because we need v to compute the relative energies in these waves, we have integrated the accelerometer signal and plotted v at both gage locations. (See Fig. 10.) The material velocity v at $x \approx 280$ m is shown as the nearly flat dotted line. The start of a weak pulse is just discernable near $t = 0.02$ s. The much larger pulse at $x \approx 580$ m is shown as a solid line. Because of the delay associated with the propagation time across 25 lengths of drill pipe, this pulse appears later in the record. The huge difference in the amplitudes of these two signals demonstrates how well the accelerometer array is isolated from transmitter array.

To calculate the isolation we notice that the combined

Douglas S. Drumheller: Wave impedances of drill strings
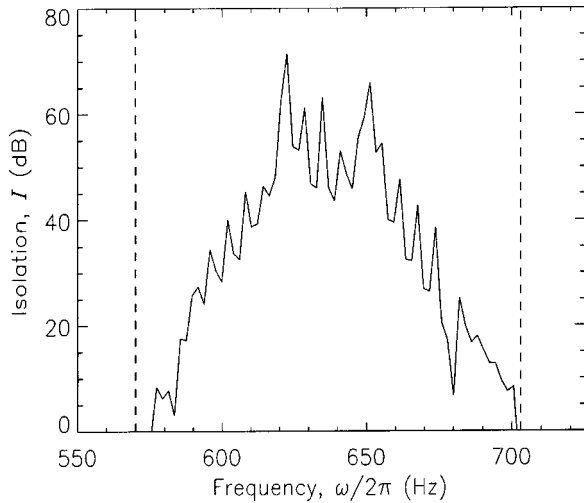
FIG. 11. Isolation of the accelerometer array. The vertical dashed lines are the boundaries of the third passband.

kinetic and potential energy $\mathcal{E}$ of a simple propagating wave is

$$\mathcal{E} = zv^2. \tag{36}$$

You will also notice that z is the same at all our gage locations because we have matched the impedance of the repeater to that of the drill string at the midpoints of all of the tubes. Thus the isolation can be computed by directly comparing these two signals. Let $\mathcal{V}_1$ and $\mathcal{V}_2$ represent the spectral amplitudes of the fast Fourier transforms of the material velocity histories of the array near $x \approx 280$ m and the single gage near $x \approx 580$ m, respectively. We compute the isolation in decibels as

$$I = 20 \log_{10}(\mathcal{V}_2 / \mathcal{V}_1). \tag{37}$$

Within the third passband between 620 to 660 Hz the isolation mostly ranges between 40 to 60 dB. (See Fig. 11.)

Now we turn to an isolation test using the constant-frequency source. Of course in a transient calculation we can only approximate a driving voltage of constant frequency. In this case we use a sequence of 500 sine waves each having a frequency of 635 Hz. The signal from the accelerometer array is integrated to obtain the material-velocity history
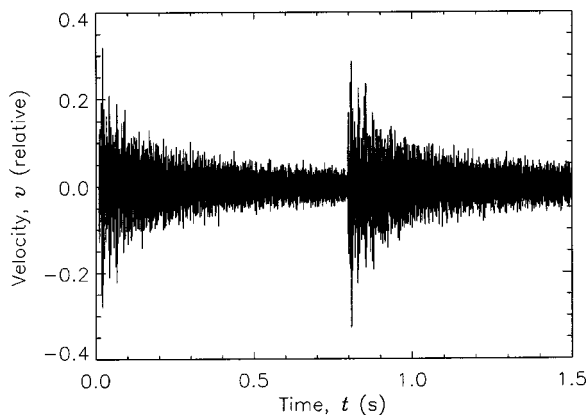
FIG. 12. The material-velocity history for the constant-frequency isolation test as determined from the measurements of the accelerometer array.
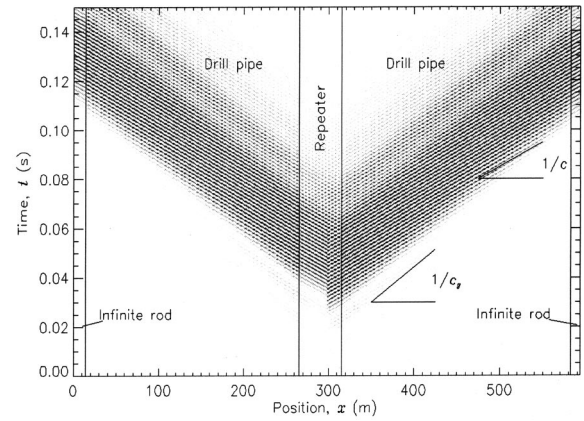
FIG. 13. The x-t diagram of the isolation test using a quarter-pipe interface.

shown in Fig. 12. We have normalized the amplitude in this illustration to the maximum material velocity v of the broadcast wave measured at $x \approx 320$ m. That wave is not shown because it is primarily a sequence of 500 sine waves of unit amplitude. The two bursts of energy in the record of the accelerometer array occur at the startup and shutdown of the drive voltage. These events generate waves in the stopband frequencies, which are trapped in the repeater. While their amplitudes seem large in the time domain, a fast Fourier transform shows a broad spectral content containing negligible amplitudes. Within the neighborhood of the third passband the isolation between the accelerometer array and the transmitters is still about 60 dB. You will also notice that these bursts ring down over a period of more than 0.5 s. This is caused by attenuation that we have included in this one calculation. The attenuation model is discussed in Ref. 10. The parameters that we use are $\tau = 200 \; \mu$s, $\eta = 0.004\,68$, and $\vartheta = 2.17$. As discussed in Ref. 10, these parameters provide good empirical estimates of drill string attenuation. When we remove attenuation from the calculation, the ring down in the stopbands does not occur; however, the isolation in the passband remains unchanged at 60 dB.

We have computed the isolation of the repeater by two methods. Both methods yield approximately the same results. To illustrate the importance of reducing injection loss and its effect on isolation, suppose we alter one dimension in the previous example. Instead of joining the repeater to the drill string on the right with a half-length tube, we shall use a quarter-length tube. Everything else in the calculation remains unaltered while the transmitter array is driven by the filtered burst of 20 sine waves. The x-t diagram for this calculation is shown in Fig. 13. Here we see that the repeater injects nearly equal levels of the wave energy into both drill strings. In this case the isolation drops to 3 dB. Indeed, this small amount of isolation is only achievable through the use of the directional accelerometer array. If instead we were to replace the accelerometer array with a single accelerometer the isolation would be degrade even further to -2 dB! This indicates that the directional capability of the transmitter array and the isolation of the accelerometer array are completely defeated by changing one of the half-length tubes to a quarter-length tube. (We might also ask if small dimensional

errors, say on the order of a few percent in length, can detune this system. In fact, they do not. Indeed, if they did we would also find that the bandwidth in Fig. 11 would be very narrow.)

B. Quarter-wave transformer

During typical drilling operations drill pipe is used in the upper section of the well while about 1000 feet of drill collar is used in the lower section directly above the drill bit. Drill collar is heavy-walled pipe that has uniform internal and external diameters. Pairs of male and female pipe threads are machined directly into ends of the collars and consequently tool joints are absent. In contrast to the light flexible drill pipe, which is supported in tension by the derrick hoist, the drill collars are heavy and quite stiff. They are allowed to support compression and provide the thrust loads necessary to push the rotating drill bit into the formation. There is often a large mismatch in wave impedance at the junction between the drill collar and drill pipe.

An ingenious device called the quarter-wave transformer is mentioned in the patent by Hixson.[14] This transformer serves as a method of matching the wave impedance of drill pipe to that of drill collar. Hixson proposed the use of "a 'transformer' length of pipe... inserted between the drill collars... and the drill pipe...," which transformer length is approximately 1/4 wave length long and has a metal cross sectional... approximately equal to the square root of the product of the cross-sectional wall area of the pipe and the cross-sectional wall area of the collars...." You will notice that because two different cross-sectional wall areas are associated with the drill pipe, that of the tube and the tool joint, Hixson's description is ambiguous. However, using our impedance analysis we can determine the appropriate acoustic cross section of the drill string and consequently the cross-sectional wall area of the Hixson transformer with precision. Indeed if we attach the transformer between the end of the drill collar and a full section of drill pipe, the transformer cross section should be based on the impedance and the acoustic cross section of the drill string at the midpoint of the tool joint. Recall that Fig. 7 shows that the wave impedance at this location is approximately 220 Mg/s. Thus the acoustic cross section for the drill pipe that should be used in the Hixson transformer formula is $\mathcal{A} = 5435$ mm^2. [See Eq. (34).]

Let's suppose this drill pipe is connected to drill collar that has an 8-in outside diameter and a 2-in inside diameter. The cross-sectional wall area of this collar is 47.1 in^2 $= 30,400$ mm^2. To join this collar to the drill pipe we need a transformer with a cross-sectional wall area of A_t, where

$$A_t = \sqrt{(30\,400 \times 5435)} = 12\,853 \text{ mm}^2 = 19.9 \text{ in}^2. \quad (38)$$

The length of the transformer is selected to be 6.5 ft, which is the quarter wavelength of a 647 Hz harmonic stress wave.

Now we test the effectiveness of the Hixson transformer by creating a single propagating impulse in velocity v in the drill collar. As this impulse strikes the transformer, part of the energy is reflected back into the drill collar and part is transmitted through the transformer and into the drill pipe.
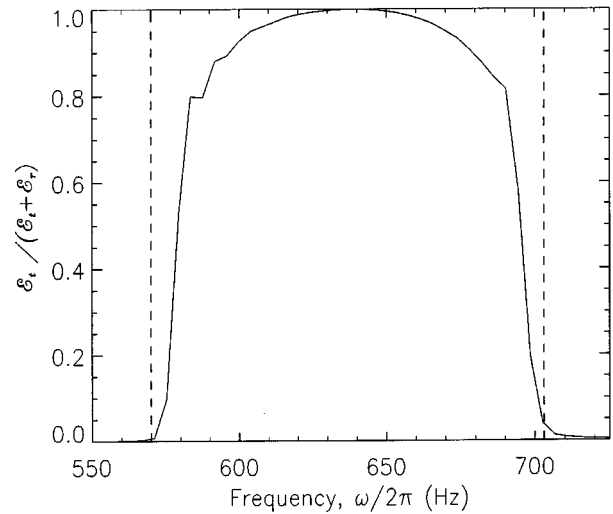
FIG. 14. The transmission ratio of the quarter-wave transformer. The vertical dashed lines are the boundaries of the third passband.

Let the spectral amplitudes of the Fourier transforms of the material velocities of the transmitted and reflected waves be $\mathcal{V}_t$ and $\mathcal{V}_r$, respectively. Then we use Eq. (36) to calculate both the transmitted energy $\mathcal{E}_t$ and the reflected energy $\mathcal{E}_r$. The transmission ratio $\mathcal{E}_t/(\mathcal{E}_t + \mathcal{E}_r)$ is shown in Fig. 14. Over the central half of the third passband this ratio is near one, which implies that only a few percent of the total energy of the wave is reflected by the transformer.

C. The terminator

In the Appendix we discuss the wave amplifier, which is mechanically identical to the repeater; however, its electrical circuit is quite different. While the repeater receives, interprets, and rebroadcasts a message at a specified wave amplitude, the wave amplifier simply magnifies everything that it sees. Conceptually the amplifier is an appealingly simple device. However, it is inherently unstable for all positive values of gain G, Eq. (A27). To see why let's return to Fig. 12 where we found that transients in the driving voltage caused the transmitters to produce energy within the stopband frequencies. This energy cannot readily leave the repeater/ amplifier housing. Indeed, regardless of how low these signal levels might be, the amplifier will continue to magnify their amplitude without bound.

However, the amplifier has one very useful function. It can be used as a wave terminator by adjusting the gain to $G = -1$. Then as a right-traveling wave passes through the terminator, the transmitter array will cancel it by producing another right-traveling wave of equal amplitude but opposite sign. We illustrate the function of a terminator by modification of the repeater geometry in Fig. 8. We replace the outer half-tubes and infinite rods with stress-free boundary conditions applied to the exposed ends of the 25 sections of drill pipe. The adjustments in gain and boundary conditions lead to the $x-t$ diagram shown in Fig. 15. We see that application of the filtered burst of 20 sine waves causes the transmitters to broadcast a wave to the right. This wave is then reflected by the right free boundary. It passes back though the termi-
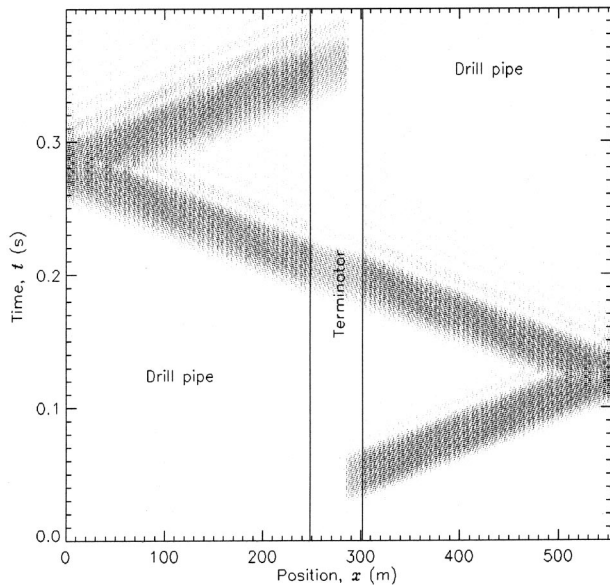
FIG. 15. The $x-t$ diagram for the terminator.

nator. Nothing happens because the accelerometer array is insensitive to left-traveling waves. However, the signal is next reflected by the left free boundary and returns to the terminator as a right-traveling wave. This time it is canceled. We compare the spectral energy of the wave that enters the terminator from the left to the spectral energy of the residual wave that manages to pass through the terminator. (See Fig. 16.) Notice that the signal levels over the central portion of the passband have been canceled by more than 30 dB. (This example plus the repeater calculation make it clear that bidirectional communication through a repeater in the same frequency band is possible. The most novel approach would require one accelerometer array between two transmitter arrays. Only weak incoming messages would be allowed in the region between the transmitter arrays. The accelerometer array would have two circuits to detect both left- and right-traveling waves.)

IV. CONCLUSIONS

We have analyzed the characteristics of extensional stress waves in a drill string. However, our results obtained
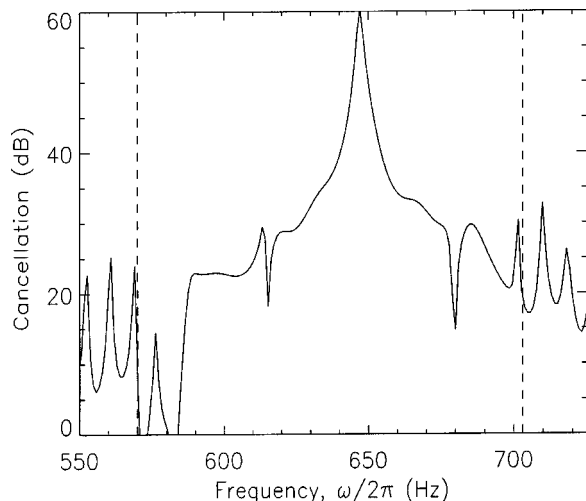
FIG. 16. The wave cancellation capability of the terminator.
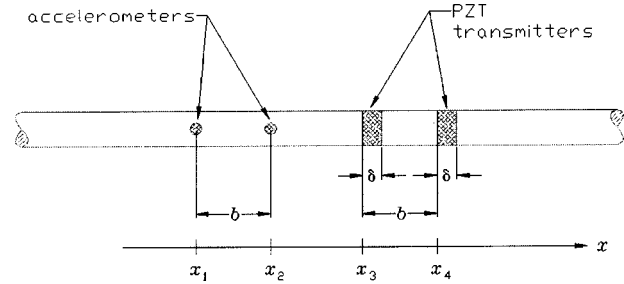
FIG. 17. The transducer arrays in an infinite rod.

through a straight-forward eigenvalue analysis are easily extended to other types of periodic media such as layered composite materials. This eigenvalue method has an historically-demonstrated usefulness in the solution of a great variety of linear wave propagation problems. Typically people evaluate the eigenvalues alone and ignore the eigenvectors. This has often been the case with solutions for elastic wave propagation in periodic media. The eigenvalues yield the phase and group velocities, which provide useful insight into the ways that waves propagate through the interior of these structures. However, when we try to understand how waves enter and leave periodic media, we require more information. As we have shown here, that is where the eigenvectors offer the crucial information. With them we can evaluate the wave impedance that the periodic structure presents to the outside world.

Here the particular periodic structure that is of most interest to us is the drill string. We have used the eigenvectors of the drill string problem to determine its wave impedance, which in general is a complex number. But at discrete physical locations the wave impedance just happens to reduce to a real number. This means that at these locations the periodic structure assumes the impedance of a homogeneous medium. As a consequence at these physical locations we can cut the drill string in two and insert a uniform diameter cylinder of any length. Provided the cylinder has a matching impedance, waves will travel from the drill string through the uniform cylinder and back again into the drill string without any reflections. This phenomena has allowed us to construct a variety of useful tools for generating and controlling waves. Among then are the repeater, the terminator, and the quarter-wave transformer. Indeed these are commercially valuable devices that can be used to develop communications systems for deep drilling operations, and U.S. Patent applications have been filed.

APPENDIX: TRANSDUCER ARRAYS

Arrays of accelerometers and PZT transducers mounted on a rod are illustrated in Fig. 17. All components of this

system have an identical wave velocity c and wave impedance z. Here we shall analyze the functions of these arrays. The two accelerometers are used to detect waves that propagate to the right but not those that propagate to the left. The two PZT transducers are used to generate stress waves that only propagate to the right. Together these arrays can be used first to detect a right-traveling wave and then either to amplify it or to cancel it. We shall begin with an analysis of the accelerometer array.

Accelerometer array

Time and position are represented by the variables t and x. Because the wave impedance is constant and boundaries are absent, we know that all possible extensional waves capable of propagating in this bar are represented by the following d'Alembert solution for the material acceleration a:

$$a(x,t) = f[t - x/c] + g[t + x/c], \tag{A1}$$

where the functions $f[\cdot]$ and $g[\cdot]$ are arbitrary and represent right-traveling and left-traveling waves, respectively. Moreover we assume that both f and g are harmonic waves with a wavelength of λ. Thus for example

$$f[t - x/c] = -f[t - (x \pm \lambda/2)/c]. \tag{A2}$$

Identical accelerometers are located at x_1 and x_2. They have negligible gage lengths, and the spacing between them is

$$x_2 - x_1 = b = \lambda/4. \tag{A3}$$

The signals $S_i(t)$ measured by the two accelerometers are

$$S_1(t) = C\{f[t - x_1/c] + g[t + x_1/c]\}, \tag{A4}$$

$$S_2(t) = C\{f[t - (x_1 + b)/c] + g[t + (x_1 + b)/c]\}, \tag{A5}$$

where the constant C represents the gage factor.

We shall delay the signal from the accelerometer at x_2 by b/c in time and then subtract it from the other accelerometer signal to obtain

$$S(t) = S_1(t) - S_2(t - b/c)$$

$$= C\{f[t - x_1/c] - f[t - (x_1 + 2b)/c\}, \tag{A6}$$

where we notice that the left-traveling wave g does not contribute to the signal $S(t)$. Moreover because of the periodic property Eq. (A2), we find that

$$S(t) = 2Cf[t - x_1/c]. \tag{A7}$$

Thus $S(t)$ is a measure of the right-traveling wave alone. It is easily shown that

$$S(t - \Delta t) = 2Cf[t - x/c], \tag{A8}$$

where

$$\Delta t \equiv (x - x_1)/c. \tag{A9}$$

Transmitter array

Now we analyze the array of PZT transmitters. We shall learn how to control them so that they only generate a right-traveling wave. The left edges of the transmitters are located at x_j ($j = 3,4$). As with the accelerometers these transmitters are also spaced a quarter wavelength apart so that $x_4 - x_3$

$= b$. We apply different harmonic voltages φ_j to the electrical leads of these transmitters causing them to expand and contract thus producing stress waves in the rod. Each transmitter operating alone produces two waves. The variables $v_j^{\pm}$ denote the material velocities of these waves. The plus sign denotes the wave that the transmitter radiates to the right, and the minus sign denotes the wave that the transmitter radiates to the left. The relationship between the applied voltage φ_j and the material velocities $v_j^{\pm}$ produced by these waves is given by Eq. (51) of Ref. 12:

$$v_j^{\pm} = \pm (i/2)\omega d_{33}\varphi_j, \tag{A10}$$

where i is the imaginary unit, ω is the harmonic frequency, and d_{33} is the piezoelectric coupling coefficient. The thickness of each transmitter is δ, where Eq. (A10) requires that $\delta \ll \lambda$. Because we are only considering harmonic waves, the material accelerations produced by the transmitters are easily computed to be

$$a_j^{\pm} = \mp B\varphi_j, \tag{A11}$$

where

$$B \equiv \tfrac{1}{2}\omega^2 d_{33}. \tag{A12}$$

Then the d'Alembert solution for the four waves generated by the transmitters are

$$a_3^+(t - x/c) = -B\varphi_3[t - (x - x_3 - \delta)/c], \tag{A13}$$

$$a_3^-(t + x/c) = +B\varphi_3[t + (x - x_3)/c], \tag{A14}$$

$$a_4^+(t - x/c) = -B\varphi_4[t - (x - x_3 - b - \delta)/c], \tag{A15}$$

$$a_4^-(t + x/c) = +B\varphi_4[t + (x - x_3 - b)/c]. \tag{A16}$$

Next we specify that the voltages are related to each other by

$$\varphi_3(t) = -\varphi(t - b/c), \tag{A17}$$

$$\varphi_4(t) = +\varphi(t). \tag{A18}$$

In the region to the right of the transmitters where $x > x_4 + \delta$, the material acceleration is

$$a^+[t - x/c] \equiv a_3^+ + a_4^+ = 2B\varphi[t - (x - x_3 - \delta + b)/c]$$

$$= 2B\varphi[t - \Delta t + \Delta \tau], \tag{A19}$$

where we have used Eqs. (A2), (A13), and (A17). In this result Δt is given by Eq. (A9), and

$$\Delta \tau \equiv (x_3 - x_1 + \delta - b)/c. \tag{A20}$$

Similarly we can show that to the left of the transmitters where $x < x_3$, the material acceleration is

$$a^- \equiv a_3^- + a_4^- = 0. \tag{A21}$$

We obtain this last result without using the periodicity condition Eq. (A2). This transmitter array only produces waves that propagate to the right.

The wave amplifier

The accelerometer and transmitter arrays can be combined to amplify right-traveling waves. To the right of both arrays we know that the right-traveling wave h exists where
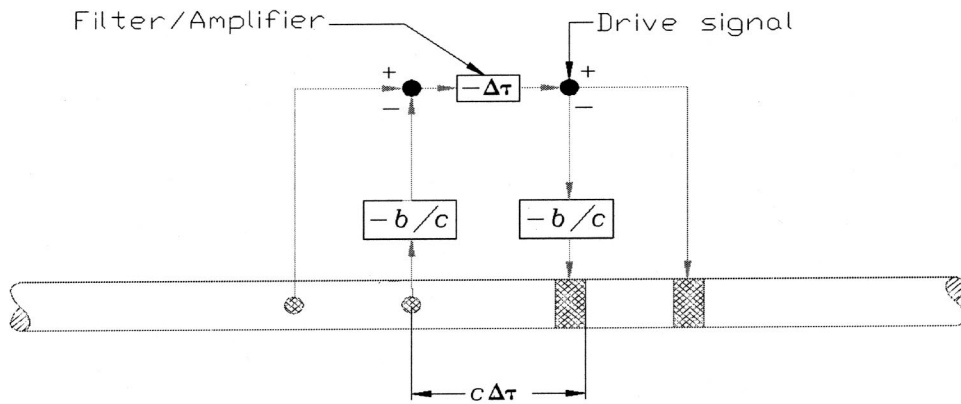
FIG. 18. Schematic of a terminator circuit.

$$h[t-x/c]=f[t-x/c]+a^+[t-x/c]. \qquad (A22)$$

Using Eqs. (A8) and (A19), we find that

$$h[t-x/c]=S(t-\Delta t)/2C+2B\varphi[t-\Delta t+\Delta\tau]. \qquad (A23)$$

Now we construct an amplifier by connecting the signal from the accelerometer array to the transmitters so that

$$\varphi(t)\equiv S(t-\Delta\tau), \qquad (A24)$$

which yields

$$h[t-x/c]=\left(\frac{1+4CB}{2C}\right)S(t-\Delta t). \qquad (A25)$$

Thus

$$h[t-x/c]=(1+G)f[t-x/c], \qquad (A26)$$

where the gain G of the amplifier is given by

$$G=4CB. \qquad (A27)$$

We find that the output of the amplifier is a right-traveling wave that is magnified and in phase with the original wave $f[t-x/c]$. As we discuss in the main body of this work, when $G>0$ the amplifier is inherently unstable when placed in a drill string; however, it is useful for cancelling a wave. This is achieved by setting

$$G=-1. \qquad (A28)$$

We call this version of the amplifier a *terminator*.

Using a terminator introduces one additional complication. The responses of the PZT transducers depend on the frequency. [See Eq. (A11).] All real systems as well as our transient computations have a spectrum of frequencies. Thus any high-frequency present in either the computation or the physical system will undergo a disproportionately large amplification. As the computation progresses or even as the physical device operates, these high-frequency components will grow without bound and eventually destabilize the system. However, this problem is easily resolved by placing a low-pass electronic filter between the accelerometer array and the transmitter array. The "roll off" in this filter only has to be greater than $1/\omega^2$ to counteract the effects of the PZT transducers.

In the physical world this can be accomplished with a simple 2-pole analog filter that introduces only minimal delay into the circuit that connects the accelerometer array to

the transmitter array. This is important because every microsecond of additional delay forces us to increase the distance x_3-x_2 another $5130\times(1\times10^{-6})\approx5$ mm. In contrast, the filtering in our transient calculations for the terminator is achieved with a finite-impulse-response filter. (See Hamming.[15]) The filter we have chosen results in the much longer delay of 3 milliseconds. Thus we have added approximately $5130\times(3\times10^{-3})\approx15.4$ meters to the spacing between the arrays in our transient calculations.

The schematic of an electrical circuit for a terminator is contained in Fig. 18. The "filter/amplifier" contains the components that low-pass filter the output from the accelerometer array and amplify the signal by the gain $G=-1$. We also show delay components to properly phase both the accelerometer and transducer arrays. At the junctions of the circuit, the $\pm$ signs indicate the proper polarity of the signals. You will notice that we can also apply a drive signal to the circuit. This is the way we initiate the transient calculation for the terminator.

[1] D. S. Drumheller, "Acoustical telemetry in a drill string using inverse distortion and echo suppression," U.S. Patent No. 5,128,901, 1991.
[2] G. S. Kino, *Acoustic Waves: Devices, Imaging, and Analog Signal Processing* (Prentice-Hall, Englewood Cliffs, NJ, 1987).
[3] D. S. Drumheller, "Acoustical properties of drill strings," J. Acoust. Soc. Am. **85**, 1048–1064 (1989).
[4] T. G. Barnes and B. R. Kirkwood, "Passband for acoustic transmission in an idealized drill string," J. Acoust. Soc. Am. **51**, 1606–1608 (1972).
[5] L. Brillouin, *Wave Propagation in Periodic Structures* (Dover, New York, 1946).
[6] D. S. Drumheller, "Electromechanical transducer for acoustic telemetry system," U.S. Patent No. 5,222,049, 1991.
[7] D. S. Drumheller, "Acoustic transducer," U.S. Patent No. 5,703,836, 1997.
[8] D. S. Drumheller, *Introduction to Wave Propagation in Nonlinear Fluids and Solids* (Cambridge University Press, Cambridge, 1998).
[9] A. Bedford and D. S. Drumheller, *Introduction to Elastic Wave Propagation* (Wiley, New York, 1994).
[10] D. S. Drumheller, "Attenuation of sound waves in drill strings," J. Acoust. Soc. Am. **94**, 2387–2396 (1993).
[11] D. S. Drumheller and S. D. Knudsen, "The propagation of sound waves in drill strings," J. Acoust. Soc. Am. **97**, 2116–2125 (1995).
[12] D. S. Drumheller, "Extensional stress waves in one-dimensional elastic waveguides," J. Acoust. Soc. Am. **92**, 3389–3402 (1992).
[13] D. S. Drumheller, "Analog circuit for controlling acoustic transducer arrays," U.S. Patent No. 5,056,067, 1991.
[14] E. L. Hixson, "Signal generator indicating vertical deviation," U.S. Patent No. 3,252,225, 1966.
[15] R. W. Hamming, *Digital Filters* (Prentice-Hall, Englewood Cliffs, NJ, 1983).

A vertical eigenfunction expansion for the propagation of sound in a downward-refracting atmosphere over a complex impedance plane

Roger Waxler
National Center for Physical Acoustics, University of Mississippi, University, Mississippi 38677

The propagation of sound in a stratified downward-refracting atmosphere over a complex impedance plane is studied. The problem is solved by separating the wave equation into vertical and horizontal parts. The vertical part has non-self-adjoint boundary conditions, so that the well-known expansion in orthonormal eigenfunctions cannot be used. Instead, a less widely known eigenfunction expansion for non-self-adjoint ordinary differential operators is employed. As in the self-adjoint case, this expansion separates the acoustic field into a ducted part, expressed as a sum over modes which decrease exponentially with height, and an upwardly propagating part, expressed as an integral over modes which are asymptotically (with height) plane waves. The eigenvalues associated with the modes in this eigenfunction expansion are, in general, complex valued. A technique is introduced which expresses the non-self-adjoint problem as a perturbation of a self-adjoint one, allowing one to efficiently find the complex eigenvalues without having to resort to searches in the complex plane. Finally, an application is made to a model for the nighttime boundary layer. © *2002 Acoustical Society of America.* [DOI: 10.1121/1.1514930]

PACS numbers: 43.20.Bi, 43.28.Js, 43.28.Fp [MSH]

I. INTRODUCTION

In this paper the propagation of sound over a complex impedance ground plane in a downward-refracting, vertically stratified atmosphere is studied. The atmosphere is vertically stratified in that the quantities characterizing the ambient state, in particular the mean density and sound speed, are assumed to depend on height. The atmosphere is downward refracting in that the sound speed increases with height. Of principal interest here is the part of the sound field which remains trapped near the ground due to the downward refraction and not the part which propagates upwards into the atmosphere.

The interaction of the sound with the ground, assumed to be a plane, is modeled by an impedance condition. The impedance is assumed to have both real and imaginary parts. The imaginary part models the compliance of the ground, while the real part models the attenuation of sound by the ground.

The propagation of sound in vertically stratified media has received much attention in both underwater and outdoor acoustics. Detailed presentations of the methods that have been developed can be found in Ref. 1 and Ref. 2. A discussion of and comparisons between the methods that have been developed in studying outdoor acoustics can be found in Ref. 3.

While expansions in vertical modes played a large role in underwater acoustics, in outdoor acoustics the parabolic equation[4,5] and horizontal wave number integration[6] techniques have been preferred. The advantage of these approaches is that they are robust and accurate numerical algorithms. They can handle a wide variety of atmospheric conditions as well as the attenuation of sound by the ground. The disadvantage of these approaches is that they are com-

putationally intensive. Further, they proceed a single frequency at a time, making it difficult to propagate an arbitrary waveform. As compared with modal expansions, these are "black box" approaches in that they provide a complete solution for the sound field without imposing a physical picture on the the propagation process.

Except for a special, and to some degree analytically tractable, case,[7] modal expansions have, until now, found little use in outdoor acoustics. The difficulty with modal expansions is twofold. They can become unwieldy if the number of modes becomes too large. Further, if the problem is intrinsically lossy, as is the case here due to the attenuation of sound by the ground, then the modes and their corresponding eigenvalues are complex. Thus, any algorithm used to find the modes must involve a two-dimensional search in the complex plane for their eigenvalues. Unless one has, at the outset, both some way of crudely estimating where the eigenvalues should be, so that one knows where to search, as well as some way of knowing how many eigenvalues there are, so that one knows when one has found them all, such searches are prone to failure.[1,8,9] In addition, as with the parabolic equation and horizontal wave number integration approaches, modal expansions proceed a single frequency at a time, making it potentially difficult to propagate an arbitrary waveform.

If, however, one has an efficient way to compute the modes, and if the number of modes is small then, once one has produced the modes, the resulting propagation model requires almost no computation at all. Further, being able to describe the sound field as a superposition of a small number of modes whose shapes are known brings insight that might not be obtained from the full solution alone. In this paper it is shown that, for typical downward-refracting sound-speed profiles and for sufficiently low frequencies, it is indeed the

case that there is an efficient way to find the modes and that the number of modes needed to describe the sound field at large distances from the source is small.

An eigenfunction expansion for the vertical part of the wave equation will be used to separate the vertical dependence of the acoustic field from the horizontal dependence. This eigenfunction expansion includes both a discrete sum over modes which are concentrated near the ground, going to zero rapidly at sufficiently large heights, as well as an integral over modes which become oscillatory with height and have, in this model, infinite extent.

The discrete sum accounts for that part of the sound field which remains ducted along the ground. The modes in the discrete sum correspond to a discrete set of complex valued horizontal wave numbers whose imaginary parts are their attenuation rates. The integral accounts for that part of the sound field which propagates upwards into the atmosphere and become unimportant near the ground at large distances from the source. The modes in the integral correspond to a continuum of horizontal wave numbers. This continuum is a real-valued half-line going from some threshold value down to negative infinity. While the continuum modes themselves do depend on the ground impedance, the threshold, and thus the continuum of horizontal wave numbers, does not. It depends only on the frequency and the asymptotic value of the sound speed at large heights.

To avoid the numerical difficulties involved in searching the complex plane for horizontal wave numbers, an equation is derived which allows one to determine the complex horizontal wave numbers from a knowledge of the real ones obtained by setting the real part of the ground impedance to zero. This equation is an exact relation from which a straightforward numerical solution can be developed. In addition to the numerical solution, a perturbation expansion valid for weak attenuation is derived. To leading order the attenuation constant for each mode is shown to be simply related to the power flux into the ground.

The organization of this paper is as follows. In Sec. II the problem is formulated and the eigenfunction expansion is introduced. In Sec. III the techniques used to find the ducted modes and the corresponding complex eigenvalues are developed. The perturbation expansion for the eigenvalues is derived in this section; the leading-order expression for the imaginary part of the eigenvalues, and thus for the attenuation, is probably the most important result in this paper because it is simple, intuitive and requires no complex eigenvalue search. The eigenvalue equation which is central to this section is derived in Appendix A. In Sec. IV a model for sound propagation in the nocturnal boundary layer is studied. Frequencies from 30 to 80 Hz are studied. Computational details are described in Appendix B. It is found that there are very few ducted modes. Values for the horizontal wave numbers associated with each mode are obtained, and it is shown that the leading-order perturbative results are quite accurate. As a result, there is no need for extensive numerical calculations to describe the ducted part of the sound field.
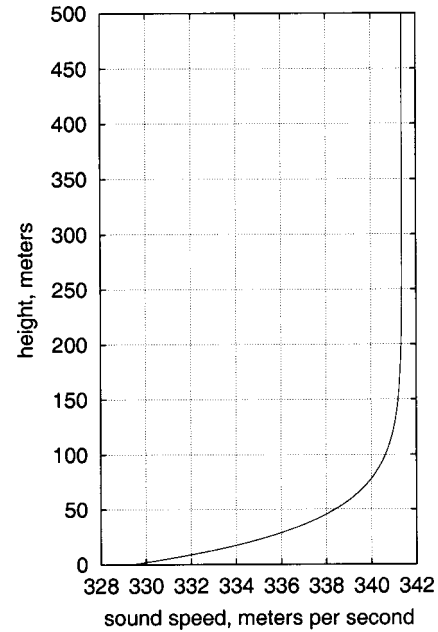
FIG. 1. A typical downward-refracting sound-speed profile.

II. FORMULATION OF THE PROBLEM

Consider the propagation of sound over a plane. Let x and y denote the coordinates parallel to the plane, let z be the coordinate perpendicular to the plane, and let t be time. Let the acoustic pressure fluctuations be given by $P(x,y,z,t)$. The coordinates x and y will be referred to as the horizontal coordinates, while z will be referred to as the vertical coordinate.

The sound speed, $c(z)$, is assumed to depend only on z and is assumed to approach a constant value, $c_0 = c(\infty)$, as $z \to \infty$. Let $k_0 = \omega/c_0$ be the resulting asymptotic form for the wave number. The sound speed is assumed to be downward refracting: if $z_1 < z_2$, $c(z_1) \le c(z_2)$. Typical of the sound-speed profiles considered is the one plotted in Fig. 1. The mean density, $\rho_0(z)$, is assumed to vary so slowly over an acoustic wavelength that $c\rho_0'/\omega\rho_0 \ll 1$.

Letting the time dependence of the acoustic pressure be harmonic

$$P(x,y,z,t) = \operatorname{Re} \hat{P}(x,y,z) e^{-i\omega t},$$

the pressure amplitude $\hat{P}$ satisfies the differential equation[2,10]

$$\left(\nabla^2 + \frac{\omega^2}{c^2} \right) \hat{P}(x,y,z) = 0. \tag{1}$$

Here, a term $(\rho_0'/\rho_0)(d/dz)$ has been dropped because of the assumptions on the slow variation of the mean density. To model the effect of the ground, an impedance condition is assumed at $z = 0$.[11,12] If the impedance is written as

$$Z(\omega) = \frac{i\omega\rho_0(0)}{\mathcal{C}(\omega)},$$

where $\mathcal{C}(\omega)$ is a complex number, then

$$\left. \frac{\partial \hat{P}(x,y,z)}{\partial z} \right|_{z=0} = -\mathcal{C}\hat{P}(x,y,0). \tag{2}$$

Equation (1) is separable. It will be solved by using an eigenfunction expansion in the vertical coordinate. The vertical equation can be written as

$$\left(\frac{d^2}{dz^2} + \frac{\omega^2}{c^2} - E\right)\psi(z) = 0, \tag{3}$$

where E is the separation parameter, $\sqrt{E}$ will be referred to as the horizontal wave number. The impedance condition (2) leads to the boundary condition

$$\psi'(0) = -\mathcal{C}\psi(0). \tag{4}$$

If $\mathrm{Im}\,\mathcal{C} \neq 0$ the differential operator defined by (3) and (4) is not self-adjoint: its adjoint operator is obtained by replacing $\mathcal{C}$ with its complex conjugate $\mathcal{C}^*$. Despite that, eigenfunction expansions for such operators have been developed[13] and similar expansions have been used, as the basis of a split-step approach, in atmospheric acoustics with constant mean temperature to model the effect of ground impedance.[5] The relevant facts are summarized below. The procedure is similar to that of the self-adjoint case, and the results can be stated either in terms of the analytic structure of the vertical Green's function[5] or as an eigenvalue problem. In this paper the eigenvalue problem formulation will be employed.

The set of complex values for E for which the solutions of (3) subject to (4) go to zero exponentially as $z \to \infty$ is a discrete set, $\{E_1, E_2, \ldots, E_N\}$, called the point spectrum. In the self-adjoint case the E_j are all real valued. Depending on the impedance and the sound-speed profile, the number of modes, N, can be anything from 0 to ∞. Let ϕ_j be the solution corresponding to $E = E_j$. The solution ϕ_j is called the eigenfunction corresponding to E_j. It is normalized in the sense that

$$\int_0^\infty \phi_j(z)^2 dz = 1. \tag{5}$$

Note that this is not the usual normalization condition which arises in the self-adjoint case. The usual normalization condition involves the integral over the modulus squared, $|\phi_j(z)|^2$, rather than the function squared, $\phi_j(z)^2$.

The set of values for E for which the solutions of (3) subject to (4) oscillate sinusoidally as $z \to \infty$ is the real half-line $(-\infty, k_0^2)$, called the continuous spectrum. For $q \in (0, \infty)$, let ψ_q be the the solution corresponding to $E = k_0^2 - q^2$. The functions ψ_q are called the continuum eigenfunctions and are not normalizable in the sense (5) (the integral diverges). Rather, they are normalized by the condition that, for sufficiently large z

$$\psi_q(z) = \sqrt{\frac{2}{\pi}} \cos(qz + \theta), \tag{6}$$

for some (possibly complex valued) phase θ. The factor $\sqrt{2/\pi}$ is chosen so that, for large z, the eigenfunction expansion below becomes a cosine transform. This is the same normalization that arises in the self-adjoint case, except that here θ is complex.

Consider two eigenvalues E and $\tilde{E}$ in the spectrum, continuum or discrete. If $E \neq \tilde{E}$, and if the corresponding eigen-

functions are ψ and $\tilde{\psi}$, then one obtains a condition similar to the usual orthogonality condition, but with the complex conjugation left out

$$\int_0^\infty \psi(z)\tilde{\psi}(z) dz = 0. \tag{7}$$

Note that this is not an orthogonality condition since it has a different geometrical interpretation: rather than ψ, it is the eigenfunction ψ^* of the adjoint operator which is perpendicular to $\tilde{\psi}$. The eigenfunctions ϕ_j and ψ_q and the adjoint eigenfunctions ϕ_j^* and ψ_q^* are said to be biorthogonal sets of eigenfunctions.

The eigenfunctions ϕ_j and ψ_q are complete in the sense that any function $f(z)$ can be expanded in the eigenfunction expansion

$$f(z) = \sum_{j=1}^N \alpha_j \phi_j(z) + \int_0^\infty \alpha(q)\psi_q(z) dq. \tag{8}$$

One finds from the biorthogonality condition (7) that the expansion coefficients are given by

$$\alpha_j = \int_0^\infty \phi_j(z) f(z) dz, \tag{9}$$

and

$$\alpha(k) = \int_0^\infty \psi_k(z) f(z) dz. \tag{10}$$

Note that (8), (9), and (10) differ from the eigenfunction expansions for self-adjoint differential operators in that, despite the fact that the eigenfunctions are complex valued, no complex conjugate is taken in computing the expansion coefficients.

Using the eigenfunction expansion (8), the solution $\hat{P}$ to (1) may be written

$$\hat{P}(x,y,z) = \sum_{j=1}^N p_j(x,y)\phi_j(z) + \int_0^\infty p(x,y,q)\psi_q(z) dq, \tag{11}$$

where, using the notation

$$\nabla_H = \begin{pmatrix} \dfrac{\partial}{\partial x} \\ \dfrac{\partial}{\partial y} \end{pmatrix}$$

for the horizontal gradient operator, $p_j(x,y)$ and $p(x,y,q)$ satisfy the horizontal wave equations

$$(\nabla_H^2 + E_j)p_j(x,y) = 0, \tag{12}$$

and

$$(\nabla_H^2 + k_0^2 - q^2)p(x,y,q) = 0, \tag{13}$$

which, given appropriate boundary conditions in x and y, are straightforward to solve.

The terms in the expansion (11) have a physical interpretation. The sum over the point spectrum is the ducted part of the sound field, the part which remains close to the earth

as it propagates. The eigenfunctions $\phi_j(z)$ are the mode shapes in the duct. The integral over the continuous spectrum is the part of the sound field which propagates upwards into the region above the mean temperature gradient, expressed as a superposition of fields which are asymptotically (for large z) plane waves.

Unlike the self-adjoint case, the ducted part of the sound field attenuates as it propagates due to its continued interaction with the ground. The imaginary parts of the horizontal wave numbers $\sqrt{E_j}$ are the attenuation rates associated with the propagation of each mode.

Further, since the modes are not orthogonal, the horizontal acoustic power flux is not, as in the self-adjoint case, the sum of the power flux per mode. Explicitly, the total horizontal power flux density vector is given by[10,14]

$$\mathbf{I}_H(x,y,\omega) = -\frac{1}{2\omega}\,\mathrm{Im}\int_0^\infty \hat{P}*\nabla_H\hat{P}\,dz.$$

Substituting from (11), one finds

$$
\begin{aligned}
\mathbf{I}_H(x,y,\omega) = -\frac{1}{2\omega}\,\mathrm{Im}\Bigg[&\sum_{j=1}^N\sum_{k=1}^N\left(\int_0^\infty \phi_j(z)*\phi_k(z)dz\right)p_j(x,y,\omega)*\nabla_H p_k(x,y,\omega)\\
&+\sum_{j=1}^N\int_0^\infty\left(\int_0^\infty \phi_j(z)*\psi_q(z)dz\right)p_j(x,y,\omega)*\nabla_H p(x,y,q,\omega)dq\\
&+\sum_{j=1}^N\int_0^\infty\left(\int_0^\infty \psi_q(z)*\phi_j(z)dz\right)p(x,y,q,\omega)*\nabla_H p_j(x,y,\omega)dq\\
&+\int_0^\infty\int_0^\infty\left(\int_0^\infty \psi_q(z)*\psi_s(z)dz\right)p(x,y,q,\omega)*\nabla_H p(x,y,s,\omega)dq\,ds\Bigg].
\end{aligned}
\tag{14}
$$

Unlike the self-adjoint case, the cross terms are not automatically zero since the modes satisfy the condition (7) rather than an orthogonality condition.

III. FINDING THE EIGENFUNCTIONS

Given a value E in the spectrum, point, or continuum, producing the corresponding eigenfunction is straightforward: substitute E into (3) and solve, either numerically or otherwise, subject to the boundary condition (4). The computational problem is thus to find an efficient way to solve for the point spectrum, since the continuum eigenvalues, $(-\infty, k_0^2)$, are known.

Finding the point spectrum can be difficult. In principle, one searches over values of E, producing, for each E, a solution ψ of equation (3) which satisfies (4) and checking to see if ψ is exponentially decaying for large z. Since this problem is not self-adjoint, the desired values of E are complex so that one needs to use a two-dimensional search algorithm. In addition to the difficulties inherent in searching in two dimensions, there is the problem of knowing if all the eigenvalues have been found.

To avoid these difficulties, the formulas derived in Appendix A are used. Explicitly, let

$$\mathcal{C} = \mathcal{A} + i\mathcal{B} \tag{15}$$

be the decomposition of $\mathcal{C}$ into its real and imaginary parts. Let $g_{\mathcal{A}}(E,z_1,z_2)$ be the Green's function for (3)

$$\left(\frac{d^2}{dz_1^2}+\frac{\omega^2}{c(z_1)^2}-E\right)g_{\mathcal{A}}(E,z_1,z_2)=\delta(z_1-z_2),$$

subject to the self-adjoint boundary condition

$$\frac{\partial g_{\mathcal{A}}(E,z_1,z_2)}{\partial z_1}\bigg|_{z_1=0}=-\mathcal{A}g_{\mathcal{A}}(E,z_1,z_2).$$

It is shown in Appendix A that the eigenvalues in the point spectrum of (3) with the non-self-adjoint boundary condition (4) are the solutions, E, of

$$1 = -i\mathcal{B}g_{\mathcal{A}}(E,0,0). \tag{16}$$

The usefulness of Eq. (16) comes from the fact that its evaluation depends only on solving the self-adjoint problem with $\mathcal{B}=0$. Computing the eigenvalues and eigenfunctions for $\mathcal{B}=0$ is straightforward. One knows *a priori* that the $\mathcal{B}=0$ eigenvalues $E_j^{(0)}$ are real valued and lie between k_0^2 and $k_0^2 + \mathcal{A} + [\omega^2/c(0)^2]$ (assuming, as is done here, that $c(0)$ is the minimum value for $c(z)$). Thus, to find the $E_j^{(0)}$ and the corresponding eigenfunctions $\phi_j^{(0)}$, one need only search a line segment. This can be done efficiently using, for example, a shooting algorithm.[8,9] Recall that, ordering the $E_j^{(0)}$ to be decreasing as j increases, the eigenfunctions $\phi_j^{(0)}$ have precisely $j-1$ nodes. Noting that when $E=k_0^2$ the solutions of (3) have the asymptotic form $a+bz$ for large z, the number of eigenvalues in the point spectrum is precisely the number of nodes of the $E=k_0^2$ solution, except in the unlikely event that $a=b=0$, in which case it is the number of nodes of the $E=k_0^2$ solution plus one.

Once the $\mathcal{B}=0$ eigenvalues and eigenfunctions have been computed, one may use them to solve (16) for the complex eigenvalues with $\mathcal{B}\neq0$. Note that if $E_j^{(0)}$, $\phi_j^{(0)}$ are the point spectra and corresponding normalized eigenfunctions,
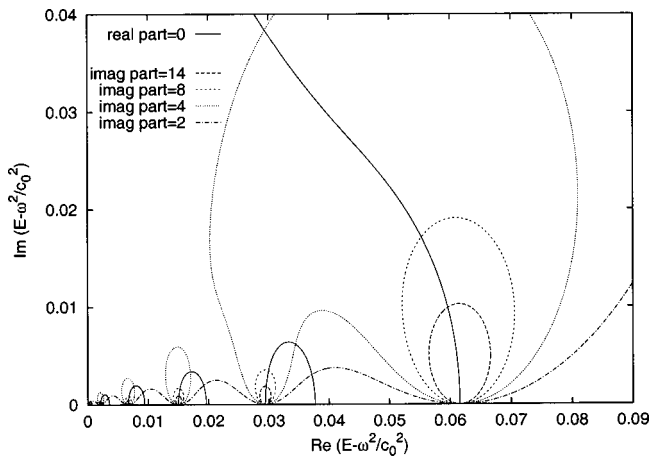
FIG. 2. Contours of $g_\mathcal{A}(E,0,0)$ at 50 Hz. Real part 0 and imaginary parts 2, 4, 8, and 14.

$j=1,2,\ldots,N$, and $\psi_q^{(0)}$ the normalized continuum eigenfunctions in the limit $\mathcal{B}=0$ (normalizations are done as in (5) and (6); in this self-adjoint case this amounts to choosing real-valued normalized eigenfunctions), then $g_\mathcal{A}(E,0,0)$ can be written

$$g_\mathcal{A}(E,0,0)=\sum_{j=1}^{N}\frac{\phi_j^{(0)}(0)^2}{E_j^{(0)}-E}+\int_0^\infty\frac{\psi_q^{(0)}(0)^2}{k_0^2-q^2-E}\,dq. \qquad (17)$$

The solutions of (16) are the points where the curve along which

$$\mathrm{Re}\,g_\mathcal{A}(E,0,0)=0$$

intersects the curves along which

$$\mathrm{Im}\,g_\mathcal{A}(E,0,0)=\frac{1}{\mathcal{B}}.$$

For small $\mathcal{B}$ the curves along which $\mathrm{Im}\,g_\mathcal{A}(E,0,0)=1/\mathcal{B}$ lie close to the singularities of $g_\mathcal{A}(E,0,0)$ at the real eigenvalues $E_j^{(0)}$, so that in this case the solutions of (16) are close to the $\mathcal{B}=0$ eigenvalues. As $\mathcal{B}\rightarrow\infty$ the boundary condition (4) approaches the Dirichlet condition $\psi(0)=0$.

The typical situation is that depicted in Fig. 2. There, the curve of the zero real part of $g_\mathcal{A}(E,0,0)$ and curves of constant imaginary part, for the values 2, 4, 8, and 14, are depicted for a 50-Hz signal in the nighttime boundary layer model studied in the next section. Given $\mathcal{B}$, the desired complex eigenvalues E_j are the points at which the curve of the zero real part intersects the curve of imaginary part $1/\mathcal{B}$. Note that the number of eigenvalues in the point spectrum is independent of $\mathcal{B}$, and is given by the number, N, of eigenvalues in the case $\mathcal{B}=0$. One can see that as $\mathcal{B}$ increases one eigenvalue moves off to infinity, while the others approach the Dirichlet eigenvalues.

Consider now the case of small $\mathcal{B}$. As $\mathcal{B}\rightarrow0$ the imaginary part of $g_\mathcal{A}(E,0,0)$ must become infinite if E is to remain an eigenvalue. Thus, as $\mathcal{B}\rightarrow0$, E must approach a singularity of $g_\mathcal{A}(E,0,0)$. These singularities are precisely the real eigenvalues $E_j^{(0)}$. Let E_j be the eigenvalue which approaches $E_j^{(0)}$ as $\mathcal{B}\rightarrow0$. To find this eigenvalue, it suffices to consider

values of E in a neighborhood of $E_j^{(0)}$ small enough so as not to come close to any of the other singularities $E_k^{(0)}$, $k\neq j$. Then, (17) shows that (16) can be written

$$1=-i\mathcal{B}\left(\frac{\phi_j^{(0)}(0)^2}{E_j^{(0)}-E}+\mathcal{F}^{(j)}(E)\right), \qquad (18)$$

where $\mathcal{F}^{(j)}(E)=g_\mathcal{A}(E,0,0)-([\phi_j^{(0)}(0)^2]/[E_j^{(0)}-E])$. The leading-order asymptotic form for E_j is obtained by solving this equation with $\mathcal{F}^{(j)}=0$. One obtains the simple asymptotic form

$$E_j=E_j^{(0)}+i\mathcal{B}\phi_j^{(0)}(0)^2+\mathcal{O}(\mathcal{B}^2). \qquad (19)$$

To improve on this approximation, set $E=E_j^{(0)}+i\mathcal{B}\phi_j^{(0)}(0)^2+\epsilon$ and substitute into (18). One obtains the fixed point equation

$$\epsilon=-i\mathcal{B}(i\mathcal{B}\phi_j^{(0)}(0)^2+\epsilon)\mathcal{F}^{(j)}(E_j^{(0)}+i\mathcal{B}\phi_j^{(0)}(0)^2+\epsilon), \qquad (20)$$

which can be solved by iteration. The first approximation, $\epsilon=0$, gives (19). To obtain the next approximation, substitute $\epsilon=0$ into (20), yielding the value $\epsilon=\mathcal{B}^2\phi_j^{(0)}(0)^2\mathcal{F}^{(j)}(E_j^{(0)}+i\mathcal{B}\phi_j^{(0)}(0)^2)$. Substituting this value for ϵ into (20) produces the next approximation, and so on, until the desired accuracy is reached.

Let $k_j+i\alpha_j=\sqrt{E_j}$ be the horizontal wave number of the jth mode, separated into its real and imaginary parts. The real part, k_j, determines the phase and group velocities of the jth mode. The imaginary part, α_j, is the attenuation rate of the jth mode. In the leading-order approximation (19) one obtains a simple and intuitive expression for the attenuation rate. Let $k_j^{(0)}=\sqrt{E_j^{(0)}}$, and let the approximate attenuation rate be
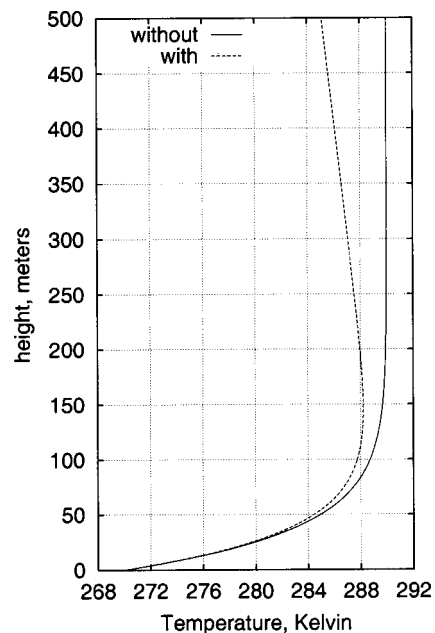
FIG. 3. A model nighttime temperature profile, with and without the adiabatic lapse rate. The explicit form taken here is an exponential fit $T_0(z)=290-20e^{-0.0275z}$. To include the adiabatic lapse rate, substitute $T_0(z)-(g/c_p)z$.
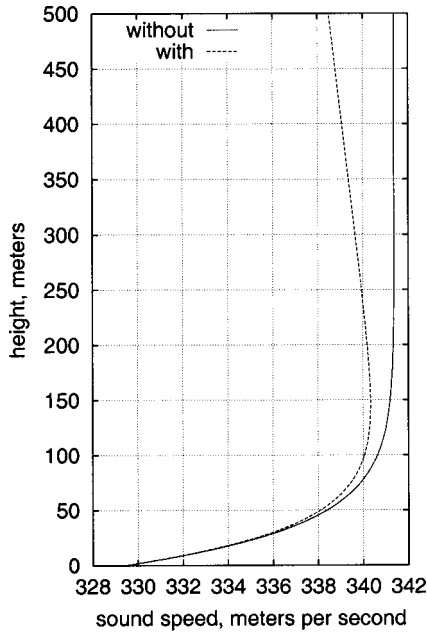
FIG. 4. A typical downward-refracting sound-speed profile, with and without the adiabatic lapse rate.

$$\alpha_j^{(0)} = \mathcal{B}\frac{\phi_j^{(0)}(0)^2}{2k_j^{(0)}}. \tag{21}$$

For small $\mathcal{B}$, (20) shows that $k_j = k_j^{(0)} + \mathcal{O}(\mathcal{B}^2)$, while $\alpha_j = \alpha_j^{(0)} + \mathcal{O}(\mathcal{B}^3)$. In particular, since the next corrections are $\mathcal{O}(\mathcal{B}^2)$ smaller, $k_j^{(0)}$ should give fairly good approximations to the phase and group velocities, while $\alpha_j^{(0)}$ should be a fairly good approximation to the attenuation rate.

To leading order in $\mathcal{B}$, the eigenfunctions can be approximated by the $\mathcal{B}=0$ eigenfunctions

$$\phi_j(z) = \phi_j^{(0)}(z) + \mathcal{O}(\mathcal{B}), \tag{22}$$

and the continuum eigenfunctions by the $\mathcal{B}=0$ eigenfunctions

$$\psi_q(z) = \psi_q^{(0)}(z) + \mathcal{O}(\mathcal{B}). \tag{23}$$

Note that the approximations (22) and (23) restore orthogonality. In particular, for small $\mathcal{B}$ the horizontal acoustic power flux density, (14), can be approximated as the sum of the power flux densities per mode. Further, by virtue of (4) and the fact that to leading order in $\mathcal{B}$ the eigenfunctions are real, one has $\mathcal{B}\phi_j(0) = -\text{Im } \phi_j'(0)$, so that, to leading order in $\mathcal{B}$

TABLE I. Eigenvalues (units of inverse square meters) and horizontal wave numbers (units of inverse meters) at 30 Hz. Here, $k_0 = 0.552$ and $\alpha_A = 6.74 \cdot 10^{-6}$ nepers/m.

j	$E_j - k_0^2$	k_j	$\left|\frac{\alpha_j^{(0)}}{\alpha_j} - 1\right|$
1	$1.68 \cdot 10^{-3} + 5.84 \cdot 10^{-5}$i	$0.567 + 5.15 \cdot 10^{-4}$i	$5.93 \cdot 10^{-5}$
2	$5.24 \cdot 10^{-3} + 9.41 \cdot 10^{-5}$i	$0.557 + 8.45 \cdot 10^{-5}$i	$1.13 \cdot 10^{-5}$
3	$1.26 \cdot 10^{-3} + 3.30 \cdot 10^{-5}$i	$0.553 + 2.98 \cdot 10^{-5}$i	$4.15 \cdot 10^{-6}$
4	$2.65 \cdot 10^{-5} + 3.98 \cdot 10^{-6}$i	$0.552 + 3.61 \cdot 10^{-6}$i	$2.28 \cdot 10^{-6}$

TABLE II. Eigenvalues (units of inverse square meters) and horizontal wave numbers (units of inverse meters) at 50 Hz. Here, $k_0 = 0.920$ and $\alpha_A = 1.79 \cdot 10^{-5}$ nepers/m.

j	$E_j - k_0^2$	k_j	$\left|\frac{\alpha_j^{(0)}}{\alpha_j} - 1\right|$
1	$5.20 \cdot 10^{-2} + 3.27 \cdot 10^{-3}$i	$0.948 + 1.72 \cdot 10^{-3}$i	$5.80 \cdot 10^{-4}$
2	$2.49 \cdot 10^{-2} + 5.99 \cdot 10^{-4}$i	$0.934 + 3.21 \cdot 10^{-4}$i	$1.15 \cdot 10^{-4}$
3	$1.27 \cdot 10^{-2} + 2.98 \cdot 10^{-4}$i	$0.927 + 1.61 \cdot 10^{-4}$i	$4.31 \cdot 10^{-5}$
4	$5.67 \cdot 10^{-3} + 1.61 \cdot 10^{-4}$i	$0.923 + 8.75 \cdot 10^{-5}$i	$2.07 \cdot 10^{-5}$
5	$1.80 \cdot 10^{-3} + 7.90 \cdot 10^{-5}$i	$0.921 + 4.29 \cdot 10^{-5}$i	$1.01 \cdot 10^{-5}$
6	$1.60 \cdot 10^{-4} + 2.13 \cdot 10^{-5}$i	$0.920 + 1.16 \cdot 10^{-5}$i	$3.83 \cdot 10^{-5}$

$$\alpha_j^{(0)} \approx -\frac{1}{2k_j} \text{Im } \phi_j(0)^* \phi_j'(0),$$

which is precisely $\rho_0 c_0$ times the power flux into the ground per horizontal wavelength.

IV. A SIMPLE MODEL FOR THE NOCTURNAL BOUNDARY LAYER

The nocturnal boundary layer develops on calm nights after the sun goes down. As the earth cools the air becomes calm and a temperature inversion forms, characterized by a mean temperature which steadily increases with height. Typically, the temperature reaches a maximum somewhere between 100 to 200 meters above the ground.[11] Above this height the mean temperature begins to decrease in a fairly linear fashion with a slope of g/c_p, or about 10 K per kilometer. The slope g/c_p is known as the "adiabatic lapse rate," here, g is the acceleration due to gravity and c_p is the specific heat of air. A model temperature profile is depicted in Fig. 3, both with and without the adiabatic lapse rate. The resulting sound-speed profile is depicted in Fig. 4, both with and without the adiabatic lapse rate. The effect of wind is not taken into account rigorously here, but for the low-angle propagation considered here it can be modeled using an effective sound speed.[2,10]

If one includes the adiabatic lapse rate, then $c(z)$ is no longer asymptotically constant but rather becomes upwardly refracting at sufficiently high altitudes. This requires some additional mathematics[12] and will be the subject of a future

TABLE III. Eigenvalues (units of inverse square meters) and horizontal wave numbers (units of inverse meters) at 80 Hz. Here, $k_0 = 1.47$ and $\alpha_A = 4.12 \cdot 10^{-5}$ nepers/m.

j	$E_j - k_0^2$	k_j	$\left|\frac{\alpha_j^{(0)}}{\alpha_j} - 1\right|$
1	$1.44 \cdot 10^{-1} + 1.64 \cdot 10^{-2}$i	$1.52 + 5.39 \cdot 10^{-3}$i	$4.94 \cdot 10^{-3}$
2	$8.58 \cdot 10^{-2} + 3.00 \cdot 10^{-3}$i	$1.50 + 1.00 \cdot 10^{-3}$i	$9.49 \cdot 10^{-4}$
3	$5.71 \cdot 10^{-2} + 1.68 \cdot 10^{-3}$i	$1.49 + 5.64 \cdot 10^{-4}$i	$3.85 \cdot 10^{-4}$
4	$3.76 \cdot 10^{-2} + 1.10 \cdot 10^{-3}$i	$1.49 + 3.69 \cdot 10^{-4}$i	$2.10 \cdot 10^{-4}$
5	$2.38 \cdot 10^{-2} + 7.47 \cdot 10^{-4}$i	$1.48 + 2.52 \cdot 10^{-4}$i	$1.28 \cdot 10^{-4}$
6	$1.40 \cdot 10^{-2} + 5.09 \cdot 10^{-4}$i	$1.48 + 1.72 \cdot 10^{-4}$i	$8.06 \cdot 10^{-5}$
7	$7.20 \cdot 10^{-3} + 3.33 \cdot 10^{-4}$i	$1.47 + 1.13 \cdot 10^{-4}$i	$4.99 \cdot 10^{-5}$
8	$2.88 \cdot 10^{-3} + 1.96 \cdot 10^{-4}$i	$1.47 + 6.64 \cdot 10^{-5}$i	$2.80 \cdot 10^{-5}$
9	$5.85 \cdot 10^{-4} + 8.30 \cdot 10^{-5}$i	$1.47 + 2.82 \cdot 10^{-5}$i	$1.15 \cdot 10^{-5}$
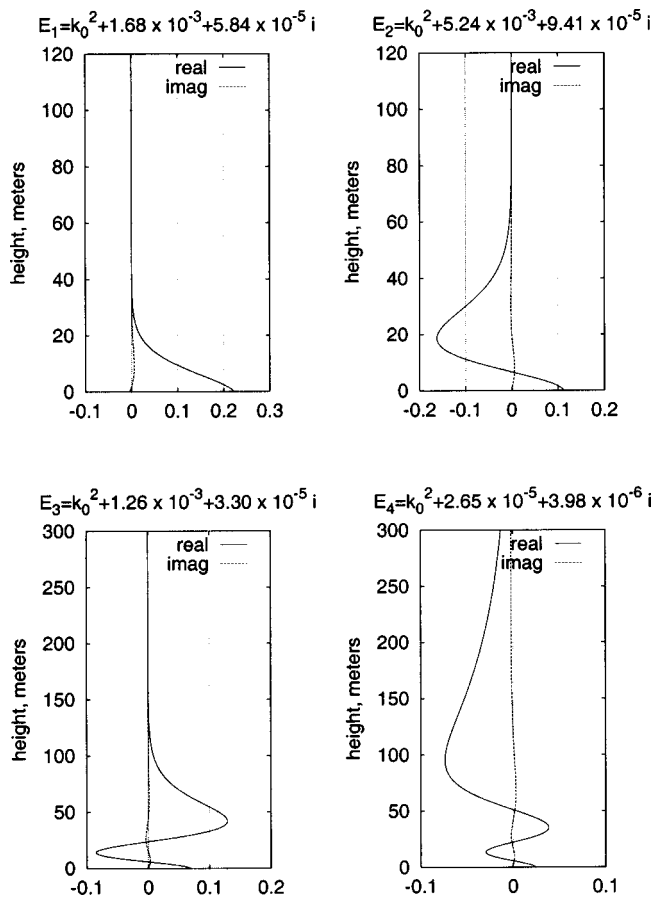
FIG. 5. The real and imaginary parts of eigenfunctions corresponding to the point spectra at 30 Hz. Ground impedance given by (24). Take note of the different vertical scales.

publication. The importance of the adiabatic lapse rate on a mode can be measured by the vertical wavelength, $\mathrm{Re}\sqrt{E_j - k_0^2}$. The adiabatic lapse rate is unimportant if the product of vertical wave number and the height at which the temperature begins to decrease is somewhat greater than 1. Put more physically, for any mode which is still nonzero at heights where the adiabatic lapse rate begins to dominate the temperature profile, the approximations made here should not be trusted.

The effect of sound interacting with the ground is often modeled by an impedance condition.[15,16] As a result of the attenuation that the ground produces, this ground impedance has a sizable real part. The computations done here use the form

$$\frac{Z(\omega)}{\rho_0(0)c(0)} = (1+i)\frac{320}{\sqrt{\omega}}$$

for the impedance, so that

$$\mathcal{C}(\omega) = (1+i)4.6 \cdot 10^{-6}\omega^{3/2}. \tag{24}$$

This choice for $Z(\omega)$ is chosen for illustrative purposes only. It fits reasonably well over the frequency range 10 to 100 Hz with the values used in Ref. 5 (these values were obtained from the model of Ref. 15) and should suffice to illustrate the technique for the three example frequencies, 30, 50, and 80 Hz, considered here. In practice, it seems likely that $Z(\omega)$ does not have a universal form, but rather differs from location to location.

The eigenvalues E_j are computed using (16) in the form (20). The $\mathcal{B}=0$ eigenvalues and eigenfunctions are computed

FIG. 6. The real and imaginary parts of eigenfunctions corresponding to the point spectra at 50 Hz. Ground impedence given by (24). Take note of the different vertical scales.

$E_1 = k_0^2 + 1.44 \times 10^{-1} + 1.64 \times 10^{-2} i$

$E_2 = k_0^2 + 8.58 \times 10^{-2} + 3.00 \times 10^{-3} i$

$E_3 = k_0^2 + 5.71 \times 10^{-2} + 1.68 \times 10^{-3} i$

$E_4 = k_0^2 + 3.76 \times 10^{-2} + 1.10 \times 10^{-3} i$

$E_5 = k_0^2 + 2.38 \times 10^{-2} + 7.47 \times 10^{-4} i$

$E_6 = k_0^2 + 1.40 \times 10^{-2} + 5.09 \times 10^{-4} i$

$E_7 = k_0^2 + 7.20 \times 10^{-3} + 3.33 \times 10^{-4} i$

$E_8 = k_0^2 + 2.88 \times 10^{-3} + 1.96 \times 10^{-4} i$

$E_9 = k_0^2 + 5.85 \times 10^{-4} + 8.30 \times 10^{-5} i$
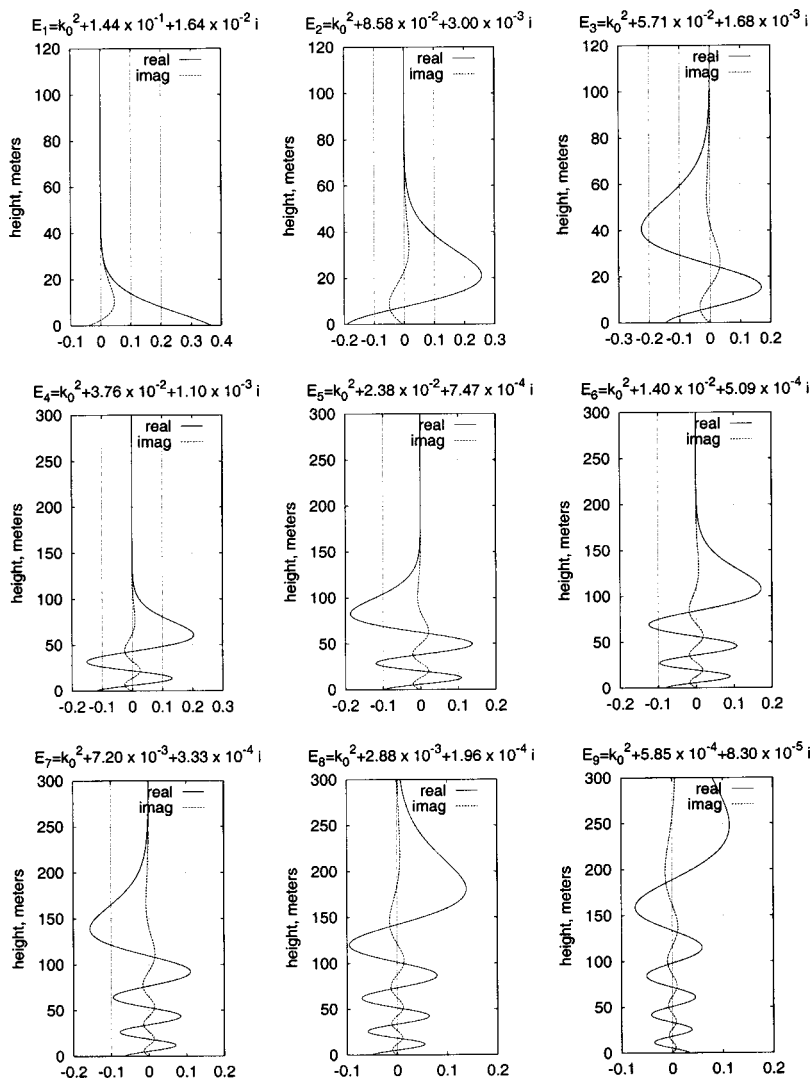
FIG. 7. The real and imaginary parts of eigenfunctions corresponding to the point spectra at 80 Hz. Ground impedance given by (24). Take note of the different vertical scales.

numerically. For the computations reported in this paper, a numerical solution of the Volterra integral equation[8] (A10) is used. To evaluate $g_\mathcal{A}(E,0,0)$ a brute force approach, without concern for the speed of the computation, is taken in that (17) is used. The are several subtleties involving the behavior of $\psi_q^{(0)}(0)^2$ which need to be understood to estimate the integral over the continuous spectrum. These are discussed in Appendix B.

The eigenvalues and horizontal wave numbers for the model sound speed of Fig. 4, ground impedance (24), and frequencies of 30, 50, and 80 Hz are listed in Tables I, II, and III, respectively. Note that the real parts of the horizontal wave numbers are all very close to k_0, regardless of the mode. The attenuation rates, however, differ significantly from mode to mode. In addition, the relative differences between the perturbative estimates from (19) and the more accurate results obtained from successive iterations of (20) are listed. Note that the perturbative estimate (19) is quite good.

It is interesting to compare the attenuation due to the interaction with the ground to the attenuation due to the atmosphere. The atmospheric attenuation can be modeled by adding an imaginary part, $\alpha_A(\omega)$, to the horizontal wave number. The values used here are taken from Fig. 10-13 of Ref. 10. At 30 Hz $\alpha_A = 6.74 \cdot 10^{-6}$ nepers/m, at 50 Hz

$\alpha_A = 1.79 \cdot 10^{-5}$ nepers/m, and at 80 Hz $\alpha_A = 4.12 \cdot 10^{-5}$ nepers/m. For the most part the attenuation due to the interaction with the ground is somewhat greater than that due to the atmosphere. The atmospheric attenuation does become important for some of the modes with greater vertical extent. For these modes, however, it is likely that the adiabatic lapse rate becomes important as well.

Given E_j, the corresponding eigenfunction is most easily produced by solving the differential equation (3) numerically. Plots of the real and imaginary parts of the normalized eigenfunctions corresponding to the point spectrum for the model sound speed of Fig. 4, ground impedance (24), and 30, 50, and 80 Hz signals are found in Figs. 5, 6, and 7, respectively. From these plots one can see that the leading-order approximation for the eigenfunctions improves with decreasing frequency. Plots of the real and imaginary parts of some normalized continuum eigenfunctions for the model sound speed of Fig. 4, ground impedance (24), and a frequency of 50 Hz are found in Fig. 8.

As a simple example, consider a point source of strength Q at height z_0 above the ground. Equation (1) must be modified by adding a δ function concentrated at the position of
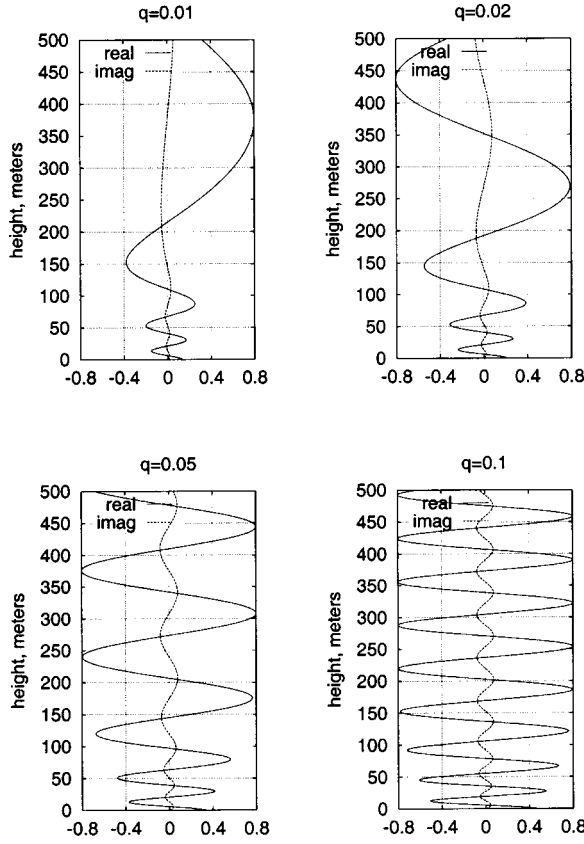
FIG. 8. The real and imaginary parts of some continuum eigenfunctions at 50 Hz. Ground impedance given by (24). Vertical wave numbers $q = 0.01$, 0.02, 0.05, 0.1 are represented.

the source to the right side. It follows from (8), (9), and (10) that

$$\delta(z-z_0) = \sum_{j=1}^{N} \phi_j(z_0)\phi_j(z) + \int_0^\infty \psi_q(z_0)\psi_q(z)dq. \quad (25)$$

Letting the horizontal position of the point source be at $x = y = 0$, one obtains from (1), (11), and (25)

$$(\nabla_H^2 + E_j)p_j(x,y) = Q\phi_j(z_0)\delta(x)\delta(y),$$

and

$$(\nabla_H^2 + k_0^2 - q^2)p(x,y,q) = Q\psi_q(z_0)\delta(x)\delta(y),$$

so that $p_j(x,y)$ and $p(x,y,q)$ are proportional to the free space Green's functions for the two-dimensional Helmholtz equation.

Let $k_j = \sqrt{E_j}$ be the horizontal wave number of the jth mode and $\kappa(q) = \sqrt{k_0^2 - q^2}$ be the horizontal wave numbers of the continuum eigenfunctions. Then, in cylindrical coordinates (r,θ,z) one has[14]

$$p_j(r) = -\frac{i}{4}Q\phi_j(z_0)H_0^{(1)}(k_j r),$$

and

$$p(r,q) = -\frac{i}{4}Q\psi_q(z_0)H_0^{(1)}(\kappa(q)r),$$

where $H_0^{(1)}$ is the Hankel function[14,17] so that

$$\hat{P}(r,z) = -\frac{iQ}{4}\left(\sum_{j=1}^{N} H_0^{(1)}(k_j r)\phi_j(z_0)\phi_j(z)\right.$$

$$\left. + \int_0^\infty H_0^{(1)}(\kappa(q)r)\psi_q(z_0)\psi_q(z)dq\right).$$

The part of the integral from k_0^2 to ∞ gives the horizontally evanescent part of the pressure field which does not propagate to the far field and can be ignored. For the rest, taking the large argument asymptotic form for the Hankel functions[14,17] one obtains the far-field approximation

$$\hat{P}(r,z) \approx -Q\sqrt{\frac{i}{8\pi r}}\left(\sum_{j=1}^{N}\frac{1}{\sqrt{k_j}}e^{ik_j r}\phi_j(z_0)\phi_j(z)\right.$$

$$\left. + \int_0^{k_0}\frac{1}{\sqrt{k(q)}}e^{i\kappa(q)r}\psi_q(z_0)\psi_q(z)dq\right). \quad (26)$$

Equation (26) has been implemented numerically. The source strength has been set to 1: $Q = 1$. The sum over the modes is straightforward to compute and the computation time required is negligible. The integral over the continuous spectrum is not as straightforward. It is complicated by the singularity in the integrand at $q = k_0$, by the sudden change from linear to quadratic behavior that occurs in ψ_q for very small q (see the discussion in Appendix B), and by the rapid oscillations in the integrand for large r. In this paper a brute force approach is taken to computing this integral without concern for the speed of the computation. The integral is computed in segments using the trapezoidal rule. For q near k_0 the integration variable is changed from q to κ before discretizing. This eliminates the singular behavior. For q near 0 a very fine grid is used to resolve the small-scale changes in the integrand. Finally, enough points are used to resolve the rapid oscillations of the integrand.

In Fig. 9(a) the magnitude of $\sqrt{r}\hat{P}(r,z)$ is shown on a gray-scale plot. The source height is 20 meters and the frequency is 50 Hz. Figure 9(b) shows the modal part alone and Fig. 9(c) the contribution from the continuous spectrum alone.

The separation into ducted and upward propagating parts is clear. At large distances from the source, only the modal part is significant at low altitudes. Further, the attenuation with distance of the modal part is clearly visible.

The continuous spectrum produces an upwardly propagating field which has some of the qualitative features of a dipole field produced by the point source and its image below the surface. This is to be expected since, for sufficiently low frequencies, $\mathcal{C}$ as given by (24) is fairly small so that the boundary condition (2) is close to the boundary condition for a hard surface.

V. CONCLUSIONS

It has been shown that modal expansions provide a simple, straightforward, and physically intuitive method for modeling the ducted part of the sound field. The eigenvalues associated with these modes are complex as a consequence of the sound field's being attenuated by the ground. An efficient method has been developed to find these eigenvalues.
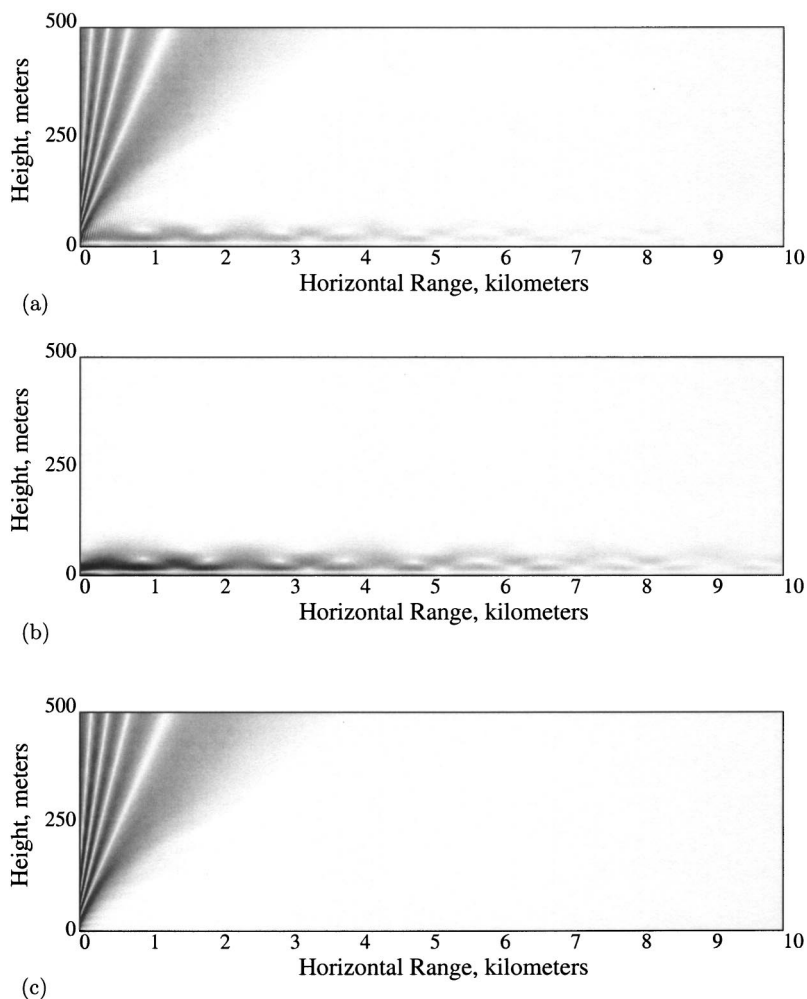
FIG. 9. (a) The magnitude of the acoustic pressure field produced by a point source 20 meters above the ground at 50 Hz. (b) The magnitude of the modal part of the acoustic pressure field produced by a point source 20 meters above the ground at 50 Hz. (c) The magnitude of the continuum part of the acoustic pressure field produced by a point source 20 meters above the ground at 50 Hz.

This method eliminates the difficulties associated with searching in the complex plane by using Eq. (16). This is an exact expression which relates the complex eigenvalues to the real ones which would arise in the absence of ground attenuation. In the case in which the attenuation of sound by the ground is small, a perturbation expansion for the imaginary parts of the eigenvalues has been developed. To leading order, a simple and intuitive analytic form for the resulting attenuation coefficient arises.

As an application, a simple model for propagation in the nighttime boundary layer has been studied. It is found that the number of modes is small for low-frequency propagation, making it particularly simple to describe the ducted part of the sound field. For the specific model considered here, there are four modes at 30 Hz, six at 50 Hz, and nine at 80 Hz. With typical values for the ground impedance, the leading-order perturbative form for the attenuation coefficient of each mode is found to be quite accurate. Comparing atmospheric with ground attenuation, the atmospheric attenuation, depending on the mode, can be comparable to the ground attenuation. Finally, while the attenuation rates differ significantly from mode to mode, the real parts of the horizontal wave numbers vary little, remaining close to what is obtained in the constant sound-speed case.

ACKNOWLEDGMENTS

APPENDIX A: FINDING THE POINT SPECTRUM

In this appendix, the numerical and analytical techniques used to find the point spectrum and the corresponding eigenfunctions are described. The new result in this appendix is the formula (A12), from which (16) immediately follows. This formula is a variation of a technique first used to solve a self-adjoint problem in the quantum mechanics of atoms in strong magnetic fields.[18]

Consider the Green's function $G_{\mathcal{C}}(\epsilon, z, z')$ for $L_{\mathcal{C}}$ given by

$$\left(\frac{d^2}{dz^2} + v(z) - \epsilon \right) G_{\mathcal{C}}(\epsilon, z, z') = \delta(z - z'),$$

subject to the boundary condition

$$\left. \frac{\partial G_{\mathcal{C}}(\epsilon, z, z')}{\partial z} \right|_{z=0} = -\mathcal{C} G_{\mathcal{C}}(\epsilon, 0, z').$$

Here, $\mathcal{C} = \mathcal{A} + i\mathcal{B}$ as in (15) is a complex number, and $v(z)$ is given by

$$v(z) = \left(\frac{\omega}{c(z)}\right)^2 - k_0^2. \tag{A1}$$

Note that v is real-valued, non-negative, bounded, and is 0 for sufficiently large z. To be definite, introduce a height H so that $v(z) = 0$ for $z > H$.

Let $\mathrm{Re}\,\epsilon > 0$ and consider solutions ψ of

$$\left(\frac{d^2}{dz^2} + v(z) - \epsilon\right)\psi(z) = 0. \tag{A2}$$

Since $\mathrm{Re}\,\epsilon > 0$, there is always a solution with $\psi(z) \to 0$ as $z \to \infty$. Call this solution $\psi_+(\epsilon,z)$. Further, for any ϵ there is always a solution which satisfies the boundary condition (4) at $z = 0$. Call this solution $\psi_-(\epsilon,\mathcal{C},z)$. Let (the prime denotes derivatives with respect to z)

$$\mathcal{W}(\epsilon,\mathcal{C}) = \psi_-(\epsilon,\mathcal{C},z)\psi'_+(\epsilon,z) - \psi'_-(\epsilon,\mathcal{C},z)\psi_+(\epsilon,z)$$

be the Wronskian of $\psi_-(\epsilon,\mathcal{C},z)$ and $\psi_+(\epsilon,z)$. Recall that $\mathcal{W}(\epsilon,\mathcal{C})$ is independent of z and that, unless ϵ is in the point spectrum of the operator $L_{\mathcal{C}}$, $\psi_-(\epsilon,\mathcal{C},z)$ and $\psi_+(\epsilon,z)$ are linearly independent so that $\mathcal{W}(\epsilon,\mathcal{C}) \neq 0$. Defining $z_> = \max\{z,z'\}$ and $z_< = \min\{z,z'\}$, one has, for ϵ not in the point spectrum of $L_{\mathcal{C}}$

$$G_{\mathcal{C}}(\epsilon,z,z') = \frac{1}{\mathcal{W}(\epsilon,\mathcal{C})}\psi_-(\epsilon,\mathcal{C},z_<)\psi_+(\epsilon,z_>). \tag{A3}$$

One may proceed similarly in the self-adjoint case $\mathcal{B} = 0$ so that, using the same notation, if ϵ is not in the point spectrum of $L_{\mathcal{A}}$ one has

$$G_{\mathcal{A}}(\epsilon,z,z') = \frac{1}{\mathcal{W}(\epsilon,\mathcal{A})}\psi_-(\epsilon,\mathcal{A},z_<)\psi_+(\epsilon,z_>).$$

Here, $\psi_+(\epsilon,z)$ is unchanged, having nothing to do with the boundary condition at $z = 0$. $\psi_-(\epsilon,\mathcal{A},z)$ is the solution of (A2) which satisfies the boundary condition $\psi'(0) = -\mathcal{A}\psi(0)$.

Since ϵ is not in the point spectrum of $L_{\mathcal{A}}$, $\psi_-(\epsilon,\mathcal{A},z)$ and $\psi_+(\epsilon,z)$ are linearly independent. It follows that $\psi_-(\epsilon,\mathcal{C},z)$ may be written as a linear combination

$$\psi_-(\epsilon,\mathcal{C},z) = \mathcal{W}(\epsilon,\mathcal{C})\left(\frac{1}{\mathcal{W}(\epsilon,\mathcal{A})}\psi_-(\epsilon,\mathcal{A},z) + \alpha\psi_+(\epsilon,z)\right),$$

for some number α depending on ϵ, $\mathcal{A}$ and $\mathcal{B}$. Substituting into (A3), one finds

$$G_{\mathcal{C}}(\epsilon,z,z') = G_{\mathcal{A}}(\epsilon,z,z') + \alpha\psi_+(\epsilon,z)\psi_+(\epsilon,z'). \tag{A4}$$

Note that if η and ψ are, respectively, the point spectrum and corresponding eigenfunctions of $L_{\mathcal{C}}$, then $1/(\eta-\epsilon)$ and ψ are, respectively, the point spectrum and corresponding eigenfunctions of the integral operator given by $G_{\mathcal{C}}$

$$\int_0^\infty G_{\mathcal{C}}(\epsilon,z,z')\psi(z')dz' = \frac{1}{\eta-\epsilon}\psi(z). \tag{A5}$$

Similarly for $L_{\mathcal{A}}$ and $G_{\mathcal{A}}$. Thus (A4) expresses the non-self-adjoint eigenvalue problem for $L_{\mathcal{C}}$ as a perturbation of the self-adjoint eigenvalue problem for $L_{\mathcal{A}}$.

The perturbation $\alpha\psi_+(\epsilon,z)\psi_+(\epsilon,z')$ in (A4) has a particularly simple form (it is known as a perturbation of rank one in the mathematical literature) which can be exploited to obtain an eigenvalue equation for $L_{\mathcal{C}}$, given that one has the Green's function $G_{\mathcal{A}}(\epsilon,z,z')$ for the self-adjoint problem. Assume that ϵ is not in the point spectrum of either $L_{\mathcal{C}}$ or $L_{\mathcal{A}}$ (it suffices to choose $\mathrm{Re}\,\epsilon$ greater than the maximum of v). Substituting (A4) into (A5), one has

$$\int_0^\infty \left(G_{\mathcal{A}}(\epsilon,z,z') - \frac{1}{\eta-\epsilon}\delta(z-z')\right)\psi(z')dz'$$

$$= -\alpha\psi_+(\epsilon,z)\int_0^\infty \psi_+(\epsilon,z')\psi(z')dz'. \tag{A6}$$

However, using $L_{\mathcal{A}} - \eta = L_{\mathcal{A}} - \epsilon - (\eta - \epsilon)$

$$G_{\mathcal{A}}(\epsilon,z,z') - \frac{1}{\eta-\epsilon}\delta(z-z')$$

$$= -\frac{1}{\eta-\epsilon}(L_{\mathcal{A}} - \eta)G_{\mathcal{A}}(\epsilon,z,z'), \tag{A7}$$

so that, substituting (A7) into (A6), multiplying on the left by $(\eta-\epsilon)(L_{\mathcal{A}}-\epsilon)G_{\mathcal{A}}(\eta,z,z'')$, integrating, using the self-adjointness of $L_{\mathcal{A}} - \eta$ and the fact that $L_{\mathcal{A}}$ and $G_{\mathcal{A}}$ commute, one has, on the left side

$$-\int_0^\infty\int_0^\infty ((L_{\mathcal{A}}-\epsilon)G_{\mathcal{A}}(\eta,z,z''))(L_{\mathcal{A}}-\eta)$$

$$\times G_{\mathcal{A}}(\epsilon,z'',z'))\psi(z')dz'\,dz''$$

$$-\int_0^\infty\int_0^\infty ((L_{\mathcal{A}}-\eta)G_{\mathcal{A}}(\eta,z,z''))(L_{\mathcal{A}}-\epsilon)$$

$$\times G_{\mathcal{A}}(\epsilon,z'',z'))\psi(z')dz'\,dz'' = -\psi(z),$$

so that

$$\psi(z) = (\eta-\epsilon)\alpha\left(\int_0^\infty (L_{\mathcal{A}}-\epsilon)G_{\mathcal{A}}(\eta,z,z'')\psi_+(\epsilon,z'')dz''\right)$$

$$\times\left(\int_0^\infty \psi_+(\epsilon,z')\psi(z')dz'\right). \tag{A8}$$

Finally, multiplying (A8) by $\psi_+(\epsilon,z)$, integrating, dividing by $\int_0^\infty \psi_+(\epsilon,z')\psi(z')dz'$, and using (A7) again with ϵ and η exchanged, one finds

$$1 = \alpha\int_0^\infty\int_0^\infty \psi_+(\epsilon,z)((\eta-\epsilon)^2 G_{\mathcal{A}}(\eta,z,z')$$

$$+ (\eta-\epsilon)\delta(z-z'))\psi_+(\epsilon,z')dz\,dz'. \tag{A9}$$

Equation (A9) is an eigenvalue equation for $L_{\mathcal{C}}$: the set of values of η which satisfy (A9) is precisely the point spectrum of $L_{\mathcal{C}}$. The value of ϵ is arbitrary, so long as ϵ is not an eigenvalue of either $L_{\mathcal{C}}$ or $L_{\mathcal{A}}$. In particular, one may let $\epsilon \to \infty$, significantly simplifying (A9).

To take the $\epsilon \to \infty$ limit, asymptotic forms for $\psi_+(\epsilon,z)$ and $\psi_-(\epsilon,\mathcal{C},z)$ are needed. It can be shown[17] that they may be chosen to be the solutions of the integral equations

$$\psi_+(\epsilon,z)=e^{-\sqrt{\epsilon}z}+\frac{1}{\sqrt{\epsilon}}\int_z^\infty \sinh(\sqrt{\epsilon}(z-z'))$$

$$\times v(z')\psi_+(\epsilon,z')dz', \qquad (A10)$$

and

$$\psi_-(\epsilon,\mathcal{C},z)=\frac{1}{2\sqrt{\epsilon}}\left(e^{\sqrt{\epsilon}z}+\frac{\sqrt{\epsilon}+\mathcal{C}}{\sqrt{\epsilon}-\mathcal{C}}e^{-\sqrt{\epsilon}z}\right)$$

$$-\frac{1}{\sqrt{\epsilon}}\int_0^z \sinh(\sqrt{\epsilon}(z-z'))$$

$$\times v(z')\psi_-(\epsilon,\mathcal{C},z')dz'. \qquad (A11)$$

Note that

$$\psi_-(\epsilon,\mathcal{C},z)=-\frac{1}{\sqrt{\epsilon}}\varphi_1(z)-\frac{\mathcal{C}}{\sqrt{\epsilon}(\sqrt{\epsilon}-\mathcal{C})}\varphi_2(z),$$

where φ_1 and φ_2 are the solutions of the integral equations

$$\varphi_1(z)=\cosh(\sqrt{\epsilon}z)+\frac{1}{\sqrt{\epsilon}}\int_0^z \sinh(\sqrt{\epsilon}(z-z'))$$

$$\times v(z')\varphi_1(z')dz',$$

and

$$\varphi_2(z)=e^{-\sqrt{\epsilon}z}+\frac{1}{\epsilon}\int_0^z \sinh(\sqrt{\epsilon}(z-z'))v(z')\varphi_2(z')dz'.$$

Similarly for $\psi_-(\epsilon,\mathcal{A},z)$.

For sufficiently large ϵ the function $v(z)$ becomes insignificant and asymptotic forms can be obtained by iterating about the $v=0$ solutions. One has

$$\psi_+(\epsilon,z)=e^{-\sqrt{\epsilon}z}+\frac{1}{\sqrt{\epsilon}}\int_z^\infty \sinh(\sqrt{\epsilon}(z-z'))$$

$$\times v(z')e^{-\sqrt{\epsilon}z'}dz'+\cdots,$$

$$\varphi_1(z)=\cosh(\sqrt{\epsilon}z)+\frac{1}{\sqrt{\epsilon}}\int_0^z \sinh(\sqrt{\epsilon}(z-z'))$$

$$\times v(z')\cosh(\sqrt{\epsilon}z)dz'+\cdots,$$

and

$$\varphi_2(z)=e^{-\sqrt{\epsilon}z}+\frac{1}{\sqrt{\epsilon}}\int_0^z \sinh(\sqrt{\epsilon}(z-z'))$$

$$\times v(z')e^{-\sqrt{\epsilon}z'}dz'.$$

Note that successive terms in these expansions are no larger in magnitude than a numerical constant times $[v(0)H]/\sqrt{\epsilon}$ times the preceding term.

Substituting these asymptotic forms into

$$\alpha=\frac{1}{\psi_+(\epsilon,z)}\left(\frac{\psi_-(\epsilon,\mathcal{C},z)}{\mathcal{W}(\epsilon,\mathcal{C})}-\frac{\psi_-(\epsilon,\mathcal{A},z)}{\mathcal{W}(\epsilon,\mathcal{A})}\right),$$

one finds, after some algebra, that

$$\alpha=-\frac{i\mathcal{B}}{\epsilon}+\cdots.$$

The $\epsilon\to\infty$ limit of (A9) can now be taken. One finds

$$1=-i\mathcal{B}\lim_{\epsilon\to\infty}\epsilon\int_0^\infty\int_0^\infty e^{-\sqrt{\epsilon}(z+z')}G_{\mathcal{A}}(\eta,z,z')dz\,dz'$$

$$=-i\mathcal{B}G_{\mathcal{A}}(\eta,0,0). \qquad (A12)$$

Equation (16) now follows immediately: set $\eta=E-k_0^2$ and notice that

$$G_{\mathcal{A}}(E-k_0^2,z,z')=g_{\mathcal{A}}(E,z,z').$$

APPENDIX B: COMPUTING THE EIGENFUNCTIONS

In this appendix, the numerical procedures used to produce the eigenfunctions are described. The exponentially decreasing solutions, $\psi_+(\epsilon,z)$, to (A2) are obtained by solving (A10). Recall that $v(z)$ as given by (A1) is zero for large enough z. Thus, the upper limit of integration can be chosen to be some finite value, say H. Equation (A10) is then of Volterra type and is straightforward to solve numerically.[8] Once the eigenvalues are determined, they can be substituted into (A10) to produce the corresponding eigenfunction.

In order to use the methods of Sec. III to find the eigenvalues, the eigenvalues and eigenfunctions for the $\mathcal{B}=0$ case are needed. For $\mathcal{B}=0$ the point spectrum is real. Thus, given solutions of (A10), a bisection algorithm[8,9] can be used to find the values of ϵ for which $\psi_+'(\epsilon,0)=-\mathcal{A}\psi_+(\epsilon,0)$. The eigenfunctions can then be determined by substituting the resulting values for ϵ into (A10) (with $\mathcal{B}$ set to zero) and solving.

To produce the continuum eigenfunctions, (3) can be transformed into the integral equation[17]

$$\psi(z)=\psi_0(z)+\frac{1}{q}\int_0^z \sin(q(z-z'))v(z')\psi(z')dz', \qquad (B1)$$

where v is given by (A1) and $\psi_0(z)$ is the solution of

$$\left(\frac{d^2}{dz^2}+q^2\right)\psi_0(z)=0$$

that satisfies (4). This integral equation is again of Volterra type and is straightforward to solve numerically.[8]

For large q the WKB (or Liouville–Green) approximation may be used.[1,17] In this approximation, one may set

$$\psi(z)\approx(\psi_-'(0)+\mathcal{C}\psi_-(0))\psi_+(z)$$

$$-(\psi_+'(0)+\mathcal{C}\psi_+(0))\psi_-(z),$$

where

$$\psi_\pm(z)=(v(z)+q^2)^{-1/4}e^{\pm i\int_0^z \sqrt{v(z')+q^2}dz'}. \qquad (B2)$$

In practice, the WKB approximation was used when $q>0.05(\omega/c_0)$.

Once the solution ψ has been produced, one normalizes as in (6) by choosing some height H large enough so that $v(z)$ is zero for $z\geq H$ and setting

$$\psi_q(z) = \sqrt{\frac{2}{\pi(\psi(H)^2 + (1/q^2)\psi'(H)^2)}}\,\psi(z). \qquad (B3)$$

That this is the proper normalization follows from the fact that for $z \geq H$, since $v(z)$ is zero, one has

$$\psi_q(z) = A\sin(qz) + B\cos(qz)$$

for some A and B. Then

$$\psi(H)^2 + \frac{1}{q^2}\psi'(H)^2 = A^2 + B^2.$$

The continuum eigenfunctions for $\mathcal{B}=0$, $\psi_q^{(0)}$ are needed in (17). They are computed as above, just with $\mathcal{B}=0$. There are, however, some subtleties in performing the integral in (17). These involve the behavior of $\psi_q^{(0)}(0)^2$.

The small and large q asymptotic forms of $\psi_q^{(0)}(0)^2$ can be extracted from the differential equation

$$\left(\frac{d^2}{dz^2} + v(z) + q^2\right)\psi_q^{(0)}(z) = 0,$$

with v given by (A1), and the normalization (B3). First, as $q \to \infty$ the term $v(z)$ becomes negligible compared to q^2, so that in the large-q limit $\psi_q^{(0)}(z)$ is a linear combination of $\sin(qz)$ and $\cos(qz)$. It follows that

$$\lim_{q\to\infty} \psi_q^{(0)}(0)^2 = \frac{2}{\pi}.$$

Similarly, if ϕ is the $q=0$ solution

$$\left(\frac{d^2}{dz^2} + v(z)\right)\phi(z) = 0,$$

which satisfies the boundary condition $\phi'(0) = -\mathcal{A}\phi(0)$, then, up to normalization, $\psi_q^{(0)}(z)$ approaches $\phi(z)$ as $q \to 0$. It follows from (B3) that, for sufficiently small q

$$\psi_q^{(0)}(0)^2 = \frac{2}{\pi}\left(\frac{\phi(0)}{\phi'(H)}\right)^2 q^2 + \cdots.$$

The function ϕ must be computed numerically (recall that the number of zeros of ϕ is the number of eigenvalues in the point spectrum). This may be done by solving the $q \to 0$ limit of (B1); this limiting equation is again of Volterra type. Note that, since $v(z)$ is asymptotically zero, ϕ is asymptotically linear so that $\phi'(H)$ is independent of H. At 50 Hz, with the sound-speed profile given in Fig. 1, one finds $\psi_q^{(0)}(0)^2 = 257.376q^2 + \cdots$.

The difficulty is that these asymptotic forms are separated from each other by several decades. In Fig. 10 $\psi_q^{(0)}(0)^2$ is plotted for the sound-speed profile given in Fig. 1 at 50 Hz. One sees that the small and large q asymptotic forms are widely separated from each. Since very small values of $E - k_0^2$ are needed (see Tables I, II, and III), and since $\psi_q^{(0)}(0)^2$ can be said to be quadratic only over a very small range of q, the contribution of the integral over the continuous spectrum cannot be ignored. Further, it is crucial that the quadratic behavior of $\psi_q^{(0)}(0)^2$ be resolved accurately in any estimate of the integral in (17), since otherwise the estimate
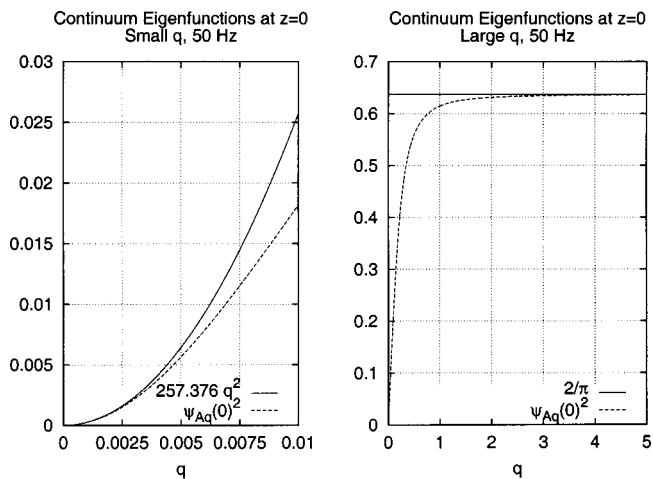
FIG. 10. The coefficients $\psi_q^{(0)}(0)^2$ at 50 Hz.

can have huge errors for small $E - k_0^2$. In particular, in estimating the integral numerically a very fine grid is needed for small values of q. For larger q a coarser grid can be tolerated.

[1] F. B. Jensen, W. A. Kuperman, M. B. Porter, and H. Schmidt, *Computational Ocean Acoustics* (American Institute of Physics, New York, 1994).
[2] E. Salomons, *Computational Atmospheric Acoustics* (Kluwer, Dordrecht, 2001).
[3] K. Attenborough, S. Taherzadeh, H. E. Bass, X. Di, R. Raspet, G. R. Becker, A. Güdesen, A. Chrestman, G. A. Daigle, A. L'Espérance, Y. Gabillet, K. E. Gilbert, Y. L. Li, M. J. White, P. Naz, J. M. Noble, and H. A. J. M. van Hoot, "Benchmark cases for outdoor sound propagation models," J. Acoust. Soc. Am. **97**, 173–191 (1995).
[4] K. Gilbert and M. J. White, "Application of the parabolic equation to sound propagation in the atmosphere," J. Acoust. Soc. Am. **85**, 630–637 (1989).
[5] K. Gilbert and X. Di, "A fast Green's function method for one-way sound propagation in the atmosphere," J. Acoust. Soc. Am. **94**, 2343–2352 (1993).
[6] R. Raspet, S. W. Lee, E. Kuester, D. C. Chang, W. F. Richards, R. Gilbert, and N. Bong, "Fast-field program for a layered medium bounded by complex impedance surfaces," J. Acoust. Soc. Am. **77**, 345–352 (1985).
[7] R. Raspet, G. Baird, and W. Wu, "Normal mode solution for low frequency sound propagation in a downward refracting atmosphere above a complex impedence plane," J. Acoust. Soc. Am. **91**, 1341–1352 (1992).
[8] W. H. Press, S. A. Teukolsky, W. T. Vetterling, and B. P. Flannery, *Numerical Recipes in C*, 2nd ed. (Cambridge University, Cambridge, 1992).
[9] J. Stoer and R. Bulirsch, *Introduction to Numerical Analysis*, 2nd ed. (Springer, New York, 1991).
[10] A. D. Pierce, *Acoustics* (Acoustical Society of America, Woodbury, NY, 1989).
[11] R. B. Stoll, *An Introduction to Boundary Layer Meterology* (Kluwer Academic, Dordrecht, 2001), Chap. 12.
[12] E. C. Titchmarsh, *Eigenfunction Expansions Associated with Second-order Differential Equations*, Parts I and II (Clarendon, Oxford, 1962).
[13] N. Dunford and J. T. Schwartz, *Linear Operators, Part III* (Wiley, New York, 1971).
[14] P. M. Morse and K. Uno Ingaard, *Theoretical Acoustics* (Princeton University, Princeton, NJ, 1986).
[15] K. Attenborough, "Acoustical impedance models for outdoor ground surfaces," J. Sound Vib. **99**, 521–544 (1985).
[16] G. A. Daigle and M. R. Stinson, "Impedance of grass-covered ground at low frequencies measured using a phase difference technique," J. Acoust. Soc. Am. **81**, 62–68 (1987).
[17] F. W. J. Olver, *Asymptotics and Special Functions* (Academic, San Diego, 1974).
[18] R. Froese and R. Waxler, "The spectrum of a hydrogen atom in an intense magnetic field," Rev. Math. Phys. **6**, 699–832 (1995), Secs. 3 and 4.

Complete mode identification for resonance ultrasound spectroscopy

Hirotsugu Ogi,[a] Keiji Sato, Takeyasu Asada, and Masahiko Hirao
*Graduate School of Engineering Science, Osaka University, Machikaneyama 1-3, Toyonaka,
Osaka 560-8531, Japan*

This study is devoted to deducing exact elastic constants of an anisotropic solid material without using any advance information on the elastic constants by incorporating a displacement-distribution measurement into resonant ultrasound spectroscopy (RUS). The usual RUS method measures free-vibration resonance frequencies of a solid and compares them with calculations to find the most suitable set of elastic constants by an inverse calculation. This comparison requires mode identification for the measured resonance frequencies, which has been difficult and never been free from ambiguity. This study then adopts a laser-Doppler interferometer to measure the displacement-distribution patterns on a surface of the vibrating specimen mounted on pinducers; comparison of the measured displacement distributions with those computed permits us to correctly identify the measured resonance frequencies, leading to unmistakable determination of elastic constants. Because the displacement patterns are hardly affected by the elastic constants, an exact answer is surely obtained even when unreasonable elastic constants are used as initial guesses at the beginning of the inverse calculation. The usefulness of the present technique is demonstrated with an aluminum alloy and a langasite crystal. © *2002 Acoustical Society of America.* [DOI: 10.1121/1.1512700]

I. INTRODUCTION

Resonant ultrasound spectroscopy (RUS)[1–5] has been recognized as a useful method for determining all of the independent elastic constants C_{ij} of an anisotropic solid in a regular shape such as a sphere, cylinder, or rectangular parallelepiped. The C_{ij} are determined in two steps. First, a swept-frequency experiment measures many of the free-vibration resonance frequencies of the specimen. Two transducers touch the specimen lightly, one for generation of a cw oscillation and the other for detection of the displacement amplitude. Second, an inverse calculation is performed to find the best fitting C_{ij} that provide the closest resonance frequencies to the measurements. The resonance frequencies can be calculated using the specimen dimensions, mass density, and all of the C_{ij}.

The successful determination of elastic constants by the RUS method relies on exact correspondence between the observed and calculated resonance frequencies in the inverse calculation, that is, correct mode identification. If modes are incorrectly identified, the elastic constants may converge to a false minimum or fail to converge. However, mode identification has never been straightforward because the measured resonance spectrum contains a large number of resonance peaks, without showing any mode information. On the other hand, the calculation identifies the resonance modes. Thus, if one knows beforehand a set of elastic constants close to the true values, the calculation is highly likely to converge o the correct modes of the specimen. If one begins with very little information about the specimen's C_{ij}, it may not converge

correctly. Several efforts have been made to overcome this difficulty. Ohno[2] noted different rates of changes of resonance frequencies when the specimen size varies. Maynard[6] switched assignments of frequencies during the iteration calculation to find the best fit. Migliori *et al.*[7] changed the specimen orientation relative to the transducers and monitored the change of signal amplitude. More recently, the present authors[8,9] developed an electromagnetic-acoustic technique to select measurable vibration modes by controlling the electromagnetic-force direction. These methods are sometimes useful but still insufficient to make *complete* mode identification. They require supplementing RUS with some other methods such as pulse-echo and rod-resonance methods.

In this study, we propose an advanced methodology for this purpose. We adopt a laser-Doppler velocimeter to map a displacement-distribution pattern of a vibrating specimen. The displacements inside the specimen can be computed. Comparison of the measurements with the computations realizes correct mode identification and then the unmistakable determination of elastic constants.

II. DISPLACEMENT MEASUREMENT AT RESONANCE

Figure 1 shows the measurement setup of the RUS/Laser combination. A rectangular-parallelepiped specimen is put on a piezoelectric tripod consisting of two pinducers for generation and detection of vibration, and one for support. A He–Ne laser beam is focused on the specimen surface (focal diameter: 15 μm) to scan the surface. The reflected beam enters the Doppler interferometer, which measures the nor-
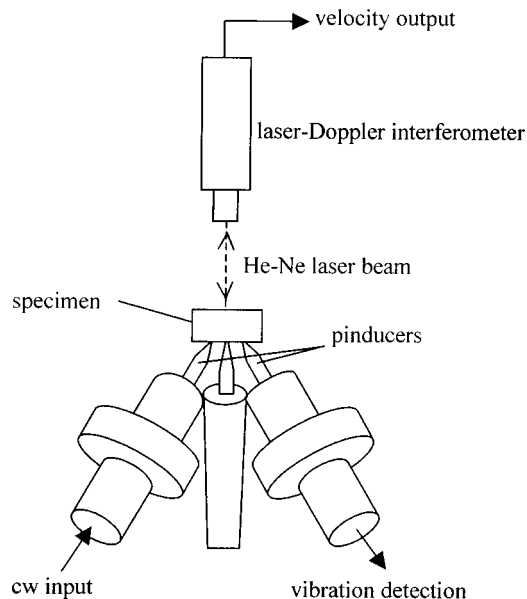
FIG. 1. RUS/Laser measurement setup.

mal component of the velocity at the focal point. The velocity is easily converted into the displacement because of harmonic oscillation.

First, we sweep the driving frequency to obtain the resonance spectrum as shown in Fig. 2 and measure the resonance frequencies by fitting a Lorentzian function around the peaks. The contact between the specimen and pinducers is weak and stable because only the specimen mass contributes to the acoustic coupling between the pinducers and specimen, which ensures high reproducibility in the resonance-frequency measurements. (Scattering of a measured resonance frequency was less than 10^{-4}.)

Second, we drive one of the pinducers at a measured resonance frequency while scanning the specimen surface with the laser-Doppler interferometer to acquire the displacement distribution. The signal-to-noise ratio can be improved by Fourier-transforming the output signal from the interferometer to extract the component at the same frequency as the driving cw signal.

This RUS/Laser technique functioned for specimens with a mass larger than 0.01 g, with a surface area larger than 2 mm-by-2 mm square, and with a Q^{-1} value smaller than 10^{-3}. Typical time needed to measure and display a displacement figure was 1 min.
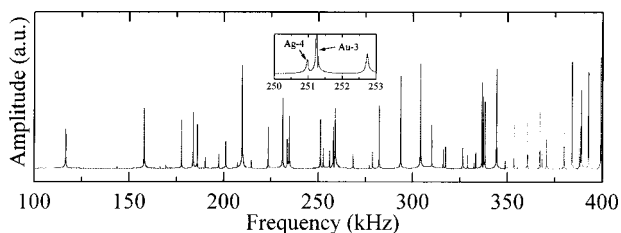
FIG. 2. Resonance spectrum measured by the pinducers for the aluminum alloy specimen. Only the specimen mass contributed to the dry acoustic coupling.

III. CALCULATION OF DISPLACEMENT DISTRIBUTION

No analytical solution exists for the displacements in a rectangular-parallelepiped solid subjected to a free vibration. Thus, the displacements have been approximated by linear combinations of basis functions, and the Rayleigh–Ritz approach has been adopted to determine the accompanying coefficients. Demarest[1] showed that use of normalized Legendre functions as basis functions result in an accurate description of the displacements of a cube specimen with a minimum number of terms. Ohno[2] applied a basis of Legendre functions to describe the displacements of a rectangular-parallelepiped specimen and established the calculation of the free-vibration resonance frequencies. We follow them in this study.

The displacement u_i along the x_i direction can be approximated as

$$u_i(x_1,x_2,x_3) = \sum_k a_k^{(i)} \Psi_k^{(i)}(x_1,x_2,x_3), \qquad (1)$$

$$\Psi_k^{(i)}(x_1,x_2,x_3) = \sqrt{\frac{8}{L_1 L_2 L_3}} \bar{P}_1(2x_1/L_1)$$
$$\times \bar{P}_m(2x_2/L_2)\bar{P}_n(2x_3/L_3), \qquad (2)$$

in a Cartesian coordinate system. $\bar{P}_\lambda$ denotes the normalized Legendre polynomial of degree λ and L_i denotes the edge length along the x_i axis of the rectangular parallelepiped. Lagrangian minimization[1–7] determines the free-vibration resonance frequencies and the coefficients $a_k^{(i)}$. The resonance frequencies have been compared with the measurements and the inverse calculation based on a least-squares fitting has inferred the C_{ij}.

There are eight vibration groups in the free vibration modes of a rectangular parallelepiped with orthorhombic symmetry, labeled as A_u, A_g, B_{1g}, B_{2g}, B_{3g}, B_{1u}, B_{2u}, and B_{3u} by Mochizuki.[10] Because the calculation of the resonance frequencies is independently performed for each vibration group, we exactly know the group and overtone order of the individual calculated frequencies, that is, we can completely identify them. On the other hand, the measured resonance frequencies never inform us of the mode information. Thus, incorrect comparison between the calculations and measurements, or mode misidentification, has easily occurred in the usual RUS method unless excellent initial guesses are adopted.

We pay attention to the coefficients $a_k^{(i)}$ to make correct mode identification. They tell us the two-dimensional pattern of the oscillating specimen surface, which is a *signature* of the individual mode. Thus, the correspondence between the measured and computed displacement distributions guarantees correct mode identification.

IV. RESULTS AND DISCUSSIONS

A. Polycrystalline aluminum alloy

First, we demonstrate the capability of the present technique with a polycrystalline aluminum alloy. The specimen measures $L_1 = 11.92$ mm, $L_2 = 10.93$ mm, and $L_3 = 9.86$ mm and has mass density 2788 kg/m^3. We assume isotropic elas-

(a) A_g-4 (250.98 kHz) (c) B_{1g}-5 (336.65 kHz)

(b) A_u-3 (251.26 kHz) (d) B_{2g}-5 (337.36 kHz)
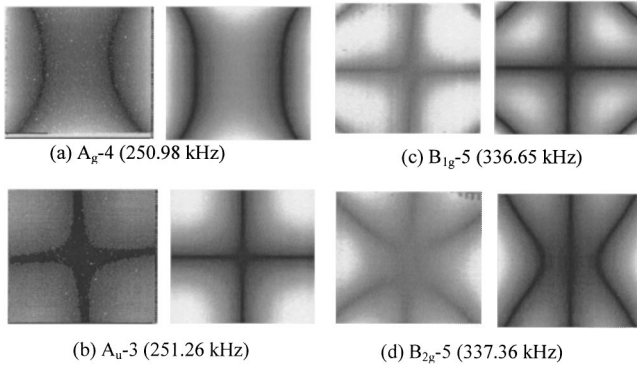
FIG. 3. Comparison of the distribution of the normal displacement amplitude between measurements (left) and computations (right) for the aluminum alloy rectangular parallelepiped. The x_1 and x_2 axes are along the horizontal and vertical directions, respectively. The origin is located at the center of the rectangular parallelepiped.

tic symmetry and two independent elastic constants C_{11} and C_{44}. Figure 2 shows the resonance spectrum measured by the piezoelectric tripod; many peaks appear and some of them overlap with each other. Thus, it is very difficult, as usual, to identify the modes without advance knowledge of the elastic constants. Figure 3 shows a comparison between the measured and computed displacement-distribution patterns. The computations used arbitrary elastic constants of $C_{11}=100$ and $C_{44}=20$ GPa. Bright regions represent high amplitude displacements and dark regions represent low amplitude displacements; black means zero amplitude, the nodal lines. Typical maximum displacement was a few nm in magnitude. [We call these figures *modern Chladni figures* after Ernst F. F. Chladni (1756–1827), who visualized the resonance oscillations of a square brass plate by putting fine sand on it.[11]] We see very good agreement between the measurements and computations. The usefulness is remarkable, especially in identifying overlapping modes. For instance, the A_g-4 and A_u-3 resonances, indicated by arrows in Fig. 2, occur at very close frequencies (only 0.1% difference) and it is hard to identify them. But, their displacement patterns are quite different from each other [Figs. 3(a) and (b)] and we can straightforwardly distinguish between them. Thus, by identifying all the observed modes (more than 80 now), we determined the C_{ij} via the inverse calculation. Table I shows the measured and calculated resonance frequencies after convergence. Owing to the complete mode identification, there are no missed or extra modes in the measurement. The *exact* elastic constants are $C_{11}=109.26$ and $C_{44}=26.72$ GPa. We tried to deduce the C_{ij} using the usual RUS approach with the initial set of C_{ij} used to compute the displacements in Fig. 3, and pairing the closest resonance frequencies from the measurements and calculations. The inverse calculation failed to converge, indicating that the usual RUS method is sensitive to the initial guesses.

Particularly significant is that the displacement-distribution patterns are insensitive to the elastic constants. In Fig. 4, we show the computed patterns for three cases; (I) isotropic symmetry with the exact C_{ij}; (II) isotropic symmetry with the C_{ij} far away from the exact values; and (III) orthorhombic symmetry with arbitrary nine components of

TABLE I. Measured (f_{meas}) and calculated (f_{calc}) resonance frequencies (kHz) after convergence for the aluminum alloy rectangular parallelepiped. Mode notation follows Mochizuki (Ref. 10). The average difference of $f_{meas}-f_{calc}$ was 0.2%.

Mode	f_{meas}	f_{calc}	Diff. (%)
A_u-1	116.716	116.32	0.33
A_u-2	143.783	143.186	0.41
$B_{1u}-1$	158.081	158.44	−0.22
$B_{2u}-1$	166.5	166.113	0.23
$B_{1g}-1$	169.523	169.338	0.11
$B_{2g}-1$	177.846	178.36	−0.29
$B_{3u}-1$	183.875	184.57	−0.38
$B_{3g}-1$	186.047	185.078	0.52
A_g-1	190.341	190.206	0.07
$B_{1u}-2$	197.386	197.692	−0.15
A_g-2	201.133	201.462	−0.16
$B_{3g}-2$	207.386	207.096	0.14
A_g-3	209.836	211	−0.56
$B_{2g}-2$	214.753	215.613	−0.40
$B_{2u}-2$	223.548	223.219	0.14
$B_{3u}-2$	231.266	230.804	0.20
$B_{3g}-3$	233.538	233.329	0.09
$B_{1g}-2$	234.717	234.758	−0.01
A_g-4	250.98	250.777	0.08
A_u-3	251.256	251.038	0.08
$B_{2g}-3$	252.742	252.303	0.17
$B_{1u}-3$	256.122	256.849	−0.28
$B_{3u}-3$	257.595	258.064	−0.18
A_g-5	258.118	258.874	−0.29
$B_{2u}-3$	259.035	259.203	−0.06
$B_{1g}-3$	268.54	267.746	0.29
$B_{2u}-4$	277.113	276.736	0.13
$B_{3u}-4$	278.762	279.144	−0.13
$B_{1u}-4$	282.311	282.773	−0.16
$B_{3u}-5$	293.686	293.016	0.22
$B_{2u}-5$	304.159	304.593	−0.14
$B_{1u}-5$	304.464	305.316	−0.27
$B_{1u}-6$	310.109	309.591	0.16
$B_{1g}-4$	316.197	315.775	0.13
$B_{2g}-4$	317.392	317.931	−0.16
A_u-4	326.462	326.556	−0.02
$B_{3g}-4$	329.034	329.369	−0.10
A_g-6	332.441	332.732	−0.08
$B_{2u}-6$	333.364	332.271	0.32
$B_{1g}-5$	336.65	336.218	0.12
$B_{2g}-5$	337.359	337.511	−0.04
A_g-7	338.276	337.71	0.16

C_{ij}. Despite the quite different C_{ij}, elastic symmetry, and accordingly resonance frequencies, the resemblance among the resultant patterns is striking, especially for the fundamental modes of the eight vibration groups. After all, such an oscillation pattern, or Chladni figure, is governed by the deformation symmetry allowed in the specimen. In the A_u-group vibrations, for example, the x_3 component of displacement, u_3, occurs only when it is an odd function of x_1 and x_2.[2] Therefore, the Chladni figures on the x_3 face of this group always contain odd numbers of nodal lines running along each of the x_1 and x_2 axes. The fundamental mode, therefore, contains the cross-shaped node signature for every case. As for the B_{3g} group, u_3 must be an even function of x_1 and an odd function of x_2, so that the fundamental-mode Chladni figure shows one center nodal line along the x_1 axis; and so forth on. Thus, a Chladni figure is not directly related to the elastic constants. Note that the overtone order is not

A_u-1 (116.3 kHz) A_g-1 (190.2 kHz) B_{1u}-1 (158.4 kHz) B_{3g}-1 (185.1 kHz) A_g-3 (211.0 kHz)

(a) case I

A_u-1 (159.1 kHz) A_g-1 (260.4 kHz) B_{1u}-1 (218.0 kHz) B_{3g}-1 (253.3 kHz) A_g-3 (288.9 kHz)

(b) case II

A_u-1 (129.3 kHz) A_g-1 (177.6 kHz) B_{1u}-1 (149.5 kHz) B_{3g}-1 (163.8 kHz) A_g-4 (309.5 kHz)

(c) case III
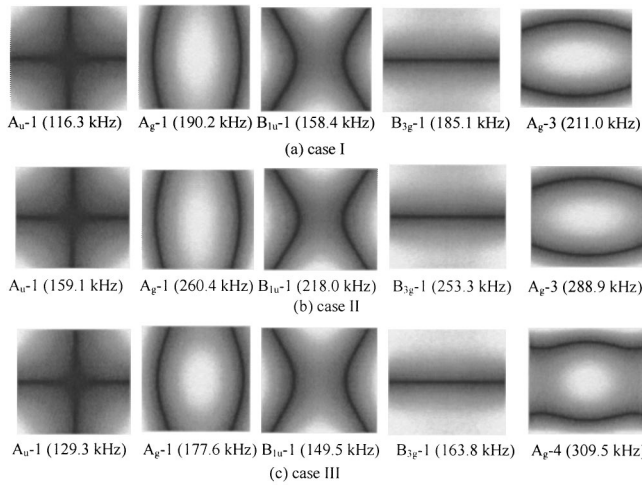
FIG. 4. Displacement-distribution patterns on the x_3 face for three cases: (a) isotropic symmetry with $C_{11}=109.26$ and $C_{44}=26.72$ GPa; (b) isotropic symmetry with $C_{11}=300$ and $C_{44}=50$ GPa; and (c) orthorhombic symmetry with $C_{11}=100$, $C_{22}=150$, $C_{33}=200$, $C_{12}=70$, $C_{13}=60$, $C_{23}=50$, $C_{44}=20$, $C_{55}=30$, and $C_{66}=40$ GPa. The x_1 and x_2 axes are along the horizontal and vertical directions, respectively. The origin is located at the center of the rectangular parallelepiped.

necessarily the same because the C_{ij} affects the resonance frequencies to a large extent; for example, the Chladni figure for the third overtone of A_g group (A_g-3) in cases I and II appears at the fourth overtone in case III (see Fig. 4).

The mode-identification procedure thus becomes an easy task with this technique. Indeed, even unrealistic initial values of $C_{11}=300$ and $C_{44}=50$ GPa allowed us to make the complete mode identification and to reach the correct answer.

B. Monocrystal langasite (La_3Ga_5SiO_14)

We applied this method to a transparent material, monocrystal langasite, by depositing a reflective thin film on the surface. Langasite is a candidate material for surface-acoustic-wave filters owing to its large piezoelectric coefficients e_{ij} and nearly temperature-independent elastic constants. The langasite's crystal structure belongs to the trigonal system with point group 32, thus involving six independent C_{ij}, two e_{ij}, and two dielectric coefficients κ_{ij}. All of them affect the free vibration, which means that e_{ij} and κ_{ij} can be determined by the RUS method together with the C_{ij}.

We used a rectangular parallelepiped crystal with dimensions of $L_1=8.027$ mm, $L_2=9.804$ mm, and $L_3=6.029$ mm. The mass density was 5725 kg/m³. We deposited a 100-nm-thick aluminum film on the surface normal to the x_3 axis (the three-fold axis of the trigonal system). The free-vibration modes for trigonal symmetry fall into the four groups of A_u, A_g, B_u, and B_g.[10] The Legendre basis functions in Eq. (2) are again available not only to describe the displacements but also to describe the electric potential. The detailed calculation procedure has been given by Ohno.[12]

We see excellent agreement between the measured and computed Chladni figures (Fig. 5). The crystal's elastic anisotropy causes asymmetric patterns about the x_1 axis (the two-fold axis). We could identify more than 80 observed resonance peaks, that is, up to more than 20 overtones in

Au-6 (367.1 kHz) Ag-7 (364.9 kHz) Bu-4 (289.0 kHz) Bg-27 (676.5 kHz)
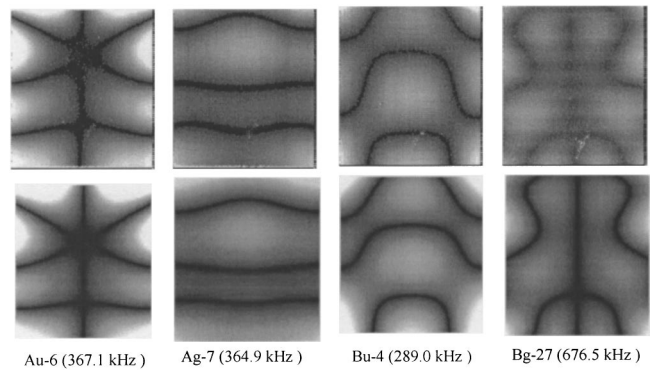
FIG. 5. Comparison of the displacement-distribution patterns on the x_3 face of the monocrystal langasite between measurements (upper) and computations (below). The x_1 and x_2 axes are along the horizontal and vertical directions, respectively. The origin is located at the center of the rectangular parallelepiped.

each group. Thus, the determination of all the material coefficients may be possible and we intend to report on this effort in near future.

V. CONCLUSIONS

We reached the following conclusions from this study.

(1) The RUS/Laser method presented here enables us to identify all observed vibration modes of a rectangular parallelepiped. This leads us to the exact elastic constants, removing the uncertainty in mode identification that has always troubled us.

(2) The displacement-distribution patterns are hardly affected by the elastic constants and elastic symmetry. Therefore, by comparing the measured and computed displacement patterns, we can obtain exact elastic constants with initial guesses far away from the truth. Even the initial values more than 200% different from the correct values resulted in the exact answer.

(3) The present technique also applies to a transparent material with a reflective thin film deposited on the specimen surface. This was demonstrated using a monocrystal langasite.

[1] H. Demarest, Jr., "Cube resonance method to determine the elastic constants of solids," J. Acoust. Soc. Am. **49**, 768–775 (1971).

[2] I. Ohno, "Free vibration of a rectangular parallelepiped crystal and its application to determination of elastic constants of orthorhombic crystals," J. Phys. Earth **24**, 355–379 (1976).

[3] J. Maynard, "Resonant ultrasound spectroscopy," Phys. Today **49**, 26–31 (1996).

[4] A. Migliori and J. Sarrao, *Resonant Ultrasound Spectroscopy* (Wiley, New York, 1997).

[5] H. Ledbetter, C. Fortunko, and P. Heyliger, "Orthotropic elastic constants of a boron–aluminum fiber-reinforced composite: An acoustic-resonance-spectroscopy study," J. Appl. Phys. **78**, 1542–1546 (1995).

[6] J. Maynard, "The use of piezoelectric film and ultrasound resonance to

determine the complete elastic tensor in one measurement," J. Acoust. Soc. Am. **91**, 1754–1762 (1992).

[7] A. Migliori, J. Sarrao, M. W. Visscher, T. Bell, M. Lei, Z. Fisk, and R. Leisure, "Resonant ultrasound spectroscopy techniques for measurement of the elastic moduli of solids," Physica B **183**, 1–24 (1993).

[8] H. Ogi, H. Ledbetter, S. Kim, and M. Hirao, "Contactless mode-selective resonance ultrasound spectroscopy: Electromagnetic acoustic resonance," J. Acoust. Soc. Am. **106**, 660–665 (1999).

[9] H. Ogi, K. Takashima, H. Ledbetter, M. L. Dunn, G. Shimoike, M. Hirao, and P. Bowen, "Elastic constants and internal friction of an SiC-fiber-reinforced Ti-alloy-matrix crossply composite: Measurement and theory," Acta Mater. **47**, 2787–2796 (1999).

[10] E. Mochizuki, "Application of group theory to free oscillations of an anisotropic rectangular parallelepiped," J. Phys. Earth **35**, 159–170 (1987).

[11] C. Taylor, *The Art and Science of Lecture Demonstration* (IOP, Bristol, 1995).

[12] I. Ohno, "Rectangular parallelepiped resonance method for piezoelectric crystals and elastic constants of alpha-quartz," Phys. Chem. Miner. **17**, 371–378 (1990).

Spatial coherence analysis applied to aberration correction using a two-dimensional array system

James C. Lacefield[a)]
Department of Electrical and Computer Engineering, University of Rochester, Rochester, New York 14627

Robert C. Waag
Departments of Electrical and Computer Engineering and Radiology, University of Rochester, Rochester, New York 14627

Complex degree of coherence functions are computed using synthetic and measured ultrasound data to demonstrate noteworthy aspects of coherence analysis in the context of aberration correction. Coherence functions calculated from synthetic data illustrate the importance of proper normalization of the constituent cross-correlation integrals when weak elements and receiver directivity are significant factors. The synthetic data also show that a spike can occur at the zero-lag position of the coherence function when the signal-to-noise ratio is reduced by element directivity near the edges of a large aperture. The latter observation is confirmed by experimental data acquired through tissue-mimicking distributed aberration phantoms using a low *f*-number two-dimensional array system. The coherence of data acquired at neighboring elements is not changed by time-shift compensation of transmit and receive focusing, but time-shift compensation does improve the coherence of echoes measured over larger separations. The resulting increase in coherence widths evaluated at levels between 0.2 and 0.5 is correlated with narrower -10 dB and -20 dB effective widths in focuses visualized using single-transmit images. Iterative focus compensation methods may benefit from aberration estimation algorithms that take advantage of these longer-range correlations in random-scattering waveforms. © *2002 Acoustical Society of America.* [DOI: 10.1121/1.1511756]

I. INTRODUCTION

Coherence functions express the correlation coefficient, a measure of the relative similarity of waveforms at two observation positions, as a function of the distance between those positions. The correlation coefficient indicates the accuracy of correlation-based estimates of time shifts between pairs of waveforms.[1] Time-shift estimation plays an integral role in several ultrasonic imaging techniques, including the measurement of blood flow velocity, elastography, and aberration correction.

In medical ultrasound, pulse-echo data are usually acquired from randomly distributed scatterers. Under distortionless propagation, the spatial coherence of an incoherently scattered wavefront is, as described by the van Cittert–Zernicke theorem,[2–4] proportional to the Fourier transform of the acoustic intensity distribution produced by the focused transmit beam. Therefore, the coherence function of a pulse-echo field can also serve as a measure of the transmit beam pattern at the focus. Measured coherence functions have thus been used to assess focusing improvements obtained from adaptive[5,6] and harmonic[7–9] imaging methods. In astronomy, the van Cittert–Zernicke theorem is employed for the reconstruction of incoherent sources observed through turbulent media, but the assumptions inherent to the theorem are not

sufficiently satisfied in ultrasound data to allow accurate reconstructions in medical imaging.[10]

Thorough discussions of the van Cittert–Zernicke theorem are available in optics textbooks,[2,3] so only a few important definitions are given here for convenient reference. The normalized form of the van Cittert–Zernicke theorem relates the intensity distribution of a spatially incoherent, quasi-monochromatic, planar source, $I(\mathbf{r}')$, to the equal time complex degree of coherence, $j(\mathbf{r}_1,\mathbf{r}_2)$, at two positions, $\mathbf{r}_1$ and $\mathbf{r}_2$, in the far field of the source. That relationship takes the form of a Fourier transform,

$$j(\mathbf{r}_1,\mathbf{r}_2) = e^{ik(r_2-r_1)}\frac{\int_\sigma I(\mathbf{r}')e^{-ik(s_2-s_1)\mathbf{r}'}\,d^2r'}{\int_\sigma I(\mathbf{r}')d^2r'}. \quad (1)$$

In Eq. (1), s_i denotes a position on the surface σ of the planar source. The source is assumed to radiate energy over a narrow band centered at a temporal frequency ν corresponding to the wave number $k=2\pi\nu/c$, where c is the propagation speed. The complex degree of coherence is a normalized cross-correlation function defined by

$$j(\mathbf{r}_1,\mathbf{r}_2)$$
$$= \frac{\langle p^*(\mathbf{r}_1,t)p(\mathbf{r}_2,t)\rangle_t}{[\langle p^*(\mathbf{r}_1,t)p(\mathbf{r}_1,t)\rangle_t]^{1/2}[\langle p^*(\mathbf{r}_2,t)p(\mathbf{r}_2,t)\rangle_t]^{1/2}}, \quad (2)$$

where $p(\mathbf{r}_i,t)$ is the radio frequency signal measured at position $\mathbf{r}_i$, the asterisk denotes complex conjugation, and $\langle \bullet \rangle_t$ indicates an expected value taken over the duration of the observation interval. The denominator of Eq. (2) is equiva-

[a)]Current address: Departments of Electrical and Computer Engineering and Medical Biophysics, University of Western Ontario, London, Ontario N6A 5B9, Canada.

lent to the geometric mean of the expected values of the intensity signals at $\mathbf{r}_1$ and $\mathbf{r}_2$. Alternatively, the normalization term in the denominator of the van Cittert–Zernicke theorem may be omitted, and the quantity on the left-hand side of Eq. (1) becomes the mutual intensity, $J(\mathbf{r}_1,\mathbf{r}_2)$, which is equivalent to the numerator of Eq. (2). The normalized definitions are used in this paper to allow comparisons of coherence functions measured under different experimental conditions.

In this paper we examine the use of the complex degree of coherence, hereafter the "coherence function" for brevity, for an analysis of aberration correction experiments performed with a large two-dimensional transducer array. Our main purposes in this paper are to describe observations about the implementation and to provide interpretations of ultrasonic coherence measurements that are not in Refs. 4–10. Coherence computations performed on synthetic data are used to demonstrate the importance of the form of the normalization term in Eq. (2) for cases where receiver element directivity, weak elements, and additive noise are significant factors. Coherence calculations are also performed using data measured through unique tissue-mimicking distributed aberration phantoms.[11] These experiments quantify changes in the coherence function that are observed under realistic, controlled levels of aberration before and after the time-shift compensation of transmit and receive focusing. The results show the conditions under which a coherence width can serve as a meaningful gauge of focusing performance. Implications of these results for future progress in aberration correction are emphasized.

II. DEMONSTRATIONS USING SYNTHETIC DATA

The procedure used for the computation of a coherence function from data acquired with a two-dimensional array is outlined here. First, a rectangular time window is applied to the signals received at each element to isolate echoes from the transmit focus. The position vectors in Eq. (2) correspond to the locations of the receiver elements, so the correlation integral in the numerator must be evaluated for each pair of windowed signals. After every correlation integral has been evaluated, the results are normalized by the autocorrelation values, as specified by the denominator of Eq. (2). The normalized correlation coefficients are then grouped by element separation and averaged to yield a two-dimensional coherence surface sampled at integer multiples of the element pitch. The entire calculation is summarized by the expression

$$\hat{j}(\Delta x,\Delta y)=\frac{1}{N_\Delta}\sum_{N_\Delta}\frac{\int_T p_i(t)p_j(t)dt}{[\int_T p_i^2(t)dt]^{1/2}[\int_T p_j^2(t)dt]^{1/2}}, \quad (3)$$

where N_Δ denotes the number of element pairs with two-dimensional Cartesian separation $(\Delta x,\Delta y)$, $p_i(t)$, and $p_j(t)$ represent the radio-frequency signals received on each of those element pairs, and T is the duration of the time window. For an $M\times N$ element array, the cumulative sum from 1 to $M\times N$ unique correlation integrals are necessary, followed by an identical number of normalization operations, so the computation can become time consuming. At the maximum aperture size used in the experiments, $M=N=79$ elements,

the calculation requires approximately ten minutes to execute on a 1.4 GHz Pentium IV workstation when implemented using Matlab 6.1 (The MathWorks, Natick, MA).

In the general case, the above algorithm uses a different normalization than the calculation defined by Eq. (17) of Ref. 4. In Ref. 4, the spatial covariance of pulse-echo data is estimated by dividing the average mutual intensity from all element pairs with the separation of interest by the signal energy averaged over the entire array. Using the notation of Eq. (3), Eq. (17) of Ref. 4 may be expressed as

$$\hat{R}_p(\Delta x,\Delta y)=\frac{[\Sigma_{N_\Delta}\int_T p_i(t)p_j(t)dt]/N_\Delta}{[\Sigma_{N_0}\int_T p_i^2(t)dt]/N_0}, \quad (4)$$

where N_0 denotes the total number of elements in the array. A Matlab implementation of Eq. (4) processes a 79×79-element dataset in approximately two minutes. The shorter computational time is obtained because a single averaged normalization is used in Eq. (4), whereas a unique normalization is computed for every cross-correlation in Eq. (3). Since the normalization terms in Eqs. (3) and (4) are a geometric and an arithmetic mean, respectively, the two calculations yield the same result only if the expected value of the intensity signal is invariant over the area of the receive array. The significance of this difference in normalization is shown in the following paragraphs using coherence curves calculated from synthetic data.

A 79×79 array of identical Gaussian-envelope sine pulses was produced with 3.0 MHz center frequency and 57% -6 dB fractional bandwidth. These parameters match the characteristics of the two-dimensional array system used in the experiments. An amplitude shading consisting of a product of one-dimensional $\sin(x)/x$ functions oriented along the lateral and elevation dimensions of the array was applied to the pulses to simulate the directivity of 2-D array elements. The amplitude shading was equivalent to the magnitude of the theoretical continuous wave far field diffraction pattern of a small rectangular element,[12]

$$|U(x,y)|\propto\frac{\sin\left[\frac{2\pi w_x x}{\lambda z}\right]}{\frac{2\pi w_x x}{\lambda z}}\frac{\sin\left[\frac{2\pi w_y y}{\lambda z}\right]}{\frac{2\pi w_y y}{\lambda z}}, \quad (5)$$

where w_x and w_y are the half-widths of the element centered at position (x,y) in the aperture plane, z denotes the distance from the aperture to the focal plane, and λ is the wavelength. For the parameters of the experimental system ($\lambda=0.5$ mm, $w_x=w_y=0.3$ mm, and $z=55$ mm), the directivity function has a maximum value of 1.0 at the center of the array and a minimum value of 0.39 at the corner elements. Weak elements were simulated by using a uniform random number distribution to select elements covering 2% of the array and attenuating the signals at those elements by 40 dB. Finally, Gaussian distributed white noise with variance equal to 0.01 or 0.1 times the peak amplitude of the original pulse was added to each signal. In the former case, the signal-to-noise ratio (SNR) was between 32 and 40 dB for the properly functioning elements and between 0 and -8 dB at the weak elements. In the latter case, the SNR was between 12 and

(a) Noiseless Synthetic Data

(b) Synthetic Data, SNR = 40 dB
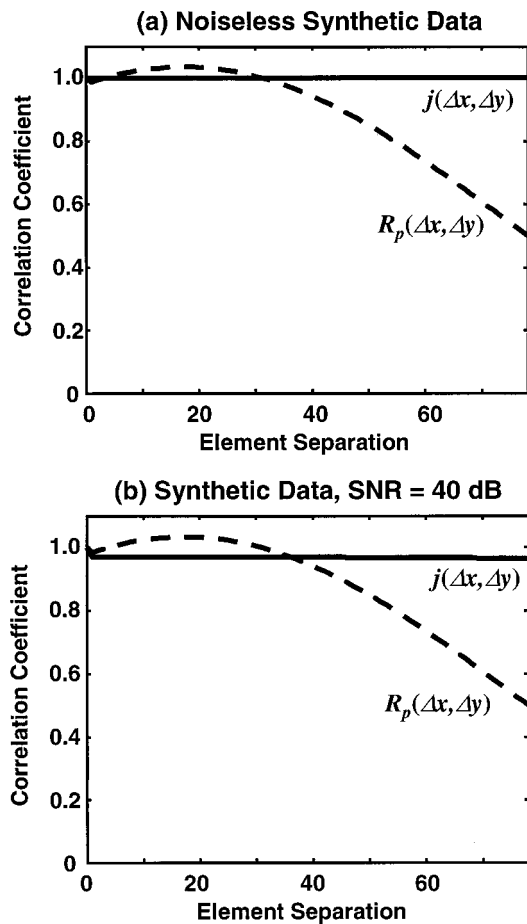
FIG. 1. Average coherence functions, $j(\Delta x, \Delta y)$ and $R_p(\Delta x, \Delta y)$, calculated using Eqs. (3) and (4), respectively, with 100 realizations of synthetic data. Error bars were omitted because they were too small to be legible. (a) Coherence curves for data that include simulated element directivity and weak elements, but no noise. (b) Coherence curves calculated after the addition of noise to the same data to reduce the maximum signal-to-noise ratio (SNR) to 40 dB.

20 dB for the properly functioning elements and between -20 and -28 dB at the weak elements. Coherence functions were calculated for the original, uniform pulses and the modified data using the two methods defined by Eqs. (3) and (4). Each case was repeated for 100 realizations of the weak element distribution and noise.

When identical, noiseless pulses were present on every array channel, both computation methods correctly return correlation coefficients equal to 1.0 for all element separations. The inclusion of element directivity and weak elements in the data alters $R_p(\Delta x, \Delta y)$, the coherence function obtained from Eq. (4). Since the two-dimensional coherence functions are, on average, radially symmetric, the radial lines presented in Fig. 1(a) sufficiently summarize the results. Weak elements decreased the lag-one value of $R_p(\Delta x, \Delta y)$, which is the estimated coherence of signals received at adjacent elements, to 0.987 ± 0.001 (mean$\pm$standard deviation over 100 realizations). The element directivity introduced an anomalous peak with magnitude 1.036 ± 0.001 at separation equal to 18.3 ± 0.9 elements. In contrast, the coherence function $j(\Delta x, \Delta y)$ estimated using Eq. (3) consistently maintained a value of 1.0 for all element separations.

The addition of noise demonstrates that $j(\Delta x, \Delta y)$ for

point-source data will not necessarily be exactly equal to 1.0 under realistic conditions. Reducing the maximum signal-to-noise ratio from infinity to 40 dB decreased the lag-one value of $j(\Delta x, \Delta y)$ to 0.969 ± 0.001, and the curve remained near that level across the rest of the aperture [Fig. 1(b)]. Noise produced a relatively small change in $R_p(\Delta x, \Delta y)$, the value of which was decreased slightly to 0.985 ± 0.001 for adjacent elements. The peak of $R_p(\Delta x, \Delta y)$ also shifted slightly to 1.034 ± 0.001 at 18.3 ± 0.9 elements separation.

A further reduction of the maximum SNR to 20 dB dropped the lag-one values of $j(\Delta x, \Delta y)$ and $R_p(\Delta x, \Delta y)$ to 0.834 ± 0.001 and 0.865 ± 0.001, respectively. This signal-to-noise ratio is comparable to the SNR observed in the experimental measurements presented in the following sections that used randomly distributed scattering. The severity of the decline in coherence from the 40 dB SNR case is partly attributable to the element directivity, which caused low signal levels near the edges of the aperture. When only the central 39×39 elements were used in the coherence calculations, the lag-one values of $j(\Delta x, \Delta y)$ and $R_p(\Delta x, \Delta y)$ increased to 0.883 ± 0.006 and 0.900 ± 0.003, respectively. The inclusion of fewer elements in the calculation also increased the variance of the results because coherence values for fewer pairs of noisy signals were averaged.

The synthetic data demonstrations are representative of the experimental data acquired by the two-dimensional array system used for the measurements in this paper. These examples verify that the analysis method summarized in Eq. (3) yields accurate results at high signal-to-noise ratios. The $j(\Delta x, \Delta y)$ coherence function is preferable for analyzing aberration correction experiments for two reasons. One reason is that the use of potentially different normalizations for each cross-correlation implies that $j(\Delta x, \Delta y)$ is relatively more sensitive to variations in pulse shape and less sensitive to variations in amplitude than is $R_p(\Delta x, \Delta y)$. If the coherence function is used to infer the expected error in time shifts estimated by cross-correlation of signal pairs, the width of a cross-correlation peak and its amplitude relative to other local maxima in the same cross-correlation function determine the accuracy of the time-shift estimate, but the absolute magnitude of the peak compared to cross-correlation peaks of other signal pairs does not influence the result.

The second advantage of $j(\Delta x, \Delta y)$ is that it apparently yields a more accurate estimate of the coherence function at large element separations. This statement is supported by Fig. 1, which shows roll-offs produced by element directivity in $R_p(\Delta x, \Delta y)$, but not in $j(\Delta x, \Delta y)$. Even in the low SNR case, which is not shown in the figure, the value of $j(\Delta x, \Delta y)$ remains approximately constant for lags greater than one, while $R_p(\Delta x, \Delta y)$ declined in a manner similar to that shown in Fig. 1. If the measured coherence function and the van–Cittert Zernicke theorem are used to compute the transmit focus, the difference in the behaviors of $j(\Delta x, \Delta y)$ and $R_p(\Delta x, \Delta y)$ at large separations can lead to significantly different estimates of the focus.

III. EXPERIMENTAL METHODS

Measurements were performed using a 3.0 MHz two-dimensional array system that consists of 6400 square,

0.6-mm-pitch elements with a −6 dB fractional bandwidth of 57%. Pulse-echo data were acquired using a synthetic aperture method from a focus 55 mm below the center of a 79×79 element aperture, which corresponds to an *f*-number equal to 1.16. The transmit aperture was apodized with the product of two one-dimensional Hamming windows applied along the lateral and elevation dimensions of the array. Receive data were sampled at 20 MHz with 12-bit resolution. Further details about the 2-D array system are available in a recent publication.[13]

Each measurement trial included a sequence of pulse-echo acquisitions that were performed in a 30 °C distilled water bath. Data were first acquired from a point reflector positioned at the transmit focus. Point-reflector data were acquired through a water path and then through one of two 35-mm thick distributed aberration phantoms[11] placed against the array and above the target. The point reflector was the polished hemispherical tip of a 0.8 mm diameter, vertically oriented stainless steel rod.

A second set of measurements was performed using a tissue-mimicking random scattering phantom[14] in place of the point reflector. Data were acquired using geometric transmit focusing through a water path and through the same locations on the aberration phantoms. Arrival time fluctuation (ATF) maps were estimated from the aberrated data, and random-scattering data were reacquired while using those ATF maps for time-shift compensation of the transmit focusing.

Both measurement sequences were repeated at eight different locations on each aberration phantom.

The aberration phantoms[11] consisted of a fat-mimicking background[15] containing randomly distributed spheres. The spheres were 6.3 and 12.7 mm in diameter and had a sound speed approximately 2% greater than the background. The aberration was produced by refraction and scattering from the spheres. The phantoms were labeled ''weak'' and ''strong'' aberrators, respectively, based on a comparison of the root-mean-square arrival time fluctuations measured through the phantoms and through human abdominal wall specimens[16] using the same transmission system. In the transmission measurements, the weak aberrator produced arrival time fluctuations with a typical root-mean-square (rms) magnitude of 45 ns and full width at half-maximum correlation length of 6 mm, while the strong aberrator produced 70 ns rms ATF with 7 mm correlation length.

Arrival time fluctuation maps were estimated from the point-reflector and random-scattering data using the method described in Ref. 17. In this method, cross-correlation functions are calculated for all pairs of signals received on horizontally, vertically, or diagonally adjacent elements. The positions of the cross-correlation peaks are used to determine differences in the echo arrival times for each element pair. Those local arrival time differences are used in an overconstrained system of equations that is solved by a least-mean-square-error method[18] to obtain a two-dimensional arrival time surface covering the aperture area. A fourth-order polynomial surface is fit to and subtracted from the output of the least-mean-square-error computation to account for geometric path length differences, and the residual time shifts are interpreted as arrival time fluctuations produced by the aberrator. Time-shift compensation was performed with 0.1 ns precision by cubic spline interpolation of the waveforms.

Two-dimensional coherence functions were calculated using geometrically corrected data before and after time-shift compensation. Results from different regions of the aberration phantoms were summarized by taking orthogonal slices along the *x* and *y* axes of the coherence functions and calculating average curves for each combination of aberrator and receive focusing method. Averaged results were plotted as radial curves since the coherence functions were symmetric through the origin. Coherence widths were evaluated the 0.8, 0.5, and 0.2 levels by interpolating the individual radial curves obtained in each trial from 0.6 mm (i.e., the array element pitch) to 0.1 mm sampling.

Coherence functions were also computed using random-scattering data from the central 39×39 receiver elements only. Truncation of the aperture increased the receive *f*-number to 2.35. This calculation was performed to demonstrate the influence of the outer elements on the estimated lag-one coherence. Those results were compared with averaged two-dimensional profiles of the signal-to-noise ratio that documented the decline in the SNR as a function of radial distance from the center of the aperture. The noise level was determined by recording 2-D array signals with no targets in the water tank. For each element, the noise level was estimated as the root-mean-square amplitude of the ''targetless'' signal averaged over four independent (average correlation coefficient=0.000 75) 5-μs windows. Signal levels were obtained by averaging the rms amplitudes within the 5-μs window over eight random scattering trials and then subtracting the estimated rms noise levels. Separate SNR profiles were determined for each combination of propagation path and transmit focusing method.

Spatial resolution was evaluated by forming single-transmit images[17] of the focus in the random scattering medium. In the focus calculation, the received waveforms were windowed with a 5-μs duration Hamming function and spatially apodized in the same manner as the transmit aperture. The windowed data were focused at 55 mm by numerical evaluation of the Rayleigh–Sommerfeld diffraction formula. The calculation produced a volume of magnitude data that was equivalent to the three-dimensional image that would be formed by scanning the receive beam in the lateral and elevation dimensions while maintaining a fixed transmit focus. The focus was characterized by effective widths[18] in the two dimensions parallel to the aperture plane at 10, 20, and 30 dB below the peak.

The effective width data were compared with the coherence widths evaluated at the 0.2 and 0.5 levels using scatter plots. The coherence widths at the 0.8 level were not used because they were shown by the calculations performed with the truncated aperture to be overly sensitive to the signal-to-noise ratio and therefore were considered not useful for characterization of the transmit focus. Six plots were produced containing two data points from each random scattering pulse-echo acquisition, for a total of 128 data points per graph. Curves of the form $y = \alpha x^{\beta}$ were fit to the scatter plots by linear regression of the transformed equation

(a) Uncompensated Point Reflector Data

(b) Receive TSC Point Reflector Data
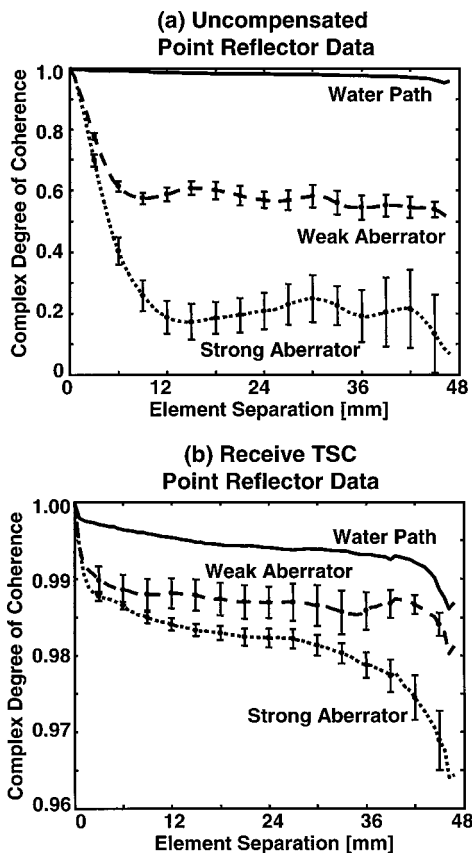
FIG. 2. Average radial coherence curves of point-reflector data. Error bars denote one standard deviation and were omitted from the water path curves because they were too small to be legible in those cases. Water path curves were computed from five acquisitions and aberrator path results from eight acquisitions at different locations on the aberration phantoms. (a) Data acquired without aberration correction. (b) Data acquired using receive time-shift compensation (TSC).

$\log(y)=\log(\alpha)+\beta\log(x)$, and coefficients of determination, r^2, were calculated for each regression curve.[19]

IV. RESULTS

Radial coherence curves calculated from point-reflector data before and after receive time-shift compensation are shown in Fig. 2. Increasing the rms ATF value (Table I) by switching from a water path to the weak and then the strong aberrator substantially reduced the uncompensated echo coherence at element separations greater than 5 mm. However, the two aberrator path curves approached the water path curve after time-shift compensation.

Table I also documents the similarity in lag-one coherence of time-shift compensated point-reflector data acquired through the two aberration phantoms. Time-shift compensation aligns the correlation peaks in the equal-time (i.e., zero

TABLE I. Noteworthy properties of point-reflector data. Root-mean-square arrival time fluctuations (rms ATF) in nanoseconds and lag-one correlation coefficients are reported as mean ± standard deviation over N trials.

Propagation path	N	rms ATF (ns)	Lag-one coherence
Water	5	5.7±0.1	0.9979±0.0003
Weak aberrator	8	40.8±3.8	0.9943±0.0020
Strong aberrator	8	64.5±6.3	0.9942±0.0008

(a) Uncompensated Random Scattering Data

(b) Receive TSC Random Scattering Data

(c) Transmit & Receive TSC Random Scattering Data
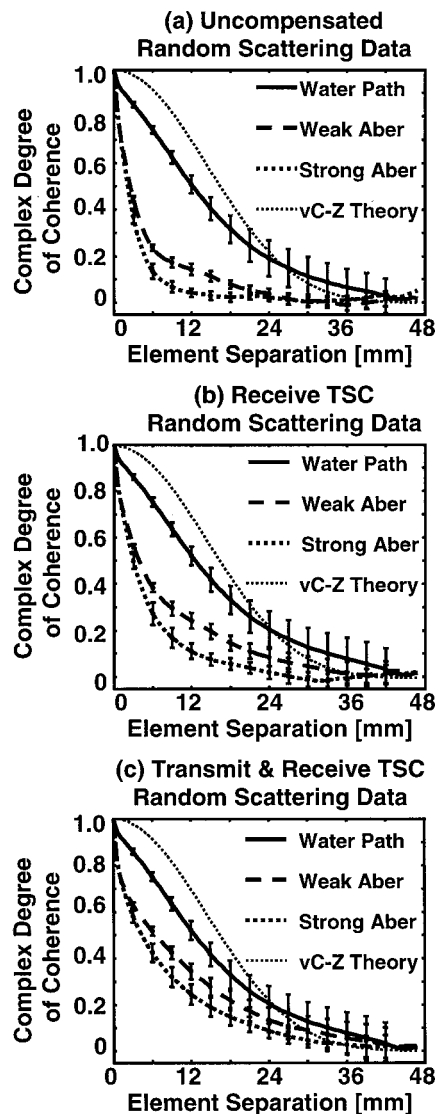
FIG. 3. Average radial coherence curves of random-scattering data. Error bars are formatted as in Fig. 2. The theoretical curve predicted by the van Cittert–Zernicke theorem (vC–Z) is shown as a dotted line in each panel. (a) Data acquired without aberration correction. (b) Data acquired using receive time-shift compensation (TSC). (c) Data acquired using time-shift compensation during both transmission and reception.

temporal lag) plane such that the coherence value at unit spatial lag is equivalent to the mean normalized correlation coefficient for signals acquired on adjacent elements. This correlation coefficient indicates the relative accuracy of the time-shift estimates.[1] Therefore, Fig. 2 and Table I demonstrate that the 2-D array hardware and computational methods perform as expected under the favorable coherence and signal-to-noise conditions provided by the point reflector.

Average radial coherence curves for the 79×79-element random-scattering data appear in Fig. 3, and the rms ATF and lag-one coherence values for that data are listed in Table II. For the random-scattering data, a coherence function was computed for data acquired using time-shift compensation during both transmission and reception, in addition to coherence functions computed from uncompensated data and after receive time-shift compensation. The coherence curve predicted by the van Cittert–Zernicke theorem, which is equal to the autocorrelation of the transmit apodization,[4] is in-

TABLE II. Noteworthy properties of random scattering data. Root-mean-square arrival time fluctuations (rms ATF) in nanoseconds and lag-one correlation coefficients are reported as mean ± standard deviation over N trials. Aberrator path results are listed for data acquired using both geometric and time-shift compensated (TSC) transmit focusing.

Propagation path	Transmit focus	N	rms ATF (ns)	Lag-one coherence 39×39 elements	Lag-one coherence 79×79 elements
Water	Geometric	8	13.8±3.7	0.972±0.010	0.945±0.008
Weak aberrator	Geometric	8	40.8±3.6	0.881±0.022	0.816±0.014
	TSC	8	44.3±5.8	0.875±0.030	0.807±0.020
Strong aberrator	Geometric	8	50.8±3.1	0.878±0.022	0.827±0.012
	TSC	8	53.4±5.2	0.869±0.027	0.816±0.018

TABLE III. Coherence widths of random scattering data evaluated at the 0.8, 0.5, and 0.2 coherence levels, reported as mean ± standard deviation over eight trials. Results are provided for data acquired using several combinations of propagation path and transmit and receive focusing methods.

Propagation path	Transmit focus	Receive focus	Coherence widths (mm) 0.8-max	Coherence widths (mm) 0.5-max	Coherence widths (mm) 0.2-max
Water	Geometric	Geometric	4.5±0.8	12.9±3.0	26.2±9.7
	Geometric	TSC	4.8±1.0	13.3±3.2	27.4±10.2
Weak aberrator	Geometric	Geometric	0.6±0.1	2.6±0.2	8.7±3.0
	Geometric	TSC	0.7±0.1	3.9±0.4	16.6±9.1
	TSC	TSC	0.7±0.1	6.8±1.5	21.2±8.3
Strong aberrator	Geometric	Geometric	0.6±0.1	2.2±0.3	4.9±1.1
	Geometric	TSC	0.7±0.1	3.1±0.6	8.4±2.8
	TSC	TSC	0.7±0.1	4.7±1.2	15.3±5.3

cluded in each panel for comparison with the water path results. The uncompensated aberrator path curves [Fig. 3(a)] are qualitatively similar to the simulated curves in Ref. 6, in that the curves obtained from measured data are characterized by a steep slope at small element separations and gentle oscillations near zero correlation at larger separations. At element separations between 5 and 25 mm, the coherence of data acquired using transmit and receive time-shift compensation together was significantly greater than the coherence of data acquired using receive compensation alone. However, the lag-one coherence values were not significantly changed by the use of transmit time-shift compensation. In other words, time-shift compensation produces larger increases in coherence width when the widths are evaluated far from the peak of the coherence function. This observation is quantified in Table III.

Maps of the signal-to-noise ratio in the aperture and complex degree of coherence are shown in Fig. 4 for random scattering received through a water path and through the strong aberrator. The maps show a decline in the signal-to-noise ratio as the distance from the center of the aperture increases. This decline is attributed to a directivity related decrease in sensitivity of the elements away from the center of the aperture. Truncation of the receive aperture increased the mean SNR of the water path random-scattering data from 26.3±3.7 dB to 29.7±2.0 dB. Similarly, the mean SNR of the weakly aberrated data increased from 14.1±4.0 dB to 18.0±1.8 dB, and the mean SNR of the strongly aberrated data rose from 15.6±3.8 dB to 19.1±1.7 dB. The effect of higher signal-to-noise ratio on the coherence is given numerically in Table II for neighboring elements and graphically in Fig. 4 for larger element separations.

Representative single-transmit images computed from strongly aberrated random scattering data are presented in

(a) SNR Map of Water Path Random-Scattering Data

(b) SNR Map of Strong Aberrator Path Random-Scattering Data

(c) Water Path Random-Scattering Data

(d) Strong Aberrator Path Random-Scattering Data
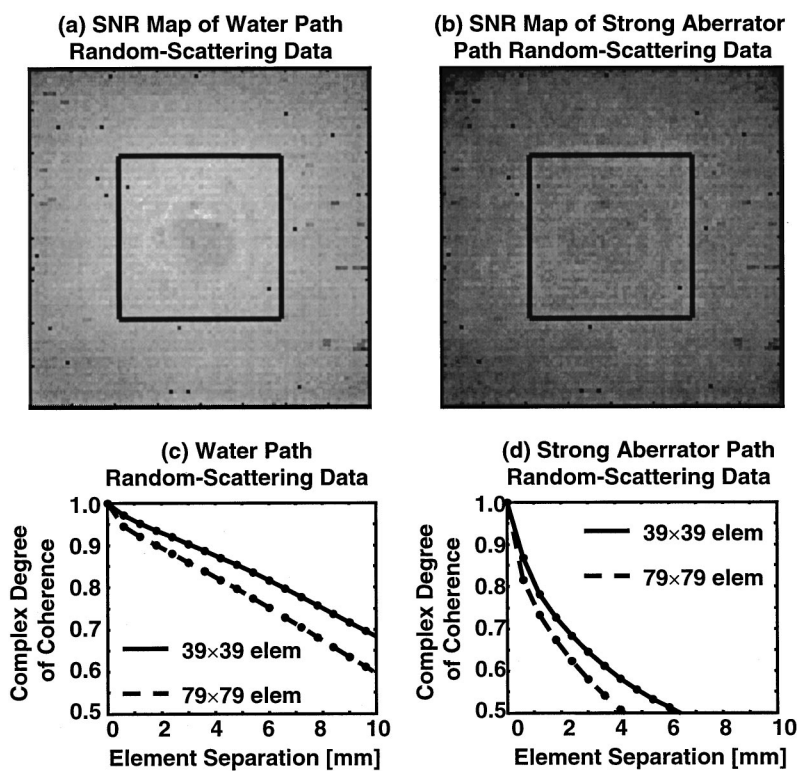
FIG. 4. Signal-to-noise ratio maps within the 2-D array aperture above segments of the corresponding coherence curves. In panels (a) and (b), the SNR maps are displayed on a logarithmic gray scale with 0 and 35 dB corresponding to black and white, respectively. The boxes outline the truncated receive aperture used to demonstrate the effect on the coherence curves of the reduced SNR at the outer elements. In panels (c) and (d), average coherence curves computed within the full 79×79-element aperture are plotted as dashed lines and coherence curves computed using the central 39×39 receive elements are shown as solid lines.
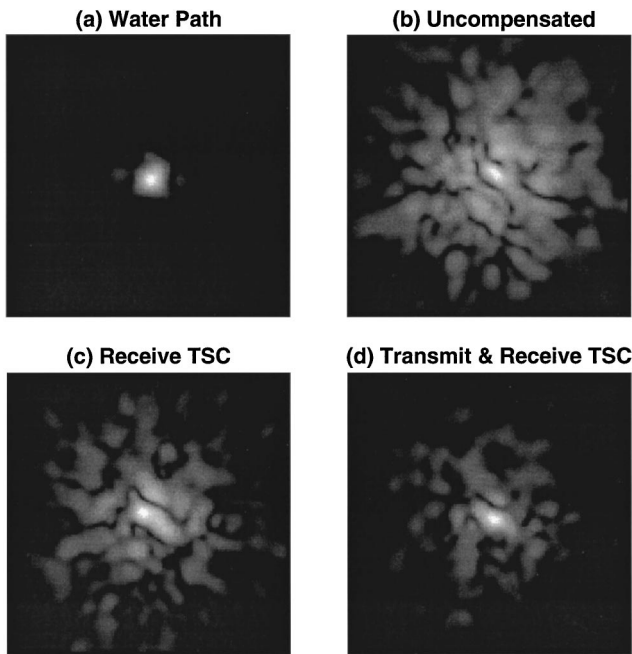
FIG. 5. Representative single-transmit images computed from random-scattering data. The images show 20×20-mm² regions in a plane through the focus and parallel to the aperture, and are displayed using a 30-dB logarithmic gray scale. (a) Water path focus. (b) Uncompensated focus produced through the strong aberrator. (c) Focus produced after receive time-shift compensation (TSC) of the data shown in Panel b. (d) Focus produced through the same aberration using time-shift compensation during both transmission and reception.

Fig. 5. Cross sections through the focus are shown in 20×20 mm² regions parallel to the aperture plane. These images are equivalent to a convolution of the receive beam with the transmit beam weighted by the scatterer distribution,[17] and thus permit comparison of compensated and uncompensated focusing. The images, which are shown on 30-dB logarithmic gray scales, demonstrate that the use of transmit and receive time-shift compensation together substantially reduced the peripheral energy level around the edges of the focus.

Selected scatter plots of coherence widths versus effective widths are shown in Fig. 6 and the regression results are summarized in Table IV. The scatter plots and regression analysis provide graphical and quantitative descriptions of the relationship between the coherence width of random scattering data and the effective width of a single transmit image when the two widths are evaluated at particular combinations of coherence and image magnitude levels. The r^2 values suggest that coherence widths evaluated at lower levels are most strongly correlated with effective widths evaluated near the peak level, and *vice versa*. This conclusion is appealing in view of the Fourier transform relationship [Eq. (1)] between the effective source distribution and the complex degree of coherence described by the van Cittert–Zernicke theorem.

V. DISCUSSION

The computation of coherence functions from experimental data raises significant practical issues. One issue is the selection of the starting time and duration of the temporal
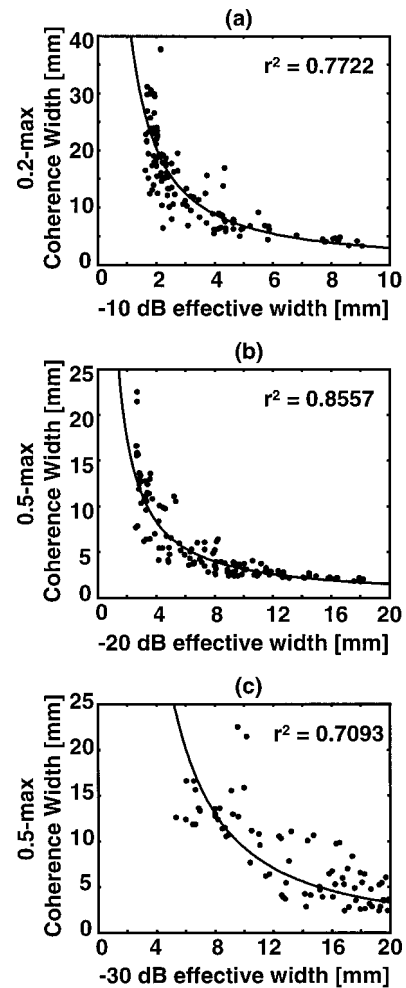
FIG. 6. Scatter plots of coherence function widths versus effective widths of single transmit images, accompanied by curves fit by linear regression of the equation $\log(y)=\log(\alpha)+\beta\log(x)$. Coefficients of determination, r^2, for the regression curves are shown on each panel. (a) Coherence widths evaluated at the 0.2 level plotted against −10 dB effective widths. (b) Coherence widths evaluated at the 0.5 level plotted against −20 dB effective widths. (c) Coherence widths evaluated at 0.5 plotted against −30 dB effective widths.

integration window represented by T in Eq. (3). A proper choice of the starting time and duration ensure that only echoes from the transmit focus contribute to the calculated coherence function.[4] In this study, the integration window was positioned by visual inspection when point-reflector data

TABLE IV. Regression coefficients for scatter plots of random scattering coherence widths versus effective widths. Results are given for several combinations of coherence width and effective width evaluation levels. The parameters listed are the coefficient of determination, r^2, obtained from linear regression of the equation $\log(y)=\log(\alpha)+\beta\log(x)$.

Effective width level	Coherence width level	Regression coefficients		
		α	β	r^2
−10 dB	0.2	46.66	−1.197	0.7722
	0.5	15.33	−1.079	0.5987
−20 dB	0.2	82.40	−0.976	0.7488
	0.5	36.47	−1.068	0.8557
−30 dB	0.2	390.8	−1.244	0.5013
	0.5	304.3	−1.514	0.7093

were analyzed, but the arrival time and duration of echoes from the transmit focus were not readily discernible in the random-scattering data. The known average sound speeds of the aberration and scattering phantoms (1460 and 1540 m/s, respectively) were used to calculate the expected arrival time of random-scattering echoes from the transmit focus. A 5-μs integration window was selected because that duration usually yielded the highest lag-one coherence. In principle, the window duration could be determined from the textbook expression for depth of field, $\Delta z = A \lambda (f/\#)^2$, but the constant of proportionality, A, is assigned different values in different references, and the most appropriate value of A for this application is unclear. A robust automated procedure for identifying the transmit focus in speckle waveforms would be useful in cases where the sound speed is unknown *a priori* and would be more efficient than a trial-and-error determination of the window duration. Such a procedure could perhaps be developed by an extension of the sound speed estimation method proposed in Ref. 20, which describes an approach similar to methods used in seismology to determine sound speeds and thicknesses of geologic layers.

Uncertainty about the arrival times of echoes from the transmit focus is also reflected by the use of a fourth-order polynomial fit during the time-shift estimation. A fourth-order polynomial was selected because it provides a more flexible fit than lower-order alternatives such as a spherical or parabolic surface. The scattering and aberration phantoms have different average sound speeds. To perform a more precise fit to the arrival time surface obtained after propagation through two layers with different average sound speeds is a nontrivial task when refraction at the interface of the layers is taken into account.[21] The remainder of the Discussion assumes that any time-shift compensation errors caused by the use of a fourth-order polynomial can be neglected. However, a recent analysis of errors caused by the failure to compensate linear or quadratic components of the arrival time profile indicates that such errors degrade the focusing performance of low f-number systems,[22] so further effort toward optimization of the time-shift estimation procedure may be worthwhile.

One benefit of the large two-dimensional array was the smoothness of the estimated coherence curves. This observation is attributed to the averaging made possible by the acquisition of 79×79 waveforms, which reduced fluctuations in the coherence function due to array nonuniformities or the random nature of speckle data. For an element separation $(\Delta x, \Delta y)$ on the 2-D coherence function, a total of $(79 - \Delta x)(79 - \Delta y)$ unique correlation integrals were used to estimate the coherence value. The one-sided curves shown in the figures were averages of slices along the x and y axes of the 2-D functions, so, for example, the lag-one coherence value obtained from a single trial was an average of $2 \times 79 \times 78 = 12\,324$ normalized cross-correlation integrals.

In the random scattering experiments, the smoothness of the coherence functions was achieved at the expense of low signal-to-noise ratios near the edges of the aperture. The reduced SNR produced a spike at the zero-lag position of the coherence function. Shen and Li[8] observed similar spikes in a study that demonstrated the effect of SNR on the coherence of second harmonic echoes. The results in this paper and Ref. 8 both indicate that the existence of a zero-lag coherence spike can serve as a flag for a low signal-to-noise ratio. The inclusion of this type of spike in a measured coherence function will create difficulties if the van Cittert–Zernicke theorem is used to estimate the transmit focus distribution, because Fourier transformation of the spike will add an anomalous constant term or floor to the estimated beam pattern.

Prior results[4–6] demonstrate that the narrowing of a random scattering coherence function produced by uncompensated aberration corresponds to a broadening of the main lobe of the point-spread function and an increase in the peripheral energy level. This and other reports[5,17] also indicate that the coherence of speckle data can be partially restored by transmit and receive focus compensation. A relationship between the coherence function and the intensity distribution at the focus could be anticipated from the van Cittert–Zernicke theorem, but the theorem assumes distortionless propagation. The purpose of the scatter plots (Fig. 6) and accompanying regression analysis is to assess whether the coherence width still provides a meaningful indication of focus quality in the presence of aberration, and, if so, whether the level at which the coherence width is measured is an important consideration. The r^2 values listed in Table IV indicate that the answer to both questions is "yes." Another approach to summarizing a coherence function with a single numerical value is to calculate a generalized correlation coefficient such as the waveform similarity factor used by Liu and Waag[17] or, analogously, the focusing criterion defined by Mallart and Fink.[5] The coherence width was used instead in this paper because coherence width has the same units as the effective width and makes a direct comparison of the two quantities appealing.

Time-shift compensation of random-scattering data may be applied iteratively using repeated pulse-echo acquisitions. In this process, time shifts are re-estimated after each acquisition to improve accuracy of the estimates. However, the lag-one coherence values in Table II and the coherence curves in Fig. 3 indicate that correlations at greater than nearest neighbor distances must be employed to obtain more accurate estimates of time shifts when low f-number systems with directivity reduced element sensitivity, like the 79×79-element aperture, $f/1.16$ configuration in this study, are used.

The aberration phantoms used in this study were designed to mimic the aberration measured through human abdominal wall specimens.[11] The moderate improvement, relative to the point-reflector results, in the coherence of random-scattering data after time-shift compensation indicates that more sophisticated compensation methods are desirable for clinical images that typically involve speckle waveforms. Since any compensation method applied to speckle waveforms will likely use comparisons of signals received at different elements of a transducer array and since the coherence function quantifies the similarity of speckle waveforms, coherence analysis can play a role in the development and validation of new compensation methods based on such waveform comparisons.

VI. CONCLUSIONS

Adherence to the analytic definition of the complex degree of coherence is necessary for a robust analysis of ultrasound data acquired with a large two-dimensional array. Figure 1 demonstrates the importance of the proper normalization of cross-correlation integrals computed from waveforms weighted by weak elements and receiver directivity. Methods that apply an identical averaged normalization to every cross-correlation integral yield artifactual peaks in the estimated coherence function. Those peaks can confound the analysis of point-target data that are expected to demonstrate approximately uniform coherence throughout the aperture.

A spike at the zero-lag position of the coherence function often indicates a low signal-to-noise ratio. In both the synthetic data and the measured random-scattering data, a coherence spike was attributed to reduced signal levels caused by element directivity near the edges of the large receive aperture. The magnitude of the spike was reduced by using a smaller aperture for the coherence computation (Fig. 4). The persistence of the spike explains the lack of improvement in the lag-one coherence of random-scattering data acquired using time-shift compensation (Table II). However, the results also show that an increase in spatial coherence is readily achieved for lags greater than unity. An iterative compensation method may produce additional focus improvement if the method takes advantage of these longer-range correlations in the reacquired data. This observation supports the assertion that coherence analysis can be employed in the development of new focus compensation methods.

Coherence width measurements are useful for assessing changes in spatial resolution produced by focus compensation provided the width is evaluated far enough below the peak of the coherence function to avoid being overly sensitive to the SNR. In Fig. 6, coherence widths evaluated at levels between 0.2 and 0.5 were shown to vary monotonically with the effective widths of point-spread functions visualized in single-transmit images (Fig. 5). Regression coefficients summarized in Table IV suggest that this relationship can be approximately modeled by a curve of the form $y = \alpha x^{\beta}$, where $\beta < 0$. However, a single coherence width may be insufficient to characterize the point-spread function at lower levels, where sidelobes become prominent.

ACKNOWLEDGMENTS

[1] W. F. Walker and G. E. Trahey, "A fundamental limit on delay estimation using partially correlated speckle signals," IEEE Trans. Ultrason. Ferroelectr. Freq. Control **42**, 301–308 (1995).

[2] J. W. Goodman, *Statistical Optics* (Wiley, New York, 1985), Chap. 5.

[3] L. Mandel and E. Wolf, *Optical Coherence and Quantum Optics* (Cambridge University Press, Cambridge, UK, 1995), Chap. 4.

[4] R. Mallart and M. Fink, "The van Cittert–Zernicke theorem in pulse echo measurements," J. Acoust. Soc. Am. **90**, 2718–2727 (1991).

[5] R. Mallart and M. Fink, "Adaptive focusing in scattering media through sound-speed inhomogeneities: The van Cittert–Zernicke approach and focusing criterion," J. Acoust. Soc. Am. **96**, 3721–3732 (1994).

[6] W. F. Walker and G. E. Trahey, "Speckle coherence and implications for adaptive imaging," J. Acoust. Soc. Am. **101**, 1847–1858 (1997).

[7] B. J. Geiman, R. C. Gauss, and G. E. Trahey, "*In vivo* comparison of fundamental and harmonic lateral transmit beam shapes," *2000 IEEE Ultrasonics Symposium Proceedings* (Institute of Electrical and Electronics Engineers, Piscataway, NJ, 2000), pp. 1669–1675.

[8] C.-C. Shen and P.-C. Li, "Tissue harmonic image analysis based on spatial covariance," IEEE Trans. Ultrason. Ferroelectr. Freq. Control **48**, 1648–1656 (2001).

[9] R. J. Fedewa, K. D. Wallace, M. R. Holland, J. R. Jago, G. C. Ng, M. R. Rielly, B. S. Robinson, and J. G. Miller, "Statistically significant differences in the spatial coherence of backscatter for fundamental and harmonic portions of a clinical beam," *2001 IEEE Ultrasonics Symposium Proceedings* (Institute of Electrical and Electronics Engineers, Piscataway, NJ, 2001), pp. 1481–1484.

[10] D.-L. Liu and R. C. Waag, "About the application of the van Cittert–Zernicke theorem in ultrasonic imaging," IEEE Trans. Ultrason. Ferroelectr. Freq. Control **42**, 590–601 (1995).

[11] J. C. Lacefield, W. C. Pilkington, and R. C. Waag, "Distributed aberrators for emulation of ultrasonic pulse distortion by abdominal wall," ARLO **3**, 47–52 (2002).

[12] J. W. Goodman, *Introduction to Fourier Optics*, 2nd ed. (McGraw-Hill, New York, 1996), Chap. 4.

[13] J. C. Lacefield and R. C. Waag, "Time-shift estimation and focusing through distributed aberration using multirow arrays," IEEE Trans. Ultrason. Ferroelectr. Freq. Control **48**, 1606–1624 (2001).

[14] E. L. Madsen, J. A. Zagzebski, R. A. Banjavic, and R. E. Jutila, "Tissue-mimicking materials for ultrasound phantoms," Med. Phys. **5**, 391–394 (1978).

[15] E. L. Madsen, J. A. Zagzebski, and G. R. Frank, "Oil-in-gelatin dispersions for use as ultrasonically tissue-mimicking materials," Ultrasound Med. Biol. **8**, 277–287 (1982).

[16] L. M. Hinkelman, T. D. Mast, L. A. Metlay, and R. C. Waag, "The effect of abdominal wall morphology on ultrasonic pulse distortion. Part I. Measurements," J. Acoust. Soc. Am. **104**, 3635–3649 (1998).

[17] D.-L. D. Liu and R. C. Waag, "Estimation and correction of ultrasonic wavefront distortion using pulse-echo data received in a two-dimensional aperture," IEEE Trans. Ultrason. Ferroelectr. Freq. Control **45**, 473–490 (1998).

[18] D.-L. Liu and R. C. Waag, "Time-shift compensation of ultrasonic pulse focus degradation using least-mean-square error estimates of arrival time," J. Acoust. Soc. Am. **95**, 542–555 (1994).

[19] J. Neter, W. Wasserman, and M. H. Kutner, *Applied Linear Statistical Models*, 2nd ed. (Richard D. Irwin, Inc., Homewood, IL, 1985), Chap. 4.

[20] M. E. Anderson and G. E. Trahey, "The direct estimation of sound speed using pulse-echo ultrasound," J. Acoust. Soc. Am. **104**, 3099–3106 (1998).

[21] S. W. Smith, G. E. Trahey, and O. T. von Ramm, "Phased array ultrasound imaging through planar tissue layers," Ultrasound Med. Biol. **12**, 229–243 (1986).

[22] Y. Li, "The influences of ambiguity phase aberration profiles on focusing quality in the very near field—Part I: Single range focusing on transmission," IEEE Trans. Ultrason. Ferroelectr. Freq. Control **49**, 57–71 (2002).

Modal decomposition method for modeling the interaction of Lamb waves with cracks

Michel Castaings,[a] Emmanuel Le Clezio,[b] and Bernard Hosten[c]

Laboratoire de Mécanique Physique, Université Bordeaux 1, UMR CNRS 5469 351, cours de la Libération, 33405 Talence Cedex, France

The interaction of the low-order antisymmetric (a_0) and symmetric (s_0) Lamb waves with vertical cracks in aluminum plates is studied. Two types of slots are considered: (a) internal crack symmetrical with respect to the middle plane of the plate and (b) opening crack. The modal decomposition method is used to predict the reflection and transmission coefficients and also the through-thickness displacement fields on both sides of slots of various heights. The model assumes strip plates and cracks, thus considering two-dimensional plane strain conditions. However, mode conversion (a_0 into s_0 and *vice versa*) that occurs for single opening cracks is considered. The energy balance is always calculated from the reflection and transmission coefficients, in order to check the validity of the results. These coefficients together with the through-thickness displacement fields are also compared to those predicted using a finite element code widely used in the past for modeling Lamb mode diffraction problems. Experiments are also made for measuring the reflection and transmission coefficients for incident a_0 or s_0 lamb modes on opening cracks, and compared to the numerical predictions. © *2002 Acoustical Society of America.* [DOI: 10.1121/1.1500756]

PACS numbers: 43.20.Gp [DEC]

I. INTRODUCTION

The presence of cracks in materials is a major preoccupation in industrial context, since even small cracks are likely to grow when the structure is under mechanical constraint or immersed into an aggressive environment. Cracks are usually caused by local small fractures or corrosion shots, and can become large defects like notches, delaminations, holes, etc. Various nondestructive testing (NDT) techniques based on x-rays magnetoscopy, eddy-current, ultrasounds or visual observation are used for locating either surface or internal defects. Among the ultrasonic techniques, different types of waves are chosen depending on the demand of the applications. High frequency bulk waves are commonly used for interrogating small areas like welds, for example.[1] Surface waves are suitable for testing structure surfaces or interfaces between materials.[2,3] However, these techniques are limited to short-range inspection, and are quite time consuming for testing large structures. Guided waves like Lamb modes or SH waves are more appropriate when large structures are to be controlled.[4] Since large specimen usually do not have a small thickness, low frequency ultrasounds are used for limiting the number of guided modes that can propagate, thus making easier the interpretation of measured signals. The drawback is a loss of sensitivity since the wavelength-to-defect-size ratio is a critical parameter. Therefore, cracks being infinitely narrow defects, the use of the low frequency ultrasounds will make it possible to detect them if they are not of too small extent. From a general point of view, the mode sensitivity depends on the stress level that it produces at the defect location, which is a function of the frequency-thickness product.[5,6] Specific components of the stress tensor are also of importance, according to the crack size, orientation and location. The ability of guided modes to detect cracks in plates has widely been demonstrated in the past.[7–10] Lamb waves seem to be a judicious choice for detecting cracks in plates, since their energy may be shared into reflected and transmitted wave packets, the proportion in amplitude of which will depend on the characteristics of the crack. However, even if the incident wave is a pure lamb mode, the wave packets reflected from and transmitted past the defect can be very complicated, since at least two Lamb modes exist at any given frequency. This is an advantage since the more modes, the more information about the defect, but the more complicated the interpretation of the diffracted Lamb waves, thus making the use of this method more difficult than conventional ultrasonic techniques. Numerical predictions are therefore necessary for simulating properly the scattering of Lamb waves by cracks of various geometries. Publications can be found on this subject, presenting models based either on the finite element (FE), the finite difference (FD) or the boundary element (BE) methods.[11–13] Various hybrid solutions are also used, combining either two of the previous methods,[14] or one of them with the Green's function integral[15–17] or wave-function expansion representation.[18–20] Some publications can also be found on the diffraction of Lamb waves by notches, which differ from crack by their nonzero width.[21,22] Although these numerical models allow the amplitude of the reflected and transmitted Lamb modes to be predicted, they usually are heavy and time-consuming methods that do not allow the inverse problem to be solved, i.e., the attributes of a defect to be numerically optimized from experimental data.

Fast and efficient methods are therefore required for simulating the problem of Lamb waves scattered by cracks.

---

[a])Electronic mail: castaings@lmp.u-bordeaux.fr
[b])Electronic mail: leclezio@lmp.u-bordeaux.fr
[c])Electronic mail: hosten@lmp.u-bordeaux.fr

Numerous works have been published on the reflection of Lamb waves by the free edge of a plate that consider the coexistence of nonpropagating and propagating Lamb modes at the plate edge, for satisfying the free boundary conditions that the incident and reflected propagating modes cannot satisfy by themselves.[23–28] The reciprocal work method[23] was also applied to predict the reflection from and transmission past a weld between the edges of two steel plates of same thickness.[29] In this study, the weld is supposed to be defect-less with a constant width running all through the plate thickness. To the authors' knowledge, few publications can be found on the consideration of nonpropagating Lamb modes for satisfying the free boundary conditions at the surfaces of a crack in a plate. S Rokhlin has used a modified version of the Wiener–Hopf technique for simulating the reflection of an incident Lamb mode from a finite crack.[30,31] This advance in the field is, however, limited to a horizontal crack situated on the plane of symmetry of an elastic layer, thus implying that any incident Lamb mode, whether it is symmetric or antisymmetric, cannot be converted into an antisymmetric or symmetric Lamb mode, respectively. B. A. Auld and M. Tan[32,33] used the variational method to predict the reflection of Lamb modes from a crack normal to the surfaces of an isotropic plate. More recently, X. M. Wang and C. F. Ying considered the case of the fundamental a_0 and s_0 Lamb wave modes scattered by a circulate cylinder embedded in an elastic plate.[34] All these studies consider the coexistence of nonpropagating and propagating Lamb modes at the vicinity of the defect, for satisfying the boundary conditions. The advantages in comparison to numerical or hybrid solutions based on FE, FD or BE methods, are the flexibility in changing the input data and the reduction in times of computation, thus making them good candidates for solving inverse problems.

The present paper is also based on this principle. It concerns the use of the modal decomposition method for simulating the interaction of the low-order symmetric (s_0) or antisymmetric (a_0) Lamb modes with cracks perpendicular to the surfaces of an 8-mm-thick aluminum plate. The frequency is chosen equal to 0.14 MHz, so that the frequency-thickness (1.12 MHz.mm) is below that of the a_1 and s_1 mode cut-off, and so that both s_0 and a_0 are relatively non-dispersive modes. The interest of this choice is that the method is thus tested for a realistic situation, since the frequency-thickness product for NDT applications is often chosen so that the generation of a pure mode is possible and the interpretation of several detected modes is as simple as possible. However, the modal decomposition method presented in this paper could be used at any other frequency-thickness. Tests have been made showing the stability of the calculations up to 10 MHz.mm where numerous propagating modes coexist. Two types of slots are considered in this study: (a) single internal crack symmetrical with respect to the middle plane of the plate and (b) single opening crack. The reflection and transmission coefficients are predicted as functions of the normalized parameter p/h, where p is the crack height and h is the plate thickness. The through-thickness displacement fields on both sides of the cracks are also predicted for various values of p/h. The model assumes
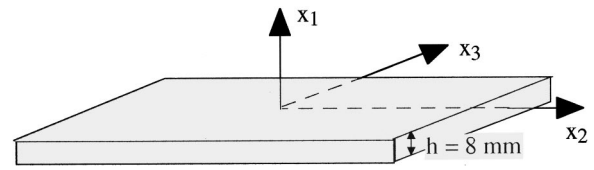
FIG. 1. Schematic of the aluminum plate and coordinate axis.

strip plates and cracks, thus considering two-dimensional, plane strain conditions. However, mode conversion (a_0 into s_0 and *vice versa*) that occurs for single opening cracks is considered. The energy balance is always calculated from the reflection and transmission coefficients, in order to check the validity of the model. The results presented in the paper are successfully compared to those predicted using a finite element code widely used in the past for modeling Lamb mode diffraction problems.[11,21,28,35] The interest in using the modal decomposition method rather than FE or FD routines is double: first it allows very fast computations to be done as said above, but it also helps in understanding the diffraction phenomena that occur at the crack location, for instance the existence of a nonpropagating modes. The reflection and transmission coefficients are also measured for the a_0 or s_0 Lamb mode incident on opening cracks of various heights manufactured in 8-mm-thick aluminum plates. Although the experimental technique is not new,[35] the good correlation obtained between the measured and predicted coefficients demonstrates that the association of this process with the modal decomposition method is a promising tool for solving inverse problems.

II. DESCRIPTION OF THE PROBLEM

The plate is 8 mm thick. It is supposed to be infinitely long in directions x_2 and x_3. Therefore, two-dimensional plane strain conditions are considered in the models, the plane of propagation being formed by axis x_1 and x_2. A schematic of the plate and coordinate axis is shown in Fig. 1. Both plate surfaces located at $x_1 = \pm h/2$ are assumed to be stress free, thus leading to the classical dispersion equation:

$$\frac{\tan (K_{T1}h/2)}{\tan (k_{L1}h/2)} + \left(\frac{4k_2^2 k_{T1} k_{L1}}{(k_{T1}^2 - k_2^2)^2} \right)^{\pm 1} = 0, \tag{1}$$

where exponent $+1$ and -1 are for symmetric or antisymmetric modes, respectively. k_2 is the Lamb wave-number along the direction of propagation (x_2 axis), and $k_{L1} = \sqrt{(\omega/c_L)^2 - k_2^2}$ and $k_{T1} = \sqrt{(\omega/c_T)^2 - k_2^2}$ are the complex components along the x_1 axis of the longitudinal and shear heterogeneous plane waves, the phase velocities of which are given in Table I. $\omega = 2\pi f$ is the circular frequency and f is the frequency. Solutions of Eq. (1) form an infinite set of (f, k_2) couples that allow dispersion curves to be plotted. At a given frequency, there are a finite number of propagating

TABLE I. Measured density (kg/m³), longitudinal and shear bulk wave velocities (m/s), and corresponding Young modulus (GPa) and Poisson coefficient for the test aluminum plate.

Density	c_L	c_T	E	v
$2660^{\pm 10}$	$6310^{\pm 50}$	$3190^{\pm 20}$	$71.8^{\pm 0.2}$	$0.33^{\pm 0.01}$

Castaings *et al.*: Modal decomposition for Lamb waves
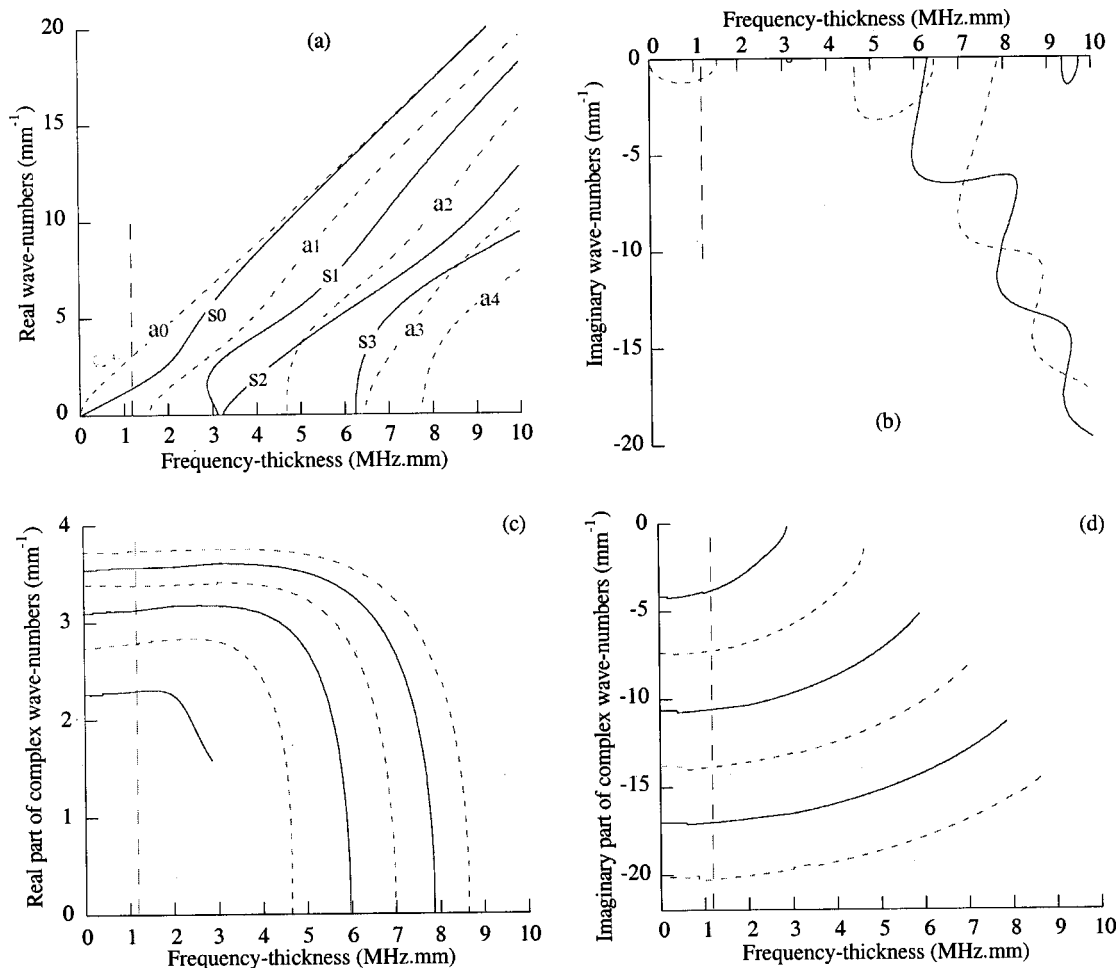
FIG. 2. Dispersion curves for anti-symmetric (---) and symmetric (—) modes in an aluminum plate: (a) propagating modes; (b) nonpropagating modes; (c) real parts of inhomogeneous modes; (d) imaginary parts of inhomogeneous modes; Vertical large-dashed line indicates the frequency-thickness product considered in the whole study for the interaction of propagating a_0 or s_0 modes with cracks.

modes having real wave-numbers, a finite number of non-propagating modes having imaginary wave-numbers and an infinite number of inhomogeneous modes having complex wave-numbers. The Newton–Raphson method[36] has been implemented to solve Eq. (1) in the real, imaginary and complex domains of k_2 and at fixed values of the frequency. Moreover, a mode pursuit routine has been developed to follow each mode in large frequency ranges. This is based on the Taylor theorem[36] for which closed form solutions of derivative functions of Eq. (1) are established. Figure 2 displays the dispersion curves in a large frequency-thickness range extending from 0 to 10 MHz.mm. Figure 2(a) shows well-known real wave-number curves that supply information concerning the velocity and dispersion behavior of the propagating modes. Figure 2(b) shows the purely imaginary wave-numbers roots, and Figs. 2(c) and (d) present the real and imaginary parts of the complex wave-number roots, respectively. These three real, imaginary and complex spaces are connected together by roots that are real above their frequency cut-off and that become either complex or imaginary below it. It must be noted that roots with negative imaginary parts have been retained for the nonpropagating and inhomogeneous modes since this has a physical meaning corresponding to decaying amplitudes in the x_2 direction sup-

posed to be that of progressive modes. Taking into account the existence of nonpropagating and inhomogeneous modes is essential for properly writing boundary conditions in diffraction problems.[37] For the frequency-thickness product considered in this study (1.12 MHz.mm pointed out by the large-dashed line in Fig. 2), there exist two propagating modes (real wave-numbers), one nonpropagating mode (imaginary root) and an infinite of inhomogeneous modes (complex roots). For each type of mode, the harmonic through-thickness displacement or stress distributions can be calculated using relations given in Ref. 37. As explained in Refs. 5 and 6, the stress distribution gives an indication of the sensitivity of a given incident propagating Lamb mode to a defect, depending on the location in the plate thickness, and on the geometry and size of that defect. Figure 3 displays the through-thickness displacement and stress distribution for the two incident propagating modes considered in this study, i.e., for a_0 and s_0, at the frequency-thickness of 1.12 MHz.mm. In these plots, the modes are set to have unit-power amplitudes, i.e., the averaged power they carry through the plate thickness and over one temporal periods is 1 W. It is clear that the stress distributions are radically different for these two modes, so meaning that they are likely to have different sensitivity to vertical slots. For solving scat-
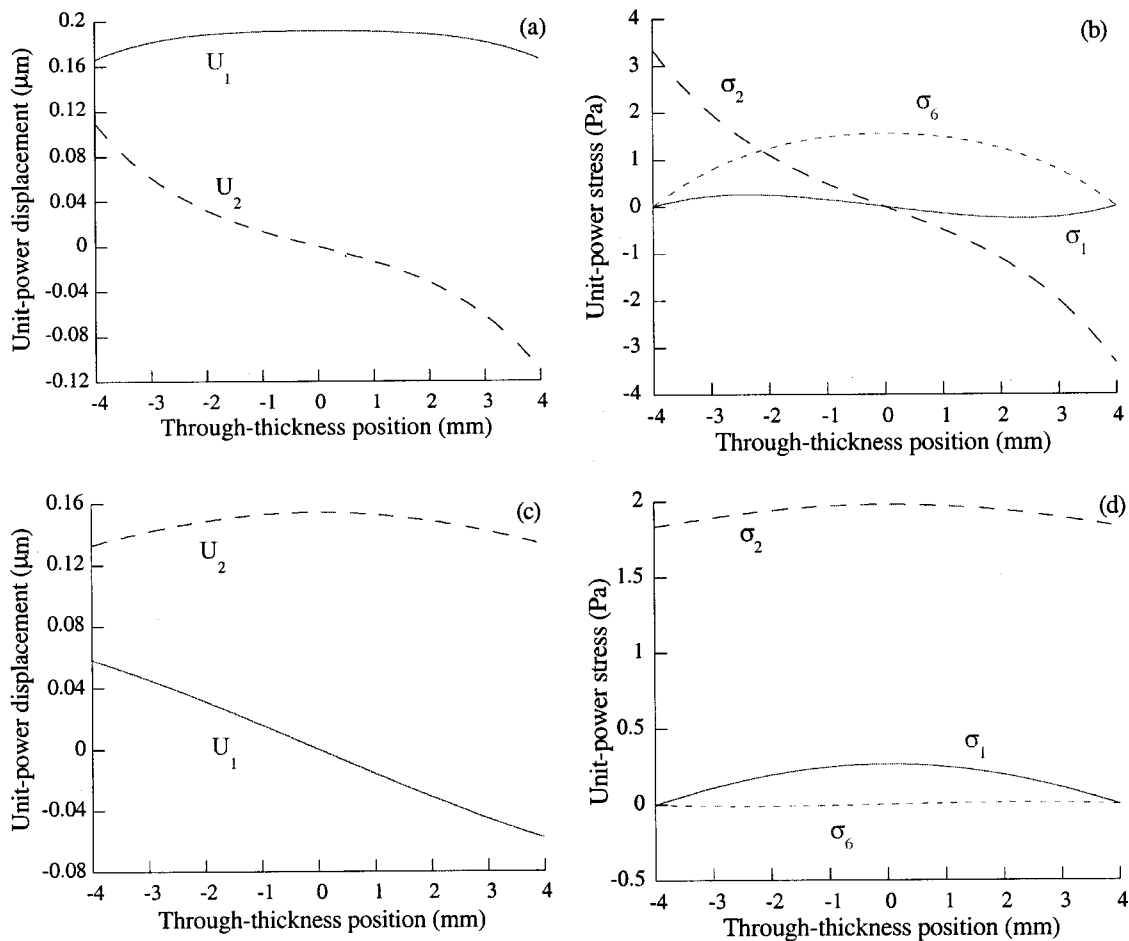
FIG. 3. Through-thickness mode shapes at 1.12 MHz.mm; (a) and (c) displacements; (b) and (d) stresses. Top plots are for a unit-power a_0 mode and bottom plots are for a unit-power s_0 mode.

tering problems as made in this paper, the through-thickness displacement and stress distributions for real, imaginary and complex wave-numbers are also calculated.

In this study, cracks are supposed to be of infinitesimal thickness, and to have motions such that their opposite surfaces do not interact at the same time. This means that there is no transfer of stresses or displacements through the cracks. As written in Ref. 30, this model is physically valid if (1) the crack width is much smaller than the plate thickness and than the wavelength, and (2) the crack width is greater than the particle displacements on its surfaces. The two types of cracks considered in this paper are presented in Fig. 4.

III. MODAL DECOMPOSITION METHOD

In a modal decomposition analysis, any acoustic field can be developed as an expansion of vibration modes of the structure. Thus, any velocity and stress fields, $\mathbf{v}$ and $\bar{\bar{\sigma}}$ can be written as a Lamb modes expansion:

$$\mathbf{v} = \Sigma_n b_n \mathbf{v_n} \quad \text{and} \quad \bar{\bar{\sigma}} = \Sigma_n b_n \bar{\bar{\sigma}}_n, \tag{2}$$

FIG. 4. Vertical crack in the aluminum plate; (a) internal crack symmetrical with respect to the middle plane of the plate, (b) opening crack.

where $\mathbf{v_n} = \mathbf{v_n}(x_1)e^{i(\omega t - k_{2n}x_2)}$ and $\bar{\bar{\sigma}}_n = \bar{\bar{\sigma}}_n(x_1)e^{i(\omega t - k_{2n}x_2)}$ are the velocity vector and stress tensor for the nth Lamb mode, t is the time, k_{2n} is the wave-number. At any given frequency, the summations above include a finite number of propagating modes, a finite number of nonpropagating modes, and an infinite number of inhomogeneous modes, which form a complete basis.[38]

In the problem of an incident Lamb wave scattered by a vertical crack, the superposition of all these modes is considered through the plate thickness, at the defect location. The coexistence of all the propagating, nonpropagating and inhomogeneous modes allows the boundary conditions to be satisfied, as illustrated by Fig. 5. The imaginary and complex modes do not propagate energy but they create a spatially transient acoustic field in the vicinity of the defect. The boundary conditions are such that points on the crack surfaces must be stress-free, while the velocity and stress fields must be continuous elsewhere in the plane normal to the plate and containing the crack. In a two-dimensional problem defined by axis x_1 and x_2 as in the present study, the stress tensor can be represented by three components noted σ_{11}, σ_{22}, and σ_{12}, or σ_1, σ_2 and σ_6, respectively, using the contraction of indices according to Ref. 37. Therefore, the boundary conditions mentioned above can be written as follows:
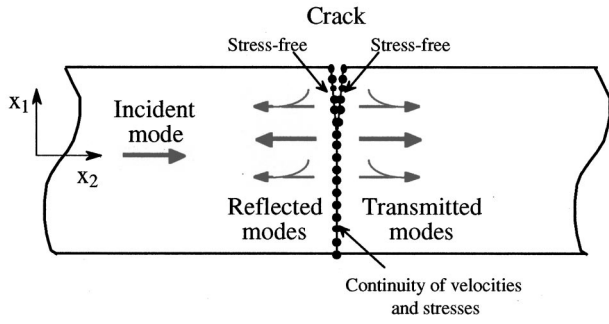
FIG. 5. Schematic of the modal decomposition method with an opening crack.

$$\bar{\bar{\sigma}} \cdot \mathbf{x}_2 = \begin{cases} \Sigma_N b_N \sigma_{N2} \\ \Sigma_N b_N \sigma_{N6} \end{cases}$$

$$= \begin{cases} 0, \\ 0, \end{cases} \quad \text{stress-free at right surface of crack,}$$

$$\bar{\bar{\sigma}} \cdot \mathbf{x}_2 = \begin{cases} a_I \sigma_{I2} + \Sigma_N b_{-N} \sigma_{-N2} \\ a_I \sigma_{I6} + \Sigma_N b_{-N} \sigma_{-N6} \end{cases}$$

$$= \begin{cases} 0, \\ 0, \end{cases} \quad \text{stress-free at left surface of crack,}$$

$$\tag{3}$$

$$\Sigma_N b_N \mathbf{v}_N = a_I \mathbf{v}_I + \Sigma_N b_{-N} \mathbf{v}_{-N},$$

velocity continuity out of crack

$$\begin{aligned} \Sigma_N b_N \sigma_{N1} \\ \Sigma_N b_N \sigma_{N2} = \\ \Sigma_N b_N \sigma_{N6} \end{aligned} \begin{cases} a_I \sigma_{I1} + \Sigma_N b_{-N} \sigma_{-N1}, \\ a_I \sigma_{I2} + \Sigma_N b_{-N} \sigma_{-N2}, \\ a_I \sigma_{I6} + \Sigma_N b_{-N} \sigma_{-N6}, \end{cases}$$

stress continuity out of crack.

The incident mode is noted I and is set to have a unit power amplitude a_I. The scattered propagating, nonpropagating and inhomogeneous modes are represented by $n = \pm N$ where $-N$ is for reflected modes and N is for transmitted modes. They have unknown complex amplitudes b_n, which have to be found.

In the numerical applications, the infinite series of complex modes is truncated, and from 10 to 25 points are considered through the thickness of the plate, at the crack location. A linear system is thus established. Its solutions b_n are obtained using the single value decomposition method (SVD).[36] An energy balance criteria is used to check the validity of the numerical results: the energy carried by the reflected and transmitted propagating modes must be as closed as possible to the energy of the incident mode. During the calculation process, the computational parameters (number of points at the crack location and/or number of complex modes) are increased until the energy balance is satisfied. When the system is correctly solved, the complex displacement field at the crack location is then computed by introducing the amplitudes b_n in the following equations:

$$\mathbf{u}(x_1, x_2^{\text{crack left}}) = a_I \mathbf{u}_I + \Sigma_N b_{-N} \mathbf{u}_{-\mathbf{N}}$$

at the left of the crack,

$$\mathbf{u}(x_1, x_2^{\text{crack right}}) = \Sigma_N b_N \mathbf{u}_\mathbf{N} \quad \text{at the right of the crack.} \tag{4}$$

The complex reflection and transmission coefficients are therefore

$$R_{-N} = \frac{b_{-N}}{a_I} \quad \text{and} \quad T_N = \frac{b_N}{a_I}. \tag{5}$$

Since the plate is purely elastic, the moduli of these coefficients are the same whatever the position along the plate is at the crack location or in the far field.

IV. FINITE ELEMENT MODEL

A. Numerical tool

This section concerns a numerical analysis package, which was developed at Imperial College in London, US, to model the propagation of plate waves and their interaction with defects.[37] This tool is based on the finite element method and includes an explicit central difference routine for producing a time marching solution. Therefore, it is possible to vary the characteristics of the exciting temporal signal, i.e., the center frequency, the number of cycles, and the envelope. The excitation can be produced at any point of the mesh, as displacements or forces. The response of the plate to various types of excitation is modeled by calculating the displacements at every point of the spatial mesh that defines the plate, as a function of time. Specific points can be monitored, thus showing the time response at particular locations in/on the plate. Results are stored in an output data file, which is processed in turn, using a specific software developed by the authors.

In the current study, the aluminum plate is modeled by a two-dimensional quadrilateral region 8 mm high in direction x_1 (plate thickness) and 800 mm long in direction x_2 (plate length). This region is meshed by 6400 square, four-nodded elements of 1-mm side. The excitation of a pure incident mode (a_0 or s_0) is produced by applying the exact through-thickness mode shape, as displacements, at the left-hand side of the region. For each of these points, the temporal excitation is a 10-cycle toneburst enclosed in a Hanning window, centered on the frequency 0.14 MHz, thus making the frequency-thickness product equal to 1.12 MHz.mm.

Since they are of infinitesimal width, cracks are simulated by disconnecting nodes, the positions of which determine the crack height and location. Any disconnected node becomes two nodes having the same position of equilibrium, and independent motions, i.e., there is no transfer of stresses or displacements between them. Cracks are running perpendicularly in the plate surfaces and are located at position $x_2 = 400$ along the plate.

B. Monitoring and processing

Series of points are monitored either along the plate surface or across the plate thickness, and different processing is done to extract the results, which are to be compared to those obtained using the modal decomposition method.

1. Reflection and transmission coefficients

Two series of 26 nodes are monitored every 4 mm at one plate surface along lines located at the left of the crack (from $x_2 = 250$ to 350 mm), and at the right of the crack (from $x_2 = 450$ to 550 mm), respectively. Displacements in both directions x_1 and x_2 were picked up at these points. These data were then used to calculate the reflection and transmission coefficients, i.e., the ratio between the amplitudes of reflected/transmitted a_0 and/or s_0 modes and the amplitude of the incident a_0 or s_0. Due to the mode conversion of a_0 into s_0 and *vice versa* that occurs when the single opening crack is modeled, two different processing are used to extract the required mode amplitudes:

(i) If the crack is symmetrical with respect to the plate thickness, then there is no mode conversion and any reflected or transmitted mode is of the same nature as that of the incident mode. The mode amplitudes are therefore obtained from signals predicted at two single points located at the left and at the right of the defect. A temporal window $w(t)$ is applied for selecting waveforms $s_i(t)$, $s_r(t)$ and $s_t(t)$ that correspond to the incident, reflected and transmitted modes, respectively. This window has a taper shape (smooth rectangular) and is as wide as possible in order not to affect the estimation of the mode amplitudes. The reflection (R) and transmission (T) coefficients are obtained simply by dividing the frequency spectrum of the appropriate waveforms multiplied by the window:

$$R(f) = \frac{\int_{-\infty}^{\infty} (s_r(t) \times w(t)) e^{-i2\pi ft} dt}{\int_{-\infty}^{\infty} (s_i(t) \times w(t)) e^{-i2\pi ft} dt},$$

$$T(f) = \frac{\int_{-\infty}^{\infty} (s_t(t) \times w(t)) e^{-i2\pi ft} dt}{\int_{-\infty}^{\infty} (s_i(t) \times w(t)) e^{-i2\pi ft} dt}. \qquad (6)$$

(ii) If the crack is not symmetrical, the mode conversion phenomena implies that both a_0 and s_0 are expected as reflected and transmitted waves, whatever the incident mode is. Because the plate is of finite length (800 mm), points monitored on both sides of the crack cannot be far enough from the crack for the reflected (or transmitted) a_0 and s_0 modes to be separated in the time domain. Therefore the temporal window mentioned above cannot be used for isolating the various reflected (or transmitted) modes and relations (6) cannot be applied for calculating the reflection and transmission coefficients. A two-dimensional Fourier transform is then applied to each set of 26 signals $s_i(x_2,t)$, $s_r(x_2,t)$ and $s_t(x_2,t)$ obtained by monitoring nodes on the plate surface, at the left and right of the crack. This transforms these data from the {time, position} space to the {frequency, wave-number} space, where reflected (or transmitted) a_0 and s_0 modes are well separated.[40] This process allows the phase velocity and the amplitude to be plotted in the frequency range of the excitation, for the incident mode and for the various reflected (or transmitted) modes. The phase velocity plots are compared to the dispersion curves obtained from Eq. (1) for identifying the nature of the modes and for checking that the incident mode (a_0 or s_0) is pure. This purity is a crucial point in the case of nonsymmetrical cracks since reflected (or transmitted) a_0 and s_0 modes

would have different amplitudes depending on the fact that the incident mode is single or not. The reflection (R) and transmission (T) coefficients are calculated from the mode amplitudes using the following relations:

$$R_{a_0 \text{ or } s_0}(f) = \frac{\int_{-\infty}^{\infty}\int_{-\infty}^{\infty} s_r(x_2,t) e^{-i2\pi ft} e^{-i2\pi k_2 x_2} dt \, dx_2}{\int_{-\infty}^{\infty}\int_{-\infty}^{\infty} s_i(x_2,t) e^{-i2\pi ft} e^{-i2\pi k_2 x_2} dt \, dx_2}$$

$$= \frac{S_r(k^-_{a_0 \text{ or } s_0}, f)}{S_i(k^+_{a_0 \text{ or } s_0}, f)},$$

$$T_{a_0 \text{ or } s_0}(f) = \frac{\int_{-\infty}^{\infty}\int_{-\infty}^{\infty} s_t(x_2,t) e^{-i2\pi ft} e^{-i2\pi k_2 x_2} dt \, dx_2}{\int_{-\infty}^{\infty}\int_{-\infty}^{\infty} s_i(x_2,t) e^{-i2\pi ft} e^{-i2\pi k_2 x_2} dt \, dx_2}$$

$$= \frac{S_t(k^+_{a_0 \text{ or } s_0}, f)}{S_i(k^+_{a_0 \text{ or } s_0}, f)},$$

where $S_i(k^+_{a_0 \text{ or } s_0}, f)$, $S_r(k^-_{a_0 \text{ or } s_0}, f)$ and $S_t(k^+_{a_0 \text{ or } s_0}, f)$ represent the variation with frequency of the amplitude of the individual incident, reflected and transmitted modes, respectively. Signs + and − mean that modes are propagating forwards or backwards in the x_2 direction, respectively. In the frequency spectrum thus obtained, only the value 0.14 MHz is considered since this study is restricted to the frequency-thickness 1.12 MHz.mm.

Careful attention must be paid to the choice of the displacement components U_1 or U_2 that are monitored at the plate surface. Indeed, the amplitudes of signals $s_i(t)$, $s_r(t)$ and $s_t(t)$ will be different according to the direction of displacements. If the reflected and transmitted modes are the same than the incident one, i.e., if they all are a_0 and s_0 modes, then the reflection and transmission coefficients will not depend on the direction of displacements that is considered, as long as the same direction is considered for the incident, reflected and transmitted modes. However, if the reflected and transmitted modes are different than the incident one, then the reflection and transmission coefficients will be different according to the direction of displacements that is considered. In this case, the through-thickness location of the monitored points will also strongly affect the resulting reflection and transmission coefficients. This is because different modes do not have the same through-thickness displacement distributions. In Sec. VI B presenting results for single opening cracks, the reflection and transmission coefficients for incident a_0 or s_0 modes are presented for both directions x_1 and x_2, the monitoring zone being at one surface of the plate.

2. Crack motion

Two series of nine nodes are also monitored every 1 mm across the plate thickness, on both sides of the cracks (at $x_2 = 400$ mm). The first series of nine points are in fact the right-hand side nodes of elements running straight left along the crack and the second series are the left-hand side nodes of elements running straight right along the crack. Displacements in both directions x_1 and x_2 were picked up at these points. Temporal waveforms predicted at these points repre-
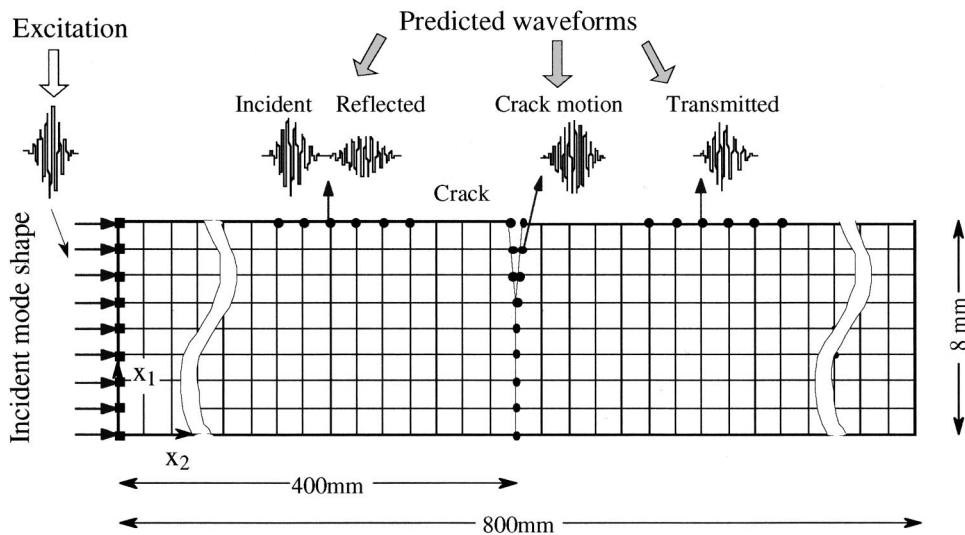
FIG. 6. Schematic of the FE model with an opening crack; (■): forced nodes; (●): monitored nodes.

sent the total field including incident and reflected/transmitted propagating modes but also nonpropagating and inhomogeneous modes. A Fourier transform is calculated for each of these waveforms, thus allowing the variation of the total displacement field across the plate thickness, along the lines located on both sides of the cracks, to be plotted at any frequency in the frequency range of the excitation. This has been done for the frequency value of 0.14 MHz, which corresponds to the 1.12 MHz.mm frequency-thickness product.

Figure 6 presents a schematic of the FE model, showing the through-thickness displacement excitation applied at the left-hand side of the plate, the modeling of an opening crack, and points monitored at the plate surface, at the left of the defect for predicting the incident and reflected modes, and at the right of the defect for predicting the transmitted modes. Also shown on this figure are points monitored through the plate thickness on both sides of the crack.

V. EXPERIMENTS

Two test aluminum square plates 8 mm thick and 400 mm long have been used for the experiments. The velocities of longitudinal and shear bulk waves propagating in this material have been measured using a conventional, ultrasonic, immersion technique, and used for calculating averaged values of the Young modulus and Poisson coefficient given in Table I. These are used in turn as input data for the numerical

models described in previous sections. Surface notches have been manufactured in the plates. They are parallel to direction x_3, 100 mm long, 0.7 mm wide and their height is p. Although these notches are not infinitely thin, the wavelength λ to their width w ratio is quite large ($\lambda/w \approx 24$ for a_0 and $\lambda/w \approx 53$ for s_0), thus making the assumptions introduced in the numerical models likely to be valid. This will be discussed in Sec. VI where numerical predictions are compared to measurements. Six single opening notches of relative height $p/h = 12.5\%$, 25%, 37.5%, 50%, 62.5%, and 75% have been manufactured in the plates. As shown in Fig. 7, these notches have been made in a noncentral position along the plates, so that two ultrasonic transducers can be placed above the 250-mm-long space: one transmitter and one receiver for generating an incident mode and for detecting waves reflected by the notches, respectively, while the remaining 150-mm-long space is sufficient for positioning one receiver necessary for measuring waves transmitted past the notches.

An ultrasonic transmitter is used for launching either the a_0 or s_0 Lamb mode along direction x_2. This transducer is an IMASONIC 1433 A101, piezoelectric, 35-mm-diam device having a frequency bandwidth centered at 250 kHz with -15-dB points at 120 and 380 kHz. The excitation signal is a five cycle, 140-kHz tone-burst, so that the frequency-thickness is identical to that in the numerical predictions
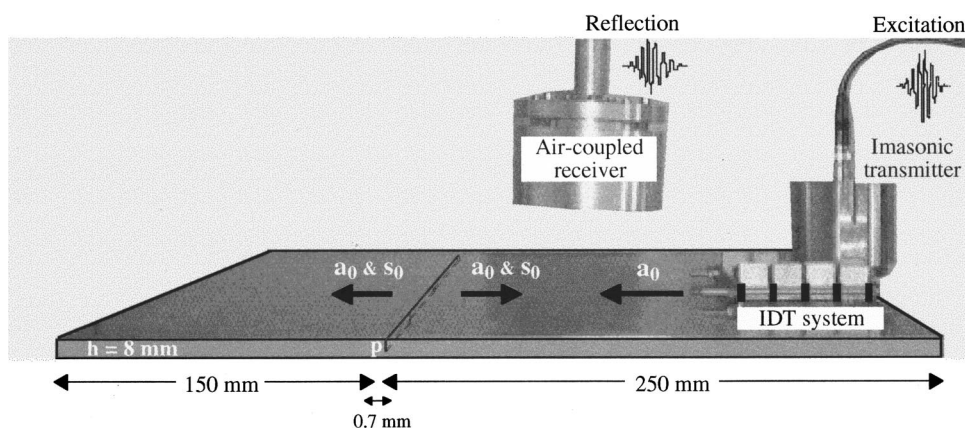
FIG. 7. Photograph of the experimental setup.

(1.12 MHz.mm). Since the plate is shorter than that modeled using the FE code, five cycle bursts must be used to avoid overlapping of signals corresponding to waves twice scattered by the notches due to reflections from the plate edges. This has no effect on the propagation of either mode since both a_0 and s_0 are nondispersive in the frequency-thickness region of interest. For launching the s_0 mode, this transmitter is placed at the left-hand side of the plate, its active face being in contact with the plate edge, and coupled using gel. The transmitter acts as a piston source through the plate thickness, thus applying a quite uniform force distribution, suitable for launching the s_0 mode as required. Moreover, to minimize the possible production of undesired a_0, the transmitter is positioned symmetrically with respect of the middle plane of the plate. For launching the a_0 mode, the same transmitter is connected to one surface of the plate via 100-mm-long Perspex fingers having rectangular sections of 10 mm high by 3 mm wide. Three fingers are coupled to the plate using gel and positioned at an equidistance of 17 mm, which corresponds to the wavelength of the a_0 mode that is to generate. The transmitter is then placed on the fingers to which it is coupled using gel for insuring a good transfer of energy to the plate through the fingers. This process launches two a_0 modes on both sides of this interdigitallike (IDT) transmitter. One mode is traveling towards the notches while the other is traveling towards one edge of the plate. In order to avoid an undesirable reflection of that wave from that edge, which would make two a_0 modes incident on the notches, the three fingers are positioned at an optimum distance from the edge, so that the reflected a_0 mode forms a constructive interference with that traveling directly to the notches. This is equivalent to having a sort of six-fingered IDT transmitter and to removing the unwanted plate edge. In that way, a strong, pure, incident a_0 mode is launched towards the notches.

The receiver is a circular, air-coupled transducer having a diameter of 50 mm, and a frequency bandwidth centered at 200 kHz with −15 dB points at 50 and 400 kHz.[41] Its angular orientation is either ±3.7 or ±8.2 degrees, so that it is sensitive to either the incident, reflected or transmitted a_0 or s_0 Lamb modes, according to the Snell-Descartes' law.[37] For accurate measurements of the amplitudes of these modes, the receiver is moved along a 40-mm-long path with 5-mm steps, in direction x_2, using a motorized translation stage. For each position, a temporal signal corresponding to either the incident, reflected or transmitted a_0 or s_0 modes, according to the orientation and location of the transducer, is visualized on a digital scope and captured. A two-dimensional Fourier transform is then applied to transform each series of nine signals so captured, from the spatial-temporal domain to the wave-number-frequency domain, as described in the previous section. The wave-number-frequency diagram thus obtained is used for computing the phase velocity and/or the amplitude for the incident, reflected and transmitted modes, in the frequency bandwidth of the input electrical signal. Then, the reflection and transmission coefficients are the ratios of the reflected and transmitted mode amplitudes by the incident one, respectively. This processing is exactly the same as that used for the finite element results, as described in the previous section.

VI. RESULTS

This section systematically presents the modulus and the phase of the reflection and transmission coefficients for the two types of defects, and for the incident mode a_0 or s_0, as functions of crack height. The moduli of the through-thickness displacement distribution at the left and right sides of the cracks are also plotted for the various situations. For each plot, except for the phase of the coefficients, results obtained using the modal decomposition method are compared to the FE predictions. Moreover, the moduli of the reflection and transmission coefficients predicted by the two methods are compared to experimental measurements, in the case of opening cracks. For the various cases of investigation, the modal decomposition method was initially solved using 15 points through the plate thickness and 10 complex modes. The energy balance was systematically checked and the number of points was increased if necessary, so that the energy balance was always correct within 5% of error. A maximum of 25 points was necessary for a satisfactory convergence in the case of a single opening crack of 50% relative height, when a_0 was incident.

A. Internal symmetrical crack

1. Reflection and transmission coefficients

Figures 8 and 9 present the modulus and the phase of the reflection and transmission coefficients, as functions of crack height, for the incident modes a_0 and s_0, respectively. The crack is internal and symmetrical with respect to the middle plane of the plate, as shown in Fig. 4(a). As expected when the crack height is null, the reflection and transmission coefficients are equal to 0 and 1, respectively, whatever the incident mode is. When the crack height is 100% of the plate thickness, the modulus of the reflection and transmission coefficients are equal to 1 and 0, respectively, whatever the incident mode is. In this case, the phase of the reflection coefficient is found to be equal to −90 or −180 degrees when a_0 or s_0 is incident, respectively. These well-known results show that the modal decomposition method is correctly used for modeling the reflection of Lamb waves on the free edge of a plate.[23–28]

The a_0 mode appears to be slightly less sensitive than the s_0 mode, to this type of crack, since both the reflection and transmission coefficients are less dependent on the crack height, for a_0 than for s_0. Indeed, the reflection coefficient for a_0 is less than 0.2 for crack heights (p) up to 60% of the plate thickness (h). In comparison, the reflection coefficient for s_0 gets bigger than 0.2 as soon as p/h is greater than 40%. This comes from the fact that s_0 and a_0 modes have different through-thickness stress distributions as shown in Fig. 3. Therefore, the use of s_0 is more suitable than that of a_0 if internal vertical cracks close to the middle plane of the plate are to be detected. The modulus of the reflection coefficient varies monotonically with the crack-height-to-plate-thickness ratio, from 0 to 1, thus meaning that this mode can also be used for easily dimensioning an internal crack. Moreover, the phase of the s_0 reflection coefficient also varies

FIG. 8. Predicted reflection and transmission coefficients for a_0 incident on internal cracks as a function of crack-height-to-plate-thickness ratio; (a) modulus; (b) phase; (- - -) finite element; (—) modal analysis.

monotonically versus the relative crack size p/h, thus meaning that it can also be used as a good indicator for crack sizing.

2. Through-thickness crack motion

Figures 10 and 11 present the modulus of the through-thickness displacement distributions on both sides of these internal cracks, for the incident mode a_0 and s_0, respectively. Plots (a), (b), (c) and (d) correspond to values of p/h equal to 25%, 50%, 75% and 100%, respectively.

Figure 10 shows that the incident a_0 mode produces identical through-thickness, in-plane motion on both sides of the internal cracks, for p/h values up to 50%. For $p/h=75\%$, the two surfaces of the crack have different in-plane displacements (U_2), as confirmed by the FE predictions. This phenomena comes from the fact that the difference in the in-plane displacements is essentially linked to the in-plane compression stress components (σ_2), which have negligible values in the vicinity of the middle plane of the plate, and that significantly increases towards the plate surfaces, for antisymmetric modes. Therefore, the difference in the in-plane motions of crack faces will be high as long as the in-plane compression stress produced by Lamb modes is high where the crack is. Moreover, the repartition of modes being different on both sides of the cracks, these motions will be different. In the same way, the out-of-plane motions (U_1) on both sides of internal cracks are different, for any value of p/h (except for $p/h=0\%$ or 100% which are particular cases) due to the shear stress components (σ_6) that have significantly high values at any position through the plate thickness, except close to the plate surfaces, for anti-symmetric modes. The unequal repartition of modes on both

FIG. 9. Predicted reflection and transmission coefficients for s_0 incident on internal cracks as a function of crack-height-to-plate-thickness ratio; (a) modulus; (b) phase; (- - -) finite element; (—) modal analysis.
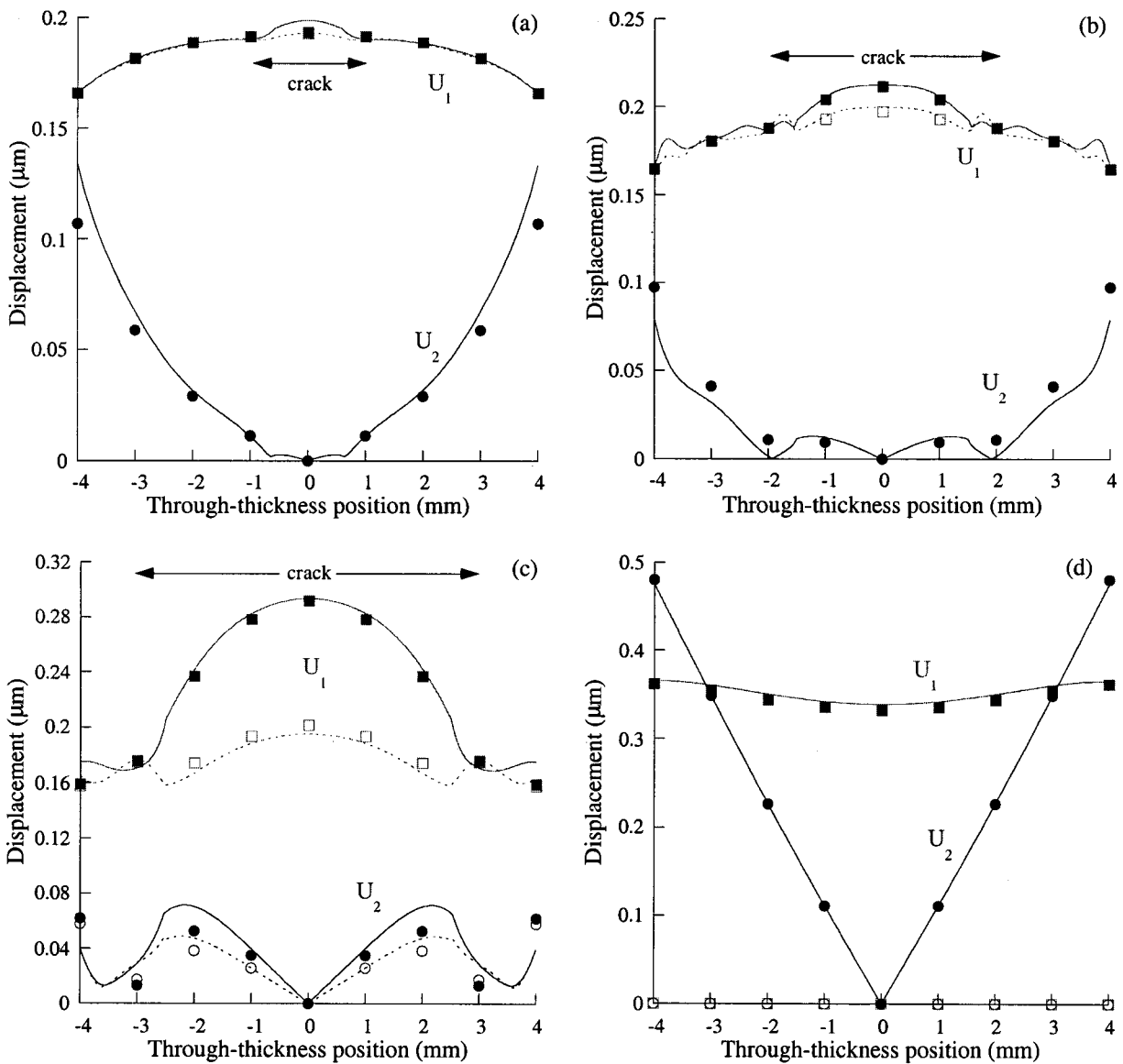
FIG. 10. Through-thickness displacements on both sides of internal cracks for incident a_0 mode; FE: out-of-plane (squares) and in-plane (circles) displacements of the right (empty) and left (full) sides; Modal analysis: displacements of the right (- - -) and left (—) sides; (a) $p/h=25\%$, (b) $p/h=50\%$, (c) $p/h=75\%$ and (d) $p/h=100\%$.

sides of the cracks thus implies different out-of-plane displacements even for small values of p/h.

Figure 11 shows that the s_0 mode always produces identical through-thickness, out-of-plane motions (U_1) on both sides of the internal cracks. This is due to the fact that the difference in the out-of-plane displacements is essentially produced by shear stress components (σ_6). Indeed, since the s_0 incident mode has a negligible shear stress component all through the plate thickness, and since stress continuity must be satisfied out of the crack, the shear stress is consequently null all through the plate. Therefore, the unequal repartition of mode on both sides of the cracks cannot induce any difference in the out-of-plane displacements of crack faces, whatever the value of p/h is. For low values of p/h, this normal displacement follows that of the mode propagating in a defectless plate. When p/h increases, the shape of this U_1 component breaks down near the plate surfaces. The in-plane displacement components (U_2) are different on both sides of

the cracks, due to strong and different in-plane compression stresses (σ_2) produced by unequal repartition of symmetric modes. It is interesting to note that in the case of the incident s_0 mode, the in-plane motion is zero and the out-of-plane motion is doubled, when the crack height is 100% of the plate thickness.

These results show that an incident a_0 or s_0 mode produces a slippery behavior or an opening behavior, respectively, of the crack lips that gets more important as p/h increases. Good correlation is obtained between the modal decomposition results and the FE predictions, both for the coefficients and for the through-thickness displacements on both sides of the internal cracks.

B. Opening crack

1. Reflection and transmission coefficients

Figures 12 and 13 present the modulus of the reflection and transmission coefficients, as functions of defect height,

FIG. 11. Through-thickness displacements on both sides of internal cracks for incident s_0 mode; FE: out-of-plane (squares) and in-plane (circles) displacements of the right (empty) and left (full) sides; Modal analysis: displacements of the right (- - -) and left (—) sides; (a) p/h=25%, (b) p/h=50%, (c) p/h=75% and (d) p/h=100%.

for the incident modes a_0 and s_0, respectively. The defect is a single opening crack of height p, as shown in Fig. 4(b). The difference with the previous case is that defects are no longer symmetrical with respect to the middle plane of the plate, thus implying mode conversion phenomena will occur. This means that an incident a_0 or s_0 mode will be reflected/transmitted into two a_0 and s_0 modes. Consequently, the values of the reflection and transmission coefficients depend on the location through the plate thickness and on the direction in the coordinate axis that are considered, as explained in Sec. IV. This is not the case when there is no mode conversion. For example, the ratio of reflected a_0 to incident a_0 is independent on the direction of displacements and on the location through the plate. In Figs. 12 and 13, graphs (a) and (b) display the reflection and transmission coefficients for directions x_2 and x_1, respectively. The FE predictions have been obtained by monitoring points at the plate surfaces as explained in Sec. IV. In order to compare the modal decom-

position results to these FE predictions, the reflection and transmission coefficients obtained from Eqs. (5) have been multiplied by the ratio of the modulus of the displacement component at the plate surface of the reflected or transmitted mode to that of the incident mode. The following relation illustrates this operation:

$$R_{-N} = \left(\frac{b_{-N}}{a_I} \right) \underbrace{\left| \frac{U_j^{-N}(x_1 = h/2)}{U_j^I(x_1 = h/2)} \right|}_{=1 \ \text{if} \ I = -N}$$

and (8)

$$T_N = \left(\frac{b_N}{a_I} \right) \underbrace{\left| \frac{U_j^N(x_1 = h/2)}{U_j^I(x_1 = h/2)} \right|}_{=1 \ \text{if} \ I = N},$$

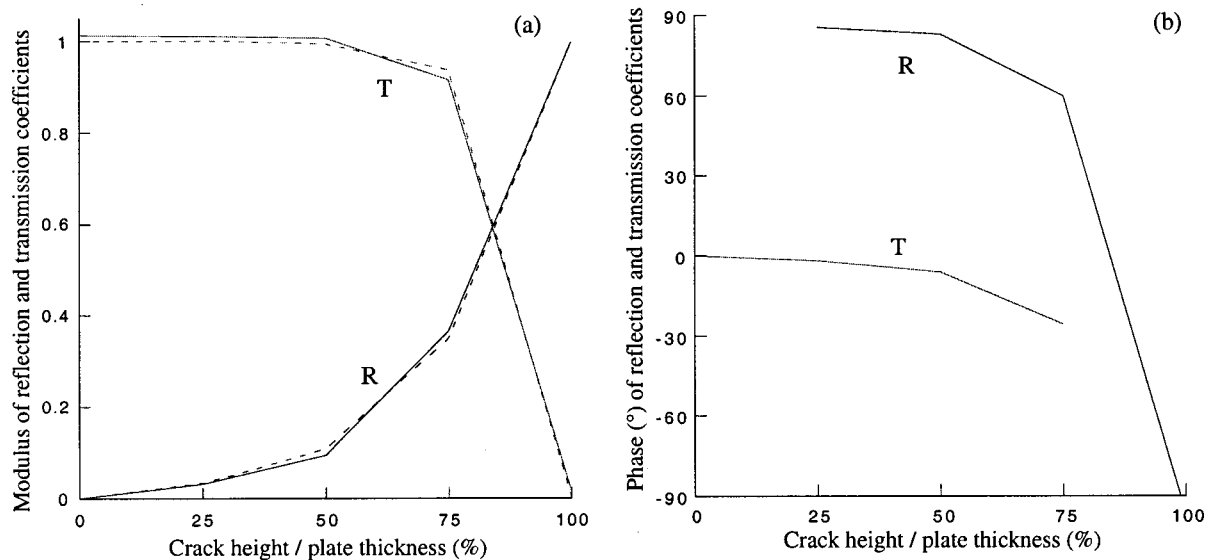where $j = 1$ or 2 (direction of displacement).
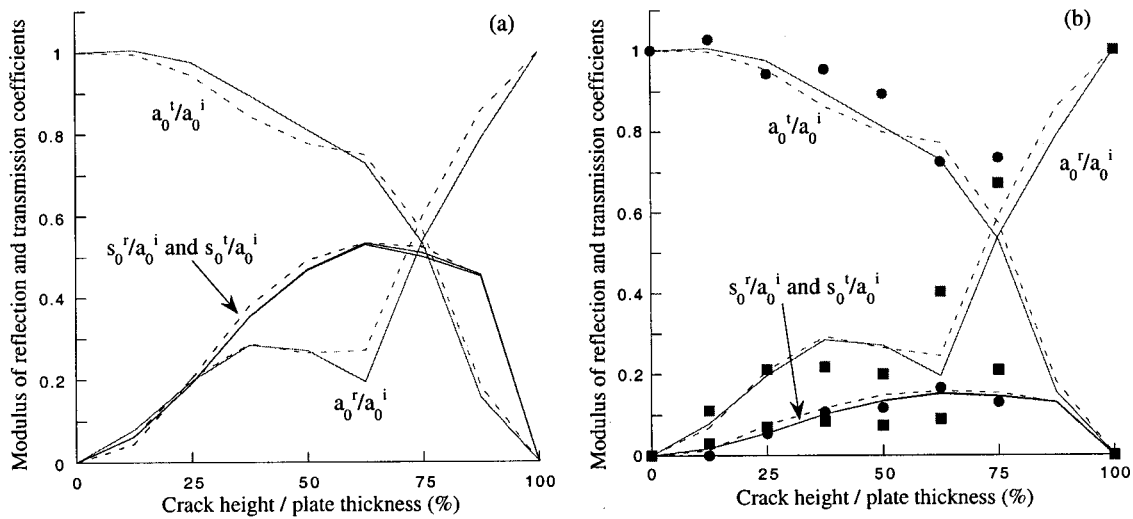
FIG. 12. Predicted and measured reflection and transmission coefficients for a_0 incident on single opening cracks as a function of crack-height-to-plate-thickness ratio; (a) in-plane surface displacement; (b) out-of-plane surface displacement; (- - -) finite element; (—) modal analysis, (●●●) measured transmission (■■■) measured reflection.

Figure 12 shows that the reflected and transmitted a_0 modes have amplitudes (relatively to that of the incident a_0 mode), which are independent of the considered direction x_1 [Fig. 12(b)] or x_2 [Fig. 12(a)]. This result comes from the explanation given above and is confirmed by the two models. The a_0 transmission coefficient decreases monotonically when the crackheight-to-plate-thickness ratio increases, thus meaning that a_0 transmitted past the crack is a good indicator for opening crack sizing problems. This is not the case of the reflected a_0 mode since its amplitude increases for values of p/h contained between 0% and 35%, then decreases for p/h bounded by 35% and 60%, and then increases again for p/h contained between 60% and 100%. This nonmonotonic variation versus p/h makes the reflected a_0 mode not appropriate for crack sizing.

The reflected and transmitted s_0 modes have the same amplitudes (relative to that of the incident a_0 mode) for a given direction of displacement. This is an interesting result

showing that the opening cracks, under the solicitation produced by the incident a_0 mode, launch equal s_0 modes from each of their sides. It must be noted, however, that the ratio of the amplitude of the diffracted s_0 to the amplitude of the incident a_0 depends on the direction of displacement. This ratio is bigger for direction x_2 than for direction x_1, as expected since s_0 produces more in-plane displacement than a_0 does, at the plate surfaces. These ratios monotonically increase for values of p/h comprised between 0% and 60%, and decreases for p/h greater than 60%. By itself, the s_0 produced by mode conversion at an opening crack when a_0 is incident is therefore not sufficient for dimensioning the crack height. However, the existence of diffracted s_0 when a_0 is incident indicates that the crack is not symmetrical with respect to the middle of the plate. Moreover, the set of reflection and transmission coefficients of the various a_0 and s_0 diffracted modes has unique values, thus meaning that the knowledge of the reflected and transmitted a_0 and s_0 modes
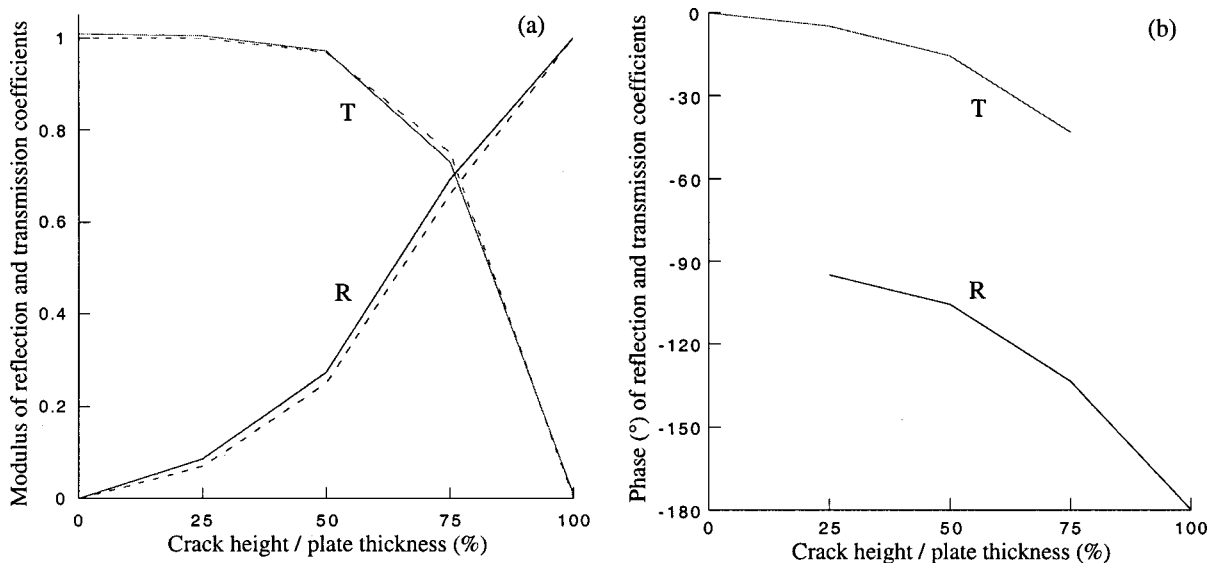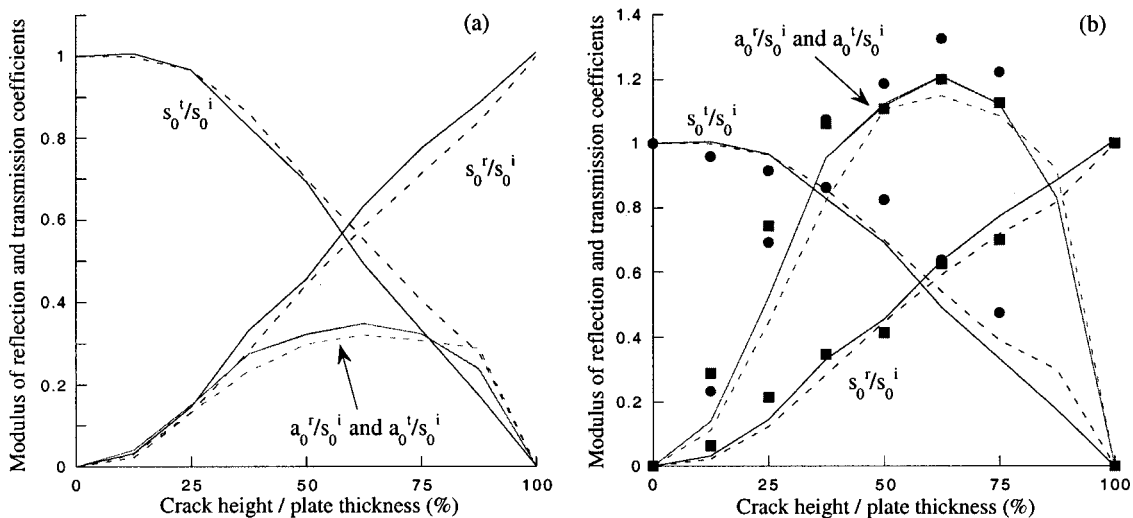

FIG. 13. Predicted and measured reflection and transmission coefficients for s_0 incident on single opening cracks as a function of crack-height-to-plate-thickness ratio; (a) in-plane surface displacement; (b) out-of-plane surface displacement; (- - -) finite element; (—) modal analysis, (●●●) measured transmission, (■■■) measured reflection.

diffracted by an opening crack is sufficient for dimensioning the crack height.

The experimental reflection and transmission coefficients have been obtained by measuring normal displacements (in direction x_1) at one surface of the plates, as described in Sec. V. As shown in Fig. 12, very good correlation is obtained between the experimental results and the numerical predictions.

As shown in Fig. 13, very similar conclusions can be drawn when the s_0 mode is incident upon the opening crack. In this case, both the s_0 reflection and transmission coefficients monotonically vary with the crack-height-to-plate-thickness ratio, thus meaning that both the reflected and transmitted s_0 are good indicators for opening crack sizing problems. Moreover, the presence of diffracted a_0 modes means that the crack is not symmetrical with respect to the middle of the plate. It is interesting to note that the diffracted a_0 amplitude to incident s_0 amplitude is greater than unity for direction x_1, due to the fact that a_0 produces more out-of-plane displacement than s_0 does, at the plate surfaces. Again, very good agreement is obtained between the experimental results and the numerical predictions, thus giving a good confidence in the models.

2. Through-thickness crack motion

Figures 14 and 15 present the modulus of the through-thickness displacement distributions on both sides of the opening cracks, for the incident mode a_0 and s_0, respectively. Plots (a), (b), (c), (d), (e) and (f) correspond to values of p/h equal to 12.5%, 25%, 37.5%, 50%, 62.5% and 75%, respectively.

Figure 14 shows that the incident a_0 mode produces different through-thickness, in-plane and out-of-plane motions on both sides of the cracks, for any value of the relative height p/h (except for p/h-12.5% where these differences are not very visible in direction x_1). This is due to an unequal repartition of antisymmetric modes having non-negligible in-plane compression (σ_2) and shear (σ_6) stress components at the crack locations. Symmetric modes are also produced by mode conversion, but, as shown in Fig. 12, the same number of these modes is launched on both sides of the cracks, so they have no effect on the difference in the displacements of the crack faces.

Figure 15 shows that the incident s_0 mode produces identical out-of-plane motions (U_1) on both sides of any opening cracks. Again, this comes from the fact that symmetric modes have negligible through-thickness shear stress (σ_6), so that the unequal repartition of these modes on both sides of the slots cannot produce differences in the out-of-plane motions of the lips. Antisymmetric modes are launched by mode conversion at the crack locations. These have significant shear stress components, but since their amplitudes are identical on both sides of the cracks (see Fig. 13), they cannot bring differences in the out-of-plane displacements of the crack surfaces. The in-plane displacement components (U_2) are different on both sides of cracks of any height, due to the strong in-plane compression stress (σ_2) produced by symmetric modes of unequal repartition.

The opening slots are shown to have both slippery and opening behavior when the a_0 mode is incident, while an opening behavior only is observed when s_0 is incident. Very good correlation is obtained for the coefficients predicted using the modal decomposition method and the FE model. Concerning the through-thickness displacements on both sides of the opening cracks, very good agreement is also obtained except when a_0 is incident on the 62.5% and 75% relative-height cracks where some differences are observed. This is due to a difficulty in choosing the optimum numbers of points and/or complex modes, so that the stress-free condition on these large cracks and the stress-velocity continuity in the small areas out of these cracks are not simultaneously satisfied. A compromise has been found, so that the system of equations that is to be solved is ill-conditioned for predicting the through-thickness displacements, but not for computing the diffraction coefficients.

VII. CONCLUSIONS

The modal decomposition method has been used for modeling the interaction of the low-order Lamb modes, a_0 and s_0, with cracks running normally to the surfaces of an aluminum plate. The frequency-thickness product was 1.12 MHz.mm, i.e., lower than the frequency cut-off of the a_1 mode, so that only a_0 and s_0 can propagate along the plate. Two types of single cracks have been considered in this model: symmetrical internal crack and opening crack. The reflection and transmission coefficients have been predicted as functions of crack-height-to-plate-thickness ratio, for each incident a_0 and s_0 mode. The through-thickness displacement fields have also been plotted on both sides of cracks of various normalized heights and for the two types of incident mode. An energy balance criteria has been used all through the calculations in order to optimize the computational parameters and to check the validity of the results. Although this was not reminded through the presentation and discussion of the numerical results, the energy balance was always correct within 5% of error.

The reflection and transmission coefficients and the through-thickness displacement fields have been compared to those predicted using a finite element code. The mode conversion phenomena that occurs for cracks, which are not symmetrical with respect to the middle plane of the plate, have been well modeled by the modal decomposition method. This simulation showed that when insonified by an a_0 (or s_0) mode, single opening cracks generate s_0 (or a_0) modes of equal amplitudes on both of their sides, at the frequency-thickness product considered in this study. Good agreement has been obtained for the various cases considered in this study.

Results concerning the motion of crack surfaces are of great importance for understanding the interaction phenomena of Lamb modes with defects. It is clear that the a_0 mode generally produces bigger out-of-plane than in-plane displacements, in comparison to the s_0 mode. This is due to the natural stress distributions of these two modes, at the frequency-thickness considered in this study. Moreover, the

J. Acoust. Soc. Am., Vol. 112, No. 6, December 2002

Castaings *et al.*: Modal decomposition for Lamb waves 2579
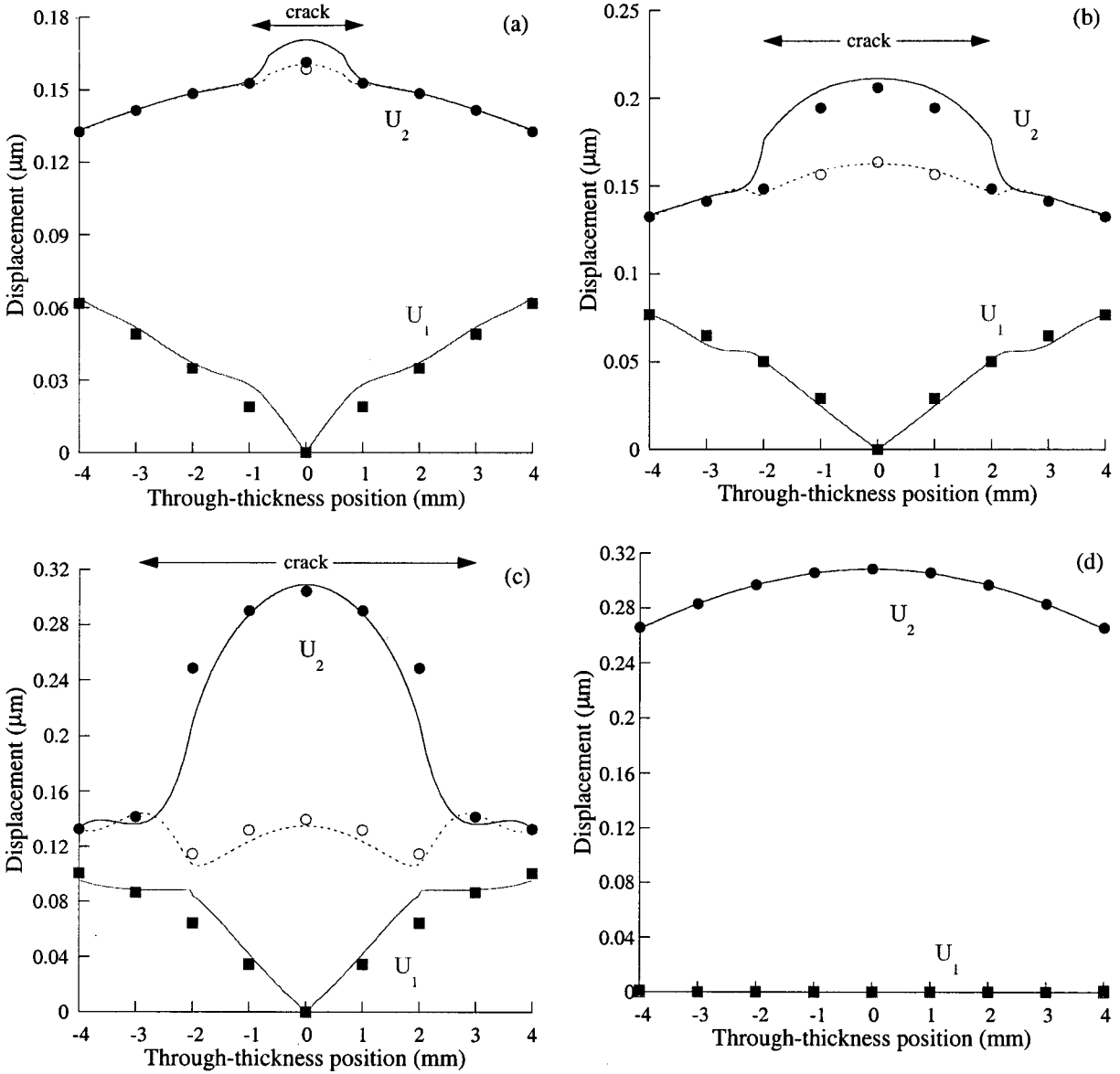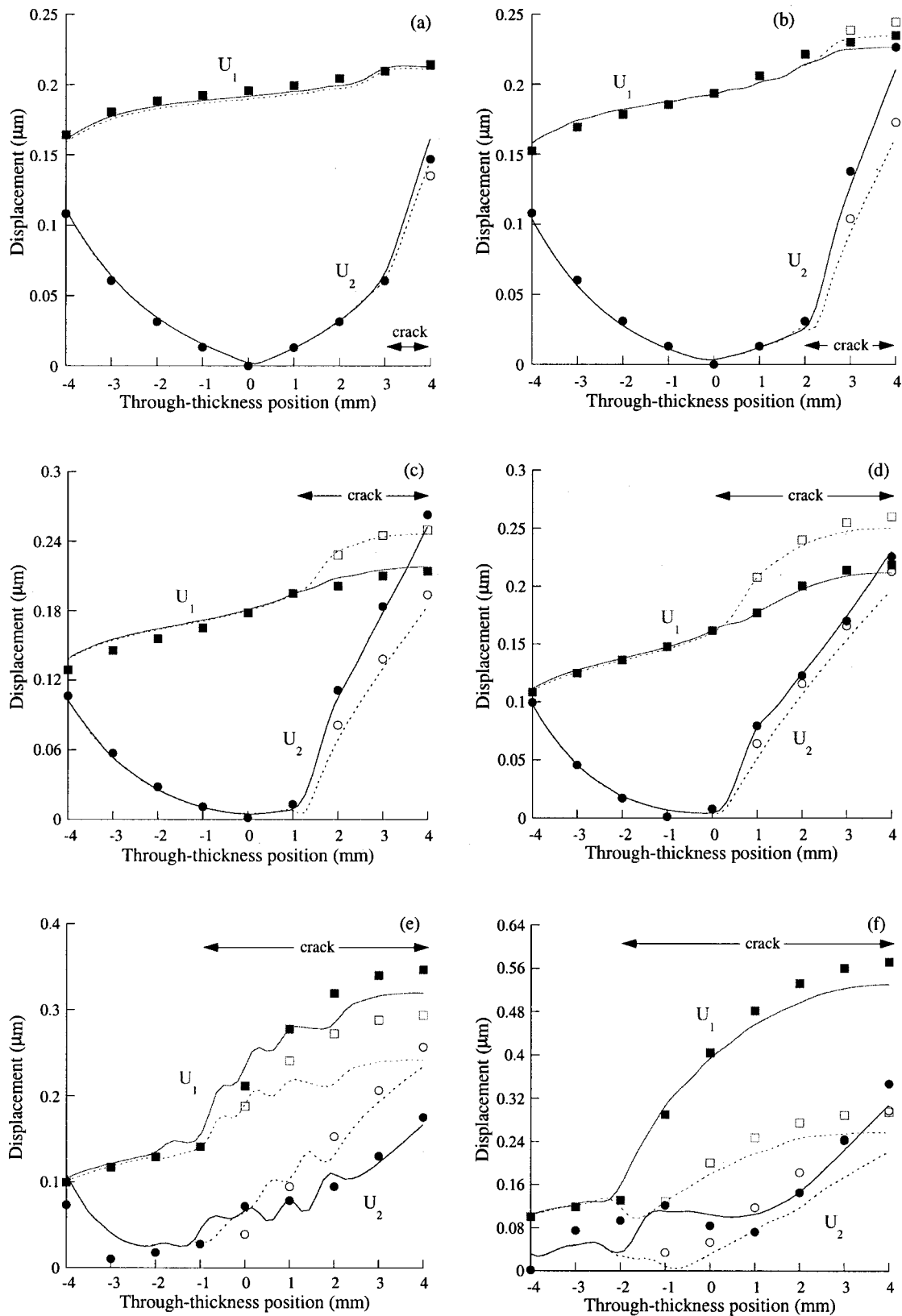
FIG. 14. Through-thickness displacements on both sides of single opening cracks for incident a_0 mode. FE: out-of-plane (squares) and in-plane (circles) displacements of the right (empty) and left (full) sides; Modal analysis: displacements of the right (- - -) and left (—) sides; (a) $p/h=12.5\%$, (b) $p/h=25\%$, (c) $p/h=37.5\%$, (d) $p/h=50\%$, (e) $p/h=62.5\%$, (f) $p/h=75\%$.

unequal repartition of Lamb modes on both sides of the slots causes differences in the motions of the faces of the slots. Thus the a_0 mode is likely to produce slippery behavior of the crack lips while the s_0 mode creates an opening behavior.

The modal decomposition method used in this study proved to be an efficient tool giving results in very good agreement with FE predictions. The reflection and transmission coefficients predicted by both of these methods are vali-
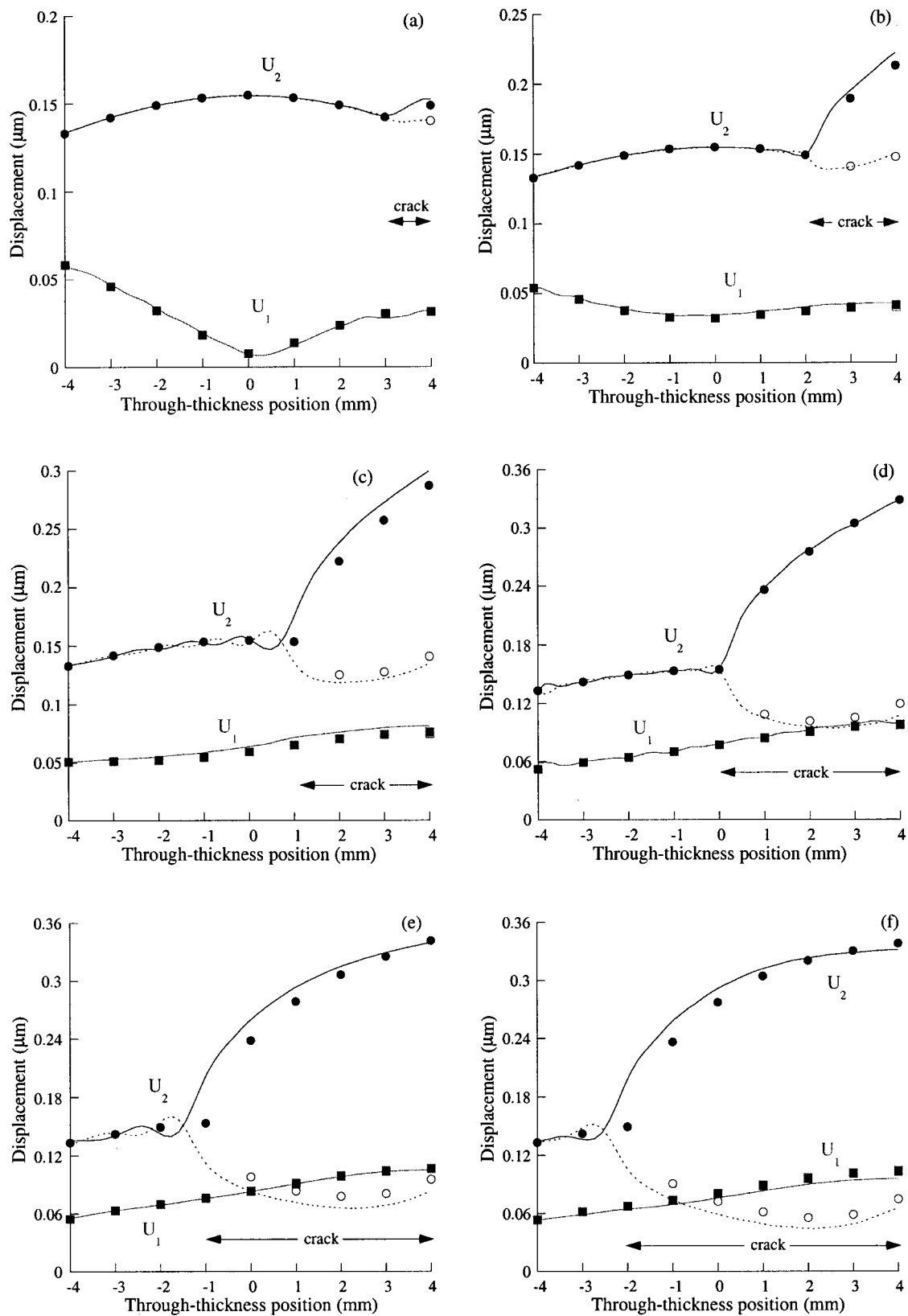
FIG. 15. Through-thickness displacements on both sides of single opening cracks for incident s_0 mode. FE: out-of-plane (squares) and in-plane (circles) displacements of the right (empty) and left (full) sides; Modal analysis: displacements of the right (- - -) and left (——) sides: (a) p/h=12.5%, (b) p/h=25%, (c) p/h=37.5%, (d) p/h=50%, (e) p/h=62.5%, (f) p/h=75%.

dated by experimental measurements made on notches manufactured in aluminum plates. These correlations show that the crack-assumption introduced in the models is valid for notch-width-to-wavelength ratios up to 0.04. This means

that nonzero widths of defects should be considered by the modal decomposition method if increase of the frequency range is planned. In terms of performances, this method supplies reflection and transmission coefficients, as well as dis-

placement fields at any location in the plate, about 100 times faster than the FE model. Therefore, it represents a suitable tool for solving inverse problems, which consist in estimating the geometry (shape and size) of cracks from experimental data. However, the authors are working on establishing closed form solutions for the crack motions in the case of incident a_0 or s_0, which would allow the reflection and transmission coefficients to be very quickly calculated using the S-parameter formalism.[37] Such solutions would be very helpful for the resolution of inverse problems.

ACKNOWLEDGMENT

[1] B. Chassignole, D. Villard, G. Nguyen Van Chi, N. Gengembre, and A. Lhémery, "Ultrasonic propagation in austenitic stainless steel welds. Approximate model and numerical methods and comparison with experiments," in *Review of Progress in Quantitative NDE*, edited by D. O. Thompson and D. E. Chimenti (Plenum, New York, 2000), Vol. 19A, pp. 153–160.

[2] A. J. Testa and C. P. Burger, "Rayleigh spectroscopy for characterizing surface cracks," in *Review of Progress in Quantitative NDE*, edited by D. O. Thompson and D. E. Chimenti (Plenum Press, New York, 1982), Vol. 1, pp. 557–564.

[3] C. Pecorari, "Scattering of Rayleigh wave by a surface-breaking crack with faces in partial contact," Wave Motion **33**, 259–270 (2001).

[4] P. Wilcox, M. Lowe, and P. Cawley, "Lamb and SH wave transducer arrays for the inspection of large areas of thick plates," in *Review of Progress in Quantitative NDE*, edited by D. O. Thompson and D. E. Chimenti (Plenum, New York, 2000), Vol. 19A, pp. 1049–1056.

[5] J. J. Ditri, J. L. Rose, and G. Chen, "Mode selection criteria for defect detection optimization using Lamb waves," in *Review of Progress in Quantitative NDE*, edited by D. O. Thompson and D. E. Chimenti (Plenum, New York, 1992), Vol. 11, pp. 2109–2115.

[6] K. Maslow and T. Kundu, "Selection of Lamb modes for detecting internal defects in composite laminates," Ultrasonics **35**, 141–150 (1997).

[7] S. K. Datta, C. M. Fortunko, and R. B. King, "Sizing of surface cracks in a plate using SH waves," in *Review of Progress in Quantitative NDE*, edited by D. O. Thompson and D. E. Chimenti (Plenum, New York, 1982), Vol. 1, pp. 227–231.

[8] M. D. Gilchrist, "Attenuation of ultrasonic Rayleigh-Lamb waves by small horizontal defects in thin aluminum plates," Int. J. Mech. Sci. **41**, 581–594 (1999).

[9] V. Dayal and V. I. Kinra, "Leaky Lamb waves in an anisotropic plate. II. Nondestructive evaluation of matrix cracks in fiber-reinforced composites," J. Acoust. Soc. Am. **89**, 1590–1598 (1991).

[10] C. Eisenhardt, L. J. Jacobs, and J. Qu, "Experimental Lamb wave spectra of cracked plates," AIP Conf. Proc. **509A**, 343–349 (2000).

[11] M. Lowe, P. Cawley, J. Y. Kao, and O. Diligent, "Prediction and measurement of the reflection of the fundamental anti-symmetric Lamb wave from cracks and notches," in *Review of Progress in Quantitative NDE*, edited by D. O. Thompson and D. E. Chimenti (Plenum, New York, 2000), Vol. 19A, pp. 193–200.

[12] A. H. Harker, "Numerical modeling of the scattering of elastic waves in plates," J. Nondestruct. Eval. **4**(2), 89–106 (1984).

[13] M. Koshiba, S. Karakida, and M. Suzuki, "Finite-element analysis of Lamb wave scattering in an elastic plate waveguide," IEEE Trans. Sonics Ultrason. **SU-31**(1), 18–25 (1984).

[14] S. W. Liu and S. K. Datta, "Scattering of ultrasonic wave by cracks in plate," ASME J. Appl. Mech. **60**(3), 352–357 (1993).

[15] J. Paffenholz, J. W. Fox, X. Gu, G. S. Jewett, S. K. Datta, and H. A. Spetzler, "Experimental and theoretical study of Rayleigh-Lamb waves in a plate containing a surface-breaking crack," Res. Nondestruct. Eval. **1**, 197–217 (1990).

[16] S. W. Liu, S. W. Datta, and T. H. Ju, "Transient scattering of Rayleigh-Lamb waves by a surface-breaking crack: comparison of numerical simulation and experiment," J. Nondestruct. Eval. **10**(3), 111–126 (1991).

[17] L. Wang and J. Shen, "Scattering of elastic waves by a crack in an isotropic plate," Ultrasonics **35**(6), 451–457 (1997).

[18] W. M. Karunasena, A. H. Shah, and S. K. Datta, "Plane-strain-wave scattering by cracks in laminated composite plates," ASCE J. Eng. Mech. **117**(8), 1738–1754 (1991).

[19] Y. Cho and J. L. Rose, "An elastodynamic hybrid boundary element study for elastic guided wave interactions with a surface-breaking defect," Int. J. Solids Struct. **37**(30), 4103–4124 (2000).

[20] J. L. Rose, W. Zhu, and Y. Cho, "Boundary element modeling for guided wave reflection and transmission factor analysis in defect classification," Proc. IEEE Ultrason. Symp. **1**, 885–888 (1998).

[21] D. N. Alleyne and P. Cawley, "The interaction of Lamb waves with defects," IEEE Trans. Ultrasonics Ferroelectr. Freq. Control **39**(3), 381–397 (1992).

[22] C. Tirado and S. Nazarian, "Impact of damage on propagation of Lamb waves in plates," Proc. SPIE **3586**, 267–278 (1999).

[23] P. J. Torvik, "Reflection of wave train in semi-infinite plates," J. Acoust. Soc. Am. **41**, 346–353 (1967).

[24] D. C. Gazis and R. D. Mindlin, "Extensional vibrations and waves in a circular disk and a semi-infinite plate," J. Appl. Mech. **27**, 541–547 (1960).

[25] B. A. Auld and E. M. Tsao, "A variational analysis of edge resonance in a semi-infinite plate," IEEE Trans. Sonics Ultrason. **24**(5), 317–326 (1977).

[26] R. D. Gregory and I. Gladwell, "The reflection of a symmetric Rayleigh-Lamb wave at the fixed or free edge of a plate," J. Elast. **13**, 185–206 (1983).

[27] M. Lowe and O. Diligent, "Reflection of the fundamental Lamb modes from the ends of plates, in *Review of Progress in Quantitative NDE*, edited by D. O. Thompson and D. E. Chimenti (Plenum, New York, 2001), Vol. 20A, pp. 89–96.

[28] E. LeClezio, M. V. Predoi, M. Castaings, B. Hosten, and M. Rousseau, "Numerical predictions and experiments on the free-plate edge mode," Ultrasonics (in press).

[29] M. V. Predoi and M. Rousseau, "Réflextion et transmission d'un mode de Lamb au niveau d'une soudure entre deux plaques," in *Proceedings of the 5th French Congress on Acoustics* (2000), pp. 173–176.

[30] S. Rokhlin, "Diffraction of Lamb waves by a finite crack in an elastic layer," J. Acoust. Soc. Am. **67**, 1157–1165 (1980).

[31] S. Rokhlin, "Resonance phenomena of Lamb waves scattering by a finite crack in a solid layer," J. Acoust. Soc. Am. **69**, 922–928 (1981).

[32] B. A. Auld and M. Tan, "Symmetrical Lamb wave scattering at a symmetrical pair of thin slots," Ultrasonics Symp. Proc., pp. 61–66 (1977).

[33] M. Tan and B. A. Auld, "Normal mode variational method for two and three dimensional acoustic scattering in an isotropic plate," Ultrasonics Symp. Proc., pp. 857–861 (1980).

[34] M. Wang and C. F. Ying, "Scattering of Lamb waves by a circular cylinder," J. Acoust. Soc. Am. **110**, 1752–1763 (2001).

[35] M. Castaings and P. Cawley, "The generation, propagation and detection of Lamb waves in plates using air-coupled ultrasonic transducers," J. Acoust. Soc. Am. **100**, 3070–3077 (1996).

[36] W. H. Press, S. A. Teukolsky, W. T. Vetterling, and B. P. Flannery, *Numerical Recipes in C—The Air of Scientific Computing,* 2nd ed. (Cambridge U.P., Cambridge, 1997).

[37] B. A. Auld, *Acoustic Fields and Waves in Solids* (Krieger, Malabar, FL, 1990).

[38] P. Kirrmann, "On the completeness of Lamb waves," J. Elast. **37**, 39–69 (1995).

[39] D. Hitchings, *FE77 user manual,* Dept. of Aeronautics, Imperial College International Report, 1995.

[40] D. Alleyne and P. Cawley, "A two-dimensional Fourier transform method for the measurement of propagating multimode signals," J. Acoust. Soc. Am. **89**, 1159–1168 (1991).

[41] M. Castaings and B. Hosten, "The propagation of guided waves in composite sandwich-like structures and their use for NDT," in *Review of Progress in Quantum NDE*, edited by D. O. Thompson and D. E. Chimenti (Plenum, New York, 2001), Vol. 20, pp. 999–1006.

On the steady-state and the transient decay methods for the estimation of reverberation time

K. S. Sum and J. Pan

Department of Mechanical and Materials Engineering, The University of Western Australia,
35 Stirling Highway, Crawley, Western Australia 6009

The discrepancy between reverberation times of an enclosed sound field measured by the steady-state method and by the transient decay method is well-known. So far, no clear explanation has been obtained. In this paper, the steady-state bandlimited energy in an enclosure and bandlimited power flow into modally reactive boundaries are derived to describe the energy balance relationship and thus the reverberation time in a frequency band. This reverberation time is then compared to that obtained from the transient decay of the sound field based on the modal analysis. The comparison provides an understanding of the discrepancy mentioned above as well as the physical interpretations of the reverberation times estimated by both methods. © *2002 Acoustical Society of America.* [DOI: 10.1121/1.1510139]

I. INTRODUCTION

It is known that the reverberation time T_{60} of an enclosed sound field or a structure in a frequency band is related to its loss factor η by $T_{60} = 4.4\pi/\eta\omega_0$, where ω_0 is the center frequency of the band. About two decades ago, Bies and Hamid[1] experimentally compared two different methods for measuring loss factors of plates, namely the steady-state method based on the energy balance relationship and the transient decay method. They observed that the loss factor measured by the former, η_{ss}, was consistently larger than that measured by the latter, η_{tr}. Subsequently, Brown and Norton[2] and Norton and Greenhalgh[3] also compared the two methods for cylindrical pipes. Their experimental observations were consistent with those of Bies and Hamid. This means T_{60}^{tr} obtained by the transient decay method is larger than T_{60}^{ss} obtained by the steady-state method. Bies and Hamid explained the discrepancy between the two methods by the concept of relaxation time and equilibrium. They suggested that during reverberant decay, the steady-state equilibrium which is initially achieved prior to gating of the excitation source is lost. Consequently, only the initial decay should give the same or close value of T_{60}^{tr} to T_{60}^{ss}. However, if T_{60}^{tr} is deduced by fitting a straight line to both the initial and late parts of the decay curve, then it would be larger than T_{60}^{ss}, since those least attenuated modes with long decay times will persist in the late decay. Interestingly, the experimental results of Ranky and Clarkson[4] for plates and shells contradicted with all the above-mentioned experimental observations. Their explanation was that the steady-state energy in a band is dominated by high energy (small loss factor) modes. The late part of the decay curve should then correspond to these modes, and should give the same or close values of η_{tr} and T_{60}^{tr} to η_{ss} and T_{60}^{ss}. Hence, when a straight line is fitted to both the initial and late decays, the weighting from the initial decay would produce a larger overall η_{tr}. Thus, the T_{60}^{tr} obtained is smaller than T_{60}^{ss}. Ranky and

Clarkson[4] also showed that both methods would yield similar results if the loss factors (or decay times) of the modes in the band are close to each other.

In many conventional acoustic measurements in rooms, the reverberation time of the enclosed sound field is usually required. Examples of such measurements are sound power radiated by acoustic sources, Sabine absorption coefficient of absorbing materials, and transmission loss of structures. The reverberation time is traditionally measured by the transient decay method because the steady-state method has not yet been accepted as a universal technique for the reverberation time estimation in rooms. Nevertheless, some experimental techniques are available for the measurements of input sound power of acoustic sources required by the latter (e.g., the impedance tube method[5] and volume velocity measurement methods[6]), and the reverberation time can then be obtained.

As building structures are modally reactive, the reverberation time in rooms is affected by acoustic–structural modal coupling even in a standard reverberation room.[7] Since the coupling is very selective,[8] it is anticipated that there is a substantial variation in the modal decay time of acoustic modes. As a result, T_{60}^{ss} and T_{60}^{tr} may not be the same unless all the modal decay times are close to each other. The implication is that the results of acoustic measurements in rooms would be different if the reverberation times obtained by both methods were different. Therefore, the study of T_{60}^{ss} and T_{60}^{tr} is essential for investigating the use of the alternative steady-state approach to obtain the reverberation time in rooms. The comparison of T_{60}^{ss} and T_{60}^{tr} may also provide a way to search for an explanation of the discrepancy between them as observed in the area of structural vibration.

This paper uses an analytical means to compare the steady-state and the transient decay methods for the reverberation time of the sound field in an enclosure. Coupling between the sound field and modally reactive boundary structures is considered as one of the acoustic energy dissipation mechanisms apart from air absorption. The results presented in this paper are in favor of the experimental ob-

servations in Refs. 1–3, but are not in full agreement with the aforementioned explanation of the discrepancy between the two methods from Ref. 4. It is shown that although the late decay corresponds to modes with small loss factors (i.e., long decay times), these modes do not necessarily dominate the steady-state energy in a band. The reason is because the energy distribution among decaying modes in transient state is not the same as in steady state. This phenomenon is justified in this paper where two issues are discussed, namely the reason for the discrepancy between T_{60}^{ss} and T_{60}^{tr}, and the physical meaning of the respective reverberation time.

II. THE STEADY-STATE METHOD

In an acoustic–structural coupled system where the enclosed sound field is directly excited by an acoustic source, an analytical expression has been derived and justified[9] for evaluating the bandlimited acoustic energy of the sound field in the medium- and high-frequency ranges. It can be extended to the case where the bare enclosure has N_F vibrating boundary structures. By considering a monopole source excitation whose location is space averaged over the enclosure volume, V_0, the bandlimited acoustic energy can be derived as

$$E_a = \sum_{i=1}^{N} E_{ai}, \tag{1}$$

$$E_{ai} = \frac{\rho_0 c_0^2 T_{ai}^c Q_p^2}{17.6\pi V_0 \Delta\omega}\left\{\tan^{-1}\left[\frac{(\omega_{ai}^c - \omega_L)T_{ai}^c}{2.2\pi}\right] - \tan^{-1}\left[\frac{(\omega_{ai}^c - \omega_U)T_{ai}^c}{2.2\pi}\right]\right\}. \tag{2}$$

E_{ai}, ω_{ai}^c, and T_{ai}^c are, respectively, the steady-state time-averaged energy, resonance frequency, and decay time of the ith coupled acoustic mode due to coupling with all the structures. $Q_p^2/\Delta\omega$ is the power spectral density of the bandlimited noise emitted by the monopole, and ω_L and ω_U are the lower and upper frequency limits of the excitation band, respectively. ρ_0 is the air density, and c_0 is the speed of sound in air. By using the derivation procedure in Ref. 9, the bandlimited power flow from the sound field into the kth structure for the space average of the excitation location can also be derived as

$$\Pi^{(k)} = \sum_{i=1}^{N} \Pi_{ai}^{(k)}, \tag{3}$$

$$\Pi_{ai}^{(k)} = \frac{A_s^{(k)2}\rho_0^3 c_0^4 Q_p^2}{2V_0 M_{ai}\Delta\omega}\sum_{j=1}^{M^{(k)}}\frac{\eta_{sj}^{(k)}\omega_{sj}^{(k)}B_{j,i}^{(k)2}}{M_{sj}^{(k)}}\int_{\Delta\omega}\frac{\omega^4}{[(\omega_{ai}^{c2} - \omega^2)^2 + (4.4\pi\omega_{ai}^c/T_{ai}^c)^2][(\omega_{sj}^{(k)2} - \omega^2)^2 + (\eta_{sj}^{(k)}\omega_{sj}^{(k)2})^2]}d\omega. \tag{4}$$

$\Pi_{ai}^{(k)}$ is the time-averaged power flow from the ith acoustic mode into the kth structure and M_{ai} is the mass of the mode. $\omega_{sj}^{(k)}$, $\eta_{sj}^{(k)}$, and $M_{sj}^{(k)}$ are the resonance frequency, loss factor, and mass of the jth uncoupled mode of the kth structure, respectively, $B_{j,i}^{(k)}$ is the coupling factor between the structural and the acoustic modes, and $A_s^{(k)}$ is the surface area of the structure. The analytical solution to the integral in Eq. (4) is available.[9] In steady state, the total power dissipated from the sound field is equal to the input power injected into the sound field by the acoustic source. Thus, from the energy balance relationship, the total dissipated power is given by

$$\Pi = \Pi_{\text{air}} + \sum_{k=1}^{N_F}\Pi^{(k)} = \eta_{ss}\omega_0 E_a = \frac{4.4\pi E_a}{T_{60}^{ss}}, \tag{5}$$

where it includes the power dissipations through air absorption and through coupling with all the structures. Therefore, T_{ai}^c in Eqs. (2) and (4) also includes the effect of the air absorption. $\Pi_{\text{air}} = \eta_{\text{air}}\omega_0 E_a$ is obtainable, as η_{air} can be evaluated.[10] Hence,

$$T_{60}^{ss} = \frac{4.4\pi E_a}{\eta_{\text{air}}\omega_0 E_a + \Sigma_{k=1}^{N_F}\Pi^{(k)}}. \tag{6}$$

If locally reactive surfaces such as those of sound absorption materials and boundary structures with a rough finish are also present in the enclosure, then the effects of the surfaces

are included in T_{ai}^c. The power dissipated by the surfaces, Π_{local}, is also added to the total dissipated power in Eq. (5).

III. THE TRANSIENT DECAY METHOD

Equation (5) also describes the rate of change of acoustic energy of the sound field such that $\tilde{\Pi} = d\tilde{E}_a/dt = -4.4\pi\tilde{E}_a/T_{60}^{tr}$. Once the sound source is shut off at time $t = 0$ s, the time-dependent energy, $\tilde{E}_a$, is then given by $\tilde{E}_a(t) = E_a e^{-4.4\pi t/T_{60}^{tr}}$. Since each acoustic mode also decays exponentially with time, the time-dependent energy of the ith mode can be similarly written as $\tilde{E}_{ai}(t) = E_{ai}e^{-4.4\pi t/T_{ai}^c}$. The total acoustic energy is then obtained as

$$\tilde{E}_a(t) = \sum_{i=1}^{N}\tilde{E}_{ai}(t) = \sum_{i=1}^{N}E_{ai}e^{-4.4\pi t/T_{ai}^c}. \tag{7}$$

The decay curve of the total energy is then evaluated by Eq. (7) and T_{60}^{tr} can be estimated from the best straight-line fit to the 60-dB range of the curve from the initial steady-state level at $t = 0$ s. However, the decay curve in practical measurements does not usually have a 60-dB dynamic range because of the presence of background noise. Therefore, the range from 5 to 35 dB below the steady-state level is commonly used in reverberation time measurements in rooms[11] and it covers a large part of the late decay. The first 10 dB of the decay is also widely used since the initial decay

K. S. Sum and J. Pan: Reverberation time of sound field

is also important from the subjective point of view. Hence, both the $[0, -10]$-dB and $[-5, -35]$-dB ranges are considered here.

In Eq. (7), $\tilde{E}_a(t)$ only decreases with time but does not fluctuate because E_{ai} was time averaged where the temporal fluctuations of the amplitude and phase of each mode were averaged out. Therefore, the true decay of the sound field, which would otherwise be obscured by the fluctuations in the decay curve, can be clearly revealed. These fluctuations depend on the amplitudes and phases of the acoustic modes at the instance when the bandlimited noise is turned off. However, these initial characteristics of the modes are random due to the temporal randomness of the excitation signal and not because of any changes in the properties of the sound field. As a result, the fluctuations in the decay curve are random, and the curve and thus the reverberation time obtained for the same driving and receiving locations in the sound field are different from trial to trial. Traditionally, the effect of the fluctuations on the measured reverberation time was minimized by taking the ensemble average of decay curves obtained from a large number of trials. Chu[12] showed that this ensemble average agreed well with the true decay of the sound field, which can be obtained by the use of Schroeder's integrated impulse method.[13] Schroeder's approach gives a smooth decay curve, where the corresponding energy decay can be written as[13]

$$\tilde{E}_a^{\text{Sch}}(t, r_s, r_r) = C \int_t^{\infty} h^2(\tau, r_s, r_r) d\tau. \tag{8}$$

C is a constant proportional to $Q_p^2/\Delta\omega$, r_s and r_r are the locations of the source and receiver, and h is the response of the sound field when excited by a filtered impulse from the bandpass filter which was used to obtain the bandlimited noise.

In order to show the closeness to the true decay, the time-average approach used in Eq. (7) is compared numerically to Schroeder's approach. In the latter, the reverberation times for a large number of combinations of source and receiver positions are obtained numerically from Eq. (8), and their averaged value, T_{60}^{Sch}, is then evaluated. A $0.88 \times 1.725 \times 1.54$-m^3 enclosure with simply supported medium density fiberboard (MDF) walls of thickness 32 mm is used. The structural properties of the walls are: longitudinal wave speed, $c_L = 2500$ ms^{-1}, material density, $\rho_{\text{walls}} = 750$ kg m^{-3}, and uncoupled loss factor, $\eta_{\text{walls}} = 0.02$. The loss factor due to air absorption, η_{air}, is taken to have an averaged value of 1.0×10^{-4} across the whole frequency range. The good agreements between T_{60}^{tr} and T_{60}^{Sch} in both the $[0, -10]$-dB and $[-5, -35]$-dB ranges indicate that the initial and late parts of the decay curves for the two approaches are similar in almost all 1/3-octave bands shown in Fig. 1. In the following sections, the time-average approach will be used because the distribution of energies among acoustic modes at any instances during the sound field decay can be conveniently obtained, while it is difficult to do so using Schroeder's approach.
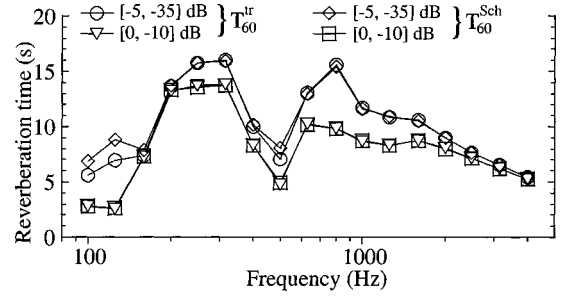
FIG. 1. Reverberation time of the sound field (comparison of the time-average and Schroeder's approaches).

IV. COMMENTS ON THE STEADY-STATE AND THE TRANSIENT ENERGIES

As shown in Eq. (2), the initial energy of each acoustic mode E_{ai} is proportional to T_{ai}^c. This is similar to Ranky and Clarkson's[4] explanation that the modal energy is inversely proportional to its loss factor. Thus, according to Eq. (7), $\tilde{E}_{ai}$ is proportional to $T_{ai}^c e^{-4.4\pi t/T_{ai}^c}$ in the transient state. If those acoustic modes in a band with close decay times are grouped together which results in G groups of modes, then from Eq. (7)

$$\tilde{E}_a \propto \sum_{m=1}^{G} N_a^{(m)} \bar{T}_a^{c(m)} e^{-4.4\pi t/\bar{T}_a^{c(m)}}, \tag{9}$$

where $\bar{T}_a^{c(m)}$ is the mean decay time of the mth group and $N_a^{(m)}$ is the population size (i.e., number of modes with $T_{ai}^c \approx \bar{T}_a^{c(m)}$) of the group. It can be seen that the initial energy of each group at $t = 0$ s is determined by the $N_a \bar{T}_a^c$ factor. However, as time increases, the exponential term in Eq. (9) provides an enormous weighting of energy towards groups of modes with long decay times because these modes tend to decay very slow with time. Thus, in the case where these groups have smaller initial energies (i.e., smaller $N_a \bar{T}_a^c$ factors) than those with short decay times, they can only partially dominate $\tilde{E}_a$ during decay in the $[0, -10]$-dB range. Therefore, T_{60}^{tr} in this decay range represents the averaged decay time of both the groups with short and long decay times. However, it represents the averaged decay time of only the latter groups if these groups have relatively larger initial energies (i.e., larger $N_a \bar{T}_a^c$ factors) because they fully dominate $\tilde{E}_a$ in the decay range. On the other hand, T_{60}^{tr} in the $[-5, -35]$-dB range also has the same physical meaning since only the groups with long decay times will remain dominant to $\tilde{E}_a$ during the late decay.

In steady state, T_{60}^{ss} depends on both E_a and $\Pi^{(k)}$ [see Eq. (6)]. Since E_a and $\Pi^{(k)}$ are the averaged energy and averaged power flow in a band, T_{60}^{ss} represents the averaged decay time of all the acoustic modes in the band. This averaged time depends on how the initial energy of each group of the acoustic modes is distributed as described below. In steady state, the exponential term does not exist, and from Eq. (9)

$$E_a \propto \sum_{m=1}^{G} N_a^{(m)} \bar{T}_a^{c(m)}. \tag{10}$$
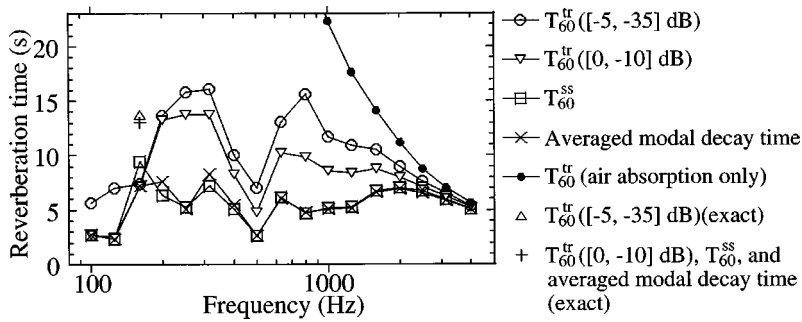
FIG. 2. Reverberation time of the sound field (comparison of the steady-state and the transient decay methods).

From Eq. (10), E_a is not necessarily weighted towards groups with long decay times, although E_{ai} is proportional to T_{ai}^c. Those groups with larger $N_a \bar{T}_a^c$ factors dominate E_a, and their averaged decay time determines the averaged decay time of all the modes in the band and thus T_{60}^{ss}. As a result, two cases exist. The first is where groups with short decay times have larger $N_a \bar{T}_a^c$ factors and thus control T_{60}^{ss}. In this case, T_{60}^{ss} is closer to T_{60}^{tr} in the $[0, -10]$-dB range than T_{60}^{tr} in the $[-5, -35]$-dB range, but smaller than both. The second case is where groups with long decay times have larger $N_a \bar{T}_a^c$ factors and thus control T_{60}^{ss}. In this case, T_{60}^{ss} is smaller but very near to both close values of T_{60}^{tr} in the two decay ranges considered. A special case is when all the modal decay times are the same. E_a is then dominated by one single group of modes in steady state. $\tilde{E}_a$ is also dominated by the same group of modes as the exponential term gives the same weighting of energy for all the modes in the transient state. Hence, both methods yield the same value of reverberation time.

From this section, it can be seen that since T_{60}^{ss} and T_{60}^{tr} have different physical interpretations, the discrepancy between them is natural. Only the distribution of energies among acoustic modes in steady state would determine whether the discrepancy is small or large.

V. RESULTS AND DISCUSSION

Some results are presented to illustrate the physical picture for the comments made in the preceding section. The same enclosure system in Sec. III is used, and T_{60}^{ss} and T_{60}^{tr} are shown in Fig. 2. The averaged modal decay time in each band as shown is obtained simply by evaluating the arithmetic mean value of the decay times of all the acoustic modes in the band. Each of the first three low-frequency bands only has one resonance acoustic mode. In the 160-Hz band, the decay time of the resonance mode and thus T_{60}^{ss} and T_{60}^{tr} are not accurately predicted by the expression for T_{ai}^c.[9] An exact full-coupling solution[9] is then used for this band, and the corresponding results are included in Fig. 2. From the figure, it can be seen that T_{60}^{ss} closely represents the averaged modal decay time in each band as argued, although both results are not exactly equal. In those bands where the values of T_{60}^{tr} in the $[0, -10]$-dB and $[-5, -35]$-dB ranges are largely different, there are distinct initial and late decays. It is obvious for both decay ranges that T_{60}^{tr} is consistently larger than T_{60}^{ss}. The results are close to each other from the 2000-Hz band and above when the coupling becomes weak

and the air absorption starts to dominate the reverberation time. The discrepancy can be explained as follows. For example, consider the 800-Hz and 4000-Hz bands where their resonance acoustic modes with close decay times are sorted into four groups. The population size expressed as the percentage of the total resonance modes and the $N_a \bar{T}_a^c$ factor of each group as a function of the mean decay time of the group are shown in Fig. 3. The energy in each group at four different instances during decay is shown in Fig. 4. In the 800-Hz band, almost 90% of the modes reside in the groups with short decay times (i.e., the 2.5-s and 7.5-s groups) (see Fig. 3). The relatively larger $N_a \bar{T}_a^c$ factors of these groups indicate that their energies dominate the total sound-field energy at the 0-dB level (i.e., $t = 0$ s). Hence, T_{60}^{ss} has a value which lies within these two groups (i.e., 4.7 s as shown in Fig. 2). However, in the transient state, the energies of these groups decay relatively fast. At the -5-dB level, the 12.5-s group then becomes dominant, while the 17.5-s group also starts to partially dominate just before the -10-dB level (see Fig. 4). This means that all four groups are in control of the sound-field energy in the $[0, -10]$-dB range. Thus, T_{60}^{tr} in this decay range has a value close to the averaged decay time of all those groups of modes (i.e., 9.8 s as shown in Fig. 2). This result also shows that although only the first 10 dB of the
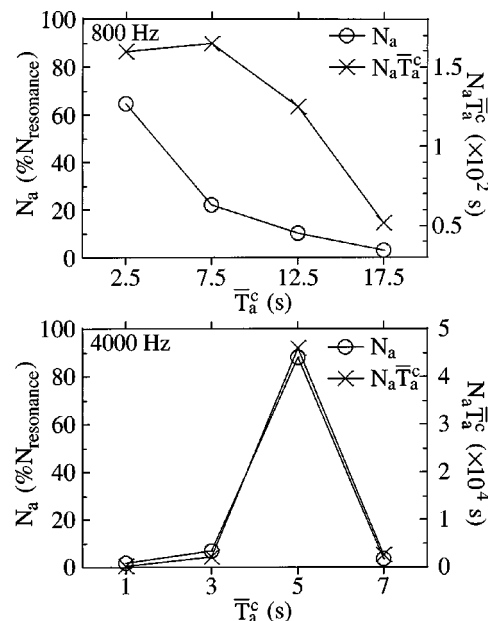
FIG. 3. Population size and $N_a \bar{T}_a^c$ factor versus the mean decay time of each group of acoustic modes.

K. S. Sum and J. Pan: Reverberation time of sound field
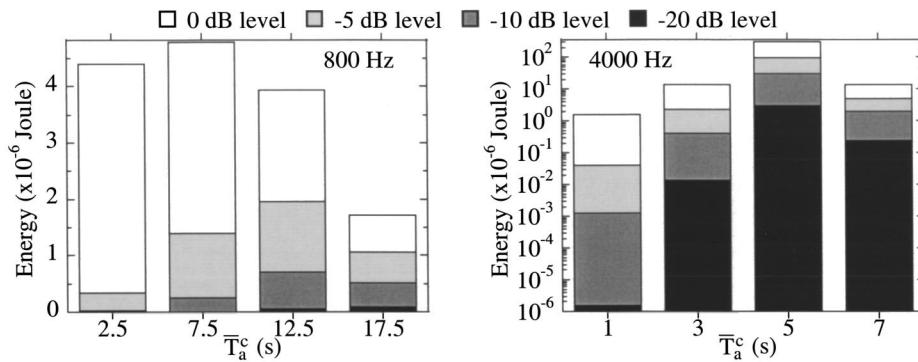
FIG. 4. Temporal acoustic energy versus the mean decay time of each group of acoustic modes.

decay is considered, the corresponding T_{60}^{tr} is still largely different from T_{60}^{ss} due to the influence of the groups with long decay times (i.e., the 12.5-s and 17.5-s groups). The 12.5-s group is largely dominant from the -5-dB level to the -20-dB level at which its energy almost levels up with that of the 17.5-s group. Since the former decays faster than the latter, the remaining sound-field decay from the -20-dB level onwards is controlled by only the 17.5-s group. As a result, T_{60}^{tr} in the $[-5, -35]$-dB range will lie within 12.5 s and 17.5 s (i.e., 15.6 s as shown in Fig. 2). In the 4000-Hz band, there is a large number of modes with long decay times which initially reside in the 5-s group (see Fig. 3). Thus, this group dominates the steady-state energy of the sound field and T_{60}^{ss} then has a value of 5.05 s as shown in Fig. 2. It can be seen from Fig. 4 that the same group also largely contributes to the sound-field energy in the $[0, -35]$-dB range. Thus, the close values of 5.2 and 5.4 s are obtained for T_{60}^{tr} in the $[0, -10]$-dB and $[-5, -35]$-dB ranges. The case in the 4000-Hz band is also an example where most acoustic modes have close or the same decay times because of poor coupling and that the absorption in each mode due to air is not as selective as that due to the coupling.

When the band has only one resonance acoustic mode, the steady-state and the decay methods only give the same or close values of reverberation time if the mode dominates the total sound-field energy at $t=0$ s as well as in the $[0, -35]$-dB range. It is the case when the mode has a long decay time (e.g., 13 s in the 160-Hz band) which results in its large initial energy. If the mode has a short decay time such as that in the 125-Hz band (i.e., 2.4 s), a discrepancy in the results can still occur (see Fig. 2). Figure 5 shows that the energy of the resonance mode is dominant at $t=0$ s. Thus, T_{60}^{ss} is con-

trolled by this mode. However, the mode decays relatively faster than the nonresonance modes, which are those whose resonance frequencies lie outside the analysis band. At the -20-dB level, its energy has leveled up with that of the nonresonance modes. The remaining decay to the -35-dB level is then controlled by the nonresonance modes. As a result, the resonance mode still controls T_{60}^{tr} in the $[0, -10]$-dB range, but T_{60}^{tr} in the $[-5, -35]$-dB range will include the effect of the nonresonance modes and is higher than T_{60}^{ss}.
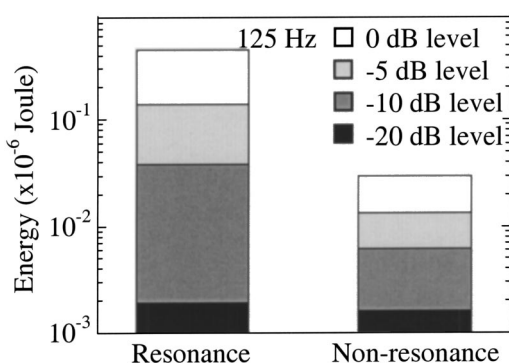
VI. CONCLUSIONS

A basic understanding of the nature of discrepancy in the sound-field reverberation times obtained by the steady-state method, T_{60}^{ss}, and by the transient decay method, T_{60}^{tr}, as well as the physical meaning of the respective reverberation time have been achieved. T_{60}^{ss} represents the averaged decay time of all the acoustic modes in a band, since it depends on the averaged energy and averaged power flow in the band. This averaged time is determined by the dominant groups of acoustic modes to the total sound-field energy in steady state. These groups do not necessarily have long decay times. On the other hand, T_{60}^{tr} in the $[-5, -35]$-dB range represents the averaged decay time of groups of modes with long decay times, since only these groups control the sound-field energy in this decay range. If these groups also dominate the initial energy of the sound field, then T_{60}^{tr} in the $[0, -10]$-dB range also has the same physical meaning. However, if groups with short decay times dominate the initial energy, then T_{60}^{tr} in the $[0, -10]$-dB range represents the averaged decay time of these groups and those with long decay times, since both of the groups also control the sound-field decay in this range. As a result, T_{60}^{tr} in the initial decay is closer to T_{60}^{ss} than T_{60}^{tr} in the late decay but both are larger than T_{60}^{ss}. Although only the first 10 dB is considered in the initial decay, the corresponding T_{60}^{tr} can still be largely different from T_{60}^{ss} due to the influence of the groups with long decay times. However, when these groups of modes control the total sound-field energy in steady state, both methods will yield close results.

FIG. 5. Temporal energies of resonance and nonresonance acoustic modes.

[1] D. A. Bies and S. Hamid, "*In situ* determination of loss and coupling loss factors by the power injection method," J. Sound Vib. **70**, 187–204 (1980).
[2] K. T. Brown and M. P. Norton, "Some comments on the experimental determination of modal densities and loss factors for statistical energy analysis applications," J. Sound Vib. **102**, 588–594 (1985).
[3] M. P. Norton and R. Greenhalgh, "On the estimation of loss factors in

lightly damped pipeline systems: Some measurement techniques and their limitations," J. Sound Vib. **105**, 397–423 (1986).

[4] M. F. Ranky and B. L. Clarkson, "Frequency average loss factors of plates and shells," J. Sound Vib. **89**, 309–323 (1983).

[5] D. A. Bies and C. H. Hansen, "Impedance-tube calibration of a reverberant room for the measurement of sound power in tones," J. Acoust. Soc. Am. **59**, 1393–1398 (1976).

[6] D. K. Anthony and S. J. Elliott, "A comparison of three methods of measuring the volume velocity of an acoustic source," J. Audio Eng. Soc. **39**, 355–365 (1991).

[7] J. Pan and D. A. Bies, "Experimental investigation into the interaction between a sound field and its boundaries," J. Acoust. Soc. Am. **83**, 1436–1444 (1988).

[8] M. C. Bhattacharya and M. J. Crocker, "Forced vibration of a panel and radiation of sound into a room," Acustica **22**, 275–294 (1969/1970).

[9] K. S. Sum and J. Pan, "An analytical model for band-limited response of acoustic–structural coupled systems. I. Direct sound field excitation," J. Acoust. Soc. Am. **103**, 911–923 (1998).

[10] D. A. Bies and C. H. Hansen, "Sound sources and outdoor sound propagation," in *Engineering Noise Control: Theory and Practice* (E&FN Spon, London, 1996), Chap. 5.

[11] L. L. Beranek, "Terminology and conversion factors," in *Concert and Opera Halls: How They Sound* (Acoustical Society of America, New York, 1996), Appendix 1.

[12] W. T. Chu, "Comparison of reverberation measurements using Schroeder's impulse method and decay-curve averaging method," J. Acoust. Soc. Am. **63**, 1444–1450 (1978).

[13] M. R. Schroeder, "New method of measuring reverberation time," J. Acoust. Soc. Am. **37**, 409–412 (1965).

The low-frequency reflection and scattering of the S_0 Lamb mode from a circular through-thickness hole in a plate: Finite Element, analytical and experimental studies

O. Diligent
Department of Mechanical Engineering, Imperial College, London SW7 2BX, United Kingdom

T. Grahn and A. Boström
Department of Applied Mechanics, Chalmers University of Technology, SE-412 96 Göteborg, Sweden

P. Cawley and M. J. S. Lowe[a)]
Department of Mechanical Engineering, Imperial College, London SW7 2BX, United Kingdom

A study of the interaction of the S_0 Lamb wave with a circular through-thickness hole in a plate is presented. The study is limited to the nondispersive frequency range of this wave, in which the distributions of stress and displacement are simple. This allows a Finite Element analysis to be undertaken using a two-dimensional membrane discretization. Predictions of the direct reflection of the S_0 mode and the lateral scattering of the SH_0 mode are made for a range of diameters of the hole. At the same time, an analytical solution based on modal superposition is developed, and this is also used to predict the reflection and scattering coefficients. Both sets of predictions are validated by experimental measurements. It is found that the trends of the reflection coefficients for different hole diameters, frequencies and distances from the hole satisfy a simple normalization. On a detailed scale, the functions exhibit undulations which are shown to result from the interference of the direct reflection with secondary reflections which arrive slightly later. © *2002 Acoustical Society of America.* [DOI: 10.1121/1.1512292]

PACS numbers: 43.20.Mv [DEC]

I. INTRODUCTION

The work presented here is motivated by the goal of developing techniques for inspecting plate structures using ultrasonic Lamb waves. Many engineering structures are composed of large areas of flat or curved plates, including, for example, oil and chemical storage tanks, pressure vessels and pipelines. The routine inspection (NDE) of these large areas to detect cracking or corrosion is very time consuming and thus expensive because conventional techniques require a test instrument to scan point by point in two dimensions over the whole area. An alternative for rapid inspection is to use ultrasonic Lamb waves which propagate along the plate and may be reflected by any defects. Each propagation of a wave can, with a suitable configuration, inspect all positions along a line; thus the time to inspect the plate can be reduced substantially.

The potential for exploiting Lamb waves for the NDE of plate structures has long been recognized[1,2] and has been discussed by many authors, for example.[3–12] A key and popular area of these investigations has been the reflection and mode conversion of the Lamb modes when they are incident at a defect such as a crack or a notch: strong interactions are clearly essential to the detection and location of the defects, and mode conversions can provide useful information about the nature of the defects. These studies normally assume a two-dimensional plane strain domain, representing a section through the plate and the defect, both of which are thus infinite in the direction normal to the plane.

Clearly this is only realistic in cases where the defect width is large compared to the width of the wave beam, but the approach is nevertheless very useful for understanding the phenomena.

In practical implementations, interestingly, the focus to date has been much more on linear waveguide structures such as pipes or solid cylindrical bars,[13–19] despite the greater complexity of their wave properties. The reason for this is that the configuration for the inspection of these structures only requires transmission along the line of the waveguide. On the other hand, the inspection of the whole area of a plate requires the propagation of multiple Lamb wave signals in order to achieve full coverage. This is not straightforward, particularly when one considers the problems of unwanted reflections from edges or other structural features. Nevertheless, some recent and ongoing work[20] is aimed at developing a technique in which the whole area of a plate may be inspected from a single transducer location.

The work presented in this paper is motivated by the developments of the techniques for Lamb wave area inspection. Specifically, it is important to extend the knowledge of the interaction of the Lamb waves with defects from the two-dimensional plane strain studies to cases in which the defect is realistically represented as a three-dimensional shape at some location in a plate. Knowledge of this will be essential in order for the area scanning approach to be exploited reliably. This work is an initial study, taking a defect with the simplest geometry of a through-thickness hole; it is anticipated that later studies will increase the complexity to address more realistic defects such as part-depth holes rep-

---

[a)]Electronic mail: m.lowe@ic.ac.uk
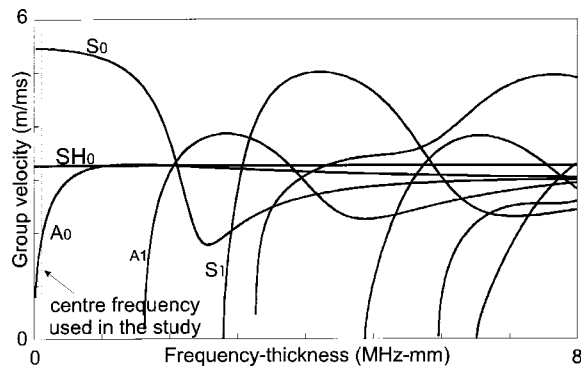
FIG. 1. Group velocity dispersion curves for Lamb waves in a steel plate.

FIG. 2. Mode shapes of the S_0 mode in a steel plate at 100 kHz-mm; (a)displacements and (b) stresses.

resenting corrosion loss. The diameters of the hole relative to the wavelength in this study are representative of the dimensions being considered in the developments reported by Wilcox et al.[20]

Two predictive studies are reported here. The first uses a Finite Element time domain model to simulate the interaction of an incident plane S_0 Lamb wave with a circular hole. The S_0 wave which is reflected straight back from the hole, and the SH_0 wave which is scattered at 90 degrees to the incident direction, are both monitored, and these are used to predict the reflection and scattering functions for a range of hole sizes, frequencies and monitoring distances from the hole. The second approach uses an analytical model to predict the same quantities. This model, whose derivation is described in some detail, is based on mode superposition. Finally a third set of results consists of a limited number of experimental measurements, using a set-up which approximates that of the predictions sufficiently well to validate the trends of the findings.

II. MODE CHARACTERISTICS AND FREQUENCY RANGE OF INTEREST

Dispersion curves for the well-known Lamb waves in a steel plate are shown in Fig. 1. These dispersion curves were calculated using the predictive model Disperse.[21,22] The group velocity curves indicate the speed of propagation of a wave packet and are therefore the curves of particular interest for long range propagation for NDE applications. Since the frequency axis may also be scaled with thickness, the scale is plotted as frequency–thickness for generality.

The low-frequency mode S_0 is attractive for NDE because it has low dispersion (the velocity is approximately constant for low frequencies), it has a high group velocity, it is equally sensitive to defects at any depth in the plate and, if the plate is immersed in a fluid medium, the attenuation due to leakage is very small. This is because its displacements and stresses are dominated by the in-plane components. Ideally for long-range NDE, this mode is best exploited at the lowest possible frequency, in order to avoid dispersion. However resolution requirements normally force the frequency of choice upwards, so that a compromise is required, and indeed an optimum can be identified logically.[23] Furthermore, another consideration is that increasing the frequency may also increase the sensitivity to defects.[12] A sensible upper limit to this increase is about 1.6 MHz-mm, in order to avoid
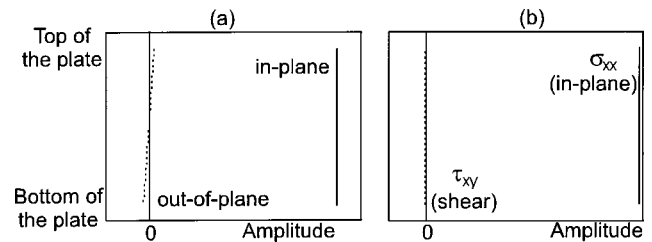
the A_1 cut-off frequency. In fact the work presented here is limited to the very low end of the range, that is below about 500 kHz-mm, where the S_0 mode is essentially nondispersive.

Figure 2 shows stress and displacement mode shapes of the S_0 mode through the plate at 100 kHz-mm. We use here the co-ordinate directions y to denote the normal to the surface of the plate, z to denote the normal to the plane of plane strain, and x to denote the direction of propagation of the wave; displacements and stresses are u and σ, respectively. It can be seen here that the mode shapes of this mode at low frequency are extremely simple. This will enable a very simple Finite Element to be employed for the modeling.

Within the same frequency range, SH_0 and A_0 can also be present. The SH_0 wave is the fundamental symmetric wave of the family of waves whose particle motion is parallel to the plate surfaces and normal to the direction of propagation. The A_0 wave has stress and displacement fields which are simple too, but these are antisymmetric with respect to the mid-plane of the plate, and it displays the characteristics of flexural behavior. Since these two waves may exist within the frequency range of interest, it is possible in principle for both of them to be excited by mode conversion when an S_0 wave is incident at a defect.

III. PROCEDURE FOR FINITE ELEMENT SIMULATION

A. Discretization

The case which was chosen for the study is sufficiently simple that it can be modeled using a two-dimensional spatial discretization. An examination of Fig. 2 shows that the behavior of the S_0 mode at low frequency is essentially that which is described by simple membrane theory. The propagation of this wave in a plate can therefore be modeled using membrane Finite Elements, the elements lying along the neutral axis of the plate. Such an approach has similarly been used by the authors to model the $L(0,2)$ mode in pipes.[18] Clearly the through-thickness hole can be introduced in such a model, although it should be noted that future development of this work to part-depth holes will later require a genuinely three-dimensional discretization. The membrane elements can also correctly represent the propagation of the SH_0 wave and so mode conversion between the incident S_0 wave and scattered SH_0 waves can be predicted.

There are two limitations of the membrane model, but fortunately neither invalidates this particular study. The first is that it cannot represent the propagation of the S_0 mode at higher frequency, that is in its dispersive region; therefore at

FIG. 3. (a) Schematic illustration of Finite Element spatial discretization for the plate and (b) mesh details around the hole.

$$\delta t \leq 0.8 \frac{\Delta x}{c}, \qquad (2)$$

where c is the velocity of the wave.

B. Simulations

The plate which was modeled was 600 mm wide and 1200 mm long. Since the membrane element models waves which are perfectly nondispersive, the thickness of the elements has no effect on the predictions and so was set arbitrarily. A circular hole was introduced by removing elements from the mesh, as discussed above, and illustrated in Fig. 3. The dimensions of the plate were chosen to be large enough to avoid the unwanted edge reflections and also to be able to separate in time the reflected signals from the input signals. The length of each element was chosen to be 3 mm, the spatial criterion of Eq. (1) being controlled in this case by the SH_0 mode which has the shortest wavelength. Thus, approximately 10 elements were present per wavelength of SH_0 at 100 kHz. Symmetry was assumed along the x axis through the center of the hole, so that only one half of the plate had to be modeled (Fig. 3). The model was repeated for different sizes of hole, its diameter varying between 1 and 3 wavelengths of S_0 at 100 kHz (one wavelength is approximately 55 mm).

The S_0 mode was excited by prescribing nodal displacements in the x direction along the whole edge of the plate, as shown in the figure. The input signal consisted of a five-cycle narrow band tone burst, defined by a sine wave modulated by a Hanning window function. The frequency of the tone was 100 kHz. The propagation of the plane wave across the plate was then simulated by the time marching algorithm.

Following the interaction of the S_0 wave with the circular hole, the scattered S_0 and SH_0 waves were received by monitoring the displacements at two series of nodes shown in the figure. The first series of points was along the axis of symmetry (defined by $y=0$), in order to extract only the S_0 wave which was reflected from the hole. The displacements in the x direction were monitored here, so that the time trace showed the input S_0 signal on its way to the hole, then the reflected S_0 signal returning. Due to the symmetry, there cannot be any SH_0 wave on this axis, so it was never present in these received signals. The second series of points was along a line 90° to the hole, and once again the displacements in the x direction were monitored here. The purpose of these monitoring points was to detect the SH_0 wave which was scattered in this direction. Thus the time traces at these points showed the incident S_0 plane wave passing through, then the scattered SH_0 wave. In general an S_0 wave is also scattered in this direction but this was not received because it has negligible displacements in the x direction.

IV. ANALYTICAL MODEL

In this section an analytical model, suitable for full three-dimensional predictions, is described. Thus this approach should apply not only for the low-frequency range which is of concern in this paper, but also for higher frequen-

all frequencies the wave propagates at the velocity which it has at zero frequency. The second is that it cannot represent the propagation of the A_0 mode. However the A_0 mode is never excited when the S_0 wave arrives at the hole, the reason being that all of the features of the geometry and of the incident wave are symmetric.

The Finite Element modeling was performed using the program FINEL which was developed at Imperial College.[24] The membrane elements which were used were four-noded quadrilaterals with 2 degrees of freedom (x, y displacements) at each node, so the solution was performed in the two-dimensional xy plane. Figure 3 illustrates the spatial domain, including detail of the mesh around the hole. An interesting issue worth mentioning here is how best to design the mesh around the hole. A smooth surface around the hole is most easily defined by designing the whole mesh in a radial form, rather like a spider's web. Another alternative is to introduce different shapes of elements in the locality of the hole, including triangular elements at the edge. However the authors' experience has shown that the most satisfactory behavior is obtained by maintaining identical element sizes and shapes throughout the model, since variations in the mesh can cause beam steering and some scattering, even when the mesh is very fine. The rather crude approach of simply omitting elements which is illustrated in the figure is therefore believed to be the best choice.

The spatial discretization was chosen to be certain of satisfying the rule

$$\lambda_{min} \geq 7 \, \Delta x, \qquad (1)$$

where λ_{min} is the shortest wavelength, within the bandwidth of the signal, of any waves which may travel in the structure, and Δx is the biggest dimension across any single element in the model. This rule has been found by the authors to be effective for ensuring accurate modeling.[18]

The program uses a diagonal mass matrix, allowing an efficient explicit time marching algorithm to be exploited. The explicit algorithm is stable provided that the time step is short enough to meet the convergence criterion:[25]

FIG. 4. Geometry of the analytical problem with: (a) a side view and (b) a top view.

cies. Furthermore, it is well configured for further development to the more advanced problems involving part-depth holes.

Analytical approaches for scattering problems in plates are quite rare. Plate theory approaches have been employed by for example McKeon and Hinders[26] to study the scattering of Lamb waves by a through hole in a plate using Kane–Mindlin higher order plate theory. Scattering of flexural waves by circular holes have been treated by Norris and Vemula using Kirchoff plate theory[27] and Mindlin theory.[28] A combined FE and mode expansion technique have been used by Chang and Mal[29] to investigate the scattering of Lamb waves by a circular hole, with or without edge cracks. In their paper the far-field is expanded in propagating Lamb modes and the region around the hole is modeled using FE.

A. Basic equations for Lamb waves

In this particular study the incoming field is defined, as discussed in the preceding section, to be a plane S_0 Lamb wave mode. However, in the general case this analytical model is applicable to other forms of incident field, such as fields that include several symmetric Lamb wave modes or Lamb waves which have been generated from a point source. The same principle would also apply for an anti-symmetric incoming field.

The geometry for the 3-D problem is given in Fig. 4. A co-ordinate system is attached to the middle of the hole and the xy-plane coincides with the mid-plane of the plate. Only time-harmonic conditions are considered, consequently the time-dependent factor $\exp(-i\omega t)$ is omitted from the equations. Here ω is the angular frequency and t is time. However, the scattering response to a pulse may still be simulated by the superposition of these monochromatic results for many frequencies; this will be treated later and examples will be given. Furthermore, since only symmetric incoming fields are considered, and since the scatterer is symmetric, the scattered field also consists solely of symmetric modes.

One way of expressing Lamb wave modes is via a potential function as shown in Achenbach and Xu.[30] In cylindrical co-ordinates, which is the most natural choice of co-ordinate system for the specific problem, Lamb wave modes can be expressed in the form

$$u_r^n = \frac{1}{k_n} V_n(z) \frac{\partial \phi}{\partial r}(r,\theta), \tag{3}$$

$$u_\theta^n = \frac{1}{k_n} V_n(z) \frac{1}{r} \frac{\partial \phi}{\partial \theta}(r,\theta), \tag{4}$$

$$u_z^n = W_n(z) \phi(r,\theta), \tag{5}$$

where the scalar potential function $\phi(r,\theta)$ satisfies Helmholtz equation, which in cylindrical co-ordinates reads as

$$\frac{\partial^2 \phi}{\partial r^2} + \frac{1}{r} \frac{\partial \phi}{\partial r} + \frac{1}{r^2} \frac{\partial^2 \phi}{\partial \theta^2} + k_n^2 \phi = 0. \tag{6}$$

For symmetric modes the wave numbers k_n are given as the roots of the Rayleigh–Lamb equation,

$$\frac{\tan(qh)}{\tan(ph)} = -\frac{4k^2 pq}{(q^2 - k^2)^2}, \tag{7}$$

where

$$q^2 = \frac{\omega^2}{c_T^2} - k^2, \quad p^2 = \frac{\omega^2}{c_L^2} - k^2. \tag{8}$$

The quantities c_T and c_L are the velocities of shear waves and longitudinal waves, respectively. The functions $V_n(z)$ and $W_n(z)$ in Eqs. (3), (4), (5) give the variation in the thickness co-ordinate and the expressions for these functions can be found in Appendix A. They are obtained from the stress-free boundary conditions of the plate surfaces.

The reflected field that is created when the incoming field hits the hole consists of Lamb wave modes and also of SH modes. The SH modes can be expressed in a similar way to the Lamb modes with the aid of a scalar potential function. Following the structure given in Achenbach and Xu,[30] SH modes can be represented in a cylindrical co-ordinate system by

$$u_r^n = \frac{1}{l_n} \cos\left(\frac{n\pi z}{2h}\right) \frac{1}{r} \frac{\partial \psi}{\partial \theta}(r,\theta), \tag{9}$$

$$u_\theta^n = -\frac{1}{l_n} \cos\left(\frac{n\pi z}{2h}\right) \frac{\partial \psi}{\partial r}(r,\theta), \tag{10}$$

$$u_z^n = 0, \tag{11}$$

where $\psi(r,\theta)$ is a solution of the Helmholtz equation,

$$\frac{\partial^2 \psi}{\partial r^2} + \frac{1}{r} \frac{\partial \psi}{\partial r} + \frac{1}{r^2} \frac{\partial^2 \psi}{\partial \theta^2} + l_n^2 \psi = 0. \tag{12}$$

The wave numbers and the mode shapes are less complicated for SH modes compared to the Lamb modes and for symmetric SH modes they are given by

$$l_n^2 = (\omega/c_T)^2 - (n\pi/2h)^2, \quad n = 0,2,4,\ldots, \tag{13}$$

$$U_n(z) = \cos\left(\frac{n\pi z}{2h}\right), \quad n = 0,2,4,\ldots. \tag{14}$$

Naturally, this wave field satisfies the condition that the surfaces of the plate are stress-free.

B. Field expansions

In order to find expressions for the different parts of the wave field, solutions of the scalar potentials have to be

found. The scalar potential $\phi(r,\theta)$, which determines the Lamb modes, satisfies Eq. (6), and a solution to this equation can be given as

$$\phi(r,\theta) = \Phi(r)e^{im\theta}, \tag{15}$$

where $\Phi(r)$ is a solution of Bessel's differential equation,

$$\frac{d^2\Phi}{dr^2} + \frac{1}{r}\frac{d\Phi}{dr} + \left(k_n^2 - \frac{m^2}{r^2}\right)\Phi = 0. \tag{16}$$

Then, using Hooke's law and Eqs. (3), (4), (5), some of the stress components for a single Lamb mode can be written as

$$\sigma_{rr}^{mn} = \left[\Sigma_{rr}^n(z)\Phi_m(k_nr) - \tilde{\Sigma}_{rr}^n(z)\left(\frac{1}{r}\Phi_m'(k_nr) \right.\right. \\ \left.\left. - \frac{m^2}{k_nr^2}\Phi_m(k_nr)\right)\right]e^{im\theta}, \tag{17}$$

$$\sigma_{r\theta}^{mn} = im\Sigma_{r\theta}^n(z)\left[\frac{1}{r}\Phi_m'(k_nr) - \frac{1}{k_nr^2}\Phi_m(k_nr)\right]e^{im\theta}, \tag{18}$$

$$\sigma_{rz}^{mn} = -\Sigma_{rz}^n(z)\Phi_m'(k_nr)e^{im\theta}, \tag{19}$$

where the z-dependent functions Σ_{ij}^n are given in Appendix A. These are the most significant stress components in this problem, since they enter the boundary conditions at a later stage.

The scalar potential for the SH modes, $\psi(r,\theta)$, satisfies the Helmholtz equation and, similarly to the Lamb wave potential, a solution to Eq. (12) can be written as

$$\psi(r,\theta) = \Psi(r)e^{im\theta}, \tag{20}$$

where $\Psi(r)$ is a solution of

$$\frac{d^2\Psi}{dr^2} + \frac{1}{r}\frac{d\Psi}{dr} + \left(l_n^2 - \frac{m^2}{r^2}\right)\Psi = 0. \tag{21}$$

Then, the relevant stresses for a single SH mode can be given as

$$\sigma_{rr}^{mn} = im\mu\cos\left(\frac{n\pi z}{2h}\right)\left[\frac{2}{r}\Psi_m'(l_nr) - \frac{2}{l_nr^2}\Psi_m(l_nr)\right]e^{im\theta}, \tag{22}$$

$$\sigma_{r\theta}^{mn} = \mu\cos\left(\frac{n\pi z}{2h}\right)\left[\frac{2}{r}\Psi_m'(l_nr) + \left(l_n - \frac{2m^2}{l_nr^2}\right)\Psi_m(l_nr)\right]e^{im\theta}, \tag{23}$$

$$\sigma_{rz}^{mn} = -im\mu\frac{n\pi}{2h}\sin\left(\frac{n\pi z}{2h}\right)\frac{1}{l_nr}\Psi_m(l_nr)e^{im\theta}. \tag{24}$$

Next, general expressions for the incoming and the reflected fields have to be found in cylindrical co-ordinates. The incoming field is given by a plane S_0 Lamb wave and the solution for the scalar potential that corresponds to this wave is

$$\phi^{\mathrm{inc}} = e^{ik_0x} = e^{ik_0r\cos\theta} = \sum_{m=-\infty}^{\infty} i^m J_m(k_0r)e^{im\theta}. \tag{25}$$

Here k_0 is the wave number for the S_0 mode and $J_m(\cdot)$ are Bessel functions of the first kind. Using this expression in Eqs. (3)–(5) gives the displacement components in cylindrical co-ordinates for the incoming field,

$$u_r^{\mathrm{inc}} = \sum_{m=-\infty}^{\infty} i^m V_0(z)J_m'(k_nr)e^{im\theta}, \tag{26}$$

$$u_\theta^{\mathrm{inc}} = \sum_{m=-\infty}^{\infty} mi^{m+1}V_0(z)\frac{J_m(k_nr)}{k_nr}e^{im\theta}, \tag{27}$$

$$u_z^{\mathrm{inc}} = \sum_{m=-\infty}^{\infty} i^m W_0(z)J_m(k_0r)e^{im\theta}. \tag{28}$$

In order to find wave expansions for the reflected field, suitable solutions of Eqs. (6) and (12) which correspond to outgoing waves have to be found. Thus, the scalar potential of an outgoing Lamb wave mode with general angle dependence is

$$\phi_{mn}(r,\theta) = H_m(k_nr)e^{im\theta}, \tag{29}$$

and for an outgoing SH mode the scalar potential is

$$\psi_{mn}(r,\theta) = H_m(l_nr)e^{im\theta}, \tag{30}$$

where $H_m(\cdot)$ are Hankel functions of the first kind. This choice of function automatically satisfies the required description of an external boundary at infinity, to which the radiating outgoing waves propagate.

For a fixed frequency, Eq. (7) has a finite number of real roots which correspond to the propagating modes and an infinite number of imaginary and complex roots. In the wave expansions for the reflected field, all real wave numbers that correspond to propagating, outgoing modes are included. Furthermore, the imaginary and complex wave numbers that correspond to evanescent modes are included. The same reasoning applies for SH modes as well, consequently their propagating and evanescent modes are included. Thus, the reflected field can be written as a sum of both propagating and nonpropagating modes. Using the expressions for the scalar potentials in Eqs. (29) and (30), and also Eqs. (3)–(5), the displacement components for the reflected field are given as

$$u_r^{\mathrm{scat}} = \sum_{n=0}^{\infty}\sum_{m=-\infty}^{\infty} A_{mn}V_n(z)H_m'(k_nr)e^{im\theta} \\ + \sum_{n=0,2,\ldots}^{\infty}\sum_{m=-\infty}^{\infty} imB_{mn}\cos\left(\frac{n\pi z}{2h}\right)\frac{H_m(l_nr)}{l_nr}e^{im\theta}, \tag{31}$$

$$u_\theta^{\mathrm{scat}} = \sum_{n=0}^{\infty}\sum_{m=-\infty}^{\infty} imA_{mn}V_n(z)\frac{H_m(k_nr)}{k_nr}e^{im\theta} \\ - \sum_{n=0,2,\ldots}^{\infty}\sum_{m=-\infty}^{\infty} B_{mn}\cos\left(\frac{n\pi z}{2h}\right)\frac{H_m'(l_nr)}{l_nr}e^{im\theta}, \tag{32}$$

$$u_z^{\mathrm{scat}} = \sum_{n=0}^{\infty}\sum_{m=-\infty}^{\infty} A_{mn}W_n(z)H_m(k_nr)e^{im\theta}. \tag{33}$$

The expansion coefficients A_{mn} and B_{mn}, which are connected to the reflected Lamb modes and the SH modes, respectively, have to be calculated in order to find the total field in the plate.

The expansions for the stresses for the incoming field, needed for the boundary conditions, can be written as

$$\sigma_{rr}^{inc} = \sum_{m=-\infty}^{\infty} i^m \left[\Sigma_{rr}^0(z) J_m(k_0 r) - \tilde{\Sigma}_{rr}^0(z) \right.$$
$$\left. \times \left(\frac{1}{r} J_m'(k_0 r) - \frac{m^2}{k_0 r^2} J_m(k_0 r) \right) \right] e^{im\theta}, \quad (34)$$

$$\sigma_{r\theta}^{inc} = \sum_{m=-\infty}^{\infty} i^{m+1} m \Sigma_{r\theta}^0(z)$$
$$\times \left[\frac{1}{r} J_m'(k_0 r) - \frac{1}{k_0 r^2} J_m(k_0 r) \right] e^{im\theta}, \quad (35)$$

$$\sigma_{rz}^{inc} = - \sum_{m=-\infty}^{\infty} \Sigma_{rz}^0(z) J_m(k_0 r) e^{im\theta}. \quad (36)$$

The relevant stresses for the scattered field are given as

$$\sigma_{rr}^{scat} = \sum_{n=0}^{\infty} \sum_{m=-\infty}^{\infty} A_{mn} \left[\Sigma_{rr}^n(z) H_m(k_n r) - \tilde{\Sigma}_{rr}^n(z) \right.$$
$$\left. \times \left(\frac{1}{r} H_m'(k_n r) - \frac{m^2}{k_n r^2} H_m(k_n r) \right) \right] e^{im\theta}$$
$$+ \sum_{n=0,2,\ldots} \sum_{m=-\infty}^{\infty} im B_{mn} \mu \cos\left(\frac{n\pi z}{2h} \right)$$
$$\times \left[\frac{2}{r} H_m'(l_n r) - \frac{2}{l_n r^2} H_m(l_n r) \right] e^{im\theta}, \quad (37)$$

$$\sigma_{r\theta}^{scat} = \sum_{n=0}^{\infty} \sum_{m=-\infty}^{\infty} im A_{mn} \Sigma_{r\theta}^n(z)$$
$$\times \left[\frac{1}{r} H_m'(k_n r) - \frac{1}{k_n r^2} H_m(k_n r) \right] e^{im\theta}$$
$$+ \sum_{n=0,2,\ldots} \sum_{m=-\infty}^{\infty} B_{mn} \mu \cos\left(\frac{n\pi z}{2h} \right)$$
$$\times \left[\frac{2}{r} H_m'(l_n r) + \left(l_n - \frac{2m^2}{l_n r^2} \right) H_m(l_n r) \right] e^{im\theta}, \quad (38)$$

$$\sigma_{rz}^{scat} = - \sum_{n=0}^{\infty} \sum_{m=-\infty}^{\infty} A_{mn} \Sigma_{rz}^n(z) H_m'(k_n r) e^{im\theta}$$
$$- \sum_{n=2,4,\ldots} \sum_{m=-\infty}^{\infty} im B_{mn} \mu \frac{n\pi}{2h} \sin\left(\frac{n\pi z}{2h} \right) \frac{1}{l_n r}$$
$$\times H_m(l_n r) e^{im\theta}. \quad (39)$$

The total stress distribution in the plate is given by the sum of the incoming field and the scattered field, i.e., $\boldsymbol{\sigma} = \boldsymbol{\sigma}^{inc} + \boldsymbol{\sigma}^{scat}$. Next, the expressions for the stresses will be used to calculate the expansion coefficients for the scattered field by applying the boundary conditions.

C. Derivation of the expansion coefficients

The boundary conditions for the stress-free hole, expressed in cylindrical co-ordinates, are

$$\sigma_{rr} = \sigma_{r\theta} = \sigma_{rz} = 0, \quad r=a, \quad -h<z<h, \quad 0<\theta<2\pi. \quad (40)$$

To obtain a system of equations for the expansion coefficients of the scattered field, the boundary conditions (40) and the expressions for the stresses (34)–(36) and (37)–(39) are employed. The boundary conditions are projected onto some complete set of orthogonal functions in order to get rid of the dependence on the z and θ co-ordinates. The orthogonality of the θ-dependent functions, $f_m(\theta) = e^{im\theta}$, suggests that they are suitable as projection functions in the θ-direction. For the z-dependency there is no obvious choice of projection functions, at least not for the Lamb wave part. However, it is always possible to project onto any complete orthogonal set of functions.

Here the mode functions for the SH modes and their derivatives are used as projection functions in the z direction. Thus, the mode shapes, $\cos(n\pi z/2h)$, $n=0,2,\ldots,N$, which is a complete function space for even functions, are projected onto the even functions σ_{rr} and $\sigma_{r\theta}$. The derivatives of the SH mode shapes, $\sin(n\pi z/2h)$, $n=2,4,\ldots,N$, which is a complete function space for odd functions are projected onto the odd function σ_{rz}. Naturally, the infinite sums for the stresses have to be truncated so that only a finite number of the expansion coefficients are kept in the expansions. The sums are truncated at $|m|=M$ and $n=N$ (N even integer). Thus, when the boundary conditions, Eq. (40), are projected onto the functions

$$\frac{1}{2\pi\mu} \cos(n\pi z/2h) e^{im\theta},$$

$$n=0,2,\ldots,N, \quad m=-M,\ldots,M, \quad \text{for} \quad \sigma_{rr} \quad \text{and} \quad \sigma_{r\theta},$$
$$\frac{1}{2\pi\mu} \sin(n\pi z/2h) e^{im\theta}, \quad (41)$$

$$n=2,4,\ldots,N, \quad m=-M,\ldots,M, \quad \text{for} \quad \sigma_{rz},$$

a system of equations for the expansion coefficients is given according to

$$\sum_{n'=0}^{N} A_{mn'} \left[H_m(k_{n'} a) K_{n'n} - \left(\frac{1}{a} H_m'(k_{n'} a) \right. \right.$$
$$\left. \left. - \frac{m^2}{k_{n'} a^2} H_m(k_{n'} a) \right) L_{n'n} \right]$$
$$+ im B_{mn} \left[\frac{2}{a} H_m'(l_n a) - \frac{2}{l_n a^2} H_m(l_n a) \right] I_{nn}^S$$
$$= -i^m \left[J_m(k_0 a) K_{0n} - \left(\frac{1}{a} J_m'(k_0 a) \right. \right.$$
$$\left. \left. - \frac{m^2}{k_0 a^2} J_m(k_0 a) \right) L_{0n} \right], \quad n=0,2,\ldots,N, \quad (42)$$

$$im\sum_{n'=0}^{N}A_{mn'}\left[\frac{1}{a}H'_m(k_{n'}a)-\frac{1}{k_{n'}a^2}H_m(k_{n'}a)\right]L_{n'n}$$

$$+B_{mn}\left[\frac{2}{a}H'_m(l_na)+\left(l_n-\frac{2m^2}{l_na^2}\right)H_m(l_na)I^S_{nn}\right]$$

$$=-i^{m+1}m\left[\frac{1}{a}J'_m(k_0a)-\frac{1}{k_0a^2}J_m(k_0a)\right]L_{0n},$$

$$n=0,2,\ldots,N, \qquad (43)$$

$$-\sum_{n'=0}^{N}A_{mn'}H'_m(k_{n'}a)M_{n'n}-imB_{mn}\frac{n\pi}{2h}\frac{1}{l_na}H_m(l_na)I^A_{nn}$$

$$=i^mJ'_m(k_0a)M_{0n}, \qquad n=2,4,\ldots,N. \qquad (44)$$

This system of equations has to be solved for every m $=-M,\ldots,M$ to find the expansion coefficients A_{mn} and B_{mn}. Once the expansion coefficients have been calculated, the scattered field is determined. The coefficients $K_{n'n}$, $L_{n'n}$, $M_{n'n}$, I^S_{nn} and I^A_{nn} that appear in Eqs. (42)–(44) due to the projections are stated in Appendix B.

As explained earlier, this set of projection functions is just one possible choice. Any complete set of functions can be used, and the final result should not depend on the choice of these functions. However, this choice may affect the convergence rate of the solution.

D. Numerical considerations

In order to find the expansion coefficients for the reflected field, the system of equations given by Eqs. (42)–(44) with $(3N/2+2)$ unknowns has to be solved for every m $(m=-M,\ldots,M)$. However, due to symmetry considerations it is sufficient to only solve for the positive m-values. The choice of the truncation parameters (M and N) is dependent on the parameters of the specific problem, such as hole size and frequency. For example, more terms are needed in the expansions for higher frequencies. In the examples which will be given later the truncation parameters are $M=15$ and $N=4$.

Before the system of equations can be solved in order to find the expansion coefficients, the wave numbers for the symmetric Lamb modes have to be obtained, including those for the complex modes. The equation for these roots are given by Eq. (7). A simple Finite Element routine was used to provide good start guesses to a root finding algorithm.

To produce results in the time domain which can be compared with the corresponding results given by the Finite Element calculations, an inverse Fourier transform is employed,

$$u(t)=\int u(\omega)F(\omega)e^{-i\omega t}d\omega. \qquad (45)$$

Here $F(\omega)$ is the frequency spectrum, in this case given by a Hanning window. In order to have almost identical input signals the frequency spectrum $F(\omega)$ which was used came from a FFT of the input signal in the Finite Element model.

The displacements in all of the examples given below are calculated at the mid-plane of the plate ($z=0$). However,
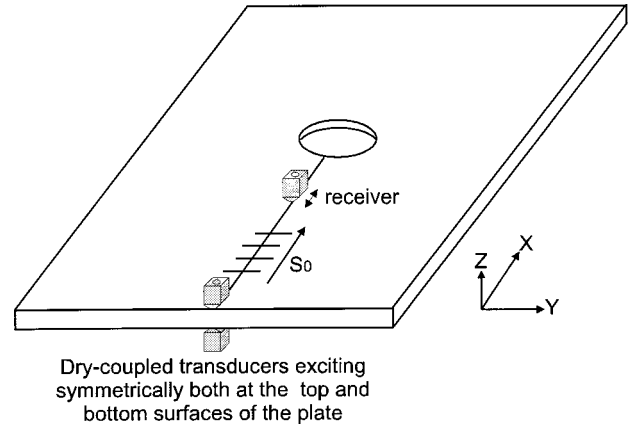
FIG. 5. Experimental set-up.

as discussed earlier, the displacements of the S_0 and SH_0 modes are more or less uniform through the plate thickness.

V. EXPERIMENTAL PROCEDURE

An experimental program was conducted in order to provide some practical validation of the findings of Finite Element and analytical modeling work. It is clearly a very difficult task to generate a plane S_0 wave across a significant width of a plate and so this was not attempted. Instead the S_0 Lamb wave was generated at a single location, approximating a point source, at a significant distance from the hole. Thus the experimental configuration was not precisely that which was modeled. Nevertheless, it is believed that this approximate approach was useful and sufficiently accurate to validate the trends and magnitudes of the cases which were predicted.

Six 1200 mm$\times$1200 mm$\times$1 mm thick steel plates, each with a through-thickness circular hole in the middle, were used for the experiments. The plates and experimental set-up are illustrated in Fig. 5. The diameters of the holes varied between approximately 1 wavelength and 2.5 wavelengths of the S_0 wave at 100 kHz center frequency (between 60 mm and 132 mm). The S_0 wave, generated using a Wavemaker (Macro Design Ltd., UK) instrument, was excited at one end of the plate by a 5-cycle 100 kHz tone burst modified by a Hanning window.

Although the S_0 mode is the simplest of the Lamb waves, and is nondispersive at low frequencies, it is actually very tricky to work with experimentally. A classic excitation method consists of creating perturbations on the surface of the plate. Typically, stresses can be induced at the surface of the plate by an ultrasonic transducer sending waves through a coupling medium such as water between it and the plate. By setting a specific angle of the incident wave with respect to the plate, a selected Lamb mode can be excited. However, S_0 at low frequency has very little out-of-plane displacement and so it is not easily excited, whereas A_0 is very readily excited. Therefore, even when the angle of the incident wave is set to excite the S_0 mode, it only excites it weakly, and at the same time the spatial bandwidth of the excitation field is such that some unwanted A_0 is also excited. Consequently it was decided to make use of dry contact transducers[31] both to
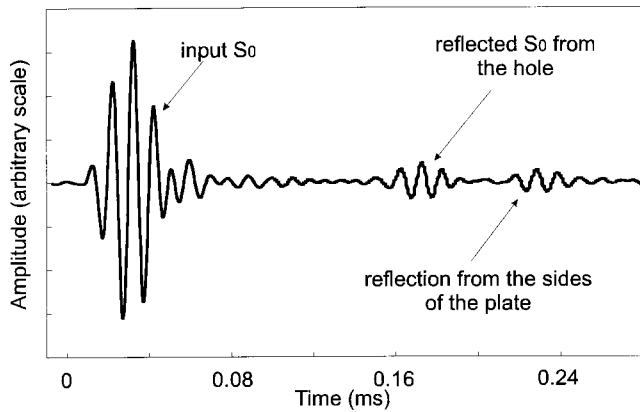
FIG. 6. Example of a measured time signal at 390 mm away from the edge of the hole; the hole is 108 mm in diameter.

FIG. 7. A comparison between typical Finite Element (solid line) and analytical (dashed line) time traces of direct S_0 reflection for a hole 120 mm in diameter and monitored at 390 mm from the edge of the hole.

excite the S_0 wave and to receive the reflected and scattered signals. These piezoelectric transducers impose a shear stress in the region of contact, therefore preferentially exciting modes with significant in-plane displacements at the surface of the plate.

These transducers are small (approximately 14 mm long) compared to the wavelengths used in this study, and so can be considered here to be point sources. In fact, although they preferentially excite the S_0 and SH_0 modes, they do excite some of the A_0 mode, so care is still needed in order to make use of them. The S_0 mode and the A_0 modes are excited along one axis (both backwards and forwards) and the SH_0 mode is excited in the perpendicular axis. Differentiation of the S_0 and A_0 modes may most easily be achieved by choosing sufficiently long propagation distances that their signals separate. A further step to minimize the excitation of A_0 is to use a pair of transducers working in parallel on opposite sides of the plate, as shown in the figure. With this set-up, any remnant A_0 can be the result only of an imbalance of the pair of transducers. The SH_0 mode is more easily separated by selection of the orientation of the transducer. Of course these arguments apply equally to the use of the transducers for excitation or reception.

Along the line of primary interest, corresponding to the axis of symmetry in the Finite Element model, and shown in the illustration in Fig. 5, there is no scattered SH_0 mode, so the measurements here contain only S_0 and any remnant A_0. These can easily be separated in time in a plate of this size and so it was possible to record reliably just the S_0 reflection. Figure 6 shows a typical measured time history at a location on this axis and 390 mm from the hole. This shows the incident S_0 mode on its way to the hole, which was in this case 108 mm in diameter, and the S_0 reflection from the hole. To calculate the reflection coefficient in the frequency domain, the frequency spectrum of the reflected S_0 signal was divided by that of the incident S_0 signal, yielding a reflection coefficient as a function of the frequency within the bandwidth of the windowed toneburst. In some cases reflection coefficients were also calculated using time domain values. This was done by calculating the envelope of the time signal, by taking the Hilbert transform, then simply dividing the value of the reflection peak by that of the incident peak.
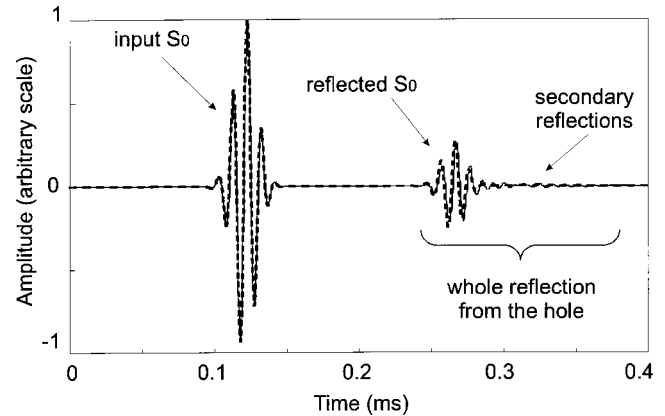
Given that the signal has rather a narrow frequency band, such an approach gives a reasonable estimate of the reflection coefficient for the center frequency.

There is negligible attenuation due to damping in a steel plate at this frequency. However there is an attenuation due to beam spreading, and indeed this will be discussed later when examining the detail of the predictions. The beam spreading attenuation in the experiments was estimated by observing the reduction in the measured reflected signal as a receiver was moved away from an edge of the plate, and assuming the decay to be a logarithmic function. This gave an attenuation of 8.2 dB/m. This figure was used to compensate the experimental measurements for a comparison with the predictions. Essentially the compensation required the received signal to be compared with the amplitude of the incident signal when it arrived at the hole, rather than when it passed the receiver on its way to the hole.

VI. RESULTS AND DISCUSSION

We present and compare here the results of the Finite Element, analytical and experimental studies. We consider first the direct reflection of the S_0 wave from the hole, then the SH_0 wave, which is scattered at 90° from the hole, and then finally we present the variation of the wave fields with angular position around the hole.

A. S_0 direct reflection from the hole

Figure 7 shows a comparison between a typical time history predicted by the analytical model with that predicted by the Finite Element simulation. The signal is monitored at a location which is 390 mm from the edge of a hole, and the hole is 114 mm in diameter. Excellent agreement is found between the two curves. The figure also shows a clean separation of the signals, so allowing reliable extraction of the incident and reflected parts for the calculation of the reflection coefficient functions.

The reflection coefficient was initially calculated using the frequency domain technique, that is, by dividing the frequency spectra of the reflected part of the signal by that of the incident part. The curve thus obtained displays amplitude (reflection coefficient) against frequency. A convenient way

Diligent *et al.*: Scattering of Lamb waves from a hole

FIG. 8. The predicted variation of S_0 reflection coefficients 390 mm away from the hole with the hole diameter normalized to the wavelength; a comparison between experimental (circle), Finite Element (filled square) and analytical (solid line) results.

FIG. 9. The Hilbert envelope of the signal from the Finite Element results in Fig. 7.

to present the results for different hole diameters is to normalize them to the wavelength of the incident mode. This has been done in Fig. 8 using results from the analytical predictions, the Finite Element predictions and the experimental measurements, and in each case for the center frequency of 100 kHz. Very good agreement of the trend is obtained in all three sets of results, and it is particularly noteworthy how well the experimental points agree with the predicted points.

However there are some differences in detail between the two sets of predictions. It is believed that the principal reason for the differences is in the Finite Element discretization around the hole. Since the surface of the hole is not smooth, but composed of a series of steps, the propagation of waves around the hole (these will be discussed shortly) is significantly affected by the detail of the mesh.[32] This was confirmed by repeating one of the cases with different discretizations of the same hole: the outcome was that there were indeed some variations of the results which were of the appropriate magnitude. On the other hand, a refined mesh, yet which retained the identical step profile of the hole, gave identical results, confirming that the mesh itself was sufficiently fine for the correct propagation of the waves. This issue could, in principle, be pursued using significantly refined meshes, but it was decided not to pursue this. The computation effort for these calculations is already large, and in any case this focus would go beyond the needs of the practical application which motivates the study.

The upward trend of the reflection function is as expected, but it also exhibits undulations which need some explanation. Additionally, it will be important to examine how this function would change for different receiver positions. We will examine each of these issues in turn, starting with the latter.

In order to see how the reflection function varies with the distance of the receiver from the hole, Finite Element
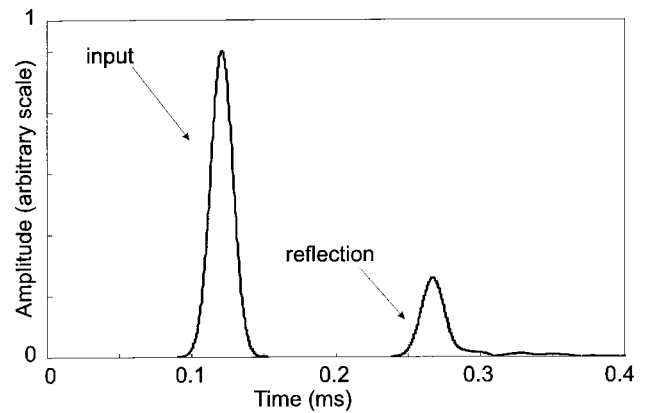
predictions of the reflection coefficient were made at a series of points along the axis. In each case the processing was performed using the time domain method which had the benefit of smoothing the undulations out of the signal, and so clarifying the comparisons for different distances. We will return to the basis of this smoothing later.

Figure 9 represents the Hilbert transform of the signal in Fig. 7. Following the explanation in Sec. V, the reflection coefficient was extracted from the figure by dividing the peak amplitude of the S_0 direct reflection by the maximum amplitude of the input S_0 wave. This was repeated for a range of distances from the hole and for three different sizes of hole. The results are presented in Fig. 10. As expected, the reflection coefficient increases with diameter and decreases with distance from the hole.

If the hole is assumed to act as a cylindrical emitter of the reflected waves, then it is possible to fit a simple decay function to these curves to describe this beam spreading behavior. The ideal spreading function of cylindrical waves is that the amplitude in the far-field is inversely proportional to the square root of the propagation distance from the source, such that

$$A(\delta) = \frac{A_{\text{refl}}}{\sqrt{\delta + \delta_0}}, \tag{46}$$

where A_{refl} is a constant related to the amplitude of the wave, δ is the distance from the edge of the hole along the axis of propagation and δ_0 is the distance from the center of the beam spreading to the edge of the hole. As the center of the hole is also the center of the curvature, a logical choice for δ_0 is to set it equal to the radius of the hole. The constant A_{refl} was calculated by fitting this equation to values from the Finite Element results. Each curve required just a single value to calculate its A_{refl}, and in each case this was taken towards the near end of the distribution in Fig. 10. The approximation functions have been superposed on the Finite Element results in the figure, showing a very good fit.

An interesting correlation is observed if we re-plot the analytical solutions (the same as plotting the approximation function curves) using the axis of the distance normalized to the hole-diameter. Figure 11 shows that all the curves plotted in this way are almost overlaid. This means that, at a given

J. Acoust. Soc. Am., Vol. 112, No. 6, December 2002

Diligent *et al.*: Scattering of Lamb waves from a hole   2597
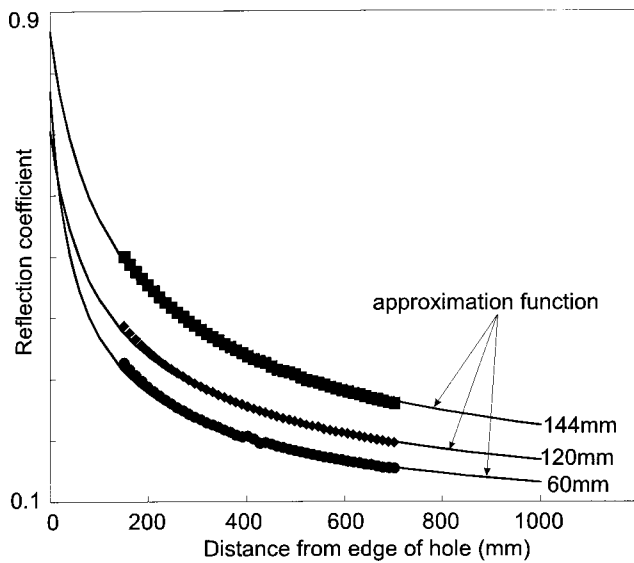
FIG. 10. Finite Element predictions (symbols) of the S_0 reflection coefficient plotted as a function of distance away from the edge of the hole, for three different diameters of the hole. Values are taken from the Hilbert envelope calculation. Lines show the approximation function which has been fitted to just one point for each hole.

FIG. 12. The reflection coefficient calculated using the whole reflection from the hole, showing the influence of the secondary reflections. An example for three different diameters: 60 mm (filled circle), 120 mm (filled diamond) and 144 mm (filled square).

distance from the hole measured in multiple diameters, all reflection coefficients at a given frequency are the same, whatever the hole size. For example, if the hole diameter is 30 mm, the reflection at 180 mm (6 diameters) away from that hole will be the same as that from a 60 mm diameter hole monitored at 360 mm. Also shown in this plot is that some curves are shorter than others. This comes from the fact that all the data were calculated for the same distance path away from the hole but different cases were normalized to different hole diameters.

Returning to the issue of the undulations, the underlying phenomenon can be shown to be the interference of the signal which is reflected directly from the near side of the hole with a second signal which arrives slightly later. The second signal is much smaller than the direct reflection, but never-

theless has an influence on the overall result. The second signal can just be seen following the direct reflection in Fig. 7, where it is labeled "secondary reflections." Sources of secondary reflections include reflected SH_0 waves, which are slower than the S_0 wave, and "creeping waves," which travel around the circumference of the hole, re-radiating time-delayed signals. SH_0 waves are present directly on the axis, but only with a radial component that decays quickly with the distance [Eq. (31)]. Creeping waves have been studied quite extensively, albeit usually in plane strain, for example, by Nagy et al.[33,34]

The secondary waves were neglected when the peak of the Hilbert transform of the direct reflection was used to construct Figs. 10 and 11, resulting in smooth distributions. However, they can be taken into account by dividing the spectra of the whole reflected wave signal by the spectra of the incident S_0 wave, using the frequency domain approach. This was done for three diameters of hole, and in each case the reflection coefficient was measured at the center frequency (100 kHz) for several points away from the edge of the hole. The results of this processing are shown in Fig. 12, exhibiting the undulations which are characteristic of the interference phenomenon. In this plot the undulations are believed to result mainly from the reflected SH_0 waves, because their amplitudes decrease with distance from the hole.

B. SH_0 reflected at 90 degrees from the hole

A very similar study was performed on the SH_0 mode which is scattered at 90 degrees from the hole. The direction of the scattering and location of the monitoring points is indicated in Fig. 3.

Figure 13 shows typical time domain predictions from the Finite Element and analytical models, and once again there is very close agreement. The predictions were made at 390 mm from the edge of the hole. The Finite Element reflection coefficients were calculated from these signals using

FIG. 11. Analytical amplitudes plotted as a distance normalized to the hole diameter.
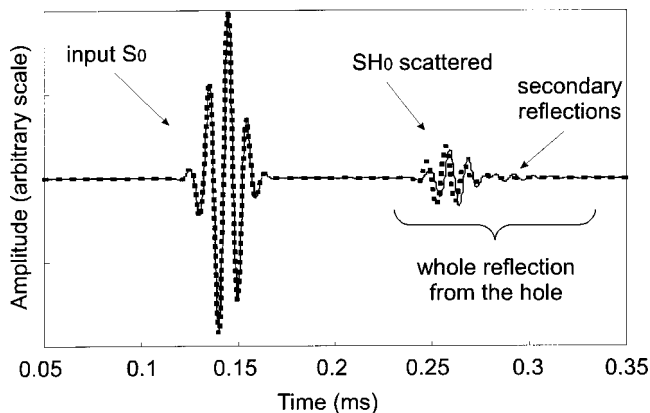
FIG. 13. A comparison between typical Finite Element (solid line) and analytical (dashed line) time traces of direct SH_0 reflection for a hole 120 mm in diameter and monitored at 234 mm from the edge of the hole.
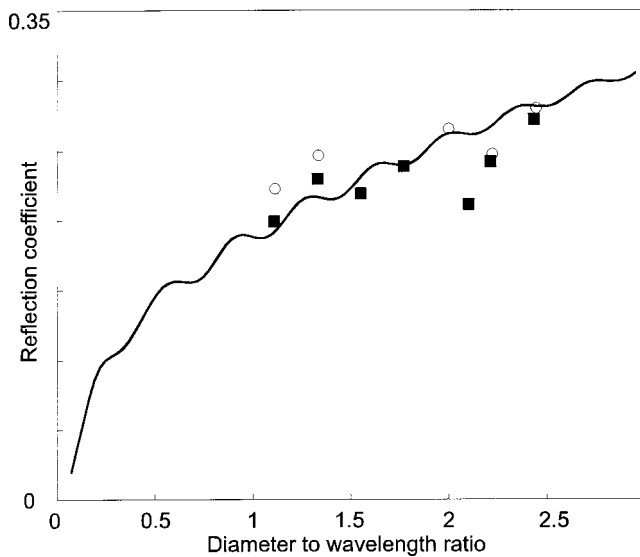

FIG. 14. Predicted variation of SH_0 reflection coefficients 390 mm away from the hole, with the hole diameter normalized to the wavelength; a comparison between analytical (solid line) and Finite Element (filled square) results at 100 kHz.

the frequency domain approach applied to the whole scattered wave signal, and extracting just the value at the center frequency of 100 kHz. The reflection coefficients are plotted against the ratio of hole diameter to wavelength in Fig. 14. Care should be taken in interpreting the reflection coefficient axis, since this relates modes of different types: this coefficient expresses the amplitude of the in-plane displacement of the scattered SH_0 wave divided by the amplitude of the in-plane displacement of the incident S_0 wave. Fairly good agreement is found between the Finite Element and the analytical results. As with the earlier work, the differences between the predictions are believed to result from the mesh details around the edge of the hole. Similarly, the undulations are expected to result from the secondary reflections, and indeed this is in evidence in the later part of the signal in Fig.

13. Experimental measurements were not obtained for this case because it proved not to be possible to avoid unwanted signals due to reflections from the edge of the plate and also the presence of the incident plane wave across the full width of the plate.

Figure 15 summarizes the results for the scattered SH_0 wave, following the sequence of analysis which was taken earlier for the reflected S_0 wave. It shows precisely the same features: (a) the amplitude of the scattered wave increases with the hole diameter and decreases with the distance from
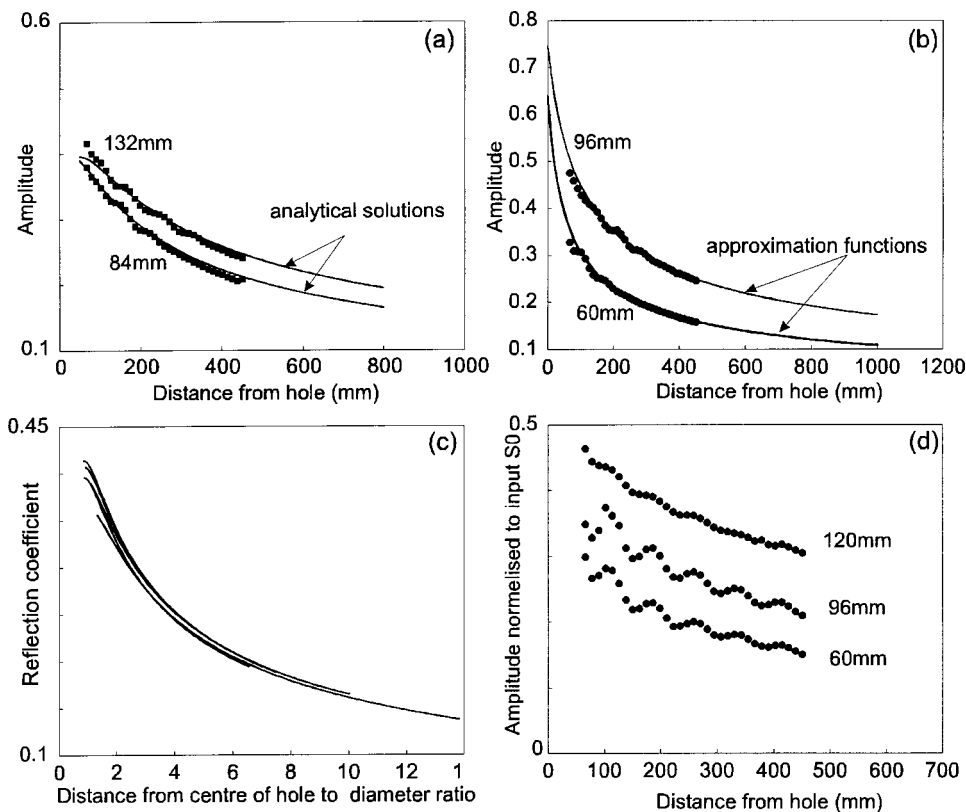
FIG. 15. (a) A comparison between analytical and Finite Element predictions for the SH_0 amplitude plotted as a function of distance away from the edge of the hole. Values are taken from the Hilbert envelope calculation. For clarity, results are plotted for only two diameters (84 mm and 132 mm); (b) a comparison between results from the S_0 specular reflection for the Finite Element and approximation function; (c) analytical results plotted as distance normalized to the hole diameter; and (d) the influence of the secondary reflections on the scattered SH_0 curves.
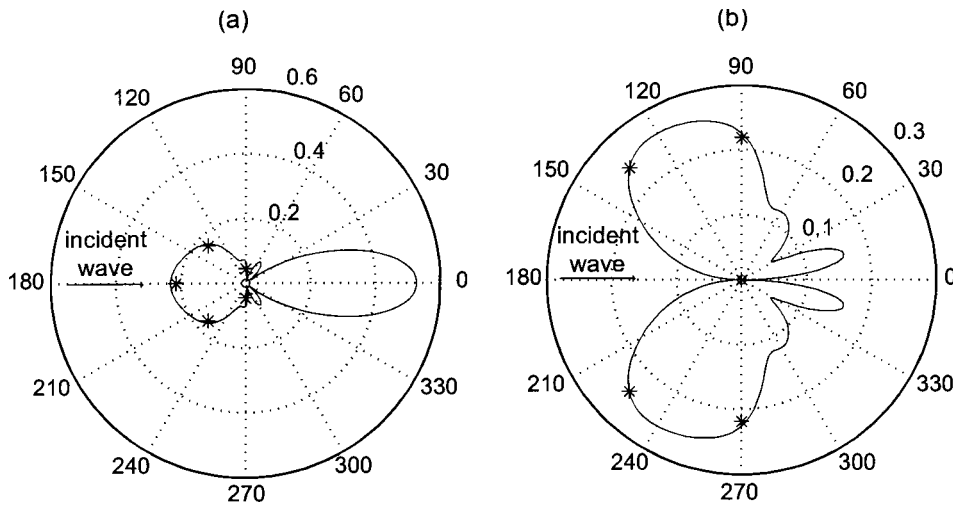
FIG. 16. Polar plots comparing analytical (solid line) and Finite Element (asterisk) predictions for a hole 84 mm in diameter, when the wave is received 390 mm away from the hole. The radial distance in the plots represents the amplitude of the received signal. The S_0 mode is incident at 100 kHz-mm. Plots show scattering of the (a) S_0 mode; and (b) SH_0 mode.

the hole; (b) the decay with distance from the hole can be described well by the cylindrical beam spreading function; (c) if the distance away from the hole is normalized to hole diameter all reflection coefficients are approximately the same whatever the hole size; and (d) secondary reflections have an effect on the results.

C. Wave field around the hole represented by polar plots

The scattered field around the hole is illustrated well by a polar plot. Figure 16 shows the predicted amplitudes of the scattered modes for a hole which is 84 mm in diameter, when the receiver is at a distance of 390 mm away from the edge of the hole. The circumferential axis of the plots corresponds directly to the angular location with respect to the center of the hole; the origin (180 degrees) corresponds to the direction of the incident wave. The radial axis of the plots corresponds to the magnitude of the displacement. The dominant displacement components are shown, that is the radial component, u_r [Fig. 16(a)], for the S_0 mode and the circumferential component, u_θ [Fig. 16(b)], for the SH_0 mode. The solid lines are calculated from the analytical model for a single frequency of 100 kHz. Results from the Finite Element models are also included at some specific angles and those points are calculated from the Hilbert envelope of the signal. Very good agreement is found between the two techniques. The reflected S_0 wave is scattered mainly forwards and backwards (at 0 and 180 degrees), while the reflected SH_0 is scattered mainly in the transverse direction. Note that the incoming S_0 wave is not plotted.

VII. CONCLUSION

The interaction of a low-frequency plane S_0 wave with a circular through-thickness hole in a plate has been studied using three different approaches: Finite Element simulation, analytical predictions, and experimental measurements. A specific focus was directed on the directly reflected S_0 mode and the laterally scattered (90 degrees) SH_0 mode, and the study was limited to hole diameters in the range of 1 to 3 wavelengths of S_0 at the frequency thickness product of 100 kHz-mm. Good agreement between the three sets of results

was obtained. The results show quite high reflection coefficients: For example, a 54 mm hole diameter has a specular reflection coefficient of 0.27 (approximately -11 dB).

Interpretation of the nature of the S_0 reflection and SH_0 scattering coefficients has indicated the same form of the behavior for each case: (a) the coefficient increases with the diameter of the hole and decreases with the distance from the hole; (b) a single function can be used to express the trend of the coefficient for all hole diameters and distances from the hole, by normalizing the distance to the diameter of the hole; (c) the trend of the decay of the coefficient with distance from the hole closely follows a cylindrical beam spreading function; (d) the trend of the coefficient is perturbed by small undulations; these are the result of interference with the main signal by secondary reflections arriving slightly later.

APPENDIX A: LAMB MODE FUNCTIONS

The thickness co-ordinate dependent functions that appear in the expressions for displacements and stresses for Lamb modes are given here. For symmetric modes they are defined as

$$V_n(z) = s_1 \cos(p_n z) + s_2 \cos(q_n z), \tag{A1}$$

$$W_n(z) = s_3 \sin(p_n z) + s_4 \sin(q_n z), \tag{A2}$$

$$\Sigma_{rr}^n(z) = \mu[s_5 \cos(p_n z) + s_6 \cos(q_n z)], \tag{A3}$$

$$\widetilde{\Sigma}_{rr}^n(z) = \Sigma_{r\theta}^n(z) = \mu[s_7 \cos(p_n z) + s_8 \cos(q_n z)], \tag{A4}$$

$$\Sigma_{rz}^n(z) = \mu[s_9 \sin(p_n z) + s_{10} \sin(q_n z)]. \tag{A5}$$

In these expressions,

$$s_1 = 2 \cos(q_n h), \tag{A6}$$

$$s_2 = -[(k_n^2 - q_n^2)/k_n^2]\cos(p_n h), \tag{A7}$$

$$s_3 = -2(p_n/k_n)\cos(q_n h), \tag{A8}$$

$$s_4 = -[(k_n^2 - q_n^2)/q_n k_n]\cos(p_n h), \tag{A9}$$

$$s_5 = [2(2p_n^2 - k_n^2 - q_n^2)/k_n]\cos(q_n h), \tag{A10}$$

$$s_6 = [2(k_n^2 - q_n^2)/k_n]\cos(p_n h), \tag{A11}$$

Diligent *et al.*: Scattering of Lamb waves from a hole

$$s_7 = 4\cos(q_n h), \tag{A12}$$

$$s_8 = -[2(k_n^2 - q_n^2)/k_n^2]\cos(p_n h), \tag{A13}$$

$$s_9 = 4p\cos(q_n h), \tag{A14}$$

$$s_{10} = [(k_n^2 - q_n^2)^2/q_n k_n^2]\cos(q_n h). \tag{A15}$$

APPENDIX B: PROJECTION COEFFICIENTS

The projection coefficients appearing in Eqs. (42)–(44) are defined as

$$
\begin{aligned}
K_{n'n} &= \frac{1}{\mu}\int_{-h}^{h}\Sigma_{rr}^{n'}(z)\cos\left(\frac{n\pi z}{2h}\right)dz \\
&= 4(-1)^{n/2}\left[\frac{q_{n'}(k_{n'}^2 - q_{n'}^2)}{k_{n'}(q_{n'}^2 - (n\pi/2h)^2)}\cos(p_{n'}h)\sin(q_{n'}h)\right. \\
&\quad \left. + \frac{p_{n'}(2p_{n'}^2 - q_{n'}^2 - k_{n'}^2)}{k_{n'}(p_{n'}^2 - (n\pi/2h)^2)}\cos(q_{n'}h)\sin(p_{n'}h)\right], \tag{B1}
\end{aligned}
$$

$$
\begin{aligned}
L_{n'n} &= \frac{1}{\mu}\int_{-h}^{h}\Sigma_{r\theta}^{n'}(z)\cos\left(\frac{n\pi z}{2h}\right)dz \\
&= 4(-1)^{n/2}\left[-\frac{q_{n'}(k_{n'}^2 - q_{n'}^2)}{k_{n'}^2(q_{n'}^2 - (n\pi/2h)^2)}\cos(p_{n'}h)\right. \\
&\quad \left. \times \sin(q_{n'}h) + \frac{2p_{n'}}{(p_{n'}^2 - (n\pi/2h)^2)}\cos(q_{n'}h)\sin(p_{n'}h)\right], \\
& \tag{B2}
\end{aligned}
$$

$$
\begin{aligned}
M_{n'n} &= \frac{1}{\mu}\int_{-h}^{h}\Sigma_{rz}^{n'}(z)\sin\left(\frac{n\pi z}{2h}\right)dz \\
&= 2(-1)^{n/2}\frac{n\pi}{2h}\left[\frac{(k_{n'}^2 - q_{n'}^2)^2}{q_{n'}k_{n'}^2(q_{n'}^2 - (n\pi/2h)^2)}\right. \\
&\quad \times \cos(p_{n'}h)\sin(q_{n'}h) \\
&\quad \left. + \frac{4p_{n'}}{(p_{n'}^2 - (n\pi/2h)^2)}\cos(q_{n'}h)\sin(p_{n'}h)\right], \tag{B3}
\end{aligned}
$$

$$I_{nn}^S = \int_{-h}^{h}\cos^2\left(\frac{n\pi z}{2h}\right)dz = \begin{cases} 2h, & n = 0, \\ h, & n \neq 0, \end{cases} \tag{B4}$$

$$I_{nn}^A = \int_{-h}^{h}\sin^2\left(\frac{n\pi z}{2h}\right)dz = h, \quad n \neq 0. \tag{B5}$$

[1] D. Worlton, "Ultrasonic testing with Lamb waves," Nondestr. Test. (Chicago) **15**, 218–222 (1957).

[2] D. Worlton, "Experimental confirmation of Lamb waves at megacycle frequencies," J. Appl. Phys. **32**, 967–971 (1961).

[3] I. A. Viktorov, *Rayleigh and Lamb Waves* (Plenum, New York, 1970).

[4] T. Mansfield, "Lamb wave inspection of aluminium sheet," Mater. Eval. **33**, 96–100 (1975).

[5] S. Rokhlin, "Resonance phenomena of Lamb waves scattering by a finite crack in a solid layer," J. Am. Ceram. Soc. **69**, 922–928 (1981).

[6] J. Paffenholz, W. Fox, X. Gu, G. Jewett, S. Datta, and H. Spetzler, "Experimental and theoretical study of Rayleigh-Lamb waves in a plate containing a surface-breaking crack," Res. Nondestruct. Eval. **1**, 197–217 (1990).

[7] D. Alleyne and P. Cawley, "The interaction of Lamb waves with defects," IEEE Trans. Ultrason. Ferroelectr. Freq. Control **39**, 381–397 (1992).

[8] D. Alleyne and P. Cawley, "Optimization of Lamb wave inspection techniques," NDT & E Int. **25**, 11–22 (1992).

[9] Y. Cho and J. Rose, "A boundary element solution for a mode conversion study on the edge reflection of Lamb waves," J. Acoust. Soc. Am. **99**, 2097–2109 (1996).

[10] Y. Cho, D. Hongerholt, and J. Rose, "Lamb wave scattering analysis for reflector characterization," IEEE Trans. Ultrason. Ferroelectr. Freq. Control **44**, 44–52 (1997).

[11] T. Ghosh, T. Kundu, and P. Karpur, "Efficient use of Lamb modes for detecting defects in large plates," Ultrasonics **36**, 791–801 (1998).

[12] M. J. S. Lowe and O. Diligent, "The low frequency reflection characteristics of the fundamental symmetric Lamb wave S_0 from a rectangular notch in a plate," J. Acoust. Soc. Am. **111**, 64–74 (2002).

[13] W. Mohr and P. Holler, "On inspection of thin-walled tubes for transverse and longitudinal flaws by guided ultrasonic waves," IEEE Trans. Sonics Ultrason. **SU-23**, 369–378 (1976).

[14] W. Bottger, H. Schneider, and W. Weingarten, "Prototype EMAT system for tube inspection with guided ultrasonics," Nucl. Eng. Des. **102**, 356–376 (1987).

[15] J. Rose, J. Ditri, A. Pilarski, K. Rajana, and F. Carr, "A guided wave inspection technique for nuclear steam generator tubing," NDT & E Int. **27**, 307–310 (1994).

[16] J. Ditri, "Utilization of guided elastic waves for the characterization of circumferential cracks in hollow cylinders," J. Acoust. Soc. Am. **96**, 3769–3775 (1994).

[17] D. Alleyne and P. Cawley, "Long range propagation of Lamb waves in chemical plant pipework," Mater. Eval. **55**, 504–508 (1997).

[18] D. Alleyne, M. Lowe, and P. Cawley, "The reflection of guided waves from circumferential notches in pipes," J. Appl. Mech. **65**, 635–641 (1998).

[19] M. Lowe, D. Alleyne, and P. Cawley, "The mode conversion of a guided wave by a part-circumferential notch in a pipe," J. Appl. Mech. **65**, 649–656 (1998).

[20] P. Wilcox, M. Lowe, and P. Cawley, "Lamb and SH wave transducer arrays for the inspection of large areas of thick plates," in *Review of Progress in Quantitative NDE*, edited by D. Thompson and D. Chimenti (Plenum, New York, 2000), Vol. 19, pp. 1049–1056.

[21] M. Lowe, "Matrix techniques for modeling ultrasonic waves in mutilayered media," IEEE Trans. Ultrason. Ferroelectr. Freq. Control **42**, 525–542 (1995).

[22] B. Pavlakovic, M. Lowe, D. Alleyne, and P. Cawley, "DISPERSE: A general purpose program for creating dispersion curves," in Ref. 20, Vol. 16, pp. 185–192.

[23] P. Wilcox, M. Lowe, and P. Cawley, "Long range Lamb wave inspection: the effect of dispersion and modal selectivity," in Ref. 20, Vol. 18, pp. 151–158.

[24] D. Hitchings, "FE77 User Manual," Tech. Rep., Imperial College of Science, Technology and Medicine, London, UK, 1994.

[25] K.-J. Bathe, *Finite Element Procedures in Engineering Analysis* (Prentice–Hall, Englewood Cliffs, NJ, 1982).

[26] J. McKeon and M. Hinders, "Lamb wave scattering from a through hole," J. Sound Vib. **224**, 843–862 (1999).

[27] A. Norris and C. Vemula, "Scattering of flexural waves on thin plates," J. Sound Vib. **181**, 115–125 (1995).

[28] A. Norris and C. Vemula, "Flexural wave propagation and scattering on thin plates using Mindlin theory," Wave Motion **26**, 1–12 (1997).

[29] Z. Chang and A. Mal, "Scattering of Lamb waves from a rivet hole with edge cracks," Mech. Mater. **31**, 197–204 (1999).

[30] J. Achenbach and Y. Xu, "Wave motion in an isotropic elastic layer generated by a time-harmonic point load of arbitrary direction," J. Acoust. Soc. Am. **106**, 83–90 (1999).

[31] D. Alleyne and P. Cawley, "The excitation of Lamb waves in pipes using dry coupled piezoelectric transducers," Nondestr. Eval. **15**, 11–20 (1996).

[32] O. Diligent, M. Lowe, and P. Cawley, "Reflection and scattering of the S_0 Lamb mode from circular defects," in Ref. 20, Vol. 20B, pp. 1134–1141.

[33] W. Hassan and P. Nagy, "Circumferential creeping waves around a fluid-filled cylindrical cavity in an elastic medium," J. Acoust. Soc. Am. **101**, 2496–2503 (1997).

[34] P. Nagy, M. Blodgett, and M. Golis, "Weep hole inspection by circumferential creeping waves," NDT & E Int. **27**, 131–142 (1994).

Sound transmission across a smooth nonuniform section in an infinitely long duct

S. K. Tang and C. K. Lau
Department of Building Services Engineering, The Hong Kong Polytechnic University, Hong Kong, People's Republic of China

Sound transmission across a nonuniform section in an infinite duct is studied numerically using the finite element method. An impedance matched absorptive portion is added to each end of the computational domain so as to avoid the undesirable higher mode reflection that will otherwise take place there. Results suggest that the sound fields downstream of the nonuniform section inlet are complicated and cannot be easily described by the conventional solution of the wave equation. The distribution of acoustic energy among the various propagating modes well downstream from the outlet of the nonuniform section is also discussed. Results show that the first symmetrical higher mode is important for all cases. The plane wave becomes important at high frequency with high rate of change of the cross-sectional area when the section is a convergent one. © *2002 Acoustical Society of America.* [DOI: 10.1121/1.1512699]

PACS numbers: 43.20.Mv [DEC]

I. INTRODUCTION

Ventilation and air conditioning systems are indispensable nowadays, especially in high-rise buildings within congested cities. Noise from the related building services equipment, such as the air handling unit and fans, therefore propagates into the interior of a building through the air conveying ductwork and affects directly the built environment. The conventional method for noise control is by installing dissipative silencers into the duct network.[1] Their design requires a calculation of the required noise attenuation. However owing to the complexity of the ductwork system, the present estimation procedure[2] may only provide good results at very low frequencies and lead to disappointing results once the noise frequency approaches the first cutoff of the duct, not to say at higher frequencies. The problem becomes more acute when the ductwork contains bends and sections of cross-sectional changes.

Changes of cross-sectional areas are common in an air conditioning duct network for controlling static pressure and flow velocity. Sometimes, such changes may result from a limitation of ceiling voids or the structural requirements of a building. All such variations of cross-sectional areas, or wave guides, are accompanied by acoustical impedance changes and therefore causing reflection within the ductwork. They also have their frequency characteristics and thus will act as filters.[3] The generation of, the propagation and the interactions between acoustic modes are important for optimal silencer provision as these phenomena have crucial effects on the sound transmission through the sections and the subsequent calculation for the required sound attenuation along the ductwork.

There have been a number of studies on this topic in the past few decades. Many of them are focused on the methodology of analysis. For instance, Alfredson[4] approximated the boundaries of a varying cross-section duct by a series of subsections whose sides were parallel to the duct axis and performed an investigation on the propagation of sound in an exponential horn. Also, Astley and Eversman[5] compared the use of finite element and weighted residual methods for the present issue. Besides, Nayfeh *et al.*[6] studied the sound transmission through an annular duct with variable cross-sectional area. However, the interaction of acoustic modes, the reflection and transmission of sound power in the duct are not clearly addressed. The recent work of Utsumi[7] introduces a semianalytical method for the study of sound propagation in non- uniform circular ducts. However, it is believed that a particular acoustic mode upstream of the non-uniform duct section will excite many modes in the downstream position and thus the results of Utsumi[7] appear incomplete. Also, both Utsumi[7] and Astley and Eversman[5] performed the matching at the inlet and exit of the nonuniform section where the acoustic modes may not be well developed. This problem becomes serious when the associated percentage change in the cross-sectional area is not small (cf. the vena contracta in fluid mechanics[8]) and/or the frequency of the exciting sound is high. The solution of the wave equation for straight duct section employed by Alfredson[4] and Utsumi[7] may thus not be able to describe the sound pressure fields at these critical areas. This will be further discussed later.

In the present study, the sound propagation through nonuniform two-dimensional ducts is investigated using the finite element method. Special efforts are made in examining how the nonuniform section affects the sound propagation and how the acoustic energies are redistributed at the exit of the section. In order to avoid the problem in doing matching of sound pressure and its gradient at the inlet and outlet of the nonuniform section, numerical anechoic sections are added to the computation domain. Details are given later. It is hoped that the present study can provide useful information on the acoustical properties of nonuniform duct sections and for improved duct noise control. For practical reason, only nonuniform sections that are symmetrical about the longitudinal axis will be considered.
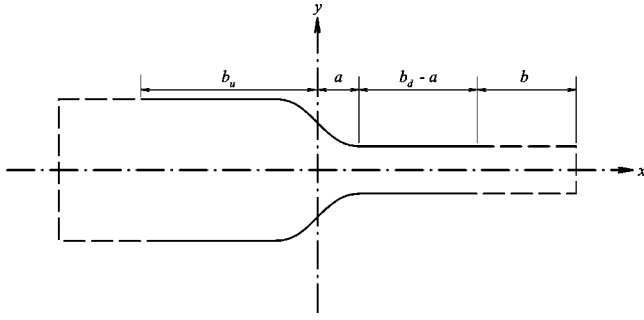
FIG. 1. Schematic diagram of the convergent section and nomenclature. —, duct boundaries; ----, anechoic termination boundaries.

II. COMPUTATIONAL DOMAINS

Effects of both convergent and divergent sections on sound transmission are investigated in the present study. The target is to solve the wave equation

$$\nabla^2 p + k^2 p = q \tag{1}$$

in the duct system, where p is the acoustic pressure, k the wave number and q the forcing. Figure 1 shows the schematic of the convergent section. The origin of the coordinate system is set to be at the center point of the nonuniform section. The forcing is applied to the system on the upstream side of the nonuniform section throughout the present investigation. Without loss of generality, the width of the narrower section is set to be unity so that all other length dimensions are normalized by this width. The wavenumber is therefore normalized by the reciprocal of this width in the foregoing analysis. The profile of the convergent section is defined by the formula

$$y = A f(x) + B, \tag{2}$$

where A and B are constants and

$$\frac{df(x)}{dx} = (x^2 - a^2)^3 \tag{3}$$

with the integration constants ignored. Expression (3) ensures the junctions between the non-uniform section and the two straight duct sections are smooth up to the second order longitudinal derivatives. A, B, and a can be adjusted to produce different convergent sections. They define the percentage change in duct width and its rate of change across the nonuniform section. The side walls are rigid so that the normal pressure gradient vanishes

$$\left. \frac{\partial p}{\partial n} \right|_{\text{wall}} = 0, \tag{4}$$

where n is the unit normal of a solid rigid boundary. In order to avoid reflections from the boundaries at the two ends of the computational domain, the boundary conditions there must be anechoic.[9] For low frequency cases where the waves in the two straight sections are planar, one can observe that for an unit strength planar sound pressure excitation to the system,

$$\frac{\partial p}{\partial n} + ikp = \begin{cases} 2ik & \text{at } x = -b_u, \\ 0 & \text{at } x = b_d \end{cases}, \tag{5}$$

are the required boundary conditions. In this case, $q = 0$.

However when higher modes are present, the corresponding boundary conditions are very complicated and are usually not easily implemented in the finite element computation context.[9] In the present study, anechoic terminations are introduced at the ends of the computational domain to damp down the higher modes before they reaches the end boundaries (chain lines in Fig. 1). In order to avoid reflections at the interface between an anechoic termination and the computational domain, the boundary conditions of the side walls of the former are set to be

$$\frac{\partial p}{\partial n} + ik\alpha p = 0, \tag{6}$$

where α is effectively an absorptive coefficient which varies with distance from each interface and is zero on the interface. In the present study, $\alpha = 0.01(x - b_i)^2$, where b_i is the longitudinal position of the interface, is adopted. The absorption of higher modes is very satisfactory when the length of this termination b is greater than 10. The standing wave ratio is nearly 0 dB up to $k = 6\pi$ (not shown here). The boundary condition at the exit of an anechoic termination is that for an outgoing plane wave

$$\frac{\partial p}{\partial n} + ikp = 0.$$

The unit strength planar sound pressure excitation to the system is obtained by setting

$$q = 2k e^{i\theta} \delta(x - b_u), \tag{7}$$

where δ is the delta function and θ is an arbitrary phase angle of the excitation. The latter has no bearing in the present study. Without loss of generality, θ equals $\pi/2$ in the present computations.

Unlike the matching scheme of Harari et al.,[10] the above computation domain enables an easy and straightforward implementation of the finite element method to solve the wave equation [Eq. (1)]. It also avoids the type of matching done by Utsumi[7] and Astley and Eversman.[5]

The computational domain for the divergent sections can be obtained by varying A, B, and a in Eqs. (2) and (3). The boundary conditions and forcing functions are again defined in the same way as those for the convergent sections and thus are not repeated here. One should note that the flow physics inside the convergent and divergent sections can be very different even if the percentage changes in cross-sectional areas of the two sections are the same. It will be shown in the next section that phenomena similar to that of the vena contracta[8] and the subsonic nozzle flows[11] can be observed at the exit of the nonuniform section provided that the percentage change in duct width and the rate of change of this width across the nonuniform section is of the right combination.

III. RESULTS AND DISCUSSIONS

For simplicity, the present investigation deals with a plane wave forcing at the upstream side of the nonuniform section. This is the case in reality as the higher mode noise is usually well attenuated some distances away from the
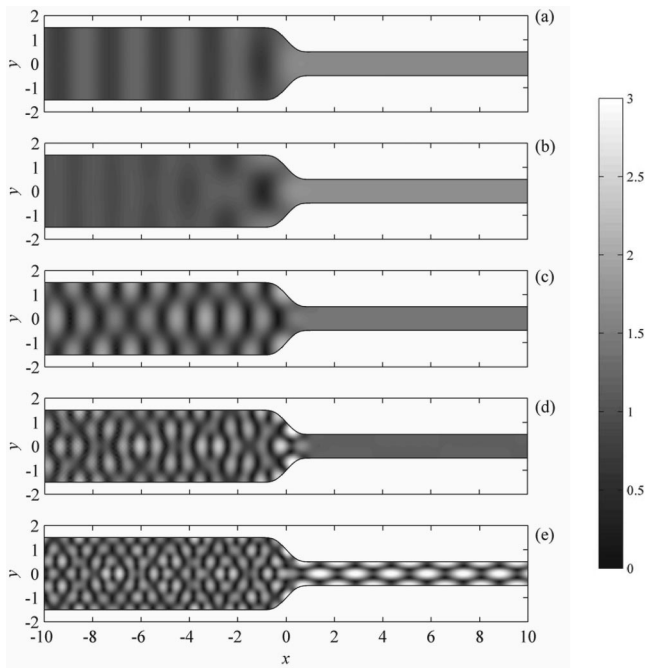
FIG. 2. Normalized sound pressure magnitude maps in the presence of a convergent section. $a=1$, $m_c=3$. (a) $k=1.5$; (b) $k=2.0$; (c) $k=3.0$; (d) $k=5.0$; (e) $k=6.5$.

FIG. 3. Effects of convergent ratio on sound field. (a) $m_c=2$; (b) $m_c=5$. $k=6.5$, $a=1$.

source. The sound field is thus symmetrical about the longitudinal axis. Also, the present investigation is restricted at $k \leq 9$. One should note that the frequency with $k \leq 9$ is practically not high. For a duct having a width of 1 m, which is not uncommon in buildings, the first cutoff frequency of the symmetrical higher mode is only 340 Hz ($k=2\pi$). Noise from air conditioning and ventilation devices still contains significant amount of energy beyond this frequency.[1] The cutoff frequency of the second symmetrical higher mode corresponds to that with $k=4\pi$, which is high enough to be reliably attenuated by duct acoustic lining of sufficient length.

A. Convergent sections

Figure 2 shows some sound field patterns across a convergent section with $A=35/32$, $B=1.5$ and $a=1$. The convergent ratio, m_c, defined as the ratio of the larger to the smaller duct width, is 3. The sound fields for $k<1$ are not presented as the waves are almost planar even inside the convergent section. For $k=1.5$, one can note the nearly circular wave pattern at $-1<x<1$ [Fig. 2(a)]. This nonplanar (higher mode) cannot propagate back into the wider duct section as expected.[12] At $k=2$, which is close to the first symmetrical higher mode cutoff value of the wider duct section (at $k=2.09$), one can observe strong non-planar sound reflection by the convergent section [Fig. 2(b)]. The sound energy is concentrated at the walls of the section, leaving a weak sound field near the center-line. The nonplanar sound penetrates a longer distance into the upstream duct section than that at $k=1.5$ as expected.[12] At increased k beyond 2.09, the upstream sound field is made up by plane waves and the first symmetrical higher mode, while that in the downstream narrower duct is a plane wave. Figure 2(c) illustrates the sound
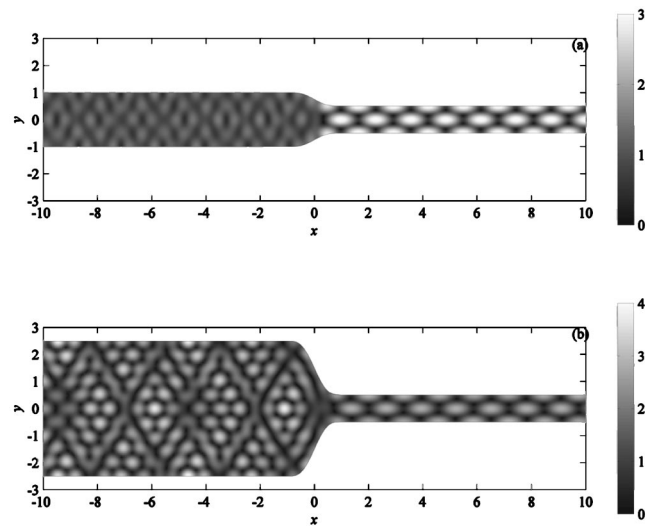
energy distribution at $k=3$, which is typical for $2.1 \leq k \leq 4$. The second symmetrical higher mode propagates into the wider duct section, while nonplanar wave pattern at the outlet of the convergent section can be observed at increased k [Fig. 2(d)]. Unlike the situation in the inlet of the convergent section, acoustic energy is concentrated at the centreline of the section outlet. This is due to the effect of vena contracta[8] where the wave is squeezed into the narrower duct section. This effect becomes more prominent as the convergent ratio increases (discussed later). For $k>6.3$, the first symmetrical higher mode propagates into the downstream without attenuation [Fig. 2(e)]. It can also be observed from Figs. 2(d) and (e) that there is a region close to the center line of the convergent section outlet where the sound pressure magnitude is very small. This is due to the higher particle velocity there under the vena contracta effect.

It can be observed that once the frequency is close to or higher than the cutoff frequency of the first symmetrical higher mode of the upstream duct section, the sound fields at the inlet and outlet of the convergent section will contain nonpropagating modes. Also, it is very clear that a plane excitation to the system will produce higher modes of substantial energy content. Therefore, the calculation of sound power transmission and reflection coefficients at a particular frequency should include all the acoustic modes involved. The analyses done by Utsumi[7] seems a bit incomplete. Besides, as the condition at the outlet of the convergent section is not equivalent to that of a straight duct section with rigid walls, the matching of solutions done by Alfredson[4] and Utsumi[7] may not be very appropriate unless the convergent ratio is close to unity. More elaboration on this point is given in the next paragraph.

At small convergent ratio, the acoustic modes are fully developed at the outlet of the convergent section [Fig. 3(a)]. However at larger convergent ratio, the flow at the outlet of the section becomes more accelerated. The higher acoustic mode may not be well developed at the convergent section outlet, especially with $k>2\pi$ [Fig. 2(e)]. Further increase in m_c makes the situation worse [Fig. 3(b)]. The convergent

S. K. Tang and C. K. Lau: Sound transmission across a nonuniform section
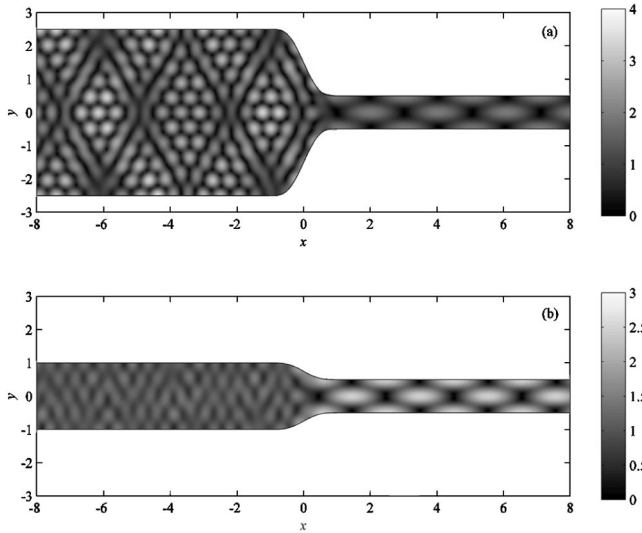
FIG. 4. Effects of convergent ratio on sound field at high frequencies. (a) $m_c=5$; (b) $m_c=2$. $k=8$, $a=1$.

FIG. 5. Effects of convergent ratio on sound power transmission coefficients. $\bigcirc$, $m_c=2$; $\triangle$, $m_c=3$; $\square$, $m_c=5$. Closed symbols, total power; open symbols, plane wave power. $a=1$.

section tends to focus the sound waves and the vena contracta acts as a variable cross-section wave guide with unknown boundary condition. Such effect becomes more pronounced at higher frequencies [Fig. 4(a)]. The solution of the wave equation within this region is therefore different from that of a straight duct.[13] The technique of mode matching[4,7] may only be appropriate for small convergent ratios, where the vena contracta is located upstream of the convergent section outlet ($x<1$), so that the wave then has sufficient distance to develop before propagating into the straight duct section [Fig. 4(b)], or when the forcing frequency is sufficiently lower than the cutoff frequency of the first symmetrical higher mode of the smaller duct section.

The increase in the length of the convergent section, a, at fixed convergent ratio allows a smoother wave propagation into the smaller duct section. The effect of the vena contracta becomes weaker. Since the corresponding wave patterns look like those presented in Figs. 3 and 4, they are not presented here. However, it will be shown later than this length has substantial effects on the sound transmission process.

Figure 5 illustrates the variations of the overall sound power transmission coefficient τ_0 and the plane wave power transmission coefficient τ_p with the forcing frequency respectively for $m_c=2$, 3, and 5 with $a=1$. The latter refers to the ratio of the power carried by the plane wave downstream of the convergent section to that of the incident power. One can easily realize that $\tau_0=\tau_p$ for forcing frequencies below the cutoff frequency of the first symmetrical higher mode of the smaller duct section. The corresponding limiting value of τ_0 at $k\rightarrow0$ ($=\tau_p$), can be calculated using the plane wave theory with abrupt contraction.[3] For the convergent ratios of 2, 3, and 5, these values are 0.89, 0.75, and 0.56, respectively.

One can observe from Fig. 5 for $k<6.3$ that τ_0 increases as the forcing frequency approaches the cutoff frequency of the first symmetrical higher mode of the larger duct section for all m_c. The overall sound power transmission coefficient
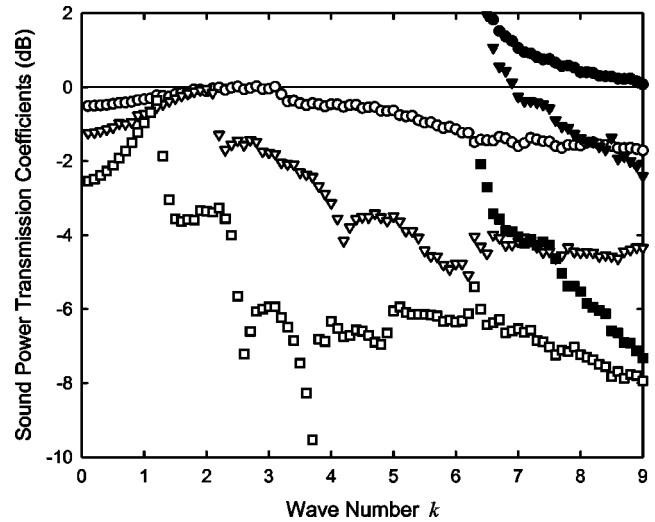
can be very close to 1. This can also be predicted using the classical plane wave calculation. At very low frequency, the length of the convergent section is very small when compared to the wavelength of the sound. The sound wave thus sees the section as an abrupt contraction. As frequency increases, the rate of contraction seen by the wave becomes lower and thus τ_0 increases as higher percentage of the incident sound power can propagate through the section. The maximum sound power transmission coefficient depends on the smoothness of the convergence. It is expected that the smoother the convergence, the closer it will be to unity.

At frequency increases beyond that of the first symmetrical higher mode of the larger duct section, higher mode propagates back to the upstream [Fig. 2(c)] and thus the power carried by the transmitted plane wave becomes less. A drop of τ_0 then follows. The τ_0 in general decreases as k further increases towards 6.3. Such phenomenon can also be predicted using the classical plane wave calculation[3] (not shown here). However, large dips of τ_0 are observed close to the cutoff frequencies of the symmetrical higher modes of the larger duct section for all m_c investigated in general. This situation becomes more acute as m_c increases. At these frequencies, the reflected waves, having the wavelength in the transverse direction greater than 1, are strong and carry substantial amount of energy under resonance. Figure 6(a) shows a typical example with $m_c=5$, $a=1$, and $k=3.7$. This phenomenon is not reported by Utsumi.[7] It should be noted that the results of Utsumi[7] are related to transmitted wave magnitudes, not the sound power transmitted. It can be noted that a dip of τ_0 is not observed at $k\sim5$ for $m_c=5$, while the corresponding forcing frequency is close to that of the fourth symmetrical higher mode of the larger duct section ($k=5.03$). At this frequency, the transverse wavelength of the reflected sound is about 0.63. The reflection is therefore not strong [Fig. 6(b)].

For $k>2\pi$, higher mode propagates along the smaller duct section and $\tau_0>\tau_p$. Large transmitted sound power is found at $k=6.3$ for all values of m_c investigated. The corre-
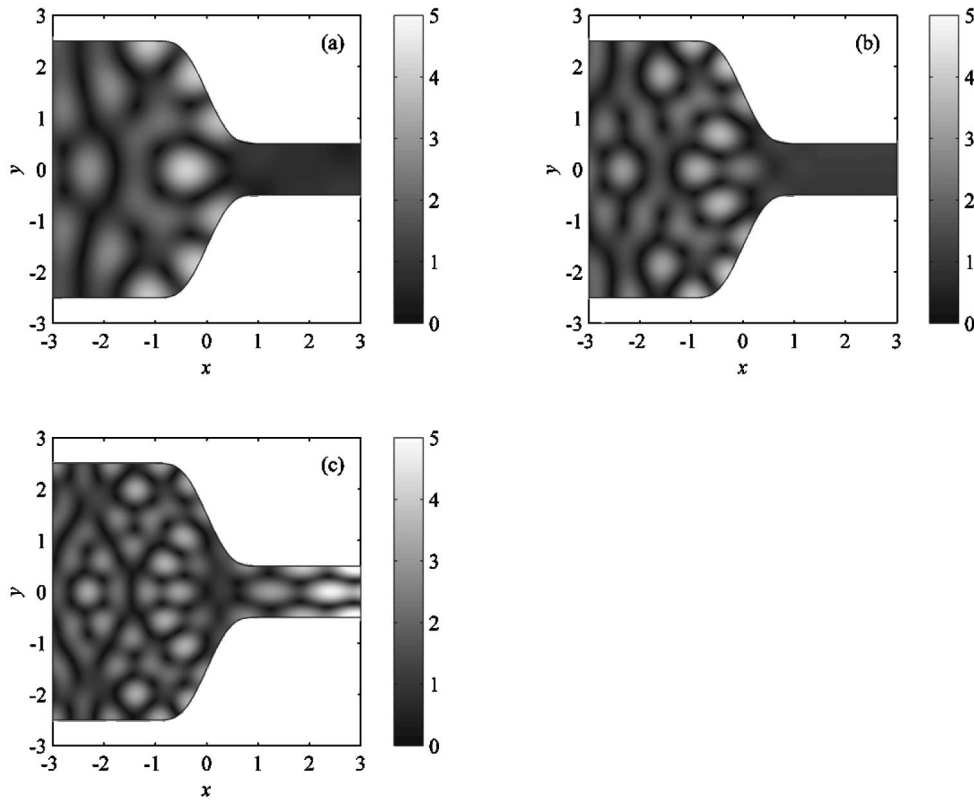
FIG. 6. Sound fields close to convergent section outlet. (a) $k=3.7$; (b) $k=5$; (c) $k=6.3$. $m_c=5$, $a=1$.

sponding forcing frequency is very close to that at which resonance can occur in both straight duct sections (wave number $k=2\pi$). Most of the transmitted sound power is carried downstream by the first symmetrical higher mode propagating in the smaller duct section as illustrated in Fig. 5. The strong higher mode propagation in the downstream direction suggests low impedance for sound propagation at the outlet of the convergent section. The corresponding pressure magnitude at this location is therefore, unlike those shown in Figs. 6(a) and (b), weak. An example of this is given in Fig. 6(c). This suggests that the overall sound power carried by the reflected waves is out-of-phase to that in the smaller duct section. As expected, a further increase of k results in lower magnitude of the symmetrical higher mode in the smaller duct section. One expects another strong rise of τ_0 above 1 at $k=4\pi$; the wave number corresponds to the cut-off frequency of the second symmetrical higher mode of the smaller duct section.

Increasing the length of the convergent section (that is, increasing a) reduces the magnitude of the dip at duct eigenfrequencies as shown in Fig. 7. For $a>1$, its effect is similar to that of reducing the convergent ratio. The smooth convergence offers a slow impedance change across the convergent section and thus helps avoiding strong reflection even close to the first and second symmetrical higher mode cutoff frequencies of the larger duct section. The convergence becomes rapid as a is reduced. For $a=1/\pi$ ($a\sim0.32$), the wave sees the convergent section as an abrupt contraction for $k\leqslant2$ (Fig. 7). Strong dips of τ_0 can also be observed at similar values of k as for the case of $a=1$, but an additional dip is observed at $k\sim2.9$. The sound fields at $k=2.4$, 2.8, 2.9, and 3.3 shown in Fig. 8 suggest relatively higher concentration of

acoustic energy at the edges of the convergent section at k around 2.8 and 2.9. Such τ_0 dip is absent for $a\geqslant1$ (Figs. 5 and 7). It is very likely to be due to the resonance inside the convergent section. If one simplifies this section as a straight taper convergent wave guide having a slope equals to the average slope of the present convergent section, which is -1.72 for $a=1/\pi$ and $m_c=3$, one will find the first even angular mode inside such wave guide resonates at $k\sim3$ (Appendix). Such resonance produces high impedance and strong reflection in form of higher mode back to the upstream. Similar resonance also occurs at $k\sim6$ (not shown
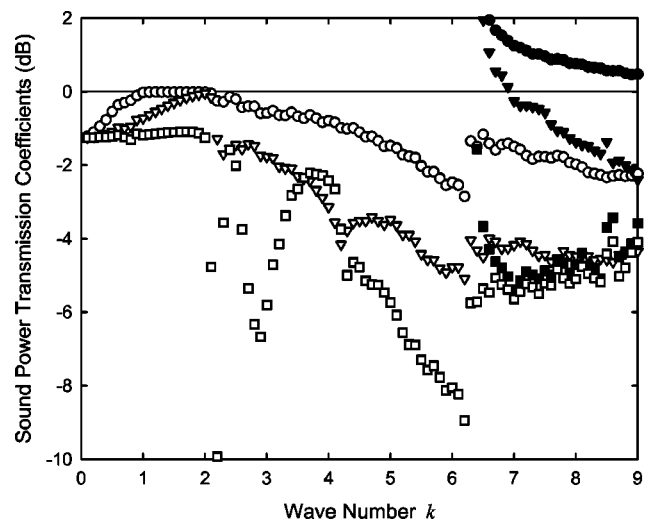
FIG. 7. Effects of convergent section length on sound power transmission coefficients. $\bigcirc$, $a=2.75$; $\triangle$, $a=1$; $\square$, $a=1/\pi$. Closed symbols, total power; open symbols, plane wave power. $m_c=3$.

S. K. Tang and C. K. Lau: Sound transmission across a nonuniform section
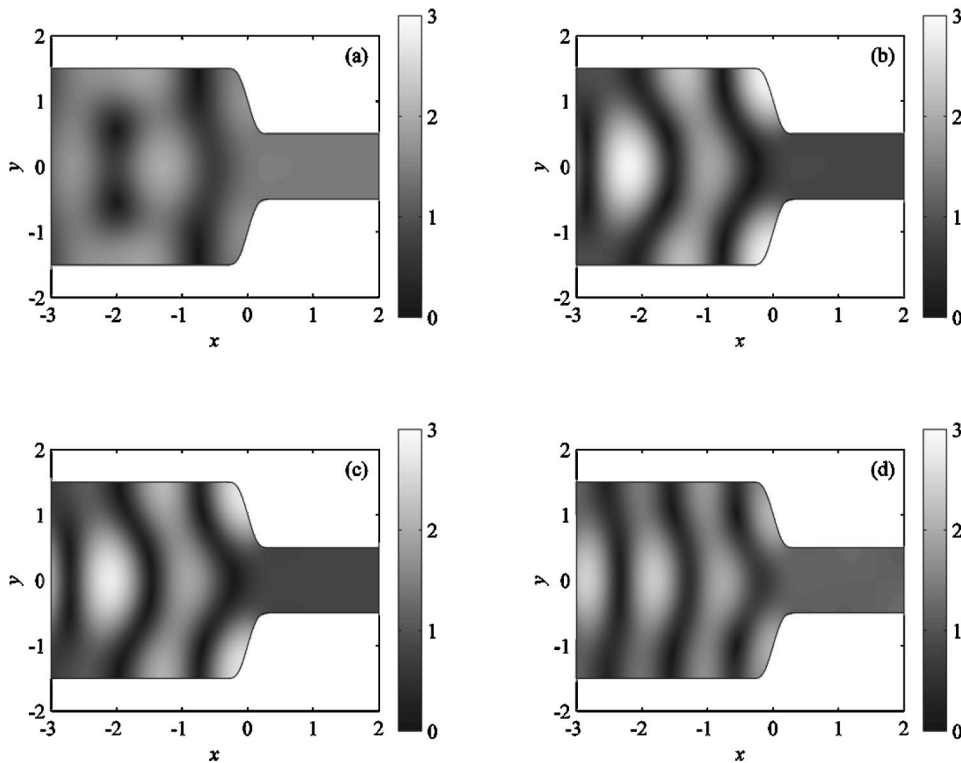
FIG. 8. Reflection of sound by convergent section at weak sound power transmission. (a) $k=2.4$; (b) $k=2.8$; (c) $k=2.9$; (d) $k=3.3$. $m_c=3$, $a=1/\pi$.

here). This effect is not found for $a=1$ or 2.75 because the corresponding wave number will be higher than 6.3. However, further investigation is necessary for clarifying the issue.

Again, resonance occurs at $k\sim6.3$ for all values of a investigated (Fig. 7). One can also observe that at small a, the plane wave in the smaller duct section carries more energy than the higher modes. The rapid contraction appears to have impeded the development of the higher mode inside the smaller duct section. The opposite is observed at large a.

B. Divergent sections

The flow across a divergent section is completely different from that across a convergent one. The divergent ratio m_d is defined as the ratio between the widths of the downstream and upstream straight duct sections. Figure 9 illustrates that the flow, with $a=1$ and $m_d=3$, is rather similar to that issuing from a subsonic nozzle,[11] when the forcing frequency is higher than the first symmetrical higher mode of the downstream larger duct section. The application of the mode matching technique for solving the present sound propagation problem as in Utsumi[7] appears questionable. Figure 9(a) suggests the high impedance of the divergent section to sound propagation at low frequencies. One can find strong reflection and standing wave patterns at these frequencies. Above the first symmetrical higher mode cutoff frequency of the larger duct section, the impedance becomes weak [Fig. 9(b)] and one can observe from Fig. 9(c) that nearly all the incident wave energy is transmitted across the divergent section. It will be further discussed later. Higher mode reflection is observed at $k>6.3$ as expected.

One can also notice from Fig. 9 that the mode patterns in the larger duct section are less ordered than those observed previously with convergent sections (Fig. 2 for instance) at high frequencies. More intensive low energy (pressure magnitude) lines and regions are found as the forcing frequency increases. This is probably due to the destructive interference from various acoustic modes inside the larger duct section. However, the patterns of these lines and/or regions do not follow any well-defined mode shapes. There are two thin low
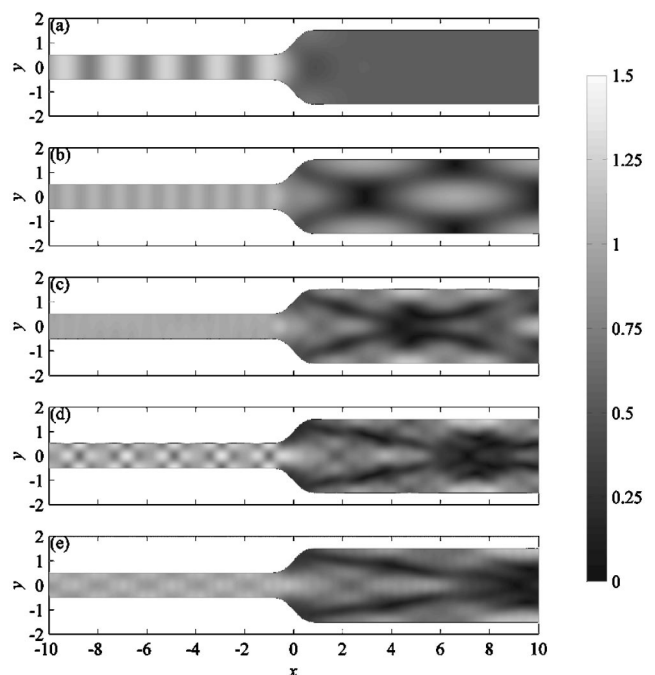
FIG. 9. Sound magnitude maps in the presence of a divergent section. (a) $k=1.5$; (b) $k=3$; (c) $k=5$; (d) $k=6.5$; (e) $k=8$; $a=1$, $m_d=3$.
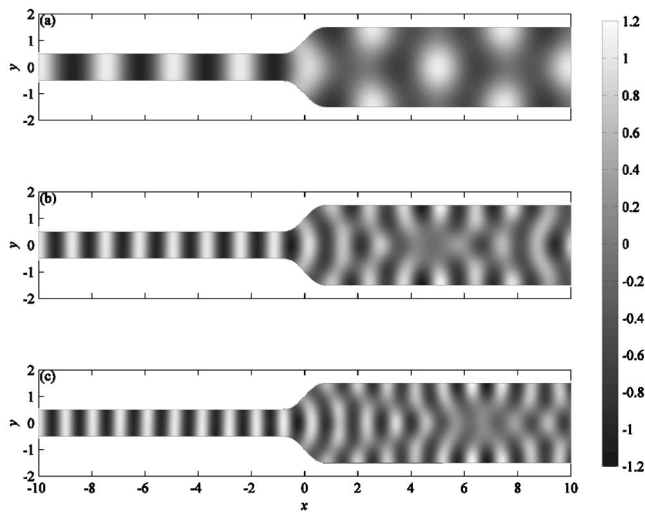
FIG. 10. Transition of sound waves into higher modes through a divergent section. (a) $k=2.5$; (b) $k=5$; (c) $k=6.2$. $a=1$, $m_d=3$.

energy regions (lines) close to the outlet of the divergent section. These regions intersect at some distances downstream of the outlet, forming a boundary, which looks like that of the potential core in a subsonic jet.[11] The wave fields close to the divergent section outlet suggest the breakup of the nearly circular wave fronts into higher duct mode patterns at frequencies higher than that of the first symmetrical higher mode of the larger duct section (Fig. 10). The lines of low energy correspond to nodal locations. The fluid velocity within the region enclosed by the two strong low energy lines close to the divergent section outlet (the potential core) appears to be higher than those outside the region; a phenomenon commonly found in the initial region of a subsonic jet.[11] A phase difference exists between waves inside and

outside the potential core. The patterns of the sound fields there thus cannot be represented by the mode shapes of the straight duct section.

The variations of m_d and a certainly affect the sound transmission processes. One can find more complicated networking of the low energy lines and regions as the rate of divergence increases (m_d increases or a decreases). However, more energy is concentrated within the potential core region at increased rate of divergence. Figure 11 gives some ideas on such phenomenon. Though the sound fields inside the larger straight duct section are complicated, one can still expect that there exist plane waves in this duct section as the transverse pressure distributions have non-vanishing mean values at a distance beyond the potential core where the flow is expected to have fully developed (not shown here). One can also expect the coexistence of many acoustic modes.

Figure 12(a) shows the energy contents of the acoustic modes well downstream from the divergent section outlet for $m_d=3$ and $a=1$ at various forcing frequencies. Only plane waves are found inside the duct at forcing frequencies below the first cutoff frequency of the symmetrical higher mode of the larger duct section and thus $\tau_0=\tau_p$. Resonance occurs at $k\sim2.09$. A rise in the first symmetrical higher mode power is resulted. It is accompanied by a fall of the plane wave power. Such phenomenon is expected to have occurred in the presence of convergent sections, but the resonance takes place in the upstream side. A dip of τ_0 (or τ_p) in Figs. 5 and 7 should be accompanied by a rise of the overall reflected wave power. The cutoff frequency of the second symmetrical higher mode of the larger duct section corresponds to a wave number $k\sim4.18$. It is found that such resonance results in a redistribution of energy from the plane wave to the symmetrical higher modes. The first symmetrical higher mode
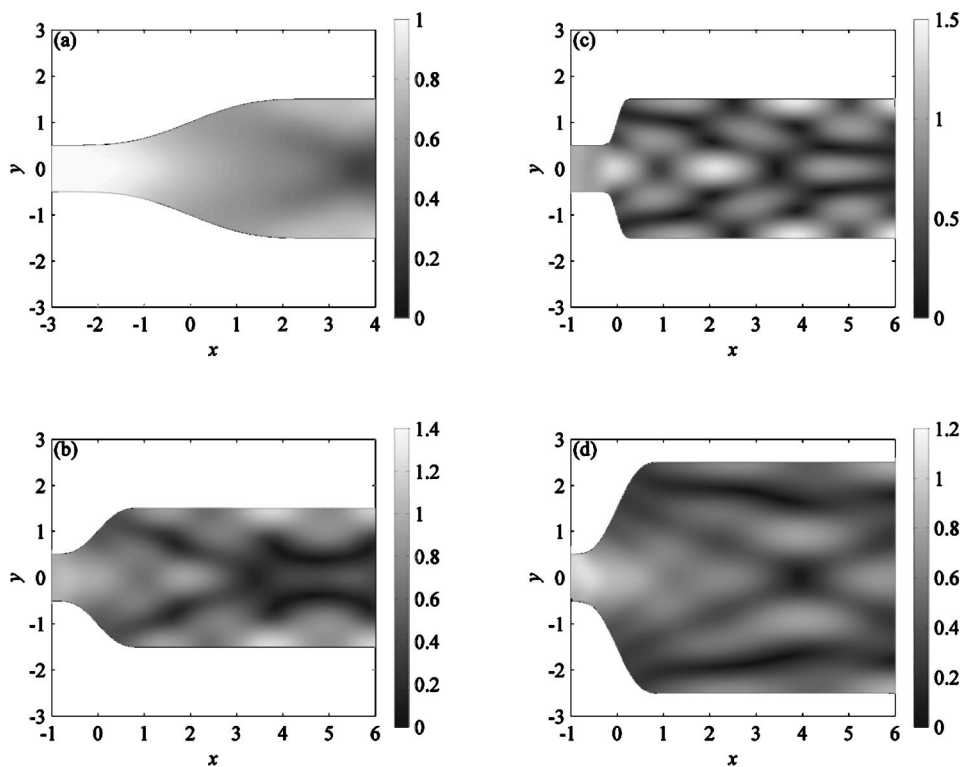
FIG. 11. Effects of rate of divergence on sound field immediate downstream of divergent section. (a) $a=2.75$, $m_d=2$; (b) $a=1$, $m_d=3$; (c) $a=1/\pi$, $m_d=3$; (d) $a=1$, $m_d=5$; $k=4.5$.

(a)

(b)

(c)
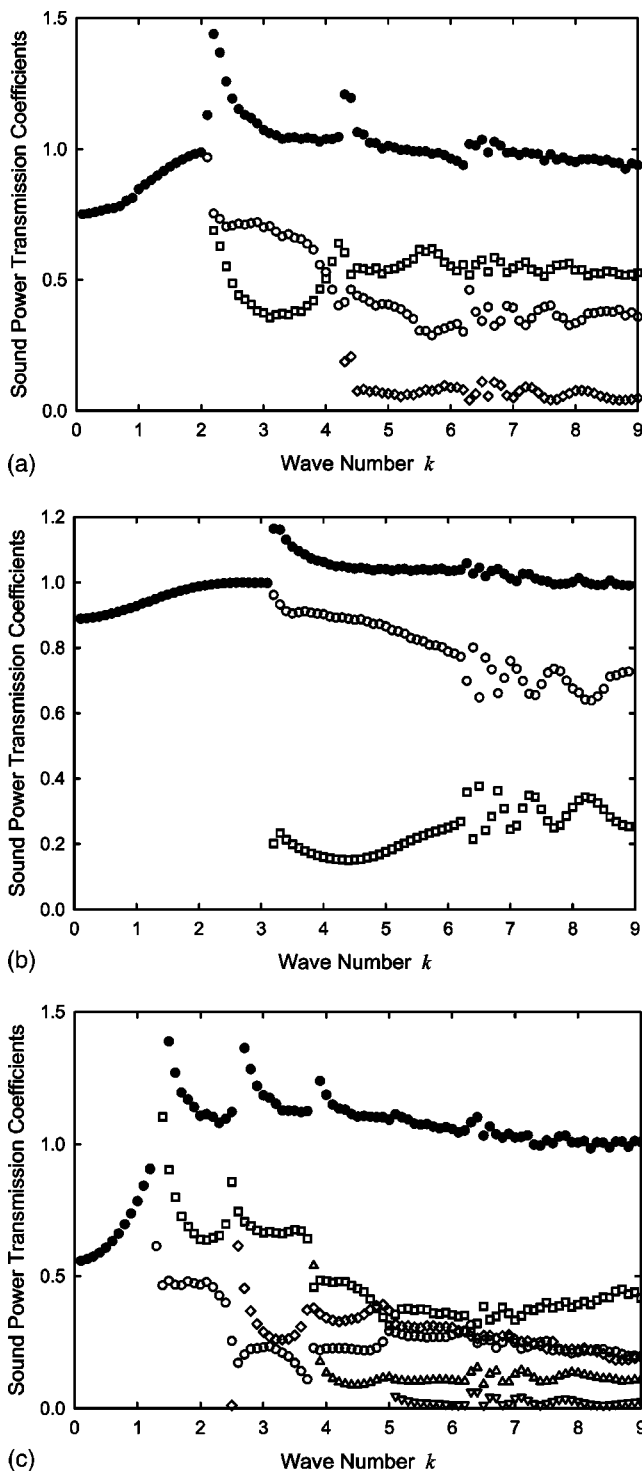
FIG. 12. Variations of sound power transmission coefficients with forcing frequency for divergent section. (a) $m_d=3$; (b) $m_d=2$; (c) $m_d=5$. ●, total; ○, plane wave; □, first symmetrical higher mode; ◇, second symmetrical higher mode; △, third symmetrical higher mode; ▽, fourth symmetrical higher mode.

becomes the dominant one for $k \geq 4.2$. A sharp drop of plane wave power is thus explained. Resonance is also observed at $k \sim 6.3$ as expected. The powers carried by the fourth and fifth symmetrical higher modes are negligible and thus are not presented.

At lower divergent ratio, less number of acoustic modes will be excited at $k<9$ [Fig. 9(b)]. At $m_d=2$, the only sig-

nificant waves that are propagating downstream are the plane wave and the first symmetrical higher mode. The plane wave basically dominates the sound field downstream of the divergent section. However at increased m_d, the first symmetrical higher mode becomes dominant when the forcing frequency is above its cutoff frequency [Fig. 12(c)]. Again as has been observed in Fig. 12(a), the resonance at the cutoff frequency of the second symmetrical higher mode results in a decrease of the plane wave power but also an increase in the power carried by the first symmetrical higher mode. The resonance at $k \sim 3.7$ of the third symmetrical higher mode produces a drop of the first symmetrical higher mode power but a rise of that of the plane wave mode. It is also observed that the plane wave energy becomes more comparable to those of the first and second symmetrical higher modes as k increases further. The on-set of the third and the fourth higher modes results in a redistribution of energy back to the plane wave mode. The reason is left to further investigations.

Results shown in Fig. 12 tend to suggest that the on-set of a symmetrical higher mode propagation in the larger duct section, except for the case of the first symmetrical higher mode which must take energy from the plane wave, is usually followed by a drop of the power carried by an acoustic mode two orders lower than this mode for $k \leq 6.2$. Also, one can observe large fluctuations of sound transmission coefficients for $k>6.3$. These fluctuations become smoother as the forcing frequency increases. However at small m_d, for example $m_d=2$, these fluctuations associated with the plane wave and the first symmetrical higher mode vary out of phase with each other in this k range [Fig. 12(b)]. Similar phenomena are expected also at larger m_d between various propagating acoustic modes, but the data would be difficult to interpret as the energy is distributed among several of these modes. The reason for the occurrence of these fluctuations is not exactly known. However, one can expect from the duct acoustics theory[14] that it is due to the form of excitation to the acoustic modes in the larger duct section. If one looks at the acoustic pressure magnitude distribution close to the nonuniform section as shown in Fig. 13, it is found that the energy is more widely spread across the inlet of the divergent section for $k=7$ and 7.7 than for $k=6.8$ and 7.3. The excitation at $k=7$ or 7.7 is therefore more uniform across the duct section and thus higher plane wave energy content can be anticipated. For $k=6.8$ or 7.3, more energy will then be redistributed to the higher mode. One can observe that it is due to the phase of the higher mode reflected back into the smaller duct section. The input impedance of the divergent section thus plays an important role for the occurrence of this phenomenon. One also expects that this impedance varies across the cross section of the divergent section inlet. Though there are studies concerning the input impedances of wave guides (for instance, Ref. 15), results related to the present type of cross sectional change are not easily found in existing literature. Further investigation is required. Similar observations as in Figs. 12 and 13 can be made when a is varied. The corresponding results are thus not presented.
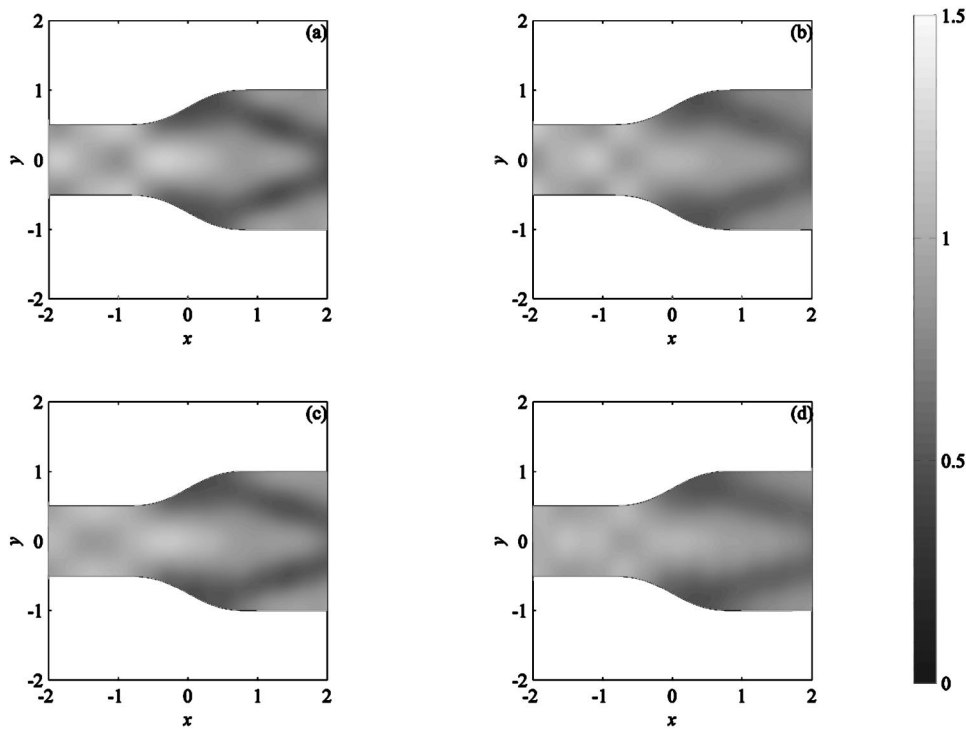
FIG. 13. Spreading of sound waves across divergent section at high frequencies. (a) $k=6.8$; (b) $k=7$; (c) $k=7.3$; (d) $k=7.7$. $a=1$, $m_d=2$.

IV. CONCLUSIONS

The sound transmission across a nonuniform section in an infinite duct is investigated by using the finite element method. Special absorption boundaries are included in the computational domains in order to avoid the erroneous reflection from the ends of the domains. The excitation is taken to be a plane wave. For practical reasons, only symmetrical divergent and convergent sections are considered in the present study. The sound field patterns and the distributions of energy among the different propagating acoustic modes under various forcing frequencies are also discussed.

Results obtained with convergent sections illustrate that there are regions of high energy content close to the center line of the section outlet when the forcing frequency is higher than the first symmetrical higher mode of the larger duct section. The situation becomes more serious as the forcing frequency increases. This is probably due to the nonparallel fluid flow near the convergent section outlet at higher frequencies. The sound power transmission coefficient increases with forcing frequency before the first symmetrical higher mode is reflected back into the larger duct section. The power carried by the transmitted plane wave decreases as the forcing frequency increases beyond the cutoff frequency of this mode in general. Sharp drop of plane wave power is found when the forcing frequency collapses with the eigenfrequencies of the larger duct section. High transmitted sound energy is observed at forcing frequencies close to the first symmetrical higher mode eigenfrequency of the smaller duct section. It is also found that the higher the rate of convergence, the lower the overall sound transmission coefficient. Besides, it is observed that the first symmetrical acoustic mode dominates the final sound field inside the smaller duct section at high frequency, unless the rate of convergence is sufficiently high.

The sound fields in the presence of a divergent section are more complicated. At a forcing frequency higher than the first symmetrical higher mode of the downstream larger duct section, the transmitted energy is concentrated on the center line within or at a location slightly downstream of the divergent section. The walls of the divergent section are usually under a weak pressure condition. The sound energy distribution pattern downstream of the inlet of the divergent section resembles that of a subsonic jet velocity field. Again, large energy content of a particular propagating mode is observed when the forcing frequency is close to its cutoff frequency. The distribution of acoustic energy among the propagating modes in the fully developed region inside the larger duct section suggests that the first symmetrical higher mode carries higher energy content than the other propagating modes once it is excited. The plane wave will only be more important when the rate of divergence is low or the forcing frequency is not high. It is also found that the impedance offered by the divergent section is important for the final distribution of energy among the propagating modes downstream of the section.

APPENDIX: ANGULAR MODES IN A SYMMETRICAL TAPER SECTION

The sound field inside a symmetrical taper section (Fig. 14) is best to be obtained by solving the wave equation in polar coordinate (r, ϕ);
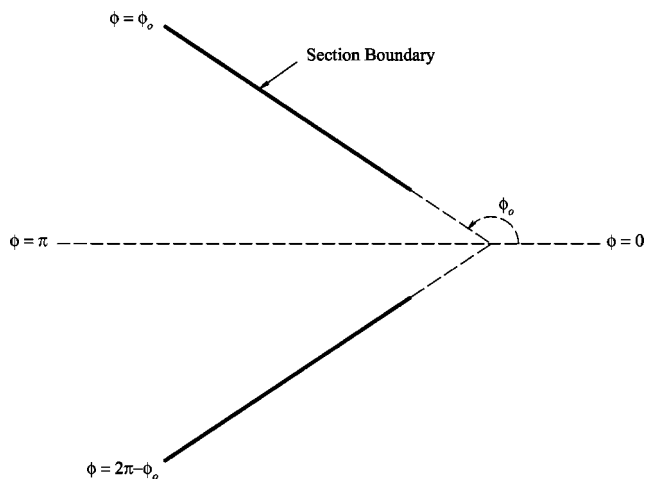
FIG. 14. Schematic diagram of a symmetrical linear taper section.

$$\nabla^2 p + k^2 p = \frac{\partial^2 p}{\partial r^2} + \frac{1}{r}\frac{\partial p}{\partial r} + \frac{1}{r^2}\frac{\partial^2 p}{\partial \phi^2} + k^2 p = 0. \qquad (A1)$$

The method of separation of variables suggests the solution is

$$p(r,\phi) = R(r)\Phi(\phi), \qquad (A2)$$

where R and Φ are sole functions of r and ϕ, respectively. Let $k\phi$ be a positive number and $rk > k_\phi$, the angular mode of the solution Φ can be obtained by solving

$$\frac{\partial^2 \Phi}{\partial \phi^2} + k_\phi^2 \Phi = 0, \qquad (A3)$$

with the hard wall boundary condition $\partial\Phi/\partial\phi_{\phi=\phi_0} = \partial\Phi/\partial\phi_{\phi=2\pi-\phi_0} = 0$. One finds

$$k_\phi = \frac{m\pi}{2(\pi - \phi_0)} \qquad (A4)$$

and

$$\Phi(\phi) = \cos(k_\phi(\phi - \phi_0)), \qquad (A5)$$

where m is an integer. A taper slope of -1.72 corresponds to $\pi - \phi_0 \approx 1.044$ and the first symmetrical angular mode ($m=2$) resonates at $k = k\phi \sim 3$.

[1] C. M. Harris, *Handbook of Noise Control* (McGraw-Hill, New York, 1979).

[2] D. D. Reynolds and J. M. Bledsoe, *Algorithms for HVAC Acoustics* (ASHRAE, 1991).

[3] L. E. Kinsler and A. R. Frey, *Fundamentals of Acoustics* (Wiley, New York, 1962).

[4] R. J. Alfredson, "The propagation of sound in a circular duct of continuously varying cross-sectional area," J. Sound Vib. **23**, 433–442 (1972).

[5] R. J. Astley and W. Eversman, "A finite element method for transmission in non-uniform ducts without flow: Comparison with the method of weighted residuals," J. Sound Vib. **57**, 367–388 (1978).

[6] A. H. Nayfeh, J. E. Kaiser, R. L. Marshell, and C. J. Hurst, "A comparison of experiment and theory for sound propagation in variable area ducts," J. Sound Vib. **71**, 241–259 (1980).

[7] M. Utsumi, "An efficient method for sound transmission in nonuniform circular ducts," J. Sound Vib. **227**, 735–748 (1999).

[8] V. L. Streeter and E. B. Wylie, *Fluid Mechanics* (McGraw-Hill, Singapore, 1983).

[9] A. Bayliss and E. Turkel, "Far field boundary conditions for compressible flows," J. Comput. Phys. **48**, 182–199 (1982).

[10] I. Harari, M. Slavutin, and E. Turkel, "Analytical and numerical studies of a finite element PML for the Helmholtz equation," J. Comput. Acoust. **8**, 121–137 (2000).

[11] A. K. M. F. Hussain and A. R. Clark, "On the coherent structure of axisymmetric mixing layer: A flow visualization study," J. Fluid Mech. **104**, 263–294 (1981).

[12] P. M. Morse and K. U. Ingard, *Theoretical Acoustics* (McGraw-Hill, New York, 1968).

[13] M. Razavy, "An acoustic waveguide with variable cross section," J. Acoust. Soc. Am. **86**, 1155–1160 (1989).

[14] P. E. Doak, "Excitation, transmission and radiation of sound from source distributions in hard-walled ducts of finite length (I): The effects of duct cross-section geometry and source distribution space-time pattern," J. Sound Vib. **31**, 1–72 (1973).

[15] N. Amir, V. Pagneux, and J. Kergomard, "A study of wave propagation in varying cross-section waveguides by modal decomposition. Part II. Results," J. Acoust. Soc. Am. **101**, 2504–2517 (1997).

The low frequency reflection characteristics of the fundamental antisymmetric Lamb wave a_0 from a rectangular notch in a plate

M. J. S. Lowe,[a] P. Cawley, J-Y. Kao, and O. Diligent
Department of Mechanical Engineering, Imperial College, London SW7 2BX, United Kingdom

An analysis of the reflection of the fundamental Lamb mode a_0 from surface-breaking rectangular notches in isotropic plates is presented. The results are obtained from finite element time domain simulations together with experimental measurements. Good agreement is found between the simulations and the measurements. Results are shown for a range of notch widths and depths, including the special case of a crack, defined as a zero-width notch. The reflection coefficient, when plotted as a function of the notch width, exhibits a cosinusoidal periodic shape, and this is explained by interference between the separate reflections from the start and the end of the notch. The reflection coefficient, when plotted as a function of notch depth, shows that in general the reflection increases with both frequency and notch depth, but the shapes of the functions are complex and there are some surprising features. An analysis of the reflection from cracks using the S-parameter scattering approach and some simplified descriptions of the crack-opening behavior yields physical explanations of the nature of these reflection functions. It is found that opening of the crack can be described adequately by a quasistatic assumption only when the crack is small, and in other cases a ray theory approach is more representative. The reflection function is shown to be a result of contributions from both the axial stress and the shear stress in the wave, and the relative importance of these varies with the crack depth and the frequency. © *2002 Acoustical Society of America.* [DOI: 10.1121/1.1512702]

PACS numbers: 43.20.Mv [DEC]

I. INTRODUCTION

The work presented in this paper was undertaken as part of ongoing research by the authors into the use of guided ultrasonic waves for the inspection (NDE) of large structures. The primary target for the research is the detection of corrosion and cracks in structures such as oil and chemical storage tanks, pressure vessels and pipelines.[1–3] Conventional NDE of these structures using point-by-point measurements, for example, using thickness gauges to detect wall-thinning, is extremely laborious. Guided waves offer the potential for much more rapid inspection because each measurement inspects a line rather than a point. However guided waves are much more complicated than bulk waves, so that a great deal of research is necessary in order to exploit them reliably in any robust industrial inspection procedure.

Since Lamb's original work on guided waves in elastic plates,[4] the theoretical aspects of guided waves in both flat plates and cylindrical structures have been addressed in many papers. Theoretically the flat plate case is much easier and was developed earlier than the cylindrical case. The publications by Worlton[5,6] anticipated the rapid progress of electronics and instrumentation which would enable the principles of guided wave inspection to be applied effectively in the field. Subsequently many authors have contributed to the knowledge of the behavior of Lamb waves and their application to inspection, for example Refs. 7–13.

In order to achieve the goal of inspecting large plate structures it will be necessary to consider the three-dimensional problem of the interaction of a finite-width guided wave beam with a defect of finite dimensions. Although there are reports of analogous problems in the scattering of bulk waves in solid media, little has been done so far to tackle this problem. Recent work[14] discusses this background and presents solutions for the simplest case of the interaction of the s_0 mode with a through-thickness hole in a plate. Nevertheless there is much to be gained by continuing in parallel to study the nature of the interaction of waves with defects in simpler two-dimensional cases when, despite the necessary approximations relating to the omitted dimension, it is possible to achieve an understanding of the physical nature of the scattering. It is this understanding which will enable the results of the complex three-dimensional problems to be interpreted properly.

A number of authors[10–12,15,16] have already reported such two-dimensional studies of the interaction of the s_0 and a_0 modes with cracks and notches, assuming a plane strain domain. Of these, the recent publication by the authors[16] concentrated particularly on explaining the physical nature of the phenomena observed in the reflection of the s_0 mode from cracks and notches. The approach taken, and which was found to be very helpful in gaining this insight, was to use the S-parameter scattering approach of Auld[17] with both low-frequency and high-frequency approximations for the crack-opening behavior. The present paper presents the equivalent analysis for the a_0 mode.

The paper starts by discussing the nature of the a_0 mode, including its stress and displacement mode shapes; these are key to understanding its scattering behavior. Descriptions

---

[a] Electronic mail: m.lowe@ic.ac.uk

FIG. 1. Group velocity dispersion curves for Lamb waves in a steel plate.

FIG. 2. Displacement and stress mode shapes of the a_0 mode; (a) at 50 kHz mm, (b) at 400 kHz mm, (c) at 1.2 MHz mm.
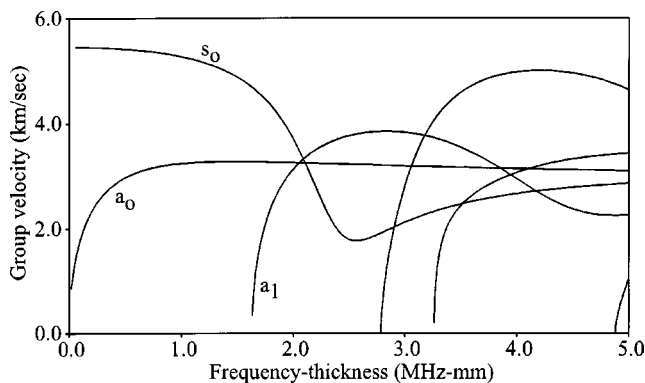
then follow an experimental setup and a finite element analysis procedure. Essentially the finite element analyses were performed as simulated experiments in order to gather a large number of reflection coefficients for notches and cracks of various widths and depths. The real experiments provided results of a significant number of the cases of these predictions and served as validation of the simulation procedure. This comparison is shown in the results section, together with some discussion of the nature of the reflection behavior from notches. Finally the particular case of a crack is examined using the *S*-parameter approach and analytical approximations in order to explain the physical behavior of the scattering.

II. PROPERTIES OF THE A_0 MODE

The dispersion curves of the Lamb waves in an isotropic plate are well known. The most useful curves for long-range NDE are the group velocity curves since these indicate the velocity of a wave packet. Group velocity curves for a steel plate are plotted in Fig. 1. The curves scale linearly with frequency and thickness so that the use of the frequency-thickness scale on the horizontal axis allows these curves to represent a plate of any thickness. These curves and the mode shapes in Fig. 2 were calculated using the computer code DISPERSE.[18,19]

A sensible aim for long-range propagation is to use wave packets whose shapes do not change significantly as they travel, since this aids the interpretation of the received signals as well as maintaining their amplitudes. In general this approach requires the use of narrow-band wave packets whose center frequency is at a nondispersive location on one of the curves, that is at a location where the group velocity does not vary with the frequency. In the case of the a_0 mode, the very low frequency range, below about 500 kHz mm, is therefore rather unattractive because it is extremely dispersive; indeed it is this feature which gives the mode the reputation of being dispersive. However in fact a_0 is one of the least dispersive modes at frequencies above about 1 MHz mm. The optimization of dispersive wave signals for distance and resolution has been discussed by Wilcox *et al.*[20]

For the present investigation we impose an upper limit of frequency thickness of interest of 1.6 MHz mm, being the frequency of the first cutoff mode, a_1. This is somewhat arbitrary because the a_0 mode is potentially useful at higher
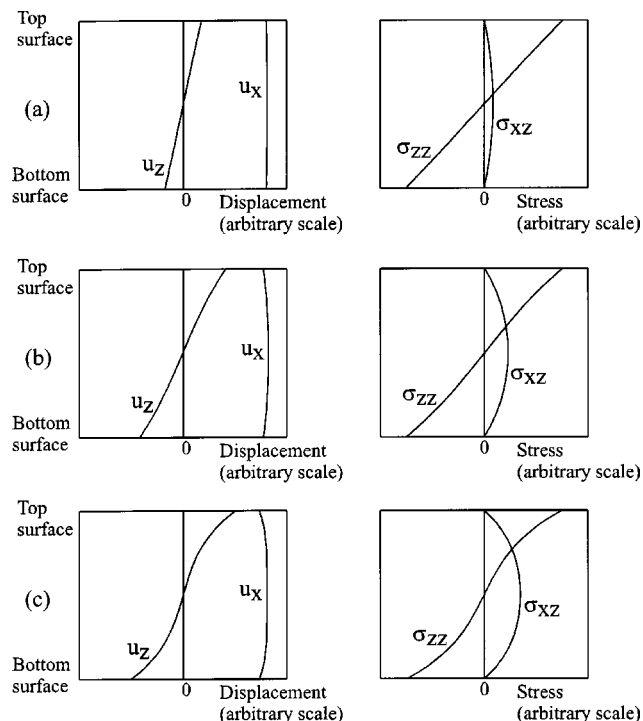
frequencies; indeed at very high frequencies it is exploitable as the Rayleigh wave. However, the approach of the authors for long-range NDE is to avoid multiple modes as far as is possible in order to aid the interpretation of signals. It is therefore desirable to work in the frequency range below the a_1 cutoff so that the a_0 mode is the only propagating antisymmetric mode.

In our earlier study of the s_0 mode,[16] we focused on its very simple displacement and stress mode shapes, and used this to bring physical understanding of the reflection phenomena. The mode shapes of the a_0 mode are not as simple as its symmetric counterpart, so that the equivalent investigation is necessarily more complex. Whereas the s_0 mode was characterized just by its dominant stress component and displacement component in the direction of travel, the a_0 mode additionally has significant shear stress and lateral displacement components. We therefore need to be aware of the influence of two stress components and two displacement components in our analysis. Furthermore, the relative significance of the different components varies with the frequency. These issues will be important for the later discussion in Sec. VI.

Figure 2 shows the displacement and stress mode shapes for the a_0 mode for three different frequencies. The labels refer to the Cartesian coordinate system xyz where x is the direction normal to the surface of the plate, z is the direction of propagation of the wave, and y is the direction normal to the plane of plane strain. The letters u and σ denote displacement and stress, respectively. Only the components which are significant to the analysis are shown, and these all lie in the plane. The shapes are plotted as real-value amplitudes, that is to say each shape is plotted at the phase in the cycle when it has its peak values, also allowing for both positive

J. Acoust. Soc. Am., Vol. 112, No. 6, December 2002

Lowe *et al.*: Reflection of a_0 Lamb wave   2613
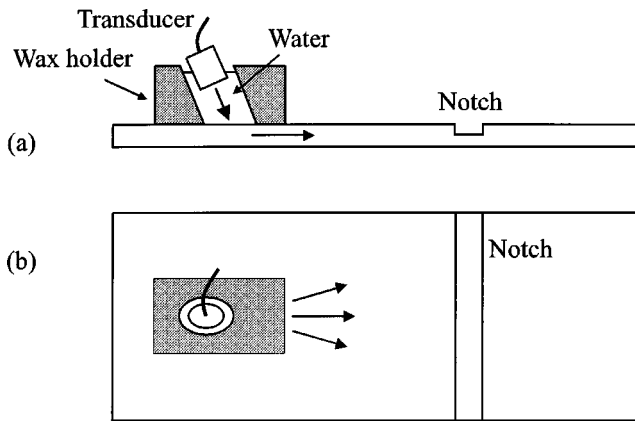
FIG. 3. Schematic diagram of experimental arrangement: (a) side view; (b) plan view.

FIG. 4. Depth profile of fatigue crack, measured by breaking specimen after experiments had been completed.

and negative values. The peak amplitudes do not occur at the same phase in the cycle for each component: if the displacement component u_z is defined (arbitrarily) to have zero phase, then the displacement u_x shown in the figure has a phase of $-\pi/2$ and similarly the stresses σ_{zz} and σ_{xz} have phases of $\pi/2$ and zero, respectively. It can be seen that at the lowest frequency the shapes are simply those of bending of the plate, in which the u_z and σ_{zz} components vary linearly through the depth of the plate, there is a large out-of-plane body motion (u_x), and the shear stress σ_{xz} is small; but at higher frequencies the through-thickness distributions are no longer linear and the shear stress is much more significant.

III. PROCEDURE FOR EXPERIMENTAL MEASUREMENTS

Experiments were performed on steel plates of dimensions 600 mm long, 200 mm wide and 3 mm thick. Rectangular notches were machined across the plates, one in each plate, as shown in Fig. 3. Each notch was positioned about 400 mm from one end of the plate. A range of notches of different widths and depths were machined, so that the effects of notch width and notch depth could be studied. The set of cases which was studied experimentally is identified in Table I. Additionally, a specimen with a fatigue crack was prepared so that the case of a zero-width notch could be included in the study. It was not possible to create a fatigue crack of constant depth across the whole of the plate, but a useful specimen with a crack whose depth varied only gradually across the width was created satisfactorily. The crack was created first in a plate of 50 mm thickness, by machining a notch, then growing the crack by cycling a three-point bending load. Once the crack had grown to a sufficient

TABLE I. Width and depth dimensions of notches used in the experimental study.

Notch depth (mm)	Notch width (mm)					
	0.5	1.0	2.0	3.0	4.0	5.0
0.5	X	X	X	X	X	X
1.0	X					
1.5	X	X	X	X	X	X
2.0	X					
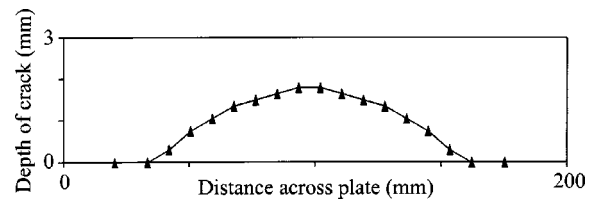
depth, the plate thickness was machined down from the notch side, from 50 mm thick to just 3 mm thick, thereby leaving just the cracked plate. Figure 4 shows the profile of the crack across the central portion of the plate; the profile was measured by breaking the plate after the guided wave experiments had been completed. The depth of the crack can be seen to be about 1.8 mm at the center of the plate where the guided wave measurements were made.

Excitation of the a_0 mode was achieved using the coincidence principle and local water immersion,[11] as illustrated in Fig. 3. The transducer was a broadband piezoelectric immersion device with a center frequency of 500 kHz (Panametrics V301). The local immersion was arranged using a block of paraffin wax;[21] this held the transducer with its axis at a fixed angle of about 40 degrees to the normal to the plate. Although strictly the angle should vary with the position along the dispersion curve, in practice there is sufficient beam spreading of the signal in the water that this fixed angle was sufficient for all of the measurements. The wax block was sealed to the surface of the plate using a rubber O-ring, in order to prevent leakage of the water. Wax was chosen for the holder in order to minimize unwanted reverberations in the water column: the acoustic impedance of the wax is close to that of water so that a lot of the unwanted sound is transmitted from the water into the block; the unwanted sound is then absorbed strongly in the wax. Another advantage of wax is that it is very easy to manufacture a specific block to suit any experiment.

The transducer was excited using a narrow band signal consisting of a toneburst multiplied by a Hanning window function. Typically the duration of the window was chosen to contain 10 cycles. The measurements were made in pulse-echo, that is to say, the same transducer was used both to emit the outgoing wave train and to receive the reflection from the notch or crack. The received signal was amplified and then stored on a digital oscilloscope. Typically 100 averages were taken of each signal in order to reduce incoherent noise. The signal generation, power amplification and received signal amplification were all done using a WAVE-MAKER instrument produced by Macro Design Ltd, UK.

A typical received signal is shown in Fig. 5, showing a number of important features. In this case the notch is rather large, its depth being 67% of the thickness of the plate, and accordingly a large a_0 wave packet is reflected; this of course is the desired signal. Unwanted signals are also present in the figure, but these are separated in time from the wanted signal. Indeed it is this need to separate the wanted and unwanted signals which determines the choice of the dimensions of the plate as well as the location of the trans-
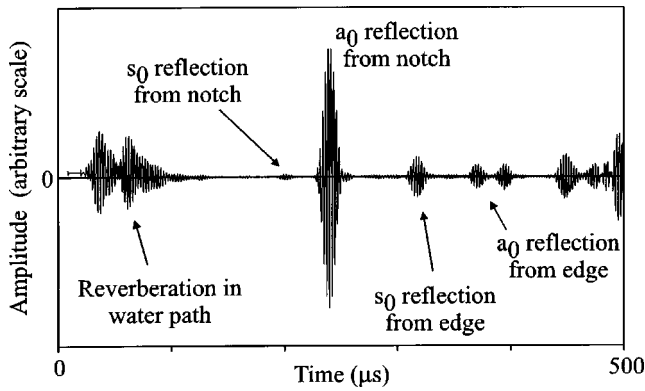
FIG. 5. Typical experimental signal; center frequency is 420 kHz, notch is 2 mm deep (67% of the plate thickness) and 0.5 mm wide.

FIG. 6. Schematic illustration of finite element spatial discretization.

ducer and the notch. The first unwanted signal is the reverberation in the water column in the transducer block; although the wax absorbs much of this, there is nevertheless always some remaining. However the propagation length from the transducer to the notch is sufficient for this to have died away before the reflection from the notch arrives. Just before the a_0 reflection arrives there is a small s_0 signal, created by mode conversion at the notch. In general the s_0 signal is not strongly excited, nor strongly received, because its displacements in the direction normal to the surface of the plate are small and so it does not couple well with the bulk wave in the water column. Therefore this small received signal is probably indicative of quite a large mode-converted s_0 wave. Even though it is small, a signal such as this would still have a significant detrimental effect on the measurements if it was not separated from the a_0 signal. The separation is achieved simply by the distance, the s_0 mode travelling significantly faster than the a_0 mode in the frequency range of the study. Finally, following the a_0 reflection, there are reflections of both a_0 and s_0 from the edge of the plate; again these are sufficiently separated in time.

Processing of the measurements to extract the reflection coefficients was performed in the frequency domain. The reflection coefficient was calculated by dividing the frequency spectrum of the a_0 wave packet by that of a reference signal, the latter representing 100% reflection. Thus the reflection coefficient could be obtained for all values of frequency within the bandwidth of the signal. The reference signal was obtained by measuring the reflection from the square-cut edge of a plate; in this case the distance of propagation was chosen to be the same as it was for the measurements from the notches, thus compensating for attenuation of the signal due to spreading of the beam. There is no other antisymmetric mode within the frequency range of the study, so the reference measurement truly represents unit reflection coefficient.

IV. PROCEDURE FOR FINITE ELEMENT SIMULATIONS

The finite element simulations were performed using a two-dimensional domain, with the assumption of plane strain. The program FINEL, developed at Imperial College,[22] was used for the calculations. A schematic illustration of the spatial models is shown in Fig. 6. A plate of 3 mm thickness
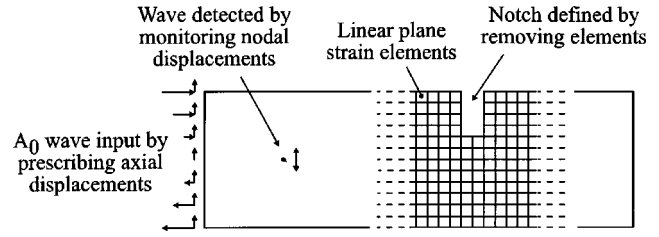
and 600 mm length was modelled for the predictions of the reflections from notches, the thickness being chosen for convenience to match the thickness of the plates used in the experimental work. The elements were defined to be perfectly square in shape. When simulating the experimental measurements of reflection from notches, the meshes used 12 elements through the thickness of the plate, but finer meshes with 24 elements through the thickness were used for the study of the reflections from cracks discussed in Sec. VI. All models respected, with significant margins, the lower limit of spatial discretization of 8 elements per wavelength which the authors have found from experience to be a good limit for accurate modelling.[11,16,23,24] In fact the limiting criterion when designing the meshes for this study was the need for sensible spatial representation of the notches and cracks, rather than the accurate simulation of propagation.

A large number of spatial models was set up in order to model the different notch and crack geometries. Rectangular notches were created simply by removing elements, as illustrated in Fig. 6. Cracks were created by disconnecting the elements at the nodes along the line defining the crack. Visually, therefore, there was no evidence of removal of material from the mesh, there was simply a discontinuity of the material. These approaches for modelling notches and cracks have been found to be reliable in previous studies of guided wave interactions with defects.[16,23] The cracks were surface-breaking, aligned normal to the surface of the plate; they were thus equivalent to the rectangular notches but with zero width.

The temporal model used a similar signal to that used in the experiments, that is, a tone burst in a Hanning window. This was applied as a displacement boundary condition in both the in-plane and the out-of-plane directions at all of the nodes at one end of the plate, as illustrated in Fig. 6. Strictly, the displacement history at each node could be specified such that the mode shape of the a_0 mode is perfectly matched at all frequencies in the bandwidth.[25] However in this case, in order to avoid the excitation of unwanted modes, it is only necessary to ensure that the excitation is perfectly antisymmetric, because the only other mode which could exist at this frequency is the symmetric s_0 mode. Therefore the excitation profile was simply matched to that of the a_0 mode at the center frequency of the signal. Explicit time integration was used, assuming a diagonal mass matrix, thus avoiding the need for global matrix assembly or inversion in the finite element solutions. Constant duration time steps were taken, within the chosen limit of maximum allowable step length of 0.8 L/C, where L is the element length and C is the wave

J. Acoust. Soc. Am., Vol. 112, No. 6, December 2002

Lowe *et al.*: Reflection of a_0 Lamb wave   2615

FIG. 7. Measured and predicted a_0 reflection coefficients from a 0.5 mm deep (17% of plate thickness) notch in a 3 mm thick plate, and various widths: (a) 0.5 mm, 1 mm, and 2 mm; (b) 3 mm, 4 mm, and 5 mm.

FIG. 8. Measured and predicted a_0 reflection coefficient from a 0.5 mm deep (17% of plate thickness) notch in a 3 mm thick plate, expressed as a function of the ratio of the notch width to the wavelength. Measurements and predictions made within frequency range of 420 to 480 kHz.

speed of the fastest wave present. This respects the stability limit of L/C for explicit time integration.[26]

The reflection coefficients were obtained from the simulations by monitoring nodal displacements at a location approximately midway between the excitation end of the plate and the notch or crack. The displacement in the out-of-plane direction (u_x) was monitored at the mid-thickness of the plate, thus ensuring that only the antisymmetric a_0 propagating mode was detected, since the symmetric s_0 mode has zero out-of-plane displacement at this depth. Since the monitoring location was many plate thicknesses away from the notch or crack, it was also considered that any nonpropagating modes generated at the notch would not be present in the received signal. Processing of the signals to calculate the reflection coefficients of the s_0 mode was performed in the frequency domain. This was done in exactly the same manner as was described for the experiments, except that the reference signal was taken simply to be the incident signal as it passed the monitoring location on its way to the notch or crack.

V. RESULTS

Figure 7 shows the measured and predicted reflection coefficient as a function of frequency at six notch widths for a 0.5 mm deep notch (17% of the plate thickness). The experiments were done at three different center frequencies with overlapping bandwidths so there are duplicated results at some frequencies. It can be seen that there is good agreement between the measurements and the predictions for most of the notches, with the exception of the widest two, but even in these cases the trends are similar. Furthermore, even for this modest range of frequency, it is evident that the nature of the frequency dependence of the reflection coefficient is markedly different for the six widths: some of them show increasing reflection with frequency, others decreasing, and the wider notches appear to have a maximum or minimum within the bandwidth.

Figure 8 shows these reflection coefficients for the 0.5 mm deep notch using the alternative horizontal axis of the

ratio of the notch width to the wavelength. The predictions were obtained for a crack and notch widths from 0.25 mm to 5 mm; the widths corresponding to different data points are indicated on the graph. At the lower widths, the bandwidth of the input toneburst was sufficient to give only a small range of notch width to wavelength ratio, but as the width increased, the range of notch width to wavelength ratio which was covered also increased. Again, there is good agreement between the measurements and predictions.

The reflection coefficient in Fig. 8 follows a clear, cosinusoidal pattern, with minima at notch width to wavelength ratios of approximately 25% and 75% and maxima at zero (a crack) and 50%. This behavior is due to interference between the reflection from the start of the notch and the reflection slightly later from the end of the notch. Thus, for example, the reflection from the end of a notch of 25% wavelength arrives back at the start of the notch with a delay corresponding to half a wavelength (length of its return trip), so that it is in opposite phase to the reflection from the start of the notch, and thus causes cancellation. The wave travels at a slightly different speed in the notch region, because the plate is thinner here; this is one reason why the maxima and minima do not occur precisely at multiples of 25%. This phenomenon of interference was also observed, and discussed in greater depth, in the earlier study of the s_0 mode.[16] In that case, in contrast, there is a phase reversal of the reflection from the end of the notch, resulting in maxima rather than minima at 25% and 75% notch widths. An important outcome of this difference is that the reflection from a crack corresponds to a minimum of the reflection function for the s_0 mode but a maximum for the a_0 mode.

Another observation from Fig. 8 is that there appear to be some discontinuities in the function. For example the reflection coefficients at a notch width to wavelength ratio of about 50% are clearly different for 2.5 mm and 3 mm wide notches. A difference of this magnitude could be accepted as an error when considering the experimental measurements, but the discontinuity is plainly evident also in the finite element results. In fact the reason for these discontinuities is that the normalization used in this figure does not encompass all the parameters of the problem. Specifically, the variation
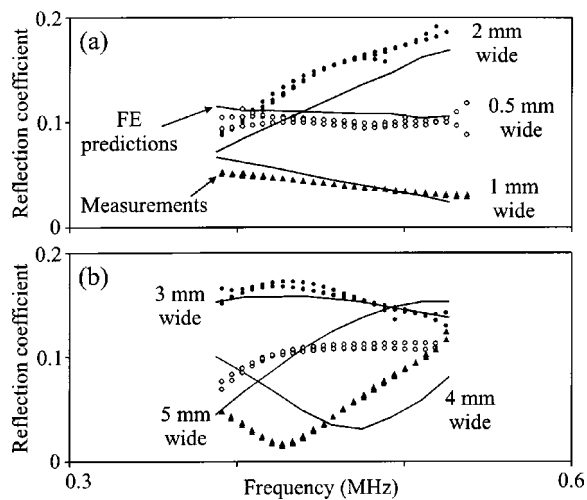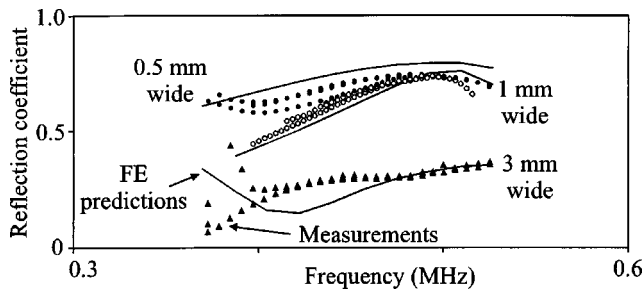
FIG. 9. Measured and predicted a_0 reflection coefficients from a 1.5 mm deep (50% of plate thickness) notch in a 3 mm thick plate, and various widths: 0.5 mm, 1 mm, and 3 mm.

of the reflection with the frequency thickness of the mode is not properly incorporated: in this example the reflection coefficient at a given value of notch width to wavelength ratio would only be the same for two different notch widths if the reflection coefficient was independent of the frequency. A further illustration is given by the presence of several different reflection coefficients, corresponding to different frequencies, when the notch width is zero (the crack case).

Figure 9 shows some examples of the measured and predicted reflection coefficient spectra when the notch is deeper. The depth now is 1.5 mm, corresponding to 50% of the plate thickness. These results show, as expected, much larger values of the reflection coefficient. A similar graph to Fig. 8 was plotted for the results at this notch depth (for brevity not shown here), but in fact it did not exhibit the clear cosinusoidal trend. The principal reason for this is that the interference phenomenon is complicated considerably by the presence also of the s_0 mode. When the notch is deep the a_0 mode arriving at the start of the notch generates a significant s_0 mode in addition to the a_0 mode in the notched region. Furthermore these two modes travel at different speeds, and each may mode convert to both types of wave when reflecting from the end of the notch. Thus the overall reflection is determined by a rather more complex summation of reflected components, and the clean pattern of the reflection function is lost.

Figure 10 shows the measured and predicted reflection coefficient as a function of frequency for four different notch depths, this time fixing the width of the notch at 0.5 mm. Again, the experiments were done at different center frequencies with overlapping bandwidths so there are duplicated results at some frequencies. As in the earlier results, there is good agreement between the measurements and the predictions. It can be seen that the form of the frequency dependence of the reflection coefficient varies considerably with the notch depth. Thus we see that the reflection coefficient is influenced significantly by all of the parameters of the problem: the notch width, the notch depth, and the frequency.

Figure 11 shows the reflection coefficient using another choice of normalization, similar in concept to the width normalization of Fig. 8, but this time with respect to the depth of the notch. Thus the horizontal axis shows the ratio of the depth of the notch to the wavelength of the incident a_0 mode. The notch width is 0.5 mm for all of these results. The coefficients for a range of notch depths are plotted and labeled
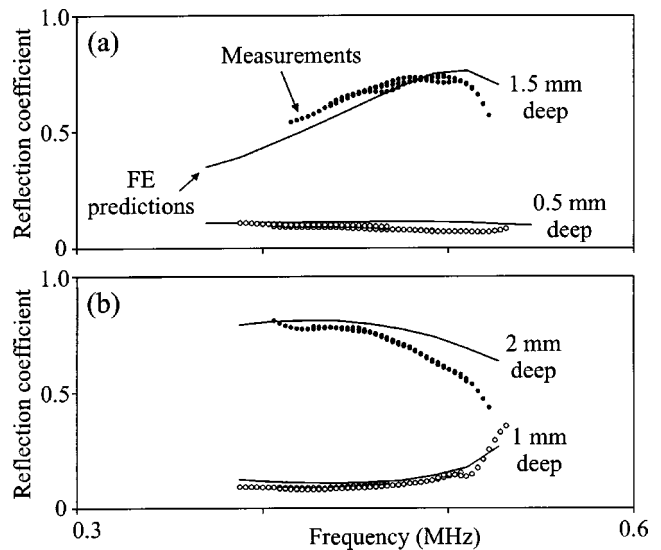
FIG. 10. Measured and predicted a_0 reflection coefficients from a 0.5 mm wide notch and various depths in a 3 mm thick plate: (a) 0.5 mm and 1.5 mm; (b) 1 mm and 2 mm.

on the graph. As with the previous results, good agreement can be seen between the measurements and the finite element predictions. Nevertheless the form of the curve is somewhat surprising. The reflection coefficient rises until the notch depth to wavelength ratio reaches about 10%, then settles on a plateau until the ratio reaches around 20%, then finally rises sharply to a value of 0.8 at a notch depth to wavelength ratio of approximately 30%. The function has this general shape at any width of notch, including the special case of the zero-width notch (crack), and an explanation for it will be presented in the context of the crack in Sec. VI.

The spectrum of the measured reflection coefficient from the fatigue crack is shown in Fig. 12. Several sets of repeated measurements are plotted together, showing good repeatability. Recalling from Fig. 4 that the depth of the fatigue crack varied according to the position across the width of the plate, it is difficult to be sure of the appropriate depth of crack to use in the finite element simulations for comparison with these measurements. The measurements were made at the center of the plate, and in this region the depth of the crack was around 1.75 to 2 mm. Finite element predictions for
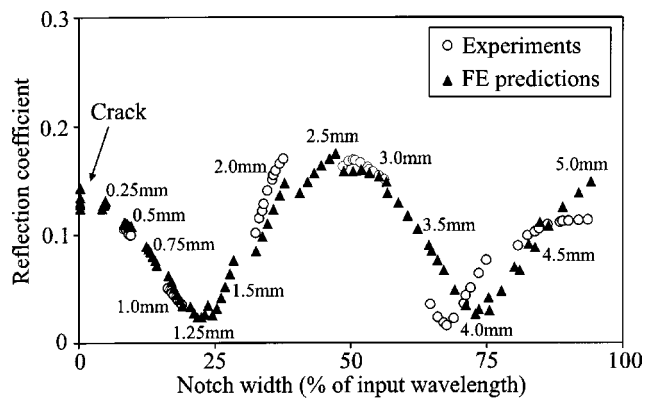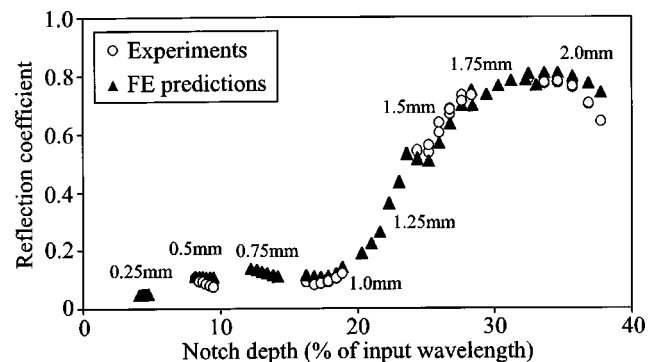

FIG. 11. Measured and predicted a_0 reflection coefficient from a 0.5 mm wide notch in a 3 mm thick plate, expressed as a function of the ratio of the notch depth to the wavelength. Measurements and predictions made within frequency range of 420 to 480 kHz.
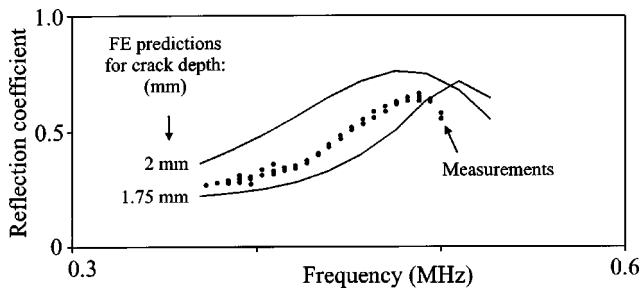
FIG. 12. Measured and predicted a_0 reflection coefficients from a fatigue crack in a 3 mm thick plate.

FIG. 14. Predicted a_0 reflection coefficient from a crack in a plate versus crack depth, for various frequencies.

these two depths are included in Fig. 12, and these convincingly bound the experimental case.

Given the difficulty of creating a fatigue crack whose depth is constant across the width, the measurement of reflection coefficients from different crack depths was not pursued. Nevertheless, the crack is a very important case for practical applications, and deserves special focus, therefore it was studied extensively using finite element simulations. A summary of the results from these simulations is presented in Fig. 13, showing the variation with frequency thickness, and Fig. 14, showing the variation with depth. It is clear that the reflection function is considerably more complex than was found for the s_0 mode in the previous work.[16] Indeed there are details which are strongly counter intuitive in both graphs; for example, Fig. 13 shows that the reflection coefficient decreases with the frequency over a significant bandwidth for several of the curves; similarly Fig. 14 shows that the reflection coefficient decreases with the depth at certain locations. The explanation of the nature of these curves was thus investigated in detail, and this will be presented in Sec. VI.

Finally we should consider some implications of these results to NDE. At first sight it is concerning that the reflection coefficient for notches exhibits the cosinusoidal shape because of the particular widths where the minima occur: the implication is that it may be difficult or impossible to detect notches at these specific widths. In practice, however, the bandwidth of a realistic test signal is likely to be wide enough that a null reflection would not occur; more significantly, defects such as corrosion patches are normally not the shape of perfect notches, and any irregularity is likely to disrupt the interference phenomenon such that the clean
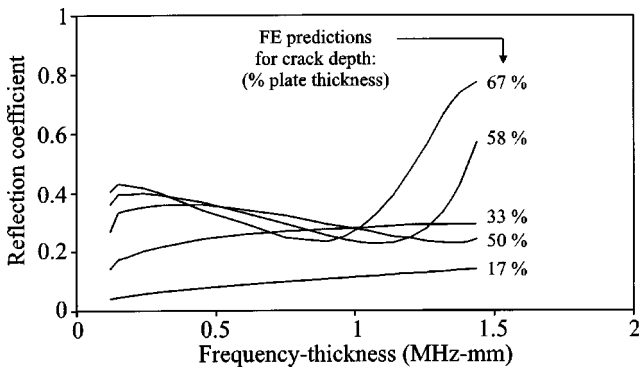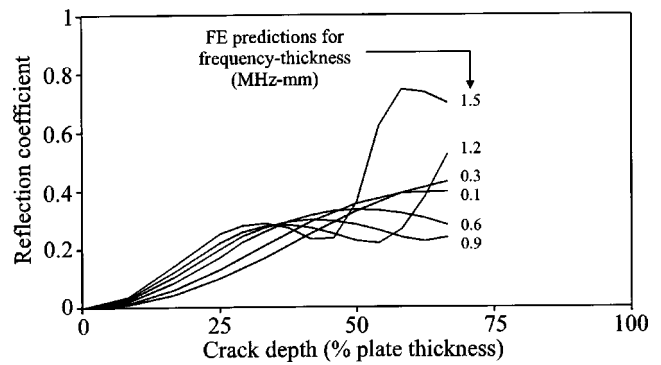
minima do not occur. The variation of the reflection coefficient with depth (Figs. 11 and 14) shows that the a_0 mode is relatively insensitive to cracks or notches whose depth is less than 20%, when compared to the sensitivity at greater depths. Nevertheless, the sensitivity to small defects is still sufficiently good to be useful for NDE. This sensitivity could in principle be improved by increasing the frequency and so reducing the wavelength. However the upper frequency of the results presented here is already close to the a_1 cut off, and above this the behavior will change radically and the signals will become much more complex.

VI. COMPARISON WITH ANALYTICAL APPROXIMATIONS FOR CRACKS

The nature of the reflection coefficient plotted as a function of depth, shown in Figs. 11 and 14, is beyond immediate interpretation and requires some further explanation. From a comparison of the different lines in Fig. 14, it seems that coefficient is strongly influenced by both the depth and the frequency. Comparison of these two figures, one of which is for a notch and the other for a crack, suggests also that the nature of the function is similar for both cracks and notches. We therefore present here an analytical study of the crack case, with the aim of explaining the features of the observed phenomena. We emphasize that our intention is not to propose a better means of making the predictions, but simply to bring some insight to the key physical phenomena.

The source of the complexity is the nature of the a_0 mode: its displacements and stresses vary through the plate thickness and these distributions also vary with the frequency. By comparison with our earlier work on the s_0 mode,[16] it can be expected solely from the increased complexity of these mode shapes that the reflection function for the a_0 mode should be less straightforward then for the s_0 mode. A physical approach to examining the significance of these distributions is to say that in a general sense we should expect the reflection to be strong when a defect or part of a defect is located at a depth where the mode has significant displacements and stresses. This should reveal some evidence of the reasons for the variation both with the depth of the crack and with the frequency.

A powerful way to pursue this idea quantitatively is to use the S-parameter technique derived from the theory of

FIG. 13. Predicted a_0 reflection coefficient from a crack in a plate versus frequency, for various depths of the crack.

reciprocity[17] and previously used to study the s_0 mode.[16] The reflection coefficient for a guided wave incident at a crack in a plate is thus expressed

$$\Delta S_{I,R} = \frac{i\omega}{4} \int_S \Delta u_I \cdot T_R \cdot \hat{n} \, dS, \qquad (1)$$

where $\Delta S_{I,R}$ is the reflection or transmission coefficient; this is the ratio of the particle displacement of the reflected or transmitted wave R to that of the incident wave I. ω is the circular frequency, Δu_I is the vector of the displacements at the crack surface, in both the normal and tangential directions, when the crack opens in response to the incident mode I. Importantly, the amplitude of mode I is defined to be such that it transmits unit power flow per unit cross-sectional area of the wave guide. T_R is the stress field of the reflected mode R if it existed in the uncracked structure and had unit power flow. $\hat{n}$ is the unit vector into the material in the direction normal to the crack face. The integral is calculated over the area S which is the whole of the surface area (both faces) of the crack. The unit power flow of the incident and reflected modes, P_I and P_R, respectively, is defined by[17]

$$P_I = \frac{-i\omega}{4} \int_A (u_I \cdot T_{-I} - u_{-I} \cdot T_I) \cdot \hat{z} \, dA = 1, \qquad (2)$$

$$P_R = \frac{-i\omega}{4} \int_A (u_R \cdot T_{-R} - u_{-R} \cdot T_R) \cdot \hat{z} \, dA = 1 \qquad (3)$$

in which a negative subscript denotes that the displacement or stress is that which would exist in a wave travelling in the opposite direction to that of the power flow. These integrals are over the cross sectional area, A, of the wave guide and the unit vector $\hat{z}$ is in the direction of propagation of the power flow.

The earlier study of the s_0 mode using this approach[16] was relatively simple because only the axial components of displacement and stress had to be considered, and so the S-parameter equation reduced to a simple scalar expression. However, the a_0 mode has two significant stress components, the axial stress (σ_{zz}) and the shear stress (σ_{xz}). These stress mode shapes are shown for three example frequency-thickness values in Fig. 2. Thus the integrand of Eq. (1) consists of two contributions. If we further expand these contributions, introducing the COD (Crack Opening Displacement) as the difference between the displacement at a location on the crack surface and that at the same location on opposite surface of the crack (that is, the displacement jump across the crack), then the integrand becomes

$$\Delta u_I \cdot T_R \cdot \hat{n} = \text{COD}_{\text{axial}} \sigma_{zz} + \text{COD}_{\text{shear}} \sigma_{xz}, \qquad (4)$$

where $\text{COD}_{\text{axial}}$ and $\text{COD}_{\text{shear}}$ relate to the opening of the crack in the axial and shear directions, respectively. These two modes of crack opening are illustrated in Fig. 15.

The COD functions are unknown without full computation of the dynamic problem and it is here that approximation is needed to proceed with the simplified analysis. At one extreme (low frequency or quasistatic approach) it may be assumed that the wavelength is very long compared to the size of the crack. Consequently at the moment when the stress is opening the crack it is assumed that the stress field is
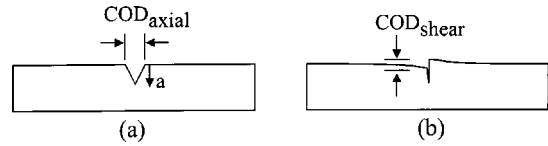
FIG. 15. The two components of crack opening: (a) axial opening and (b) shear opening.

constant over a long length of the plate. This assumption allows the use of a static function for the crack opening due to a remotely applied static load. Such functions for various structural forms, cracks and loads are widely published in the fracture mechanics literature, and we will use one shortly. At the other extreme (high frequency or ray approach), the wavelength is assumed to be sufficiently small compared to the size of the crack that it is acceptable to model the behavior by individual rays simply reflecting from the free surface at the crack. The displacement at any location on the crack surface where the wave is incident can then be assumed simply to be twice the value of the particle displacement of the incident mode at that depth in an uncracked plate, while the displacement on the opposite (downstream) face of the crack is zero.

Previous work by the authors[16,23,27,28] has discussed the nature of these two limiting assumptions in the context of Lamb wave reflections, indicating that for many typical practical cases the reflection characteristic is represented neither by one nor by the other of these limiting assumptions, but lies somewhere between. Nevertheless, the cases with low frequency and small crack sizes tend towards the quasistatic behavior, while the cases with high frequency and large crack size tend towards the ray behavior. Indeed, given the differences between these limiting assumptions, the extent to which they represent the reflection function is an important part of the revelation of the nature of the physical behavior. We will consider each approach in turn now for the a_0 mode incident at the crack.

At very low frequency only the axial component of the stress mode shapes of the a_0 mode is present, and it corresponds closely to the stress distribution of pure bending of the plate. Our quasistatic analysis is based on this case, for which a static COD solution exists in the literature. At higher frequencies the linearity of the axial stress distribution is lost, and furthermore the shear stress becomes significant. Both of these features preclude the pursuit of static solutions because these fields cannot be found in a static analysis but only exist in the dynamic problem. Thus we can only make predictions here of the axial component of the COD. The axial COD at the mouth of the crack for a remotely applied bending moment is given in the handbook by Tada et al.,[29]

$$\text{COD}_{\text{axial,mouth}} = \frac{4\sigma_{zz}a}{E'} V, \qquad (5)$$

where E' is the effective stiffness modulus of the material (in this case the plane strain modulus), a is the depth of the crack, and σ_{zz} is the axial stress at a location remote from the crack, caused by the bending moment. The function V is[29]

J. Acoust. Soc. Am., Vol. 112, No. 6, December 2002

Lowe *et al.*: Reflection of a_0 Lamb wave   2619
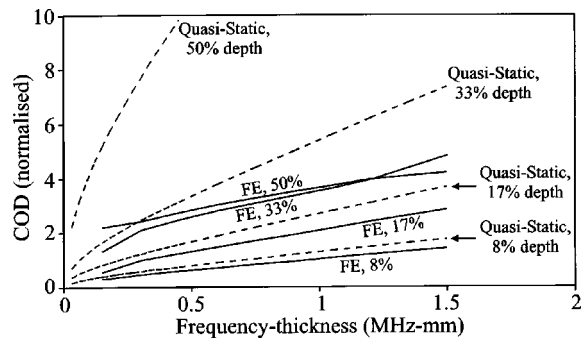
FIG. 16. Axial crack opening displacement (COD) at the mouth of the crack versus frequency thickness: comparison between quasistatic predictions and maximum values monitored during the finite element simulations (FE). Values are normalized to the axial displacement of the wave at the surface of the plate at a location remote from the crack.

FIG. 17. Axial and shear crack opening displacements (COD) at the mouth of the crack versus depth of the crack: comparison between quasistatic predictions and maximum values monitored during the finite element simulations (FE). All values are normalized to the axial displacement of the wave at the surface of the plate at a location remote from the crack.

$$V = 0.8 - 1.7\left(\frac{a}{b}\right) + 2.4\left(\frac{a}{b}\right)^2 + \frac{0.66}{(1-a/b)^2} \tag{6}$$

in which b is the thickness of the plate. The strain-displacement and stress–strain relationships are given by

$$\epsilon_{zz} = i u_z k = i u_z \frac{\omega}{C}, \tag{7}$$

$$\sigma_{zz} = E' \epsilon_{zz}, \tag{8}$$

in which ϵ_{zz} is the axial strain, k is the wave number, C is the phase velocity, and i^2 is -1. For convenience of presentation of the results, we will normalize the COD value to the in-plane component of the displacement (u_z) at the surface of the plate for the power-normalized incident mode when it is remote from the crack, and denote the magnitude of this quantity $\widehat{COD}$. Substitution of Eqs. (7) and (8) into (5) gives this normalized COD at the crack mouth

$$\widehat{COD}_{axial,mouth} = \frac{4a\omega}{C} V. \tag{9}$$

The extent to which this quasistatic estimate of the COD matches the true behavior can be judged by comparing the results of this function with crack opening values taken from the finite element simulations. The COD was obtained from the finite element simulations simply by monitoring the in-plane displacements at the two nodes at the crack mouth; the COD at the mouth is the difference between the displacement values at each side of the mouth.

Figures 16 and 17 show the results of the quasistatic COD predictions together with the finite element simulations, respectively, versus frequency thickness and crack depth. It can be seen that the quasistatic predictions are reasonable when the crack depth is small but only up to about 20% depth. This is most evident in Fig. 17 where the finite element curves can be seen to diverge dramatically for larger depths. Interestingly the limit of validity of the quasistatic predictions is not much affected by frequency: the depth at which the curves start to diverge is fairly similar for the three values of frequency thickness shown. We may conclude therefore that the quasistatic approach will only predict the reflection coefficient adequately for these smaller cracks.
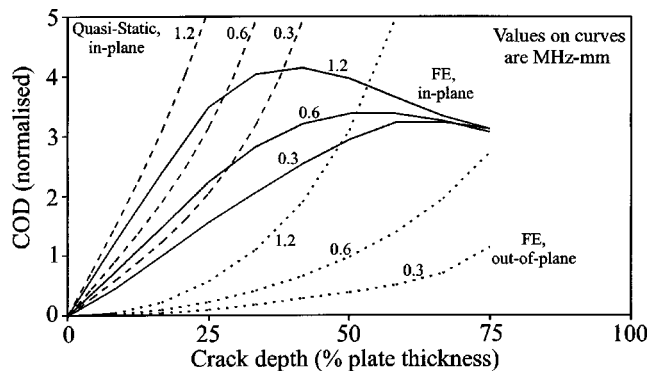
As a point of interest, the shapes of the quasistatic curves reveal the nature of the components of Eq. (9). In Fig. 16 the shape of each curve represents the variation of the ratio of the frequency to the phase velocity; thus these curves would be linear with frequency except for the dispersion of the a_0 mode which is characterized by a varying value of C. In Fig. 17 the shapes show the nature of the function V.

As discussed earlier, there is no static solution for the shear crack opening, so we cannot make the parallel comparison for this contribution to the reflection behavior. Nevertheless, we can monitor the shear opening in the finite element simulations, and these results have been added into Fig. 17. These show that the shear crack opening rises quickly with both the crack depth and the frequency. Indeed this should be expected by observing the stress mode shapes in Fig. 2: the shear component increases with the frequency, and also increases with depth at all frequencies. Returning to Fig. 17, the shapes of the shear crack opening curves can be seen to be smooth and simple, and in this respect they are like the quasistatic curves for the axial opening, and do not have the complexity of shape of the finite element axial curves. A reasonable interpretation of this observation is that the shear opening is probably described adequately by quasistatic-like behavior throughout this range of frequency and crack depth.

Substitution of the COD results into Eq. (4) and then into Eq. (1) yields a prediction of the reflection coefficient function when the a_0 mode is incident. Our interest here is in the strength of the reflection solely of the a_0 mode, and so we use the stresses σ_{zz} and σ_{xz} from this mode in Eq. (4) (the use of the stresses from the s_0 mode could alternatively have been used to predict the strength of mode conversion to that mode). Thus results for the a_0 incident—a_0 reflected reflection coefficient are shown in Fig. 18 for the example frequency-thickness value of 1.2 MHz mm. At this stage we observe only two of the curves in the figure. The dashed curve labeled "quasistatic, axial component only" is the prediction made using the axial COD, following the preceding discussion. The solid curve shows the prediction from the finite element simulation for comparison; this is the result of the full elastodynamic calculation and so should be consid-

2620   J. Acoust. Soc. Am., Vol. 112, No. 6, December 2002

Lowe *et al.*: Reflection of a_0 Lamb wave
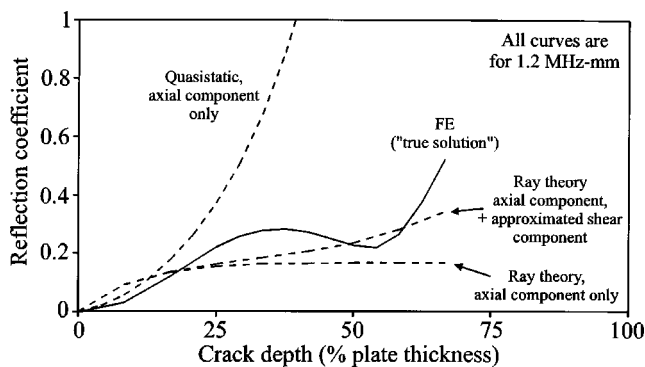
FIG. 18. Predicted a_0 reflection coefficient from a crack in a plate versus crack depth, at 1.2 MHz mm: comparison of results from finite element (FE) simulations and three analytical approximations.

ered to represent the true function. This is in fact one of the curves from Fig. 14. It is no surprise to see that the quasistatic prediction is reasonably representative of the true function for crack depths up to about 20%, but the curves diverge strongly for deeper cracks. This is consistent with the range of validity of the quasistatic COD predictions. It does also confirm that the contribution from the shear component of crack opening is not significant in this range; again, this should be expected because the shear stress is small near the surfaces of the plate.

We turn now to the ray analysis, and consider the axial component of the crack opening. The ray theory assumes simply that any ray arriving at the crack face is reflected perfectly, while any ray arriving at the remaining ligament of the plate is transmitted perfectly. When a wave reflects from a free surface the particle displacement at the surface is twice that of the wave (it is the sum of the displacements of the incident and reflected waves), so we assume that the axial displacement at the surface of the crack is twice the axial particle displacement of the power-normalized a_0 mode. This varies, according to the a_0 mode shape, for all positions along the upstream face of the crack. The downstream face of the crack does not receive any ray and so remains motionless in this analysis. Thus the COD is given just by the value of the upstream surface displacement. Substitution of this COD profile into Eqs. (4) and (1) yields the predicted reflection coefficient function. This has been calculated for the example case of 1.2 MHz mm and has been added into Fig. 18; the curve is labeled "Ray theory, axial component only." It is clear immediately that the ray theory provides a much improved representation of the behavior for the large crack depths, and indeed the agreement with the true solution is moderately good. The fact that the reflection coefficient is approximately constant over the majority of this range can be explained by recognizing that the majority of the contribution of the axial component comes from the near-surface part of the crack; at greater depths the axial displacement of the a_0 mode is small and so the COD contribution here is small. However, only the middle region of the curve is well modelled. At very low values of crack depth the ray theory prediction is not as good as the quasistatic prediction; the COD here is overestimated. Furthermore, at the large depth end of the curves the ray theory does not show any indication of the

rise of reflection coefficient which is evident in the true solution.

Finally therefore we consider the contribution of the shear COD to the predictions of the reflection coefficient. As discussed earlier, it seems probable that the shear COD is described by quasistatic-like behavior rather than ray-like behavior. Indeed, a calculation of the shear contribution using ray theory made very little change to the curves of Fig. 18 (not shown here). Unfortunately there is no quasistatic solution for the COD. Therefore, just by way of illustration, we include here predictions for the shear contribution using the monitored COD from the finite element simulations. The COD at the mouth was taken directly from the data plotted in Fig. 17; the COD at other positions along the crack was then assumed to vary linearly from the surface value to zero at the crack tip. The reflection coefficient results using this shear model together with the ray theory axial model are shown as the fourth and final line in Fig. 18, labeled "ray theory axial component, + approximated shear component." This shows that the shear COD is responsible for the observed upturn of the reflection coefficient at large crack depth. It also shows, as expected, that the shear COD plays no significant part when the crack depth is small.

In summary, it seems that the complexity of the reflection function can be explained by the axial and shear COD contributions, their relative importance at different depths and frequencies according to the mode shapes, and a combination of quasistatic and ray theory behavior. We can identify the key features in three regions of the reflection function.

0–20 % crack depth. The reflection coefficient rises with the crack depth, the increasing function being stronger than linear. The behavior is controlled by the axial component of the COD; shear crack opening is negligible. A quasistatic analysis of the crack opening is a reasonably representative model. Ray theory analysis overestimates the crack opening and so overestimates the reflection coefficient.

20–50 % crack depth. The reflection coefficient varies little over this range of depth. The behavior is still dominated by the axial COD contribution, but the shear COD begins to contribute at the deeper end of this range. Furthermore, the behavior is dominated by the near-surface part of the crack, the deeper parts making little contribution; this explains why the function does not vary much with the crack depth. A ray theory provides moderate representation, and should certainly be the preferred choice for physical interpretation. The quasistatic analysis predicts excessively large opening of the crack and is clearly ruled out.

50% + crack depth. The reflection coefficient rises sharply with the crack depth. This is where the shear crack opening makes its contribution. The shear crack opening displacement cannot be calculated statically; nevertheless the nature of the shear crack opening appears to be similar to quasistatic behavior rather than ray theory.

VII. CONCLUSIONS

Finite element predictions and experimental measurements have been obtained for the reflection coefficient of the

J. Acoust. Soc. Am., Vol. 112, No. 6, December 2002

Lowe *et al.*: Reflection of a_0 Lamb wave   2621

a_0 mode incident at rectangular notches of various widths and depths. Comparison of the measurements and predictions has shown very good agreement.

The examination of the reflection coefficient as a function of the notch width has identified the important phenomenon of the interference between the reflections from the two sides of the notch. This leads to a periodic shape of the function when the notch depth is small or moderate. Conceptually this is similar to the periodic shape of the s_0 reflection coefficient which was published in earlier work, except that the s_0 interference behavior involves a phase reversal whereas the a_0 case does not; consequently the minima of the reflection functions for these two modes do not occur at the same notch widths.

The examination of the reflection coefficient as a function of notch depth has revealed complex shape, and includes some counter-intuitive details, such as some cases of a decrease of reflection coefficient with frequency or notch depth.

An analytical study of the reflection coefficient for a crack has shed light on the complexity of the function of depth. It has been found that the reflection results from contributions both from the axial stress and from the shear stress; these cause the crack to open in the in-plane and shear directions, respectively. The amplitude of the opening is best characterized by a ray theory approach representing just the axial contribution, except in the case of a very shallow crack, when a quasistatic analysis is appropriate, and the case of a very deep crack, when the shear contribution must also be taken into account.

[1] D. Alleyne and P. Cawley, "Optimization of Lamb wave inspection techniques," NDT & E Int. **25**, 11–22 (1992).

[2] D. Alleyne, B. Pavlakovic, M. Lowe, and P. Cawley, "Rapid, long range inspection of chemical plant pipe work using guided waves," Insight **43**, 93–101 (2001).

[3] P. Wilcox, M. Lowe, and P. Cawley, "Lamb and SH wave transducer arrays for the inspection of large areas of thick plates," in *Review of Progress in Quantitative NDE*, edited by D. Thompson and D. Chimenti (Plenum, New York, 2000), Vol. 19, pp. 1049–1056.

[4] H. Lamb, "On waves in an elastic plate," Proc. R. Soc. London, Ser. A **93**, 114–128 (1917).

[5] D. Worlton, "Ultrasonic testing with Lamb waves," Nondestr. Test. (Chicago) **15**, 218–222 (1957).

[6] D. Worlton, "Experimental confirmation of Lamb waves at megacycle frequencies," J. Appl. Phys. **32**, 967–971 (1961).

[7] I. A. Viktorov, *Rayleigh and Lamb waves* (Plenum, New York, 1970).

[8] T. Mansfield, "Lamb wave inspection of aluminium sheet," Mater. Eval. **33**, 96–100 (1975).

[9] S. Rokhlin, "Resonance phenomena of Lamb waves scattering by a finite crack in a solid layer," J. Am. Ceram. Soc. **69**, 922–928 (1981).

[10] J. Paffenholz, W. Fox, X. Gu, G. Jewett, S. Datta, and H. Spetzler, "Experimental and theoretical study of Rayleigh-Lamb waves in a plate containing a surface-breaking crack," Res. Nondestruct. Eval. **1**, 197–217 (1990).

[11] D. Alleyne and P. Cawley, "The interaction of Lamb waves with defects," IEEE Trans. Ultrason. Ferroelectr. Freq. Control **39**, 381–397 (1992).

[12] Y. Cho, D. Hongerholt, and J. Rose, "Lamb wave scattering analysis for reflector characterization," IEEE Trans. Ultrason. Ferroelectr. Freq. Control **44**, 44–52 (1997).

[13] T. Ghosh, T. Kundu, and P. Karpur, "Efficient use of Lamb modes for detecting defects in large plates," Ultrasonics **36**, 791–801 (1998).

[14] O. Diligent, T. Grahn, A. Boström, P. Cawley, and M. Lowe, "The low-frequency reflection and scattering of the S_0 Lamb mode from a circular through-thickness hole in a plate: Finite Element, analytical and experimental studies," J. Acoust. Soc. Am. **112**, 2589–2601 (2002).

[15] Y. Cho and J. Rose, "A boundary element solution for a mode conversion study on the edge reflection of Lamb waves," J. Acoust. Soc. Am. **99**, 2097–2109 (1996).

[16] M. J. S. Lowe and O. Diligent, "The low frequency reflection characteristics of the fundamental symmetric Lamb wave S_0 from a rectangular notch in a plate," J. Acoust. Soc. Am. **111**, 64–74 (2002).

[17] B. Auld, *Acoustic Fields and Waves in Solids* (Krieger, Malabar, Florida, 1990), Vol. 2.

[18] M. Lowe, "Matrix techniques for modeling ultrasonic waves in multilayered media," IEEE Trans. Ultrason. Ferroelectr. Freq. Control **42**, 525–542 (1995).

[19] B. Pavlakovic, M. Lowe, D. Alleyne, and P. Cawley, "DISPERSE: A general purpose program for creating dispersion curves," in *Review of Progress in Quantitative NDE*, edited by D. Thompson and D. Chimenti (Plenum, New York, 1997), Vol. 16, pp. 185–192.

[20] P. Wilcox, M. Lowe, and P. Cawley, "The effect of dispersion on long range inspection using ultrasonic guided waves," NDT & E Int. **34**, 1–9 (2001).

[21] R. Dalton, P. Cawley, and M. Lowe, "The potential of guided waves for monitoring large areas of metallic aircraft fuselage structure," J. Nondestruct. Eval. **20**, 29–46 (2001).

[22] D. Hitchings, "FE77 User Manual," Tech. Rep., Imperial College of Science, Technology and Medicine, London, UK, 1994.

[23] D. Alleyne, M. Lowe, and P. Cawley, "The reflection of guided waves from circumferential notches in pipes," J. Appl. Mech. **65**, 635–641 (1998).

[24] M. Lowe, R. Challis, and C. Chan, "The transmission of Lamb waves across adhesively bonded lap joints," J. Acoust. Soc. Am. **107**, 1333–1345 (2000).

[25] B. Pavlakovic, D. Alleyne, M. Lowe, and P. Cawley, "Simulation of Lamb wave propagation using pure mode excitation," in *Review of Progress in Quantitative NDE*, edited by D. Thompson and D. Chimenti (Plenum, New York, 1998), Vol. 17, pp. 1003–1010.

[26] K.-J. Bathe, *Finite Element Procedures in Engineering Analysis* (Prentice-Hall, Englewood Cliffs, NJ, 1982).

[27] M. Lowe, D. Alleyne, and P. Cawley, "The mode conversion of a guided wave by a part-circumferential notch in a pipe," J. Appl. Mech. **65**, 649–656 (1998).

[28] M. Lowe, "Characteristics of the reflection of Lamb waves from defects in plates and pipes," in *Review of Progress in Quantitative NDE*, edited by D. Thompson and D. Chimenti (Plenum, New York, 1998), Vol. 17, pp. 113–120.

[29] H. Tada, P. Paris, and G. Irwin, *The Stress Analysis of Cracks Handbook* (Del Research Co., St. Louis, MO, 1973).

Analysis of piezoelectric strip waveguides based on the effective index and pseudospectral element methods

Oscar A. Peverini[a)]
IEIIT–CNR, C.so Duca degli Abruzzi 24, 10129 Torino, Italy

Renato Orta
Dipartimento di Elettronica Politecnico di Torino, C.so Duca degli Abruzzi 24, 10129 Torino, Italy

Riccardo Tascone
IEIIT–CNR, C.so Duca degli Abruzzi 24, 10129 Torino, Italy

Integrated acousto-optical circuits in $LiNbO_3$ are attractive devices for applications especially in advanced WDM systems. In order to increase the scale of integration and to reduce the RF driving power of these devices, one promising approach is to use acoustical waveguides with smaller lateral dimensions. In this paper the combination of a pseudospectral elements method (PSEM) and an effective index method (EIM) for the analysis of film-loaded surface acoustic waveguides (SAWG's) is presented. Numerical results demonstrate the exponential rate of convergence of the PSEM and agree with the computations performed via the transverse resonance technique. Due to the exponential rate of convergence of the PSEM and to a mapping transformation in the substrate, the piezoelectric problem in the depth direction of the structures is evaluated by a low number of Legendre polynomials. The method is applied to the analysis of several layered SAWG's of practical interest for AO devices, such as $metal/SiO_2/X-Y\,LiNbO_3$, in which the metal is either Au, Al, In, or Ti. © *2002 Acoustical Society of America.* [DOI: 10.1121/1.1512293]

PACS numbers: 43.20.Mv, 43.35.Pt, 43.35.Sx [DEC]

I. INTRODUCTION

Tunable filters and wavelength selective switches are key components for a variety of applications especially in wavelength division multiplexed (WDM) optical communication systems and for optical instrumentation. In particular, integrated acousto-optical filters and switches in $LiNbO_3$ are very attractive because of a broad tuning range, a fast tuning speed and specifically because of their unique property of simultaneous filtering capability.[1,2]

These devices consist of a combination of collinear acousto-optical polarization converters and polarizing elements. The operation of the acousto-optical polarization converter is based on the interaction between two waveguide optical modes with orthogonal polarizations (TE, TM) and the guided surface acoustic wave (SAW). The polarization conversion is maximized if the phase-matching condition $|\beta_{TE} - \beta_{TM}| = K_{AC}$ is satisfied, i.e., the difference of the propagation constants of the TE and TM polarized modes β_{TE}, β_{TM} has to be matched by the SAW propagation constant K_{AC}. A wavelength-selective behavior is achieved since $\beta_{TE} - \beta_{TM}$ varies with the optical wavelength. A challenge for improving these devices is to increase the scale of integration and to reduce the RF driving power. A promising approach to increase the integration density and to reduce the RF driving power is to use acoustical waveguides with smaller lateral dimensions.

The most common technique to fabricate SAW waveguides (SAWG's) is via Ti-indiffusion into the cladding regions of the waveguide. In spite of low losses, these SAWG's are quite wide (≈ 110 μm) because of the small relative change of the SAW velocity induced by Ti-indiffusion and the need for sufficient distance between the Ti cladding regions of the SAWG and the Ti optical waveguides. Recently, it has been demonstrated that these disadvantages can be overcome by using a new film-loaded SAWG,[3] in which the SAW velocity is decreased in the core region by deposition of an optically transparent material such as In_2O_3-doped SiO_2. In the case of a pure SiO_2 film the confinement of the SAW is almost the same as in the Ti-indiffused SAWG, but it can be remarkably increased by adding the In_2O_3 compound. The guiding mechanism in this new SAWG depends on the combination of mass-loading effect, electrical short-circuiting effect and a stiffness effect. In order to perform a detailed analysis of piezoelectric film loaded SAWG's, as sketched in Fig. 1, in this paper we present a numerical method, which is based on the combination of the effective index method and the pseudo-spectral elements method. The effective index method requires the computation of the SAW velocity in each planar piezoelectric layered structure composing the 3D waveguide. Planar stratified media are typically analyzed along the depth direction via the T-matrix model,[4,5] matrix methods[6–8] and the impedance model.[9] The propagation constants of guided modes can then be found by imposing the transverse resonance condition and solving the resulting transcendental dispersion equation. Though complex-function theory can be invoked, automated search for the roots is however a hard task and some of them may be missed. To overcome these drawbacks we developed a pseudospectral elements method

_____

[a)]Electronic mail: peverini@athena.polito.it
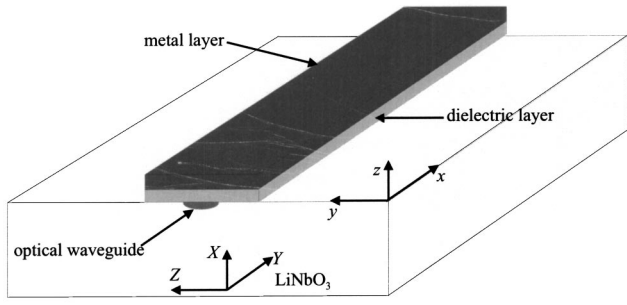
FIG. 1. Film-loaded surface acoustic waveguide with crystal (X,Y,Z) and coordinate (x,y,z) axes.

FIG. 2. Planar multilayered structure and coordinate system.

that allows the computation of modal fields and propagation constants without solving any transcendental equation. The basic concept is the expansion of the fields on a set of functions. The differential problem turns into an algebraic generalized eigenvalue one, where the eigenvalues are the propagation constants; the field configuration are readily obtained as linear combinations of the expansion functions, the weights of which are the eigenvector elements. In principle, an entire domain basis might be chosen,[10] but this would cause a slow (power-law) convergence, owing to the fact that the fields are infinitely differentiable everywhere in space but at an interface. Hence, separate bases in each piezoelectric layer are required to ensure a correct modeling of the discontinuities. An exponential convergence ensues adopting Legendre polynomials as expansion functions.[11] Moreover, the sought mode is a SAW, that is tightly confined at the surface of the substrate; therefore, it is convenient to introduce a mapping transformation in the substrate, in order to enhance the convergence properties of the method. As a consequence of the mapping, the coefficients of the differential equations describing the piezoelectric problem in the parent domain are no longer constant and, then, a pseudospectral element method has to be adopted. A similar method was applied in Ref. 12 to study the modes of a slab with continuously varying parameters.

II. EFFECTIVE INDEX METHOD

A simple and computational efficient method of investigation of three-dimensional piezoelectric waveguides, Fig. 1, is the effective index method.[13,14] The procedure is similar to that used in the case of optical stripe waveguides. A SAW in a piezoelectric material like $LiNbO_3$ is completely described by four components: the elongations along the three geometrical axes and the electrical potential. For X-cut, Y-propagating SAW's the amplitude of the elongation parallel to the crystalline X direction (geometrical z axis in Fig. 1) is dominant.[15] Therefore, one assumes that the SAW can be described reasonably well in a scalar approximation by this component only. Similarly to the EIM for optical strip waveguides, a reduction to a one dimensional problem is performed by introducing a velocity profile $V_{SAW}(y)$, which refers to a SAW propagating along the x direction and which is a function of the transverse y direction. This profile is obtained by applying the pseudospectral elements method to the two-dimensional modal analysis in the depth direction of
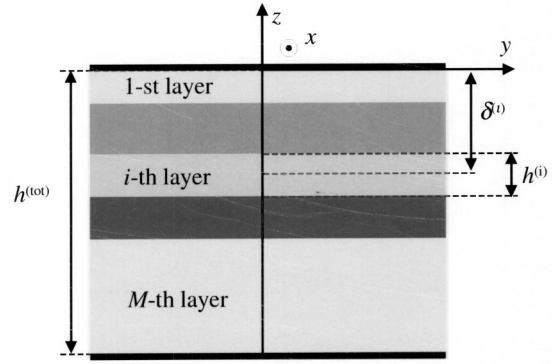
the piezoelectric layered structure. Once the velocity profile $V_{SAW}(y)$ has been computed, one needs to handle the following transversal, scalar and one-dimensional wave equation:

$$\left\{\frac{\partial^2}{\partial y^2}-(2\pi f)^2\left(\frac{1}{V_{SAW,eff}^2}-\frac{1}{V_{SAW}^2(y)}\right)\right\}u_z(y)=0, \qquad (1)$$

where $u_z(y)$ and $V_{SAW,eff}$ are, respectively, the transversal field distribution of the elongation along the z direction and the propagation velocity of the guided SAW. In the EIM the influence of the strip corners is not taken into account and this approximation appears to be quite reasonable for sufficiently flat strips. By assuming that $u_z(y)$ and its first derivatives are continuous at the boundaries, one can easily solve this equation and obtain the modes of the structure. Furthermore, by applying a beam propagation method to the scalar equation (1), one can determine the elastic field distributions in amplitude and phase for arbitrarily shaped acoustic structures including S bends and coupled or tapered waveguides.[16]

III. 2D PIEZOELECTRIC PROBLEM IN THE DEPTH DIRECTION

A. Formulation

As explained above, the first step in the application of the EIM is the determination of the velocity V_{SAW} in the different multilayered structures composing the 3D SAWG's. Therefore, one has to solve the vectorial piezoelectric wave equations in two-dimensional multilayered structure depicted in Fig. 2. The ith layer is characterized by its stiffness tensor $\mathbf{c}^{(i)}$ measured under constant electric field conditions, its piezoelectric tensor $\mathbf{e}^{(i)}$, its permittivity tensor $\boldsymbol{\epsilon}^{(i)}$ measured under constant strain conditions and its mass density $\rho^{(i)}$. The orientation of the crystal axes is specified in terms of the Euler Angles $(\Phi_{EA},\Theta_{EA},\Psi_{EA})$. In the usual *quasistatic approximation*, according to which the rotational part of the electric field $\mathbf{E}$ as well as the magnetic field $\mathbf{H}$ are neglected, the field equations governing the wave propagation in each piezoelectric medium can be written according to the symbolic notation[17] as

$$\boldsymbol{\nabla}_s^\dagger\cdot\mathbf{c}^{(i)}:\boldsymbol{\nabla}_s\mathbf{v}-\rho^{(i)}\frac{\partial^2\mathbf{v}}{\partial t^2}=-\boldsymbol{\nabla}_s^\dagger\cdot\left(\mathbf{e}^{(i)}\cdot\frac{\partial\boldsymbol{\nabla}\Phi}{\partial t}\right), \qquad (2)$$

$$0 = -\mu_0 \nabla \cdot \left(\epsilon^{(i)} \frac{\partial^2 \nabla \Phi}{\partial t^2} \right) + \mu_0 \nabla \cdot \left(\mathbf{e}^{(i)\dagger} : \nabla_s \frac{\partial \mathbf{v}}{\partial t} \right), \tag{3}$$

where μ_0 is the vacuum permeability, $\mathbf{v} = [v_x \ v_y \ v_z]^\dagger = J\omega[u_x \ u_y \ u_z]^\dagger$ is the vector of the acoustical velocities (time derivatives of the elongations u_i), and Φ is the electrical potential. Moreover, the symbol $[\ ]^\dagger$ denotes transposition operation and ∇_s and ∇ are the following operators:

$$\nabla_s = \begin{bmatrix} \dfrac{\partial}{\partial x} & 0 & 0 & 0 & \dfrac{\partial}{\partial z} & \dfrac{\partial}{\partial y} \\[8pt] 0 & \dfrac{\partial}{\partial y} & 0 & \dfrac{\partial}{\partial z} & 0 & \dfrac{\partial}{\partial x} \\[8pt] 0 & 0 & \dfrac{\partial}{\partial z} & \dfrac{\partial}{\partial y} & \dfrac{\partial}{\partial x} & 0 \end{bmatrix}^\dagger,$$

$$\tag{4}$$

$$\nabla = \begin{bmatrix} \dfrac{\partial}{\partial x} \\[8pt] \dfrac{\partial}{\partial y} \\[8pt] \dfrac{\partial}{\partial z} \end{bmatrix}.$$

Besides, within each layer the following piezoelectric constitutive relations hold:

$$\mathbf{T} = -\mathbf{e}^{(i)} \cdot \mathbf{E} + \mathbf{c}^{(i)} : \mathbf{S}, \tag{5}$$

$$\mathbf{D} = \epsilon^{(i)} \cdot \mathbf{E} + \mathbf{e}^{(i)\dagger} : \mathbf{S}, \tag{6}$$

where, according to the symbolic notation, the stress vector $\mathbf{T}$ and the strain vector $\mathbf{S}$ are defined as

$$\mathbf{T} = [T_{xx} \ T_{yy} \ T_{zz} \ T_{yz} \ T_{xz} \ T_{xy}]^\dagger, \tag{7}$$

$$\mathbf{S} = [S_{xx} \ S_{yy} \ S_{zz} \ 2S_{yz} \ 2S_{xz} \ 2S_{xy}]^\dagger. \tag{8}$$

The boundary conditions at the interface between two layers require the continuity of the normal components of the stress, $\mathbf{T}_z = [T_{xz} \ T_{yz} \ T_{zz}]^\dagger$, of the particle displacement velocity, $\mathbf{v}$, of the normal component of the electrical displacement, D_z, and of the electrical potential, Φ. Although acoustical modes decaying in the substrate are not influenced by the boundary condition on the bottom surface of the substrate (M layer), the clamped condition, $\mathbf{v} = 0$, and the short-circuiting condition, $\Phi = 0$, are enforced on that surface. Finally, on the upper surface of the first layer the stress-free condition, $\mathbf{T}_z = 0$, and the open-circuit condition, $D_z = 0$, are imposed. The last condition is approximated but its accuracy is acceptable when the dielectric permittivity of the crystal is large.

For modal harmonic solutions of Eqs. (2) and (3), each field component is of the form $C_l \exp(J(\omega t - \xi x - \eta y))$, where C_l is an appropriate constant factor and ξ and η are the wave vector components along the x direction and y direction, respectively. In the 2D analysis both the structures and the fields are assumed to be uniform along the y direction and, then, hereinafter η is set to zero, i.e., $\partial/\partial_y = 0$. Therefore, the operators ∇_s and ∇ can be decomposed as

$$\nabla_s = -J\xi \mathbf{A}^\dagger + \mathbf{F}^\dagger \frac{d}{dz}, \quad \nabla = -J\xi \mathbf{M} + \mathbf{N} \frac{d}{dz}, \tag{9}$$

where the matrix $\mathbf{A}$, $\mathbf{F}$, $\mathbf{M}$, and $\mathbf{N}$ are reported in the Appendix. Insertion of the representation (9) of the dyadic operators in Eqs. (2) and (3) yields the following second-order differential system for the ith medium:

$$-\xi^2 \mathbf{Q}_2^{(i)} \mathbf{\Psi}^{(i)} - J\xi \mathbf{Q}_1^{(i)} \frac{d\mathbf{\Psi}^{(i)}}{dz} + \mathbf{Q}_0^{(i)} \mathbf{\Psi}^{(i)} + \mathbf{Q}_0^{z,z(i)} \frac{d^2 \mathbf{\Psi}^{(i)}}{dz^2} = 0, \tag{10}$$

where the state vector is defined as $\mathbf{\Psi}^{(i)} = [v_x^{(i)} \ v_y^{(i)} \ v_z^{(i)} \ J\Phi^{(i)}]^\dagger$. This definition of the state vector leads to real matrices $\mathbf{Q}_2^{(i)}$, $\mathbf{Q}_1^{(i)}$, $\mathbf{Q}_0^{(i)}$, and $\mathbf{Q}_0^{z,z(i)}$ for lossless media. These matrices are reported in the Appendix and depend on the physical constants of the layer and on the angular frequency ω.

The continuity and the boundary conditions must also be written in terms of the state vector $\mathbf{\Psi}^{(i)}$ and, then, one needs to represent $\mathbf{T}_z^{(i)}$ and $D_z^{(i)}$ as functions of $\mathbf{\Psi}^{(i)}$. By substitution of Eq. (9) into the following relationships:

$$\mathbf{S} = \frac{\nabla_s \mathbf{v}}{J\omega}, \tag{11}$$

$$\mathbf{E} = -\nabla \Phi, \tag{12}$$

and using Eqs. (5) and (6) one obtains

$$\mathbf{\Gamma}^{(i)} = -J\xi \mathbf{P}_1^{(i)} \mathbf{\Psi}^{(i)} + \mathbf{P}_0^{(i)} \frac{d\mathbf{\Psi}^{(i)}}{dz}, \tag{13}$$

where the vector $\mathbf{\Gamma}^{(i)} = [JT_{xz}^{(i)} \ JT_{yz}^{(i)} \ JT_{zz}^{(i)} \ J\omega D_z^{(i)}]^\dagger$ is defined such that the matrices $\mathbf{P}_1^{(i)}$ and $\mathbf{P}_0^{(i)}$ (see the Appendix) are real for lossless media. Therefore, the continuity conditions between the ith and $(i+1)$th layers can be written in $z = -\delta^{(i)} - h^{(i)}/2$ as

$$\mathbf{\Psi}^{(i)} = \mathbf{\Psi}^{(i+1)}, \tag{14}$$

$$-J\xi \mathbf{P}_1^{(i)} \mathbf{\Psi}^{(i)} + \mathbf{P}_0^{(i)} \frac{d\mathbf{\Psi}^{(i)}}{dz}$$
$$= -J\xi \mathbf{P}_1^{(i+1)} \mathbf{\Psi}^{(i+1)} + \mathbf{P}_0^{(i+1)} \frac{d\mathbf{\Psi}^{(i+1)}}{dz}. \tag{15}$$

The stress-free and open-circuit conditions on the upper surface of the first layer are stated as

$$-J\xi \mathbf{P}_1^{(1)} \mathbf{\Psi}^{(1)} + \mathbf{P}_0^{(1)} \frac{d\mathbf{\Psi}^{(1)}}{dz} = 0 \quad \text{in } z = 0 \tag{16}$$

and the clamped and short-circuiting conditions on the bottom surface of the Mth layer have the form

$$\mathbf{\Psi}^{(M)} = 0 \quad \text{in } z = -h^{\text{tot}}. \tag{17}$$

Equation (10), completed with the relevant continuity and boundary conditions, is a quadratic differential eigenvalue, where the eigenvalue is proportional to the mode propagation constant ξ. This equation, however, can be turned into a linear problem by introducing an auxiliary unknown $\mathbf{\Theta}^{(i)} = -J\xi \mathbf{\Psi}^{(i)}$. In terms of it, the differential system (10) becomes

$$-J\xi\mathbf{Q}_2^{(i)}\mathbf{\Theta}^{(i)}-J\xi\mathbf{Q}_1^{(i)}\frac{d\mathbf{\Psi}^{(i)}}{dz}+\mathbf{Q}_0^{(i)}\mathbf{\Psi}^{(i)}+\mathbf{Q}_0^{z,z(i)}\frac{d^2\mathbf{\Psi}^{(i)}}{dz^2}=0,$$

$$(18)$$

whereas the continuity (15) and boundary (16) conditions are rewritten, respectively, as

$$\mathbf{P}_1^{(i)}\mathbf{\Theta}^{(i)}+\mathbf{P}_0^{(i)}\frac{d\mathbf{\Psi}^{(i)}}{dz}=\mathbf{P}_1^{(i+1)}\mathbf{\Theta}^{(i+1)}+\mathbf{P}_0^{(i+1)}\frac{d\mathbf{\Psi}^{(i+1)}}{dz}$$

$$\text{in } z=-\delta^{(i)}-h^{(i)}/2 \qquad (19)$$

and

$$\mathbf{P}_1^{(1)}\mathbf{\Theta}^{(1)}+\mathbf{P}_0^{(1)}\frac{d\mathbf{\Psi}^{(1)}}{dz}=0 \quad \text{in } z=0. \qquad (20)$$

B. Spectral elements method

Equation (18) is a differential equation with piecewise constant coefficients, so that its solution can be obtained by standard analytical techniques. In this way, the eigenvalue ξ is computed by solving a complicated transcendental equation, which is obtained by setting to zero a suitable determinant. This is the well-known transverse resonance technique. The solutions of this equation are in general complex (also for lossless media) and may be difficult to find. For this reason, in this paper Eq. (18) is solved by the Lanczos method,[18] which allows the use of standard eigenvalue techniques. The method consists in representing the unknowns on a set of Legendre polynomials $\{P_n(r)\}_{n=0}^{N_i-1}$ defined in the interval $r\in[-1,1]$ (parent domain). Each object domain is uniformly mapped onto the parent domain by the mapping function:

$$r=\frac{2}{h^{(i)}}(z+\delta^{(i)}),$$

$$\forall z\in[-\delta^{(i)}-h^{(i)}/2,-\delta^{(i)}+h^{(i)}/2]. \qquad (21)$$

Hence, one writes each scalar component of the state vector $\mathbf{\Psi}^{(i)}$ in the parent domain as

$$\Psi_l^{(i)}=\sum_{n=0}^{N_i-1}\psi_{l,n}^{(i)}P_n(r), \quad l=1,...,4. \qquad (22)$$

By defining the vectors $\mathbf{b}_n^{(i)}=[\psi_{1,n}^{(i)}\ \psi_{2,n}^{(i)}\ \psi_{3,n}^{(i)}\ \psi_{4,n}^{(i)}]^\dagger$ we can express $\mathbf{\Psi}^{(i)}$ and $\mathbf{\Theta}^{(i)}$ as

$$\mathbf{\Psi}^{(i)}=\sum_{n=0}^{N_i-1}\mathbf{b}_n^{(i)}P_n(r), \quad \mathbf{\Theta}^{(i)}=\sum_{n=0}^{N_i-1}\mathbf{c}_n^{(i)}P_n(r), \qquad (23)$$

where

$$\mathbf{c}_n^{(i)}=-J\xi\mathbf{b}_n^{(i)}. \qquad (24)$$

The introduction of representation (23) in Eq. (18) and the projection on the mth Legendre polynomial lead to the following linear algebraic system:

$$-J\xi\mathbf{Q}_2^{(i)}\sum_{n=0}^{N_i-1}\mathbf{c}_n^{(i)}\int_{-1}^1 P_n(r)P_m(r)dr-\frac{J2\xi}{h^{(i)}}\mathbf{Q}_1^{(i)}$$

$$\times\sum_{n=0}^{N_i-1}\mathbf{b}_n^{(i)}\int_{-1}^1\frac{dP_n(r)}{dr}P_m(r)dr$$

$$+\mathbf{Q}_0^{(i)}\sum_{n=0}^{N_i-1}\mathbf{b}_n^{(i)}\int_{-1}^1 P_n(r)P_m(r)dr+\frac{4}{h^{(i)2}}\mathbf{Q}_0^{z,z(i)}$$

$$\times\sum_{n=0}^{N_i-1}\mathbf{b}_n^{(i)}\int_{-1}^1\frac{d^2P_n(r)}{dr^2}P_m(r)dr=0 \qquad (25)$$

$\forall i=1,...,M$ and $\forall m=0,...,N_i-3$.

The projection integrals are analytically evaluated as

$$\int_{-1}^1 P_n(r)P_m(r)dr=\begin{cases}\dfrac{2}{2m+1}, & \text{for } n=m, \\ 0, & \text{otherwise,}\end{cases}$$

$$\int_{-1}^1\frac{dP_n(r)}{dr}P_m(r)dr=\begin{cases}1-(-1)^{(m+n)}, & \text{for } n\geq m+1, \\ 0, & \text{otherwise,}\end{cases}$$

$$(26)$$

$$\int_{-1}^1\frac{dP_n^2(r)}{d^2r}P_m(r)dr$$

$$=\begin{cases}\frac{1}{2}(1-(-1)^{(m+n+1)})(n+m+1)(n-m), \\ \qquad\text{for } n\geq m+2, \\ 0, \quad \text{otherwise.}\end{cases}$$

The total number of unknowns are $N_{\text{tot}}=8\Sigma_{i=1}^M N_i$, whereas from Eqs. (24) and (25) one obtains $4\Sigma_{i=1}^M N_i+4\Sigma_{i=1}^M(N_i-2)$ scalar equations: the further $8M$ equations are provided by the continuity and boundary conditions. In fact, insertion of the representation (23) in the continuity equations between the ith and $(i+1)$th layers, Eqs. (14) and (19), and evaluation in $r=\pm 1$ yields, respectively,

$$\sum_{n=0}^{N_i-1}\mathbf{b}_n^{(i)}P_n(-1)=\sum_{n=0}^{N_{i+1}-1}\mathbf{b}_n^{(i+1)}P_n(+1) \qquad (27)$$

and

$$\mathbf{P}_1^{(i)}\sum_{n=0}^{N_i-1}\mathbf{c}_n^{(i)}P_n(-1)+\frac{2}{h^{(i)}}\mathbf{P}_0^{(i)}\sum_{n=0}^{N_i-1}\mathbf{b}_n^{(i)}\frac{dP_n}{dr}(-1)$$

$$=\mathbf{P}_1^{(i+1)}\sum_{n=0}^{N_{i+1}-1}\mathbf{c}_n^{(i+1)}P_n(1)$$

$$+\frac{2}{h^{(i+1)}}\mathbf{P}_0^{(i+1)}\sum_{n=0}^{N_{i+1}-1}\mathbf{b}_n^{(i+1)}\frac{dP_n}{dr}(1). \qquad (28)$$

In implementing them, account has to be taken of the values of Legendre polynomials and their first derivatives at the ends of the orthogonality interval $[-1,+1]$,

$$P_n(\pm 1)=(\pm 1)^n,$$

$$(29)$$

$$\frac{dP_n}{dr}(\pm 1)=(\pm 1)^{(n+1)}\frac{n(n+1)}{2}.$$

The same procedure applied to the boundary conditions (17) and (20) yields

$$\sum_{n=0}^{N_M-1} \mathbf{b}_n^{(M)} P_n(-1)=0 \tag{30}$$

and

$$\mathbf{P}_1^{(1)}\sum_{n=0}^{N_1-1} \mathbf{c}_n^{(1)} P_n(1)+\frac{2}{h^{(1)}}\mathbf{P}_0^{(1)}\sum_{n=0}^{N_1-1} \mathbf{b}_n^{(1)}\frac{dP_n}{dr}(1)=0. \tag{31}$$

If all the relevant equations are collected and the unknowns are arranged in the column vector $\mathbf{Y}=[\mathbf{b}_1^{(1)\dagger}\cdots\mathbf{b}_{N_M}^{(M)\dagger}\ \mathbf{c}_1^{(1)\dagger}\cdots\mathbf{c}_{N_M}^{(M)\dagger}]^\dagger$, a generalized eigenvalue problem is obtained,

$$\mathbf{\Pi}\cdot\mathbf{Y}=\lambda\mathbf{\Xi}\cdot\mathbf{Y}, \tag{32}$$

where the eigenvalues λ's are related to the propagation constants of the modes via $\lambda=J\xi$. Furthermore, the acoustic velocities are computed as $V=\omega/\xi$. The matrix $\mathbf{\Xi}$ is rank deficient due to the fact that some boundary and continuity conditions do not involve ξ. As a consequence, some eigenvalues may be infinite[19] and, of course, do not correspond to any physical solution.

C. Pseudospectral elements method

In integrated acousto-optical devices the only modes of interest in a multilayered structure are those tightly confined at the surface of the substrate (Mth layer), such as surface acoustic waves. Therefore, in order to enhance the convergence properties of the present method, it is convenient to introduce a nonuniform mapping function for the Mth layer:

$$r=f(z) \quad \forall z\in[-\delta^{(M)}-h^{(M)}/2,-\delta^{(M)}+h^{(M)}/2]. \tag{33}$$

The nonuniform mapping leads to a differential system in the parent domain with variable coefficients. Indeed, Eq. (18) is transformed in

$$-J\xi\mathbf{Q}_2^{(m)}\mathbf{\Theta}^{(M)}-J\xi\mathbf{Q}_1^{(M)}g(r)\frac{d\mathbf{\Psi}^{(M)}}{dr}+\mathbf{Q}_0^{(M)}\mathbf{\Psi}^{(M)}+\mathbf{Q}_0^{z,z(M)}$$

$$\times\left(g(r)h(r)\frac{d\mathbf{\Psi}^{(M)}}{dr}+g(r)^2\frac{d^2\mathbf{\Psi}^{(M)}}{dr^2}\right)=0, \tag{34}$$

where the following functions have been introduced:

$$g(r)=\frac{dr}{dz}, \quad h(r)=\frac{dg(r)}{dr}. \tag{35}$$

By applying to Eq. (34) the same procedures of expansion and projection adopted in the preceding section one obtains

$$-J\xi\mathbf{Q}_2^{(M)}\sum_{n=0}^{N_M-1}\mathbf{c}_n^{(M)}\int_{-1}^{1}P_n(r)P_m(r)dr-J\xi\mathbf{Q}_1^{(M)}\sum_{n=0}^{N_M-1}\mathbf{b}_n^{(M)}$$

$$\times\int_{-1}^{1}g(r)\frac{dP_n(r)}{dr}P_m(r)dr$$

$$+\mathbf{Q}_0^{(M)}\sum_{n=0}^{N_M-1}\mathbf{b}_n^{(M)}\int_{-1}^{1}P_n(r)P_m(r)dr+\mathbf{Q}_0^{z,z(M)}$$

$$\times\sum_{n=0}^{N_M-1}\mathbf{b}_n^{(M)}\left(\int_{-1}^{1}g(r)h(r)\frac{dP_n(r)}{dr}P_m(r)dr\right.$$

$$\left.+\int_{-1}^{1}g^2(r)\frac{d^2P_n(r)}{dr^2}P_m(r)dr\right)=0, \tag{36}$$

$\forall_m=0,...,N_M-3$. The projection integrals involving $g(r)$ and $h(r)$ are efficiently evaluated by a Gauss–Legendre quadrature rule.

The nonuniform mapping does not change the boundary condition (17) but it transforms the continuity condition (19) between the $(M-1)$th and M layers as follows:

$$\mathbf{P}_1^{(M-1)}\sum_{n=0}^{N_{M-1}-1}\mathbf{c}_n^{(M-1)}P_n(-1)+\frac{2}{h^{(M-1)}}\mathbf{P}_0^{(M-1)}$$

$$\times\sum_{n=0}^{N_{M-1}-1}\mathbf{b}_n^{(M-1)}\frac{dP_n}{dr}(-1)$$

$$=\mathbf{P}_1^{(M)}\sum_{n=0}^{N_M-1}\mathbf{c}_n^{(M)}P_n(1)+g(1)\mathbf{P}_0^{(M)}\sum_{n=0}^{N_M-1}\mathbf{b}_n^{(M)}\frac{dP_n}{dr}(1). \tag{37}$$

Various mapping transformations may be used to achieve a better description of the modes decaying into the substrate;[20] in this paper the following rational mapping function has been adopted:

$$r=\frac{2}{h^{(M)}}\left(\frac{-\alpha}{(z+\delta^{(M)}-\beta)}-\gamma\right),$$

$$\forall z\in[-\delta^{(M)}-h^{(M)}/2,-\delta^{(M)}+h^{(M)}/2], \tag{38}$$

where

$$\beta=\sqrt{\alpha+\left(\frac{h^{(M)}}{2}\right)^2}, \quad \gamma=-\left(\frac{h^{(M)}}{2}+\frac{\alpha}{\left(\frac{h^{(M)}}{2}-\beta\right)}\right), \tag{39}$$

and α is the main parameter controlling the nonlinearity of the mapping transformation.

IV. RESULTS

A. Code validation and convergence analysis

The generalized eigenvalue problem (32) is implemented in MATLAB[21] using the routine **spatarn.m** based on the Arnoldi's algorithm with spectral transformation. This routine enables to select the spectral range ξ in which the eigenvalue search is carried out and, then, it is very useful when only few eigenvalues are required, i.e., the ones corresponding to the modes tightly confined on the upper surface of the substrate. As a validation of the code, a $SiO_2/X-Y$ $LiNbO_3$ planar structure is analyzed via the present method and via the transverse resonance technique.[4,5] For all the materials the physical constants are taken from Ref. 17, apart from $LiNbO_3$, for which the data reported in Ref. 22 are used. Figure 3 reports for both methods the SAW velocity versus the thickness of the SiO_2 layer, h_{SiO_2}, at a fixed frequency $f=170$ MHz, that is a typical value of RF conversion frequency in AO $LiNbO_3$ devices. The PSEM computa-

J. Acoust. Soc. Am., Vol. 112, No. 6, December 2002

Peverini *et al.*: Piezoelectric strip waveguides 2627
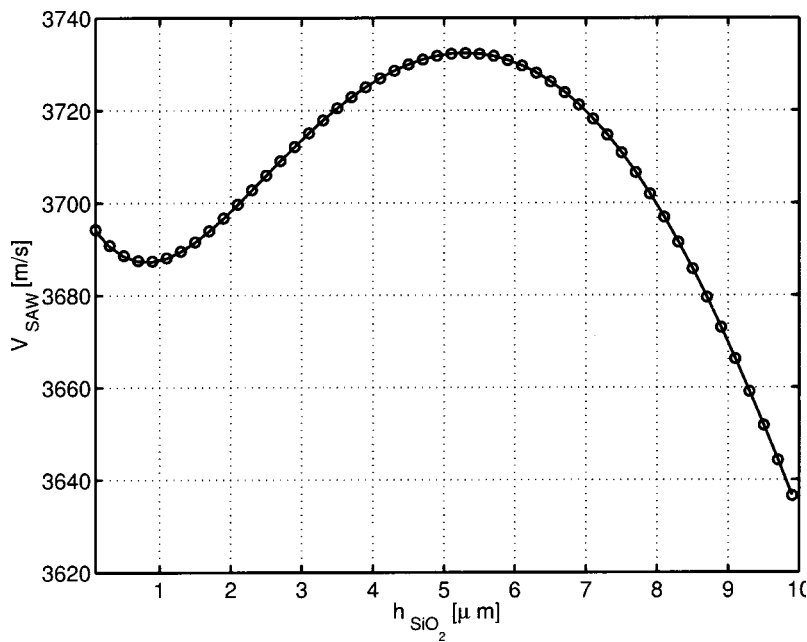
FIG. 3. SAW velocity V_{SAW} vs h_{SiO_2} for a $SiO_2/X-Y$ $LiNbO_3$ planar structure: PSEM (—), transverse resonance technique ($\bigcirc$).

tion is carried out with $N_1 = 7$, $N_2 = 10$, and $h_{LiNbO_3} = h^{(2)}$ $= 1$ mm. The mapping coefficient is set to $\alpha = \lambda_{est} h^{(2)}$, where $\lambda_{est} = 2\pi/(\omega s_{est})$ and $s_{est} = 0.27$ ms/m. From this analysis one can infer that the PSEM provides results that agree with those obtained with the transverse resonance technique. Moreover, the maximum relative change of V_{SAW} for $h_{SiO_2} \in [0.1,2]$ μm with respect to the unloaded substrate is about 0.3% as experimentally observed in Ref. 3. In comparison with the transverse resonance technique the present method has the advantage of automatically providing all the modes of the planar layered structure. Figure 4 shows the velocity of all the modes decaying into the substrate versus the thickness h_{SiO_2}. The lower curve is related to the fundamental mode of the structure, i.e., the SAW. This curve starts at 3696 m/s for $h_{SiO_2} = 0$ (SAW velocity in $X-Y$ $LiNbO_3$) and for $h_{SiO_2} \geqslant 30$ μm reaches its asymptotic value of about

3411 m/s, corresponding to the SAW velocity in the SiO_2 layer. The other curves starting at $V_{bulk,QSV} = 3940$ m/s (cut-off velocity of bulk waves with quasishear vertical polarization in $X-Y$ $LiNbO_3$) correspond to higher order modes.

The profiles of the field components, that are the elongation components u_x, u_y, u_z and the electrical potential Φ, are readily obtained as linear combination of the expansion functions, weights of which are the eigenvector elements. The modal fields are normalized so that the associated power (per unit length in the y direction) equals 1 W. Figure 5 shows the field components of the SAW for a value of SiO_2 thickness $h_{SiO_2} = 5$ μm. As it is expected, the SAW is prevalently polarized in the sagittal plane (xz) and the acoustical and electrical fields are coupled via the piezoelectric effect in the $X-Y$ $LiNbO_3$ substrate. In Fig. 6 the field components of the SAW are reported for $h_{SiO_2} = 25$ μm. As the SiO_2 thick-
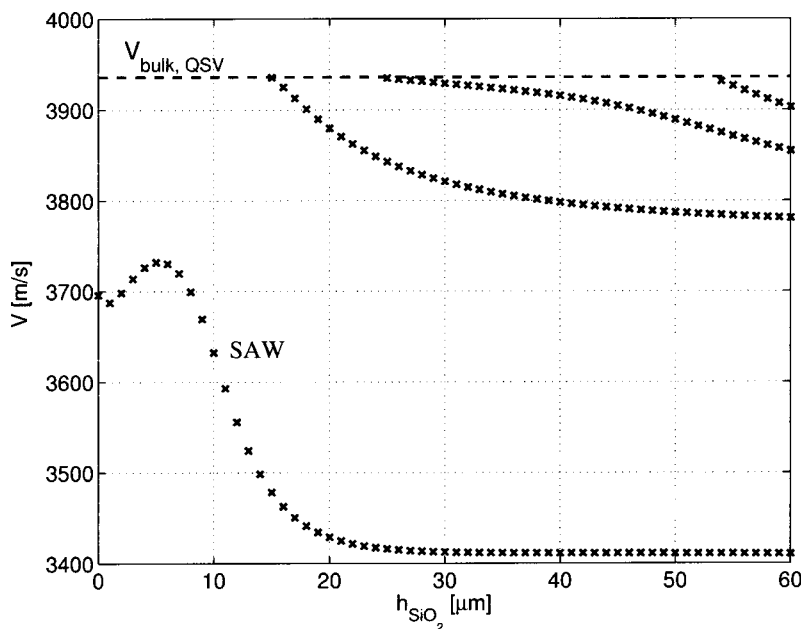
FIG. 4. Mode velocity V vs h_{SiO_2} for a $SiO_2/X-Y$ $LiNbO_3$ planar structure.

Peverini *et al.*: Piezoelectric strip waveguides
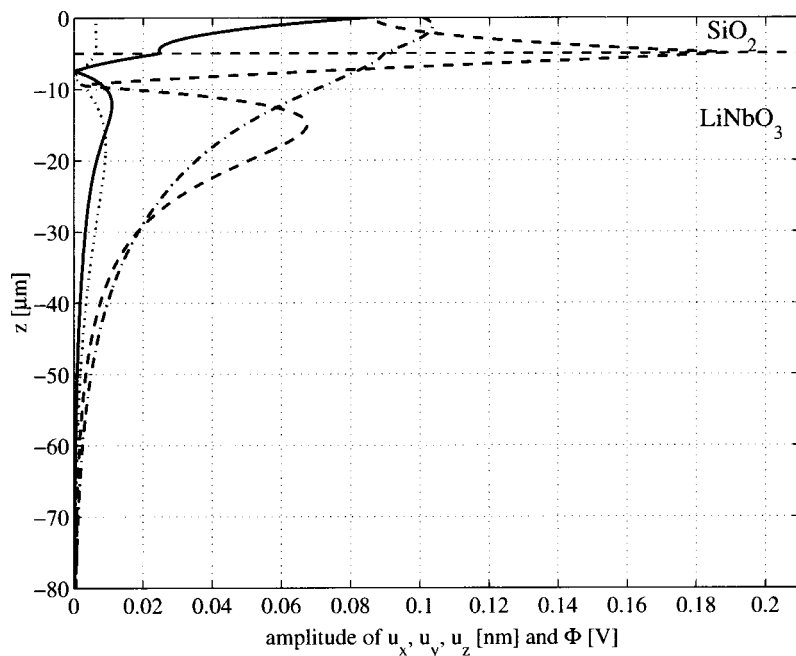
FIG. 5. Amplitude of the field components of a SAW in a $SiO_2/X-Y$ LiNbO$_3$ planar structure with $h_{SiO_2} = 5$ μm and $h_{LiNbO_3} = 1$ mm: u_x (——), u_y (···), u_z (-·-), Φ (---).

ness is increased the SAW gets more confined in the SiO$_2$ layer and the electrical component decreases, since the film layer is not piezoelectric. For this value of h_{SiO_2}, also another mode with quasishear horizontal polarization decays into the substrate and its fields components are plotted in Fig. 7.

The convergence properties and the influence of the mapping function are illustrated in Fig. 8, which shows the relative error on V_{SAW} versus the number of Legendre polynomials N_2 for the $SiO_2/X-Y$ LiNbO$_3$ planar structure. The layers thickness are $h_{SiO_2} = h^{(1)} = 5$ μm and $h_{LiNbO_3} = h^{(2)} = 1$ mm, and $f = 170$ MHz. The number of polynomials in the SiO$_2$ layer is set to $N_1 = 7$ in order to assure a good capability of representation of the fields inside it and two values of λ_{est} are used corresponding to $s_{est,0} = 0.2$ ms/m and $s_{est,1} = 0.27$ ms/m.

From this analysis one can note the exponential rate of convergence of the PSEM and its remarkable dependence on the mapping factor α. Furthermore, the relation $\alpha = \lambda_{est} h_z^{(substrate)}$ appears to be the best choice for the mapping factor, even if it does not depend severely on the exact value of s_{est}. Therefore, one can infer that the introduction of a correct mapping increases the capability of the method when searching for solutions decaying into the substrate.

B. Metal/SiO$_2$ SAWG's

The developed and validated method can be applied to investigate new types of SAWG's for AO devices.

From Fig. 3 it is evident that the deposition of a $\sim$0.6 μm thick SiO$_2$ layer over $X-Y$ LiNbO$_3$ produces a small
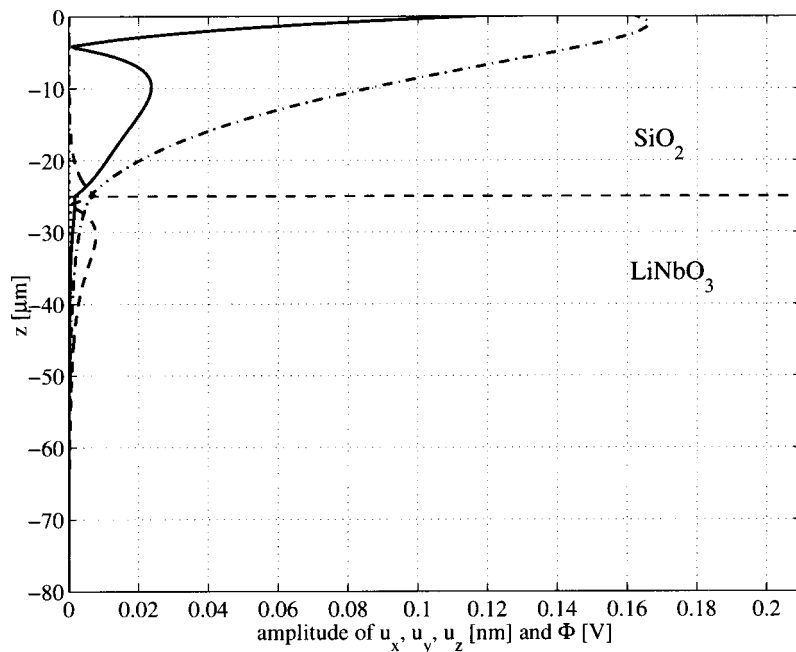
FIG. 6. Amplitude of the field components of a SAW in a $SiO_2/X-Y$ LiNbO$_3$ planar structure with $h_{SiO_2} = 25$ μm and $h_{LiNbO_3} = 1$ mm: u_x (——), u_y (···), u_z (-·-), Φ (---).
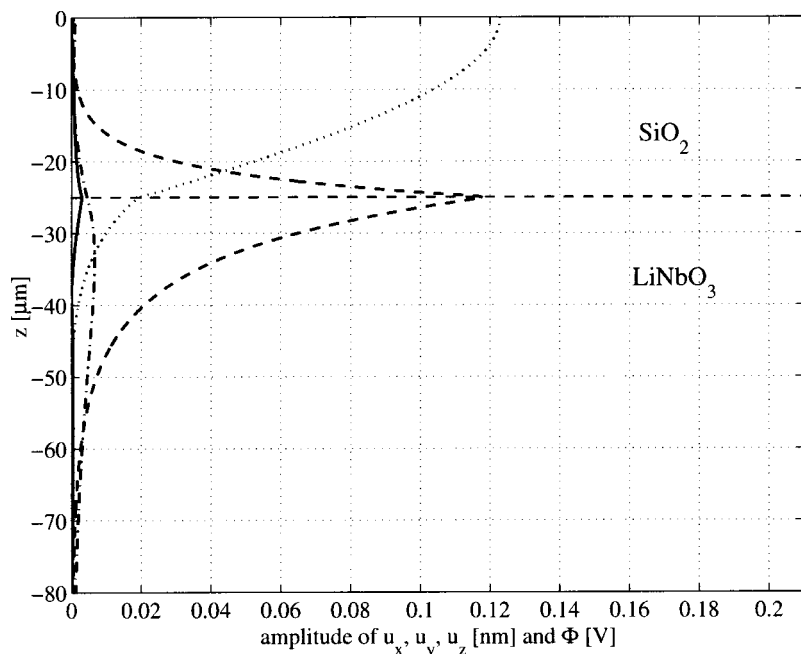
FIG. 7. Amplitude of the field components of the first order mode in a $SiO_2/X-Y$ $LiNbO_3$ planar structure with $h_{SiO_2} = 25$ μm and $h_{LiNbO_3} = 1$ mm: u_x (—), u_y ($\cdots$), u_z (-·-), Φ (---).

decrease of V_{SAW}, ~0.3%, comparable with that obtained via Ti-indiffusion. Indeed, the new type of SAWG's proposed in Ref. 3 is based on a film of SiO_2 doped with In_2O_3 compound. By changing the doping percentage the SAW velocity may be controlled and values of relative change of 1–2 % are obtained. The variation of V_{SAW} is caused by both the increased mass-loading effect and the partial short-circuiting of the electrical potential due to the presence of In. Therefore, it is interesting for AO applications to investigate planar metal/SiO_2/$X-Y$ $LiNbO_3$ structures, in which the metal is either Al, Ti, In, and Au. The range of thickness values under investigation is related to fabrication feasibility of the films. The results for Al and Au are reported in Figs. 9 and 10, respectively. Each figure shows the relative change of SAW velocity, ΔV_{SAW}, versus the SiO_2 thickness, h_{SiO_2},

for different thickness of the metal. Besides, each plot reports also the case in which the metallic film has no thickness, i.e., no mass, and, therefore, induces only a change in the electrical boundary conditions on the top surface of the SiO_2 layer. In all cases $|\Delta V_{SAW}|$ increases when h_{SiO_2} approaches zero, because the metal film gets closer to the free surface of the $X-Y$ $LiNbO_3$ substrate and this orientation of $LiNbO_3$ crystal is very sensible to the electrical boundary condition. Increasing the thickness of the SiO_2 layer provides higher electrical insulation from the metal film, since SiO_2 is not a piezoelectric material and the electrical potential decays exponentially away from the free surface of $X-Y$ $LiNbO_3$. On the other hand, for a fixed value of h_{SiO_2} the SAW can be slowed down if a denser metal is used, such as
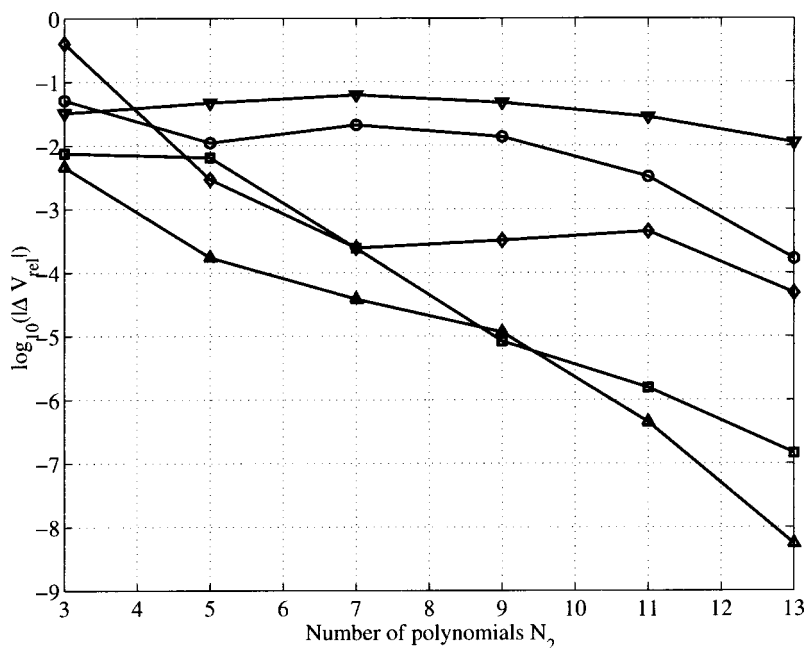
FIG. 8. Relative error on V_{SAW} versus the number of Legendre polynomials N_2 for different mappings in a $SiO_2/X-Y$ $LiNbO_3$ planar structure with $h_{SiO_2} = 5$ μm and $h_{LiNbO_3} = 1$ mm: no mapping ($\triangledown$), mapping factor $\alpha = 10\lambda_{est,1}h_{LiNbO_3}$ ($\bigcirc$), mapping factor $\alpha = 0.1\lambda_{est,1}h_{LiNbO_3}$ ($\diamond$), mapping factor $\alpha = \lambda_{est,0}h_{LiNbO_3}$ ($\square$), mapping factor $\alpha = \lambda_{est,1}h_{LiNbO_3}$ ($\triangle$).
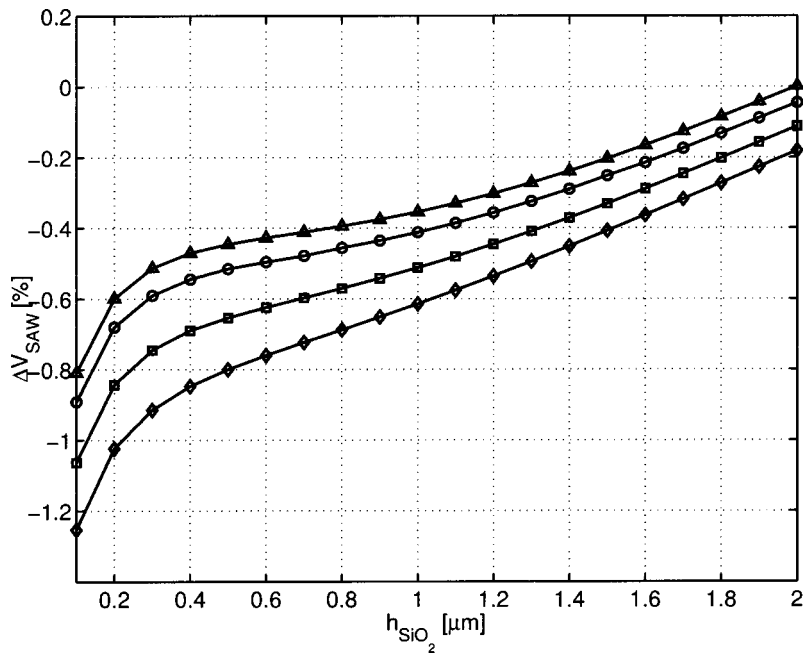
FIG. 9. Relative change on SAW velocity, ΔV_{SAW}, vs h_{SiO_2} in an Al/SiO$_2$/$X-Y$ LiNbO$_3$ planar structure with $h_{LiNbO_3}=1$ mm: $h_{Al}=0$ nm ($\triangle$), $h_{Al}=50$ nm ($\bigcirc$), $h_{Al}=200$ nm ($\square$), $h_{Al}=400$ nm ($\diamond$).

Au or In. In this configuration of SAWG's the SiO$_2$ provides only the necessary insulation to the optical waveguides from the metal film in order to prevent additional optical losses, whereas the mass-loading effect due to the metal film slows down the SAW.[23] By changing the metal and its thickness one can control the mass-loading effect and, therefore, the SAW velocity.

After the computation of the V_{SAW} in the multilayered structure, defining the core of the 3D strip guide, one can apply the EIM to obtain the dispersion curves of the 3D guide versus the strip width W_{strip}. In Fig. 11 the dispersion curves of a film-loaded Au/SiO$_2$/$X-Y$ LiNbO$_3$ SAWG for different values of h_{Au} at $f=170$ MHz are reported. The SiO$_2$ film has thickness $h_{SiO_2}=0.6$ μm. All the dispersion curves start at $V_{cl}\cong3696$ m, which is the value of V_{SAW} in

the unloaded $X-Y$ LiNbO$_3$ substrate. From this figure one can state that at already $W_{strip}\cong30$ μm and $h_{Au}\cong60$ nm one obtains a single mode waveguide in which the fundamental mode is strongly confined in the transverse direction. Therefore, with this new type of SAWG's both the scale of integration and the acousto-optical interaction is increased.

V. CONCLUSIONS

In this paper a method of analysis for film-loaded surface acoustic waveguides based on the combination of the effective index method and the pseudospectral elements method has been reported. The method provides a flexible and computationally efficient tool for the analysis of a variety of film-loaded SAWG's. Interesting results have been
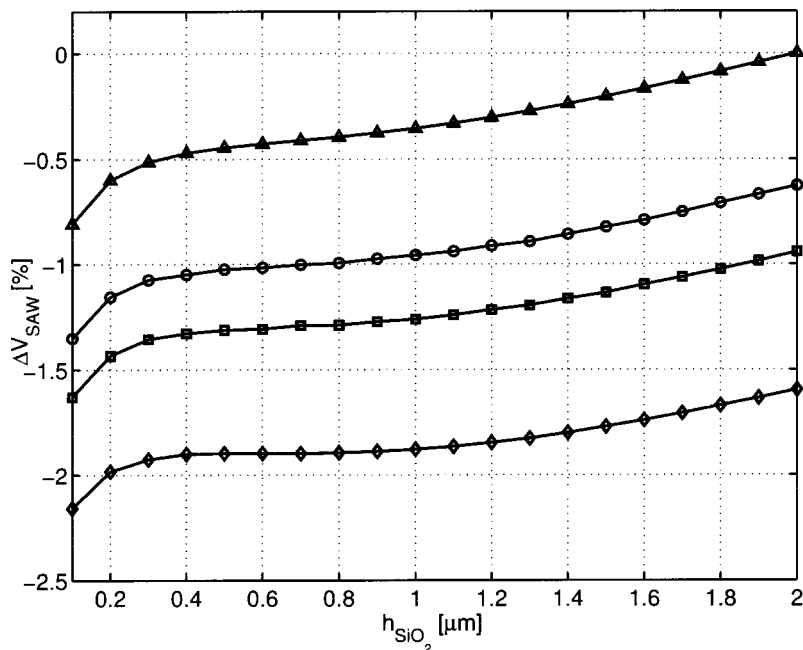
FIG. 10. Relative change on SAW velocity, ΔV_{SAW} vs h_{SiO_2} in an Au/SiO$_2$/$X-Y$ LiNbO$_3$ planar structure with $h_{LiNbO_3}=1$ mm: $h_{Au}=0$ nm ($\triangle$), $h_{Au}=20$ nm ($\bigcirc$), $h_{Au}=30$ nm ($\square$), $h_{Au}=50$ nm ($\diamond$).
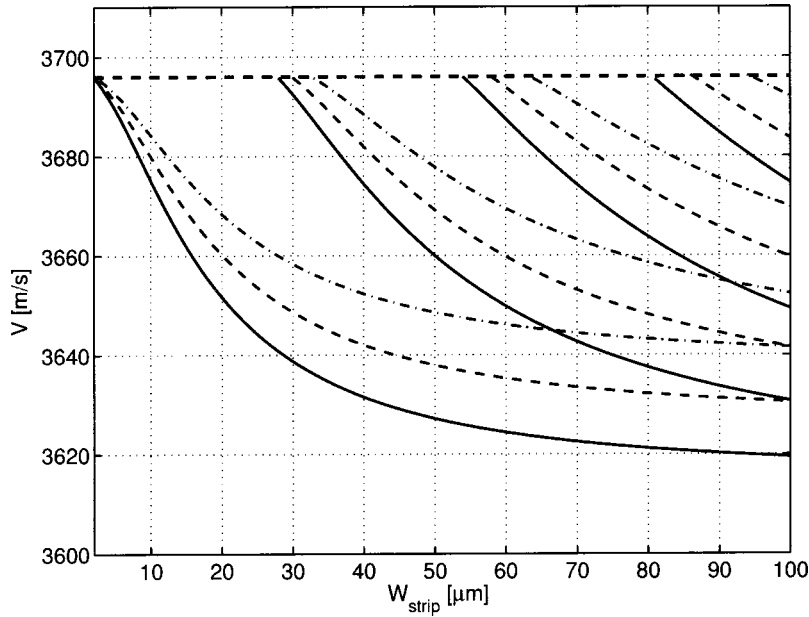
FIG. 11. Dispersion curves for a film-loaded Au/SiO$_2$/X–Y LiNbO$_3$ SAWG with $h_{SiO_2} = 0.6$ μm and $h_{LiNbO_3} = 1$ mm: $h_{Au} = 40$ nm (-··-), $h_{Au} = 50$ nm (---), $h_{Au} = 60$ nm(—).

obtained for metal/SiO$_2$/X–Y LiNbO$_3$ SAWG's, that are very attractive structures for integrated AO components. The velocity profile has been obtained by a pseudospectral method instead of the classical matrix method. This is advantageous because it avoids the solution of the transcendental equation which is difficult to carry out automatically.

A further merit of this method is that it is not limited to the determination of the SAW wave. It provides also the propagation constants of all guided modes, an information that is necessary for the solution of the stripe guide problem by a more rigorous approach, such as the mode-matching technique, described in Ref. 24.

ACKNOWLEDGMENTS

APPENDIX

In this Appendix the expressions for the matrices introduced in Eqs. (9), (10), and (13) are reported

$$\mathbf{A} = \begin{bmatrix} 1 & 0 & 0 & 0 & 0 & 0 \\ 0 & 0 & 0 & 0 & 0 & 1 \\ 0 & 0 & 0 & 0 & 1 & 0 \end{bmatrix}, \quad \mathbf{F} = \begin{bmatrix} 0 & 0 & 0 & 0 & 1 & 0 \\ 0 & 0 & 0 & 1 & 0 & 0 \\ 0 & 0 & 1 & 0 & 0 & 0 \end{bmatrix}, \quad \mathbf{M} = \begin{bmatrix} 1 \\ 0 \\ 0 \end{bmatrix}, \quad \mathbf{N} = \begin{bmatrix} 0 \\ 0 \\ 1 \end{bmatrix},$$

$$\mathbf{Q}_2^{(i)} = \begin{bmatrix} \mathbf{A}c^{(i)}\mathbf{A}^\dagger & \omega\mathbf{A}e^{(i)}\mathbf{M} \\ \omega\mathbf{M}^\dagger e^{(i)\dagger}\mathbf{A}^\dagger & -\omega^2\mathbf{M}^\dagger\epsilon^{(i)}\mathbf{M} \end{bmatrix}, \quad \mathbf{Q}_1^{(i)} = \begin{bmatrix} \mathbf{A}c^{(i)}\mathbf{F}^\dagger + \mathbf{F}c^{(i)}\mathbf{A}^\dagger & \omega\mathbf{A}e^{(i)}\mathbf{N} + \omega\mathbf{F}e^{(i)}\mathbf{M} \\ \omega\mathbf{M}^\dagger e^{(i)\dagger}\mathbf{F}^\dagger + \omega\mathbf{N}^\dagger e^{(i)\dagger}\mathbf{A}^\dagger & -\omega^2\mathbf{M}^\dagger\epsilon^{(i)}\mathbf{N} - \omega^2\mathbf{N}^\dagger\epsilon^{(i)}\mathbf{M} \end{bmatrix},$$

$$\mathbf{Q}_0^{(i)} = \begin{bmatrix} \omega^2\rho^{(i)}\mathbf{I}_{3\times 3} & \mathbf{0}_{3\times 1} \\ \mathbf{0}_{1\times 3} & \mathbf{0}_{1\times 1} \end{bmatrix}, \quad \mathbf{Q}_0^{z,z(i)} = \begin{bmatrix} \mathbf{F}c^{(i)}\mathbf{F}^\dagger & \omega\mathbf{F}e^{(i)}\mathbf{N} \\ \omega\mathbf{N}^\dagger e^{(i)\dagger}\mathbf{F}^\dagger & -\omega^2\mathbf{N}^\dagger\epsilon^{(i)}\mathbf{N} \end{bmatrix},$$

$$\mathbf{P}_1^{(i)} = \begin{bmatrix} \frac{1}{\omega}\mathbf{c}^{(i)}([5,4,3],:)\mathbf{A}^\dagger & \mathbf{e}([5,4,3],:)\mathbf{M} \\ \mathbf{e}^\dagger(3,:)\mathbf{A}^\dagger & -\omega\epsilon(3,:)\mathbf{M} \end{bmatrix}, \quad \mathbf{P}_0^{(i)} = \begin{bmatrix} \frac{1}{\omega}\mathbf{c}^{(i)}([5,4,3],:)\mathbf{F}^\dagger & \mathbf{e}([5,4,3],:)\mathbf{N} \\ \mathbf{e}^\dagger(3,:)\mathbf{F}^\dagger & -\omega\epsilon(3,:)\mathbf{N} \end{bmatrix}.$$

[1] H. Herrmann, U. Rust, and K. Schafer, "Tapered acoustical directional couplers for integrated acousto-optical mode converters with weighted coupling," J. Lightwave Technol. **13**, 364–374 (1995).

[2] H. Herrmann and H. Mendis, "Broadly tunable integrated acoustooptical polarization converters in LiNbO$_3$," Proceedings ECIO'99, 1999, pp. 229–232.

[3] T. Nakazawa, S. Taniguchi, and M. Seino, "Ti:LiNbO$_3$ acousto-optic tunable filter (AOTF)," Fujitsu Sci. Tech. J. **35**, 107–112 (1999).

[4] C. Potel and J. de Belleval, "Propagation in an anisotropic periodically

multilayered medium," J. Acoust. Soc. Am. **93**, 2669–2677 (1993).

[5] M. N. Armenise, V. M. Passaro, and F. Impagnatiello, "Acoustic-mode analysis of a homogeneous multilayer guiding structure," J. Opt. Soc. Am. B **8**, 443–448 (1991).

[6] E. L. Adler, "SAW and pseudo-SAW properties using matrix methods," IEEE Trans. Ultrason. Ferroelectr. Freq. Control **41**, 876–882 (1994).

[7] E. L. Adler, "Matrix methods applied to acoustic waves in multilayers," IEEE Trans. Ultrason. Ferroelectr. Freq. Control **37**, 485–490 (1990).

[8] E. L. Adler, J. K. Slaboszewicz, G. W. Farnell, and C. K. Jen, "PC Soft-

ware for SAW propagation in anisotropic multilayers," IEEE Trans. Ultrason. Ferroelectr. Freq. Control **37**, 215–223 (1990).

[9] S. V. Biryukov, Y. V. Gulyaev, V. V. Krylov, and V. P. Plessky, *Surface Acoustic Waves in Inhomogeneous Media* (Springer-Verlag, Berlin, 1995), Chap. 3.

[10] Y. Kim and W. D. Hunt, "Acoustic fields and velocities for surface-acoustic-wave propagation in multilayered structures: An extension of the Laguerre polynomial approach," J. Appl. Phys. **68**, 4993–4997 (1990).

[11] V. Lancellotti and R. Orta, "Guided waves in layered cubic media: Convergence study of a polynomial expansion approach," J. Acoust. Soc. Am. **104**, 2638–2644 (1998).

[12] J. E. Lefebvre, V. Zhang, J. Gazalet, T. Gryba, and V. Sadaune, "Acoustic wave propagation in continuous functionally graded plates: An extension of the Legendre polynomial approach," IEEE Trans. Ultrason. Ferroelectr. Freq. Control **48**, 1332–1340 (2001).

[13] G. B. Hocker and W. K. Burns, "Mode dispersion in diffused channel waveguides by the effective index method," Appl. Opt. **16**, 113–118 (1977).

[14] A. A. Oliner, *Acoustic Surface Waves* (Springer Verlag, Berlin, 1978), Chap. 5.

[15] A. J. Slobodnik, E. D. Conway, and R. T. Delmonico, "Surface wave velocities," *Microwave Acoustics Handbook* (Air Force Cambridge Research Labs, Cambridge, 1973), Vol. 1A.

[16] A. Bove, G. Donato, S. Schmid, E. DeAmbrogi, I. Montrosset, and G. Perrone, "BPM simulations of surface acoustic waves in planar waveguide structures on LiNbO$_3$," Proceedings ECIO'99, 1999, pp. 51–54.

[17] B. A. Auld, *Acoustic Fields and Waves in Solids* (Krieger, New York, 1990), Vol. I, Chap. 8.

[18] S. A. Orzag and D. Gottlieb, *Numerical Analysis of Spectral Methods: Theory and Applications* (SIAM, Philadelphia, PA, 1977), pp. 37–42.

[19] C. B. Moler and G. W. Stewart, "An algorithm for generalized matrix eigenvalue problem," SIAM (Soc. Ind. Appl. Math.) J. Numer. Anal. **10**, 241–256 (1973).

[20] J. P. Boyd, *Chebyshev and Fourier Spectral Methods* (Springer-Verlag, Berlin, 1989).

[21] MATLAB, The Language of the Technical Computing, Version 5.3, The MathWorks, Inc., 1999.

[22] G. Kovacs, M. Anhorn, H. E. Engan, G. Visintini, and C. C. W. Ruppel, "Improved material constants for LiNbO$_3$ and LiTaO$_3$," IEEE Ultrasonics Symposium Proceedings, 1990, pp. 435–438.

[23] O. A. Peverini, H. Herrmann, and R. Orta, "Film-loaded strip- and slot-type SAW waveguides for integrated acousto-optical polarization converters in LiNbO$_3$," Proceedings ECIO'01, 2001, pp. 31–34.

[24] M. P. da Cunha and E. L. Adler, "Scattering of SAW at discontinuities: Some numerical experiments," IEEE Trans. Ultrason. Ferroelectr. Freq. Control **42**, 168–173 (1995).

Tube-wave propagation in a fluid-filled borehole generated by a single point force applied to the surrounding formation

Pavel M. Bokov and Andrei M. Ionov

Department of Modeling of Physical Processes in Environment, Moscow State Engineering Physics Institute (State University), 31 Kashirskoe Shosse, 115409 Moscow, Russia

Propagation of tube waves in an infinite fluid-filled borehole, generated by a single-force point source placed in the elastic surrounding formation, is analyzed in the long-wave approximation. Integral representations of the precise solution are obtained both for fast and slow formations. An asymptotic analysis of tube-wave propagation in the fluid-filled borehole is performed on the basis of these two integral representations. The complete asymptotic wave field in the borehole fluid for a fast formation consists of P and SV phases and the lowest eigenmode of the Stoneley wave (tube wave). For a slow formation the conical Stoneley wave (Mach wave) is generated. It appears only behind the critical angle defined by the ratio of the S wave velocity in the formation to the low-frequency Stoneley wave velocity and decays weakly with an offset. Asymptotic wave forms are in good agreement with wave forms obtained by straightforward calculations. © *2002 Acoustical Society of America.* [DOI: 10.1121/1.1508781]

I. INTRODUCTION

It is well known that tube-wave amplitude and travel-time characteristics in a fluid-filled borehole carry important information about properties of the surrounding formation. Theoretical and experimental data show that both the velocity and quality factor of tube waves depend on the shear modulus of the surrounding formation, permeabilities, and porosities of permeable strata. Moreover, tube-wave phases include information about all multiple reflections arising at internal interfaces. Incident elastic waves in the surrounding formation generate in a fluid-filled borehole both P, SV, and Stoneley waves. The last-named phase is the superposition of tube-wave eigenmodes and consists of the lowest mode only in the long-wave limit,[1,2] when the wavelength exceeds essentially the borehole radius.

Most of analytic results, which are not restricted by the long-wave approximation, were obtained for tube waves in a fluid-filled borehole generated by a point source placed in the borehole interior. For simple geometries exact solutions can be obtained by integral transforms as double integrals over the horizontal slowness and frequency and can be investigated numerically. A further analysis of the exact solution is simplified significantly for the far field, when asymptotic methods are valid. Thus, Lee and Balch[3] investigated theoretically seismic wave radiation and tube-wave generation by a pulse point source placed in the borehole interior. Their asymptotic analysis was restricted by fast formations, when the shear-wave velocity of the surrounding formation exceeds the tube-wave velocity. Meredit *et al.*[4] demonstrated that for a slow formation the conical Stoneley wave (Mach wave) appears. They showed its wave front to be conical and calculated aperture of the cone and its moveout velocity. Peng *et al.*[5] found small absorption and dispersion corrections for the conical Stoneley wave velocity in the low-frequency limit from the exact dispersion equation.

The problem of tube-wave propagation generated by in-cident elastic waves in the formation, in general, is rather complicated. It can be significantly simplified in the seismic wavelength range, when the long-wave approximation is valid. Thus, White[1] showed that incident plane elastic P or SV waves propagating through fast formations do not excite Stoneley waves in the long-wave limit. Thus, the complete wave field in the borehole fluid consists of P or SV waves only. Shear elastic SH waves incident on a fluid-filled borehole do not generate tube waves at all, because they do not induce a volumetric change of the borehole fluid. Amplitudes of P or SV responses in the borehole fluid are finite and do not contain peculiarities for fast formations. In contrary, an impermissible singularity in the SV wave amplitude arises at some critical angle of incidence[1,6] for slow formations. This alludes to the fact that more sophisticated analysis is required near the critical point.

Ionov and Maximov[7] solved in the long-wave approximation the problem of tube-wave propagation generated by an isotropic point source placed at some offset from the fluid-filled borehole axis. As distinct from incident plane elastic waves, the spherical P wave, propagating through the surrounding formation, induces not only the P wave in the borehole fluid, but the tube wave as well. It is caused by a nonzero curvature of the incident wave front.

Tube-wave propagation generated by a single-force point source applied to the surrounding formation at some offset from a fluid-filled borehole is considered in this work in the long-wave approximation. The simplifying assumption is made that the force vector is parallel to the borehole axis. The reasoning behind this suggestion is the following. The radiation problem from the single-force source has the axial symmetry in the coordinate system, which vertical axis co-incides with the force vector. Thus, the incident wave field radiated by the source depends only on the vertical coordinate along the borehole, because the radial coordinate (the offset) is fixed. This simplifies considerably mathematical

solution and analysis of 1D problem of tube-wave propagation in the borehole fluid.

In contrary, when the force vector and the borehole axis are out-of-parallelism, the radiated wave field, being dependent on the azimuth angle, invalidates the axial symmetry.[8] Moreover, SH-polarized waves appear in addition to P and SV waves.

It should be pointed out that vertical seismic vibrators and pulse radiators used for sounding of geological formations are very common in exploration seismology.[1,9] Thus, the problem solved in this paper can be feasible for problems of borehole seismics, because tube-wave amplitudes and wave forms give valuable information about acoustic parameters of the surrounding formation.

Our work focuses on asymptotic analysis of tube waves arising in the problem. The treatment of the problem is presented in Sec. II. Definition of the effective stress at the borehole axis induced by elastic waves radiated by the single-force point source is fulfilled in Sec. III. Precise integral representations of the solution convenient for asymptotic tube-wave analysis both for fast and slow formations are derived in Secs. IV A and IV B. The asymptotic analysis of tube-wave phases is performed in Secs. V A and V B. Comparison of wave forms obtained with the aid of asymptotic formulas and straightforward calculations both for fast and slow formations is presented in Sec. VI.

II. FORMULATION OF THE PROBLEM

Propagation of tube waves in the long-wave approximation $\lambda \gg b$ (where λ is the wavelength, b is the borehole radius) through a fluid-filled borehole embedded in an elastic formation is governed by the wave equation[1,10]

$$\frac{\partial^2 P}{\partial z^2} - \frac{1}{c_{tw}^2} \frac{\partial^2 P}{\partial t^2} = \frac{2\rho_f}{E} \frac{\partial^2 \sigma_{\text{eff}}^{\text{inc}}}{\partial t^2}. \tag{1}$$

In Eq. (1), P is the dynamic borehole fluid pressure, c_{tw} is the low-frequency Stoneley wave velocity,[1] ρ_f is the fluid density, E is the Young modulus of the surrounding formation, z is the vertical coordinate along the borehole. The incident effective stress at the borehole axis $\sigma_{\text{eff}}^{\text{inc}}$ is expressed *via* components of the stress tensor σ_{ij}^{inc} in cylindrical coordinates as

$$\sigma_{\text{eff}}^{\text{inc}} = \sigma_{rr}^{\text{inc}} + \sigma_{\phi\phi}^{\text{inc}} - \nu\sigma_{zz}^{\text{inc}}, \tag{2}$$

where ν is the Poisson ratio.

Tube-wave propagation, generated by the single point force $\mathbf{f} = F(t)\delta(\mathbf{r})\mathbf{e_z}$ applied to an isotropic, purely elastic, homogeneous formation at some offset r from the fluid-filled borehole, is investigated in this work. It is assumed that the surrounding formation and the fluid-filled borehole are of infinite extent. Here $\mathbf{e_z}$ is the unit vector along the borehole axis, $\delta(\mathbf{r})$ is the Dirac delta function, $F(t)$ is the seismic source function, $\mathbf{r}$ is the radius vector.

Geometry of the problem is shown in Fig. 1. To solve the problem, it is necessary to define the effective stress $\sigma_{\text{eff}}^{\text{inc}}$ at the borehole axis generated by the single-force point source. The required solution of Eq. (1) must obey Sommerfeld's radiation conditions at infinity $z \to \pm\infty$.
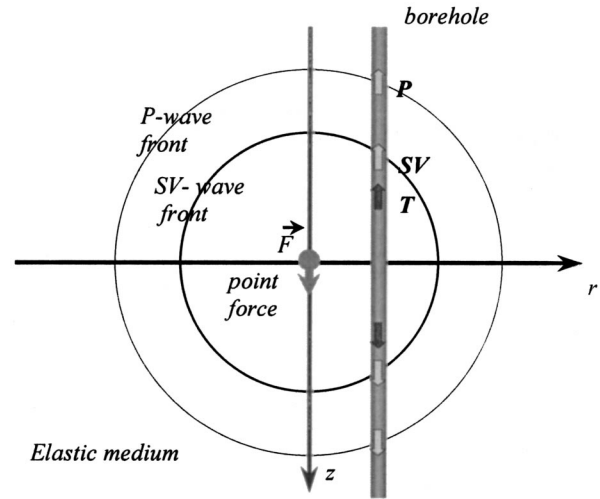
FIG. 1. Geometry of the problem.

III. EFFECTIVE STRESSES AT THE BOREHOLE AXIS FROM A SINGLE-FORCE POINT SOURCE

Propagation of elastic waves is defined by the equation of dynamic theory of elasticity[7]

$$\frac{\partial^2 \mathbf{u}}{\partial t^2} = \alpha^2 \boldsymbol{\nabla} \, \text{div} \, \mathbf{u} - \beta^2 \, \text{rotrot} \, \mathbf{u} + \mathbf{f}/\rho_s, \tag{3}$$

in which α and β are longitudinal and shear wave velocities, respectively, in the elastic formation, ρ_s is the density of the elastic medium, $\mathbf{u}$ is the displacement. It is convenient to solve Eq. (3) through the scalar ϕ and vector $\boldsymbol{\psi}$ potentials defined as $\mathbf{u} = \boldsymbol{\nabla}\phi + \text{rot}\,\boldsymbol{\psi}$. In this case it is necessary to represent the single-force point source *via* Helmholtz potentials Φ and $\boldsymbol{\Psi}$ as $\mathbf{f} = \boldsymbol{\nabla}\Phi + \text{rot}\,\boldsymbol{\Psi}$. The vector potentials $\boldsymbol{\psi}$ and $\boldsymbol{\Psi}$ satisfy the gauge conditions:[11] $\text{div}\,\boldsymbol{\psi} = 0$, $\text{div}\,\boldsymbol{\Psi} = 0$. The procedure is described in detail by Aki and Richards.[11] The result for the vertical force is given by

$$\Phi = -\frac{F(t)}{4\pi}\frac{\partial}{\partial z}\left(\frac{1}{R}\right), \quad \boldsymbol{\Psi} = \frac{F(t)}{4\pi}\text{rot}\left(\frac{\mathbf{e_z}}{R}\right), \tag{4}$$

where $R = |\mathbf{r}|$ is the distance from the source point.

Substitution of the displacement and force potentials (4) in Eq. (3) leads to a vector partial differential equation, involving both scalar and vector potentials. Successive application of the divergence and curl operators to the equation gives separate equations for the vector and scalar potentials. Elimination of the Laplace operator Δ according to the Lamé theorem[11] leads to the inhomogeneous wave equations

$$\frac{\partial^2 \phi}{\partial t^2} - \alpha^2 \Delta\phi = -\frac{F(t)}{4\pi\rho_s}\frac{\partial}{\partial z}\left(\frac{1}{R}\right),$$

$$\frac{\partial^2 \psi}{\partial t^2} - \beta^2 \Delta\psi = \frac{F(t)}{4\pi\rho_s R}. \tag{5}$$

The well-known equation[11] of the vector analysis $\boldsymbol{\nabla}\,\text{div}\,\mathbf{B} = \Delta\mathbf{B} + \text{rotrot}\,\mathbf{B}$ is used at derivation of Eqs. (5), where $\mathbf{B}$ is an arbitrary vector. The vector displacement potential in Eqs. (5) has only one nonzero component due to the axial symmetry of the problem.

It is easy to see that the sources in the right-hand sides of Eqs. (5) are spatially nonlocal. Let's apply the Laplace operator to eliminate this nonlocality from Eqs. (5). This leads to wave equations for values $\phi_0 = \Delta\phi$ and $\psi_0 = \Delta\psi$,

$$\frac{\partial^2 \phi_0}{\partial t^2} - \alpha^2 \Delta \phi_0 = \frac{F(t)}{\rho_s} \frac{\partial}{\partial z} \delta(\mathbf{r}),$$

$$\frac{\partial^2 \psi_0}{\partial t^2} - \beta^2 \Delta \psi_0 = -\frac{F(t)}{\rho_s} \delta(\mathbf{r}). \tag{6}$$

The well-known equality $\Delta(1/R) = -4\pi\delta(\mathbf{r})$ is used in Eq. (6).

Equations (6) can be solved using integral transforms. It is convenient to find the solution in cylindrical coordinates (r,z). After making the double Fourier transform with respect to time t and the vertical coordinate z, and the Hankel transform of zero order over the radial coordinate r,

$$\begin{Bmatrix} \phi_0(p,a,\omega) \\ \psi_0(p,a,\omega) \end{Bmatrix} = \int_{-\infty}^{+\infty}\int_{-\infty}^{+\infty} dt\, dz \exp(i\omega az - i\omega t) \int_0^\infty r\, dr$$

$$\times J_0(\omega pr) \begin{Bmatrix} \phi_0(r,z,t) \\ \psi_0(r,z,t) \end{Bmatrix} \Leftrightarrow \begin{Bmatrix} \phi_0(r,z,t) \\ \psi_0(r,z,t) \end{Bmatrix}$$

$$= \frac{1}{(2\pi)^2} \int_{-\infty}^{+\infty}\int_{-\infty}^{+\infty} \omega^2\, d\omega\, da$$

$$\times \exp(-i\omega az + i\omega t) \int_0^\infty p\, dp\, J_0(\omega pr)$$

$$\times \begin{Bmatrix} \phi_0(p,a,\omega) \\ \psi_0(p,a,\omega) \end{Bmatrix}, \tag{7}$$

where $J_0(x)$ is the Bessel function of zero order, the solution of Eqs. (6) is given by

$$\phi_0(p,a,\omega) = -\frac{iF(\omega)}{2\pi\rho_s\omega\alpha^2} \frac{a}{a^2 - \zeta^2(p)},$$

$$\psi_0(p,a,\omega) = -\frac{F(\omega)}{2\pi\rho_s\omega^2\beta^2} \frac{1}{a^2 - \eta^2(p)}. \tag{8}$$

In Eqs. (8) p is the horizontal slowness, $\zeta(p) = \pm\sqrt{\alpha^{-2} - p^2}$ and $\eta(p) = \pm\sqrt{\beta^{-2} - p^2}$ are the vertical P wave and S wave slowness, respectively. The parameter a is related with the vertical wave number k_z as $a = k_z/\omega$.

Integrals over the variable a can be easily evaluated as residues in the poles of the integrands in Eqs. (8). The only one pole, satisfying the Sommerfeld's condition, contributes to each integral. This leads to the result for ϕ_0 and ψ_0,

$$\phi_0(r,z,\omega) = -\frac{F(\omega)\omega^2}{4\pi\rho_s\alpha^2} \mathrm{sgn}(z) \int_0^\infty p\, dp\, J_0(\omega pr)$$

$$\times \exp(-i\omega\zeta(p)|z|),$$

$$\psi_0(r,z,\omega) = -\frac{F(\omega)\omega}{4\pi\rho_s\beta^2} \int_0^\infty \frac{p\, dp}{i\eta(p)} J_0(\omega pr)$$

$$\times \exp(-i\omega\eta(p)|z|), \tag{9}$$

where $\mathrm{sgn}(x)$ is the sign function.

Taking into account Eqs. (9), the final result for ϕ and ψ is given by

$$\phi(r,z,\omega) = \frac{F(\omega)}{4\pi\rho_s} \mathrm{sgn}(z) \int_0^\infty dp\, p J_0(\omega pr)$$

$$\times \exp(-i\omega\zeta(p)|z|) + \frac{F(\omega)}{4\pi\rho_s\omega^2} \frac{\partial}{\partial z}\left(\frac{1}{R}\right),$$

$$\tag{10}$$

$$\psi(r,z,\omega) = \frac{F(\omega)}{4\pi\rho_s} \int_0^\infty dp\, \frac{p}{i\omega\eta(p)} J_0(\omega pr)$$

$$\times \exp(-i\omega\eta(p)|z|) - \frac{F(\omega)}{4\pi\rho_s\omega^2 R}.$$

It is easy to see from Eqs. (10), that the scalar potential ϕ is antisymmetric and the vector one ψ is symmetric with respect to the vertical coordinate. It follows also from the symmetry of Eqs. (5).

Finally, the incident effective stress $\sigma_{\mathrm{eff}}^{\mathrm{inc}}$ at the borehole axis, located at an offset r from the source point, is derived from Eqs. (10),

$$\sigma_{\mathrm{eff}}^{\mathrm{inc}}(r,z,\omega) = -\frac{\omega^2 F(\omega)}{4\pi\rho_s} E\, \mathrm{sgn}(z) \int_0^\infty dp\, p J_0(\omega pr)$$

$$\times [(p^2 + \beta^{-2}/2 - \alpha^{-2})\exp(-i\omega\zeta(p)|z|)$$

$$- p^2 \exp(-i\omega\eta(p)|z|)]. \tag{11}$$

This expression should be used further as a disturbing force at the right-hand side of Eq. (1) to model propagation of tube waves in a fluid-filled borehole.

IV. PRECISE SOLUTION OF TUBE-WAVE EQUATION BY INTEGRAL TRANSFORMS

A. Representation through an integral over the horizontal slowness

Let's perform the double Fourier transform of Eq. (1) in the (t,z) domain. This leads to the solution of Eq. (1) for the dynamic pressure in the (ω,k) domain

$$P(r,k,\omega) = \frac{2\rho_f}{E} \frac{\omega^2 \sigma_{\mathrm{eff}}^{\mathrm{inc}}(r,k,\omega)}{k^2 - \omega^2/c_{tw}^2}. \tag{12}$$

This solution is as yet formal, because bypass rules of the poles in Eq. (12) are not determined. Moreover, it is necessary to evaluate the Fourier transform of the effective stress $\sigma_{\mathrm{eff}}^{\mathrm{inc}}$ given by Eq. (11) over the vertical coordinate z to write the required solution explicitly. It follows from Eq. (11) that this procedure involves integrals over the vertical coordinate of the kind

$$\int_{-\infty}^{+\infty} dz \exp(ikz)\mathrm{sgn}(z)\exp(-i\omega\zeta(p)|z|) = \frac{2ik}{k^2 - \omega^2\zeta^2(p)}. \tag{13}$$

These integrals can be evaluated using the principle of ultimate absorption.[11] Thus, the Fourier transform of the effective stress $\sigma_{\mathrm{eff}}^{\mathrm{inc}}$ is given by

P. M. Bokov and A. M. Ionov: Tube waves in a borehole

$$\sigma_{\text{eff}}^{\text{inc}}(r,k,\omega)=-\frac{\omega^2 F(\omega)ik}{2\pi\rho_s}\int_0^\infty p\,dp\,J_0(\omega pr)$$

$$\times\left[\frac{p^2+\beta^{-2}/2-\alpha^{-2}}{k^2-\omega^2\zeta^2(p)}-\frac{p^2}{k^2-\omega^2\eta^2(p)}\right].$$

$$(14)$$

Substitution of Eq. (14) into Eq. (12) gives the formal solution of Eq. (1). Further manipulations involve evaluation of inverse Fourier transforms with respect to the vertical tube-wave wave number k. Thus, the following integrals have to be evaluated:

$$I=\int_{-\infty}^{+\infty}\frac{ik\exp(-ikz)dk}{(k^2-\omega^2\zeta^2(p))(k^2-\omega^2/c_{tw}^2)}. \qquad (15)$$

The Jordan's lemma and residue theorem can be applied to evaluate such integrals over k. The integration contour and

location of poles in the case $z>0$ are shown in Fig. 2. Inversely, path integration for $z<0$ has to be performed in the upper k plane. The principle of ultimate absorption is used to shift poles away from the real axis.[11] It is easy to see, that this principle leads to a shift of the poles $k_1=+\omega\zeta$ and $k_2=+\omega/c_{tw}$ ($\omega>0$) in the lower half-plane $\text{Im}\,k<0$. Therewith, other two poles $k_3=-\omega\zeta$ and $k_4=-\omega/c_{tw}$ ($\omega>0$) are shifted in the upper half-plane $\text{Im}\,k>0$. The procedure of contour integration leads to the resultant integral

$$I=\frac{\pi}{\omega^2}\frac{\text{sgn}(z)}{c_{tw}^{-2}-\zeta^2(p)}[\exp(-i\omega|z|/c_{tw})-\exp(-i\omega\zeta(p)|z|)].$$

$$(16)$$

Evaluations for the second term in Eq. (14) are quite analogous, so the precise solution of Eq. (1) is

$$P(r,z,\omega)=-\frac{\omega^2 F(\omega)}{2\pi}\frac{\rho_f}{\rho_s}\text{sgn}(z)\left\{\exp\left(-\frac{i\omega|z|}{c_{tw}}\right)\int_0^\infty p\,dp\,J_0(\omega pr)\left[\frac{p^2+\beta^{-2}/2-\alpha^{-2}}{p^2+c_{tw}^{-2}-\alpha^{-2}}-\frac{p^2}{p^2+c_{tw}^{-2}-\beta^{-2}}\right]\right.$$

$$+\left.\int_0^\infty p\,dp\,J_0(\omega pr)\left[\frac{p^2+\beta^{-2}/2-\alpha^{-2}}{p^2+c_{tw}^{-2}-\alpha^{-2}}\exp(-i\omega\zeta|z|)-\frac{p^2}{p^2+c_{tw}^{-2}-\beta^{-2}}\exp(-i\omega\eta|z|)\right]\right\}. \qquad (17)$$

Because the relations $J_0(x)=[H_0^{(1)}(x)+H_0^{(2)}(x)]/2$ and $H_0^{(2)}(-x)=-H_0^{(1)}(x)$ hold, where $H_\mu^{(1,2)}(x)$ are Hankel functions of the first and second kind of order μ, the resultant solution can be written as an integral over the real p axis

$$P(r,z,\omega)=I_1+I_2=-\frac{\omega^2 F(\omega)}{4\pi}\frac{\rho_f}{\rho_s}\text{sgn}(z)\left\{\exp\left(-\frac{i\omega|z|}{c_{tw}}\right)\int_{-\infty}^{+\infty}p\,dp\,H_0^{(2)}(\omega pr)\left[\frac{p^2+\beta^{-2}/2-\alpha^{-2}}{p^2+c_{tw}^{-2}-\alpha^{-2}}-\frac{p^2}{p^2+c_{tw}^{-2}-\beta^{-2}}\right]\right.$$

$$+\left.\int_{-\infty}^{+\infty}p\,dp\,H_0^{(2)}(\omega pr)\left[\frac{p^2+\beta^{-2}/2-\beta^{-2}}{p^2+c_{tw}^{-2}-\alpha^{-2}}\exp(-i\omega\zeta|z|)-\frac{p^2}{p^2+c_{tw}^{-2}-\beta^{-2}}\exp(-i\omega\eta|z|)\right]\right\}. \qquad (18)$$

In Eq. (18) I_1 and I_2 designate corresponding integral terms, the first one is proportional to $\exp(-i\omega|z|/c_{tw})$. A superscript will be used to mark internal terms in I_1 and I_2 in the order corresponding to Eq. (18).

This integral representation of the exact solution is convenient for asymptotic evaluation of tube-wave propagation in fast formations, when the shear velocity exceeds the fundamental Stoneley wave velocity. Another representation of the exact solution, suitable for asymptotic tube-wave analysis in slow formations, is presented in Sec. IV B.

B. Representation through path integrals along edges of the cuts of $\zeta(p)$ and $\eta(p)$ functions in the complex p plane

Equation (18) consists of two terms. The first term I_1 is an analytic function in the whole complex p plane cut along the negative real semiaxis. It can be evaluated precisely in the complex p plane using the residue theorem.

Taking into account asymptotic behavior of the Hankel function at large values of its argument $H_0^{(2)}(w)\to\sqrt{2/(\pi w)}\exp(-iw+i\pi/4)$, we have to complete the integration path along a large semicircle in the lower complex half-plane $\text{Im}\,p<0$, where exponential decay of the integrand

proportional to $\exp(-i\omega pr)=\exp(-i\omega r(\text{Re}\,p+i\,\text{Im}\,p))\sim\exp(+\omega r\,\text{Im}\,p)$ occurs. Then, the first integral I_1 in Eq. (18) reduces to residues at the simple poles $p_1=-i\sqrt{c_{tw}^{-2}-\alpha^{-2}}$ and $p_3=-i\sqrt{c_{tw}^{-2}-\beta^{-2}}$. This leads to the result

$$P_{\text{Re}\,s}=I_1^{(1)}+I_1^{(2)}=\frac{i\omega^2 F(\omega)}{4}\frac{\rho_f}{\rho_s}\exp\left(-\frac{i\omega|z|}{c_{tw}}\right)\text{sgn}(z)$$

$$\times\left[\left(\frac{1}{2\beta^2}-\frac{1}{c_{tw}^2}\right)H_0^{(2)}(-i\omega\sqrt{c_{tw}^{-2}-\alpha^{-2}}r)\right.$$

$$+\left.\left(\frac{1}{c_{tw}^2}-\frac{1}{\beta^2}\right)H_0^{(2)}(-i\omega\sqrt{c_{tw}^{-2}-\beta^{-2}}r)\right].$$

$$(19)$$

Note, that for slow formations, when $c_{tw}>\beta$, the poles $p_{3,4}=\mp i\sqrt{c_{tw}^{-2}-\beta^{-2}}=\pm\sqrt{\beta^{-2}-c_{tw}^{-2}}$ lay at the real axis and have different signs. The principle of ultimate absorption dictates the positive and negative pole to be shifted to the lower and upper half-plane, respectively. So, only the residue in the positive pole contributes to the integral I_1.
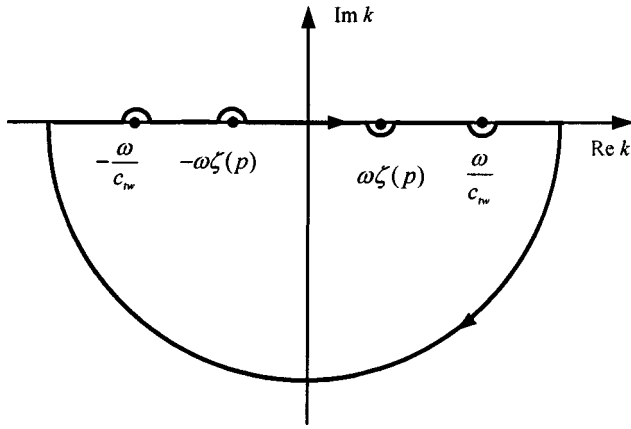
FIG. 2. The integration path in the complex wave number k plane.

FIG. 3. The integration path along with cuts and poles in the complex horizontal slowness p plane. The real part of the vertical slowness $\mathrm{Re}\,\zeta(p)$ is discontinuous at passing through the cut.

The second term I_2 in Eq. (18) is transformed in a more sophisticated manner. To perform further transformations in the complex p plane, for example, in $I_2^{(1)}$, it is necessary to apply the conditions $\mathrm{Im}\,p<0$ and $\mathrm{Im}\,\zeta(p)<0$. Thus, the complex p plane has to be cut to distinguish the branch $\mathrm{Im}\,\zeta(p)<0$. According to the principle of ultimate absorption[11] α^{-1} has to be replaced by $\alpha^{-1}-i\varepsilon$ ($\varepsilon>0$) in the P wave vertical slowness $\zeta(p)=\sqrt{\alpha^{-2}-p^2}$ to obtain

$$(\mathrm{Re}\,\zeta+i\mathrm{Im}\,\zeta)^2=(\alpha^{-1}-i\varepsilon)^2-(\mathrm{Re}\,p+i\,\mathrm{Im}\,p)^2. \quad (20)$$

Separation of real and imaginary parts in Eq. (20) results in the system

$$(\mathrm{Re}\,\zeta)^2-(\mathrm{Im}\,\zeta)^2=\alpha^{-2}-\varepsilon^2-(\mathrm{Re}\,p)^2+(\mathrm{Im}\,p)^2,$$
$$\mathrm{Re}\,\zeta\cdot\mathrm{Im}\,\zeta=-\varepsilon/\alpha-\mathrm{Re}\,p\cdot\mathrm{Im}\,p. \quad (21)$$

Because the cut is defined by the condition $\mathrm{Im}\,\zeta=0$, the hyperbolic equation for the cut in the complex p plane follows from the second equality in Eq. (21),

$$\mathrm{Re}\,p\cdot\mathrm{Im}\,p=-\varepsilon/\alpha. \quad (22)$$

At $\varepsilon\to0$ the cut consists of the imaginary semiaxis ($\mathrm{Im}\,p<0$, $\mathrm{Re}\,p=0$) and the intercept ($-\alpha^{-1}<\mathrm{Re}\,p<0$, $\mathrm{Im}\,p=0$). Note, that function $\mathrm{Re}\,\zeta(p)$ is subject to discontinuity in moving from the upper edge of the cut to the lower one. Thus, the integration path of the first term $I_2^{(1)}$ in Eq. (18) along the real axis can be transformed into the integration contour in the complex p plane shown in Fig. 3. The latter consists of the real axis, upper and lower edges of the cut, and a large semicircle in the lower complex half p plane. The integrand is an everywhere analytic function inside the domain bounded by this contour except for the simple pole $p_1=-i\sqrt{c_{tw}^{-2}-\alpha^{-2}}$.

According to the residue theorem, the integral along the path shown in Fig. 3 can be evaluated as

$$I_2^{(1)}+\int_{\mathrm{cut}_1}dp\cdots+\int_{\cap}dp\cdots$$
$$=-2\pi i\,\mathrm{Res}_1(p_1=-i\sqrt{c_{tw}^{-2}-\alpha^{-2}}), \quad (23)$$

where $\int_{\mathrm{cut}_1}dp\cdots$ is the path integral along the upper and lower edges of the cut of $\zeta(p)$, $\int_\cap dp\cdots$ is the path integral along a large semicircle in the lower complex half p plane,

$\mathrm{Res}_1(p_1=-i\sqrt{c_{tw}^{-2}-\alpha^{-2}})$ is the residue of $I_2^{(1)}$ in the pole p_1. Taking into account that $\int_\cap dp\cdots\to0$ and the equality

$$2\pi i\,\mathrm{Res}_1(p_1=-i\sqrt{c_{tw}^{-2}-\alpha^{-2}})$$
$$=\frac{i\omega^2 F(\omega)}{4}\frac{\rho_f}{\rho_s}\mathrm{sgn}(z)\left(\frac{1}{2\beta^2}-\frac{1}{c_{tw}^2}\right)$$
$$\times H_0^{(2)}(-i\sqrt{c_{tw}^{-2}-\alpha^{-2}}\,\omega r)\exp\left(-\frac{i\omega|z|}{c_{tw}}\right)=I_1^{(1)}, \quad (24)$$

the summary integral $I_1^{(1)}+I_2^{(1)}$ can be represented as the path integral along edges of the cut for function $\zeta(p)$

$$I_1^{(1)}+I_2^{(1)}=-\int_{\mathrm{cut}_1}dp\cdots. \quad (25)$$

The second term $I_2^{(2)}$ in I_2 is transformed quite analogous along the cut for the S wave vertical slowness $\eta(p)$ in the complex p plane. The summarized result is

$$P(r,z,\omega)=I_1+I_2=I_1^{(1)}+I_1^{(2)}+I_2^{(1)}+I_2^{(2)}$$
$$=-\int_{\mathrm{cut}_1}dp\cdots-\int_{\mathrm{cut}_2}dp\cdots. \quad (26)$$

Change of integration variables $p\to\zeta$ and $p\to\eta\to\zeta$ in the path integrals in Eq. (26) leads to

$$P(r,z,\omega)=\frac{\omega^2 F(\omega)}{4\pi}\frac{\rho_f}{\rho_s}\mathrm{sgn}(z)\int_{-\infty}^{+\infty}\frac{\zeta d\zeta}{c_{tw}^{-2}-\zeta^2}\exp(-i\omega\zeta|z|)$$
$$\times[(\beta^{-2}/2-\zeta^2)H_0^{(2)}(\sqrt{\alpha^{-2}-\zeta^2}\,\omega r)$$
$$-(\beta^{-2}-\zeta^2)H_0^{(2)}(\sqrt{\beta^{-2}-\zeta^2}\,\omega r)]. \quad (27)$$

It follows from Eq. (27) that the integrand has pole singularities at the integration path. Their contribution to the integral value can be separated by expansion of the integrand denominator in Eq. (27) into partial fractions and using the principle of ultimate absorption $c_{tw}^{-1}\to c_{tw}^{-1}-i\varepsilon(\varepsilon>0)$. Taking into account that the well-known equalities[12] hold

P. M. Bokov and A. M. Ionov: Tube waves in a borehole

$$\frac{1}{\zeta \pm c_{tw}^{-1}} \rightarrow \frac{1}{\zeta \pm c_{tw}^{-1} \mp i\varepsilon} = \text{v.p.} \frac{1}{\zeta \pm c_{tw}^{-1}} \pm i\pi\delta(\zeta \pm c_{tw}^{-1}), \tag{28}$$

where v.p. designates a Cauchy principle-value integral, the desired integral representation of the solution is obtained by combining Eq. (27) and Eq. (28) and after some transformations can be presented as

$$P(r,z,\omega) = \frac{\omega^2 F(\omega)}{4\pi} \frac{\rho_f}{\rho_s} \text{sgn}(z) \text{v.p.} \int_{-\infty}^{+\infty} \frac{\zeta\, d\zeta}{c_{tw}^{-2} - \zeta^2} \exp(-i\omega\zeta|z|)[(\beta^{-2}/2 - \zeta^2)H_0^{(2)}(\sqrt{\alpha^{-2} - \zeta^2}\,\omega r)$$

$$- (\beta^{-2} - \zeta^2)H_0^{(2)}(\sqrt{\beta^{-2} - \zeta^2}\,\omega r)] - \frac{\omega^2 F(\omega)}{4\pi} \frac{\rho_f}{\rho_s} \text{sgn}(z)[\exp(-i\omega|z|/c_{tw}) - \exp(+i\omega|z|/c_{tw})]$$

$$\times \left[(\beta^{-2}/2 - c_{tw}^{-2})K_0(\omega\sqrt{c_{tw}^{-2} - \alpha^{-2}}\,r) + \frac{\pi i}{2}(\beta^{-2} - c_{tw}^{-2})H_0^{(2)}(\omega\sqrt{\beta^{-2} - c_{tw}^{-2}}\,r) \right], \tag{29}$$

where $K_0(x) = -i\pi H_0^{(2)}(-ix)/2$ is the Macdonald function of zero order of a real variable x.

Both representations given by Eq. (18) and Eq. (29) are equivalent. The latter is suitable to find tube-wave asymptotics in slow formations.

V. ASYMPTOTIC FAR-FIELD ANALYSIS OF TUBE-WAVE PROPAGATION IN FAST AND SLOW FORMATIONS

A. Fast formations

It is essential to distinguish tube-wave propagation in fast ($\beta > c_{tw}$) and slow ($\beta < c_{tw}$) formations. Asymptotic P and SV wave forms generated by a single-force point source in a fluid-filled borehole, embedded in a fast formation, can be found by the method of stationary phase[13] applied to the second integral term I_2 in Eq. (18). The first and second items in I_2 describe asymptotically P and SV wave propagation, respectively. The procedure of their evaluation is quite analogous, so we consider it for the P wave only.

Taking into account the asymptotics of the Hankel function at great arguments, the following expression for the phase of the integrand is obtained:

$$\vartheta(p) = -i\omega(pr + \zeta(p)|z|). \tag{30}$$

The stationary point is determined by the stationary-phase condition $d\vartheta/dp = 0$, which leads to

$$p_0(r/R) = r/(\alpha R) = \sin\gamma/\alpha, \tag{31}$$

where $\sin\gamma = r/R$. After expansion of the phase $\vartheta(z)$ in Taylor series near the stationary point up to the second order and then integration of the resultant integrand over the slowness, the P wave asymptotics contributed by the incident P wave is derived

$$P_P(r,z,\omega) = \frac{\omega^2 F(\omega)}{4\pi} \frac{\rho_f}{\rho_s} \text{sgn}(z) \int_{-\infty}^{+\infty} p\, dp \frac{p^2 + \beta^{-2}/2 - \alpha^{-2}}{p^2 + c_{tw}^{-2} - \alpha^{-2}}$$

$$\times \exp(-i\omega\zeta|z|)H_0^{(2)}(\omega pr)$$

$$\rightarrow \frac{i\omega F(\omega)}{4\pi} \frac{\rho_f}{\rho_s} \text{sgn}(z)$$

$$\times \cos\gamma \frac{(\beta^{-2} - 2\beta^{-2}\cos^2\gamma)}{(c_{tw}^{-2} - \alpha^{-2}\cos^2\gamma)} \frac{\exp(-i\omega R/\alpha)}{\alpha R}. \tag{32}$$

The final asymptotic solution for the $P + SV$ wave is obtained by adding together the P wave acoustic pressure given by Eq. (32) with the similar result for the S wave

$$P_{P+SV} = \frac{\rho_f}{\rho_s} \frac{\text{sgn}(z)}{4\pi} \frac{\cos\gamma}{R}$$

$$\times \left[\frac{(\beta^{-2} - 2\beta^{-2}\cos^2\gamma)}{(c_{tw}^{-2} - \alpha^{-2}\cos^2\gamma)} \frac{\dot{F}(t - R/\alpha)}{\alpha} \right.$$

$$\left. - \frac{2\beta^{-2}\sin^2\gamma}{(c_{tw}^{-2} - \beta^{-2}\cos^2\gamma)} \frac{\dot{F}(t - R/\beta)}{\beta} \right]. \tag{33}$$

It follows from Eq. (33) that wave forms and travel times of the P and SV waves in the borehole fluid coincide with such ones for P and SV elastic waves in a fast formation. Their amplitudes decay as R^{-1}. Amplitudes of the P and SV waves are free of singularity, because the Stoneley wave velocity obeys the condition $c_{tw} < \beta < \alpha$.

Taking into account analytic features of the integrand in the first integral I_1 in Eq. (18), it can be reduced to residues at the simple poles $p_1 = -i\sqrt{c_{tw}^{-2} - \alpha^{-2}}$ and $p_3 = -i\sqrt{c_{tw}^{-2} - \beta^{-2}}$. Straightforward calculations for the Stoneley wave lead to

$$P^{St}(r,z,\omega) = P_P^{St} + P_{SV}^{St}$$

$$= -\frac{\omega^2 F(\omega)}{2\pi} \frac{\rho_f}{\rho_s} \text{sgn}(z)\exp\left(-\frac{i\omega|z|}{c_{tw}}\right)$$

$$\times \left\{ \left(\frac{1}{2\beta^2} - \frac{1}{c_{tw}^2}\right) K_0(\omega\sqrt{c_{tw}^{-2} - \alpha^{-2}}\,r) \right.$$

$$\left. - \left(\frac{1}{\beta^2} - \frac{1}{c_{tw}^2}\right) K_0(\omega\sqrt{c_{tw}^{-2} - \beta^{-2}}\,r) \right\}. \tag{34}$$

It follows from Eq. (34) that the Stoneley wave P^{St} has its own internal structure due to contribution of the longitudinal wave P_P^{St} and the shear wave P_{SV}^{St}. The complete asymptotic wave field $P_{P+SV}+P^{St}$ in the fluid-filled borehole embedded in a fast formation is given by the sum of Eq. (33) and Eq. (34). Analysis of the Stoneley wave form given by Eq. (34) shows, that in the case when the signal duration T is small as compared with the width $\sqrt{c_{tw}^{-2}-\alpha^{-2}}r$, its amplitude decreases proportional to r^{-3} and its duration is determined by this width. In the reverse limiting case, when $T \gg \sqrt{c_{tw}^{-2}-\beta^{-2}}r$, its amplitude decays as r^{-1}.

B. Slow formations

The SV wave amplitude in a slow formation ($\beta < c_{tw}$) described by the second term in Eq. (33) becomes singular at the critical point given by

$$\cos \gamma_c = \pm \beta/c_{tw}, \qquad (35a)$$

or, equivalently, by the condition

$$z_c = \pm r/\sqrt{c_{tw}^2/\beta^2-1}. \qquad (35b)$$

This peculiarity was intimated repeatedly by White,[1] Peng et al.,[6] and other researchers.

This SV wave singularity at the critical point is not surprising, because the standard stationary-phase method does not lead to the correct result in this case. The reason is that the stationary-phase point (or the saddle point) coincides with the simple pole of the integrand as pointed out by Fedoryuk[14] and Petrashen.[15]

In fact, there is no singularity for SV wave at the critical point. However, its appearance is not accidental for a slow formation. For fast formations the apparent velocity of the incident shear wave along the borehole is always greater than the low-frequency Stoneley wave velocity. Otherwise, for a slow formation only the limited borehole section ($|z|<z_c$) exists, where this statement is true, because the Stoneley wave velocity exceeds the moveout shear velocity at $|z| > z_c$.

The method of stationary phase has to be modified to evaluate the asymptotic behavior of the SV wave near the critical point. The SV wave contribution to the complete wave field in the fluid-filled borehole is proportional to the second integral term in Eq. (29),

$$I_{SV}=\text{v.p.} \int_{-\infty}^{+\infty} \frac{\zeta d\zeta}{(c_{tw}^{-2}-\zeta^2)}(\beta^{-2}-\zeta^2)\exp(-i\omega\zeta|z|)$$
$$\times H_0^{(2)}(\omega\sqrt{1/\beta^2-\zeta^2}r). \qquad (36)$$

Taking into account the asymptotic behavior of the Hankel function, the stationary point of the phase $\vartheta_{SV}(\zeta) = -i\omega(\zeta|z|+\sqrt{\beta^{-2}-\zeta^2}r)$ in this integrand is given by

$$\zeta_0^{SV}=|z|/(\beta R)=\cos \gamma/\beta. \qquad (37)$$

After expansion of the phase near the critical point in Taylor series up to the second order the considered integral can be asymptotically transformed to

$$I_{SV}\rightarrow -\sqrt{\frac{2}{\pi\omega r}} \frac{\zeta_0^{SV}(\beta^{-2}-(\zeta_0^{SV})^2)^{3/4}}{(c_{tw}^{-1}+\zeta_0^{SV})} \exp\left(-\frac{i\omega R}{\beta}+\frac{i\pi}{4}\right)$$
$$\times I(\delta,\sigma), \qquad (38)$$

where

$$I(\delta,\sigma)=\text{v.p.} \int_{-\infty}^{+\infty} \frac{dx}{x-\delta}\exp(i\sigma x^2),$$

$$\delta=\beta/c_{tw}-\cos \gamma, \qquad \sigma=\omega R^3/(2\beta r^2).$$

Equation (38) contains the Cauchy principle-value integral $I(\delta,\sigma)$. This integral can be expressed via the Fresnel integrals[16] $C(x)$ and $S(x)$. Thus, the expression for the SV wave near the critical point is

$$P_{SV}=\frac{i\omega^{3/2}F(\omega)}{2\sqrt{2\pi}} \frac{\rho_f}{\rho_s} \text{sgn}(z) \frac{\zeta_0^{SV}(\beta^{-2}-(\zeta_0^{SV})^2)^{3/4}}{\sqrt{r}(c_{tw}^{-1}+\zeta_0^{SV})}$$

$$\times\exp\left(-\frac{i\omega R}{\beta}+\frac{i\pi}{4}+i\sigma\delta^2\right)$$

$$\times\left\{-\text{sgn}(\delta)+\sqrt{2}\left[\exp\left(\frac{i\pi}{4}\right)C\left(\sqrt{\frac{2\sigma}{\pi}}\delta\right)\right.\right.$$

$$\left.\left.+\exp\left(-\frac{i\pi}{4}\right)S\left(\sqrt{\frac{2\sigma}{\pi}}\delta\right)\right]\right\}. \qquad (39)$$

Taking into account the asymptotic behavior[16] of the Fresnel integrals $C(x)$ and $S(x)$, so that $I(\delta,\sigma)$ $\rightarrow -(\pi/\sigma)^{1/2}\exp(i\pi/4)/\delta$, Eq. (39) can be transformed to the standard WKBJ[13] result at $\delta \gg \sigma^{-1/2}$ for the SV wave given by the second term in Eq. (33).

In addition to the stationary point ζ_0^{SV}, the pole singularities at $\zeta=\pm c_{tw}^{-1}$ contribute to the integral given by Eq. (36). After decomposition of the denominator in Eq. (36) on partial fractions, replacement of the Hankel function by its asymptotics at great arguments and the change of variables $\zeta \pm c_{tw}^{-1} \rightarrow x$ in corresponding integrals, the result is

$$I_{SV}^{pol}=\frac{c_{tw}}{2}\sqrt{\frac{2}{\pi\omega r}}\exp\left(\frac{i\pi}{4}\right)\left[-\text{v.p.}\int_{-\infty}^{+\infty}\frac{dx}{x}f_1(x)\right.$$

$$\times\exp[i\omega S_1(x)]+\text{v.p.}\int_{-\infty}^{+\infty}\frac{dx}{x}$$

$$\left.\times f_2(x)\exp[i\omega S_2(x)]\right], \qquad (40)$$

where functions f_i and phases S_i ($i=1,2$) are given by

$$f_1(x)=(c_{tw}^{-1}+x)[\beta^{-2}-(c_{tw}^{-1}+x)^2]^{3/4},$$

$$f_2(x)=(-c_{tw}^{-1}+x)[\beta^{-2}-(-c_{tw}^{-1}+x)^2]^{3/4},$$

$$\qquad\qquad\qquad\qquad\qquad\qquad\qquad\qquad (41)$$

$$S_1(x)=-[(c_{tw}^{-1}+x)|z|+\sqrt{\beta^{-2}-(c_{tw}^{-1}+x)^2}r],$$

$$S_2(x)=-[(-c_{tw}^{-1}+x)|z|+\sqrt{\beta^{-2}-(-c_{tw}^{-1}+x)^2}r].$$

Asymptotic evaluation of such integrals is considered in detail by Fedoryuk.[14] Their asymptotic behavior at $\omega \to \infty$ is governed by a local value of the first derivative $S'(0)$. If $S'(0) \neq 0$, the result is

$$\text{v.p.} \int_{-\infty}^{+\infty} \frac{dx}{x} f(x) \exp[i\omega S(x)]$$

$$\to i\pi f(0)\exp[i\omega S(0)]\text{sgn}[S'(0)]. \qquad (42)$$

It can easily be shown that the equality $\text{sgn}[S'(0)]=-1$ holds invariably. However, the value $S'_1(0)$ changes its sign in passing through the critical point

$$S'_1(0)=|z_c|-|z|. \qquad (43)$$

Taking into account the above mentioned, the contribution of the poles can be written as

$$-\frac{\omega^2 F(\omega)}{4\pi}\frac{\rho_f}{\rho_s}\text{sgn}(z)I_{SV}^{\text{pol}}$$

$$\to \frac{i\omega^2 F(\omega)}{4\sqrt{2\pi\omega r}}\frac{\rho_f}{\rho_s}\text{sgn}(z)(\beta^{-2}-c_{tw}^{-2})^{3/4}$$

$$\times \exp\left(-i\omega\sqrt{\beta^{-2}-c_{tw}^{-2}}\,r+\frac{i\pi}{4}\right)$$

$$\times \left[\exp\left(-\frac{i\omega|z|}{c_{tw}}\right)\text{sgn}(|z_c|-|z|)-\exp\left(\frac{i\omega|z|}{c_{tw}}\right)\right]. \qquad (44)$$

Summation of Eq. (44) and the pole terms in Eq. (29) leads to the final result for the partial Stoneley wave P_{SV}^{St} contributed by the incident SV wave in a slow formation

$$P_{SV}^{\text{St}}\to \frac{i\omega^2 F(\omega)}{4\sqrt{2\pi\omega r}}\frac{\rho_f}{\rho_s}\text{sgn}(z)[\text{sgn}(|z_c|-|z|)-1]$$

$$\times (\beta^{-2}-c_{tw}^{-2})^{3/4}$$

$$\times \exp(-i\omega(\sqrt{\beta^{-2}-c_{tw}^{-2}}\,r+|z|/c_{tw})+i\pi/4).$$

$$(45)$$

Thus, the Stoneley wave P_{SV}^{St} exists only in the post-critical region $|z|>|z_c|$. This statement has been proved in the strict sense only asymptotically at $\lambda \ll r$. However, straightforward calculations made in Sec. VI for slow formations show the truth of this statement in a wide range of the ratio λ/r. The conic Stoneley wave amplitude decays with an offset rather slowly ($r^{-1/2}$) as compared to the P_P^{St} amplitude (r^{-3}).

It follows from Eq. (45), that the wave front of the Stoneley wave P_{SV}^{St} is a cone with a vertex laying at the axis passing through the source and parallel to the borehole:

$$z=\pm\sqrt{c_{tw}^2/\beta^2-1}\,r+C.$$

Hence, it is a conical wave or Mach wave. It will be referred further in this work as the conical Stoneley wave.

It would be reasonable to make the following remark. Peng et al.[5] solved the problem about tube-wave propagation in a fluid-filled borehole generated by a source placed in the borehole interior. It was assumed the ratio λ/r to be arbitrary. They obtained the asymptotic speed for the conical Stoneley wave in the long-wave approximation, when the wavelength λ is much greater than the borehole radius b. It was shown for a slow formation, when the condition $\beta < c_{tw}$ holds, that the speed of the conical Stoneley wave has additional terms of the order $(b/\lambda)^2 \ll 1$ in the long-wave approximation. The imaginary and real additives to the speed of the conical Stoneley wave describe absorption and dispersion, respectively. It should be emphasized that in the approach considered here these additives are precisely equal to zero. Estimates show that for small enough values of the ratio b/λ, characteristic for the most part of applied seismic problems, the integral influence due to absorption and dispersion on the conical Stoneley tube wave is negligible. However, these effects for a fluid-filled borehole of infinite extent lead at large distances to distortion and decay of the conical Stoneley wave. Note, that the absorption and dispersion can be introduced explicitly in the Fourier analog of Eq. (1) through the low-frequency limit[1] of the Stoneley wave velocity.

Asymptotic expressions obtained for the P wave and the partial contribution P_P^{St} to the Stoneley wave for a fast formation are also valid for a slow formation.

VI. ASYMPTOTIC AND STRAIGHTFORWARD NUMERICAL MODELING OF TUBE-WAVE PROPAGATION

The straightforward solution of the problem as a superposition of delayed tube waves, generated by incident elastic waves in the surrounding formation, was obtained by White.[1] In a slightly different form it can be written as[10]

$$P(r,z,t)=-\frac{\rho_f c_{tw}}{E}\int_{-\infty}^{+\infty}dz'\frac{\partial}{\partial t}\left[\sigma_{\text{eff}}^{\text{inc}}\left(r,z',t-\frac{|z-z'|}{c_{tw}}\right)\right]. \qquad (46)$$

Cumbersome, but straightforward evaluations for the single-force point source based on Eq. (11) and the Sommerfeld's representation of a spherical wave as a superposition of cylindrical waves lead to

$$\frac{\partial\sigma_{\text{eff}}^{\text{inc}}(r,z,t)}{\partial t}=-\frac{E\cos\gamma}{4\pi\rho_s}\left\{\left[\frac{1}{2\beta^2}-\frac{\cos^2\gamma}{\alpha^2}\right]\frac{\ddot{F}(t-R/\alpha)}{\alpha R}-\frac{(1-\cos^2\gamma)}{\beta^3 R}\ddot{F}(t-R/\beta)+\left[\frac{1}{2\beta^2}+\frac{3(1-2\cos^2\gamma)}{\alpha^2}\right]\frac{\dot{F}(t-R/\alpha)}{R^2}\right.$$

$$\left.+\frac{2(3\cos^2\gamma-2)}{\beta^2 R^2}\dot{F}(t-R/\beta)+\frac{3(3-5\cos^2\gamma)}{R^3}\left[\frac{F(t-R/\alpha)}{\alpha}-\frac{F(t-R/\beta)}{\beta}+\frac{1}{R}\int_{t-R/\beta}^{t-R/\alpha}F(\tau)d\tau\right]\right\}, \qquad (47)$$
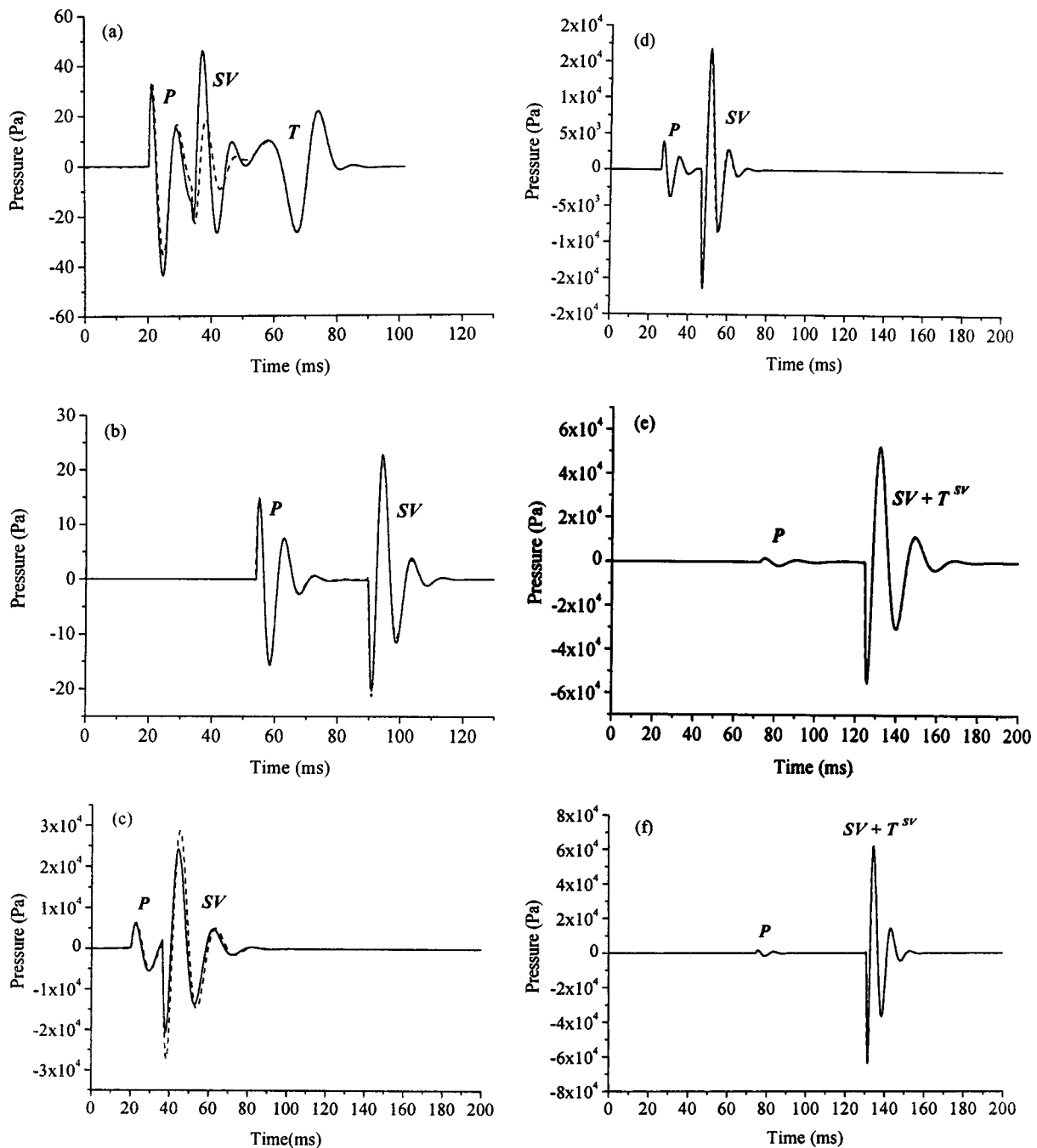
FIG. 4. Pressure wave forms in the fluid-filled borehole generated by a single-force point source. Solid line, straightforward calculations; dashed line, asymptotic solution. Sketches (a) and (b) correspond to the fast formation with acoustic parameters $\alpha = 5000$ m/s, $\beta = 3000$ m/s. Sketches (c), (d), (e), and (f) correspond to the slow formation with acoustic parameters $\alpha = 1440$ m/s, $\beta = 780$ m/s; wave forms (c) and (d) are calculated for a subcritical distance, wave forms (e) and (f) are calculated for post-critical distances. The ratio between the dominant wavelength and the offset $\lambda/r > 1$ for (b), (d), (f), and $\lambda/r < 1$ for (a), (c), (e). (a) Wave forms at $r = 20$ m, $z = 100$ m, $f_0 = 100$ Hz; (b) wave forms at $r = 100$ m, $z = 100$ m, $f_0 = 100$ Hz; (c) wave forms at $r = 20$ m, $z = 100$ m, $f_0 = 50$ Hz; (d) wave forms at $r = 30$ m, $z = 100$ m, $f_0 = 100$ Hz; (e) wave forms at $r = 20$ m, $z = 20$ m, $f_0 = 50$ Hz; (f) wave forms at $r = 30$ m, $z = 20$ m, $f_0 = 100$ Hz.

where a dot over a letter designates differentiation with respect to time.

Results of modeling of tube-wave propagation generated by the single-force point source in a fluid-filled borehole are presented in this section. Calculations were performed both on the base of asymptotic formulas derived in Sec. V and the straightforward integral representation in the form of retarded potentials given by Eqs. (46) and (47). We adhere to

the following notations for tube-wave phases: P and SV denote P and SV waves in the borehole fluid, the Stoneley wave corresponding to $P^{\mathrm{St}} = P_P^{\mathrm{St}} + P_{SV}^{\mathrm{St}}$ is designated as $T = T^P + T^{SV}$. If required, the partial additives in the Stoneley wave are designated separately.

The seismic source function is chosen in the form $F(t) = At \exp(-\pi f_0 t)\sin(2\pi f_0 t)\Theta(t)$, where $\Theta(t)$ denotes the Heaviside unit step function. The normalizing factor A is
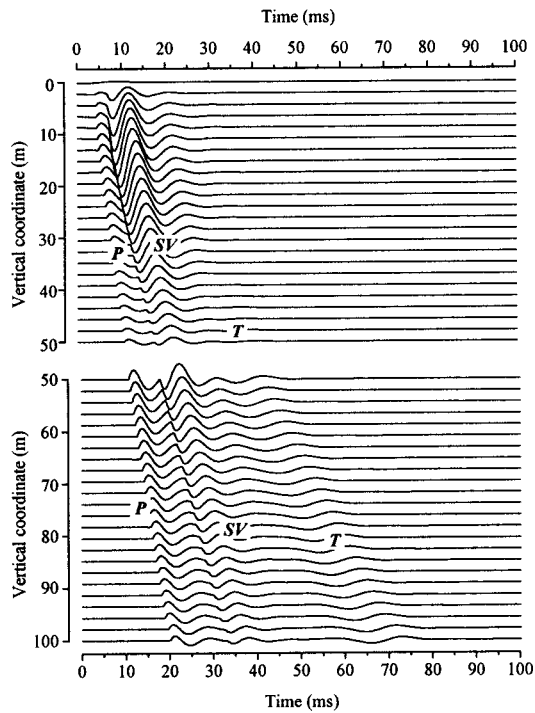
FIG. 5. Synthetics of the dynamic pressure in the fluid-filled borehole embedded in the fast formation with acoustic parameters $\alpha = 5000$ m/s, $\beta = 3000$ m/s. The offset is $r = 20$ m. The dominant frequency of the source is $f_0 = 100$ Hz. The lower part of seismic traces is presented on a fourfold enlarged amplitude scale.

supposed to be equal to unity throughout all calculations.

Results of calculations made on the base of these two approaches both in a fast and slow formation are shown in Fig. 4. Numerical tube-wave modeling for a slow formation is fulfilled in both subcritical and post-critical regions. The ratio λ/r is also varied in the set of calculations, being less or more than unity by several times. Though asymptotic formulas obtained in Sec. V are formally valid only in the case $\lambda/r \ll 1$, an analysis of wave forms shows that these two approaches lead to very similar results in a wide range of the ratio.

Synthetics of the dynamic pressure in a fluid-filled borehole embedded in a fast formation are shown in Fig. 5. Receivers are distributed equidistantly through each 2 m from 0 m up to 100 m. The borehole is filled with water of the density $\rho_f = 1000$ kg/m^3 and the sound speed $c_f = 1600$ m/s. Three phases are clearly visualized in Fig. 5: P and SV waves, and the Stoneley wave. These phases are not distinguished separately at small vertical distances along the borehole axis, but they can be easily identified at long distances.

The lower part of seismic traces shown in Fig. 5 is presented on a fourfold enlarged amplitude scale, because the P and SV wave amplitudes decrease due to a geometrical decay. As observed in Fig. 5, the amplitude of the Stoneley wave, being free of any geometrical decay, becomes comparable at some distance with P and SV wave amplitudes. At longer distances the Stoneley wave turns to be the dominant phase.

It is of interest to compare the ratio between the Stoneley wave and P wave amplitudes for the explosive (isotropic) and the single-force source. This ratio is equal to
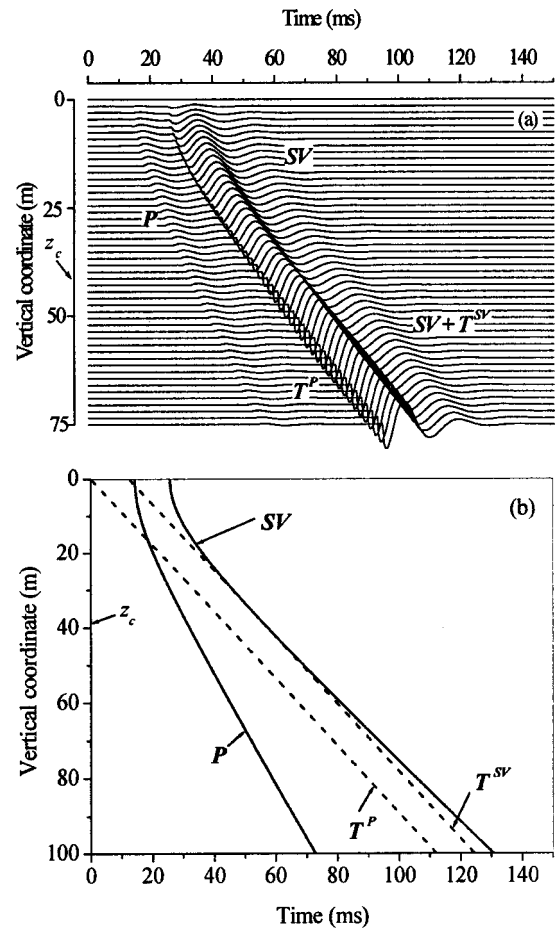
FIG. 6. Wave propagation in the fluid-filled borehole embedded in the slow formation with acoustic parameters $\alpha = 1440$ m/s, $\beta = 780$ m/s. The offset is $r = 20$ m. The dominant frequency of the source is $f_0 = 50$ Hz. (a) Seismic traces; (b) travel times of different phases.

$$\left(\frac{A(T^P)}{A(P)}\right)_{\text{explosive}} = \frac{c_{tw}|z|}{\alpha R}\left(\frac{A(T^P)}{A(P)}\right)_{\text{vertical force}}, \quad (48)$$

where asymptotic results for an isotropic source[7] and asymptotics found in this work are used.

Thus, the Stoneley wave amplitude at the same P wave amplitude is greater for a single-force point source. However, its amplitude is essentially suppressed. The reason is that the two components T^P and T^{SV} of the Stoneley wave have various polarities and about the same widths, thus the overall Stoneley wave amplitude differs substantially from the result given by Eq. (48). Note, that the Stoneley wave in Fig. 5 is suppressed not only due to compensation of its two components, but also due to an offset geometrical factor. It is possible to increase essentially P and SV wave amplitudes by placing the source point closer to the borehole.

Travel times and synthetics in a slow formation are shown in Fig. 6. As observed in Fig. 6(b), the travel-time curves of P and SV waves are hyperbolas in the (t,z) plane and coincide with the incident P and SV wave travel-time curves. The travel-time curves of the partial Stoneley waves T^P and T^{SV} are straight parallel lines and intersect the abscissa t axis at the points $t=0$ and $t=r/\beta$, respectively. Though the T^P and T^{SV} time-distance curves are shown in Fig. 6(b) for all non-negative z values, there is some domain

where they are meaningless, because these tube-wave phases have not been formed yet. Thus, the partial Stoneley wave T^{SV} as shown in Sec. V B does not exist at subcritical distances $|z| < |z_c|$. At the critical point z_c the travel-time curves for the SV and T^{SV} phases are tangent to one another. At post-critical distances $|z| > |z_c|$ first these curves are very close to one another, so these two phases interfere, and then diverge slowly at increase of the vertical coordinate. It happens because in a slow formation the low-frequency Stoneley wave velocity is close to the S wave velocity. Another example concerns the P and T^P phases. It can be shown[7] that they are separated at distances $z > r \sqrt{\alpha^2 / c_{tw}^2 - 1}$.

Three phases are clearly distinguished in Fig. 6(a): P and SV waves, and the conic Stoneley wave T^{SV}. The Stoneley partial response T^P has very small amplitude as compared to other phases to be clearly visualized. As observed in Fig. 6(a), the amplitude of SV wave grows up to the critical point, whereas the conic Stoneley wave T^{SV} is absent in accordance with the results of asymptotic analysis fulfilled in Sec. V B. In the post-critical region the conic Stoneley wave appears and interferes with the SV wave. The wave interference leads to wave form changes of the combined wave field $SV + T^{SV}$.

The SV wave decays strongly at large distances along the borehole axis, just as the conic Stoneley wave amplitude is constant. Thus, the conic Stoneley wave becomes asymptotically a dominant phase. Note, that for a slow formation in contrast to a fast one, the total amplitude of the Stoneley wave is great enough as compared with other phases and so can be easily visualized and discriminated.

VII. CONCLUSION

Tube-wave propagation in a fluid-filled borehole of infinite extent, generated by a single point force applied to an isotropic, purely elastic surrounding formation, is considered in the long-wave approximation. The precise solution is obtained as a double integral over the horizontal slowness and frequency. Another integral representation of the problem is derived in an easy-to-use form to analyze asymptotically tube-wave propagation for slow formations, when the Stoneley wave velocity exceeds the transversal velocity in the surrounding formation. Therewith, corresponding integrals over the slowness real axis are transformed into contour integrals in the slowness complex plane and converted to integrals over edges of cuts for vertical slowness functions and semiresidues in poles. An asymptotic analysis of tube-wave propagation in a fluid-filled borehole is fulfilled on the base of these two integral representations both for fast and slow surrounding formations.

It is shown that the asymptotic wave field in the borehole fluid for a fast formation consists of P and SV waves and the lowest eigenmode of the Stoneley wave (tube wave), which, in its turn, is a superposition of contributions due to the incident P and SV waves. The Stoneley wave amplitude is significantly suppressed as compared with such one generated by an isotropic source, because its two additives have inverse polarities. Asymptotic wave forms are obtained and analyzed for the P and SV waves, and the Stoneley wave.

The SV wave far-field asymptotics in the borehole fluid is derived from the exact integral representation for a slow formation. It is shown that far away from the critical point, which is determined by the ratio of the shear-wave velocity in the formation to the tube-wave velocity, it is described by the standard WKBJ expression. In the critical point and in its neighborhood the SV wave field is free of the singularity peculiar to the WKBJ wave field. It is shown that for a slow formation the conic Stoneley wave (Mach wave) is generated. It appears after the critical angle defined by the ratio of the S wave velocity in the formation to the low-frequency Stoneley wave velocity. The conic Stoneley wave does not exist within the borehole section viewed from the double critical angle of the source point. This statement is proven by analytic methods only asymptotically. The conic Stoneley wave amplitude decays weakly with an offset (asymptotically as $r^{-1/2}$). Therefore it has significant amplitude at large distances as compared with other tube-wave phases.

Wave forms obtained with the aid of asymptotic formulas and straightforward calculations in the form of superposition of delayed tube waves are compared. Numerical modeling is performed both for fast and slow formations at various ratios of the dominant wavelength to the offset. These two approaches lead to very similar wave forms.

[1] J. E. White, *Underground Sound—Application of Seismic Waves* (Elsevier Science, New York, 1983).

[2] L. Tsang and D. Rader, "Numerical evaluation of the transient acoustic waveform due to a point source in a fluid-filled borehole," Geophysics **44**, 1706–1720 (1979).

[3] M. W. Lee and A. H. Balch, "Theoretical seismic wave radiation from a fluid-filled borehole," Geophysics **47**, 1308–1314 (1982).

[4] J. A. Meredith, M. N. Toksöz, and C. H. Cheng, "Secondary shear waves from source boreholes," Geophys. Prospect. **41**, 287–312 (1993).

[5] Chengbin Peng, C. H. Cheng, and M. N. Toksöz, "Cased borehole effects on downhole seismic measurements," Geophys. Prospect. **42**, 777–811 (1994).

[6] Chengbin Peng, C. H. Cheng, and M. N. Toksöz, "Borehole effects on downhole seismic measurements," Geophys. Prospect. **41**, 883–912 (1993).

[7] A. M. Ionov and G. A. Maximov, "Excitation of a tube wave in a borehole by an external seismic source," Acoust. Phys. **45**, 311–316 (1999).

[8] G. Müller, "The reflectivity method: a tutorial," J. Geophys. **58**, 153–174 (1985).

[9] R. E. Sheriff and L. P. Geldart, *Exploration Seismology. History, Theory and Data Acquisition* (Cambridge University Press, Cambridge, 1985), Vol. 1.

[10] A. M. Ionov and G. A. Maximov, "Propagation of tube waves generated by an external source in layered permeable rocks," Geophys. J. Int. **124**, 888–906 (1996).

[11] K. Aki and P. G. Richards, *Quantitative Seismology—Theory and Methods* (Freeman & Co, San Francisco, 1980), Vol. 1.

[12] J. Mathews and R. L. Walker, *Mathematical Methods of Physics* (W. A. Benjamin, New York, Amsterdam, 1964).

[13] A. H. Nayfeh, *Introduction to Perturbation Techniques* (Wiley-Intersience, New York, 1981).

[14] M. V. Fedoryuk, *Asymptotics: Integrals and Series* (Nauka, Moscow, 1987) (in Russian).

[15] G. I. Petrashen, *Wave Propagation in Anisotropic Elastic Media* (Nauka, Leningrad, 1984) (in Russian).

[16] M. Abramowitz and I. Stegun, *Handbook of Mathematical Functions with Formulas, Graphs, and Mathematical Tables* (Dover, New York, 1964).

Prediction of sound level at high-frequency bands by means of a simplified boundary element method

Jae-Kwon Kim and Jeong-Guon Ih[a]

Center for Noise and Vibration Control, Department of Mechanical Engineering, Korea Advanced Institute of Science and Technology, Science Town, Taejon 305-701, Korea

A simplified boundary element method (BEM) for dealing with high-frequency sound is proposed. The boundary integral equation is modified into a quadratic form to enable the prediction of sound levels in the one-third octave band analysis. Monopole and dipole source terms in the conventional BEM are transformed into the auto- and cross-spectra of two vibrating sources, in which the cross-spectra are eventually neglected by assuming that the correlation coefficients involved are negligible. The present method is compared with the Rayleigh integral for calculating the sound pressure radiated from a baffled panel, in terms of the application limit. The characteristic length of the boundary element and the applicable frequency range can be determined by the lower limit value of the correlation coefficient. As a test example, the field pressure radiated from a partially vibrating sphere is predicted and the resultant trend is in good agreement with the analytic solution as far as the related correlation coefficient satisfies the assumption. The overdetermination process for overcoming nonuniqueness in exterior radiation problems is unnecessary in the present method because phase information can be ignored. The results of the calculation show that the proposed method is acceptable for solving the exterior radiation problem at a high-frequency range in a timely manner. © *2002 Acoustical Society of America.* [DOI: 10.1121/1.1517254]

PACS numbers: 43.20.Rz, 43.20.Tb [MO]

I. INTRODUCTION

The direct boundary element method (BEM), based on the Kirchhoff–Helmholtz integral equation, is currently used for the low-frequency analysis of various vibroacoustic systems, typically for the $ka < 20$ range, because the sound energy from most radiators is concentrated at low frequencies. The applicable frequency range is determined by the maximum size of the elements. Although the number of elements can be increased in order to achieve fine precision, the available high frequency is limited because of computer capacity and numerical errors. Typically, six constant elements or four quadratic elements are required per wavelength to ensure a certain acceptable accuracy.[1,2] A recent thorough analysis on this matter[2] reveals that at least five constant elements should be used for a wavelength when the error in the Euclidean norm is to be within five percent, whereas the number of constant elements per wavelength should be at least eight when the maximum norm is employed for the error description. Anyway, although a number of elements are needed for analyzing practical machines, including major frequency components, the BEM has been used to evaluate the overall level or the energy envelope of radiated sound. However, usually most of the audible high-frequency range cannot be analyzed using the conventional BEM, notwithstanding the fact that the high frequency is related to auditory sensitivity, speech communication, and sound quality perception. For

example, objective noise evaluation indices,[3] such as the AI (Articulation Index), NC (Noise Criterion), RC (Room noise Criterion), etc., are based on the one-third octave band sound spectrum, including high-frequency bands at a few kHz. In addition, international and domestic standards are usually prescribed up to high-frequency bands, which are supported by the fact that the bandwidth of the one-third octave band is very similar to the critical bandwidth at high frequencies. Although other analysis techniques for high frequencies are available for use above the Schroeder frequency, e.g., the statistical energy analysis[4,5] and the ray tracing method,[6] a new technique is clearly needed for dealing with high-frequency sound radiation problems.

Seybert and Rengarajan[7] utilized the fact that the radiation impedance becomes the characteristic impedance, ρc_0, at high frequencies, assuming a plane wave. They derived a brief boundary integral equation and the sound radiation from a cylinder was predicted as a demonstration example. This method appears to be useful in the prediction of sound levels at high frequencies, notwithstanding the fact that erroneous results could be obtained in the low-frequency range because the bulk reacting feature was not considered. The plane wave solution was also used as an initial value of the iterative method by Makarov and Ochmann.[8] After full iterations, this method showed more accurate results than the plane wave solution, but it required a large number of elements at high frequencies. Rokhlin[9] and Rosen *et al.*[10] suggested considerably different techniques for reduction of computational effort by using the sparse coefficient matrices. Both approaches are more efficient for solving a matrix equation than the conventional BEM. However, these meth-

[a]Author to whom correspondence should be addressed. Jeong-Guon Ih, Dept. of Mechanical Engineering, KAIST, Science Town, Taejon 305-701, Korea. Electronic mail: ihih@sorak.kaist.ac.kr

ods need a bit more time to make matrix equations than the conventional BEM because additional matrix manipulations when the same number of elements are required. Wu et al.[11] employed the interpolated Green's function in the frequency domain. In spite of the advantage of its short computation time, this method is difficult to apply to large models because a huge amount of memory is required for saving the interpolation data. Guyader[12] and Guyader and Loyau[13,14] proposed a method that uses the frequency-averaged quadratic pressure for the calculation of the modified Rayleigh integral. This method considered the vibrating surface as the distributed monopole sources and neglected the surface pressure, which constructs the dipole source distribution. Therefore, the neglected dipole term could cause errors when the surface is nearly rigid. Mahe et al.[15] introduced the radiation coefficient τ and the normalized impedance σ into the boundary integral equation, in which both parameters depend on the geometrical parameters of the source and the distance between the source and receiver. These coefficients must be determined by the user and therefore depends on the individual's knowledge of the system. Fahnline and Koopmann[16] described boundary sources with monopoles, dipoles, and tripoles, although they finally used the monopole only, i.e., using the Rayleigh integral form. Consequently, it was possible to evaluate the boundary integral with fewer boundary elements than the conventional BEM in evaluating the far-field pattern, although an additional modeling effort was needed. The aforementioned studies were attempts to extend the applicable high-frequency range or to reduce the calculation time for a given boundary element model.

In this paper, a method is proposed to undertake the aforementioned high-frequency analysis for the radiated sound from machines. To expand the applicable range to higher-frequency bands, the source terms in the Kirchhoff–Helmholtz integral equation are modeled by incoherent autospectra source elements and the phase term is removed. The resulting trend in frequency spectrum shows that the proposed method can be used for the approximate prediction of exterior radiated sound pressure levels in the high-frequency band.

II. THEORETICAL FORMULATION

When a vibrating object is considered in the following Kirchhoff–Helmholtz integral equation as[17]

$$c(\mathbf{r})p(\mathbf{r}) = \int_{S_0} \left[\frac{\partial G(\mathbf{r},\mathbf{r}_0)}{\partial \mathbf{n}} p(\mathbf{r}_0) - G(\mathbf{r},\mathbf{r}_0) \frac{\partial p(\mathbf{r}_0)}{\partial \mathbf{n}} \right] dS,$$
(1)

the acoustic pressure p at a receiver point $\mathbf{r}$ produced by the vibration of the surface with an area S_0 is given by
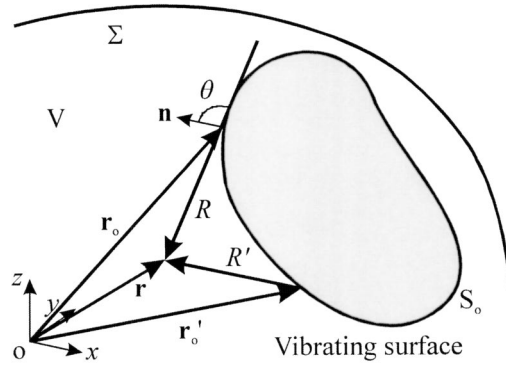
FIG. 1. Geometrical notations for the sound radiation from a vibrating source.

$$c(\mathbf{r})p(\mathbf{r}) = \int_{S_0} \left\{ -p(\mathbf{r}_0)\left(\frac{1}{R}+jk\right) \right.$$

$$\left. \times \cos\theta + \rho a(\mathbf{r}_0) \right\} \frac{e^{-jkR}}{R} dS.$$
(2)

Here, $\mathbf{r}_0$ is a point on the surface S_0, $\partial/\partial\mathbf{n}$ is the normal derivative on the surface, as depicted in Fig. 1, $G(\mathbf{r},\mathbf{r}_0)$ is the free-field Green's function, $c(\mathbf{r})$ is the solid angle, $p(\mathbf{r})$ is the sound pressure, $a(\mathbf{r}_0)$ is the normal acceleration at $\mathbf{r}_0$, ρ is the density of medium, R is the distance between field point and boundary point, k is the wave number, and θ is the direction angle.

A. Simplified boundary integral equation

At very high frequencies, the magnitude of the acoustic pressure is sufficient for the evaluation of various noise indices, whereas the phase information is insignificant.[13] This fact can be utilized to simplify the basic equation for application to the high-frequency analysis. Guyader[12] formulated a quadratic form of the Rayleigh integral equation using the same concept. In order to remove the phase component from Eq. (1), it is expressed in a quadratic form as

$$c^2 |p(\mathbf{r})|^2 = \int_{S_0}\int \left[\frac{\partial G^*}{\partial \mathbf{n}} p^*(\mathbf{r}_0') - G^* \frac{\partial p^*(\mathbf{r}_0')}{\partial \mathbf{n}} \right]$$

$$\times \left[\frac{\partial G}{\partial \mathbf{n}} p(\mathbf{r}_0) - G \frac{\partial p(\mathbf{r}_0)}{\partial \mathbf{n}} \right] dS' \, dS,$$
(3)

where R' is $|\mathbf{r}-\mathbf{r}_0'|$, as shown in Fig. 1 and the superscript "*" denotes the complex conjugate. From this equation, one can obtain the quadratic pressure at a field point $\mathbf{r}$, when the solid angle c is 4π due to the prescribed acceleration a at $\mathbf{r}_0$ and $\mathbf{r}_0'$ on S_0. Expanding Eq. (3), it follows that

$$16\pi^2|p(\mathbf{r})|^2 = \int_{S_0}\int p(\mathbf{r}_0)p^*(\mathbf{r}_0')\left\{\frac{1}{RR'}+k^2-jk\left(\frac{1}{R}-\frac{1}{R'}\right)\right\}\cos\theta\cos\theta'\frac{e^{-jk(R-R')}}{RR'}\,\mathrm{d}S'\,\mathrm{d}S$$

$$+\rho^2\int_{S_0}\int a(\mathbf{r}_0)a^*(\mathbf{r}_0')\frac{e^{-jk(R-R')}}{RR'}\,\mathrm{d}S'\,\mathrm{d}S + \rho\int_{S_0}\int a^*(\mathbf{r}_0')p(\mathbf{r}_0)\left(-jk-\frac{1}{R}\right)\cos\theta\frac{e^{-jk(R-R')}}{RR'}\,\mathrm{d}S'\,\mathrm{d}S$$

$$+\rho\int_{S_0}\int a(\mathbf{r}_0)p^*(\mathbf{r}_0')\left(jk-\frac{1}{R'}\right)\cos\theta'\frac{e^{-jk(R-R')}}{RR'}\,\mathrm{d}S'\,\mathrm{d}S. \tag{4}$$

For the computational ease of Eq. (4), the surface can be discretized into N boundary elements with a constant shape function, which results in the following equation:

$$16\pi^2|p(r)|_i^2 = \sum_m^N\sum_{m'}^N (\mathbf{p}^*\mathbf{p})_{m'm}\mathbf{A}_{im'm}$$

$$+\sum_m^N\sum_{m'}^N (\mathbf{a}^*\mathbf{a})_{m'm}\mathbf{B}_{im'm}$$

$$+\sum_m^N\sum_{m'}^N (\mathbf{a}^*\mathbf{p})_{m'm}\mathbf{C}_{im'm}$$

$$+\sum_m^N\sum_{m'}^N (\mathbf{p}^*\mathbf{a})_{m'm}\mathbf{D}_{im'm}. \tag{5}$$

Here, m and m' denote the positions of boundary elements and the coefficients for the expression of ith field pressure are given by

$$\mathbf{A}_{im'm} = \int_{S_{m'}}\int \frac{1}{R^2R'^2}\{1+RR'k^2+jk(R-R')\}$$

$$\times\cos\theta\cos\theta' e^{-jk(R-R')}\,\mathrm{d}S'\,\mathrm{d}S, \tag{6a}$$

$$\mathbf{B}_{im'm} = \rho^2\int_{S_{m'}}\int \frac{1}{RR'}e^{-jk(R-R')}\,\mathrm{d}S'\,\mathrm{d}S, \tag{6b}$$

$$\mathbf{C}_{im'm} = \rho\int_{S_mS_{m'}}\int \frac{1}{RR'}\cos\theta\left(-jk-\frac{1}{R}\right)e^{-jk(R-R')}\,\mathrm{d}S'\,\mathrm{d}S, \tag{6c}$$

$$\mathbf{D}_{im'm} = \rho\int_{S_{m'}}\int \frac{1}{RR'}\cos\theta'\left(jk-\frac{1}{R'}\right)e^{-jk(R-R')}\,\mathrm{d}S'\,\mathrm{d}S. \tag{6d}$$

When m does not coincide with m', the terms $(\mathbf{p}^*\mathbf{p})_{m'm}$, $(\mathbf{a}^*\mathbf{a})_{m'm}$, $(\mathbf{a}^*\mathbf{p})_{m'm}$ signify the cross-spectra between sound pressures and/or particle accelerations at different positions on the radiator surface. In other words, when $m=m'$, these terms represent the autospectra of pressure, the autospectra of acceleration, and the cross-spectra of pressure and acceleration at the mth element. The cross-spectra of sound pressures or accelerations between two different posi-

tions on the surface are generally smaller than their autospectra in the case of random excitation with small damping.[18,19] With this assumption of a relatively smaller cross-spectra than an autospectra and also with the aid of the assumption of similarity in R and R' on a single element, Eq. (5) can be approximated as

$$16\pi^2 p_i^2 \approx \sum_m^N (\mathbf{p}^*\mathbf{p})_m\mathbf{A}_{im} + \sum_m^N (\mathbf{a}^*\mathbf{a})_m\mathbf{B}_{im}$$

$$+\sum_m^N 2\,\mathrm{Re}[(\mathbf{a}^*\mathbf{p})_m\mathbf{C}_{im}], \tag{7}$$

where

$$\mathbf{A}_{im} = \int_{S_m}\frac{\cos^2\theta_{im}}{R_{im}^2}\left(\frac{1}{R_{im}^2}+k^2\right)\mathrm{d}S\int_{S_m}\mathrm{d}S', \tag{8a}$$

$$\mathbf{B}_{im} = \rho^2\int_{S_m}\frac{1}{R_{im}^2}\,\mathrm{d}S\int_{S_m}\mathrm{d}S', \tag{8b}$$

$$\mathbf{C}_{im} = \rho\int_{S_m}\frac{\cos\theta_{im}}{R_{im}^2}\left(-jk-\frac{1}{R_{im}}\right)\mathrm{d}S\int_{S_m}\mathrm{d}S'. \tag{8c}$$

It should be noted that the small cross-spectra assumption introduced in deriving Eq. (7) reduces the amount of calculation, although the equation still consists of monopole and dipole terms. In Eq. (7), both the autospectra and the system matrices $\mathbf{A}$, $\mathbf{B}$ are real. The exponential function $\exp[-jk(R-R')]$ in Eq. (4) takes the phase information into account, whereas Eq. (7) is composed of the autospectra, which ignore the phase. The element size is related only to the distribution of vibration energy because the phase term is no longer required, in spite of the fact that the interference due to phase differences between any two elements cannot be reflected in the calculation result. This indicates that the model division in the present method can be coarser than that of the conventional BEM, in which the element size is related to the wavelength. The first and second terms of Eq. (7) represent the dipole and the monopole, respectively. These two terms describe the radiated sound energy from the vibrating surface and the third term represents the correction term caused by the phase difference between the pressure and acceleration of the vibrating surface. It should be noted that the magnitudes of all three terms in Eq. (7) are inversely proportional to R^2, although the directional characteristics are different.

The sound pressures and particle accelerations on the radiator surface are considered when the field point $\mathbf{r}$ is located on the surface. Therefore, if we rearrange Eq. (2) for pressure and acceleration, the following equation can be derived:

$$\int_{S_0}\left\{2\pi p(\mathbf{r})\delta(\mathbf{r}-\mathbf{r}_0)+p(\mathbf{r}_0)\left(\frac{1}{R}+jk\right)\cos\theta\frac{e^{-jkR}}{R}\right\}dS=\int_{S_0}\rho a(\mathbf{r}_0)\frac{e^{-jkR}}{R}dS. \tag{9}$$

If each side of Eq. (9) is multiplied by its complex conjugate, and the following equation can be obtained:

$$4\pi^2|p(\mathbf{r})|^2\int\int_{S_0}\delta(\mathbf{r}-\mathbf{r}_0)\delta(\mathbf{r}-\mathbf{r}_0')dS'\,dS+\int\int_{S_0}\frac{1}{R^2R'^2}p(\mathbf{r}_0)p^*(\mathbf{r}_0')\{1+RR'k^2+jk(R-R')\}\cos\theta\cos\theta'e^{-jk(R-R')}dS'\,dS$$

$$+2\pi p(\mathbf{r})\int\int_{S_0}\delta(\mathbf{r}-\mathbf{r}_0)p^*(\mathbf{r}_0')\left(\frac{1}{R'}-jk\right)\cos\theta'\frac{e^{jkR'}}{R'}dS'\,dS+2\pi p(\mathbf{r})\int\int_{S_0}\delta(\mathbf{r}-\mathbf{r}_0')p(\mathbf{r}_0)\left(\frac{1}{R}+jk\right)\cos\theta\frac{e^{-jkR}}{R}dS'\,dS,$$

$$=\rho^2\int\int_{S_0}\frac{1}{R^2}a(r_0)a^*(r_0')dS'\,dS. \tag{10}$$

Using the same constant shape function and the same assumptions used in deriving Eq. (5), one can derive

$$[\mathbf{A}'_{im}]\{(\mathbf{p}^*\mathbf{p})_m\}=[\mathbf{B}_{im}]\{(\mathbf{a}^*\mathbf{a})_m\}. \tag{11}$$

Here, the coefficient matrix $\mathbf{B}$ is identical with Eq. (8b) and the coefficient matrix $\mathbf{A}'$ for the ith element is given by

$$\mathbf{A}'_{im}=\begin{cases}\int_{S_m}\left\{\frac{1}{R_{im}^2}+k^2\right\}\frac{1}{R_{im}^2}\cos^2\theta_{im}\,dS\int_{S_m}dS', & (i\neq m) \tag{12a}\\[2mm]\int_{S_m}\left\{\frac{1}{R_{im}^2}+k^2\right\}\frac{1}{R_{im}^2}\cos^2\theta_{im}\,dS\int_{S_m}dS'+\int_{S_m}\left\{4\pi^2+4\pi\,\mathrm{Re}\left[\left(\frac{1}{R_{im}}-jk\right)\cos\theta_{im}\frac{e^{-jkR_{im}}}{R_{im}}\right]\right\}dS\int_{S_m}dS' & (i=m). \tag{12b}\end{cases}$$

Because the number of unknown variables in Eq. (7) is $2N$, additional N equations are required to solve the problem. The remaining N equations can be obtained by multiplying the complex conjugate of the right side of Eq. (9) to both sides as follows:

$$\mathrm{LHS}=2\pi p(\mathbf{r})\rho\int_{S_0}\delta(\mathbf{r}-\mathbf{r}_0)a^*(\mathbf{r}_0')\frac{e^{jkR'}}{R'}dS\int_{S_0}dS'$$

$$+\rho\int_{S_0}p(\mathbf{r}_0)a^*(\mathbf{r}_0')\left(\frac{1}{R}+jk\right)$$

$$\times\cos\theta\frac{e^{-jk(R-R')}}{RR'}dS\int_{S_0}dS'. \tag{13}$$

Here, the resulting expression of the right side is exactly same as in the Eq. (10). In a similar manner in deriving Eq. (11), one can rewrite Eq. (13) in the matrix form as

$$[\mathbf{C}'_{im}]\{(\mathbf{a}^*\mathbf{p})_m\}=[\mathbf{B}_{im}]\{(\mathbf{a}^*\mathbf{a})_m\}, \tag{14}$$

where the coefficient of matrix $\mathbf{C}'$ for the ith element is given by

$$\mathbf{C}'_{im}=\rho\int_{S_m}\left\{\delta_{im}2\pi R_{im}+\left(\frac{1}{R_{im}}+jk\right)\right.$$

$$\left.\times\cos\theta_{im}\right\}\frac{1}{R_{im}^2}dS\int_{S_m}dS'. \tag{15}$$

Here, δ_{im} denotes the Kronecker delta. From Eqs. (11) and (14), the autospectrum of the sound pressure and the cross-spectrum between pressure and acceleration on the surface can be calculated.

When Eq. (4) is integrated for a frequency band between $\Omega-\epsilon$ and $\Omega+\epsilon$, one can derive

$$16\pi^2\langle|p(\mathbf{r})|^2\rangle=\int_{-\epsilon}^{\epsilon}\int\int_{S_0}p(\mathbf{r}_0)p^*(\mathbf{r}_0')\left\{\frac{1}{RR'}+\frac{(\Omega+\omega)^2}{c_0^2}-\frac{j(\Omega+\omega)}{c_0}\left(\frac{1}{R}-\frac{1}{R'}\right)\right\}\cos\theta\cos\theta'G_\Omega(R,R',\omega)dS'\,dS\,d\omega$$

$$+\rho^2\int_{-\epsilon}^{\epsilon}\int\int_{S_0}a(\mathbf{r}_0)a^*(\mathbf{r}_0')G_\Omega(R,R',\omega)dS'\,dS\,d\omega+\rho\int_{-\epsilon}^{\epsilon}\int\int_{S_0}\left\{\frac{1}{R}p(\mathbf{r}_0)a^*(\mathbf{r}_0')\cos\theta\right.$$

$$\left.+\frac{1}{R'}p^*(\mathbf{r}_0')a(\mathbf{r}_0)\cos\theta'\right\}G_\Omega(R,R',\omega)dS'\,dS\,d\omega+j\rho\int_{-\epsilon}^{\epsilon}\int\int_{S_0}\frac{(\Omega+\omega)}{c_0}$$

$$\times\{p(\mathbf{r}_0)a^*(\mathbf{r}_0')\cos\theta-p^*(\mathbf{r}_0')a(\mathbf{r}_0)\cos\theta'\}G_\Omega(R,R',\omega)dS'\,dS\,d\omega, \tag{16}$$

Jae-Kwon Kim and Jeong-Guon Ih: Simplified boundary element method

where

$$G_\Omega(R,R',\omega) = \frac{e^{-(j\Omega/c_0)(R-R')}}{RR'}$$

$$\times\left(1 + \sum_{q=1}^{\infty} \frac{(-j(\omega/c_0)(R-R'))^q}{q!}\right).$$

$$(17)$$

Here, $\langle\ \rangle$ indicates the frequency averaging, ω is the circular frequency, Ω is the arithmetic center frequency of calculation band, and c_0 is the speed of sound. For the percentage bandwidth analysis, Ω and ϵ are of the $1/n$-octave band determined by the following equations using the geometric center frequency of the percentage band, Ω_c, as

$$\Omega = \frac{\Omega_c}{2}(2^{n/2}+2^{-n/2}),$$

$$(18a)$$

$$\epsilon = \frac{\Omega_c}{2}(2^{n/2}-2^{-n/2}),$$

$$(18b)$$

where ϵ denotes the half-bandwidth in linear scale. Under the assumption of a small cross-spectrum between pressure and acceleration, Eq. (16) can be rewritten in the matrix form as

$$16\pi^2\langle p_i^2\rangle = \sum_m^N \langle \mathbf{p}^*\mathbf{p}\rangle_m \hat{\mathbf{A}}_{im} + \sum_m^N \langle \mathbf{a}^*\mathbf{a}\rangle_m \hat{\mathbf{B}}_{im}$$

$$+ \sum_m^N 2\,\text{Re}[\langle \mathbf{a}^*\mathbf{p}\rangle_m \hat{\mathbf{C}}_{im}],$$

$$(19)$$

where

$$\hat{\mathbf{A}}_{im} = \int_{S_m} \frac{\cos^2\theta_{im}}{R_{im}^2}\left\langle\left(\frac{1}{R_{im}^2} + \frac{\Omega^2+\epsilon^2}{c_0^2}\right)\right\rangle dS \int_{S_m} dS',$$

$$(20a)$$

$$\hat{\mathbf{B}}_{im} = \rho^2 \int_{S_m} \frac{\langle 1\rangle}{R_{im}^2}dS \int_{S_m} dS',$$

$$(20b)$$

$$\hat{\mathbf{C}}_{im} = \rho \int_{S_m} \frac{\cos\theta_{im}}{R_{im}^2}\left\langle\left(\frac{j\Omega}{c_0} - \frac{1}{R_{im}}\right)\right\rangle dS \int_{S_m} dS'.$$

$$(20c)$$

One can find in Eq. (20a) that, in the frequency band of concern, i.e., from $-\epsilon$ to ϵ, the linear term in ϵ is ignored, while the quadratic term in ϵ is retained. Although direct interference due to the phase differences at a single frequency is neglected, it is still acceptable, in terms of engineering usage, because the radiated sounds are usually wide band and smooth at the mid- to high-frequency bands. When the radiated sounds from two different source positions are
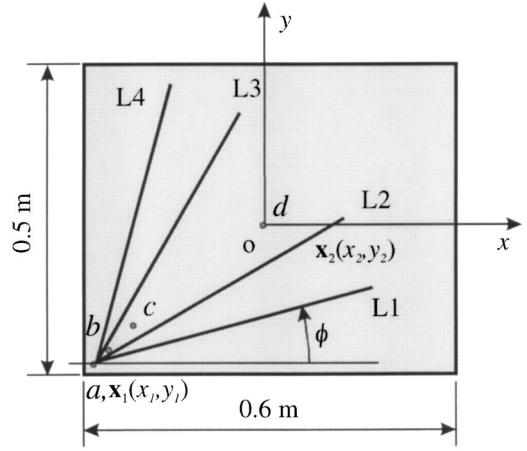
FIG. 2. Geometric description of a baffled rectangular plate for estimating the correlation coefficient between reference point $\mathbf{x}_1$ and response points $\mathbf{x}_2$ along four skewed lines: L1 (ϕ=15°), L2 (ϕ=30°), L3 (ϕ=60°), and L4 (ϕ=75°). Excitation points used for the prediction of radiated sound are a (−0.28 m, −0.23 m), b (−0.25 m, −0.2 m), c (−0.2 m, −0.15 m), and d (0 m, 0 m).

of the same frequency, a smearing effect in phase occurs, whereas the interference is rare in the case of two different frequencies.

If the radiator is baffled, the Kirchhoff–Helmholtz integral can be simplified into the Rayleigh integral that predicts the field pressure with only monopole sources on the radiator surface. Similar with the preceding paragraph, the quadratic pressure for a frequency band can be easily derived as

$$4\pi^2\langle p_i^2\rangle = \sum_m^N \langle \mathbf{a}^*\mathbf{a}\rangle_m \hat{\mathbf{B}}_{im},$$

$$(21)$$

where $\hat{\mathbf{B}}_{im}$ has the same expression as Eq. (20b). One can find that Eq. (21) is described simply by the autospectrum $\langle \mathbf{a}^*\mathbf{a}\rangle_m$ and by the distance R_{im} between the source and receiver. This equation is identical to the diagonal parts of the equation derived by Guyader.[12]

B. Consideration of the element size

In deriving Eq. (7), the cross-spectra of pressures and/or accelerations between two different positions are assumed to be negligible. In the present method, the phase term in Eq. (4) is $\exp[-jk(R-R')]$, which is eliminated in Eq. (7). This means that a larger element is sufficient to describe the energy distribution than that of the conventional BEM. Note that the characteristic size of the constant element should be less than about $\lambda/6$ in order to appropriately describe the wave motion in using the conventional BEM.[1,2] As a simple demonstration example, on two positions at $\mathbf{x}_1$ and $\mathbf{x}_2$ of a baffled rectangular plate as depicted in Fig. 2, the ratio of the cross-spectrum and the autospectrum for a frequency band is described by the following correlation coefficient:[20]

$$\gamma_{12}(\mathbf{x}_1,\mathbf{x}_2,\Omega) = \frac{\int_{\Omega-\epsilon}^{\Omega+\epsilon}\text{Re}[G_{12}(\mathbf{x}_1,\mathbf{x}_2,\omega)]d\omega}{(\int_{\Omega-\epsilon}^{\Omega+\epsilon}\text{Re}[G_1(\mathbf{x}_1,\omega)]d\omega)^{1/2}(\int_{\Omega-\epsilon}^{\Omega+\epsilon}\text{Re}[G_2(\mathbf{x}_2,f)]d\omega)^{1/2}}.$$

$$(22)$$

When the modal density is sufficiently high, the mode integration technique[18] can be applied to Eq. (22) using the mode function of a simply supported plate as

$$\gamma_{12}(\mathbf{x}_1,\mathbf{x}_2,\Omega)=\frac{N(x_1,x_2,y_1,y_2;k_b)}{D(x_1,x_2,y_1,y_2;k_b)}, \tag{23}$$

where

$$N(x_1,x_2,y_1,y_2;k_b)$$
$$=J_0(k_b\sqrt{(x_1-x_2)^2+(y_1-y_2)^2})$$
$$-J_0(k_b\sqrt{(x_1-x_2)^2+(y_1+y_2)^2})$$
$$-J_0(k_b\sqrt{(x_1+x_2)^2+(y_1-y_2)^2})$$
$$+J_0(k_b\sqrt{(x_1+x_2)^2+(y_1+y_2)^2}), \tag{24a}$$

$$D(x_1,x_2,y_1,y_2;k_b)$$
$$=\prod_{i=1}^{2}\sqrt{1-J_0(2k_bx_i)-J_0(2k_by_i)+J_0(2k_b\sqrt{(x_i^2+y_i^2)})}. \tag{24b}$$

Here, k_b is the bending wave number of the plate and J_0 denotes the zeroth-order Bessel function of the first kind. When the radiator is excited uniformly for all the involved modes, Eq. (23) can be reduced to[18]

$$\gamma_{12}(\mathbf{x}_1,\mathbf{x}_2,\Omega_c)\approx J_0(k_bl), \tag{25}$$

where l is the distance between $\mathbf{x}_1$ and $\mathbf{x}_2$. This rather simple equation would suggest the characteristic size of the boundary element for modeling most of the cases. On the other hand, when the excitation position $\mathbf{x}_0$ is considered important, Eq. (22) can be rewritten to include a mode function ϕ as follows:[18]

$$\gamma_{12}(\mathbf{x}_1,\mathbf{x}_2,\omega)=\frac{\Sigma_q\phi_q(\mathbf{x}_1)\phi_q(\mathbf{x}_2)\phi_q^2(\mathbf{x}_0)}{[\Sigma_q\phi_q^2(\mathbf{x}_1)\phi_q^2(\mathbf{x}_0)]^{1/2}[\Sigma_q\phi_q^2(\mathbf{x}_2)\phi_q^2(\mathbf{x}_0)]^{1/2}}. \tag{26}$$

III. DISCUSSION ON THE BASIC CHARACTERISTICS OF THE METHOD

A. Validation of the basic assumption: Baffled vibrating plate

As an initial test example of the present method, the sound radiated from a baffled steel plate, which was 0.6 m long, 0.5 m wide, 0.001 m thick was considered. The material properties of the steel plate were as follows: Young's modulus was 200 Gpa, the density 7700 kg/m^3, the Poisson ratio 0.27, and the loss factor 0.01. The density of air was 1.21 kg/m^3 and the speed of sound was 343 m/s. The element size was approximately determined by Eq. (25) with the assumptions of a high modal density and a low correlation coefficient for the frequency bands of interest. One can easily calculate[21] that the mode count, N_m, is more than nine for any one-third octave band above 500 Hz. At these frequency bands, the correlation coefficients with 100 random excitation points were calculated along the lines in Fig. 2. Four lines on the plate were chosen to have different direction angles without appreciable symmetry. The correlation coef-
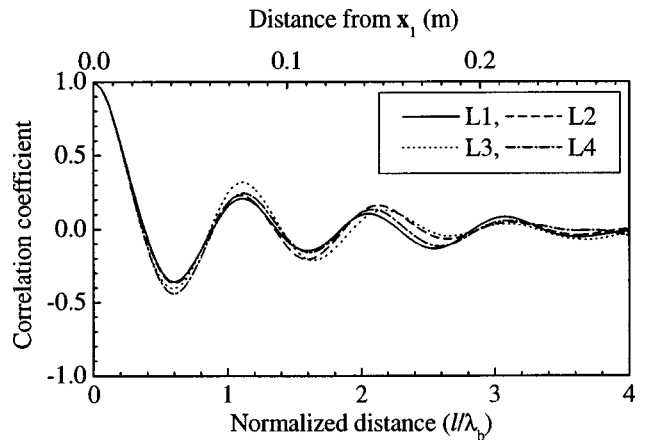
FIG. 3. Correlation coefficients along the lines, as shown in Fig. 2. The averaged result of the excitation at 100 randomly chosen points is shown for 2 kHz in 1/3-octave band ($\eta=0.01$).

ficients with a reference to the point a at (-0.28 m, -0.23 m) were calculated by averaging all 100 responses due to excitations with the same magnitude at 100 uniform random points. Figure 3 shows the calculated correlation coefficient for one-third octave bands along each line in Fig. 2. It can be seen that the calculated correlation coefficient is sufficiently small for satisfying the basic assumption when the distance is longer than the bending wavelength, λ_b. Figure 4 shows a similar trend for other frequency bands except 200 Hz: For this relatively low-frequency band, in which $N_m=4$, the distance between the two response positions should be longer than about λ_b in order to satisfy the basic assumption. It can be seen from Figs. 3 and 4 that the correlation coefficients are very similar, in spite of the directional and frequency differences. The variation of the correlation coefficient becomes small for high-frequency bands as in Fig. 5, including that the correlation coefficient is not strongly influenced by the exciting position at high-frequency bands.

If the positions $\mathbf{x}_1$ and $\mathbf{x}_2$ are sufficiently far from the boundary, the correlation coefficient can be calculated using Eq. (25), which ignores the boundary effect. This coefficient represents the contribution to the radiated sound caused by the cross-terms of two different sources. The ratio of the side
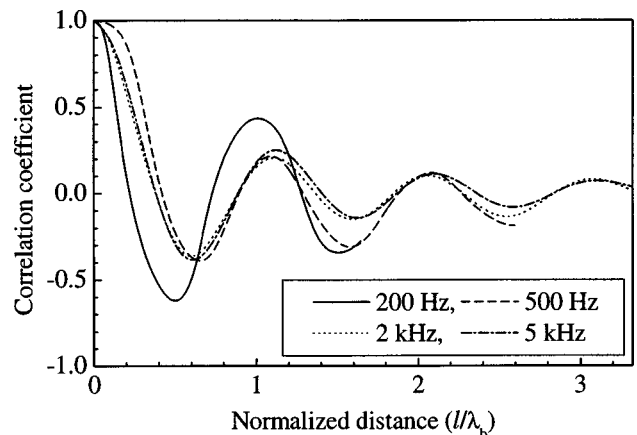
FIG. 4. Correlation coefficients along the line L1, which is the averaged result of the excitation at the 100 randomly chosen points, varying the center frequencies in 1/3-octave bands ($\eta=0.01$).
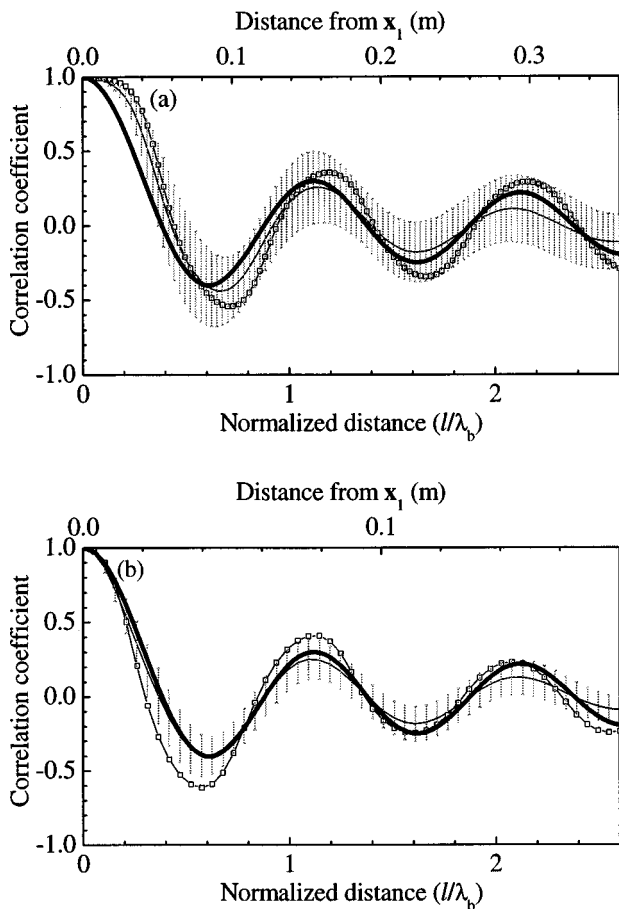
FIG. 5. Averaged correlation coefficient along the four lines shown in Fig. 2 ($\eta=0.01$): —, excitation at randomly chosen 100 points [Eq. (26)]; —□—, mode integral [Eq. (23)]; —, $J_0(k_b l)$ [Eq. (25)]. Here, "I" denotes the standard deviation of the result. (a) 500 Hz in a 1/3-octave band; (b) 2 kHz in a 1/3-octave band.

FIG. 6. Calculated 1/3-octave band level radiated from a baffled plate excited at point b (-0.25 m, -0.2 m) ($\eta=0.01$): —■—; Rayleigh integral; —○—, present method ($L_c=0.2$ m); $-+-$, present method ($L_c=0.15$ m); $-\times-$, present method ($L_c=0.1$ m).

three parameters was performed and the results are shown in Fig. 7(a). As the loss factor increases from 0.01 to 0.1, the errors decrease by approximately 2 dB because of the increase in the modal overlap factor. If the characteristic length of an element decreases from 0.2 to 0.05, the averaged error increases by approximately 7 dB because the assumed con-

lobes to the main lobe of the coefficient is usually small, *viz.*, the ratio is 0.041 when nine periods are considered for side lobes in the $1.1 < l/\lambda_b < 10$ range, whereas one period in $l/\lambda_b < 1.1$ is considered as the main lobe. It appears that the proper range of the correlation coefficient for complying, with the assumption of the present method is within ± 0.3 when the lower limit frequency is 500 Hz, and the smallest characteristic size of an element should then be at least 0.15 m, as shown in Fig. 5(a). The radiation from the baffled plate was analyzed for cases in which the characteristic lengths of the element were 0.2, 0.15, and 0.1 m. The receiver position was at a distance of 1 m from the center of the plate in a normal direction. When the plate is excited at point b, the sound pressure level at the receiver point is shown in Fig. 6. For the purpose of comparison, the Rayleigh integral was numerically evaluated using the trapezoidal rule. Equally spaced 60×50 abscissas were used for the integration over the source surface and equally spaced 30 abscissas were used for the frequency band integration. The present method has a tendency to overestimate and to fluctuate in frequency in comparison with the Rayleigh integral method. The error becomes large as the element size becomes small because the basic assumption cannot be satisfied. Because the exciting position, loss factor, and element size influence the accuracy of the prediction, an error analysis taking into account all

FIG. 7. Errors of the present method compared with the Rayleigh integral in the prediction of the sound level radiated from a baffled plate excited with a white noise. (a) Excitation at point d (0, 0) varying the loss factor of panel; (b) effect of the variation of the excitation position ($\eta=0.01$).
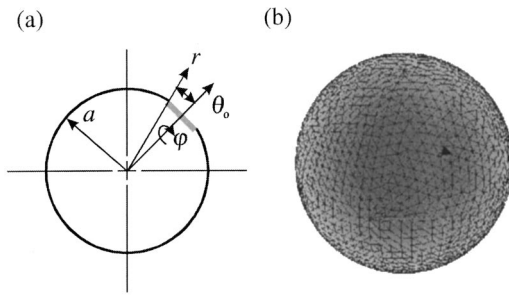
FIG. 8. (a) A partially vibrating sphere; (b) a boundary element model.

dition on the correlation coefficient has not been fulfilled. Figure 7(b) shows a comparison of errors for variations in the exciting position and element size when $\eta = 0.01$. The error is more than 5 dB when the exciting point is located near the boundary and the element is small. The overall trend shows that the element size should be larger than 0.15 m in order to satisfy the basic assumption.

B. Prediction of the field sound level: Partially vibrating sphere

As a test example of sound radiation from a three-dimensional body, a partially vibrating sphere with the radius of 0.35 m was considered. One element was used for a source and other surface elements were maintained rigid as shown in Fig. 8, and this boundary condition satisfied the prescribed assumption. The number of constant elements was 3042 and the characteristic length of the element was 0.034 m, which would pose limitations in an analysis by the conventional BEM to 1680 Hz.

The nonuniqueness problem always occurs when the acoustic BEM deals with an exterior problem due to the inherent nature of the Fredholm equation. For a pulsating sphere of radius a, the nonuniqueness problem occurs at $ka = n\pi$ ($n = 1,2,3,...$) because of the excitation of the zeroth-order spherical mode and the additional number of high-order modes, which cause a serious error. In order to avoid the nonuniqueness problem, the conventional direct BEM typically employs the CHIEF method[22] or the Burton and Miller method.[23] In this case, nine CHIEF points are used for the conventional BEM calculation. The analytic solution of the radiated sound pressure at field position (r,θ) due to a partially vibrating sphere is given by[24]

$$p = \sum_m A_m P_m(\cos\theta) h_m(kr) e^{j\omega t}, \quad (27)$$

where

$$A_m = \frac{\rho c_0 U_m}{B_m} e^{i\delta_m}, \quad (28a)$$

$$U_m = \left(m + \frac{1}{2}\right) \int_0^\pi U(\theta) P_m(\cos\theta) \sin(\theta) d\theta. \quad (28b)$$

Here, P_m is the mth-order Legendre function, h_m is the mth-order spherical Hankel function, $U(\theta)$ describes the normal velocity of the surface, and δ_m, U_m, and B_m are the modal coefficients. The present method does not suffer from nonu-
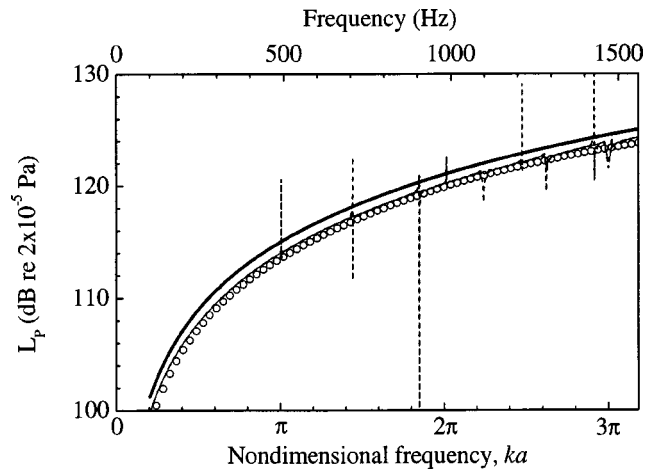
FIG. 9. The predicted surface sound pressure of a partially vibrating sphere: ○, analytic solution; —, present method; ---, conventional BEM without an overdetermined point; —, conventional BEM with nine overdetermined points.

niqueness problems because Eq. (7) contains no phase term. Figure 9 shows a comparison of the present method with the analytic solution and conventional BEM results. The amount of singularity reduction by the CHIEF method depends on the number and position of the overdetermined points. The present method overestimates by approximately 1.5 dB, compared to the analytic solution. The conventional BEM has large errors at singular frequencies without the use of the overdetermination technique and shows a 1–2 dB error at some high frequencies, even after using the overdetermination technique. The latter nonuniqueness errors can be removed by additional CHIEF points.

The field pressures are evaluated at $r = 0.4$, 0.5, 1.0, 2.0 m and $\theta = 0°–180°$ at 10° intervals. Five types of boundary element models, as listed in Table I, were used to investigate the effect of the characteristic length, L_c, of boundary elements. The high-frequency analysis method proposed by Seybert and Rengarajan[7] was also adopted as a comparison. However, the method proposed by Mahe *et al.*[15] was not used in the comparison because it requires an intuitive factor for the calculation of the involved coefficients. The plane wave solution was also used as an initial value of the iterative method by Makarov and Ochmann.[8] After a number of iterations, the iterative method seems better than the present method in the viewpoint of the convergence. However, it should be recalled that the present method uses coarser mesh than the conventional BEM and the iterative method, which makes the band analysis possible due to its energy-like variables. This strong feature reduces modeling effort and calcu-

TABLE I. Boundary element models for the radiation analysis of a partially vibrating sphere.

Model	Number of elements	Characteristic length (L_c)	High-frequency limit ($c_0/6L_c$)
A	76	0.28 m	205 Hz
B	220	0.15 m	380 Hz
C	448	0.1 m	570 Hz
D	782	0.07 m	815 Hz
E	3042	0.034 m	1681 Hz
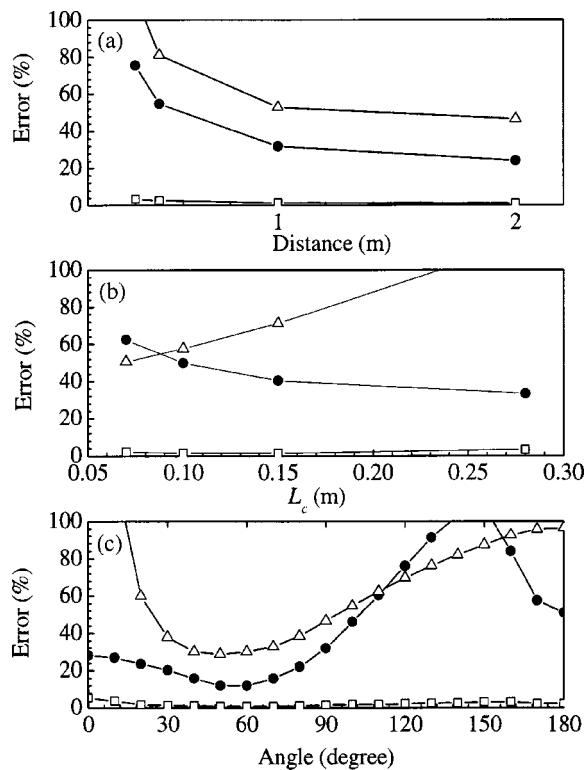
FIG. 10. Errors in the predicted field pressure compared to the analytic solution in the frequency range of $f<c_0/6L_c$: —□—, conventional BEM; —●—, present method; —△—, the Seybert and Rengarajan method (Ref. 6). (a) Receiver position distance r; (b) the characteristic length of the element L_c; (c) the angular position of the receiver point θ.

FIG. 11. Errors in the predicted field pressure compared to the analytic solution in the frequency range of $c_0/2L_c<f<2c_0/L_c$ and angle range of $\theta<70°$: —□—, conventional BEM; —●—, present method; —△—, the Seybert and Rengarajan method (Ref. 6). (a) Receiver position distance r; (b) the characteristic length of the element L_c; (c) the angular position of the receiver point θ.

lation time. As expected, the conventional BEM results in small errors of less than 1% in the frequency range of $f<c_0/6L_c$ at the whole field positions. However, the present method shows errors in excess of 100% at some backside points, as can be seen in Fig. 10(c). The method proposed by Seybert and Rengarajan also shows errors larger than 100% at some front–side points because their assumption is not satisfied at low frequencies. The reason for this is that the assumed dipole source strength is too large and, as a result, the pressures on the surrounding surface affect the radiated sound. The difference between the above two high-frequency methods is caused by the differences in the applicable frequency range and the assumption used. The assumption used in the present method is satisfied better for larger elements, whereas the assumption used by Seybert and Rengarajan is satisfied better for higher-frequency ranges. When high frequencies ($c_0/2L_c<f<2c_0/L_c$) are considered, as in Fig. 11, the conventional direct BEM yields a 20%–40% error because the analyzed frequency range exceeds the upper limit frequency of the conventional BEM for the given element size. In contrast, the error of the present method is less than 20%, which is similar to that found for the Seybert and Rengarajan method for the $\theta<70°$ range. Figure 12 shows a comparison of errors represented in the ka domain. The conventional BEM shows a number of spiky errors due to nonuniqueness in spite of the fact that a fine boundary element model (as designated by "model E") is used, but the proposed method yields less than a 20% error in $ka<20$. The model E was not used for the present method because an

excess fine boundary element model does not satisfy the assumption of the small correlation coefficient. Figure 12(b) shows that the high-frequency limit of the present method is not limited by element size, but depends on the entire geometric size of the system. The applicable range of the present method is limited by $ka\approx20$, because the overestimating error becomes larger than 20% in the $ka>20$ range.

The conventional BEM has a fully populated, complex system matrix, which requires complex operations. However, the present method requires only simple real operations. Because of this fact, the amount of calculations is nearly the same as for the conventional BEM, although more terms are involved in the present method than that of the conventional direct BEM. Calculation times in a personal computer (AMD Duron, clock speed=800 MHz) are compared in Fig. 13. The conventional BEM requires more time for the assembling of a system equation than the present method, because the CHIEF method is employed to remove the nonuniqueness errors in the conventional BEM. The conventional BEM requires 3000 elements for analyzing a system of up to ka =10, which would require more than 3 h per single frequency. This implies that it would be, in practice, impossible to apply to a high-frequency analysis near $ka\approx20$, because the time required for the solution process is proportional to N^2, where N is the number of elements. In contrast, the present method can be used for such a high-frequency analysis ($ka\approx20$) without any severe problems, as long as the assumptions are satisfied.
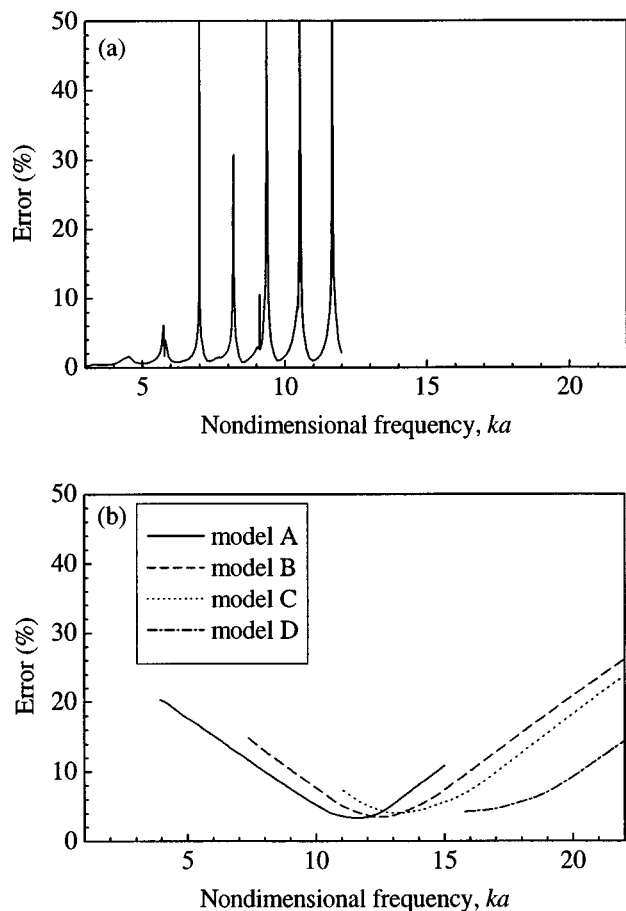
FIG. 12. Errors in the predicted field pressure compared to the analytic solution for the angle range of $\theta < 70°$. (a) Conventional BEM in the frequency range of $f < c_0/6L_c$ using model E in Table I; (b) the present method in the frequency range of $c_0/2L_c < f < 2c_0/L_c$ using four other boundary element models in Table I.

FIG. 13. Computational effort in the prediction of field pressure radiated from a partially vibrating sphere: —□—, conventional direct BEM; —●—, present method. (a) Time for assembling the equation; (b) time for solving the equation; (c) time for calculating the field pressure.

IV. CONCLUDING REMARKS

In this paper, a simplified boundary element method was formulated based on the Kirchhoff–Helmholtz integral equation, which is derived for calculating the one-third octave sound level and extending the applicable high-frequency range. To this end, the assumption was introduced, that the correlation coefficient between any two different points is negligibly small on the surface of the general vibrating structure. The element size is determined by the correlation coefficient: too fine an element division yields a high correlation coefficient and this causes the errors in the present method. The correlation coefficient, which converges to $J_0(k_b r)$ when the modes of the plate are uniformly excited, within the value of ± 0.3 is suggested for the application of the present method. The sound pressure, which was radiated from a baffled steel plate with an exciting point b, was calculated and the results were compared with those of the Rayleigh integral. A maximum error of about 5 dB was observed when the loss factor was 0.01 and the characteristic length was 0.15 m, but there was an evident trend that the result was improved with an increase in element size. In addition, the sound pressure radiated from a partially vibrating sphere was predicted by the present method. The results were compared with those using the conventional BEM, the method

proposed by Seybert and Rengarajan,[7] and an analytic solution. The nonuniqueness errors in the conventional BEM can be removed by the present method and the Seybert and Rengarajan method. At the high-frequency range of $5 < ka < 20$, the present method and the Seybert and Rengarajan method yielded errors of less than 20%, which can be considered acceptable for engineering usage, while the conventional BEM showed peak errors larger than 50% at some singular frequencies, even though the over determination process was employed. For the low-frequency range of $ka < 5$, it was found that the conventional BEM has a small error of less than 1%, but the Seybert and Rengarajan method yields a large error in excess of 100%, and the present method produces an error of less than 30% in front of the vibrating surface. It is also found that the assembling time of the present method is quite small compared to the conventional BEM, because the latter requires additional time to deal with the nonuniqueness problem. Therefore, the present method requires far less time for the field calculation, even though the same number of elements is used in both methods. However, the present method yields a 20%–30% overestimating error with a fluctuating tendency. This error may be acceptable for an abrupt calculation of the field sound pressure level in engineering usage, but, nevertheless, it should be further reduced. For this purpose, the errors caused by the crossterm, which are ignored in the assumption need to be analyzed quantitatively in a future study.

[1] Anonymous, *SYSNOISE Rev. 5.0 User's Manual* (Numerical Integration Technologies N.V., Belgium, 1993).

[2] S. Marburg, "Six boundary elements per wavelength: is that enough?," J. Comput. Acoust. **10**, 25–51 (2002).

[3] L. L. Beranek and I. L. Vér, *Noise and Vibration Control Engineering: Principles and Applications* (Wiley, New York, 1992).

[4] R. H. Lyon and G. Maidanik, "Power flow between linearly coupled oscillators," J. Acoust. Soc. Am. **34**, 640–647 (1962).

[5] R. H. Lyon and R. G. DeJong, *Theory and Application of Statistical Energy Analysis*, 2nd ed. (MIT Press, Cambridge, 1975).

[6] M. R. Schroeder, "Digital simulation of sound transmission in reverberant spaces," J. Acoust. Soc. Am. **47**, 424–431 (1969).

[7] A. F. Seybert and T. K. Rengarajan, "The high frequency radiation of sound from bodies of arbitrary shape," Trans. ASME, J. Vib., Acoust., Stress, Reliab. Des. **109**, 381–387 (1987).

[8] S. N. Makarov and M. Ochmann, "An iterative solver of the Helmholtz integral equation for high-frequency acoustic scattering," J. Acoust. Soc. Am. **103**, 742–750 (1998).

[9] V. Rokhlin, "Rapid solution of integral equations of scattering theory in two dimensions," J. Acoust. Soc. Am. **86**, 414–439 (1990).

[10] E. M. Rosen, F. X. Canning, and L. S. Couchman, "A sparse integral equation method for acoustic scattering," J. Acoust. Soc. Am. **98**, 599–610 (1995).

[11] T. W. Wu, W. L. Li, and A. F. Seybert, "An efficient boundary element algorithm for multi-frequency acoustical analysis," J. Acoust. Soc. Am. **94**, 447–452 (1993).

[12] J. L. Guyader, "Method to reduce computing time in structural acoustics," *Proceedings of the 3rd International Congress on Air- and Structureborne Sound and Vibration*, 1994, pp. 5–12.

[13] J. L. Guyader and T. Loyau, "Sound radiation from structures: The frequency averaged quadratic pressure approach," *Proceedings of Inter-noise 96*, 1996, pp. 1267–1272.

[14] J. L. Guyader and T. Loyau, "Acoustic radiation from structures: the frequency averaged quadratic pressure prediction," *Proceedings of the 5th International Congress on Air- and Structure-Borne Sound and Vibration*, 1997, pp. 2492–2436.

[15] H. Mahe, P. Maurel, and N. Hamzoui, "Simple approach of noise radiated by industrial structures," *Proceedings of Euro-noise 95*, 1995, pp. 457–462.

[16] J. B. Fahnline and G. H. Koopmann, "Numerical implementation of the lumped parameter model for the acoustic power output of a vibrating structure," J. Acoust. Soc. Am. **102**, 179–192 (1997).

[17] B. B. Baker and E. T. Copson, *The Mathematical Theory of Huygens' Principle* (Oxford, London, 1939).

[18] M. W. Bonilha and F. J. Fahy, "On the vibration field correlation of randomly excited flat plate structures, I: Theory," J. Sound Vib. **214**, 443–467 (1998).

[19] M. W. Bonilha and F. J. Fahy, "On the vibration field correlation of randomly excited flat plate structures, II: Experimental verification," J. Sound Vib. **214**, 469–496 (1998).

[20] J. S. Bendat and A. G. Piersol, *Random Data*, 2nd ed. (Wiley, Singapore, 1991).

[21] F. J. Fahy, *Sound and Structural Vibration: Radiation, Transmission and Response* (Academic, London, 1985).

[22] L. G. Copley, "Integral equation method for radiation from vibrating bodies," J. Acoust. Soc. Am. **42**, 807–816 (1967).

[23] P. J. Harris and S. Amini, "On the burton and miller boundary integral formulation of the exterior acoustic problem," Trans. ASME, J. Vib., Acoust., Stress, Reliab. Des. **114**, 540–545 (1992).

[24] P. M. Morse and K. U. Ingard, *Theoretical Acoustics* (McGraw-Hill, New York, 1968).

Supercritical parametric phase conjugation of ultrasound. Numerical simulation of nonlinear and nonstationary mode

Alain Merlen[a]
LML, Cité Scientifique, USTL, 59655 Villeneuve d'Ascq Cédex, France

Vladimir L. Preobrazhensky[b]
IEMN–DOAE, Ecole Centrale de Lille, B.P. 48, 59651 Villeneuve d'Ascq Cédex, France
and Wave Research Center GPI RAS, Moscow, Russia

Philippe Pernod[c]
IEMN–DOAE, Ecole Centrale de Lille, B.P. 48, 59651 Villeneuve d'Ascq Cédex, France

This paper investigates the saturation mechanism of the nonstationary supercritical mode of parametric wave phase conjugation in a magnetostrictive medium. The numerical simulation considers the two most probable nonlinear mechanisms of interaction between elastic deformation and electromagnetic excitation. For the qualitative study of the dynamics of the system, a one-dimensional numerical simulation is sufficient if applied to an infinite medium with a finite active zone. The temporal form of the conjugate wave is obtained for both hypotheses. Comparison with experiments shows that only one mechanism corresponds to the experimental behavior. © 2002 Acoustical Society of America. [DOI: 10.1121/1.1506687]

I. INTRODUCTION

Parametric wave phase conjugation (WPC) of sound is of interest for various applications in acoustics. Acoustic echo was observed first in the hypersonic frequency band by means of microwave pumping of piezoelectric[1] and magnetic[2] crystals. For WPC in ultrasound frequency band various mechanisms of parametric interaction were considered theoretically[3–5] and studied experimentally.[6–8] Supercritical electromagnetic pumping of magnetic ceramics[9] was found as a most effective method of WPC in the ultrasound frequency band. Giant amplification of phase conjugate waves (exceeding 80 dB) and a number of manifestations of acoustic time reversal were demonstrated by means of supercritical magnetoacoustic phase conjugator (MAPC).[10] Applications of parametric WPC are discussed extensively.[11,12] The general problem of supercritical WPC has no analytical solution. Recently a numerical technique based on Godunov-type procedure was elaborated for description of WPC supercritical dynamics and was demonstrated on an example of a linear WPC mode at the given pumping field approximation.[13]

Nevertheless, the problem of nonlinear pumping mode is of principle importance for the study of the output power limitation by nonlinear effects in parametric wave phase conjugators. In this paper, the same numerical technique includes the nonlinearity of the parametric pumping in two situations of interaction between the elastic field and the electromagnetic energy supply. These numerical results allow a deeper understanding of the coupling mechanism between the excitation source and the elastic field. This work provides useful direction of research for the optimization of the magnetostrictive samples needed for the applications of wave phase conjugation.

II. PHYSICAL MODEL

Generally parametric wave phase conjugation uses an active material of limited length, a part of which (active zone) is under the effect of a pumping field. When an incident acoustic wave of frequency ω penetrates the active zone, a pumping field at double frequency $\Omega = 2\omega$ (parametric resonance condition) is applied to the active material and the conjugate wave is created. The supercritical mode of giant amplification occurs when the pumping amplitude is higher than a threshold value, function, for a given material, of the length of the sample. At the first stage of this process, the nonlinear effects are small and a numerical simulation with a linear pumping[13] is in good agreement with multiscale asymptotic expansions (MSAE)[14] and experimental data when the deformation remains small at the end of the pumping.[15]

Nevertheless, this linear mode can be applied only for relatively short pumping in the beginning of amplification. For consideration of stationary states of the system or evaluation of output power of the system when pumping is long enough, the nonlinear effects have to be introduced in the numerical model.

The most important nonlinear mechanism of amplitude limitation is the feedback of the system on the pumping source.[10] Dependent on the electrical scheme of the pumping circuit, two main mechanisms are possible.

The first one is a pumping depletion in which the feedback is in phase with the pumping field. This situation occurs, for example, in magnetostrictive conjugators when the pumping coil with active material is introduced in the reso-

nance serial electrical circuit. In this case, the modulation of sound velocity $c(t)$ by the external magnetic field is described analogously to Ref. 16 by the following formula:

$$c^2(t) = c_0^2 \left[1 + m \left(\cos(\Omega t + \psi) + \frac{mMc_0^2}{2P_e l} \int_0^l \frac{\partial}{\partial t} \left(\frac{\partial u}{\partial x} \right)^2 dx \right) \right],$$

where u is the elastic displacement, M and l are the mass and length of the active part of the sample; and $P_e = U_0^2/R$ is the electric power of the pumping source, U_0 is the tension amplitude of the electric source, and R is the active resistance of the circuit. Moreover, m is a small parameter ($m \ll 1$) referred to the "modulation depth" and ψ is an arbitrary phase shift.

The second mechanism is a phase mechanism in which the feedback leads to a phase shift of the pumping field. This mechanism could be observed, for example, if the electrical tension source were loaded directly by the pumping coil around the active magnetostrictive medium. Such a case corresponds to the following form of the sound velocity modulation:

$$c^2(t) = c_0^2 \left[1 + m \left(\cos(\Omega t + \psi) + \frac{mMc_0^2 \Omega}{2P_e l} \int_0^l \left(\frac{\partial u}{\partial x} \right)^2 dx \right) \right]$$

but here, $P_e = U_0^2/\Omega L$, where L is the inductance of the coil.

The present paper describes the development of the phase conjugation process in time and space for both mechanisms. The influence of the mechanism on the output shape of the conjugate wave is demonstrated. The numerical simulations allow a detailed analysis of the saturation process and provide explanations to some dynamic behaviors observed in experiments but not understood until now.

III. MATHEMATICAL MODEL

The problem can be written as a hyperbolic conservation system[13]

$$\left(\begin{array}{l} \dfrac{\partial U}{\partial t} + \dfrac{\partial F(U)}{\partial x} = S, \quad \forall x \in IR, t \geqslant 0 \\ U(x,0) = U_0(x), \quad \forall x \in IR \end{array} \right), \tag{1}$$

with

$$F(U) = \begin{pmatrix} c_0 \, w_1 \\ -c_0 \, w_2 \end{pmatrix}, \quad U = \begin{pmatrix} w_1 \\ w_2 \end{pmatrix},$$

where w_1 and w_2 can be considered as the displacement velocities associated, respectively, with the direct and the conjugate wave. Calling $v = \partial u/\partial t$ the physical displacement velocity and σ_{xx} the normal stress in the x direction, we can write $w_1 = v + \theta$, $w_2 = v - \theta$ where $\theta = -\sigma_{xx}/\rho c_0$.

The source term S is given by

$$S = - \begin{pmatrix} m(w_1 - w_2) \left(\dfrac{\Omega}{4} \sin(\Omega t + \psi) - s \right) \\ -m(w_1 - w_2) \left(\dfrac{\Omega}{4} \sin(\Omega t + \psi) - s \right) \end{pmatrix},$$

where s is the nonlinear pumping term.

For the mechanism of pumping depletion, we have

$$s = \frac{mMc_0^2}{2P_e l} \left(\int_0^l \left(\frac{\partial w_1}{\partial x} \right) \left(\frac{\partial w_2}{\partial x} \right) dx + \frac{1}{4} \left[(w_1 - w_2) \frac{\partial(w_1 - w_2)}{\partial x} \right]_0^l \right).$$

For the phase mechanism, the expression of s is

$$s = \frac{mMc_0 \Omega}{16 P_e l} \left(\int_0^l (w_1 - w_2) \frac{\partial}{\partial x} (w_1 + w_2) dx \right).$$

In both expressions, s is expressed in terms of spatial derivatives using Eq. (1) to replace any time derivatives by spatial ones. This supposes also that deformations remain sufficiently small to enable s and Ω to be of the same order of magnitude.

When the pumping is stopped, the linear term has to be switched off, but the nonlinear term still remains active. In experiments the electric power cannot be cut instantaneously because the inertia of the circuit that has been simulated in the calculation through a quality factor by an exponential decay of the linear term at the end of the pumping.

In the following section, the system (1) is solved numerically by an explicit finite volume method already used in the linear case and described in more details in Refs. 13 and 17. The nonlinear term is computed by a classical Newton–Cotes quadrature. With the very refined meshes used in this work a trapezoidal rule is sufficient.

IV. NUMERICAL RESULTS

Numerical simulations presented in this part were made for an infinite active material with finite active zone for the two nonlinear mechanisms of amplitude limitation. From the numerical point of view, the sample of active material is situated between $x = 0$ cm and $x = 4$ cm. The active zone lies between $x = 1$ cm and $x = 3.5$ cm. The mesh contains 8000 points. The boundary conditions at $x = 0$ cm and $x = 4$ cm are nonreflexive as if the domains $x < 0$ and $x > 4$ cm were filled by the material too. The initial condition is given in the following form:

$$w_1 = A \sin \left(\frac{2\pi}{\lambda} (x - x_l) \right) \quad \text{for } x_1 < x < 0.5 \text{ cm},$$

$$w_2 = 0 \quad \text{for } x_1 < x < 0.5 \text{ cm},$$

$$w_1 = w_2 = 0, \quad \text{elsewhere}.$$

Abscissa x_1 is chosen such as $(0.5 - x_1) = 3\lambda$, where λ is the wavelength $\lambda = 2\pi c_0/\omega$ with $\omega = 2\pi \times 10^7 \text{ s}^{-1}$ and $c_0 = 4000$ m/s. Parameter $A = 2.5 \times 10^5$ Pa is the initial amplitude. Actually, the value of A is irrelevant because the pumping duration is chosen long enough to reach the saturation in any case. This level will be shown as independent of the initial condition. Moreover the giant amplification being exponential a variation of A does produce a noticeable delay of the saturation. The beginning of the pumping is the origin of time. Of course, in order to produce the parametric resonance, the pumping frequency is $\Omega = 2\omega$. The density of the magnetostrictive material is $\rho_0 = 5000$ kg/m^3.

Pumping signal (s⁻¹) — Modulation rate of the compression modulus: $\dfrac{\partial c}{c\,\partial t}$ (s⁻¹)

Normal stress (Pa) — Normal stress at the limit of the active zone
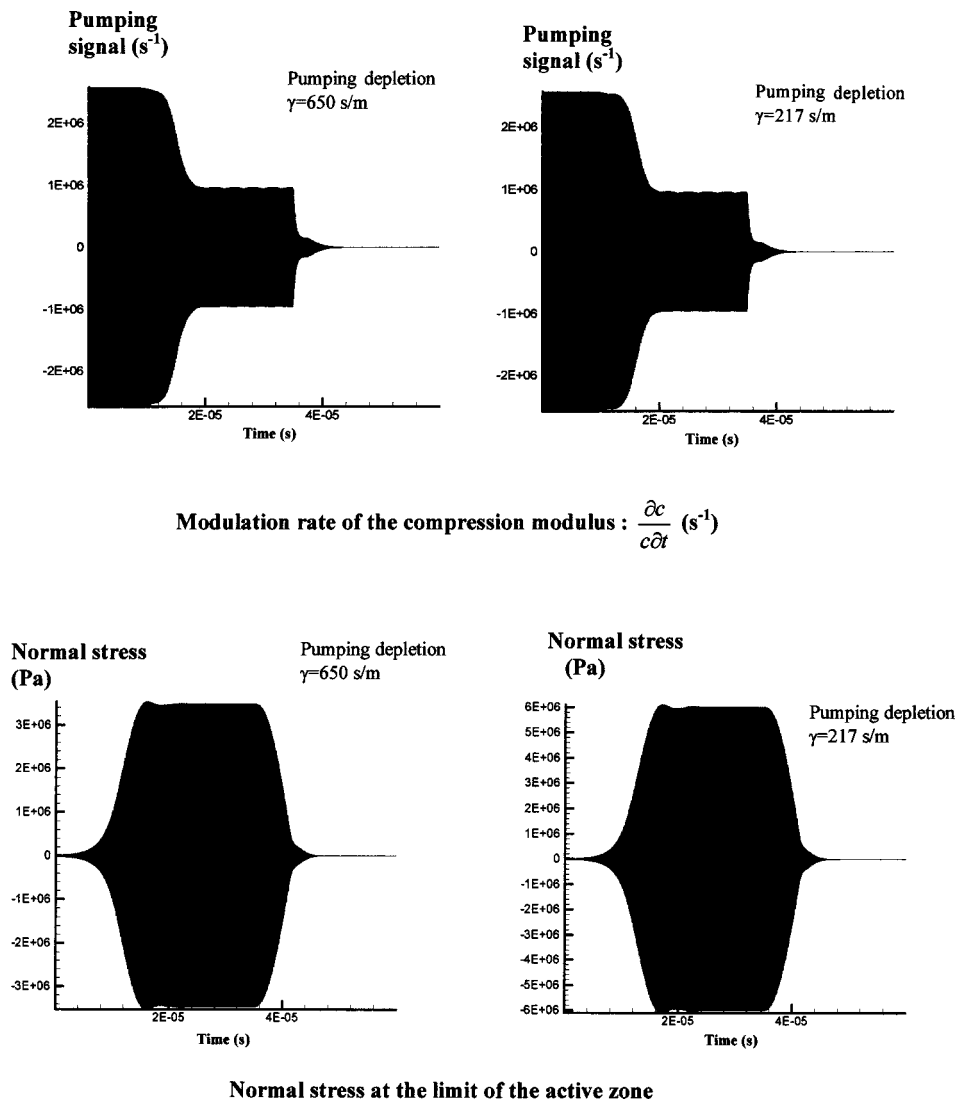
FIG. 1. Time evolution of the pumping signal and the normal stress at the left edge of the active zone for $\gamma = 650$ s/m and $\gamma = 217$ s/m. The pumping signal is the value of $dc/c\,dt$ which is the source term in the primitive formulation in θ and v. This signal is directly proportional to the electromagnetic signal of the excitation as it can be measured in experiments. The stress signal at the left edge of the active zone gives the time evolution of the conjugate wave. Its shape can be compared with the pressure measured in water in wave conjugation experiments.

A. Pumping depletion mechanism

Figure 1 shows the results obtained with the first mechanism of amplitude limitation (pumping depletion). The results were made for a pumping duration of $Tp = 35\ \mu s$, a modulation depth of $m = 4.1 \times 10^{-2}$. Two values of coefficient $\gamma = Mmc_0^2/P_e l = 650$ and 217 are selected. The first choice corresponds approximately to the experimental conditions of Ref. 9.

The pumping signal corresponds to the rate of variation of the compressibility modulus of the medium and is directly proportional to the electromagnetic signal measured in experiments. At the beginning of the process, the modulation is essentially governed by the linear term and is nothing but a sinusoidal function of time of amplitude $m\Omega/2$. Suddenly the nonlinear term reaches the order of magnitude of the linear one, the pumping decays and the saturation of the stress signal begins. Finally the pumping and the stress signal stabilize at a constant value, showing that the system reaches a neutral stability. It is not surprising that the variation of the compressibility modulus stabilizes at a value that is totally independent of γ and m. This is because this neutral stability corresponds exactly to the threshold value of pumping: $m_0\Omega/2$ which is $m_0 = 1.6 \times 10^{-2}$ for this sample. This value

of m only depends on the length of the sample. At the end of the pumping all the signals decrease according to the quality factor of the circuit. This is exactly the behavior observed in experiments.

The temporal form of the conjugate stress signal is computed at the left output of the active zone. This signal clearly exhibits the exponential amplification of the conjugate wave followed by a saturation of the amplitude due to the pumping depletion. An important feature is the variation of the saturation level with γ, it is 3.4 Mpa for $\gamma = 650$ s/m and 5.9 Mpa for $\gamma = 217$ s/m. One can imagine that this is due to the fact that the saturation takes place later when the nonlinear term is small. This delay is observable by comparison of the pumping signal in both cases. The decay of the pumping happens about 2 μs before for $\gamma = 650$ s/m. Nevertheless a more interesting way for explanation is to analyze the saturation level in terms of balance between the linear and nonlinear term. It is clear that the smallest γ the highest the stress amplitude is needed for balancing the linear term.

Figure 2 presents the evolution of the spatial distribution of the normal stress field (in Pa) inside the sample. The view corresponding to $t = 0.75\ \mu s$ shows the incident pulse (on the right) and the origin of the direct wave created by parametric
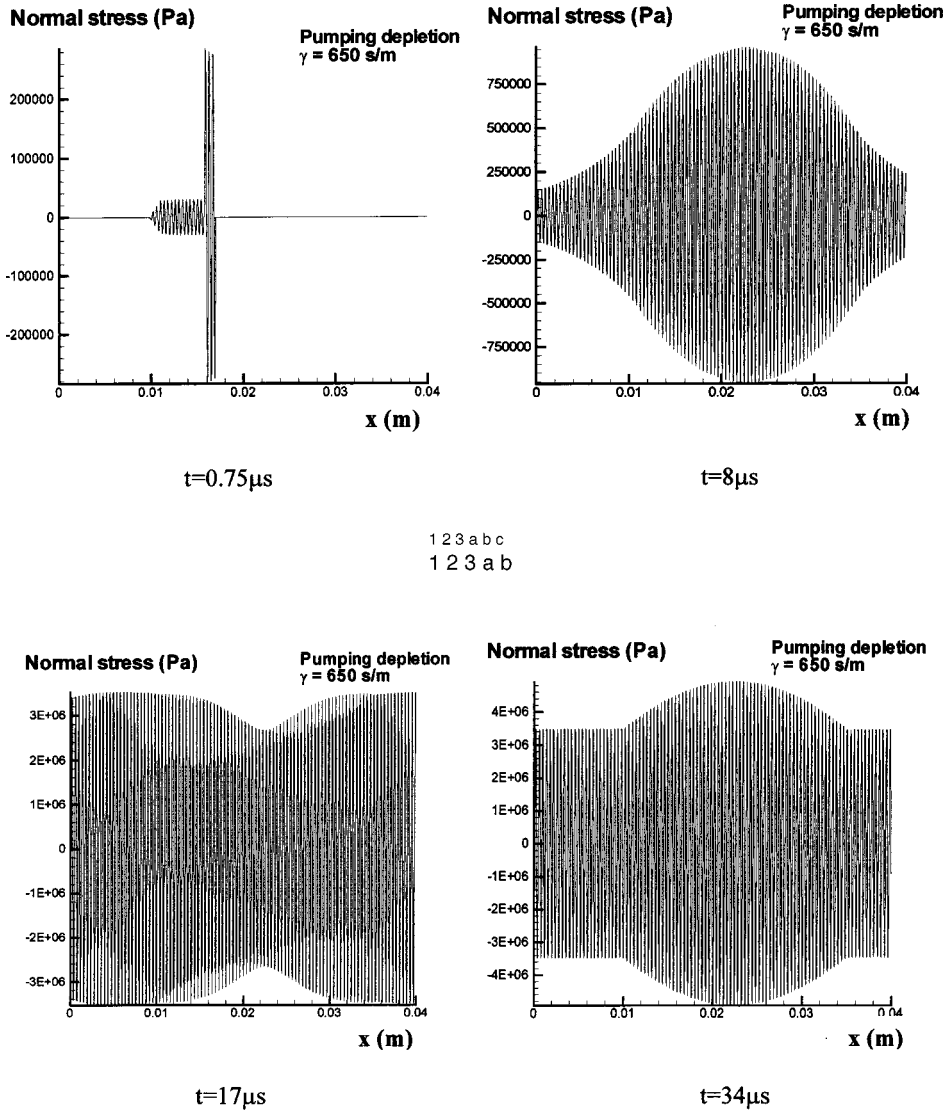
FIG. 2. Spatial repartition of normal stress in the sample for the pumping depletion process and a pumping duration of 35 μs. At $t = 0.75$ μs, the initial condition is observable as well as the beginning of the direct wave. After the incident wave evacuated the sample, both direct and conjugate waves are amplified ($t = 8$ μs). At time $t = 17$ μs, the saturation takes place and the last picture shows the typical repartition of stress during the saturation for a modulation depth $m = 4.1$ $e-2$. A similar sequence is available for $\gamma = 217$ s/m.

interaction. At the same time the conjugate wave develops and after evacuation of the incident wave the stress tends to become symmetric relatively to the middle of the sample ($t = 8$ μs). Due to the amplification process, the amplitude of this distribution increases over time and, due to the growth of the nonlinear terms, tends progressively to the one presented in the next picture which corresponds to $t = 17$ μs. After saturation, the spatial distribution is to the one presented for $t = 34$ μs. The constant amplitude of the direct (on the right) and conjugate (on the left) waves going out from the active zone is observed. Finally, when the pumping is stopped, the direct and the backward waves separate like in the linear case,[13] but here the quality factor of the circuit is simulated. The linear pumping is exponentially damped and the nonlinear term follows with the decrease of the elastic power. This explains the smooth decay on the temporal signal.

B. Phase mechanism

The results obtained with the phase mechanism are shown in Fig. 3, for similar conditions as for the previous situation: pumping duration $Tp = 35$ μs, $m = 4.1 \times 10^{-2}$, and $\gamma = 650$. The behavior is slightly changed. The saturation takes place after a sharp decay of the pumping signal followed by oscillations. Nevertheless the threshold value is also obtained and the signals stabilize. This difference with the amplitude depletion process can be explained by the phase shift between the linear and nonlinear source term.

The oscillations of the source term lead to some oscillations too on the stress signal of the conjugate wave. Another important fact is the difference of the saturation level, which is of 4.3 MPa here instead of 3.4 Mpa for the pumping depletion.

Computations with $\gamma = 217$ leads towards the same observations except that the stress saturation level at the left edge of the active zone is 7.5 Mpa.

V. ANALYSIS

We focus our analysis on the saturation level considered as a balance between the linear and nonlinear source terms. In terms of primitive variables θ and v, the source term can be written

$$\frac{dc}{c\,dt} = -\frac{m}{2}\left[\Omega\sin(\Omega t + \psi) - \frac{\gamma}{2c_0^2}\int_0^l \frac{\partial^2 \theta^2}{\partial t^2}\,dx\right]$$

Pumping signal (s⁻¹) / **Normal stress (Pa)** (top two plots)

Pumping signal $\dfrac{dc}{cdt}$ / **Stress signal of the conjugate wave** (bottom two plots)

$t=8\mu s$ (left), $t=34\mu s$ (right)

Stress repartition in the sample
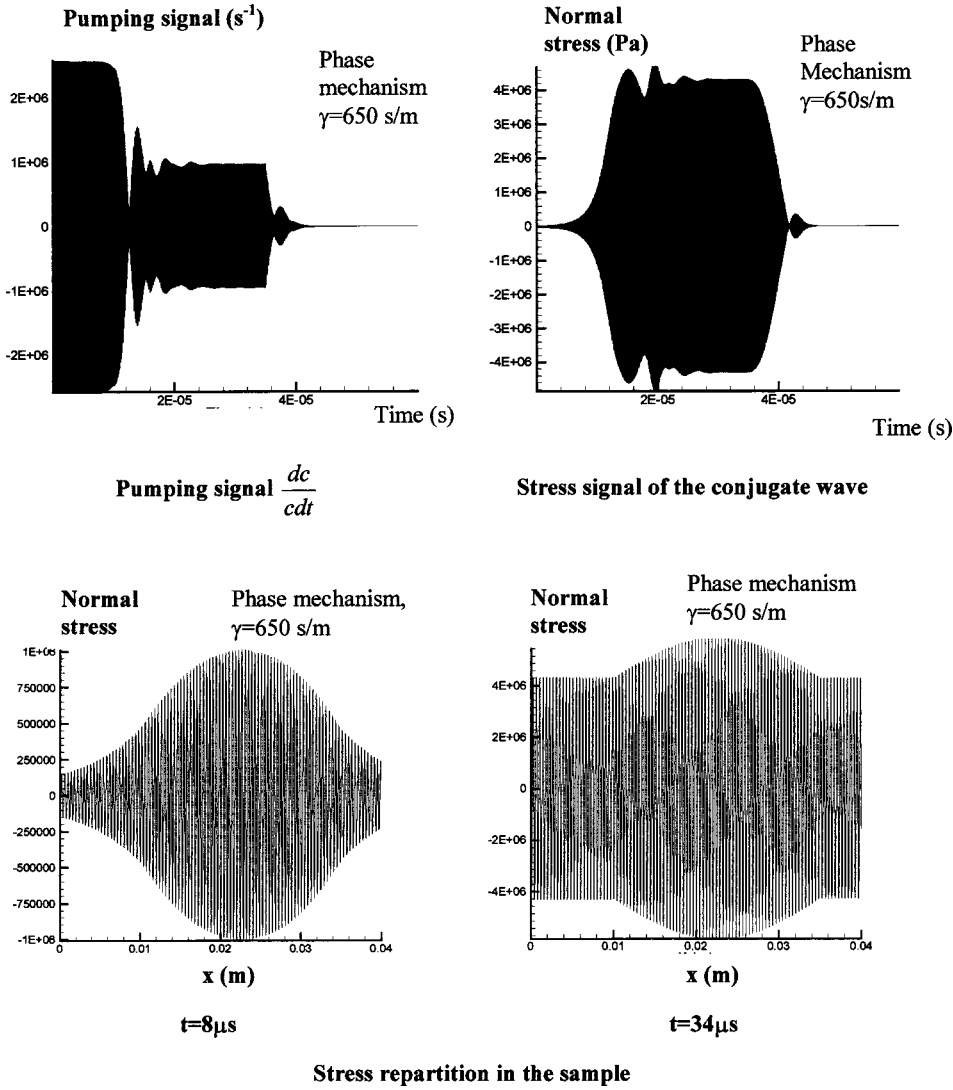
FIG. 3. Results for the phase mechanism. The pumping signal fluctuates more than for the pumping depletion, nevertheless the saturation level is the same and corresponds to the threshold of the exponential amplification. The conjugate wave stress signal is also more agitated than for the depletion process and reaches a saturation level slightly higher. The stress repartition in the sample does not seem to be very different from the depletion process. The situation during the saturation is exactly the same as for the depletion except the overall level slightly higher. The same results are available for $\gamma = 217$ s/m.

for the amplitude depletion, and

$$\frac{dc}{cdt} = -\frac{m}{2}\left[\Omega\,\sin(\Omega t + \psi) + \frac{\gamma\Omega}{c_0}\int_0^l \theta\frac{\partial v}{\partial x}\,dx\right]$$

for the phase mechanism.

In a very general formulation, the direct and conjugate waves are

$$w_1 = A_0 F_1\left(\frac{x}{l}\right)\cos(\omega t - kx + \psi_1)$$

and

$$w_2 = A_0 F_2\left(\frac{x}{l}\right)\cos(\omega t + kx + \psi_2),$$

where F_1 and F_2 are "slow" functions of x compared with $\cos(kx)$ and $k = \omega/c_0$. Function F_1 always fulfills the condition $F_1(0) = 0$ and $F_1(1) = 1$, A_0 being the amplitude at the edge of the active zone. At the saturation we have $F'_1(1) = 0$ since the direct wave is totally evacuated at the right edge of the active zone. The symmetry condition leads to $F_2(x/l) = F_1[1 - (x/l)]$. The simplest pair (F_1, F_2) is $F_1(x/l) = \sin(\pi x/2l)$ and $F_2(x/l) = \cos(\pi x/2l)$, which is the configuration obtained numerically at saturation for both pro-

cesses (Fig. 4). With these assumptions and using the relations

$$\theta = \frac{w_1 - w_2}{2}$$

and

$$\frac{\partial v}{\partial x} = -\frac{\partial \theta}{c_0 \partial t}(1 + 0(m)),$$

it can be shown, by standard techniques, that

$$\int_0^l \frac{\partial^2 \theta^2}{\partial t^2}\,dx = -\frac{A_0^2\Omega^2 l}{4\pi}\cos(\Omega t + \phi)(1 + 0(1/kl))$$

and

$$\int_0^l \theta\frac{\partial v}{\partial x}\,dx = \frac{A_0^2\Omega l}{8\pi}\sin(\Omega t + \phi)(1 + 0(1/kl)),$$

where $\phi = \psi_1 + \psi_2$ and $kl \sim 4\times 10^2$. Therefore, neglecting very small terms, the pumping can be written at saturation

$$\frac{dc}{c\,dt} = -\frac{m\Omega}{2}\left[\sin(\Omega t + \psi) - \frac{\gamma\Omega l}{8\pi c_0^2}A_0^2\sin(\Omega t + \Phi)\right],$$

W₁ — Amplitude depletion m= 4.1 x 10⁻²

W₂ — Amplitude depletion m=4.1 x 10⁻²
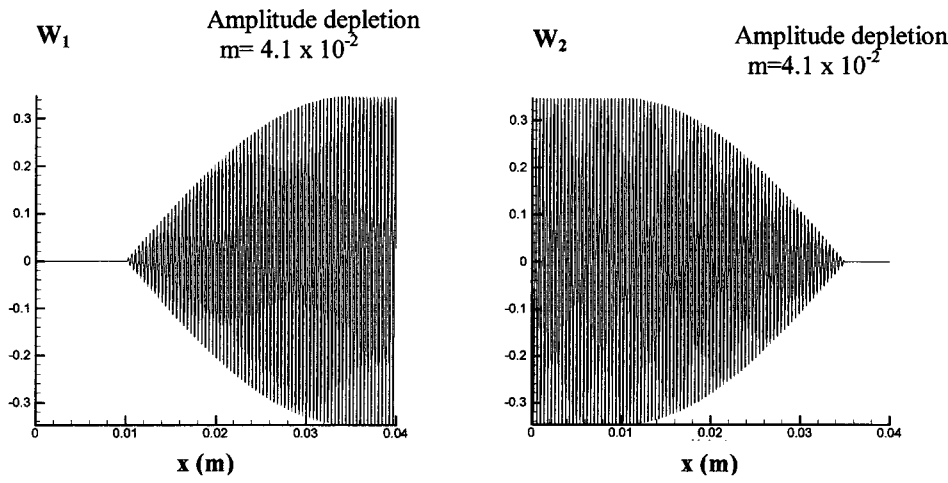
Amplitude depletion: direct (W₁) and conjugate (W₂) waves during saturation

x (m)

FIG. 4. Spatial repartition of the direct and conjugate waves during saturation. The amplitude of the waves inside the active zone $(0.01\,\text{m} < X < 0.035\,\text{m})$ is given by $F_1 = A_0 \times \sin(\pi x/2l)$ and $F_2 = A_0 \cos(\pi x/2l)$. The constant value A_0 depends on the process.

W₁ — Phase mechanism m=4.1 x 10⁻²

W₂ — Phase mechanism m=4.1 x 10⁻²
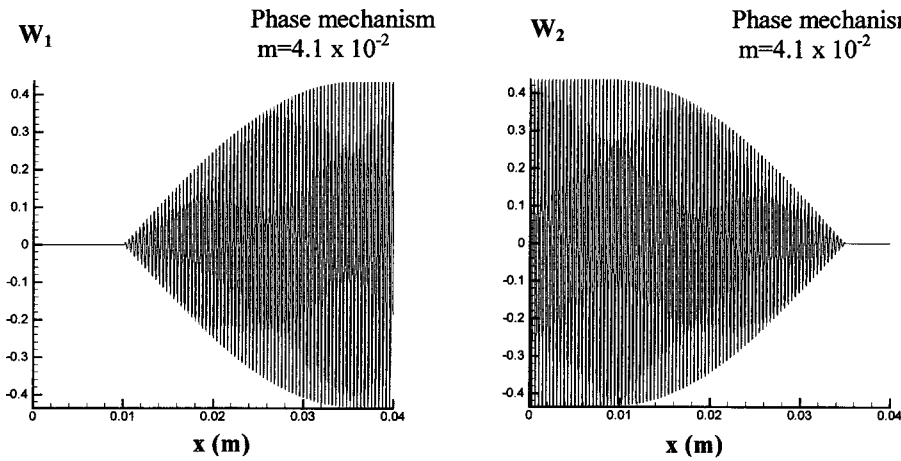
Phase mechanism: direct (W₁) and conjugate (W₂) waves during saturation

x (m)

where $\Phi = \psi_1 + \psi_2 + (\pi/2)$ for the pumping depletion and $\Phi = \psi_1 + \psi_2$ for the phase mechanism.

We define

$$K = \left[\frac{\gamma \Omega l}{8\pi c_0^2} A_0^2 \right]$$

and

$$tgH = -\frac{K\sin(\Phi - \psi)}{1 - K\cos(\Phi - \psi)},$$

and write

$$\frac{dc}{c\,dt} = -\frac{m_0\Omega}{2}\sin(\Omega t + \psi + H)$$

$$= -\frac{m\Omega}{2}\sqrt{1 + K^2 - 2K\cos(\Phi - \psi)}$$

$$\times [\sin(\Omega t + \psi + H)].$$

The general solution is

$$K = \cos(\Phi - \psi) \pm \sqrt{\cos^2(\Phi - \psi) - \left(1 - \frac{m_0^2}{m^2}\right)}.$$

For the amplitude depletion we expect that the threshold is reached without phase shift, hence $H=0$, $\Phi = \psi$, and $K = 1 - (m_0/m)$ which is the lowest root in this case gives

$$A_0 = 2c_0 \sqrt{\frac{2\pi}{\gamma \Omega l}\left(1 - \frac{m_0}{m}\right)}$$

and a stress level at saturation

$$\sigma_0 = \rho_0 c_0^2 \sqrt{\frac{2\pi}{\gamma \Omega l}\left(1 - \frac{m_0}{m}\right)}. \tag{2}$$

With our data, this formula gives $\sigma_0 = 3.46$ Mpa for $\gamma = 650$ s/m and $\sigma_0 = 6$ Mpa for $\gamma = 217$ s/m which is in total agreement with the numerical results.

For the phase mechanism, the level is higher and corresponds roughly to $H = \pi/2$, which gives $\cos(\Phi - \psi) = 1/K$ and

Direct wave
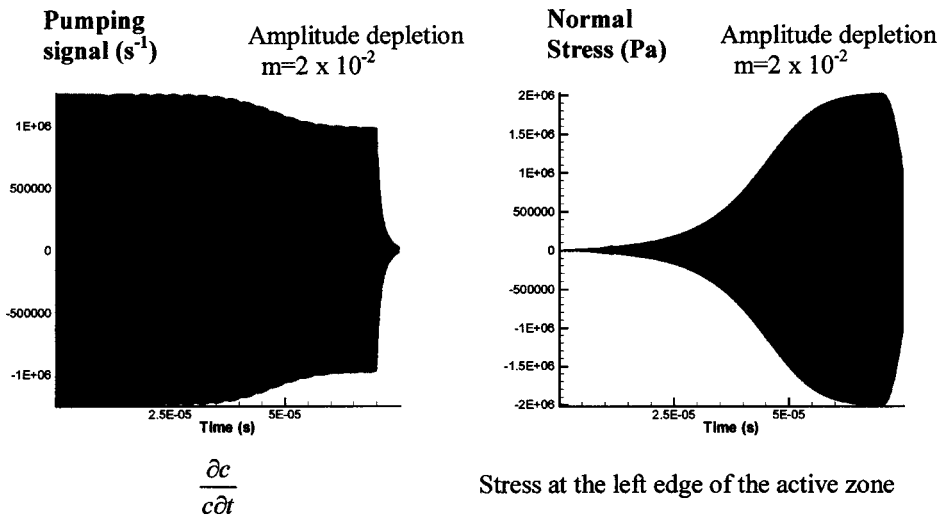
Conjugate wave

FIG. 5. Amplitude depletion, numerical results for $m = 2 \times 10^{-2}$. For this value of m near the threshold, formula (2) gives the right saturation value. The direct and conjugate waves have the same spatial repartition as for $m = 4.1 \times 10^{-2}$.
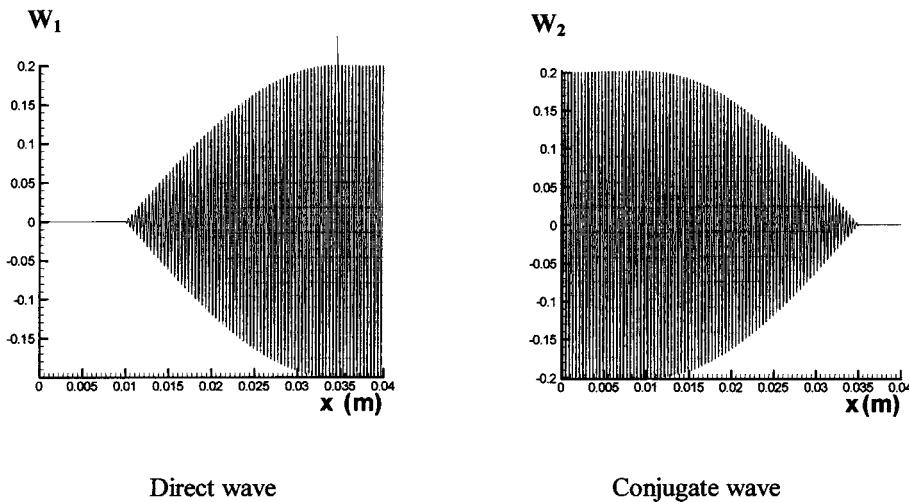
$$\sigma_0 = \rho_0 c_0^2 \sqrt{\frac{2\pi}{\gamma \Omega l}} \sqrt{\left(1 + \frac{m_0^2}{m^2}\right)} \qquad (3)$$

leading to $\sigma_0 = 4.6$ Mpa for $\gamma = 650$ s/m and $\sigma_0 = 7.9$ Mpa for $\gamma = 217$ s/m. These values are both 6% higher than the computed values. This means that H is slightly lower than $\pi/2$ but does not depend on γ. We must underline that formula (3) is not as general as formula (2), which can be applied for any value of m since for the amplitude depletion, H is always zero. On the contrary, H varies with m in the phase mechanism and formula (3) is just the limit value when H tends toward $\pi/2$.

These considerations are confirmed by Fig. 5 which presents the results for $m = 2 \times 10^{-2}$ and $\gamma = 650$ s/m for a pumping duration of 70 μs. This value of m is relatively close to the threshold, which explains the slower growth rate and the necessity of a long pumping before reaching the saturation. Formula (2) forecasts the value of 2 Mpa for σ_0 in the pumping depletion mechanism, which is in total agreement with the computation.

For the phase mechanism (Fig. 6) $\sigma_0 = 3.5$ Mpa which gives $K \approx 0.5$ and $H = -0.51$ radian which means that the phase shift $\Phi - \psi$ between the linear and nonlinear pumping terms is about 0.9 radian.

A systematic study of functions $H(m)$ and $K(m)$ is needed in order to obtain, in the future, general formulas for the phase mechanism. Nevertheless before starting such an investigation, it is more important to compare our conclusions with experiments. That is the purpose of the next section but before starting with it, we must recall that the numerical simulation can provide much more information that experiments in such a problem. For example, experiments cannot provide the stress repartition in the sample, which is not as simple as it seems looking the very simple repartitions of w_1 and w_2.

Figure 7 shows the repartitions obtained for both processes in the case $m = 2 \times 10^{-2}$. This result is unexpected according to the similarity of the repartitions of w_1 and w_2 in all the configurations. But it must be reminded that the condition on the phase concerns $\psi_1 + \psi_2$ and allows a degree of freedom between the respective values of these angles. The

Pumping Signal (s⁻¹)

$$\frac{\partial c}{c\partial t}$$

W₁

x (m)

Direct wave (Saturation)

Normal stress

Stress at the left edge of the active zone

W₂

x (m)

Conjugate wave (Saturation)
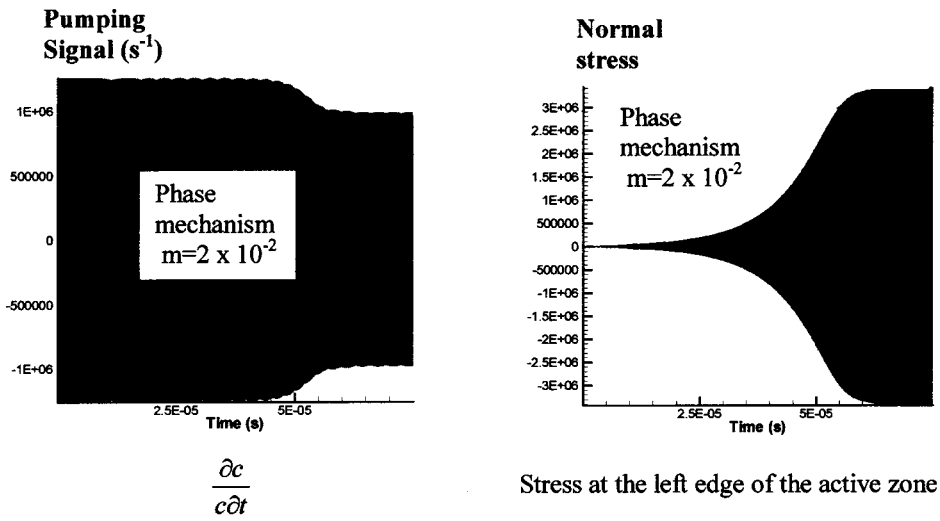
FIG. 6. Phase mechanism, numerical results for $m = 2 \times 10^{-2}$. For this value of m near the threshold, $K \approx 0.5$ and $H \approx -0.51$ radian. The phase shift between the linear and nonlinear pumping is about 0.9 radian at saturation. The direct and conjugate waves have the same spatial repartition as for the other cases.
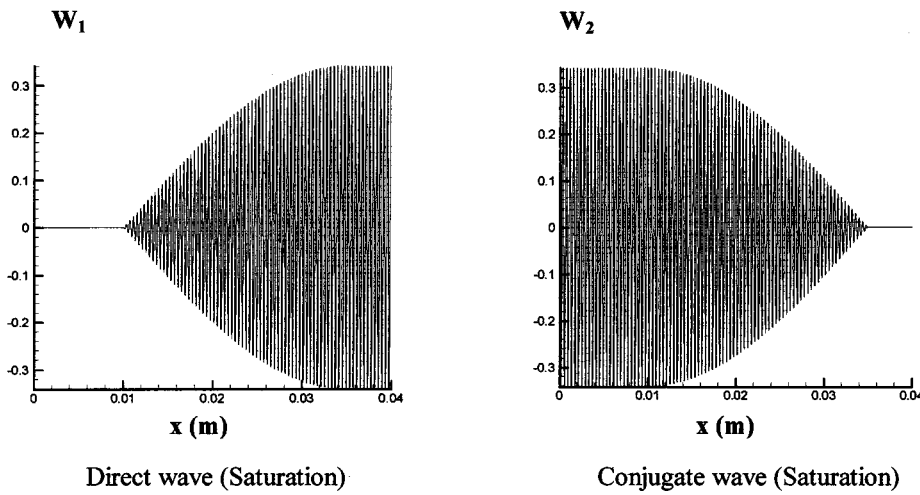
actual values of ψ_1 and ψ_2 are fixed by the boundary condition through the higher order terms in $1/kl$ that we neglected in our analysis. Results for $m = 4.1 \times 10^{-2}$ (Figs. 2 and 3) correspond to a situation where $\psi_1 \approx \psi_2$ whereas the results for $m = 2 \times 10^{-2}$ (Fig. 7) correspond to $\psi_1 \approx \psi_2 + \pi$. This very little detail emphasized by the numerical simulation can have non-negligible consequences on the resistance of the sample.

VI. COMPARISON WITH EXPERIMENTS

In the previous simulation the pumping duration T_p was sufficiently long for a good examination of the phenomenon

Normal stress (Pa)

x (m)

Amplitude depletion

Normal stress (Pa)

x (m)

Phase mechanism
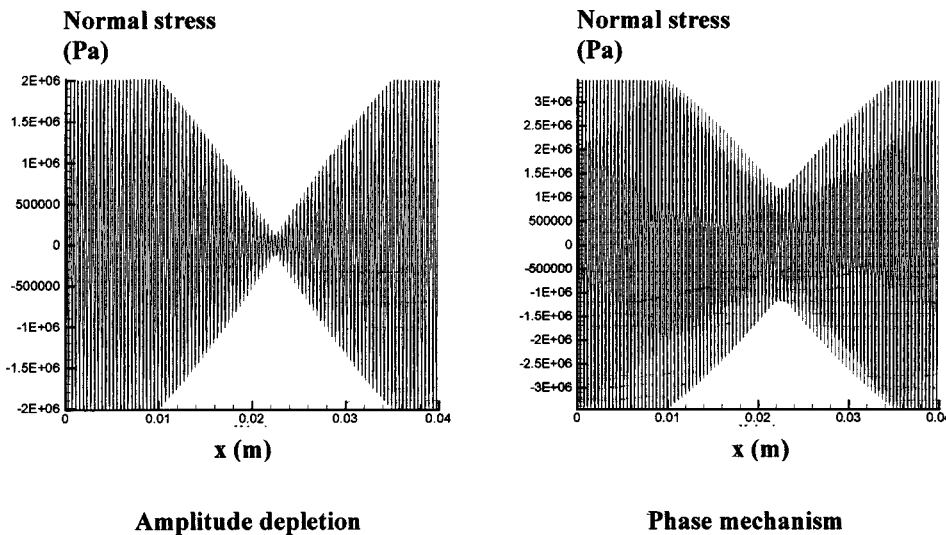
FIG. 7. Stress repartition in the sample for $m = 2 \times 10^{-2}$. The phase shift between the direct and conjugate wave is π instead of 0 for the case $m = 4.1 \times 10^{-2}$. The stress is minimum in the middle of the sample.
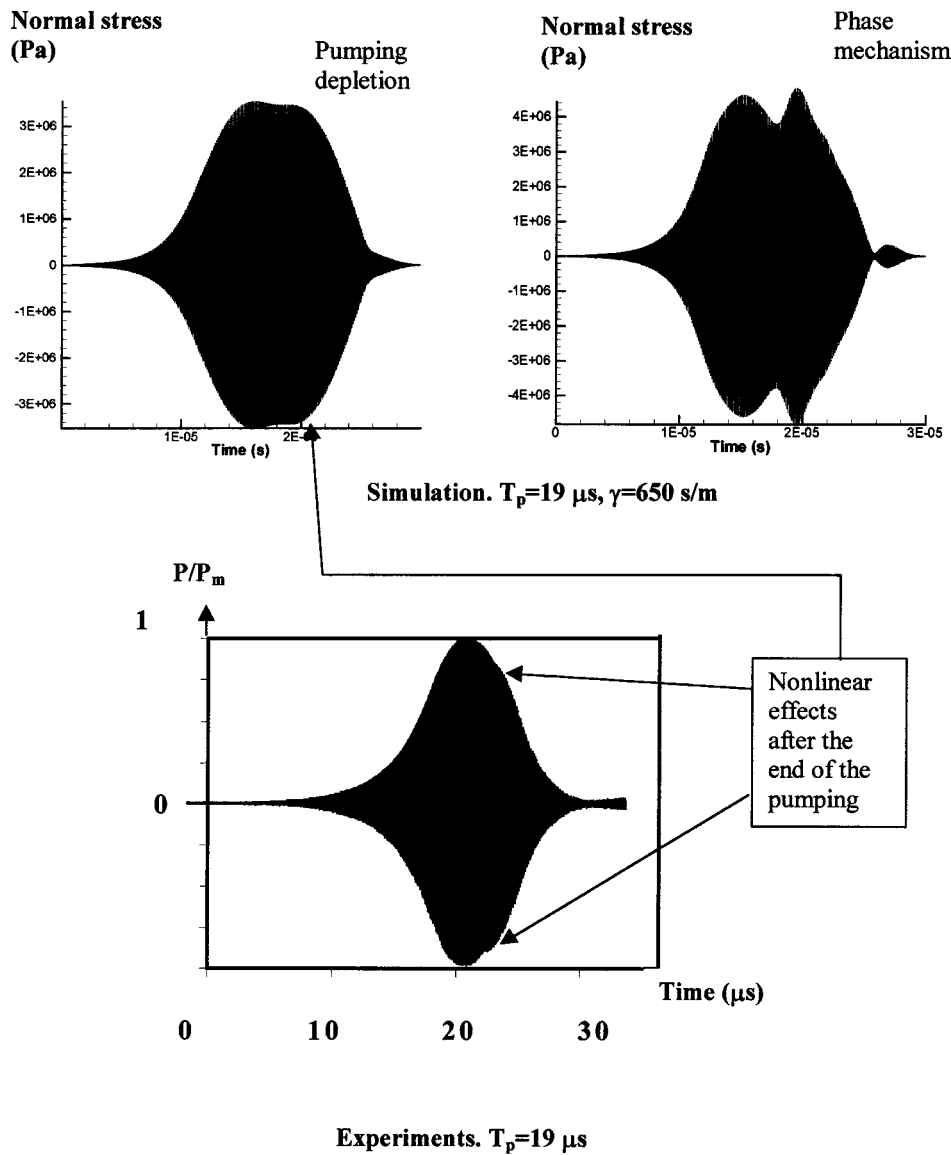
FIG. 8. Comparison with experiments for a pumping duration of 19 μs. The experimental signal is a pressure measurement of the conjugate wave outside the sample. It has been normalized by the maximum pressure since only the shape is relevant here. The general feature of the experimental signal is similar to the results given by the amplitude depletion process. No oscillation before saturation is observed and a similar decay takes place after the end of the pumping with a small flattening after the maximum. A careful adaptation of parameter m and γ must provide simulations very similar with the experimental result for the amplitude depletion process.

of saturation. In experiments the pumping duration is often shorter. The first comparison with experiments consisted in fitting the rate of the exponential growth. This task, focalized, on the linear pumping was achieved in previous works.[13] The value of $m=4.1\times10^{-2}$ was fixed according to these previous results. In this paper we compare the behavior of the stress signal at the end of the pumping. In experiments T_p was 19 μs and the full saturation had no time to take place. Nevertheless the nonlinear terms play an important role in the dynamical behavior of the signal just before the pumping is switched off. Figure 8 presents a comparison between simulations and experiments. Of course the experimental signal is not the stress inside the sample at the edge of the active zone but the conjugate wave signal in water after emission from the sample. Consequently, the comparison of the levels is irrelevant. The important issue is the capacity of the simulation to reproduce the shape of the signal. Figure 8 is clearly in favor of the amplitude depletion process, which is able to reproduce the experimental decay including the slight flattening that follows the peak value and was unexplained until now. The phase mechanism is much

more agitated and the decay sharper. By a careful adaptation of m and γ the pumping depletion model must provide a signal very similar to the experimental one.

This result does not mean that the phase mechanism cannot take place in experiments: not enough experiments are available for the moment to allow such a conclusion. Nevertheless these numerical simulations and the corresponding analysis provide excellent touchstones to recognize the characteristic features of these nonlinear effects in experiments.

VII. CONCLUSION

It is shown that the one-dimensional numerical model used in this work allows the simulation of amplitude limitation due to the feedback of the system on the pumping source in the process of parametric phase conjugation. The two mechanisms considered are physically relevant, but the amplitude depletion seems to be the most probable since it corresponds to the experimental features. For that mechanism the universal analytical formula (2) provides the relation be-

tween the saturation level and the parameters of the experiments. For this fundamental study, the model was applied in this paper for an infinite medium in order to isolate the only feedback effect, but the numerical approach can be used for a sample of finite length[13] and provides information on the influence of boundaries on the nonlinear process. A two-dimensional (2D) model is now in preparation for the study of the process for primary wave with an arbitrary angle of incidence and on a laterally limited sample. This model will describe nonstationary and nonlinear processes of WPC taking into account acoustic mode conversion clearly observed in experiments. Despite the very refined mesh needed in these computations because of the high frequency of the waves, the 2D approach is still technically possible. Nevertheless, for simulations of real three-dimensional situations a hybrid asymptotic–numerical formulation has to be developed in order to simulate only the amplitude evolutions without having to reproduce the high frequency oscillations. The difficulty in this approach is the correct description of the interfaces.

ACKNOWLEDGMENTS

[1] R. B. Thomson and C. E. Quate, "Nonlinear interaction of microwave electric fields and sound in LiNbO$_3$," J. Appl. Phys. **42**, 907–919 (1971).

[2] H. van de Vaart, D. H. Lyons, and R. W. Damon, "Parametric excitation and amplification of magnetoelastic waves," J. Appl. Phys. **38**, 360–374 (1967).

[3] F. V. Bunkin, D. V. Vlasov, and Y. E. Kravtzov, "On wave phase conjugation of sound with amplification of the reversed wave," Kvant. Elektron. (Moscow) **8**, 1144–1145 (1981). Translated in Sov. J. Quantum Electron. **11**, 687–688 (1981).

[4] V. M. Levin and L. A. Chernozatonskii, "Propagation of acoustic waves in a piezo-seimconductor placed to alternating electrical field," Zh. Eksp. Teor. Fiz. **32**, 142–145 (1970). Translated in Sov. Phys. JETP **32**, 79–82 (1971).

[5] V. N. Strel'tsov, "Phase conjugation of a sound wave and photo-acoustic interaction in a electroacoustic amplifier," BRAS. Physics/supplement Physics of vibrations **59**, 78–82 (1995).

[6] Y. Nakagawa and S. Kawanago, "Surface acoustic wave parametric generation with pumping of light," J. Appl. Phys. **61**, 1415–1421 (1987).

[7] V. Krasil'nikov, T. Mamatova, and V. Prokoshev, "Parametric amplification at wave phase conjugation of magneto-elastic wave in hematite," Fiz. Tverd. Tela (Leningrad) **28**, 615–617 (1986). Translated in Sov. Phys. Solid State **28**, 346–348 (1986).

[8] M. Ohno and K. Takagi, "Enhancement of the acoustic phase conjugate reflectivity in nonlinear piezoelectric ceramics by applying static electric or static stress field," Appl. Phys. Lett. **69**, 3483–3485 (1996).

[9] A. P. Brysev, F. V. Bunkin, D. V. Vlasov, L. M. Krutyansky, V. L. Preobrazhensky, and A. D. Stakhovsky, "Regenerative amplification of acoustic waves with phase conjugation in a ferrite," Akust. Zh. **34**, 986–990 (1988). Translated in Sov. Phys. Acoust. **34**, 567–569 (1988).

[10] A. Brysev, L. Krutyanskii, and V. Preobrazhenskii, "Wave phase conjugation of ultrasonic beams," Usp. Fiz. Nauk **39**, 555–567 (1998). Translated in Sov. Phys. Usp. **41**, 793–805 (1998).

[11] K. Yamamoto, M. Ohno, A. Kokubo, K. Sakai, and K. Takagi, "Acoustic phase conjugation by nonlinear piezoelectricity. Part II. Visualization and application to imaging systems" J. Acoust. Soc. Am. **106**, 1339–1345 (1999).

[12] A. Brysev, L. Krytyansky, P. Pernod, and V. Preobrazhensky, "Acoustic microscope based on magneto-elastic wave phase conjugator," Appl. Phys. Lett. **76**, 3133–3135 (2000).

[13] S. Ben Khelil, A. Merlen, V. Preobrazhensky, and P. Pernod, "Numerical simulation of acoustic wave phase conjugation in active media," J. Acoust. Soc. Am. **109**, 75–83 (2001).

[14] D. L. Bobroff and H. A. Haus, "Impulse response of active coupled wave systems," J. Appl. Phys. **38**, 390–403 (1967).

[15] P. Pernod and V. Preobrazhensky, "Parametric phase conjugation of a wide-band acoustic pulse in supercritical mode," Appl. Phys. Lett. **76**, 387–389 (2000).

[16] V. Preobrazhensky, "Radiation power in the case of parametric phase conjugation of ultrasound in a magnet," Akust. Zh. **46**, 847–849 (2000). Translated in Acoust. Phys. **46**, 746–748 (2000).

[17] E. F. Toro, "The Weighted average flux method applied to the Euler equations," Philos. Trans. R. Soc. London, Ser. A **341**, 499–530 (1992); **341**, 499–530 (1992).

Strain wave evolution equation for nonlinear propagation in materials with mesoscopic mechanical elements

Vitalyi Gusev
Laboratoire de Physique de l'Etat Condensé, UPRESA-CNRS 6087, Faculté des Sciences,
Ecole Nationale Supérieure d'Ingénieurs du Mans, Université du Maine, 72085 Le Mans, France

Vladislav Aleshin
Laboratoire d'Acoustique, UMR-CNRS 6613, IAM, Faculté des Sciences, Université du Maine,
avenue O. Messiaen, 72085 Le Mans Cedex 09, France

Nonlinear wave propagation in materials, where distribution function of mesoscopic mechanical elements has very different scales of variation along and normally to diagonal of Preisach–Mayergoyz space, is analyzed. An evolution equation for strain wave, which takes into account localization of element distribution near the diagonal and its slow variation along the diagonal, is proposed. The evolution equation provides opportunity to model propagation of elastic waves with strain amplitudes comparable to and even higher than characteristic scale of element localization near Preisach–Mayergoyz space diagonal. Analytical solutions of evolution equation predict nonmonotonous dependence of wave absorption on its amplitude in a particular regime. The regime of self-induced absorption for small-amplitude nonlinear waves is followed by the regime of self-induced transparency for high-amplitude waves. The developed theory might be useful in seismology, in high-pressure nonlinear acoustics, and in nonlinear acoustic diagnostics of damaged and fatigued materials. © *2002 Acoustical Society of America.* [DOI: 10.1121/1.1517252]

PACS numbers: 43.25.Dc, 91.60.Lj [MFH]

LIST OF SYMBOLS

c	the sound velocity
c_0	the velocity of the infinitely weak acoustic disturbance (the velocity of the linear sound)
$c^H = c - c_0$	the local variation in sound velocity due to strain variation in the acoustic wave
$c_H = \sqrt{2}c^H/(h^H s_\perp^0 c_0)$	the normalized variation in sound velocity
$c_{H,0}$	the normalized variation of the zero-point velocity (of the point $S=0$ in the wave profile)
$c_{H,e}$	the normalized variation of the velocity of the extrema of the wave profile
E	the elastic modulus
E_0	the elastic modulus corresponding to static preloading of the material
$E^H = E - E_0$	the elastic modulus variation due to variable strain action on hysteretic elements
$E_H = E^H/(\sqrt{2}h^H s_\perp^0 E_0)$	the normalized variation of the modulus
$f_{12}(s_1, s_2)$	the density distribution of the mechanical elements in coordinate plane (s_1, s_2)
$f^H = f^H(s_1, s_2)$	the surface density of the hysteretic elements (those with $s_2 > s_1$)
$f^{NH} = f^{NH}(s_1, s_1)$	the density of the nonhysteretic elements (those with $s_2 = s_1$)
$\tilde{f}^H\left(\dfrac{s_\parallel}{s_\parallel^H}, \dfrac{s_\perp}{s_\perp^0}\right)$	the surface density of the hysteretic elements in the coordinates $(s_\parallel, s_\perp)$
$\sqrt{2}\tilde{f}^{NH}(s_\parallel/s_\parallel^{NH})$	the linear density of the nonhysteretic elements along the coordinate $s_\parallel$
$\tilde{f}_{ch}^H$	the characteristic density of the hysteretic elements
$\tilde{f}_{ch}^{NH}$	the characteristic density of the nonhysteretic elements
$F^H = \tilde{f}^H(0, s_\perp/s_\perp^0)/\tilde{f}^H(0,0)$	the normalized distribution function of hysteretic elements
$\beta = \tilde{f}^{NH}/(\tilde{f}^H s_\perp^0)$	the nondimensional parameter characterizing relative contribution of nonhysteretic and hysteretic elements to the total number of the mesoscopic mechanical elements
$\Phi = G_+^{-1} - G_-^{-1}$	the compact notation (where $GG^{-1}(S) = S$)
G	the function describing the acoustic wave profile at the boundary of the medium
G_+	the function describing the part of the initial wave profile where the strain increases $(\partial S/\partial\eta > 0)$
G_-	the function describing the part of the initial wave profile where the strain decreases $(\partial S/\partial\eta < 0)$
h^{NH}	the characteristic nondimensional nonlinear parameter related to the changes of the nonhysteretic element

h^H — the characteristic nondimensional nonlinear parameter due to the presence of the hysteretic mechanical elements

$p_0(s)$ — the nonspecified parameter characterizing the presence of mesoscopic mechanical elements

$p_0(s,s_1,s_2)$ — the parameter characterizing the state of an individual mechanical element

$\Delta p = p_2 - p_1$ — the difference between the values of the parameter $p_0(s,s_1,s_2)$ of an individual mesoscopic element in two admissible states

$P = s_0/\sqrt{2}s_\perp^0$ — the nondimensional parameter characterizing the importance of element localization near the diagonal of the Preisach–Mayergoyz (PM) space

s — the strain

s_1 — the strain level necessary to "close" an individual hysteretic element

s_2 — the strain level necessary to "open" an individual hysteretic mechanical element

$s_\perp^0$ — the characteristic strain scale for the localization of the mechanical elements near the diagonal of the PM space

$s_\parallel^0$ — the characteristic strain scale for the variation of the mechanical elements distribution along the diagonal of the PM space

s_0 — the initial (boundary) amplitude of the strain wave

s^A — the current amplitude of the strain wave

$S^A = s^A/s_0$ — the normalized wave amplitude

$\bar{s}$ — the strain magnitude in the middle of the interval of strain variation

$s_\parallel = (s_2 + s_1)/\sqrt{2}$ — the strain coordinate parallel to the PM space diagonal

$s_\perp = (s_2 - s_1)/\sqrt{2}$ — the strain coordinate perpendicular to the PM space diagonal

$S_\perp = s_\perp/s_0$ — the normalized coordinate for the description of element localization in the direction perpendicular to the PM space diagonal

$s' = s - \bar{s}$ — the strain disturbance relative to the middle level of the strain variation

$S = s'/s_0$ — the normalized strain variation

S_e — the normalized strain value in the extremum (maximum or minimum) of the strain wave profile

s_0^{cr} — the characteristic wave amplitude, above which the along diagonal variation of the mesoscopic elements should be taken into account even in the case of much stronger localization of the elements perpendicular to the diagonal of the PM space in comparison with their variation along the diagonal

$\mu = s_\perp^0/s_\parallel^0$ — the parameter characterizing the shape of elements distribution in the PM space

σ — the contribution to stress due to mesoscopic mechanical elements

ρ_0 — the equilibrium density of the material

t — the time variable

τ_0 — the characteristic time scale of the acoustic disturbance at the boundary

$\tau = t - x/c_0$ — the retarded time

$\theta = \tau/\tau_0$ — the normalized retarded (fast) time variable

$\eta = \theta - \int_0^\zeta \{S^A(\zeta') - (P/2)[S^A(\zeta')]^2\}d\zeta'$ — the modified fast time variable

u — the mechanical particle displacement

x — the spatial coordinate

x_{SH} — the characteristic length for the nonlinear effects induced by the variation of the nonhysteretic element density along the diagonal of the PM space

x_H — the characteristic length for the nonlinear effects induced by presence of hysteretic mechanical elements

$\zeta = x/x_H$ — the normalized slow spatial coordinate

$\zeta_{abs} = x_{abs}/x_H$ — the characteristic nondimensional length of nonlinear sound absorption

$\bar{\zeta}_{abs} = \zeta_{abs}/P$ — the renormalized characteristic nondimensional length of nonlinear sound absorption

ζ_{SH}^β — the characteristic normalized distance for shock formation (induced by the variation along the PM space diagonal of both nonhysteretic and hysteretic elements)

$\chi = \zeta - P\int_0^\zeta S^A(\zeta')d\zeta'$ — the modified slow spatial variable

ω — the characteristic frequency of the acoustic signal ($\omega \propto 1/\tau_0$).

I. INTRODUCTION

It is currently acknowledged that the nonlinear hysteretic stress/strain relationship observed in micro-inhomogeneous materials can be modeled by introducing mesoscopic mechanical elements with stress (strain) dependent parameters.[1–3] An individual mechanical element "opens" at strain level $s = s_2$ and "closes" at strain level $s = s_1$. The system of mesoscopic elements is characterized by their density distribution $f_{12}(s_1,s_2)$ in coordinate plane (s_1,s_2) [in Preisach–Mayergoyz (PM) space].[1–4] It should be noted that

in mechanics of solids PM space can be presented both as the (stress, stress) coordinate plane[1,2] and as the (strain, strain) coordinate plane (see Ref. 4 and the references therein). The mechanical elements on the diagonal $s_1 = s_2$ of PM space are nonhysteretic. The off-diagonal elements ($s_1 < s_2$) exhibit hysteresis in their behavior: when $s_1 < s < s_2$ the state of hysteretic element (is it opened or closed) depends on whether the strain decreases or increases.[2,4] The distribution function $f_{12}(s_1, s_2)$ of mesoscopic elements can be found from the experimental stress/strain curves of material. The results obtained[2,3] demonstrate that in rocks the distribution function $f_{12}(s_1, s_2)$ is localized near PM space diagonal in the band with characteristic width $s_\perp^0 \propto 10^{-4}$ (at atmospheric pressure) and varies along the diagonal at characteristic scale $s_\parallel^0$, which is larger ($s_\parallel^0 > s_\perp^0$). It is clear that elastic wave propagation should depend on relative magnitude of strain amplitude s^A in the wave and characteristic strains $s_\perp^0$ and $s_\parallel^0$. However until now the fact of $f_{12}(s_1, s_2)$ inhomogeneity in PM space has been included in theoretical analysis only through a simplified model valid in the asymptotic case $s^A \ll s_\perp^0, s_\parallel^0$.[5-7] In this model the distribution $f_{12}(s_1, s_2)$ is separated into hysteretic and nonhysteretic parts $f_{12}(s_1, s_2) \equiv f^H + f^{NH}\delta(s_1 - s_2)$, where f^H is the surface density of hysteretic elements, f^{NH} is the linear density of nonhysteretic elements, and δ is Riemann's delta function. The density f^H of hysteretic elements has always been considered to be a constant.[5-7] This assumption leads, in particular, to prediction of linear dependence of resonance frequency shift of a bar on its vibration amplitude, providing an explanation for multiple experimental observations[8-12] at strain levels $s^A \lesssim 10^{-6}$. It has also been demonstrated that, if the variation of f^{NH} along the PM diagonal is modeled by a linear dependence, then nonhysteretic elements contribute to quadratic nonlinearity of classical form (one leading to cascade process of frequency mixing.[5-7]

In the present publication we propose an extension of the theory, which takes into account variation of f_{12} both in the direction perpendicular to the PM space diagonal and in the direction along the diagonal. There are at least three indications that theory generalization of this kind might be useful.

First, there are multiple experimental observations[9,10,12] demonstrating that the dependence of resonance frequency shift of a bar on vibration amplitude deviates from linear law at strain levels $s^A \gtrsim 10^{-6}$.

Second, the model with $f^H \equiv$ const does not take into account the so-called ΔE effect (observed[13] at strain levels $s^A \gtrsim 10^{-4}$), which is one of the manifestations of f^H localization near the PM space diagonal. The experiments[2,3,13] clearly indicate that inhomogeneity of hysteretic elements distribution in the direction perpendicular to the PM diagonal should be included in theoretical analysis of waves with strain amplitudes $s^A \gtrsim 10^{-4}$.

Finally, there is a growing interest nowadays in different manifestations of nonlinear wave processes in seismology.[14-17] Even in detection point (in far field) the amplitudes of seismic signals can be of the order of $s^A \propto 10^{-4}$ corresponding to strong ground motion.[14-17] Consequently, for analysis of nonlinear propagation of these sig-

nals the existing theory for strain levels $s^A \ll s_\perp^0 \propto 10^{-4}$ should be extended to the region $s^A \gtrsim s_\perp^0 \propto 10^{-4}$. Moreover, the registration of seismic signals with $s^A \propto 10^{-4}$ from strong earthquakes indicates that strain amplitude near the earthquake source is much higher ($s^A \gg 10^{-4}$). Consequently, for the analysis of the problem of source identification from far-field observations, the existing theory should be extended to the case $s^A \gg s_\perp^0 \propto 10^{-4}$.

In the present publication we derive an evolution equation for strain propagation in the case of arbitrary relation between the magnitudes of s^A and $s_\perp^0$, retaining however the assumption $s^A \ll s_\parallel^0$. In this regime strain wave may be sensitive to the details of f^H distribution to its localization region near the PM space diagonal and feels weak inhomogeneity of both f^H and f^{NH} along the diagonal as well.

II. GENERAL FORM OF EVOLUTION EQUATION

The equation for propagation of plane acoustic wave (longitudinal or shear) has the form

$$\rho_0\left[\frac{\partial^2 u}{\partial t^2} - c_0^2\frac{\partial^2 u}{\partial x^2}\right] = \frac{\partial \sigma}{\partial x}, \qquad (1)$$

where u is particle displacement (parallel or perpendicular to the x axis, along which the wave propagates). In Eq. (1) c_0 is the sound velocity, which does not take into account the presence of mesoscopic elements, ρ_0 is the density of the material, and σ is the contribution to stress due to mesoscopic mechanical elements. It is assumed[2,5-7] that the presence of mesoscopic elements and their behavior can be described by a nonspecified strain-dependent parameter $p_0 = p_0(s)$, and that stress depends on this parameter ($\sigma = \sigma(p_0(s))$). Consequently, the right-hand side of Eq. (1) can be rewritten in the form

$$\frac{\partial \sigma}{\partial x} = \frac{\partial \sigma}{\partial p_0}\frac{\partial p_0}{\partial s}\frac{\partial s}{\partial x}. \qquad (2)$$

It is admitted that the parameter $p_0 = p_0(s)$ for material under consideration can be obtained from linear superposition of parameters $p_0(s, s_1, s_2)$ of individual mesoscopic elements

$$p_0(s) = \int_{-\infty}^{+\infty} ds_1 \int_{-\infty}^{+\infty} ds_2 \; p_0(s, s_1, s_2) f_{12}(s_1, s_2). \qquad (3)$$

The behavior of an individual mechanical element [the value of its parameter $p_0(s, s_1, s_2)$] depends on two critical strain values s_1 and s_2, and also on the direction of current strain variation (as has been described in the Introduction). In Eq. (3) $f_{12}(s_1, s_2)$ is the density of mesoscopic mechanical elements in PM space.[2-4] By considering linear superposition in Eq. (3), possible interaction between mesoscopic elements is neglected. Under this approximation it is reasonable to assume that $\partial\sigma/\partial p_0$ in Eq. (2) does not depend on p_0. Note that classical nonlinear elasticity[18,19] can be included in the analysis, formally assuming[7] additional explicit dependence of stress σ on strain $\sigma = \sigma(p_0(s), s)$. However, this opportunity will be neglected, due to experimental evidence that in the mesoscopic materials the nonlinearity caused by mesoscopic elements dominates over the classical one.[2,6-10] For the same reason, the strain will be approxi-
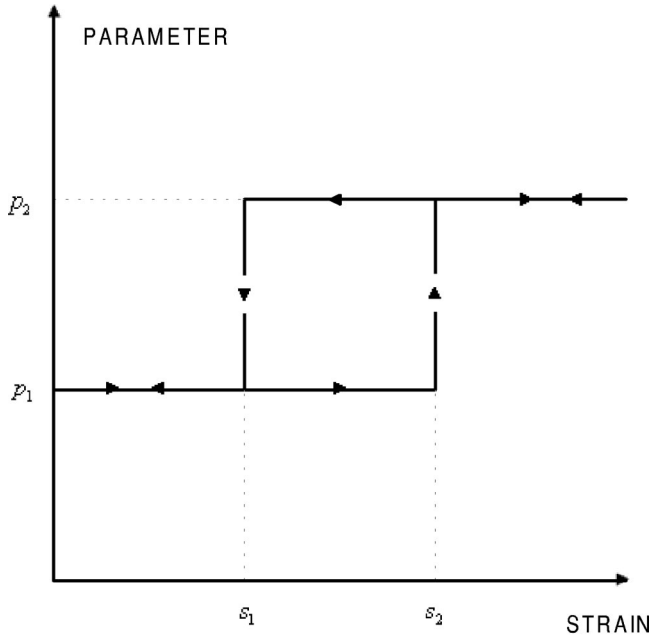
FIG. 1. Two-level mechanical element with hysteresis. The element switches from level, characterized by parameter p_1 to level characterized by parameter p_2 (it "opens") at strain s_2, which is higher than strain s_1 for the inverse process (of "closing"). Arrowheads indicate direction of strain variation in time.

mated by its linear part ($s \cong \partial u / \partial x$). In other words, kinematic nonlinearity[18,19] will also be neglected in comparison with mesoscopic nonlinearity. In brief, the arguments presented above give us opportunity to consider $\partial \sigma / \partial p_0$ in Eq. (2) as a constant and also approximate $s \cong \partial u / \partial x$. Then, the nonlinearity in Eq. (2) and in Eq. (1) is due only to the dependence of $\partial p_0 / \partial s$ on strain.

In order to evaluate $\partial p_0 / \partial s$ we first separate the contributions to the total density $f_{12}(s_1, s_2)$ from the hysteretic and nonhysteretic elements

$$f_{12}(s_1, s_2) = f^H(s_1, s_2)[1 + \text{sign}(s_2 - s_1)]/2$$
$$+ f^{NH}(s_1, s_2) \delta(s_1 - s_2). \quad (4)$$

Substituting Eq. (4) into Eq. (3), we derive

$$p_0(s) = \int_{-\infty}^{s_2} ds_1 \int_{s_1}^{+\infty} ds_2 \, p_0(s, s_1, s_2) f^H(s_1, s_2)$$
$$+ \int_{-\infty}^{+\infty} ds_1 \, p_0(s, s_1, s_1) f^{NH}(s_1, s_1). \quad (5)$$

Note that substituting of the function $[1 + \text{sign}(s_2 - s_1)]$ in the integral (3) limits in Eq. (5) the integration both over s_2 (to begin at s_1) and over s_1 (to finish at s_2). Accepting for mesoscopic mechanical elements the two-level model presented in Fig. 1, we find that for individual elements, that are changing their state under the influence of the acoustic wave

$$\frac{\partial p_0}{\partial s}(s, s_1, s_2) = \begin{cases} \Delta p \, \delta(s - s_2) & \text{if } \partial s / \partial t > 0, \\ \Delta p \, \delta(s - s_1) & \text{if } \partial s / \partial t < 0. \end{cases}$$

Here, $\Delta p = p_2 - p_1$ is the difference between the values of the parameter of an individual mesoscopic element in two states (opened and closed; see Fig. 1). With the help of these

relations, the differentiation of Eq. (5) is straightforward

$$\frac{\partial p_0}{\partial s}(s) = \Delta p \left\{ \left[\begin{array}{l} \int_{-\infty}^{s} f^H(s_1, s) ds_1 \text{ if } s_t \equiv \partial s / \partial t > 0 \\ \int_{s}^{+\infty} f^H(s, s_2) ds_2 \text{ if } s_t \equiv \partial s / \partial t < 0 \end{array} \right] \right.$$
$$\left. + f^{NH}(s, s) \right\}. \quad (6)$$

It should be pointed out here that only the elements that are changing their state upon strain changes contribute to integrals in Eq. (6).

In the modeling adopted here, the control parameter in the problem is the strain. In this case it is useful (though unnecessary) to associate the jump of the parameter $p_0(s, s_1, s_2)$ of an individual mechanical element with the abrupt change of the stress in the vicinity of the crack due to its opening/closing (because this abruptly creates/destroys mechanically free surface with zero stress). However, to describe nonlinear acoustic phenomena in the (stress, stress) coordinate plane it is sufficient to change the control parameter from strain to stress (using the linear Hooke's law) and to consider that the parameter $p_0(s, s_1, s_2)$ is related to the volume of the crack-containing mechanical element. Then, the jump of the parameter $p_0(s, s_1, s_2)$ for an individual element might be viewed as the abrupt change in crack volume due to its opening/closing.[2]

In the following we will be interested in the analysis of a periodic process with a single maximum and a single minimum over a period ("simplex" process.[6]) In this case the variation of strain takes place in the interval $\bar{s} - s^A \leq s \leq \bar{s} + s^A$, where $\bar{s}$ is the strain in the middle of the interval and s^A is the amplitude of strain oscillations. Because of this, the integration limits $\pm \infty$ in Eq. (6) can be changed for $\bar{s} \pm s^A$, respectively.

For the analysis of different physical situations, it is useful to describe the distribution of the elements in coordinates $s_\parallel = (s_2 + s_1)/\sqrt{2}$ and $s_\perp = (s_2 - s_1)/\sqrt{2}$, which are along and perpendicular to the PM space diagonal, respectively

$$f^H(s_1, s_2) \equiv \tilde{f}^H(s_\parallel / s_\parallel^H, s_\perp / s_\perp^0),$$

$$f^{NH}(s, s) \equiv \sqrt{2} \tilde{f}^{NH}(s_\parallel / s_\parallel^{NH}) = \sqrt{2} \tilde{f}^{NH}(\sqrt{2} s / s_\parallel^{NH}).$$

Here, $s_\parallel^H$ and $s_\parallel^{NH}$ are characteristic scales of the distribution functions variation along the PM space diagonal, and $s_\perp^0$ is the characteristic scale of hysteretic elements localization in the direction normal to the diagonal. We use the notation "$\tilde{f}$" to define the distribution functions in the new coordinates. For simplicity, we consider that characteristic scales of $\tilde{f}^H$ and of $\tilde{f}^{NH}$ variation along the diagonal are equal ($s_\parallel^H = s_\parallel^{NH} \equiv s_\parallel^0$). This assumption qualitatively corresponds to the results extracted from the analysis of experimental data.[3] Then, Eq. (6) can be presented in the form

$$\frac{\partial p_0}{\partial s}(s) = \sqrt{2}\Delta p \left\{ \int_0^{[s^A + \text{sign}(s'_t)s']/\sqrt{2}} \right.$$

$$\left. \times \tilde{f}^H\left(\frac{\sqrt{2}s - \text{sign}(s'_t)s_\perp}{s_\parallel^0}, \frac{s_\perp}{s_\perp^0} \right) ds_\perp + \tilde{f}^{NH}\left(\frac{\sqrt{2}s}{s_\parallel^0} \right) \right\}. \tag{7}$$

Here, $s' \equiv s - \bar{s}$ denotes elastic disturbance relative to the middle level of strain variation. For the particular form of $\partial p_0/\partial s$ in Eq. (7), the evolution equation, following from Eq. (1) for slow variation of strain $s' = \partial u/\partial x$ in elastic wave propagating in the positive direction of the x axis $[s' = s'(x,\tau = t - x/c_0)]$, takes the form

$$\frac{\partial s'}{\partial x} = \frac{\Delta p}{\sqrt{2}\rho_0 c_0^3}\left(\frac{\partial\sigma}{\partial p_0} \right)\left\{ \int_0^{[s^A + \text{sign}(s'_t)s']/\sqrt{2}} \right.$$

$$\times \tilde{f}^H\left(\frac{\sqrt{2}(\bar{s} + s') - \text{sign}(s'_t)s_\perp}{s_\parallel^0}, \frac{s_\perp}{s_\perp^0} \right) ds_\perp$$

$$\left. + \tilde{f}^{NH}\left(\frac{\sqrt{2}(\bar{s} + s')}{s_\parallel^0} \right) \right\} \frac{\partial s'}{\partial\tau}. \tag{8}$$

To derive Eq. (8) the method of slowly varying wave profile[20,21] has been applied. This is the most general form for an evolution equation derived in the present publication. As already mentioned in the Introduction, the evolution equations for nonlinear wave propagation in material with mesoscopic mechanical elements were proposed before only for the asymptotic case $s^A \ll s_\perp^0, s_\parallel^0$, where dependence of distribution functions $\tilde{f}^{NH}$ and $\tilde{f}^H$ in Eq. (8) on acoustic strain s' can be neglected or can be considered as weak. In this case the evolution equation contains ordinary (of classical form) and hysteretic quadratic nonlinearities.[5–7] Cubic nonlinearity of classical form can be included in the evolution equation as a correction.[5,6] In the present publication we are interested in the analysis of Eq. (8) in a more general case, where strain amplitude s^A might be comparable or might even exceed one of the characteristic scales $s_\perp^0, s_\parallel^0$. Processing of the experimental data[3] indicates that, at least in sandstones, $s_\perp^0$ is smaller than $s_\parallel^0$ (in Fig. 2 we present qualitatively the distribution of mechanical elements in PM space.[2,3]) That is why, in the following analysis, in order to understand the influence on nonlinear wave propagation of mesoscopic elements localization near the PM space diagonal, we will be interested in the asymptotic regime $s^A, s_\perp^0 \ll s_\parallel^0$. It is important that the condition $s^A, s_\perp^0 \ll s_\parallel^0$ is not sufficient to completely neglect the role of variation of $\tilde{f}^{NH}$ and $\tilde{f}^H$ along the diagonal. This conclusion follows from the analysis of separate influence of the scales $s_\perp^0$ and $s_\parallel^0$ on wave propagation.

A. Variation of distribution function along the PM space diagonal

Assuming $s^A \ll s_\perp^0, s_\parallel^0$, we approximate the expression in curled brackets in Eq. (8) by
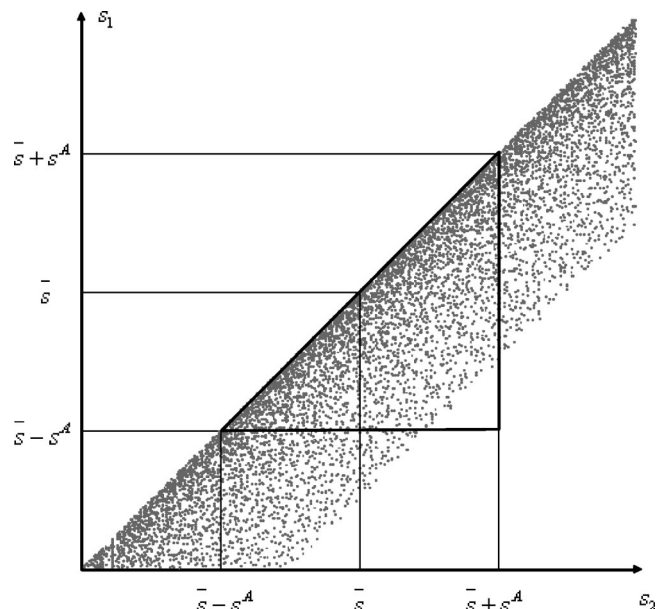
FIG. 2. Qualitative presentation of the distribution of mesoscopic elements in Preisach–Mayergoyz space. The density of elements is proportional to surface density of points on (s_1, s_2) coordinate plane. Periodic strain wave influences the elements in the triangle between the diagonal $s_2 = s_1$, horizontal line $s_1 = \bar{s} - s^A$, and vertical line $s_2 = \bar{s} + s^A$. Here, $\bar{s}$ is the mean strain level and s^A is strain amplitude.

$$\int_0^{[s^A + \text{sign}(s'_t)s']/\sqrt{2}} \tilde{f}^H\left(\frac{\sqrt{2}(\bar{s} + s') - \text{sign}(s'_t)s_\perp}{s_\parallel^0}, \frac{s_\perp}{s_\perp^0} \right) ds_\perp$$

$$+ \tilde{f}^{NH}\left(\frac{\sqrt{2}(\bar{s} + s')}{s_\parallel^0} \right)$$

$$\cong \tilde{f}^H\left(\frac{\sqrt{2}\bar{s}}{s_\parallel^0}, 0 \right)\frac{s^A + \text{sign}(s'_t)s'}{\sqrt{2}}$$

$$+ \tilde{f}^{NH}\left(\frac{\sqrt{2}\bar{s}}{s_\parallel^0} \right) + \frac{\partial\tilde{f}^{NH}}{\partial s_\parallel}\left(\frac{\sqrt{2}\bar{s}}{s_\parallel^0} \right)\sqrt{2}s'. \tag{9}$$

In the right-hand side of Eq. (9) the term $\tilde{f}^{NH}(\sqrt{2}\bar{s}/s_\parallel^0)$ contributes to the change in linear properties of material (due to the presence of mesoscopic elements). Considering that this influence is incorporated in the modified sound velocity c_0, we neglect the terms of this type everywhere in the following. It might be argued that the term $\tilde{f}^{NH}(\sqrt{2}\bar{s}/s_\parallel^0)$ in combination with nonlinear contribution $s^{NL} \propto (\partial u/\partial x)^2$ to longitudinal strain s in Eq. (2) [i.e., when $s = \partial u/\partial x + s^{NL}$ is substituted in Eq. (2)] could provide important contribution to quadratic nonlinearity. However, this is not true. This contribution to nonlinearity will be negligible even in comparison with ordinary elastic nonlinearity as far as the contribution of $\tilde{f}^{NH}(\sqrt{2}\bar{s}/s_\parallel^0)$ to sound velocity is small. Here it should be mentioned that nonlinearity, described by the term $\propto (\partial\tilde{f}^{NH}/\partial s_\parallel)s'$ in Eq. (9), can be dominant not because $\tilde{f}^{NH}$ is large but because the variation of $\tilde{f}^{NH}$ with strain is large. Strong dependence of the mesoscopic elements density on strain is expected because they are softer than atomic scale elastic mechanical elements. In other words, $s_\parallel^0$ is expected

(and is observed[2,3]) to be significantly smaller than the characteristic scale $\propto 0.1-1$ of important elastic interatomic deformations.

From the experimental data processing it follows[3] that the total numbers of hysteretic and of nonhysteretic elements are comparable

$$\tilde{f}^H s_\perp^0 \propto \tilde{f}^{NH}. \tag{10}$$

With the help of Eq. (10), we can estimate the ratio of the first and the third contribution to the right-hand side in Eq. (9) by

$$\frac{\tilde{f}^H}{\partial \tilde{f}^{NH}/\partial s_\parallel} \propto \frac{\tilde{f}^H}{\tilde{f}^{NH}/s_\parallel^0} \propto \frac{s_\parallel^0}{s_\perp^0}.$$

Consequently, if we formally assume $s_\parallel^0 \ll s_\perp^0$ or just $s_\perp^0 = \infty$ (in order to understand the separate role of the distribution function variation along the diagonal), we are able to neglect the first term in the right-hand side of Eq. (9). As a result we present evolution equation (8) in the form

$$\frac{\partial s'}{\partial x} + \frac{h^{NH}}{c_0} s' \frac{\partial s'}{\partial \tau} = 0, \tag{11}$$

where

$$h^{NH} \equiv -\frac{\Delta p}{\rho_0 c_0^2}\left(\frac{\partial \sigma}{\partial p_0}\right)\left(\frac{\partial \tilde{f}^{NH}}{\partial s_\parallel}\right) \propto \frac{\Delta p}{\rho_0 c_0^2}\left(\frac{\partial \sigma}{\partial p_0}\right)\frac{\tilde{f}^{NH}}{s_\parallel} \tag{12}$$

is the characteristic nondimensional nonlinear parameter related to the changes of $\tilde{f}^{NH}$ distribution along the diagonal. The methods for solution of Eq. (11) are well known[21,22] and will not be presented here. Importantly, the characteristic scale for variation of acoustic signal [with initial amplitude $s^A(x=0) \equiv s_0$ and characteristic time scale τ_0] is estimated by

$$x_{SH} \propto \frac{c_0 \tau_0}{h^{NH} s_0} \propto \frac{1}{s_0}. \tag{13}$$

We have used in Eq. (13) the subscript "SH," because Eq. (13) provides the estimate for shock front formation distance and for the scale of nonlinear attenuation at the shock as well.[20] Note that in accordance with Eq. (13) the role of along-diagonal gradients of distribution function $\tilde{f}^{NH}$ increases with increasing wave amplitude. So, due to the scale $s_\parallel^0$ existence the self-induced absorption of strain waves can be expected.

B. Variation of distribution function perpendicular to the PM space diagonal

Assuming $s_\parallel^0 = \infty$, we approximate the expression in curled brackets in Eq. (8) by

$$\int_0^{[s^A + \text{sign}(s_t')s']/\sqrt{2}} \tilde{f}^H\left(0, \frac{s_\perp}{s_\perp^0}\right) ds_\perp + \tilde{f}^{NH}(0).$$

The second term here can be taken into account in the wave equation by modification of linear sound velocity c_0. The evolution equation (8) takes the form

$$\frac{\partial s'}{\partial x} + \frac{h^H}{\sqrt{2}c_0}\left\{\int_0^{[s^A + \text{sign}(s_t')s']/\sqrt{2}}\left[\frac{\tilde{f}^H(0, s_\perp/s_\perp^0)}{\tilde{f}^H(0,0)}\right]ds_\perp\right\}\frac{\partial s'}{\partial \tau} = 0, \tag{14}$$

where

$$h^H \equiv -\frac{\Delta p}{\rho_0 c_0^2}\left(\frac{\partial \sigma}{\partial p_0}\right)\tilde{f}^H(0,0) \tag{15}$$

is the characteristic nondimensional nonlinear parameter due to hysteretic mesoscopic elements.[7,22] In normalized variables $S \equiv s'/s_0, S_\perp \equiv s_\perp/s_0, \theta \equiv \tau/\tau_0, \zeta \equiv x/x_H$ [where $x_H = 2c_0\tau_0/(h^H s_0)$] and $F^H(s_\perp/s_\perp^0) \equiv f^H(0, s_\perp/s_\perp^0)/f^H(0,0)$, we rewrite Eq. (14) as

$$\frac{\partial S}{\partial \zeta} + \sqrt{2}\left\{\int_0^{[S^A + \text{sign}(S_\theta)S]/\sqrt{2}} F^H(\sqrt{2}PS_\perp)dS_\perp\right\}\frac{\partial S}{\partial \theta} = 0. \tag{16}$$

Here, $P \equiv s_0/\sqrt{2}s_\perp^0$ is the nondimensional parameter characterizing the importance of element localization near the PM space diagonal. In the limiting case $P = 0$ ($F^H(0) = 1$) of homogeneous distribution of hysteretic elements in the diapason of strain action, Eq. (16) reduces to the form already analyzed analytically[7,22]

$$\frac{\partial S}{\partial \zeta} + [S^A + \text{sign}(S_\theta)S]\frac{\partial S}{\partial \theta} = 0. \tag{17}$$

Equation (17) can be also derived, by taking the limit $s_\parallel^0 \to \infty$ ($\partial/\partial s_\parallel \to 0$) in Eq. (9). Note that in Eq. (17) the unknown normalized wave amplitude $S^A(\zeta)$ can be excluded by the variable transformation.[22,23] In the more general case of Eq. (16) $S^A(\zeta)$ can be excluded only if the solution of Eq. (16) is first found for the arbitrary function $S^A(\zeta)$. Thus, Eq.(16) presents a new type of equation for nonlinear acoustics.

For the analysis of nonlinear wave propagation in the frame of Eq. (16), we model distribution of hysteretic mesoscopic elements by an exponential function [$F^H = \exp(-s_\perp/s_\perp^0) = \exp(-\sqrt{2}PS_\perp)$] as was proposed earlier.[3] Then, Eq. (16) takes the form

$$\frac{\partial S}{\partial \zeta} + \frac{1}{P}\{1 - e^{-P[S^A + \text{sign}(S_\theta)S]}\}\frac{\partial S}{\partial \theta} = 0. \tag{18}$$

Even without finding its solutions, Eq. (18) provides opportunity for theoretical predictions, which can be qualitatively compared with available experimental data. In fact, the coefficient in front of $\partial S/\partial \theta$ in Eq. (18) has a direct relation to local variation c^H in sound velocity c due to hysteretic elements ($c = c_0 + c^H$, $|c^H| \ll c_0$)[20,21]

$$\frac{c^H}{c_0} = -\frac{h^H s_\perp^0}{\sqrt{2}}\{1 - e^{-P[S^A + \text{sign}(S_\theta)S]}\}. \tag{19}$$

Taking into account the relation between sound velocity and elastic modulus E ($E \propto c^2$, $E_0 \propto c_0^2$, $E^H \propto 2c_0 c^H$), we present the normalized changes of the modulus [$E_H \equiv E^H/(E_0\sqrt{2}h^H s_\perp^0)$] in the form

$$E_H = -\{1 - e^{-P[S^A + \text{sign}(S_\theta)S]}\}. \tag{20}$$
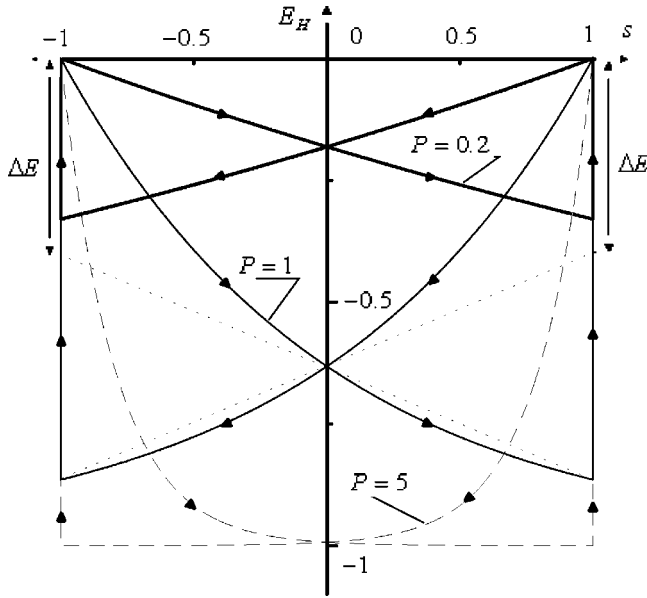
FIG. 3. Periodic dimensionless contribution E_H to elastic modulus due to nonlinearity hysteresis for different values of the local parameter $P(\zeta) = PS^A(\zeta)$. Arrowheads indicate the direction of strain (S) variation in time. With increasing wave amplitude [increasing parameter $P(\zeta)$] the bow ties become more and more asymmetric relative to mean level of E_H.

The relation (20) predicts bow tie behavior of nonlinear contribution to elastic modulus (Fig. 3). The presentation in Fig. 3 is valid at arbitrary distance for renormalized (local) value of the parameter $P(\zeta) = PS^A(\zeta)$. In the limiting case $P \ll 1$ the bow tie is composed of straight lines $E_H \cong -P(S^A + \text{sign}(S_\theta)S)^{6,22}$ (Fig. 3, bow tie for $P = 0.2$), symmetric relative to $E_H = -P$ level. However with increasing parameter P this symmetry disappears (Fig. 3, bow ties for $P = 1$ and $P = 5$). It looks like there is an excess variation of elastic modulus, when it abruptly increases (jumps) in the end points $S = \pm S^A$. In Fig. 3 we present the comparison of the bow tie for $P = 1$ with a symmetric bow tie (presented by points). The excess variation of elastic modulus denoted by ΔE in Fig. 3 was observed experimentally[2,3,13] and was called the ΔE effect.[13] We conclude that (in terms of the model analyzed here) the ΔE effect is due to inhomogeneity of mechanical element distribution in the direction perpendicular to PM space diagonal. It manifests itself strongly when acoustic strain feels localization of the elements in the vicinity of the diagonal ($P \geq 1$).

Another opportunity to compare the predictions of the model in Eq. (18) with experimental observations is provided by an estimate of wave velocity dependence on wave amplitude. In accordance with Eq. (19) the presence of hysteretic elements always diminishes local sound velocity ($c^H \leq 0$). With the help of Eq. (19) the nondimensional velocity $c_H \equiv \sqrt{2}c^H/(c_0 h^H s_\perp^0)$ of zero points ($S = 0$) can be estimated as

$$c_{H,0} = -\{1 - e^{-PS^A}\}. \tag{21}$$

In accordance with Eq. (21), the diminishing of wave velocity with increasing wave amplitude is first proportional to wave amplitude ($c_{H,0} \cong -PS^A$ if $P \ll 1$), but at higher wave amplitudes it continues sublinearly, and finally it saturates ($c_{H,0} \cong -1$ if $P \geq 1$). This prediction correlates with experi-

mental observations of variation of resonance frequency of a bar with increasing amplitude.[9,10,12] There are reports that the initially linear decrease in resonance frequency is followed for sufficiently high amplitudes ($s^A \geq 10^{-6}$) by a region of slower (sublinear) diminishing of frequency as a function of s^A. We conclude that in terms of the model [Eq. (18)] analyzed here the diminishing of the rate of resonance frequency variation can be attributed to a manifestation of hysteretic elements localization near the PM space diagonal. It should be mentioned here that quadratic nonlinearity related to variation of element distribution along the diagonal [for example, one in Eq. (11)] does not contribute at all to changes in velocity of initially sinusoidal wave.[20] Due to the fact that density of hysteretic elements diminishes with distance from the PM space diagonal, the effective nonlinearity of the medium (related to the existence of these elements) diminishes with increasing wave amplitude. In the frame of the model Eq. (18), material is more nonlinear for weak amplitude waves ($s^A \leq s_\perp^0$, $P \leq 1$) than for high-amplitude waves ($s^A \geq s_\perp^0$, $P \geq 1$). In PM space acoustic wave interacts with hysteretic elements located in the triangle between diagonal $s_1 = s_2$, the horizontal line $s_1 = \bar{s} - s^A$ and the vertical line $s_2 = \bar{s} + s^A$ (Fig. 2). Clearly, if the elements are localized near the diagonal, then with increasing s^A the average density of the elements inside interaction triangle diminishes, leading to decrease of effective nonlinearity.

1. Weak variation of distribution function perpendicular to the PM space diagonal

In the case $s_0 \ll s_\perp^0$ (but $s_\perp^0 \neq \infty$) or, in other terms, in the case $P \ll 1$ ($P \neq 0$) we expand exponential function in Eq. (18) in power series. Let us introduce new nondimensional variables

$$\chi = \zeta - P \int_0^\zeta S^A(\zeta')d\zeta',$$

$$\eta = \theta - \int_0^\zeta \{S^A(\zeta') - (P/2)[S^A(\zeta')]^2\}d\zeta'. \tag{22}$$

By using Eq. (22) and by retaining the terms only of zero and first order in small parameter $P \ll 1$, we derive

$$\frac{\partial S}{\partial \chi} + \text{sign}\left(\frac{\partial S}{\partial \eta}\right)S\frac{\partial S}{\partial \eta} - \frac{P}{2}S^2\frac{\partial S}{\partial \eta} = 0. \tag{23}$$

In the case $P = 0$ the analytical solutions of Eq. (23) have been found earlier.[7,22] The corrective term proportional to small parameter $P \ll 1$ has a form of classical cubic nonlinearity.[24] In the presence of this term each point of wave profile on the plane (S, η) (on the phase plane[21]) exhibits additional horizontal motion along the η-axis

$$d\eta = -\frac{P}{2}S^2 d\chi. \tag{24}$$

In accordance with Eq. (24), all the points of the profile move faster than the zero points ($S = 0$). In Fig. 4 we present the transformation of initially sinusoidal wave with propagation distance as it is predicted by Eq. (23). Profile 1 [$S(\chi = 0) = \sin \eta$] is the initial sinusoidal profile. Profile 2 in Fig. 4 is the theoretical prediction[22] for wave profile at the dis-

FIG. 4. Transformation of initially sinusoidal profile (1) of a small-amplitude ($P \ll 1$) acoustic wave with increasing propagation distance. Profiles (2) and (3) are presented at distance $\chi = 1.2$ for $P = 0$ and $P = 0.5$, respectively. The arrowheads indicate the displacement direction of profile points with propagation distance.

tance $\chi = 1.2$ in the case $P = 0$. Profile 3 is the theoretical prediction at the same distance but in the case $P = 0.5$. The observed tendency of forward shift of wave maximum and wave minimum corresponds to their faster propagation.

2. General solution in the case of mesoscopic elements localization near the PM space diagonal

To derive a general solution of Eq. (18) it is useful to introduce the change of the independent variables $(\zeta, \theta) \rightarrow (\zeta, \eta = \theta - P^{-1}\zeta)$. Then, Eq. (18) takes the form

$$\frac{\partial S}{\partial \zeta} - \frac{1}{P} e^{-P[S^A(\zeta) + \mathrm{sign}(S_\eta)S]} \frac{\partial S}{\partial \eta} = 0. \tag{25}$$

The solution of Eq. (25) should satisfy the boundary condition

$$S(\zeta = 0) = G(\eta), \tag{26}$$

where $G(\eta)$ is a periodic function with a single maximum and a single minimum over a period. We consider odd functions for definiteness. Formal solution of the problem (25), (26) can be presented in form of explicit dependence of the variable η on acoustic strain S (see the solutions of the similar equations in Refs. 20 and 21)

$$\eta = G^{-1}(s) - \frac{1}{P} e^{-P\,\mathrm{sign}(S_\eta)S} \int_0^\zeta e^{-PS^A(\zeta')}d\zeta'. \tag{27}$$

In Eq. (27) $G^{-1}(s)$ denotes the inverse function $[G(G^{-1}(S)) = S]$. An important general result can be obtained at this point after differentiating Eq. (27) over η

$$\frac{\partial S}{\partial \eta} = \frac{1}{\dfrac{\partial G^{-1}}{\partial S} + \mathrm{sign}(S_\eta)e^{-P\,\mathrm{sign}(S_\eta)S}\displaystyle\int_0^\zeta e^{-PS^A(\zeta')}d\zeta'}.$$

From this formula it follows that if for a particular function G the sign of $\partial G^{-1}/\partial S$ coincides with $\mathrm{sign}(S_\eta)$, then both terms in the denominator have the same sign, the denominator never equals zero, and consequently $\partial S/\partial n$ never diverges ($|\partial S/\partial n| \neq \infty$). In other words, there is no shock front formation in the profile of acoustic strain. This conclusion is valid, in particular, for initially sinusoidal wave profile.

It should be noted that in Eq. (27) the acoustic wave amplitude $S^A(\zeta)$ is still an undetermined function. The dependence of S^A on propagation distance and the positions of acoustic wave extrema $\eta = \eta_e(\zeta)$ can be found by matching the solutions in Eq. (27) for $S_\eta > 0$ and $S_\eta < 0$ in the points of extrema $S = S_e = S^A(\zeta)\mathrm{sign}(S_e)$

$$\eta_e(\zeta) = G_{(+)}^{-1}(S_e) - \frac{1}{P} e^{-PS_e} \int_0^\zeta e^{-PS^A(\zeta')}d\zeta' \quad \text{if } S_\eta > 0, \tag{28}$$

$$\eta_e(\zeta) = G_{(-)}^{-1}(s_e) - \frac{1}{P} e^{PS_e} \int_0^\zeta e^{-PS^A(\zeta')}d\zeta' \quad \text{if } S_\eta < 0. \tag{29}$$

Here, the values of the inverse function in the extrema depend on the branch of the function G ($S_\eta > 0$ or $S_\eta < 0$), along which the extremum S_e is approached. To clarify this we have introduced in Eq. (28) and Eq. (29) the subscripts $(+)$ and $(-)$ $[G_{(+)}^{-1}(S_e) \neq G_{(-)}^{-1}(S_e)]$. By eliminating $\eta_e(\zeta)$ between Eq. (28) and Eq. (29), the integral equation for the wave amplitude is obtained

$$\frac{2}{P}\sinh(PS^A)\int_0^\zeta e^{-PS^A(\zeta')}d\zeta' + \Phi(S^A) = 0. \tag{30}$$

Here, we have introduced compact notation $\Phi(s^A) \equiv G_{(+)}^{-1}(S^A) - G_{(-)}^{-1}(S^A)$ and we have taken into account assumed symmetry of the G function. By differentiating over ζ and then excluding $\int_0^\zeta \exp[-PS^A(\zeta')]d\zeta'$ with the help of Eq. (30), a differential equation for wave amplitude is derived

$$\frac{\partial S^A}{\partial \zeta} + \frac{1}{P}\frac{1 - \exp(-2PS^A)}{\partial\Phi/\partial S(S^A) - P\coth(PS^A)\Phi(S^A)} = 0. \tag{31}$$

If for a particular initial wave profile $G(\eta)$ Eq. (31) is integrated (analytically or numerically), then Eq. (27) provides the description of wave profile transformation in propagation. The extrema of the profile can be determined from Eq. (28) [or Eq. (29)]. In particular, the positions of the peaks and, consequently, their velocities can be followed in wave propagation process.

Analytical solution of Eq. (31) is possible if we use piecewise linear approximation for the initial wave profile. In particular, for the initial profile 4 in Fig. 4 ($G(\eta) = (2/\pi)\eta$ if $|\eta| \leq \pi/2$, $G(\eta) = 2\,\mathrm{sign}(\eta) - (2/\pi)\eta$ if $\pi/2 \leq |\eta| \leq \pi$), which provides the simplest piecewise linear approximation of initially sinusoidal wave, the integration of Eq. (31) gives

$$\zeta = \frac{\pi}{2}\left\{\frac{1}{2}\left[Li_2(e^{-2P}) - Li_2(e^{-2PS^A})\right]\right.$$

$$-P(1-S^A)\ln(e^{2PS^A} - 1) + P^2[1-(S^A)^2] - 2P$$

$$\left.\times\left[\frac{1}{e^{2P}-1} - \frac{1}{e^{2PS^A}-1} - \frac{1}{1-e^{-2P}} + \frac{S^A}{1-e^{-2PS^A}}\right]\right\}. \tag{32}$$

In Eq. (32) Li_2 denotes polylog of second order ($Li_2(x) \equiv \Sigma_{k=1}^{\infty} x^k / k^2$). Solution (32) provides in an implicit form the dependence of wave amplitude S^A on propagation distance ζ and the parameter P. In the limiting case $P \ll 1$ (when the acoustic wave does not feel inhomogeneity of the mesoscopic elements distribution in PM space) solution (32) reduces to

$$S^A(P \ll 1) \cong \frac{1}{1 + \frac{2}{\pi}\zeta}. \tag{33}$$

The result in Eq. (33) resembles one obtained in Ref. 22. It predicts that in the regime $P \ll 1$ the medium becomes less acoustically transparent for the waves of higher amplitude (self-induced attenuation).[22] However, in the asymptotic case $P \gg 1$ the situation is quite different. In this case the solution (32) reduces to

$$S^A(P \gg 1) \cong 1 + \frac{1}{P}\left(1 - \sqrt{1 + \frac{2\zeta}{\pi}}\right). \tag{34}$$

Analysis of the result in Eq. (34), which is valid in the case of strong localization of mesoscopic elements in the interaction triangle (Fig. 2), leads to a few important conclusions.

(a) From Eq. (34) it follows that at distances $\zeta \ll 1$ acoustic wave amplitude diminishes linearly with propagation distance

$$S^A(P \gg 1, \zeta \ll 1) \cong 1 - \frac{1}{\pi P}\zeta \cong \exp\left(-\frac{1}{\pi P}\zeta\right). \tag{35}$$

Importantly, because $\zeta = x/x_H = h^H s_0 x/(2c_0\tau_0) \propto s_0$ and $P = s_0/\sqrt{2}s_\perp^0 \propto s_0$, this initial stage of amplitude diminishing does not depend on initial wave amplitude s_0

$$S^A(P \gg 1, \zeta \ll 1) \cong \exp\left(-\frac{h^H s_\perp^0}{\sqrt{2}\pi c_0\tau_0}x\right). \tag{36}$$

The coefficient of hysteretic absorption $\alpha^H \equiv h^H s_\perp^0/(\sqrt{2}\pi c_0\tau_0)$ defined by Eq. (36) is independent of wave amplitude and is proportional to wave fundamental frequency ω (because $1/\tau_0 \propto \omega$). We conclude that in the regime $P \gg 1$, $\zeta \ll 1$ interaction of strain wave with hysteretic mechanical elements contributes to amplitude-independent (linear) absorption proportional to frequency, which is observed experimentally in such materials as rocks and sands.[25–28] It should be mentioned here that currently there is no consensus on the mechanism of this experimentally observed absorption.[25,26,29–33] Different linear mechanisms were proposed.[25,26,29–33] In Refs. 25 and 26 it was demonstrated that amplitude independent proportional to frequency absorption may be caused by a nonlinear mechanism due to a very particular form of the dependence of local sound velocity changes on strain
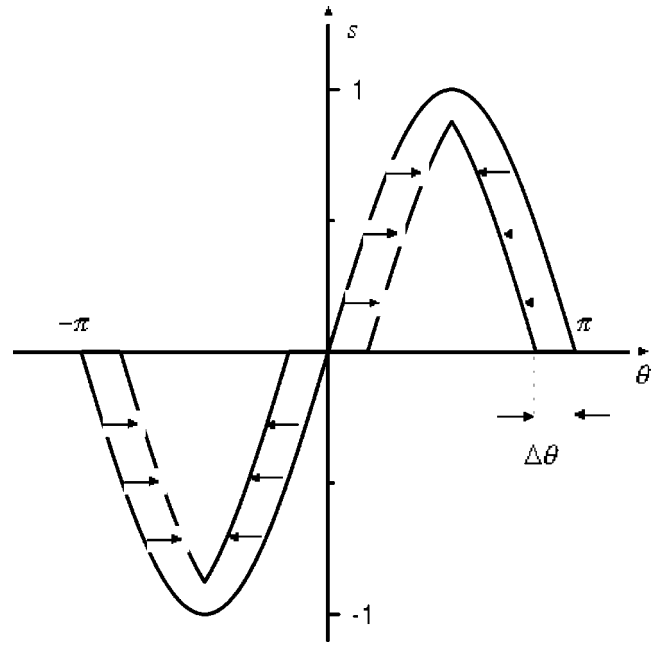
FIG. 5. Transformation of initially sinusoidal strain wave with increasing propagation distance in the frame of Knopoff's model. Arrowheads indicate the direction for the shift of profile points with increasing distance. The magnitude $|\Delta\theta|$ of the time shift at fixed propagation distance is the same for all the points.

$$\Delta c \propto -\text{const}\,\text{sign}(s_\theta)\text{sign}(s), \tag{37}$$

where the constant is positive. Note that in Eq. (37) the velocity changes do not depend on wave amplitude but only on the sign of strain and direction of its variation. A qualitative picture of initially sinusoidal profile transformation in the frame of the model (37) is presented in Fig. 5. The arrowheads in Fig. 5 indicate the direction for the shift of profile points with increasing propagation distance. Spectral analysis of the nonlinearly deformed profile in Fig. 5 demonstrates that at short propagation distances (when $|\Delta\theta| \ll \pi/2$) the absorption of fundamental frequency $\omega = 1/\tau_0$ is proportional to frequency and does not depend on wave amplitude. It can be noted that in the case of Knopoff's model (37) energy dissipation takes place everywhere along the profile.

In the case of mesoscopic nonlinearity considered in the present analysis, predicted transformation of wave profile is very different. As it follows directly from Eq. (25), in the case $P \gg 1$ the transformation of the profile takes place only near the extremums, where $(S^A(\zeta) + \text{sign}(S_\eta)S) \lesssim 1/P \ll 1$. Everywhere else the second term in Eq. (25) is exponentially small. Consequently, the qualitative picture of initially sinusoidal profile transformation looks as it is presented in Fig. 6. The spectral analysis of nonlinearly deformed profile (with cut extrema of sinusoid) demonstrates that at short propagation distances (when strain fall ΔS in Fig. 6 is small) the absorption of fundamental frequency is proportional to frequency and does not depend on wave amplitude (similar to Knopoff's model). However, in contrast to Knopoff's model,

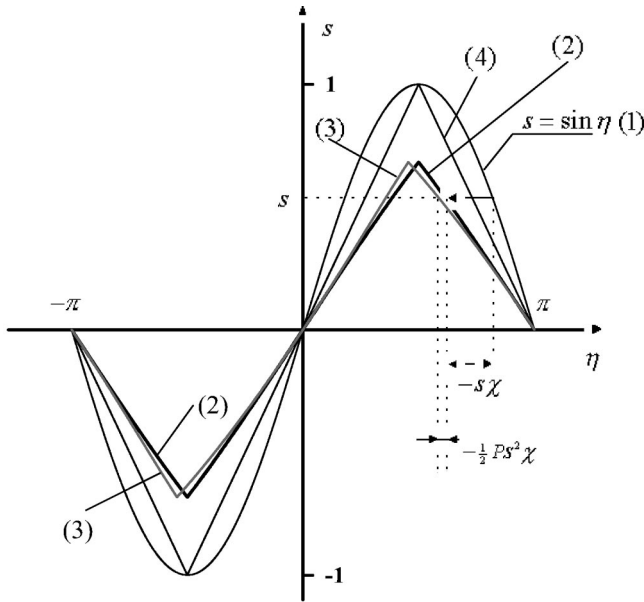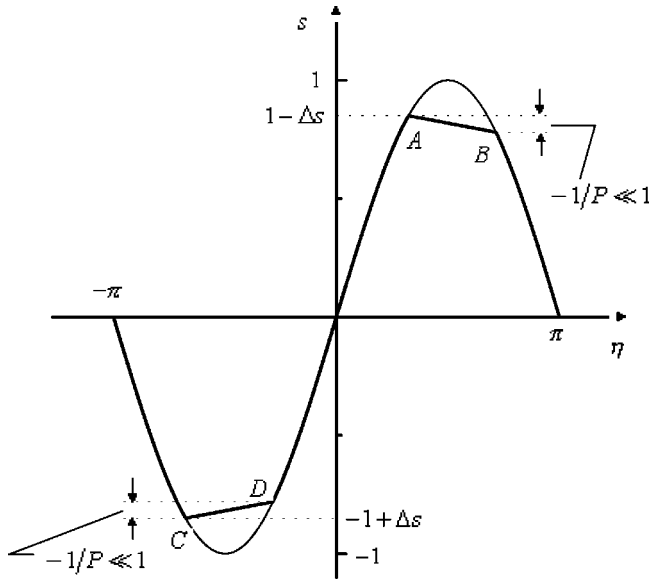FIG. 6. Qualitative picture for transformation of initially sinusoidal profile of a high-amplitude ($P \gg 1$) acoustic wave with increasing propagation distance, which is valid at distances where the diminishing ΔS of the wave amplitude is small ($\Delta S \ll 1$). Acoustic attenuation takes place near the extrema of wave profile. The 'huts' of nonlinearly transformed profile are slightly inclined relative to horizontal axis.

in the case of hysteretic nonlinearity absorption takes place only in the vicinity of wave maximum and wave minimum.

We have presented cuts ("huts") of profiles in Fig. 6 to be slightly inclined relative to the horizontal axis to reflect a more tiny feature of the exact solution of evolution equation (25). In fact, from Eq. (28) and Eq. (29) it follows that in the regime $P \gg 1$ maximum of wave profile moves along the part $S_\eta > 0$ of the initial profile [$\eta_{\max}(\zeta, P \gg 1) \cong G_{(+)}^{-1}(S^A(\zeta))$], while minimum of wave profile moves along the part $S_\eta < 0$ of the initial profile [$\eta_{\min}(\zeta, P \gg 1) \cong G_{(-)}^{-1}(S^A(\zeta))$]. So, the inclination introduced for the lines AB and CD in Fig. 6 reflects qualitatively the fact that the extrema of the wave are located in points A and C. This tendency in the regime $P \gg 1$ correlates with the tendency of wave transformation in the case $P \ll 1$ presented in Fig. 4.

In the present publication we are very far from the statement that nonlinear mechanism considered here provides a physical explanation for classical experimental observations.[25–28] The proposed mechanism is amplitude independent only for high-amplitude elastic waves (beyond the strain levels $s_0 \lesssim 10^{-5}$ analyzed in the experiments[25–28]). If we estimate from Ref. 3 that $s_\perp^0 \propto 10^{-4}$, then amplitude-independent absorption due to hysteretic elements is expected for elastic strains $s_0 \gtrsim 10^{-3}$. We know that in experiments[34–37] the attenuation is observed to be an increasing function of wave amplitude in the strain interval $10^{-6}–10^{-5} \lesssim s_0 \lesssim 10^{-3}$. However, we have failed to find any data on strain attenuation in the diapason $s_0 \gtrsim 10^{-3}$. It should also be mentioned that in accordance with Ref. 2 and Ref. 3 $s_\perp^0$ diminishes with increasing confining pressure. Because of this the considered mechanism will be more interesting, perhaps, for seismic wave propagation in Earth crust or for high-pressure acoustics than for acoustics at ambient pressures. It is also possible that artificially damaged (or fa-

tigued) materials have $s_\perp^0$ significantly smaller than natural rocks.

In contrast to other models proposed for nonlinear attenuation in rocks and sands (predicting increased attenuation with increasing wave amplitude[11,22,27,38–41]) the model in Eq. (34) predicts that absorption does not increase with increasing wave amplitude.

Finally, it should be mentioned that linear absorption predicted by Eq. (36) is estimated to be rather high. Specific dissipation function Q of the medium[25,26] $Q \equiv (2\alpha^H c_0/\omega)^{-1} = (\sqrt{2} h^H s_\perp^0/\pi)^{-1} \propto 1/(h^H s_\perp^0)$ is estimated to be $Q \lesssim 10$ for $s_\perp^0 \propto 10^{-4}$ and typical values[8,10,42] $h^H \gtrsim 10^3$. Consequently this mechanism might provide an important contribution to absorption of high-amplitude strain pulses and, in general, cannot be neglected even though it does not control the absorption length of high-amplitude acoustic pulses [see paragraph (b) just below].

(b) As it follows from Eq. (34) and Eq. (35), the absorption law considered just above is valid only at initial stage $\zeta \ll 1$ of high-amplitude strain wave evolution. In this regime strain amplitude variation ΔS in Fig. 6 is small, $\Delta S \ll 1$. The regime of the nonlinear absorption of the wave changes before the high-amplitude wave is significantly absorbed. Significant variation in wave amplitude in the regime $P \gg 1$ is possible only at distances $\zeta \gtrsim 1$. For $\zeta \gg 1$ the result in Eq. (34) can be approximated by

$$ S^A(P \gg 1, \zeta \gg 1) \cong 1 - \sqrt{\frac{2\zeta}{\pi P^2}}. \tag{38} $$

From Eq. (38) we find that characteristic nondimensional length of wave absorption in the regime $P \gg 1$ [defined by $S^A(\zeta = \zeta_P) \cong 1/2$] is $\zeta_P = \pi P^2/8$. Consequently, the characteristic dimensional length of wave absorption in this regime is

$$ x_P = \zeta_P x_H = \frac{\pi c_0 \tau_0}{8 h^H s_\perp^0} \left(\frac{s_0}{s_\perp^0} \right) \propto s_0. \tag{39} $$

With increasing wave amplitude s_0, characteristic length of elastic wave absorption increases. In other words, the regime $P \gg 1$ is the regime of self-induced transparency for high-amplitude strain waves.

From comparison of Eq. (39) with Eq. (13) the following important conclusion can be derived. If (as it is in reality) the distribution function of mesoscopic elements varies along and normally to PM space diagonal, then the condition $s_\perp^0, s_0 \ll s_\parallel^0$ (between the scales of distribution function and initial wave amplitude) is insufficient to neglect along-diagonal variation of mechanical element density. As we see from Eq. (39) and Eq. (13) the role of elements localization near the diagonal diminishes with increasing wave amplitude (for high-amplitude waves), while the role of along-diagonal variation of distribution function increases. Consequently, even in the case $s_\perp^0 \ll s_\parallel^0$ there is critical wave amplitude s_0^{cr} [defined by $x_P(s_0^{cr}) \propto x_{SH}(s_0^{cr})$] when both effects should be taken into account simultaneously. From Eq. (39) and Eq. (13), we get

$$ (s_0^{cr})^2 \propto \frac{8}{\pi} \left(\frac{h^H}{h^{NH}} \right) (s_\perp^0)^2. \tag{40} $$
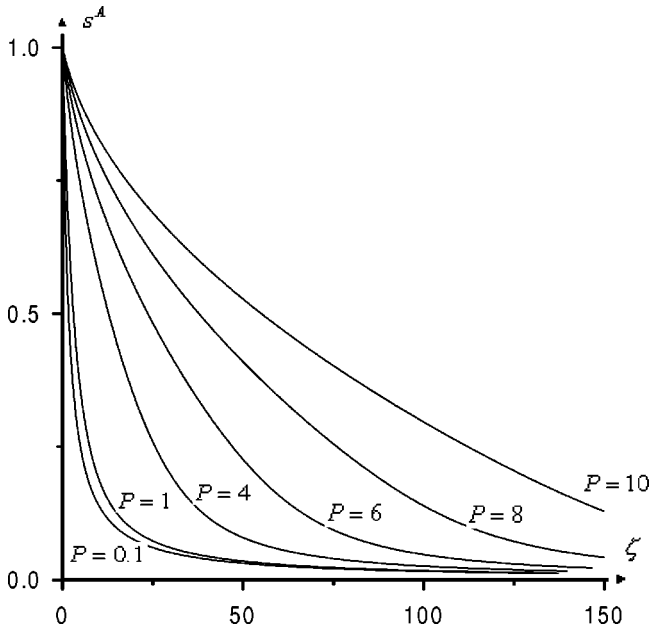
FIG. 7. The dependence of normalized wave amplitude S^A on normalized propagation distance for different values of the parameter P (P = 0.1,1,4,6,8,10), which characterizes wave sensitivity to localization of hysteretic elements near the diagonal of Preisach–Mayergoyz space.

FIG. 8. The dependence of characteristic length of nonlinear acoustic absorption on the parameter P (which is proportional to strain wave amplitude). For $P \lesssim 2$ the self-induced absorption takes place and for $P \gtrsim 2$ self-induced transparency is predicted.

The ratio (h^H/h^{NH}) is estimated with the help of Eq. (12), Eq. (15), and Eq. (10) as $(h^H/h^{NH}) \propto (\tilde{f}^H(0,0)/\tilde{f}^{NH})s_{\parallel}^0 \propto (s_{\parallel}^0/s_{\perp}^0)$. Consequently, the estimate in Eq. (40) for critical strain amplitude s_0^{cr} reduces to

$$s_0^{cr} \propto \sqrt{s_{\perp}^0 s_{\parallel}^0}. \qquad (41)$$

We are now in position to formulate the following general conclusion. The variation of the distribution function along PM space diagonal can be neglected in the evolution equation for strain amplitudes in the diapason

$$s_{\perp}^0, s_0 \ll \sqrt{s_{\perp}^0 s_{\parallel}^0}. \qquad (42)$$

The role of distribution function variation along PM space diagonal plays important role in the diapason

$$\sqrt{s_{\perp}^0 s_{\parallel}^0} \lesssim s_0, \qquad (43)$$

even if $s_0 \ll s_{\parallel}^0$. It should be pointed out that hysteretic mechanical elements cannot be neglected completely even if Eq. (43) is replaced by the strong inequality $\sqrt{s_{\perp}^0 s_{\parallel}^0} \ll s_0$. As it follows from the next section, these elements still control the diminishing of wave amplitude before shock front formation. Moreover, the variation of their density along the PM space diagonal provides an important contribution to quadratic nonlinearity in Eq. (11) (when the latter is generalized for the case $s_{\perp}^0 \neq \infty$).

To conclude this section we present in Fig. 7 the results for the dependence of the wave amplitude on propagation distance and the parameter P, which is described by Eq. (32). To characterize wave absorption we define the characteristic nondimensional length of wave absorption ζ_{abs} by the condition $S^A(\zeta = \zeta_{abs}) = S^A(\zeta = 0)/2 = 1/2$. Then, the right-hand side of Eq. (32) with substitution $S^A = 1/2$ gives the dependence of $\zeta_{abs} = x_{abs}/x_H = (h^H s_0/(2c_0\tau_0))x_{abs}$ on the parameter P. Finally, additional division of Eq. (32) by P provides

the dependence of normalized absorption length $\bar{\zeta}_{abs} \equiv \zeta_{abs}/P = (h^H s_{\perp}^0/(2c_0\tau_0))x_{abs}$ on wave amplitude ($s_0 \propto P$). We present the dependence $\bar{\zeta}_{abs} = \bar{\zeta}_{abs}(P)$ in Fig. 8. It is clear from Fig. 8 that the initial increase in wave absorption ($\partial\bar{\zeta}_{abs}/\partial P < 0$, $\bar{\zeta}_{abs} \propto 1/P$ for $P \ll 1$) is followed by its saturation for $P \approx 2$ and then by an induced transparency region, where $\partial\bar{\zeta}_{abs}/\partial P > 0$. These results are in accordance with analysis of asymptotic regimes $P \ll 1$ and $P \gg 1$ fulfilled earlier in this section. Localization of hysteretic elements near the PM space diagonal leads to nonmonotonous dependence of absorption length on wave amplitude.

As it was demonstrated,[43] the Granato and Lucke theory of sound damping by dislocation breakaway predicts the diminishing of the nonlinear acoustic absorption at stress levels σ_0 exceeding the characteristic breakaway stress Γ. The predicted maximum in the breakaway loss as a function of the acoustic wave amplitude was observed experimentally in aluminum at low temperatures.[44] For high enough values of the parameter (σ_0/Γ) the decrement diminishes proportionally to $(\sigma_0/\Gamma)^{-1}$ due to the saturation in the number of dislocations, which are able to participate in the breakaway process. In other words the number of dislocations, which might participate in the acoustic wave absorption, grows with increasing wave amplitude slower than the acoustic wave energy. Clearly the physics of the decrement diminishing at high wave amplitudes ($s_0 \gg s_{\perp}^0$) predicted by our formula (39) is similar (that is due to the slower growth of the number of sound-absorbing hysteretic mechanical elements in comparison with the acoustic energy increase). The asymptotic behavior of the decrement at high acoustic amplitudes is also similar to that in the Granato and Lucke theory. In accordance with Eq. (39), the decrement in the

V. Gusev and V. Aleshin: Evolution equation for mesoscopic materials

regime $(s_0/s_\perp^0)\gg 1$ $(P\gg 1)$ diminishes proportionally to $(s_0/s_\perp^0)^{-1}$.

III. MODEL FORM OF EVOLUTION EQUATION

In this section we will be interested in the simplification of general equation (8), avoiding the assumption $s_\parallel^0=\infty$ applied in the previous Sec. II B. We will study the regime $s_\perp^0, s_0 \ll s_\parallel^0 \neq \infty$. Without significant loss of generality, we assume factorization of the distribution function of hysteretic elements

$$\tilde{f}^H = \tilde{f}_\parallel^H\left(\frac{\sqrt{2}(\bar{s}+s')-\mathrm{sign}(s_t')s_\perp}{s_\parallel^0}\right)\tilde{f}_\perp^H\left(\frac{s_\perp}{s_\perp^0}\right). \quad (44)$$

For simplicity, we assume identical distribution of hysteretic and nonhysteretic elements along the PM space diagonal. In the case

$$s_0 \ll s_\parallel^0 \quad (45)$$

of interest here, this distribution can be modeled as a linear one

$$\tilde{f}_\parallel^H\left(\frac{\sqrt{2}(\bar{s}+s')-\mathrm{sign}(s_t')s_\perp}{s_\parallel^0}\right)$$

$$\equiv \left(1+\frac{\sqrt{2}s'-\mathrm{sign}(s_t')s_\perp}{s_\parallel^0}\right)f_{ch}^H, \quad (46)$$

$$\tilde{f}^{NH}\left(\frac{\sqrt{2}(\bar{s}+s')}{s_\parallel^0}\right)\equiv\left(1+\frac{\sqrt{2}s'}{s_\parallel^0}\right)\tilde{f}_{ch}^{NH}. \quad (47)$$

In the right-hand side of Eq. (46) and Eq. (47), f_{ch}^H and f_{ch}^{NH} denote characteristic densities of mechanical elements in the interaction triangle of PM space. Then, if F^H is modeled by exponential distribution $F^H(s_\perp/s_\perp^0)=\exp(-s_\perp/s_\perp^0)$, the substitution of (46) and (47) into Eq. (8) leads to

$$\frac{\partial S}{\partial\zeta}+\left\{(1+2\mu PS)\frac{1}{P}(1-e^{-P[S^A+\mathrm{sign}(S_\theta)S]})\right.$$

$$-\frac{\mu}{P}\mathrm{sign}(S_\theta)[1-e^{-P[S^A+\mathrm{sign}(S_\theta)S]}$$

$$\left.-P(S^A+\mathrm{sign}(S_\theta)S)e^{-P[S^A+\mathrm{sign}(S_\theta)S]}]+2\beta\mu S\right\}\frac{\partial S}{\partial\theta}=0. \quad (48)$$

Equation (48) is written in nondimensional variables introduced earlier in Sec. II B. As before, amplitude-independent contribution to sound velocity is assumed to be included in renormalized sound velocity. Two additional parameters are introduced in Eq. (48). The parameter $\beta\equiv\tilde{f}^{NH}/(\tilde{F}^H s_\perp^0)\propto 1$ characterizes relative contribution of nonhysteretic and hysteretic elements to total number of mesoscopic elements. Small parameter $\mu\equiv s_\perp^0/s_\parallel^0\ll 1$ specifies particular character of element distributions, which are analyzed in this section. Combining $\mu\equiv s_\perp^0/s_\parallel^0$ with $P\equiv s_0/\sqrt{2}s_\perp^0$ and Eq. (45), we get $P\ll 1/\mu$. The latter inequality is useful for some of the simplifications in the following.

In the limiting case $P\ll 1$, Eq. (48) reduces to the form in Eq. (17). In the intermediate regime $P\propto 1$, Eq. (48) reduces to the form in Eq. (18). In the limiting case $P\gg 1$ the transformation of the variables $(\zeta,\theta)\to(\zeta,\eta=\theta-P^{-1}\zeta)$ (see Sec. II B 2) is useful. However, in the more general case considered here (where $s_\parallel^0\neq\infty$) Eq. (48) reduces to the form in Eq. (25) only near the extrema of wave profile (in the regions of width $\propto 1/P\ll 1$ near the extrema; see Fig. 6). Everywhere else the exponentials $\exp\{-P(S^A+\mathrm{sign}(S_\eta)S)\}$ can be neglected and an asymptotic form of Eq. (48) in the limit $P\gg 1$ is

$$\frac{\partial S}{\partial\zeta}+2(\beta+1)\mu S\frac{\partial S}{\partial\eta}=0. \quad (49)$$

Importantly, along-diagonal variation both of nonhysteretic and hysteretic elements distributions contributes to quadratic nonlinearity of classical form in Eq. (49). This prediction should be compared to Eq. (11) derived in the case $s_\perp^0=\infty$.

Combining Eq. (49) with Eq. (25), we get a model evolution equation, which is asymptotically valid in the regime $P\ll 1/\mu$

$$\frac{\partial S}{\partial\zeta}-\frac{1}{P}e^{-P[S^A(\zeta)+\mathrm{sign}(S_\eta)S]}\frac{\partial S}{\partial\eta}+2(\beta+1)\mu S\frac{\partial S}{\partial\eta}=0. \quad (50)$$

As it follows from our previous analysis in Sec. II B 2, the third term in Eq. (50) can be neglected in the regime (42): $s_\perp^0, s_0 \ll \sqrt{s_\perp^0 s_\parallel^0}$ $(P\ll 1/\sqrt{\mu})$. Importantly, Eq. (50) can be applied for the analysis of initial regime $s_\perp^0\ll\sqrt{s_\perp^0 s_\parallel^0}\leqslant s_0\ll s_\parallel^0$ $(1\ll 1/\sqrt{\mu}\leqslant P\ll 1/\mu)$. We are starting this analysis in the following.

At the beginning the method for solution of Eq. (50) is the same as the one for solution of Eq. (25). Generalization of the solution (27) to the case of Eq. (50) is

$$\eta=G^{-1}(S)-\frac{1}{P}e^{-P\mathrm{sign}(S_\eta)S}\int_0^\zeta e^{-PS^A(\zeta')}d\zeta'$$

$$+2(\beta+1)\mu S\zeta. \quad (51)$$

The modified conditions of matching solution (51) in the extrema of wave profile [modified Eq. (28) and Eq. (29)] are

$$\eta_e(\zeta)=G_{(+)}^{-1}(S_e)-\frac{1}{P}e^{-PS_e}\int_0^\zeta e^{-PS^A(\zeta')}d\zeta'$$

$$+2(\beta+1)\mu S_e\zeta \quad \text{if} \quad S_\eta>0, \quad (52)$$

$$\eta_e(\zeta)=G_{(-)}^{-1}(S_e)-\frac{1}{P}e^{PS_e}\int_0^\zeta e^{-PS^A(\zeta')}d\zeta'$$

$$+2(\beta+1)\mu S_e\zeta \quad \text{if} \quad S_\eta<0. \quad (53)$$

By eliminating $\eta_e(\zeta)$ between Eq. (52) and Eq. (53), the additional (third) terms in the right-hand side are also eliminated. Due to this, quadratic nonlinearity of classical form does not modify Eqs. (30) and (31) for acoustic wave amplitude. Consequently, for initial strain profile 4 in Fig. 4 the dependence of wave amplitude on propagation distance is provided (for $P\gg 1$) by the solution in Eq. (34). As it follows from Eq. (52) and Eq. (53), in the regime $P\gg 1$ under con-

sideration, the positions of wave maximum and wave minimum can be approximately found from

$$\eta_{max}(\zeta) = G_{(+)}^{-1}(S^A(\zeta)) + 2(\beta+1)\mu S^A(\zeta)\zeta, \qquad (54)$$

$$\eta_{min}(\zeta) = G_{(-)}^{-1}(-S^A(\zeta)) - 2(\beta+1)\mu S^A(\zeta)\zeta. \qquad (55)$$

In accordance with Eq. (54) and Eq. (55), quadratic nonlinearity of classical form (which is here due to mesoscopic mechanical elements, both nonhysteretic and hysteretic) induces the motion of maximum and minimum of wave profile in opposite directions [compare the signs of the second terms in the right-hand side of Eq. (54) and Eq. (55)]. This indicates possible formation of a shock front, and this is exactly the case. From Eq. (51) we find

$$\frac{\partial S}{\partial \eta} = \frac{1}{\frac{\partial G^{-1}}{\partial S} + \text{sign}(S_\eta)e^{-P\text{sign}(S_\eta)S}\int_0^\zeta e^{-PS^A(\zeta')}d\zeta' + 2(\beta+1)\mu\zeta}. \qquad (56)$$

Starting from characteristic distance $\zeta = \zeta_{SH}^\beta$, the condition $\partial S/\partial \eta = \infty$ is fulfilled in some points of initially descending ($S_\eta < 0$) parts of the profile. Estimating the second term in the denominator of Eq. (56) with the help of solution (34) for $S^A(\zeta)$, we find that this term provides exponentially small [$\propto \exp(-P)$] contribution to shock formation distance. Consequently, shock formation distance in the regime $P \gg 1$ can be found as though only classical form quadratic nonlinearity is present [from the condition $\partial G_{(-)}^{-1}/\partial S(S=0) + 2(\beta+1)\mu\zeta_{SH}^\beta = 0$]. For the initial profile 4 in Fig. 4, this gives

$$\zeta_{SH}^\beta = \frac{\pi}{4(\beta+1)\mu} \propto \frac{1}{\mu} \gg 1. \qquad (57)$$

Note that we have introduced superscript ''β'' to indicate that in comparison with the case $s_\perp^0 \to \infty$ (considered in Sec. II A) shock formation is due to both nonhysteretic and hysteretic elements ($\beta \neq 0$).

In accordance with Eq. (55) it is the minimum of strain wave that is located on the part $S_\eta < 0$ of the initial wave profile. So, it is expected that minimums of acoustic wave will be first influenced by shock formation, and that asymmetry of the shock relative to $S=0$ will induce its motion from the initial points $\eta = (2n+1)\pi$ ($n = \pm 1, \pm 2, ...$) of its formation. It is important that starting from $\zeta = \zeta_{SH}^\beta$ the amplitudes of positive and negative half periods of the wave become different. Consequently, the derivation of generalized equation (50) should be re-examined, perhaps, taking this into account. Also, a law for shock front installation in the profile of the wave in the case where hysteretic absorption takes place at shock front (as it is expected starting $\zeta = \zeta_{SH}^\beta$, because wave minimum will be located at the shock) should be established. We leave these topics for future research. It is quite possible that better understanding of a rather complicated problem of shock propagation in the presence of hysteretic absorption might be obtained from the analysis of strain pulse propagation. For this purpose nonlinear equations for acoustic pulses derived in Ref. 23 for the regime $P \ll 1$ should be generalized for the regimes $P \geqslant 1$ and $P \gg 1$ by the methods proposed in the present publication.

IV. CONCLUSIONS

Nonlinear wave propagation in materials, where distribution function of mesoscopic mechanical elements has very different scales of variation along and normally to diagonal of PM space ($s_\perp^0 \ll s_\parallel^0$), is analyzed. An evolution equation for strain waves with amplitudes $s^A \ll s_\parallel^0$, which takes into account localization of elements distribution near the diagonal and its slow variation along the diagonal, is proposed. Analytical solutions of the evolution equation predict nonmonotonous dependence of wave absorption on its amplitude in the asymptotic regime $s_\perp^0, s^A \ll \sqrt{s_\perp^0 s_\parallel^0}$. The regime of self-induced absorption for small-amplitude ($s^A \ll s_\perp^0$) waves is followed by the regime of self-induced transparency for high-amplitude ($s^A \gg s_\perp^0$) waves. It is demonstrated that even under the condition $s_\perp^0 \ll s_\parallel^0$ inhomogeneity of elements distribution along the PM space diagonal (when $s_\parallel^0 \neq \infty$) plays an important role in the propagation of strain waves with amplitudes $\sqrt{s_\perp^0 s_\parallel^0} \leqslant s^A \ll s_\parallel^0$.

The proposed evolution equation provides opportunity to model propagation of elastic waves with strain amplitudes s^A comparable to and even higher than characteristic scale $s_\perp^0$ of element localization near the PM space diagonal. The developed theory might be useful, in particular, in seismology, where earthquakes generate strain wave of sufficiently high amplitudes s^A. At the same time, it is known that localization scale $s_\perp^0$ diminishes with increasing confinement pressure. Consequently, the developed theory might be applied in high-pressure nonlinear acoustics. It might be also applied in nonlinear acoustic diagnostics of damaged and fatigued materials even at ambient pressures if $s_\perp^0$ is sufficiently low.

[1] D. J. Holcomb, "Memory, relaxation, and microfracturing in dilatant rock," J. Geophys. Res. **86**, 6235–6248 (1981).
[2] R. A. Guyer, K. R. McCall, and G. N. Boitnott, "Hysteresis, discrete memory, and nonlinear wave propagation in rock: A new paradigm," Phys. Rev. Lett. **74**, 3491–3494 (1995).
[3] R. A. Guyer, K. R. McCall, G. N. Boitbott, L. B. Hillbert, Jr., and T. J. Plona, "Quantitative implementation of Preisach-Mayergoyz space to find static and dynamic elastic moduli in rock," J. Geophys. Res. **102**, 5281–5293 (1997).
[4] A. Visintin, "On hysteresis in elasto-plasticity and in ferromagnetism," Int. J. Non-Linear Mech. **37**, 1283–1298 (2002).
[5] K. R. McCall and R. A. Guyer, "A new theoretical paradigm to describe hysteresis, discrete memory and nonlinear elastic wave propagation in

rock," Nonlinear Processes in Geophys. **3**, 89–101 (1996).

[6] Koen E-A Van den Abeele, P. A. Johnson, R. A. Guyer, and K. R. McCall, "On the quasi-analytical treatment of hysteretic nonlinear response in elastic wave propagation," J. Acoust. Soc. Am. **101**, 1885–1898 (1997).

[7] V. E. Gusev, W. Lauriks, and J. Thoen, "Dispersion of nonlinearity, nonlinear dispersion, and absorption of sound in micro-inhomogeneous materials," J. Acoust. Soc. Am. **103**, 3216–3226 (1998).

[8] V. E. Nazarov, L. A. Ostrovsky, I. A. Soustova, and A. M. Sutin, "Anomolous acoustic nonlinerity in metals," Akust. Zh. **34**, 491–499 (1985) [English Transl.: Sov. Phys. Acoust. **34**, 284–289 (1988)].

[9] P. A. Johnson, B. Zinszner, and P. N. J. Rasolofosaon, "Resonance and elastic nonlinear phenomena in rock," J. Geophys. Res. **101**, 11553–11564 (1996).

[10] R. A. Guyer and P. A. Johnson, "Nonlinear mesoscopic elasticity: Evidence of a new class of materials," Phys. Today **52**, 30–35 (1999).

[11] R. A. Guyer, J. TenCate, and P. Johnson, "Hysteresis and the dynamic elasticity of consolidated granular materials," Phys. Rev. Lett. **82**, 3280–3283 (1999).

[12] Koen Van den Abeele and J. De Visscher, "Damage assessment in reinforced concrete using spectral and temporal nonlinear vibration techniques," Cem. Concr. Res. **30**, 1453–1464 (2000).

[13] G. N. Boitnott, "Nonlinear rheology of rock at moderate strains: Fundamental observations of hysteresis in the deformation of rock," in *Proceedings of the 15th Annual Seismic Research Symposium, Vail, Colorado,* edited by J. F. Lewkowicz and J. M. McPhetres (Philips Laboratory of the Air Force Material Command, Handsom Air Force Base, MA, 1993), Environmental Research Papers no. 125, pp. 121–133.

[14] I. A. Beresnev and K.-L. Wen, "Nonlinear soil response–a reality?" Bull. Seismol. Soc. Am. **86**, 1964–1978 (1996).

[15] I. A. Beresnev and K.-L. Wen, "The possibility of observing nonlinear path effect in earthquake-induced seismic wave propagation," Bull. Seismol. Soc. Am. **86**, 1028–1041 (1996).

[16] E. H. Field, P. A. Johnson, I. A. Beresnev, and Y. Zeng, "Nonlinear ground-motion amplification by sediments during the 1994 Northridge earthquake," Nature (London) **390**, 599–602 (1997).

[17] E. H. Field, S. Kramer, A.-W. Elgamal, J. D. Bray, N. Matasovic, P. A. Johnson, C. Cramer, C. Roblee, D. J. Wald, L. F. Bonilla, P. P. Dimitriu, J. G. Anderson, "Nonlinear site response: Where we're at (A report from SCEE/PEER seminar and workshop)," Seismol. Res. Lett. **69**, 230–234 (1998).

[18] L. D. Landau and E. M. Lifshitz, *Theory of Elasticity* (Pergamon, London, 1959).

[19] L. V. Zarembo and V. A. Krasilnikov, "Nonlinear phenomena in the propagation of elastic waves in solids," Usp. Fiz. Nauk **102**, 549–586 (1970) [English transl.: Sov. Phys. Usp. **13**, 778–797 (1971)].

[20] O. V. Rudenko and S. I. Soluyan, *Theoretical Foundations of Nonlinear Acoustics* (Consultants Bureau, New York, 1977).

[21] V. E. Gusev and A. A. Karabutov, *Laser Optoacoustics* (AIP, New York, 1993), Chap. 6.

[22] V. E. Gusev, C. Glorieux, W. Lauriks, and J. Thoen, "Nonlinear bulk and surface shear waves in materials with hysteresis and end-point memory," Phys. Lett. A **232**, 77–86 (1997).

[23] V. E. Gusev, "Propagation of acoustic pulses in material with hysteretic nonlinearity," J. Acoust. Soc. Am. **107**, 3047–3059 (2000).

[24] O. V. Rudenko and O. A. Sapozhnikov, "Wave beams in cubically nonlinear nondispersive media," Zh. Eksp. Teor. Fiz. **106**, 395–413 (1994) [English transl.: JETP **79**, 220–229 (1994)].

[25] L. Knopoff, "Attenuation of small amplitude stress waves in solids," Rev. Mod. Phys. **30**, 1178–1192 (1958).

[26] L. Knopoff, "Attenuation of elastic waves in the earth," in *Physical Acoustics*, edited by W. P. Mason (Academic, New York, 1965), Vol. III, Part B, Chap. 7.

[27] J. Duffy and R. D. Mindlin, "Stress-strain relations and vibrations of a granular medium," J. Appl. Mech., Trans. ASME **79**, 585–593 (1957).

[28] M. J. Buckingham, "Wave propagation, stress relaxation, and grain-to-grain shearing in saturated, unconsolidated marine sediments," J. Acoust. Soc. Am. **108**, 2796–2815 (2000).

[29] J. C. Savage, "Thermoelastic attenuation of elastic waves by cracks," J. Geophys. Res., **71**, 3929–3938 (1966).

[30] G. M. Lundquist and V. C. Cormier, "Constraints on the absorption band model of *Q*," J. Geophys. Res. **85**, 5244–5256 (1980).

[31] I. A. Chaban, "Sound attenuation in sediments and rock," Akust. Zh. **39**, 362–369 (1993) [English transl.: Acoust. Phys. **39**, 190–193 (1993)].

[32] M. J. Buckingham, "Theory of acoustic attenuation, dispersion, and pulse propagation in unconsolidated granular materials including marine sediments," J. Acoust. Soc. Am. **102**, 2579–2596 (1997).

[33] V. Yu. Zaitsev and V. E. Nazarov, "Linear frequency dependence of attenuation coefficient of elastic waves in micro-inhomogeneous solids," Akust. Zh. **45**, 622–627 (1999) [English transl.: Acoust. Phys. **45**, 552–556 (1999)].

[34] R. B. Gordon and L. A. Devis, "Velocity and attenuation of seismic waves in imperfectly elastic rock," J. Geophys. Res. **73**, 3917–3935 (1968).

[35] K. Winkler, A. Nur, and M. Gladwin, "Friction and seismic attenuation in rocks," Nature (London) **277**, 528–531 (1979).

[36] R. R. Stewart and M. N. Toksoz, "Strain dependent attenuation: observations and a proposed mechanism," J. Geophys. Res. **88**, 546–554 (1983).

[37] A. N. Tutuncu, A. L. Podio, A. R. Gregory, and M. M. Sharma, "Nonlinear viscoelastic behaviour of sedimentary rocks, Part I: Effect of frequency and strain amplitude," Geophysics **63**, 184–194 (1998).

[38] W. P. Mason, "Internal friction mechanism that produces an attenuation in the Earth's crust proportional to the frequency," J. Geophys. Res. **74**, 4963–4966 (1969).

[39] G. M. Mavko, "Frictional attenuation: An inherent amplitude dependence," J. Geophys. Res. **84**, 4769–4775 (1979).

[40] M. M. Sharma and A. N. Tutuncu, "Grain contact adhesion hysteresis: A mechanism for attenuation of seismic waves," Geophys. Res. Lett. **21**, 2323–2326 (1994).

[41] A. N. Tutuncu, A. L. Podio, A. R. Gregory, and M. M. Sharma, "Nonlinear viscoelastic behaviour of sedimentary rocks, II: Hysteresis effects and influence of type of fluid on elastic moduli," Geophysics **63**, 193–203 (1998).

[42] V. E. Nazarov, L. A. Ostrovsky, I. A. Soustova, and A. M. Sutin, "Nonlinear acoustics of micro-inhomogeneous media," Phys. Earth Planet. Inter. **50**, 65–73 (1988).

[43] D. H. Rogers, "An extension of a theory of mechanical damping due to dislocations," J. Appl. Phys. **33**, 781–792 (1962).

[44] T. S. Hutchinson and D. H. Rogers, "Ultrasonic damping at kilocycle frequencies in aluminum at low temperatures," J. Appl. Phys. **33**, 792–799 (1962).

Traffic noise prediction with the parabolic equation method: Validation of a split-step Padé approach in complex environments

Benoit Gauvreau[a)] and Michel Bérengier[b)]
Laboratoire Central des Ponts et Chaussées, Section Acoustique Routière et Urbaine, BP4129, 44341 Bouguenais Cedex, France

Philippe Blanc-Benon[c)]
Ecole Centrale de Lyon, Laboratoire de Mécanique des Fluides et d'Acoustique, UMR CNRS 5509, BP 163, 69131 Ecully, France

Claude Depollier[d)]
Institut d'Acoustique et de Mécanique, Université du Maine, BP 535, 72017 Le Mans, France

This study deals with sound propagation in typical traffic noise conditions. The numerical results are obtained through the split-step Padé method and the discrete random Fourier modes technique. These are first evaluated *qualitatively*, by color contour maps showing noise propagation, diffraction by an impedance discontinuity or a screen edge, and scattering by atmospheric turbulence. Next, our numerical results are *quantitatively* validated by comparison with analytical models and other parabolic equation models. For all the atmospheric conditions and geometrical configurations available in literature, the agreement between the different methods is very good, except for some cases involving the atmospheric turbulence. However, in those particular cases, the split-step Padé results are shown to be more consistent with physical theory. Finally, our method seems to be very powerful and reliable for traffic noise prediction. © *2002 Acoustical Society of America.*
[DOI: 10.1121/1.1509074]

I. INTRODUCTION

The present work focuses on traffic noise propagation, which often occurs above a plane and mixed ground (asphalt/grass) with topographical irregularities (barrier). The typical configuration and the parameters notations of this study are summarized in Fig. 1. The propagation medium (atmosphere) is either homogeneous or stratified, and eventually turbulent. We consider frequencies from 100 Hz to 5 kHz. This range is representative of the traffic noise spectrum, mainly generated by tire–road contact beyond 60 km/h. Experimental works carried out in the Laboratoire Central des Ponts et Chaussées (LCPC) showed that the equivalent sound source height is very low (of the order of a few centimeters, typically 3 cm) and that this source can be correctly modeled by a monopole.[1]

In recent past years, propagation of sound above a plane and heterogeneous ground in a homogeneous[2–9] or stratified[10] atmosphere has been extensively studied. In addition, other studies more specifically dealing with the introduction of an obstacle along the sound wave path in a homogeneous[11–18] or stratified[19–28] or turbulent[29,30] atmosphere have been carried out. When a noise barrier (or berm, slope, etc.) is located between the source and the receiver, an acoustic shadow zone appears behind the screen and can be reinforced for upward refraction. To obtain reliable predictions in this region, it is now well known that atmospheric turbulence must be taken into account.

The parabolic equation (PE) based methods seem to be the more appropriate ones, because of their ability to solve the problem of propagation above a mixed ground with topographical irregularities in a both refractive and turbulent atmosphere. Among these, the split-step Padé method[31] stands to be the more convenient within the framework of the traffic noise propagation, because of the good compromise between CPU time, accuracy in the heterogeneities location, and wide-angle properties.[32] Thus, in this paper, numerical results are obtained through the resolution of the parabolic equation with the split-step Padé method. The atmospheric turbulence is assumed to be only due to temperature fluctuations, and is numerically generated using the discrete random Fourier modes. Both theories are briefly reviewed in the following and then our model is validated. The split-step Padé results are first analyzed from a qualitative point of view: sound level contour maps effectively underline acoustic refraction, diffraction by an impedance discontinuity or a barrier edge, and scattering by atmospheric turbulence. Next, split-step Padé predictions are quantitatively compared to numerical, analytical, and experimental results already published for homogeneous and/or heterogeneous ground and/or atmosphere.

II. THE MODEL

In the linear acoustic approximation, the sound-pressure p is a solution of the elliptic Helmholtz propagation equation:

[a)]Electronic mail: Benoit.Gauvreau@lcpc.fr
[b)]Electronic mail: Michel.Berengier@lcpc.fr
[c)]Electronic mail: Philippe.Blanc-Benon@ec-lyon.fr
[d)]Electronic mail: Claude.Depollier@univ-lemans.fr
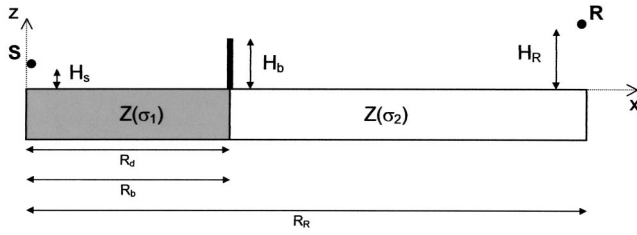
FIG. 1. Schematic representation and parameter notations.

$$\Delta p + k_0^2 p = 0, \tag{1}$$

where $k_0 = 2\pi f/c(z)n(z)$ is a reference wave number, f the frequency, c the sound speed, and n the refraction index. Assuming the azimuthal symmetry for the acoustic field, the sound-pressure $p(r,z)$ can be split into two components: a two-dimensional (2D) far field approximation for the Hankel function and a function $u(r,z)$ that is slowly range dependent. Then, assuming that the range dependence of the refraction index $n(r,z)$ is weak and neglecting the backscattering by index fluctuations, the acoustic field is dominated by forward propagating waves which are solutions of the one-way parabolic equation written in the 2D cylindrical coordinates system:[33]

$$\frac{\partial u(r,z)}{\partial r} = ik_0(Q-1)u(r,z), \tag{2}$$

where Q is the pseudo-differential operator defined as $Q^2 = 1 + \xi + \eta$ with $\xi = (1/k_0^2)(\partial^2/\partial z^2)$ and $\eta = n^2 - 1$. Assuming that Q varies very slowly in the interval $[r_0, r_0 + \Delta r]$, Eq. (2) can be directly integrated. This introduces an exponential operator[31] $\exp[\sigma(Q-1)]$, where $\sigma = ik_0\Delta r$. The next and major idea of the method is to approximate this exponential operator by a second-order Padé expansion of $Q = \sqrt{1 + \xi + \eta} = \sqrt{1 + \Im}$, which yields[34,35]

$$u(r_0 + \Delta r, z) = \exp[\sigma(Q-1)]u(r_0, z)$$

$$\approx \frac{1 + p_1\Im + p_2\Im^2}{1 + q_1\Im + q_2\Im^2} u(r_0, z), \tag{3}$$

where the coefficients p_1, p_2, q_1, and q_2 are easily deduced from a fourth-order Taylor series: $p_1 = (3+\sigma)/4$; $p_2 = (\sigma^2 + 6\sigma + 3)/48$; $q_1 = (3-\sigma)/4$; $q_2 = (\sigma^2 - 6\sigma + 3)/48$. Finally, the marching algorithm to obtain $u(r_0 + \Delta r, z)$ from $u(r_0, z)$ is expressed in terms of the coefficients p_1, p_2, q_1, q_2, η and of the operator ξ, as

$$[1 + q_1(\eta + \xi) + q_2(\eta + \xi)^2]u(r_0 + \Delta r, z)$$

$$= [1 + p_1(\eta + \xi) + p_2(\eta + \xi)^2]u(r_0, z). \tag{4}$$

The numerical scheme deduced from Eq. (4) leads to a linear system with pentadiagonal matrices, solved at each step with a standard LU decomposition method.[36] Its stability is guaranteed by imposing that the denominator and the numerator elements of the rational approximation are complex conjugates of each other, so that the resulting rational function always has a modulus equal to unit. This second-order Padé scheme can accommodate very large included angles, which is really convenient for traffic noise propagation with acoustic barriers often close to the sound source.

The ground is modeled as a locally reacting surface with a complex impedance, which may change along the sound wave path. The impedance values are calculated from the air flow resistivity σ through the Delany and Bazley model.[37] We notice that, even if the impedance discontinuity and the barrier positions (R_d and R_b, rspectively, see Fig. 1) are set identical in the presented configurations, they are of course allowed to differ in our numerical code.

The mean vertical sound speed profiles are set constant along the distance and are logarithmically shaped as previously presented by Gilbert and White:[38]

$$c(z) = c_0 + a \ln(z/z_0), \tag{5}$$

where z_0 is the roughness parameter and "a" the refraction parameter.

A nonreflecting boundary condition is imposed at the top of the computational domain by adding an absorption layer of several wavelengths thickness, so that no significant acoustic energy is artificially introduced by reflection on the upper boundary of the waveguide.

The starting field required for the initialization of the marching algorithm has a Gaussian shape, an adjustable width, and takes into account the image source weighed by a complex reflection coefficient.

The atmospheric turbulence is considered as isotropic and homogeneous, and only due to temperature fluctuations. It is modeled by an averaging on N realizations of the refraction index, which random field is generated by a superposition of discrete random Fourier modes.[39] The turbulent energy spectrum (and thus the index fluctuations) depends on the choice of the turbulence spectrum, which profile is determined by the intensity μ_0^2 and the external (or macro) scale L_0 of turbulence. The Gaussian distribution is the most commonly used for modeling this turbulence spectrum.[40] However, except when indicated, we use a von Kàrmàn spectrum of the turbulent eddies.[41] The latter introduces an internal (or micro) scale of turbulence l_0. Its special domain is wider, and thus, better takes into account the turbulent eddies responsible for acoustic scattering in the atmosphere.[39]

The introduction of an acoustic barrier along the sound wave path is modeled by setting all the $u(r,z)$ to zero at the range step $r = R_b$ for $z \leq H_b$. This induces spurious oscillations due to numerical integration. Thus, as mentioned in Refs. 19 and 29, a spatial averaging is required to obtain smooth curves and reliable predictions. Moreover, it must be noticed that no diffraction coefficient has been considered in the PE code: the diffracted energy is only due to coupling between the equations in the linear system of Eq. (4).

The computation of the sound-pressure levels up to a distance of 1 km without turbulence is done with a grid spacing $\Delta r = \lambda/2$ and $\Delta z = \lambda/6$. On a SUN Ultra 10 360 MHz work station, the CPU time is 30 s for $f = 100$ Hz and 20 min for $f = 5$ kHz.

III. MAP ILLUSTRATIONS

A. Ground effects

For conciseness, we only present here results for 4 kHz, for heights up to 20 m and for distances up to 200 m. Other
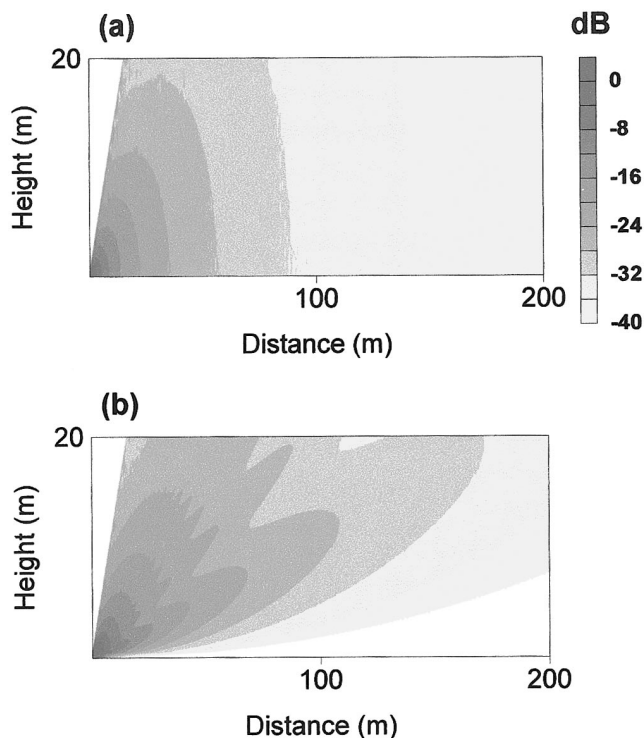
FIG. 2. Ground effects modeling. $f=4$ kHz; $H_S=10^{-2}$ m. (a): $\sigma_1=\sigma_2=3\times10^5$ kPa s m^{-2}. (b): $\sigma_1=3\times10^5$ kPa s m^{-2}; $\sigma_2=3\times10^2$ kPa s m^{-2}; $R_d=5$ m.

FIG. 3. Atmospheric effects modeling. Numerical predictions in the case of upward refraction for a nonturbulent (a) or turbulent (b) atmosphere. $f=5$ kHz; $H_S=0.03$ m; $\sigma_1=\sigma_2=3\times10^5$ kPa s m^{-2}; $a=-2$ m/s. von Kàrmàn spectrum (20 realizations); $\mu_0^2=8\times10^{-6}$; $L_0=1.1$ m; $I_0=0.05$ m.

maps with higher sound source have clearly shown interference fringes, whose number increases with the frequency and with the source height.[32] In this part, the atmosphere is assumed to be homogeneous.

In Figs. 2(a) and (b), we plotted sound-pressure levels (SPLs) relative to a reference microphone installed close to the source. For both Figs. 2(a) and (b), the sound source elevation is 10^{-2} m, the frequency is 4 kHz, and the relative sound pressure level range $[-40$ dB; 0 dB$]$, with a color step each 4 dB. For a source very close to the ground ($H_S/\lambda \ll 1$) and for homogeneous and acoustically perfectly hard ground, no interference fringes occur and the propagation lobes turn to plane wave foreheads [Fig. 2(a)]. In Fig. 2(b), the air flow resistivity turns rapidly from 3×10^5 kPa s m^{-2} (sealed concrete for instance) to 3×10^2 kPa s m^{-2} (grass) 5 m from the source position. The introduction of an impedance jump leads to *diffraction* of the acoustic energy on this discontinuity, which then acts as a secondary source and which generates new propagation lobes [Fig. 2(b)]. We also verified that the main propagation lobes due to the impedance discontinuity are turned either upward or downward depending upon whether the sound speed gradient is, respectively, negative or positive.[23,32] In comparing Fig. 2(a) to Fig. 2(b), we also observe the intuitive phenomena that the ground absorption is reinforced and that the sound energy is considerably less important for the lowest receiver heights of the 2D waveguide. In both cases, the angular limitation of the method is easily visible.

B. Atmospheric effects

For a perfectly homogeneous and reflective ground, we specifically study the effects of the medium heterogeneities on the sound propagation due to refraction and turbulence. The atmospheric turbulence has a stronger effect on the highest frequencies. This is the reason why Figs. 3(a) and (b) focus on the highest traffic noise frequency: 5 kHz. The source, surface, and atmosphere parameters values are indicated in figure captions.
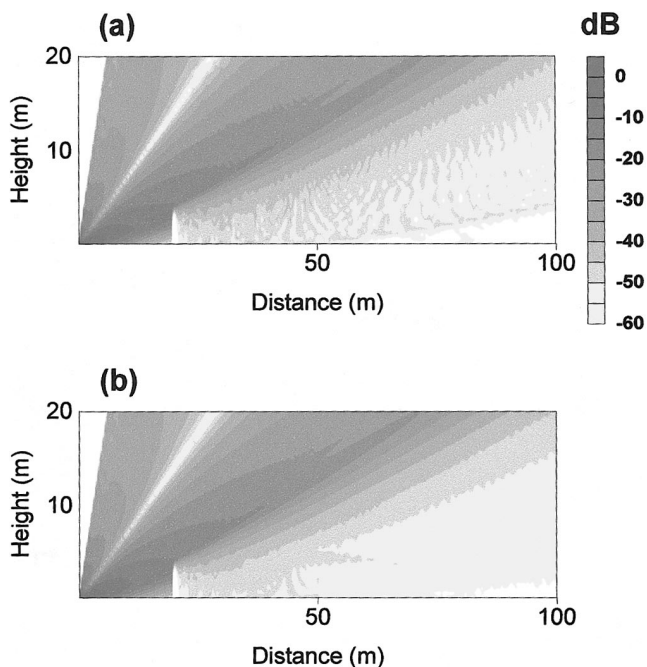
FIG. 4. Screen effects modeling. Numerical predictions in the case of upward refraction for a nonturbulent (a) or turbulent (b) atmosphere. $f=5$ kHz; $H_S=0.03$ m; $\sigma_1=\sigma_2=3\times10^5$ kPa s m^{-2}; $a=-2$ m/s; $R_b=20$ m; $H_b=4$ m. von Kàrmàn spectrum (20 realizations); $\mu_0^2=8\times10^{-6}$; $L_0=1.1$ m; $I_0=0.05$ m.

Temperature and wind vertical gradients induce vertical sound speed gradients, either positive or negative. In the first case ($a < 0$ for downward refraction), interference fringes can even appear with very low source heights compared to the wavelength. These interference patterns are minimized by the decorrelation role of the atmospheric turbulence. Our method explicitly shows this phenomena in Refs. 30, 32, 34, and 35. In the second case ($a < 0$ for upward refraction), an acoustic shadow zone appears. In this zone, relative sound-pressure levels theoretically decrease down to -60 dB, i.e., without turbulence [Fig. 3(a)]. The atmospheric turbulence enhanced the SPL in this region, by scattering the acoustic energy down to the ground. This is verified in Fig. 3(b).

C. Screen effects

We now introduce a thin screen along the sound wave path above a perfectly reflective ground. In the case of sound propagation for upward refraction, the effect of an acoustic barrier is reinforced: the diffraction fringes are turned upward as the diffraction lobes are in the presence of an impedance discontinuity,[23,32] and the acoustic shadow zone is even more emphasized. This is the most unfavorable situation for acoustic propagation [Fig. 4(a)].

When turbulence is considered [Fig. 4(b)], the sound levels behind the screen are not enhanced such as in an only *refractive* shadow zone [cf. Figs. 3(a) and (b)]. The preponderant mechanism responsible for the enhanced sound levels just behind the screen is the *diffraction* by its edge, and the sound field is almost *homogeneized* by the decorrelation role of turbulence. This implies a cancellation of the interference fringes between Figs. 4(a) and (b). For longer distances and for upward refraction, the *scattering* role of turbulence reappears and the relative contribution of diffraction and scattering to the sound spreading in the shadow region is inverted.

IV. QUANTITATIVE VALIDATION

The stability and the accuracy of the split-step Padé method have been tested for a large number of propagation conditions and frequencies.[32] In this part, the split-step Padé results are compared to those found in the literature for gradually more complex situations: homogeneous, heterogeneous, or screened ground, for a homogeneous, stratified, or turbulent atmosphere (except the case involving an impedance discontinuity in turbulent conditions, for which neither theoretical nor experimental data exist yet). Thus, we present sound-pressure levels calculated with our numerical code (SSP) under the same propagation conditions as detailed by the different authors. If there is no specific indication, the sound-pressure levels are relative to free field.

A. Homogeneous ground and atmosphere

In the trivial case that both the ground and atmosphere are homogeneous, we can compare the split-step Padé results with those given by PROPATE, a ray tracing alogirithm developed at the LCPC from Ref. 42 and largely validated by comparison with experimental data. In [100 Hz; 5 kHz] frequencies and [3×10^2 kPa s m^{-2}; 3×10^5 kPa m^{-2}] flow resistivities ranges, perfect agreement has been found for all
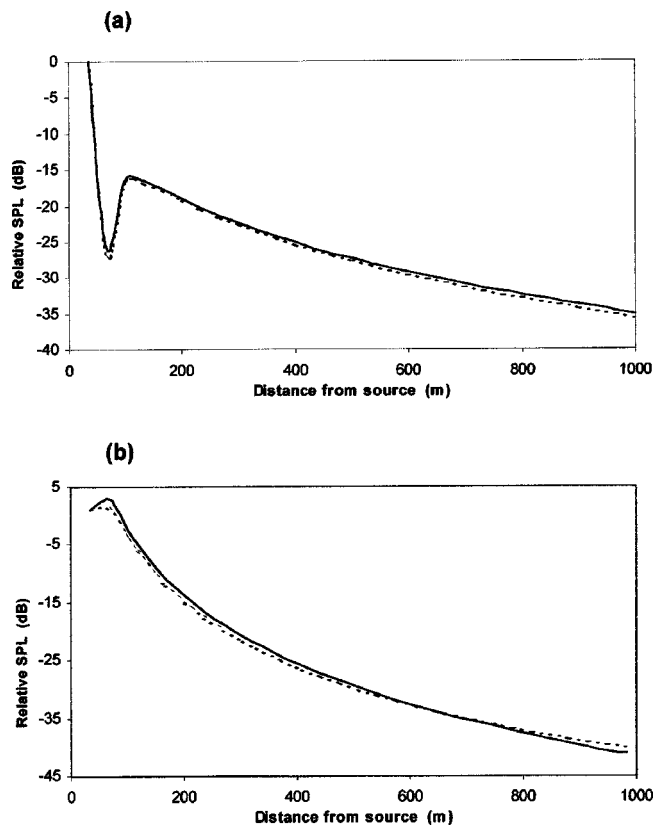
FIG. 5. Split-step Padé predictions (—) compared with ray method results (- - -) from PROPATE (Ref. 42). $f = 5$ kHz; $H_S = H_R = 1$ m. (a): $\sigma_1 = \sigma_2 = 2 \times 10^5$ kPa s m^{-2}. (b): $\sigma_1 = \sigma_2 = 3 \times 10^2$ kPa s m^{-2}.

cases. Figures 5(a) and (b) show two examples of SPL relative to a reference microphone, calculated with both methods for the highest traffic noise frequency 5 khz. The curves are always almost overlaying, including in destructive interference regions which appear when $H_S/\lambda \gg 1$ and for high flow resistivity values [Fig. 5(a)].

B. Homogeneous ground-stratified atmosphere

SPL representation versus distance from the source position for a monochromatic acoustic sound wave in a stratified atmosphere has been treated by Galindo among others. She compared her PE calculations (CNPE) with Green's function parabolic equation and with fast field program predictions.[7] For distances from the sound source up to 1 km, the agreement was very satisfactory. Thus, her numerical results are used as *reference* data in these propagation conditions, involving homogeneous porous ground. In Figs. 6(a) and (b), we have plotted the relative SPL computed with our numerical code in the cases of, respectively, upward refraction ($a = -2$ ms^{-1}) and downward refraction ($a = +2$ ms^{-1}). Numerical data are obtained for $f = 500$ Hz.

Figure 6(a) shows a rapid decay in the relative sound levels, as pronounced with the SSP predictions as with the CNPE ones. After 150 m, the relative level are less than -68 dB and strong oscillations occur, with a mean value nearly constant: this is identified with the acoustic shadow zone, where analytical theories do not predict any acoustic energy. In reality, we know that atmospheric turbulence scatters

(a)

(b)

FIG. 6. Split-step Padé predictions (——) compared with CNPE results (■) from Galindo (Ref. 7). $f = 500$ Hz; $H_S = 1.5$ m; $H_R = 2$ m; $\sigma_1 = \sigma_2 = 2 \times 10^2$ kPa s m^{-1}. (a) Upwind conditions, $a = -2$ m/s, (b) downwind conditions, $a = +2$ m/s.

FIG. 7. Split-step Padé predictions in deterministic ($\times$) or turbulent cases: (---) 10 realizations; (——) 20 realizations; (—) 40 realizations compared with experimental data (●) from Wiener and Keast (Ref. 45). $f = 424$ Hz; $H_S = 1.2$ m; $H_R = 0.6$ m; $\sigma_1 = \sigma_2 = 3 \times 10^2$ kPa s m^{-2}; $a = -0.5$ m/s. von Kàrmàn spectrum; $\mu_0^2 = 7.7 \times 10^{-6}$; $L_0 = 1.1$ m; $l_0 = 0.05$ m.

predictions with and without turbulence in the same propagation conditions as in the Wiener and Keast experiments.[45] For nonturbulent conditions, the relative SPL predictions rapidly decrease, whereas turbulent predictions are very close to the experimental values. Turbulent results are indicated for three different numbers of realizations, in order to give an idea of their convergence. The slight discrepancy between experimental and numerical results can be explained in terms of uncertainty in the acoustic, climatic, and impedance measurements. However, the relative SPL profiles are very similar as far as turbulence is considered.

D. Impedance discontinuity-homogeneous atmosphere

Craddock and White[2] have first introduced an impedance discontinuity in a numerical code based on the PE (finite differences with the Cranck–Nicolson scheme—CNPE). They validated their results by comparing them with analytical models predictions, in particular one from Rasmussen.[46] They next chose a SPL representation versus distance (and thus for a fixed frequency) to illustrate in a better way the jump in the impedance values, but for which there were neither experimental nor numerical data available for comparison. Their results for either a homogeneous and perfectly reflective ground or heterogeneous hard/soft ground are plotted in Fig. 8 and compared to split-step Padé results for the same cases. We also mentioned in Fig. 8 the results given by an analytical model developed at the LCPC and based on Rasmussen's technique.[46]

The agreement between the three methods is excellent, except in the destructive interference region where the sound-pressure levels dramatically fall and where the accuracy in the grid spacing is of great importance.

E. Impedance discontinuity-stratified atmosphere

For this more complex situation involving a sound wave propagating above a heterogeneous ground (without screen) through a stratified atmosphere, only upward refraction cases exist in the literature. In Ref. 10, Bérengier and Daigle compared indoor experimental data obtained for propagation of

acoustic energy in this region. When distance and frequency increase, the introduction of these effects is necessary to obtain reliable numerical predictions. It will be discussed later in this paper.

In downwind conditions [Fig. 6(b)], the predictions obtained with the two numerical methods are identical for distances up to 1 km: the respective relative SPL values are very close to each other, except in the destructive interference regions. A slight difference appears in those values and increases with the distance. The nature of these errors has been presented by Galindo in terms of a *level* error introduced by the selection of the starting field, and of a *phase* error generated by the rational linear approximation [Eq. (3)] and worsened in strong downward refraction conditions.[7,43]

C. Homogeneous ground-turbulent atmosphere

The first effect of atmospheric turbulence on acoustic field is decorrelation of coherent wave front, which minimizes destructive interferences and which smooths sound level profiles when $H_S/\lambda \gg 1$, or for downward refraction ($a > 0$), or if the surface is concave. In Refs. 32, 34, and 35, good agreement has been found between split-step Padé predictions and Daigle's experimental data[44] for those propagation situations.

The sound effect of turbulence is scattering of sound energy downward into the shadow region when we consider propagation above a convex surface or for upward refraction ($a < 0$). This latter case is studied in Fig. 7. We plot SSP

FIG. 8. Split-step Padé predictions for a homogeneous (---) and heterogeneous (——) ground compared with CNPE results from Craddock and White (Ref. 2) in the same conditions (♦ and ■, respectively). Also plotted: results from Rasmussen model (Ref. 46) for heterogeneous ground (●). f = 160 Hz; H_S = 1.5 m; H_R = 1.8 m; $\sigma_1 = 2 \times 10^5$ kPa s m^{-2}; $\sigma_2 = 2 \times 10^2$ kPa s m^{-2}; R_d = 50 m.

sound above a curved surface having an impedance discontinuity, with analytical predictions given by a residue series solution. Assuming a far field approximation in our PE method, we proceed to a scale change in order to correctly compare our results to Bérengier and Daigle's data (Fig. 9). We thus multiply by 10 the geometrical parameters, and divide by 10 the frequency and the air flow resistivity.

In Fig. 9, the shorter range split-step Padé results provide a better fit to experimental data than Bérengier and Daigle's analytical predictions. According to the authors, this deviation beyond the discontinuity could be explained by the choice of the edge diffraction coefficient $D = 1$ in their model.[10] The discrepancy between the split-step Padé calculations and the experimental acquisitions at ''long'' distances could be attributed, in one part, to the inaccuracy in the experimental air flow resistivity measurement and, in another part, to the impedance discontinuity location. This last point is amplified by the scale factor and by the very strong linear gradient value, due to the analogy between sound propagation in a homogeneous atmosphere above a curved surface and sound propagation in a stratified atmosphere above a plane surface.[10]
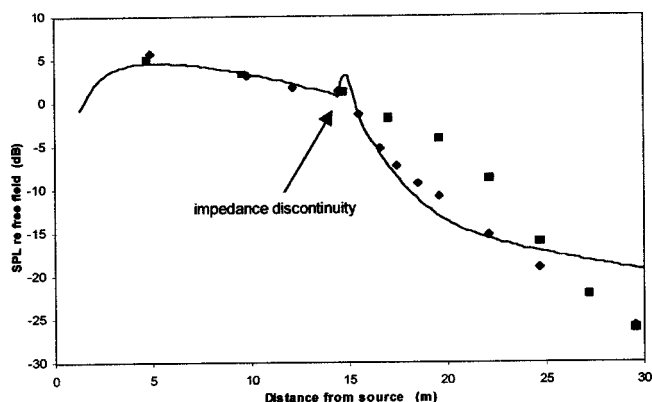
FIG. 9. Split-step Padé predictions (——) compared with experimental (♦) and theortical (■) results from Bérengier and Daigle (Ref. 10). f = 400 Hz; $H_S = H_R$ = 0.5 m; $\sigma_1 = 5 \times 10^4$ kPa s m^{-2}; σ_2 = 50 kPa s m^{-2}; R_d = 15 m. a = -68.8 m/s (linear gradient until the altitude z = 1.2 m).
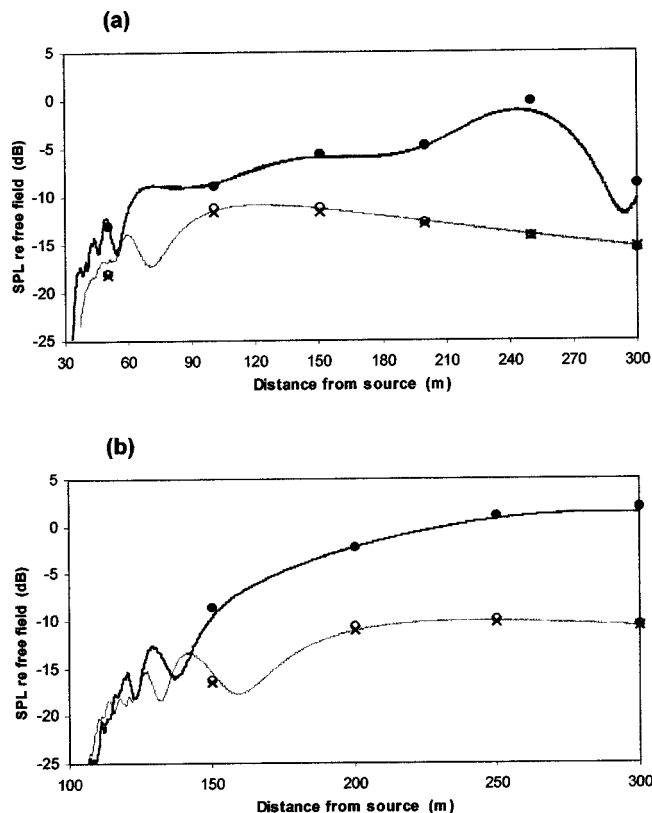
FIG. 10. Split-step Padé predictions for a = 0 m/s (thin line) and a = 2 m/s (thick line) compared with Salomons predictions (Ref. 19) for the same values (○ and ●, respectively), and those from Hadden and Pierce—Ref. 47 (×) for a homogeneous atmosphere (a = 0 m/s). f = 1 kHz; $H_S = H_R$ = 2 m; $\sigma_1 = \sigma_2 = 3 \times 10^2$ kPa s m^{-2}. (a) R_b = 30 m; H_b = 4 m. (b) R_b = 100 m; H_b = 6 m.

F. Acoustic barrier-homogeneous and stratified atmosphere

The predicted results are directly compared to those from Salomons[19] in a downward refracting and nonturbulent atmosphere, for the same physical parameters values (see captions) and for identical screen locations and dimensions: R_b = 30 m, H_b = 4 m [Fig. 10(a)] and R_b = 100 m, H_b = 6 m [Fig. 10(b)]. In each figure, we plot as a reference Hadden and Pierce's analytical predictions, given for a homogeneous atmosphere and an absorbent barrier.[47] It must be emphasized that no diffraction coefficient has been considered in our PE code: the diffracted energy is only due to coupling in the linear system of Eq. (4). The agreement between the various models is very good for all the propagation conditions and geometrical configurations, except just downstream from the screen, where some oscillations occur in the relative SPL due to numerical instabilities in the PE solution just behind the screen edge [Figs. 10(a) and (b)].

G. Acoustic barrier-homogeneous and turbulent atmosphere

Now, the split-step Padé results are compared to those from Forssén[29] for a turbulent but nonstratified atmosphere, and for the frequencies f = 500 Hz [Figs. 11(a) and (b)] and f = 1 kHz [Figs. 12(a) and (b)]. They are calculated with an averaging on 10 realization, using a Gaussian spectrum for

(a)

(b)
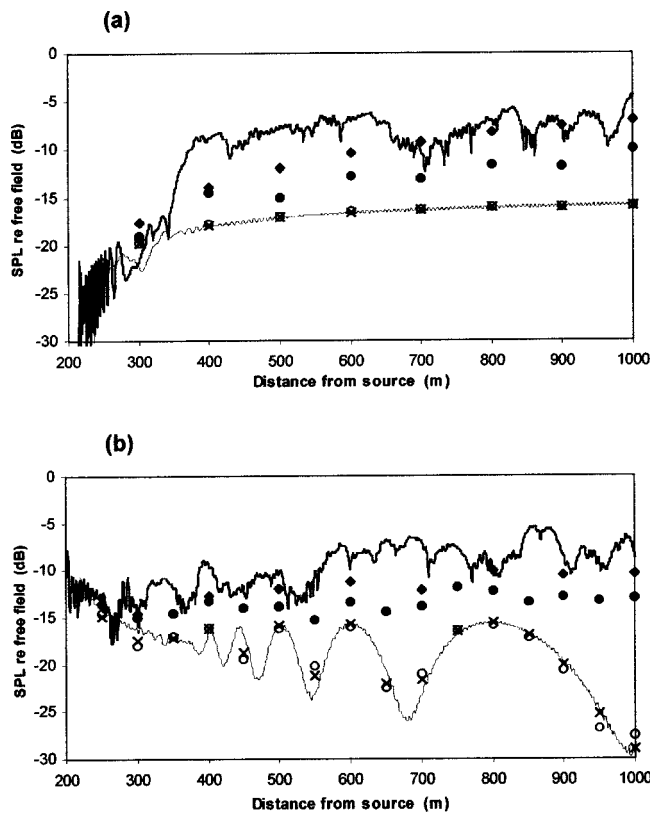
FIG. 11. Split-step Padé predictions for a homogeneous (thin line) and turbulent (thick line) atmosphere compared with Forssén predictions (Ref. 29) for the same values ($\bigcirc$ and $\bullet$, respectively). Also plotted: results from the Hadden and Pierce model (Ref. 47) for a homogeneous atmosphere ($\times$) and results from the Daigle model (Ref. 48) for a turbulent atmosphere ($\blacklozenge$). $f = 500$ Hz; $H_S = 0$ m; $\sigma_1 = \sigma_2 = 3 \times 10^5$ kPa s m^{-2}; $R_b = 200$ m; $H_b = 20$ m; Gaussian distribution (10 realizations); $\mu_0^2 = 3 \times 10^{-6}$; $L = 1.1$ m. (a) $H_R = 0$ m. (b) $H_R = 20$ m.

the turbulence as the author did. In this case again, the Hadden and Pierce calculations for a homogeneous atmosphere and an absorbent barrier are indicated as a reference. In the turbulent cases, we also plot predictions given by Daigle's model, which uses diffraction and scattering cross section theories.[48] The relative SPLs existing *behind the screen* are given for receiver heights $H_R = 0$ m [Figs. 11(a) and 12(a)] and $H_r = H_b$ [Figs. 11(b) and 12(b)]. Location and dimension of the barrier are, respectively, $R_b = 200$ m and $H_b = 20$ m for Fig. 11, and $R_b = 100$ m and $H_b = 10$ m for Fig. 12.

In deterministic cases, the three methods (split-step Padé, Forssén, Hadden, and Pierce) give exactly the same results, except immediately behind the screen as previously explained. When $H_R / \lambda \ll 1$, no interference occurs, and the relative SPL tends toward an asymptotic limit [Figs. 11(a) and 12(a)]. For higher receivers, interference fringes appear where the different methods give very similar predictions [Figs. 11(b) and 12(b)].

In order to limit the variation parameter number in the turbulent cases, we use a *Gaussian* distribution for the index fluctuations as Forssén did. Generally speaking, our results are very close to Daigle's and slightly stronger than Forssén's. As mentioned by Forssén[29] by comparison with Daigle's model, Forssén's predictions sometimes underestimate the sound-pressure levels existing in the shadow zone

(a)

(b)
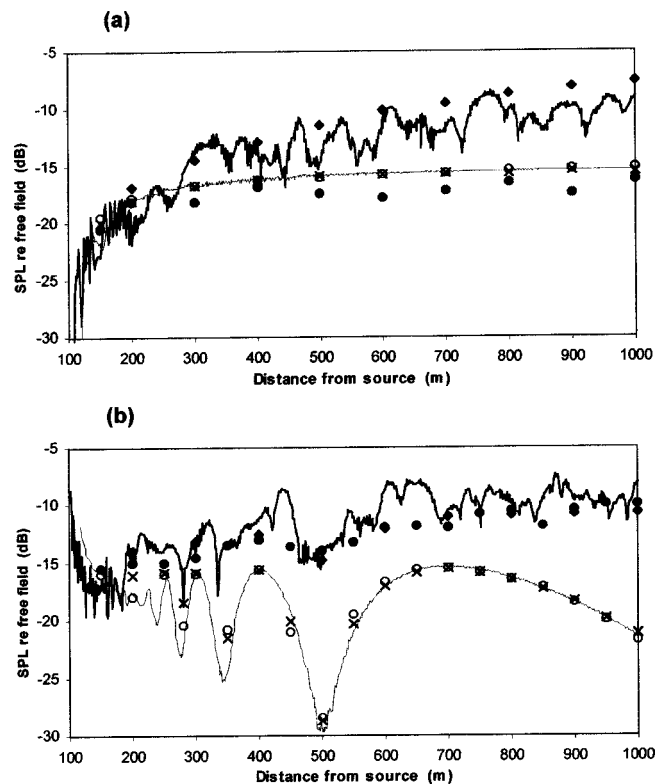
FIG. 12. Split-step Padé predictions for a homogeneous (thin line) and turbulent (thick line) atmosphere compared with Forssén predictions (Ref. 29) for the same values ($\bigcirc$ and $\bullet$, respectively). Also plotted: results from the Hadden and Pierce model (Ref. 47) for a homogeneous atmosphere ($\times$) and results from the Daigle model (Ref. 48) for a turbulent atmosphere ($\blacklozenge$). $f = 1000$ Hz; $H_S = 0$ m; $\sigma_1 = \sigma_2 = 3 \times 10^5$ kPa s m^{-2}; $R_b = 100$ m; $H_b = 10$ m; Gaussian distribution (10 realizations); $\mu_0^2 = 3 \times 10^{-6}$; $L = 1.1$ m. (a) $H_R = 0$ m. (b) $H_R = 10$ m.

[Fig. 12(a)]. On the contrary, the discrete random Fourier modes technique predicts more enhanced sound levels in this region and demonstrates again its efficiency and its accuracy.

V. CONCLUSION

The split-step Padé method coupled with the discrete random Fourier modes technique have been validated for a large number of propagation configurations. Qualitatively, sound maps illustrated propagation mechanisms in the presence of a monopole source very close to the ground, an impedance discontinuity, an acoustic barrier, and a stratified or turbulent atmosphere.

Then, sound-pressure levels computed with the split-step Padé method were compared with relevant data from the literature. The quantitative agreement is generally very good, without introducing any additional heuristic coefficient in screened configurations. Thus, our PE-based method appears to be reliable to predict traffic noise propagation in such complex environments.

This work opens the field for further investigations, notably the more precise description of sound speed profiles in the vicinity of multishaped obstacles. Outdoor controlled experiments have been realized in order to validate the code for such complex configurations, for which no data exist yet. This will be the subject of a further paper.

[1] J. F. Hamet, M. A. Pallas, D. Gaulin, and M. Bérengier, "Acoustical modeling of road vehicles for traffic noise predictions: Determination of the source height," 16th ICA-ASA Congress, Seattle, USA, J. Acoust. Soc. Am. **103**, 2919 (1998).

[2] J. M. Craddock and M. J. White, "Sound propagation over a surface with varying impedance: A parabolic equation approach," J. Acoust. Soc. Am. **91**, 3184–3191 (1992).

[3] K. B. Rasmussen, "Scale model simulation of sound propagation over an impedance discontinuity," Proceedings of Inter-Noise **93**, 1711–1714 (1993).

[4] M. Galindo, "Application of the parabolic approximation method to sound propagation above ground with impedance variations," Proceedings of the Sixth International Symposium on Long Range Sound Propagation, Ottawa, Canada, 12–14 June 1994, pp. 394–407.

[5] D. C. Hothersall and J. N. B. Harriott, "Approximate models for sound propagation above multi-impedance plane boundaries," J. Acoust. Soc. Am. **97**, 918–926 (1995).

[6] J. S. Robertson, P. J. Schlatter and W. L. Siegmann, "Sound propagation over impedance discontinuities with the parabolic approximation," J. Acoust. Soc. Am. **99**, 761–767 (1996).

[7] M. Galindo, "The parabolic equation method for outdoor sound propagation," Ph.D. thesis, Technical University of Denmark, 1996.

[8] M. R. Stinson and G. A. Daigle, "Surface wave formation at an impedance discontinuity," J. Acoust. Soc. Am. **102**, 3269–3275 (1997).

[9] P. Boulanger, T. Waters-Fuller, K. Attenborough, and K. M. Li, "Models and measurements of sound propagation from a point source over mixed impedance ground," Proceedings of the Seventh International Symposium on Long Range Sound Propagation, Lyon, France, 24–26 July 1996, pp. 291–305.

[10] M. Bérengier and G. A. Daigle, "Diffraction of sound above a curved surface having an impedance discontinuity," J. Acoust. Soc. Am. **84**, 1055–1060 (1988).

[11] Y. W. Lam and S. C. Roberts, "A simple method for accurate prediction of finite barrier insertion loss," J. Acoust. Soc. Am. **93**, 1445–1452 (1993).

[12] D. J. Saunders and R. D. Ford, "A study of the reduction of explosive impulses by finite sized barriers," J. Acoust. Soc. Am. **94**, 2859–2875 (1993).

[13] K. B. Rasmussen, "Model experiments related to outdoor propagation over an earth berm," J. Acoust. Soc. Am. **96**, 3617–3620 (1994).

[14] E. M. Salomons, "Sound propagation in complex outdoor situations with a non-refracting atmosphere: Model based on analytical solutions for diffraction and reflection," Acustica **83**, 436–454 (1997).

[15] S. S. T. Ho, I. J. Busch-Vishniac, and D. T. Blastock, "Noise reduction by a barrier having a random edge profile," J. Acoust. Soc. Am. **101**, 2669–2676 (1997).

[16] M. Salomons, A. C. Geerlings, and D. Duhamel, "Comparison of a ray model and a Fourier-boundary element method for traffic noise situations with multiple diffractions and reflections," Acustica **83**, 35–47 (1997).

[17] J. P. Chambers, G. J. Wadsworth, M. Kelly, and R. Raspet, "Scale model experiments on the insertion loss of wide and double barriers and barriers under turbulent conditions," Proceedings of the Eighth International on Long Range Sound Propagation, Penn State College, 1998, pp. 153–167.

[18] J. S. Robertson, "Sound propagation over a large wedge: A comparison between the geometrical theory of diffraction and the parabolic equation," J. Acoust. Soc. Am. **106**, 113–119 (1999).

[19] E. M. Salomons, "Diffraction by a screen in downwind sound propagation: A parabolic equation approach," J. Acoust. Soc. Am. **95**, 3109–3117 (1994).

[20] K. B. Rasmussen, "Sound propagation over screened ground under upwind conditions," J. Acoust. Soc. Am. **100**, 3581–3586 (1996).

[21] E. M. Salomons, "Noise barriers in a refracting atmosphere," Appl. Acoust. **47**, 217–238 (1996).

[22] K. B. Rasmussen and M. Galindo Arranz, "The insertion loss of screens under the influence of wind," J. Acoust. Soc. Am. **104**, 2692–2698 (1998).

[23] B. Gauvreau, M. Bérengier, Ph. Blanc-Benon, and C. Depollier, "Impedance discontinuity and range dependent refraction profile: A numerical study," in Ref. 17, pp. 225–240.

[24] K. M. Li and Q. Wang, "A BEM approach to assess the acoustic performance of noise barriers in a refracting atmosphere," J. Sound Vib. **211**, 663–681 (1998).

[25] S. Taherzadeh, K. M. Li, and K. Attenborough, "Sound propagation in a refracting medium above an uneven terrain," in Ref. 17, pp. 101–111.

[26] N. Barriere and Y. Gabillet, "Sound propagation over a barrier with realistic wind gradients. Comparison of wind tunnel experiments with GFPE computations," Acustica **85**, 325–334 (1999).

[27] D. Zhu, "Use of the parabolic equation method for predictions of outdoor sound propagation in complex environments," Proceedings of the Sixth International Congress on Sound and Vibration, Copenhagen, Denmark, 1999, pp. 669–676.

[28] E. M. Salomons, "Reduction of the performance of a noise screen due to screen-induced wind-speed gradients. Numerical computations and wind-tunnel experiments," J. Acoust. Soc. Am. **105**, 2287–2293 (1999).

[29] J. Forssén, "Calculation of sound reduction by a screen in a turbulent atmosphere using the parabolic equation method," Acustica **84**, 599–606 (1998).

[30] B. Gauvreau, M. Bérengier, Ph. Blanc-Benon, and C. Depollier, "A numerical method to predict sound propagation for realistic road environments," J. Acoust. Soc. Am. **105**, 1335(A) (1999).

[31] M. D. Collins, "A split-step Padé solution for the parabolic equation method," J. Acoust. Soc. Am. **93**, 1736–1742 (1993).

[32] B. Gauvreau, "Influence des conditions micrométéorologiques sur l'efficacité des écrans acoustiques," Ph.D. thesis, Université du Maine, Le Mans, France, 1999.

[33] F. D. Tappert and R. H. Hardin, "Computer simulation of long-range ocean acoustic propagation using the parabolic equation method," Proceedings of the Eighth International Congress on Acoustics, 1974, p. 452.

[34] P. Chevret, "Simulation numérique des effets de la turbulence atmosphérique sur la propagation du son dans l'atmosphère," Ph.D. thesis, Ecole Centrale de Lyon, France, 1994, No. 94-18.

[35] P. Chevret, Ph. Blanc-Benon, and D. Juvé, "A numerical model for sound propagation through a turbulent atmospheres near the ground," J. Acoust. Soc. Am. **100**, 3587–3599 (1996).

[36] W. H. Press, B. P. Flannery, S. A. Teukolsky, and W. T. Vetterling, *Numerical Recipes* (Cambridge University Press, Cambridge, 1992).

[37] M. E. Delany and E. N. Bazley, "Acoustical properties of fibrous absorbent materials," Appl. Acoust. **3**, 105–116 (1970).

[38] K. E. Gilbert and M. J. White, "Application of the parabolic equation to sound propagation in a refracting atmosphere," J. Acoust. Soc. Am. **85**, 630–637 (1989).

[39] D. Juvé, Ph. Blanc-Benon, and P. Chevret, "Numerical simulation of sound propagation through a turbulent atmosphere," Proceedings of the Fifth International Symposium on Long Range Sound Propagation, Milton Keynes, UK, 24–26 May 1992, pp. 282–296.

[40] G. A. Daigle, J. E. Piercy, and T. F. W. Embleton, "Line-of-sight propagation through atmospheric turbulence near the ground," J. Acoust. Soc. Am. **74**, 1505–1513 (1983).

[41] A. Ishimaru, *Wave Propagation and Scattering in Random Media* (Academic, New York, 1978), Vol. 2.

[42] J. E. Piercy, T. F. W. Embleton, and L. C. Sutherland, "Review of noise propagation in the atmosphere," J. Acoust. Soc. Am. **61**, 1403–1418 (1977).

[43] M. Galindo, "Approximations in the PE method. Phase and level errors in a downward refracting atmosphere," Proceedings of the Seventh International Symposium on Long Range Sound Propagation, Lyon, France, 1996, pp. 235–255.

[44] G. A. Daigle, J. E. Piercy, and T. F. W. Embleton, "Effects of atmospheric turbulence on the interference of sound waves near a hard boundary," J. Acoust. Soc. Am. **64**, 622–630 (1978).

[45] F. M. Wiener and D. N. Keast, "Experimental study of the propagation of sound over ground," J. Acoust. Soc. Am. **31**, 724–733 (1959).

[46] K. B. Rasmussen, "A note on the calculation of sound propagation over impedance jumps and screens," J. Sound Vib. **84**, 598–602 (1982).

[47] W. J. Hadden and A. D. Pierce, "Sound diffraction around screens and wedges for arbitrary point source locations," J. Acoust. Soc. Am. **69**, 1266–1276 (1981). Erratum **71**, 1290 (1982).

[48] G. A. Daigle, "Diffraction of sound by a noise barrier in the presence of atmospheric turbulence," J. Acoust. Soc. Am. **71**, 847–854 (1982).

Computation of scattering from N spheres using multipole reexpansion

Nail A. Gumerov[a] and Ramani Duraiswami[b]

Perceptual Interfaces and Reality Laboratory, Institute for Advanced Computer Studies,
University of Maryland, College Park, Maryland 20742

A computational technique for the solution of problems of wave scattering from multiple spheres is developed. This technique, based on the T-matrix method, uses the theory for the translation and reexpansion of multipole solutions of the Helmholtz equation for fast and exact recursive computation of the matrix elements. The spheres can have prescribed radii, impedances, and locations. Results are validated by comparison with boundary element calculations, and by convergence analyses. The method is much faster than numerical methods based on discretization of space, or of the sphere surfaces. An even faster method is presented for the case when the spheres are aligned coaxially. © *2002 Acoustical Society of America.* [DOI: 10.1121/1.1517253]

PACS numbers: 42.30.Fn [LLT]

I. INTRODUCTION

Numerous practical problems of acoustic and electromagnetic wave propagation require computation of the field scattered by multiple objects. Examples include the scattering of acoustic waves by objects (e.g., the scattering of sound by humans and the environment), light scattering by clouds and the environment, electromagnetic waves in composite materials and the human body, pressure waves in disperse systems (aerosols, emulsions, bubbly liquids), etc. Our interest is in modeling the cues that arise due to scattering of sound and light, and to use this information in simulating audio and video reality (Duda and Martens, 1998; Duraiswami *et al.*, 2000).

In many cases the scatterers are spheres, or can be modeled as such. Such modeling is convenient for parametrization of large problems, since each sphere can be characterized by a few quantities such as the coordinates of its center, its radius, and its impedance. This impedance will in general be a complex quantity, and characterizes the absorbing/reflecting properties of the body/surface. For example, we are exploring the head and the torso (Gumerov *et al.*, 2002; Algazi *et al.*, 2002). In fluid mechanical problems, bubbles, droplets, or dust particles can be assumed spherical (Gumerov *et al.*, 1988; Duraiswami and Prosperetti, 1995).

We are interested in computing the solution of multiple scattering from N spheres, with specified impedance boundary conditions at their surfaces. Numerical methods such as boundary-element methods (BEM), finite-element methods (FEM), or finite difference methods (FDM) are well known. Despite the relative advantages of these methods they all share a common deficiency related to the necessity of discretization of either the boundary surfaces or of the complete space. Discretization introduces a characteristic size (or length scale) l_* of the surface or spatial element. For accu-

rate and stable computations the change of discretization length l_* must not affect the results. This leads to a requirement that this size should be much smaller than the wavelength λ, i.e., $l_* \ll \lambda$. Practically this condition is $l_* < B\lambda$, where B is some constant smaller than 1. If computations are required for high frequencies (or short waves), this leads to very fine surface or spatial meshes. For example, in computations of scattering of sound by human heads (Kahana, 2001; Katz, 2001), for 20 kHz sound in air in normal conditions, the wavelength is 1.7 cm, while the diameter of the typical human head is $D = 17$ cm. For accuracy the length of a surface element should be, say, 6 times smaller than 1.7 cm, i.e., 60 times smaller than the diameter of the head. This gives a 24 000-element discretization of the head surface in the case where triangular elements are used in the BEM. Such discretizations require solution of very large linear systems with dense interinfluence matrices in the case of the BEM, and even larger but sparse matrices in the case of the FEM/FDM. Solutions of these equations using direct or iterative methods are costly in terms of CPU time and memory.

Another approach to solve this problem is a semi-analytical method such as the T-matrix method (Waterman and Truell, 1961; Peterson and Strom, 1974; Varadan and Varadan, 1980; Mischenko *et al.*, 1996; Koc and Chew, 1998). In this method, the scattering properties of a scatterer and of the collection are characterized in terms of the so-called T-matrices that act on the coefficients of the local expansion of the incoming wave, centered at the scatterer, and transform them into the coefficients of an outgoing wave from the scatterer.

There are two basic challenges related to using the T-matrix method to solve multiple scattering problems. The first challenge is to obtain the solution for a single scatterer. In the case of complex shapes and boundary conditions this solution can be obtained either numerically or via analytical or semi-analytical techniques, based on decomposition of the original shape to objects of simpler geometry. The field scattered by sound-soft, sound-hard, and elastic spheres placed

---

[a] Electronic mail: gumerov@umiacs.umd.edu;
 URL: http://www.umiacs.umd.edu/users/gumerov
[b] Electronic mail: ramani@umiacs.umd.edu;
 URL: http://www.umiacs.umd.edu/users/ramani

in the field of a plane wave were considered in several papers (e.g., Marnevskaya, 1969, 1970; Huang and Gaunaurd, 1995). In the present paper we consider the practically important case of spherical objects with impedance boundary conditions in an arbitrary incident field (in particular that generated by a source). In this case a solution for a single scatterer in an arbitrary incident field can be obtained analytically.

The second challenge is related to computation of the T-matrices (or matrices of the translation coefficients for the Helmholtz equation). Several studies that are dedicated to scattering by two spheres (Marnevskaya, 1969, 1970; Gaunnaurd and Huang, 1994; Gaunaurd *et al.*, 1995) use representations of the translation coefficients via the Clebsch–Gordan coefficients or 3-*j* Wigner symbols. We should notice that while this method provides exact computation of T-matrix elements, it is time consuming, and perhaps is practical only for a small number of spheres. Brunning and Lo (1971) considered the multiple scattering of electromagnetic waves by spheres, and pointed out that the computational work can be reduced by several orders of magnitude if the computation of the translation coefficients could be performed more efficiently, e.g., recursively. In their study they applied recursive computation of these coefficients for the case when the sphere centers are located on a line. This is always true for two spheres, and is a special case for three or more spheres. In the present paper we refer to this as the "coaxial" case. A general three-dimensional case of acoustical scattering by *N* objects using the T-matrix method was considered by Koc and Chew (1998). They proposed using a numerical evaluation of integral forms of the translation operators (Rokhlin, 1993) and the fast multipole method (FMM) applied to an iterative solution of a large system of equations that appear in the T-matrix method.

In this paper we use a variant of the T-matrix technique that is specialized to the solution of the problem of multiple scattering from *N* spheres arbitrarily located in three-dimensional space. The distinguishing feature of our algorithm is utilization of a fast recursive procedure for exact computation of the T-matrix elements. We should note that the recurrence relations for the three-dimensional scalar addition theorem for the Helmholtz equation were obtained by Chew (1992). These relations were derived for local-to-local (regular-to-regular) translations of the solutions of the Helmholtz equation, but can be extended to far-to-far and far-to-local translations. This was mentioned by Chew (1992) and details can be found in our study (Gumerov and Duraiswami, 2001a) where also relations for arbitrary rotations and simplified expressions for coaxial translations are presented. The savings that would arise from use of fast multipole methods can also be realized in our problem though they are not considered here as our focus is on the case of relatively small numbers of scatterers.

We have developed software implementing this technique. We compare the results of the computations with numerical and analytical solutions, and demonstrate the computational efficiency of our method in comparison with commercial BEM software. The results show that the developed method compares favorably in both accuracy and speed
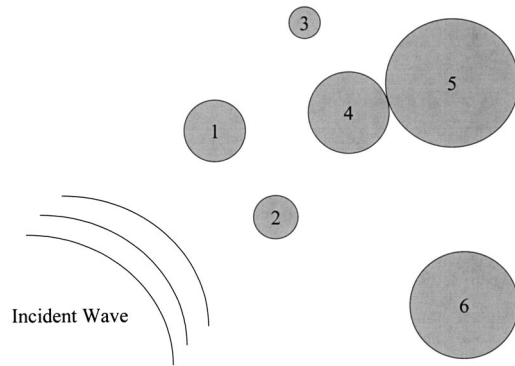
FIG. 1. The multiple scattering problem considered in this paper.

up of computations (in some cases by several orders of magnitude).

II. STATEMENT OF THE PROBLEM

Consider the problem of sound scattering by *N* spheres with radii $a_1, \ldots, a_N$ situated in an infinite three-dimensional space as shown in Fig. 1. The coordinates of the centers of the spheres are denoted as $\mathbf{r}'_p = (x'_p, y'_p, z'_p)$, $p = 1, \ldots, N$. The scattering problem in the frequency domain is reduced to solution of the Helmholtz equation for complex potential $\psi(\mathbf{r})$,

$$\nabla^2 \psi + k^2 \psi = 0, \tag{1}$$

with the following general impedance boundary conditions on the surface S_p of the pth sphere:

$$\left(\frac{\partial \psi}{\partial n} + i \sigma_p \psi \right) \bigg|_{S_p} = 0, \quad p = 1, \ldots, N, \tag{2}$$

where k is the wave number and σ_p are complex admittances, and $i = \sqrt{-1}$. In the particular case of sound-hard surfaces ($\sigma_p = 0$) we have the Neumann boundary conditions,

$$\partial \psi / \partial n |_{S_p} = 0, \tag{3}$$

and in the case of sound-soft surfaces ($\sigma_p = \infty$) we have the Dirichlet boundary conditions,

$$\psi |_{S_p} = 0. \tag{4}$$

Usually the potential is represented in the form:

$$\psi(\mathbf{r}) = \psi_{\text{in}}(\mathbf{r}) + \psi_{\text{scat}}(\mathbf{r}), \tag{5}$$

where $\psi_{\text{scat}}(\mathbf{r})$ is the potential of the scattered field. Far from the region occupied by spheres the scattered field should satisfy the Sommerfeld radiation condition:

$$\lim_{r \to \infty} r \left(\frac{\partial \psi_{\text{scat}}}{\partial r} - i k \psi_{\text{scat}} \right) = 0. \tag{6}$$

III. SOLUTION USING MULTIPOLE TRANSLATION AND REEXPANSION

A. Decomposition of the scattered field

Due to the linearity of the problem the scattered field can be represented in the form

$$\psi_{\text{scat}}(\mathbf{r}) = \sum_{p=1}^{N} \psi_p(\mathbf{r}), \qquad (7)$$

where $\psi_p(\mathbf{r})$ can loosely be thought of as the change in the scattered field introduced by the pth sphere, though of course it contains the influence of all the spheres. More precisely, each potential $\psi_p(\mathbf{r})$ is regular outside the pth sphere and satisfies the Sommerfeld radiation condition

$$\lim_{r \to \infty} r\left(\frac{\partial \psi_p}{\partial r} - ik\psi_p\right) = 0, \quad p = 1, \ldots, N. \qquad (8)$$

B. Multipole expansion

Let us introduce N reference frames connected with the center of each sphere. In spherical polar coordinates $\mathbf{r} - \mathbf{r}_p' = \mathbf{r}_p = (r_p, \theta_p, \varphi_p)$, the solution of the Helmholtz equation that satisfies the radiation condition (8) can be represented in the form

$$\psi_p(\mathbf{r}) = \sum_{n=0}^{\infty} \sum_{m=-n}^{n} A_n^{(p)m} S_n^m(\mathbf{r}_p), \quad p = 1, \ldots, N. \qquad (9)$$

Here $A_n^{(p)m}$ are coefficients multiplying the $S_n^m(\mathbf{r})$, which are multipoles of order n and degree m, given by

$$S_n^m(\mathbf{r}_p) = h_n(kr_p)Y_n^m(\theta_p, \varphi_p), \quad p = 1, \ldots, N. \qquad (10)$$

Here $h_n(kr)$ are spherical Hankel functions of the first kind that satisfy the Sommerfeld condition, and $Y_n^m(\theta, \phi)$ are orthonormal spherical harmonics, which also can be represented in the form

$$Y_n^m(\theta, \varphi) = (-1)^m \sqrt{\frac{2n+1}{4\pi} \frac{(n-|m|)!}{(n+|m|)!}} P_n^{|m|}(\cos\theta)e^{im\varphi}, \qquad (11)$$

where $P_n^m(\mu)$ are the associated Legendre functions.

The problem now is to determine the coefficients $A_n^{(p)m}$ so that *the complete potential*

$$\psi(\mathbf{r}) = \psi_{\text{in}}(\mathbf{r}) + \sum_{p=1}^{N} \sum_{n=0}^{\infty} \sum_{m=-n}^{n} A_n^{(p)m} S_n^m(\mathbf{r}_p) \qquad (12)$$

satisfies all boundary conditions on the surface of all spheres.

C. Multipole reexpansion

To solve this problem let us consider the qth sphere. Near the center of this sphere, $\mathbf{r} = \mathbf{r}_q'$, all the potentials $\psi_p(\mathbf{r})$, $p \neq q$, are regular. Accordingly the singular solutions [multipoles $S_n^m(\mathbf{r}_p), p \neq q$] can be then reexpanded into a series of terms of *regular elementary solutions* near the qth sphere, $|\mathbf{r}_q| \leq |\mathbf{r}_p' - \mathbf{r}_q'|$ using the following expression:

$$S_n^m(\mathbf{r}_p) = \sum_{l=0}^{\infty} \sum_{s=-l}^{l} (S|R)_{ln}^{sm}(\mathbf{r}_{pq}')R_l^s(\mathbf{r}_q),$$

$$p, q = 1, \ldots, N, \quad p \neq q. \qquad (13)$$

Here $R_n^m(\mathbf{r}_q)$ are regular elementary solutions of the Helmholtz equation in spherical coordinates connected with the qth sphere:

$$R_n^m(\mathbf{r}_q) = j_n(kr_q)Y_n^m(\theta_q, \varphi_q), \quad p = 1, \ldots, N, \qquad (14)$$

where $j_n(kr)$ are spherical Bessel functions of the first kind. The coefficients $(S|R)_{ln}^{sm}(\mathbf{r}_{pq}')$ are the translation reexpansion coefficients, and depend on the relative location of the pth and qth spheres, $\mathbf{r}_{pq}'$. Since $\mathbf{r} = \mathbf{r}_p + \mathbf{r}_p' = \mathbf{r}_q + \mathbf{r}_q'$, we have

$$\mathbf{r}_p = \mathbf{r}_q + \mathbf{r}_{pq}', \quad \mathbf{r}_{pq}' = \mathbf{r}_q' - \mathbf{r}_p' = \mathbf{r}_p - \mathbf{r}_q, \qquad (15)$$

where $\mathbf{r}_{pq}'$ is the vector directed from the center of the pth sphere to the center of the qth sphere. Aspects of the multipole reexpansion coefficients, their properties, and methods for their efficient computations are considered in Chew (1992) and Gumerov and Duraiswami (2001a).

Near the center of expansion the incident field can also be represented using a similar series, the radius of convergence for which is not smaller than the radius of the qth sphere:

$$\psi_{\text{in}}(\mathbf{r}) = \sum_{l=0}^{\infty} \sum_{s=-l}^{l} C_l^{(\text{in})s}(\mathbf{r}_q')R_q^s(\mathbf{r}_q). \qquad (16)$$

Substituting the local expansions from Eqs. (13) and (16) into Eq. (12) we obtain the following representation of the field near $\mathbf{r} = \mathbf{r}_q'$:

$$\psi(\mathbf{r}) = \sum_{l=0}^{\infty} \sum_{s=-l}^{l} C_l^{(\text{in})s}(\mathbf{r}_q')R_l^s(\mathbf{r}_q)$$

$$+ \sum_{n=0}^{\infty} \sum_{m=-n}^{n} A_n^{(q)m} S_n^m(\mathbf{r}_q) + \sum_{\substack{p=1 \\ p \neq q}}^{N} \sum_{n=0}^{\infty} \sum_{m=-n}^{n} A_n^{(p)m}$$

$$\times \sum_{l=0}^{\infty} \sum_{s=-l}^{l} (S|R)_{ln}^{sm}(\mathbf{r}_{pq}')R_l^s(\mathbf{r}_q). \qquad (17)$$

Here the incident field is also expanded in terms of the regular functions centered at $\mathbf{r}_q'$, the singular multipole expansion around $\mathbf{r}_q'$ is kept as is, while the other multipole expansions are converted to local expansions in terms of regular functions around $\mathbf{r}_q'$.

Let us change the order of summation in the latter term in Eq. (17) and substitute Eqs. (10) and (14) for S_n^m and R_n^m. This expression can then be rewritten as

$$\psi(\mathbf{r}) = \sum_{l=0}^{\infty} \sum_{s=-l}^{l} [B_l^{(q)s}j_l(kr_q) + A_l^{(q)s}h_l(kr_q)]Y_l^s(\theta_q, \varphi_q), \qquad (18)$$

$$B_l^{(q)s}(\mathbf{r}_1', \ldots, \mathbf{r}_N')$$

$$= C_l^{(\text{in})s}(\mathbf{r}_q') + \sum_{\substack{p=1 \\ p \neq q}}^{N} \sum_{n=0}^{\infty} \sum_{m=-n}^{n} (S|R)_{ln}^{sm}(\mathbf{r}_{pq}')A_n^{(p)m}. \qquad (19)$$

D. Boundary conditions

From these equations we have the boundary values of ψ and $\partial\psi/\partial n$ on the surface of the qth sphere as

$$\psi|_{S_q} = \sum_{l=0}^{\infty} \sum_{s=-l}^{l} [B_l^{(q)s} j_l(ka_q)$$

$$+ A_l^{(q)s} h_l(ka_q)] Y_l^s(\theta_q, \varphi_q), \qquad (20)$$

$$\frac{\partial \psi}{\partial n}\bigg|_{S_q} = k \sum_{l=0}^{\infty} \sum_{s=-l}^{l} [B_l^{(q)s} j_l'(ka_q)$$

$$+ A_l^{(q)s} h_l'(ka_q)] Y_l^s(\theta_q, \varphi_q). \qquad (21)$$

To obtain the coefficients, we must satisfy the boundary condition Eq. (2), which on the surface of the qth sphere leads to

$$\sum_{l=0}^{\infty} \sum_{s=-l}^{l} \{B_l^{(q)s} [kj_l'(ka_q) + i\sigma_q j_l(ka_q)]$$

$$+ A_l^{(q)s} [kh_l'(ka_q) + i\sigma_q h_l(ka_q)]\} Y_l^s(\theta_q, \varphi_q) = 0. \qquad (22)$$

Orthogonality of the surface harmonics yields

$$B_l^{(q)s} [kj_l'(ka_q) + i\sigma_q j_l(ka_q)]$$

$$= -A_l^{(q)s} [kh_l'(ka_q) + i\sigma_q h_l(ka_q)], \qquad (23)$$

where $l=0,1,\ldots$, $s=-l,\ldots,l$. Note that the boundary values of $\psi|_{S_q}$ and $\partial \psi/\partial n|_{S_q}$ can be expressed in terms of the coefficients $A_l^{(q)s}$, since

$$B_l^{(q)s} = -A_l^{(q)s} \frac{kh_l'(ka_q) + i\sigma_q h_l(ka_q)}{kj_l'(ka_q) + i\sigma_q j_l(ka_q)},$$

$$l=0,1,\ldots, \quad s=-l,\ldots,l, \qquad (24)$$

and Eqs. (20) and (21) yield

$$\psi|_{S_q} = \sum_{l=0}^{\infty} \sum_{s=-l}^{l} \left[h_l(ka_q) - j_l(ka_q) \right.$$

$$\left. \times \frac{kh_l'(ka_q) + i\sigma_q h_l(ka_q)}{kj_l'(ka_q) + i\sigma_q j_l(ka_q)} \right] A_l^{(q)s} Y_l^s(\theta_q, \varphi_q). \qquad (25)$$

$$\frac{\partial \psi}{\partial n}\bigg|_{S_q} = k \sum_{l=0}^{\infty} \sum_{s=-l}^{l} \left[h_l'(ka_q) - j_l'(ka_q) \right.$$

$$\left. \times \frac{kh_l'(ka_q) + i\sigma_q h_l(ka_q)}{kj_l'(ka_q) + i\sigma_q j_l(ka_q)} \right] A_l^{(q)s} Y_l^s(\theta_q, \varphi_q). \qquad (26)$$

These relations can be also rewritten in a compact form using the Wronskian for the spherical Bessel functions,

$$W\{j_l(ka), h_l(ka)\} = j_l(ka) h_l'(ka) - j_l'(ka) h_l(ka)$$

$$= i(ka)^{-2} \qquad (27)$$

as

$$\psi|_{S_q} = \frac{1}{ika_q^2} \sum_{l=0}^{\infty} \sum_{s=-l}^{l} \frac{A_l^{(q)s} Y_l^s(\theta_q, \varphi_q)}{kj_l'(ka_q) + i\sigma_q j_l(ka_q)}, \qquad (28)$$

$$\frac{\partial \psi}{\partial n}\bigg|_{S_q} = -\frac{\sigma_q}{ka_q^2} \sum_{l=0}^{\infty} \sum_{s=-l}^{l} \frac{A_l^{(q)s} Y_l^s(\theta_q, \varphi_q)}{kj_l'(ka_q) + i\sigma_q j_l(ka_q)}$$

$$= -i\sigma_q \psi|_{S_q}. \qquad (29)$$

For the particular case of a sound-hard sphere ($\sigma_q = 0$) this gives

$$\psi|_{S_s} = \frac{1}{ik^2 a_q^2} \sum_{l=0}^{\infty} \sum_{s=-l}^{l} \frac{A_l^{(q)s} Y_l^s(\theta_q, \varphi_q)}{j_l'(ka_q)},$$

$$\qquad (30)$$

$$\frac{\partial \psi}{\partial n}\bigg|_{S_q} = 0,$$

while for sound-soft spheres ($\sigma_q = \infty$) we have

$$\psi|_{S_q} = 0, \quad \frac{\partial \psi}{\partial n}\bigg|_{S_q} = \frac{i}{ka_q^2} \sum_{l=0}^{\infty} \sum_{s=-l}^{l} \frac{A_l^{(q)s} Y_l^s(\theta_q, \varphi_q)}{j_l(ka_q)}. \qquad (31)$$

E. Matrix representation

To determine the boundary values of the potential and/or its normal derivative and obtain a spatial distribution according to Eq. (12) we need to determine the coefficients $A_l^{(q)s}$ in Eqs. (23) and (19), which are valid for any sphere, $q = 1,\ldots,N$. These equations form a linear system that may be represented in standard matrix-vector form.

First, we note that coefficients of expansions to spherical harmonics, such as A_n^m, $n=0,1,2,\ldots$; $m=-n,\ldots,n$, can be stacked into one column vector, e.g.,

$$\mathbf{A} = (A_0^0, A_1^{-1}, A_1^0, A_1^1, A_2^{-2}, A_2^{-1}, A_2^0, A_2^1, A_2^2, \ldots)^T, \qquad (32)$$

where the superscript T denotes the transpose. In this representation the elements of the vector $\mathbf{A}$ are related to coefficients A_n^m by

$$A_t = A_n^m, \quad t = (n+1)^2 - (n-m),$$

$$n=0,1,2,\ldots; \quad m=-n,\ldots,n; \quad t=1,2,\ldots. \qquad (33)$$

The same reduction in dimension can be applied to the reexpansion coefficients $(S|R)_{ln}^{sm}$. The coefficients can then be stacked in a two-dimensional matrix as

$$(\mathbf{S}|\mathbf{R}) = \begin{vmatrix} (S|R)^{00}_{00} & (S|R)^{0-1}_{01} & (S|R)^{00}_{01} & (S|R)^{01}_{01} & (S|R)^{0-2}_{02} & \cdots \\ (S|R)^{-10}_{10} & (S|R)^{-1-1}_{11} & (S|R)^{-10}_{11} & (S|R)^{-11}_{11} & (S|R)^{-1-2}_{12} & \cdots \\ (S|R)^{00}_{10} & (S|R)^{0-1}_{11} & (S|R)^{00}_{11} & (S|R)^{01}_{11} & (S|R)^{0-2}_{12} & \cdots \\ (S|R)^{10}_{10} & (S|R)^{1-1}_{11} & (S|R)^{10}_{11} & (S|R)^{11}_{11} & (S|R)^{1-2}_{12} & \cdots \\ (S|R)^{-20}_{20} & (S|R)^{-2-1}_{21} & (S|R)^{-20}_{21} & (S|R)^{-21}_{21} & (S|R)^{-2-2}_{22} & \cdots \\ \cdots & \cdots & \cdots & \cdots & \cdots & \cdots \end{vmatrix}, \tag{34}$$

with the following correspondence of the matrix elements and coefficients:

$$(S|R)_{rt} = (S|R)^{sm}_{ln},$$

$$r = (l+1)^2 - (l-s),$$

$$t = (n+1)^2 - (n-m), \quad l, n = 0, 1, 2, \ldots;$$

$$m = -n, \ldots, n; \quad s = -l, \ldots, l. \tag{35}$$

Using this representation we introduce the following vectors and matrices

$$\mathbf{A}^{(q)} = \{A^{(q)}_t\}^T, \quad \mathbf{D}^{(q)} = \{D^{(q)}_t\}^T, \quad \mathbf{L}^{(qp)} = \{L^{(qp)}_{rt}\},$$

$$q = 1, \ldots, N, \quad p = 1, \ldots, N, \tag{36}$$

where

$$A^{(q)}_t = A^{(q)m}_n,$$

$$D^{(q)}_t = -\frac{kj'_n(ka_q) + i\sigma_q j_n(ka_q)}{kh'_n(ka_q) + i\sigma_q h_n(ka_q)} C^{(\text{in})m}_n(\mathbf{r}'_q), \tag{37}$$

$$L^{(qp)}_{rt} = \frac{kj'_l(ka_q) + i\sigma_q j_l(ka_q)}{kh'_l(ka_q) + i\sigma_q h_l(ka_q)} (S|R)^{sm}_{ln}(\mathbf{r}'_{pq}),$$

$$\text{for } p \neq q, \quad L^{(qq)}_{rt} = \delta_{rt},$$

$$t = (n+1)^2 - (n-m),$$

$$n = 0, 1, 2, \ldots; \quad m = -n, \ldots, n;$$

$$r = (l+1)^2 - (l-s), \quad l = 0, 1, 2, \ldots;$$

$$s = -l, \ldots, l; \quad q = 1, \ldots, N, \quad p = 1, \ldots, N,$$

where δ_{rt} is the Kronecker delta; $\delta_{rt} = 0$ for $r \neq t$ and $\delta_{rr} = 1$.

Equations (23) and (19) then can be represented in the form

$$\sum_{p=1}^{N} \mathbf{L}^{(qp)} \mathbf{A}^{(p)} = \mathbf{D}^{(q)}, \quad q = 1, \ldots, N, \tag{38}$$

or as a single equation

$$\mathbf{LA} = \mathbf{D}, \tag{39}$$

where the matrices and vectors are

$$\mathbf{L} = \begin{vmatrix} \mathbf{L}^{(11)} & \mathbf{L}^{(12)} & \cdots & \mathbf{L}^{(1N)} \\ \mathbf{L}^{(21)} & \mathbf{L}^{(22)} & \cdots & \mathbf{L}^{(2N)} \\ \cdots & \cdots & \cdots & \cdots \\ \mathbf{L}^{(N1)} & \mathbf{L}^{(N2)} & \cdots & \mathbf{L}^{(NN)} \end{vmatrix},$$

$$\mathbf{A} = \begin{vmatrix} \mathbf{A}^{(1)} \\ \mathbf{A}^{(2)} \\ \cdots \\ \mathbf{A}^{(N)} \end{vmatrix}, \quad \mathbf{D} = \begin{vmatrix} \mathbf{D}^{(1)} \\ \mathbf{D}^{(2)} \\ \cdots \\ \mathbf{D}^{(N)} \end{vmatrix}. \tag{40}$$

This linear system can be solved numerically using standard routines, such as LU-decomposition. The block-structure can also be exploited using block-oriented solvers, though we do not pursue this here.

An important issue is the truncation of the infinite series and corresponding truncation of the associated matrices. A first way to truncate the series is to truncate the outer sum at a fixed number M in each expansion, and is the approach taken here. This number is selected via a heuristic based on the magnitude of the smallest retained term. In this case $n = 0, 1, \ldots, M$; $m = -n, \ldots, n$, then the length of each vector $\mathbf{A}^{(p)}$ and $\mathbf{D}^{(p)}$ will be $(M+1)^2$, and the size of each sub-matrix $\mathbf{L}^{(qp)}$ will be $(M+1)^2 \times (M+1)^2$, the size of the total vectors $\mathbf{A}$ and $\mathbf{D}$ will be $N(M+1)^2$ and the size of the total matrix $\mathbf{L}$ will be $N(M+1)^2 \times N(M+1)^2$.

Several ideas could be employed to improve this heuristic. For example, the use of fast multipole methods could lead to accelerated schemes to solve these equations iteratively (Koc and Chew, 1998). Further, the expressions used to select the truncation of the series could be selected in a more rigorous manner. However, as will be seen below, even with a fixed size of M we are able to solve large problems using conventional techniques.

F. Computation of multipole reexpansion coefficients

The $(S|R)$-multipole translation coefficients can be computed in different ways including via numerical evaluation of integral representations, or using the Clebsch–Gordan or Wigner 3-j symbols (e.g., see Epton and Dembart, 1995; Koc *et al.*, 1999). For fast, stable, exact and efficient computations of the entire truncated matrix of the reexpansion coefficients we used a method based on Chew (1992) recurrence relations and symmetries, who derived them first for the $(R|R)$-translation coefficients [translation of regular-to-regular elementary solution, see Eq. (14)]. Fortunately (since the singular and regular elementary solutions of the Helmholtz equation satisfy the same recurrence relations) these relations hold for $(S|R)$-multipole translation coefficients

also, but with different initial values for recursive computations (44). This was also pointed out by Chew (1992). Note that for other equations (e.g., for the Laplace equation) the singular and regular elementary solutions may not satisfy the same recursions. In Gumerov and Duraiswami (2001a) proofs and details may be found. We only provide necessary relations and initial values for using the recurrence procedures here.

All the $(S|R)_{ln}^{sm}(\mathbf{r}'_{pq})$ translation reexpansion coefficients can be computed in the following way. First, we compute the so-called "sectorial coefficients" of type $(S|R)_{l|m|}^{sm}$ and $(S|R)_{|s|n}^{sm}$ using the following relations:

$$b_{m+1}^{-m-1}(S|R)_{l,m+1}^{s,m+1} = -b_l^{-s}(S|R)_{l-1,m}^{s-1,m}$$
$$- b_{l+1}^{s-1}(S|R)_{l+1,m}^{s-1,m}, \qquad (41)$$

$$b_{m+1}^{-m-1}(S|R)_{l,m+1}^{s,-m-1} = b_l^s(S|R)_{l-1,m}^{s+1,-m}$$
$$- b_{l+1}^{-s-1}(S|R)_{l+1,m}^{s+1,-m},$$

$$l=0,1,\dots, \quad s=-l,\dots,l,$$

$$m=0,1,2,\dots, \qquad (42)$$

where

$$b_n^m = \begin{cases} \sqrt{\dfrac{(n-m-1)(n-m)}{(2n-1)(2n+1)}}, & 0 \le m \le n, \\[3mm] -\sqrt{\dfrac{(n-m-1)(n-m)}{(2n-1)(2n+1)}}, & -n \le m < 0, \\[3mm] 0, & |m| > n, \end{cases} \qquad (43)$$

and the recurrence process starts with

$$(S|R)_{l0}^{s0}(\mathbf{r}'_{pq}) = \sqrt{(4\pi)}(-1)^l S_l^{-s}(\mathbf{r}'_{pq}),$$
$$(S|R)_{0n}^{0m}(\mathbf{r}'_{pq}) = \sqrt{(4\pi)} S_n^m(\mathbf{r}'_{pq}). \qquad (44)$$

Due to the symmetry relation

$$(S|R)_{|m|l}^{-m,-s} = (-1)^{l+m}(S|R)_{l|m|}^{sm},$$

$$l=0,1,2,\dots, \quad s=-l,\dots,l, \quad m=-n,\dots,n, \qquad (45)$$

all of the sectorial coefficients $(S|R)_{|s|n}^{sm}$ can be obtained from the coefficients $(S|R)_{l|m|}^{sm}$.

Once the sectorial coefficients are computed, all other coefficients can be derived from them using the following recurrence relation, which does not change the degrees s,m of the reexpansion coefficients:

$$a_{n-1}^m(S|R)_{l,n-1}^{sm} - a_n^m(S|R)_{l,n+1}^{sm}$$
$$= a_l^s(S|R)_{l+1,n}^{sm} - a_{l-1}^s(S|R)_{l-1,n}^{sm},$$

$$l,n=0,1,\dots, \quad s=-l,\dots,l, \quad m=-n,\dots,n, \qquad (46)$$

where

$$a_n^m = \begin{cases} \sqrt{\dfrac{(n+1+|m|)(n+1-|m|)}{(2n+1)(2n+3)}}, & n \ge |m|, \\[3mm] 0, & |m| > n. \end{cases} \qquad (47)$$

Due to the symmetry

$$(S|R)_{ln}^{sm} = (-1)^{n+l}(S|R)_{nl}^{-m,-s},$$

$$l,n=0,1,\dots, \quad s=-l,\dots,l, \quad m=-n,\dots,n, \qquad (48)$$

only those coefficients with $l \ge n$ need be computed using recurrence relations.

In addition, the $(S|R)$ coefficients for any pair of spheres p and q need be computed only for the vector $\mathbf{r}'_{pq}$, since for the opposite directed vector we have the symmetry

$$(S|R)_{ln}^{sm}(\mathbf{r}'_{pq}) = (-1)^{l+n}(S|R)_{ln}^{sm}(\mathbf{r}'_{pq}),$$

$$l,n=0,1,\dots, \quad m=-n,\dots,n. \qquad (49)$$

Software based on this algorithm was developed and entitled MultisphereHelmholtz. Results of tests using this software are presented and discussed in Sec. V.

IV. COAXIAL SPHERES

The case of two spheres is interesting, since on the one hand the scattered fields due to the spheres interact with each other (multiple scattering), while on the other, the interaction is still simple enough that it can be investigated in detail and understood more intuitively than the general case of N spheres. Additionally, in this case, the computation of the reexpansion matrices can be simplified via a proper selection of the reference frames. Indeed, for two spheres we can introduce a reference frame which has its z axis directed from the center of one sphere to the center of the other sphere. Since the reexpansion coefficients depend only on the relative location of the spheres, for this frame orientation, there will be no angular dependence for the reexpansion coefficients. This does not require the incident fields to be symmetric with respect to this axis. The same statement holds for the case when there are N spheres arranged along a line, taken to be the z axis. In these particular cases, the general reexpansion formula Eq. (13) simplifies to

$$S_n^m(\mathbf{r}_p) = \sum_{l=|m|}^{\infty} (S|R)_{ln}^{mm}(\mathbf{r}'_{pq}) R_l^m(\mathbf{r}_q),$$

$$p=1,\dots,N, \quad p \ne q. \qquad (50)$$

The coefficients

$$(S|R)_{ln}^m(r'_{pq}) = (S|R)_{ln}^{mm}(\mathbf{r}'_{pq}),$$

$$l,n=0,1,\dots, \quad m=-n,\dots,n, \qquad (51)$$

satisfy general recurrence relations and can be computed using the general algorithm we have developed. However, there are simpler relations that take advantage of the coaxiality of the spheres, while resulting in substantially lower dimensional matrices.

Note that the sign of coefficients $(S|R)_{ln}^m(r'_{pq})$ depends on the direction of the vector $\mathbf{r}'_{pq}$. To be definite, we use the convention that r'_{pq} corresponds to $\mathbf{r}'_{pq}$ and r'_{qp} corresponds to $\mathbf{r}'_{qp} = -\mathbf{r}'_{pq}$. Since $(S|R)_{ln}^{mm}(\mathbf{r}'_{pq}) = (-1)^{l+n}$ $(S|R)_{ln}^{mm}(-\mathbf{r}'_{pq}) = (-1)^{l+n}(S|R)_{ln}^{mm}(\mathbf{r}'_{qp})$, we will have

$$(S|R)_{ln}^m(r'_{pq}) = (-1)^{l+n}(S|R)_{ln}^m(r'_{qp}),$$

$$l,n=0,1,\dots, \quad m=-n,\dots,n. \qquad (52)$$

A. Matrix representation

According to Eq. (50) harmonics of each order m can be considered independently. Equations (19) and (23) can be rewritten in the form

$$\frac{kj'_l(ka_q)+i\sigma_q j_l(ka_q)}{kh'_l(ka_q)+i\sigma_q h_l(ka_q)} \sum_{\substack{p=1 \\ p \neq q}}^{N} \sum_{n=|m|}^{\infty} (S|R)^m_{ln}(r'_{pq})A^{(p)m}_n$$

$$+A^{(q)m}_l = D^{(q)m}_l,$$

$$m=0,\pm 1,\pm 2,\ldots, \quad l=|m|,|m|+1,\ldots,$$

$$q=1,\ldots,N, \tag{53}$$

where

$$D^{(q)m}_l = -\frac{kj'_l(ka_q)+i\sigma_q j_l(ka_q)}{kh'_l(ka_q)+i\sigma_q h_l(ka_q)} C^{(\mathrm{in})m}_l(\mathbf{r}'_q). \tag{54}$$

This linear system can be represented in the following form

$$\sum_{p=1}^{N} \mathbf{L}^{(qp)m}\mathbf{A}^{(p)m} = \mathbf{D}^{(q)m},$$

$$m=0,\pm 1,\pm 2,\ldots, \quad q=1,\ldots,N, \tag{55}$$

where the vectors $\mathbf{A}^{(q)m}$ and $\mathbf{D}^{(q)m}$ and matrices $\mathbf{L}^{(qp)m}$ are stacked as follows:

$$\mathbf{A}^{(q)m}=\{A^{(q)m}_n\}^T, \quad \mathbf{D}^{(q)m}=\{D^{(q)m}_n\}^T,$$

$$\mathbf{L}^{(qp)m}=\{L^{(qp)m}_{ln}\}, \tag{56}$$

$$q=1,\ldots,N, \quad p=1,\ldots,N,$$

$$m=0,\pm 1,\pm 2,\ldots, \quad l,n=|m|,|m|+1,\ldots,$$

with the individual matrix elements given by

$$L^{(qp)m}_{ln}=\frac{kj'_l(ka_q)+i\sigma_q j_l(ka_q)}{kh'_l(ka_q)+i\sigma_q h_l(ka_q)}(S|R)^m_{ln}(r'_{pq}),$$

$$\text{for } p\neq q, \quad L^{(qq)m}_{ln}=\delta_{ln}. \tag{57}$$

Since all equations can be considered separately for each m, the linear system Eq. (55) can be written as

$$\mathbf{L}^m\mathbf{A}^m=\mathbf{D}^m, \quad m=0,\pm 1,\pm 2,\ldots, \tag{58}$$

where

$$\mathbf{L}^m = \begin{pmatrix} \mathbf{L}^{(11)}m & \mathbf{L}^{(12)m} & \cdots & \mathbf{L}^{(1N)m} \\ \mathbf{L}^{(21)m} & \mathbf{L}^{(22)m} & \cdots & \mathbf{L}^{(2N)m} \\ \cdots & \cdots & \cdots & \cdots \\ \mathbf{L}^{(N1)m} & \mathbf{L}^{(N2)m} & \cdots & \mathbf{L}^{(NN)m} \end{pmatrix},$$

$$\mathbf{A}^m = \begin{pmatrix} \mathbf{A}^{(1)m} \\ \mathbf{A}^{(2)m} \\ \cdots \\ \mathbf{A}^{(N)m} \end{pmatrix}, \quad \mathbf{D}^m = \begin{pmatrix} \mathbf{D}^{(1)m} \\ \mathbf{D}^{(2)m} \\ \cdots \\ \mathbf{D}^{(N)m} \end{pmatrix}. \tag{59}$$

As in the general case considered above, the infinite series and matrices need to be truncated for numerical computation. If we limit ourselves to the first M modes for each expansion

of spherical harmonics, so that $m=0,\pm 1,\ldots,\pm M$, $n=|m|, |m|+1,\ldots,M$, then the length of each vector $\mathbf{A}^{(p)m}$ and $\mathbf{D}^{(p)m}$ is $M+1-|m|$, the dimensions of each matrix $\mathbf{L}^{(qp)m}$ is $(M+1-|m|)\times(M+1-|m|)$, the size of the total vectors $\mathbf{A}^m$ and $\mathbf{D}^m$ are $N(M+1-|m|)$, and the size of the total matrix $\mathbf{L}^m$ is $N(M+1-|m|)\times N(M+1-|m|)$. The problem then is reduced to solution of $2M+1$ *independent* linear systems for each m. Note that the coaxial, or diagonal, translation coefficients $(S|R)^m_{ln}(r'_{pq})$ are symmetrical with respect to the sign of the degree m, $(S|R)^m_{ln}(r'_{pq})=(S|R)^{-m}_{ln}(r'_{pq})$ (see Gumerov and Duraiswami, 2001a). Therefore the matrices $\mathbf{L}^m$ are also symmetrical [see Eq. (57)]

$$\mathbf{L}^m=\mathbf{L}^{-m}, \quad m=0,1,2,\ldots, \tag{60}$$

and can be computed only for non-negative m. At the same time the right-hand side vector $\mathbf{D}^m$, generally speaking, does not coincide with $\mathbf{D}^{-m}$, so that the solution $\mathbf{A}^m$ can be different from $\mathbf{A}^{-m}$.

Let us compare the number of operations required for determination of all expansion coefficients $A^{(q)m}_n$, $m=0,\pm 1,\ldots,\pm M$, $n=|m|, |m|+1,\ldots,M$, $q=1,\ldots,N$, using the general algorithm and using the algorithm for coaxial spheres. Assuming that a standard solver requires CK^3 operations to solve a linear system with matrix of dimension $K\times K$, where C is some constant, we can find solution using general algorithm with

$$N^{(\mathrm{general})}_{\mathrm{operations}}=CN^3(M+1)^6 \tag{61}$$

operations. Using the algorithm for coaxial spheres we will spend $CN^3(M+1-|m|)^3$ operations to obtain $A^{(q)m}_n$ for each $m=0,\pm 1,\ldots,\pm M$. The total number of operations will be therefore

$$N^{(\mathrm{coaxial})}_{\mathrm{operations}}=CN^3 \sum_{m=-M}^{M} (M+1-|m|)^3$$

$$=CN^3\left[(M+1)^3+2\sum_{m=1}^{M} m^3\right]$$

$$=CN^3[(M+1)^3+\tfrac{1}{2}M^2(M+1)^2]$$

$$=\tfrac{1}{2}CN^3[(M+1)^4+(M+1)^2]. \tag{62}$$

Therefore, for $M\gg 1$, we have

$$\frac{N^{(\mathrm{general})}_{\mathrm{operations}}}{N^{(\mathrm{coaxial})}_{\mathrm{operations}}}\sim 2M^2 \tag{63}$$

which shows much higher efficiency of the algorithm for coaxial spheres.

Note also that in the case of coaxial spheres the number of the multipole reexpansion coefficients that needs to be computed for each pair $p\neq q$ requires $O(M^3)$ operations, while in the general case such computations can be performed in $O(M^4)$ operations. These numbers are smaller than the leading order term in the complexity, that are required for solution of linear equations, and thus Eqs. (61)–(63) provide a comparison between the two methods.

The above expressions for coaxial spheres assume that the z axis coincides with the direction from the center of one

of the spheres to the center of some other sphere. If coordinates of spheres are specified in the original reference frame, with the axis z oriented arbitrarily with respect to the line connecting the sphere centers, we can rotate them so that the new reference frame is convenient for use with the coaxial algorithm.

B. Computation of coaxial reexpansion coefficients

Due to the symmetry relations [see Eqs. (49) and (51)]

$$(S|R)_{ln}^{m}=(S|R)_{ln}^{-m}, \quad m=0,1,2,\ldots, \quad (64)$$

the coaxial coefficients $(S|R)_{ln}^{m}(\mathbf{r}'_{pq})$ can be computed only for $l\geq n\geq m\geq 0$. The process of filling the matrix $\{(S|R)_{ln}^{m}\}$ can be performed efficiently using recurrence relations that first fill the layers with respect to the orders l and n followed by advancement with respect to the degree m. If such a procedure is selected, then the first step is filling of the layer $m=0$. The initial value depends on the orientation of $\mathbf{r}'_{pq}$ vector relative to the axis $\mathbf{i}_z$ (or $\mathbf{i}_{\hat{z}}$ if rotation is performed), and is given by

$$(S|R)_{l0}^{0}(r'_{pq})=(S|R)_{l0}^{00}(\mathbf{r}'_{pq})\sqrt{4\pi}(-1)^{l}S_{l}^{0}(\mathbf{r}'_{pq})$$

$$= \epsilon_{lpq}\sqrt{2l+1}\,h_{l}(kr'_{pq}), \quad (65)$$

where

$$\epsilon_{lpq}=\left(-\frac{\mathbf{r}'_{pq}\cdot\mathbf{i}_{z}}{|\mathbf{r}'_{pq}|}\right)^{l}=\begin{cases}(-1)^{l}, & \text{for } \mathbf{r}'_{pq}\cdot\mathbf{i}_{z}=|\mathbf{r}'_{pq}|,\\ 1, & \text{for } \mathbf{r}'_{pq}\cdot\mathbf{i}_{z}=-|\mathbf{r}'_{pq}|.\end{cases} \quad (66)$$

To advance with respect to the order n at fixed $m\geq 0$ we can use Eq. (46) for $s=m$,

$$a_{n}^{m}(S|R)_{l,n+1}^{m}=a_{n-1}^{m}(S|R)_{l,n-1}^{m}-a_{l}^{m}(S|R)_{l+1,n}^{m}$$

$$+a_{l-1}^{m}(S|R)_{l-1,n}^{m}, \quad n=m,m+1,\ldots, \quad (67)$$

with the a's given by Eq. (47). For advancement with respect to m it is convenient to use Eq. (41) for $s=m+1$,

$$b_{m+1}^{-m-1}(S|R)_{l,m+1}^{m+1}$$

$$= b_{l}^{-m-1}(S|R)_{l-1,m}^{m}-b_{l+1}^{m}(S|R)_{l+1,m}^{m},$$

$$l=m+1,m+2,\ldots, \quad (68)$$

with the b's given by Eq. (43) and then obtain the other $(S|R)_{ln}^{m+1}$ using Eq. (67).

V. COMPUTATIONAL RESULTS

We apply our method to several example problems. First, we compare the present technique with the BEM for problems involving two and three spheres, and show that the present method is accurate, and much faster. Next, we consider problems that, due to their size, would be impractical to handle with the BEM, and demonstrate that the present technique can deal with them. Convergence for these cases is demonstrated as the truncation number M is increased.
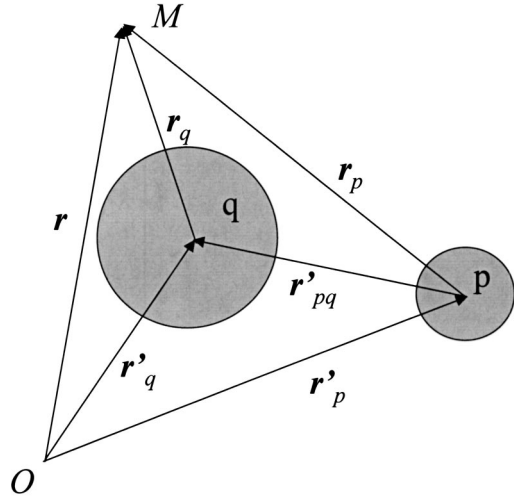
FIG. 2. Notation denoting the different reference frames used in the multipole reexpansion technique.

A. Single sphere

For the case of a single sphere there are no multiple scattering effects. Despite this, the case is interesting from a practical viewpoint. We were unable to find this solution in the standard handbooks, and we include this limiting case to provide an analytical solution for both an arbitrary incident field and for a monopole source. From Eqs. (37)–(40) we have $\mathbf{L}^{(1)}=\mathbf{I}$, $\mathbf{A}^{(1)}=\mathbf{D}^{(1)}$, or

$$A_{n}^{(1)m}=-\frac{kj'_{n}(ka)+i\sigma j_{n}(ka)}{kh'_{n}(ka)+i\sigma h_{n}(ka)}C_{n}^{(\text{in})m}(\mathbf{r}'_{1}). \quad (69)$$

Here we will drop subscript 1 for σ and a, while keeping them for the coordinates. Substituting this expression into Eqs. (28) and (29), we obtain expressions for the potential and its normal derivative on the sphere surface as

$$\psi|_{S_{1}}=-\frac{1}{ika^{2}}\sum_{l=0}^{\infty}\sum_{s=-l}^{l}\frac{C_{l}^{(\text{in})s}(\mathbf{r}'_{1})Y_{l}^{s}(\theta_{1},\varphi_{1})}{kh'_{l}(ka)+i\sigma h_{l}(ka)}, \quad (70)$$

$$\frac{\partial\psi}{\partial n}\bigg|_{S_{1}}=\frac{\sigma}{ka^{2}}\sum_{l=0}^{\infty}\sum_{s=-l}^{l}\frac{C_{l}^{(\text{in})s}(\mathbf{r}'_{1})Y_{l}^{s}(\theta_{1},\varphi_{1})}{kh'_{l}(ka)+i\sigma h_{l}(ka)}$$

$$= -i\sigma\psi|_{S_{1}}. \quad (71)$$

The coefficients $C_{n}^{(\text{in})m}(\mathbf{r}'_{1})$ are determined using Eq. (16) and depend on the incident field. In the case of a monopole source located at some point $\mathbf{r}=\mathbf{r}_{\text{source}}$, the incident field corresponds to the fundamental solution of the Helmholtz equation

$$\psi_{in}(\mathbf{r})=QG_{k}(\mathbf{r}-\mathbf{r}_{\text{source}})=Q\frac{e^{ik|\mathbf{r}-\mathbf{r}_{\text{source}}|}}{4\pi|\mathbf{r}-\mathbf{r}_{\text{source}}|}, \quad (72)$$

where Q is the source intensity (complex, if the phase Φ is not zero),

$$Q=|Q|e^{i\Phi}. \quad (73)$$

For multiple spheres, expansion of this function near the center of the qth sphere $\mathbf{r}=\mathbf{r}'_{q}$ (see Fig. 2) can be found else-
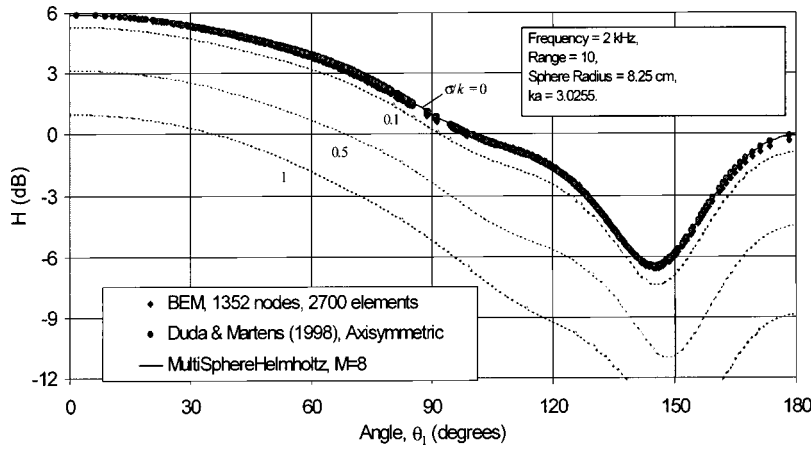
FIG. 3. The normalized surface transfer function H, Eq. (81), for a single sphere of radius $a = 8.25$ cm and a monopole source, located at a distance $d/a = 10$ from the center of the sphere for spheres of different values of σ/k (shown near the curves). The continuous and dashed lines show results of computations using the present method with truncation number $M = 8$. Circles and diamonds respectively show the results of Duda and Martens (1998) and of BEM computations for $\sigma = 0$. In the BEM the sphere surface was discretized using 2700 linear elements.

where (e.g., Morse and Feshbach, 1953),

$$\psi_{\text{in}}(\mathbf{r}) = Q i k \sum_{n=0}^{\infty} \sum_{m=-n}^{n} S_n^{-m}(\mathbf{r}_{\text{source}} - \mathbf{r}_q') R_n^m(\mathbf{r}_q),$$

$$|\mathbf{r}_q| \leq |\mathbf{r}_{\text{source}} - \mathbf{r}_q'| . \tag{74}$$

Comparing Eqs. (16) and (74) we obtain

$$C_n^{(\text{in})m}(\mathbf{r}_q') = Q i k S_n^{-m}(\mathbf{r}_{\text{source}} - \mathbf{r}_q'). \tag{75}$$

A simplification of the general formula for $C_n^{(\text{in})m}$, Eq. (75), is possible, since the problem for monopole source and a single sphere is axisymmetric relative to the axis connecting the sphere center and the source location. Setting the axis z_1 to be this axis, we have

$$C_n^{(\text{in})m} = Q i k \delta_{m0} h_n(k|\mathbf{r}_{\text{source}} - \mathbf{r}_1'|) Y_n^0(0,0)$$

$$= Q i k \delta_{m0} \sqrt{\frac{2n+1}{4\pi}} h_n(kd), \tag{76}$$

where d is the distance between the source and the sphere center. The expression for the surface values of the potential and its derivative Eqs. (70) and (71) become

$$\psi|_{S_1} = -\frac{Q}{4\pi a^2} \sum_{l=0}^{\infty} \frac{(2l+1)h_l(kd)P_l(\cos \theta_1)}{kh_l'(ka) + i\sigma h_l(ka)}, \tag{77}$$

$$\frac{\partial\psi}{\partial n}\bigg|_{S_1} = \frac{iQ\sigma}{4\pi a^2} \sum_{l=0}^{\infty} \frac{(2l+1)h_l(kd)P_l(\cos \theta_1)}{kh_l'(ka) + i\sigma h_l(ka)}$$

$$= -i\sigma\psi|_{S_1}. \tag{78}$$

For the particular case of a sound-hard ($\sigma = 0$) surface this gives

$$\Psi|_{S_1} = -\frac{Q}{4\pi ka^2} \sum_{l=0}^{\infty} (2l+1) \frac{h_l(kd)}{h_l'(ka)} P_l(\cos \theta_1),$$

$$\frac{\partial\psi}{\partial n}\bigg|_{S_q} = 0, \tag{79}$$

while for sound-soft ($\sigma = \infty$) surfaces we have

$$\psi|_{S_1} = 0,$$

$$\frac{\partial\psi}{\partial n}\bigg|_{S_1} = \frac{Q}{4\pi a^2} \sum_{l=0}^{\infty} (2l+1) \frac{h_l(kd)}{h_l(ka)} P_l(\cos \theta_1), \tag{80}$$

These limiting cases are classical and their expressions can be found elsewhere (e.g., see Hanish, 1981).

We compared results of computations of the potential on the surface with those provided by Eq. (79) and that obtained using the BEM, as realized in the software package COMET. The figures below illustrate comparisons of the following transfer function H measured in dB, which represents the ratio of the amplitude of the acoustic field at a specified location of the surface to the amplitude of the incident field at the center of the sphere:

$$H = 20 \lg \left| \frac{\psi|_{S_1}}{\psi_{\text{in}}(\mathbf{r}_1')} \right|. \tag{81}$$

The solution, Eq. (79), for a single sphere was used by Duda and Martens (1998), for an investigation of scattering cues in audition. Figure 3 shows good agreement between computations using all methods. In this example we include also computations for different impedances of the sphere.

We also tested the results of computations obtained using different truncation numbers. Duda and Martens (1998) used truncation based on comparison of subsequent terms in the series (in this particular case the series was truncated when the ratio of such terms is smaller than 10^{-6}). Experiments showed that excellent agreement with these results is achieved, if the truncation number is selected using the heuristic

$$M = [eka], \quad e = 2.718\,28\ldots, \tag{82}$$

which shows that it increases with the wave number. For large ka good agreement was observed for $M \geq [1/2eka]$, while differences were visible for smaller M. For moderate ka such differences appeared for truncation numbers below the value provided in Eq. (82).

B. Two spheres

Since there is no closed-form analytical solution for two spheres in a simple form, we compared the numerical results obtained using our code, and by using the BEM. As an example we considered computation of the function Eq. (81).

FIG. 4. An example of BEM (COMET 4.0) computations of potential distribution over the surface of two spheres generated by a monopole source. Each sphere surface is discretized to 2700 triangular elements. The ratio of sphere radii is 1.3253 and they touch in one point.

The model consists of two spheres, which are touching at one point. In the computations the ratio of sphere radii was taken to be 1.3253. The origin of the reference frame was located at the center of the smaller sphere and the direction of the y axis was from the larger sphere to the smaller one. The z axis was directed towards a monopole source, generating the incident field, which was located at the distance of 10 radii from the smaller sphere. The frequency of the incident wave nondimensionalized with the radius of the smaller sphere corresponded to $ka_1 = 3.0255$. The mesh for computations using the BEM contained 5400 triangular elements (2700 elements for each sphere). A picture of this two-sphere configuration with computational mesh and distribution of the acoustic pressure is shown in Fig. 4. In the computations the admittances of both spheres were set to zero.

For computations using MultisphereHelmholtz the truncation number was automatically set to

$$M = \left[\tfrac{1}{2} e k r'_{12}\right]. \tag{83}$$

For the above given values of a_2/a_1 and ka_1, this provided $M = 9$, so that the total number of modes n in the multipole expansion was 10 for each sphere (or 100 A_n^m coefficients for each sphere).

Figure 5 shows a comparison between the BEM and the MultisphereHelmholtz computational results for function H calculated for sphere 1 according to Eq. (81). Each curve corresponds to a fixed value of the spherical polar angle θ_1 and demonstrates dependence on the angle φ_1. Note that dependence on the angle φ_1 is only due to the presence of the sphere 2. The comparison shows a good agreement between the results obtained by different methods. Some small dispersion of the points obtained using BEM is due to the mesh discretization of the sphere surface, which normally can be avoided by additional smoothing/interpolation procedures (we did not apply such smoothing in the results plotted). Our code far outperformed BEM computationally, both in achieving much faster computations (seconds as opposed to tens of minutes on the same computer) and memory usage.

Figure 6 demonstrates computations of H for the two sphere geometry with the parameters described above, but for a higher wave number, and with different impedances for the larger sphere. For the given geometry, the automatically selected truncation number was $M = 31$. This number is large enough to observe a substantial difference in speed of computations and memory usage between the general algorithm and the coaxial one [see Eq. (63)].

Proper selection of the truncation number is an important issue for applications of multipole translation techniques. Figure 7 shows convergence of the computations with increasing truncation numbers for H at a specified point on the surface ($\theta_1 = 60$ degrees and $\varphi_1 = 0$ degrees in the case shown in the figure). Computations with low truncation numbers may provide poor accuracy. At some particular truncation number (depending on the nondimensional wave number ka) the computational results stabilize (note that since the solution H depends on the wave number, and so for each ka the solution asymptotes to the corresponding value). Further increase in the truncation number increases both the accuracy of the results and computational time/memory, since the matrix size grows in proportion to M^4 in the general case, and to M^3 for coaxial spheres. However, at some

FIG. 5. Comparison of the angular dependence of function H, Eq. (81), over the surface of a smaller sphere computed for the two sphere geometry shown in Fig. 4 using the BEM and the multipole reexpansion technique. Both spheres are sound-hard.
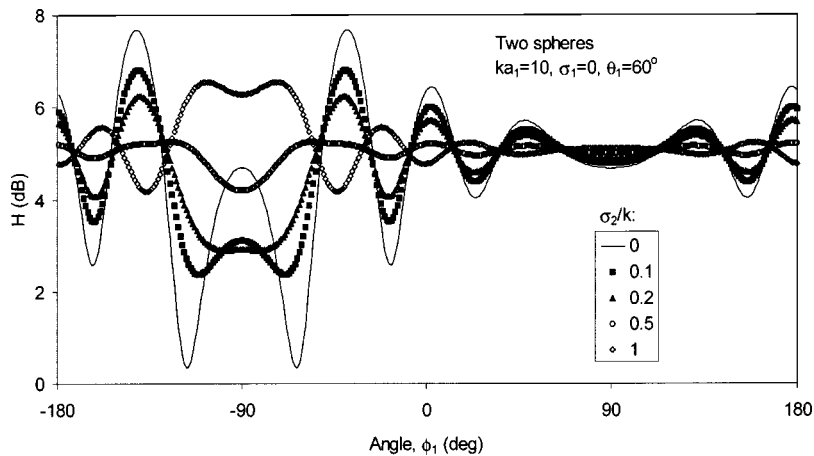
FIG. 6. Angular dependence of H in Eq. (81) over the surface of the sound-hard smaller sphere for the geometry shown in Fig. 4 for different admittances of the larger sphere. Results computed using the present method with automatically selected truncation number $M=31$.

truncation numbers, which slightly exceed the value provided by Eq. (83), the computations can encounter difficulties that arise from the exponential growth of portions of the terms in the expansions, leading to overflow related errors. These are due to the spherical Hankel functions of large order, $h_n(kr'_{pq})$, entering the reexpansion system matrix. Asymptotic expansion of the Hankel function at large n and fixed kr'_{12} shows that the growth starts at $n \sim 1/2ekr'_{12}$. This is used as the basis for automatic selection of the truncation number Eq. (83). Of course, this limitation is purely based on the order of computation of the elements, and the product of terms remains finite, and calculations can be performed for much larger M than given by Eq. (83). However, we have not yet modified our software to use this order of computation.

The computations presented in Fig. 7 show that the actual stabilization occurs at smaller M than those given by Eq. (83) (where we have for $ka_1 = 1,5,10,20,30$ the following values: $M = 3,15,31,63,94$, respectively). Results of our numerical experiments show that for large kr'_{12} reasonable accuracy can be achieved at $M^* \sim 1/2M_{\max}$, where $M_{\max}$ is provided by Eq. (83). At the same time, for lower kr'_{12} formula (83) provides values which cannot be reduced, and accurate computations can be achieved with M slightly larger than $M_{\min}$, with $M_{\min}$ provided by Eq. (83).

In a recent paper (Gumerov and Duraiswami, 2001b) we presented results of the computation of the surface potential for a sphere near a rigid wall. In this case the rigid wall could be replaced by an image sphere and an image source and the

coaxial multipole reexpansion can be used. The problem of sound scattering by a sphere near a rigid wall is in some sense a simplification of the general problem for two spheres, since both the real and the image spheres in this case have the same radius and impedance. For this case, the coefficients of the multipole expansions near each sphere $A_n^{(1)m}$ and $A_n^{(2)m}$ are symmetrical and the dimension of the system can be reduced using this symmetry by a factor of 2. In that paper, we also provided a study and discussion of the influence of the distance between the sphere and the wall and frequency of the field on the surface potential.

C. Three arbitrarily located spheres

If the cases of one and two spheres can be covered using simplified codes, the case of three non-coaxial spheres requires the general three-dimensional multipole translation. As in the case of two spheres discussed above, we compared results of computations for three spheres using Multisphere-Helmholtz and the COMET BEM software.

For this computational example we placed an additional sphere (3) to the case described above. The distance between the centers of spheres 1 and 3 was the same as the distance between the centers of spheres 1 and 2. The parameters of the incident field were the same as for the case of two spheres. The mesh for computations using the BEM contained 5184 triangular elements, 1728 elements for each sphere. A picture of this configuration with the computational
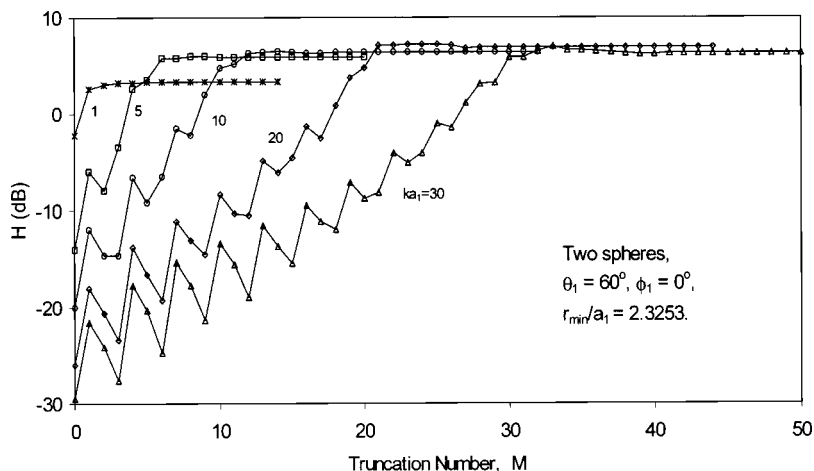
FIG. 7. Dependence of the computations of H, Eq. (81), for the two sphere geometry (see Fig. 4) on the truncation number M for different nondimensional wave numbers.
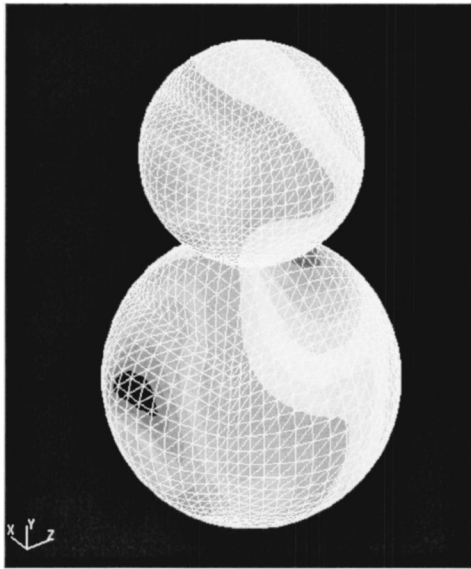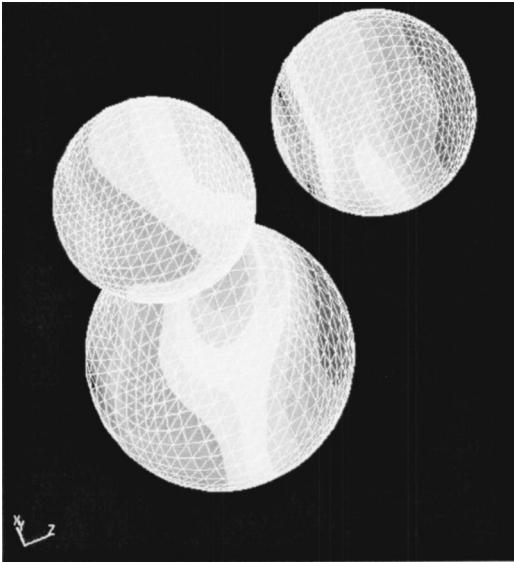
FIG. 8. BEM (COMET 4.0) computations of the potential distribution over the surface of three spheres generated by a monopole source. Each sphere surface is discretized using 1728 triangular elements. Two spheres of non-dimensional radii 1 (sphere 1) and 1.3253 (sphere 2) touch at one point. Sphere 3, with nondimensional radius 1, is located at a distance 2.3253 from the center of sphere 1, on the line connecting the source and the center of sphere 1.

mesh and distribution of the acoustic pressure is shown in Fig. 8. In the computations the three spheres were all taken to be sound-hard.

Results of comparisons between BEM and Multisphere-Helmholtz computations with $M=9$ are shown in Fig. 9. The comparison is as good as in the case of two spheres. Since Figs. 5 and 9 represent similar dependence, we can notice that the presence of the third sphere reduced (at some points by 3–4 dB) the amplitude of the sound field on sphere 1.

D. Many spheres

The case of sound and electromagnetic wave scattering by many arbitrarily located spheres has numerous practical and theoretical applications, including acoustics and hydro-dynamics of multiphase flows, sound propagation in com-
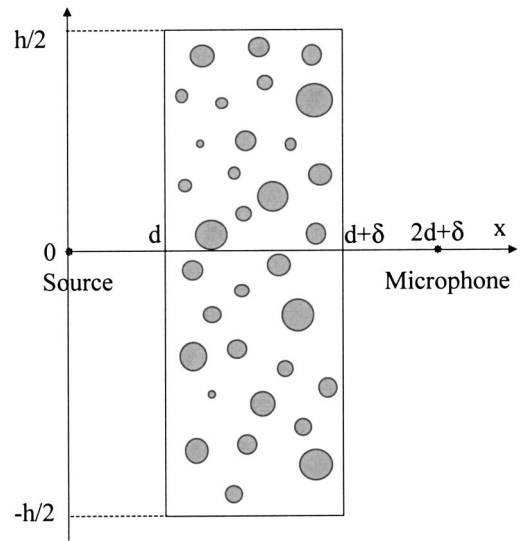
FIG. 10. A sketch of the problem geometry for sound propagation through a screen of spherical particles.

posite materials, electromagnetic waves in clouds, and inverse problems, such as the detection of buried objects, medical tomography, etc.

We considered the following hypothetical problem of sound scattering by a screen of spherical particles. The geometry of the problem is shown in Fig. 10. Here the incident field is generated by a monopole source located at distance d from a flat particle screen of thickness δ. A sensor (e.g., a microphone) measuring the acoustic pressure is located behind the screen at the same distance as the source. N spheres with the same acoustic impedance (in the examples below we took the spheres as sound-hard), but with possibly different sizes, are distributed according to some distribution density over their radii, and have locations of their centers within a box $\delta \times h \times h$ representing the screen. The objective is to evaluate the effect of the screen on the sound propagation.

This effect can be evaluated by defining a "screen transfer function" (STF), which we define as

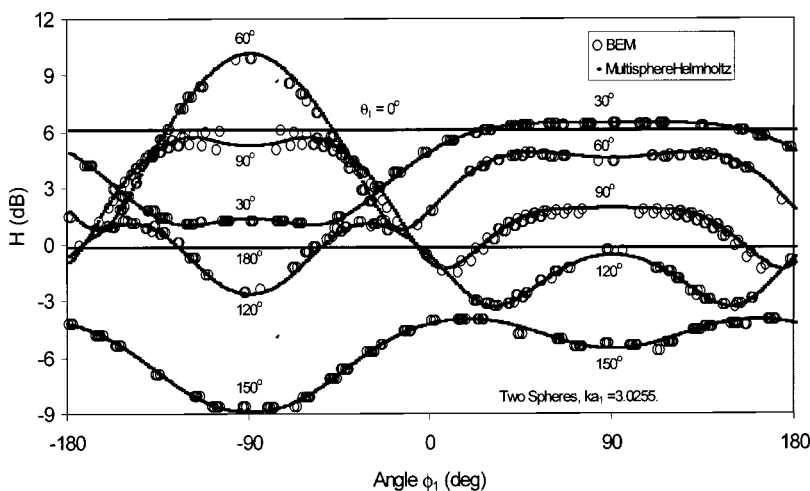$$\text{STF} = 20 \lg |\psi(\mathbf{r}'_{\text{mic}})/\psi_{\text{in}}(\mathbf{r}'_{\text{mic}})|, \tag{84}$$
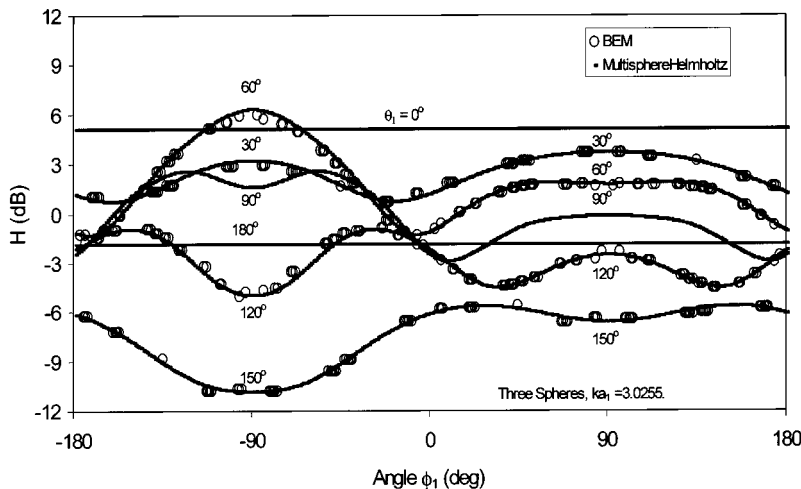
FIG. 9. Comparison of the angular dependence of H (81) over the surface of smaller sphere computed for the three sphere geometry shown in Fig. 8 using the BEM and the multipole reexpansion technique. All three spheres have sound-hard surfaces.
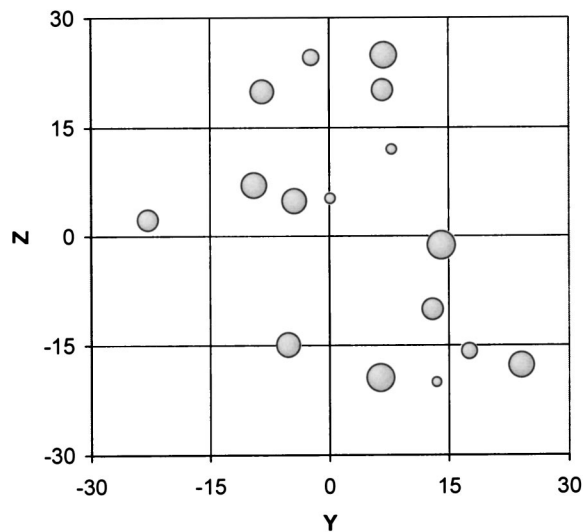
FIG. 11. A scattering screen of 16 spheres with random sizes and random locations of their centers. The centers are uniformly distributed inside a box $10 < x < 15$, $-25 < y < 25$, $-25 < z < 25$. The radii are uniformly distributed over $0.5 < a < 1.5$.

where $\mathbf{r}'_{\text{mic}}$ is the radius-vector of the microphone location and which is measured in decibels.

Two examples of computations with many spheres are presented below. In the first example we placed 16 spheres with uniform random distribution of their dimensionless radii from $a_{\min} = 0.5$ to $a_{\max} = 1.5$. Dimensionless parameters of the screen were $d = 10$, $\delta = 5$, and $h = 50$. The sphere centers were distributed uniformly within the screen. The view of this screen in the yz plane is shown in Fig. 11. In the computations we chose three different wave numbers, $ka = 1$, $ka = 3$, and $ka = 5$, where a is the length scale (the characteristic sphere radius). Computations were performed using the general software with increasing truncation number M. Dependences of the STF on M at various ka are shown in Fig. 12. It is seen that results converge to some value de-
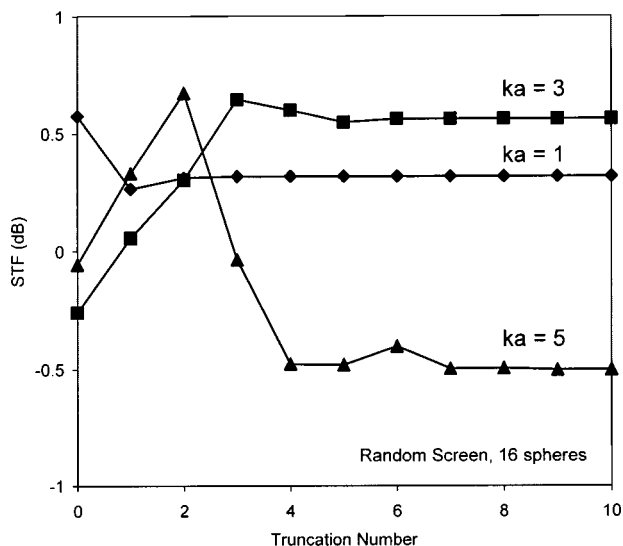
FIG. 12. Convergence test for the problem of sound scattering by a screen of 16 randomly sized spheres with random location of their centers (as shown in Fig. 11). Three different curves computed at different ka, where a is the mean of the sphere radii distribution.
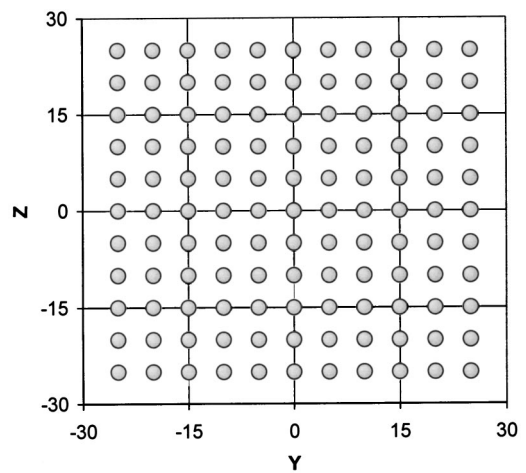
FIG. 13. The view of a scattering screen of 121 spheres of the same size $a = 1$ and location of their centers at the nodes of a square grid $-25 < y < 25$, $-25 < z < 25$ with the grid size $\Delta y = \Delta z = 5$.

pending on ka. This type of check shows that for the given geometry relatively low truncation numbers can be used, which are much smaller than given by Eq. (83), where instead of r'_{12} some representative intersphere distance r'_{pq} is selected. We noticed, however, that in some cases when we have many spheres with very different intersphere distances (from touching spheres, to spheres located at large kr'_{pq}), stabilization of computation only occurs at higher truncation numbers than prescribed by Eq. (83). Thus, at this point the procedure we recommend is an experimental one to check the results of several calculations and find the truncation number at which results converge.

In the second example we put a regular monolayer screen ($d = 10$, $\delta = 0$, and $h = 50$) of 121 spheres of the same radii $a = 1$, which centers form a regular grid in plane $x = d$ (see Fig. 13). Again we compared results obtained with the aid of MultisphereHelmholtz at increasing M and different wave numbers and found fast convergence (see Fig. 14).

VI. CONCLUSIONS

We have developed a procedure for solution of the Helmholtz equation for the case of N spheres of various radii and impedances arbitrarily located in three-dimensional space. This solution uses a T-matrix method where the matrices are computed using a multipole reexpansion technique. We presented computational results for two and three spheres obtained both using the boundary element method with fine discretization of the surfaces (thousands of elements), and showed that our solutions are correct. For the case of larger numbers of spheres, we demonstrated that our results are consistent, by showing that they converge as the truncation number increases.

An open problem that remains is the proper choice of the truncation number as a function of the wave number, sphere sizes, and intersphere distances. In the case where the truncation number is properly selected, the solution showed high accuracy, and substantial speed-up in comparison to the boundary element method. In cases when the centers of the spheres are located on a line (which is always true for two
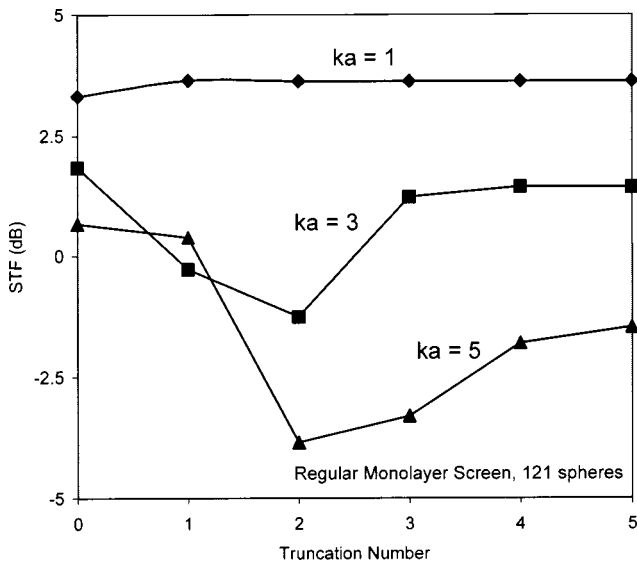
FIG. 14. Convergence test for the problem of sound scattering by a screen of 121 equal sized spheres located at the nodes of a regular grid (as shown in Fig. 13). Three different curves are computed at different *ka* indicated near the curves.

spheres, and can be realized in particular problems for *N* spheres) computations using a coaxial multipole reexpansion can be performed with much higher efficiency than in the general case.

Future improvements to the method proposed here may include use of spatial grouping of nearby spheres into clusters represented by one multipole expansion, variable truncation numbers depending on the particular distribution of spheres, implementation of a fast multipole method based evaluation of the matrix-vector product in Eq. (39), and development of iterative algorithms for solution of that equation.

ACKNOWLEDGMENTS

Algazi, V. R., Duda, R. O., Duraiswami, R., Gumerov, N. A., and Tang, Z. (**2002**). "Approximating the head-related transfer function using simple geometric models of the head and torso," J. Acoust. Soc. Am. **112**, 2053–2064.

Brunning, J. H., and Lo, Y. T. (**1971**). "Multiple scattering of EM waves by spheres, parts I and II," IEEE Trans. Antennas Propag. **AP-19**(3), 378–400.

Chew, W. C. (**1992**). "Recurrence relations for three-dimensional scalar addition theorem," J. Electromagn. Waves Appl. **6**(2), 133–142.

Duda, R. O., and Martens, W. L. (**1998**). "Range dependence of the re-

sponse of a spherical head model," J. Acoust. Soc. Am. **104**, 3048–3058.

Duraiswami, R., and Prosperetti, R. (**1995**). "Linear pressure waves in fogs," J. Fluid Mech. **299**, 187–215.

Duraiswami, R., Gumerov, N. A., Davis, L., Shamma, S. A., Elman, H. C., Duda, R. O., Algazi, V. R., Liu, Q-H., and Raveendra, S. T. (**2000**). "Individualized HRTFs using computer vision and computational acoustics," J. Acoust. Soc. Am. **108**, 2597(A). Also available on the web at http://www.acoustics.org/press/140th/duraiswami.htm.

Epton, M. A., and Dembart, B. (**1995**). "Multipole translation theory for the three-dimensional Laplace and Helmholtz equations," SIAM J. Sci. Comput. **4**, 865–897.

Gaunaurd, G. C., and Huang, H. (**1994**). "Acoustic scattering by a spherical body near a plane boundary," J. Acoust. Soc. Am. **96**, 2526–2536.

Gaunaurd, G. C., Huang, H., and Strifors, H. (**1995**). "Acoustic scattering by a pair of spheres," J. Acoust. Soc. Am. **98**(1), 495–507.

Gumerov, N. A., and Duraiswami, R. (**2001a**). "Fast, Exact, and Stable Computation of Multipole Translation and Rotation Coefficients for the 3-D Helmholtz Equation," University of Maryland Institute for Advanced Computer Studies Technical Report UMIACS-TR-#2001-44. Also CS-TR-#4264. (Available at http://www.cs.umd.edu/Library/TRs/CS-TR-4264/CS-TR-4264.pdf).

Gumerov, N. A., and Duraiswami, R. (**2001b**). "Modelling the effect of a nearby boundary on the HRTF," Proc. International Conference on Acoustics, Speech, and Signal Processing 2001, Salt Lake City, UT, 7–11 May 2001, Vol. 5, pp. 3337–3340.

Gumerov, N. A., Duraiswami, R., and Tang, Z. (**2002**). "Numerical study of the influence of the torso on the HRTF," to appear in Proc. of the International Conference on Acoustics, Speech and Signal Processing, Orlando, FL, 2002.

Gumerov, N. A., Ivandaev, A. I., and Nigmatulin, R. I. (**1988**). "Sound waves in monodisperse gas-particle or vapour-droplet mixtures," J. Fluid Mech. **193**, 53–74.

Hanish, S. (**1981**). *A Treatise on Acoustical Radiation*, Naval Research Laboratory, Washington, DC, pp. 123–125.

Huang, H., and Gaunaurd, G. C. (**1995**). "Acoustic scattering of a plane wave by two spherical elastic shells," J. Acoust. Soc. Am. **98**, 2149–2156.

Kahana, Y. (**2001**). "Numerical modeling of the head-related transfer function," Ph.D. thesis, University of Southampton.

Katz, B. F. G. (**2001**). "Boundary element method calculation of individual head-related transfer function. I. Rigid model calculations," J. Acoust. Soc. Am. **110**, 2440–2448.

Koc, S., and Chew, W. C. (**1998**). "Calculation of acoustical scattering from a cluster of scatterers," J. Acoust. Soc. Am. **103**, 721–734.

Koc, S., Song, J., and Chew, W. C. (**1999**). "Error analysis for the numerical evaluation of the diagonal forms of the scalar spherical addition theorem," SIAM (Soc. Ind. Appl. Math.) J. Numer. Anal. **36**, 906–921.

Marnevskaya, L. A. (**1969**). "Diffraction of a plane scalar wave by two spheres," Sov. Phys. Acoust. **14**(3), 356–360.

Marnevskaya, L. A. (**1970**). "Plane wave scattering by two acoustically-rigid spheres," Sov. Phys. Acoust. **15**(4), 499–502.

Mishchenko, M. I., Travis, L. D., and Mackowski, D. W. (**1996**). "T-matrix computations of light scattering by nonspherical particles: a review," J. Quant. Spectrosc. Radiat. Transf. **55**, 535–575.

Morse, P. M., and Feshbach, H. (**1953**). *Methods of Theoretical Physics—I* (McGraw–Hill, New York).

Peterson, B., and Strom, A. (**1974**). "Matrix formulation of acoustic scattering from an arbitrary number of scatterers," J. Acoust. Soc. Am. **56**, 771–780.

Rokhlin, V. (**1993**). "Diagonal forms of translation operators for the Helmholtz equation in three dimensions," Appl. Comp. Harmonic Analysis **1**, 82–93.

Varadan, V. K., and Varadan, V. V. (**1980**). *Acoustic, Electromagnetic and Elastic Wave Scattering: Focus on the T-Matrix Approach* (Pergamon, New York).

Waterman, P. C., and Truell, R. (**1961**). "Multiple scattering of waves," J. Math. Phys. **2**, 512–537.

Time domain investigation of transceiver functions using a known reference target

C. Feuillade[a)] and R. W. Meredith
Naval Research Laboratory, Stennis Space Center, Mississippi 39529-5004

N. P. Chotiros
Applied Research Laboratory, University of Texas, Austin, Texas 78713-8029

C. S. Clay
Geophysical and Polar Research Center, University of Wisconsin-Madison, Madison, Wisconsin 53706

During August 1998, a bottom scattering tank experiment was performed at the Applied Research Laboratory, University of Texas to measure wideband acoustic reverberation from multiple objects (e.g., cobbles and pebbles) placed on a sediment simulation of the sea floor. In preparation for processing and analyzing the experimental data, time domain scattering measurements made with stainless steel and glass balls suspended in the water column were used to calibrate the sonar transceiver system by deconvolving the theoretical impulse response for steel and glass spheres, obtained via the Faran elastic sphere scattering model, from the scattered time signals. It is the analysis of these calibration measurements which forms the subject of this paper. Results show the critical importance of accurate input–output system calibrations for time domain sound scattering research, and successfully demonstrate a time domain method for accurately calibrating the complete sonar transceiver function, i.e., both the amplitude and time dependence, using a known reference target. The work has implications for boundary and volume scattering applications. © *2002 Acoustical Society of America.* [DOI: 10.1121/1.1512704]

I. INTRODUCTION

The use of reference targets for underwater sound research and sonar development is a familiar concept. Such targets have a range of applications, including acoustic source calibration and testing. A helpful experimental survey of several types of sonar targets has been given by Wallace *et al.*[1]

Spherical forms are an obvious choice for reference targets, since their backscattering characteristics are independent of orientation. The theory of acoustic scattering from spheres has received much attention, beginning with Rayleigh, who derived a solution for the case of a sphere which is small compared to the wavelength.[2] Morse gave solutions without wavelength restrictions, but for cases where there is no acoustic penetration of the sphere.[3] The issue of acoustically penetrable spheres was subsequently treated by Anderson,[4] who developed a method for describing scattering from fluid spheres, and Faran,[5] who obtained solutions for the scattering of sound by elastic spheres and cylinders. Faran's formalism is general, and has been shown[6] to contain both Anderson's solution and Hickling and Wang's "movable rigid sphere" solution[7] as limiting cases.

Experimental studies of scattering from solid spheres in water have been performed by a number of investigators.[8–10] Dragonette *et al.*[11] used the technique of time separating the rigid body and elastic components within short pulse, broadband, scattering returns from a metal sphere, to calibrate test

targets for acoustic measurements. In 1982, Foote[12] demonstrated a precision technique for cw calibration of sonar equipment, by normalizing the scattering from a reference copper sphere target with the return theoretically predicted by Faran's formalism. Copper is determined to be a superior material since its properties appear to be stable, in contrast to the variabilities induced by variations in the annealing processes of alloys. Foote's calibration procedure has subsequently been widely adopted within the fisheries community. Typically, before a stock assessment exercise is begun, a known test target is suspended below a survey ship, and scattering returns from it are used to calibrate the sonar system that is going to be used.

A recent innovation in bioacoustics research is the application of time domain scattering methods to investigate the internal structure of organisms in the water column. Chu and Stanton[13] used pulse compression techniques, via chirp pulses with narrow autocorrelation functions to achieve fine time–space sampling, to identify and explore the inner structures of several different species of zooplankton. There is growing interest in the use of techniques like this to develop fisheries technologies which are capable of simultaneously coupling biomass estimation with species identification.

One of the requirements needed to enable time domain approaches of this type to be used in biomass survey exercises, and in other volume and boundary scattering applications, is the development of an accurate and reliable method for calibrating the time dependence of the sonar system used. The work described here demonstrates such a calibration method by presenting a technique for determining the com-

---

[a)]Electronic mail: cf@nrlssc.navy.mil

plete time signature of a sonar, which works by deconvolving the theoretically derived impulse response of a known reference target from an experimental scattering signal. The work also has a secondary purpose, which is to explore in some detail the use of impulse response methods to investigate both scatterers and transient acoustic sources.

In order to process and analyze the data from a bottom scattering tank experiment at the Applied Research Laboratory, University of Texas (ARL-UT), a procedure was used to calibrate the sonar transceiver system, by deconvolving the theoretical impulse response for steel and glass spheres, obtained via the Faran elastic sphere scattering model, from scattered time signals from stainless steel and glass balls suspended in the water column. These calibration measurements are the subject of this present work. The results show the importance of accurate input–output system calibrations for time domain sound scattering applications, and successfully demonstrate that the complete sonar transceiver function, i.e., both the amplitude *and* time dependence, can be accurately calibrated in the time domain by deconvolving the impulse response of a known reference target from the experimental scattered signal.

Section II of this paper describes the experiment performed and the data collected. Section III describes the time domain filtering and convolution/deconvolution methods used to perform the sonar calibrations, and briefly summarizes the Faran elastic sphere scattering model used to calculate the impulse responses for steel and glass spheres. Section IV describes the results of the theoretical calculations, deconvolutions, and data comparisons. Section V provides a summary of conclusions. Two appendices are included, which provide background information on filtering and deconvolution using polynomial multiplication and division methods, and also the amplitude of the geometrical scattering component from spheres.

II. THE EXPERIMENT

The overall technical objective of the tank experiment, which was performed at the Applied Research Laboratory, University of Texas, in August 1998, was to study scattering from objects, i.e., cobbles and pebbles, placed on a simulated seafloor. Before the main part of the experiment was performed, preliminary tests were made to calibrate the sonar transceiver system.

One method of calibrating a sonar is to direct it toward a plane water/air interface, and measure the reflected signal. Since the dynamic response of the interface is a spike, this should enable the sonar function to be directly observed and calibrated. This technique cannot readily be used if the water surface is not flat (e.g., during deployment at sea), but was indicated under the controlled conditions of the ARL-UT experiment. In our case, an initial attempt to calibrate the sonar was made by directing it vertically upwards and measuring the reflected signal from the flat water surface in the tank. Unfortunately, however, subsequent analysis showed that the large amplitude of the reflected signals had induced a nonlinear response in the transceiver system and thereby invalidated the procedure.
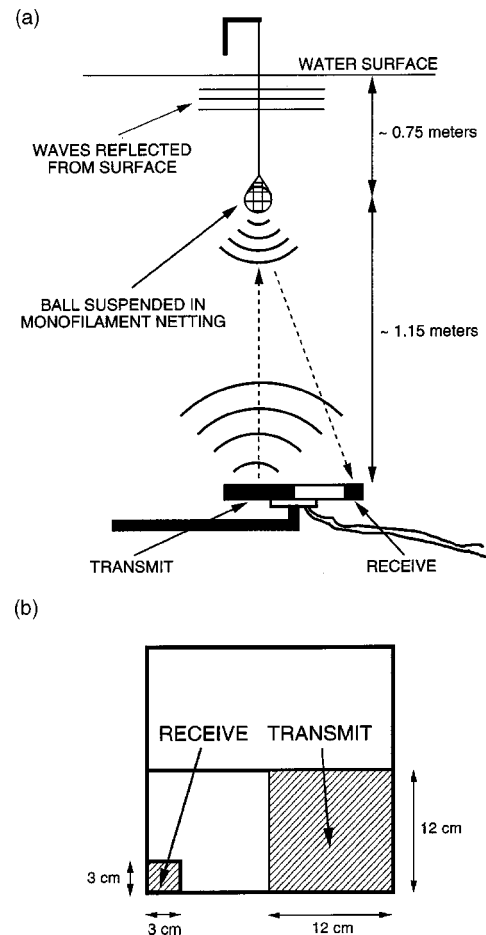
FIG. 1. The experiment. (a) Schematic diagram of the experiment. Careful tests were made to ensure that the target balls were suspended directly over the center of the transmit transducer. The scattered/reflected signals were detected at the receive transducer. (b) The transmit and receive transducers were subdivided panels of a larger flat plate transducer.

Another method of calibrating a sonar is to use a known reference target. This is the basis of the technique for cw calibration developed by Foote,[12] who advocated the use of copper sphere targets. During the same series of preliminary tests at ARL-UT, another experiment was performed using the same vertical configuration, but with steel and glass balls interposed directly between the sonar transducer and the water surface. Due to the problems experienced with the reflected signals, an alternative procedure was followed to determine the sonar transceiver function. This required that the theoretical impulse response for elastic steel or glass spheres, obtained via the Faran scattering model, should be deconvolved from the signals scattered from the balls. These measurements were not originally performed for calibration purposes, and the targets were not optimally made from copper. Nevertheless, the deconvolution is achievable if the material properties of the steel and glass balls can be determined to sufficient accuracy. It is the performance and resulting analysis of the subsequent calibration/deconvolution procedure which forms the subject of this present work.

A schematic diagram of the experiment is shown in Fig. 1(a). The sonar transmit and receive system consisted of two subdivided panels of a ≈ 25 cm square flat plate transducer [Fig. 1(b)] with primary frequency output between about 25

and 120 kHz, and peaking near 80 kHz. The ball targets were carefully suspended ~ 1.15 m directly above the center of the 12 cm square transmit panel and ~ 0.75 m below the water surface. The signal was directed vertically upwards, and was scattered from the balls and also reflected back down from the water surface. The scattered/reflected signals were detected at the 3 cm square receive panel, as shown in Fig. 1(a). The distance from the transducers to the balls was greater than the Rayleigh distance for the transducers throughout the primary operational frequency range of the sonar system, indicating that the targets are located in the "far-field" of the transducers. The transmit transducer was always driven using the same electrical signal throughout the experiment. The receiver system was operated within a linear range, so that the output $e(t)$ in volts was proportional to the pressure field $p_{bs}(t)$ at the face of the receive transducer. The scattering data were sampled and recorded at 1 MHz. The water in the tank had a measured sound speed of $c = 1482$ m/s throughout the experiment.

The 3 dB beamwidth of the transmit transducer is calculated as $\approx 7.8°$ at 80 kHz. The 3 dB beamwidth of the receiver transducer is $\approx 31.2°$ at the same frequency. The ball targets were located within the main beam of both transducers. The physical separation of the centers of the two transducers was ≈ 17.6 cm, which corresponds to an angular separation, as subtended at the location of the center of the balls, of $\approx 8.7°$. Recent time domain studies of scattering from elastic spheres[14] indicate that the scattered impulse wave is essentially unchanged within $\pm 10°$ of the backscattering axis, which implies that the scattering geometry of the experiment described here is effectively monostatic. For this reason, we have utilized the backscattered impulse response (which is widely used) in the analysis described here.

The balls were supported in cradles of fine monofilament netting, which were knotted to monofilament line suspended from a retort stand placed above the water surface. During the steel ball measurements, the acoustic scattering response of the evacuated cradle and line was tested separately, and found to have a peak-to-peak variation ≈ 100 mV, which is about 10 dB lower than the steel ball. However, the evacuated netting tended to bunch together to form, with the knot, a somewhat compact and coherent target. With the steel ball enclosed, the netting expanded to become a more diffuse target, and the knot was then situated in the acoustic shadow of the ball, in the forward scattering direction, where it would have a smaller influence on the backscattered field. For these reasons, it was assumed that the influence of the netting on the backscattered field for the steel ball was negligible. No similar tests were performed on the cradle used for the larger and more massive glass ball, but the same assumption was made in the backscattering measurements for this object also.

Figure 2(a) depicts a typical output from the experiment. It shows the output, coherently averaged over ten pings, of the time signal backscattered from one of the steel balls placed in the water column, together with the surface reflection (other secondary features, i.e., the initial transmit disturbance and multiple reflections in the surface, can also be seen). Figure 2(b) shows the current input drive to the trans-
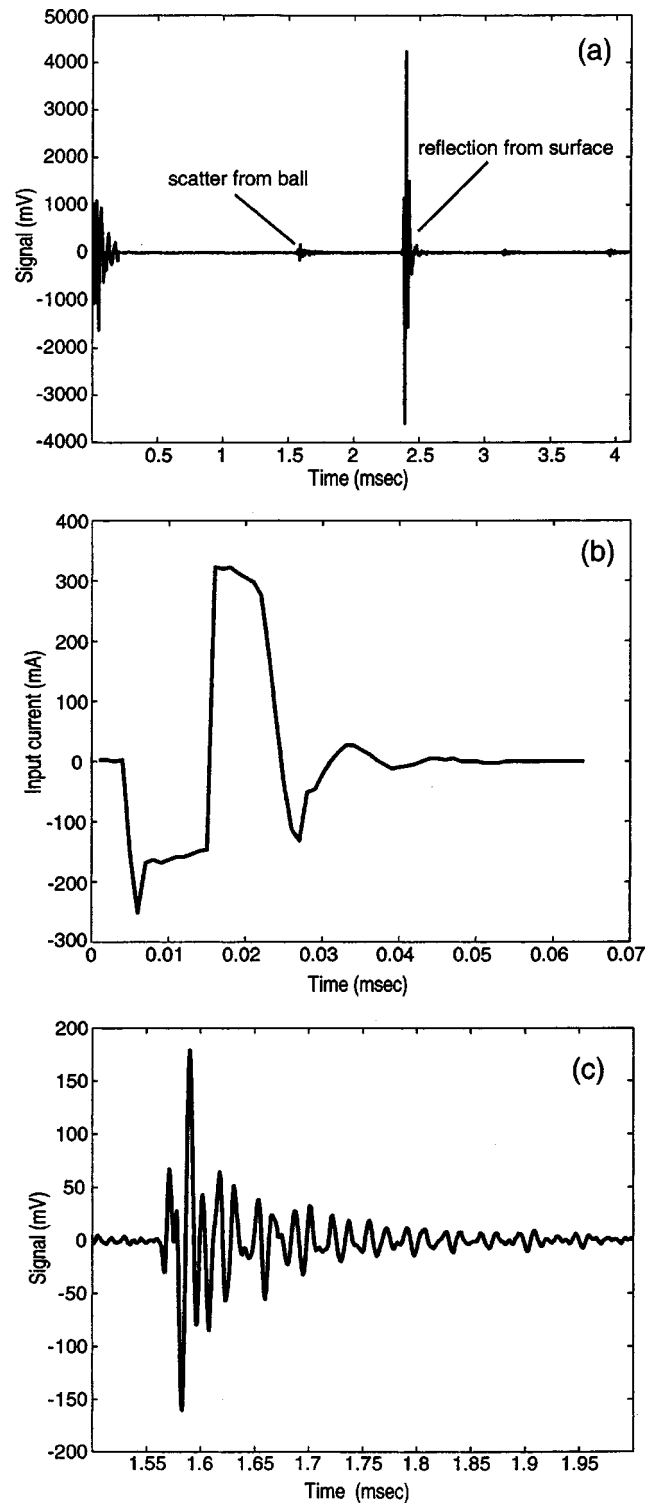
FIG. 2. Typical output from the experiment. (a) The time signal $p_{bs}(t)$ backscattered from a steel ball averaged over ten pings is shown, together with the surface reflection. Other secondary features can also be seen. The experimental data have units of mV at the output of the amplifier. (b) Input drive current to the transducer for the signal recorded in (a) and (c). (c) Magnification of the signal scattered from the steel ball in (a). The peak values for this section of the signal are much smaller than for the surface reflection component, and did not give rise to nonlinearities.

mit transducer which was used to produce this output. The same current drive was used unchanged throughout the experiment. In Fig. 2(a), the large amplitude of the surface reflection part of the signal ($\sim \pm 4$ V) exceeded the linear

Feuillade *et al.*: Time domain transceiver functions investigations

range of the receiving amplifier in the transceiver system. Normally, the impulse response of the sonar system may be determined by deconvolving the corresponding current input drive [Fig. 2(b)] from the reflected signal, but this procedure was not valid in this case. Figure 2(c) shows a magnification of the section of the signal in Fig. 2(a) scattered from the steel ball. The signal amplitudes in this section were within the linear range of the receiving amplifier, and provide the data for deconvolving the sonar transceiver function, as we shall describe in the following.

After the experiment was completed, further tests at a lower current drive were subsequently made to calibrate the sonar transceiver system using the surface reflection method. While the problem of nonlinearities was eliminated, these tests had another different problem. Figure 3(a) shows the average of 50 pings of the reflected signal from one of these later tests. The corresponding input current to the sonar is shown in Fig. 3(b). Unfortunately, the first data point in the input current data stream was not recorded, and the value of this datum [denoted by the leftmost point in Fig. 3(b)] had to be estimated in order to achieve a reliable deconvolution of the sonar impulse response. Figure 3(c) shows the most stable deconvolution result that could be obtained from this data.

As described earlier, the primary intention of this paper is to demonstrate the method of deconvolving the theoretical impulse response of a known reference target from scattering data to calibrate the time signature of a sonar. The desired operational *result* of the work, however, is the confirmation of the sonar impulse response seen in Fig. 3(c), which then enables the remaining data from the ARL-UT experiment to be analyzed. Since Fig. 3(c) was obtained at a lower current, this result also indicates that the transmit transducer output relative to the current drive appears to be linear in the range where it was used during the experiment.

In the development of the theory and method used in this present work, we have followed the format used in a recent textbook,[18] which expresses the acoustic field in terms of sound pressure in the water. The work described here demonstrates that it is not necessary to have independently calibrated pressure responses for the transmitter and receiver. If the same transmitter and receiver system (i.e., transceiver) is used for the reference target calibration measurements and the subsequent experimental scattering measurements, then the impulse response of the reference target can be used to determine the impulse response of the sonar system. Further details about the relation of instrument outputs and inputs to sound pressures are given in Medwin and Clay's book (Ref. 18, Sec. 4.6).

III. THE TIME DOMAIN DECONVOLUTION

A. Time domain filters

The deconvolution result shown in Fig. 3(c) was obtained by discrete Fourier transform division, using the fast Fourier transform (FFT) algorithm. However, the method of sonar calibration described in this present work uses time domain deconvolution and filtering techniques. The concept of minimum delay wavelets is borrowed from exploration
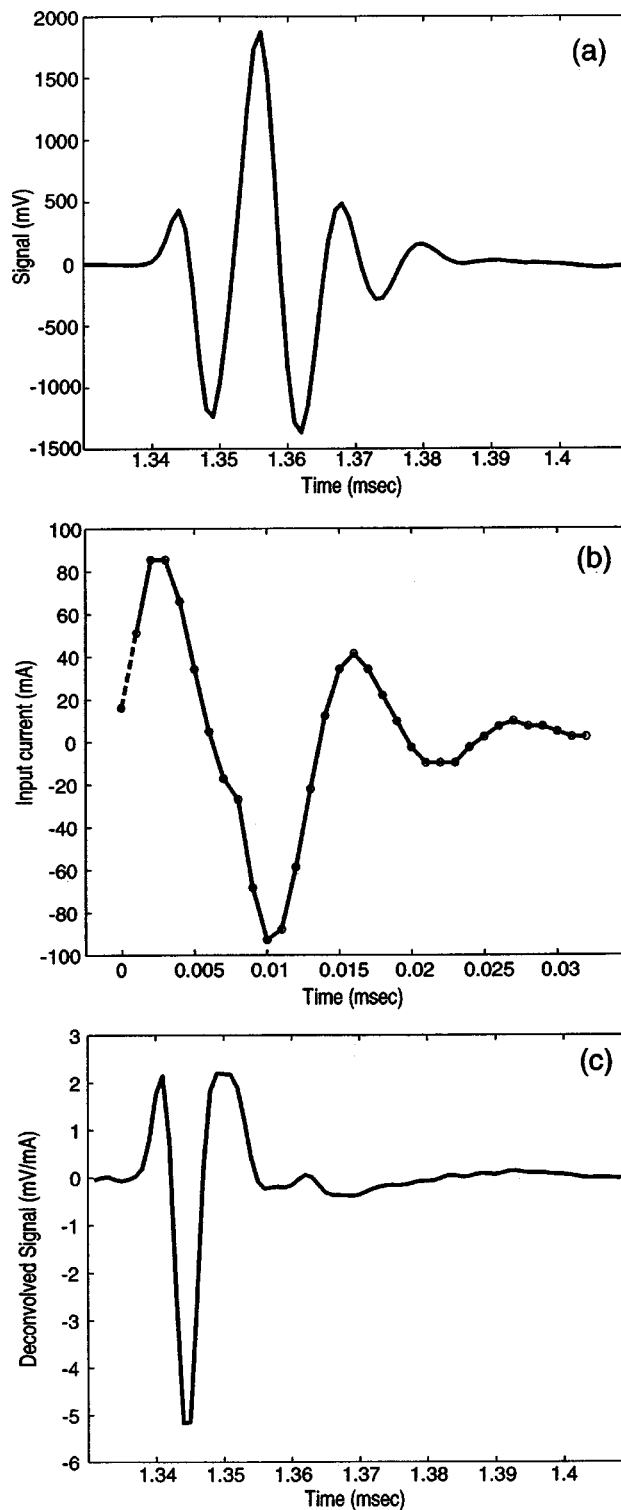
FIG. 3. Calibration signal at lower current drive. Subsequent to the experiment, further measurements at a lower current drive were made to calibrate the sonar transceiver system. (a) Reflected signal averaged over 50 pings. (b) Input current to the sonar. The datum denoted by the leftmost point was missing, and its location had to be estimated. (c) Sonar impulse response derived by deconvolving the input current (including the estimated datum) from the average reflected signal.

geophysics, and one-sided time domain filters are constructed to concentrate energy toward the front, and minimize distortions, of the input signals.[15,16]

The signal processing uses numerical vectors and

Laplace z-transform polynomial notation for the sampled signals and for convolution and deconvolution operations. The Laplace z-transform polynomial and corresponding row vector of a signal E are written

$$E(z) = e_1 z^1 + e_2 z^2 + e_3 z^3 + e_4 z^4 + \cdots, \tag{1}$$

$$E = [e_1 \quad e_2 \quad e_3 \quad e_4 \quad \cdots], \tag{2}$$

where the time increment is Δt, and a time delay $n\Delta t$ is indicated by the power of z^n (the notation z^{-n} is also sometimes used in the literature). A minimum delay filter is constructed that is the product of minimum delay wavelets. In z-transform notation we write:

$$w_1 = [1 + z/2], \quad w_2 = [1 + 2z/3], \quad w_3 = [1 + 3z/4],$$
$$w_4 = [1 + 4z/5], \quad w_5 = [1 + 5z/6], \tag{3}$$

with polynomial product

$$\mathcal{W} = w_1 * w_2 * w_3 * w_4 * w_5, \tag{4}$$

where the asterisk represents convolution. This product, together with other similar polynomial operations, is rapidly performable in MATLAB.[17] (Examples of the MATLAB coding procedures used in this work are given in Appendix A.) The wavelets in Eq. (3) were chosen because they are simple low distortion filters that do not advance any of the signal components ahead of the actual arrival time.[15] Figure 4(a) represents the time domain filter $\mathcal{W}$, normalized so that the numerical sum of its row vector elements is unity. To understand the filtering action of $\mathcal{W}$, its spectrum is computed using the FFT and shown in Fig. 4(b), with the frequency spectrum of the surface reflection used in the calibration measurements [Fig. 3(a)] overlaid for comparison. We see that $\mathcal{W}$ is a low-pass filter. It is used here in convolution calculations to suppress Nyquist oscillations in the theoretical impulse responses for spherical scatterers, and also as a simple smoother to reduce high-frequency noise in the experimental signals and to suppress Nyquist oscillations in the deconvolutions.

B. The theoretical impulse response of an elastic sphere

The theory of scattering from an elastic sphere was introduced by Faran. We will not reproduce the theory here, but refer the reader to Faran's paper.[5] His method uses spherical wave expansions around an origin placed at the center of the sphere. The incident and scattered fields are compressional waves in the external fluid. The acoustic wave inside the elastic sphere consists of both compressional and shear components. To determine the coefficients in the expansion of the scattered field, three boundary conditions are applied at the surface of the sphere. The normal displacement and normal stress must be continuous, and the tangential stress must be zero. To facilitate later discussion, we note the following expressions for the speed of propagation of compressional waves (c_L) and shear waves (c_T) in the internal elastic medium, i.e.,

$$c_L = \sqrt{\frac{\lambda + 2\mu}{\rho}}, \tag{5}$$
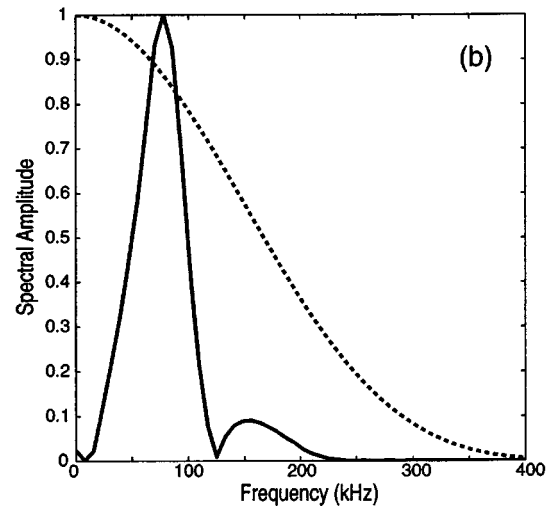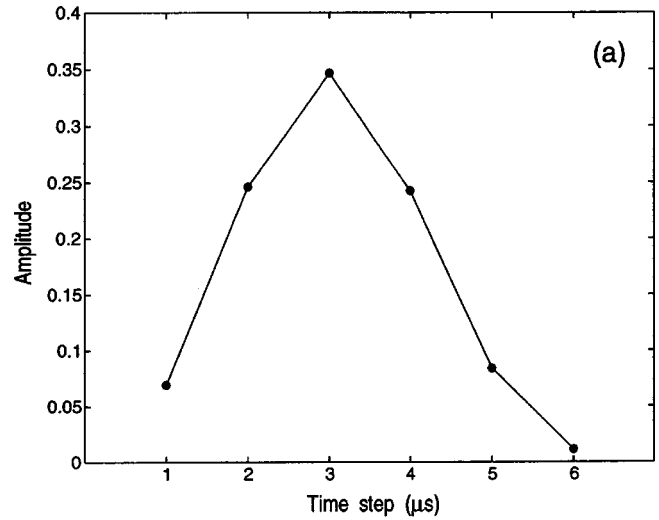
FIG. 4. The time domain filter. (a) Graphical depiction of the minimum delay filter $\mathcal{W}$ constructed by convolving a series of minimum delay wavelets [see Eqs. (3) and (4)]. The filter is normalized so the sum of its elements is unity. The points (closed circles) are joined by lines to accent the variations. (b) The dashed line is the absolute value of the Fourier spectrum of the filter $\mathcal{W}$. $\Delta t = 1$ μs, $\Delta f = 7.8125$ kHz. The absolute value of the spectrum of the surface reflection used in the calibration measurements [Fig. 3(a)] is overlaid for comparison (solid line). The amplitudes have been normalized to unity for display.

$$c_T = \sqrt{\frac{\mu}{\rho}}, \tag{6}$$

where ρ is the density of the sphere, and λ and μ are the elastic Lamé constants. In particular, μ is the shear rigidity modulus.

The backscattered impulse response of an object may be formally written by means of the inverse Fourier transform

$$l_{bs}(t) = \int_{-\infty}^{\infty} L_{bs}(f) \, e^{i2\pi ft} \, df, \tag{7}$$

where $L_{bs}(f)$ is the backscattering length in m (Ref. 18, pp. 237–238). For a sphere $L_{bs}(f)$ is often referred to $a/2$, where a is the spherical radius. The impulse response $l_{bs}(t)$ has units m/s. These units are appropriate for $l_{bs}(t)$, because it enters convolution integrals over time.

Feuillade *et al.*: Time domain transceiver functions investigations

The impulse responses for the elastic spheres in this analysis were computed by evaluating Eq. (7) numerically using the inverse discrete Fourier transform (via the inverse FFT), i.e.,

$$l_{\text{bs}}(n\Delta t) = \sum_{m=0}^{M-1} L_{\text{bs}}(m\Delta f) e^{i2\pi mn/M} \Delta f, \tag{8}$$

where M is the number of points in the inverse FFT. In the computations presented here, $M = 2048$, and Δf was chosen to correspond to $\Delta t = 1$ μs, i.e., the sampling period used to record and store data in the experiments. The values of $L_{\text{bs}}(m\Delta f)$ were computed by means of the Faran theory, using appropriate values of ρ, c_L, and c_T, for stainless steel and glass.

As described previously, for the data analyzed here, the spherical targets were located in the far-field of the transmit/receive transducers. Tests were made to determine whether a plane wave assumption could be used to represent the incident field in the computation of $L_{\text{bs}}(f)$. To examine this issue, the spherical wave expansion for a point source (i.e., not a plane wave expansion) was used to calculate the incident field, and the distance from the point source to the sphere adjusted to match the particular data analyzed. In every case it was found that, when direct comparisons were made between the impulse responses resulting from the point source expansion and those obtained using the plane wave assumption, the differences were practically negligible. A plane wave expansion was therefore used throughout to calculate $L_{\text{bs}}(f)$.

C. The scattered sound pressure

The frequency domain expression for the backscattered sound pressure, in the case where the transmit and receiver transducers are colocated (as is effectively the case in the present experiment) and have the same directivity D is written (Ref. 18, pp. 350–353)

$$P_{\text{bs}}(f) = D^2 \frac{S_{\text{rc}}(f) R_0 L_{\text{bs}}(f)}{R^2} 10^{-\alpha R/10}, \tag{9}$$

where $S_{\text{rc}}(f)$ is the source sound pressure, R is the range from the scatterer to the transducer in m, and α is the attenuation coefficient in dB/m. The far field sound pressure output of the transducer $S_{\text{rc}}(f)$ is referred to $R_0 = 1$ m. The inverse Fourier transform gives

$$p_{\text{bs}}(t) = \int_{-\infty}^{\infty} D^2 \frac{S_{\text{rc}}(f) R_0 L_{\text{bs}}(f)}{R^2} 10^{-\alpha R/10} e^{i2\pi ft} df, \tag{10}$$

and the inverse discrete Fourier transform expression corresponding to Eq. (10) is

$$\begin{aligned} p_{\text{bs}}(n\Delta t) = \sum_{m=0}^{M-1} D^2 \frac{S_{\text{rc}}(m\Delta f) R_0 L_{\text{bs}}(m\Delta f)}{R^2} \\ \times 10^{-\alpha R/10} e^{i2\pi mn/M} \Delta f. \end{aligned} \tag{11}$$

In the time domain, the scattered sound pressure is the convolution of the transducer sound pressure $s_{\text{rc}}(t)$ and the scattering length $l_{\text{bs}}(t)$, i.e.,

$$p_{\text{bs}}(t) = \frac{10^{-\alpha R/10} R_0}{R^2} \int D^2 s_{\text{rc}}(\tau - 2R/c) l_{\text{bs}}(t - \tau) d\tau, \tag{12}$$

where the frequency dependence of the attenuation α is ignored. Both $s_{\text{rc}}(t)$ and the backscattered pressure $p_{\text{bs}}(t)$ have the same units. The solution of Eq. (12) for $s_{\text{rc}}(t)$ is achieved through deconvolution.

D. Discrete sampled signals

To perform the time domain operations here, the first step is to write equivalent z-transform polynomials for the functions p_{bs}, s_{rc}, and l_{bs}, as indicated by Eq. (1). In MATLAB these are represented by row vectors as shown in Eq. (2). Convolution is accomplished by polynomial algebraic multiplication, and deconvolution by polynomial algebraic division. Using z-transform and row vector notations, the scattered signal and source signal are

$$p_{\text{bs}}(z) = s_{\text{rc}}(z) l_{\text{bs}}(z) R_0 \frac{D^2}{R^2}, \tag{13}$$

$$s_{\text{rc}}(z) = [p_{\text{bs}}(z) / l_{\text{bs}}(z)] \frac{1}{R_0} \frac{R^2}{D^2}, \tag{14}$$

where the attenuation is neglected (it is typically very small for the ranges and conditions which apply in the present experiment). In MATLAB, the scattered signal p_{bs} is the convolution

$$p_{\text{bs}} = \left(\frac{R_0 D^2}{R^2}\right) \text{conv}(s_{\text{rc}}, l_{\text{bs}}), \tag{15}$$

and the deconvolution for the source function s_{rc} is

$$[s_{\text{rc}} \text{ rem}] = \left(\frac{R^2}{R_0 D^2}\right) \text{deconv}(p_{\text{bs}}, l_{\text{bs}}), \tag{16}$$

where rem is the remainder from the long division. [Further details are given in Appendix A.] The deconvolutions are rendered more tractable when l_{bs} approximates a "minimum delay" signal, i.e., the function has finite length, is large at the beginning, and decreases to small values at the end.

IV. RESULTS AND ANALYSIS

A. Deconvolution using a steel ball

The first set of scattering measurements were made using a standardized 440-C stainless steel spherical ball which, for convenience, we denote SB. SB had a measured diameter of 1.876 in (4.764 cm) and a mass of 0.956 lb (0.4336 kg). Several measurements of the diameter of SB at different orientations were made to verify the sphericity of the ball. Using the measured values for diameter and mass, the density of stainless steel is calculated as 7.661 g/cc for SB.

The acoustic properties of the steel from which the ball was constructed (i.e., the compressional and shear sound speeds) were not supplied by the manufacturer. In earlier scattering experiments at ARL-UT, using 440-C stainless steel balls which were smaller than that used here, the com-

FIG. 5. Scattering by a stainless steel sphere (SB). $c_L = 5980$ m/s, $c_T = 3350$ m/s, $\rho = 7.661$ g/cc, $a = 2.382$ cm. (a) Theoretical spectrum of the scattering length, or form function, $L_{bs}/(a/2)$. (b) Raw theoretical impulse response for $a = 2.382$ cm, calculated using the inverse FFT. (c) Convolution of the impulse response with the low-pass filter $\mathcal{W}$. (d) Backscatter data averaged over ten pings. This signal is obtained by deconvolving the current drive in Fig. 2(b) from the scattered signal seen in Fig. 2(c).

pressional and shear sound speeds input to the Faran model were adjusted to fit the measured backscattering form function in the frequency domain. By this means, the compressional and shear sound speeds for that particular manufacturing lot of type 440-C stainless steel were determined to be $c_L = 5980$ m/s and $c_T = 3350$ m/s, respectively. These values were used as initial estimates for input to the time domain Faran calculations in the present work. It was found that the computed impulse response of the steel balls was relatively insensitive to the compressional sound speed. This parameter was therefore not varied, but maintained at the $c_L = 5980$ m/s value determined in the previous frequency domain analysis. Considerable efforts were made, however, to refine the value of c_T, which was found to be the parameter which primarily determined the time domain backscattering response of the elastic spheres.

Figure 5(a) shows the variation of the scattering length with frequency, calculated using the Faran theory, for a stainless steel sphere with the density of SB, and using the initial values of $c_L = 5980$ m/s and $c_T = 3350$ m/s (which was later adjusted to be $c_T = 3315$ m/s, as explained in the following). The radius a of SB has been factored out of the

calculation (so that nondimensional units are used both for the scattering length and the frequency) to display the scattering "form function," which is the way this information is often presented in the literature. Figure 5(b) shows the corresponding theoretical impulse response for SB, which is calculated via Eq. (8) using a bandwidth ranging from 0 Hz to slightly greater than 500 kHz. Nyquist oscillations are superimposed on the signal. Figure 5(c) shows the result of convolving the impulse response in Fig. 5(b) with the low pass filter $\mathcal{W}$. The filter removes the oscillations and gives an impulse that is followed by several arrivals. A factor $\Delta t = 1$ μs is multiplied into the impulse response in the convolution. Appendix B provides some comments on the magnitude of the impulsive functions shown in Fig. 5(c) and Fig. 7(c).

The following procedure was used to refine the value of c_T for stainless steel in this experiment. In the impulse response shown in Fig. 5(c), two strong spike features ("f1" and "f2") are particularly noticeable. The first spike f1 is due to the initial reflection of the input pulse from the front face of the ball. The second f2 appears to be due to elastic wave propagation within the ball, interior reflection from the

Feuillade *et al.*: Time domain transceiver functions investigations

rear curved boundary, and repropagation to the front of the ball and then back to the receiver transducer. Figure 5(d) shows the backscatter from SB averaged over 10 pings. This curve was derived from the time signal shown in Fig. 2(c) by deconvolving out the current input to the sonar system for this set of measurements [Fig. 2(b)] using FFT division. Close examination of Fig. 5(d) reveals the occurrence of two strong features (''d1'' and ''d2'') embedded within other elastic oscillations of the ball. The time separation between d1 and d2 is very close to that between f1 and f2 in Fig. 5(c), which suggests that they may well be the result of the convolution of the transceiver function with the spikes in the impulse response. The value of the shear sound speed for analysis of the present experiment was finely tuned by assuming that the two sets of features are directly related in this way, and then adjusting the value of c_T used as input to the Faran calculation until the time separation between f1 and f2 closely matched that between d1 and d2. By this means, the shear speed was determined to be $c_T = 3315$ m/s. This value of c_T was subsequently used for all of the substantive calculations in this work. The justification for this procedure will be evident from the accuracy of the results to follow. We have not shown the raw and filtered impulse responses for SB, calculated using $c_T = 3315$ m/s, since they are visually indistinguishable from the signals seen in Figs. 5(b) and (c).

The main purpose here is the deconvolution of the theoretical impulse response of the steel ball from the experimental scattering signal to produce a time domain representation of the transceiver function. In preparation for deconvolution, the experimental data [Fig. 2(c)] were first smoothed using the filter $\mathcal{W}$, and then the initial section of the signal [spanning a time period slightly greater than that separating d1 and d2 in Fig. 5(d)] was selected, as shown in Fig. 6(a). A section of similar length was also selected from the theoretical impulse response $l_{bs}(t)$ [Fig. 5(c)], as shown in Fig. 6(b). In this case, the selected section begins at a data point which is large enough to ensure a stable deconvolution. As described previously, the deconvolution method uses an algorithm based upon polynomial long-division of the time-series values (see Appendix A). Selecting the first point of the impulse response within the initial spike causes it to approach a minimum delay signal which facilitates a stable causal inverse.[19]

Figure 6(c) shows the result of deconvolving the impulse response from the experimental signal for SB, using Eq. (16). The dashed line, which is the raw deconvolution, has oscillations at the Nyquist frequency superimposed on the signal. The solid line is the deconvolution after smoothing with $\mathcal{W}$. Since the experimental range R for this set of data is used in Eq. (16), the deconvolution in Fig. 6(c) represents the ''transceiver function'' referred to $R_0 = 1$ m. It can be seen that smoothing with $\mathcal{W}$ also introduces a small time delay.

B. Testing the transceiver function

A second set of scattering measurements were made using a spherical glass ball, which we denote GB. The ball was of nonspecific manufacture, and neither the acoustical prop-
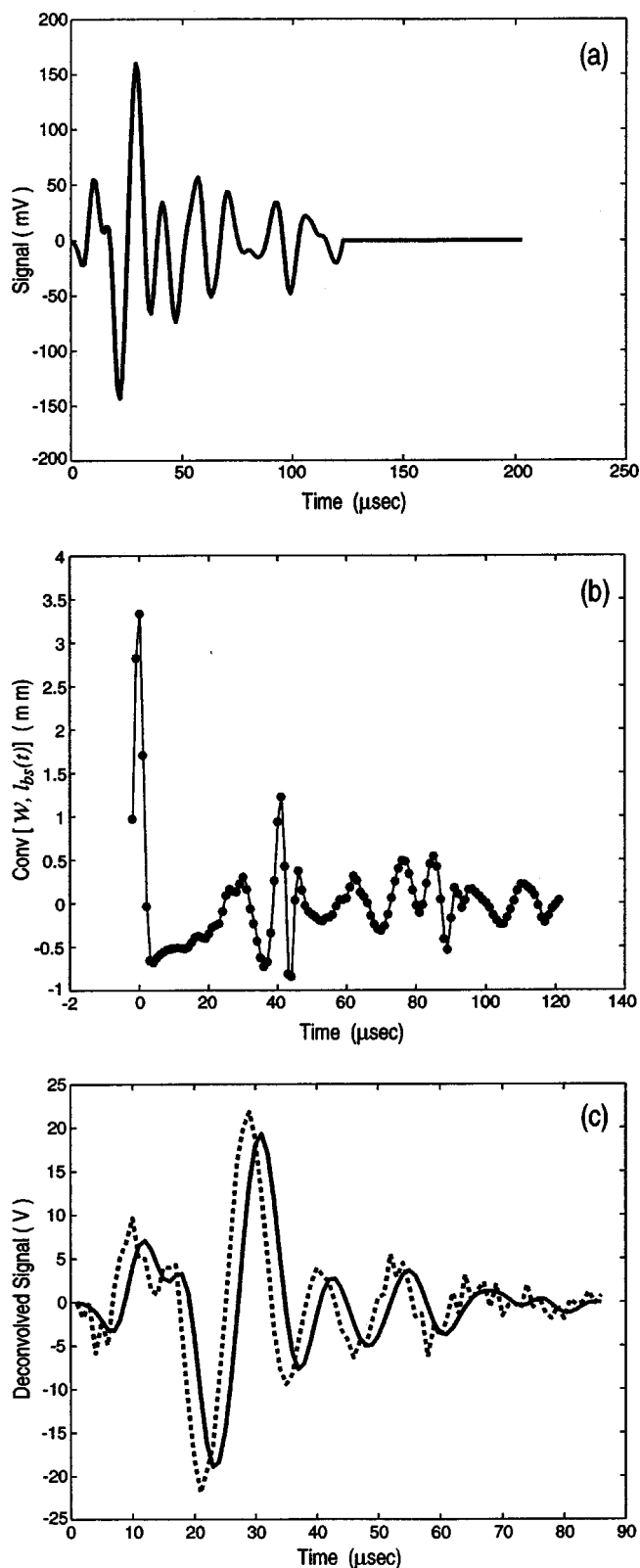
FIG. 6. Deconvolving the transceiver function from SB. (a) Data selected from the signal in Fig. 2(c), and low-pass filtered in preparation for deconvolution. (b) Selected region of the theoretical impulse response [Fig. 5(c)]. The data points (closed circles) are joined by lines to accent the variations. (c) The transceiver function is achieved by deconvolution of the theoretical impulse response from the experimental scattering data. The dashed line is the raw result, which contains oscillations at the Nyquist frequency. The solid line is the result of smoothing with $\mathcal{W}$, which also introduces a small time delay.

erties of the glass, nor its exact chemical composition, were available from the supplier. In the original experimental plan, this (and several other) glass balls were intended to be used as discrete bottom scattering targets.

Several measurements of the diameter of GB at perpendicular orientations indicated that it was not quite spherical. Three measurements of the diameter produced the following values: 3.869 in.; 3.898 in.; 3.882 in., with an average of 3.883 in. (9.863 cm). Since the deviation of the diameter from perfect sphericity was $<0.5\%$ from the average value, it seems reasonable to assume that GB is spherical and to use the average radial value for input to the Faran model. The mass of GB was measured as 2.732 lb (1.239 kg), which enabled the density of the glass to be determined as 2.467 g/cc.

Initial estimates of $c_L = 5800$ m/s and $c_T = 3525$ m/s were obtained from the CRC Handbook[20] by averaging the values for fused silica and Pyrex glass. Since we know, from the analysis of the steel ball data, that the impulse response is relatively insensitive to the compressional sound speed, the value of c_L was not varied. However, the value of the shear sound speed was refined using a procedure equivalent to that used earlier for SB, and determined to be $c_T = 3500$ m/s.

Figure 7(a) shows the variation of the scattering form function for a glass sphere with the density of GB, and using values of $c_L = 5800$ m/s and $c_T = 3500$ m/s. Figure 7(b) shows the corresponding impulse response for GB [calculated via Eq. (8) using the same bandwidth as for SB], which again contains Nyquist oscillations. Figure 7(c) shows the result of convolving the impulse response in Fig. 7(b) with $\mathcal{W}$. Again, a factor $\Delta t = 1$ μs is multiplied into the impulse response in the convolution. Comparison with Fig. 7(c) shows that the time separation between the arrivals f1 and f2 is almost exactly twice as long as for SB. If, as we suspect, f2 is due to interior reflection from the rear face of GB, this is presumably due to the fact that the diameter of GB is greater than that of SB by a factor of about 2.07, while the elastic sound speeds of the two materials are comparable.

In Fig. 8(a), the solid line shows backscatter data for GB averaged over 10 pings. The data have been smoothing using $\mathcal{W}$, and the amplitude has been scaled to refer the data to $R_0 = 1$ m. The dashed line is the convolution, using Eq. (15), of the transceiver function derived from the SB data shown in Fig. 6(c) with the theoretical impulse response for GB shown in Fig. 7(c). The close correlation between the two time signals is evident, both in overall time dependence and amplitude. In Fig. 8(b), the solid line shows the transceiver function deconvolved from the SB data, as shown in Fig. 6(c). The dashed line shows the convolution, again using Eq. (15), of the sonar impulse response derived from reflection calibration measurements [Fig. 3(c)], referred to $R_0 = 1$ m, with the current drive to the transducer for the SB scattering data set [Fig. 2(b)]. The convolution signal is smoothed using $\mathcal{W}$. Again, there is good time dependence and amplitude agreement between the signals which, in this case, represent two independent realizations of the transceiver function in the SB measurements. The result shown in Fig. 8(b) is very important. It confirms the impulse response curve seen in Fig. 3(c), which means that the complete transceiver func-
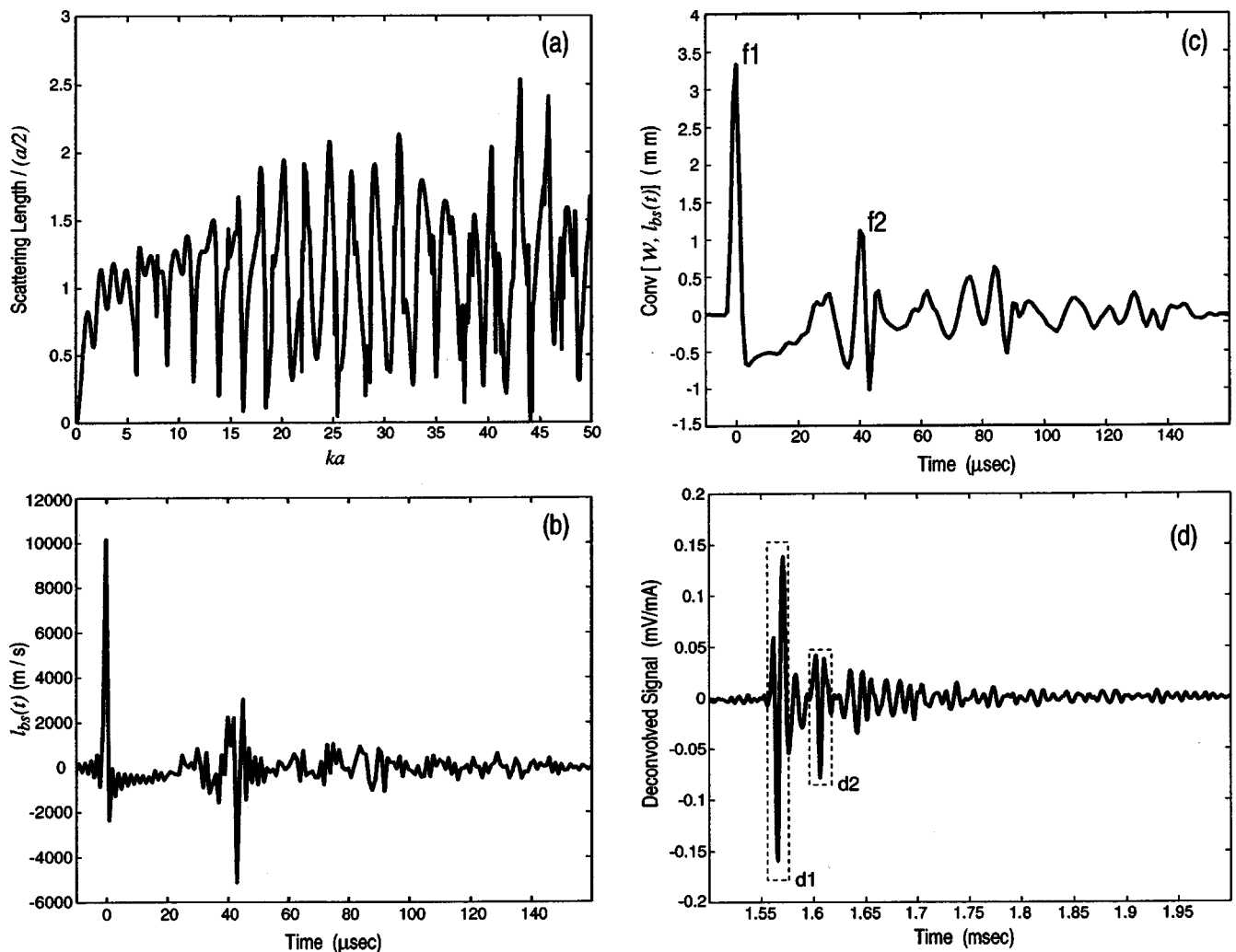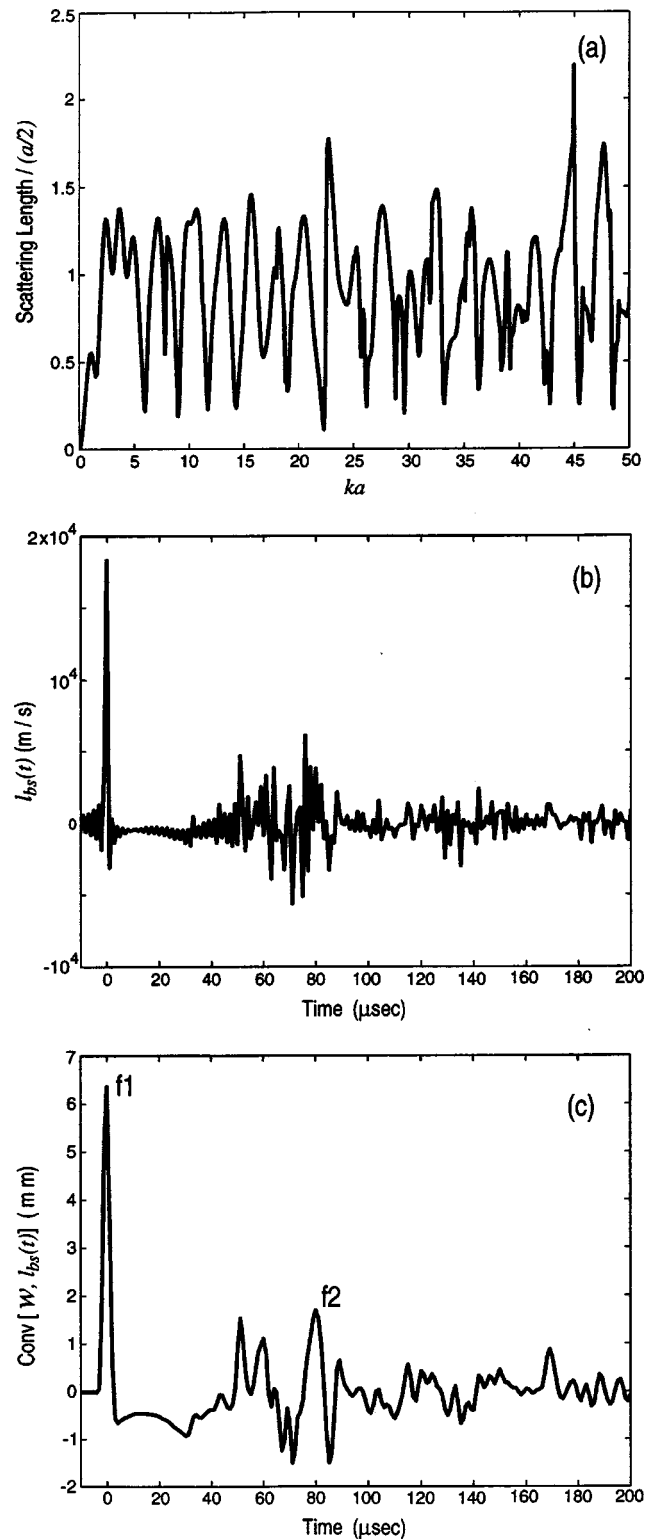

FIG. 7. Scattering by a glass sphere (GB). $c_L = 5800$ m/s, $c_T = 3500$ m/s, $\rho = 2.467$ g/cc, $a = 4.9315$ cm. (a) Theoretical spectrum of the scattering length, or form function, $L_{bs}/(a/2)$. (b) Raw theoretical impulse response for $a = 4.9315$ cm, calculated using the inverse FFT. (c) Convolution of the impulse response with the low-pass filter $\mathcal{W}$.

tion, i.e., both the time dependence and amplitude, for any other set of measurements from the ARL-UT experiment can be accurately determined by convolving this curve with the corresponding transducer current drive, and scaling the amplitude for the target range which applies to those measurements.
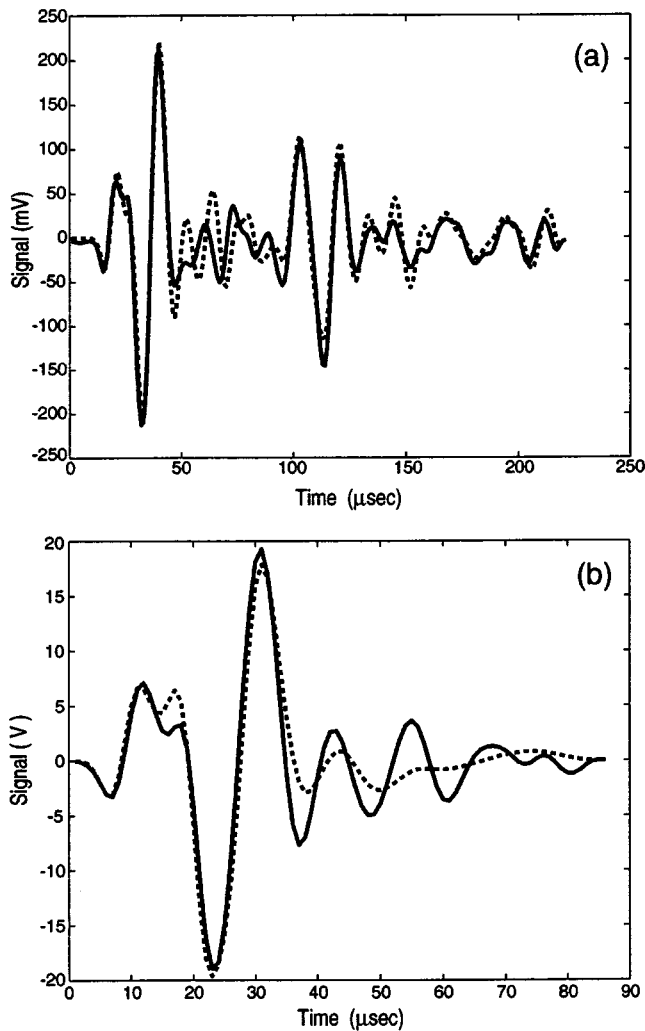
FIG. 8. Tests of the transceiver function. (a) The solid line shows backscatter data for GB, averaged over ten pings and smoothed using $\mathcal{W}$. The dashed line is the convolution of the transceiver function deconvolved from SB [solid line in Fig. 6(c)] with the theoretical impulse response for a glass sphere shown in Fig. 7(c). Note the time dependence and amplitude correlation between the two signals. (b) Two independent realizations of the transceiver function. The solid line shows the transceiver function deconvolved from SB [Fig. 6(c)]. The dashed line is the convolution of the sonar impulse response obtained from calibration measurements [Fig. 3(c)] with the current drive for the SB measurements [Fig. 2(b)], smoothed using $\mathcal{W}$.

V. CONCLUSIONS

Time domain measurements in an experimental water tank have been used to calibrate the time signature of a sonar transceiver system by deconvolving the theoretical impulse response for stainless steel and glass spheres, obtained via the Faran elastic sphere scattering model, from experimental time signals scattered from steel and glass balls suspended in the water column. The work described successfully demonstrates that the complete transceiver function of a sonar, i.e., both the amplitude *and* time dependence, can be accurately and practicably calibrated in the time domain by deconvolving the impulse response of a known reference target from the experimental scattered signal. The use of impulse response methods to investigate both scatterers and transient acoustic sources has also been explored in some detail. The results obtained indicate the importance of accurate input–output system calibrations for time domain sound scattering research, and have implications for boundary and volume scattering applications, such as biomass survey exercises.

APPENDIX A: DECONVOLUTIONS AND FILTER OPERATIONS

The use of filters in deconvolution operations requires care. In MATLAB, a polynomial such as

$$A = a_1 + a_2 z + a_3 z^2 + \cdots + a_i z^i + \cdots \tag{A1}$$

is written as an array

$$A = [a_1 \ a_2 \ a_3 \cdots a_i \cdots]. \tag{A2}$$

Similarly, let polynomials B and C be written:

$$B = [b_1 \ b_2 \ b_3 \ \ldots \ b_n \ \ldots \ ], \tag{A3}$$

$$C = [c_1 \ c_2 \ c_3 \ \ldots \ c_m \ \ldots \ ]. \tag{A4}$$

Let C be the polynomial product of A and B, i.e.,

$$C = A * B . \tag{A5}$$

In MATLAB, this product is given by $C = \text{conv}(A, B)$. Let A and B be

$$A = [1 \ \ 1 \ \ -2 \ \ ], \tag{A6}$$

$$B = [1 \ \ -2 \ \ 3 \ \ -1 \ \ 1 \ \ -2], \tag{A7}$$

so that

$$C = [1 \ \ -1 \ \ -1 \ \ 6 \ \ -6 \ \ 1 \ \ -4 \ \ 4]. \tag{A8}$$

The corresponding polynomial long division solution of Eq. (A5) for B is

$$B = C/A, \tag{A9}$$

and, in MATLAB, $B = \text{deconv}(C, A)$.

In signal processing, filters are routinely used to "clean" time signals. For example, following Eq. (3), let $\mathcal{W} = w_1 = [1 + z/2]$ which, in array format, is $\mathcal{W} = [1 \ \ 0.5]$. The filter operation on A is $\mathcal{W}A = \mathcal{W} * A$, or $\mathcal{W}A = \text{conv}(\mathcal{W}, A)$. Applying the filter to A, B, and C, yields:

$$\mathcal{W}A = [1.0 \ \ 1.5 \ \ -1.5 \ \ -1.0], \tag{A10}$$

$$\mathcal{W}B = [1.0 \ \ -1.5 \ \ 2.0 \ \ 0.5 \ \ 0.5 \ \ -1.5 \ \ -1.0], \tag{A11}$$

$$\mathcal{W}C = [1.0 \ -0.5 \ -1.5 \ 5.5 \ -3.0 \ -2.0 \ -3.5 \ 2.0 \ 2.0]. \tag{A12}$$

Using $\mathcal{W}C$ [from Eq. (A12)] rather than C [from Eq. (A8)], the deconvolution operation (A9) becomes

$$\mathcal{W}B = \mathcal{W}C/A = \text{deconv}(\mathcal{W}C, A), \tag{A13}$$

which yields

$$\mathcal{W}B = [\, 1.0 \quad -1.5 \quad 2.0 \quad 0.5 \quad 0.5 \quad -1.5 \quad -1.0 \,], \tag{A14}$$

in agreement with Eq. (A11). We can also perform

$$B = \text{deconv}(\mathcal{W}C, \mathcal{W}A) = [\, 1 \quad -2 \quad 3 \quad -1 \quad 1 \quad -2 \,], \tag{A15}$$

which agrees with Eq. (A7). The operations are what one would expect.

If the filters for the A and C are not the same, then the deconvolution operation gives rather different results. Consider

$$B' = C/(\mathcal{W}*A)[\text{ or } C/\mathcal{W}A\,], \tag{A16}$$

$$B' = [\, 1.0 \quad -2.5 \quad 4.25 \quad -3.125 \quad 2.5625\,], \tag{A17}$$

which should be contrasted with Eq. (A15). These examples demonstrate the need to be careful when using filters.

APPENDIX B

The geometrical scatter from a sphere, $a/2$, is often used as a reference (Ref. 18, pp. 268–271). Sun *et al.*[21] used $a/2$ in their composite scattering model for the impulse response scattered at the first surface. On the basis of our numerical studies of the modal solutions, we suggest an empirical method. First, the value $a/2$ for the geometrical scatter is effectively the result of an impulse integration of a time domain scattered signal (Ref. 18, pp. 72, 73). Recall the signal peaks labeled "f1" in Figs. 5(c) and 7(c). Let the duration of the positive part be t_{f1}. The impulse integral is

$$\text{Impulse} = \int_0^{t_{f1}} l_{f1}(t)\, dt. \tag{B1}$$

First, this impulse can be compared to the total (optical) scatter from a rigid sphere of $\sigma_{\text{total}} = a^2/4$ (or amplitude $a/2$). Second, the inverse Fourier transform of the wave number solution $L_{\text{bs}}(ka)$ to the time domain gives an initial peaked function $l_{f1}(t)$ that corresponds to the backscattered reflec-

tion from the rigid sphere. The height $l_{f1}(t)$ and width t_{f1} depend on the bandwidth of the $L_{\text{bs}}(ka)$. Third, the impulse is the integral of $l_{f1}(t)$ over its duration t_{f1}. The backscattered impulses from the steel and glass spheres are roughly 85%–95% of $a/2$.

[1] R. H. Wallace, H. V. Hillery, G. R. Barnard, B. M. Marks, and C. M. McKinney, "Experimental investigation of several passive sonar targets," J. Acoust. Soc. Am. **57**, 862–869 (1975).

[2] Lord Rayleigh, *The Theory of Sound* (1st American ed., Dover, New York, 1945), Sec. 334.

[3] P. M. Morse, *Vibration and Sound*, 2nd ed. (reprinted by American Institute of Physics, New York, 1981), pp. 354–357.

[4] V. C. Anderson, "Sound scattering from a fluid sphere," J. Acoust. Soc. Am. **22**, 426–431 (1950).

[5] J. J. Faran, Jr., "Sound scattering by solid cylinders and spheres," J. Acoust. Soc. Am. **23**, 405–418 (1951).

[6] C. Feuillade and C. S. Clay, "Anderson (1950) revisited," J. Acoust. Soc. Am. **106**, 553–564 (1999).

[7] R. Hickling and N. M. Wang, "Scattering of sound by a rigid movable sphere," J. Acoust. Soc. Am. **39**, 276–279 (1966).

[8] L. D. Hampton and C. M. McKinney, "Experimental study of the scattering of acoustic energy from solid metal spheres in water," J. Acoust. Soc. Am. **33**, 664–673 (1961).

[9] W. G. Neubauer, R. H. Vogt, and L. R. Dragonette, "Acoustical reflection from elastic spheres. I. Steady-state signals," J. Acoust. Soc. Am. **55**, 1123–1129 (1974).

[10] L. R. Dragonette, R. H. Vogt, L. Flax, and W. G. Neubauer, "Acoustical reflection from elastic spheres. II. Transient analysis," J. Acoust. Soc. Am. **55**, 1130–1137 (1974).

[11] L. R. Dragonette, S. K. Numrich, and L. J. Frank, "Calibration technique for acoustic scattering measurements," J. Acoust. Soc. Am. **69**, 1186–1189 (1981).

[12] K. G. Foote, "Optimizing copper spheres for precision calibration of hydroacoustic equipment," J. Acoust. Soc. Am. **71**, 742–747 (1982).

[13] D. Chu and T. K. Stanton, "Application of pulse compression techniques to broadband acoustic scattering by live individual zooplankton," J. Acoust. Soc. Am. **104**, 39–55 (1998).

[14] C. Feuillade, "Impulse scattering processes of an elastic sphere," J. Acoust. Soc. Am. **110**, 2777(A) (2001).

[15] E. A. Robinson and S. Treitel, *Geophysical Signal Analysis* (Prentice–Hall, Englewood Cliffs, NJ, 1980), pp. 112–118.

[16] J. F. Claerbout, *Imaging the Earth's Interior* (Blackwell, Oxford, 1985).

[17] N. J. Higham and D. J. Higham, *MATLAB Guide* (S.I.A.M. Press, Philadelphia, 2000).

[18] H. Medwin and C. S. Clay, *Fundamentals of Acoustical Oceanography* (Academic, San Diego, 1998).

[19] E. A. Robinson, *Physical Applications of Stationary Time-Series* (Macmillan, New York, 1980), pp. 118–124.

[20] *CRC Handbook of Chemistry and Physics*, 64th ed., edited by R. C. Weast (CRC Press, Boca Raton, FL, 1983), p. E-43.

[21] Z. Sun, G. Gimenez, D. Vray, and F. Denis, "Calculation of the impulse response of a rigid sphere using the physical optic method and modal method jointly," J. Acoust. Soc. Am. **89**, 10–18 (1991).

Circumferential-wave phase velocities for empty, fluid-immersed spherical metal shells

Herbert Überall[a)]
Department of Physics, Catholic University of America, Washington, DC 20064

A. Claude Ahyi and P. K. Raju
Department of Mechanical Engineering, Auburn University, Auburn, Alabama 36849-5341

Irina K. Bjørnø[b)] and Leif Bjørnø[b)]
Department of Industrial Acoustics, Technical University of Denmark, DK-2800 Lyngby, Denmark

In earlier studies of acoustic scattering resonances and of the dispersive phase velocities of surface waves that generate them [see, e.g., Talmant *et al.*, J. Acoust. Soc. Am. **86**, 278–289 (1989) for spherical aluminum shells] we have demonstrated the effectiveness and accuracy of obtaining phase velocity dispersion curves from the known acoustic resonance frequencies. This possibility is offered through the condition of phase matching after each complete circumnavigation of these waves [Überall *et al.*, J. Acoust. Soc. Am. **61**, 711–715 (1977)], which leads to a very close agreement of resonance results with those calculated from three-dimensional elasticity theory whenever the latter are available. The present investigation is based on the mentioned resonance frequency/elasticity theory connection, and we obtain comparative circumferential-wave dispersion-curve results for water-loaded, evacuated spherical metal shells of aluminum, stainless steel, and tungsten carbide. In particular, the characteristic upturn of the dispersion curves of low-order shell-borne circumferential waves (A or A_0 waves) which takes place on spherical shells when the frequency tends towards very low values, is demonstrated here for all cases of the metals under consideration. © *2002 Acoustical Society of America.* [DOI: 10.1121/1.1512290]

PACS numbers: 43.30.Jx, 43.40.Ey [DEC]

I. INTRODUCTION

Acoustic scattering from bounded objects is often dominated by the associated creation of circumferential waves (surface waves) that can circumnavigate the object along closed paths (great circles on a spherical scatterer, circles or even helical paths on a cylinder, geodesics in general). When returning to their point of origin after each circumnavigation, a "phase matching condition" may apply at certain well-defined "resonance frequencies" that are determined by the form of the phase velocity vs frequency dispersion curve of these waves. This phase matching leads to a resonant build-up of the circumferential wave that becomes manifest in the scattering process through the radiation of the wave into the ambient field. Such a mechanism has first been pointed out by us quite early,[1] and has subsequently been explored through many specific applications.[2–11]

The circumferential-wave dispersion curves are related to the scattering-resonance frequencies by the formula[1,2] (for the case of spherical scatterers):

$$c/c_w = k_n a(n + \tfrac{1}{2}), \tag{1}$$

where c_w is the sound speed in the ambient fluid (e.g., water), k is the acoustic propagation constant in this fluid, c is the dispersive phase velocity of a circumferential wave, a is the sphere radius, and n is the modal vibration order (which,

by phase matching, is the number of circumferential wavelengths spanning the sphere, the term $\tfrac{1}{2}$ arising from the fact that a quarter-wavelength phase jump takes place as the waves converge at each of the two focal points on the sphere[12]). The corresponding resonance value of k is designated k_n. Equation (1) constitutes the mentioned connection between resonance frequencies k_n and phase-velocity dispersion curves $c(k)$, so that known values of k_n determine the points $c(k_n)$ on the dispersion curves, or vice versa[2] (for cylindrical shells, see Ref. 11).

In Ref. 2, Eq. (1) has been used in order to obtain some limited portions of circumferential-wave dispersion curves for evacuated, water-immersed thin shells of aluminum, stainless steel, and tungsten carbide (WC), based on the calculated resonance frequencies up to $ka=8$ (Al), 3(WC), and 2.3 (steel) that were available at that time. Upturning dispersion curves were found here as ka (i.e., the frequency) tended to lower values (below $ka \cong 3$); this is not the case for cylindrical shells nor for plates[13,14] where the corresponding dispersion curves tend to zero monotonically as the frequency decreases.

The various types of surface waves on shells that are involved here, have dispersion curves that resemble those of the Lamb waves A_0, S_0, A_1, S_1, etc., on a free plate[13–15] when scaled from one to the other object by a formula

$$fh = (c_w/2\pi)ka(1 - b/a) \tag{2}$$

due to Dragonette.[16] Here f is the frequency, a is the external shell radius, and b the internal one, and h is the thickness of

---
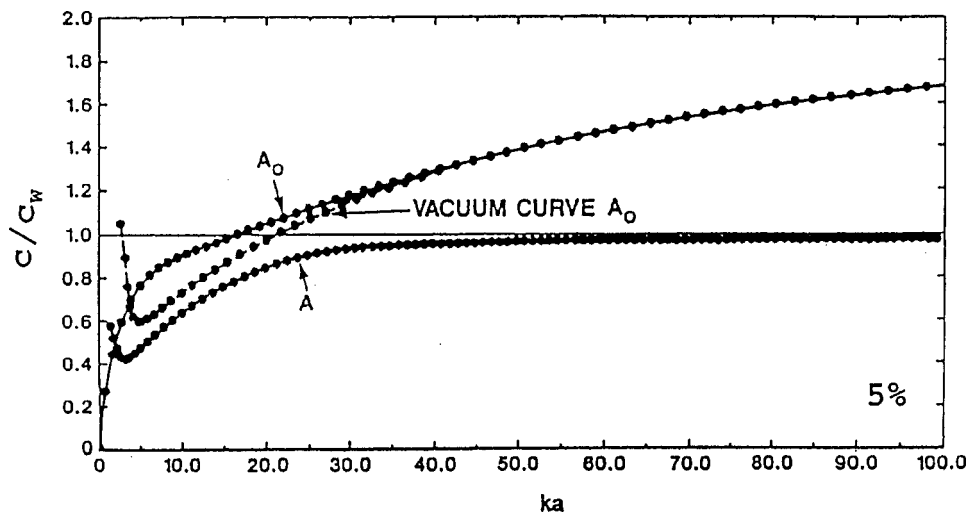
FIG. 1. A_0- and A-wave dispersion curves on a water-loaded, evacuated spherical aluminum shell (5% thick) and A_0 curve for a shell in vacuum. From Refs. 15 and 17 (with permission).

the plate [or, $h \equiv (a-b)$ for the shell]. This resemblance is close for cylindrical shells; for a spherical shell, however, the work of Sammelmann et al.[17] has obtained [using three-dimensional (3D)-elasticity theory] phase velocity dispersion curves for aluminum shells that show the mentioned upturn. This is presented here in Fig. 1 in a version adapted[15] from Ref. 17.

Seen in Fig. 1 is, first, the dispersion curve of the A_0 Lamb-type wave for an evacuated aluminum shell in vacuum (designated "vacuum curve A_0"), which shows an upturn at very low values of the dimensionless frequency ka. [The thickness indication "5%" of the shell here refers to the value of $(a-b)/a \equiv h/a$]. For the water-loaded, evacuated shell, the A_0 curve now tends toward zero, however. An additional surface wave A (also called[16] a_{0-} and generally referred to as the "Scholte-Stoneley wave"[2,5,6,10]) now appears here, being present due to the water loading of the shell, and it is now the dispersion curve of this A wave that shows the low-frequency upturn. At first thought, the A_0 wave, since existing on the shell with or without fluid loading could be expected to be shell-borne throughout, and the A wave which exists only with the presence of fluid loading could be considered to be fluid-borne throughout (especially since its dispersion curve at $ka \rightarrow \infty$ tends towards the sound speed in the ambient fluid). If this were correct, the switch-over of the low-frequency upturn from the A_0 to the A wave upon application of fluid loading would appear to be unexplained.

An explanation for this switch-over phenomenon can be found using a physical argument.[15] The A_0 and the A waves are coupled together (they "interact") by the boundary conditions of the shell-fluid interface. With phase velocities for $f \rightarrow \infty$ tending towards the Rayleigh[14] plate-speed (for A_0), and towards c_w (for A), respectively, these limits identify A_0 as being shell-borne, and A as being fluid-borne at large frequencies. With f descending towards the coincidence frequency where $c(A_0)$ approaches c_w, the coupling takes effect, causing the previously converging A_0 and A curves to undergo a "repulsion."[15] During this repulsion the physical nature of the two waves switches around,[18] so that at still lower frequencies (below coincidence), A now is a shell-borne and A_0 a fluid-borne wave. The switch-over of the physical character of modes during curve repulsions as

caused by modal coupling is also known in other branches of physics, e.g., in atomic physics.[19]

With this change-over of the nature of the A_0 and A waves, the interpretation of the dispersion curves in Fig. 1 now becomes thus: as low frequencies are approached, it is always the shell-borne wave whose dispersion curve shows the upturn, while the dispersion curve of fluid-borne wave tends towards zero.

In the following, the generality of this behavior of A_0 and A wave dispersion curves, including their low-frequency upturn, will be demonstrated on the basis of the connection between resonance frequencies and dispersion curves. This will be carried out for water-loaded, evacuated spherical shells of aluminum, stainless steel, and tungsten carbide (WC) of various shell thicknesses. In this way, comprehensive information will be obtained on the quantitative behavior of the corresponding dispersion curves, not previously demonstrated in the literature, for a variety of shell dimensions and suitable for comparisons between shells of different materials.

The approach to be followed here is more general than just being an application to the interacting A_0 and A dispersion curves. As stated, it consists in a comparison of now available calculated dispersion curves with calculated resonance frequency data pertaining to these dispersion curves, in order to show the suitablity of the resonance data for determining the dispersion curves, and the degree of accuracy that can be achieved with this procedure. All this is being carried out here for the A_0 and A-type surface waves, and also for the S_0 wave and even the A_1, S_1, and S_2 waves wherever possible. The shell thickness considered were 1%, 2%, 2.5%, and 5% for aluminum, 1%, 2.3%, and 2.5% for stainless steel, and 1%, 2.5%, and 5% for tungsten carbide (although shells of other thicknesses also are available). As a result, we obtain a comprehensive overview of dispersion curves for the A wave and the lowest Lamb-type waves based on results from calculations and from resonance data, as they are available at present for the mentioned materials; this also allows comparisons between different materials and different shell thickness.

It should be noted that for a given shell material (Al, SS, or WC where SS designates stainless steel), the literature

contains different assumptions about its material parameters. For example, the SS parameters have been taken as $c_L = 5.854 \times 10^5$ cm/s (longitudinal velocity), $c_T = 3.150 \times 10^5$ cm/s (shear velocity) and $\rho = 7.84$ g/cm^3 (density) for 440c stainless steel by Ref. 20, or as $c_L = 5.675 \times 10^5$ cm/s, $c_T = 3.141 \times 10^5$ cm/s, and $\rho = 7.57$ g/cm^3 for 304 stainless steel by Ref. 3. It has been found, however,[3] that, e.g., the A-wave amplitude is only very wealy dependent on the material parameters and the shell thickness. We may assume, therefore, that dispersion and resonance data obtained using material parameters differing from each other by only the small amounts illustrated above, may be used interchangeable in the following for our comparison purposes. If necessary, a curvature correction due to Marston[21] may be applied in order to convert dispersion curves valid for a plate to those for a shell of given radius and thickness; such results are illustrate for 16.2% steel shells[20] and are significant for substantial shell thicknesses only.

II. ALUMINUM SHELLS

Application of the phase matching procedure which furnishes the resonance/dispersion curve connection has been initiated by Talmant et al.[2] for the case of spherical aluminum shells. In this reference, the Scholte-Stoneley wave (called the A wave) has first been identified on spherical shells, simultaneously with the work of Sammelmann et al.[17] where it was called the a_0-wave), see Fig. 1. To illustrate this connection, Fig. 2(a) shows the calculated resonances in the far-field backscattering amplitude (or from function) plotted vs ka ($k = \omega/c_w$, a = outer shell radius) for an air-filled aluminum shell in water, of thickness 5%, and Fig. 2(b) shows the A-wave dispersion curve for this aluminum shell (or rather, the resonance points thereof) obtained from Eq. (1). This curve displays the low-flow-frequency upturn of the A-wave curve that was mentioned earlier. Also shown in Fig. 2(b) are portions of the A-wave dispersion curves for 1% steel and 1% WC shells as they have been available in Ref. 2, and which shall be discussed below. These portions belong solely to the upturning regions of the corresponding dispersion curves.

A very instructive picture of the calculated resonance response (i.e., of the form function after coherent subtraction of the specular reflection amplitude) is given in Fig. 3 for a 2.5% shell (from Ref. 2), which distinguishes between the resonances of the A wave and those of the S_0 wave with their mode orders n as indicated. Further, more extended resonance graphs are given in the same reference. These will be used here for establishing the resonance/dispersion curve connection for aluminum shells.

Calculated dispersion curves are shown in Fig. 1, or are contained in several figures of Ref. 2 for the A and A_0 waves. For obtaining further Lamb mode dispersion curves, it is possible to use the values for a one-sided water-loaded plate,[13] or even for a free plate[15] as stated in Ref. 6; as a matter of fact, the agreement of the resonance value predictions with the free-plate dispersion curves as shown in the following figures (e.g., for the S_0 wave) is a demonstration of the validity of such a procedure. The frequency scale for plates, usually given by the variable fd (in units mm/μs
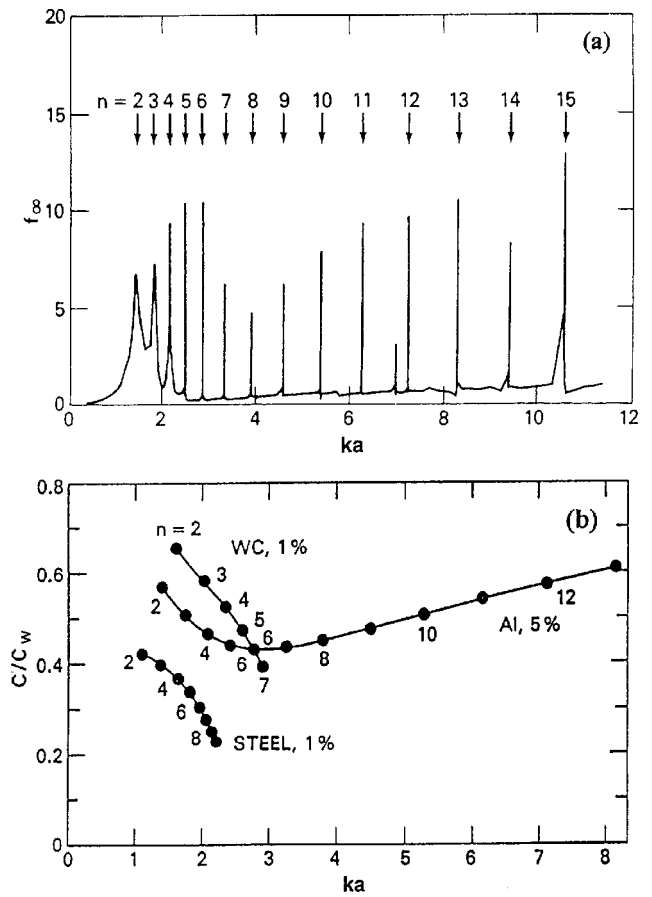
FIG. 2. (a) Resonances in the form function ($\equiv$ far field backscattering amplitude) of an air-filled aluminum shell in water, of thickness 5%, plotted vs ka. (b) Dispersion curve of the A wave on the aluminum shell, plotted vs ka. Also shown are portions of the dispersion curves for 1% steel and 1% WC shells. From Ref. 2.

where d is the plate thickness) is related by Eq. (2) (where the plate thickness was called h) to the ka scale for shells. Figure 4 shows this fd scale and simultaneously the ka scales for 1%, 2.5%, and 5% shells, the curves thus being in a sense universal for all shell thickness (it should be kept in mind that this applies to thin shells only). Note that a conversion of the dispersion curves for a shell of one thickness to the plate scale by the Dragonette formula Eq. (2), with a subsequent reconversion to a shell of different thickness, allows to convert dispersion curves from a shell of one thickness to those of a different thickness, as we shall occasionally do below.

Figure 4 shows our results for the A, A_0, and S_0 wave dispersion curves of an aluminum shell. The calculated dispersion curves labeled A_0, $A_{0,\text{sph}}^{\text{vac}}$ are obtained from the 5%-shell curves of Fig. 1, and those labeled $A_{0,\text{pl}}^{\text{vac}}$, $S_{0,\text{pl}}^{\text{vac}}$, and $A_{1,\text{pl}}^{\text{vac}}$ (the free-plate curves) from Ref. 2 or 15. The cutoff frequency of $A_{1,\text{pl}}^{\text{vac}}$ is obtained from Brekhovskikh,[22] and it is known that the A_1, S_1, etc., curves for $f \rightarrow \infty$ tend towards the shear speed c_T in the plate material while those of the A_0 and S_0 wave tends towards[14] the Raleigh speed c_R as indicated; the A-wave speed tends toward the sound speed in water, c_w. The aluminum parameters were here assumed[2] as $c_L = 6350$ m/s, $c_s = 3050$ m/s, and $\rho = 2.7$ g/cm^3, differing only insignificantly from those of Ref. 15. The (selected)

J. Acoust. Soc. Am., Vol. 112, No. 6, December 2002

Überall et al.: Phase velocities for metal shells   2715
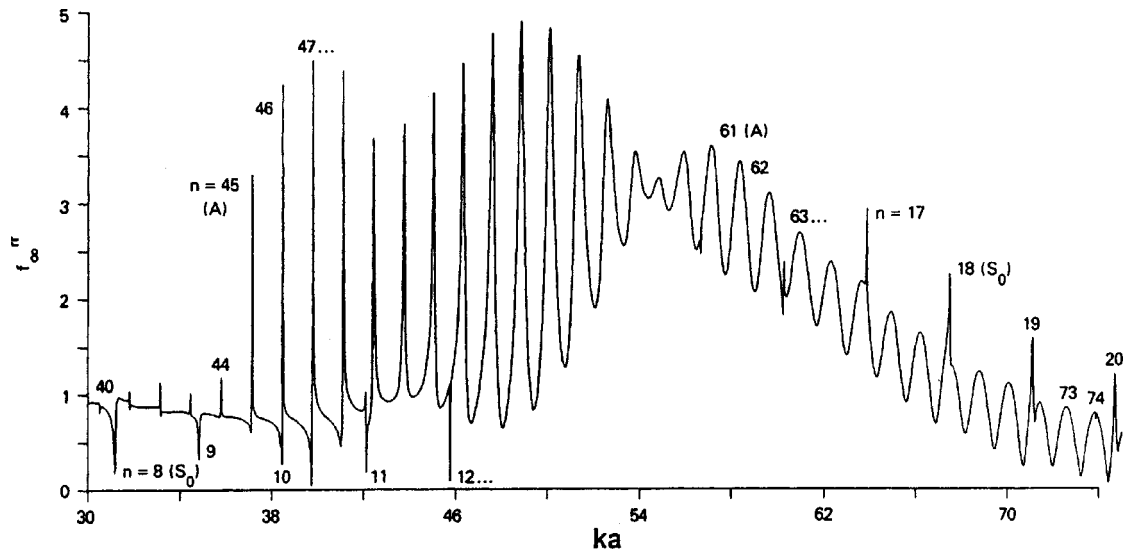
FIG. 3. Resonance response of a 2.5% Al shell plotted vs ka. From Ref. 2.

resonance points in Fig. 4, labeled by their numbers n, are found from the resonance frequency values of Ref. 2, Figs. 1, 2, 10, and 12. The agreement is perfect, even for the S_0 wave where the resonance values are compared to the plate-wave dispersion curve.

Figure 5 shows the A_0 and A wave results of Fig. 4 on an enlarged scale, and Fig. 6 those of the A wave, further enlarged, for the 5% shell and with the calculated 2% shell dispersion curves added on either the 2% scale or on the 5% scale. The results presented here illustrate the power of the resonance/dispersion curve comparisons, and demonstrate the agreement between the two approaches for the A, A_0, and S_0, waves in thin aluminum shells of various thickness. Similar results will now be shown for shells of stainless steel and of tungsten carbide.

III. STAINLESS STEEL SHELLS

For the case of evacuated, water-immersed stainless steel shells there exist previous calculations of both surface-wave dispersion curves,[3,4,20,24] and of the resonances caused by them.[23–26] These will be useful for the present study in which resonance results will be superimposed with the dispersion curves.

The calculated dispersion curves in Fig. 2 of Ref. 3 for the A_0 and A waves of a stainless steel shell are the analogs of our present Fig. 1 for the aluminum shell. They refer to a 2.3% SS 304 empty spherical shell immersed in water. Since we will use these resulting curves to compare with the resonances of a 2.5% thick spherical shell, we can readjust the curves to the 2.5% scale by employing Dragonette's formula Eq. (2) twice. In addition, we may rescale in the variable ka, as indicated, e.g., in Fig. 4, to other shell thicknesses, e.g., to a 5% shell.

For that latter case, we present our comparisons in Fig. 5(a) where the solid dispersion curves are those of Ref. 3 (re-scaled as mentioned) for the A_0 and A waves, and that for the S_0 wave is from Ref. 20 which also shows A_1 and S_1 curves. The upturn of this latter curve for low frequencies was found[20] to be eliminated (rendered horizontal) by Mar-

ston's curvature correction;[21] both versions are indicated here. For the Lamb wave curves, we used those for a free plate. Here, the A_1, S_1, and S_2 waves are included, and their low-frequency cutoff values were obtained from the formulas of Brehovshikh.[22]

The resonance-generated curve points come from the calculated resonance values of Ref. 24, marked by their mode numbers n. As to the agreement of the A_1 and S_1 resonance points with the dispersion curves for plates that were employed here, this is by and large satisfactory, with the more important deviations occurring in the right direction predicted by Marston's curvature corrections as illustrated in Fig. A2 of Ref. 20.

The A_0 and A wave results form a crucial part of Fig. 5(a), for which the Kaduchak–Marston curves[3] provided the same clarification for the stainless steel shells that the results of Sammelmann et al.[17] (reproduced in our Fig. 1) did for the aluminum shells; we shall elaborate on this in the following portions of Fig. 5 below. The Lamb-wave parts in Fig. 5(a) have the same layout as in Fig. 4 of Ref. 24; however, the A_0 and A parts in that latter reference are incomplete insofar as they only present limited portions of the two curves one at a time not indicated by their labeling. The reason for this is that calculated resonance response of the steel shell in Ref. 24 (the analog to our Fig. 3 for Al) does not show all the resonances present, with the S_0 and A wave resonances clearly visible but those of the A_0 wave totally obscured due to their overlapping widths (thus forming just one broad hump in Fig. 3, referred to as the "midfrequency enhancement" by Marston et al.[3]). The visible A-wave resonances become increasingly narrow in the low-frequency region, but have nevertheless been calculated in an approach effective for ultranarrow resonances by Ref. 23. In Fig. 5(c) the calculated A_0 and A wave dispersion curves are shown correctly (as well as that for the A_0 wave for a shell in vacuum) but only on a smaller scale; in the following Fig. 5(b) we increase this scale and add the resonance results.

The low frequency upturn of the A (or A_0^{vacuum}) curves seen for Al in Fig. 1 is also present for SS shells, cf. Figs.
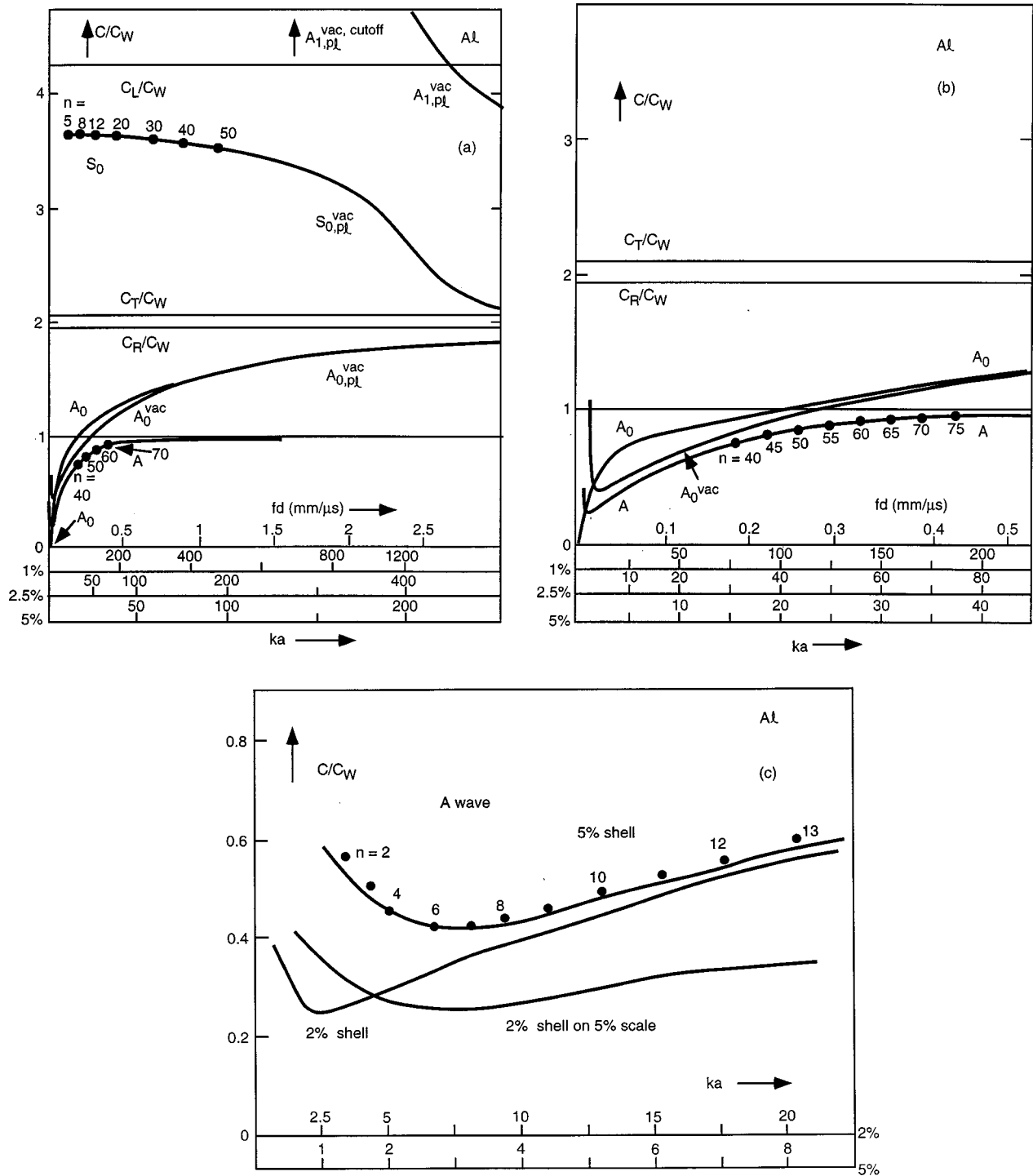
FIG. 4. Comparison of calculated dispersion curves on water-loaded, evacuated spherical aluminum shells with results obtained from calculated resonance frequencies (5% thickness); (a) for A, A_0, and S_0 waves (A_1 wave also indicated); (b) for A and A_0 waves on an extended scale; (c) for the A wave, further extended scale and 2% shell curve added.

4(b) and (c). It is interesting to note, however, that this upturn does not proceed to infinity but that at even lower frequencies, it goes through a maximum and is followed by a downturn, so that the A curve finally ends up at zero for $f \rightarrow 0$ as shown in Ref. 4.

The low-frequency portions of the dispersion curves of Fig. 5(a) are plotted on a larger scale in Fig. 5(b). The calculated A_0, A_0^{vac}, and A wave dispersion curves for 2.5% steel shells are entered following Kaduchak and Marston,[3]

except that their A-wave curve is extended to lower frequencies, drawn through the resonance points to guide the eye. The resonance points originate with Marston and Sun[23] (2.5% shells, open circles), with Ref. 25 (2.5% and 1% shells, crosses), and with Ref. 2 (1% shells, solid circles). These latter points were first obtained by Junger,[27] constituting his "lower ($j=1$) branch" of spherical shell vibrations, and may be referred to as the resonances of the "Junger wave."
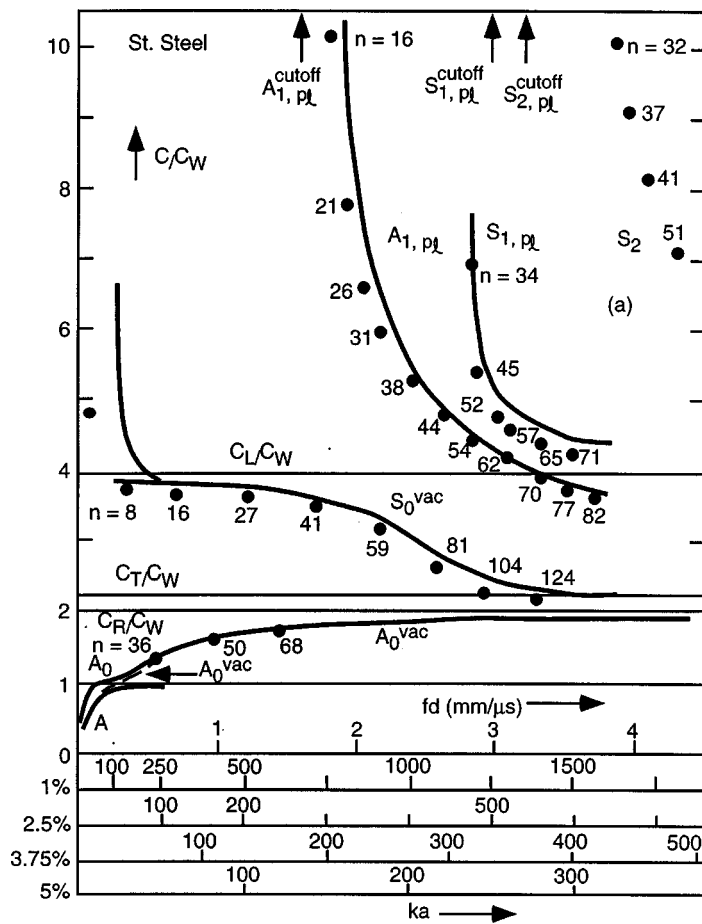
FIG. 5. Comparison of calculated dispersion curves on water-loaded, evacuated spherical stainless steel shells with results obtained from calculated resonance frequencies: (a) for A, A_0, S_0, A_1, and S_1 waves (S_2 wave also indicated), 5% thickness; (b) for A and A_0 waves at 2.5% thick shells (1% resonance points added).
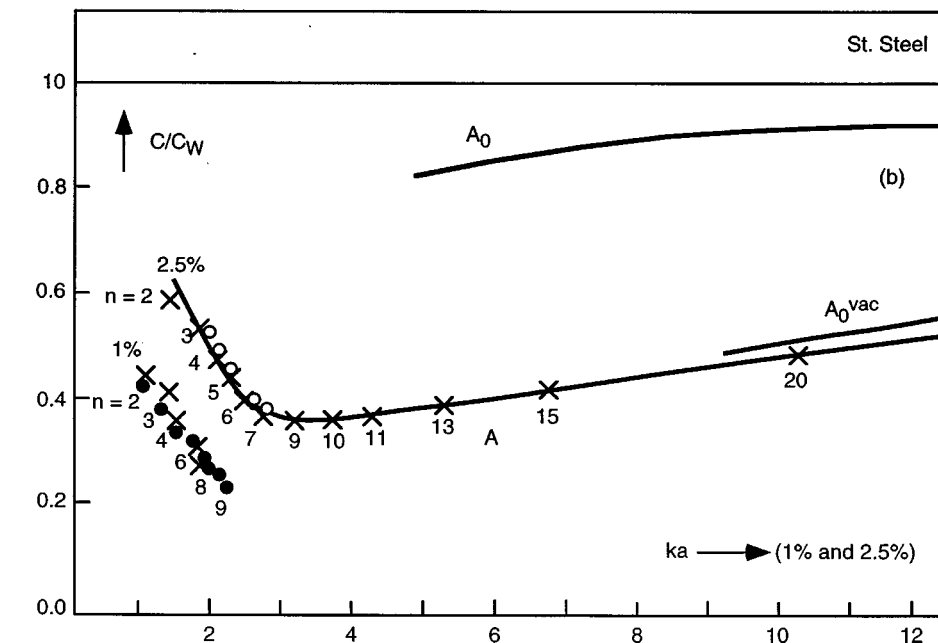
The results for the 2.5% steel shell as shown here demonstrate the low-frequency upturn of the A wave, as noted earlier for the Al shell; cf., e.g., Fig. 4(c). By comparison with the 5% and 2% A curves for Al, Fig. 5(b) shows analogous 2.5% and 1% A curves for steel, and by this analogy, it becomes clear that the Junger wave on a 1% steel shell is the low-frequency upturning extension of the A-wave dispersion curve of the water-loaded shell.[28]

IV. TUNGSTEN CARBIDE SHELLS

For the case of evacuated tungsten carbide (WC) shells immersed in water, the literature contains calculated dispersion curves for 1% and 2.5% shell thicknesses,[2] as well as a calculated resonance spectrum for a 1% shell [Fig. 3(a) of Ref. 2]. For that calculation, we assumed WC material parameters $\rho = 13.80$ g/cm^3, $c_L = 6.860 \times 10^5$ cm/s, and c_T
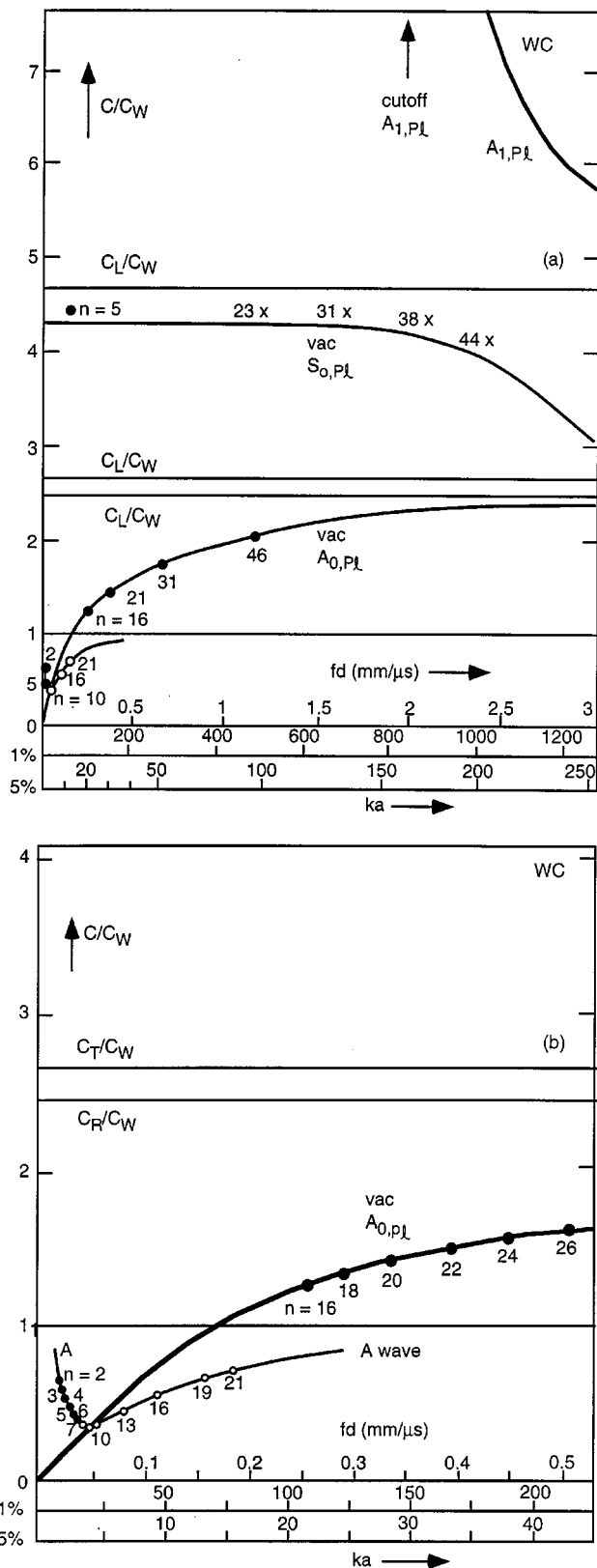
FIG. 6. Comparison of calculated dispersion curves on water-loaded, evacuated spherical tungsten-carbide shells with results obtained from calculated resonance frequencies: (a) for A, A_0, and S_0 waves (A_1 wave also indicated); (b) for A and A_0 waves at 1% shell thickness.

$=4.185\times10^5$ cm/s; for water $\rho_w=1$ g/cm^3 and $c_w=1.4825$ km/s. Low-frequency resonances were calculated for a 1% shell, and the resulting resonance points of the A wave were entered in the present Fig. 2(b). While Ref. 29 contains cal-

culated resonances for 1% and 5% shells, only the dispersion curves for WC plates are exhibited in this reference. The resonances are shown here in the fashion of the present Fig. 3, and are analyzed only for the S_0 and A_0 wave resonances. However, the A-wave resonances are also visible in Figs. 2 and 3 of Ref. 29, and are here extracted by us for the purposes of the present study.

Our results are shown in Fig. 6. Here, Fig. 6(a) which is patterned after Fig. 4(a) for Al and Fig. 5(a) for SS, exhibits the dispersion curves of the Lamb waves A_0, and S_0, and A_1 for plates, as well as of the A wave with its characteristic low-frequency upturn; resonance points from Refs. 2 and 29 have also been entered, indicating their mode numbers n. As we did before, only selected resonance points are entered in our figures, sufficient to assess their agreement with the calculated curves.

The low-frequency behavior of the A and A_0 waves is visible in the lower left corner of Fig. 6(a), but is shown in detail in Fig. 6(b) on an extended scale. The A_0-wave points of $n=16,18,\ldots$ and the A-wave points $n=8,9,10,13,\ldots$ come from Fig. 2 or 3 of Ref. 29 which, as stated, are amenable to having their resonances interpreted in terms of these waves. The resonance points $n=2-7$ are those of Fig. 2(b), stemming from Ref. 2; the resulting curve joins smoothly with that through the $n\geq8$ points and legitimizes their interpretation in terms of the A-wave curve with its familiar low-frequency upturn.

V. SUMMARY AND CONCLUSIONS

The present study constitutes an overview of the dispersion curves for the Lamb waves A_0, S_0, A_1, S_1, etc., and for the Scholte-Stoneley A wave on thin, water-immersed and evacuated (or, alternately, the closely similar air-filled) spherical shells of aluminum, stainless steel, and tungsten carbide. This study is based on all the information available in the literature for these shells, regarding the dispersion curves for A, A_0, S_0, etc., waves, as well as the resonance frequencies generated by the phase matching during circumferential propagation of these waves around the shells. The resonance frequencies have been used to obtain individual points on the dispersion curves, enabling us to judge their fits with the calculated continuous dispersion curves. Our Figs. 4, 5, and 6 form the gist of our present study.

Of special interest here is the clarification of the low-frequency behavior of the interacting dispersion curves of the A and A_0 waves, which the previous literature showed to be known only in a tentative, or even ill-understood fashion. For all three shell materials considered here, the clarifying picture of calculated dispersion curves for Al of Fig. 1 (due to Sammelmann *et al.*[17]), as well as the corresponding clarification for SS due to Kaduchak and Marston,[3] has been conformed by the fits of the resonance points superimposed on these curves. The same has been shown here to hold for WC shells, so that the low-frequency upturn of the A-wave dispersion curve, together with the progression to zero of the A_0-wave curve, is now recognized as a quite universal phenomenon. We believe that our present overview of the Lamb and Scholte-Stoneley wave behavior (regarding dispersion curves and resonance frequencies) for thin spherical shells

J. Acoust. Soc. Am., Vol. 112, No. 6, December 2002

Überall *et al.*: Phase velocities for metal shells   2719

with the different shell materials considered here constitutes a comprehensive picture of the physical phenomena involved, that had been presented in the previous literature only in a disjoint, and sometimes only partially understood, fashion.

ACKNOWLEDGMENTS

[1] H. Überall, L. R. Dragonette, and L. Flax, "Relation between creeping waves and normal modes of vibration of a curved body," J. Acoust. Soc. Am. **61**, 711–715 (1977).

[2] M. Talmant, H. Überall, R. D. Miller, M. F. Werby, and J. W. Dickey, "Lamb waves and fluid-borne waves on water-loaded, air-filled thin spherical shells," J. Acoust. Soc. Am. **86**, 278–289 (1989).

[3] G. Kaduchak and P. L. Marston, "Observation of the midfrequency enhancement of tone bursts backscattered by a thin spherical shell in water near the coincidence frequency," J. Acoust. Soc. Am. **96**, 224–230 (1993).

[4] G. Kaduchak, C. S. Kwiatkowski, and P. L. Marston, "Measurement and interpretation of the impulse response for backscattering by a thin spherical shell using a broad-bandwidth source that is nearly acoustically transparent," J. Acoust. Soc. Am. **97**, 2699–2708 (1995).

[5] G. Maze, F. Léon, J. Ripoche, A. Klauson, J. Metsaveer, and H. Überall, "Nature de l'onde d'interface de Scholte sur une coque cylindrique," Acustica **81**, 201–213 (1995).

[6] H. Überall, A. Gérard, A. Guran, J. Duclos, M. Khelil, X. L. Bao, and P. K. Raju, "Acoustical scattering resonances: relation to external and internal surface waves," Appl. Mech. Rev. **49**, S63–S71 (1996).

[7] J. P. Sessarego, J. Sageloli, R. Guillermin, and H. Überall, "Scattering by an elastic sphere embedded in an elastic isotropic medium," J. Acoust. Soc. Am. **104**, 2836–2844 (1998).

[8] A. C. Ahyi, P. Pernod, O. Gatti, V. Latard, A. Merlen, and H. Überall, "Experimental demonstration of the pseudo-Rayleigh (A_0) wave," J. Acoust. Soc. Am. **104**, 2727–2732 (1998).

[9] X. L. Bao, P. K. Raju, and H. Überall, "Circumferential waves on an immersed, fluid-filled elastic cylindrical shell," J. Acoust. Soc. Am. **105**, 2704–2709 (1999).

[10] H. Überall, "Acoustic of a shell," Acoustical Physics **47**, 115-139 (2001), translated from Russian [Akusticheskii Zhurnal **47**, 149–177 (2001)].

[11] X. L. Bao, H. Überall, P. K. Raju, A. C. Ahyi, I. K. Bjørnø and L. Bjørnø, "Waves on fluid-loaded shells and their resonance frequency spectrum," preprint.

[12] See, e.g., A. Sommerfeld, *Optics* (Dover, New York, 1945).

[13] X. L. Bao, H. Franklin, P. K. Raju, and H. Überall, "The splitting of dispersion curves for plates fluid-loaded on both sides," J. Acoust. Soc. Am. **102**, 1246–1248 (1997).

[14] M. F. Werby and H. Überall, "The analysis and interpretation of some special properties of higher-order symmetric Lamb waves: The case for plates," J. Acoust. Soc. Am. **111**, 2686–2691 (2002). See also M. F. Werby and H. Überall, "A systematic study of water-filled, submerged elastic spherical shells and the resolution of elastic and water-included resources," J. Acoust. Soc. Am. **112**, 896–905 (2002).

[15] H. Überall, B. Hosten, M. Deschamps, and A. Gérard, "Repulsion of phase velocity dispersion curves and the nature of plate vibrations," J. Acoust. Soc. Am. **96**, 908–917 (1994).

[16] L. R. Dragonette, Ph.D. thesis, The Catholic University of America, Washington, DC, 1978; also NRL Report 8216, Naval Research Laboratory, Washington, DC, 1978.

[17] G. S. Sammelmann, D. H. Trivett, and R. H. Hackman, "The acoustic scattering by a submerged spherical shell I," J. Acoust. Soc. Am. **85**, 114–124 (1989).

[18] M. Talmant, G. Quentin, J. L. Rousselot, J. V. Subrahmanyam, and H. Überall, "Acoustic resonances of thin cylindrical shells and the resonance scattering theory," J. Acoust. Soc. Am. **84**, 681–688 (1988).

[19] See, e.g., P. H. E. Meijer and E. Bauer, *Group Theory* (North-Holland, Amsterdam, 1965), p. 52.

[20] S. G. Kargl and P. L. Marston, "Ray synthesis of Lamb wave contributions to the total scattering cross section for an elastic spherical shell," J. Acoust. Soc. Am. **88**, 1103–1113 (1990).

[21] P. L. Marston, "Phase velocity of Lamb waves on a spherical shell: Approximate dependence on curvature from kinematics," J. Acoust. Soc. Am. **85**, 2663–2665 (1989).

[22] L. Brekhovskikh, *Waves in Layered Media*, 1st ed. (Academic, New York, 1960), Chap. 1.

[23] P. L. Marston and N. H. Sun, "Resonance and interference scattering near the coincidence frequency of a thin spherical shell. An approximate ray synthesis," J. Acoust. Soc. Am. **92**, 3315–3319 (1992).

[24] G. C. Gaunaurd and M. F. Werby, "Lamb and creeping waves around submerged spherical shells resonantly excited by sound scattering II: Further applications," J. Acoust. Soc. Am. **89**, 1656–1667 (1991).

[25] H. C. Strifors and G. C. Gaunaurd, "Multipole character of the large-amplitude, low-frequency resonances in the sonar echoes of submerged spherical shells," Int. J. Solids Struct. **29**, 121–130 (1992).

[26] G. C. Gaunaurd and M. F. Werby, "Sound scattering by resonantly excited, fluid-loaded elastic spherical shells," J. Acoust. Soc. Am. **90**, 2536–2550 (1991).

[27] M. C. Junger, "Normal modes of submerged plates and shells," in *Fluid–Solid Interaction*, edited by J. E. Greenspan (Proc. ASME Colloquium, New York, 1967), p. 95.

[28] H. Überall, I. K. Bjørnø, and L. Bjørnø, "Dispersion of circumferential waves on evacuated, water-loaded spherical steel shells," Ultrasonics **37**, 673–675 (2000).

[29] V. M. Ayres, G. C. Gaunaurd, C. Y. Tsui, and M. F. Werby, "The effects of Lamb waves on the sonar cross-sections of elastic spherical shells," Int. J. Solids Struct. **23**, 937–946 (1987).

2720   J. Acoust. Soc. Am., Vol. 112, No. 6, December 2002

Überall *et al.*: Phase velocities for metal shells

Source bearing estimation in the Arctic Ocean using ice-mounted geophones

Stan E. Dosso
School of Earth and Ocean Sciences, University of Victoria, Victoria, British Columbia V8W 3P6, Canada

Garry J. Heard
Defence Research and Development Canada–Atlantic, Dartmouth, Nova Scotia B2Y 3Z7, Canada

Michael Vinnins
Defence Research and Development Canada–Ottawa, Ottawa, Ontario K1A 0Z4, Canada

This paper investigates the use of geophones mounted on the surface of Arctic sea ice for estimating the bearing to acoustic sources in the water column. The approach is based on measuring ice seismic waves for which the direction of particle motion is oriented radially outward from the source. However, the analysis is complicated by the fact that sea ice supports several types of seismic waves, producing complex particle motion that includes significant nonradial components. To suppress seismic waves with transverse particle motion, seismic polarization filters are applied in conjunction with a straightforward rotational analysis (computation of particle-motion power as a function of angle). The polarization filters require three-dimensional (3D) measurements of particle motion, and apply theoretical phase relationships between vertical and horizontal components for the various waves types. In addition, the 180° ambiguity inherent in the rotational analysis can be resolved with 3D measurements by considering particle motion in the vertical–radial plane. Arctic field trials were carried out involving two components. First, a hammer source was used to selectively excite the various ice seismic waves to investigate their propagation properties and relative importance in bearing estimation. Second, impulsive acoustic sources were deployed in the water column at a variety of bearings and ranges from 200–1000 m. For frequencies up to 250 Hz, source bearings are typically estimated to within an average absolute error of approximately 10°.
© *2002 Acoustical Society of America.* [DOI: 10.1121/1.1516758]

PACS numbers: 43.30.Ma, 43.40.Dx [DLB]

I. INTRODUCTION

This paper investigates the use of geophones mounted on the surface of Arctic sea ice to estimate the bearing of an acoustic source located in the water column. While a number of previous studies have been reported that used ice-mounted geophones to investigate sources within the ice layer, e.g., ice cracking and ridging,[1–5] relatively little work has been published considering acoustic sources in the water. The approach to bearing-estimation developed here is based on measuring ice seismic waves for which the direction of wave oscillation (particle motion) is oriented radially outward from the source. For such waves, seismic recordings at two orthogonally mounted horizontal geophones can be combined geometrically to compute the wave power in horizontal look angles from 0°–360°. The angle of maximum power provides the optimal estimate of the source bearing, to within an ambiguity of 180° due to rotational symmetry (this ambiguity can be resolved by consideration of the three-dimensional particle motion, as described later). This approach is attractive in that it provides a bearing estimate based on a single, ice-mounted sensor, and does not require penetrating the ice to deploy a dipole hydrophone or use of an array of sensors for beamforming.[5,6] However, the rotational analysis is complicated by the fact that sea ice supports several types of seismic waves,[7–9] producing complex

particle motion at the sensor which includes significant nonradial components that degrade bearing estimates.

Effective source-bearing estimation requires suppressing seismic waves with transverse particle motion (i.e., motion perpendicular to the source bearing direction) while passing waves with radial motion. To this end, seismic polarization filters, developed in earthquake seismology[10] and previously applied to ice fracturing events,[4] are adapted here for a water-column source and applied in conjunction with the rotational analysis. Polarization filters make use of three-dimensional (3D) measurements of the particle motion, and apply theoretical phase relationships between vertical and horizontal components for the various wave types to selectively suppress or enhance particular waves. In addition, with 3D measurements, the 180° bearing ambiguity inherent in the horizontal rotational analysis can be resolved using the known phase relationship between the vertical and radial components of particle motion.

To investigate this approach to bearing estimation, field trials were carried out in April, 2000, on the ice cover of the Lincoln Sea north of Ellesmere Island, Canada, as part of the Iceshelf 2000 research program. The trials were performed on an ice floe, approximately 2 m thick, consisting predominantly of annual (first-year) ice, with some multiyear ice blocks frozen in place. The water depth at the experimental site was about 50 m. The trials were based on recording

seismic arrivals from controlled sources using a set of three-component geophones coupled to the ice surface. The trials consisted of two components. First, an ice seismic survey was carried out using a linear array of three-component geophones and a swinging hammer apparatus to provide a repeatable seismic source. This allowed estimation of the propagation velocities and attenuations of various ice seismic waves, as well as a consideration of the coupling between waves and the relative importance of the different wave types in source bearing estimation. Second, the effectiveness of ice-mounted geophones as directional sensors in the Arctic was investigated using impulsive sources (imploding glass light bulbs[11]) in the water column deployed at ranges from 200–1000 m and bearings of 0°–90° with respect to the geophones. Source-bearing estimates were computed using rotational analysis with polarization filtering, and compared to the actual bearings.

The remainder of this paper is organized as follows. Section II briefly describes seismoacoustic propagation in sea ice, and analyzes the hammer seismic survey. Section III presents the theoretical basis of the rotational analysis and seismic polarization filtering, and considers the bearing estimation survey. Finally, Sec. IV summarizes the results.

II. SEISMO-ACOUSTIC PROPAGATION IN SEA ICE

A. Ice seismic waves

The theory of wave propagation in a floating ice sheet is well developed[7,8] and a number of field studies have been reported.[1–5,9] This paper will not consider the general theory; however, a basic description of the fundamental seismic wave types is required. Acoustic energy from an underwater source is transmitted to an ice-mounted geophone both as seismic plate waves propagating along the ice (due to acoustic energy transmitted into the ice between source and receiver), and as acoustic waves that arrive at the underside of the ice directly below the geophone and couple locally into seismic waves. For an acoustic wave incident on a planar water/ice interface, the transmitted components include compressional (P) waves with particle motion parallel to the direction of propagation, and vertically polarized shear (S_V) waves with particular motion perpendicular to the propagation direction. In addition, horizontally polarized shear (S_H) waves with transverse particle motion are typically generated due to roughness at the water/ice interface and inhomogeneous internal ice structure that causes out-of-plane coupling between S_H and $P-S_V$ components.[3]

At low frequencies, where the wavelengths are long compared to ice thickness, ice seismic waves propagate in three fundamental modes, longitudinal plate (L_P) waves, S_H waves, and flexural (F_L) waves. Longitudinal plate waves involve prograde elliptically polarized particle motion in the radial/vertical plane (i.e., $P-S_V$ motion with particle motion in the direction of wave propagation at the top of the ellipse), and propagate at a velocity slightly less than the bulk compressional velocity of the ice. L_P waves represent plate modes that are not fully trapped, and continuously lose energy via radiation into the water. S_H waves involve transverse motion and propagate at the ice bulk shear velocity. F_L

(a)

(b)
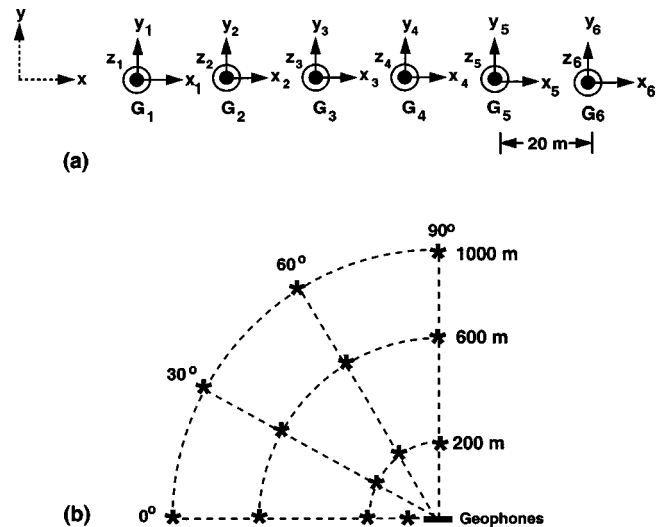
FIG. 1. Plan view of the experiment geometry. The sensor array is shown in (a), with $G_1 - G_6$ representing geophones with three components: x (along array axis), y (perpendicular to axis), and z (vertical). Source positions are indicated by asterisks in (b). The hammer seismic survey involved the sources along 0° bearing.

waves involve $P-S_V$ particle motion, exhibit strong inverse dispersion (i.e., high-frequency components travel faster than low-frequency components), and propagate with a maximum velocity slightly less than the shear velocity.

B. Hammer seismic survey

An important component of the field trials was a hammer seismic survey carried out to investigate the properties of elastic waves propagating within the ice layer. Analysis of the hammer seismic survey guides in identifying and understanding the seismo-acoustic arrivals at an ice-mounted geophone due to an acoustic source in the water. The ability to preferentially excite particular seismic wave types by directional hammer blows allows the three fundamental plate waves to be examined individually and their properties to be measured. Finally, the survey allows the importance of coupling between wave types, which can degrade source bearing estimation, to be examined.

The hammer seismic survey was based on recordings made at a linear array of six tri-axial (x,y,x) geophones, spaced at 20-m intervals, deployed on the surface of the ice, as shown in Fig. 1(a). The geophones were positioned accurately using a laser surveying instrument, and frozen to the ice surface using a small amount of water [Fig. 2(a)]. The geophone signals were transmitted via over-ice cables to a heated recording tent located near the center of the array, where they were recorded on a 16-channel digital seismograph at a sampling rate of 2000 Hz. Because of the recording limitation of 16 channels, signals from only five of the tri-axial geophone could be recorded at one time; for the hammer seismic survey, signals from geophones $G_1 - G_5$ were recorded. The weather during the hammer seismic survey and subsequent source bearing-estimation trials (described in Sec. III D) was clear and cold ($-35°$ to -45 °C), with little or no wind, conditions that typically result in minimal ambient noise due to ice-cracking or ridge-building events.[12,13]

Dosso *et al.*: Source bearing estimation using ice-mounted geophones

FIG. 2. (a) Hand-planting a three-component geophone on the sea ice surface (tents of the Arctic field camp in the background); (b) the swinging seismic-hammer apparatus (photo credit: Janice Lang, DRDC–Ottawa).

The seismic sources consisted of sledge hammer blows to wooden four-by-four posts that had been frozen into the ice at ranges of 70, 200, 600, and 1000 m endfire from the array center, as shown in Fig. 1(b). Longitudinal waves in the ice were preferentially generated by hammer blows directed toward the array ($+x$ direction, referred to as radial hammer blows). Horizontally polarized shear waves were generated by hammer blows perpendicular to the array ($+y$ direction, transverse blows). Flexural waves were generated by vertical hammer blows ($-z$ direction). To measure the attenuation of L_P and S_H waves requires repeatable source levels for the radial and transverse hammer blows at different ranges. This was accomplished using a simple mechanical apparatus in which the hammer swung freely on a pivot from a constant backswing angle [Fig. 2(b)]. A precise time for the hammer

blows was measured by affixing a trigger geophone directly to the wooden post.

To measure wave propagation velocities, seismic sections were plotted of waveform arrivals as a function of time and range. Figure 3 shows a seismic section for the longitudinal plate wave, corresponding to the x-component seismograms recorded for radial hammer blows at ranges of 70, 200, 600, and 1000 m from the center of the geophone array. Seismic traces have been normalized to a common maximum amplitude so that the details of long-range arrivals can be readily discerned. To determine the L_P-wave velocity, v_L, first-break arrival-time picks were chosen by examining individual traces at high magnification. The slope of the least-squares line that best fits the arrival-time picks (included in Fig. 3) provides an estimate of the L_P wave propagation
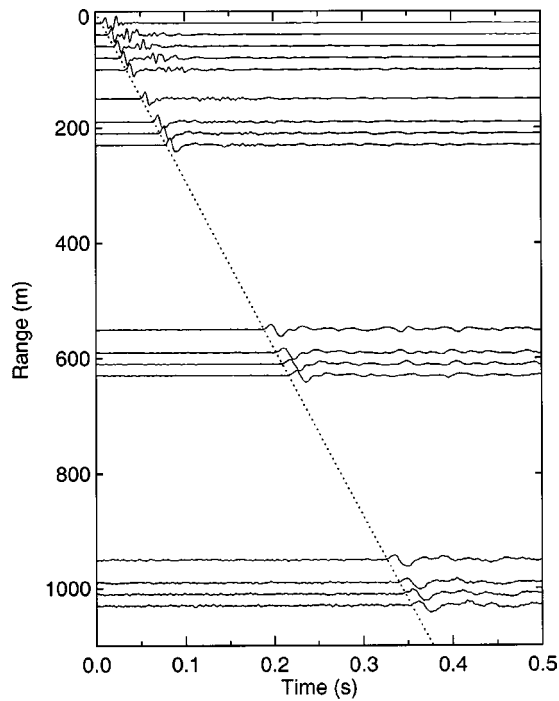
FIG. 3. Seismic section of L_P waves recorded at x-component geophones for radial hammer blows at four ranges. Dotted line indicates the first-break arrival time picks. Channel 2 is not plotted for all sources due to recording difficulties.
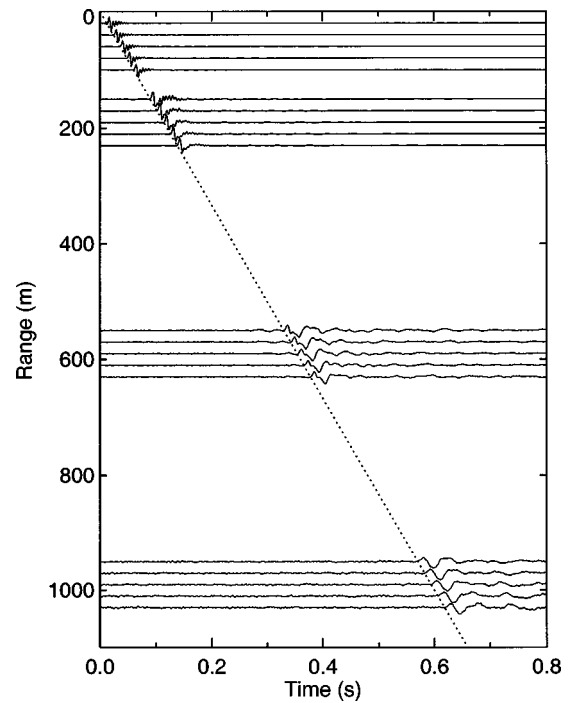
FIG. 4. Seismic section of horizontal shear waves recorded at y-component geophones for transverse hammer blows at four ranges. Dotted line indicates the first-break arrival time picks.

velocity. In this case, $v_L = (2900 \pm 20)$ m/s, in good agreement with reported values for Arctic sea ice, as summarized in Table I for previous studies carried out as part of the Iceshelf program (unpublished), and in Table II for published values.

A similar procedure was applied to compute the propagation velocity of the horizontal shear wave, which corresponds directly to the bulk shear velocity, v_S, of the pack ice. Figure 4 shows a seismic section for the S_H wave, corresponding to the y-component seismograms recorded for transverse hammer blows. Least-squares analysis indicates a shear velocity of $v_S = (1670 \pm 20)$ m/s, again in good agreement with reported values (Tables I and II).

For completeness, Fig. 5 shows a seismic section for flexural waves, corresponding to the z-component seismograms recorded for vertical hammer blows at ranges of 70 and 200 m (flexural waves could not be clearly discerned at longer ranges). The strong inverse dispersion of the flexural wave is evident in Fig. 5. Because of this dispersion, the arrival instant and propagation velocity of the flexural wave is not well defined. Figure 5 includes lines corresponding to the propagation velocities of L_P and S_H waves, as deter-

mined from Figs. 3 and 4. The flexural wave is seen to propagate at a maximum velocity slightly below the shear velocity, as expected from theory.

In addition to propagation velocities, the attenuation factors associated with longitudinal and shear waves are important to understand seismo-acoustic propagation in an Arctic environment. Attenuation coefficients of the various wave types can be estimated from an analysis of the exponential decay of signal amplitude A with range r:

$$A(r) = A(0)S(r)\exp[-\alpha r], \qquad (1)$$

where $S(r)$ represents geometric (cylindrical) spreading, and α is the attenuation coefficient in Nepers/meter. According to Eq. (1), the attenuation coefficient can be estimated as the (negative) slope of $\log_e A(r)/S(r)$ as a function of r. By transforming to the frequency domain, this procedure can be carried out for a number of different frequency bands to investigate the frequency dependence of the attenuation (a linear frequency dependence is typically assumed, allowing the attenuation to be expressed in units of decibels per wavelength). Figure 6 shows plots of $\log_e A(r)/S(r)$ vs r for third-octave frequency band averages centered at frequencies from 40–160 Hz for the longitudinal plate waves shown in

TABLE I. Summary of propagation velocities and attenuations for shear and longitudinal waves in Arctic sea ice from the Iceshelf program.

Ice type	Iceshelf 95		Iceshelf 96	Iceshelf 97	Iceshelf 2000
	Smooth annual	Rough annual	Multiyear	Multiyear	Mixed Annual
v_S (m/s)	1710	1710	1740	1720	1670
v_L (m/s)	3100	3100	3080	3000	2900
α_S (dB/λ)					1.6
α_L (dB/λ)					2.6

TABLE II. Summary of published propagation velocities and attenuations of shear and longitudinal waves in Arctic sea ice.

	Stein (Ref. 1)	Miller and Schmidt (Ref. 3)			Brooke and Ozard (Ref. 9)				Yang and Giellis (Ref. 5)
		1.2-m ice	2.4-m ice		Smooth ice		Rough ice		
Date	1982	1987	1987		1986	1987	1986	1987	1988
v_S (m/s)	1800	1590	1750		1891	1705	1746	1660	1650
v_L (m/s)					2960	3084	2864	2893	2800
α_S (dB/λ)	1.57	2.66	2.99	20–40 Hz	0.45	0.32	1.26	2.33	1.10
				40–80 Hz	0.57	1.00	0.84	2.55	0.91
				80–160 Hz	0.49	0.38	0.48	1.33	0.69
α_L (dB/λ)				20–40 Hz					1.87
				40–80 Hz					2.10
				80–160 Hz					1.77

Fig. 3. In this plot, L_P wave records with a signal-to-noise ratio SNR<5 dB were automatically rejected, resulting in the reduction in the number of long-range data points at higher frequencies in Fig. 6. The least-squares line at each frequency is included in Fig. 6. As mentioned above, the negative slope of each line provides an estimate of the L_P-wave attenuation coefficient at the corresponding frequency. These estimates (converted to dB/m) are plotted as a function of frequency in Fig. 7(a), and are consistent with a linear increase in attenuation with frequency. The slope of the least-squares line in Fig. 7(a) is $(9.0\pm0.7)\times10^{-4}$ dB/m/Hz; assuming the velocity of the L_P wave is $v_L=2900$ m/s, the attenuation can be expressed in decibels per wavelength as $\alpha_L=(2.6\pm0.2)$ dB/λ.

A similar analysis was applied to estimate the ice shear attenuation from the exponential decay of the S_H waves shown in Fig. 4. Figure 8 shows plots of $\log_e A(r)/S(r)$ vs r for the S_H wave for third-octave band averages from 40–160 Hz. Figure 7(b) shows the attenuation estimates derived from Fig. 8 plotted as a function of frequency. The results are consistent with a linear increase in attenuation with frequency, with a slope given by $(9.6\pm1.0)\times10^{-4}$ dB/m/Hz or $\alpha_S=(1.6\pm0.2)$ dB/λ (assuming $v_S=1670$ m/s). The attenuation coefficients estimated here for L_P and S_H waves are in good agreement with previously reported results (Table II).

Given the seismic-wave velocities and attenuations determined above, it is informative to consider the 3D seismic waveforms recorded at the geophone array for all source types (i.e., radial, transverse and vertical hammer blows). Figure 9 shows the seismic waves recorded for a radial hammer blow at a range of 200 m, with all signals plotted in true relative amplitude. Dotted lines in the figure indicate the expected arrival times for waves propagating at the longitudinal- and shear-wave velocities (on left and right, respectively). As expected, the largest signal is the L_P arrival on the radial (x) geophones. Weaker arrivals at this velocity
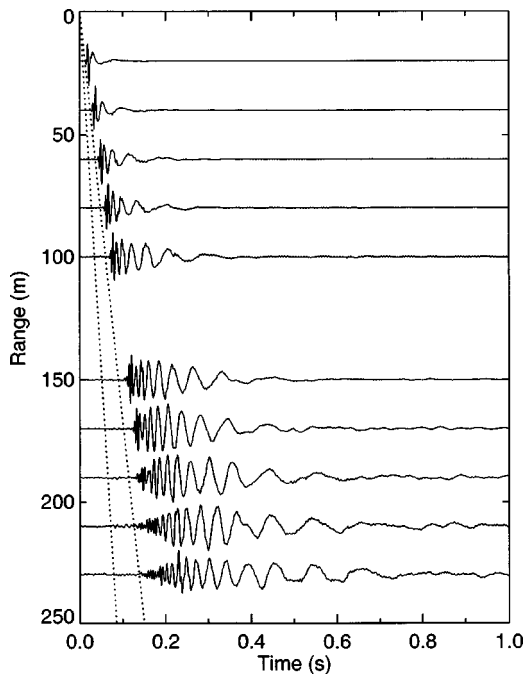
FIG. 5. Seismic section of flexural waves recorded at z-component geophones for vertical hammer blows at two ranges. Dotted lines correspond to the propagation velocities of L_P wave (on left) and S_H waves (on right).
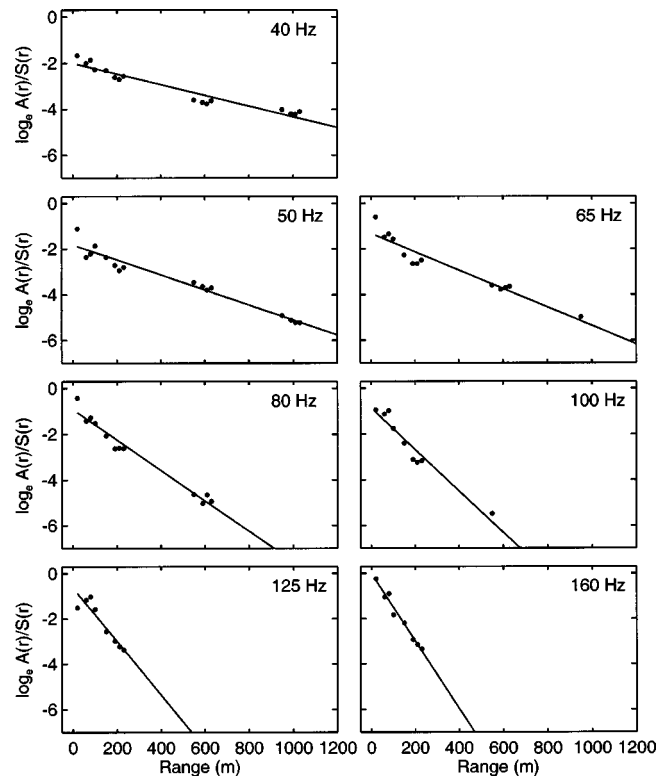
FIG. 6. Plots of $\log_e A(r)/S(r)$ vs r for L_P waves in third-octave band averages centered at the indicated frequencies. Least-squares lines fitting the data points are included on each plot; the negative of the slope for each line gives α_L in Nepers/m.
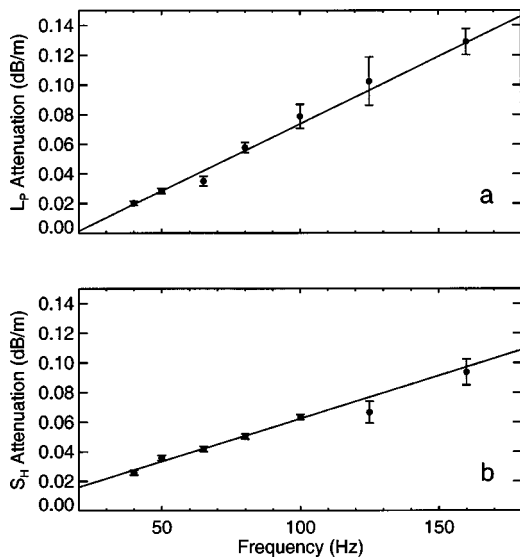
FIG. 7. Attenuation coefficients α_L and α_S as a function of frequency are shown in (a) and (b), respectively. The least-squares line fitting the data points is included on each plot.

are also evident on the vertical (z) geophones, consistent with the radial–vertical ($P-S_V$) particle motion of this wave. Dispersive flexural waves are also evident on the vertical geophones, with the highest-frequency components arriving shortly after the expected shear-wave arrival times. Of interest are the significant S_H arrivals at the y-component geophones. In theory, shear waves should not be excited in a direction perpendicular to the hammer blow for a uniform ice
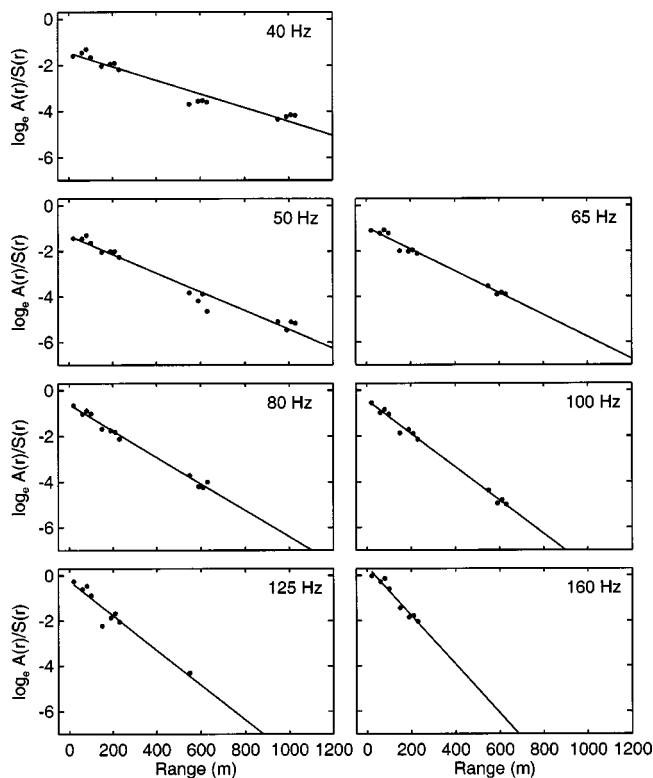
FIG. 8. Plots of $\log_e A(r)/S(r)$ vs r for S_H waves in third-octave band averages centered at the indicated frequencies. Least-squares lines fitting the data are indicated for each plot; the negative of the slope for each line gives α_S in Nepers/m.
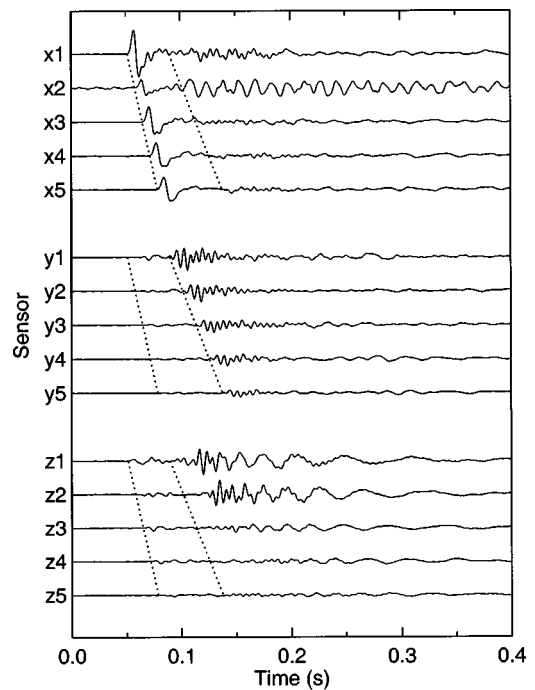
FIG. 9. 3D seismic arrivals for a radial hammer blow at 200-m range. Dotted lines indicate expected arrival times for L_P and S_H waves (left and right, respectively).

plate. Their existence here is likely due to coupling between $P-S_V$ and S_H waves at the source and at inhomogeneities within the ice, and possibly to hammer blows that were not precisely perpendicular to the y-component geophones. In particular, the signals arriving at the y-component geophones at velocity v_S must have been generated at or near the source, while the weaker signals arriving at velocities intermediate between v_L and v_S (i.e., between the dotted lines in Fig. 9) must result from wave coupling in the ice between the source and receivers.

Seismic waveforms recorded for a transverse hammer blow are illustrated in Fig. 10. The strongest arrival is the S_H wave at the transverse (y) geophones. No arrivals are evident at the longitudinal-wave velocity at any sensors, and only very weak arrivals appear at the shear velocity on the radial and vertical geophones. Figure 11 shows the waveforms recorded for a vertical hammer below. In this case, the strongest arrival is the flexural wave on the x and z geophones, with the highest-frequency components arriving shortly after the expected shear-wave arrival times. A weak L_P wave is also evident on the x geophones. Noteworthy again is the significant S_H-wave arrival on the y geophones. As a vertical hammer blow cannot have a component in the transverse direction, the S_H energy must arise from coupling between $P-S_V$ and S_H waves in the ice.

Finally, it is interesting to consider the seismo-acoustic arrivals at a ice-mounted geophone due to an impulsive acoustic source in the water column. Figure 12 shows seismic waveforms recorded for a light-bulb implosion at $0°$ bearing and 200-m range (the deployment procedure is described in Sec. III D). In Fig. 12, the dashed lines indicate the expected arrival time for an acoustic wave propagating over the slant range from source to receivers at the water
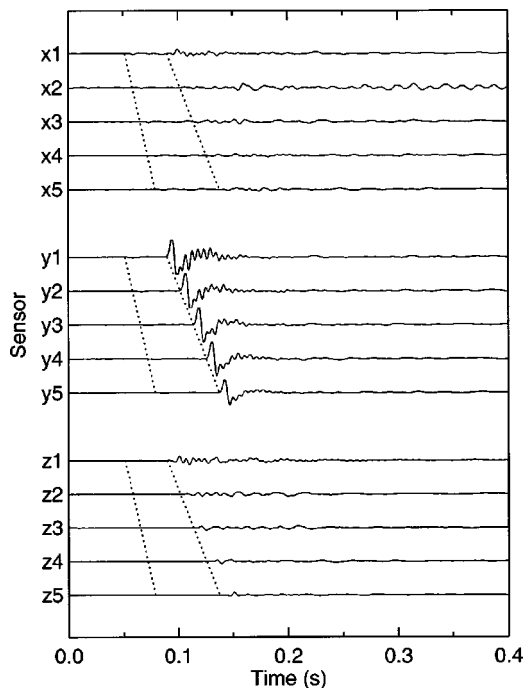
FIG. 10. 3D seismic arrivals for a transverse hammer blow at 200-m range. Dotted lines indicate expected arrival times for L_P and S_H waves (left and right, respectively).

FIG. 12. 3D seismic arrivals for a light bulb implosion at 200-m range, 40-m depth, and 0° bearing. Dotted and dashed line indicate expected arrival times for the critically refracted L_P wave and water-borne acoustic wave, respectively.

sound velocity of $v_w = 1440$ m/s. The strongest arrival in Fig. 12 appears on the z geophones at the acoustic-wave arrival times. The corresponding arrivals on the x geophones actually begin at times slightly before the acoustic arrival time; the reason for the early arrival of these waveforms is not completely clear, but could be related to coupling between water-borne acoustic waves and ice seismic waves with a

FIG. 11. 3D seismic arrivals for a vertical hammer below at 200-m range. Dotted lines indicate expected arrival times for L_P and S_H waves (left and right, respectively).

dominant P component in the vicinity of the geophone. Significant arrivals at approximately the water velocity are also evident on the y geophones, apparently due to coupling between the acoustic and S_H waves at the underside of the ice. The dotted lines in Fig. 12 indicate the arrival time for a critically refracted L_P wave, i.e., an arrival that propagates as an acoustic wave through the water, intersects the ice at the critical angle $\theta_c = \sin^{-1} v_w / v_L \approx 60°$, and propagates the remaining distance through the ice as an L_P wave. The critically refracted L_P wave is clearly evident at the x geophones. There is no evidence of a flexural wave on any of the seismograms. Water-column multiples are evident, particularly on the x and z recordings.

III. SOURCE BEARING ESTIMATION

A. Rotational analysis

The relative importance of the various types of seismic waves in the ice is an important factor in source-bearing estimation. This section describes a straightforward rotational analysis for waves with particle motion in the radial–vertical propagation plane; the following section describes a set of polarization filters that suppress nonradial wave components. The coordinate system for the problem is defined in Fig. 13(a). The geophone is located on the ice surface at the origin of a Cartesian coordinate system with the $+z$ axis oriented vertically upward. A seismo-acoustic wave (indicated by a ray) is incident at an angle θ in the horizontal plane and an angle ϕ (with respect to the normal) in the vertical plane. Let x_t, y_t, z_t, $t = 1, \ldots, T$ denote the discrete time series of particle motion recorded on the x-, y-, and
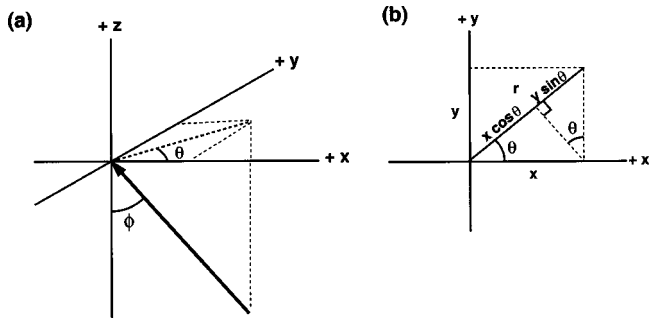
FIG. 13. Coordinate system for the source-bearing estimation problem. A seismic wave, indicated by a ray, is incident at an angle ϕ with respect to the z axis, and a bearing θ with respect to the x axis, as shown in (a). The projection of x and y onto r at a bearing θ is shown in (b).

z-component geophones, respectively. Then at any instant of time, the horizontal (radial) particle motion is given by

$$r_t = x_t \cos \theta + y_t \sin \theta, \tag{2}$$

as shown in Fig. 13(b). For waves with particle motion confined to the radial–vertical plane, the bearing angle θ can be determined from x_t and y_t by maximizing the rotational power function consisting of the (squared) projection of the horizontal components along a bearing θ:

$$\Psi(\theta) = \sum_{t=1}^{T} r_t^2(\theta)$$

$$= \cos^2 \theta \sum x_t^2 + \sin^2 \theta \sum y_t^2 + 2 \cos \theta \sin \theta \sum x_t y_t. \tag{3}$$

Setting $\partial \Psi / \partial \theta = 0$ for a maximum leads to the solution

$$\theta_{\max} = 1/2 \tan^{-1} \left[\frac{2\Sigma x_t y_t}{\Sigma x_t^2 - \Sigma y_t^2} \right]. \tag{4}$$

Equation (4) provides a closed-form solution for the optimal source-bearing estimate based on the particle motion. However, it is more instructive to consider the angular dependence of the particle motion in a format analogous to a beamformer output plot. This can be accomplished by projecting the horizontal components of particle motion onto a series of look angles from 0°–360°, and computing the power $\Psi(\theta)$ of the projection at each angle θ. The angle at which the power is maximum corresponds to the analytic solution given by Eq. (4). Considering the particle-motion power as a function of look angle provides an indication of how well the maximum is defined relative to the power at other look angles. Note that resolving the particle motion in the horizontal plane results in a 180° ambiguity in bearing; this ambiguity can be resolved by also considering the vertical motion (dealt with in Sec. III C). The procedure for source-bearing estimation is illustrated in Fig. 14. Figure 14(a) shows the x, y, and z time series recorded for an impulsive source (an imploding glass light bulb) at a bearing of 30° and a range of 1000 m (described in Sec. III D). The value of $\theta_{\max}$ as determined by Eq. (4) is 39°. Figure 14(b) shows a polar plot of $\Psi(\theta)$ in decibels, i.e., $10 \log \Psi(\theta)$. The source-bearing estimate is taken to be the angle θ at
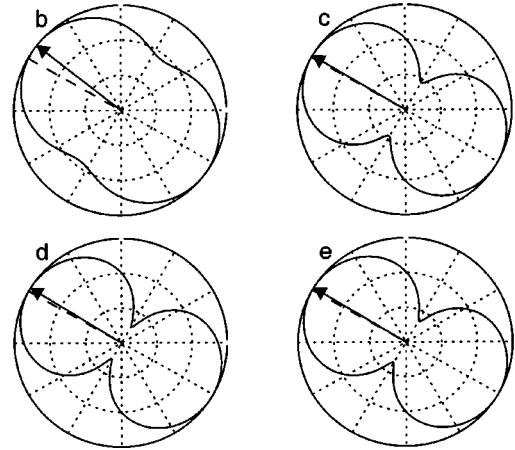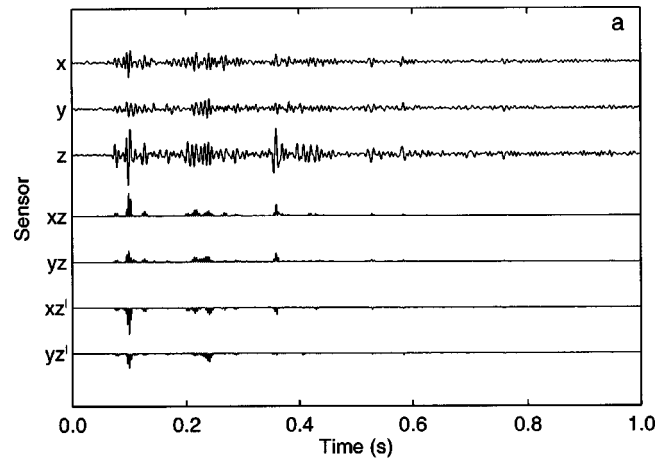
FIG. 14. Example of rotational analysis. (a) Recorded time series x, y, z for a light-bulb source at 30° bearing and 1000-m range; xz, yz, xz', and yz' are polarization-filtered time series. (b) The result of the rotational analysis (no polarization filtering). (c), (d), and (e) The results of z filtering, z' filtering, and combining z and z' filtering. Dotted circles indicate 5-dB increments; dashed lines indicate true source bearing, arrows indicate optimal bearing estimate.

which the maximum value of $\Psi(\theta)$ occurs: in Fig. 14(b) this is $\theta = 39°$. The minimum value of $\Psi(\theta)$ occurs at a direction perpendicular to $\theta_{\max}$. The difference between the maximum and minimum values provides a measure of the level of discrimination of the bearing estimate (i.e., how well the angle is determined). In Fig. 14(b), this discrimination level is approximately 6 dB. The rotational analysis is degraded by S_H waves which have particle motion perpendicular to the radial–vertical plane, by P and S_V waves which have been scattered out of the propagation plane, and by ambient noise.

B. Seismic polarization filters

The rotational analysis described in the previous section assumes particle motion in the radial–vertical propagation plane. When significant non-radial wave components exist, poor bearing estimates can be obtained. Wave polarization filters have been developed in the field of earthquake seismology and applied to enhance bearing estimation for seismic sources within the earth (e.g., an earthquake or underground explosion). A straightforward and effective set of polarization filters was developed by White.[10] By considering the particle motion at the surface of the earth due to

incident, reflected, and converted waves, White determined the coherency between the vertical and horizontal particle motion of the fundamental seismic wave types in the earth: P, S_V, S_H, Rayleigh and Love waves (Rayleigh waves are analogous to flexural waves in ice; Love waves are horizontally polarized surface waves).[14] These coherency results are exploited to enhance or suppress certain wave types by using the vertical-component signal and/or its time derivative as time-domain filters for the horizontal signals. This section provides an overview of the theory; the following section adapts the approach to the Arctic acoustic application of interest here.

Consider first the application of the vertical-component signal as a time-domain filter and its effect on the various wave types. For instance, for an incident P wave with an arbitrary waveform function $p(t)$, it can be shown that the x, y, and z components of particle motion at the earth's surface are given by[10]

$$p_x(t)=Ap(t)\cos\,\theta,\quad p_y(t)=Ap(t)\sin\,\theta,\quad p_z(t)=Bp(t),$$
$$(5)$$

where A and B are real, positive constants (expressions for A and B can be derived in terms of ϕ, v_p, and v_S, but are not required for the present application). Multiplication of each of the horizontal-component signals by the vertical signal yields

$$p_{xz}(t)\equiv p_x(t)p_z(t)=ABp^2(t)\cos\,\theta,$$
$$p_{yz}(t)\equiv p_y(t)p_z(t)=ABp^2(t)\sin\,\theta.$$
$$(6)$$

Similarly, for an S_V wave $s(t)$ incident at an angle $\phi < \sin^{-1}(v_S/v_p)$, the particle motion components are

$$s_x(t)=Cs(t)\cos\,\theta,\quad s_y(t)=Cs(t)\sin\,\theta,\quad s_z(t)=-Ds(t),$$
$$(7)$$

where C and D are real, positive constants. Multiplying the horizontal signals by the vertical signal yields

$$s_{xz}(t)=-CDs^2(t)\cos\,\theta,$$
$$s_{yz}(t)=-CDs^2(t)\sin\,\theta.$$
$$(8)$$

Equations (6) and (8) show that since the horizontal- and vertical-component seismograms are in phase for P and (steep) S_V waves, multiplying the horizontal signals by the vertical signal has the effect of extracting these waveforms as positive and negative rectified signals, respectively. This multiplication also has the effect of suppressing other wave types which are not in phase. For instance, the particle motion at the surface associated with an incident S_V wave $s(t)$ at $\phi \geqslant \pi/4$ can be shown to be[10]

$$s_x(t)=-Es_1(t)\cos\,\theta,$$
$$s_y(t)=-Es_1(t)\sin\,\theta,\quad s_z(t)=-F[s_1(t)]_{\pi/2},$$
$$(9)$$

where $s_1(t)$ is an altered waveform (the exact form is not required here), $[s_1(t)]_{\pi/2}$ is a waveform that leads $s_1(t)$ by $\pi/2$ in phase, and E and F are real, positive constants. Multiplying the horizontal components by the vertical component yields

$$s_{xz}(t)=EFs_1(t)[s_1(t)]_{\pi/2}\cos\,\theta,$$
$$s_{yz}(t)=EFs_1(t)[s_1(t)]_{\pi/2}\sin\,\theta.$$
$$(10)$$

Since $s_{xz}(t)$ and $s_{yz}(t)$ are the product of waveforms that are out of phase, the net contribution due to S_V waves at $\phi > \pi/4$ is expected to be small. Similarly, S_V waves at angles of incidence $\sin^{-1}(v_S/v_p)\leqslant\phi\leqslant\pi/4$ and Rayleigh waves of waveform $R(t)$ can be shown to yield particle motion

$$R_x(t)=Es_1(t)\cos\,\theta,$$
$$s_y(t)=Es_1(t)\sin\,\theta,\quad s_z(t)=-F[s_1(t)]_{\pi/2},$$
$$(11)$$

and

$$R_x(t)=G[R(t)]_{\pi/2}\cos\,\theta,$$
$$R_y(t)=G[R(t)]_{\pi/2}\sin\,\theta,\quad R_z(t)=HR(t),$$
$$(12)$$

where G and H are positive constants. Since the horizontal and vertical components in Eqs. (11) and (12) are out of phase by $\pi/2$, the multiplication of these components generally suppresses the contributions of S_V waves $[\sin^{-1}(v_S/v_p)\leqslant\phi\leqslant\pi/4]$ and Rayleigh waves.

Next, consider the effect of multiplying the horizontal signals of the various wave types by the time derivative of the vertical signal. Taking the derivative introduces a phase shift of $\pi/2$ to the vertical component. Hence, for an incident P wave, the products of horizontal- and vertical-component seismograms, Eq. (5), are

$$p_{xz'}(t)\equiv p_x(t)p_z'(t)=ABp(t)[p(t)]_{\pi/2}\cos\,\theta,$$
$$p_{yz'}(t)\equiv p_y(t)p_z'(t)=ABp(t)[p(t)]_{\pi/2}\sin\,\theta,$$
$$(13)$$

where $'\equiv\partial/\partial t$. Since these equations contain products of signals that are out of phase by $\pi/2$, this filter generally suppresses P waves. A similar result holds for S_V waves at angles $\phi<\sin^{-1}(v_S/v_p)$ as expressed by Eq. (7). However, for S_V waves at angles greater than $\pi/4$

$$s_{xz'}(t)=EFs_1(t)[s_1(t)]_{\pi}\cos\,\theta=-EFs_1^2(t)\cos\,\theta,$$
$$s_{yz'}(t)=EFs_1(t)[s_1(t)]_{\pi}\sin\,\theta=-EFs_1^2(t)\sin\,\theta,$$
$$(14)$$

since $[s_1(t)]_{\pi}=-s_1(t)$, and the vertical-derivative filter is in phase with the horizontal signals. A similar result holds for S_V waves at angles $\sin^{-1}(v_S/v_p)>\phi>\pi/4$, as expressed by Eq. (10), except with opposite sign,

$$s_{xz'}(t)=EFs_1^2(t)\cos\,\theta,\quad s_{yz'}(t)=EFs_1^2(t)\sin\,\theta.\quad(15)$$

For Rayleigh waves given by Eq. (12),

$$R_{xz'}(t)=GH[R(t)]_{\pi/2}^2\cos\,\theta,$$
$$R_{yz'}(t)=GH[R(t)]_{\pi/2}^2\sin\,\theta,$$
$$(16)$$

and the filter is again in phase with and enhances the horizontal signals.

In summary, multiplication of the horizontal-component seismograms with the vertical seismogram produces a positive signal for P waves and a negative signal for S_V waves

with $\phi < \sin^{-1}(v_S/v_p)$; S_V waves at shallower angles and Rayleigh (or F_L) waves are suppressed. Multiplication by the derivative of the vertical seismogram produces a negative signal for S_V waves with $\phi > \pi/4$, a positive signal for S_V waves with $\sin^{-1}(v_S/v_p) < \phi < \pi/4$, and a positive signal for Rayleigh (or F_L) waves; P waves and S_V waves with $\phi < \sin^{-1}(v_S/v_p)$ are suppressed. In addition, since S_H and Love waves have no vertical-component motion, multiplying the horizontal-component signals by either the vertical signal or its derivative tends to suppress these wave types. Finally, it is shown in Ref. 10 that random (incoherent), isotropic noise is also generally suppressed by both filters.

C. Application of polarization filters to rotational analysis

In earthquake seismology, long propagation paths and large differences in wave velocities typically result in the arrivals of different wave types being well separated in time. This fact is exploited by time integrating polarization-filtered signals to provide source bearing estimates for earthquake sources.[10] However, in the problem of interest here, the assumption of well-separated arrivals is not valid, since seismic waves of all types are excited by the water-borne acoustic wave incident on the ice in the immediate vicinity of the receiver. Therefore, in this paper, acoustic source bearings are estimated from the two sets of filtered signals (xz, yz and xz', yz') by applying the rotational analysis described in Sec. III B. The filtering has the effect of suppressing S_H waves and incoherent noise while enhancing the P and shallow-angle S_V waves, which provide the primary information regarding source bearing.

Figure 14(a) shows the filtered signals for a light-bulb source at 30° bearing and 1-km range. The strong positive signals in xz and yz correspond to the P-wave component; the strong negative signals in xz' and yz' correspond to the shallow-angle S_V component ($\phi > \pi/4$). In theory, xz and yz should also contain S_V-wave components [$\phi < \sin^{-1}(c_s/c_p) \approx 30°$ for sea ice] as a negative signal, and xz' and yz' should contain S_V components [$\sin^{-1}(c_s/c_p) < \phi < \pi 4$] and flexural-wave components as positive signals. However, these components are expected to be small for the following reasons. By Snell's Law, a propagation angle of $\pi/4 = 45°$ in the ice corresponds to an angle of approximately 36° (with respect to the normal) in the water column: Arctic acoustic propagation at these steep angles is strongly attenuated with range. Also, F_L waves in the ice are not well excited by a water-column source much deeper than one quarter of the flexural wavelength. In Fig. 14(a) the negative components in xz and yz are the positive components in xz' and yz' are indeed seen to be negligibly small. Such weak signals may be dominated by noise and are of dubious value in bearing estimation. In fact, by considering all of the data sets described in Sec. III D of this paper, it was found that the best source-bearing estimates were obtained by setting the negative component of xz and yz and the positive component of xz' and yz' to zero prior to carrying out rotational analysis. To apply the rotational analysis to the two sets of filtered

signals, rotational functions are computed for each set according to

$$\Psi_z(\theta) = \cos^2 \theta \sum (x_t z_t)^2 + \sin^2 \theta \sum (y_t z_t)^2$$

$$+ 2 \cos \theta \sin \theta \sum (x_t z_t)(y_t z_t),$$

$$\Psi_{z'}(\theta) = \cos^2 \theta \sum (x_t z_t')^2 + \sin^2 \theta \sum (y_t z_t')^2$$

$$+ 2 \cos \theta \sin \theta \sum (x_t z_t')(y_t z_t'). \tag{17}$$

The two rotational functions can then be combined as

$$\Psi_{zz'}(\theta) = \Psi_z(\theta)/\mathrm{Min}\{\Psi_z(\theta)\} + \Psi_{z'}(\theta)/\mathrm{Min}\{\Psi_{z'}(\theta)\}. \tag{18}$$

In combining $\Psi_z(\theta)$ and $\Psi_{z'}(\theta)$, some form of normalization is required since their relative amplitudes are determined by the relative amplitudes of z and z', which is not physically meaningful. Normalizing each rotational function by its minimum value in Eq. (18) allows each function to contribute to the sum at its peak according to the difference between its maximum and minimum values (the discrimination level). Figures 14(c)–(e) shows $\Psi_z(\theta)$, $\Psi_{z'}(\theta)$, and $\Psi_{zz'}$, respectively, for the impulsive source at 30° bearing. The maximum of $\Psi_z(\theta)$ in Fig. 14(c) occurs at 30.5° with a discrimination level of 11 dB. The maximum of $\Psi_{z'}(\theta)$ in Fig. 14(d) occurs at 31.5° with a level of 12.5 dB. Finally, the maximum of the combined rotational function $\Psi_{zz'}(\theta)$ in Fig. 14(e) occurs at 31° with a level of 12 dB. This example shows that the filtered rotational function represent a substantial improvement over the unfiltered version $\Psi(\theta)$ shown in Fig. 14(b).

The rotational functions shown in Figs. 14(b)–(e) contain a 180° ambiguity that is inherent in the definition of $\Psi(\theta)$ in terms of the horizontal particle motion, Eq. (3). However, this ambiguity can be resolved by considering the particle motion in the radial–vertical plane to provide a unique estimate of the source bearing. Figure 15(a) shows the radial- and vertical-component seismograms for the impulsive source considered in Fig. 14. The radial component is calculated using

$$r_t = x_t \cos \theta_{max} + y_t \sin \theta_{max}, \tag{19}$$

where $\theta_{max} = 31°$ was determined from the combined rotational function shown in Fig. 14(e). Figure 15(b) shows a hodogram of the vertical versus radial particle motion. The $P - S_V$ waves combine to produce prograde elliptical particle motion (i.e., the z component leads the r component). That this should be the case is evident from Eqs. (5) and (9) which indicate that for P waves the vertical and horizontal components are in phase, while for (shallow-angle) S_V waves the vertical component leads the horizontal components by $\pi/2$. Hence, the direction to the source can be determined by choosing one of the two possible values of θ_{max} from the rotational function and checking if this choice results in prograde particle motion. If so, this choice of θ_{max} represents the unique optimal bearing estimate; if not, the other choice of

FIG. 16. Rotational power for light-bulb sources at 200-m and geophones G_1, G_3, G_4, and G_5. Dotted circles indicate 5-dB increments; dashed lines indicate true source bearings, arrows indicate optimal bearing estimates.

FIG. 15. Example of particle motion in the $r-z$ plane. (a) The time series for the source in Fig. 14 resolved into radial r and vertical z components. (b) A vertical–radial hodogram, with arrows indicating direction of motion.

θ_{max} is indicated. An effective method to determine if a set of $r-z$ seismograms are dominated by prograde or retrograde particle motion is to form the sum

$$\sigma = \sum_{t=2}^{T-1} z_t(r_{t+1} - r_{t-1}). \qquad (20)$$

If $\sigma > 0$, prograde motion dominates; if $\sigma < 0$, retrograde motion dominates. The unique source bearing estimates determined in this manner are indicated by arrows in Figs. 14(b)–14(e).

D. Bearing estimation trials

The overall purpose of the Arctic field trials was to investigate estimating the bearing of an acoustic source in the water column using a geophone mounted on the ice surface. To this end, recordings were made at the geophone array of impulsive sources deployed at 40-m depth in the water and ranges of 200 m, 600 m, and 1000 m along lines at 0°, 30°, 60°, and 90° bearing with respect to the array axis (endfire), as shown in Fig. 1(b). The impulsive sources consisted of glass light bulbs imploded under hydrostatic pressure at depth.[11] To control the depth at which the light bulbs imploded, the bulbs were attached to a weight and lowered on a line through a hole in the ice to the desired depth. A messenger weight was then dropped along the line, breaking the

bulb on impact. At least two light-bulb sources were deployed at all ranges and bearings. It should be noted that the structure of the ice floe was not isotropic. Towards 0° bearing, the floe consisted of generally smooth annual ice. The ice roughness increased with bearing angle from 0°–90°, with several inclusions of large multi-year ice blocks towards 90° bearing.

An estimate of the bearing to each acoustic source was obtained from the 3D particle motion at each geophone by applying the rotational analysis in conjunction with seismic polarization filtering, as described in Sec. III C. The results are illustrated in terms of polar plots of the rotational power, $\Psi_{zz'}(\theta)$, computed by combining the two sets of polarization-filtered signals according to Eq. (18). The optimal bearing estimate is determined as the angle of maximum rotational power, with the 180° ambiguity resolved by considering the vertical–radial particle motion. Figure 16 shows the rotational power for sources at 200-m range and bearings of 0°, 30°, 60°, and 90°. For the results shown here, the recorded time series were digitally filtered with a pass-band filter of 50–250 Hz to attenuate ambient noise at low frequencies where the light-bulb power is low, and to attenuate signals at frequencies above the upper limit of the geophone calibration band. However, virtually identical results were obtained using a low-pass filter of 0–250 Hz (i.e., passing all low-frequency energy). The rotational power is plotted for geophones G_1, G_3, G_4, and G_5. Recordings for geophone G_2 exhibited unusual oscillatory behavior due to electronics problems (e.g., Figs. 3 and 9) which strongly degraded the bearing estimates, and so were omitted from this analysis. The rotational power plots in Fig. 16 have been corrected for the fact that the true bearing to the source for each geophone differs from the bearing as measured at the array center. Figure 16 shows that reasonably good estimates of the source bearing are obtained in all cases. The rotational power along
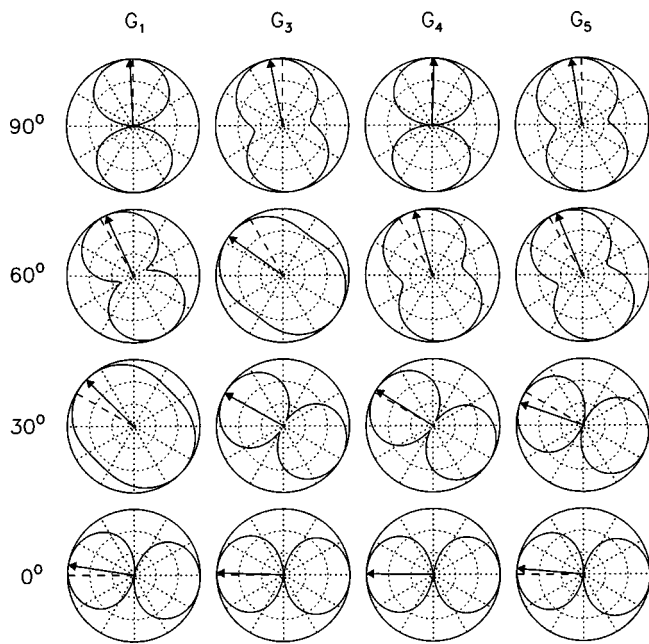
FIG. 17. Rotational power for light-bulb sources at 600-m range and indicated source bearings. Dotted circles indicate 5-dB increments; dashed lines indicate true source bearings, arrows indicate optimal bearing estimates.

FIG. 19. Rotational power for light-bulb sources at 1000-m range and indicated source bearings, *without* polarization filtering. Dotted circles indicate 5-dB increments; dashed lines indicate true source bearings, arrows indicate optimal bearing estimates.

the optimal bearing is typically 10–15 dB greater than the power in the perpendicular direction. Figures 17 and 18 show the rotational power for light-bulb sources at 600-m and 1000-m range, respectively. In each case, good estimates of the true source bearing are obtained with discrimination levels of 5–15 dB. To illustrate the benefits of the polarization filters, Fig. 19 shows the rotational power plots obtained for the sources at 1000-m range without the application of the polarization filters. Comparison of Figs. 18 and 19 indicates that polarization filtering leads to bearing estimates that

are significantly more accurate and to considerably higher discrimination levels.

For simplicity, Figs. 16–18 show the bearing estimates for just one light-bulb source at each bearing and range. Considering all sources, the average absolute error in bearing estimates for geophones G_1, G_3, G_4, and G_5 are 11.6°, 10.8°, 5.4°, and 10.5°, respectively. The 180° ambiguity is correctly resolved in all cases (a total of 104 bearing esti-

FIG. 18. Rotational power for light-bulb sources at 1000-m range and indicated source bearings. Dotted circles indicate 5-dB increments; dashed lines indicate true source bearings, arrows indicate optimal bearing estimates.

FIG. 20. Absolute errors in bearing estimates as a function of source range.

FIG. 21. Absolute errors in bearing estimates as a function of source bearing.

the various geophones at particular source bearings, there is no clear pattern between error size and bearing angle. In particular, the rougher ice with included blocks at 90° bearing did not lead to uniformly larger errors at this bearing, likely because the most important arrivals appear to be due to the acoustic wave incident on the ice below the geophone, and not due to seismic plate waves propagating along the ice. Finally, Fig. 22 shows that although there is a tendency for the largest errors to be associated with low SNRs, a strong relationship between bearing errors and data noise is not evident. Hence, the cause of the uncertainties in source bearing incurred in this study is not readily apparent.

IV. SUMMARY AND DISCUSSION

This paper described and analyzed field trials carried out on the polar ice pack to investigate estimating the bearing of an acoustic source in the water column using geophones coupled to the surface of the sea ice. The approach pursued here is based on rotational analysis of ice seismic waves with particle motion directed radially outward from the source, which provides a source-bearing estimate using a single tri-axial geophone. Seismic polarization filters were applied in conjunction with the rotational analysis to suppress waves with transverse particle motion (S_H waves), while passing waves with radial motion ($P-S_V$ waves). Polarization filters will not remove out-of-plane $P-S_V$ waves due to reflections from ice inclusions or 3D bathymetry; however, these components are generally expected to be small relative to the direct acoustic wave. In addition, the 180° ambiguity inherent in the rotational analysis of horizontal seismograms was resolved by requiring outgoing (prograde) particle motion in the vertical-radial plane, providing a unique bearing estimate.

A hammer seismic survey was carried out to determine propagation velocities and attenuations of the principle seismic waves, with results in good agreement with previously reported values. This study indicated significant coupling between $P-S_V$ (radial) waves and S_H (transverse) waves in the ice. Comparison of seismograms recorded for a water-column source with the hammer seismograms indicated that the dominant arrival appears to be the acoustic water wave that couples into ice seismic waves immediately below the geophone, although significant S_H and L_P waves were observed.

To investigate source-bearing estimation, ice-mounted geophones were used to record impulsive sources in the water, consisting of light bulbs imploded at ranges varying from 200–1000 m, and at bearings of 0°, 30°, 60°, and 90°. The analysis was applied to an upper frequency limit of 250 Hz due to the calibration limit of the geophones. Good source-bearing estimates were obtained, with average absolute bearing errors of 5°–11° per geophone. Polarization filtering was shown to significantly improve the bearing estimates by removing S_H particle motion, and may also be useful for determining ice properties from elastic waves,[15] although this approach was not applied here. Overall, the results in this paper indicate that ice-mounted geophones can provide useful bearing estimates for acoustic sources in Arctic waters.

mates). To further investigate the bearing-estimate errors, in Figs. 20–22 all bearing-estimate errors are plotted as a function of range, source bearing, and SNR, respectively. Figure 20 shows that the bearing errors generally do not increase with range for ranges of 200–1000 m. Figure 21 shows that although there are obvious differences between the errors for

FIG. 22. Absolute errors in bearing estimates as a function of SNR.

[1] P. J. Stein, "Interpretation of a few ice event transients," J. Acoust. Soc. Am. **83**, 617–622 (1988).

[2] Y. Xie and D. M. Farmer, "Acoustical radiation from thermally stressed sea ice," J. Acoust. Soc. Am. **89**, 2215–2230 (1991).

[3] B. E. Miller and H. Schmidt, "Observation and inversion of seismo-acoustic waves in a complex arctic ice environment," J. Acoust. Soc. Am. **89**, 1668–1685 (1991).

[4] Y. V. Dudko and H. Schmidt, "Near-field polarization processing of ice fracturing events," J. Acoust. Soc. Am. **102**, 3193 (1997).

[5] T. C. Yang and G. R. Giellis, "Experimental characterization of elastic waves in a floating ice sheet," J. Acoust. Soc. Am. **96**, 2993–3009 (1994).

[6] J. L. Becklehimer, "A Fortran program for computing beam patterns for geophone arrays," Comput. Geosci. **17**, 633–640 (1991).

[7] F. Press and W. M. Ewing, "Propagation of elastic waves in a floating ice sheet," Trans., Am. Geophys. Union **32**, 673–678 (1951).

[8] W. M. Ewing, W. S. Jardetzky, and F. Press, *Elastic Waves in Layered Media* (McGraw-Hill, New York, 1957), pp. 293–299.

[9] G. H. Brooke and J. M. Ozard, "In-situ measurement of elastic properties of sea ice," in *Underwater Acoustic Data Processing*, edited by Y. T. Chan (Kluwer Academic, Dordrecht, The Netherlands, 1989), pp. 113–118.

[10] J. E. White, "Motion product seismograms," Geophysics **29**, 288–298 (1964).

[11] G. J. Heard, M. McDonald, N. R. Chapman, and L. Haschke, "Underwater light bulb implosions: A useful acoustic source," Proc. IEEE Oceans '97, Vol. 2, pp. 755–762 (1997).

[12] M. V. Greening and P. Zakarauskas, "Spatial and source level distributions of ice cracking in the Arctic Ocean," J. Acoust. Soc. Am. **95**, 783–790 (1994).

[13] M. V. Greening and P. Zakarauskas, "Pressure ridging spectrum level and a proposed origin of the infrasonic peak in Arctic ambient noise spectra," J. Acoust. Soc. Am. **95**, 791–797 (1994).

[14] K. E. Bullen, *An Introduction to the Theory of Seismology* (Cambridge University Press, London, 1965).

[15] P. J. Stein, S. E. Euerle, and J. C. Parinella, "Inversion of pack ice elastic wave data to obtain ice physical properties," J. Geophys. Res., [Oceans] **103**, 21783–21793 (1998).

A numerical optimization approach to acoustic hull array design

Thomas A. Wettergren, John P. Casey, and Roy L. Streit

Naval Undersea Warfare Center, 1176 Howell Street, Newport, Rhode Island 02841

A numerical optimization approach is presented to optimize passive broadband detection performance of hull arrays through the adjustment of array shading weights. The approach is developed for general hull arrays in low signal-to-noise ratio scenarios, and is shown to converge rapidly to optimal solutions that maximize the array's deflection coefficient. The beamformer is not redesigned in this approach; only the shading weights of the conventional beamformer are adjusted. This approach allows array designers to use the array to minimize the impact of known sources of noise on detection at the beamformer output while maintaining acoustic array gain against an unknown source. The technique is illustrated through numerical examples using hull-borne structural noise as the noise source; however, the design concept can be applied to other design parameters of the array such as element position, material selection, etc. © *2002 Acoustical Society of America.* [DOI: 10.1121/1.1518982]

PACS numbers: 43.30.Wi, 43.40.Ph, 43.30.Yj [WMC]

I. INTRODUCTION

Traditional approaches to acoustic hull array design have focused on the optimization of desirable beam properties such as the maximization of array gain or the minimization of sidelobe levels. Passive arrays typically employ data-independent beamforming, where the beamformer weights are chosen *a priori* to approximate a desired response oriented in the steered direction. Beam pattern design for linear and planar array geometries has been studied analytically for decades (see, e.g., the classic papers by Dolph[1] and Taylor[2]), but these approaches base their design on achieving some desirable beam characteristics at a fixed frequency, and they focus on trade-offs between beamwidth and sidelobe structure. Single-frequency approaches (see Ref. 3, for example) only indirectly support the fundamental design goal of a passive acoustic hull array, which is to obtain an optimal broadband detection capability in a specified frequency band. Furthermore, the response of the array to nonacoustic noise cannot be assessed through standard beam pattern design techniques.

Passive broadband detection capability of a hull array is degraded by the presence of structural noise. This noise is often reduced by mechanical means (such as isolating mounts, pressure release materials, etc.). A supplementary means to reduce the impact of structural noise on passive detection is to adjust the beamformer weightings to reduce the impact of this noise while maintaining desirable beam characteristics for incoming acoustic waves. This is accomplished (for Gaussian signals) by numerically maximizing the deflection coefficient of a classical square-law detector under the assumption of a small signal-to-noise ratio (SNR). Under this approach, the underlying detection processor is not altered; rather, the conventional beamformer processor is used and the shading weights are treated as available design parameters to be optimized. The design concept is to predict the noise at the hydrophone outputs and then use this local noise field information to mitigate its effect on broadband array detection processing. The parameters which are ad-justed are the beamformer weighting (shading) coefficients, and the optimization finds optimal values that replace any conventionally derived weightings. While the example herein is for shading weight adjustment, the design concept can be applied to other design parameters of the array such as element position, material selection, etc.

A computational approach is feasible since structural noise is highly predictable, and current computer hardware and software capabilities enable the numerical optimization of very large degree-of-freedom systems. In this paper, the improvement of passive hull array detection performance through numerical optimization of shading weights is developed. The underlying formulation of this problem has been discussed in Ref. 4 and the references therein. In Sec. II, the broadband hull array detection problem presents a performance metric which can be optimized through shading weights against an unknown acoustic signal. In Sec. III, this detection problem is formulated as a numerical optimization problem and its solution is discussed. In Sec. IV, the approach is applied to a simple numerical example to demonstrate its utility. The paper concludes with recommendations about the use of the method in hull array design.

II. HULL-MOUNTED BROADBAND SONAR DETECTION

Consider a conformal array of sensors (hydrophones) that is electronically steered to receive an incoming acoustic plane wave in the look direction given by the unit vector $\boldsymbol{\xi}_l$. This passive array system is looking for weak signals of unknown spectrum in the presence of noise. The hydrophone array receives noise as well as signal, where the signal is assumed small in received level compared to the noise, and the signal and noise are statistically independent. In this context, noise refers to all contributions to hydrophone response other than the desired acoustic plane wave, so that noise includes ambient noise, structure-borne noise, electronic noise, and acoustic sources outside of the look direction. The hydrophone array is beamformed using a standard broadband

delay-and-sum beamformer, and a square-law postbeam-forming detection processing scheme is used.

The detection performance of the passive broadband array is measured by the deflection coefficient. In standard hypothesis testing, the deflection coefficient d for distinguishing signal-plus-noise from noise alone, where both hypotheses are governed by Gaussian random variables, is given by[5]

$$d = \frac{\mu_{SN} - \mu_N}{\sigma_N}, \qquad (2.1)$$

if the two hypotheses have the same variance, as is the case of low SNR. We use μ and σ to denote the mean and standard deviation, and subscripts S and N to represent the signal-only and noise-only hypotheses, respectively, and SN to represent the combined signal-plus-noise hypothesis. In a standard square-law detector scheme, the standard deviation σ_N of the noise-only hypothesis is given by (see Ref. 5 for details)

$$\sigma_N = \left[\frac{1}{\pi T} \int_{-\infty}^{+\infty} |H_0(\omega)|^4 V_N^2(\omega) d\omega \right]^{1/2}, \qquad (2.2)$$

where T is the system averaging time, $V_N(\omega)$ is the beamformer output power spectrum due to noise only, and $H_0(\omega)$ is the predetection filter transfer function. Expression (2.2) assumes that the averaging time T is large compared to the correlation time of the beamformer output under the noise-only conditions. Since the SNR is small, the standard deviation of the signal-plus-noise hypothesis is the same as (2.2). The mean value of the signal-plus-noise hypothesis is given by

$$\mu_{SN} = \frac{1}{2\pi} \int_{-\infty}^{+\infty} |H_0(\omega)|^2 V_{SN}(\omega) d\omega, \qquad (2.3)$$

where, due to the statistical independence of signal and noise, $V_{SN}(\omega) = V_S(\omega) + V_N(\omega)$, with $V_S(\omega)$ and $V_N(\omega)$ representing the signal-only and noise-only beamformer output power spectra, respectively, in the given look direction ξ_l. The mean difference in Eq. (2.1) is thus given by

$$\mu_{SN} - \mu_N = \frac{1}{2\pi} \int_{-\infty}^{+\infty} |H_0(\omega)|^2 (V_{SN}(\omega) - V_N(\omega)) d\omega$$

$$= \frac{1}{2\pi} \int_{-\infty}^{+\infty} |H_0(\omega)|^2 V_S(\omega) d\omega. \qquad (2.4)$$

When the source spectrum is completely unknown, the predetection filter $H_0(\omega)$ is typically omitted, in which case the deflection coefficient is given by

$$d = \frac{\frac{1}{2}\sqrt{T/\pi} \int_{-\infty}^{+\infty} V_S(\omega) d\omega}{[\int_{-\infty}^{+\infty} V_N^2(\omega) d\omega]^{1/2}}. \qquad (2.5)$$

This expression is used for the remainder of this paper; if a specific predetection filter is to be used in the system under study, the deflection coefficient is easily modified appropriately.

The beamformer output spectrum is dependent on unknown signal characteristics, so it cannot be improved through a passive array design optimization. However, the beamformer output spectrum $V_N(\omega)$ due to noise alone can be written, in part, in terms of predictable structural noise terms. The noise prediction is accomplished through physics-based models of array structural response, empirical data, or a combination of the two. It is through this predictable contribution that the array design is optimized.

An array of M hydrophones is located along a hull at the positions $\{\mathbf{p}_m\}_{m=1}^M$. The beamformer output in the look direction ξ_l is given by the autocorrelation of the time output beamformed response as

$$V(\omega) = \int_{-\infty}^{+\infty} E[v(t)v(t+\tau)] e^{-i\omega\tau} d\tau, \qquad (2.6)$$

where $E[\cdot]$ represents the expected value operation and $v(t)$ is the time-domain beamformer output. The time-domain beamformer output for the M hydrophones with look direction ξ_l is given by

$$v(t) = \sum_{m=1}^M w_m u_m(t - (\mathbf{p}_m \cdot \xi_l)/c), \qquad (2.7)$$

where c is the sound speed and $u_m(t)$ is the time-domain response of the mth hydrophone. The time-domain array element response $u_m(t)$ is due to either (1) the incident plane wave for the source-only case $V_S(\omega)$ or (2) the combination of noise sources for the noise-only case $V_N(\omega)$.

For omnidirectional hydrophones, the electronically steered array phasing matches that of an incident source plane wave in the look direction, so that

$$V_S(\omega) = S(\omega) \left(\sum_{m=1}^M w_m \right)^2, \qquad (2.8)$$

where $S(\omega)$ is the power spectrum of the source signal. The hydrophone response to a single noise source on the hull is given by the convolution of the noise source waveform $\alpha(t)$ with the impulse response function $h_m(t)$ of the mth hydrophone relative to a unit impulse force at the noise source location. The impulse response function $h_m(t)$ is well defined because the structural-acoustics problem is modeled as a linear system; thus,

$$u_m(t) = \int_{-\infty}^{+\infty} h_m(\mu) \alpha(t - \mu) d\mu. \qquad (2.9)$$

Substituting (2.9) into (2.7), it can be shown that the noise-only beamformer output power spectrum is given by

$$V_N(\omega) = A(\omega) \left| \sum_{m=1}^M w_m H_m(\omega) e^{i\omega(\mathbf{p}_m \cdot \xi_l)/c} \right|^2, \qquad (2.10)$$

where

$$A(\omega) = \int_{-\infty}^{+\infty} E[\alpha(t)\alpha(t+\tau)] e^{-i\omega\tau} d\tau \qquad (2.11)$$

is the power spectrum of the noise source $\alpha(t)$, and

$$H_m(\omega) = \int_{-\infty}^{+\infty} h_m(\mu) e^{-i\omega\mu} d\mu \qquad (2.12)$$

is the spectral transfer function (or spectral Green's function) between the noise source location and the mth hydrophone.

The expression derived above for the array response to a single-point noise source with power spectrum $A(\omega)$ is written in vector-matrix form as

$$V_N(\omega) = \mathbf{X}^*(w,\omega)\mathbf{H}^*(\omega)A(\omega)\mathbf{H}(\omega)\mathbf{X}(w,\omega), \quad (2.13)$$

where $(\cdot)^*$ represents the complex conjugate transpose. In this expression, $\mathbf{H}(\omega)$ is a row vector of the spectral transfer functions $[H_1(\omega),H_2(\omega),\ldots,H_M(\omega)]$ and $\mathbf{X}(w,\omega)$ is the beamformer process (column) vector, which is given by

$$\mathbf{X}(w,\omega) = \begin{bmatrix} w_1\exp(ik_0(\mathbf{p}_1\cdot\boldsymbol{\xi}_l)) \\ \vdots \\ w_M\exp(ik_0(\mathbf{p}_M\cdot\boldsymbol{\xi}_l)) \end{bmatrix}, \quad (2.14)$$

where $k_0 = \omega/c$ is the free-space wave number. Since $\mathbf{H}(\omega)$ is a row vector of length M, the term $\mathbf{H}^*(\omega)A(\omega)\mathbf{H}(\omega)$ is an $M\times M$ matrix representing the relative complex responses of the M hydrophones to the noise source.

The analysis for multiple known structural noise sources follows the analysis for the single noise source. For K discrete (possibly correlated) noise sources, the beamformer output spectrum is given by the Fourier transform of the autocorrelation of the linear superposition of the beamformed responses of the individual noise sources. Thus

$$V_N(\omega) = \int_{-\infty}^{+\infty} E\left[\sum_{k=1}^{K} v_k(t)\sum_{j=1}^{K} v_j(t+\tau)\right]e^{-i\omega\tau}d\tau$$

$$= \sum_{k=1}^{K}\sum_{j=1}^{K}\int_{-\infty}^{+\infty} E[v_k(t)v_j(t+\tau)]e^{-i\omega\tau}d\tau,$$

$$(2.15)$$

where $v_k(t)$ is the time-domain beamformer output for the kth noise source alone. This is equivalent to

$$V_N(\omega) = \mathbf{X}^*(w,\omega)\mathbf{H}^*(\omega)\mathbf{C}(\omega)\mathbf{H}(\omega)\mathbf{X}(w,\omega), \quad (2.16)$$

where $\mathbf{H}(\omega)$ is now the $K\times M$ matrix of transfer functions whose (k, m) component is the transfer function from the kth source to the mth hydrophone, and $\mathbf{C}(\omega)$ is the $K\times K$ matrix of noise source cross correlations such that the (j, k) component of $\mathbf{C}(\omega)$ is given by

$$\mathbf{C}_{jk}(\omega) = \int_{-\infty}^{+\infty} E[\alpha_j(t)\alpha_k(t+\tau)]e^{-i\omega\tau}d\tau, \quad (2.17)$$

where $\alpha_j(t)$ is the time-domain source function for the jth source.

The matrix $\mathbf{M}(\omega)$, given by

$$\mathbf{M}(\omega) = \mathbf{H}^*(\omega)\mathbf{C}(\omega)\mathbf{H}(\omega), \quad (2.18)$$

is seen to be the cross-correlation matrix of sensor responses due to the combination of noise sources. The beamformer output spectrum for the combined noise sources is thus given by

$$V_N(\omega) = \mathbf{X}^*(w,\omega)\mathbf{M}(\omega)\mathbf{X}(w,\omega). \quad (2.19)$$

It is easy to see that this expression reduces to (2.13) in the case of a single noise source, and furthermore, for uncorrelated noise sources, it reduces to

$$V_N(\omega) = \sum_{j=1}^{K} V_N^{(j)}(\omega), \quad (2.20)$$

where $V_N^{(j)}(\omega)$ is the beamformer output power spectrum for the jth noise source.

The beamformer output spectrum due to noise as shown in (2.16) is a Hermitian form in the array weights w_j. To see this, write $\mathbf{X}(w,\omega)$ as

$$\mathbf{X}(w,\omega) = \mathbf{U}(\omega)\mathbf{W}, \quad (2.21)$$

where

$$\mathbf{W} = [w_1,w_2,\ldots,w_M]^T, \quad (2.22)$$

and

$$\mathbf{U}(\omega) = \mathrm{Diag}\{\exp(ik_0(\mathbf{p}_1\cdot\boldsymbol{\xi}_L)),\exp(ik_0(\mathbf{p}_2\cdot\boldsymbol{\xi}_L)),\ldots,$$

$$\exp(ik_0(\mathbf{p}_M\cdot\boldsymbol{\xi}_L))\}. \quad (2.23)$$

Thus, the general form of the beamformer output power spectrum for the response of a hull array to structural noise is given by

$$V_N(\omega) = \mathbf{W}^T\mathbf{U}^*(\omega)\mathbf{M}(\omega)\mathbf{U}(\omega)\mathbf{W}. \quad (2.24)$$

Under the limit of small SNR assumption, the incident acoustic signal excites only the hydrophones, and not the hull, so the signal and noise responses are uncorrelated and expression (2.5) for the deflection coefficient holds. Then, using the noise-only beamformer output spectrum $V_N(\omega)$ given by (2.24) and the signal-only beamformer output spectrum $V_S(\omega)$ given by (2.8) in the expression for the deflection coefficient d, we arrive at

$$d = \frac{\frac{1}{2}\sqrt{T/\pi}\,(\Sigma_{m=1}^{M}w_m)^2}{[\int_{-\infty}^{+\infty} V_N^2(\omega)d\omega]^{1/2}}\int_{-\infty}^{+\infty} S(\omega)d\omega, \quad (2.25)$$

as the deflection coefficient. The conditions of omnidirectional hydrophones and of negligible acoustic hull excitation are easily removed at the expense of a more complicated mathematical model; however, these more general conditions somewhat obscure the insight obtained from this derivation, and are therefore not presented here.

III. PERFORMANCE OPTIMIZATION

To optimize the broadband detection performance of a passive sonar array, we seek to find a weighting coefficient vector $\mathbf{W}$ [given by Eq. (2.22)] that maximizes the deflection coefficient d over the frequency band of interest, the upper limit of which is denoted by frequency B. We assume appropriate bandpass filters are placed to minimize the out-of-band effects. The effect of these filters is to limit the integrals in (2.25) to the interval $[-B,B]$. By inspection, the deflection coefficient d is invariant to the scale of the weight vector $\mathbf{W}$, so we fix $\Sigma w_m = 1$ without loss of generality, thus removing the Σw_m term from expression (2.25) for d.

For a fixed averaging time T and unknown signal $S(\omega)$, the only component of the deflection coefficient that can be optimized at the design stage is the noise-only beamformer output spectrum $V_N(\omega)$. Since the square-root function found in (2.25) is monotonic, it is removed from the optimi-

J. Acoust. Soc. Am., Vol. 112, No. 6, December 2002

Wettergren *et al.*: Numerical hull array design   2737

zation to leave the following objective function which maximizes the deflection coefficient (and hence, the detection performance):

$$J = \int_{-B}^{+B} V_N^2(\omega) d\omega$$

$$= \int_{-B}^{+B} [\mathbf{W}^T \mathbf{U}^*(\omega) \mathbf{M}(\omega) \mathbf{U}(\omega) \mathbf{W}]^2 d\omega. \qquad (3.1)$$

The available design parameters in this optimization are the beamformer weighting coefficients w_m which enter the objective function J through the vector $\mathbf{W}$. The complete mathematical optimization problem is stated as follows:

$$\min_{w_m} \int_{-B}^{+B} V_N^2(\omega) d\omega$$

$$\text{subject to } \sum w_m = 1 \text{ and } w_m \geq 0 \text{ for all } m, \qquad (3.2)$$

where

$$V_N(\omega) = \mathbf{W}^T \mathbf{U}^*(\omega) \mathbf{M}(\omega) \mathbf{U}(\omega) \mathbf{W}, \qquad (3.3)$$

and $\mathbf{W}$ and $\mathbf{U}$ are given by Eqs. (2.22) and (2.23), respectively. Numerical optimization techniques are used to obtain the solution to this optimization problem for each desired look direction $\boldsymbol{\xi}_l$. It is interesting to note that the optimization problem in Eq. (3.2) is equivalent to the adaptive beamforming technique of minimum variance distortionless response (MVDR) in the limit as frequency bandwidth goes to zero.

The objective function (3.1) is the square of a quadratic form of the design parameters $\mathbf{W}$. Locally, this is well approximated by a positive definite quadratic form, so it is expected that sequential quadratic programming (SQP) would be an effective method of numerical optimization. The principle of SQP methods of optimization is to model the optimization problem (objective function plus constraints) by a quadratic subproblem at each step of the optimization process. The solution of the subproblem defines a search direction for the next step of the algorithm. This method has been found by experience to be very effective in a number of application areas, and it is now a standard technique in numerical optimization. SQP methods are known to work well on problems which have smooth nonlinear functions in both the objective and the constraints. The linear constraints in this problem are obviously smooth, and the objective being the integral of a square of a quadratic form is also smooth. Details of the SQP method are found in a number of references, a good survey of the method is in Ref. 6.

Several software packages exist for solving general SQP optimization problems. A discussion of practical numerical issues when implementing SQP methods is found in Ref. 7. For this problem, the package NPSOL[8] from Stanford University's Systems Optimization Laboratory was used, since it performs few evaluations of the objective function, and since each evaluation in our application is a relatively computationally intensive integral over frequency. The performance

of the optimization method is measured by tracking the improvement in the objective function at each step. While local convergence (vs global convergence) is an issue with Newton-type optimization methods such as SQP, this is not an issue for this problem because the optimization problem is convex. That is, the objective function J and the constraint functions are convex functions of the unknown weights, which guarantees that any locally optimal solution is a global optimum. (Moreover, in the examples in Sec. IV, numerous starting points are chosen, and it is observed that all arrived at the same optimum.)

For this implementation, the gradient of the objective function is explicitly evaluated as a subroutine call in the software. For the objective function given in Eq. (3.1), the gradient with respect to the unknowns w_m is given by

$$\nabla J = 2 \int_{-B}^{+B} V_N(\omega) \nabla V_N(\omega) d\omega$$

$$= 2 \int_{-B}^{+B} V_N(\omega)(2\mathbf{U}^*(\omega)\mathbf{M}(\omega)\mathbf{U}(\omega)\mathbf{W}) d\omega$$

$$= 4 \left(\int_{-B}^{+B} V_N(\omega)\mathbf{U}^*(\omega)\mathbf{M}(\omega)\mathbf{U}(\omega) d\omega \right) \mathbf{W}. \qquad (3.4)$$

A useful numerical check on the accuracy of the gradient evaluation is made by verifying the identity

$$\mathbf{W}^T \nabla J = 4J. \qquad (3.5)$$

This identity is checked at each evaluation. All integrals in the numerical evaluations of the objective function and its gradient are computed using the method of overlapping parabolas as discussed in Ref. 9.

IV. NUMERICAL RESULTS

To illustrate the utility of the beamformer shading optimization technique, consider an 11-element line array that is conformal to the exterior of a spherical steel shell as shown in Fig. 1. The array elements are equally spaced and extend across a 60° arc along the sphere. The shell's thickness-to-radius ratio is 0.01. The interior of the shell is assumed to be air-filled, so that the magnitude of acoustic waves propagating within the cavity is negligible in the context of the structural-acoustics problem, and the shell is immersed in an unbounded water medium. For this example, it is assumed that the array elements provide negligible impact on the shell's response to external forcing. Element to element coupling is also assumed negligible. Thus, the array elements measure the structural acoustic response of the spherical shell to whatever forcing is applied, combined with the acoustic response to an incident acoustic wave. The structural acoustic analysis of such a spherical shell responding to both incident acoustic waves and point forces is well-studied, and results can be found in numerous references, such as Junger and Feit.[10]

Assume the array in Fig. 1 is electronically steered to its main response axis (MRA), which is the direction of the south pole. The array straddles the south pole (the negative z direction). The broadband design frequency for the array under consideration is given by $3 \leq ka \leq 10$, where k is the
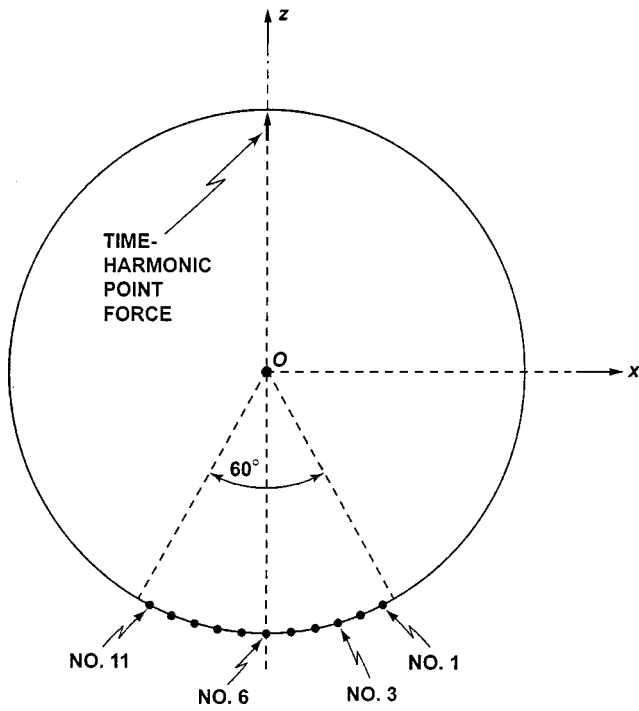
FIG. 1. Array geometry for a spherical shell with conformal 11-element line array.

FIG. 2. Cross correlation of sensor responses to the point force: solid line is for sensor 1 correlated with itself, dotted line is for sensor 1 correlated with sensor 2.

acoustic wave number in the fluid and a is the shell's exterior radius. At the lower end of this frequency band, the array length is given by $3\lambda/2\pi \approx \lambda/2$, so the low end of the band is the lowest frequency that the array can resolve. The upper frequency is below the Nyquist frequency and large enough to provide a broad sensor frequency band (in this case, the bandwidth is greater than 100% of the center frequency).

An external broadband point force is applied at the north pole of the array, as illustrated in Fig. 1. The spectral content of this force is assumed white over the sensor design frequency band. By computing the array element responses to this force over the entire design frequency band (at 2000 evenly spaced frequency samples), the sensor noise cross-correlation matrix $\mathbf{M}(\omega)$, given by Eq. (2.18), is evaluated. The evaluation of the transfer function in (2.18) is performed using expressions from Junger and Feit.[10] The components of this matrix are functions of frequency, and the (1,1) and (1,2) components are shown in Fig. 2. Note that the (1,1) component is the autocorrelation of the response of element 1 to the broadband point noise source, and the (1,2) component is the cross correlation of elements 1 and 2. The large variations in the structural response over this frequency band show that it is sufficiently broadband that single frequency heuristic designs may do little to improve signal detection performance.

Using the analytical sensor noise cross-correlation matrix in the optimization problem (3.2), with $\mathbf{U}(\omega)$ defined by electronic steering of the array geometry of Fig. 1 to its MRA at the south pole, an optimization of the beamformer shading weights is performed. The results of the optimization are shown as case A in Fig. 3. The symmetry of the optimized weights is a result of the problem symmetry; that is, the array geometry, electronic steering, and noise source all share the same symmetry about the array center. The
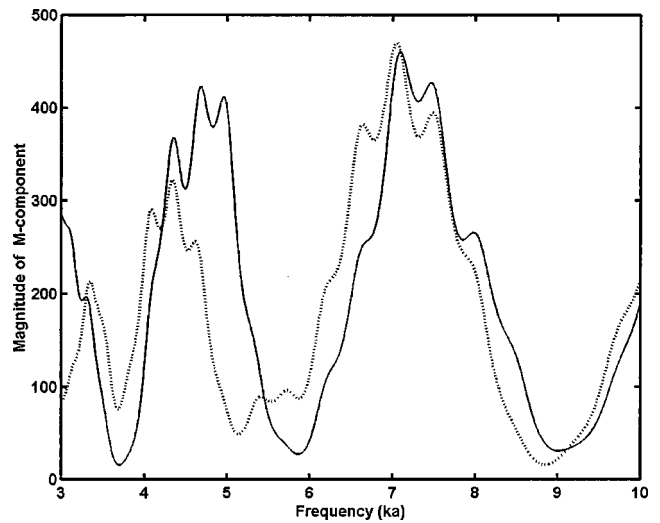
"notch" in the center of the array shadings is caused by a large structural vibration response at the middle element of the array over most of the frequency band, which is expected since that element lies at the antipode of the noise forcing function on the thin spherical shell.

To assess the performance of the optimized shading weights, it is illustrative to look at the improvement in deflection coefficient that is achieved by using optimized shading over some nominal shading. The broadband SNR of the beamformer output is proportional to the deflection coefficient d, with the proportionality constant independent of the shading coefficients (given that the noise model includes all sources of noise). By referencing the iterative design improvements to a nominal shading design, the SNR improvement is shown in a manner that is independent of the signal spectrum $S(\omega)$. The SNR improvement of the optimized shading over a uniform shading is given by
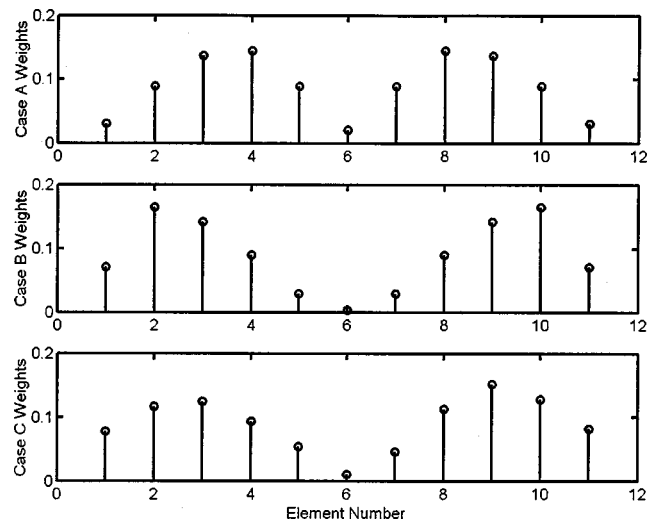
FIG. 3. Optimized weights for 11-element array shown in Fig. 1. Case A is with broadband point noise source steered to MRA. Case B is with broadband equatorial ring noise source steered to MRA. Case C is with broadband point noise source steered to 30° off MRA.

J. Acoust. Soc. Am., Vol. 112, No. 6, December 2002

Wettergren *et al.*: Numerical hull array design 2739
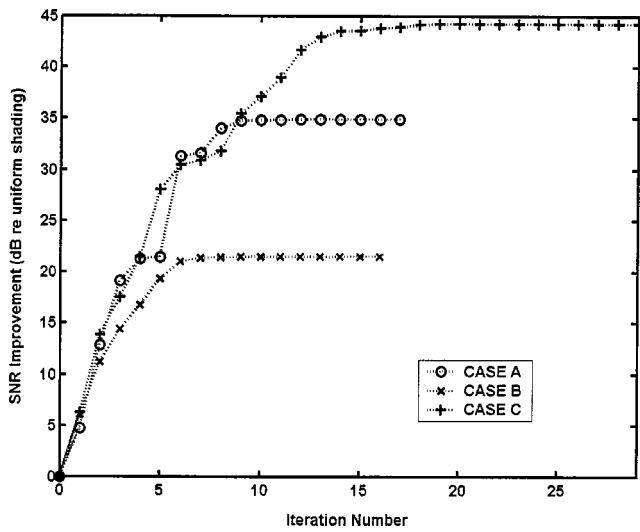
FIG. 4. Convergence of deflection coefficient for optimized results shown in Fig. 3.

FIG. 5. Array geometry for a spherical shell with equatorial ring force.

$$\text{SNR improvement} = \frac{d(\text{optimum weights})}{d(\text{uniform weights})}. \qquad (4.1)$$

For the example of case A, the improvement in SNR of optimal shading weights over uniform shading weights is shown in Fig. 4. In this plot, the improvement in deflection coefficient (relative to uniform shading) is shown as a function of iteration step in the optimization. The improvement starts at 0-dB since the initial condition for the optimization is uniform shading. Numerical experiments were performed with a variety of other initial conditions, but the final optimization results shown are insensitive to the choice of initial condition (as expected because of the problem's convexity).

From Fig. 4, the optimization is seen to converge monotonically, which is expected for a quadratic optimization of a positive definite superquadratic (quartic) objective function. Also note that the convergence is rapid in the early iterations, improving the deflection coefficient by more than 19-dB in just the first three iterations. The surprisingly good results of approximately 35-dB improvement after the convergence of the optimization should be tempered with the realization that the idealized point-driven spherical shell has large resonances that the beamformer shading is able to compensate for by acting as a spatial filter. If the aggregate noise is matched to the noise source model, this improvement translates to 35-dB SNR improvement in detection capability. However, the real situation is mismatched from the single source model in that it has many more components of noise (such as ambient noise, electronics noise, etc.) that combine as in Eq. (2.20) to affect the true deflection coefficient. In practice, it is required that the most dominant of these noise sources be modeled (or measured) and included in the objective function for optimization.

To examine the effect of other types of structural forcing functions, an equatorial ring force was simulated through a series of in-phase broadband point forces distributed along the equator, as shown in Fig. 5. The frequency band of these noise forces was maintained at $3 \leq ka \leq 10$. The resulting optimized shading weights are shown as case B in Fig. 3 and the convergence of the deflection coefficient over the optimization for case B is shown in Fig. 4. A comparison of these weights with those from the point source show that more of the array center is down weighted, which is expected due to the limited number of modes excited by this force relative to a point force. The more complicated forcing also limits the improvement in deflection performance to only approximately 22-dB. This suggests that adding more noise mechanisms to the model will lower the effectiveness of the optimized array. However, there is still considerable improvement over the nominal case (uniform weights), and the convergence is still monotone. For a specified noise source distribution, any implementation of this method will produce results which are at least as good as the starting values.
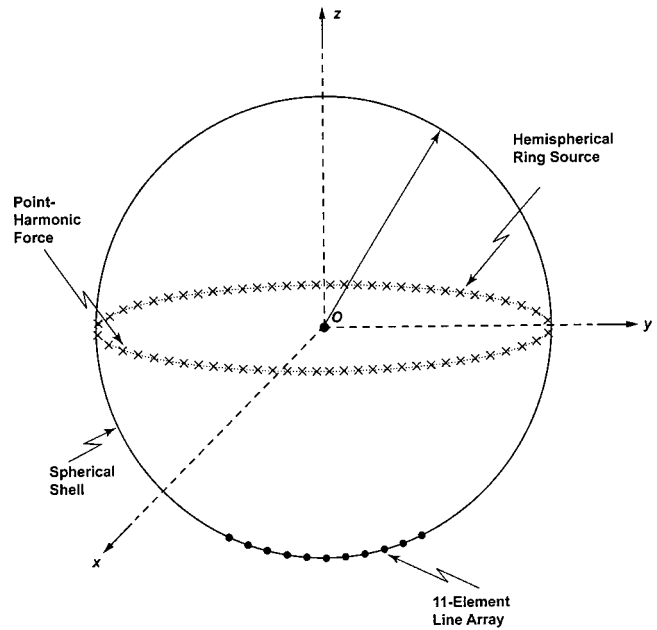
The examples of case A and case B were both steered to the array MRA. As an example of the effects of steering, optimization is performed on an array steered to 30° off of the MRA with the point forcing as shown in Fig. 1. The results of this optimization are shown as case C in Figs. 3 and 4. This example shows a slight asymmetry in the weightings, as is expected for a steered array. The resulting performance gain is very large at approximately 44-dB. This large improvement compared to the previous cases is due to the center element of the array sitting at a nodal center of the vibration modes. The center element has a large noise response over most of the band and must be lowered to minimize noise effects. However, minimizing the center element will negatively impact the acoustic reception performance of an array steered to an MRA at the south pole. When the MRA is steered off the south pole, the reception performance is not as severely degraded because of a low center element weighting; thus, total broadband detection performance (deflection coefficient) improves dramatically.

The cases previously shown all consider the bandwidth of the array to be $3 \leq ka \leq 10$. In Fig. 6, the effect of design
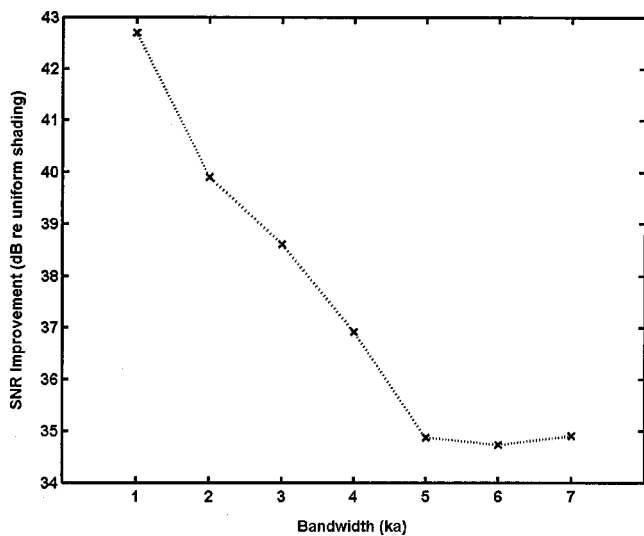
FIG. 6. Optimized deflection coefficient over nominal as a function of bandwidth for the case of the point force with the array steered to MRA.

bandwidth on optimization performance is shown for the case of the point force with the array steered to MRA as the design bandwidth is varied. For this analysis, the frequency range (given by $ka_{min} \leq ka \leq ka_{max}$) is varied with the center frequency held at $ka = 6.5$. As expected, the relative performance improvement due to optimization increases dramatically as the bandwidth is lowered. The performance degradation for increasing bandwidth reaches a plateau near $ka_{max} - ka_{min} = 5$. Above this bandwidth, the additional complexity of the additional modes of vibration is beyond the spatial resolution of the 11-element array.

The results shown are very encouraging for practical problems since the optimization produced (a) a constant set of shading weights that reduces the impact of structural noise over the entire broadband frequency range and (b) also maintains enough signal gain to provide improved detection performance over standard designs. To apply the method to arrays that are conformal to large complex structures, the computation of noise transfer functions over the entire broadband frequency range (at as many finely resolved frequency steps as necessary) must be performed. Numerical approaches to efficiently compute these broad frequency sweeps are currently under investigation.

For computational time, the entire 16 iterations of the broadband array shading optimization shown as case A took less than 10 s to run on a 300-MHz workstation. Other cases had similar timing performance. This computation timing assumes that the data matrix $\mathbf{M}(\omega)$ was computed *a priori* and stored as a large text file to be read in at run time. In practical situations, this is accomplished by either running models of all noise sources over the entire band of interest prior to optimization or taking noise data of an actual array and computing $\mathbf{M}(\omega)$ as an average of the measured noise field.

The question of robustness of the numerical optimization with respect to noise uncertainty is not addressed here. The use of a broadband objective function is employed in an attempt to minimize the impact of noise variations on the objective function (3.1). Given the availability of a noise variation model, the extent of the optimal solution's robustness can be measured by forming the Hessian of the objective function (3.1). Such an analysis is a subject of future interest.

V. CONCLUSION

A numerical optimization method is used to optimize passive broadband detection performance of hull arrays through the adjustment of array shading weights. The method is applied to simple examples of a spherical shell with a conformal line array under structural noise. The method shows gains in performance of greater than 20-dB over unity shading for simple noise sources. Convergence of the optimization technique is rapid and guaranteed. The method uses the conventional beamformer framework and optimizes the available design parameters (shading weights). This approach is applicable to any broadband hull array design where problematic noise is known through either measurements or models. Since the approach is to optimize at the design stage, the optimal shading weights obtained can be tabulated for each steering angle in a look-up table in the array beamformer software. Further investigations of the performance of this method with varying types of noise sources (ambient, structural, electronic, etc.) as well as studies of the robustness of the method are planned in the future. While the example shown in this paper is shading weight adjustment, the design concept can be applied to other design parameters of the array such as element position, material selection, etc.

ACKNOWLEDGMENTS

[1] C. L. Dolph, "A current distribution for broadside arrays which optimizes the relationship between beam width and sidelobe level," Proc. IRE **34**, 335–348 (1946).

[2] T. T. Taylor, "Design of line-source antennas for narrow beamwidth and low side lobes," IRE Trans. Antennas Propag. **AP-1**, 17–20 (1955).

[3] B. D. Van Veen and K. M. Buckley, "Beamforming: A versatile approach to spatial filtering," IEEE ASSP Mag. **5**, 4–24 (1988).

[4] J. P. Casey, and D. Wu, "Numerical acoustic hull array optimization," NUWC-NPT Technical Report 11239, Naval Undersea Warfare Center Division, Newport, RI (2000).

[5] H. L. Van Trees, *Detection, Estimation, and Modulation Theory* (Wiley, New York, 1968), Part I, Chap. 2.

[6] P. T. Boggs and J. W. Tolle, "Sequential quadratic programming," Acta Numerica **4**, 1–51 (1996).

[7] J. Nocedal and S. J. Wright, *Numerical Optimization* (Springer, New York, 1999), Chap. 18.

[8] P. E. Gill, W. Murray, M. A. Saunders, and M. H. Wright, "User's guide for NPSOL 5.0: A FORTRAN package for nonlinear programming," Report SOL 86-1, Dept. of Operations Research, Stanford University (1998), available online at ⟨http://www.stanford.edu/group/SOL⟩.

[9] P. J. Davis and P. Rabinowitz, *Methods of Numerical Integration* (Academic, New York, 1975), Sec. 2.3.

[10] M. C. Junger and D. Feit, *Sound, Structures, and Their Interaction* (MIT Press, Cambridge, MA, 1986), Secs. 7.17–7.19.

A high frequency amplitude-steered array for real-time volumetric imaging

Catherine H. Frazier[a)]
Bioacoustics Research Laboratory, Department of Electrical and Computer Engineering, University of Illinois at Urbana-Champaign, Urbana, Illinois 61801

W. Jack Hughes[b)]
Applied Research Laboratory, The Pennsylvania State University, P.O. Box 30, State College, Pennsylvania 16801

William D. O'Brien, Jr.[c)]
Bioacoustics Research Laboratory, Department of Electrical and Computer Engineering, University of Illinois at Urbana-Champaign, Urbana, Illinois 61801

Real-time three-dimensional acoustic imaging is difficult in water or tissue because of the slow speed of sound in these media. Conventional pulse–echo data collection, which uses at least one transmit pulse per line in the image, does not allow for the real-time update of a volume of data at practical ranges. Recently, a linear amplitude-steered array was presented that allows the collection of a plane of data with a single transmit pulse by spatially separating frequencies in the lateral direction. Later, by using a linear array with frequency separation in the vertical direction and rotating the array in the horizontal direction, volumetric data were collected with a small number of transmit pulses. By expanding the linear array to a two-dimensional array, data can now be collected for volumetric imaging in real time. In this study, the amplitude-steered array at the heart of a real-time volumetric sonar imaging system is described, giving the design of the array and describing how data are collected and processed to form images. An analysis of lateral resolution in the vertical and horizontal directions shows that resolution is improved in the direction of frequency separation over systems that use a broad transmit beam. Images from simulated data are presented. © *2002 Acoustical Society of America.* [DOI: 10.1121/1.1518699]

PACS numbers: 43.30.Yj, 43.30.Wi [DLB]

I. INTRODUCTION

The concept of steering the maximum response of an array using amplitude weighting was introduced by Hughes and Thompson in 1976.[1] At that time, the intent of amplitude steering was to steer the maximum response of the beam patterns without using phase-shift networks or multiple delay lines. Initially, amplitude weighting was applied with an electronic gain.[2] When large-area transducer material became available, shaped hydrophones were developed where shading for low sidelobes was achieved geometrically.[3,4] It was realized that in addition to the low sidelobes, geometrical amplitude steering could also be used to form a set of steered beams. In the original concept, the beam was steered to a particular direction at a single frequency, and the fact that the steering direction changed with frequency was considered a drawback of the design. With the availability of broadband large-area 1–3 composite material, a transducer array was built which could form multiple beams at multiple frequencies.[5] The imaging concept was introduced when it was realized that a single FM pulse could be used to sweep the maximum response axis over a range of steering angles. A plane of data is created from a single receive signal using a short-time Fourier transform (STFT) where the frequencies contained within the window give the azimuth of the targets and the temporal position of the STFT window gives the range of the targets. Three-dimensional acoustic imaging is an extension, where beams in the orthogonal plane are obtained by mechanical or time-delay steering. The potential advantages of using the amplitude weighting for steering and imaging are greatly reduced size of the electronics and high frame rate volumetric imaging.

Volumetric acoustic imaging has received attention recently for both sonar and medical applications because it allows better visualization of structures or anatomy than a series of two-dimensional slice images. Real-time volumetric imaging, meaning updating the volume of data at a rate of at least 30 Hz, is even more valuable. In sonar, volumetric imaging is most often considered for short-range applications (less than 10 meters) such as fish counting, assisting divers, monitoring remotely operated vehicles, or mine hunting. Real-time three-dimensional imaging could provide the visibility required for a diver to locate objects such as damaged pipes in turbid water. In medical imaging, three-dimensional images could provide information on the shape of a solid mass, one of the parameters used to distinguish between benign and malignant tumors. Real-time three-dimensional im-

---

[a)]Electronic mail: hillsley@brl.uiuc.edu. Current address: Johns Hopkins University Applied Physics Laboratory, 11100 Johns Hopkins Road, Laurel, MD 20723.
[b)]Electronic mail: wjh2@psu.edu
[c)]Electronic mail: wdo@uiuc.edu

aging would allow a physician to view the structures of the heart throughout the cardiac cycle.

Data collection for a three-dimensional image using techniques of two-dimensional imaging requires too much time for volumes to be scanned in real time. Although the speed of sound is similar for sonar and medical applications, the maximum ranges of interest are very different. Collecting data for a two-dimensional medical image with a maximum range of 20 cm requires 25 ms, where the speed of sound is assumed to be 1540 m/s and where 128 pulses are used to create 128 lines in the image. A three-dimensional image formed with 128^2 pulses under the same conditions requires 3.19 seconds. Real-time three-dimensional imaging using conventional data collection techniques would be impossible. For sonar imaging, with a maximum range of 5 m and a speed of sound of 1500 m/s, transmitting and receiving a single pulse requires 6.7 ms. No more than 5 pulses could be used to scan the volume in real time.

A solution to this problem is to form several receive beams for one transmitted pulse and to separate reflections from different directions through processing. Several other groups have worked on developing such techniques in both sonar and medicine. Sonar systems were discussed in Ref. 5. Three-dimensional medical ultrasound exists; however, with one exception, it is not real time. Currently available systems typically scan two-dimensional planes using linear arrays and then translate or rotate the array to scan the next plane. Three-dimensional images are then formed off-line.[6] For cardiac imaging, where real-time data collection is most critical, data are often collected over several heart beats, and then the data from different cycles are combined so that a single heart cycle can be recreated as a cineloop. Successive heart beats must be similar enough for the reconstruction. In many cases, irregular heart beats are thrown out,[7,8] making it impossible to use these systems to diagnose a heart abnormality.

Researchers from Duke University have a real-time volumetric imaging system, which is in operation.[9] Their system uses a sparse, two-dimensional array. As reported in 1991, the volume is scanned in a pyramidal scheme, with 12 transmit pulses in the elevation direction and 52 transmit pulses in the azimuthal direction, for a total of 624 transmit pulses per volume. Parallel beamforming is used in the elevation direction so that eight receive beams are formed for each transmit pulse. The volume can be scanned eight times per second. Initial image quality was poor. To improve the image quality, they have been working on improving the two-dimensional array, increasing channel count and frequency. Their method is unsuitable for sonar because of the large number of transmitted pulses used.

Lu[10] has proposed a technique for three-dimensional imaging using limited diffraction beams. A plane-wave pulse is transmitted from the two-dimensional array to illuminate the scene. In reception the same transducer array is used to form an array of limited diffraction beams by weighting the elements of the array. A complete data set is formed by varying the element weighting. Using a three-dimensional inverse Fourier transform, a three-dimensional image is created. This technique requires a fairly large, broadband array. The largest cross-sectional area that can be imaged without greatly reducing the speed of data collection is equal to the area of the array. The method has been tested using a phantom with embedded point scatterers.[11] The results look promising, although the images reveal the dependence of the technique on the broad bandwidth of the transducer.

Shen and Ebbini[12] have worked on coded excitation in combination with a pseudoinverse operator so that multiple beams from different steering directions can be received at one time. Independent codes are transmitted on each element, resulting in different impulse responses in each steering direction. Returns from different directions are then separated using pseudoinverse filters. The number of beams that can be formed simultaneously depends on the number of filters in the filter bank. Previous images formed using coded-excitation methods with matched filter operators have suffered because correlations between beams in different directions produce artifacts in the images. Shen and Ebbini's technique is reported not to have this drawback; however, the pseudoinverse operator suffers from consequences of the assumption that targets occur on a grid pattern. If target positions differ from the grid pattern, the image quality is degraded.

We are interested in a real-time sonar system with high resolution. Our current application is a diver-held sonar system intended for real-time detection and identification of submerged mines. We expect the mines to be metallic or plastic targets suspended in water or sitting on the soft bottom of the water body, with characteristic dimension of 50 cm and features on the order of 1 cm. The goal is to image a volume from 3 to 5 meters in front of the array, with a resolution voxel of 1 cm. The imaged volume is 20° wide in the vertical direction and 30° wide in the horizontal direction. The resolution requirement leads to the choice of 1 to 5 MHz as the desired operating frequency range. Current volumetric sonar systems have low resolution due to the broad transmit beam. As discussed above, medical systems use too many transmit pulses to be adapted for sonar, or they have other drawbacks. Our solution is to extend the amplitude-steered array for real-time volumetric sonar imaging. Our system could also work for medical imaging; however, in that case we might make different choices for operating frequency and array dimensions.

In Ref. 5, the linear amplitude-steered array was used for volumetric imaging by rotating the array. A plane of data was collected with each transmit pulse. However, the rate of data collection can be increased by using a transmit beam that is narrow and steered in the vertical direction and broad in the horizontal direction.

In order to image a volume of interest with a single transmit pulse, the received signal must contain information to give vertical, horizontal, and range position of the target. The linear-phased amplitude-steered array uses frequency separation to determine vertical position and conventional beamforming to determine horizontal location. The range of the target is obtained from the time elapsed until the reflected signal is received. The vertical position information is determined by the frequency of the returned signal. The horizontal position of the target is found by using conventional, linear

phased array processing of the signals from the *staves* or columns of elements.

In Sec. II, we describe the new array layout for achieving amplitude steering, which results in lower peak sidelobe levels than the previous design. In Sec. III, we discuss the procedure for data collection and the algorithms for image formation including time–frequency processing beyond the STFT. In Sec. IV, we describe simulations and show resulting images. In addition, we compare resolution results in the vertical and horizontal lateral directions. Section V discusses the relationship between the amplitude-steered array and Lu's imaging with nondiffracting beams. Finally, we give a conclusion.

II. ARRAY LAYOUT AND BEAM PATTERN

Amplitude steering has been described in detail previously (see Ref. 1), so we limit this discussion to changes in the array design. Amplitude steering in the vertical direction is achieved by applying weights to each row. [The weights are $\cos\{(2n-1)\phi\}$, $\sin\{(2n-1)\phi\}$, where n is the row number, $\phi = (k_0 d/2)\sin\theta_0$, k_0 is the wave number at the design frequency, d is the row spacing, and θ_0 is the design steered angle.] Weights are applied geometrically, not by scaling the signals, but by grouping elements together. Earlier versions of the amplitude-steered array assigned elements to sine and cosine regions by trying to match regions that would be created for a shaped PVDF transducer. This array layout produced undesirable peak sidelobe levels. For the linear-phased amplitude-steered array, weighting is still applied by dividing the available area into regions; however, now the division is done on a row-by-row basis. The sine and cosine weightings are implemented by selecting the number of elements in each row that are connected together as sine or cosine elements. The signals from the sine elements must pass through an additional 90° phase shift before summing.

Each active element of a row must be assigned to the cosine or sine group such that the proper $\cos((2n-1)\phi)$ and $\sin((2n-1)\phi)$ row weightings are maintained. The numbers of each type of element in a row are determined by the equations

$$N_C(n) = \frac{N_n^{\max}}{1.414}\left|\cos\left((2n-1)\frac{k_0 d}{2}\sin\theta_0\right)\right|, \qquad (1)$$

$$N_S(n) = \frac{N_n^{\max}}{1.414}\left|\sin\left((2n-1)\frac{k_0 d}{2}\sin\theta_0\right)\right|, \qquad (2)$$

where N_C is the number of cosine elements, N_S is the number of sine elements, $N_n^{\max}$ is the maximum number of elements in the nth row, d is the spacing between the rows, k_0 is the design wave number, and θ_0 is the design steering angle in the vertical direction. For a rectangular array, $N_n^{\max}$ would be a constant for all n. For our array, which has a circular aperture, $N_n^{\max}$ depends on the row number. The $\cos((2n-1)\phi)$ and $\sin((2n-1)\phi)$ terms may represent positive or negative values. Thus, there are four element assignments: positive and negative cosine, and positive and negative sine. In each row, there are either positive cosine or negative cosine elements, not both. Also, there are either positive sine or

negative sine elements, not both. We refer to elements by their group, e.g., cosine elements or sine elements.

The optimal beam pattern is that of an electronically steered array of the same size. The electronic phase gives each element both a cosine weight and a sine weight. For the amplitude-steered array, each element can contribute to either the cosine or the sine weighting, but not to both; therefore, we are essentially designing two sparse arrays, one cosine and one sine array.

An alternating element design, in which elements of the cosine and sine groups are alternated until $2 \times \min(N_C, N_S)$ is reached, leads to high grating lobes in the horizontal direction at positions corresponding to an interelement spacing of $2d$. The positioning of the elements within the row was made random to avoid grating lobes. Patterns of random sparse arrays are characterized by a sidelobe pedestal level. The average sidelobe level of the intensity pattern is approximately N^{-1}, where N is the number of elements in the array.[13,14] Steinberg analyzed and compared the peak sidelobe level of sparse arrays designed using algorithmically aperiodic arrays and random placement of elements. He found that both produced the same mean peak sidelobe level, but that the variance of the random arrays was much smaller than that of algorithmically designed arrays, when all algorithmically designed arrays were compared as a group regardless of design method.

The random design was implemented as follows. Each element of the array was given a probability of being a cosine element and a probability of being a sine element, where the probabilities depended on the row of the array. The sum of these probabilities does not equal 1 for every row; therefore, it is also possible for the element to be nulled, or not used, in order to keep the proper relative row weighting for steering. A random number generator was used to assign element type. Figure 1 shows the array layout used for the simulations. Part (b) of the figure gives an expanded view of the region indicated by the white box in part (a). In the figure, there are five gray-scale levels for the four element assignments and the null elements. In each row there is a maximum of three gray-scale levels: one cosine, one sine, and one for the null elements. Figure 2 shows the beam pattern produced. The random array design produced a beam pattern whose main lobe has the same width as the main lobe of the full array, and the random array has no grating lobes or large sidelobes. The predicted average sidelobe level using Steinberg's expression is −51.12 dB. The average sidelobe level in the figure is approximately −44 dB. The peak sidelobe level is only 2.3 dB above the mean.

One potential advantage of using this array for volumetric imaging is the reduced electronics requirement compared to proposed array systems that must address each element individually. For the amplitude-steered array, a separate channel is not required for each element. Only four channels are required per stave. One channel is assigned for each element type: positive cosine, negative cosine, positive sine, and negative sine. The number of wires that must connect the array elements to the processor is also reduced, thereby reducing the required cable size.
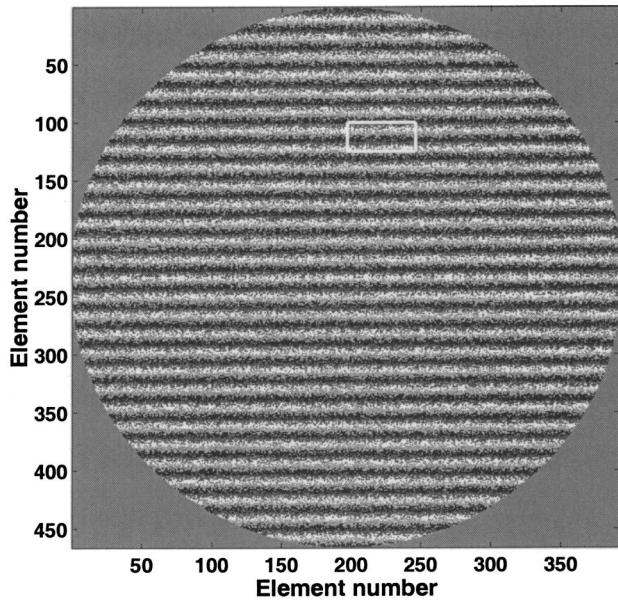
(a)
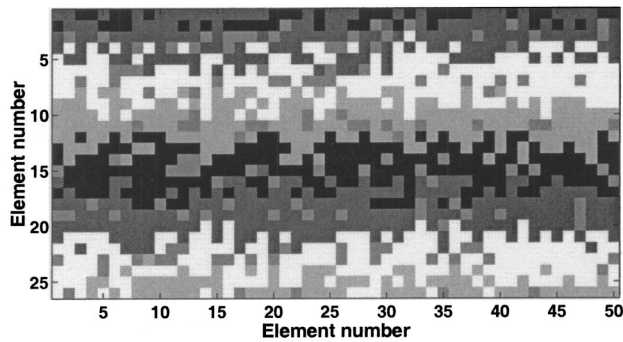
(b)

FIG. 1. (a) Array layout for 2D array with random placement of the four element phases. Four gray-scale levels represent the four phases of elements: white, cosine; black, negative cosine; light gray, sine; dark gray, negative sine. (b) Zoom of (a) to show detail. Isolated gray squares within more continuous regions indicate null elements.

III. DATA COLLECTION AND IMAGE FORMATION

Real-time data collection with the linear-phased amplitude-steered array is accomplished as follows. A linear FM chirp pulse is transmitted from the center two staves, which means that at a given frequency, the transmitted beam is wide in the horizontal direction and narrow in the vertical direction. The narrow beam in the vertical direction results in better resolution than current sonar systems that use a broad transmit beam in all directions. Frequencies are separated in the vertical direction with high frequencies steered deeper than low frequencies.

The reflected signal is received by the whole array. Signals from individual staves are digitized separately and are stored for further processing. Following the data collection, forming the complete three-dimensional data set consists of two steps. First, the signals from individual staves must be processed to give horizontal position information. Second, time–frequency processing is performed on signals corre-
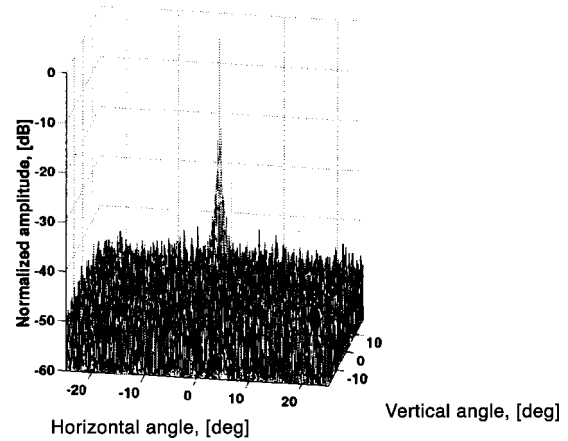
FIG. 2. Field pattern for array with random placement of elements.

sponding to each horizontal steering direction to give vertical position and range information.

A. Horizontal position information

The raw signals from individual staves are processed to give horizontal position information. The focusing delays do not change with horizontal steering direction, so they are applied first. The output from the array, with focusing delays applied, is a two-dimensional matrix with stave number along one direction and time sample number along the other. Then beam steering is accomplished using the Radon transform. The discrete Radon transform sums through a matrix at different angles, resulting in beams steered to several directions.[15]

Once the Radon transformation is complete, the two-dimensional data matrix contains one time signal for each horizontal steering direction. For a complete set of volumetric data, we then apply time–frequency processing to the time signal from each horizontal steering direction.

B. Time–frequency processing

Range and vertical position information are determined using time–frequency processing. Time resolution corresponds to range resolution and frequency resolution corresponds to vertical resolution for our application. Time–frequency processing has been used to identify targets in sonar signals based on characteristics of the received signals,[16,17] but has not been used to form an image of targets until Ref. 5.

We limit ourselves to Cohen's class of time–frequency distributions whose kernels are independent of the signal. Cohen's class of distributions is bilinear in the signal, and therefore is characterized by oscillating cross terms.[18] In this study, we implement two members of Cohen's class: the spectrogram, which is the magnitude squared of the short-time Fourier transform, and the smoothed pseudo-Wigner distribution (SPWD). The spectrogram is the most likely to be implemented for early arrays; however, with the spectrogram, there is a trade-off in time- and frequency resolution that depends on the length of the filter used. In an earlier study, an analysis of resolution using different time–frequency distributions to form images of point targets with the linear array showed that the SPWD gave the best overall results in terms of cross-term level and resolution in the

time- and frequency directions.[19] Of the distributions considered in that study, the SPWD had the most parameters available for optimization, allowing independent smoothing in the time- and frequency directions.

For the current study, parameters such as the filter lengths and shapes were determined by forming images of point targets and optimizing those images for visual appearance. The final window for the spectrogram was chosen to be a Hanning window with a length of 1024 samples or 50 μs. For the SPWD, the filters used for smoothing in the time and frequency directions were Gaussian windows, described by the expression $\exp(-t^2/\alpha^2 - \omega^2/\beta^2)$, where α is 3.4 μs and β is 125.7×10^3 rad/s.

The result of time-frequency processing is a three-dimensional data set, where for each horizontal steering direction, vertical position and range have been obtained.

C. Resolution

The image resolution is dependent not only on the size of the array, but also on the processing used to form the images.[20] First, we describe the resolution that is achievable by the array, without considering the processing. Then, we will consider the resolution obtained when using the spectrogram or SPWD. Range resolution will be given in millimeters. It is dependent on the bandwidth of the received signal and the size of the array, as in the case of the linear amplitude-steered array. Vertical and horizontal resolutions are measured in degrees. In the vertical direction, the lateral resolution is very much like that of the linear amplitude-steered array, which is described in Ref. 20. The resolution will get worse as the vertical angle increases because the high frequencies are steered downward. In the horizontal direction, the resolution is similar to that of an electronically phased array.

The theoretical description of resolution is complicated by the multiple frequencies and multiple foci in the horizontal direction. For the lowest frequencies used, the volume of interest is in the far field; therefore, focusing will not be effective. Horizontal resolution could be estimated by determining the far-field beam spread of the array. For the highest frequencies, the region of interest is in the near field. Six different focal regions are used. A theoretical value for horizontal resolution can be determined at the location of the foci. At other locations, the diffraction-limited spreading must be taken into account. Vertical resolution depends on the frequency separation. Resolution is investigated through simulations because of the many different cases within our volume of interest.

IV. SIMULATIONS AND RESULTS

The operation of the linear-phased amplitude-steered array for imaging and the results of projection images are demonstrated through simulation.

A. Processing

Data collection with the random two-dimensional amplitude-steered array is simulated using the FIELD II program by Jensen.[21,22] A block diagram of the simulations is
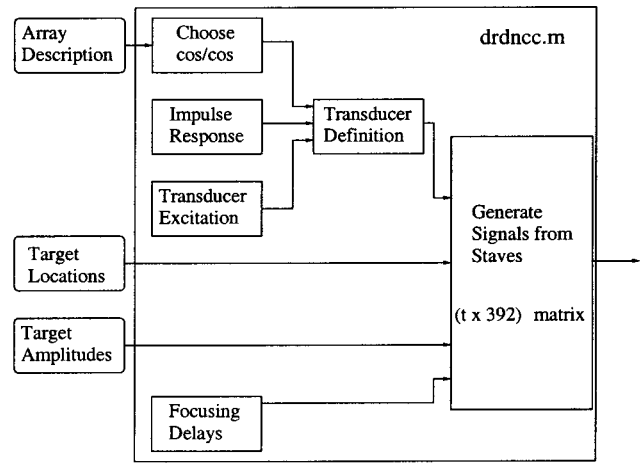
(a)
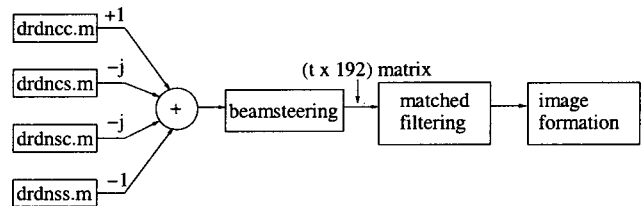
(b)

FIG. 3. Block diagram of simulation. The variable t in the matrix sizes indicates the number of time samples received, which depends on the distance between the closest and farthest point targets and the sampling rate.

shown in Fig. 3. Data collection was simulated in four parts: cosine elements transmitting, cosine elements receiving; cosine elements transmitting, sine elements receiving; sine elements transmitting, cosine elements receiving; and sine elements transmitting, sine elements receiving.

Part (a) of Fig. 3 shows the diagram for one of the four parts. The array description, frequency response of the transducer, point target locations, and point target amplitudes were generated separately and stored as MATLAB files for input into the simulation program. Within the simulation program, the transducer characteristics such as stave and row spacing were defined and focusing delays were calculated.

The simulated transducer was an array with an approximately circular aperture. The diameter was 10 cm, with a row spacing of 215.9 μm and a stave spacing of 254 μm. The simulated transducer impulse response was given by Fig. 4. The center frequency of the response was 4.74 MHz, calculated as $(f^+_{-3 \text{ dB}} - f^-_{-3 \text{ dB}})/2$, and the relative bandwidth was 82.5%. The lowest frequencies transmitted are below the -3-dB bandwidth; however, higher frequencies suffer greater attenuation. The transmitted signal was a linear FM chirp with frequency swept from 1 to 5 MHz, corresponding to steering angles of 24° to 5°. Simulating the actual data collection, a linear FM chirp was transmitted by the center two staves of the array.

The FIELD II program assumes a linear frequency dependence of attenuation, which is an appropriate assumption for tissue but not for water. In order to include attenuation in the

Frazier *et al.*: HF amplitude-steered array for volumetric imaging

(a)

(b)

FIG. 4. Simulated transducer impulse response. The transducer has a center frequency of 4.74 MHz and an 82.5% bandwidth.

FIELD II was used to generate the received output voltage signal for each stave. The reflected signals were received by each of the elements in a stave, and the sum of the signals from elements in the same stave was calculated using the appropriate phase shift to simulate a lossless lens focused at 4 m in the vertical direction. The stave signals were stored in a matrix with stave number along one direction and time sample in the other direction. Before storing the time signal from a stave as one column of the matrix, appropriate time delays were implemented for focusing in the horizontal direction. Six depths of focus were used. They were 3.0, 3.3, 3.65, 4.0, 4.6, and 5.2 m.

Figure 3(b) shows how the four parts were combined to form an image. The $-j$ and -1 terms indicate phase shifts between the parts. Considering the array operating in receive mode, signals received on the sine channel must be phase shifted by $\pm 90°$ before combining them with signals received on the cosine channel in order to obtain the correctly steered beam. An identical phase shift is required on transmit. Therefore, a signal transmitted on the sine channel and received on the cosine channel requires a $\pm 90°$ phase shift. A signal transmitted on the cosine channel and received by the sine channel also requires a $\pm 90°$ phase shift. The sign of the 90° phase shift determines whether the beam is steered above or below broadside. A signal transmitted and received on the sine channel requires a 180° phase shift to be combined with the signal transmitted and received on the cosine channel.

B. Resolution analysis

Resolution analysis is performed by placing one simulated point target in the field at a time, and measuring the extent of the point spread function. Point targets were placed at 0° or 15° horizontally. Vertical positions ranged from 5° to 24° at 1-deg intervals. Range positions ranged from 3 to 5 m at 10-cm intervals. Range resolution is found using the time signal after the Radon transform for the correct horizontal steering direction. Envelope detection is performed using the Hilbert transform. Then, the envelope is log compressed and the points 6 dB below the maximum are found. The time difference between these points is then converted to distance using the speed of sound. Vertical resolution is found by first calculating the magnitude squared of the FFT of the entire received signal. Those data are then log compressed and the frequency values 6 dB below the maximum are found. That frequency information is then converted to angular information using[20]

$$\theta = \sin^{-1}\left(\frac{f_0 \sin \theta_0}{f}\right), \qquad (4)$$

where θ is the steering direction for frequency f, θ_0 is the design steering angle, and f_0 is the design frequency. Finally, horizontal resolution is found by calculating the Radon transform for a range of angles around the target's actual angular position. This calculation forms part of an image in the horizontal angle/range plane. The horizontal resolution is the lateral extent of the point spread function measured by -6-dB points.

simulation, the target strengths were modified according to their range and vertical position, where vertical position determines the center frequency of the signal that will insonify the point. Attenuation was calculated using the equation for the plane-wave amplitude attenuation coefficient given by Tolstoy and Clay[23]

$$\alpha = \left(\frac{2.34 \times 10^{-6} S f_T f^2}{f_T^2 + f^2} + \frac{3.38 \times 10^{-6} f^2}{f_T}\right)$$
$$\times (1 - 6.54 \times 10^{-4} P), \qquad (3)$$

where α is the attenuation coefficient in Np/m, $S = 30$ is the salinity, given in parts per thousand, $P = 1$ is the pressure in atm, $T = 15°$ is the temperature in °C, $f_T = 21.9 \times 10^{6 - 1520/(T + 273)} = 115.52$ is a frequency parameter given in kHz, and f is the operating frequency in kHz. Point target amplitudes were reduced according to the round-trip attenuation to that point. The target was placed at 4 m, centered at 0° horizontally and 10° vertically.

TABLE I. Horizontal resolution in degrees.

Vertical angle (deg)	Range (m)				
	3	3.5	4	4.5	5
5	0.239	0.237	0.231	0.237	0.238
7	0.332	0.335	0.329	0.322	0.316
9	0.429	0.432	0.427	0.419	0.407
11	0.525	0.527	0.521	0.465	0.457
13	0.619	0.575	0.570	0.565	0.559
15	0.710	0.710	0.704	0.700	0.694
17	0.810	0.811	0.806	0.802	0.799
19	0.907	0.911	0.907	0.902	0.900
21	0.983	0.981	0.974	0.970	0.966
23	1.082	1.081	1.079	1.078	1.076

TABLE III. Range resolution in mm.

Vertical angle (deg)	Range (m)				
	3	3.5	4	4.5	5
5	4.76	5.42	3.52	3.52	3.66
7	6.34	7.03	7.62	8.13	8.31
9	8.09	8.75	9.38	9.78	10.1
11	9.96	10.5	11.1	11.6	11.9
13	12.0	12.5	13.0	13.5	13.8
15	13.0	13.5	14.2	14.6	15.1
17	15.5	15.9	16.3	16.7	17.0
19	16.8	17.4	17.9	18.3	18.7
21	18.8	19.2	19.5	19.9	20.1
23	20.3	20.9	21.1	21.5	21.8

Tables showing the results for horizontal, vertical, and range resolution for targets at 0° horizontally are given in Tables I, II, and III, respectively. Horizontal resolution stays fairly constant in range due to the multiple foci. Horizontal resolution degrades as vertical steering angle increases because lower frequencies are steered to larger angles. Vertical resolution degrades with range because only one focal zone is used. Vertical resolution degrades with increasing steering angle due to the change in frequency. Range resolution degrades slightly as range increases and it degrades as steering angle increases because of the change in frequency.

At very high frequencies (small steering angles), vertical resolution is better than horizontal resolution at closer ranges, but comparable to horizontal resolution at far ranges, because there is only one focus in the vertical direction. At low frequencies, vertical resolution is fairly stable because targets are in the far field, and therefore, focusing does not have any effect. Also, for low frequencies vertical resolution is better than horizontal resolution because of the transmit–receive combination. The transmit beam pattern is wide in the horizontal direction, but narrow in the vertical direction. The main lobe of the receive beam pattern is narrow both in the horizontal and vertical directions. The comparison between vertical and horizontal resolution shows one of the advantages of the amplitude-steered array over a system that uses a broad transmit and a conventional phased array to receive. Better resolution in the vertical direction than in the horizontal direction is a result of having a narrow transmit

beam in the vertical direction for each frequency.

Resolutions are also measured for data following time–frequency processing. In this case, only range and vertical resolutions are measured. The Radon transform is calculated for the appropriate steering angle, then two-dimensional images are formed using either the spectrogram or the SPWD. The comparison is thus made for slice images at one horizontal steering direction rather than for projections through the horizontal steering direction. Resolutions are measured from the image as the −6-dB range and vertical extent of the pulse spread function.

Plots showing the comparisons of range and vertical resolutions for the case of no time–frequency processing or processing with the spectrogram and SPWD are given in Fig. 5. Part (a) shows the range resolutions for the three cases. The solid line respresents the results for no processing, and should be the lowest line for all angles. However, the dotted line, representing the results for the SPWD, dips below the solid line. The SPWD can produce resolution very close to the limit of no processing, but it cannot do better. Part (b) shows the results for the vertical resolution. Again, the SPWD resolution approaches that of no processing.

For both range and vertical resolution, the spectrogram results are not as good as the others. We could improve one at the expense of the other by changing the window length. For comparison, in (b), the dashed-dotted line shows the horizontal resolution measured with no processing. It is worse than the resolution in the vertical direction because the transmit beam in the horizontal direction is broad.

C. Simulated target

To demonstrate the array operation, projection images were produced by simulating data collection from a more complicated target. The target used for these simulations was designed to include some features of a mine, including representations of bolts and a slanted face. A diagram of the target with dimensions is shown in Fig. 6. The bolts are approximately 2 cm across and raised 1 cm above the planar surface of the mine to test the resolution limits. The slanted face is intended to provide information about depth resolution. The original computer model of this target was created at the Applied Research Laboratory at the Pennsylvania State University using AUTOCAD. In this study, we use the model by assuming the node positions of AUTOCAD were point tar-

TABLE II. Vertical resolution in degrees.

Vertical angle (deg)	Range (m)				
	3	3.5	4	4.5	5
5	0.151	0.178	0.310	0.260	0.213
7	0.221	0.231	0.244	0.275	0.340
9	0.283	0.292	0.301	0.317	0.333
11	0.338	0.344	0.356	0.363	0.373
13	0.403	0.407	0.413	0.418	0.426
15	0.521	0.526	0.537	0.547	0.555
17	0.547	0.549	0.556	0.561	0.563
19	0.643	0.648	0.653	0.658	0.664
21	0.688	0.701	0.698	0.706	0.710
23	0.766	0.773	0.778	0.780	0.788
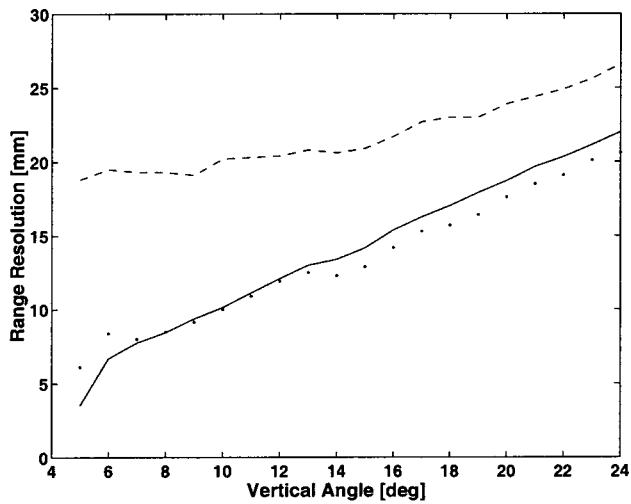
(a)
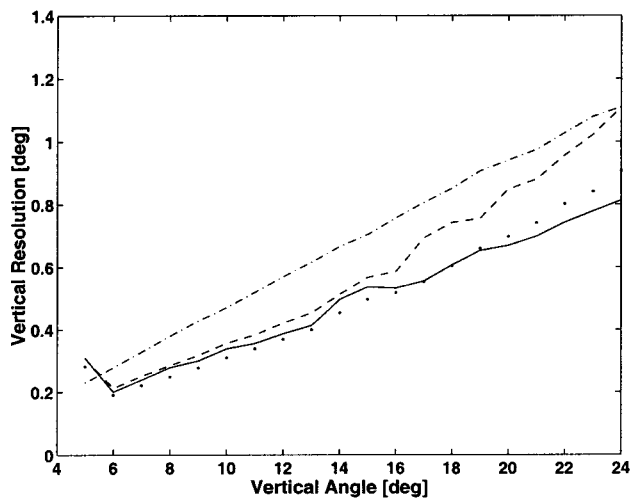
(b)

FIG. 5. Comparison of resolutions for no processing (solid line), spectrogram processing (dashed line), and SPWD processing (dotted line), for (a) range resolution and (b) vertical resolution. For comparison, the dashed-dotted line in (b) shows the horizontal resolution measured with no processing.

gets in the FIELD II program. The definition of the bolts required many nodes. Therefore, they were highly dense targets, making them easier to detect.

The point-target representation of the target is shown in Fig. 7. The orientation of the target in these figures corresponds to the orientation in which it is imaged. The axis labeled *X-Lateral direction* corresponds to horizontal steering directions. The axis labeled *Y-Lateral direction* corresponds to vertical steering angles. *Height* corresponds to axial distance. The bolts are closest to the array in range.

D. Image results

Sample projection images are shown in Figs. 8, 9, 10, and 11. In each of these projection images, one dimension of resolution that is present in the data is given up to display the image.
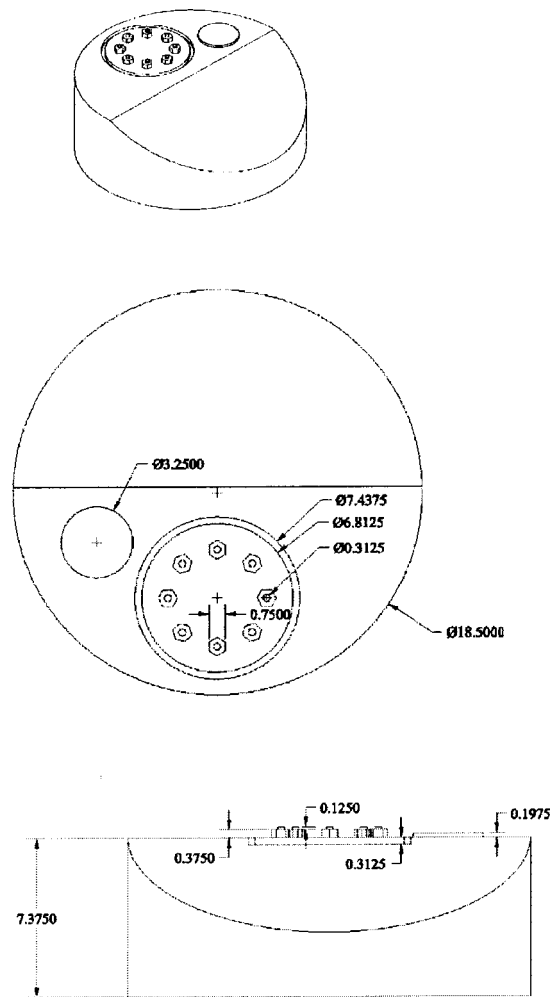
FIG. 6. Diagram of test target. Dimensions are given in inches.

Figure 8 shows the projection image through the vertical direction or the view from the top. At this orientation, which corresponds to Fig. 7(b), the observer sees the cylindrical target along its height; therefore, it appears as a rectangle. The bolts appear as white spots at the top of the image which corresponds to the closest range. Figure 9 shows the projection through range or the front view. This is a C-mode image in that the plane of view is parallel to the plane containing the transducer. At this orientation, which corresponds to Fig. 7(a), the observer views the top of the cylinder, so that the target appears as a circle. The slanted face is not apparent in the projection image. It is apparent in an image displaying the range of the first maximum (not shown). The bolts appear as a ring of bright spots near the bottom of the circle. The bottom of the circle, which corresponds to higher frequencies, appears more dim due to the greater attenuation despite the better frequency response of the transducer at higher frequencies. The top of the circle, corresponding to lower incident frequencies, appears more blurred due to the wider beamwidths at lower frequencies.

Figures 10 and 11 show the projection through the horizontal direction or the side view. Figure 10 uses the spectrogram to calculate the projection, and Fig. 11 uses the SPWD. In both cases, the bottom of the image is more dim and the top is more blurred for the reasons discussed above. Also in
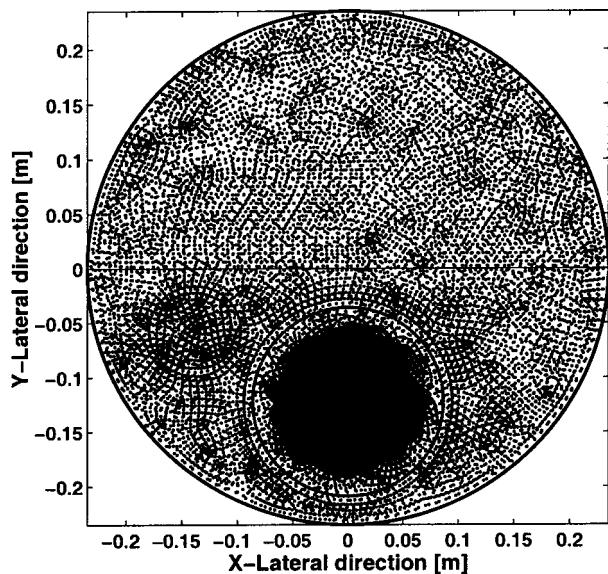
(a)
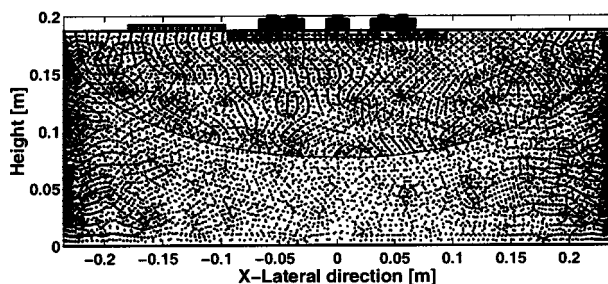
(b)
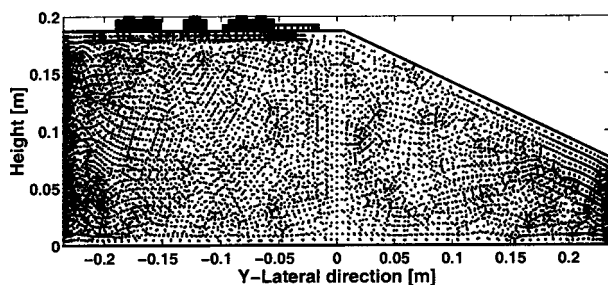
(c)

FIG. 7. View of target as point sources: (a) top; (b) from horizontal, with the sloped surface facing the reader; and (c) from vertical.

both cases, the overall shape of the target with the slanted face in the vertical direction is apparent. The SPWD image is much sharper than the spectrogram image. The SPWD image suffers from streaking in the vertical direction. The streaking can be reduced at the expense of resolution in the vertical direction by increasing the smoothing in that direction.

The three projection images allow us to display the data with reduced processing. Together, the three projection images produce an impression of the shape of the target. Resolution of small features can be improved by increasing the diameter of the array. Resolution may also be improved by
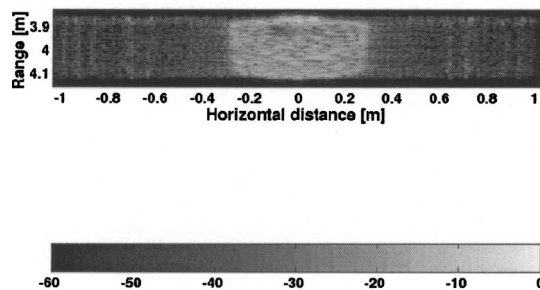
FIG. 8. Projection through the vertical direction, formed by envelope-detecting data following the Radon transform. The gray scale is in dB.

increasing the frequency; however, increasing the frequency may cause additional problems due to the increase in attenuation.

V. DISCUSSION

We have shown that by using frequency steering in one direction, the lateral resolution is improved in that direction, over the resolution achieved using a wide transmit beam. To improve resolution in both directions, we would like to be able to transmit a single pulse, using the full array rather than two staves, and then form images using frequency steering in both vertical and horizontal directions. We would consider this the full two-dimensional amplitude-steered array. Our current system for volumetric imaging is more accurately described as a linear-phased amplitude-steered array, because amplitude steering is used in the vertical direction, and conventional phased-array beam steering is used in the horizontal direction.

We are not able to achieve the full two-dimensional amplitude-steered array by applying fixed amplitude weighting along both rows and staves. With amplitude weighting only in the vertical direction, and assuming no phased-array steering in the horizontal direction, a pulse collects a plane of data perpendicular to the array face that is vertical. If we applied fixed amplitude weighting in both vertical and horizontal directions, a single pulse would produce a two-dimensional image representing a plane perpendicular to the array face and rotated around the array axis.
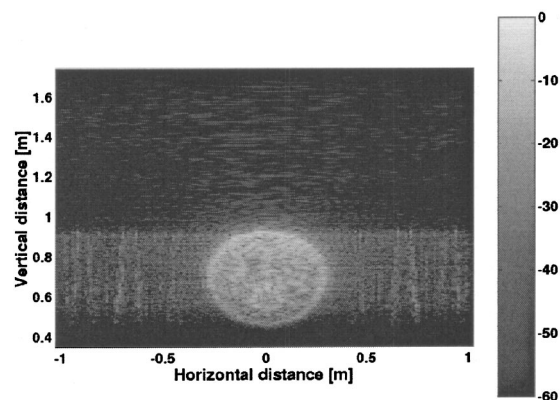
FIG. 9. Projection through the range direction, formed by calculating the Fourier transform of each signal following the Radon transform. The gray scale is in dB.

Frazier *et al.*: HF amplitude-steered array for volumetric imaging
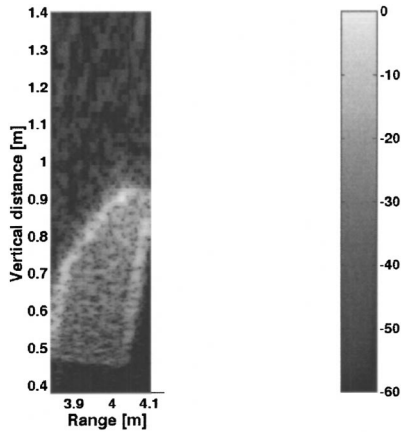
FIG. 10. Projection through the horizontal direction, formed using the spectrogram processing on the summed output of the Radon transform. The gray scale is in dB.

Lu's array, which forms *grid array beams*, could be considered a full two-dimensional amplitude-steered array, in that array weighting is used in both lateral directions. However, his amplitude weighting is not fixed. An extensive bibliography of Lu's work in limited diffraction beams is available in Ref. 11.

Forming grid array beams requires amplitude weighting on the elements of a two-dimensional array which is derived from Eq. (11) of Ref. 24:

$$\Phi_G(x,y,z-c_1t) = (\cos k_x x)(\cos k_y y)e^{ik_z(z-c_1t)}, \qquad (5)$$

where Φ_G is a three-dimensional wave field, the subscript G refers to grid array beams, x and y are the lateral directions, z is the axial direction, and (k_x, k_y, k_z) are the components of the vector wave number. Equation (5) is a limited diffraction solution to the wave equation because the transverse beam pattern does not change as z increases. The weighting on the elements is given by

$$A(x,y) = \cos(k_x x)\cos(k_y y). \qquad (6)$$

Choosing values for the parameters k_x and k_y gives one set of grid array beams, and therefore, one received signal. That single signal cannot be processed by itself to give target po-

sition in three dimensions. Multiple grid array beams are formed in order to obtain the data for target localization. Forming an image requires changing the weighting on the elements by changing k_x and k_y. By calculating the output of the array for many different values of k_x and k_y, i.e., summing signals from array elements with different weightings, a three-dimensional data set is formed. Multiple sets of beams can be formed by storing signals from individual elements of the transducer array or by using electronics to calculate multiple grid array beams, and therefore multiple received signals, at once. The image is obtained using a three-dimensional inverse Fourier transform.
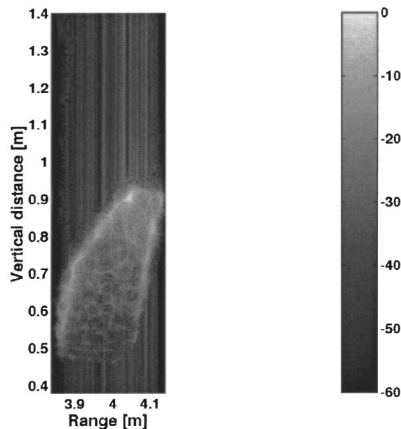
We can put our amplitude weighting in the form of Eq. (5); however, our weighting is only in the x direction, and it is fixed. For each row, we have weighting terms $\cos((2n-1)\phi)$ and $\sin((2n-1)\phi)$, where n was an index used to enumerate the row and $\phi = (k_0 d/2)\sin\theta_0$. These weighting terms are discretized versions of $\cos(k_x x)$ and $\sin(k_x x)$, where $k_x = k_0 \sin\theta_0$ and $x = (2n-1)(d/2)$. With fixed weighting, we have only a single value of k_x, whereas the limited diffraction beam system uses variable k_x and k_y. The result is that our lateral resolution varies with angle. Lu's lateral resolution remains constant at a particular range.

One final difference between our work and that of Lu is that, although we apply similar weighting to our array, we do not claim to be using limited diffraction beams. For a finite array size, the transmitted and receive beams will diffract; however, Lu forms his images well within the near field and finds that diffraction effects are not important. We form our images before the near-field/far-field transition for part of our frequency range; however, for the lower frequencies, our targets are assumed to be in the far field of the array.

VI. CONCLUSIONS

We have introduced the linear-phased amplitude-steered array and associated processing for real-time volumetric imaging.[25] A previous implementation of the amplitude-steered array suffered from grating lobes and large beamwidths. The array layout has been modified with randomized element assignment so that sidelobes are low. And, the aperture is large compared with a wavelength even at the lowest frequency, so the beamwidths have been improved.

The main obstacle to collecting a volume of high-resolution, high SNR data in real time is the time required to scan a beam in two dimensions. Often, to avoid scanning the transmit beam in many directions, a broad transmit beam is used; however, the result is poorer resolution than would be achieved by using a narrow transmit and receive beam. Using the amplitude-steered array, the beam, which is narrow in the vertical dimension, is scanned in the vertical direction as the frequency of the transmitted pulse changes. Received signals from different directions are separated by frequency content, not by time, greatly reducing the time required to collect data and with improved lateral resolution in the direction of frequency separation. The amplitude-steered array offers the additional benefit of reducing the number of channels required to process data from a dense two-dimensional array. The array uses only four channels per column of elements rather than one channel for each array element.

FIG. 11. Projection through the horizontal direction, formed using SPWD processing on the summed output of the Radon transform. The gray scale is in dB.

We chose to transmit a broad beam in the horizontal direction and to focus in that dimension only on receive because the large ranges associated with our application required collecting a volume of data with a single transmit pulse. For medical imaging, with shorter ranges of interest and greater demand for high resolution, we could transmit beams that are narrow and steered in the horizontal direction as well as in the vertical direction. The volume of data would be collected in the same time that it currently takes to form a two-dimensional image using standard ultrasonic imaging techniques.

ACKNOWLEDGMENTS

[1] W. J. Hughes and W. Thompson, Jr., "Tilted directional response patterns formed by amplitude weighting and a single 90° phase shift," J. Acoust. Soc. Am. **59**, 1040–1045 (1976).

[2] W. J. Hughes, W. Thompson, Jr., and R. D. Ingram, "Transducer array scanning system," United States Patent 3,905,009, 9 Sept. 1975.

[3] W. J. Hughes and C. W. Allen, "A shaped PVDF hydrophone for producing low sidelobe beampatterns," Proceedings of the 1992 Symp. on Autonomous Underwater Vehicle Technology, 2–3 June 1992, Washington, D.C.

[4] W. J. Hughes and C. W. Allen, "A spatially phased transducer to form steered beams," Proceedings of SPIE, Medical Imaging 1999: Ultrasonic Transducer Engineering **3664**, 138–146 (1999).

[5] C. H. Frazier, W. J. Hughes, and W. D. O'Brien, Jr., "Volumetric imaging with an amplitude-steered array," J. Acoust. Soc. Am. **112**, 2753–2762 (2002).

[6] T. R. Nelson and D. H. Pretorius, "Three-dimensional ultrasound imaging," Ultrasound Med. Biol. **24**(9), 1243–1270 (1998).

[7] S. Berg, H. Torp, D. Martens, E. Steen, S. Samstad, I. Høivik, and B. Olstad, "Dynamic three-dimensional freehand echocardiography using raw digital ultrasound data," Ultrasound Med. Biol. **25**(5), 745–753 (1999).

[8] R. Canals, G. Lamarque, and P. Chatain, "Volumetric ultrasound system for left ventricle motion imaging," IEEE Trans. Ultrason. Ferroelectr. Freq. Control **46**(6), 1527–1538 (1999).

[9] S. W. Smith, H. G. Pavy, Jr., and O. T. von Ramm, "High-speed ultrasound volumetric imaging system. I. Transducer design and beam steering," IEEE Trans. Ultrason. Ferroelectr. Freq. Control **38**(2), 100–108 (1991).

[10] J.-Y. Lu, "2D and 3D high frame rate imaging with limited diffraction beams," IEEE Trans. Ultrason. Ferroelectr. Freq. Control **44**(4), 839–856 (1997).

[11] J.-Y. Lu, "Experimental study of high frame rate imaging with limited diffraction beams," IEEE Trans. Ultrason. Ferroelectr. Freq. Control **45**(1), 84–97 (1998).

[12] J. Shen and E. S. Ebbini, "A new coded-excitation ultrasound imaging system. I. Basic principles," IEEE Trans. Ultrason. Ferroelectr. Freq. Control **43**(1), 131–140 (1996).

[13] B. D. Steinberg, "Comparison between peak sidelobe of the random array and algorithmically designed aperiodic arrays," IEEE Trans. Antennas Propag. **AP-21**(3), 366–370 (1973).

[14] B. D. Steinberg, "The peak sidelobe of the phased array having randomly located elements," IEEE Trans. Antennas Propag. **AP-20**(2), 129–136 (1972).

[15] D. H. Johnson and D. E. Dudgeon, *Array Signal Processing: Concepts and Techniques* (Prentice-Hall, Englewood Cliffs, NJ, 1993).

[16] P. Chevret, N. Gache, and V. Zimpfer, "Time-frequency filters for target classification," J. Acoust. Soc. Am. **105**, 3168–3175 (1999).

[17] L. R. Dragonette, D. M. Drumheller, C. F. Gaumond, D. H. Hughes, B. T. O'Connor, N.-C. Yen, and T. J. Yoder, "The application of two-dimensional signal transformations to the analysis and synthesis of structural excitations observed in acoustical scattering," Proc. IEEE **84**(9), 1249–1263 (1996).

[18] L. Cohen, "Time–frequency distributions—A review," Proc. IEEE **77**(7), 941–981 (1989).

[19] C. H. Frazier and W. D. O'Brien, Jr., "Image formation with the amplitude-steered array using time–frequency processing," Acoust. Imaging **25**, 535–542 (2000).

[20] C. H. Frazier, W. J. Hughes, and W. D. O'Brien, Jr., "Resolution analysis for an amplitude steered array," J. Acoust. Soc. Am. **107**, 2430–2436 (2000).

[21] J. A. Jensen, "FIELD: A program for simulating ultrasound systems," Med. Biol. Eng. Comput. **34**(1), Suppl. 1, 351–353 (1996).

[22] Program is available at http://www.it.dtu.dk/˜jaj/field/field.html

[23] I. Tolstoy and C. S. Clay, *Ocean Acoustics: Theory and Experiment in Underwater Sound* (McGraw-Hill, St. Louis, 1966).

[24] J.-Y. Lu, "Limited diffraction array beams," Int. J. Imaging Syst. Technol. **8**(1), 126–136 (1997).

[25] C. A. H. Frazier, "A two-dimensional amplitude-steered array for real-time volumetric acoustic imaging," Ph.D. thesis, University of Illinois at Urbana-Champaign, 2000.

Volumetric imaging with an amplitude-steered array

Catherine H. Frazier[a]
Bioacoustics Research Laboratory, Department of Electrical and Computer Engineering,
University of Illinois at Urbana-Champaign, Urbana, Illinois 61801

W. Jack Hughes[b]
Applied Research Laboratory, The Pennsylvania State University, P.O. Box 30, State College,
Pennsylvania 16801

William D. O'Brien, Jr.[c]
Bioacoustics Research Laboratory, Department of Electrical and Computer Engineering,
University of Illinois at Urbana-Champaign, Urbana, Illinois 61801

Volumetric acoustic imaging is desirable for the visualization of underwater objects and structures; however, the implementation of a volumetric imaging system is difficult due to the high channel count of a fully populated two-dimensional array. Recently, a linear amplitude-steered array with a reduced electronics requirement was presented, which is capable of collecting a two-dimensional set of data with a single transmit pulse. In this study, we demonstrate the use of the linear amplitude-steered array and associated image formation algorithms for collecting and displaying volumetric data; that is, proof of principle of the amplitude-steering concept and the associated image formation algorithms is demonstrated. Range and vertical position are obtained by taking advantage of the frequency separation of a vertical linear amplitude-steered array. The third dimension of data is obtained by rotating the array such that the mainlobe is mechanically steered in azimuth. Data are collected in a water tank at the Pennsylvania State University Applied Research Laboratory for two targets: a ladder and three pipes. These data are the first experimental data collected with an amplitude-steered array for the purposes of imaging. The array is 10 cm in diameter and is operated in the frequency range of 80 to 304 kHz. Although the array is small for high-resolution imaging at these frequencies, the rungs of the ladder are recognizable in the images. The three pipes are difficult to discern in two of the projection images; however, the pipes separated in range are clear in the image showing vertical position versus range. The imaging concept is demonstrated on measured data, and the simulations agree well with the experimental results. © *2002 Acoustical Society of America.* [DOI: 10.1121/1.1518698]

PACS numbers: 43.30.Yj, 43.30.Wi [DLB]

I. INTRODUCTION

Volumetric imaging is of interest in sonar and other applications because of the additional information provided by the third dimension of data. Three-dimensional sonar imaging has been developed for applications such as fish counting, mine hunting, and inspecting structures. In general, systems are designed to complement or replace optical systems, which are ineffective in turbid water.

Several of the systems discussed in the literature are based on transmitting a single pulse with a broad region of coverage and then focusing or processing the received signals to produce an image. Jones[1] uses a conceptually simple system, transmitting a chirp over a broad region and then using a sparse two-dimensional array to steer and focus the receive beam. The broad transmit beam lowers the achievable resolution. Such a system also suffers from poor signal-to-noise ratio due to the broad spread of transmitted energy and the high average sidelobe level of the receive beam pattern.

Murino *et al.* also use a single transmit pulse to insonify a region and a two-dimensional transducer array to receive reflected signals; however, the processing is not conventional beamforming of the received signals.[2] Instead, the processing involves a noncoherent correlation of the received signals, or correlation of the envelopes of the received signals. The proposed method is reported to have the advantages of reduction in speckle and no grating lobes regardless of interelement spacing. Thus, the array can be sparse to reduce complexity. However, it is acknowledged that the method will have poor angular resolution. In addition, although the −3-dB beamwidth of the correlation system can be made comparable to that of a focused beamforming system, the −10-dB and −20-dB beamwidths of the correlation system are much larger than those of the focused beamforming system, leading to poor image contrast.

Papazoglou and Krolik[3] have improved an imaging system for studying zooplankton by using adaptive beamforming. The original system, referred to as *FishTV*, uses two linear arrays of eight elements each in the typical geometry of a Mills Cross array. The composite pattern has 64 pencil

---

[a]Electronic mail: hillsley@brl.uiuc.edu. Current address: Johns Hopkins University Applied Physics Laboratory, 11100 Johns Hopkins Road, Laurel, MD 20723.
[b]Electronic mail: wjh2@psu.edu
[c]Electronic mail: wdo@uiuc.edu

beams. A minimum variance distortionless response beam-former is used to lower sidelobes from -10 dB to -20 dB and improve resolution from $2°$ to $0.25°$. The frame rate is reported to be 4 frames per second. Images contain few pixels and are difficult to interpret.

Other researchers are developing lens-based systems. Belcher has developed three small, high-frequency sonars that use lenses.[4,5] The transmitter is a single element or row of the two-dimensional array. The receiver is the two-dimensional array located in the focal plane of the lens. Erikson *et al.* are developing an acoustic camera. It is also a lens-based system using a transducer hybrid array (THA) and a C-scan format for data collection.[6] A separate transmitter, with a wide beam, is used to insonify the region of interest. Then, an acoustic lens is used to image multiple planes onto the acoustic array. In all of these systems, the lens accomplishes the focusing, so that the electronics requirement is reduced. A small number of range planes can be collected with a single transmit pulse; more range planes are collected with successive pulses. The total range depth that can be imaged is determined by the depth of focus of the acoustic lens, which is limited.

Recently, a linear amplitude-steered array was presented that is capable of collecting a two-dimensional set of data with a single transmit pulse and has a reduced requirement for electronics.[7] The linear amplitude-steered array steers the mainlobe by changing frequency. The potential for beam steering and imaging by changing frequency had been recognized by Lizzi and Weil.[8] Using a curved transducer with tapered thickness and exciting the transducer with different frequencies, beams with different origins and steering directions are radiated. By changing the frequency continuously, the beam is scanned through a sector. The system is limited by the fact that the ratio of highest to lowest excitation frequency cannot be more than 3. Otherwise, at the highest frequencies, multiple beams will be radiated with different orientations and steering directions, as the transducer will radiate from all places where the excitation frequency is an odd multiple of a half wavelength of thickness.

The concept of steering the maximum response of an array using amplitude weighting was introduced by Hughes and Thompson in 1976.[9] At that time, the intent of amplitude steering was to tilt the maximum response of the beam pattern without using phase-shift networks or multiple delay lines, which are bulky. A steered beam was achieved by summing the signals from two appropriately weighted subarrays with a single $90°$ phase shift. Initially, amplitude weighting was applied with an electronic gain,[10] but as shaped hydrophones were developed,[11] amplitude weighting was achieved geometrically, further reducing the electronics requirement.[12]

In the original formulation, the beam was steered to a particular direction at a single frequency, and the fact that the steering direction changed with frequency was considered a drawback of the design. By operating a vertical linear amplitude-steered array in broadband mode, with an impulsive or chirp excitation, the maximum response axis is swept over a range of vertical steering angles. A vertical plane of data is created from a received signal using a short-time Fourier transform (STFT). The temporal position of the STFT

window gives the range of the target, and the frequencies contained within the window give the vertical angle of the target.

There have not been any experimental tests for this new volumetric imaging concept using amplitude steering. In this study a small experimental array, which was used for the low-frequency validation of the two-dimensional amplitude-steering concept, is utilized for the three-dimensional volumetric imaging. It would have been preferable to have a large aperture array with random element assignments, but one was not available. Another contribution[13] that introduced this new imaging method had demonstrated feasibility with simulated data, not experimental results. Despite the shortcomings of this array, and the fact that resolution of the images is low, the experimental results verify the simulations and support the work in the higher frequency medical imaging.

In order to collect volumetric data with a linear amplitude-steered array, the array is rotated such that the mainlobe is mechanically steered in the azimuthal direction and one pulse is transmitted for each steering direction. Data are collected in a water tank and images of three targets are produced. Section II gives a description of the array used for data collection. The experimental system used to collect the data is described in Sec. III. The image formation algorithms are briefly discussed in Section IV. And, in Sec. V, results are compared to simulations formed using the FIELD II program.[14,15] FIELD II has been widely used for simulations of transducer beam patterns and for simulations of imaging scenarios.[16–18] Following the comparison of images from simulated and experimental data, a conclusion is given.

II. DESCRIPTION OF THE ARRAY

Amplitude steering using a linear array has been described previously.[7,9,12,19] It is reviewed here briefly. The array pattern for a steered linear array with an even number of point sources/receivers can be written as

$$
H(\theta) = \frac{2}{N} [\cos \phi \cos u
$$
$$
+ \cdots + \cos((2n-1)\phi)\cos((2n-1)u)
$$
$$
+ \cdots + \cos((N-1)\phi)\cos((N-1)u)
$$
$$
+ \sin \phi \sin u + \cdots + \sin((2n-1)\phi)\sin((2n-1)u)
$$
$$
+ \cdots + \sin((N-1)\phi)\sin((N-1)u)] \quad n=1,...,N/2,
$$
$$
(1)
$$

where θ is the angular position in the field, N is the (even) number of elements, d is the interelement spacing, k is the wave number at the operating frequency, k_0 is the wave number at the designed frequency, θ_0 is the designed steering angle, and $\phi = (k_0 d/2)\sin \theta_0$ and $u = (kd/2)\sin \theta$. Equation (1) is interpreted as beam steering by amplitude weighting the elements. Steering by amplitude weighting is accomplished using two sets of weightings, one phase symmetric and one phase antisymmetric. In the phase-symmetric case, the weights on each element are $\cos((2n-1)\phi)$, where

Frazier *et al.*: Volumetric imaging with an amplitude-steered array

$n \in [-(N/2)+1, N/2]$ is an index used to enumerate the elements. Elements placed symmetrically about the center of the array are added with equal weights and in phase. In the phase-antisymmetric case, the weights on each element are $\sin((2n-1)\phi)$. Elements placed symmetrically about the center of the array are added with equal weights and with a 180° phase shift. The output signal of the phase-antisymmetric array must be phase shifted by 90° before combining with the output of the phase-symmetric array in order to achieve the steered beam. The parameter ϕ is a fixed value as defined above. By changing the frequency, the steering angle of the mainlobe is changed as

$$\phi = \frac{k_0 d}{2} \sin \theta_0 = \frac{k_f d}{2} \sin \theta_f, \qquad (2)$$

$$\theta_f = \sin^{-1}\left(\frac{f_0}{f} \sin \theta_0\right), \qquad (3)$$

where the subscript f has been added to emphasize the new operating frequency, and θ_f is the new steering direction.

The amplitude weighting can be achieved geometrically rather than electronically by dividing the available area of a single piezoelectric crystal into cosine and sine regions according to the ratio of the weights, as shown by Fig. 1. To derive this figure, we first imagine that we can phase a continuous rectangular transducer to steer its main beam. We use the following equation to determine the phase at each point along the length of the transducer:

$$H_{\text{continuous}}(\theta) = \int e^{jk_0 x \sin(\theta_0)} e^{-jkx \sin(\theta)} dx, \qquad (4)$$

where θ is the angular argument of the beam pattern measured relative to the broadside direction, k_0 is the wave number at the design frequency, θ_0 is the design steering angle, and x is the spatial position along the transducer. We separate the phase into its real and imaginary parts to obtain

$$H_{\text{continuous}}(\theta) = \int \cos(k_0 x \sin \theta_0) e^{-jkx \sin \theta} dx$$

$$+ j \int \sin(k_0 x \sin \theta_0) e^{-jkx \sin \theta} dx, \qquad (5)$$

where the first term of the sum corresponds to the cosine array and the second term corresponds to the sine array.

Part (a) of Fig. 1 shows the regions belonging to the cosine and sine arrays for the continuous transducer. The solid line represents the cosine array, and the dashed line represents the sine array. The weighting is achieved by changing the shape of the transducer. In part (b) of Fig. 1, we show that the two different weightings must occupy the same space. In Fig. 1(c), we show that the correct weighting at each x is achieved by using a cosine function and a (sine +cosine) function for weighting.

The array used in these experiments is a two-dimensional matrix of elements with elements assigned to sine or cosine regions, corresponding approximately to the regions shown in Fig. 1. The cosine and sine weightings can be positive or negative; therefore, there are four possible subgroups of elements: positive and negative cosine, and positive and negative sine. Figure 2 shows the layout of the

(a)

(b)

(c)
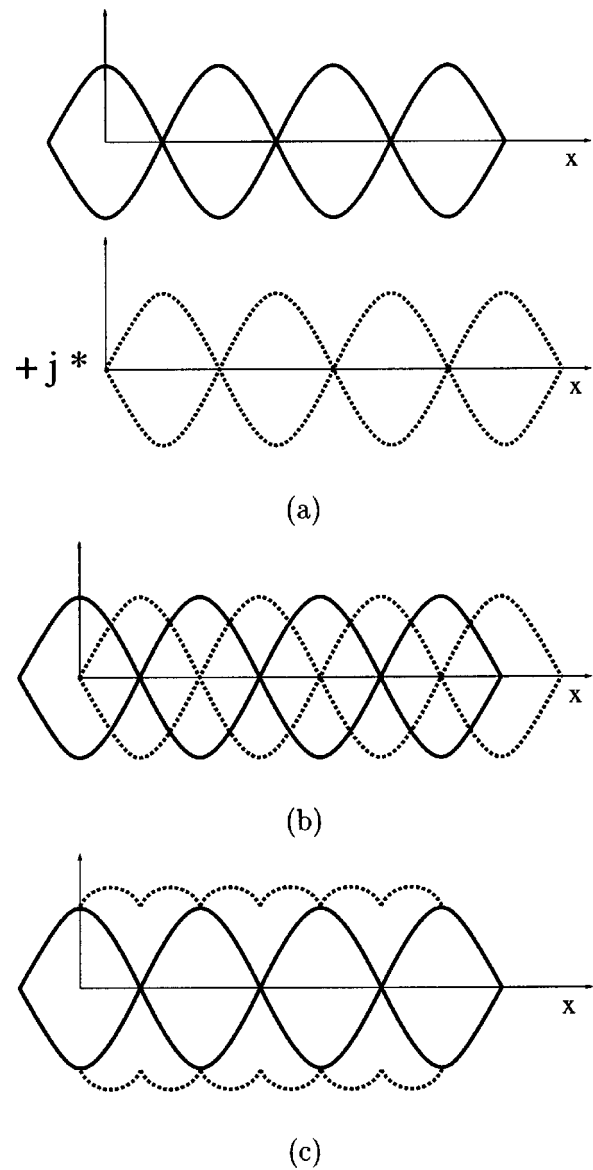
FIG. 1. Array layout for linear array. (a) The cosine (solid line) and sine (dashed line) phased elements. (b) Cosine and sine phased elements must share space. (c) In the linear array the sharing is calculated using cosine and (sine+cosine) functions.

array with four gray levels representing four subgroups of elements. In Fig. 1, the frequency separation is in the horizontal direction, and in Fig. 2, the frequency separation is in the vertical direction. Although the array layout is largely based on the "shaped crystal" implementation, the flexibility offered by using a matrix of elements rather than a single crystal is used to increase the intermixing of the types of elements.

The array used for data collection is approximately circular with a diameter of 10 cm. The maximum array dimensions are 52 by 55 elements. Interelement spacing is 2.11 mm in both the vertical and horizontal directions. The array has a geometric focus at 0.61 m formed by curving the array slightly; however, the focus does not have much effect as it is very close to the near-field/far-field transition even at the highest frequencies used. The array was built for purposes other than imaging, but has been used for this work to demonstrate the volumetric imaging concept on measured data.
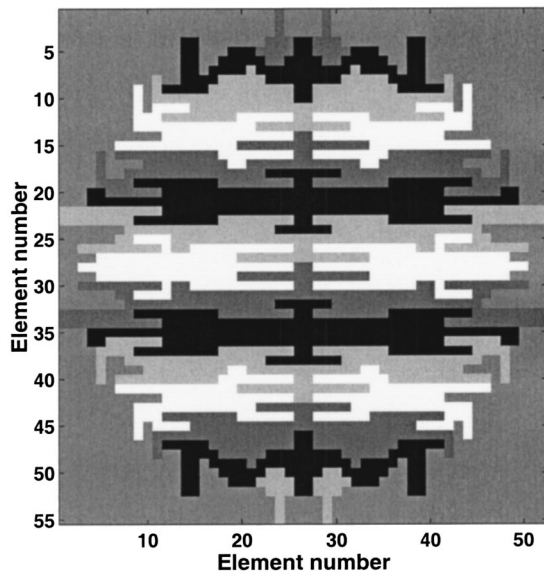
FIG. 2. Array layout for 2D array based on implementation of linear array. Four gray-scale levels represent the four phases for elements: white, cosine; black, negative cosine; light gray, sine; dark gray, negative sine.

FIG. 4. Diagram of data acquisition system.

The array is designed to steer to 30° at 100 kHz. The peak frequency response of the array is at 220 kHz. In Fig. 3, the calculated beam pattern is shown for 400 kHz. The 400 kHz beam is steered to approximately 7°. Additional major lobes appear at 49.8° in the vertical direction and ±1.59° in the horizontal direction, and they are only 12.4 dB below the mainlobe. The presence of high sidelobes reveals that this array layout or assignment of elements is nonideal. A discussion of how the beam pattern will be improved by changing the layout of the array is included in Ref. 13. Grating lobes are eliminated by randomizing the assignment of elements of different types, and the mainlobe width is improved by increasing the frequency while keeping the array diameter the same.

III. DATA COLLECTION SYSTEM

The data were collected in an anechoic tank at the Applied Research Laboratory (ARL) at the Pennsylvania State University. The tank measured 5.49 m deep by 5.33 m long by 7.92 m wide and was filled with stale water. The array

FIG. 3. Field pattern for 2D array based on implementation of linear array.

was held by a custom-built positioning system (Scientific-Atlanta, Inc., Atlanta, GA) with 0.318 cm (1/8-in.) depth resolution and ±0.02° rotational resolution around a vertical axis. Data were collected in 1° rotational steps.

A diagram of the system used to collect pulse–echo data is shown in Fig. 4. An HP 3314 function generator was used to manually trigger data collection. The transmit signal was generated by an HP 89410A vector signal analyzer. The transmit signal was split so that one signal path proceeded through a 90° phase shift to produce the excitation signal for the elements designated as sine elements. Each signal path then went through a power amplifier (model L6, Instruments, Inc., San Diego, CA). The output from each amplifier was fed into a current voltage sensor (model VIT-13, Instruments, Inc., San Diego, CA), used to monitor the current and voltage into the array electronics. The outputs from both sensors were input into the custom-built phased array electronics box (ARL), which excited the amplitude-steered array. The output from one current voltage sensor was also fed into an HP 59307A VHF switch so that the transmit voltage could be recorded by a second HP 89410A vector signal analyzer.

The received signal from the amplitude-steered array was returned back through the phased array electronics, through a Krohn-Hite 3103A filter with a passband between 500 Hz and 1 MHz, to the VHF switch, and finally to channel 2 of the second vector signal analyzer. The vector signal analyzer digitized both transmit and receive signals at a sampling rate of 1.024 MHz. Signals were stored on disk in HP format and later converted to MATLAB format using software provided by HP.

The transmit signal generated by the first vector signal analyzer is a linear FM chirp, 0.5 ms in length. The start frequency is 304 kHz and the stop frequency is 80 kHz, giving angular coverage from 9.5° to 38.7°. The lower frequencies are given greater initial amplitude to partially compensate for the frequency response of the transducer. The

Frazier *et al.*: Volumetric imaging with an amplitude-steered array

array is oriented such that lower frequencies are steered farther downward than higher frequencies.

In order to process the signals, the received signals from each horizontal steering direction were first time gated to remove the initial bleed-through of the transmit. Then, the signals were filtered with a matched filter for pulse compression. The two-dimensional matrix of data contains one time signal for each azimuthal steering direction. For a complete set of volumetric data, we then apply time–frequency processing to the time signal from each azimuthal steering direction to determine vertical position and range. The STFT window is a 0.02-ms Hanning window.

IV. IMAGE FORMATION ALGORITHMS

Once the three-dimensional data set has been calculated, the data must be displayed. Surface or volume rendering requires significant processing. Surface rendering is difficult when targets have flat surfaces with significant reflectivity because reflected energy may be directed away from the receiver, resulting in a low received signal despite the presence of a surface. Surface rendering also may be particularly difficult in the presence of noise or when resolution is not high enough.

Kamgar-Parsi et al.[5] studied many possible alternatives to volume and surface rendering including range images that display the first maximum above a threshold, and acoustic photographs which integrate the backscatter intensities along each beam. They found that displaying the maximum produced images similar to surface rendering. Taking the depth to the first maximum produced better results. These methods are limited to displaying the data at one orientation.

Projection images are another alternative to surface or volume rendering. Projection images integrate through one dimension to display the other two as an image, in which brightness indicates target strength. An image of vertical versus horizontal position is formed by summing through the range information. An image of range versus horizontal position is formed by summing through the vertical position information. And, an image of vertical position versus range is formed by summing through the horizontal information.

One way to form projection images is to begin with the full three-dimensional volume of data and sum through the various directions; however, in our case projection images are formed more directly from the received signals. Forming the three-dimensional data set requires time–frequency processing for each horizontal beam. The projection images can be formed faster using different processing. The projection image of range versus horizontal position is formed by envelope detecting the received signals from each horizontal steering direction. Range resolution is better than time–frequency methods that use a sliding window, effectively averaging over the samples in the window. The image of vertical position versus horizontal position is formed by taking a single Fourier transform of the entire received signal for each steering direction. Since the image does not display any range information, time–frequency processing is not necessary for this image. Also, by using the entire signal, the best frequency resolution is obtained, giving the best resolution of vertical position. These two images represent the extremes of
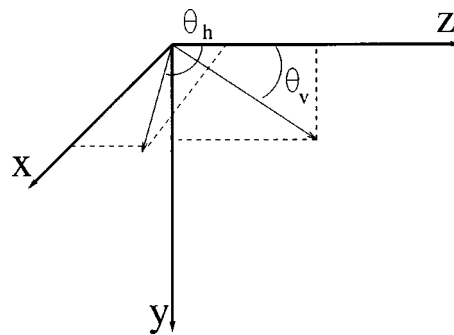
FIG. 5. Illustration to show axes and angles used to define target positions.

using the STFT, with very short or very long processing windows. Finally, to form the image of vertical position versus range, time–frequency processing is required. Rather than performing the calculation for every horizontal beam, the sum through the horizontal beams is taken first, and then the time–frequency distribution is calculated only once.

The image resolution is dependent not only on the size of the array,[7] but also on the processing used to form the images. Also, because of the frequency separation, resolution will vary throughout the insonified field. Following the analysis of Ref. 7, which defines resolution as the -3-dB width of the point spread function, the best range resolution we could achieve is $0.4423c/\Delta f$, which corresponds to 3.0 mm. The best lateral resolution we could achieve is 4.4 cm at 304 kHz and 16.6 cm at 80 kHz at a range of 1 m. Image formation algorithms are described in greater detail in Ref. 19.

V. SIMULATED AND EXPERIMENTAL RESULTS

Pulse–echo data were collected for several targets using the system described above. To describe target locations, we give two sets of coordinates, which are pictured in Fig. 5. The first set of coordinates is in (x,y,z) form, where x is the horizontal position parallel to the face of the array, y is the depth, and z is the horizontal position perpendicular to the face of the array. Thus, x and y are lateral positions and z is an axial position. Positive y is down, and positive z is away from the array in the broadside direction. Positive x follows from the right-hand rule. This convention is in agreement with that used by the FIELD II program.

The second set of coordinates is in (r,θ_v,θ_h) form, where r is the range from the center of the array, θ_v is the vertical angle relative to horizontal with the origin at the center of the array, and θ_h is the horizontal angle relative to the broadside direction, also with the origin at the center of the array. Both sets of coordinates are given because the images of the targets are given using both coordinates.

In the simulations, the frequency response of the transducer was assumed to be flat, and the excitation signal did not change amplitude with frequency. The target positions were rotated to simulate the rotation of the array. Processing of the simulated data was the same as processing of the experimental data, with the exception of the initial time gating, which was not necessary for the simulated data.

Comparisons between the simulations and experiments are made on a qualitative basis. Target positions were measured at the water surface and therefore are known only approximately. Gross differences between the images from simulated and experimental data are apparent visually. Numerical comparisons, for example using the energy of a difference image or a correlation technique, would require multiple time-consuming simulations as the targets are translated and rotated to provide a better match, and not much insight would be gained.

A. Ladder target

The ladder target was a standard 6-ft. wooden step ladder with rungs that were 30.5 cm (1 ft.) apart. The ladder was placed in the water in the folded position so that it hung approximately vertically, 1.2 m away from the array. Figure 6(a) shows a picture of the target and array. The target position and orientation are shown in Fig. 6(b). Two rungs appear within the insonified region; however, a third rung is very close in depth to the insonified region. The locations of these three rungs are given by the coordinates (± 0.152 m, 0.406 m, 1.2 m); (± 0.152 m, 0.711 m, 1.2 m); and (± 0.152 m, 1.02 m, 1.2 m). In terms of angles, the coordinates are (1.27 m, 18.7°, ± 7.2°); (1.40 m, 30.7°, ± 7.2°); and (1.57 m, 40.2°, ± 7.2°). The positive and negative values in the x and θ_h coordinates represent a range which is the extent of a rung. Data were collected over a range of horizontal angles from -30° to 30°. In the simulation, the sides of the ladder and each rung were represented as a line of point targets. To represent the targets, 53 636 points were used.

Figure 7 shows the projection images through the vertical angle using simulated and experimental data. The three rungs should be present at 1.27, 1.4, and 1.57 m. All three rungs are visible at the correct ranges in the image from simulated data. The farthest rung is less bright because it is not fully within the insonified region. Preceding the closest rung in range, there is a very thin line that extends across the image. This artifact is due to the discontinuity at the onset of the received signal. The artifact is also present in the image from experimental data, to a lesser extent. The third rung is not visible in the image from experimental data, due to the low response of the array at lower frequencies, and due to the position of the rung just outside of the insonified region. At the closest/highest rung, reflections from the sides of the ladder appear. Also, there is an additional reflection at the top rung in the experimental data probably due to the fact that the ladder is a folding ladder, and there is a step behind the rung.

Figure 8 shows the projection images through range using simulated and experimental data. Both the image from simulated data and the image from experimental data show two rungs. The third rung is below the range shown in the image. The upper rung appears smaller, indicating the smaller beamwidth at the higher frequency. In both cases, the lower rung appears wider. In the image from experimental data, the lower rung also appears less bright, due to the smaller response of the transducer at the lower frequency.

Figure 9 shows the projection images through the horizontal angle using simulated and experimental data. Both the

(a)
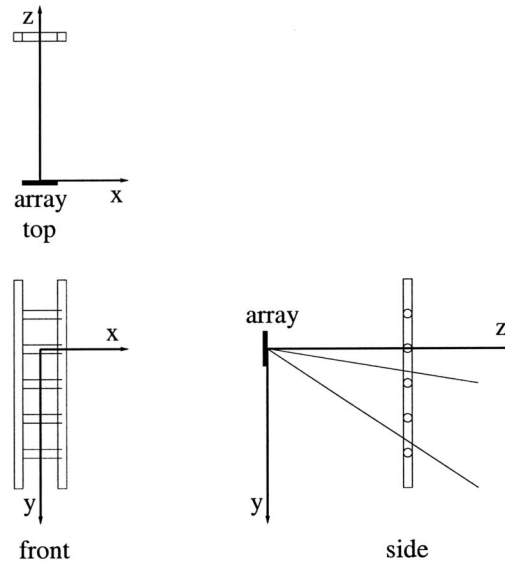
(b)

FIG. 6. (a) Picture of the ladder target prepared for data collection. The array is the circular object held by a frame behind the ladder (above the ladder in the picture.) The structure that holds the array is reflected in the water surface. (b) Top, front, and side views to show position and orientation of ladder target.

images from simulated and experimental data show three rungs. The highest rung appears to be closest to the transducer in range. The third (lowest) rung appears in this projection because summing across the horizontal angles has increased the signal level above the threshold for display. However, only part of the lowest rung is visible. The middle rung appears the brightest because of the summing operation. The simulated image is very smooth. There is a reflection that extends through most of the vertical distance just before the highest rung. That reflection is due to the artifact described above caused by the onset of the signal. The image from experimental data also has a reflection before the first (highest) rung, due to the artifact. In addition, there is a reflection behind the highest rung and above the middle rung. It may be a reflection from the flat step behind the rung. Although the ladder is hanging vertically, the rungs

Frazier *et al.*: Volumetric imaging with an amplitude-steered array
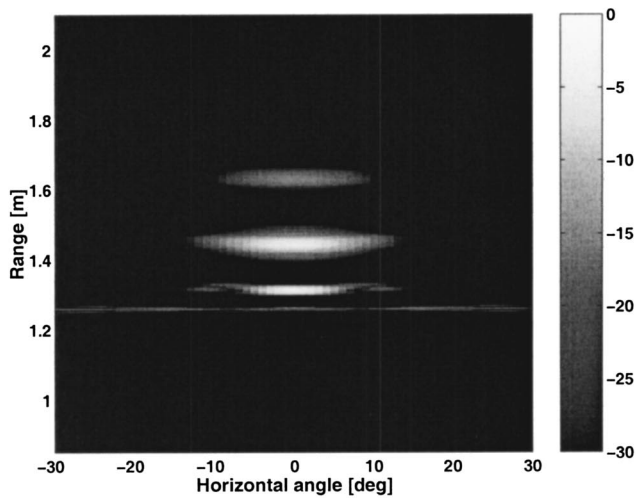
(a)
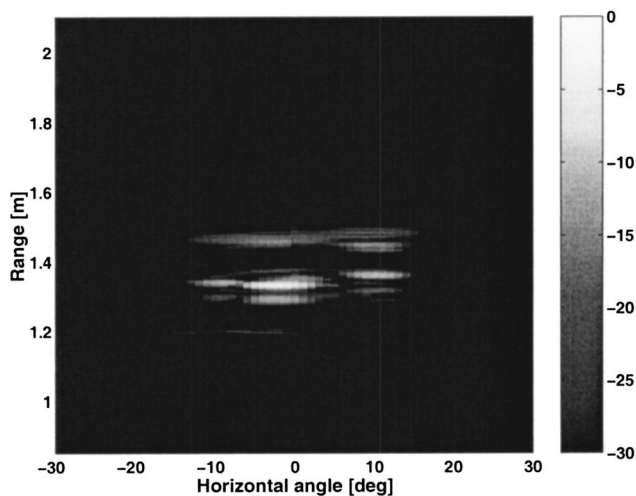
(b)

FIG. 7. Images of the ladder target [corresponding to the top view of Fig. 6(b)]. Range versus horizontal angle (a) simulated; (b) experimental. The gray scale is in dB.

appear to move away from the transducer in range as they become deeper because the insonified region is off-broadside, directed downward.

In the three images, the rungs of the ladder are clearly long in the horizontal direction and compact in the vertical and range directions. There is excellent agreement between the simulated and experimental data for these three sets of images. The rungs of the ladder are perpendicular to the direction of frequency separation, and therefore each rung reflects a small range of frequencies. There are some differences that show more structure in the experimental data due to the model of the ladder and due to the fact that the simulation assumes simple reflection.

B. Three-pipe target

The next targets used were three steel pipe targets. The pipes are each 3.05 m (10 ft.) long, with an outer diameter of
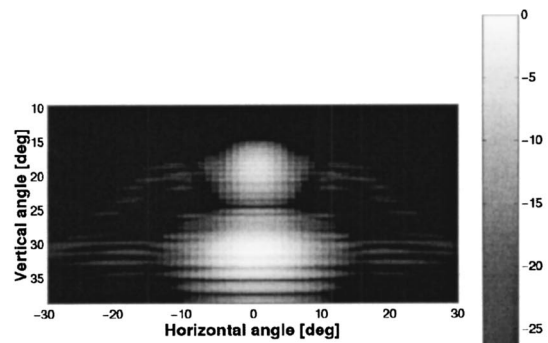
(a)
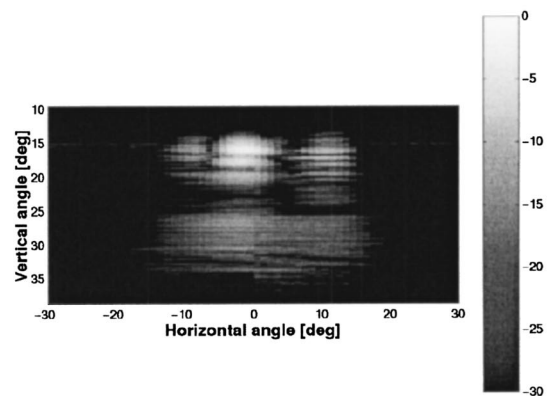
(b)

FIG. 8. Images of the ladder target [corresponding to the front view of Fig. 6(b)]. Vertical angle versus horizontal angle (a) simulated; (b) experimental. The gray scale is in dB.

2.54 cm (1 in.) and an inner diameter of 0.794 cm (5/16 in.). The targets are arranged as three corners of a square, where the side of the square has a length of 30.5 cm (1 ft.). The target positions and orientations are shown in Fig. 10. The pipe locations are given by the coordinates (0 m, −, 1.0 m); (0 m, −, 1.305 m); and (−0.305 m, −, 1.305 m). For the pipe targets, no y coordinate (depth) is specified because the targets extend through the entire depth coverage of the array. In terms of (r, θ_v, θ_h) coordinates, the targets are at (1.0 m, −, 0°); (1.305 m, −, 0°); and (1.340 m, −, −13.15°). θ_v is the entire insonified depth of the array, 9.5° to 38°. Data were collected over a range of horizontal angles from −25° to 10°. In the simulation, each pipe was represented as a single line of points. The three pipe targets were defined by 60 003 points.

Figure 11 shows the projection through the vertical direction. In the simulated image, each pipe target appears as a very thin horizontal line. The horizontal lines extend across the whole image because the beamwidth of the lowest frequency (80 kHz) is 20°, and the image shows only a 35° sector. The image formed with experimental data agrees in character with the image formed with simulated data. The separation in range between the pipes appears to be larger than 0.305 m. This difference in separation is probably due to the pipes hanging at an angle and not perfectly vertical.
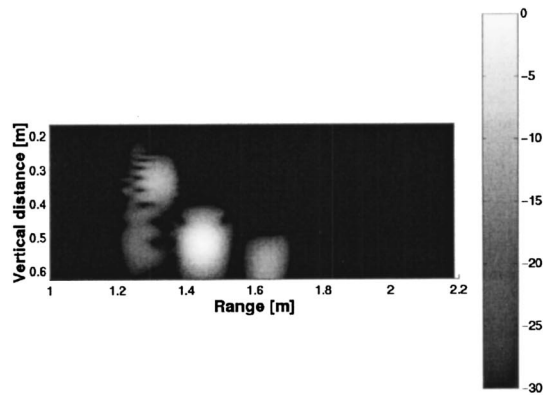
(a)
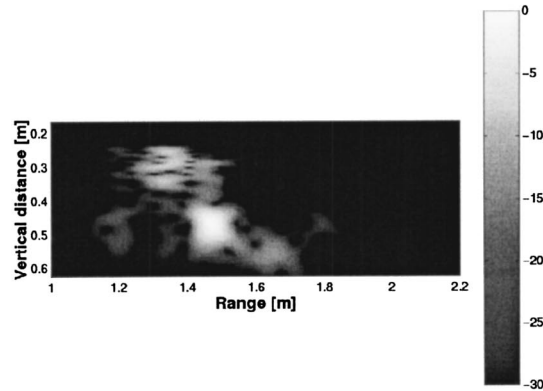
(b)

FIG. 9. Images of the ladder target formed using the STFT [corresponding to the side view of Fig. 6(b)]. Vertical angle versus range (a) simulated; (b) experimental. The gray scale is in dB.

The distances between the pipes were measured at the top of the pipes, slightly above the water level. If the pipe that is nominally at $x=0$ m and $z=1.305$ m is hanging at a 3° angle, the farther pipe in range would appear to be 0.4 m from the closer pipe, rather than 0.3 m, as expected. The image formed with experimental data also has a distinct bright spot at 0° in the horizontal direction and 1.0 m in
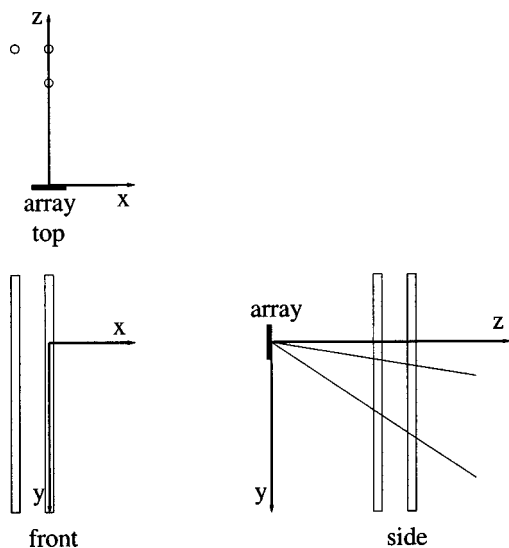
FIG. 10. Top, front, and side looks at the three-pipes targets.
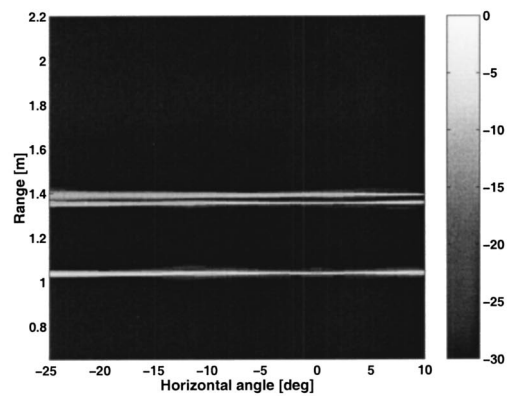
(a)
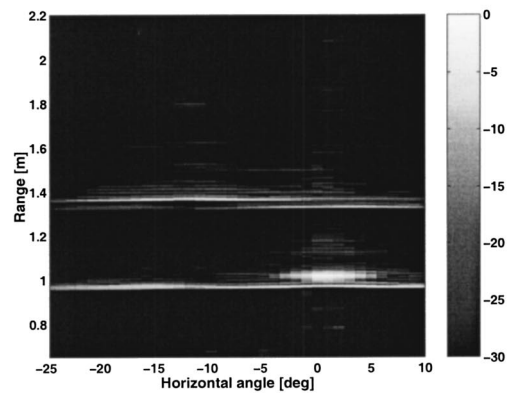
(b)

FIG. 11. Images of the three-pipes target (corresponding to the top view of Fig. 10). Range versus horizontal angle (a) simulated; (b) experimental. The gray scale is in dB.

range. This reflection is probably a particularly strong reflection from the closest pipe, perhaps due to reverberation in the pipe or a flaw in the pipe. There were no other targets in the water, and there should not have been any air trapped in the pipe.

Figure 12 shows the simulated and experimental results for the projection through range. Again, the images formed using simulated and experimental data are similar. In particular, both have the bright diagonal returns that fill the image. This characteristic is more noisy in the image from experimental data, and it is also less bright because of the brighter spot at 0° horizontally and 15° vertically, as discussed above. Both images are filled with reflections because the targets extend through the entire vertical region and because the beamwidths are wide in the horizontal direction, particularly at the lower frequencies which appear at the bottom of the image. Although it would be difficult to discern three pipes in this image, this image is valuable for showing that the simulations agree with the experimental data.

Figure 13 shows the simulated and experimental results for the projection through horizontal angle. Signals from −10° to 10° were included in the sum to form the projection through the horizontal angle, so that signals were summed symmetrically about $\theta_h=0°$ even though the data were not collected symmetrically around the $\theta_h=0°$ angle. The im-

(a)

(b)
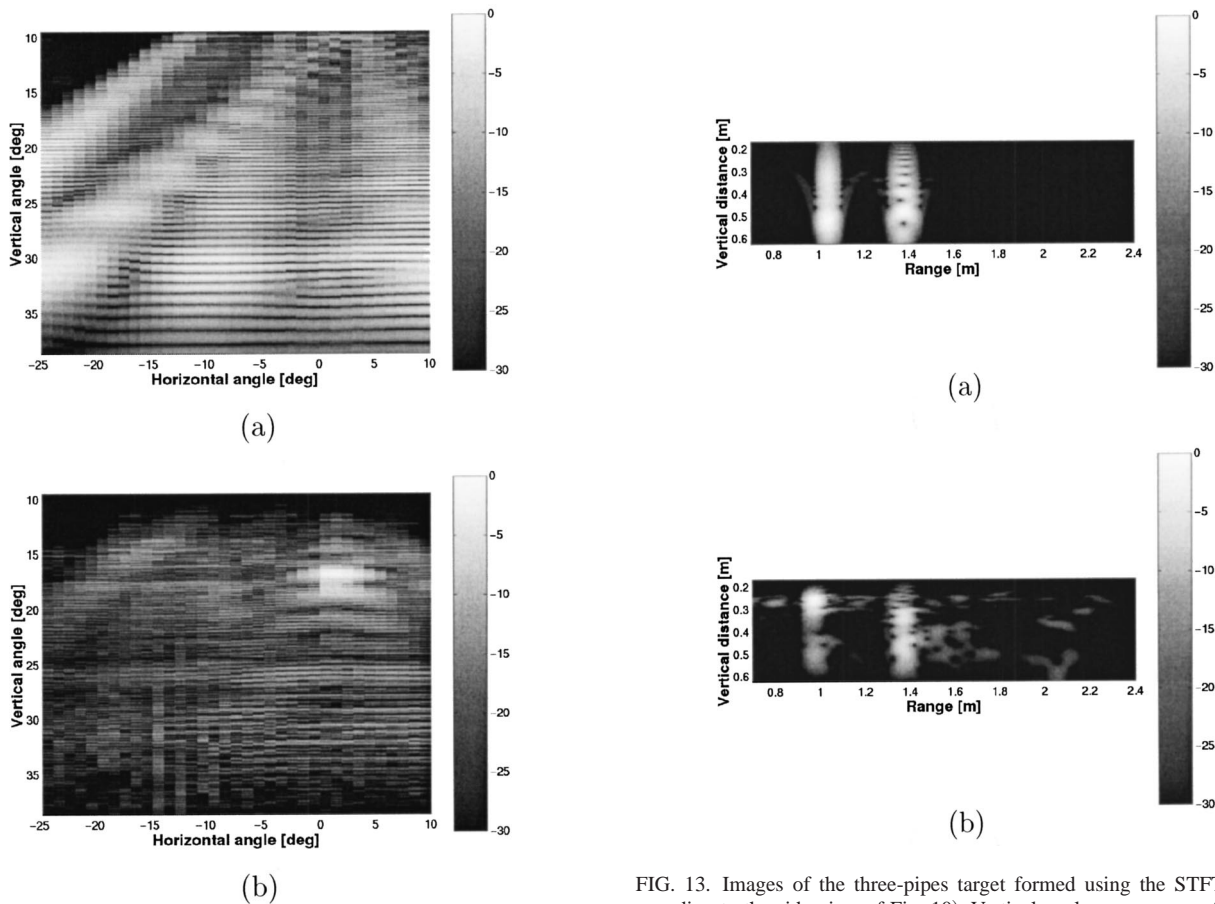
FIG. 12. Images of the three-pipes target (corresponding to the front view of Fig. 10). Vertical angle versus horizontal angle (a) simulated; (b) experimental. The gray scale is in dB.

(a)

(b)

FIG. 13. Images of the three-pipes target formed using the STFT (corresponding to the side view of Fig. 10). Vertical angle versus range (a) simulated; (b) experimental. The gray scale is in dB.

ages are similar in character, showing two vertical lines, one at 1.0 m and one farther in range. The difference in range separation has been discussed previously. The two vertical lines represent the three targets. In this projection, two targets at the same range cannot be separated. In the image from simulated data, the brightest reflections occur at lower vertical distances. In the image from experimental data, the brightest reflection occurs at the top of the closer target. This location of the brightest reflection agrees with that of the other two projections for experimental data.

The images of the three pipes are poorly resolved in the horizontal direction due to the wide horizontal beamwidths of this array; however, there is good agreement between images formed with simulated and experimental data. Differences arise because of a particularly strong echo in the experimental data, although the origin of this bright echo is unknown. Horizontal beamwidths can be improved by increasing the array diameter. In this case, the array diameter is 20 wavelengths at the highest frequency and 5 wavelengths at the lowest.

VI. DISCUSSION AND CONCLUSIONS

This study demonstrates with experimental data the use of the linear amplitude-steered array for volumetric imaging on measured data. The rungs of the ladder were fairly well

represented by the three projection images. The three pipes were best represented by the projection through the horizontal direction, which showed that the targets were discrete in range and extended in the vertical direction. The projection through range and through the vertical direction suffered from poor horizontal resolution, which made it difficult to see the pipe that was separated laterally from the other two.

Simulations of the array operation were confirmed with experiments conducted in the water tank at the Pennsylvania State University Applied Research Laboratory. There was excellent agreement between simulations and experiments. The three-pipes target introduced additional complexity in that the target was line-like rather than point-like in a vertical plane; however, the agreement between simulation and experimental data was still good. Hard targets with broad smooth surfaces are more difficult to represent as a collection of point targets, for the purposes of simulation, requiring large numbers of densely spaced points. The effects of shadowing must be included in the calculations. Difficulty in imaging hard smooth surfaces is a problem with acoustic imaging systems in general, in that the bulk of the energy may be reflected away from the receiver for monostatic imaging with a high angle of incidence. The amplitude-steered array is not an exception. Data collected from a water-filled aluminum shell showed a bright reflection from a particular region of the front surface and smaller reflections from each end of the cylinder, but the shape of the cylinder was not apparent in the images.

In this study, we rotated the linear array to obtain the third dimension in the data. For imaging longer ranges or for truly real-time volumetric imaging, the configuration would be modified such that the transmitted beam is broad in the horizontal direction and phased array beamforming would be used on receive in the horizontal direction to steer and focus the beam. Such an array, operating at a higher frequency is the subject of Ref. 13. In that work, the array layout is modified to lower sidelobes. The beamwidths are improved by increasing frequency while keeping the size of the array the same. Focusing is also implemented. Frequency and size of the modified array layout are chosen for a particular underwater imaging application.

ACKNOWLEDGMENTS

[1] I. S. F. Jones, "High resolution underwater acoustic imaging," in Proceedings of Oceans 1999 MTS/IEEE, 1999, pp. 1093–1097.

[2] V. Murino, C. S. Regazzoni, A. Trucco, and G. Vernazza, "A noncoherent correlation technique and focused beamforming for ultrasonic underwater imaging: A comparative analysis," IEEE Trans. Ultrason. Ferroelectr. Freq. Control **41**(5), 621–630 (1994).

[3] M. Papazoglou and J. L. Krolik, "High resolution adaptive beamforming for three-dimensional acoustic imaging of zooplankton," J. Acoust. Soc. Am. **100**, 3621–3630 (1996).

[4] E. O. Belcher, H. Q. Dinh, D. C. Lynn, and T. J. Laughlin, "Beamforming and imaging with acoustic lenses in small, high-frequency sonars," Proceedings of Oceans 1999 MTS/IEEE **3**, 1495–1499 (1999).

[5] B. Kamgar-Parsi, B. Johnson, D. L. Folds, and E. O. Belcher, "High-resolution underwater acoustic imaging with lens-based systems," Int. J. Imaging Syst. Technol. **8**(4), 377–385 (1997).

[6] K. Erikson, A. Hairston, A. Nicoli, J. Stockwell, and T. White, "128×128 (16 K) ultrasonic transducer hybrid array," Acoust. Imaging **23**, 485–494 (1998).

[7] C. H. Frazier, W. J. Hughes, and W. D. O'Brien, Jr., "Resolution analysis for an amplitude steered array," J. Acoust. Soc. Am. **107**, 2430–2436 (2000).

[8] F. L. Lizzi and K. W. Weil, "Frequency-controlled scanning of ultrasound beams," United States Patent 4,350,917, 21 Sept. 1982.

[9] W. J. Hughes and W. Thompson, Jr., "Tilted directional response patterns formed by amplitude weighting and a single 90° phase shift," J. Acoust. Soc. Am. **59**, 1040–1045 (1976).

[10] W. J. Hughes, W. Thompson, Jr., and R. D. Ingram, "Transducer array scanning system," United States Patent 3,905,009, 9 Sept. 1975.

[11] W. J. Hughes and C. W. Allen, "A shaped PVDF hydrophone for producing low sidelobe beampatterns," Proceedings of the 1992 Symposium on Autonomous Underwater Vehicle Technology, 2–3 June 1992, Washington, D.C.

[12] W. J. Hughes and C. W. Allen, "A spatially phased transducer to form steered beams," Proceedings of SPIE, Medical Imaging 1999: Ultrasonic Transducer Engineering **3664**, 138–146 (1999).

[13] C. H. Frazier, W. J. Hughes, and W. D. O'Brien, Jr., "A high frequency amplitude-steered array for real-time volumetric imaging," J. Acoust. Soc. Am. **112**, 2742–2752 (2002).

[14] J. A. Jensen, "FIELD: A program for simulating ultrasound systems," Med. Biol. Eng. Comput. **34**(1), 351–353 (1996).

[15] Program is available at http://www.it.dtu.dk/~jaj/field/field.html

[16] M. E. Anderson, M. S. Soo, R. C. Bentley, and G. E. Trahey, "The detection of breast microcalcifications with medical ultrasound," J. Acoust. Soc. Am. **101**, 29–39 (1997).

[17] W. F. Walker and G. E. Trahey, "Speckle coherence and implications for adaptive imaging," J. Acoust. Soc. Am. **101**, 1847–1858 (1997).

[18] E. Maione, P. Tortoli, G. Lypacewicz, A. Nowicki, and J. M. Reid, "PSPICE modeling of ultrasound transducers: Comparison of software models to experiment," IEEE Trans. Ultrason. Ferroelectr. Freq. Control **46**(2), 399–406 (1999).

[19] C. A. H. Frazier, "A two-dimensional amplitude-steered array for real-time volumetric acoustic imaging," Ph.D. thesis, University of Illinois at Urbana-Champaign, 2000.

Laser ultrasonics in copy paper: Bending stiffness dependence on temperature and moisture content

Matthew A. Cornwell and Yves H. Berthelot[a]

Woodruff School of Mechanical Engineering, Georgia Institute of Technology, Atlanta, Georgia 30332-0405

The A_0 Lamb mode in copy paper is generated and detected by using laser ultrasonics. The frequency dependence of the group velocity of the A_0 mode is found from the wavelet transform of the measured signal. A best fit of the dispersion curve against predictions based on orthotropic plate theory yields an estimate of the bending stiffness of the sample. The sample is enclosed in an environmental chamber so that the effects of temperature and humidity can be controlled. Results indicate that the bending stiffness decreases with increasing temperature at an approximate rate of 4×10^{-6} N m/°C, and that it decreases with increasing percent moisture content (PMC) at an approximate rate of 2×10^{-5} (N m)/PMC. © *2002 Acoustical Society of America.*
[DOI: 10.1121/1.1518986]

I. INTRODUCTION

An on-line, nondestructive determination of the mechanical properties of paper is mandatory for adequate quality and process control during manufacturing. To this end, there is a need to develop a noncontact sensor capable of measuring the mechanical properties of the product on-line. The first successful method was reported by Luukkala *et al.*,[1] who used a loudspeaker and a microphone to measure the dependence of the transmission of sound through the plate as a function of angle of incidence. This so-called plate-wave resonance technique is based on the coincidence effect and it is consequently limited to bending waves that travel faster than the sound speed in air.[2] Recent advances in miniature air-coupled transducers[3,4] have allowed noncontact material characterization at ultrasonic frequencies despite some limitations due to the impedance mismatch between the air and the sample. An alternative approach is laser ultrasonics,[5] where a pulsed laser generates waves by thermoelastic expansion or ablation, and where detection is achieved with a laser interferometric system. Despite its limitations (such as cost, potential damage at the generation spot, and nontrivial detection system), laser ultrasonic enables direct measurements of the elastic wave propagating in the sample, without limitations imposed by impedance mismatch between air and the sample, or by wave velocity in the sample. Preliminary work by Johnson *et al.*[6,7] demonstrated that laser ultrasonics could be used on paper samples. Recently, Ridgway *et al.*[8] used laser ultrasonics on a variety of paper products moving at velocities up to 15 m/s. They also compared various detecting systems and found that a Mach–Zehnder interferometer gave best results. Recently, Telschow and Deason[9] have proposed an interesting detection system capable of measuring plate-wave motion simultaneously in all planar directions without scanning. It is based on dynamic holography and photorefractive interferometry.

Paper is a very complex material. It is an intricate network of fibers that exhibits some strong anisotropy in its mechanical properties because of fiber alignment in a preferential direction during manufacture. This preferential direction is referred to as the machine direction (MD), while the direction perpendicular to MD is referred to as the cross direction (CD). A third principal axis (ZD), perpendicular to both MD and CD, corresponds to stacking of fiber networks in the thickness direction. Paper is therefore modeled as an orthotropic material,[10] i.e., a medium described by nine elastic constants, or alternately, by three moduli (Young's modulus, shear modulus, and Poisson ratio) in each of the three principal directions, MD, CD, and ZD. Unlike many orthotropic composite plates, paper exhibits an extremely compliant behavior in the thickness direction compared to the other two directions. To add further to the complexity, each fiber contains cellulose, a viscoelastic material, so that the elastic moduli are actually complex quantities.[11,12] Paper is therefore a heterogeneous, anisotropic, viscoelastic material. Nevertheless, ultrasonic velocities of plate waves in paper offer a convenient way to measure some of its elastic constants[10] and its mechanical moduli of elasticity in the linear regime.

The literature on Lamb waves for material characterization is voluminous, as shown in a recent review article by Chimenti.[13] The propagation of laser-generated Lamb waves in anisotropic materials, and the inversion methods to determine the elastic constants of the material, have both been the object of many articles. Every and Sachse[14] showed that the elastic constants could be determined from measurements of group velocities. Castagnède *et al.*[15,16] demonstrated the technique using laser-generated ultrasound in a unidirectional composite plate. The recovery of elastic constants of anisotropic materials by immersion ultrasonic techniques, using transmission and reflection of plane waves, has been extensively studied by Rokhlin and Wang.[17,18] Hosten[12] studied the effects of viscoelasticity on the complex stiffnesses of an orthotropic plate immersed in water, using reflection and transmission of plane waves. Cheng *et al.*[19,20] used the normal-mode expansion method to solve the transient Lamb problem of laser-generated ultrasound in orthotropic plates.

[a]Electronic mail: yves.berthelot@me.gatech.edu

Deschamps and Bescond[21] proposed a clever numerical method to recover the elastic constants of a composite from group velocities, and Audoin *et al.*[22] validated the technique using ultrasound generated and detected by lasers. Guilbaud and Audoin[23] used the wavelet transform of the analytic signal to calculate group velocities and determine the stiffness coefficients of a viscoelastic composite material. Recently, Leymarie *et al.*[24] improved the robustness of the inversion technique by using an objective function based on the maximum-likelihood principle.

An important issue for practical implementation of a laser ultrasonic system in a paper mill is the to assess the effect of environmental conditions close to or on the sheet of paper during manufacture. To obtain meaningful results, it is necessary to measure dependence of bending stiffness on temperature and moisture content. Except for the recent results of Griggs[25] and Cornwell,[26] work in this area has been done by considering only the static moduli[27,28] or by using low-frequency ultrasonic transducers.[29,30] If a laser ultrasonic system is to be implemented for on-line inspection, it is necessary to measure the dependence of the elastic moduli on temperature and moisture by laser ultrasonics. This is the objective of the research presented herein. The method consists of generating, under controlled environmental conditions, a short ultrasonic pulse (A_0 Lamb mode) that propagates in the paper in either the machine direction (MD) or the cross direction (CD). The frequency dependence of the group velocity of the A_0 mode is found from the wavelet transform of the measured signal. A best fit of the measured dispersion curve against predictions based on orthotropic plate theory yields estimates of the bending stiffness and the shear rigidity of the material, in either MD or CD. The main advantage of the wavelet transform in this context is that the dispersion curve can be obtained from a single waveform, whereas two waveforms, recorded at two different source–receiver distances, are needed to measure the phase velocity. In fact, the method proposed here was compared[26] to results obtained by taking the fast Fourier transform of two waveforms. The relative phase dependence on frequency, $\phi(\omega) = k(\omega) \ d$, where d is the separation distance between the two detected signals, is then used to extract the phase velocity $C_{ph}(\omega) = \omega/k(\omega)$. The drawback of the phase method is that it requires a rather delicate handling of phase unwrapping. Unlike other techniques[14–18,21–24] that require signals measured along many angles, and whose objective is to characterize as many elastic constants as possible, the goal of the work presented here is to measure the effects of temperature and moisture on the bending stiffness in either MD or CD. The main objective is not to determine all the elastic constants of the medium. The experimental arrangement and procedure are presented in Sec. II. Signal-processing issues are discussed in Sec. III, specifically the determination of the bending stiffness of the sample from the wavelet transform of the signal. The results are presented and discussed in Sec. IV.

II. EXPERIMENTAL ARRANGEMENT AND PROCEDURE

A block diagram of the experiment is shown in Fig. 1. A Q-switched Nd:Yag laser with a 6-ns pulse duration and an
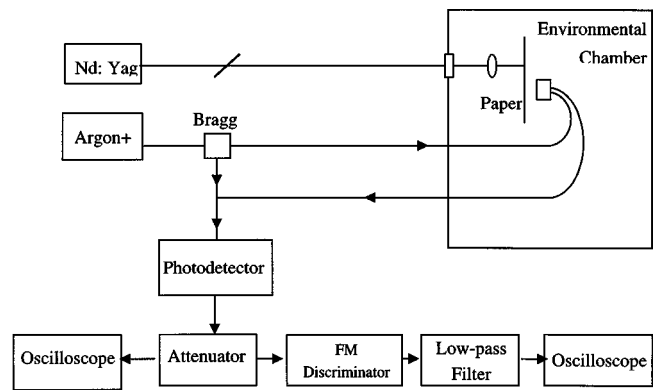
FIG. 1. Block diagram of the experimental arrangement.

energy of 450 mJ at 1064 nm is used for the generation. The energy incident on the paper is reduced to 15–35 mJ by using a half-wave plate and polarizer combination. The light pulse enters an environmental chamber through a fused silica window. The light is focused onto the paper by means of a lens with an 8-mm focal length. The generation spot size is about 1 mm in diameter.[31] Under these conditions, an ultrasonic pulse is launched into the sample. For copy paper with thickness of about $h = 90 \ \mu$m, the frequency-thickness product is sufficiently low that only the lowest Lamb modes are excited: the S_0 and A_0 modes, i.e., the lowest symmetric and antisymmetric plate modes. The quantity $B = \rho h$, which is 80 grams/m^2 for the samples considered, is commonly referred to as the grammage in the paper industry. A fiberoptic Mach–Zehnder interferometer[5] (200 milliwatt argon ion laser, 514 nm) is used to detect the normal component of the particle displacement of the Lamb wave at a distance ranging from 5 to 30 mm from the source. The sample and the detecting probe are placed on a 50-mm translation stage that can be controlled from the outside of the chamber. The fiberoptic probe uses two separate fibers to illuminate the sample and detect the light scattered at the sample surface. This separate fiber arrangement significantly increased the signal-to-noise ratio in our experiment as compared with the single send–receive fiber arrangement initially tested. The fibers are terminated by miniature lenses with graded index of refraction (GRIN lenses). The probe beam is focused with a 20× microscope objective and the detection spot diameter on the sample is estimated to be 10 μm. The Mach–Zehnder interferometer is heterodyned (Bragg cell shift at 40 MHz) and the signal is subsequently FM demodulated, with a low-pass frequency of 750 kHz. The detected signals are captured on a digital oscilloscope and downloaded to a computer for signal analysis. The paper sample is typically a strip of copy paper 30 cm long and about 5 cm wide. The sample is placed on a 20-cm by 20-cm square frame, as shown in Fig. 2. It is held in position with a large clip at one end and with a clip attached to a rubber band at the other end, to ensure some small tension in the sample. The environmental chamber is capable of reaching temperatures between -20 °C and 93 °C, and relative humidities between 7% and 95%. Although some data were taken close to these extreme conditions, most experiments were conducted between 25 °C and 75 °C, and from 10% RH to 70% RH.
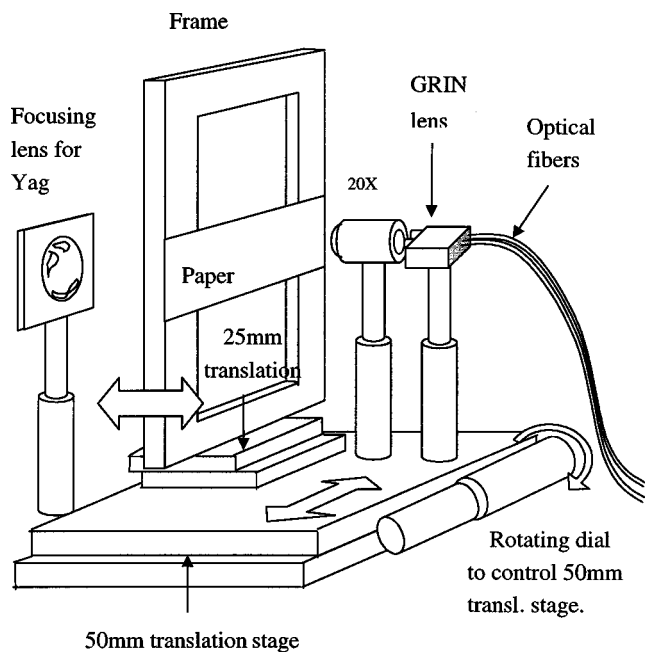
FIG. 2. Experimental setup inside the environmental chamber.

FIG. 3. Signal recorded by the interferometer. The source–receiver distance was 21 mm, the temperature was 50 °C, and the relative humidity was 25%.

The percent moisture content of paper (PMC) is a quantity of importance for pulp products such as paper.[32] It is defined as $(W_1 - W_2)/W_2 \times 100\%$, where W_1 is the weight of the sample under test and W_2 is the weight of the dry paper (at 0% relative humidity). There is no simple, direct relationship between moisture content and relative humidity because there is a hysteresis effect between the two. At a fixed relative humidity, the moisture content differs depending on whether the sample is drying or moisturizing. To calculate the PMC, another sample taken from the same sheet of paper is hung inside the environmental chamber and it is connected to a balance (accurate to 1 mg) positioned outside the chamber by a hook entering the chamber through a small hole bored into the top. The exact mass of water absorbed by the sample can be determined with sufficient accuracy and precision to satisfy the TAPPI standard[32] for measuring moisture content of paper products. Additional details about the experimental arrangements can be found in Ref. 26.

Before taking data, the detection laser is allowed to stabilize for at least 30 min to avoid any amplitude fluctuations in the carrier signal. It is also necessary to let the environmental chamber stabilize at the desired conditions (temperature and humidity). Since paper absorbs moisture and heat more slowly than the air inside the chamber, the system was left at the desired conditions for at least another 15 min before taking data. Then, the power to the chamber is switched off to stop any vibrations and currents from motors and fans. The generation laser is manually triggered and a waveform is recorded for the initial source–receiver distance, $L = 29$ mm. Waveforms are typically averaged two to six times. The translation stage is then adjusted to decrease L by 2.5 mm and the experiment is repeated until L is 11.5 mm. Although ablation at the generation spot on the sample is usually not noticeable after a single shot, it is clearly visible, without a microscope, after five shots at the same location on the sample. In our experiment, the emphasis is not on the
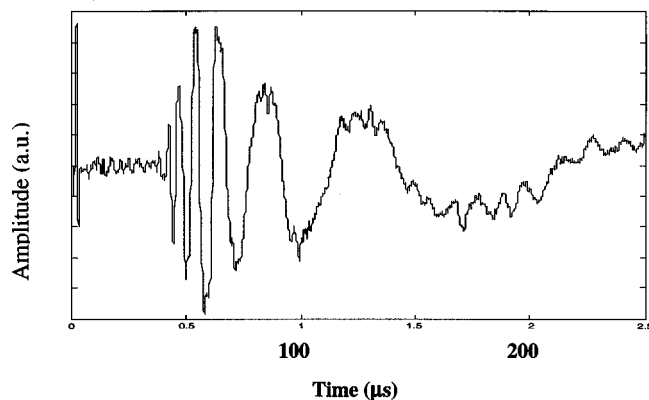
nondestructive capability of the method, but rather it is to obtain signals with sufficiently good signal-to-noise ratios, even at high temperatures and moisture content, to determine the dependence of bending stiffness on temperature and moisture. Ablation was therefore acceptable for this experiment.

III. WAVELET PROCESSING TO OBTAIN BENDING STIFFNESS

A typical signal recorded by the interferometer is shown in Fig. 3. The distance between the source and the receiver is $L = 21$ mm. The signal was propagating in the MD direction of the paper. The temperature is 50 °C and the relative humidity is 25%. The initial spike is the electromagnetic pick-up during the laser discharge. It is followed by a noisy signal (approximately in the interval 10–30 μs) which could correspond to the fast traveling compressional S_0 wave. The out-of-plane amplitude of the S_0 mode is usually very small in copy paper. It is not clearly seen in Fig. 3 because of limitations in signal-to-noise-ratio. The signal of interest for the present study, the A_0 Lamb mode, is clearly seen in Fig. 3. It shows a dispersive trend characteristic of flexural waves, with high frequencies arriving before low-frequency components. To process the signal, a time window is applied to capture only the large-amplitude dispersive signal. In addition, a running average smoothing filter is applied to the later portion of the signal to remove the small high-frequency components superposed to the low-frequency oscillations. Several authors[33–37] have shown that the wavelet transform of the measured signal is a useful tool to measure the dispersion of the signal. Essentially, the wavelet transform is a time–frequency decomposition of the signal. It can be used to plot the amplitude received around a given time in a narrow frequency band. This information leads directly to the group velocity dependence on frequency according to

$$C_{gr}(f) = \frac{L}{t_{\max}(f)}, \qquad (1)$$

where $t_{\max}(f)$ is the arrival time of the maximum amplitude of the wave packet centered around the frequency f. The continuous analytic Morlet wavelet is chosen.[38] The magnitude of the wavelet transform yields a contour plot showing
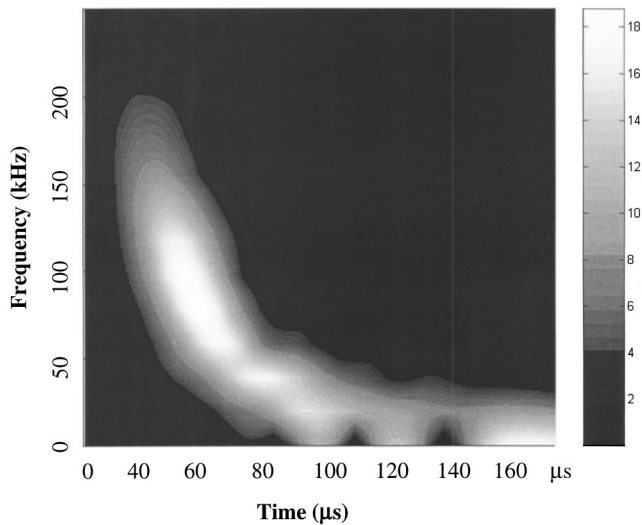
FIG. 4. Wavelet coefficients for the time–frequency decomposition of the signal shown in Fig. 3.

the magnitude of the signal as functions of both scale and arrival time. The scale parameter of the transform is inversely proportional to frequency. The time–frequency plot, an example of which is shown in Fig. 4, shows what is often referred[34] to as a "ridge" that captures the dispersion of the signal. The peak amplitude of the ridge defines the variable denoted by $t_{max}(f)$ in Eq. (1). The peak amplitude can be found either with a simple peak-finder routine or with more sophisticated tools such as a ridge extractor. It should be noted that the analytic Morlet wavelet (complex) gives better results than its real-valued counterpart. The reason is that it is equivalent to using the real transform on the analytic signal, and, as shown by Audoin *et al.*,[22] it represents the energy in the signal, at time t and frequency f. In a recent article, Bernard *et al.*[39] have pointed out that, at some frequencies, the group velocity may actually differ substantially from the energy velocity (Poynting vector integral) when the medium is very absorbing. This effect is neglected in the present paper. The result of the wavelet processing is shown in Fig. 5, which represents the frequency dependence of the group ve-
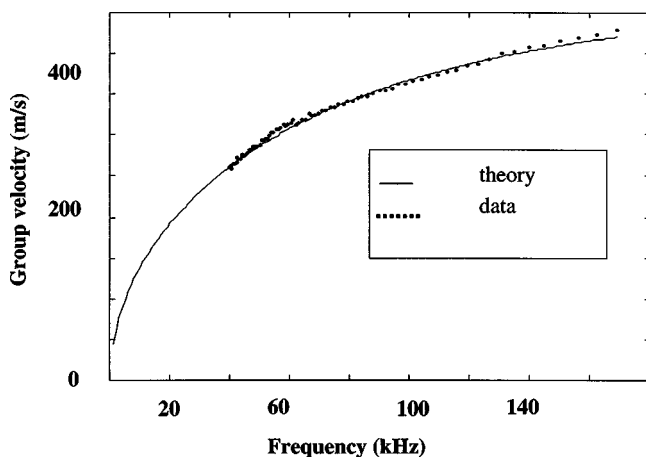
FIG. 5. Frequency dependence of the group velocity extracted from the waveform shown in Fig. 3. The dots correspond to experimental data processed with the wavelet transform. The solid line corresponds to a best fit based on orthotropic plate theory.
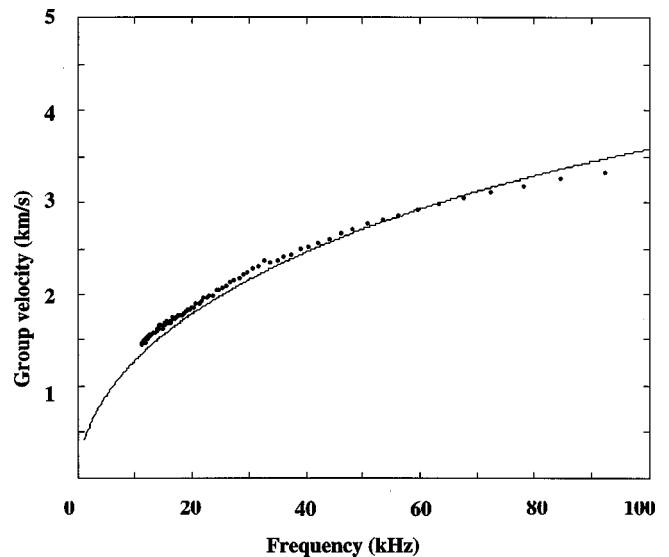
FIG. 6. Validation of the wavelet processing to measure dispersion. Comparison of experimental and predicted dispersion curves for a silicon wafer 304 μm thick, for waves propagating in the [100] direction.

locity extracted from the waveform shown in Fig. 3. The dots correspond to experimental data processed with the wavelet transform. The solid line corresponds to a best fit based on orthotropic plate theory that will be discussed later. Similar results were obtained by using the reassigned short-time Fourier transform spectogram[40] instead of the wavelet transform.

To validate the approach, experiments were conducted with a silicon wafer instead of paper. The properties of the wafer are precisely known. The thickness is 304 μm and the elastic constants are $C_{11} = 16.57 \times 10^{10}$ N/m^2, $C_{12} = 6.39 \times 10^{10}$ N/m^2, and $C_{44} = 7.96 \times 10^{10}$ N/m^2. The dispersion curve is then calculated by solving the Christoffel equation.[41] Figure 6 shows a comparison of the predicted dispersion curve for A_0 waves propagating in the [100] direction with that obtained from experimental data processed with the wavelet transform approach as discussed above. The agreement between measured and predicted dispersion is very good. Note that there are no adjustable parameters in the comparison between the two curves.

The dispersion is often given in terms of phase velocity dependence on frequency, $C_{ph}(\omega)$. The relationship between phase velocity and group velocity[42] is given below in Eq. (2).

$$C_{gr}(\omega) = \frac{C_{ph}(\omega)}{1 - \left[\frac{\omega}{C_{ph}(\omega)}\right]\left[\frac{dC_{ph}}{d\omega}\right]}$$

and

$$C_{ph}(\omega) = \frac{\omega}{\int_0^\omega [d\omega'/C_{gr}(\omega')]}. \tag{2}$$

For pure bending waves, the phase velocity varies as the square root of frequency,[43] so that, at any given frequency, the group velocity is exactly twice the phase velocity. As pointed out by Degtyar and Rokhlin,[44] the determination of elastic constants of orthotropic plates from measurements of phase or group velocities is sensitive to the direction of wave

propagation. In the experiments reported here, only the 0° (MD) and 90° (CD) orientations are considered.

Paper is usually modeled as an orthotropic plate.[10] The full dispersion equation for the A_0 mode in paper, including the effects of rotary inertia, and tension, is rather complicated. Habeger and Jong[45] have shown that, for paper under standard experimental conditions, a highly accurate dispersion equation, valid only along either the MD or CD direction, is given by

$$C_{ph}^4 + \omega^2 \left(\frac{D}{S}\right) C_{ph}^2 - \omega^2 \left(\frac{D}{\rho h}\right) = 0, \qquad (3)$$

where $C_{ph}(\omega)$ is the phase speed of the A_0 mode along the principal axis under consideration (MD or CD). In Eq. (3), $D = Qh^3/12$ is the flexural rigidity (bending stiffness) in the direction of propagation, Q is the planar stiffness defined by $Q = E/(1 - \nu_{12}\nu_{21})$, where E is the Young's modulus and ν are the planar Poisson ratios in the direction of propagation. In Eq. (3), ρ and h are the plate density and thickness, respectively, and $\kappa^2 = h^2/[12(1 - \nu^2)] = D/S$, where S is the shear rigidity. Equation (3) can be rewritten as

$$\left(\frac{D}{\rho h}\right) k^4 - \omega^2 - \kappa^2 k^2 \omega^2 = 0, \qquad (4)$$

or

$$k^4 = \omega^2 (a + k^2 b), \qquad (5)$$

where $k = \omega/C_{ph}$ is the wave number, and where the constants a and b are defined as $a = \rho h/D$ and $b = \rho h/S$, which define the properties of interest in the direction of propagation MD or CD. The quantity a is the ratio of grammage to bending stiffness (units of s^2/m^4), and the quantity b is the ratio of grammage to shear rigidity (units of s^2/m^2). Near-field effects, tension in the sample, and rotary inertia are all neglected in this simplified formulation which is only valid for either MD or CD. The objective of the method is simply to determine the constants a and b; it is not capable of finding the nine elastic constants of the material.

One of the advantages of the technique proposed in this paper is that the material properties a and b can be determined from a single waveform. If the wavelet processing method described previously is used effectively, one obtains the group velocity dispersion curve which can then be compared with the predicted group velocity dispersion curve, $C_{gr}(\omega) = \partial \omega/\partial k$. It was decided to compare group velocities instead of phase velocities because the data processed with the wavelet transform yield group velocity. From Eq. (5), the group velocity dispersion explicitly depends on the constants a and b according to

$$C_{gr} = \frac{\sqrt{2}\sqrt{b\omega^2 + \sqrt{b^2\omega^4 + 4a\omega^2}}}{b\omega + \dfrac{b^2\omega^3 + 2a\omega}{\sqrt{b^2\omega^4 + 4a\omega^2}}}. \qquad (6)$$

The dispersion is mostly dependent on the bending stiffness. The shear rigidity becomes important at the very high frequencies. Equation (6) differs from Eq. (21) of Ref. 35 because the authors base their derivation on a Taylor series

TABLE I. Average material constants and their variances for each set of conditions.

Temp.	RH	PMC	Avg. bending stiffness (Nm×10⁻⁴)	% Standard deviation	Avg. shear rigidity (N/m×10⁴)	% Standard deviation
25 °C	10	4.8	6.05	6.81	1.48	12.19
	25	5.9	5.81	5.11	1.31	10.45
	50	7.7	5.78	3.46	1.41	10.92
	60	8.2	5.54	9.73	1.38	9.89
	70	10.2	5.36	8.56	1.31	14.74
50 °C	10	4.0	5.36	8.23	1.49	11.21
	25	5.2	5.15	6.86	1.35	9.71
	50	6.6	4.81	7.52	1.37	9.37
	60	7.5	4.41	5.54	1.24	10.71
75 °C	10	3.4	4.30	11.46	1.43	12.48
	25	4.8	3.87	13.28	1.41	16.79
	50	6.3	3.64	11.38	1.29	11.41
	60	7.0	3.39	10.01	1.22	12.32

approximation of the dispersion relation, initially proposed by Hutchins et al.,[46] whereas Eq. (5) above does not require such an approximation. To measure material properties from the data, the dispersion curve is compared to a prediction in which the material parameters are adjusted to minimize (in the least-square sense, using the function "fmins" under the MATLAB™ environment) the difference between the measured and predicted dispersion curves.

IV. RESULTS AND DISCUSSION

A standard piece of copy paper with grammage of 80 grams/m² was placed in the environmental chamber. For each set of environmental conditions, signals were recorded along the machine direction (MD) for source–receiver distances decreasing from 29 mm to 11.5 mm, by steps of 2.5 ± 0.1 mm. Each signal was averaged two to six times. Occasionally, some signals were found to be of poor quality and, consequently, discarded. The experiment was repeated for the same environmental conditions along two physically different paths in the paper, also in the machine direction. The paths were parallel and separated by a distance of about 10 mm. Therefore, each "measured" material property represents a spatial average over the paper sample. Collecting such a large number of waveforms enables one to calculate the standard deviation of the measured properties. This is a useful measure because of the intrinsic spatial variability of paper. The bending stiffness and the shear rigidity were extracted from the data using the wavelet procedure described in Sec. II. The results are shown in Table I. Figure 7 shows the dependence of bending stiffness on temperature for relative humidity of 10% and 60%. Figure 8 shows the dependence of the bending stiffness on percent moisture content (PMC) at 25 °C, 50 °C, and 75 °C. The vertical bars represent a 1-σ standard deviation. The results show that the bending stiffness decreases with increasing temperature at a rate of about 4×10^{-6} N m/°C, and that it decreases with increasing percent moisture content (PMC) at a rate of about 2×10^{-5} (N m)/PMC. The trends for the shear rigidity cannot be extracted from the data because the standard deviations exceed the measured dependence on temperature or moisture content.
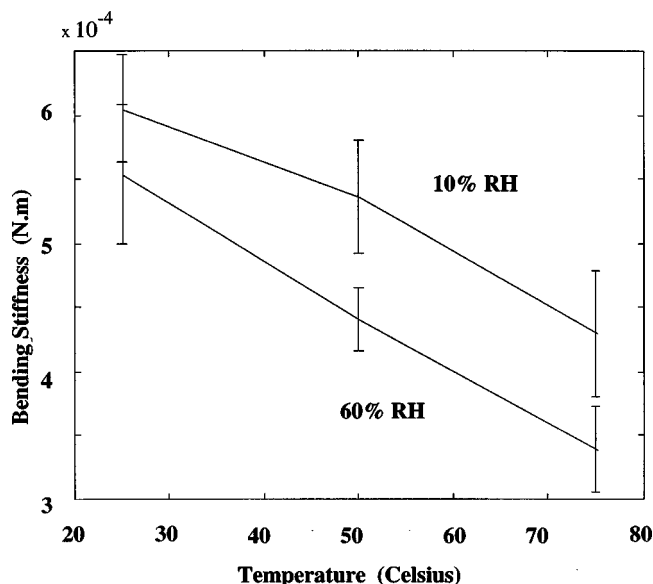
FIG. 7. Dependence of the bending stiffness of copy paper (MD) on temperature at 10% and 60% relative humidity. The vertical bars represent a $1-\sigma$ standard deviation.

Equation (1) shows that the relative error on the group velocity is the sum of the relative error on the source–receiver distance and the relative error on the determination of the time at which the dispersion contour is maximum. The positioning system is such that the source–receiver distance is known within 0.1 mm. Thus, the relative error on source–receiver distance is less than 1%. In contrast, the relative error on arrival time can be substantial, up to 10% at the higher frequencies, and it clearly sets the limit on the relative error of the group velocities.

The decrease of bending stiffness with increasing temperature is consistent with the expectation that activation en-

FIG. 8. Dependence of the bending stiffness of copy paper (MD) on percent moisture content (PMC), at 25 °C, 50 °C, and 75 °C. The vertical bars represent a $1-\sigma$ standard deviation.

ergy leads to redistributions of polymer conformations[29,30] and subsequent fiber mobility. When a polymer such as cellulose is stressed, there is a redistribution of molecular states that requires thermal energy. There is a spectrum of thermal relaxations in cellulose, each one with its own time constant. As temperature increases, more thermal energy per degree of freedom is available for polymer motion, and redistributions of polymer conformations occur more rapidly in response to stress changes. Consequently the mass-specific modulus of elasticity (expressed as Young's modulus divided by density, E/ρ) is decreased at higher temperatures. Using contact low-frequency transducers, Berger et al.[29,30] have shown that the ratio E/ρ decreases almost linearly with increasing temperature, in the range of temperatures experienced online. Bending stiffness is related to this parameter with an additional dependency on thickness. However, with standard online conditions, dimensional changes with temperature are typically small and can be neglected. Thus, it would be expected that bending stiffness would also decrease linearly with increasing temperature, a trend that is confirmed by the results shown in Fig. 7.

At constant temperature, added moisture increases the free volume of the polymeric structure. The result is a reduction in the required activation energy. The relaxations are generally intensified, and shifted to lower temperatures. Thus, moisture is called a "plasticizer" and, as with temperature, added moisture will decrease the mass-specific modulus of elasticity E/ρ. Berger et al.[29,30] reported a linear dependence for PMC less than 20%. It should be noted that moisture has a significant effect on the length of the paper sample, but thickness changes can still be neglected. Therefore, bending stiffness should also decrease linearly with an increase in moisture, a trend that is confirmed by the results shown in Fig. 8.

It is important to realize that measuring dispersion to extract bending stiffness is not a very sensitive method. Indeed, for purely flexural waves, the phase velocity is proportional to the fourth root of the bending stiffness.[43] This dependence on a small power is a fundamental limitation of the method presented here. Recently, Yang et al.[47] have used a method based on neural networks to analyze the data and extract material properties without the need to calculate the dispersion curves from the data but the computation time is, however, significantly larger than with the wavelet method presented here.

A separate experiment was conducted to distinguish between the intrinsic measurement error and the spatial variability of the paper sample. The intrinsic measurement error is understood to encompass all errors associated with the experiment and the processing of the signals. Results indicate that the standard deviation of relative errors in bending stiffnesses measured over an identical source–receiver path is about 4%, but that it becomes 14% if the measurements are made over different paths (albeit with the same source–receiver distance). This "error" actually captures the physical nature of paper, which has strong spatial heterogeneities. Finally, we note that a possible source of bias error in the data is the localized heating associated with the detection laser (CW). However, the time during which the laser was
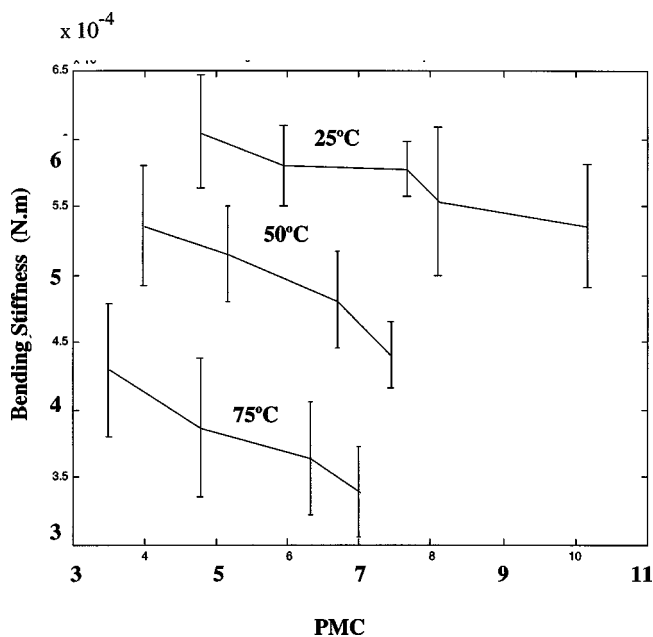
Matthew A. Cornwell and Yves H. Berthelot: Laser ultrasonics in copy paper

actually illuminating the paper was kept to a minimum, and first-order estimates of the error associated with this added heating indicates that this effect is very small. Most of the scatter in the estimated bending stiffnesses is caused by the spatial variability of the paper.

V. CONCLUSIONS

A laser ultrasonic system has been used to generate and measure the A_0 Lamb mode in copy paper placed inside an environmental chamber with controlled temperature and relative humidity. The frequency dependence of the group velocity was determined by using the wavelet transform of the signals. One advantage of the wavelet transform is that the dispersion curve can be obtained from a single measurement. The bending stiffness of the sample was found by comparing the dispersion curve with that predicted from orthotropic plate theory. The experiment was repeated for a range of temperatures and relative humidity. Results indicate that the bending stiffness decreases with increasing temperature at an approximate rate of 4×10^{-6} N m/°C, and that it decreases with increasing percent moisture content (PMC) at an approximate rate of 2×10^{-5} (N m)/PMC. These results are consistent with results obtained at lower frequencies with contact transducers.[16,17] The relatively large errors associated with the measured bending stiffnesses are mostly due to two factors. First, the phase velocity depends only on the fourth root of the bending stiffness, and, second, paper is inherently heterogeneous and its mechanical properties vary throughout the sample. Despite its limitations, the laser ultrasonics method combined with the wavelet processing was found to be useful in measuring the dependence of the bending stiffness of copy paper on both temperature and moisture content.

[1] M. Luukkala, P. Heikkila, and J. Surakka, "Plate wave resonance—A contactless test method," Ultrasonics **10**, 201–208 (1971).

[2] M. Khoury, G. Tourtollet, and A. Schroder, "Contactless measurement of elastic Young's modulus of paper by an ultrasonic technique," Ultrasonics **37**, 133–139 (1999).

[3] D. Schindel and D. A. Hutchins, "Applications of micro-machined capacitance transducers in air-coupled ultrasonics and nondestructive evaluation," IEEE Trans. Ultrason. Ferroelectr. Freq. Control **42**(1), 51–58 (1995).

[4] M. Castaings and P. Cawley, "The generation, propagation, and detection of Lamb waves in plates using air-coupled ultrasonic transducers," J. Acoust. Soc. Am. **100**, 3070–3077 (1996).

[5] C. B. Scruby and L. E. Drain, *Laser Ultrasonics: Techniques and Applications* (Hilger, New York, 1990).

[6] M. A. Johnson, Y. H. Berthelot, P. H. Brodeur, and L. A. Jacobs, "Investigation of laser generation of Lamb waves in copy paper," Ultrasonics **34**, 703–710 (1996).

[7] M. A. Johnson and Y. H. Berthelot, "Laser ultrasonics in copy paper," Opt. Eng. **36**(2), 408–416 (1997).

[8] P. L. Ridgway, A. J. Hunt, M. Quinby-Hunt, and R. E. Russo, "Laser ultrasonics on moving paper," Ultrasonics **37**, 395–403 (1999).

[9] K. L. Telschow and V. A. Deason, "Imaging laser ultrasonics measurement of the elastodynamic properties of paper," International Ultrasonics Symposium, 2001 IEEE, New York, edited by D. Yuhas and S. Schneider, Vol. 1, 737–745 (2001).

[10] C. C. Habeger, R. W. Mann, and G. A. Baum, "Ultrasonic plate waves in paper," Ultrasonics **17**, 57–62 (1979).

[11] A. Bonnin, R. Huchon, and M. Deschamps, "Ultrasonic waves propagation in absorbing thin plates: Application to paper characterization," Ultrasonics **37**, 555–563 (2000).

[12] B. Hosten, "Reflection and transmission of acoustic plane waves on an immersed orthotropic and viscoelastic solid layer," J. Acoust. Soc. Am. **89**, 2745–2752 (1991).

[13] D. E. Chimenti, "Guided waves in plates and their use in materials characterization," Appl. Mech. Rev. **50**(5), 247–284 (1997).

[14] A. G. Every and W. Sachse, "Determination of the elastic constants of anisotropic solids from acoustic wave group velocity measurements," Phys. Rev. B **42**, 8196–8205 (1990).

[15] B. Castagnède, J. T. Jenkins, and W. Sachse, "Optimal determination of the elastic constants of composite materials from ultrasonic wave-speed measurements," J. Appl. Phys. **67**(6), 2753–2761 (1990).

[16] B. Castagnède, K. Y. Kim, W. Sachse, and M. O. Thompson, "Determination of the elastic constants of anisotropic materials using laser-generated ultrasonic signals," J. Appl. Phys. **70**(1), 150–157 (1991).

[17] S. I. Rokhlin and W. Wang, "Double through-transmission bulk wave method for ultrasonic phase velocity measurement and determination of elastic constants of composite materials," J. Acoust. Soc. Am. **91**, 3303–3312 (1992).

[18] S. I. Rokhlin and W. Wang, "Measurements of elastic constants of very thin anisotropic plates," J. Acoust. Soc. Am. **94**, 2721–2730 (1993).

[19] J.-C. Cheng and Y. H. Berthelot, "Theory of laser-generated transient Lamb waves in orthotropic plates," J. Phys. D **29**, 1857–1867 (1996).

[20] J.-C. Cheng and S. Y. Zhang, "Quantitative theory for laser-generated Lamb waves in orthotropic thin plates," Appl. Phys. Lett. **74**(14), 2087–2089 (1999).

[21] M. Deschamps and C. Bescond, "Numerical method to recover the elastic constants from ultrasound group velocities," Ultrasonics **33**(3), 205–211 (1995).

[22] B. Audoin, C. Bescond, and M. Deschamps, "Measurement of stiffness coefficients of anisotropic materials from pointlike generation and detection of acoustic waves," J. Appl. Phys. **80**(7), 3760–3771 (1996).

[23] S. Guilbaud and B. Audoin, "Measurement of the stiffness coefficients of a viscoelastic composit material with laser-generated and detected ultrasound," J. Acoust. Soc. Am. **105**, 2226–2235 (1999).

[24] N. Leymarie, C. Aristégui, B. Audoin, and S. Baste, "Identification of complex stiffness tensor from waveform reconstruction," J. Acoust. Soc. Am. **111**, 1232–1244 (2002).

[25] D. A. Griggs, "A laser-based ultrasonic system to measure the mechanical properties of paper products in a controlled," Master thesis, Georgia Institute of Technology, April 2001.

[26] M. A. Cornwell, "Determination of the bending stiffness of copy paper and its dependence on temperature and moisture using laser ultrasonics Lamb waves," Master thesis, Georgia Institute of Technology, December 2001.

[27] N. L. Salmen, "Responses of paper properties to changes in moisture content and temperature," in *Products of Papermaking, Transactions of the Tenth Symposium held at Oxford: September 1993*, edited by C. F. Baker (Pira International, Surrey, United Kingdom, 1994), Vol. 1.

[28] N. L. Salmen and E. L. Back, "Moisture-dependent termal softening of paper, evaluated by its elastic modulus," Tappi J. **63**(6), 117–120 (1980).

[29] B. J. Berger, C. C. Habeger, and B. M. Pankonin, "The influence of moisture and temperature on the ultrasonic viscoelastic properties of cellulose," J. Pulp Pap. Sci. **15**(5), 170–177 (1989).

[30] B. J. Berger and C. C. Habeger, "Influences of nonequilibrium moisture conditions on the in-plane ultrasonic stiffnesses of cellulose," J. Pulp Pap. Sci. **15**(5), 160–165 (1989).

[31] To reduce ablation effects, a line source with length 8 mm was initially used instead of a point source. However, it was found that diffraction effects associated with the length of the source complicated the interpretation of the results.

[32] TAPPI standard T 412 om-94, "Moisture in pulp, paper, and paperboard," 1994.

[33] J.-B. Han, J.-C. Cheng, and Y. H. Berthelot, "Wavelet analysis of ultrasonic Lamb waves excited by pulsed laser in a composite plate," in *Review of Progress in Nondestructive Evaluation*, edited by R. Thompson and D. Chimenti (Plenum, New York, 1999), Vol. 18, pp. 695–701.

[34] A. Abbate, D. Klimek, P. Kotidis, and B. Anthony, "Analysis of dispersive ultrasonic signals by the ridges of the analytic wavelet transform," in *Review of Progress in Nondestructive Evaluation*, edited by R. Thompson and D. Chimenti (Plenum, New York, 1999), Vol. 18, pp. 703–710.

[35] Y. Hayashi, S. Ogawa, H. Cho, and M. Takemoto, "Noncontact estimation of thickness and elastic properties of metallic foils by the wavelet transform of laser-generated ultrasound," NDT & E Int. **32**, 21–27 (1999).

[36] H. C. Park and D.-S. Kim, "Evaluation of the dispersive phase and group velocities using harmonic wavelet transform," NDT & E Int. **34**, 457–467 (2001).

[37] M. Cornwell, Y. H. Berthelot, and C. C. Habeger, "Noncontact determination of the bending stiffness of paper using laser ultrasonics and wavelet analysis: Effects of temperature and moisture content," International Ultrasonics Symposium, 2001 IEEE, New York, edited by D. Yuhas and S. Schneider, Vol. 1, 747–750 (2001).

[38] E. Foufoula-Georgiou and P. Kumar, *Wavelets in Geophysics* (Academic, New York, 1994).

[39] A. Bernard, M. J. S. Lowe, and M. Deschamps, "Guided waves energy velocity in absorbing and nonabsorbing plates," J. Acoust. Soc. Am. **110**, 186–196 (2001).

[40] M. Niethammer, L. J. Jacobs, J. Qu, and J. Jarzynski, "Time-frequency representation of Lamb waves using the reassigned spectogram," J. Acoust. Soc. Am. **107**(5), pt. 1, L19–L23 (2000).

[41] B. A. Auld, *Acoustic Fields and Waves in Solids*, 2nd ed. (Krieger, Malabar, FL, 1990), Vol. I.

[42] M. Born and E. Wolf, *Principles of Optics*, 6th ed. (Pergamon, New York, 1980), p. 21.

[43] A. D. Pierce, *Acoustics: An Introduction to Its Physical Principles and Applications* (McGraw-Hill, New York, 1981), p. 128.

[44] A. D. Degtyar and S. I. Rokhlin, "Comparison of elastic constant determination in anisotropic materials from ultrasonic group and phase velocity data," J. Acoust. Soc. Am. **102**, 3458–3466 (1997).

[45] C. Habeger and J. Jong, "Paper A_0 Signal Analysis," Institute of Paper Science and Technology, private communication (February 2000). A useful reference for the case of an isotropic plate is J. W. S. Rayleigh, *The Theory of Sound*, 2nd ed. (Dover, New York, 1945), Vol. I, Art. 188, pp. 296–297.

[46] D. A. Hutchins and K. A. Lundgren, "A laser study of transient Lamb waves in thin materials," J. Acoust. Soc. Am. **85**, 1441–1448 (1989).

[47] J. Yang, J.-C. Cheng, and Y. H. Berthelot, "An inversion method to determine the elastic constants of fiber-reinforced composite plates by means of wavelet transforms and artificial neural networks," J. Acoust. Soc. Am. **111**, 1245–1250 (2002).

The effect of large openings on cavity amplification at ultrasonic frequencies

Michael J. Anderson,[a] K. Scott Line, and Ralph S. Budwig
Department of Mechanical Engineering, University of Idaho, Moscow, Idaho 83844

It is sometimes desired to exploit acoustic amplification in a cavity that is not entirely enclosed. Because of the presence of openings in the cavity, acoustic energy will leave the cavity and degrade the degree of amplification. The extent of this problem is unknown when the size of the openings becomes large relative to a wavelength. The present paper describes a quantitative estimation of the effect of large openings on the amplification performance of an acoustic cavity. Air was assumed to be the working medium. The amplification taking place in a rigid-walled rectangular channel excited by a transducer flush-mounted in one wall was compared to the amplification that would take place in a bounded rectangular resonator excited by the same transducer. It was found, for frequencies in the range 25 kHz–1 MHz, that source ka's greater than 37 and 42 were required in order for the collimation of the transducer beam to overcome the leakage of acoustic energy through the openings for one- and two-half wavelength resonances, respectively. Experimental measurements conducted over source ka's ranging from 6.5 to 26.1, resulted in quality factors 8%–18% lower than theoretically predicted values for one-, two-, and three-half wavelength resonances. © *2002 Acoustical Society of America.* [DOI: 10.1121/1.1513649]

PACS numbers: 43.35.Zc [YHB]

I. INTRODUCTION

Resonant acoustic cavities have many applications. They are used to determine properties of fluids,[1] absorb sound,[2] and to amplify sound pressure levels when intense sound fields are required. An application requiring intense acoustic sound pressure fields is the use of acoustic radiation pressure to apply forces to particles entrained in a fluid. The forces may be used to levitate,[3,4] deform,[5,6] or concentrate[7–13] the particles. In these applications, it is often easier to achieve high sound pressure levels using resonant cavity amplification rather than a direct application of powerful, but inefficient transducers.

It is often the case that one wishes to employ acoustic radiation forces to move small particles entrained in a flowing,[7–9,11,12] rather than static[10,13] fluid. If a cavity is used in this application to achieve high sound pressure levels, openings are required to allow fluid flow through the cavity. Because the openings are often large relative to a wavelength, it is presumed that the presence of openings could degrade the degree of cavity amplification.

A question of practical interest is the effect of large openings on resonant cavity amplification. Misalignment between the exciting transducer and the opposite reflecting wall can cause acoustic energy to leave the cavity through a large opening.[8] Otherwise, if the cavity walls are aligned with the exciting transducer, the amount of acoustic energy that escapes through the openings is not quantitatively known.

The effect of small openings on resonator performance is well known. The fundamental Helmholtz resonator, defined by the resonator volume, neck area, and neck length, all smaller than a wavelength, will radiate sound as a simple source. The quality factor of the Helmholtz resonator is related to the hole size, cavity volume, and neck length.[14] Other models, such as for automobiles,[15] musical instruments,[16] or mufflers,[17] relax the condition that the volume is less than a wavelength in size, but still require that the opening(s) is (are) much smaller than a wavelength.

In this paper, we calculated the acoustic energy loss through large openings in a three-dimensional resonator. By exploiting the resonator geometry and limiting consideration to a resonance of plane longitudinal modes, the calculation was performed with a two-dimensional model. The working fluid was assumed to be air, and mean motion of the working fluid was not considered. The resonator was modeled as a rectangular channel, unbounded in one dimension. Embedded in one of the walls of the channel was a plane piston transducer. Absorption was modeled in the body of the air medium, and approximate boundary layer losses were included. Acoustic energy loss was quantified by comparing quality factors predicted by the rectangular channel model to those that would take place in a similarly sized resonator without openings.

II. RESONATOR MODELS

The three-dimensional resonator under consideration was a rectangular channel, shown in Fig. 1. The channel consisted of four planar rigid walls. The channel was of width b, and depth L, and its extent in the x direction was unbounded. A rectangular transducer, modeled to be a rigidly vibrating plane, was fixed to the bottom surface of the resonator. The transducer was of width $2a$. If the transducer vibrated as a rigid plane, and the width dimension b was much greater than a wavelength, it would be appropriate to consider a two-dimensional model of the resonator, defined
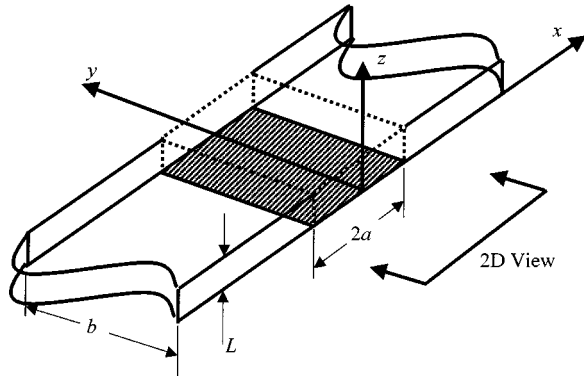
FIG. 1. Three-dimensional geometry for channel cavity. The shaded region is the area occupied by the transducer. The dotted lines define the volume directly in front of the transducer. The resonator is unbounded in the x direction.

by the two-dimensional view shown in Fig. 1. If the transducer width $2a$ was much greater than a wavelength, the collimated acoustic field would be concentrated in the volume directly in front of the transducer, indicated by dotted lines in Fig. 1. We considered openings of depth dimension L that were $\lambda/2$ or greater, and a width b much larger than λ.

A comparison of two models was used to estimate the effect of large openings on resonant cavity amplifications. One model, denoted as the "open resonator," consisted of a rectangular channel with rigid walls as shown in Fig. 2. The depth dimension L as shown separated the walls. A rectangular transducer was flush-mounted to one of the walls. The two-dimensional open-resonator configuration shown in Fig. 2 coincides with the view indicated in Fig. 1. A second model, denoted the "closed resonator," consisted of a rectangular cavity excited by a transducer of equal size to that contained in the open-resonator configuration. A diagram of the closed resonator is shown in Fig. 3. It too had a depth dimension L. A rigid piston of width $2a$ that moved harmonically with velocity amplitude U excited each cavity. A comparison area for the open-resonator configuration was defined by the region directly in front of the exciting transducer, indicated by the dotted lines in Fig. 2. It would be expected that the acoustic field in the comparison area of the open-resonator configuration would be less than that encountered in the closed-resonator configuration.

For frequencies $\Delta\omega$ near a longitudinal depth resonance of a closed rectangular cavity, i.e., $\Delta\omega = \omega - \omega_n$, where $\omega_n \approx n2\pi c_0/2L$, an approximation for the acoustic pressure is

$$p_n(x,z)e^{-i\omega t} \approx \rho_0 c_0 U \left(\frac{2Q_n}{k_n L} \right) \frac{\cos[k_n(L-z)]}{1 - i2Q_n \dfrac{\Delta\omega}{\omega_n}} e^{-i\omega t}. \quad (1)$$
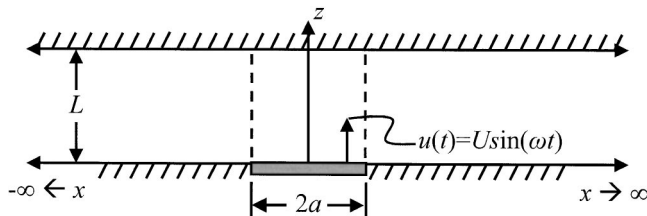
FIG. 2. Open-resonator configuration.
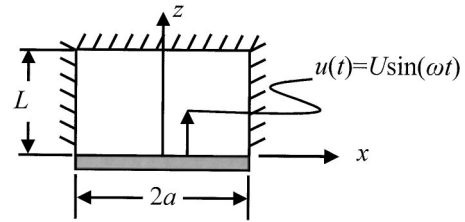
FIG. 3. Closed-resonator geometry.

In this expression, ρ_0 and c_0 are the ambient density and equilibrium sound speed of air, $k_n = \beta_n - i\alpha_n$ is the nominal wave number at resonance; $\beta_n \approx \omega_n/c_0$ is the real (propagating) part of the wave number, and α_n is the cavity absorption at the resonance frequency. The model adopted for the wave number k is contained in the appendix. The quality factor

$$Q_n \approx \frac{n\pi}{2\alpha_n L} \quad (2)$$

is a measure of the potential amplification that can be provided by the cavity at the nth longitudinal resonance, when $L \approx n\lambda/2$. In the following, the harmonic factor $e^{-i\omega t}$ will be suppressed.

An expression for the acoustic pressure in the air between the walls of the open-resonator configuration can be obtained using a Fourier transform method. The equation to be solved is

$$\nabla^2 p + k^2 p = 0, \quad (3)$$

where k, including a model for absorption, is the complex wave number as before. The boundary conditions are

$$\left. \frac{\partial p}{\partial z} \right|_{z=0} = i\rho_0 \omega U H(x), \quad (4a)$$

$$\left. \frac{\partial p}{\partial z} \right|_{z=L} = 0. \quad (4b)$$

The expression $H(x)$ is a Heaviside function, where $H(x) = 1$ for $|x| < a$ and zero elsewhere. Using the following form of the Fourier transform,

$$\Im[p(x,z)] = \frac{1}{2\pi} \int_{-\infty}^{\infty} p(x,z,t) e^{ik_x x} dx = \hat{p}(k_x, z),$$

the Helmholtz equation (3) and boundary conditions (4) are transformed to

$$\frac{\partial^2 \hat{p}}{\partial z^2} + (k^2 - k_x^2)\hat{p} = 0, \quad (5)$$

$$\left. \frac{\partial \hat{p}}{\partial z} \right|_{z=0} = i\omega\rho_0 U \frac{a}{\pi} \mathrm{sinc}(k_x a), \quad (6a)$$

$$\left. \frac{\partial \hat{p}}{\partial z} \right|_{z=L} = 0. \quad (6b)$$

The Fourier transform of pressure satisfying Eqs. (5) and (6) is

Anderson *et al.*: Ultrasonic resonators with large openings

$$\hat{p}(k_x,z)=i\omega\rho_0 UL\frac{\cos[\sqrt{k^2-k_x^2}(L-z)]}{\sqrt{k^2-k_x^2}L\sin[\sqrt{k^2-k_x^2}L]}\frac{a}{\pi}\text{sinc}(k_xa).$$

$$(7)$$

The acoustic pressure $p(x,z)$ in the open-resonator configuration is given by the inverse Fourier transform of Eq. (7),

$$p(x,z)=i\omega\rho UL\int_{-\infty}^{\infty}\left[\frac{\cos[\sqrt{k^2-k_x^2}(L_z-z)]}{\sqrt{k^2-k_x^2}L\sin[\sqrt{k^2-k_x^2}L]}\right.$$

$$\left.\times\frac{a}{\pi}\text{sinc}(k_xa)\right]e^{-ik_xx}dk_x.$$

$$(8)$$

In general, a closed form expression for $p(x,z)$ is not known. In this paper, computations of $p(x,z)$ were obtained by numerical evaluation of the inverse transform integral.

There are a number of practical considerations relevant to the numerical inversion of the Fourier transform of the acoustic pressure, Eq. (8). For $z>0$, the integrand is bounded by the evanescent behavior of the acoustic field when $k_x>\beta$. When $z=0$, the aperture function $(a/\pi)\text{sinc}(k_xa)$ bounds the integrand. Consequently, for sources with $ka\gg1$, the limits of the integral can be replaced with a finite k_x^* appropriately larger than β. Second, because of the smallness of the absorption coefficient α for air, the poles of the integrand can dominate the integral. We found that the sharpness of the poles prevented the use of a direct adaptive integrator of the type described in Ref. 18. In general, an inverse Fourier transform integral with finite limits is written as

$$p(k_x^*,x,z)=\int_{-k_x^*}^{k_x^*}\hat{p}(k_x,z)e^{-ik_xx}dk_x,$$

where k_x^* is the limit of the truncated integral. Using the fundamental theorem of calculus,[19] the integral can be transformed to

$$\frac{\partial p(k_x^*,x,z)}{\partial k_x^*}=\hat{p}(k_x^*,z)e^{-ik_x^*x},$$

$$(9)$$

which is a differential equation with the dependent variable being the acoustic pressure $p(k_x^*,x,z)$. Since the contributions to acoustic pressure are evanescent for $|k_x^*|>\beta$, we may safely use the initial condition $p(-k_x^*,x,z)=0$ to solve the differential equation (9). Specifically, to invert the Fourier transform of the acoustic pressure (8), one solves the differential equation

$$\frac{\partial p(k_x^*x,z)}{\partial k_x^*}$$

$$=i\omega\rho UL\left[\frac{\cos[\sqrt{k^2-k_x^*}(L_z-z)]}{\sqrt{k^2-k_x^*}L\sin[\sqrt{k^2-k_x^*}L]}\frac{a}{\pi}\text{sinc}(a)\right]e^{-ik_x^*x},$$

subject to the initial condition $p(-k_x^*,x,z)=0$. The value of the inverse transform $p(k_x^*,x,z)$ can be obtained using a differential equation solver designed for stiff systems[20] (we used function ODE15S in MATLAB). It may be the case that the properties of the inverse Fourier transform for acoustic pressure just described may also allow an asymptotic approximation in closed form.
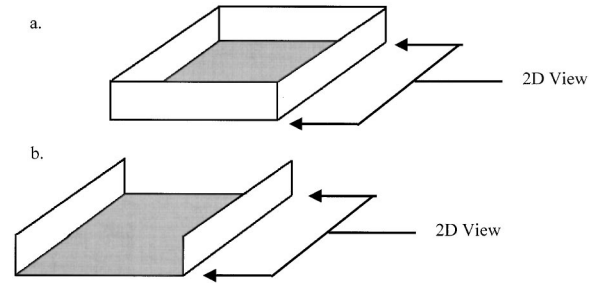
FIG. 4. Walls used in absorption model for closed- (a) and open- (b) resonator configurations. The shaded portion is the transducer, and the walls are perpendicular to the transducer.

Since resonators are designed to operate at a resonance frequency, predicting their performance depends crucially on the model used for absorption. A simple absorption model for the open- and closed-resonator configurations was chosen to capture the appropriate physics. The total attenuation α, was modeled by three components,

$$\alpha=\alpha_{vt}+\alpha_r+\alpha_b,$$

$$(10)$$

where α_{vt} is the viscous and thermal body absorption within the cavity volume, α_r is the molecular relaxation absorption withing the cavity volume, and α_b models the viscous shear and thermal conduction at the boundaries. In general, each component of the absorption model is dependent on frequency, and a detailed description of the attenuation models is contained in the Appendix.

The absorption models adopted in the present investigation used a different sidewall area for the open- and closed-resonator configurations. For the closed-resonator configuration, the boundary layer losses were assumed to be caused by the presence of four sidewalls, as shown in Fig. 4. For the open-resonator configuration, it was reasoned that fluid shear and thermal conduction would occur at the two sidewalls. Acoustic waves propagating in the $\pm x$ direction would not encounter a boundary in the open-resonator configuration. The two-wall model for boundary layer losses in the open-resonator configuration is shown in Fig. 4. The contribution to wave number by viscous shear and heat conduction at the boundaries was modeled by

$$\alpha_b=\frac{C}{2A}\left(1+\frac{(\gamma-1)}{\sqrt{\text{Pr}}}\right)\sqrt{\frac{2\mu\omega}{\rho_0c_0^2}}+\frac{1}{L}\sqrt{\frac{2\mu\omega}{\rho_0c_0^2}}\frac{(\gamma-1)}{\sqrt{\text{Pr}}},$$

$$(11)$$

where C is the wall perimeter, and A is the transducer cross section $A=(2a)^2$. For the open-resonator configuration, the wall perimeter was set to $C=2(2a)$, while for the closed-resonator configuration, the wall perimeter was set to $C=4(2a)$. The second term in α_b accounts for thermal conduction at the ends—this includes the source transducer. Viscous boundary layer losses at the end were assumed to be minimal. Details of the boundary layer absorption coefficient α_b in the wave number model are discussed in the Appendix.

III. NUMERICAL RESULTS

As would be expected, a trade-off between beam collimation and absorption will determine the performance of the

a.
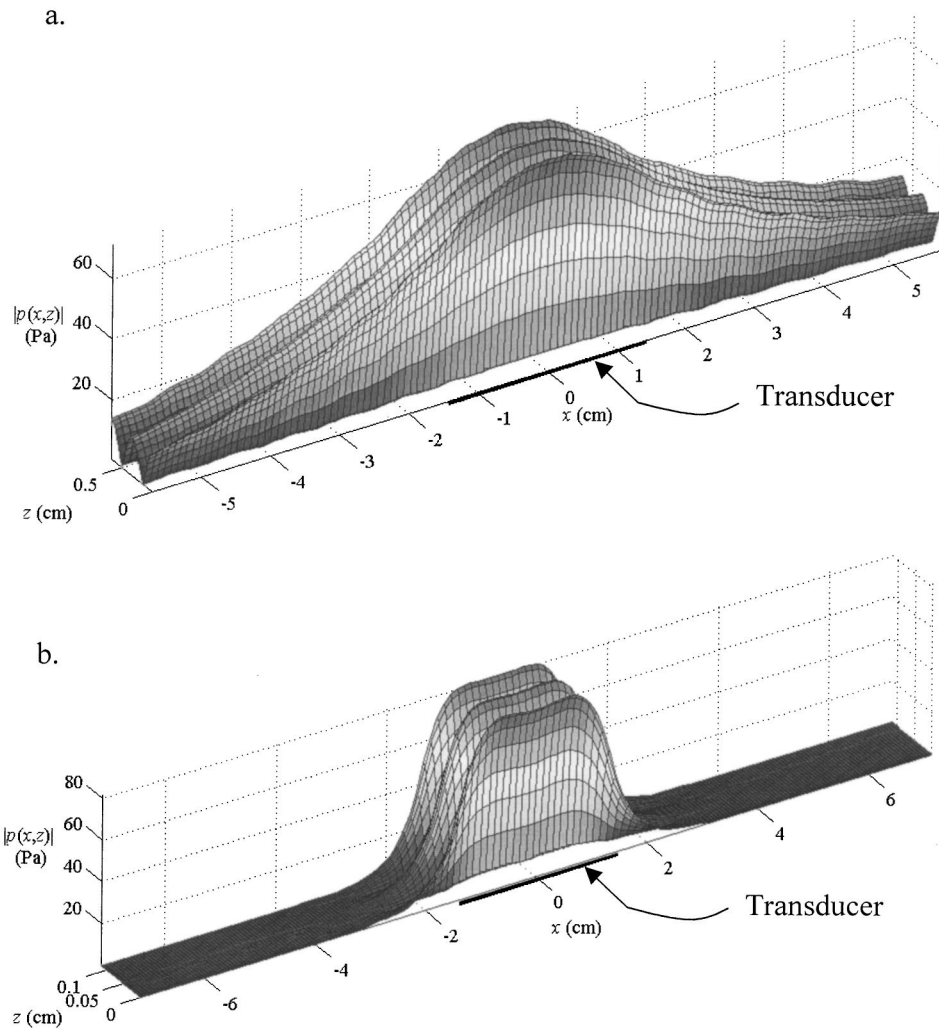
FIG. 5. Computed acoustic pressure amplitude in two open resonators: (a) $f = 50$ kHz, (b) $f = 300$ kHz.

b.

open-resonator configuration. At low frequencies, the acoustic field in front of the transducer is poorly collimated, and a relatively large amount of energy will propagate out the openings. As frequency increases, and the beam becomes more collimated, less energy will propagate out the boundaries. However, at high frequencies, absorption will tend to limit the magnitude of the acoustic field. An example of this behavior is shown in Fig. 5. Both plots show the acoustic pressure magnitude in front of the transducer for the open-resonator configuration. A velocity amplitude of $U = 2.95$ mm/s, transducer width $2a = 28.57$ mm, and a resonator depth of one wavelength was common for both examples. Figure 5(a) shows the pressure amplitude when the frequency was 50 kHz ($ka = 13$), and Fig. 5(b) shows the pressure amplitude when the frequency was 300 kHz ($ka = 78$). As would be expected, the acoustic field at 50 kHz was not collimated in front of the transducer. Consequently, a substantial amount of energy propagated out through the openings of the resonator at 50 kHz. At 300 kHz, the acoustic field was concentrated in front of the transducer. Less acoustic energy propagated out the openings.

The resonator models from Eqs. (8) and (1) were used to numerically compare the acoustic amplification that could be obtained in the open- and closed-resonator configurations. We believe that the most useful comparison metric is the quality factor Q_n of the resonator. The quality factor quantifies the energy loss per cycle of excitation, without reference to the performance of the transducer used to excite the cavity. The quality factor for the open-resonator configuration was determined by computing the acoustic pressure at $(x,z) = (0,L)$ over a suitable frequency range and identifying the half power frequencies. A corresponding quality factor was computed for a closed-resonator configuration using Eq. (2).

A plot summarizing a comparison of quality factors for the open- and closed-resonator factors as they depend upon ka of the source is shown in Fig. 6. These calculations were performed over a frequency range of 25 kHz–1 MHz; the transducer width was $2a = 28.57$ mm, and the depth $L \approx nc_0/2f$ ranged from 0.343 to 6.86 mm. The horizontal axis shows ka of the source as the frequency was swept. The vertical axis is quality factor Q_n. Quality factors Q_1 and Q_2 for resonators of $L \approx \lambda/2$ and $L \approx \lambda$ ($n = 1,2$) depths were determined for each frequency. The source ka's corresponding to the frequencies 50 and 300 kHz used for the computations of acoustic pressure contained in Fig. 5 are indicated with arrows in Fig. 6 for reference.

The quality factors for the open- and closed-resonator configurations shared some similar features. The quality factors for the $\lambda/2$ resonance were smaller than for the λ reso-

Anderson *et al.*: Ultrasonic resonators with large openings
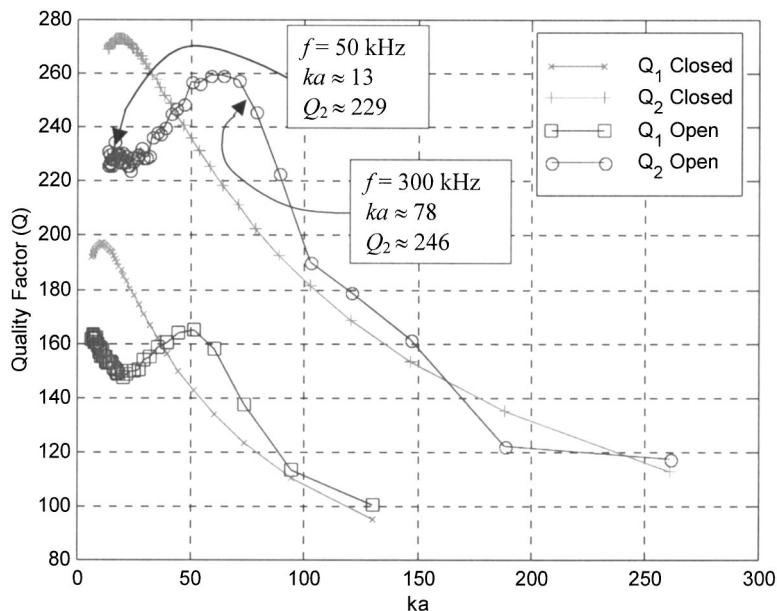
FIG. 6. Quality factor vs source ka for the open- and closed-resonator configurations. Q_1 and Q_2 are associated with the $\lambda/2$ and λ depth resonances, respectively.

nance. This is caused by the fact that the resonant wave number k_n increases linearly with frequency, while absorption per unit wavelength does not build up as fast. The quality factors all trended downward as source ka is increased. Increasing absorption associated with thermal conduction at the ends caused this behavior.

The plots of quality factors contained in Fig. 5 quantitatively address the tradeoff between collimation and absorption with respect to the amplification that can be achieved with the open resonator configuration. For source ka's less than 37, the quality factor Q_1 for the open-resonator configuration was lower than that for the closed-resonator configuration. In this range of source ka, the deficit in quality factor for the open-resonator configuration was presumably caused by leakage of acoustic energy through the openings. For the quality factor Q_2, the break-even source ka was approximately 42. As the source ka became higher, the quality factor for the open-resonator configuration exceeded that of the closed-resonator configuration. In this source ka range, the open-resonator configuration actually suffered less absorption because little energy escaped through the openings, and viscous and thermal absorption occurred at two sidewalls instead of four. As ka of the source became very high, body absorption within the volume of air in front of the transducer dominated the energy loss per cycle, and the quality factors became approximately equal for the two configurations. For the frequency range 25 kHz–1 MHz, and air as the medium, it is evident that a source ka of at least 37 is needed for optimal performance of an open-resonator configuration operating at a $\lambda/2$ depth resonance. An open-resonator operating at a λ depth resonance would require a source ka of at least 42 to achieve as much amplification as a closed-resonator configuration.

Given that source ka's of approximately 37 and 42 were optimal for the type of open-resonator configuration being considered, it is of interest to consider the practical aspects of building such a resonator. High source ka implies a wide transducer, and a relatively high frequency. A relatively high

frequency implies a short resonator depth L. To assess the consequences of the source ka condition, the quality factor data in Fig. 6 were replotted against resonator aspect ratio $2a/L$ on the horizontal axis. Figure 7 contains a plot of open- and closed-resonator quality factors as they depend upon resonator aspect ratio. Locations on the two curves corresponding to the two acoustic pressure computations contained in Fig. 5 are indicated with arrows in Fig. 7. As before, for small aspect ratios, the quality factor for the open-resonator configuration was lower than for closed-resonator configuration. At a particular aspect ratio the quality factor for the open-resonator configuration became equal to the quality factor for the closed-resonator configuration. For an open-resonator design whose depth L was $\lambda/2$, the break-even aspect ratio was approximately 24, at a predicted quality factor of 159. The break-even aspect ratio for an $L \approx \lambda$ depth resonator was approximately 14, at a predicted quality factor of 246.

IV. EXPERIMENTAL MEASUREMENTS

Experimental measurements were performed to validate some of the predictions of the numerical model in Eq. (8). Quality factors for the open-resonator configuration were obtained, but practical problems prevented unambiguous measurements in the closed-resonator configuration. These problems are discussed in the following. The measurements with the open-resonator configuration do provide a reference point to the achievable quality factors for the open-resonator configuration.

A resonator corresponding to the rectangular channel configuration shown in Fig. 1 was constructed. The width b of the channel was 28.575 ± 0.025 mm, the depth was $L = 6.86 \pm 0.025$ mm, and the total length in the x direction was 107.1 ± 0.025 mm. A PZT transducer (type APC 841 manufactured by APC International Ceramics Ltd.), of dimensions $2a = 28.575 \pm 0.38$ mm and thickness 4.064 ± 0.025 mm was used to excite the resonator. Based upon
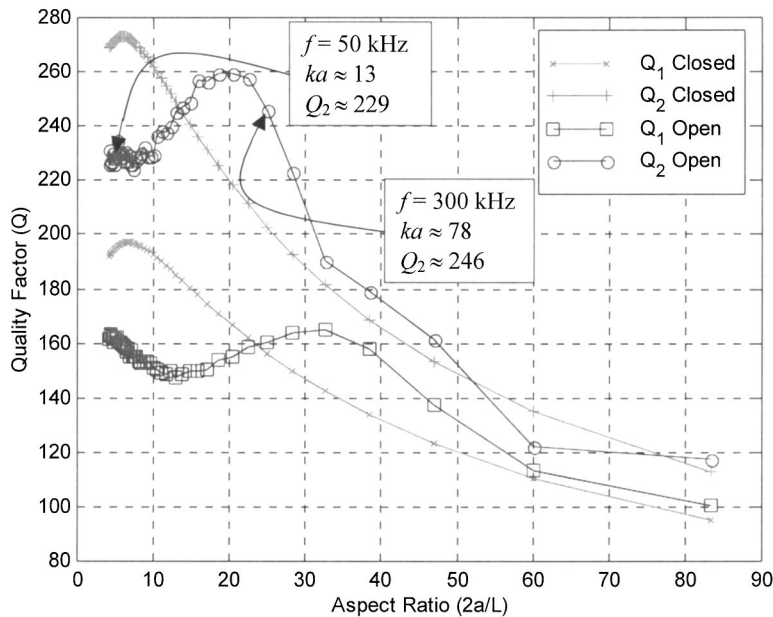
FIG. 7. Quality factor vs resonator aspect ratio ($2a/L$).

The figure shows a plot of Quality Factor (Q) on the y-axis (80 to 280) versus Aspect Ratio (2a/L) on the x-axis (0 to 90). Legend entries: Q_1 Closed, Q_2 Closed, Q_1 Open, Q_2 Open. Annotations in the figure:

$f = 50$ kHz
$ka \approx 13$
$Q_2 \approx 229$

$f = 300$ kHz
$ka \approx 78$
$Q_2 \approx 246$

data provided by the manufacturer, this transducer had a through-thickness resonance frequency of 493 kHz, and experimental measurements indicated that the first transverse (width) resonance frequencies were 67 and 98 kHz. With the exception of 100 kHz, the resonance frequencies of the open-resonator cavity were well separated from the transducer resonance frequencies, so that the transducer was operating in the stiffness regime near the cavity resonance frequencies. Opposite the exciting PZT transducer, a 1/8-in.-diam Bruel & Kjear type 4138 microphone was flush mounted to the wall. This microphone had a nominal sensitivity of 0.906 mV/Pa, and was capable of measuring acoustic pressure amplitude up to a frequency of 150 kHz. The PZT source was driven by a computer-controlled oscillator and audio amplifier, and the microphone signal was measured by a digital oscilloscope (bandwidth 100 MHz) and recorded with a personal computer. In a typical experiment, a computer set the frequency provided by the oscillator, recorded the microphone voltage amplitude, and repeated this process over frequency range at specified increments.

Experimental measurements of quality factor obtained with the open-resonator apparatus are summarized in Table I. Quality factors were experimentally measured at four longitudinal depth resonance frequencies, corresponding to depths $L \approx \lambda/2$, λ, $3\lambda/2$, and 2λ. A half-power point method was used to compute the quality factors from the experimental data. As is evident, the ka value for the source transducer was relatively low, 6.5 to 26.1, corresponding to the lowest

values included in numerical predictions discussed in Sec. III. The fifth and sixth columns contain the theoretically predicted and experimentally determined quality factors for the open-resonator apparatus. For the first three resonances, occurring at 25, 50, and 75 kHz, the measured quality factor for the open-resonator configuration ranged 8%–18% lower than the quality factors that were predicted by the model (8). The measured quality factor for the resonance occurring at 100 kHz was 42% lower than the experimentally predicted value.

We believe, in general, that the disparity in measured and predicted quality factors was due to geometric imperfections in the resonator used for experiments. While the model from Eq. (8) assumes that the resonator geometry is perfectly rectangular, the actual resonator used in experiments contained imperfections in parallelism, and curvature. Loss of parallelism between the transducer and reflecting wall is known to cause energy loss.[8] This mechanism would cause experimental measurements of quality factor to be consistently less than would be predicted by a theoretical model that assumed parallelism. The cavity resonance frequency at 100 kHz was near a transducer resonance at 98 kHz, and this fact may have affected the experimental determination of cavity quality factor, causing it to be excessively low.

It would be valuable to obtain experimental measurements at higher source ka's, extending to the region $ka > 37$, in order to explore the break-even point in quality fac-

TABLE I. Predicted and measured quality factors for the open-resonator configuration.

Frequency (kHz)	L (λ)	ka	Aspect ratio $2a/L$	Open Predicted Q	Open Measured Q	Closed Predicted Q
25	$\lambda/2$	6.54	4.1655	161	148	191
50	λ	13.10	4.1655	226	184	269
75	$3\lambda/2$	19.63	4.1655	284	255	323
100	2λ	26.17	4.1655	322	187	364

Anderson *et al.*: Ultrasonic resonators with large openings

tor that is predicted by the numerical computations summarized in Figs. 6 and 7. The experimental measurements were limited to an upper frequency limit of 150 kHz, due to available microphone technology. For practical size transducers, large source ka's cannot be obtained with this upper frequency limit.

Another apparatus, corresponding to the closed-resonator configuration with the same dimensions as the open-resonator apparatus, was constructed to benchmark theoretical predictions and achievable quality factors for the closed-resonator configurations. Our efforts were not successful, as the presence of extra cavity boundaries and a degeneracy caused by a square cross-section caused excessive mode frequency packing, and we were unable to isolate the longitudinal modes of the closed-resonator configuration.

V. CONCLUSIONS

The amplification performance of open- and closed-configuration two-dimensional resonators was compared over the frequency range 25 kHz–1 MHz with air as the working fluid. Theoretical computations showed that source ka's greater than 37 and 42 were required in order for the quality factor of the open-resonator configuration to be as high as the closed-resonator configuration for the half- and one-wavelength resonances. This condition corresponded to a source-width-to-depth aspect ratio of 24 for a half-wavelength depth resonator, and 14 for a one-wavelength depth resonator. Experimental measurements at low source ka's, in the range 6.5–26.1, showed that quality factors for the one-, two-, and three-half wavelength resonances were 8%–18% lower than the theoretically predicted values.

ACKNOWLEDGMENTS

APPENDIX

The model used for acoustic wave number and absorption was

$$k = \frac{\omega}{c_0} + i\alpha_{vt} + (1+i)\alpha_b + \frac{1}{\pi}\frac{\omega}{c}\sum_{\nu}(\alpha_{\nu}\lambda)_m\frac{i\omega\tau_{\nu}}{1-i\omega\tau_{\nu}}$$

$$= \beta - i\alpha. \tag{A1}$$

A form similar to this is found in Ref. 21, to which dissipation α_b caused by viscous and thermal losses at the boundary have been added.

The model used for body dissipation α_{vt} caused by viscosity and thermal conductivity was

$$\alpha_{vt} = \frac{\omega^2\mu}{2\rho_0 c^3}\left[\frac{4}{3} + \frac{\mu_B}{\mu} + \frac{\gamma-1}{\text{Pr}}\right], \tag{A2}$$

where $\mu = 1.81\times10^{-5}$ Ns/m^2, $\mu_B = 0.6\mu$ Ns/m^2, $\rho_0 = 1.21$ kg/m^3, $\gamma = 1.4$, and $\text{Pr} = 4\gamma/(9\gamma-5)$ were the shear viscosity, bulk viscosity, ambient density, isentropic coefficient of compression, and Prandtl number for air.

The model contained in Ref. 21 for α_b is

$$\alpha_b = \frac{C}{2A}\left(1 + \frac{(\gamma-1)}{\sqrt{\text{Pr}}}\right)\sqrt{\frac{2\mu\omega}{\rho_0 c_0^2}}. \tag{A3}$$

This expression accounts for viscous and thermal losses at the sidewalls of the resonator. To account for thermal conduction at the ends, an equivalent absorption coefficient must be derived. This absorption coefficient can be derived by solving for the acoustic pressure in a one-dimensional waveguide, with the acoustic velocity specified at one end, and a near-rigid impedance at the other end. Thermal conduction at the end boundary may be modeled as an impedance Z of[21]

$$\frac{1}{Z} = \frac{\sqrt{2}(1-i)}{2\rho_0 c_0}\sqrt{\frac{\omega\mu}{\rho_0 c_0^2}}\frac{\gamma-1}{\sqrt{\text{Pr}}}. \tag{A4}$$

Upon solving for the acoustic pressure in this problem, one obtains an effective absorption coefficient of

$$\alpha = \frac{1}{2L}\sqrt{\frac{2\omega\mu}{\rho_0 c_0^2}}\frac{(\gamma-1)}{\sqrt{\text{Pr}}}, \tag{A5}$$

that will account for the impedance boundary condition at the end. For the open- and closed-resonator configurations, the effective thermal conduction at the end (A5) was doubled to account for thermal conduction at the source, and the total boundary losses α_b were modeled to be

$$\alpha_b = \frac{C}{2A}\left(1 + \frac{(\gamma-1)}{\sqrt{\text{Pr}}}\right)\sqrt{\frac{2\mu\omega}{\rho_0 c_0^2}} + \frac{1}{L}\sqrt{\frac{2\mu\omega}{\rho_0 c_0^2}}\frac{(\gamma-1)}{\sqrt{\text{Pr}}}. \tag{A6}$$

Molecular relaxation taking place in the body of the fluid in the cavity was modeled by the third term in Eq. (A1) with the frozen sound speed c as

$$c = c_0\left(1 + \frac{1}{\pi}\sum(\alpha_{\nu}\lambda)_m\right), \tag{A7}$$

and $(\alpha_1\lambda)_m = 0.0011$, $\tau_1 = 1.74\times10^{-5}$ s; $(\alpha_2\lambda)_m = 0.0002$, $\tau_2 = 0.0013$ s were used for the O$_2$ and N$_2$ relaxations, respectively.

With these definitions, the molecular relaxation absorption coefficient α_r was defined as

$$\alpha_r = \text{Im}\left[\frac{1}{\pi}\frac{\omega}{c}\sum_{\nu}(\alpha_{\nu}\lambda)_m\frac{i\omega\tau_{\nu}}{1-i\omega\tau_{\nu}}\right], \tag{A8}$$

and the propagating part β of the wave number k was defined as

$$\beta = \frac{\omega}{c_0} + \alpha_b + \text{Re}\left[\frac{1}{\pi}\frac{\omega}{c}\sum_{\nu}(\alpha_{\nu}\lambda)_m\frac{i\omega\tau_{\nu}}{1-i\omega\tau_{\nu}}\right] \approx \frac{\omega}{c_0}. \tag{A9}$$

A subscript n was added to the absorption coefficient α and propagating part β of the wave number to indicate that they were evaluated at the frequency ω_n.

[1] J. P. M. Trusler, *Physical Acoustics and Metrology of Fluids* (Adam Hilger, Boston, 1991).

[2] L. L. Beranek and I. L. Ver, *Noise and Vibration Control Engineering, Principles and Applications* (Wiley, New York, 1992).

[3] M. F. Hamilton and D. T. Blackstock, *Nonlinear Acoustics* (Academic, New York, 1998).

[4] M. Seaver, A. Galloway, and T. J. Manuccia, "Acoustic levitation in a free-jet wind tunnel," Rev. Sci. Instrum. **60**, 3452–3459 (1989).

[5] R. E. Apfel and W. T. Shi, "Deformation and position of acoustically levitated liquid drops," J. Acoust. Soc. Am. **99**, 1977–1984 (1996).

[6] R. G. Holt, Y. Tian, J. Jankovsky, and R. E. Apfel, "Surface-controlled drop oscillations in space," J. Acoust. Soc. Am. **102**, 3802–3805 (1997).

[7] M. Groschl, "Ultrasonic separation of suspended particles. I. Fundamentals," Acustica **84**, 432–447 (1998).

[8] M. Groschl, "Ultrasonic separation of suspended particles. II. Design and operation of separation devices," Acustica **84**, 632–642 (1998).

[9] M. Groschl, W. Burger, and B. Handl, "Ultrasonic separation of suspended particles. III. Application in biotechnology," Acustica **84**, 815–822 (1998).

[10] W. T. Coakley, G. Whitworth, M. A. Grundy, R. K. Gould, and R. Allman, "Ultrasonic manipulation of particles and cells," Bioseparation **4**, 73–83 (1994).

[11] P. H. Brodeur, "Acoustic separation in a laminar flow," Proc. IEEE Ultranson. Symp. **3**, 1359–1362 (1994).

[12] J. J. Hawkes, D. Barrow, J. Cefai, and W. T. Coakley, "A laminar flow expansion chamber facilitating downstream manipulation of particles concentrated using an ultrasonic standing wave," Ultrasonics **36**, 901–903 (1998).

[13] G. Whitworth and W. T. Coakley, "Particle column formation in a stationary ultrasonic field," J. Acoust. Soc. Am. **91**, 79–85 (1992).

[14] L. E. Kinsler, A. R. Frey, A. B. Coppens, and J. V. Sanders, *Fundamentals of Acoustics*, 3rd ed. (Wiley, New York, 1982).

[15] J. D. Jeong, S. W. Yoo, H. G. Choi, C. G. Ahn, and J. M. Lee, "Acoustic mode control method using additional cavity and holes," Proceedings of the International Modal Analysis Conference and Exhibit, 2000, pp. 1737–1742.

[16] N. H. Fletcher and T. D. Rossing, *The Physics of Musical Instruments* (Springer, Berlin, 1991).

[17] M. L. Munjal, *Acoustics of Ducts and Mufflers* (Wiley, New York, 1987).

[18] F. B. Jensen, W. A. Kuperman, M. B. Porter, and H. Schmidt, *Computational Ocean Acoustics* (AIP Press, New York, 2000).

[19] E. W. Swokowski, *Calculus with Analytic Geometry* 2nd ed. (Prindle, Weber and Schmidt, 1979).

[20] L. F. Shampine and M. W. Reichelt, "The MATLAB ODE Suite," SIAM J. Sci. Comput. (USA) **18**, 1–22 (1997).

[21] A. D. Pierce, *Acoustics: An Introduction to its Physical Principles and Applications* (Acoustical Society of America, 1989).

Electrode surface profile and the performance of condenser microphones

N. H. Fletcher[a)]
Research School of Physical Sciences and Engineering, Australian National University, Canberra,
ACT 0200, Australia

S. Thwaites
CSIRO Telecommunications and Industrial Physics, Lindfield, NSW 2070, Australia

Condenser microphones of all types are traditionally made with a planar electrode parallel to an electrically conducting diaphragm, additional diaphragm stiffness at acoustic frequencies being provided by the air enclosed in a cavity behind the diaphragm. In all designs, the motion of the diaphragm in response to an acoustic signal is greatest near its center and reduces to zero at its edges. Analysis shows that this construction leads to less than optimal sensitivity and to harmonic distortion at high sound levels when the diaphragm motion is appreciable compared with its spacing from the electrode. Microphones of this design are also subject to acoustic collapse of the diaphragm under the influence of pressure pulses such as might be produced by wind. A new design is proposed in which the electrode is shaped as a shallow dish, and it is shown that this construction increases the sensitivity by about 4.5 dB, and also completely eliminates harmonic distortion originating in the cartridge. © *2002 Acoustical Society of America.* [DOI: 10.1121/1.1515971]

PACS numbers: 43.38.Bs, 43.38.Kb, 43.58.Ry [AJZ]

I. INTRODUCTION

Condenser microphones of various designs are central to the whole of audio engineering practice and to scientific research in acoustics. At one end of the range we find relatively simple high quality omnidirectional microphones with diameters ranging from 3 to 25 mm for use with sound level meters and other types of precision measuring equipment,[1] while at the other end there are much more complicated studio microphones with adjustable directional patterns.[2] Alongside these there are simple, rugged, and inexpensive electret microphones for a whole variety of less demanding uses.

In all cases the basic principle of operation is the same—a thin conducting diaphragm is held under tension a very small distance away from a planar conducting electrode, and matching charges are induced on the diaphragm and electrode by a voltage applied between the two through a very high resistance. (In the case of an electret microphone, the charge is generated by electret polarization so that an external bias is not required.) Motion of the diaphragm then causes a corresponding change in the potential between the diaphragm and the electrode, and this voltage signal is amplified through a device with very high input impedance to provide the output signal. Of course, many refinements are involved in order to ensure a flat response over a wide frequency range and, in the case of studio microphones, to provide control over directional response. These refinements will not be of concern in the present paper.

The purpose of the present discussion is to analyze certain aspects of this basic microphone design and to propose that a significant improvement in performance can be achieved by modifying the plane electrode to an appropriately specified dished shape. It is difficult, in retrospect, to believe that such a modification has not been suggested, and perhaps implemented, during the past 80 or more years of microphone technology, but the possibility is not mentioned in classic papers on microphone design[1–3] or in two comprehensive modern texts on the subject,[4,5] and no reference to it has been found in the course of a search of published scientific or patent literature.

II. ANALYSIS OF THE PLANAR-ELECTRODE DESIGN

A. Microphone types

For the purposes of the present discussion, we identify two main classes of condenser microphone. The first class, designated here as type I and shown schematically in Fig. 1(a), is typical of measurement microphones. The diaphragm is of thin metal under high tension so that its natural frequency is typically in the range 10–150 kHz, depending on diaphragm diameter. This tension then provides the main restoring force for any displacement of the diaphragm. In the second class, characteristic of inexpensive electrets as well as of many studio microphones, and here designated as type II, the diaphragm is of metal-coated polymer material under only moderate tension so that its resonance frequency is only 1–2 kHz. In this case the air volume enclosed within the microphone capsule must be relied upon to raise the resonance frequency to a value of around 15 kHz, and this air volume provides most of the dynamic restoring force upon the diaphragm. The cavity is necessarily vented through a very small opening for static pressure equalization, however, so that the diaphragm tension must provide the restoring force against static electrical stress.

Two subclasses of type II microphones can be distinguished. In a type IIA microphone, the structure of which is

_____
[a)]Electronic mail: neville.fletcher@anu.edu.au

metal diaphragm

vented electrode

air cavity   insulator   slow leak

(a)

polymer diaphragm

gold coating

cavity electrode   slow leak

(b)
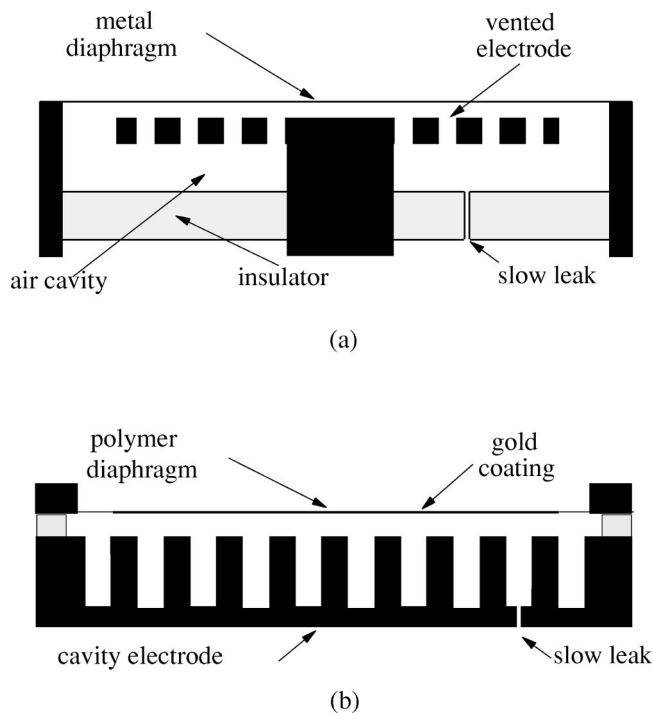
FIG. 1. Schematic of the main types of condenser microphone in current use. (a) Type I: a precision measurement microphone with a metal diaphragm under high tension. The directional pattern of such a microphone can be made cardioid by providing vents with appropriate acoustic resistance into the back of the cartridge from the environment. (b) Type II: a basic studio microphone with a metalized plastic diaphragm and restoring force provided by air enclosed in cavities in the thick electrode. A studio microphone consists essentially of two type II microphone cartridges mounted back-to-back and linked by a structure with high acoustic resistance. By varying the potentials on the two diaphragms, the response can be made omnidirectional, cardioid, or figure-eight.

otherwise similar to that shown in Fig. 1(a) for a type I microphone, there is a single air cavity behind the diaphragm and electrode. In microphones with cardioid directional characterstics this cavity is vented through an appropriate rear acoustic resistance. In a type IIB microphone, the air cavity is subdivided into a large number of small cells located in a rather thick metallic electrode, as shown in Fig. 1(b). In a microphone with variable directionality, two such capsules are placed back-to-back and acoustically coupled through a narrow intervening space and small holes in the electrodes.[2] The directional response can then be varied by changing the voltages applied to the two diaphragms. Simple electret microphones are generally of type IIA, while studio microphones are usually of type IIB.

Suppose that, for a microphone of either type I or II, the diaphragm tension is T and the reservoir volume is Δ_0. Then the local mechanical restoring force $F(r)$ per unit area on the diaphragm when it is displaced normally inwards by an amount $z(r)$, is

$$F(r) = -\frac{T}{r}\frac{\partial}{\partial r}\left(r\frac{\partial z}{\partial r}\right) + \frac{\rho c^2}{\Delta_0}\int_0^a 2\pi z r\, dr, \quad (1)$$

where a is the radius of the electrode. The form of the tension-dependent term assumes that only circularly symmetric displacements are considered,[6] while the second term on the right-hand side is simply the acoustic pressure devel-

oped in the air cavity by the diaphragm displacement $z(r)$. For a type I microphone T is very large, so that the first term is dominant and the second term can be neglected. For a type II microphone, however, the diaphragm tension is smaller by a factor of order 1000 and the second term is dominant in many features of the behavior. The first term, however, determines the behavior under electrostatic loading, since the reservoir is necessarily vented through a small opening and the pressure of the enclosed air quickly decays to atmospheric.

It might appear that the volume-dependent restoring term in Eq. (1) should have a different form in a type-IIB microphone, since the air cavity is distributed over the surface of the diaphragm in small cells that might be expected to provide a local rather than a global pressure response. The RC time-constant for the individual cells, where C is the acoustic compliance of the enclosed air and R the flow resistance of the thin air film between the electrode and the diaphragm, is however about equal to the inverse of the cavity-supported resonance frequency of the diaphragm, so that, at the frequencies well below this limit with which we are primarily concerned, the cavities are effectively interconnected and behave as one single cavity.

In what follows, the somewhat different but related behavior of these two microphone types under both static electrostatic forces and oscillatory acoustic pressures is considered. The design complications associated with studio microphones of variable directionality will not be of concern here, but only the behavior or the basic microphone cartridge.

B. Electrostatic deflection

The behavior of all microphone types under electrostatic loading is formally the same, except for the magnitude of the diaphragm tension T. The analysis is well known[7] but is repeated here to make clear the subsequent developments. Suppose that the separation between the diaphragm and the plane electrode is h when no voltage is applied, and that the diaphragm is deflected a distance $z(r)$ toward the electrode by an applied voltage V. Then, by Eq. (1) with the enclosed volume term omitted,

$$\frac{T}{r}\frac{d}{dr}\left(r\frac{dz}{dr}\right) = -\frac{\epsilon_0 V^2}{(h-z)^2}, \quad (2)$$

where ϵ_0 is the permittivity of free space. If the electrode has a radius $b < a$, where a is the diaphragm radius, then Eq. (2) still applies provided we take $V = 0$ for $b < r < a$.

This equation is easy to solve in the linearized limit $z \ll h$, in which case

$$z = \frac{\epsilon_0 V^2 b^2}{4Th^2}\left(1 - \frac{r^2}{b^2} - 2\log\frac{b}{a}\right), \quad r < b, \quad (3)$$

$$= -\frac{\epsilon_0 V^2 b^2}{2Th^2}\log\frac{r}{a}, \quad b < r < a. \quad (4)$$

In this limit the shape is a paraboloid of revolution for $r < b$ and a logarithmic surface of opposite curvature for $b < r < a$.

N. H. Fletcher and S. Thwaites: Condenser microphone electrode profile
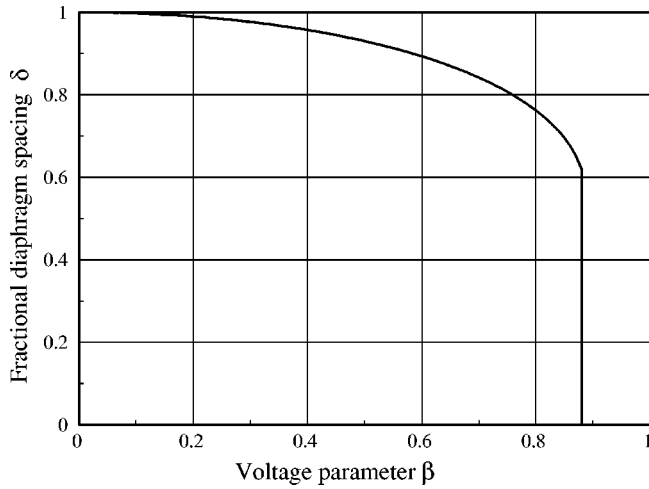
FIG. 2. Calculated variation of the normalized diaphragm spacing δ from the electrode as a function of the polarization voltage parameter $\beta = (\epsilon_0 b^2/4Th^2)^{1/2}V$. The diaphragm collapses onto the electrode when β exceeds 0.88.

FIG. 3. Calculated normalized profiles of the diaphragm, as a function of the parameter β, for electrostatic loadings up to the point of collapse. All profiles are approximately parabolic.

A general solution for larger deflections is necessarily numerical, since the equation is nonlinear. Such a solution is most usefully parametrized in terms of the quantities

$$\beta=\left(\frac{\epsilon_0 b^2}{4Th^2}\right)^{1/2}V, \quad \delta=\frac{h-z}{h}, \tag{5}$$

which represent, respectively, the normalized polarizing voltage and the fractional value of the separation between the diaphragm and the electrode. The calculated result is shown in Fig. 2. As the potential on the diaphragm (the parameter β) is increased, the diaphragm moves steadily toward the electrode until suddenly, at about $\beta=0.88$, it collapses onto the electrode. Just before the collapse, the separation between the diaphragm and the electrode has been reduced to about 0.63 of its unpolarized value. The physical reason for the collapse is that the maintenance of diaphragm potential at the center of the diaphragm requires an inflow of charge from the supply to the center of the diaphragm, thus increasing the electrostatic force and further reducing the separation, which in turn requires more charge to maintain the diaphragm potential. This electrostatic force, which increases about as $(h-z)^{-2}$, ultimately overbalances the elastic restoring force, which increases only linearly with z.

When values for the relevant physical parameters are inserted into the parameter β, it is found that for a typical type I microphone $\beta<0.01$, while for a type II microphone $\beta\sim0.3$. This means that the electrostatic displacement of the diaphragm is almost negligibly small for a type I microphone, while a type II microphone has a significant static displacement and may be close to the condition for collapse if excess voltage is applied. Computed profiles of the diaphragm for various values of the parameter β are shown in Fig. 3. It can be seen that the profile is approximately parabolic right up to the value of β giving collapse.

C. Acoustic deflection

Suppose that there is an extra inward diaphragm deflection $\psi(r)$ in a uniform acoustic pressure field $p(\omega)$, and for simplicity let $b=a$ so that the whole diaphragm is electrically active. Since the diaphragm (or the electrode, depending on the microphone design) is essentially electrically isolated at acoustic frequencies, the total charge Q upon it remains fixed at the value
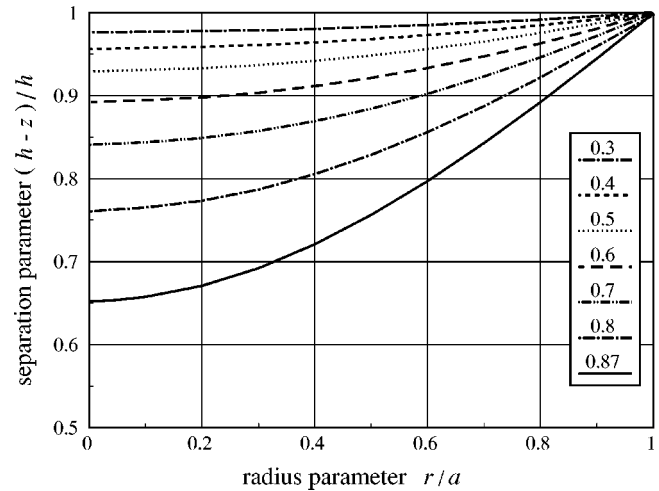
$$Q=2\pi\epsilon_0 V_0 \int_0^a \frac{r\,dr}{h-z(r)}, \tag{6}$$

where V_0 is the steady supply voltage, h is the initial diaphragm separation from the electrode, and $z(r)$ is the electrostatic displacement of the diaphragm. The diaphragm potential V under the influence of the additional acoustic displacement $\psi(r)$ is then

$$V=V_0 \int_0^a \frac{r\,dr}{h-z(r)} \Big/ \int_0^a \frac{r\,dr}{h-z(r)-\psi(r)}, \tag{7}$$

and the time-varying part of this potential constitutes the electrical signal from the microphone.

The behavior of $\psi(r)$ is given by

$$\rho\frac{\partial^2\psi}{\partial t^2}=-F(\psi,r)+G(\psi,r)+p, \tag{8}$$

where ρ is the mass of the diaphragm per unit area, $F(\psi,r)$ is the additional elastic restoring force as given by Eq. (1) with $z(r)$ replaced by $\psi(r)$, and $G(r)$ is the additional electrostatic force, given by Eq. (7) as

$$G(r)=\frac{\epsilon_0 V^2}{(h-z+\psi)^2}-\frac{\epsilon_0 V_0^2}{(h-z)^2}. \tag{9}$$

The second term on the right-hand side of Eq. (1) simply contributes a constant times the average magnitude of ψ across the diaphragm and so is proportional to p. Since at high sound levels the acoustic vibration amplitude $\psi(r)$ of the diaphragm may be not much less than the diaphragm spacing $h-z$, the nonlinear terms in Eq. (9) are significant, so that the electrical signal V will suffer an appreciable amount of harmonic distortion, as will be discussed in Sec. III.

At low acoustic levels $\psi(r)$ is everywhere much less than the diaphragm spacing $h-z(r)$ so that, from Eq. (9), $G(r)$ is approximately zero and $F(r)$ is simply proportional to ψ. It is then simple to solve the linearized version of Eq. (8). For very low frequencies, the left-hand side of Eq. (8) can be neglected, leading to $F(\psi,r)=p$ and hence, if we take $b=a$ for simplicity, to the result

$$\psi(r)=Ap\left(1-\frac{r^2}{a^2}\right),\tag{10}$$

where A is a constant. For frequencies approaching that of the cavity-supported diaphragm resonance, the left-hand side of Eq. (8) cannot be neglected, and the solution has the well-known form[6]

$$\psi(r)=BpJ_0(2.4r/a),\tag{11}$$

where J_0 is a Bessel function of order zero and B is another constant. The profile shapes given by Eqs. (10) and (11) are very similar.

When the diaphragm displacement is no longer negligibly small compared with the diaphragm separation h, then the redistribution of charge on the deflected diaphragm must be taken into account by including the force term $G(r)$ from Eq. (9) with V given by Eq. (7). This clearly introduces more nonlinear terms and so more harmonic distortion of the electrical output signal δV. This will not be pursued further here.

III. DISTORTION AND SENSITIVITY

To examine the effect of electrode shape on sensitivity and distortion, it is simplest to consider first an idealized type I microphone with no electrostatic distortion of the diaphragm. Suppose that the diaphragm radius is a and that its equilibrium spacing from the electrode is h. As derived previously in Eq. (10), the acoustic displacement has the form

$$z(r)=\psi_0\left(1-\frac{r^2}{a^2}\right)\cos\omega t,\tag{12}$$

where ψ_0 is the acoustic displacement at the center of the diaphragm. If it is assumed for simplicity that the electrode extends to the edge of the diaphragm, then the microphone capacitance is

$$C=2\pi\epsilon_0\int_0^a\frac{r\,dr}{h-\psi_0(1-r^2/a^2)\cos\omega t},\tag{13}$$

$$=\frac{\pi a^2\epsilon_0}{\psi_0\cos\omega t}\log\left(\frac{h}{h-\psi_0\cos\omega t}\right).\tag{14}$$

If $Q=C_0V_0$ is the charge on the electrode when the polarizing voltage is V_0 and $C_0=\pi a^2\epsilon_0/h$ is the capacitance when the acoustic displacement amplitude $\psi_0=0$, then the potential V of the electrode in the presence of acoustic displacement is

$$V=\frac{Q}{C}=-\frac{V_0(\psi_0\cos\omega t/h)}{\log[1-(\psi_0/h)\cos\omega t]}.\tag{15}$$

Expansion of this expression as a power series in $\cos\omega t$ and conversion to a series in $\cos n\omega t$ involves tedious algebra, but the first few terms are given approximately by

$$V\approx V_0\left[1-0.56\frac{\psi_0}{h}\cos\omega t-0.06\left(\frac{\psi_0}{h}\right)^2\cos 2\omega t\right.$$
$$\left.-0.03\left(\frac{\psi_0}{h}\right)^3\cos 3\omega t+\cdots\right].\tag{16}$$

This means that the relative amplitude of second-harmonic distortion is about $0.11\psi_0/h$ and of third-harmonic distortion about $0.05(\psi_0/h)^2$. Converting to distortion levels shows that, when $\psi_0=0.1h$ so that the amplitude of the electrical signal is $0.06V_0$, second-harmonic distortion is about -40 dB relative to the fundamental, and third-harmonic distortion is about -66 dB. The electrostatic modification of the acoustic deflection function, referred to briefly earlier, will add further distortion terms. These figures require some modification when the fact that the electrically active part of the diaphragm does not extend to its full diameter is taken into account. Formally, this is done by changing the upper limit of the integral in Eq. (13) from a to b, which significantly complicates the algebra. The result is a reduction in both the electrical output and also the distortion.

From a practical point of view it must be pointed out, however, that the acoustic level required to achieve a diaphragm displacement of $0.1h$ is much larger than would normally be contemplated for a microphone. Indeed the output signal amplitude would then be about one-tenth of the polarizing voltage, so that the preamplifier would be forced into severe clipping. The consequent distortion would completely obscure the microphone distortion.

There is one other feature of the planar-electrode design that is worthy of comment, and that is the possibility of what might be termed acoustic collapse. If the acoustic signal has a large positive pressure, then this will bring the center of the diaphragm close to the electrode and the migration of charge will cause it to collapse into contact, thus short-circuiting the microphone and rendering it inoperative for perhaps several seconds until the charge has been restored through the very high supply resistance. This phenomenon can be investigated in the quasi-static limit by adding an acoustic pressure term p, independent of r, to the right-hand side of Eq. (2).

IV. IMPROVED ELECTRODE DESIGN

Referring back to Eq. (7), it is immediately apparent that, if the electrode is curved so that the static diaphragm separation $h-z(r)$ is made everywhere proportional to the acoustic displacement $\psi(r)$ so that $[h-z(r)]=\gamma\psi(r,t)/p(t)$, where $p(t)$ is the acoustic pressure signal and γ is a constant, then Eq. (7) simplifies to the form

$$V=V_0[1+\gamma^{-1}p(t)],\tag{17}$$

and the electrical output mirrors the acoustic input without distortion. In physical terms, this means that the diaphragm motion does not cause any redistribution of charge, so that the electrostatic force on all parts of the diaphragm remains constant, thus ensuring that the displacement ψ, and thus the reciprocal of the microphone capacitance, faithfully follows the acoustic pressure signal p.

These observations are the basis of the proposed improved microphone design. The electrode profile that will
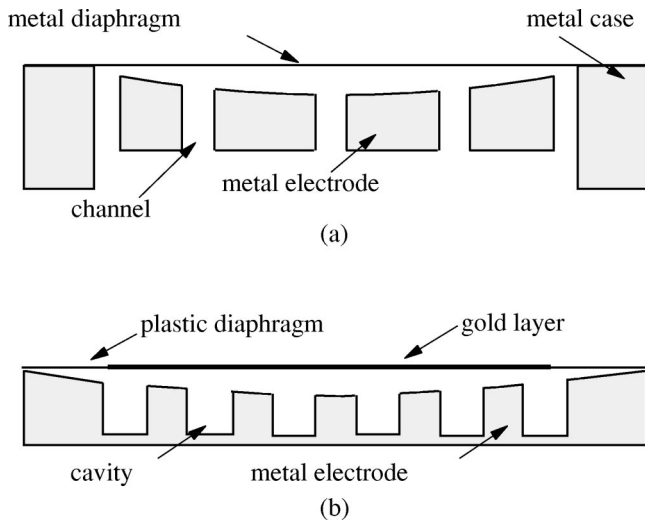
FIG. 4. Optimal electrode profile. (a) In practice the electrode will terminate a small distance from the edge of the diaphragm in a type I microphone; (b) in a type II microphone the diaphragm metallization should terminate at 0.9 times the diaphragm radius.

give optimal performance does not differ greatly between type I and type II microphones, though there are significant quantitative variations associated with the extent to which the diaphragm is deflected by electrostatic forces.

A. Type I microphones

As discussed previously, the tension in the diaphragm of a type I microphone is so high that the static deflection is only of order 10^{-3} of the electrode spacing. This means that the diaphragm can be treated as essentially planar, and this assumption forms the basis for an initial evaluation of optimal electrode profile. It has already been shown that the vibration amplitude of the diaphragm has a parabolic profile at low frequencies and a rather similar Bessel-function profile near the major resonance, in each case vanishing at the circumference. An optimum electrode shape should therefore follow a similar profile, vanishing at the edge of the diaphragm, and with a central displacement chosen to optimize other features of the design, as shown in Fig. 4(a).

Suppose that the radius of the diaphragm is a and that of the electrode b and that the central diaphragm spacing is h_0. Then the electrode shape is $h(r) = h_0[1 - (r/a)^2]$ and the low-frequency acoustic displacement has the similar form $\psi(r) = \psi_0[1 - (r/a)^2]$. The electrical capacitance has the value

$$C = \epsilon_0 \int_0^b \frac{2\pi r\, dr}{h(r)} = \frac{\epsilon_0 \pi b^2}{h_0} \log\left(\frac{a^2}{a^2 - b^2}\right). \quad (18)$$

To avoid a short circuit at the edge of the diaphragm, b must be significantly less than a, and a choice of $b = 0.9a$ will later be shown to be optimal, giving a capacitance of $1.7\epsilon_0 \pi b^2/h_0$. The diaphragm spacing at the edge of the electrode will be 0.2 times that at the center.

The electrical output under a polarizing voltage V_0 when the central acoustic displacement is ψ_0 is given by Eq. (7) with the upper limit of both integrals taken as b rather than a. The result is

$$\delta V = \frac{V_0 \psi_0}{h_0}, \quad (19)$$

and there are no higher terms, so that harmonic distortion is identically zero.

This should be compared with a microphone with a planar electrode with the same values of a and b, and a constant electrode spacing $h(r) = h_0$. The electrical capacitance is $\epsilon_0 \pi b^2/h_0$, which, for the case $b = 0.9a$, is about half that of the curved electrode design. Evaluation of the modified integrals in Eq. (7) for this case shows that, to first order,

$$\delta V = \frac{V_0 \psi_0}{h_0}\left(1 - \frac{b^2}{2a^2}\right). \quad (20)$$

If $b = 0.9a$, then the voltage signal is smaller than that for the curved-electrode design by a factor of about 0.6, which is about 4.5 dB. As discussed previously, there are also higher terms of all orders that contribute harmonic distortion.

It can be concluded that the curved-electrode design offers significant advantages in terms of increased sensitivity (about 4.5 dB), increased capacitance (factor about 1.7), and freedom from distortion, compared with the corresponding planar electrode design. Some practical issues will be discussed in a later section.

B. Type II microphones

The major difference between a type I and a type II microphone in the present context is the fact that the diaphragm of the type II microphone suffers appreciable curvature under the influence of electrostatic forces, the separation at the diaphragm center being reduced by perhaps a factor 0.7 in a normal plane-electrode design. These microphones also usually employ a greater electrode separation from the diaphragm, typically about 40 μm, partly for this reason. An optimal electrode design will therefore be dished to about 50 μm at its center and come close to the level of the diaphragm mount at the circumference as in Fig. 4(b).

Because of the appreciable electrostatic deflection of the diaphragm, however, it must be questioned whether the paraboloidal or near-spherical electrode shape is still appropriate. The form of the electrostatic deflection is once again given by Eq. (2), but now with the electrode separation varying with radius r. If we define the shape of the electrode by the curve $h(r)$ as in Fig. 5 and the shape of the diaphragm under electrostatic deflection by $f(r)$, then minimum distortion and maximum sensitivity is achieved if $h(r) - f(r)$ is proportional to the acoustic deflection of the diaphragm which, as has been shown previously, is approximately parabolic at low frequencies. The equation for the electrostatic deflection $f(r)$ is then

$$\frac{T}{r}\frac{d}{dr}\left(r\frac{df}{dr}\right) = -\frac{\epsilon_0 V^2}{[h(r) - f(r)]^2}. \quad (21)$$

The problem then is to choose an electrode profile $h(r)$ so that $h(r) - f(r)$ is parabolic.

If the paraboloidal-electrode design is appropriate, then we can assume that $h(r) = h_0[1 - (r/a)^2]$, where a is the radius of the diaphragm. Substituting this into Eq. (21) gives
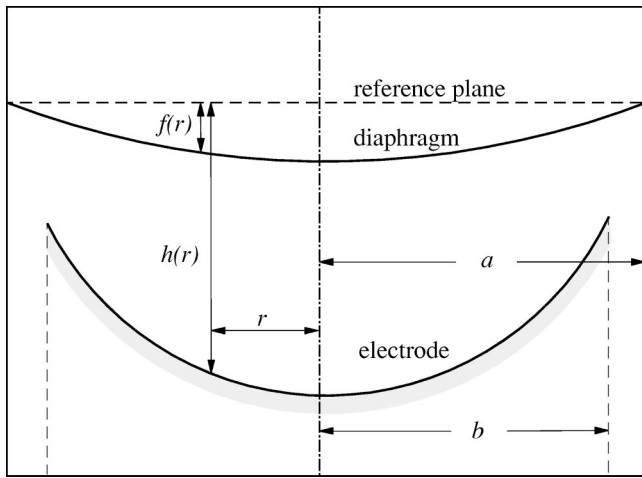
FIG. 5. Definition of the curves $h(r)$ specifying the shape of the electrode relative to the undisplaced diaphragm plane, and $f(r)$ specifying the shape of the diaphragm under electrostatic deflection.

a nonlinear equation that must be solved numerically, though the solution has a quite general form when the boundary condition that $z=0$ at $r=a$ is inserted. The electrostatic force per unit area, however, is greater at the edge of the diaphragm than at its center, because of the smaller separation there, and this leads to a displaced diaphragm shape that is approximately that of one half of a very oblate spheroid, the slope of the diaphragm being very steep at its edges, if the metalization is assumed to cover the entire diaphragm.

The escape from this difficulty is, however, quite simple. If the diaphragm metallization radius b is assumed to be approximately $0.9a$, then numerical evaluation shows that the steep diaphragm slope at its edge is eliminated, and the shape of the diaphragm is quite closely parabolic for $0 \leq r \leq b$, thus following the shape of the electrode as desired. This is a quite adequate solution. The improvements to be expected in sensitivity are similar to those for a type I microphone, and harmonic distortion in the microphone cartridge itself should be eliminated.

C. Electrode venting

As shown in Figs. 1 and 4, the electrodes in all condenser microphone designs have vent holes to relieve the compressive pressure in the thin air layer between the diaphragm and the electrode. Flow to the vent holes in this air layer is impeded by air viscosity, and the flow resistance increases inversely as the cube of the separation between the diaphragm and the electrode. In current manufacturing, the design of each microphone is optimized so that the damping provided by this resistance reduces appropriately the peak in the response at the resonance frequency.

To achieve uniform response over the whole area of the diaphragm in accord with the design objectives set out earlier, it is necessary that the size and spacing of the vent holes through the electrode also be optimized. The decreased diaphragm spacing toward its edges leads to a great increase in flow resistance in the enclosed air layer, which varies as h^{-3}. While the local acoustic impedance of the diaphragm is also higher, it is necessary to change the size and spacing of the

vent holes toward the edge of the diaphragm in order to achieve uniform damping behavior. The exact solution is outside the scope of the present paper.

D. Acoustic collapse

Another incidental advantage of the curved-electrode design is that such a microphone does not suffer from acoustically induced collapse of the diaphragm at very high sound pressure levels. In a planar-electrode design, particularly in a type II microphone, redistribution of charge on the diaphragm under very large acoustic deflection can cause collapse onto the electrode. No such charge redistribution occurs in the curved-electrode design, so the problem is not encountered.

E. Practical issues

The microphone designs discussed previously were idealized to a small extent. In the case of a type I microphone, for example, the electrostatic diaphragm deflection is not zero, though it is much smaller than for a type II microphone. As has been shown, however, the distorting effect on the diaphragm of this electrostatic displacement can be minimized if the electrode diameter is about 0.9 times the diaphragm diameter, and this is desirable for simple electrical reasons in any case. Electrical discharge between diaphragm and electrode should not be a problem, though a slightly curved edge to the electrode is probably desirable.

In practice it is also probably not reasonable to shape the electrode to a parabolic profile because of manufacturing difficulties. Because of the small curvature required, however, a spherical-dish shape is completely adequate. Indeed, almost any shallow dish shape should yield an improvement in microphone performance. To place the dimensions in context, the diaphragm spacing of a conventional 1 in. (25 mm) measuring microphone is typically about 20 μm, so the dished electrode, which is about 20 mm in diameter, will have a curvature radius of about 2.5 m. In the case of a conventional type II studio microphone cartridge, the unpolarized diaphragm separation is 40–50 μm, so that the curvature radius is about 1 m. Lapping tables to produce such curvatures in the electrodes are straightforward to produce since, in contrast with optical components, a surface accuracy of ± 1 μm is completely adequate. A lapping table with diameter 20 cm would typically require a central elevation of 2–5 mm, which is easily made and measured.

V. CONCLUSIONS

This analysis suggests that the behavior of all types of condenser microphones could be improved, both in relation to sensitivity and distortion, by using a shallowly dished electrode instead of the normal planar electrode design. While this adds minor manufacturing complications, it turns out that simple spherical dishing with a radius of curvature between about 1 and 2.5 m is adequate for most common microphone types, and this should not be difficult to implement. The appropriate electrode curvature depends on the type of microphone, the unpolarized diaphragm spacing and

tension, and the operating voltage. The analysis presented here allows the optimal electrode design to be calculated in each case.

It is a matter for discussion whether or not these advantages are of sufficient practical benefit to justify the required modifications to current microphone designs. An improvement in sensitivity of 4.5 dB is certainly helpful, but the same result could have been achieved with a planar design by reducing the diaphragm spacing by a factor 0.6 or by increasing the polarizing voltage by a factor 1.7. Similarly, the actual distortion level in a conventional microphone design depends upon the preamplifier as well as the cartridge, and this must be taken into account. Nevertheless, these are all advantages of the proposed new design, and there may be special applications in which they become important.

[1] G. Rasmussen, "A new condenser microphone," Brüel & Kjaer Technical Review No. 1, 1959; reprinted in *Measuring Microphones* (Brüel & Kjaer, Naerum, Denmark, 1972), pp. 1–11.

[2] F. W. O. Bauch, "New high-grade condenser microphone. I, II," Wireless World **59**, 50–54; **59**, 111–114 (1953).

[3] A. J. Zuckerwar, "Theoretical response of condenser microphones," J. Acoust. Soc. Am. **64**, 1278–1285 (1978).

[4] *Microphone Engineering Handbook*, edited by M. Gayford (Focal, Butterworth-Heinemann, Oxford, 1994).

[5] *AIP Handbook of Condenser Microphones*, edited by G. S. K. Wong and T. F. W. Embleton (AIP Press, New York, 1995).

[6] P. M. Morse, *Vibration and Sound*, 2nd ed. (reprinted by Acoustical Society of America, New York, 1948), pp. 183–208.

[7] A. J. Zuckerwar, "Principles of operation of condenser microphones," in Ref. 5, pp. 37–69.

Optimal source distribution for binaural synthesis over loudspeakers[a]

Takashi Takeuchi[b] and Philip A. Nelson
Institute of Sound and Vibration Research, University of Southampton, Highfield, Southampton SO17 1BJ, United Kingdom

When binaural sound signals are presented with loudspeakers, the system inversion involved gives rise to a number of problems such as a loss of dynamic range and a lack of robustness to small errors and room reflections. The amplification required by the system inversion results in loss of dynamic range. The control performance of such a system deteriorates severely due to small errors resulting from, e.g., misalignment of the system and individual differences in the head related transfer functions at certain frequencies. The required large sound radiation results in severe reflection which also reduces the control performance. A method of overcoming these fundamental problems is proposed in this paper. A conceptual monopole transducer is introduced whose position varies continuously as frequency varies. This gives a minimum processing requirement of the binaural signals for the control to be achieved and all the above problems either disappear or are minimized. The inverse filters have flat amplitude response and the reproduced sound is not colored even outside the relatively large "sweet area." A number of practical solutions are suggested for the realization of such optimally distributed transducers. One of them is a discretization that enables the use of conventional transducer units. © *2002 Acoustical Society of America.*
[DOI: 10.1121/1.1513363]

I. INTRODUCTION

A. Introduction

Binaural technology[1–3] is often used to present a virtual acoustic environment to a listener. The principle of this technology is to control the sound field at the listener's ears so that the reproduced sound field coincides with what would be produced when he is in the desired real sound field. One way of achieving this is to use a pair of loudspeakers (electroacoustic transducers) at different positions in a listening space with the help of signal processing to ensure that appropriate binaural signals, which contain all the spatial information, are obtained at the listener's ears.[4–7] Then the listener would experience an extremely realistic three dimensional sound environment.

One of the objectives of this study is to investigate a number of problems that arise from the multichannel system inversion involved in such binaural synthesis over loudspeakers. A basic analysis with a free field transfer function model illustrates the fundamental difficulties that such systems can have. The singular value decomposition helps to understand the role of the inverse filters more intuitively. The amplification required by the system inversion results in loss of dynamic range. The inverse filters obtained are likely to contain large errors around ill-conditioned frequencies. Regularization is often used to design practical filters but this also results in poor control performance around those frequencies. Sound radiation by transducers in directions other than that of the listener can be very large and this results in severe reflection and degrades control performance. Further analysis with a more realistic plant matrix, where the sound signals are controlled at a listener's ears in the presence of the listener's body (pinnae, head, etc.), demonstrates that this is still the case. Such problems are often noted as noise, distortion, fatigue of transducers, loss of directional and spatial perception, and coloration.

The investigation has resulted in the proposal of a system concept that we refer to as the Optimal Source Distribution (OSD). The OSD system overcomes these fundamental problems by means of a conceptual pair of monopole transducers whose span varies continuously as a function of frequency. The underlying theoretical principle is described in detail. The significance is that all of the above problems that are associated with the multichannel system inversion are solved by using this principle. The limitations with this principle are also made clear in terms of the operational frequency range. Several examples of practical solutions that can realize a variable transducer span are also described. One of them is the discretization and it enables the use of conventional transducer units and crossover filter networks with only a little decrease in performance from theoretical limit. The practical system realized has a very good performance over a wide frequency range (e.g., over the whole audible frequency range).
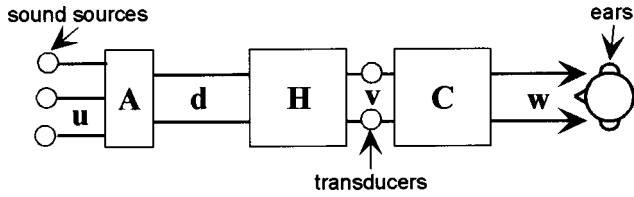
FIG. 1. Block diagram for multichannel sound control with system inversion.

B. Principles of binaural synthesis over loudspeakers

System inversion is often used for multichannel sound control including binaural reproduction over loudspeakers. The principle of such systems is described below with 2-channel case as an example and is illustrated in Fig. 1. The objective of the system is to feed to each ear of the listener independently the binaural signals that contain spatial information of sound as well as the signals associated with the sources in a virtual sound environment. However, when loudspeakers are used for this purpose, each loudspeaker feeds its signal to both ears. There is a matrix of acoustic paths between the loudspeakers and the listener's ears, and this can be expressed as a matrix of transfer functions (plant matrix). Independent control of two signals (such as the binaural sound signals) at two receivers (such as the ears of a listener) can be achieved with two electroacoustic transducers (such as loudspeakers), by filtering the input signals to the transducers with the inverse of the transfer function matrix of the plant. This process is also referred as system inversion. The signals and transfer functions involved are defined as follows. Two monopole transducers produce source strengths (volume accelerations) defined by the elements of the complex vector $\mathbf{v}=[\nu_1(j\omega) \quad \nu_2(j\omega)]^T$. The resulting acoustic pressure signals are given by the elements of the vector $\mathbf{w}=[w_1(j\omega)w_2(j\omega)]^T$. This is given by

$$\mathbf{w}=\mathbf{Cv}, \tag{1}$$

where $\mathbf{C}$ is the plant matrix (a matrix of transfer functions between sources and receivers). The two signals to be synthesised at the receivers are defined by the elements of the complex vector $\mathbf{d}=[d_1(j\omega) \quad d_2(j\omega)]^T$. In the case of audio applications, these signals are usually the signals that would produce a desired virtual auditory sensation when fed to the two ears independently. They can be obtained, for example, by recording sound source signals $\mathbf{u}$ with a recording head (e.g., a dummy head) or by filtering the signals $\mathbf{u}$ by matrix of synthesised binaural filters $\mathbf{A}$.

Therefore, a filter matrix $\mathbf{H}$ which contains inverse filters is introduced (the inverse filter matrix) so that $\mathbf{v}=\mathbf{Hd}$, where

$$\mathbf{H}=\begin{bmatrix} H_{11}(j\omega) & H_{12}(j\omega) \\ H_{21}(j\omega) & H_{22}(j\omega) \end{bmatrix} \tag{2}$$

and thus

$$\mathbf{w}=\mathbf{CHd}. \tag{3}$$

For convenience in later analysis, we also define the control performance matrix $\mathbf{R}$ given by
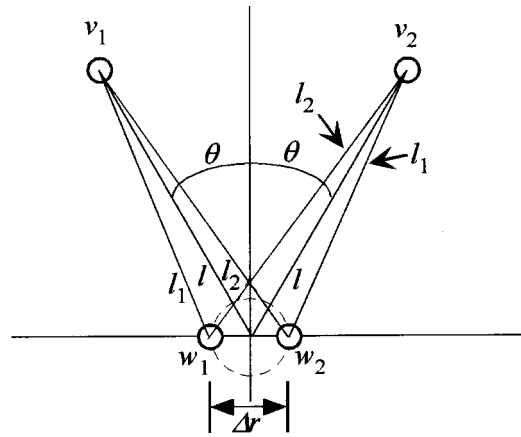
FIG. 2. Geometry of a 2-source 2-receiver system under investigation.

$$\mathbf{R}=\mathbf{CH}. \tag{4}$$

The inverse filter matrix $\mathbf{H}$ can be designed so that the vector $\mathbf{w}$ is a good approximation to the vector $\mathbf{d}$ with a certain delay.[8,9] When the independent control at two receivers is perfect, the matrix $\mathbf{R}$ becomes the identity matrix $\mathbf{I}$. However, various factors introduce errors into the process. When errors are present, the diagonal term of the matrix $\mathbf{R}$ shows the portion of desired signal transmission and the other terms are the cross-talk components.

II. ANALYSIS WITH A FREE FIELD MODEL AND THE SINGULAR VALUE DECOMPOSITION

A simple case involving the control of two monopole receivers with two monopole transducers (sources) under free field conditions is first considered here in order to understand the physics underlying binaural synthesis over loudspeakers. The fundamental problems with regard to system inversion can be illustrated in this simple case where the effect of path length difference dominates the problem. The singular value decomposition helps to understand the role of the inverse filter matrix more intuitively, since it decomposes the matrix into multiple parts and each of these has a simple physical role. A matrix of Head Related Transfer Functions (HRTFs) is also analyzed in the later section as an example of a more realistic plant matrix. In such a case, the acoustic response of the human body (pinnae, head, torso, and so on) also comes to affect the problem. However, the fundamental difficulties inherit to such systems can still be seen predominantly.

A. Inverse filter matrix

A symmetric case with the intersource axis parallel to the inter-receiver axis is considered for an examination of the basic properties of the system. The geometry is illustrated in Fig. 2. In the free field case, the plant transfer function matrix can be modelled as

$$\mathbf{C}=\frac{\rho_0}{4\pi}\begin{bmatrix} e^{-jkl_1}/l_1 & e^{-jkl_2}/l_2 \\ e^{-jkl_2}/l_2 & e^{-jkl_1}/l_1 \end{bmatrix}, \tag{5}$$

where an $e^{j\omega t}$ time dependence is assumed with $k=\omega/c_0$, and where ρ_0 and c_0 are the density and sound speed. When the ratio of and the difference between the path lengths con-

necting one source and two receivers are defined as $g = l_1/l_2$ and $\Delta l = l_2 - l_1$,

$$\mathbf{C} = \frac{\rho_0 e^{-jkl_1}}{4\pi l_1}\begin{bmatrix} 1 & ge^{-jk\Delta l} \\ ge^{-jk\Delta l} & 1 \end{bmatrix}. \tag{6}$$

Now consider the case

$$\mathbf{d} = \frac{\rho_0 e^{-jkl_1}}{4\pi l_1}\begin{bmatrix} D_1(j\omega) \\ D_2(j\omega) \end{bmatrix}, \tag{7}$$

i.e., the desired signals are the acoustic pressure signals which would have been produced by the closer sound source alone whose values are either $D_1(j\omega)$ or $D_2(j\omega)$ without disturbance due to the other source (cross-talk). This normalization enables a description of the effect of system inversion as well as ensuring a causal solution. The elements of $\mathbf{H}$ can be obtained from the exact inverse of $\mathbf{C}$ and can be written as

$$\mathbf{H} = \mathbf{C}^{-1} = \frac{1}{1 - g^2 e^{-2jk\Delta l}}\begin{bmatrix} 1 & -ge^{-jk\Delta l} \\ -ge^{-jk\Delta l} & 1 \end{bmatrix}. \tag{8}$$

When $l \gg \Delta r$, we have the approximation $\Delta l \approx \Delta r \sin\theta$ where $\Theta = 2\theta$ is the source span (hence $0 < \Theta \leq \pi$) and under these conditions,

$$\mathbf{H} = \frac{1}{1 - g^2 e^{-2jk\Delta r \sin\theta}}\begin{bmatrix} 1 & -ge^{-jk\Delta r \sin\theta} \\ -ge^{-jk\Delta r \sin\theta} & 1 \end{bmatrix}. \tag{9}$$

B. Singular value decomposition

The singular value decomposition helps to understand the role of the inverse filter matrix $\mathbf{H}$ more intuitively. As described in the Appendix, the inverse filter matrix $\mathbf{H}$ can be expressed as

$$\mathbf{H} = \mathbf{U}\mathbf{\Sigma}^{-1}\mathbf{V}^H = \begin{bmatrix} \frac{1}{\sqrt{2}} & \frac{1}{\sqrt{2}} \\ \frac{1}{\sqrt{2}} & -\frac{1}{\sqrt{2}} \end{bmatrix}\begin{bmatrix} \sigma_i & 0 \\ 0 & \sigma_o \end{bmatrix}$$
$$\times \frac{1}{\sqrt{2}}\begin{bmatrix} \sqrt{\frac{1+ge^{jk\Delta l}}{1+ge^{-jk\Delta l}}} & \sqrt{\frac{1+ge^{jk\Delta l}}{1+ge^{-jk\Delta l}}} \\ \sqrt{\frac{1-ge^{jk\Delta l}}{1-ge^{-jk\Delta l}}} & -\sqrt{\frac{1-ge^{jk\Delta l}}{1-ge^{-jk\Delta l}}} \end{bmatrix},$$

where

$$\sigma_i = \frac{1}{\sqrt{(1 + ge^{-jk\Delta r \sin\theta})(1 + ge^{jk\Delta r \sin\theta})}}$$

and

$$\sigma_o = \frac{1}{\sqrt{(1 - ge^{-jk\Delta r \sin\theta})(1 - ge^{jk\Delta r \sin\theta})}}. \tag{10}$$

The unitary matrix $\mathbf{V}^H$ extracts the in-phase and out-of phase components out of the binaural signals. (Superscript H denotes the Hermitian transpose of a matrix; that is the complex conjugate of the transpose.) It also introduces phase rotation according to the property of the plant but does not change their amplitude. The two singular values are denoted
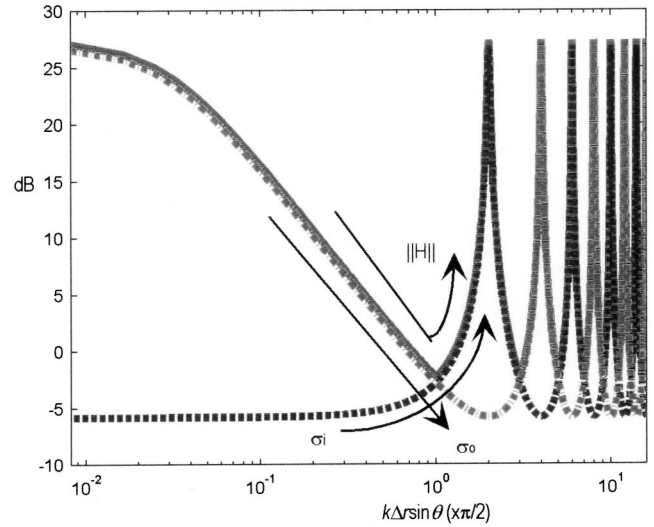
FIG. 3. Norm and singular values of the inverse filter matrix $\mathbf{H}$ as a function of $k\Delta r \sin\theta$.

by σ_i and σ_o, and correspond to orthogonal components of the inverse filters. The singular value σ_i corresponds to the amplification factor of the in-phase component of the binaural signals and the other singular value σ_o corresponds to the amplification factor of the out-of-phase component of the binaural signals. The unitary matrix $\mathbf{U}$ distributes the suitably amplified in-phase and out-of phase components into the pair of transducers.

The net effect of the inverse filter matrix $\mathbf{H}$ depends largely on the content of the input signals $\mathbf{d}$, i.e., the characteristics of the sound source signal contents and the auditory virtual space being created. However, the maximum amplification of the source strengths required for the arbitrary binaural signal input at each frequency can be found from the 2-norm of $\mathbf{H}$ ($\|\mathbf{H}\|$). Since $\|\mathbf{U}\| = \|\mathbf{V}\| = 1$, this is equal to the largest of the singular values. Thus

$$\|\mathbf{H}\| = \|\mathbf{\Sigma}\| = \max(\sigma_i, \sigma_o). \tag{11}$$

Plots of σ_i, σ_o, and $\|\mathbf{H}\|$ with respect to $k\Delta r \sin\theta$ are illustrated in Fig. 3. The examples throughout this paper use typical values of the distance between the adult human ears for Δr. As seen in Eq. (10) and Fig. 3, the singular values σ_i and σ_o interchange their amplitude as a function of frequency and source span, periodically giving peaks of $\|\mathbf{H}\|$ where k and θ satisfy the following relationship with even values of the integer number n:

$$k\Delta r \sin\theta = \frac{n\pi}{2}. \tag{12}$$

This is where a term in the denominator of the singular values becomes very small (nearly zero) so the singular values become very large. The singular value σ_i has peaks at $n = 2, 6, 10, \ldots$ where the system is required to use large effort to reproduce the in-phase component of the desired signals. The singular value σ_o has peaks at $n = 0, 4, 8, \ldots$ where the system is required to use large effort to reproduce the out-of-phase component. Around these frequencies, sound signals from control sources interfere destructively with each other, leaving little response left. In other words, the signals

FIG. 4. Dynamic range loss due to system inversion.
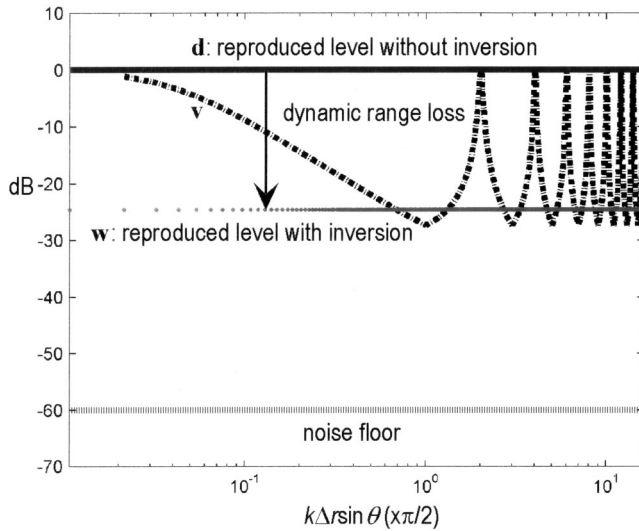
FIG. 5. Dynamic range loss as a function of source span.

cancel each other. Therefore, the solution for the inverse, i.e., the amplification required to produce the desired sound pressure at each receiver, becomes substantially large. The low frequency boost as a consequence of the peak at $n=0$ has often been addressed in several papers[3] but the other features, especially the peak for the in-phase component, has drawn less attention.

III. FUNDAMENTAL PROBLEMS OF EXISTING SYSTEMS

A. Loss of dynamic range

In practice, since the maximum source output is given by $\|\mathbf{H}\|_{max}$, this must be within the range of the system in order to avoid clipping of the signals. The required amplification by the inverse filter matrix $\mathbf{H}$ results directly in the loss of dynamic range illustrated in Fig. 4. The level of the output source signals ($\mathbf{d}$: without system inversion, $\mathbf{v}$: with inversion) and the resulting level of the acoustic pressure at listener's ears ($\mathbf{d}$: without inversion, $\mathbf{w}$: with inversion) are plotted assuming that the maximum output levels and dynamic range of the systems are the same. Where $\|\mathbf{H}\|$ is large, each transducer is emitting very large sound most of which is cancelled by the sound from the other transducers. As a result, the levels of synthesized binaural signals at the listener's ears are significantly smaller than that those without cancellation. The given dynamic range is distributed into the system inversion and the remaining dynamic range that is to be used by the binaural auditory space synthesis, and also most importantly, by the sound source signal itself. Thus the signal-to-noise ratio of the signals $\mathbf{w}$ becomes low. Since the transducers are working much harder than usual use to produce usual sound level at the ears, nonlinear distortion becomes more significant and is often audible. For the same reason, fatigue of the transducers is more severe. Conventional driver units are not designed to be used in this manner and they can be easily destroyed by fatigue.

The dynamic range loss is defined by the difference between the signal level at the receiver with one monopole source and the signal level reproduced by two sources having
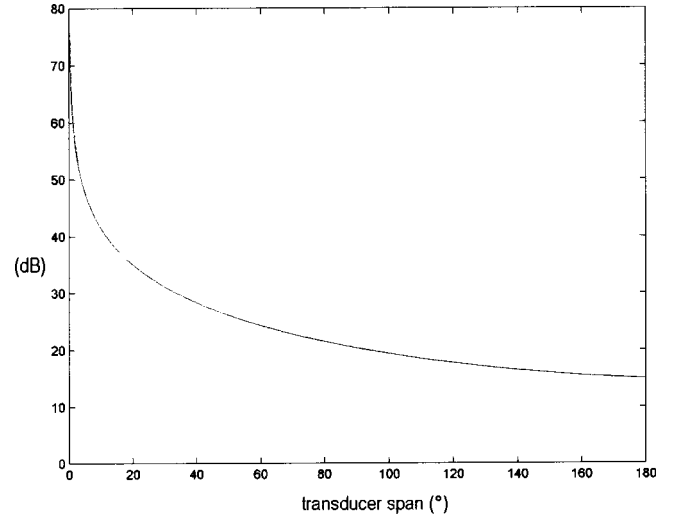
the same maximum source strength when the system is inverted. The frequency of the peaks of $\|\mathbf{H}\|$ do not affect the amount of dynamic range loss but the magnitude of the peaks do. Since $\|\mathbf{H}\|$ here is normalized by the case without system inversion by Eq. (7), the dynamic range loss Γ is given by $\|\mathbf{H}\|_{max}$. For example, when $n=2,6,10,\ldots$, $k\Delta r \sin \theta=\pi,3\pi,5\pi,\ldots$, therefore, $e^{-jk\Delta r \sin \theta}=e^{-jk\Delta r \sin \theta}=-1$. Thus

$$\Gamma=\|\mathbf{H}\|_{max}=\max(\sigma_i)=\max(\sigma_o)=\frac{1}{1-g}. \quad (13)$$

The dynamic range loss given by Eq. (13) as a function of source span is shown in Fig. 5. Since $g\approx 1-\Delta r \sin \theta/l$, then Γ can be approximated as

$$\Gamma\approx\frac{l}{\Delta r \sin \theta} \quad (14)$$

as a function of θ. Figure 5 and Eq. (14) show that the larger the source span, the less is the dynamic range loss. It varies from more than 70 dB when two transducers are very close together to about 15 dB when they are on opposite sides of the ears. When there is a head between the ears, this is relaxed a little.

B. Robustness to error in the plant

A problem is said to be well-conditioned if small changes in parameters produce small changes in the solution, and ill-conditioned if relatively large changes are produced. The extent to which a process can be regarded as well-conditioned can be evaluated by calculating the condition number.[10] Equation (1) implies that the system inversion (which determines $\mathbf{v}$ and leads to the design of the filter matrix $\mathbf{H}$) is very sensitive to small errors in the assumed plant $\mathbf{C}$ (which is often measured and thus small errors are inevitable) where the condition number of $\mathbf{C}$, $\kappa(\mathbf{C})$, is large.[10] Such errors include individual differences of HRTFs,[11–13] and misalignment of the head and loudspeakers.[14] The condition number of $\mathbf{C}$ is given by
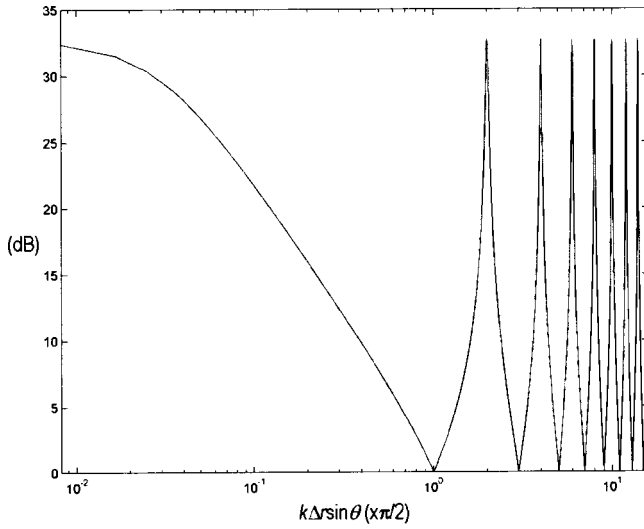
FIG. 6. Condition number $\kappa(\mathbf{C})$ as a function of n.

$$\kappa(\mathbf{C}) = \|\mathbf{C}\|\|\mathbf{C}^{-1}\| = \|\mathbf{C}\|\|\mathbf{H}\| = \|\mathbf{H}^{-1}\|\|\mathbf{H}\|$$

$$= \max\left(\sqrt{\frac{(1+g\mathrm{e}^{-jk\Delta r\sin\theta})(1+g\mathrm{e}^{jk\Delta r\sin\theta})}{(1-g\mathrm{e}^{-jk\Delta r\sin\theta})(1-g\mathrm{e}^{jk\Delta r\sin\theta})}}, \right.$$

$$\left. \sqrt{\frac{(1-g\mathrm{e}^{-jk\Delta r\sin\theta})(1-g\mathrm{e}^{jk\Delta r\sin\theta})}{(1+g\mathrm{e}^{-jk\Delta r\sin\theta})(1+g\mathrm{e}^{jk\Delta r\sin\theta})}} \right) \quad (15)$$

and is shown in Fig. 6. As seen in Eq. (15) and Fig. 6, $\kappa(\mathbf{C})$ has peaks where Eq. (12) is satisfied with an even value of the integer number n. The frequencies which give peaks of $\kappa(\mathbf{C})$ are consistent with those which give the peaks of $\|\mathbf{H}\|$.

Around the frequencies where $\kappa(\mathbf{C})$ is large, the system is very sensitive to small errors in $\mathbf{C}$.[15] The calculated inverse filter matrix $\mathbf{H}$ is likely to contain large errors due to small errors in $\mathbf{C}$ and results in large errors in the reproduced signal $\mathbf{w}$ at the receiver. This is because such errors are magnified by the inverse filters but remain uncancelled in the plant. On the contrary, $\kappa(\mathbf{C})$ is small around the frequencies where n is an odd integer number in Eq. (12). For the same value of n, the robust frequency range becomes lower as the source span becomes larger. With a logarithmic frequency scale, which is related to the perceptual attributes of the human auditory system, the frequency range of robust inversion is more or less constant for different source spans for the same value of n, even though it looks wider for smaller source spans on a linear frequency scale.

C. Robustness to error in the inverse filters

In addition, since

$$\mathbf{v} = \mathbf{C}^{-1}\mathbf{w} \quad (16)$$

and $\kappa(\mathbf{C}^{-1}) = \kappa(\mathbf{C})$, a practical and close to ideal inverse filter matrix $\mathbf{H}$ is easily obtained where $\kappa(\mathbf{C})$ is small. However, the reproduced signals $\mathbf{w}$ are less robust to small changes in the inverse of the plant matrix $\mathbf{C}^{-1}$, hence $\mathbf{H}$, where $\kappa(\mathbf{C})$ is large. Even if $\mathbf{C}$ does not contain any errors, the reproduction of the signals at the receiver is too sensitive to the small errors within the inverse filter matrix $\mathbf{H}$ to be useful.
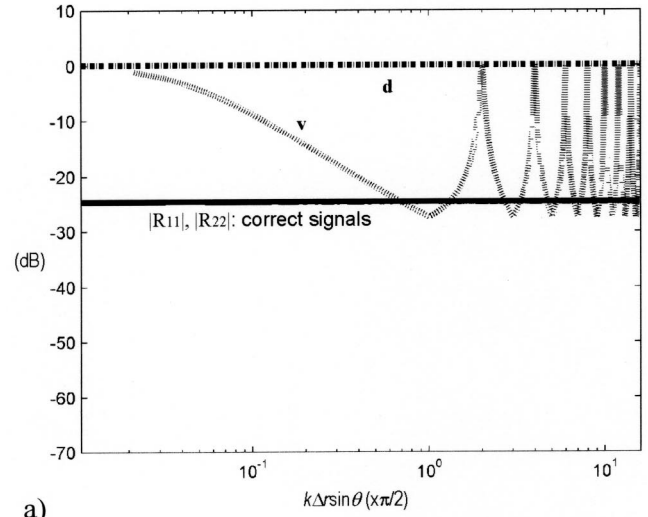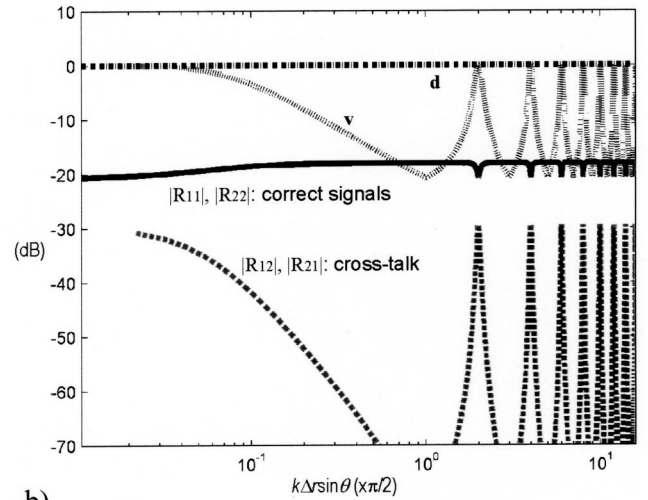
FIG. 7. Dynamic range improvement and loss of control performance with regularization. (a) Without regularization. (b) With regularization.

One common example of such an error is that due to regularisation, where a small error is deliberately introduced to improve the condition of matrix to design practical filters.[16] It is also possible to reduce the excess amplification and hence the dynamic range loss by means of regularization, where the pseudoinverse filter matrix $\mathbf{H}$ is given by

$$\mathbf{H} = [\mathbf{C}^{\mathrm{H}}\mathbf{C} + \beta\mathbf{I}]^{-1}\mathbf{C}^{\mathrm{H}}, \quad (17)$$

where β is a regularization parameter. The regularization parameter penalizes large values of $\mathbf{H}$ and hence limits the dynamic range loss of the system. Since $\|\mathbf{H}\|$ is normalized by the case without system inversion by Eq. (7), the regularization parameter limits the dynamic range loss to less than about

$$\Gamma \approx -10\log_{10}\beta - 6 \quad \text{(dB)}. \quad (18)$$

However, the regularization parameter intentionally, hence inevitably, introduces a small error in the inversion process. This gives rise to a problem for filter design at frequencies where $\kappa(\mathbf{C})$ is large. An example of this is illustrated in Fig. 7. The dynamic range loss is reduced by regularization from

about 27 dB (without regularization) as in Fig. 7(a) to 14 dB as shown in Fig. 7(b) ($\beta = 10^{-2}$). However, it can be clearly seen that the control performance of the system deteriorates around the frequencies where n is an even integer number in Eq. (12). The contribution of the correct desired signals (R_{11} and R_{22}) is reduced only slightly but the contribution of the wrong desired signals (R_{12} and R_{21}, the cross-talk component) is increased significantly. In other words, the system has little control (cross-talk cancellation) around these frequencies. This problem is significant at lower frequencies [$n < 1$ in Eq. (12)] in the sense that the region without cross-talk suppression is large, and at higher frequencies [$n > 1$ in Eq. (12)], in the sense that there are many frequencies at which the plant is ill-conditioned. With an equivalent dynamic range loss, making the source span larger leads to a better control performance at lower frequencies but a poorer performance at higher frequencies. On the contrary, making the source span smaller leads to better control performance at higher frequencies but poorer performance at lower frequencies.

D. Robustness to reflections

Reflections from surrounding objects (e.g., walls, floors, and ceilings) affect the control performance. The effect of reflections on this kind of system has been studied with a simple image source model and subjective experiments.[17] Although the perceptual aspects of sound localization such as the precedence effect suggest that the performance of this kind of system will be retained to some extent,[18] reflected sound with a much larger level than the control sound arriving directly at the listener's ears destroys the correct perception. Therefore, the relative level of sound radiation in directions other than towards listener's ears is a very good measure of the robustness of the system to reflections. Figure 8 shows an example ($n \approx 2$) of far field sound radiation by the control transducers with reference to the receiver directions. The horizontal axis is the intersource axis and the receivers (ears) are at the directions of the vertical axis. At frequencies where Eq. (12) is not satisfied with an odd value of the integer number n, as in this example, the sound radiation in directions other than receiver directions can be significantly larger (typically +30 dB~+40 dB) than those at the receiver directions (0 dB and $-\infty$ dB). The maximum amount of this excessive radiation is the same as the amount of dynamic range loss as in Eq. (13) and Fig. 5. When the environment is not anechoic, as is normally the case, this obviously results in severe reflections and the control performance of the system deteriorates. In addition, the sound radiated in directions other than that of receiver has a peaky frequency response due to the response of inverse filter matrix **H** and normally result in severe coloration.

IV. A SYSTEM TO OVERCOME THE PROBLEMS

As discussed above, there is a trade-off between dynamic range, robustness, and control performance. However, a system which aims to overcome these fundamental problems is proposed in what follows.
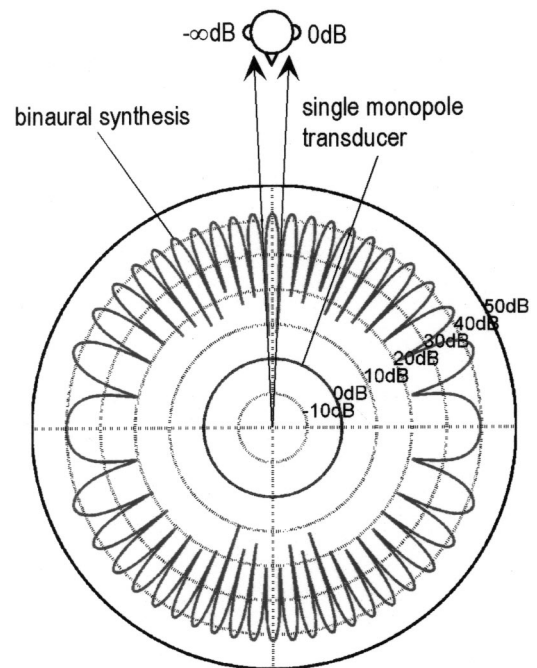
FIG. 8. Sound radiation by the control transducer pairs with reference to the receiver directions (0 dB and $-\infty$ dB).

A. Principle of the optimal source distribution

Equation (12) can be rewritten in terms of the source span Θ as

$$\Theta = 2\theta = 2\arcsin\left(\frac{n\pi}{2k\Delta r}\right).$$ (19)

As seen from the analysis above, systems with the source span where n is an odd integer number in Eq. (19) gives the best control performance as well as robustness. This implies that the optimal source span must vary as a function of frequency.

We now consider a pair of conceptual monopole transducers whose span varies continuously as a function of frequency (Fig. 9) in order to satisfy the requirement for n to be an odd integer number in Eq. (19) (Fig. 10). This relationship is where σ_i and σ_o are balanced and the source span becomes smaller as frequency becomes higher. With this concept, the expression for the inverse filter matrix **H** [Eq. (9)] becomes very simple as

$$\mathbf{H} = \frac{1}{1+g^2}\begin{bmatrix} 1 & -jg \\ -jg & 1 \end{bmatrix}.$$ (20)
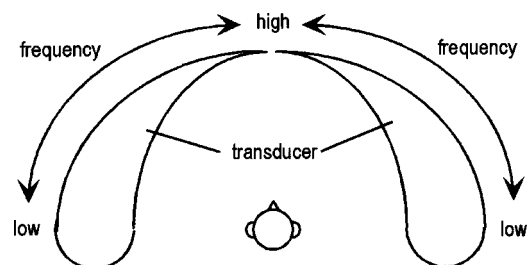
FIG. 9. Principle of the "OSD" system.
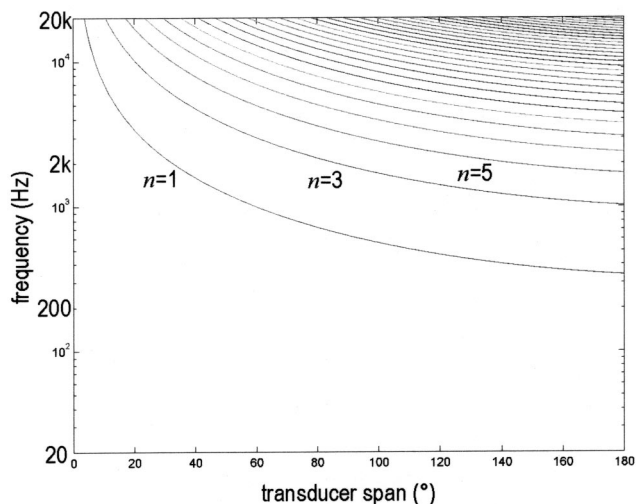
FIG. 10. Relationship between source span and frequency for different odd integer number n.

Note that $\|\mathbf{H}\|=1/\sqrt{2}$ for all frequencies. Therefore, there is no dynamic range loss compared to the case without system inversion. In fact, there is a dynamic range gain of 3 dB since the two orthogonal components of the desired signals are $\pi/2$ out of phase. This means the system has good signal to noise ratio and advantage over distortion or fatigue of transducers. The inverse filters have flat frequency response so there is no coloration, in excess of that produced by room response, at any location in the listening room even outside the sweet area. When the listener is far away from the sweet spot, the spatial information perceived may not be ideal. However, the spectrum of the sound signals are not changed by the inverse filters. Therefore, the listener can still enjoy the natural production of sound together with some remaining spatial aspects. The sound radiation by the transducer pair in all directions is always smaller than those at the receiver directions, which is also smaller than the sound radiation by a single monopole transducer producing the same sound level at the ears as shown in Fig. 11. In contrast to Fig. 8, the system
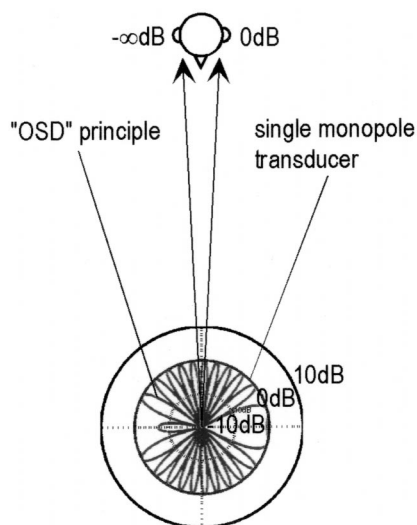
FIG. 11. Sound radiation by the "OSD" loudspeakers with reference to the receiver directions (0 dB and $-\infty$ dB).

does not radiate excessive sound all around so it is also robust to reflections in a reverberant environment, and these small reflections do not have any coloration other than that caused by the reflecting materials. Note also that $\kappa(\mathbf{C})=1$ which is constant over all frequencies and which is the smallest possible value. The error in calculating the inverse filter is small and the system has very good control over the reproduced signals. The system is also very robust to the changes in plant matrix.

Also note that when $l \gg \Delta r$, $g \approx 1$ therefore,

$$\mathbf{H} \approx \frac{1}{2}\begin{bmatrix} 1 & -j \\ -j & 1 \end{bmatrix}. \tag{21}$$

This implies that independent control of the two signals is nearly achieved just by addition of the desired signals with a $\pi/2$ relative phase shift between them.

B. Aspects of the proposed system

From Eq. (19), the range of variable source span Θ is given by the frequency range of interest as can be seen from Fig. 10. A smaller value of n gives a smaller source span for the same frequency. Therefore, the smallest source span Θ_h for the same high frequency limit is given by $n=1$ and this is about 4° to give control of the sound field at two positions separated by the distance between two ears (about 0.13 m for KEMAR dummy head[19]) up to a frequency of 20 kHz.

Equation (12) can also be rewritten in terms of frequency as

$$f = \frac{nc_0}{4\Delta r \sin\theta}, \tag{22}$$

The smallest value of n gives the lowest frequency limit for a given source span. Since $\sin\theta \leqslant 1$,

$$f \geqslant \frac{nc_0}{4\Delta r}, \tag{23}$$

i.e., the physically maximum source span of $\Theta=2\theta=180°$ gives the lowest frequency limit, f_l, associated with this principle. A smaller value of n gives a lower low frequency limit so the system given by $n=1$ is normally the most useful among those with an odd integer number n. The low frequency limit given by $n=1$ of a system designed to control the sound field at two positions separated by the distance between two ears is about $f_l=300\sim400$ Hz.

C. Consideration of the head related transfer function model

The condition number $\kappa(\mathbf{C})$ of the plant matrix plotted as a function of frequency and source span is shown in Fig. 12 for the audible frequency range (20 Hz$\sim$20 kHz). Figure 13 shows the condition number of the more realistic plant matrix with HRTFs. The HRTFs were measured with the KEMAR dummy head at MIT Media Lab[20] and the loudspeaker response was deconvolved later. Those between sampled directions are obtained by bilinear interpolation on the virtual spherical surface of magnitude and phase spectra in the frequency domain.[14] A similar trend can clearly be seen as in the free field case. However, additional "ill-
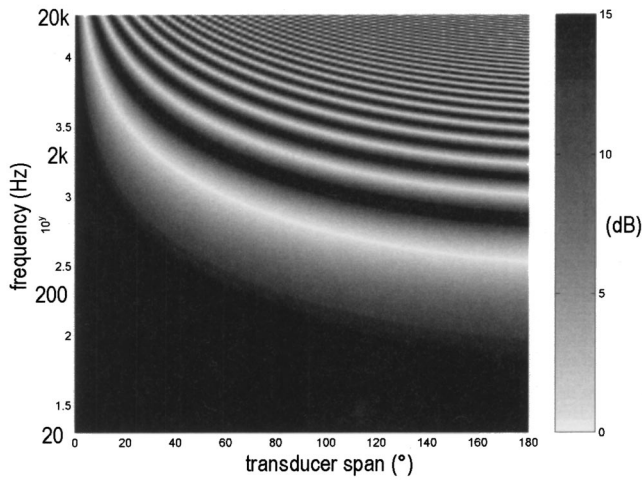
FIG. 12. Condition number $\kappa(\mathbf{C})$ of a free field plant matrix $\mathbf{C}$ as a function of source span and frequency.

a)

b)

FIG. 14. Flat panel transducers. (a) Individual excitation. (b) Point excitation.

conditioned frequencies'' can be observed around 9 kHz and 13 kHz where the HRTFs have minima. It is possible that the signal-to-noise ratio of the measured data around these frequencies is poor.

It should also be noted that where the incidence angle θ is small, the peak frequencies obtained with the HRTF plant matrix are similar to that of the free field plant with the receiver distance $\Delta r \approx 0.13$. This corresponds to the shortest distance between the entrances of the ear canals of the KEMAR dummy head. However, where the incidence angle θ is large, the peak frequencies obtained with the HRTF plant matrix are similar to that of the free field plant with the receiver distance $\Delta r \approx 0.25$. This is a much larger distance than the shortest distance between the entrances of the ear canals of the KEMAR dummy head and is a result of diffraction around the head. A correction to the receiver distance Δr can be made in order to match the frequency-span characteristics of the free field model. Following is an example of a linear approximation,

$$\Delta r = \Delta r_0 (1 + \Theta / \pi), \tag{24}$$

FIG. 13. Condition number $\kappa(\mathbf{C})$ of a plant matrix $\mathbf{C}$ with HRTFs as a function of source span and frequency.

where Δr_0 is the geometrical distance between the ears. Figure 12 incorporates Eq. (24) and shows good agreement with Fig. 13 which is obtained from more realistic KEMAR data.

D. Transducers for the optimal source distribution

This principle requires a pair of monopole type transducers whose position from which sound is radiated varies continuously as frequency varies. This might, for example, be realized by exciting a plate at each position individually [Fig. 14(a)]. The requirement of such a transducer is that a certain frequency of vibration is excited most at a particular position such that sound of that frequency is radiated mostly from that position. Relatively large damping would be required to suppress unwanted plate vibration modes. Such characteristics may also be achieved by exciting a triangular shaped plate with large damping at one end whose width and stiffness varies along its length in a controlled manner [Fig. 14(b)]. The narrow and stiff excited end radiates most high frequency sound whereas the wide and floppy end of the plate radiates the lower frequency sound. This principle is very similar to the way the basilar membrane of the human auditory system performs frequency decomposition. Alternatively, a similar effect might be obtained by changing the width of a slot along an acoustic waveguide (Fig. 15). Again a relatively large damping would be necessary in order to suppress peaks at resonance. In both cases, the vibration characteristics of the plate or air particles would differ along the length, and so as the radiation impedance. Then, transducers which effectively distribute each frequency components to desired position may be designed.
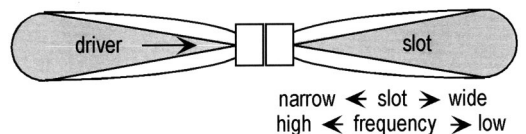
FIG. 15. Acoustic waveguide type transducers.
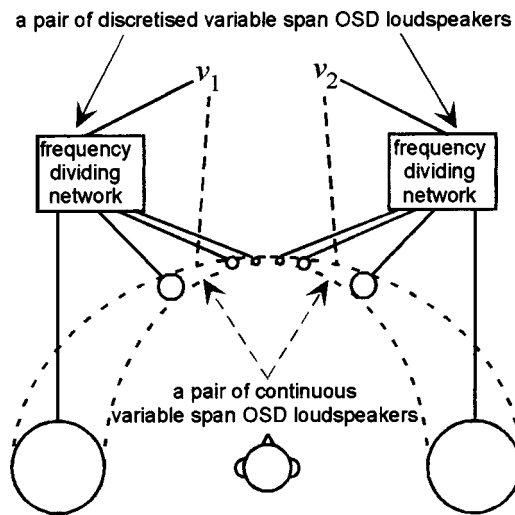
FIG. 16. Discretized variable frequency/span transducers.

V. DISCRETE SYSTEM

A. Discretization of frequency-span relationship

In practice, a monopole transducer whose position varies continuously as a function of frequency is not easily available. However, it is possible to realize a practical system based on this principle by discretizing the transducer span as illustrated in Fig. 16 and Fig. 17. With a given span, the frequency region where the amplification is relatively small and plant matrix $\mathbf{C}$ is well conditioned is relatively wide around the optimal frequency. Therefore, by allowing n to have some width, say $\pm\nu$ $(0<\nu<1)$, which results in a small amount of dynamic range loss and slightly reduced robustness, a certain transducer span can nevertheless be allocated to cover a certain range of frequencies where control performance and robustness of the system is still reasonably good (Fig. 17). Consequently, it is possible to discretize the continuously varying transducer span into a finite number of discrete transducer spans. A system with a smaller n gives a wider region with the same performance on a logarithmic scale as can be seen in Figs. 12 and 13.

It is important to design the system to ensure $\|\mathbf{H}\|$ and $\kappa(\mathbf{C})$ that are as small as possible over a frequency range that is as wide as possible. Therefore, the transducer spans for
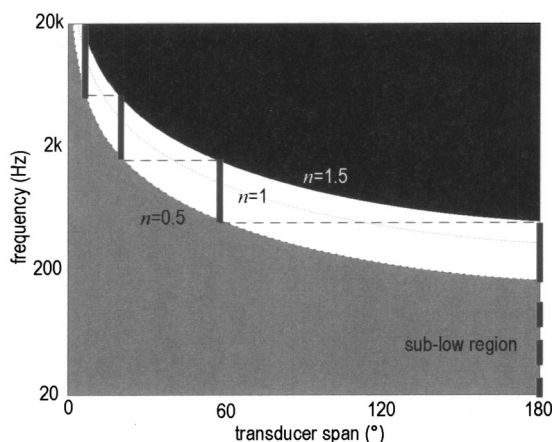
FIG. 17. An example of frequency/span region and discretization.

each pair of transducers in each frequency range can be decided to ensure that the smallest possible values of n are used over all frequency ranges of interest above f_1.

It is also possible to discretize, i.e., decide the transducer spans and frequency ranges to be covered by each pair of driver units (i.e., range of n), in terms of a tolerable dynamic range loss. The dynamic range loss of the entire system is now given by the maximum value among the values given by each discretized transducer span.

A number of examples of the discrete OSD system have been simulated.[21] The effect has been calculated of discretization number and the allocated dynamic range loss on the cross-talk cancellation performance. Studies have been undertaken of the spans for each discretized control transducers arrangement, crossover frequencies, and width of ν. Practical consideration above a number of possibilities for designing crossover filters and inverse filters have also been described in detail. In short, the dynamic range loss is more than 40 dB when the discretization is one way. It reduces to 18 dB when the discretization is two way and to less than 7 dB when discretization is three way.

B. Consequence of the discretization of variable source span

The discretization is extremely useful and practical because a single transducer which can cover the whole audible frequency range is not practically available either. Therefore, this principle also gives the ideal background for multiway systems for binaural reproduction over loudspeakers which maximize the frequency range to be produced and controlled. Conventional driver units and crossover filters can easily be accommodated to be used for this system. It should be noted that this is still a simple "2 channel" control system where only two independent control signals are necessary to control any form of virtual auditory space. This in principle can synthesize an infinite number of virtual source locations with different source signals with any type of acoustic response of the space. The difference for this discrete system from the conventional 2-channel system is that the two control signals are divided into multiple frequency bands and fed into the different pairs of driver units with different spans. Ironically, substantial effort has been invested in conventional multiway loudspeakers for stereophony in order to approximate a point source by multiple driver units. The discrete OSD system requires just the opposite; different driver units are required to be at different locations. A "poor" performance unit in the sense of stereophony which has relatively narrow operational frequency range may perform very well with this principle.

It should be noted that the low frequency limit f_1 given by odd integer numbers n in Eq. (23) is extended towards a lower frequency by discretization because now the region for frequency and transducer span where n is not an integer number is also used. For example, a practical system discretized from the ideal system with $n=1$ can now make use of the region $1-\nu<n<1+\nu$ so that the low frequency limit is given by $n=1-\nu$.

As can be seen from Figs. 10 and 17, in the higher frequency range where the source span is very small, the frequency range to be covered is very sensitive to small
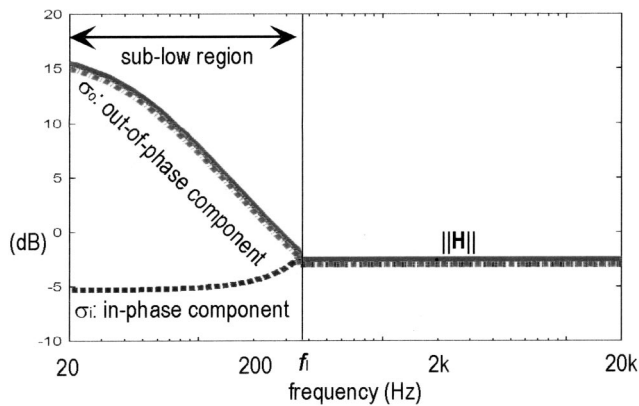
FIG. 18. Norm and two singular values of the inverse filter matrix **H** with "OSD" principle.

differences in transducer span. On the contrary, it is very insensitive to the source span at lower frequencies. Consequently, the range of practical span for the low frequency units is very large, which can practically be anywhere from about 60° to 180° with only a very slight increase of low frequency limit.

VI. CONSIDERATIONS FOR THE SUB-LOW-FREQUENCY REGION

At the frequencies below f_1 ($n < 1 - \nu$) where $\|\mathbf{H}\|$ and $\kappa(\mathbf{C})$ is larger than other frequencies, the requirement for dynamic range loss and robustness of the system are more severe than at other frequencies. Figure 18 illustrates the 2-norm of **H** and the two singular values (σ_i and σ_o) with the "OSD" principle. As described in Sec. IV A, $\|\mathbf{H}\|$ shows the flat amplitude response of the inverse filters above f_1. However, below f_1, it still increases moderately as frequency becomes lower. In this region, although the system has difficulty in reproducing the out-of-phase component of the desired signal, it still can produce the in-phase component as well as before.

When f_1 is reasonably low, where interaural difference may not be crucial for binaural reproduction, one can avoid system inversion and simply add a single subwoofer unit for this frequency region to avoid the extra dynamic range loss required by this region. As seen in Eq. (10), adding two channels of signals results in complete cancellation of the out-of-phase component of the binaural signals and producing the in-phase component only. Then, there is no independent control of binaural signals in this region.

It is possible to cover this sub-low-frequency region with the lowest frequency pair of units without sacrificing performance for other frequencies. The large σ_o, the out-of-phase component, in this region can be regularized with the method described in Sec. III C. In such case, even though little cross-talk suppression is available, the low-frequency pair can still work as a subwoofer mostly producing the in-phase component, while it is working perfectly within the OSD frequency range. In the sub-low region, the control performance deteriorates severely due to heavy regularization. However, $\|\mathbf{R}\|$ and hence the norm of the reproduced signal, is the same as that without regularization. This

may be acceptable in binaural reproduction since the difference between the two desired signals is normally not so large and sometimes negligible in the very low-frequency range.

When slight dynamic range loss is acceptable, the regularization can be used to limit the amplification, and hence avoid too much dynamic range loss, without sacrificing robustness for other frequencies. The cross-talk performance with regularization in the frequency range below f_1 is not as good as at the other frequencies. However, there can still be reasonable cross-talk suppression available. If more dynamic range loss is allowed, a relatively small regularization can be used to suppress the out-of-phase component in the sub-low region. The cross-talk cancellation performance in this region is very sensitive to the allocated dynamic range loss. Therefore, it is possible to design the system by selecting the required low frequency cross-talk cancellation performance. The amount of the dynamic range loss required by the discretization often gives relatively good control performance also in the sub-low-frequency region, especially when the discretization is coarse.

One might choose to allow all the dynamic range loss necessary for the full control of the sub-low-frequency region. The overall dynamic range loss is determined by the lowest frequency pair, which has the largest span. As discussed in Sec. III A, the dynamic range loss by the largest span is the smallest value among all other pairs.

VII. CONCLUSIONS

Analysis with a free field model and more realistic plant matrix with head related transfer functions reveals a number of fundamental problems related to multichannel sound control with system inversion such as binaural synthesis over loudspeakers. A principle of 2-channel (binaural) sound control with loudspeakers is proposed which overcomes the fundamental problems with system inversion by utilizing a variable transducer span. Practical ways to tackle the sub-low-frequency region are also described where outside the OSD principle.

The proposed principle has various advantages. No dynamic range loss due to system inversion directly means good signal-to-noise ratio but also leads to less distortion and longer life of transducers. The robustness to errors has advantages in many respects, e.g., incorrect inverse filters due to restriction of hardware resources, differences between individuals or products, and the misalignments that is inevitable in practical use. The minimal sound radiation in directions other than receiver directions reduces the chance of the 3D effect being destroyed by reflections from surrounding objects. The system inversion does not result in coloration because of the flat response of the inverse filters, and this adds practicality by enabling the listener to enjoy the reproduced sound signals even outside the "sweet region." As a natural consequence of this, the reflections or reverberation of the room are not colored either.

The practical system can be realized in a number of ways including discretizing the theoretical continuously variable transducer span that results in multiway sound control system. The discretization enables the use of conventional

transducer units and crossover filter networks. The relationship between the position of a driver unit and the frequency region to be covered can be determined easily. Further developments to realize ideal continuously distributed transducer will be beneficial to improve the performance of such systems.

APPENDIX

When the desired signals are defined as Eq. (7), this effectively normalizes the plant transfer function matrix $\mathbf{C}$ with respect to the acoustic pressure signals which would have been produced by the closer of two sound sources to the receiver point. Then this normalized plant transfer function matrix $\mathbf{C}$ can be written as

$$\mathbf{C}=\begin{bmatrix} 1 & g\mathrm{e}^{-jk\Delta l} \\ g\mathrm{e}^{-jk\Delta l} & 1 \end{bmatrix}. \tag{A1}$$

It is possible to express $\mathbf{C}$ with unitary matrices $\mathbf{U}$ and $\mathbf{V}$ such that

$$\mathbf{C}=\mathbf{U}\mathbf{\Sigma}\mathbf{V}^{\mathrm{H}}, \tag{A2}$$

where $\mathbf{\Sigma}$ is the diagonal matrix whose elements are singular values of $\mathbf{C}$, σ_1, and σ_2. The singular values of $\mathbf{C}$ can be found from the square roots of eigenvalues of $\mathbf{C}^{\mathrm{H}}\mathbf{C}$,

$$\mathbf{C}^{\mathrm{H}}\mathbf{C}=\begin{bmatrix} 1 & g\mathrm{e}^{jk\Delta l} \\ g\mathrm{e}^{jk\Delta l} & 1 \end{bmatrix}\begin{bmatrix} 1 & g\mathrm{e}^{-jk\Delta l} \\ g\mathrm{e}^{-jk\Delta l} & 1 \end{bmatrix}$$
$$=\begin{bmatrix} 1+g^2 & g(\mathrm{e}^{jk\Delta l}+\mathrm{e}^{-jk\Delta l}) \\ g(\mathrm{e}^{jk\Delta l}+\mathrm{e}^{-jk\Delta l}) & 1+g^2 \end{bmatrix}. \tag{A3}$$

The eigenvalues of $\mathbf{C}^{\mathrm{H}}\mathbf{C}$ are given by

$$\lambda_{1,2}=(1+g\mathrm{e}^{jk\Delta l})(1+g\mathrm{e}^{-jk\Delta l}),(1-g\mathrm{e}^{jk\Delta l})(1-g\mathrm{e}^{-jk\Delta l}). \tag{A4}$$

Therefore, the singular values of $\mathbf{C}$ are given by

$$\sigma_{1,2}=\sqrt{\lambda_{1,2}}=\sqrt{(1+g\mathrm{e}^{jk\Delta l})(1+g\mathrm{e}^{-jk\Delta l})},$$
$$\sqrt{(1-g\mathrm{e}^{jk\Delta l})(1-g\mathrm{e}^{-jk\Delta l})}. \tag{A5}$$

It is possible to find an orthonormal set of eigenvectors $\mathbf{x}_i$ such that

$$\mathbf{C}^{\mathrm{H}}\mathbf{C}\mathbf{x}_i=\sigma_i^2\mathbf{x}_i. \tag{A6}$$

Therefore,

$$\mathbf{V}=\begin{bmatrix} \dfrac{1}{\sqrt{2}} & \dfrac{1}{\sqrt{2}} \\ \dfrac{1}{\sqrt{2}} & -\dfrac{1}{\sqrt{2}} \end{bmatrix}. \tag{A7}$$

The vectors comprising $\mathbf{U}$ are given by

$$\mathbf{y}_i=\frac{1}{\sigma_i}\mathbf{C}\mathbf{x}_i. \tag{A8}$$

Hence

$$\mathbf{U}=\frac{1}{\sqrt{2}}\begin{bmatrix} \sqrt{\dfrac{1+g\mathrm{e}^{-jk\Delta l}}{1+g\mathrm{e}^{jk\Delta l}}} & \sqrt{\dfrac{1-g\mathrm{e}^{-jk\Delta l}}{1-g\mathrm{e}^{jk\Delta l}}} \\ \sqrt{\dfrac{1+g\mathrm{e}^{-jk\Delta l}}{1+g\mathrm{e}^{jk\Delta l}}} & -\sqrt{\dfrac{1-g\mathrm{e}^{-jk\Delta l}}{1-g\mathrm{e}^{jk\Delta l}}} \end{bmatrix}. \tag{A9}$$

The singular value decomposition of $\mathbf{C}$ may therefore be written as

$$\mathbf{C}=\mathbf{U}\mathbf{\Sigma}\mathbf{V}^{\mathrm{H}}=\frac{1}{\sqrt{2}}\begin{bmatrix} \sqrt{\dfrac{1+g\mathrm{e}^{-jk\Delta l}}{1+g\mathrm{e}^{jk\Delta l}}} & \sqrt{\dfrac{1-g\mathrm{e}^{-jk\Delta l}}{1-g\mathrm{e}^{jk\Delta l}}} \\ \sqrt{\dfrac{1+g\mathrm{e}^{-jk\Delta l}}{1+g\mathrm{e}^{jk\Delta l}}} & -\sqrt{\dfrac{1-g\mathrm{e}^{-jk\Delta l}}{1-g\mathrm{e}^{jk\Delta l}}} \end{bmatrix}\begin{bmatrix} \sqrt{(1+g\mathrm{e}^{jk\Delta l})(1+g\mathrm{e}^{-jk\Delta l})} & 0 \\ 0 & \sqrt{(1-g\mathrm{e}^{jk\Delta l})(1-g\mathrm{e}^{-jk\Delta l})} \end{bmatrix}$$
$$\times\begin{bmatrix} \dfrac{1}{\sqrt{2}} & \dfrac{1}{\sqrt{2}} \\ \dfrac{1}{\sqrt{2}} & -\dfrac{1}{\sqrt{2}} \end{bmatrix}. \tag{A10}$$

Note that

$$\mathbf{C}^{-1}=[\mathbf{U}\mathbf{\Sigma}\mathbf{V}^{\mathrm{H}}]^{-1}=\mathbf{V}\mathbf{\Sigma}^{-1}\mathbf{U}^{\mathrm{H}}, \tag{A11}$$

since $\mathbf{V}^{\mathrm{H}}\mathbf{V}=\mathbf{I}$, $[\mathbf{V}^{\mathrm{H}}]^{-1}=\mathbf{V}$, $\mathbf{U}^{\mathrm{H}}\mathbf{U}=\mathbf{I}$, and $\mathbf{U}^{-1}=\mathbf{U}^{\mathrm{H}}$. Therefore,

$$\mathbf{H} = \mathbf{C}^{-1} = \mathbf{V}\mathbf{\Sigma}^{-1}\mathbf{U}^{\mathrm{H}} = \begin{bmatrix} \dfrac{1}{\sqrt{2}} & \dfrac{1}{\sqrt{2}} \\[2ex] \dfrac{1}{\sqrt{2}} & -\dfrac{1}{\sqrt{2}} \end{bmatrix} \begin{bmatrix} \dfrac{1}{\sqrt{(1+g\mathrm{e}^{jk\Delta l})(1+g\mathrm{e}^{-jk\Delta l})}} & 0 \\[3ex] 0 & \dfrac{1}{\sqrt{(1-g\mathrm{e}^{jk\Delta l})(1-g\mathrm{e}^{-jk\Delta l})}} \end{bmatrix}$$

$$\times \frac{1}{\sqrt{2}} \begin{bmatrix} \sqrt{\dfrac{1+g\mathrm{e}^{jk\Delta l}}{1+g\mathrm{e}^{-jk\Delta l}}} & \sqrt{\dfrac{1+g\mathrm{e}^{jk\Delta l}}{1+g\mathrm{e}^{-jk\Delta l}}} \\[3ex] \sqrt{\dfrac{1-g\mathrm{e}^{jk\Delta l}}{1-g\mathrm{e}^{-jk\Delta l}}} & -\sqrt{\dfrac{1-g\mathrm{e}^{jk\Delta l}}{1-g\mathrm{e}^{-jk\Delta l}}} \end{bmatrix}. \tag{A12}$$

Hence

$$\sigma_i = \frac{1}{\sqrt{(1+g\mathrm{e}^{-jk\Delta r \sin\theta})(1+g\mathrm{e}^{jk\Delta r \sin\theta})}}, \quad \sigma_o = \frac{1}{\sqrt{(1-g\mathrm{e}^{-jk\Delta r \sin\theta})(1-g\mathrm{e}^{jk\Delta r \sin\theta})}} \tag{A13}$$

are the singular values of the inverse filter matrix $\mathbf{H}$.

[1] J. Blauert, *Spatial Hearing: The Psychophysics of Human Sound Localization* (MIT Press, Cambridge, MA, 1997), Chap. 2, pp. 50–136.

[2] H. Møller, "Fundamentals of Binaural Technology," Appl. Acoust. **36**, 171–218 (1992).

[3] D. R. Begault, *3-D Sound for Virtual Reality and Multimedia* (AP Professional, Cambridge, MA, 1994).

[4] M. R. Schroeder and B. S. Atal, "Computer simulation of sound transmission in rooms," IEEE Intercon. Rec. Pt7, 150–155, 1963.

[5] P. Damaske, "Head-related two-channel stereophony with reproduction," J. Acoust. Soc. Am. **50**, 1109–1115 (1971).

[6] J. L. Bauck and D. H. Cooper, "Generalized transaural stereo and applications," J. Audio Eng. Soc., **44**, 683–705 (1996).

[7] P. A. Nelson, O. Kirkeby, T. Takeuchi, and H. Hamada, "Sound fields for the production of virtual acoustic images," J. Sound Vib. **204**, 386–396 (1997).

[8] P. A. Nelson, F. Orduna-Bustamante, and H. Hamada, "Inverse filter design and equalisation zones in multi-channel sound reproduction," IEEE Trans. Speech Audio Process. **3**, 185–192 (1995).

[9] O. Kirkeby, P. A. Nelson, F. Orduna-Bustamante, and H. Hamada, "Local sound field reproduction using digital signal processing," J. Acoust. Soc. Am. **100**, 1584–1593 (1996).

[10] S. Barnett, *Matrices—Methods and Applications* (Oxford University Press, Oxford, 1990), Chap. 8, pp. 218–225, 396–401.

[11] E. M. Wenzel, M. Arruda, D. J. Kistler, and F. L. Wightman, "Localisation using nonindividualized head-related transfer functions," J. Acoust. Soc. Am. **94**, 111–123 (1993).

[12] H. Møller, M. F. Sørensen, D. Hammershøi, and C. B. Jensen, "Head-related transfer functions on human subjects," J. Audio Eng. Soc., **43**, 300–321 (1995).

[13] T. Takeuchi, P. A. Nelson, O. Kirkeby, and H. Hamada, "Influence of individual head related transfer function on the performance of virtual acoustic imaging systems," 104th AES Convention Preprint 4700 (P4-3), 1998.

[14] T. Takeuchi, P. A. Nelson, and H. Hamada, "Robustness to Head Misalignment of Virtual Sound Imaging Systems," J. Acoust. Soc. Am. **109**, 958–971 (2001).

[15] D. B. Ward and G. W. Elko, "Effect of loudspeaker position on the robustness of acoustic crosstalk cancellation," IEEE Signal Process. Lett. **6**, 106–108 (1999).

[16] W. H. Press, S. A. Teukolsky, W. T. Vetterling, and B. P. Flannery, *Numerical Recipes in C*, 2nd ed. (Cambridge University Press, Cambridge, 1992).

[17] T. Takeuchi, P. A. Nelson, O. Kirkeby, and H. Hamada, "The effects of reflections on the performance of virtual acoustic imaging systems" in Proceedings of the Active 97, The International Symposium on Active Control of Sound and Vibration, Budapest, Hungary, 1997, pp. 955–966.

[18] B. Rakerd, and W. M. Hartmann, "Localization of sound in rooms. II. The effects of a single reflecting surface," J. Acoust. Soc. Am. **78**, 524–533 (1985).

[19] U. Burandt, C. Poesselt, S. Ambrozus, M. Hosenfeld, and V. Knauff, "Anthropometric contribution to standarising manikins for artificial head microphones and to measuring headphones and ear protectors," Appl. Ergonomics **22**, 373–378 (1991).

[20] B. Gardner and K. Martin, "HRTF Measurements of a KEMAR Dummy-Head Microphone," MIT Media Lab Perceptual Computing—Technical Report No. 280, 1994.

[21] T. Takeuchi and P. A. Nelson, "Optimal source distribution for virtual acoustic imaging," ISVR Technical Report No. 288, University of Southampton, 2000.

Cluster control of a distributed-parameter planar structure—Middle authority control

Nobuo Tanaka[a]
Mechanical Engineering Department, Tokyo Metropolitan Institute of Technology, 6-6 Asahigaoka, Hino-shi, Tokyo 191-0065, Japan

Scott D. Snyder
Mechanical Engineering Department, The University of Adelaide, Adelaide, SA 5005, Australia

This paper proposes a generalized active vibration control approach, "cluster control," that explicitly targets sets of structural modes with some common property. The approach falls into a category of MAC (middle authority control) between conventionally used LAC (low authority control) and HAC (high authority control), possessing the benefit of stability and control law simplicity analogous to LAC, while providing high control performance as well as some flexibility of control gain assignment similar to HAC. The structure of a cluster control system is outlined, showing that it is possible to control a target cluster without affecting the other clusters. A design procedure for the cluster control system is then proposed. Experimental results are also presented. © 2002 Acoustical Society of America. [DOI: 10.1121/1.1518984]

I. INTRODUCTION

A difficulty faced in actively controlling vibration is the infinite number of structural modes that exist in the real system. At some point, the control system designer must truncate the set of modes used in the model of the system, typically extending consideration to just a handful of low-order, low-frequency system modes. When the control system is then implemented, spillover effects appear. In particularly bad cases, spillover can lead to destabilization of the control system.[1] One active vibration control approach that avoids the spillover problem is direct velocity feedback (DVFB)[2] with collocated sensors and actuators. DVFB augments the damping of structural modes over a very wide (theoretically infinite) frequency range without spillover. However, DVFB implementations treat all structural modes equally, and are not able to preferentially damp modes that are more bothersome while ignoring modes that are inconsequential to the final result. In effect, the overall result is spread thinly over all modes, leading to the label "low authority control" (LAC).[3]

One area where the limitations of LAC are particularly troublesome is in the active control of structural acoustic radiation using vibration inputs. It is well known[4,5] that minimization of structural kinetic energy does not necessarily lead to the minimization of total acoustic power on a given structure, and so any control implementation should preferentially target attenuation of modes with the greatest radiation efficiency. Spreading the control effort evenly over all modes will not give the optimum result.

Control approaches that can specially target the most vexatious modes are often labeled "high authority control" (HAC).[6] HAC approaches, which include observer-based optimal control[7] and robust control,[8] generally aim to suppress the targeted modes in a very narrow frequency band without collocation. However, the risk of significant control spillover effects is high, and, particularly in the case of robust control, system complexity can limit practicality.

It would be highly desirable to build a control system that is simple, effective, and robust, one that can avoid spillover without relinquishing the ability to preferentially target the most bothersome modes. The key to moving some way towards this result lies in the sensing system.

As mentioned, the most common way to handle the problem of an infinite number of structural modes in the control design stage is to truncate on the basis of frequency. Low-pass filters are then installed on the inputs in an attempt to limit observation spillover. However, a more efficient way to approach the problem, particularly when structural acoustic radiation is of interest, is to "cluster" structural modes with similar properties and truncate the number of clusters under consideration. Clustering can be approached using criteria as rudimentary as shape. For example, like-index modes on a rectangular plate (odd–odd modes, odd–even modes, etc.) could be grouped. However, a more rigorous approach to the exercise is to formulate a quadratic measure of the unwanted phenomenon, such as radiated acoustic power, and use the eigenvectors of the defining weighting matrix to generate the clusters. This is the approach taken in generating "power modes"[9–12] or "radiation modes,"[13–15] which are groups of structural modes that radiate independently (from other groups).

This paper proposes a novel active control approach referred to as "cluster control," where emphasis is placed on controlling designated groupings of structural modes. The approach falls into a category of MAC (middle authority control) between conventionally used LAC and HAC, possessing the benefits of stability and control law simplicity analogous to LAC, while providing high control performance as well as some flexibility of control gain assignment

[a]Electronic mail: ntanaka@cc.tmit.ac.jp
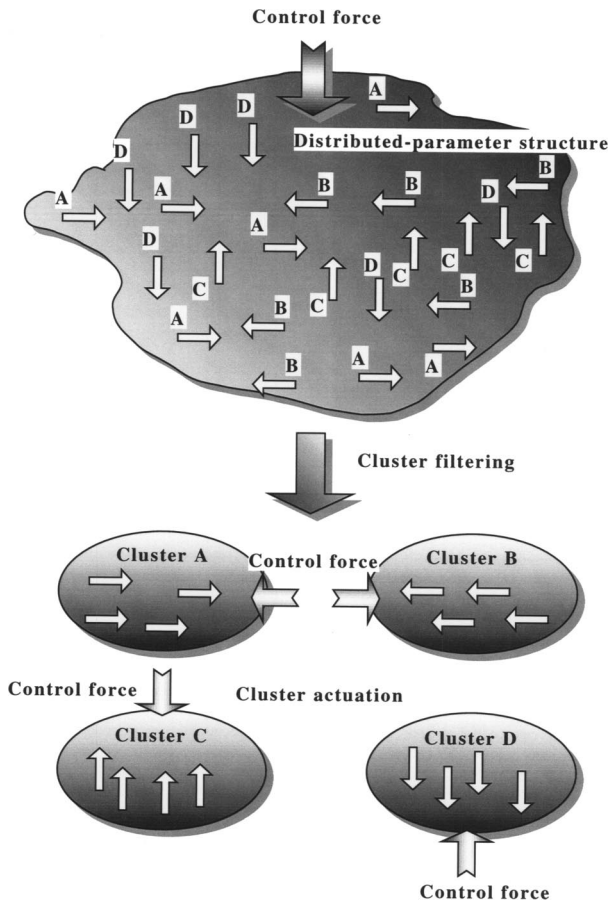
FIG. 1. Conceptual diagram of a cluster control of a distributed-parameter structure.

similar to HAC. This paper begins by presenting the concept of cluster filtering of a distributed-parameter planar structure, whereby the eigenfunctions of the structure are placed into groups, or "clusters," based upon some defining characteristic. Cluster actuation based upon the reciprocity principle between sensing and actuation is then discussed, followed by cluster control. It will be shown that conventional DVFB is a special case of the cluster control methodology proposed in the work. Finally, experimental demonstration of cluster control for suppressing groups of modes in a planar structure is presented.

II. CLUSTER CONTROL

A. What is cluster control?

Before mathematically developing the cluster control framework, it is worthwhile outlining the basic idea. Illustrated in Fig. 1 is a distributed-parameter structure where an infinite number of eigenvectors exist. For the purposes of description, the relative phases of these eigenvectors are assumed to fall into four groupings; A, B, C, D. When a control force acts on the structure as shown in the figure, the eigenvectors in the group labeled C may be suppressed due to the 180-deg phase difference between the control force vector and the eigenvector. Eigenvectors in the groups A and B will not be significantly affected due to the 90-deg phase difference. The eigenvectors in the D group will be amplified, possibly leading to destabilization of the control system.

To overcome this problem, the eigenvectors in the structure are grouped in a finite number of clusters in which all eigenvectors possess some common property. In the case of Fig. 1, this property is phase. The amplitudes of these clusters can be sensing using some form of input filtering (to be derived here). Different, appropriate control forces can then be applied to different clusters to ensure attenuation, or at least avoid amplification, of all eigenvectors. This application is achieved via actuation reciprocal to the filtering. Combining both the cluster filtering and cluster actuation, a cluster control system can be constructed.

B. Theoretical development of cluster filtering/ actuation

Consider the partial differential equation of motion of an undamped planar structure on which m point forces f_i ($i = 1,2,...m$) act

$$\mathbf{L}[w(\mathbf{r},t)]+m(\mathbf{r})\ddot{w}(\mathbf{r},t)=\sum_{i=1}^{m} f_i(t)\,\delta(\mathbf{r}-\mathbf{r}_i)=\mathbf{f}^T\boldsymbol{\delta}, \quad (1)$$

where $w(\mathbf{r},t)$ is the deflection of the structure at $\mathbf{r}=(x,y)$, $\cdot$ the time derivative, $m(\mathbf{r})$ the mass density, $\mathbf{L}$ a self-adjoint differential operator, ^{T}transpose of a vector, and δ a Dirac delta function. The force vector $\mathbf{f}$ and a location vector $\boldsymbol{\delta}$ are defined as

$$\mathbf{f}=\begin{pmatrix} f_1(t) \\ f_2(t) \\ \vdots \\ f_m(t) \end{pmatrix}, \quad (2)$$

$$\boldsymbol{\delta}=\begin{pmatrix} \delta(\mathbf{r}-\mathbf{r}_1) \\ \delta(\mathbf{r}-\mathbf{r}_2) \\ \vdots \\ \delta(\mathbf{r}-\mathbf{r}_m) \end{pmatrix}. \quad (3)$$

Using the eigenfunctions $\varphi_k(\mathbf{r})$ and modal amplitudes η_k ($k=1,2,3...$), $w(\mathbf{r},t)$ may be expressed as

$$w(\mathbf{r},t)=\sum_{k=1}^{\infty} \varphi_k(\mathbf{r})\,\eta_k(t). \quad (4)$$

Owing to the properties of the self-adjoint operator $\mathbf{L}$, the eigenfunctions are orthogonal, and are normalized as

$$\int_D \varphi_r(\mathbf{r})\mathbf{L}[\varphi_s(\mathbf{r})]d\mathbf{r}=\omega_r^2\,\delta_{rs}, \quad (5)$$

$$\int_D \varphi_r(\mathbf{r})m(\mathbf{r})\varphi_s(\mathbf{r})d\mathbf{r}=\delta_{rs}, \quad (6)$$

where ω_r, δ_{rs}, and D are the eigenfrequency of the rth structural mode, a Kronecker delta, and the domain of the structure, respectively. The modal amplitude $\eta_k(t)$ is then expressed as

$$\eta_k(t)=\int_D \varphi_k(\mathbf{r})m(\mathbf{r})w(\mathbf{r},t)d\mathbf{r}. \quad (7)$$

Multiplying Eq. (1) by $\varphi_s(\mathbf{r})$ and integrating over the domain D leads to

$$\int_D \varphi_s(\mathbf{r})\mathbf{L}[w(\mathbf{r},t)]d\mathbf{r} + \int_D \varphi_s(\mathbf{r})m(\mathbf{r})\ddot{w}(\mathbf{r},t)d\mathbf{r}$$

$$= \ddot{\eta}_s(t) + \omega_s^2 \eta_s(t) = \mathbf{f}^T \boldsymbol{\varphi}_s \quad (s=1,2,3,...), \tag{8}$$

where

$$\boldsymbol{\varphi}_s = \begin{pmatrix} \varphi_s(\mathbf{r}_1) \\ \varphi_s(\mathbf{r}_2) \\ \vdots \\ \varphi_s(\mathbf{r}_m) \end{pmatrix}. \tag{9}$$

When attaching n velocity point sensors at $\tilde{\mathbf{r}}_i$ ($i=1,2,...,n$) of the structure, a velocity vector $\mathbf{v}$ comprising the velocity sensor outputs $v(\tilde{\mathbf{r}}_i,t)$ is defined as

$$\mathbf{v} = (v(\tilde{\mathbf{r}}_1,t),v(\tilde{\mathbf{r}}_2,t),v(\tilde{\mathbf{r}}_3,t),...,v(\tilde{\mathbf{r}}_n,t))^T. \tag{10}$$

Using the eigenfunctions $\varphi_k(\tilde{\mathbf{r}}_i)$ and modal amplitudes $\eta_k(t)$, velocity $v(\tilde{\mathbf{r}}_i,t)$ at $\tilde{\mathbf{r}}_i$ is described as

$$v(\tilde{\mathbf{r}}_i,t) = \sum_{k=1}^{\infty} \varphi_k(\tilde{\mathbf{r}}_i)\dot{\eta}_k(t). \tag{11}$$

Substituting Eq. (11) into Eq. (10), the velocity vector $\mathbf{v}$ yields

$$\mathbf{v} = \tilde{\boldsymbol{\varphi}}_s \dot{\eta}_s(t) + \bar{\boldsymbol{\varphi}}_s, \tag{12}$$

where

$$\tilde{\boldsymbol{\varphi}}_s = \begin{pmatrix} \varphi_s(\tilde{\mathbf{r}}_1) \\ \varphi_s(\tilde{\mathbf{r}}_2) \\ \vdots \\ \varphi_s(\tilde{\mathbf{r}}_n) \end{pmatrix}, \tag{13}$$

and where

$$\bar{\boldsymbol{\varphi}}_s = \begin{pmatrix} \sum_{k=1,k\neq s}^{\infty} \varphi_k(\tilde{\mathbf{r}}_1)\dot{\eta}_k(t) \\ \sum_{k=1,k\neq s}^{\infty} \varphi_k(\tilde{\mathbf{r}}_2)\dot{\eta}_k(t) \\ \vdots \\ \sum_{k=1,k\neq s}^{\infty} \varphi_k(\tilde{\mathbf{r}}_n)\dot{\eta}_k(t) \end{pmatrix}. \tag{14}$$

Assume that all the sensors and actuators are collocated; then, $m=n$ and

$$\mathbf{r}_i = \tilde{\mathbf{r}}_i \quad (i=1,2,3,...,m), \tag{15}$$

hence

$$\boldsymbol{\varphi}_s = \tilde{\boldsymbol{\varphi}}_s. \tag{16}$$

Introducing an orthonormal matrix $\mathbf{T}$, the velocity vector $\mathbf{v}$ is transformed into a cluster vector $\tilde{\mathbf{v}}$, and this procedure is termed a "cluster filtering" in the work

$$\tilde{\mathbf{v}} = \mathbf{T}\mathbf{v}. \tag{17}$$

Further, introducing subvectors $\mathbf{t}_i$ ($i=1,2,...,m$), the matrix $\mathbf{T}$ is partitioned as

$$\mathbf{T} = \begin{pmatrix} \mathbf{t}_1^T \\ \mathbf{t}_2^T \\ \cdot \\ \cdot \\ \cdot \\ \mathbf{t}_m^T \end{pmatrix}, \tag{18}$$

where

$$\mathbf{T} \in \mathcal{R}^{m\times m}, \quad \mathbf{t} \in \mathcal{R}^{m\times 1}. \tag{19}$$

Consider that a cluster information $\tilde{v}_i$, the ith entry of a cluster vector $\tilde{\mathbf{v}}(t)$ expressed as

$$\tilde{v}_i(t) = \mathbf{t}_i^T \mathbf{v}, \tag{20}$$

is fed back to a set of collocated actuators located at $\mathbf{r}_1 - \mathbf{r}_m$ with the same weights used when extracting the cluster information $\tilde{v}_i$ from a set of velocity sensor outputs. This procedure is referred to as "cluster actuation." The control force vector is then given by

$$\mathbf{f} = \begin{pmatrix} f_1(t) \\ f_2(t) \\ \vdots \\ f_m(t) \end{pmatrix} = -g_i\tilde{v}_i\mathbf{t}_i = -g_i\tilde{v}_i \begin{pmatrix} t_{i1} \\ t_{i2} \\ \vdots \\ t_{im} \end{pmatrix}, \tag{21}$$

where $g_i > 0$ is a feedback gain and t_{ij} is the jth element of the subvector $\mathbf{t}_i$. The feedback signal input into the ith actuator is expressed as $-g_i\tilde{v}_i t_{ii}$.

Substituting Eq. (21) into the right-hand side of Eq. (1), multiplying by $\varphi_s(\mathbf{r})$, and integrating over the domain D of the panel leads to

$$\int_D \varphi_s(\mathbf{r})\mathbf{f}^T \boldsymbol{\delta} d\mathbf{r} = -\int_D \varphi_s(\mathbf{r})g_i\tilde{v}_i\mathbf{t}_i^T \boldsymbol{\delta} d\mathbf{r}$$

$$= -g_i\tilde{v}_i\mathbf{t}_i^T \int_D \varphi_s(\mathbf{r})\boldsymbol{\delta} d\mathbf{r} = -g_i\tilde{v}_i\mathbf{t}_i^T \boldsymbol{\varphi}_s. \tag{22}$$

Moreover, substituting Eqs. (12) and (20) into Eq. (22) yields

$$\int_D \varphi_s(\mathbf{r})\mathbf{f}^T \boldsymbol{\delta} d\mathbf{r} = -g_i\mathbf{t}_i^T \mathbf{v}\mathbf{t}_i^T \boldsymbol{\varphi}_s$$

$$= -g_i\mathbf{t}_i^T (\boldsymbol{\varphi}_s\dot{\eta}_s(t) + \bar{\boldsymbol{\varphi}}_s)\mathbf{t}_i^T \boldsymbol{\varphi}_s$$

$$= -g_i(\mathbf{t}_i^T \boldsymbol{\varphi}_s)^2 \dot{\eta}_s(t) - g_i\mathbf{t}_i^T \bar{\boldsymbol{\varphi}}_s\mathbf{t}_i^T \boldsymbol{\varphi}_s. \tag{23}$$

Then, the equation of motion in a modal coordinate system is written as

$$\ddot{\eta}_s(t) + g_i(\mathbf{t}_i^T \boldsymbol{\varphi}_s)^2 \dot{\eta}_s(t) + \omega_s^2 \eta_s(t)$$

$$= -g_i\mathbf{t}_i^T \bar{\boldsymbol{\varphi}}_s\mathbf{t}_i^T \boldsymbol{\varphi}_s \quad (s=1,2,3,...). \tag{24}$$

Observe from Eq. (24) that the cluster feedback *always* performs as negative feedback in all the modal coordinate system, so that stability of the cluster feedback system can be guaranteed. Further, by choosing $\mathbf{r}_i$ ($i=1,2,...,m$) such that $\boldsymbol{\varphi}_s$ is not a null vector, damping on all structural modes is augmented.

Figure 2 shows a signal flow diagram of a control system for a single cluster. Note that a feedback signal from all sensor outputs is input to all actuators at $\mathbf{r}_i$ ($i=1,2,...,m$).
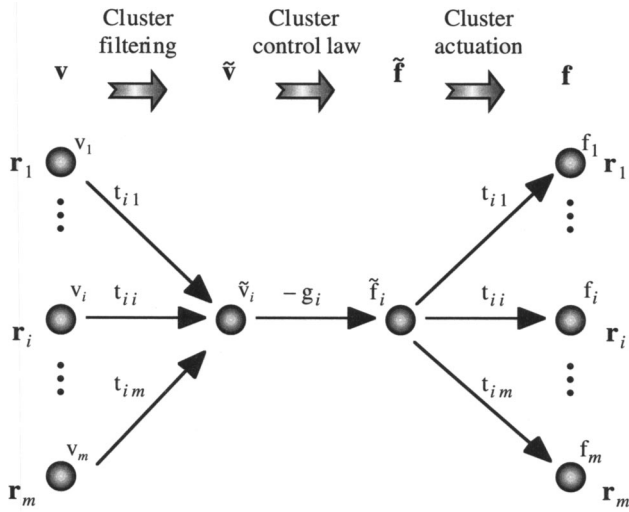
FIG. 2. Signal flow of a cluster control with a single cluster feedback.

FIG. 3. Signal flow of a cluster control with all of the cluster feedback.

However, the control system is stable, and the damping on every structural mode is increased. Thus, the cluster filtering enables the extraction of target cluster information out of a set of sensor outputs, while the cluster actuation explicitly excites the target cluster without spillover. Note that this is valid for the case where sensors and actuators are collocated.

C. Theoretical development for multiple clusters with actuation

Consider that all cluster velocities $\tilde{v}_i$ $(i=1,2,...,m)$ obtained through the filtering process of Eq. (17) are fed into a set of collocated actuators, using the same weights to distribute this input as were used to extract the cluster velocities. This operation will be referred to as "cluster feedback." To do this, a transformed control vector $\tilde{\mathbf{f}}$ must be calculated by multiplying the cluster vector $\tilde{\mathbf{v}}$ in Eq. (17) by a gain matrix $\mathbf{G} \in \mathcal{R}^{m \times m}$ that is assumed to be positive definite

$$\tilde{\mathbf{f}} = -\mathbf{G}\tilde{\mathbf{v}}. \tag{25}$$

The control force vector $\mathbf{f}$ is derived using the transformation matrix $\mathbf{T}$ and the transformed control vector $\tilde{\mathbf{f}}$

$$\mathbf{f} = \mathbf{T}^T \tilde{\mathbf{f}} = -\mathbf{T}^T \mathbf{G}\tilde{\mathbf{v}} = -\mathbf{T}^T \mathbf{G}\mathbf{T}\mathbf{v} = -\mathbf{T}^{-1}\mathbf{G}\mathbf{T}\mathbf{v}. \tag{26}$$

Figure 3 shows a signal flow diagram of cluster control with cluster feedback. Observe that by transforming a group of velocity sensor measurements (cluster filtering), cluster velocity $\tilde{v}_i$ $(i=1,2,...,m)$ is extracted. With the information, a transformed control vector $\tilde{\mathbf{f}}$ is calculated using the gain matrix $\mathbf{G}$. A single element $\tilde{f}_k$, the kth element of $\tilde{\mathbf{f}}$, can be expressed as

$$\tilde{f}_k = -\sum_{j=1}^{m} g_{kj}\tilde{v}_j, \tag{27}$$

where g_{kj} represents the ith row and jth column element of the gain matrix $\mathbf{G}$. The transformed vector $\tilde{\mathbf{f}}$ is then fed back into a set of actuators with weights $\mathbf{T}$ (cluster actuation/feedback).

Next, substituting Eq. (26) into Eq. (1), multiplying by $\varphi_s(\mathbf{r})$, and integrating over the domain D gives

$$\int_D \varphi_s(\mathbf{r})\mathbf{f}^T \boldsymbol{\delta} d\mathbf{r} = -\boldsymbol{\varphi}_s^T \mathbf{T}^{-1}\mathbf{G}\mathbf{T}\boldsymbol{\varphi}_s \dot{\eta}_s(t) - \overline{\boldsymbol{\varphi}}_s^T \mathbf{T}^{-1}\mathbf{G}\mathbf{T}\boldsymbol{\varphi}_s. \tag{28}$$

The equation of motion in a modal coordinate system is now given by

$$\ddot{\eta}_s(t) + \boldsymbol{\varphi}_s^T \mathbf{T}^{-1}\mathbf{G}\mathbf{T}\boldsymbol{\varphi}_s \dot{\eta}_s(t) + \omega_s^2 \eta_s(t)$$
$$= -\overline{\boldsymbol{\varphi}}_s^T \mathbf{T}^T \mathbf{G}\mathbf{T}\boldsymbol{\varphi}_s \quad (s=1,2,3,...). \tag{29}$$

Consider the second term $\boldsymbol{\varphi}_s^T \mathbf{T}^{-1}\mathbf{G}\mathbf{T}\boldsymbol{\varphi}_s$ on the left-hand side of Eq. (29). Given a positive definite matrix $\mathbf{T}^{-1}\mathbf{G}\mathbf{T}$, the second term $\boldsymbol{\varphi}_s^T \mathbf{T}^{-1}\mathbf{G}\mathbf{T}\boldsymbol{\varphi}_s$ is positive, with the result that negative feedback of cluster velocities is performed on all the structural modes, thereby guaranteeing the stability of the feedback system. As the gain matrix $\mathbf{G}$ is positive definite from assumption, $\mathbf{T}^{-1}\mathbf{G}\mathbf{T}$ is also positive definite due to similarity between these matrices, and hence the stability of the cluster control system is ensured.

Equation (26) further expands to

$$\mathbf{f} = -\mathbf{Q}\mathbf{v}, \tag{30}$$

where

$$\mathbf{Q} = \mathbf{T}^{-1}\mathbf{G}\mathbf{T}. \tag{31}$$

The expression in Eq. (30) is similar to that of DVFB.[1,2] Regarding DVFB, however, it is unclear how to determine a gain matrix $\mathbf{Q}$, and hence the control objective is also ambiguous. On the contrary, cluster control possesses an unequivocal purpose; extraction of target cluster information out of a set of sensor outputs, and preferential suppression of the target cluster without spillover. In addition, DVFB is highly likely to treat the gain matrix $\mathbf{Q}$ as a diagonal matrix in practice, thereby constructing a self-feedback loop that is a commonly used fundamental structure for DVFB. Such a case will be shown as a special case of the cluster control with a special gain matrix $\mathbf{G}$ as expressed in the following.

1. Case A: G is a diagonal matrix

Consider a gain matrix $\mathbf{G}$ expressed as
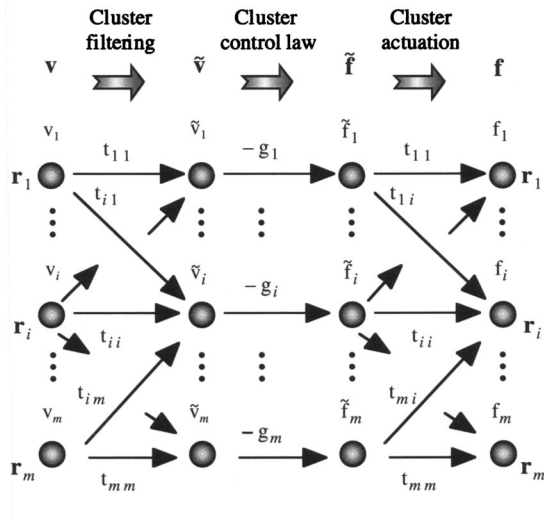
FIG. 4. Signal flow of a cluster control with independent cluster feedback.

$$\mathbf{G}=\mathbf{\Lambda}=\begin{pmatrix} g_1 & & & \mathbf{0} \\ & g_2 & & \\ & & \ddots & \\ \mathbf{0} & & & g_m \end{pmatrix},$$

$$g_i>0 \quad (i=1,2,3,...,m). \tag{32}$$

With this, Eq. (26) can be written as

$$\mathbf{f}=-\mathbf{T}^{-1}\mathbf{\Lambda}\mathbf{T}\mathbf{v}. \tag{33}$$

The signal flow of this case is depicted in Fig. 4. Observe that there is no cross talk between clusters in the derivation of the control signals because of the mode cluster sets being uncoupled in the modal domain. A given cluster velocity $\tilde{v}_i$ is directly transformed into a control variable $\tilde{f}_i$ with a feedback gain $-g_i$. The equation of motion in a modal coordinate system for this case becomes

$$\ddot{\eta}_s(t)+\sum_{i=1}^{m} g_i(\mathbf{t}_i^T\boldsymbol{\varphi}_s)^2 \dot{\eta}_s(t)+\omega_s^2 \eta_s(t)$$

$$=-\sum_{i=1}^{m} g_i\mathbf{t}_i^T\overline{\boldsymbol{\varphi}}_s\mathbf{t}_i^T\boldsymbol{\varphi}_s \quad (s=1,2,3,...). \tag{34}$$

Note from Eq. (34) that damping is augmented on all structural modes by an amount $\sum_{i=1}^{m}g_i(\mathbf{t}_i^T\boldsymbol{\varphi}_s)^2$, and hence the control system is stabilized. The control force acting at a position "i" is given by

$$f_i=\sum_{k=1}^{m} t_{ki}\tilde{f}_k=-\sum_{k=1}^{m} g_k\tilde{v}_k t_{ki}. \tag{35}$$

To each control actuator, all the cluster velocities $\tilde{v}_k$ ($k=1,2,...,m$) weighted by t_{ki} (ith row and jth column element of $\mathbf{T}$) are fed back.

It has been stated[1] that by introducing an infinite number of point sensors and point actuators to a lossless distributed parameter structure, DVFB enables a control system to be asymptotically stable. However, as is clear from Eq. (34), as long as the second term on the left-hand side of Eq. (34) is

TABLE I. Modal frequency and modal number of a simply supported plate ($88 \text{ cm} \times 180 \text{ cm} \times 9 \text{ mm}$).

Mode number	Mode	Modal frequency Hz	Mode number	Mode	Modal frequency Hz
1	(1,1)	35.292	12	(3,2)	283.588
2	(1,2)	55.716	13	(2,5)	284.136
3	(1,3)	89.756	14	(3,3)	317.628
4	(2,1)	120.744	15	(2,6)	359.024
5	(1,4)	137.412	16	(1,7)	362.077
6	(2,2)	141.168	17	(3,4)	365.284
7	(2,3)	175.208	18	(3,5)	426.556
8	(1,5)	198.684	19	(2,7)	447.529
9	(2,4)	222.864	20	(4,1)	462.551
10	(3,1)	263.164	21	(1,8)	464.197
11	(1,6)	273.573	22	(4,2)	482.975

nonzero, asymptotic stability is guaranteed. A phenomenon in which the second term becomes zero takes place *only* when all the nodal lines of a targeted structure run over all the sensor/actuator locations at the same time; therefore, avoiding such a case leads to an asymptotically stable control system implemented with fewer sensors and actuators.

2. Case B: G is diagonalized using T

Consider now the case where a gain matrix $\mathbf{G}$ is diagonalized using an orthonormal matrix $\mathbf{T}$. With this, Eq. (26) is given by

$$\mathbf{f}=-\mathbf{T}^{-1}\mathbf{G}\mathbf{T}\mathbf{v}=-\mathbf{\Lambda}\mathbf{v}. \tag{36}$$

In this case, the matrix $\mathbf{Q}$ in Eq. (30) becomes a diagonal matrix $\mathbf{\Lambda}$, and the cluster control yields a traditional DVFB with a self-loop feedback.
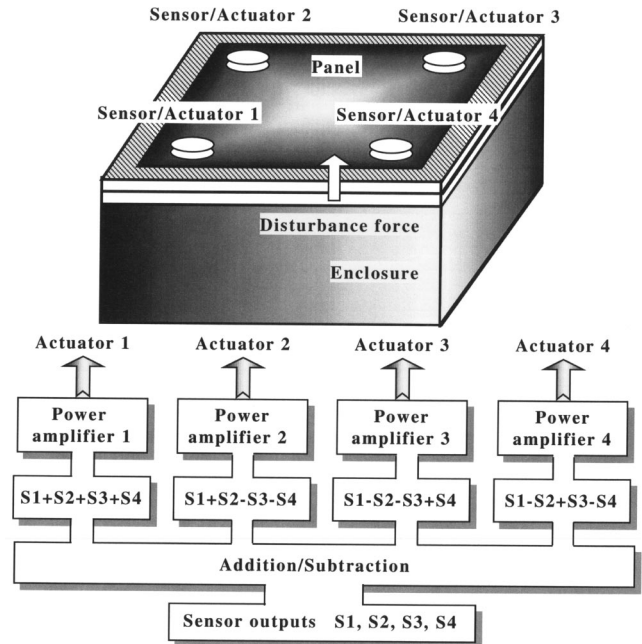
FIG. 5. Schematic diagram of cluster control system consisting of cluster filtering and cluster actuation.

Nobuo Tanaka and Scott D. Snyder: Distributed cluster control
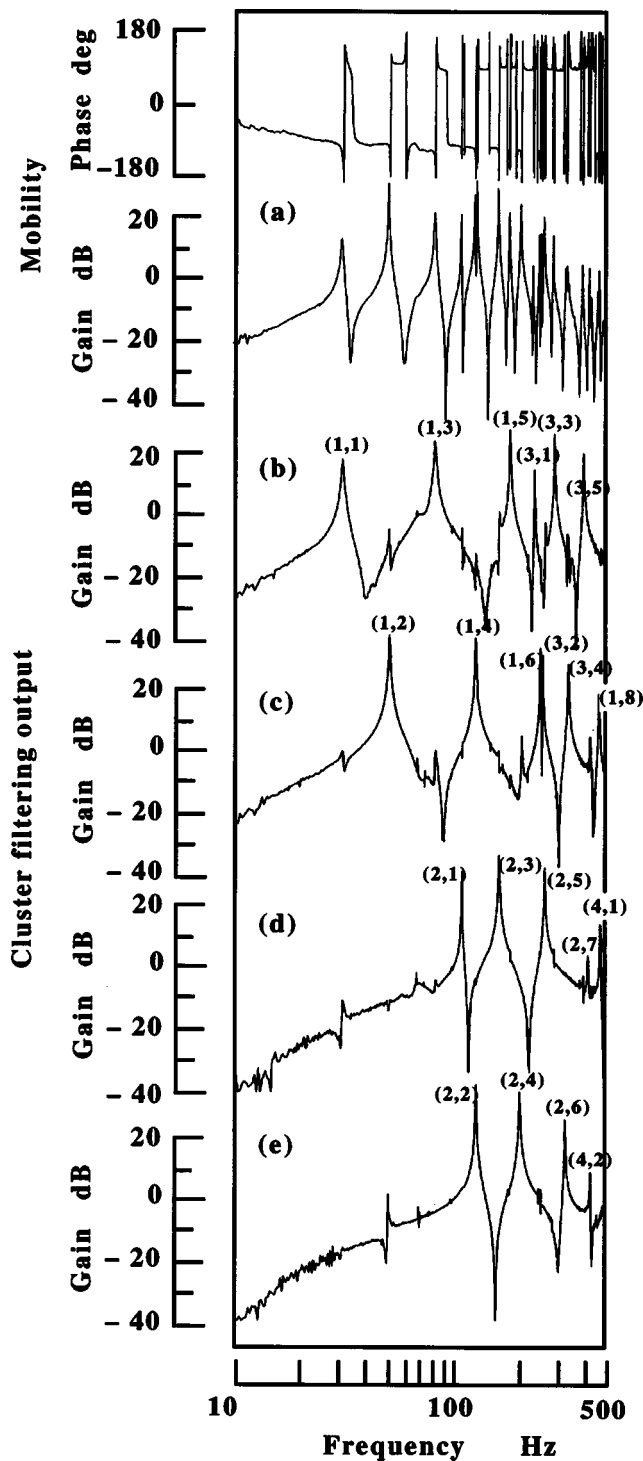
FIG. 6. Driving point mobility of the panel and the cluster filtering sensor outputs (a) Driving point mobility. (b)–(e) Each cluster filtering output.

3. Case C: G is an identity matrix

Consider the case when all elements of the gain matrix $\mathbf{\Lambda}$ are equal, and of value g_o. Then, $\mathbf{\Lambda}$ can be written as

$$\mathbf{\Lambda} = g_0 \mathbf{I}, \tag{37}$$

where $\mathbf{I}$ represents an identity matrix. Equation (26) then expands to

$$\mathbf{f} = -\mathbf{T}^T \mathbf{\Lambda} \mathbf{T} \mathbf{v} = -g_0 \mathbf{T}^T \mathbf{T} \mathbf{v} = -g_0 \mathbf{T}^{-1} \mathbf{T} \mathbf{v} = -g_0 \mathbf{v}. \tag{38}$$
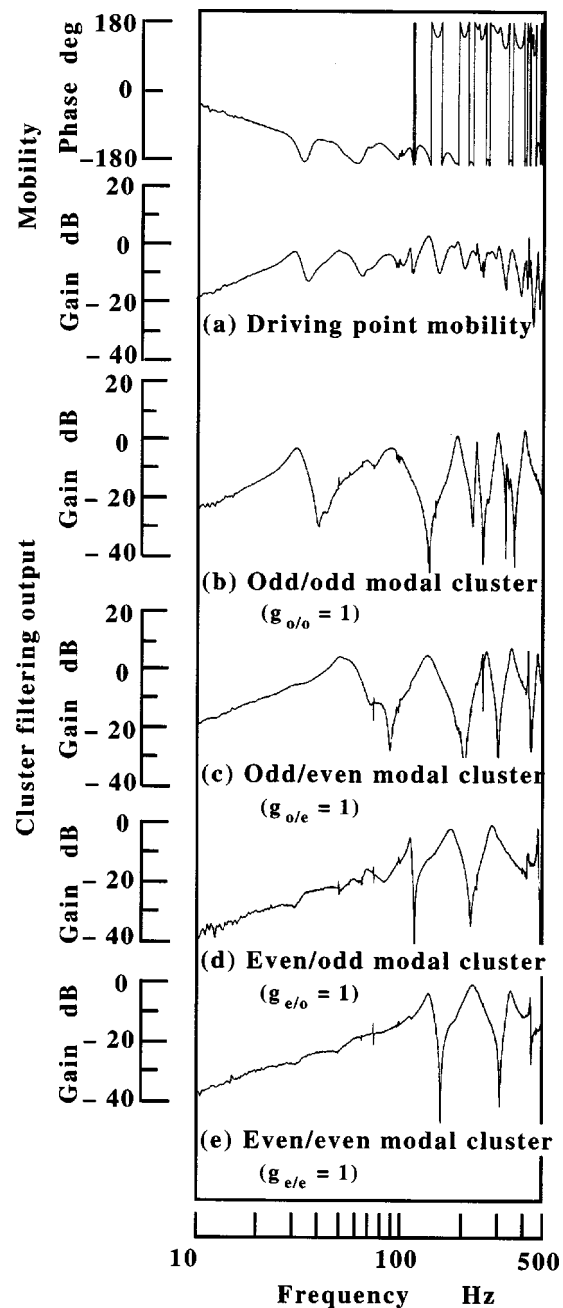
FIG. 7. Cluster control effect for suppressing all the clusters with feedback gains: $g_{o/o} = g_{o/e} = g_{e/o} = g_{e/e} = 1$. (a) Driving point mobility. (b)–(e) Each cluster filtering output.

From Eq. (38), when the gain matrix $\mathbf{G}$ is expressed by an identity matrix multiplied by a constant, cluster control results in DVFB with a self-loop.

III. CLUSTER CONTROL OF A RECTANGULAR PANEL

Consider a simply supported rectangular panel with the dimension of $L_x \times L_y \times h$. Then, all the modal functions $\varphi_k(\mathbf{r})$ of the panel are classified into four clusters.[12,13]

A. Odd/odd modal cluster set

All the modal functions $\varphi_k^{o/o}(\mathbf{r})$—superscript denotes that the numbers of nodal areas of a panel in x- and y-directions are odd and odd, respectively—belonging to this cluster satisfy the following formula:
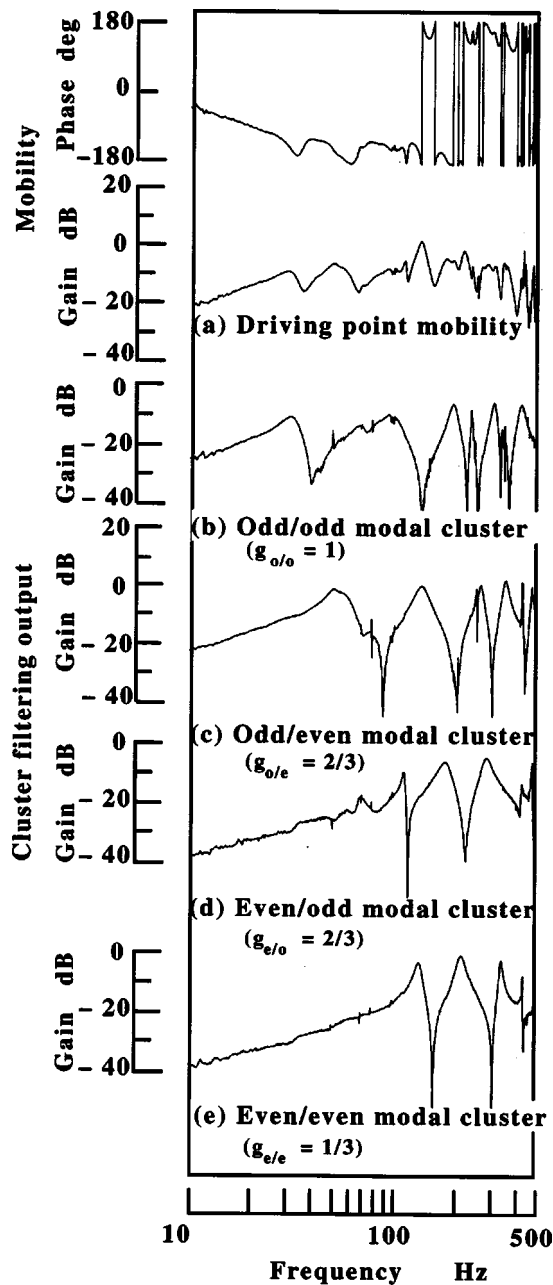
FIG. 8. Cluster control effect for suppressing all the clusters with feedback gains: $g_{o/o}=1$, $g_{o/e}=2/3$, $g_{e/o}=2/3$, and $g_{e/e}=1/3$. (a) Driving point mobility. (b)–(e) Each cluster filtering output.

$$\varphi_k^{o/o}(\mathbf{r}_1)=\varphi_k^{o/o}(\mathbf{r}_2)=\varphi_k^{o/o}(\mathbf{r}_3)=\varphi_k^{o/o}(\mathbf{r}_4), \qquad (39)$$

where

$$\mathbf{r}_1=(x_1,y_1), \qquad (40)$$

$$\mathbf{r}_2=(-x_1,y_1), \qquad (41)$$

$$\mathbf{r}_3=(-x_1,-y_1), \qquad (42)$$

$$\mathbf{r}_4=(x_1,-y_1), \qquad (43)$$

and where

$$0<x_1<L_x/2, \quad 0<y_1<L_y/2. \qquad (44)$$

Equation (39) simply states that the four corners of the panel vibrate in phase. In addition, the odd/odd modal cluster in
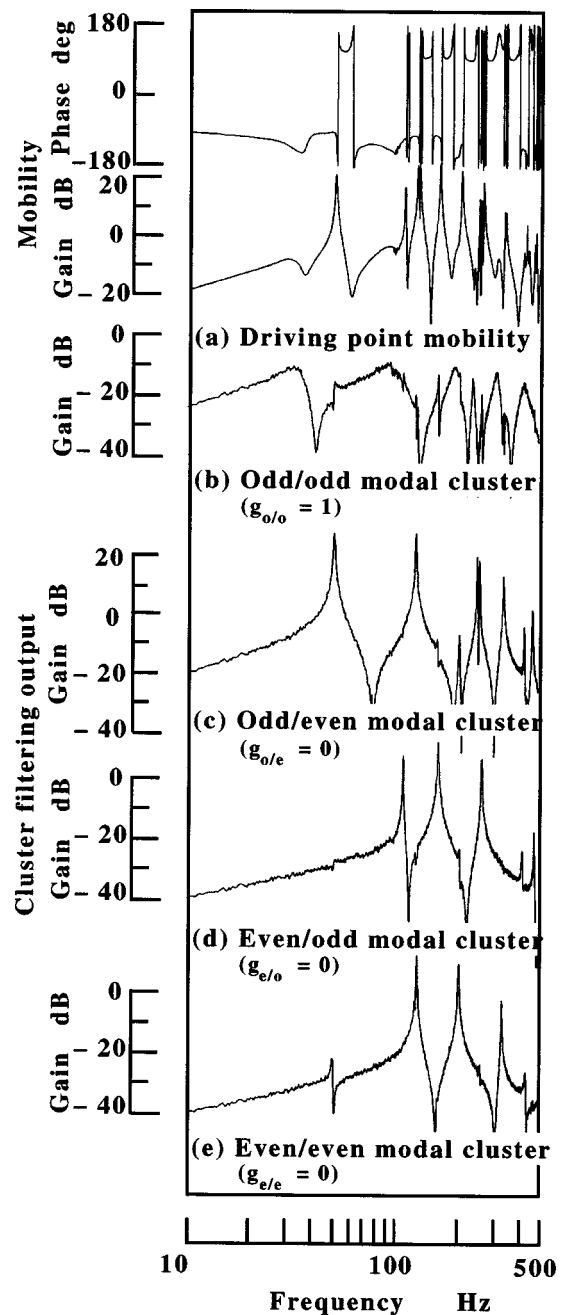
FIG. 9. Cluster control effect for suppressing the odd/odd modal cluster ($g_{o/o}=1$, $g_{o/e}=0$, $g_{e/o}=0$, $g_{e/e}=0$). (a) Driving point mobility. (b)–(e) Each cluster filtering output.

the subsonic frequency range is the greatest contributor[9–12] to the total acoustic power radiated from a vibrating panel, and hence suppressing this cluster leads to efficient suppression of the acoustic power.

B. Odd/even modal cluster set

All the modal functions $\varphi_k^{o/e}(\mathbf{r})$ belonging to this cluster satisfy the following formula:

$$\varphi_k^{o/e}(\mathbf{r}_1)=\varphi_k^{o/e}(\mathbf{r}_2)=-\varphi_k^{o/e}(\mathbf{r}_3)=-\varphi_k^{o/e}(\mathbf{r}_4), \qquad (45)$$

meaning that the corners of the panel at $\mathbf{r}_1$ and $\mathbf{r}_2$ and those at $\mathbf{r}_3$ and $\mathbf{r}_4$ vibrate out of phase.

Nobuo Tanaka and Scott D. Snyder: Distributed cluster control
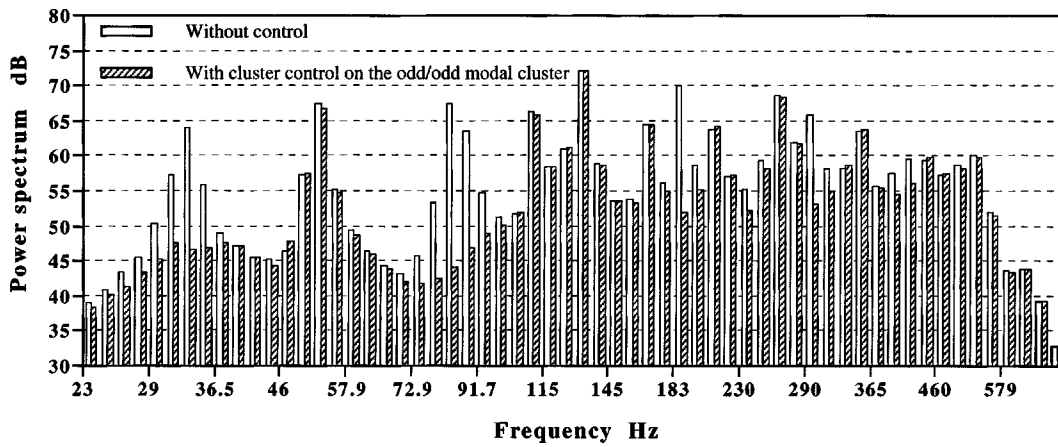
FIG. 10. Power spectrum of total acoustic power radiating from a vibrating simply supported plate after the cluster control on the odd/odd modal cluster.

C. Even/odd modal cluster set

All the modal functions $\varphi_k^{e/o}(\mathbf{r})$ belonging to this cluster satisfy the following formula:

$$\varphi_k^{e/o}(\mathbf{r}_1) = -\varphi_k^{e/o}(\mathbf{r}_2) = -\varphi_k^{e/o}(\mathbf{r}_3) = \varphi_k^{e/o}(\mathbf{r}_4), \qquad (46)$$

meaning that the corners of the panel at $\mathbf{r}_1$ and $\mathbf{r}_4$ and those at $\mathbf{r}_2$ and $\mathbf{r}_3$ vibrate out of phase.

D. Even/even modal cluster set

All the modal functions $\varphi_k^{e/e}(\mathbf{r})$ belonging to this cluster satisfy the following formula:

$$\varphi_k^{e/e}(\mathbf{r}_1) = -\varphi_k^{e/e}(\mathbf{r}_2) = \varphi_k^{e/e}(\mathbf{r}_3) = -\varphi_k^{e/e}(\mathbf{r}_4), \qquad (47)$$

meaning that the corners of the panel at $\mathbf{r}_1$ and $\mathbf{r}_3$ and those at $\mathbf{r}_2$ and $\mathbf{r}_4$ vibrate out of phase.

Boundary conditions that satisfy the properties written by Eqs. (39)–(47) are, for instance, simply support of four edges (SSSS), clamped support (CCCC), free support (FFFF), and the combinations of thereof such as (SCSC), (FCFC), where an eigenfunction is expressed as a symmetrical or skew-symmetrical function.

Consider the case where four point sensors/actuators are placed at $\mathbf{r}_1 - \mathbf{r}_4$. Then, the cluster vector in Eq. (17) yields

$$\begin{pmatrix} \tilde{v}_1(t) \\ \tilde{v}_2(t) \\ \tilde{v}_3(t) \\ \tilde{v}_4(t) \end{pmatrix} = \begin{pmatrix} 1 & 1 & 1 & 1 \\ 1 & 1 & -1 & -1 \\ 1 & -1 & -1 & 1 \\ 1 & -1 & 1 & -1 \end{pmatrix} \begin{pmatrix} v(\mathbf{r}_1, t) \\ v(\mathbf{r}_2, t) \\ v(\mathbf{r}_3, t) \\ v(\mathbf{r}_4, t) \end{pmatrix}. \quad (48)$$

Note that there is an Hadamard matrix in Eq. (48). Let $\tilde{v}_1(t)$, $\tilde{v}_2(t)$, $\tilde{v}_3(t)$, and $\tilde{v}_4(t)$, the velocities of the clusters of odd/odd, odd/even, even/odd, and even/even modal functions, respectively, be denoted as $v^{o/o}$, $v^{o/e}$, $v^{e/o}$, and $v^{e/e}$. Similarly, let $g_{o/o} = g_1$, $g_{o/e} = g_2$, $g_{e/o} = g_3$, and $g_{e/e} = g_4$. Applying again the Hadamard matrix, Eq. (26) now becomes

$$\begin{pmatrix} f_1 \\ f_2 \\ f_3 \\ f_4 \end{pmatrix} = \begin{pmatrix} 1 & 1 & 1 & 1 \\ 1 & 1 & -1 & -1 \\ 1 & -1 & -1 & 1 \\ 1 & -1 & 1 & -1 \end{pmatrix} \begin{pmatrix} \tilde{f}_1 \\ \tilde{f}_2 \\ \tilde{f}_3 \\ \tilde{f}_4 \end{pmatrix}$$

$$- \begin{pmatrix} g_{o/o}v^{o/o} + g_{o/e}v^{o/e} + g_{e/o}v^{e/o} + g_{e/e}v^{e/e} \\ g_{o/o}v^{o/o} + g_{o/e}v^{o/e} - g_{e/o}v^{e/o} - g_{e/e}v^{e/e} \\ g_{o/o}v^{o/o} - g_{o/e}v^{o/e} - g_{e/o}v^{e/o} + g_{e/e}v^{e/e} \\ g_{o/o}v^{o/o} - g_{o/e}v^{o/e} + g_{e/o}v^{e/o} - g_{e/e}v^{e/e} \end{pmatrix},$$

$$(49)$$

where the gain matrix $\mathbf{G}$ is set to be a diagonal matrix

$$\mathbf{G} = \mathbf{\Lambda} = \begin{pmatrix} g_{o/o} & 0 & 0 & 0 \\ 0 & g_{o/e} & 0 & 0 \\ 0 & 0 & g_{e/o} & 0 \\ 0 & 0 & 0 & g_{e/e} \end{pmatrix}. \qquad (50)$$

IV. EXPERIMENTAL IMPLEMENTATION OF CLUSTER CONTROL

A steel rectangular panel of dimensions ($L_x = 88$ cm, $L_y = 180$ cm, $h = 9$ mm) fixed on top of an enclosure constructed from 10-cm-thick concrete walls was used to experimentally test the cluster control approach. The uppermost edges of the walls have a "knife blade" in order to simulate simply supported boundary conditions. The enclosed cavity is packed with glasswool to dampen acoustic resonances. An electro-dynamic shaker attached at $\mathbf{r}_a = (24 \text{ cm}, 25 \text{ cm})$ provided the panel with an impact force as disturbance, while four point velocity sensors used for cluster filtering were mounted at $\mathbf{r}_1 = (20 \text{ cm}, 21 \text{ cm})$, $\mathbf{r}_2 = (68 \text{ cm}, 21 \text{ cm})$, $\mathbf{r}_3 = (68 \text{ cm}, 159 \text{ cm})$, and $\mathbf{r}_4 = (20 \text{ cm}, 159 \text{ cm})$. Twenty-two structural modes (see Table I) are resonant in the frequency spectrum of the impact force used in experiment, which rolls off at 500 Hz. Four noncontact shakers consisting of "neogium" permanent magnets with a maximum force of 200 N were attached at the sensor locations.

Illustrated in Fig. 5 is a schematic diagram of cluster control consisting of both cluster filtering with four point
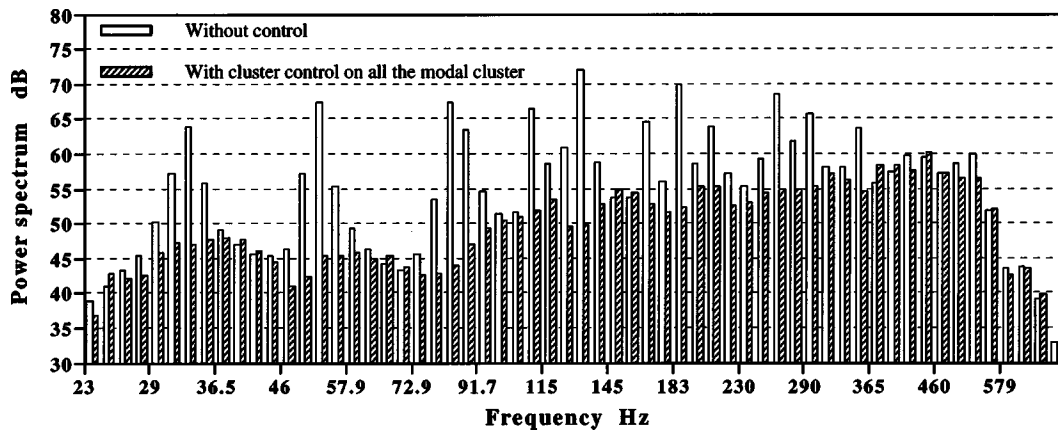
FIG. 11. Power spectrum of total acoustic power radiating from a vibrating simply supported plate after the cluster control on all the modal clusters.

sensors and cluster actuation with four collocated point actuators. As seen from the figure, control signals obtained by combining sensor outputs with appropriate polarities are fed back into power amplifiers to drive point actuators.

Figure 6(a) shows the driving point mobility of the panel driven at $\mathbf{r}_a$, while Figs. 6(b)–(e) depict the frequency response of the cluster filtering outputs on the odd/odd modal cluster, odd/even modal cluster, even/odd modal cluster, and even/even modal cluster, respectively. The odd/odd modal cluster filtering output, for example, was obtained by combining the four sensor outputs with the same polarity.

Figure 7 shows the driving point mobility obtained by the cluster control under the condition of equal feedback gains, $g_{o/o}=g_{o/e}=g_{e/o}=g_{e/e}=1$, in an effort to suppress all the structural modes uniformly. In the experiment, high-pass/low-pass filters were not used for the purpose of avoiding influence on the phase characteristics of the control signals. Thus, even with a simple direct feedback control, cluster control allows high feedback gain, thereby providing satisfactory control performance on all modes of the distributed-parameter planar structure. Figures 7(b)–(e) show the control effect for suppressing the cluster components—odd/odd modes, odd/even modes, even/odd modes, and even/even modes.

Unlike DVFB, cluster control offers the opportunity to assign different control gains to each cluster. Figure 8 shows the control effect for suppressing all the clusters with different gains on each cluster; $g_{o/o}=1$, $g_{o/e}=2/3$, $g_{e/o}=2/3$, and $g_{e/e}=1/3$. Figure 8(a) depicts the driving point mobility. By comparing Figs. 8(b)–(e) with Figs. 7(b)–(e), differences are noticeable, especially on the odd/odd modal cluster filtering output level. In the case of Fig. 7(b), where the equal weighting factors are assigned on each cluster, the maximum gain is 1 dB. However, this is reduced to −8 dB in Fig. 8(b), where the largest weight is placed upon the odd/odd modal cluster.

An extreme case of preferential damping is shown in Fig. 9, where only the odd/odd modal cluster is targeted: i.e., $g_{o/o}=1$, $g_{o/e}=0$, $g_{e/o}=0$, and $g_{e/e}=0$. Figure 9(a) illustrates the driving point velocity, revealing that only the targeted 7 odd/odd modes among 22 in the frequency band of interest are suppressed, while the other modes remain unaffected. The maximum gain in this case is further reduced to −10 dB, 2 dB lower than that of Fig. 8(b).

Illustrated in Fig. 10, corresponding to Fig. 9, is the power spectrum of total acoustic power radiating from the panel after the cluster control on the odd/odd modal cluster. When measuring the acoustic power, a pair of microphones located 10 cm high above the panel was traversed over the panel to measure the acoustic intensity distribution. With the data, the power spectrum in the figure is obtained. Among 22 peaks, only the odd/odd modal cluster set is suppressed, while the other peaks remain intact.

Figure 11, corresponding to Fig. 7, shows the power spectrum of total acoustic power after the cluster control on all the modal clusters. Observe that all the peaks in the spectrum are suppressed, and hence it is verified that the suppression of all the modal cluster set leads to the suppression of the acoustic power radiating from the vibrating panel.

V. CONCLUSIONS

For the purpose of suppressing the vibration of a distributed parameter planar structure, cluster control has been presented, the relationship between a conventional DVFB and the cluster control being clarified. Using a set of sensor outputs, cluster information with some common property may be extracted. Due to the reciprocity principle, cluster actuation allows one to explicitly excite the target cluster without causing control spillover. Employing both the cluster filtering and the cluster actuation, cluster control is constructed which falls into a category of MAC, possessing the benefit of stability and control law simplicity analogous to LAC, while providing high control performance as well as some flexibility of control gain assignment similar to HAC. If the gain matrix is positive definite, cluster control is found to be stabilized. It is also found that a conventional DVFB is a special case of the cluster control when a special gain matrix is introduced. With a view to verifying the validity of the cluster control, an experiment was conducted using a rectangular panel, demonstrating the significant control effect for suppressing the target cluster without causing instability.

[1] M. J. Balas, "Active control of flexible systems," J. Optim. Theory Appl. **25**, No. 3, 415–436 (1978).
[2] M. J. Balas, "Direct velocity feedback control of large space structure," J. Guid. Control **2−3**, 252–253 (1979).

[3] J. N. Aubrun, "Theory of the control of structures by low-authority control," J. Guid. Control **3**, 444–451 (1980).

[4] C. R. Fuller, "Active control of sound transmission/radiation from elastic plates by vibration inputs. I. Analysis," J. Sound Vib. **136**(1), 1–15 (1990).

[5] S. D. Snyder and C. H. Hansen, "Mechanisms of active noise control using vibration sources," J. Sound Vib. **147**, 519–525 (1991).

[6] J. N. Aubrun, "ACOSS FIVE (Active Control of Space Structure)," PHASE IA, LMSC Technical Report, RAND-TR-82-21, March (1982).

[7] See for instance, B. D. O. Anderson and J. B. Moor, *Linear Optimal Control* (Prentice-Hall, Englewood Cliffs, NJ, 1971).

[8] See for instance, B. A. Francis, *A Course in H-infinity Control Theory* (Springer-Berlin, 1987).

[9] S. D. Snyder and N. Tanaka, "On feedforward active control of sound and vibration using vibration error signals," J. Acoust. Soc. Am. **94**, 2181–2193 (1993).

[10] S. D. Snyder, N. Tanaka, and Y. Kikushima, "The use of optimally shaped piezo-electric film sensors in the active control of free field structural radiation. I. Feedforward control)," ASME J. Vibr. Acoust. **117**, 311–322 (1995).

[11] S. D. Snyder, N. Tanaka, and Y. Kikushima, "The use of optimally shaped piezo-electric film sensors in the active control of free field structural radiation. II. Feedback control)," ASME J. Vibr. Acoust. **118**, 112–121 (1996).

[12] N. Tanaka, S. D. Snyder, and C. H. Hansen, "Distributed parameter modal filtering using smart sensors," ASME J. Vibr. Acoust. **118**, 630–640 (1996).

[13] S. J. Elliott and M. E. Johnson, "Radiation modes and the active control of sound power," J. Acoust. Soc. Am. **94**, 2194–2204 (1993).

[14] K. A. Cunefare and M. N. Currey, "On the exterior acoustic radiation modes of structures," J. Acoust. Soc. Am. **96**, 2302–2312 (1994).

[15] M. N. Currey and K. A. Cunefare, "The radiation modes of baffled finite plates," J. Acoust. Soc. Am. **98**, 1570–1580 (1995).

Analysis of flexural wave velocity and vibration mode in thin cylindrical shell

Kenji Saijyou[a)]
Fifth Research Center, Technical R & D Institute, Japan Defense Agency, 3-13-1 Nagase, Yokosuka 239-0826, Japan

Shigeru Yoshikawa[b)]
Department of Acoustical Design, Kyushu Institute of Design, 4-9-1 Shiobara, Minami-ku, Fukuoka 815-8540, Japan

The relationship between the flexural wave velocity and the excited vibration mode of a thin cylindrical shell is investigated. The natural frequency corresponding to the vibration mode is obtained as the solution of characteristic equation of thin cylindrical shell. However, all of these vibration modes are not excited actually. To estimate the excited vibration mode, the concept of ''modified bending stiffness'' is introduced, and the influence of each stress component upon the modified bending stiffness is analyzed. The excited mode is theoretically discriminated from the nonexcited mode based on the smallness of this modified bending stiffness. The validity of our theory is confirmed by an excellent agreement between theoretical and experimental results on flexural wave velocity. © *2002 Acoustical Society of America.* [DOI: 10.1121/1.1513787]

I. INTRODUCTION

Structural vibration of thin cylindrical shell has been an interesting research topic for a long time because of its many engineering applications. For the control of noise and vibration of a cylindrical shell, it is important to characterize the vibration mode. However, the analysis of vibration mode of cylindrical shells is not straightforward, because the equation of motion for cylindrical shells together with boundary conditions are complex.

The studies of vibration mode of cylindrical shell are generally divided into two kinds of researches. The first one mainly discusses the relationship between vibration modes and natural frequencies, because acoustic radiation is strong at the natural frequency corresponding to the vibration mode. Zhang *et al.*[1] treated the natural mode of cylindrical shell as a combination of standing waves in the circumferential and axial directions to easily obtain the natural frequency. The natural frequencies associated with vibration modes are obtained by solving the algebraic equation, that is, by setting the determinant of the coefficient of the equation of motion for cylindrical shell equal to zero. This equation is called ''characteristic equation.'' [2,3] To solve the characteristic equation for a cylindrical shell of finite length, the specification of boundary condition is required, and the simplest set is that of simply supported cylindrical shell. We can estimate the natural frequency corresponding to the (*m,n*) mode from this characteristic equation for simply supported cylindrical shell, where *m* and *n* are the axial and circumferential mode numbers, respectively. However, it is not so straightforward to theoretically predict which vibration mode is actually excited.

The second one treats the mobility function or the impedance of cylindrical shell, and investigates the vibrational power flow. Approximate formulas of the point impedance of thin cylindrical shells were derived by Franken[4] and Heckl[5] in 1960s. Feit[6] also approximately derived vibrational response of a point-excited cylindrical shell for high frequencies in 1970s. Their methods are very simple and easy to understand intuitively. However, the applicable frequency ranges of their approximate theories are restricted. For example, Feit[6] treated the vibrational response of a cylindrical shell as that of a thin elastic plate, therefore, the applicable frequency range of his method is restricted to $\Omega \gg 1$, where Ω is the natural frequency which is non-dimensionalized by the ring frequency.[7]

Fuller[8] investigated the input mobility of fluid-filled cylindrical shell in 1980s. He calculated the point mobility of a cylindrical shell as the sum of mobilities individually obtained at each circumferential mode number. Xu *et al.*[9] investigated the vibrational power flow from a harmonic line force with cosine distribution along the circumference into fluid-filled elastic shell and *in vacuo* shell. However, many terms of circumferential mode are necessary to assure the accuracy of the calculated mobility, therefore their methods are too complicated to estimate the truly excited vibration mode.

Ming *et al.*[10,11] theoretically derived the expressions of the mobility functions of finite cylindrical shell and proposed a new method for the measurement of the structural mobility and power flow. A point-force excitation is employed instead of a circumferential modal force excitation which is difficult to implement in a practical experiment. However, the estimated results of structural mobilities cannot bring us the dominant vibration mode directly. Their theory needs the equation of motion for the cylindrical shell together with the effective transverse force, the bending moment, the exten-

---

[a)]Electronic mail: saijyou@jda-trdi.go.jp
[b)]Electronic mail: shig@kyushu-id.ac.jp

sional stress, and the effective shear stress, therefore, this procedure for calculating structural mobilities is relatively complicated.

In order to readily estimate the excited vibration mode, we introduce the concept of "modified bending stiffness" from the equation of motion for simply supported thin cylindrical shell. The modified bending stiffness is defined as the equivalent plate bending stiffness which includes the influence of curvature of the cylindrical shell, and derived from the equation of motion for the simply supported cylindrical shell only. A larger driving force is necessary to excite a stiffer mode. For example, if two vibration modes are degenerate, in other words, if the natural frequencies of these vibration modes are the same, a more flexible mode is excited. Moreover, we investigate the influence of each stress component on the modified bending stiffness in detail. The investigated result shows that the modified bending stiffness approaches to the bending stiffness of a thin plate in higher frequencies. This result explains how the flexural wave velocity of cylindrical shell is close to that of thin plate as the driving frequency is increased.

To confirm this theoretical consideration, experiments are carried out. A comparison between theoretical and experimental results demonstrates the validity of this prediction method of excited vibration mode. Theoretical explanations on the characteristics of flexural wave velocity, excited vibration mode, and modified bending stiffness are described in Sec. II. Theoretical calculations of the modified bending stiffness, natural frequencies of vibration mode, and flexural wave velocities are described in Sec. III. Comparison between theoretical and experimental results is also described there. The experimental results on a finite cylindrical shell are obtained by generalized near-field acoustical holography.[12] In our conclusions of Sec. IV, the validity of our theory will be summarized.

II. THEORY

A. Flexural wave velocity at the natural frequency

At first, let us review the flexural wave velocity of thin cylindrical shell at the natural frequency. The flexural wave velocity at the natural frequency corresponding to vibration mode (m,n) is described as

$$c_{\text{flex},(m,n)} = \lambda_{\text{flex},(m,n)} f_{(m,n)} = \frac{2\pi f_{(m,n)}}{k_{\text{flex},(m,n)}}, \tag{1}$$

$$k_{\text{flex},(m,n)} = \sqrt{\left(\frac{m\pi}{L}\right)^2 + \left(\frac{n}{a}\right)^2}, \tag{2}$$

where $f_{(m,n)}$ is the natural frequency of (m,n) mode, a the shell radius, L the shell length, $\lambda_{\text{flex},(m,n)}$ the wavelength, and $k_{\text{flex}(m,n)}$ the wave number, respectively. The algebraic equation defining $f_{(m,n)}$ is written as follows:[2,3]

$$|L| = 0, \tag{3}$$

$$L \equiv \begin{bmatrix} L_1 & L_2 & L_3 \\ L_2 & L_4 & L_5 \\ L_3 & L_5 & L_6 \end{bmatrix}, \tag{4}$$

$$L_1 = -\Omega^2 + (k_m a)^2 + \frac{1-\nu}{2} n^2 (1+\beta^2), \tag{5}$$

$$L_2 = \frac{1+\nu}{2} k_m a n, \tag{6}$$

$$L_3 = k_m a \left\{ \nu + \beta^2 \left[(k_m a)^2 - \frac{1-\nu}{2} n^2 \right] \right\}, \tag{7}$$

$$L_4 = -\Omega^2 + \frac{1-\nu}{2} (k_m a)^2 (1+3\beta^2) + n^2, \tag{8}$$

$$L_5 = n \left[1 + \frac{3-\nu}{2} \beta^2 (k_m a)^2 \right], \tag{9}$$

$$L_6 = \beta^2 \{1 - 2n^2 + [(k_m a)^2 + n^2]^2\} + 1 - \Omega^2, \tag{10}$$

$$\Omega = \frac{\omega_{(m,n)} a}{c_p}, \tag{11}$$

$$\beta^2 = \frac{h^2}{12 a^2}, \tag{12}$$

$$k_m = \frac{m\pi}{L}, \tag{13}$$

$$c_p^2 = \frac{E}{\rho(1-\nu^2)}, \tag{14}$$

$$\omega_{(m,n)} = 2\pi f_{(m,n)}, \tag{15}$$

where Ω is the nondimensional natural frequency, ν Poisson's ratio, ρ the density of the shell, E Young's modulus, and L_ℓ ($\ell = 1,2,3,4,5,6$) are the coefficients in the K-space representation of the Flügge–Bryne–Lur'ye equation of motion (abbreviated as "Flügge's equation" hereafter), which defines the radial, axial, and circumferential displacements W, U, and V in K space as[2]

$$L(U,V,W)^T = (0,0,F_W)^T, \tag{16}$$

where $(0,0,F_W)$ is the driving force vector and T defines the transposition of the matrix.

We can estimate the flexural wave velocity corresponding to the (m,n) mode from Eq. (1). However, it is difficult to predict whether the (m,n) mode is an actually excited vibration mode or not. To estimate the excited vibration mode, the "modified bending stiffness" should be derived from Flügge's equation according to our scheme proposed in the next section.

B. Modified bending stiffness

In order to derive the modified bending stiffness, let us examine the relationship between flexural wave velocity and bending stiffness. First, we consider the equation of motion for thin plate,[3] which is written using flexural wave velocity of thin plate $c_{\text{flex,plate}}$ in K space as

$$c_{\text{flex,plate}}^4 (k_x^2 + k_y^2)^2 W - \omega^4 W = 0, \tag{17}$$

$$c_{\text{flex,plate}} = \left(\frac{D\omega^2}{h\rho}\right)^{1/4}, \tag{18}$$

$$D = \frac{Eh^3}{12(1-\nu^2)}, \tag{19}$$

where D is the bending stiffness of thin plate, k_x and k_y are the wave numbers corresponding to x and y, respectively. If we define the wave number of flexural wave k_f as

$$k_f = \sqrt{k_x^2 + k_y^2}, \tag{20}$$

then Eq. (17) is rewritten as

$$c_{\text{flex,plate}}^4 k_f^4 = \omega^4. \tag{21}$$

Next, we examine Flügge's equation in K space. The K-space representation of axial and circumferential displacements are expressed as

$$U = \frac{L_2 L_5 - L_3 L_4}{L_1 L_4 - L_2^2} W = L_u W, \tag{22}$$

$$V = \frac{L_2 L_3 - L_1 L_5}{L_1 L_4 - L_2^2} W = L_v W. \tag{23}$$

Therefore, the substitution of Eqs. (22) and (23) to the third equation of Eq. (16) brings us the modified equation

$$F_W = \beta^2 [(k_m a)^2 + n^2]^2 W - \Omega^2 W + L_{\text{shell}(m,n)} W, \tag{24}$$

$$L_{\text{shell}(m,n)} \equiv L_3 L_u + L_5 L_v + [1 + \beta^2(1 - 2n^2)], \tag{25}$$

which defines the relationship between the driving force and radial displacement. Here, the term $(\beta^2[(k_m a)^2 + n^2]^2 - \Omega^2)W$ is exactly the same as that occurring in the equation of motion for thin plates.[3] Therefore, the term $L_{\text{shell},(m,n)}W$ in Eq. (24) describes the difference between an equation of motion for a thin plate and that for a thin cylindrical shell. Now, we set $F_W = 0$ and rewrite Eq. (24) using flexural wave velocity of thin plate as

$$\left[c_{\text{flex,plate}}^4 \left(k_m^2 + \left(\frac{n}{a}\right)^2 \right)^2 - \omega_{(m,n)}^4 \right.$$

$$\left. + L_{\text{shell}(m,n)} \left(\frac{c_p \omega_{(m,n)}}{a} \right)^2 \right] W = 0. \tag{26}$$

If we rewrite Eq. (26) as

$$c_{\text{flex,plate}}^4 k_{\text{flex},(m,n)}^4 + L_{\text{shell}(m,n)} \left(\frac{c_p \omega_{(m,n)}}{a} \right)^2 = \omega_{(m,n)}^4 \tag{27}$$

using Eq. (17) and modify Eq. (1) as

$$c_{\text{flex},(m,n)}^4 k_{\text{flex},(m,n)}^4 = \omega_{(m,n)}^4, \tag{28}$$

then we have the following relationship between flexural wave velocity of thin plate and that of cylindrical shell:

$$c_{\text{flex},(m,n)}^4 = c_{\text{flex,plate}}^4 + \frac{c_p^2 \omega_{(m,n)}^2}{a^2} \frac{L_{\text{shell}(m,n)}}{[k_m^2 + (n/a)^2]^2}. \tag{29}$$

Moreover, if we express the flexural wave velocity of cylindrical shell as

$$c_{\text{flex},(m,n)} = \left(\frac{D_{\text{shell},(m,n)} \omega_{m,n}^2}{h\rho} \right)^{1/4} \tag{30}$$

in comparison with Eq. (18), the modified bending stiffness of the shell $D_{\text{shell},(m,n)}$ is defined as

$$D_{\text{shell},(m,n)} = D \left[1 + \frac{12}{a^2 h^2} \frac{L_{\text{shell},(m,n)}}{[k_m^2 + (n/a)^2]^2} \right] \tag{31}$$

from Eqs. (29) and (30).

Now, let us consider the relationship between modified bending stiffness and each stress component. In Eq. (24), the term $L_{\text{shell},(m,n)}W$ is the sum of the stress components induced by axial ($L_3 L_u W = L_3 U$), circumferential ($L_5 L_v W = L_5 V$) and radial ($[1 + \beta^2(1 - 2n^2)]W$) displacements. Once the driving frequency is fixed, the flexural wave velocity of thin plate is determined by Eq. (18), and the contribution of the stress caused by the plate-like motion is uniquely determined, even if the vibration mode number (m,n) is changed. On the other hand, the contribution of the stresses caused by axial, circumferential, and radial displacements to the modified bending stiffness is changed if the vibration mode (m,n) is varied. The larger the term $12L_{\text{shell},(m,n)}/\{[k_m^2 + (n/a)^2]ah\}^2$ in Eq. (31) is, the stronger driving force is necessary to excite the vibration mode (m,n). In other words, if the modified bending stiffness of (m_0,n_0) is large, a large driving force is necessary to excite this (m_0,n_0) mode, and this mode is called as a "stiff" mode. When the modified bending stiffness of (m_1,n_1) is small, the (m_1,n_1) mode is called as a "flexible" mode. Therefore, if the natural frequencies of (m_0,n_0) and (m_1,n_1) modes are the same, then (m_1,n_1) mode is only excited, because (m_1,n_1) mode is the "flexible" mode. Namely, the vibration mode whose modified bending stiffness $D_{\text{shell},(m,n)}$ defined by Eq. (31) is smallest can be estimated as the excited vibration mode.

Moreover, the influences of each stress components on the modified bending stiffness are discussed in detail. Each stress component in $L_{\text{shell},(m,n)}W$, except that induced by circumferential displacement, is positive. The stress caused by circumferential displacement is always negative because L_v is always negative. Also, from Eqs. (7), (9), (22), and (23), we know that the amplitude of $L_5 L_v W$ at $m=1$ in each series of $n = \text{const}$ is larger than that of $[L_3 L_u + 1 + \beta^2(1 - 2n^2)]W$. Therefore, the modified bending stiffness of $(1,n)$ mode, $D_{\text{shell},(1,n)}$, is always less than D, and

$$c_{\text{flex},(1,n)} < c_{\text{flex,plate}} \quad \text{at } f_{1,n}. \tag{32}$$

In higher frequency regions ($\Omega \gg 1$), it is well known that the flexural wave velocity of cylindrical shell is close to that of the thin plate.[6,13] We now discuss this mechanism in terms of modified bending stiffness. The denominator of Eqs. (22) and (23) is

$$L_1 L_4 - L_2^2 = \Omega^4 \left(1 - \frac{(k_m a)^2 + \frac{1-\nu}{2}n^2(1+\beta^2)}{\Omega^2} \right)$$

$$\times \left(1 - \frac{\frac{1-\nu}{2}(k_m a)^2(1+3\beta^2) + n^2}{\Omega^2} \right), \tag{33}$$

therefore, from Eq. (25)

$$\lim_{\omega_{(m,n)} \to \infty} L_{\text{shell},(m,n)} = 1 + \beta^2(1 - 2n^2) \tag{34}$$
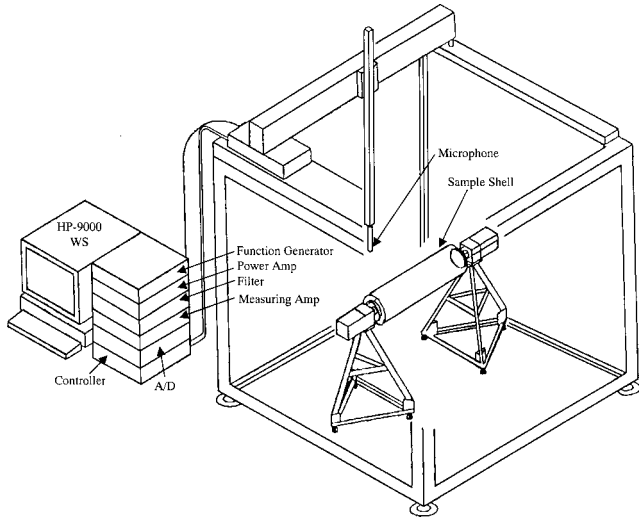
FIG. 1. A block diagram of the measurement system in the GENAH experiment for airborne sounds.

because $L_1 L_4 - L_2^2 \to \infty$. As the natural frequency is increased, the circumferential mode number is also increased. Therefore, from Eq. (31),

$$\lim_{\omega_{(m,n)} \to \infty} D_{\text{shell},(m,n)} = \lim_{\omega_{(m,n)} \to \infty} D \left[1 + \frac{12}{(ah)^2} \frac{L_{\text{shell},(m,n)}}{[k_m^2 + (n/a)^2]^2} \right]$$

$$= \lim_{n \to \infty} D \left[1 + \frac{12}{(ah)^2} \right.$$

$$\left. \times \frac{1 + \beta(1 - 2n^2)}{\{(k_m/n)^2 + (1/a)^2\}^2 n^4} \right] = D, \qquad (35)$$

therefore, Eqs. (30) and (18) give

$$\lim_{\omega_{(m,n)} \to \infty} c_{\text{flex},(m,n)} = \lim_{\omega_{(m,n)} \to \infty} \left(\frac{D_{\text{shell},(m,n)} \omega_{(m,n)}^2}{h \rho} \right)^{1/4}$$

$$= \lim_{\omega_{(m,n)} \to \infty} \left(\frac{D \omega_{(m,n)}^2}{h \rho} \right)^{1/4}$$

$$= \lim_{\omega_{(m,n)} \to \infty} c_{\text{flex,plate}} . \qquad (36)$$

In the next section, theoretical calculation of the modified bending stiffness and flexural wave velocities is carried out. Comparison between theoretical and experimental results is also described to exhibit the validity of the theory.

III. THEORETICAL CALCULATION AND EXPERIMENT

A. Experimental apparatus and model description

GENAH is performed by scanning the sound-pressure field over a defined cylindrical contour. This task is accomplished experimentally by means of a robotic scanning system that allows movement of a measuring microphone using several degrees of freedom. This scanning system was developed for the experimental implementation of GENAH for airborne sound (cf. Fig. 1) based on our underwater GENAH.[14−16]

A simply-supported shell is held by a rotating robot. A WILCOXON F9/Z9/F3 shaker, which drives the sample shell, is attached inside a shell. A Brüel & Kjær Type 4182 probe microphone is placed at the prescribed position with automatic scanners. A two-dimensional measurement contour is thus scanned by stepwise rotational and horizontal movement of the shell. Measured data of the measurement contour are taken in 5.625(=360/64) degree steps along the rotational scanning and in 25-mm steps along the horizontal scanning. The mesh size is sufficiently smaller than the size of the vibration mode cell. Thus, 64×64 points data make one hologram. The received and amplified signals from the microphone are digitized and transferred to the HP-9000 Workstation. Sampling inception time is accurately controlled by the computer, which acts as the reference source for holographic interference. The analysis computation is executed with the HP-9000 Workstation.

An experimental cylindrical shell is made of SUS 304 stainless steel. The shell is 800 mm in length, 0.105 m in inner diameter, and 3.0 mm in thickness. The Young's modulus is 1.95×10^{11} (N/m), Poisson's ratio is 0.28, and density is 7.83×10^3 (kg/m^3). The shaker is attached at the distance of 300 mm from the bottom of the shell. The shaker is driven by a broadband (300–6000 Hz) linear frequency modulation signal. Ten consecutive responses of the excitation are added to enhance the signal-to-noise ratio.

B. Comparison between theoretical and experimental result

The modified bending stiffness calculated by Eq. (31) is shown in Fig. 2. The dimensions and material constants of the shell for this calculation correspond to the experimental model. As explained in Sec. II, a larger driving force is necessary to excite the vibration mode with a larger modified bending stiffness. Therefore, it is supposed that the modified bending stiffness of the excited vibration mode should be smaller than that of the nonexcited vibration mode. For example, the natural frequencies of (2,5) mode and that of (4,4) mode are almost the same. However, the modified bending stiffness of (2,5) mode is smaller than that of (4,4) mode, and the difference between these is 2.5 dB. Therefore, we can easily estimate that (2,5) mode is an actually excited vibration mode. As inferred from the above-mentioned discussion, we can estimate the excited vibration mode by calculating the modified bending stiffness. In Fig. 2, the most "flexible" modes are indicated by circles, while modes indicated by triangles correspond to stiffer modes. As the result, we may assume that the modes indicated by circles will be really excited.

To confirm the validity of such theoretical estimation of the excited modes, we compare the theoretical and experimental results. Figure 3 shows the driving-point mobility of the shell measured by an impedance head. This mobility is normalized by the maximum value. In Fig. 3, the vibration mode is shown in (m,n). These mode numbers are obtained from the results of the shell surface velocity reconstructed by GENAH.[15] A comparison between Figs. 2 and 3 shows that all of the excited vibration modes, which are theoretically predicted (cf. Fig. 2), are only observed in the experimental
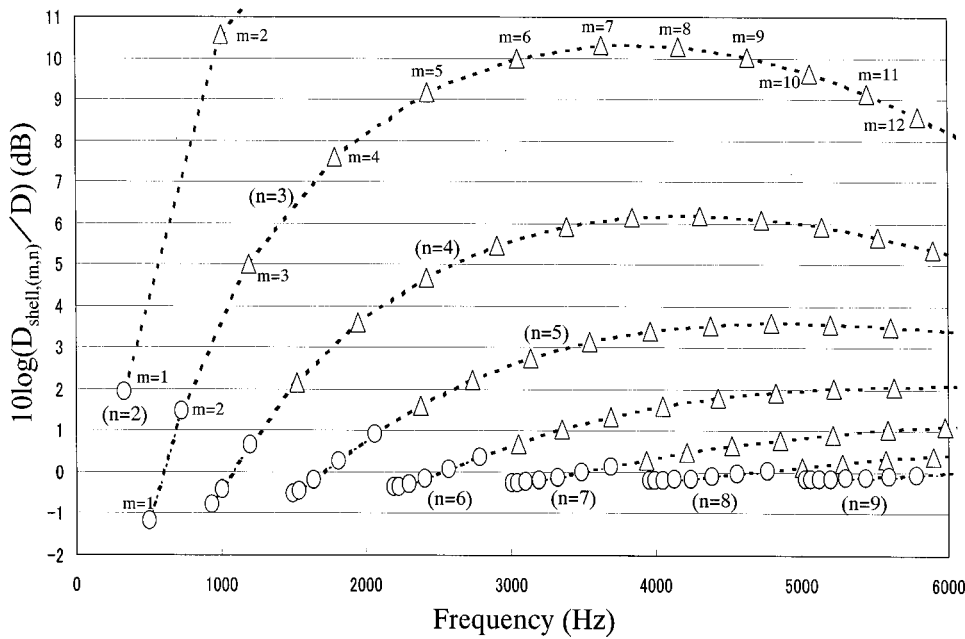
FIG. 2. Calculation of the modified bending stiffness of individual vibration mode. Symbol ○, the lowest modified bending stiffness at the natural frequency; △, the nonlowest modified bending stiffness. The broken line connects the loci of a constant n.

result (cf. Fig. 3), and nonexcited vibration modes in Fig. 2, such as (3,3), (4,4), etc., are not shown in Fig. 3. Therefore, the validity of our proposed prediction method of the excited vibration mode is confirmed.

Figure 4 shows the experimental results (●) of flexural wave velocity. The flexural wave velocity obtained by the characteristic equation (◇ and △) and that of the thin plate (solid line) are also shown in Fig. 4. Theoretically predicted excited modes are shown as ◇, and nonexcited modes as △. An excellent agreement between ◇ and ● is indicated in Fig. 4, and the difference between these experimental and theoretical values of $c_{\text{flex},(m,n)}$ is about 1.4%.

Figure 5 shows the difference between the flexural wave velocity of the shell and that of the plate. Comparison between theoretical (△) and experimental (●) results shows an excellent agreement. In all series of $n = \text{const}$, as the axial mode number m is increased, the relative velocity of flexural wave, which are normalized by the flexural wave velocity of thin plate, is also increased. Also, the flexural wave velocity

of the shell with $m = 1$ is smaller than that of the plate. From Eq. (30) we obtain

$$\frac{(c_{\text{flex},(m,n)} - c_{\text{flex,plate}})}{c_{\text{flex,plate}}} = \left(\frac{D_{\text{shell},(m,n)}}{D}\right)^{1/4} - 1. \tag{37}$$

Therefore, $(1,n)$ mode is the most flexible mode in all series of $n = \text{const}$, and as m is increased, the modified bending stiffness is increased. If $f_{(m,n)} > f_{(1,n+1)}$, then $(1,n+1)$ mode is more flexible than (m,n) mode, therefore, $(1,n+1)$ mode is excited instead of (m,n) mode. As the driving frequency increases, the difference between the flexural wave velocity of the shell and that of the plate becomes very small. These experimental results reconfirm the validity of theoretical consideration of the influence of each stress component on the modified bending stiffness described in Sec. II B.

FIG. 3. Driving-point mobility of the airborne shell. The (m,n) denotes the vibration mode.
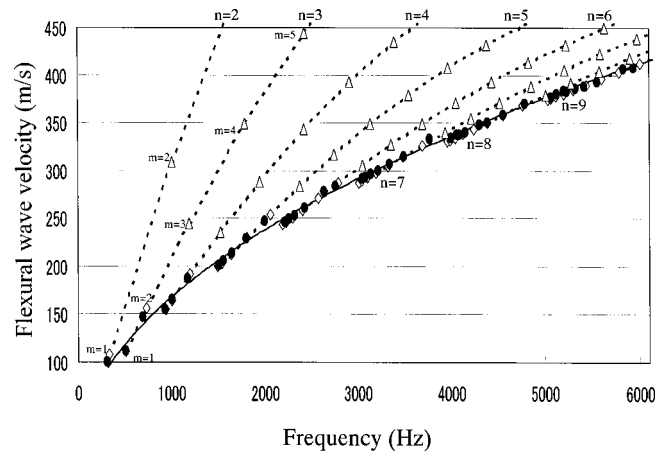
FIG. 4. Flexural wave velocity of the airborne shell. Symbol ●, experimental result of flexural wave velocity of the excited vibration mode; ◇, flexural wave velocity of the excited mode calculated from Eqs. (1) and (2), and the characteristic equation; △, flexural wave velocity of the nonexcited mode similarly calculated. The solid line gives the flexural wave velocity of thin plate; the broken line that of the (m,n) shell modes for constant n.
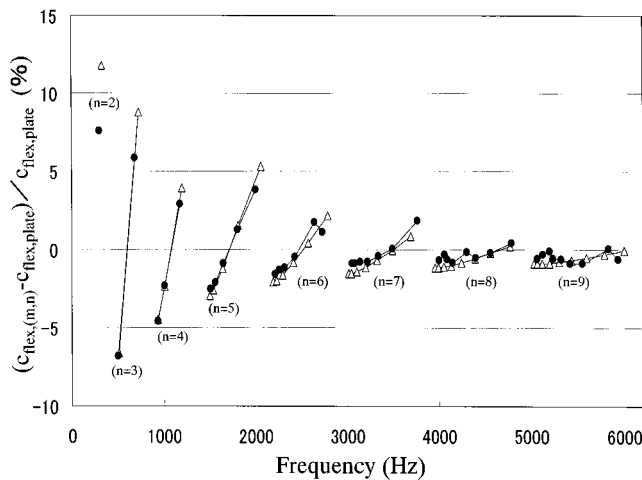
FIG. 5. The relative % difference between the flexural wave velocity of the shell and that of the plate. Symbol ●, the experimental result; △, the result calculated from Eqs. (1) and (2) and the characteristic equation. The solid line gives a series of $n = $ const.

Also, the validity of the proposed prediction method of the excited mode is well illustrated.

IV. CONCLUSION

We propose a prediction method of the excited vibration mode of the shell by introducing the concept of "modified bending stiffness," which indicates the "stiffness" of each vibration mode. A stronger driving force is necessary to excite a stiffer mode, while a weaker driving force is able to excite a flexible mode. The influence of each stress component on the modified bending stiffness is discussed in detail. The investigation result shows that the stress component caused by circumferential displacement reduces the modified bending stiffness. Since the amplitude of this stress component at $m = 1$ in a series of $n = $ const is larger than the sum of stress components caused by radial and axial displacements, the flexural wave velocity of $(1,n)$ mode is always less than that of thin plate. In higher wavenumber regions ($\Omega \gg 1$), the difference between the modified bending stiffness of the excited vibration mode and the bending stiffness of thin plate becomes very close. As the result, the flexural wave velocity of the shell is close to that of thin plate. The validity of our proposed method is confirmed by an excellent agreement between experimental and theoretical results.

However, we have to consider the effect of the "fluid loading" in order to apply our estimation method to sub-

merged cylindrical shells. The natural frequency of the vibration mode of thin plate is easily determined in the air, but this is not the case in the water. Calculation of this fluid loading requires the inclusion of the force term caused by the radiated pressure into the equation of motion and then into $L_{\text{shell},(m,n)}$ of Eq. (25). And for the estimation of the excited vibration mode of the submerged plate, the radiated pressure term should be treated as the modification term of the bending stiffness. This modification term can be treated the same as $L_{\text{shell},(m,n)}$ of the motion equation of the cylindrical shell. Such a modification to apply our proposed method to estimate the excited vibration mode of submerged structures will be discussed in our next paper.

[1] X. M. Zhang, G. R. Liu, and K. Y. Lan, "Vibration analysis of cylindrical shells using wave propagation approach," J. Sound Vib. **239**, 397–403 (2001).

[2] W. Leissa, *Vibration of Shells* (Acoustical Society of America, New York, 1993).

[3] M. C. Junger and D. Feit, *Sound, Structures, and Their Interaction*, 2nd ed. (MIT Press, Cambridge, MA, 1986).

[4] P. A. Franken, "Input impedances of simple cylindrical shells," J. Acoust. Soc. Am. **32**, 473–477 (1960).

[5] M. Heckl, "Vibrations of point-driven cylindrical elastic shells," J. Acoust. Soc. Am. **34**, 1553–1557 (1962).

[6] D. Feit, "High-frequency response of a point-excited cylindrical shells," J. Acoust. Soc. Am. **49**, 1499–1504 (1971).

[7] L. Cremer, M. Heckl, and E. E. Ungar, *Structure-Borne Sound*, 2nd ed. (Springer-Verlag, New York, 1988).

[8] C. R. Fuller, "The input mobility of an infinite circular cylindrical elastic shell filled with water," J. Sound Vib. **87**, 409–427 (1983).

[9] M. B. Xu and X. M. Zhang, "Vibration power flow in a fluid-filled cylindrical shell," J. Sound Vib. **218**, 587–598 (1998).

[10] R. S. Ming, J. Pan, and M. P. Norton, "The mobility functions and their application in calculating power flow in coupled cylindrical shells," J. Acoust. Soc. Am. **105**, 1702–1713 (1999).

[11] R. Ming, J. Pan, and M. P. Norton, "The measurement of structural mobilities of a circular cylindrical shell," J. Acoust. Soc. Am. **107**, 1374–1383 (2000).

[12] E. G. Williams, H. D. Dardy, and K. B. Washburn, "Generalized nearfield acoustic holography for cylindrical geometry: Theory and experiment," J. Acoust. Soc. Am. **81**, 389–405 (1987).

[13] P. W. Smith, Jr., "Minimum axial phase velocity in shells," J. Acoust. Soc. Am. **30**, 140–141 (1958).

[14] K. Saijyou and S. Yoshikawa, "Sound scattering of an arbitrary wave incident on a simply-supported cylindrical shell," J. Acoust. Soc. Jpn. (E) **16**, 223–232 (1995).

[15] K. Saijyou and S. Yoshikawa, "Structural intensity measurement of cylindrical shell based NAH technique and influences of a rib on the acoustic energy flow," J. Acoust. Soc. Jpn. (E) **20**, 125–136 (1999).

[16] K. Saijyou and S. Yoshikawa, "Reduction methods of the reconstruction error for large-scale implementation of near-field acoustical holography," J. Acoust. Soc. Am. **110**, 2007–2023 (2001).

Sound radiation from a water-filled pipe, radiation into light fluid

Bilong Liu,[a] Jie Pan,[b] Xiaodong Li, and Jing Tian

*Institute of Acoustics, Chinese Academy of Sciences, P.O. Box 2712, Beijing100080,
People's Republic of China*

This paper is concerned with the sound radiation from a water-filled exhaust pipe. The pipe opening and a plate attached to it form a vibrating surface for this radiation. Fluid-structural coupling between the pipe and enclosed fluid is included in the system modeling, but light fluid assumption is used for sound radiation into the space above the vibrating surface. In this paper, a numerical study on the $n=0$ mode in the pipe shows that the wave types associated with this mode have different characteristics in two regions of the nondimensional frequency Ω. In the first region of $0<\Omega<0.5$ and $1<\Omega<1.3$, the fluid and structural waves are weakly coupled, and the fluid and structural response of the pipe is governed by the resonance of each wave type. The fluid and structural waves are strongly coupled in the second region $(0.5<\Omega<1)$. Simple correlation between the pipe response and uncoupled mode distributions does not exist. Significant contribution of multiple wave-types to the model energy is evident. The ultimate goal of our system modeling is to illustrate the contribution of all wave types (structural-borne and water-borne waves of the system) to sound radiation from the pipe opening and the attached plate. This paper also demonstrates the effect of these waves and their coupling in the water-filled pipe and across the plate and pipe boundary on the radiated sound pressure. Experimental results obtained in a semi-anechoic room are used to partially validate the theoretical and numerical predictions. © *2002 Acoustical Society of America.* [DOI: 10.1121/1.1515794]

PACS numbers: 43.40.Ey, 43.20.Tb [ANN]

I. INTRODUCTION

Water-filled exhaust pipes find many applications in industries. Typical example is the exhaust pipes in some ocean surface ships and underwater vehicles, where the outlets of the exhaust are underneath the water surface. The determination of vibration transmission from a water-filled pipe to the structure attached to the pipe opening and of subsequent structural-borne/water-borne sound radiation from the pipe and the structure is an important step before any control treatment. Much research has been devoted to the understanding of the wave travelling characteristics in pipes for two cases, *in vacuo* and in fluid filled. Harari[1] and Fuller[2] studied wave propagation in cylindrical shells with structural discontinuity. Schlesinger,[3] Tso and Hansen[4] investigated the wave propagation through cylindrical/plate junction. The dispersion relations and energy distributions for wave travelling in a fluid-filled elastic pipe were thoroughly analyzed by Fuller and Fahy.[5]

In this paper, the water-filled exhaust pipe system is modeled as a water-filled pipe coupled with a finite plate at the pipe opening. The disturbance from the source end of the pipe is transmitted to the pipe opening as water-borne sound and to the attached plate as structural-borne sound radiated into the medium above the plate. The paper concentrate on the water/structure coupling in the pipe and pipe/plate coupling, and the effect of these coupling on the radiated sound.

The fluid-structural coupling in a water-filled pipe is included in the mathematical modelling and the ''light fluid'' assumption (such as air) is used for the medium above the plate. This assumption allows us to neglect the effect of fluid loading on the plate vibration. A simple experiment of sound radiation into air within a semianechoic room was conducted for comparison. According to Crighton's analysis,[6] the fluid loading (e.g., water loading) on the radiating plate can be regarded as ''light'' if the operating frequency is above the ''null frequency.'' Thus above the null frequency, the analysis presented in this paper is also valid for sound radiation into water.

II. SYSTEM DESCRIPTION AND DISPERSION CURVES

The system model used in this paper is shown in Fig. 1, where (z, σ, θ) denote, respectively, axial, radial and circumferential coordinates above the plate, (u, v, w) and (u_p, v_p, w_p) represent displacements in the three orthogonal directions of the pipe wall and the plate. The length and radius of the pipe are denoted as L and a, respectively. The flat plate is finite and circular and b is the outside radius, the inner boundary of the plate is connected rigidly to the pipe opening and the outer boundary is clamped on a rigid infinite baffle. A velocity source located at the bottom of the pipe is used to generate sound and vibration.

The characteristics of sound propagation in a fluid-filled pipe are described by the dispersion curves of waves in the fluid-filled pipe of infinite length. Figure 2 shows a typical

---
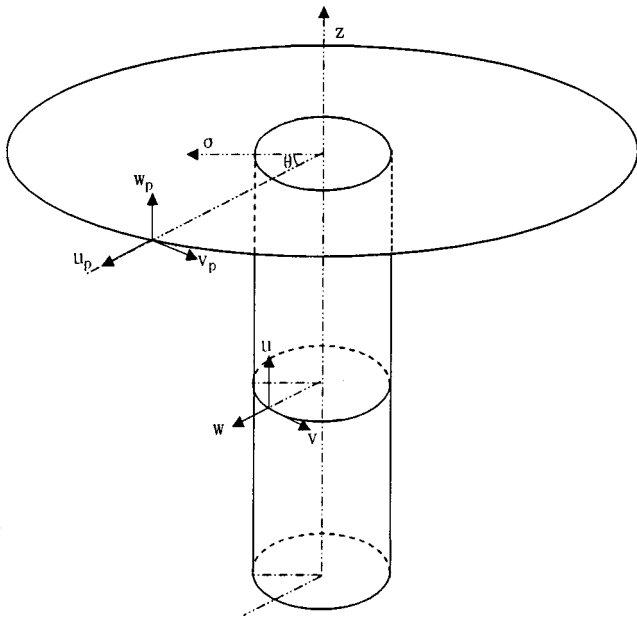
FIG. 1. System model and coordinates definition.

plot of the dispersion curves first obtained by Fuller,[5] and this paper do a decent job explaining the dispersion curves.

The curves in Fig. 2 are classified into s and r branches. s ranges from 1 to 4 while r from 0 to infinity. At the low frequencies ($0<\Omega<0.5$), the fluid and pipe is weakly coupled. Each r branch represents an acoustic traveling wave in a rigid pipe. The number of radial nodes of the wave equals r. s corresponds to the structural wave types *in vacuo* shell. For example, $r=0$ denotes fluid plane waves, $r=1,2,3,...$ represent high order fluid waves and $s=1$ corresponds to extensional waves *in vacuo*, $s=2$ represents torsional waves, and $s=3,4$ to flexure waves. Increasing the nondimensional frequency ($0.5<\Omega<1$), the pipe stiffness in the radial direction decreases and fluid-structural coupling becomes strong. In this region, $r=0$ branch changes its characteristics of pure fluid plane waves and $s=1$ also deviates from characteristics of structural extensional waves. After the frequency Ω exceeds 1, $r=0$ changes from initially fluid
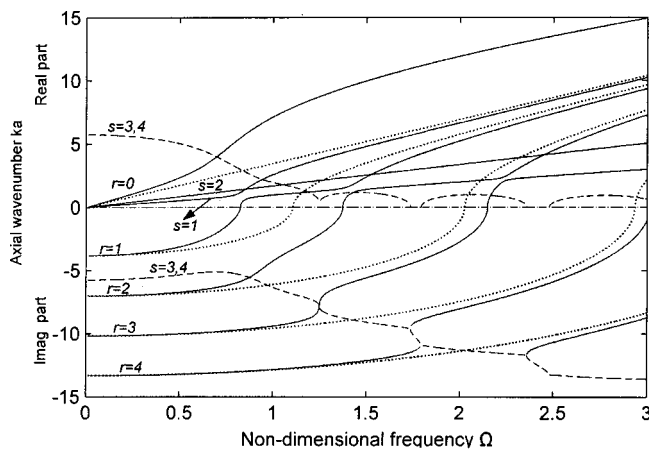
FIG. 2. Dispersion curves of a water-filled steel shell with thickness/radius ratio $h/a=0.05$ and for $n=0$. Solid lines, purely real and imaginary wave number; dashed lines, real and imaginary parts of complex wave number; dotted lines, rigid walled duct solution.

plane waves to shell extensional waves and in the same time $s=1$ changes from initially shell extensional waves to fluid plane waves. So the fluid-structural coupling in this region returns to be weak.

$r=1$ branch corresponds to high order of evanescent fluid dominant waves at low frequencies. It changes from imaginary number to real number at $\Omega=0.8$. Above this frequency, $r=1$ represents the characteristics of shell longitudinal waves. Furthermore at $\Omega>1.5$ it corresponds the characteristics of the first cross-mode of fluid-dominated propagating waves.

As s and r branches co-exist, to determine the travelling wave response of shell we need four boundary conditions at each end of the pipe. At the same time we can expand fluid particle velocity at each end for N_r r branches using Bessel functions. The radial modes are truncated into finite orders and only N_r r branches are used in the expansion. Then we have $4+N_r$ boundary conditions at each end for total $2(4+N_r)$ coefficients of the travelling wave solution.

III. SOLUTION OF THE SYSTEM RESPONSE

A. Sources and boundary conditions of water filled pipe

The dynamical response of a water-filled pipe is described by (u,v,w,p) representing three vibration components on the pipe wall and sound pressure inside the pipe. Such response is due to the external forces, moment exerted on the pipe wall and volume velocity at bottom of the pipe at $z=-L$. The boundary conditions at other end of the pipe $z=0$ are described by the forces and moment per unit length, which are related to the elastic stresses at the pipe/plate joint, and by the air particle velocity at the pipe opening. In the following deduction, the polarization angle is assumed to be zero. The analysis can be readily extended to include arbitrary sound velocity distribution and nonsymmetrical pipes. Detailed analysis and experimental method to resolve the effect of wave polarization have been investigated by Ming, Pan, and Norton.[7]

The transverse shear force, torsional shear force, axial force and bending moment are related to the displacement of the pipe wall as the follows:[8]

$$Q_z=\{-Eh^3/12(1-\mu^2)\}\left\{\frac{\partial^3 w}{\partial z^3}+[(2-\mu)/a^2]\frac{\partial^3 w}{\partial z\partial\theta^2}\right\}, \quad (1)$$

$$N_{z\theta}=\{Eh/2(1+\mu)\}\left\{\frac{\partial u}{a\partial\theta}+\frac{\partial v}{\partial z}-(h^2/6a^2)\frac{\partial^2 w}{\partial z\partial\theta}\right\}, \quad (2)$$

$$N_z=\{Eh/(1-\mu^2)\}\left\{\frac{\partial u}{\partial z}+(\mu/a)\frac{\partial v}{\partial\theta}+(\mu/a)w\right\}, \quad (3)$$

$$M_z=\{Eh^3/12(1-\mu^2)\}\left\{\frac{\partial^2 w}{\partial x^2}+(\mu/a^2)\frac{\partial^2 w}{\partial\theta^2}\right\}. \quad (4)$$

The sound pressure and the normal particle velocity are related at the boundaries by

$$\hat{v} = j \frac{1}{\rho \omega} \frac{\partial p}{\partial z}. \tag{5}$$

B. Pipe response

The wave motion of a thin-walled cylindrical pipe containing an acoustic field can be most conveniently described by the Donnell–Mushtari shell equations,[9] and the response of the water-filled pipe can be represented by the superposition of the circumferential and axial modes. Corresponding to each circumferential modal number n (u,v,w,p), have several propagating modes in the axial direction, and they coexist (except for $n=0$, where the torsional component v is uncoupled from all other modes). Furthermore, even for the same circumferential and axial propagating mode, the sound pressure may have different radial distribution.

The axial wave numbers k_{nm} can be calculated from the characteristic equation[5]

$$\begin{bmatrix} L_{11} & L_{12} & L_{13} \\ L_{21} & L_{22} & L_{23} \\ L_{31} & L_{32} & L_{33} \end{bmatrix} \begin{bmatrix} U_{nm} \\ V_{nm} \\ W_{nm} \end{bmatrix} = \begin{bmatrix} 0 \\ 0 \\ 0 \end{bmatrix}, \tag{6}$$

where (U_{nm},V_{nm},W_{nm}) are amplitudes of three wave types on the pipe wall and the matrix elements are

$$L_{11} = -\Omega^2 + (k_{nm}a)^2 + \tfrac{1}{2}(1-\nu)n^2, \tag{7a}$$

$$L_{12} = \tfrac{1}{2}(1+\nu)n(k_{nm}a), \tag{7b}$$

$$L_{13} = \nu(k_{nm}a), \tag{7c}$$

$$L_{21} = L_{12}, \tag{7d}$$

$$L_{22} = -\Omega^2 + \tfrac{1}{2}(1-\nu)(k_{nm}a)^2 + n^2, \tag{7e}$$

$$L_{23} = n, \tag{7f}$$

$$L_{31} = L_{13}, \tag{7g}$$

$$L_{32} = L_{23}, \tag{7h}$$

$$L_{33} = -\Omega^2 + 1 + \beta^2[(k_{nm}a)^2 + n^2]^2 - FL. \tag{7i}$$

In Eqs. (7), $\Omega = \omega a / C_L$ is defined as nondimensional frequency, C_L is the extensional phase speed of the shell, ν is the Possion's ratio of the pipe material and $\beta^2 = h^2/12a^2$ is the thickness parameter, where h is the thickness of the pipe wall. FL is the fluid loading of the contained fluid:

$$FL = \Omega^2(\rho_f/\rho_s)(h/a)^{-1}(k_m^r a)^{-1}[J_n(k_m^r a)/J_n'(k_m^r a)], \tag{8}$$

where ρ_f and ρ_s are the densities of the fluid and pipe wall, respectively. The radial wave number can be obtained from the wave number vector relationship as

$$k_m^r a = \pm[\Omega^2(C_L/C_f)^2 - (k_{nm}a)^2]^{1/2}, \tag{9}$$

where C_f is the sound speed in the fluid.

In Eq. (6), the coefficients of travelling modes are related. Considering the continuity of the structural/fluid par-

ticle velocities on the pipe wall, the amplitudes of (n,m) travelling mode in the pipe are expressed as

$$[\Phi_{nm}] = \begin{bmatrix} U_{nm} \\ V_{nm} \\ W_{nm} \\ P_{nm} \end{bmatrix} = W_{nm} \begin{bmatrix} j\alpha_{nm}^U \\ \alpha_{nm}^V \\ 1 \\ \alpha_{nm}^P \end{bmatrix}, \tag{10}$$

where

$$\begin{bmatrix} j\alpha_{nm}^U \\ \alpha_{nm}^V \end{bmatrix} = -\begin{bmatrix} L_{11} & L_{12} \\ L_{21} & L_{22} \end{bmatrix}^{-1}\begin{bmatrix} L_{13} \\ L_{23} \end{bmatrix},$$

and (11)

$$a_{nm}^P = \omega^2 \rho_f / k_m^r J_n'(k_m^r a).$$

Then the pipe response is due to superposition of all the travelling modes

$$\begin{bmatrix} u \\ v \\ w \\ p \end{bmatrix} = \sum_{n,m} \begin{bmatrix} u_{nm} \\ v_{nm} \\ w_{nm} \\ p_{nm} \end{bmatrix}$$

$$= \sum_{n=0}^{\infty} \sum_{m=1}^{2(4+Nr)} W_{nm} \begin{bmatrix} j\alpha_{nm}^U \\ \alpha_{nm}^V \\ 1 \\ \alpha_{nm}^P \end{bmatrix}$$

$$\times \begin{bmatrix} \cos n\theta & & & 0 \\ & \sin n\theta & & \\ & & \cos n\theta & \\ 0 & & & \cos n\theta J_n(k_m^r\sigma) \end{bmatrix}$$

$$\times e^{-jk_{nm}z}. \tag{12}$$

For each circumferential mode, $2(4+N_r)$ equations are required for W_{nm}, $m=1,...,2(4+N_r)$. At boundary $z=-L$, the boundary forces and moment are expanded in the circumferential direction as the follows:

$$Q_z = \sum_{n=0}^{\infty} Q_{zn}\cos(n\theta, \tag{13a}$$

$$N_{z\theta} = \sum_{n=0}^{\infty} N_{z\theta n}\sin(n\theta), \tag{13b}$$

$$N_z = \sum_{n=0}^{\infty} N_{zn}\cos(n\theta), \tag{13c}$$

$$M_z = \sum_{n=0}^{\infty} M_{zn}\cos(n\theta). \tag{13d}$$

Combined with Eqs. (1)–(4), Eq. (13) provides four equations for the solution of W_{nm} of each circumferential mode.

The particle velocity of the fluid at $z=-L$ is expanded as

$$\hat{v}_1 = \sum_{n,r} \hat{V}_{nr}^{(1)}\cos(n\theta)J_n(k^r\sigma), \tag{14}$$

where the velocity in the radial direction is expanded by the mode shape functions of sound pressure in a pipe with the rigid wall condition $[J_n'(k^r\sigma)|_{\sigma=a}=0]$. The convergence of this expansion depends upon the orthogonality between $J_n(k^r\sigma)$ and $J_n(k_m^r\sigma)$. Nevertheless, the spatial coherence between the functions with the same radial numbers should be much larger that that with different radial numbers. Therefore good convergence property of this expansion is expected.

As a result, the evaluation of Eqs. (5), (11), (12), and (14) at the boundary $z=-L$ suggests

$$\sum_{n,r} \hat{V}_{nr}^{(1)} \cos n\theta J_n(k^r\sigma)$$

$$= \frac{j}{\rho_o\omega} \sum_{n,m} (-jk_{nm})\alpha_{nm}^P W_{nm} \cos n\theta J_n(k_m^r\sigma)e^{jk_{nm}L}. \tag{15}$$

Multiplying $J_n(k^{r'}\sigma)$ on both sides of Eq. (15) and integrating the resultant equation from 0 to a gives rise to following equation:

$$\hat{V}_{nr'}^{(1)}\bar{\Lambda}_{nr'} = \frac{1}{\rho_o\omega} \sum_m k_{nm}\alpha_{nm}^P W_{nm}\chi_{nr',nm}e^{jk_{nm}L}, \tag{16}$$

where

$$\bar{\Lambda}_{nr'} = \int_0^a J_n^2(k^{r'}\sigma)\sigma\, d\sigma, \tag{17}$$

$$\chi_{nr',nm} = \int_0^a J_n(k^{r'}\sigma)J_n(k_m^r\sigma)\sigma\, d\sigma. \tag{18}$$

Given the velocity distribution of the sound source at $z=-L$, Eq. (16) provides N_r equations for W_{nm} of each circumferential mode.

C. Sound radiation from the pipe opening

The normal particle velocity at the pipe opening is expressed as

$$\hat{v}_2 = \sum_{n,r} \hat{V}_{nr}^{(2)} \cos(n\theta)J_n(k^r\sigma), \tag{19}$$

which contribute to the radiated sound pressure (air-borne noise) in $z>0$ space

$$p_A(\sigma,\theta,z) = \frac{j\omega\rho_o}{2\pi} \sum_{n,r} \hat{V}_{nr}^{(2)} \int_0^a \int_0^{2\pi} \frac{\cos n\theta' J_n(k^r\sigma')}{R}$$

$$\times e^{-j\vec{k}\cdot\vec{R}}\sigma'\, d\sigma'\, d\theta', \tag{20}$$

where $R=\sqrt{(\sigma\cos\theta-\sigma'\cos\theta')^2+(\sigma\sin\theta-\sigma'\sin\theta')^2+z^2}$ is the distance between the vibrating element at $(\sigma,\theta',0)$ and observation point at (σ,θ,z), ρ_o is the density of medium above the plate. If the circumferential mode $n=0$ is considered only, the radiated sound in Eq. (20) can be approximated by first N_r modal velocity coefficients $(\hat{V}_{0r}^{(2)}, r=1,2,...,N_r)$.

The sound pressure at the opening $(\sigma \leq a)$ is the sum of the self-radiated pressure and pressure loading $p_S(\sigma,\theta,0)$ due to the plate vibration (structural borne sound of the plate)

$$p_1(\sigma,\theta,0) = \sum_{n,r} \hat{V}_{nr}^{(2)}Z_{nr}(\sigma,\theta,0)+p_S(\sigma,\theta,0), \tag{21}$$

where

$$Z_{nr}(\sigma,\theta,0) = \frac{j\omega\rho_o}{2\pi} \int_0^a \int_0^{2\pi} \frac{\cos n\theta' J_n(k^r\sigma')}{R_{z=0}}$$

$$\times e^{-j\vec{k}\cdot\vec{R}_{z=0}}\sigma'\, d\sigma'\, d\theta'. \tag{22}$$

To calculate the modal velocity $\hat{V}_{nr}^{(2)}$, Use the boundary condition at $z=0$ so that the sound pressure inside the pipe and that radiated into the space must be continue at the opening

$$\sum_{n,m} \alpha_{nm}^P W_{nm} \cos n\theta J_n(k_m^r\sigma)$$

$$= \sum_{n,r} \hat{V}_{nr}^{(2)}Z_{nr}(\sigma,\theta)+p_S(\sigma,\theta,0). \tag{23}$$

Multiplying $\cos(n'\theta)J_{n'}(k^{r'}\sigma)$ on both sides of Eq. (23) and integrating the resultant equation on the opening surface, the modal velocity is then related to the modal amplitude of the pipe flexural waves

$$\sum_m \alpha_{n'm}^P \Lambda_{n'}\chi_{n'm,n'r'}W_{n'm} = \sum_{n,r} \hat{V}_{nr}^{(2)}\sigma_{nr,n'r'}+p_{Sn'r'}, \tag{24}$$

where

$$\Lambda_{n'} = \int_0^{2\pi} \cos^2 n'\theta\, d\theta. \tag{25}$$

In Eq. (24), $\sigma_{nr,n'r'}$ are modal radiation efficiency factors and defined as

$$\sigma_{nr,n'r'} = \frac{j\omega\rho_o}{2\pi} \int_0^a \int_0^{2\pi} \int_0^a \int_0^{2\pi} \frac{\cos n'\theta\cos n\theta' J_{n'}(k^{r'}\sigma)J_n(k^r\sigma')}{R_{z=0}} e^{-j\vec{k}\cdot\vec{R}_{z=0}}\sigma\sigma'\, d\sigma\, d\theta\, d\sigma'\, d\theta'. \tag{26}$$

The modal pressure due to plate sound radiation is

$$p_{Sn'r'} = \int_0^a \int_0^{2\pi} p_S(\sigma,\theta,0) \cos n'\theta J_{n'}(k^{r'}\sigma)\sigma\,d\sigma\,d\theta. \tag{27}$$

For $n=n'=0$, there are total N_r equations in Eq. (24) as $r'=1,2,...,N_r$. However, Eq. (24) also includes $p_{S0r'}$ which is determined by the plate response.

In the mean time, the combination of Eqs. (5), (11), (12), and (19) suggests

$$\sum_{n,r} \hat{V}_{nr}^{(2)} \cos n\theta J_n(k^r\sigma)$$

$$= \frac{j}{\rho_o\omega} \sum_{n,m} (-jk_{nm})\alpha_{nm}^P W_{nm} \cos n\theta J_n(k_m^r\sigma), \tag{28}$$

which gives rise to

$$\hat{V}_{nr'}^{(2)}\bar{\Lambda}_{nr'} = \frac{1}{\rho_o\omega} \sum_m k_{nm}\alpha_{nm}^P W_{nm}\chi_{nr',nm}. \tag{29}$$

Equations (24) and (29) provide total $2\times N_r$ equations. However N_r velocity modal amplitudes $\hat{V}_{0r}^{(2)}$ are introduced. If the light fluid (such as air) is assumed for medium above the plate, the fluid loading on the pipe opening can be ignored. Equation (24) is simplified as

$$\sum_m \alpha_{nm}^P \Lambda_n \chi_{nr',nm} W_{nm} = 0, \tag{30}$$

which includes N_r equations uncoupled with $\hat{V}_{0r}^{(2)}$. It should be noted that the simplification from Eq. (24) to Eq. (30) due to light fluid loading will result in a significant error if sound radiation from an air-filled pipe is considered.

D. Plate response

The rest four equations are obtained by considering the plate response and the sound radiation from the plate into the space ($z\geq 0$) filled with light fluid. The effect of pressure loading on the plate response is ignored due to the light fluid assumption. For this case, the flexural displacement in the plate ($b\geq\sigma\geq a$) is expressed as[10]

$$W^{(P)}(\sigma,\theta) = \sum_{n=0}^{\infty} W_n^{(P)} \cos n\theta$$

$$= \sum_{n=0}^{\infty} [W_{An}^{(P)} J_n(\beta\sigma) + W_{Bn}^{(P)} Y_n(\beta\sigma)$$

$$+ W_{Cn}^{(P)} I_n(\beta\sigma) + W_{Dn}^{(P)} K_n(\beta\sigma)]\cos n\theta, \tag{31}$$

where $\beta^4 = \rho_s h\omega^2/D$ and $D = Eh^3/12(1-\nu^2)$ is the plate bending stiffness. J_n and Y_n are the Bessel functions of first and second kinds, I_n and K_n are the modified Bessel functions of the first and second kinds. The coefficients $W_{An}^{(P)},...,W_{Dn}^{(P)}$ determine the mode shape and are solved from the boundary conditions.

The coefficients of the nth plate mode are determined by the boundary conditions. We denote the transverse shearing force and bending moment acting on the plate at the pipe/plate joint ($z=0$, $\sigma=a$) as
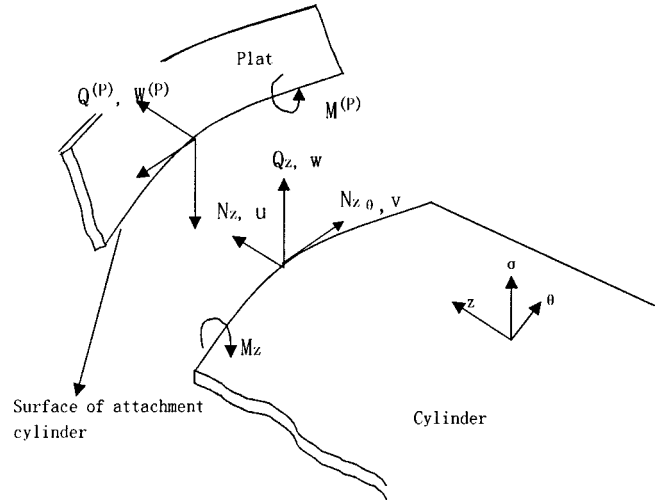
FIG. 3. Forces, moments, and displacements at the pipe/plate joint.

$$Q^{(P)} = \sum_{n=0}^{\infty} Q_n^{(P)} \cos n\theta, \tag{32a}$$

$$M^{(P)} = \sum_{n=0}^{\infty} M_n^{(P)} \cos n\theta. \tag{32b}$$

They are related to the flexural displacement of the plate by[8]

$$Q^{(P)} = D\frac{\partial}{\partial\sigma}\left(\frac{\partial^2 W^{(P)}}{\partial\sigma^2} + \frac{1}{\sigma}\frac{\partial W^{(P)}}{\partial\sigma} + \frac{1}{\sigma^2}\frac{\partial^2 W^{(P)}}{\partial\theta^2}\right), \tag{33a}$$

$$M^{(P)} = D\left[\frac{\partial^2 W^{(P)}}{\partial\sigma^2} + \nu\left(\frac{1}{\sigma}\frac{\partial W^{(P)}}{\partial\sigma} + \frac{1}{\sigma^2}\frac{\partial^2 W^{(P)}}{\partial\theta^2}\right)\right]. \tag{33b}$$

On the clamped plate edge, the boundary conditions at ($z=0$, $\sigma=b$) are

$$W(b) = 0, \quad \left.\frac{\partial W}{\partial\sigma}\right|_{\sigma=b} = 0. \tag{34}$$

Substituting Eqs. (31), (32) into Eq. (33) and Eq. (31) into Eqs. (34), a matrix equation for the coefficients of the nth mode in the plate is obtained,

$$\begin{bmatrix} Z_{An}^{(Q)} & Z_{Bn}^{(Q)} & Z_{Cn}^{(Q)} & Z_{Dn}^{(Q)} \\ Z_{An}^{(M)} & Z_{Bn}^{(M)} & Z_{Cn}^{(M)} & Z_{Dn}^{(M)} \\ Z_{An}^{(1)} & Z_{Bn}^{(1)} & Z_{Cn}^{(1)} & Z_{Dn}^{(1)} \\ Z_{An}^{(2)} & Z_{Bn}^{(2)} & Z_{Cn}^{(2)} & Z_{Dn}^{(2)} \end{bmatrix} \begin{bmatrix} \dot{W}_{An}^{(P)} \\ \dot{W}_{Bn}^{(P)} \\ \dot{W}_{Cn}^{(P)} \\ \dot{W}_{Dn}^{(P)} \end{bmatrix} = \begin{bmatrix} Q_n^{(P)} \\ M_n^{(P)} \\ 0 \\ 0 \end{bmatrix}. \tag{35}$$

The modal force and moment on the right-hand side of Eq. (33) must be equal to the axial force and the bending moment in the pipe wall at the pipe/plate joint (as illustrated in Fig. 3)

$$\begin{bmatrix} Q_n^{(P)} \\ M_n^{(P)} \end{bmatrix}_{\sigma=a} = \begin{bmatrix} -N_{zn} \\ M_{zn} \end{bmatrix}_{z=0}. \tag{36}$$

Inverting the impedance matrix in Eq. (35) gives rise to the conductance matrix

$$\begin{bmatrix} Z_{An}^{(Q)} & Z_{Cn}^{(Q)} & Z_{Cn}^{(Q)} & Z_{Dn}^{(Q)} \\ Z_{An}^{(M)} & Z_{Bn}^{(M)} & Z_{Cn}^{(M)} & Z_{Dn}^{(M)} \\ Z_{An}^{(1)} & Z_{Bn}^{(1)} & Z_{Cn}^{(1)} & Z_{Dn}^{(1)} \\ Z_{An}^{(2)} & Z_{Bn}^{(2)} & Z_{Cn}^{(2)} & Z_{Dn}^{(2)} \end{bmatrix}^{-1} \begin{bmatrix} Y_{11} & Y_{12} & Y_{13} & Y_{14} \\ Y_{21} & Y_{22} & Y_{23} & Y_{24} \\ Y_{31} & Y_{32} & Y_{33} & Y_{34} \\ Y_{41} & Y_{42} & Y_{43} & Y_{44} \end{bmatrix},$$

(37)

which allows the mobility functions to be expressed explicitly as

$$\gamma_n^{N_z} = j\omega \frac{W_n^{(p)}}{N_{zn}} = -\frac{\dot{W}_n^{(p)}}{Q_n^{(P)}}$$

$$= -[Y_{11}J_n + Y_{21}Y_n + Y_{31}I_n + Y_{41}K_n]$$

$$+ [Y_{12}J_n + Y_{22}Y_n + Y_{32}I_n$$

$$+ Y_{42}K_n] \frac{M_{zn}}{N_{zn}} \bigg|_{\sigma=a},$$

(38a)

$$\gamma_n^{M_z} = j\omega \frac{W_n^{(p)}}{M_{zn}} = \frac{\dot{W}_n^{(p)}}{M_n^{(P)}}$$

$$= [Y_{12}J_n + Y_{22}Y_n + Y_{32}I_n + Y_{42}K_n]$$

$$+ [Y_{11}J_n + Y_{21}Y_n + Y_{31}I_n$$

$$+ Y_{41}K_n] \frac{N_{zn}}{M_{zn}} \bigg|_{\sigma=a}.$$

(38b)

We also obtained the mobility functions in terms of the angular displacement

$$\hat{\gamma}_n^{N_z} = j\omega \frac{\partial W_n^{(p)}/\partial z}{N_{zn}}$$

$$= -\frac{\partial \dot{W}_n^{(p)}/\partial \sigma}{Q_n^{(P)}}$$

$$= -[Y_{11}J_n' + Y_{21}Y_n' + Y_{31}I_n' + Y_{41}K_n']$$

$$+ [Y_{12}J_n' + Y_{22}Y_n' + Y_{32}I_n' + Y_{42}K_n'] \frac{M_{zn}}{N_{zn}} \bigg|_{\sigma=a},$$

(38c)

$$\hat{\gamma}_n^{M_z} = j\omega \frac{\partial W_n^{(p)}/\partial z}{M_{zn}}$$

$$= \frac{\partial \dot{W}_n^{(p)}/\partial \sigma}{M_n^{(P)}}$$

$$= [Y_{12}J_n' + Y_{22}Y_n' + Y_{32}I_n' + Y_{42}K_n']$$

$$- [Y_{11}J_n' + Y_{21}Y_n' + Y_{31}I_n' + Y_{41}K_n'] \frac{N_{zn}}{M_{zn}} \bigg|_{\sigma=a}.$$

(38d)

Assume that the plate is thin and in-plane response may be ignored. Therefore the boundary conditions of the pipe may be simplified as

$$U_n = W_n^{(P)},$$ (39a)

$$V_n = 0,$$ (39b)

$$W_n = 0.$$ (39c)

However, future work should consider the significance of the contribution of in-plane modes to the sound radiation into water through the Poisson effect. Recent work [Pan and Farag (2002)] on the characteristics of in-plane vibration in circular clamped plates has paved a way towards such understanding.[11] Also note that the angular displacements of the pipe and plate should be continuous at the joint ($z = 0, \sigma = a$),

$$\frac{\partial W_n}{\partial z} = \frac{\partial W_n^{(P)}}{\partial \sigma}.$$ (39d)

In summary, the four boundary conditions [Eqs. (38a), (39a), (38b), (38c), and (38d), (39d)] for the pipe response at $z = 0$ are provided. Together with Eq. (30), $4 + N_r$ equations are available at $z = 0$. These equations and $4 + N_r$ equations at $z = -L$ allow the solution of $2(4 + N_r)$ coefficients for the response of the nth circumferential pipe mode.

E. Sound radiation from the plate

The plate flexural vibration described by Eq. (31) radiates sound pressure into $z \geq 0$ space,

$$p_S(\sigma, \theta, z)$$

$$= -\frac{\omega^2 \rho_o}{2\pi} \int_a^b \int_0^{2\pi} \frac{W^{(p)}(\sigma', \theta')}{R} e^{-j\vec{k}\cdot\vec{R}} \sigma' d\sigma' d\theta'. \quad (40)$$

Finally, the total sound pressure from the plate and the pipe opening is obtained as

$$p_T = p_A(\sigma, \theta, z) + p_s(\sigma, \theta, z). \quad (41)$$

F. Schematics of system solution

For each circumferential mode, Fig. 4 summarizes the process of using $2(4 + N_r)$ equations to determine $2(4 + N_r)$ coefficients of W_{nm}, and finally to obtain the sound pressure radiated from the system.

IV. NUMERIC RESULTS

A. Sound radiation due to volume velocity source at $z = -L$

Following example is used to illustrate the sound radiation and associated mechanisms. The system is excited by a uniformly distributed velocity source at $z = -L$. Only the waves and sound radiation due to $n = 0$ circumferential modes are considered here. The system parameters are $L = 1$ m, $a = 0.1$ m, $b = 0.4$ m, $h_s = h_p = 0.005$ m, $c_L = 5200$ m/s, $\rho_s = 7800$ kg/m^3, $\rho_f = 1000$ kg/m^3, $\rho_o = 1.21$ kg/m^3, $c_f = 1500$ m/s, $V_i = 0.000001$ m/s, $E = 1.92 \times 10^{11}$ N/m^2, $\nu = 0.3$. In the calculation, damping is ignored.

In order to understand the characteristics of system conveniently, two quantities are defined

$$T1 = 10 * \log 10 \left(\frac{|P|^2}{|V_i|^2} \right), \quad T2 = 10 * \log 10 \left(\frac{|\overline{V_o}|^2 * S_o}{|V_i|^2 * S_i} \right), \quad (42)$$

in which $T1$ represents the transfer impedance level between the radiated sound pressure P and the input velocity V_i, $T2$ denotes the magnitude of the frequency response function

J. Acoust. Soc. Am., Vol. 112, No. 6, December 2002

Liu *et al.*: Sound radiation from water-filled pipe   2819

| Combine equations ((1)-(4))/(13) and (16), we have 4+Nr equations at Z=-L. | Combine equations ((38a)/(39a), (38b), (38c), (38d)/(39d)), and (24)/(29), we have 4+Nr equations at Z=0. |

These 2(4+Nr) equations are used to determine 2(4+Nr) coefficients Wnm. Then the response of the nth circumferential mode in the pipe is determined by Equation (10)

The plate response is calculated using equations (38a)/(39a) and (38d)/(39d).

The sound pressures radiated from pipe opening and the plate are then calculated using (20)/(29) and (31)/(40),respectively. The summation of the two pressures gives rise to the total sound pressure.

FIG. 4. Schematics of calculating the system response.

between the volume velocity $\overline{V_o}*S_o$ at the radiation surface (plate, pipe opening or the total surface at $z=0$) and that of the sound source $\overline{V_i}*S_i$ at $z=-L$.

Figure 5 shows $T1$ where P is at the position of (0,0,10 m). The sound pressure in Fig. 5(a) may be divided into two regions. The first region includes $0<\Omega<0.5$ and $1<\Omega<1.3$, where the fluid and structural waves are weakly coupled because the characteristics of coupled waves are similar to that of fluid waves in rigid-walled pipe and structural waves *in vacuo* pipe, respectively. In this region, the density of resonance peak is sparse and the fluid and structural response of the pipe is governed by the resonance of each wave type. The interaction between the fluid and structural waves can be approximately modeled by weakly coupled subsystems. For example, when the originally uncoupled resonance frequencies of the two subsystems are close and the corresponding distributions of the mode shapes match spatially, the approximate coupling occurs. Within the second region ($0.5<\Omega<1$), the fluid and structural waves are strongly coupled for the characteristics of coupled waves are no longer similar to that of fluid waves in rigid-walled pipe and structural waves *in vacuo* pipe. In this region, it is difficult to find simple correlation between the pipe response and uncoupled mode distributions, the level of sound radiation is relatively low and the

density of the peaks is increased. In Fig. 5(a), the resonance peaks in the first region are classified in terms of the number of antinodes in the distributed sound field in the pipe. Each index of the peak is also attached with (f) to show that wave type in the pipe is dominated by the fluid waves, and fluid wave radiation at the pipe opening contribute significantly to the total sound pressure radiated. Other peaks correspond to the large sound radiation from the plate and indexed by a number attached with (s). The number equals the number of antinodes in the plate vibration along the radial direction. The resonance peaks in the second region are labeled with *mc* for difference.

The radiated sound pressure is due to the water borne sound from the pipe opening and the structure borne sound from the plate. A comparison of the peak magnitudes of these two pressure components [Fig. 5(b)] illustrates that both of the fluidic and structural modes are important to the sound radiation, and the fluid and structure type of modes couple more or less in different frequency ranges.

The difference of the structure borne and water borne sound radiation shown in Fig. 5(b) can be explained by examining the system response at several resonance frequencies.

Figure 6 illustrates the system response at $m=4(f)$ (for
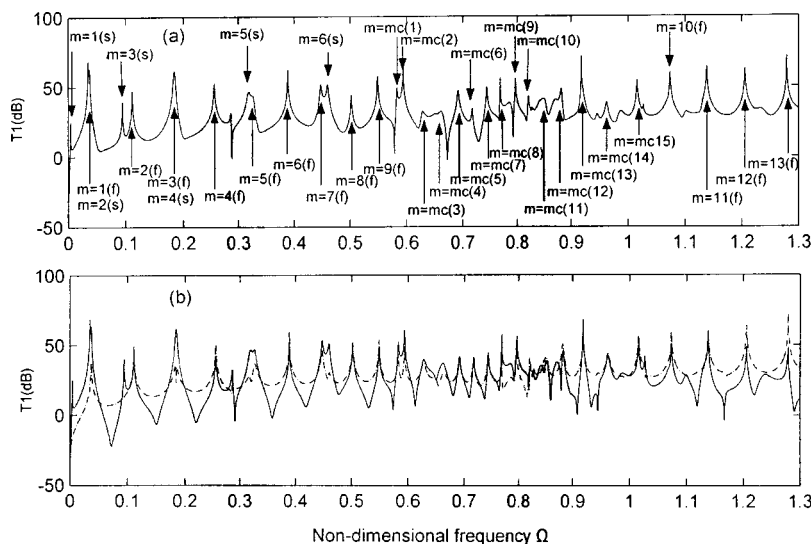
FIG. 5. $T1$ as a function of nondimensional frequency. (a) Total sound radiation from the plate and pipe opening; (b) solid line is the sound radiation from the plate and dashed–dotted line is that from pipe opening.
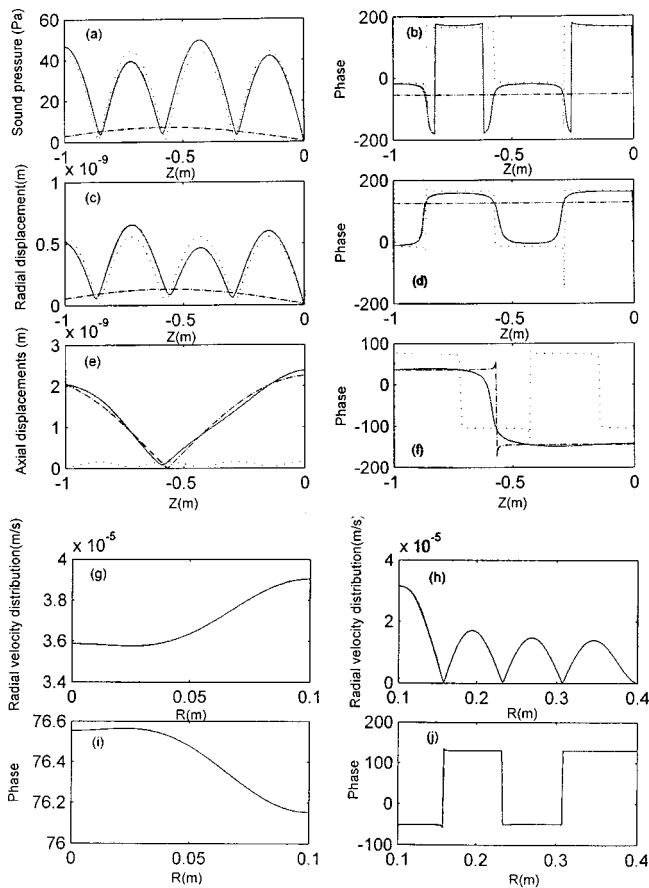
FIG. 6. The system response at $m=4(f)$. (a)–(f) illustrate the axial distribution of sound pressure in the pipe, radial and axial displacements on the pipe wall. In (a)–(f), solid line is contributed by all branches, dashed–dotted line corresponds to branch $s=1$, dotted line corresponds to branch $r=0$. (g)–(j) illustrate the radial velocity distribution on the radiation surface.

FIG. 7. The system response at $m=8(f)$. (a)–(f) illustrate the axial distribution of sound pressure in the pipe, radial and axial displacements on the pipe wall. In (a)–(f), solid line is contributed by all branches, dashed–dotted line corresponds to branch $s=1$, dotted line corresponds to branch $r=0$. (g)–(j) illustrate the radial velocity distribution on the radiation surface.

$\Omega<0.53$). The sound pressure distribution in the pipe [Figs. 6(a) and (b)] shows that the fluid wave (branch $r=0$) is the dominant component. The contribution of the structural wave ($s=1$) only slightly affects this sound pressure distribution. Also shown in Figs. 6(c) and (d) are the radial and axial displacements on the pipe wall. For the radial displacement, the fluid wave component is clearly dominating the response. While the axial displacement is part of the branch $s=1$, where extensional and flexural waves are coupled.

The radial velocity distributions on the radiation surface are demonstrated in Figs. 6(g) and (h). The velocity at the pipe end is close to uniform and the slight variation is due to the contribution of $r=1$ branch. While on the plate surface, the velocity distribution already has a modal structure with four antinodes in the radial direction. However, the fourth resonance frequency of the plate is not in the vicinity of the fourth organ mode of the pipe.

The second plate resonance frequency is located very close to the first fluid mode. At this frequency the plate is a stronger sound radiator than the pipe opening, as a result, the structural borne sound for $m=1(f)$ dominates the sound radiation. Similar sound radiation mechanism is observed at $m=3(f)$, where the resonance frequency of the fourth plate modes coincides with that of the third organ mode of the pipe.

The peak denoted by $m=3(s)$ is due to the resonance radiation by the third plate modes. However, as this mode is not generated by the resonance response of the pipe system, its sound radiation is relatively small.

The peak of $m=8(f)$ is due to the mode close to strong fluid/structural coupled region. Shown in Fig. 7, the sound pressure distribution the pipe is spatially modulated. This is due to the superposition of two modal branches ($s=1$ and $r=1$). Close the strong-coupled region the two wave types start to have comparable magnitudes and to produce interference patterns in sound field. Similar to the sound pressure distribution, the radial and axial displacement distributions also are spatially modulated. In the same time, the number of anti-nodes on the plate is added as a result of increased frequency [see Fig. 7(h)].

Above the strong-coupled region ($1<\Omega<1.3$), the $m=13(f)$ in Fig. 8 for example has distribution of sound field in the pipe of two branches ($s=1$ and $r=1$), while that of the radial displacement has contributions of three branches ($s=1$, $r=0$, and $r=1$) and the radial displacement has one branch ($r=1$). The reason for this is that the contribution of the $r=0$ wave type to the sound field despaired in this region, as it has evolved into structural mode. While the original structural modes ($s=1$) stand for the fluid modes as frequency increases. Furthermore the $r=1$ branch has al-
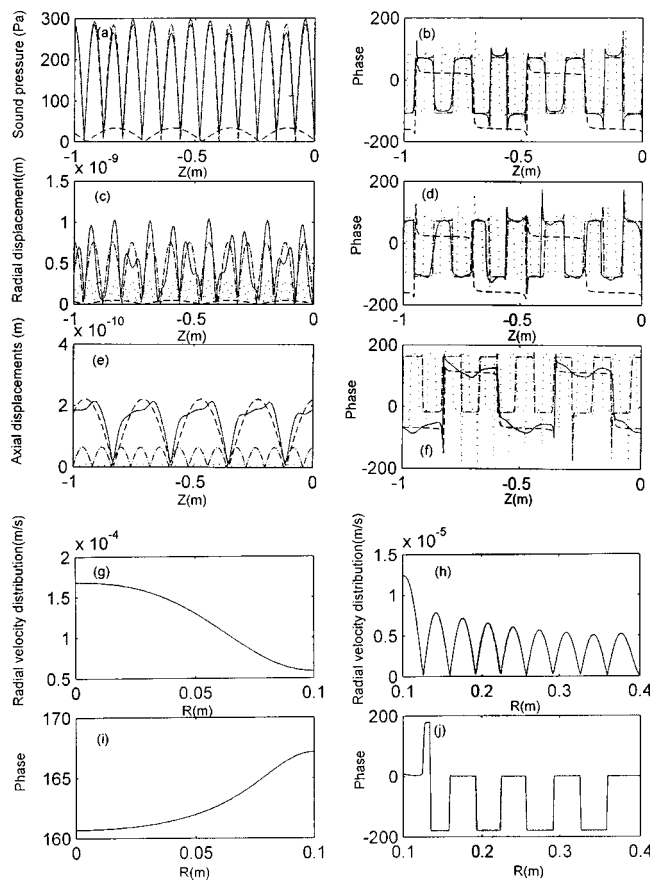
FIG. 8. The system response at $m=13(f)$. (a)–(f) illustrate the axial distribution of sound pressure in the pipe, radial, and axial displacements on the pipe wall. In (a)–(f), solid line is contributed by all branches, dashed–dotted line correspond to branch $s=1$, dotted line corresponds to branch $r=0$, dashed line corresponds to branch $r=1$. (g)–(j) illustrate the radial velocity distribution on the radiation surface.

FIG. 9. The system response at $m=mc(5)$. (a)–(f) illustrate the axial distribution of sound pressure in the pipe, radial and axial displacements on the pipe wall. In (a)–(f), solid line is contributed by all branches, dashed–dotted line corresponds to branch $s=1$, dotted line corresponds to branch $r=0$, dash line correspond to branch $r=1$. (g)–(j) illustrate the radial velocity distribution on the radiation surface.

ready cut on and it's characteristics are similar to that of shell longitudinal waves. In this region, the sound radiation of the plate modes is reduced because of the increased antinode in the radial direction, and the corresponding sound radiation from the higher order modes of the plate becomes low due to the cancellation of the volume velocity on the surface of the plate. As a result, the sound radiation is dominated by the water-borne sound.

It is interesting to note that the sound radiation within the strong-coupled region is relatively low and the density of the peaks is also increased. In this region, we observed the following phenomena from the system response shown in Fig. 9.

(1) Both sound field and structural vibration of the pipe are contributed by more than one wave types of comparable magnitudes.
(2) The contribution of $r=0$ branch to the sound field gradually reduces as frequency increases, while that of the $s=1$ gradually takes the place.
(3) Similar switch over of two wave types is also observed in the radial displacement, $r=1$ branch gradually dominate the radial response.

The total sound power from the radiation surface is de-

termined by both level and directivity of radiated sound pressure. The lower order peak $[m=1(f)]$ is characterized by the monopole radiation pattern. For the higher order peaks, the radiated sound fields are by nonmonopole directivities. The nonuniform distribution of sound pressure is mainly due to complex directivity of the higher order plate modes. The sound radiation from the pipe opening is relatively simple for $n=0$, and is close to a piston sound radiation. In all the cases, the sound pressure in the z direction has the maximum value. Another important observation (see Fig. 10) is that the higher order peak sound radiation from the plate and from the opening has significantly different radiation patterns.

V. EXPERIMENT

The theory and numerical results shown above are validated experimentally. Figure 11 shows the schematics of experimental rig installed in a semianechoic room. The testing plate is clamped all around and a sound source located at the bottom of the pipe is used to excite the system.

The sound source is made of a simply supported copper plate excited by a piezoelectric actuator and the radius of its vibration surface is 0.04 25 m. The steel pipe is filled with water and the medium above the plate is air, which is consistent with the assumption of light fluid in the radiation
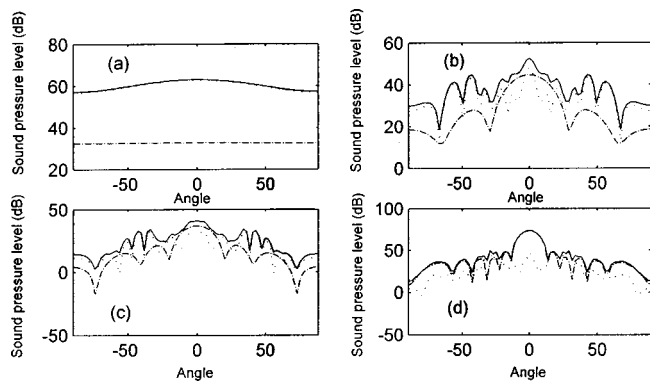
FIG. 10. Direction patterns, dotted line corresponds to that of the plate, dashed line corresponds to that of the pipe opening and solid line is the total sound radiation directivity. (a) $m=1(f)$, (b) $m=8(f)$, (c) $m=mc(5)$, (d) $m=13(f)$.
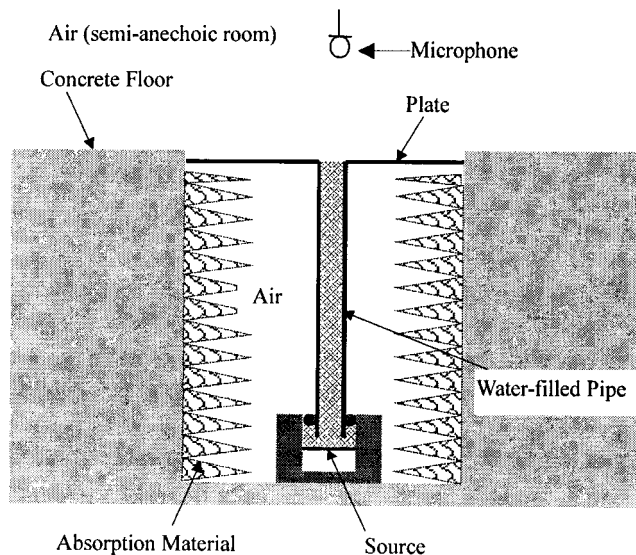
FIG. 11. Schematics of experimental rig.

space. The system parameters used in the experimentation are $L=0.55$ m, $a=0.03$ m, $b=0.18$ m, $h_s=h_p=0.003$ m.

Nor-840 was used in the measurement. The measured frequency range is up to 25 000 Hz, which correspond approximately to $\Omega=0.95$. The microphone was located at the position of (0,0,0.35 m), one of the accelerometers was glued at the bottom of the pipe to measure the velocity of the source and another was fixed on the plate to measure average velocity of the vibrating plate at six different points. The experimental results are showed in Fig. 12, where numeric results and dispersion curves of the water-filled pipe are also provided for comparison.

Although the measured impedance level $T1$ and the frequency response function between volume velocities of the plate and the sound source are presented below $\Omega=0.95$, two frequency regions ($0\leq\Omega\leq0.5$ and $0.5\leq\Omega\leq0.95$) for the water/pipe coupling are available for comparison. As shown in Fig. 12, the theoretical prediction agrees with the experi-

mental result in terms of the general trend of resonance peak distribution and levels at the antiresonance frequencies. Figure 12(b) clearly shows the sound radiation feature in the two regions. In the range of $0.65\leq\Omega\leq0.95$, the feature of clear resonance peaks as observed $0\leq\Omega\leq0.5$ is no longer there. Instead, the strong coupling between the sound waves in water and pipe wall vibration results in the modal response contributed by multiple wave types. In the transition region of $0.4\leq\Omega\leq0.7$, the decreased distance of resonance peaks can also be observed for the reason of decreased phase velocity of fluid dominated waves.

It is not the author's intention to have a quantitative comparison between the experimental and analytical results. The main discrepancies of the experimental setup from the theoretical model are due to the following.
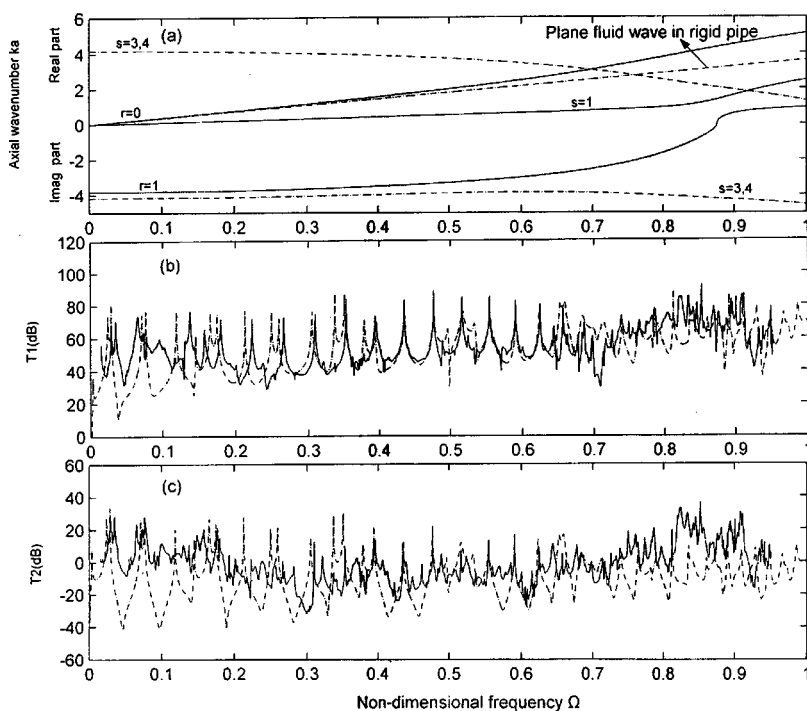
FIG. 12. (a) Dispersion curves of water filled experimental pipe. (b) $T1$ vs nondimensional frequency, (c) $T2$ vs nondimensional frequency, the concerned volume velocity is the plate. In (b) and (c), solid lines are experimental data, dashed–dotted lines are theoretic calculation.

(1) Negligence of the structural damping in pipe and plate materials, in the coupling plate/pipe boundary and the fluid damping of the water in the pipe.
(2) Imperfect boundary conditions of the plate and excitation.

As a result, only qualitative comparison is possible. Further experimental work will focus on the energy distributions in each coupled modes as more meaningful comparison may be made with predicted phenomena.

VI. CONCLUSIONS

In this paper, the method of traveling waves is used to investigate the sound transmission from a finite water-filled pipe to an attached circular plate and subsequent sound radiation from the pipe opening and the plate. Numeric and experimental results demonstrate that the wave characteristics in the water-filled pipe can be classified into strongly coupled and weakly coupled regions. In the weakly coupled region ($0 < \Omega < 0.5$ and $1 < \Omega < 1.3$), the fluid and structural response of the pipe is governed by the resonance of each wave type. In the strongly coupled region ($0.5 < \Omega < 1$), the simple correlation between the pipe response and uncoupled mode distributions does not exist. Significant contribution of multiple wave types to the model energy becomes evident.

The sound radiation by the weakly coupled waves is often due to an individual wave type which is dominating at the operating frequency. In this region, the peak sound radiation can be correlated to resonance frequencies pipe acoustical modes and pipe/plate coupled modes.

The level of sound radiation within the strong-coupled region is relatively low and the density of the peaks is increased. In this region, both sound field and structural vibration of the pipe are contributed by more than one wave type of comparable magnitude.

This paper provides a method to investigate the sound radiation from a water-filled exhaust pipe. Although the medium for sound radiation is assumed to be ''light,'' the relative importance of structural-borne and water-borne sound radiation at different frequencies, and qualitative understanding obtained may be useful guidance for control of the radiated sound. The study of sound radiation from a water-filled pipe into heavy fluid is currently underway.

[1] A. Harari, ''Wave propagation in cylindrical shells with finite regions of structural discontinuity,'' J. Acoust. Soc. Am. **162**, 1196–1205 (1977).
[2] C. R. Fuller, ''Elastic wave transmission on the propagation of flexural waves in cylindrical shells,'' J. Sound Vib. **75**, 207–317 (1981).
[3] A. Schlesinger, ''Transmission of elastic waves from a cylinder to an attached flat plate,'' J. Sound Vib. **186**, 761–780 (1995).
[4] Y. K. Tso and C. H. Hansen, ''Wave propagation through cylinder/plate junctions,'' J. Sound Vib. **186**, 447–461 (1995).
[5] C. R. Fuller and F. J. Fahy, ''Characteristic of wave propagation and energy distributions in cylindrical elastic shells filled with fluid,'' J. Sound Vib. **81**, 501–518 (1982).
[6] D. G. Crighton, ''The 1988 Rayleigh Medal Lecture: fluid loading—the interaction between sound and vibration,'' J. Sound Vib. **133**, 1–27 (1989).
[7] R. Ming, J. Pan, and M. P. Norton, ''The measurement of structural mobilities of a circular cylindrical shell,'' J. Acoust. Soc. Am. **107**, 1374–1382 (2000).
[8] A. W. Lessia, ''Vibration of shells,'' NASA SP-288, 1973.
[9] M. C. Junger and D. Feit, *Sound, Structures and Their Interaction* (MIT Press, Cambridge, MA, 1972).
[10] A. W. Lessia, ''Vibration of plates,'' NASA SP-160, 1969.
[11] J. Pan and N. H. Farag, ''A study of in-plane vibration of circular clamped plates,'' 9th International Congress on Sound and Vibration, Orlando, USA, 2002.

Crack detection by measurement of mechanical impedance of a rotor-bearing system

S. Prabhakar, A. R. Mohanty,[a] and A. S. Sekhar
Department of Mechanical Engineering, Indian Institute of Technology, Kharagpur 721 302, India

Measurements were done to determine the influence of a transverse crack on the mobility of a rotor-bearing system. The results show that the mobility changes substantially due to the presence of crack and follows definite trends with the crack depth and direction of force application. The significant changes in mobility were observed at the natural frequency and at the running frequency of the rotor system. Good agreement between the experimental results and numerical simulations has been observed. The measurement of mobility has been suggested for crack detection and condition monitoring of rotor-bearing systems. © *2002 Acoustical Society of America.*
[DOI: 10.1121/1.1515792]

I. INTRODUCTION

The present day requirement for ever-increasing reliability in the field of rotating machinery is now more important than ever before and continues to grow constantly. Most of the breakdowns in modern machinery are due to fatigue of the material. Fatigue of the material results in the formation of cracks, which may lead to catastrophic failure if not detected in time. The dynamic analysis of cracked rotors has been a subject of great interest for the last three decades and excellent reviews on this are available.[1–4] The identification of crack location and magnitude through the measurement of changes in system characteristics has been studied by various researchers.[5–7] Imam *et al.*[8] presented an on-line rotor crack diagnosis system that will detect even a very small crack by a so-called histogram signature analysis technique. Chondros *et al.*[9] developed a continuous cracked beam vibration theory for the lateral vibration of cracked Euler–Bernoulli beams with experimental validation. Some works on nonlinear vibration of cracked shaft and structures have also been reported recently.[10,11] Many other crack detection and monitoring techniques were discussed in Ref. 4.

Even though a great deal of achievement in the area of the dynamics of cracked rotors has been obtained, not enough attention has been paid to the studies on the variation of mechanical impedance of the cracked rotors. Nezu[12] investigated a nondestructive test method using mechanical impedance for detecting damages in the structural member. Bamnios and Trochidis[13] have developed the influence of transverse crack on the mechanical impedance of the cantilever beam with experimental validation. However, the above techniques[12,13] on the determination of mechanical impedance are applied, not to rotors but to structures having open cracks. Recently, the authors[14] have studied numerically the influence of a transverse surface crack on the mechanical impedance of a rotor-bearing system. Both open and breathing crack detections were discussed.

In the present paper, the influence of a transverse surface crack on the mechanical impedance of a rotor-bearing system was investigated experimentally to validate the numerical analysis.[14] A parametric study has been done with different crack parameters and for different force locations in an attempt to use the change of mobility for crack detection and monitoring.

II. ROTOR-BEARING TEST RIG AND EXPERIMENTAL MEASUREMENTS

The rotor-bearing test rig is shown in Fig. 1. It was designed and developed to run at a maximum speed of 9000 RPM and has a first critical speed of 2820 RPM (47 Hz), which enables us to observe the vibrational behavior of the rotor while passing through the critical speed.

A. Rig description

The rotor-bearing test rig, essentially, consists of a shaft supported on two bearings at the ends and driven by a motor. The rotor shaft of 12 mm diameter and 500 mm length is supported on two self-aligned deep groove ball bearings of type SKF 2201. A balanced rigid disk is mounted on the shaft by radial screws and is located at the midspan of the shaft. The mass, polar, and diametral moment of inertia of the disk are 0.8 kg, 0.001 kg m^2, and 0.005 kg m^2, respectively. The rotor shaft is driven by a 0.125 kW ac/dc universal motor connected through a jaw coupling. The power supply to the motor can be varied through an autotransformer, thus controlling the speed of the motor from 0 to 9000 RPM. Experiments were carried out on the rotor system with and without the presence of crack in the shaft. A saw cut crack (width of 300 μm) of different depths was made at a distance of 23 mm from the disk toward bearing number 2 of the rotor system. The crack depth was measured with the help of a traveling microscope. Here, the nondimensional crack depth ($\bar{\alpha}$) is defined as the ratio of crack depth (α) to the shaft diameter (D).

[a]Author to whom correspondence should be addressed. Electronic mail: amohanty@mech.iitkgp.ernet.in
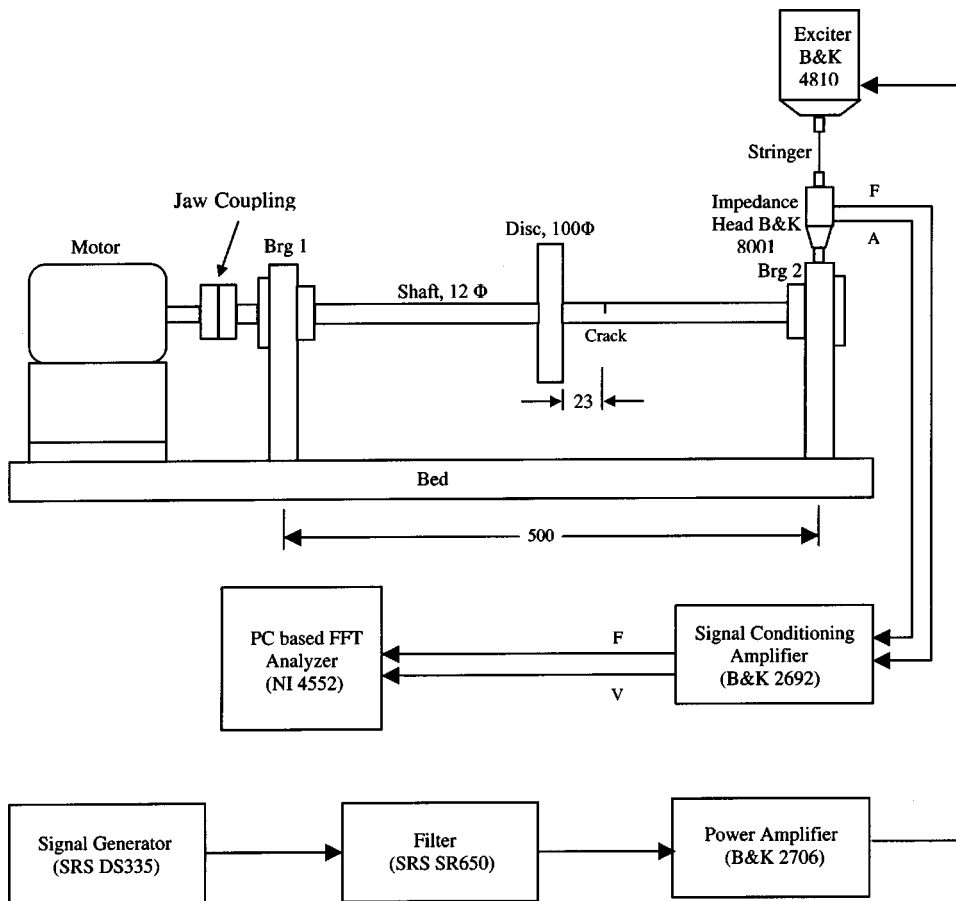
FIG. 1. Rotor-bearing test rig.

B. Instrumentation details

The necessary instrumentation for measuring the mobility of the rotor-bearing test rig are shown in Fig. 1. A signal generated at the function generator (SRS DS335) drives a power amplifier (B&K 2706) through a LP/HP filter set (SRS SR650). The bandwidth of the signal can be selected by setting the appropriate low- and high-frequency cutoffs in the LP/HP filter set. The signal from the power amplifier is used to drive the vibration exciter (B&K 4810) (see Fig. 1). An impedance head (B&K 8001) connected on the stringer of the exciter is used to measure the excitation force and the acceleration response at the point of excitation. The acceleration and force response signals from the impedance head are then conditioned in a signal amplifier (B&K 2692). The acceleration response from the impedance head is integrated in the signal conditioning amplifier (B&K 2692) to get a velocity response, which is required for mobility measurements. The velocity and force signals from the signal conditioning amplifier are then fed to a PC-based FFT analyzer (National Instruments, 4552).

C. Mobility measurements

Mechanical impedance $Z(X_f)$ of the rotor-bearing system at any force location X_f is defined as the ratio of force $F(X_f)$ to the velocity response $V(X_f)$. Mathematically,

$$Z(X_f) = F(X_f)/V(X_f). \tag{1}$$

However, for convenience, the mobility plots were considered in the present analysis, where the mobility is reciprocal of the impedance. In the present work, mobility measurements were made at the bearing locations in horizontal and vertical directions because the natural frequencies of the test-rig are different in two directions (given in the next section).

The experimental setup for mobility measurements in the vertical direction at bearing location 2 is shown in Fig. 1. A swept sine excitation signal with a frequency range of 0.1–210 Hz and an amplitude of 0.2 N was used to drive the vibration exciter. The sweep rate was 0.5 Hz/s and was set in the signal generator. The vibratory force from the exciter was then applied in the vertical direction at the bearing location of the rotor test rig. The vibration exciter was suspended with soft springs while performing the mobility measurements in the vertical direction. The frequency response function (FRF) (a complex quantity with magnitude and phase of the mobility) data, after performing 32 averages, was stored in a personal computer from the PC-based FFT analyzer for a further analysis. The dynamic range of NI 4552 is 90 dB with a maximum sampling frequency of 102.4 kHz. A flat-top window function was used for all FRF measurements. The FRF data of 800 lines with a frequency resolution of 0.39 Hz were stored in a PC for further analysis. In a similar way, mobility measurements were made in the horizontal direction.

III. ANALYSIS OF EXPERIMENTAL RESULTS

In all the cases, mobility instead of mechanical impedance was measured for convenience. Before the mobility measurements of a rotor system, natural frequencies of the
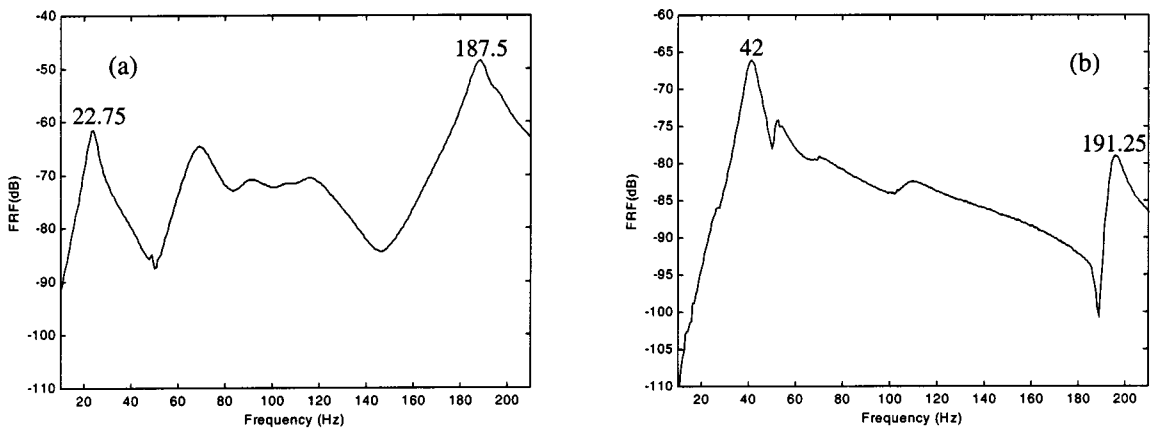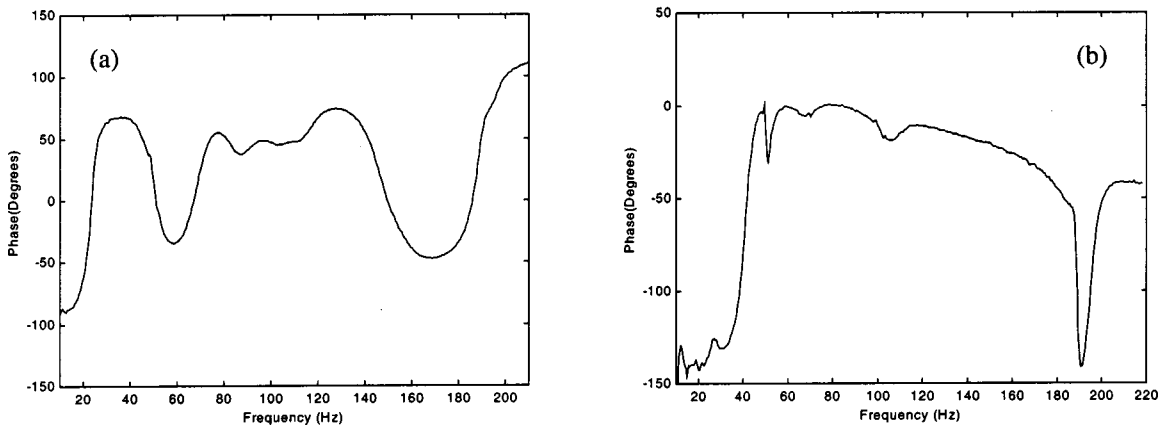
FIG. 2. Natural frequency plots of a rotor-bearing system. (a) FRF for excitation and response in the horizontal direction. (b) FRF for excitation and response in the vertical direction.

rotor-bearing rig were determined. The reciprocity theorem of mobility was checked to ensure the linearity of the behavior.

For determining the natural frequency of the rotor system, a modal test was made[15] using the impulse excitation technique. An instrumented hammer (B&K 8202) with a rubber tip was used for excitation. Figure 2 shows the frequency response function (FRF) and phase measurements when force was applied at bearing number 2 in horizontal and vertical directions. From these measurements, it was found that the natural frequency of the rotor system in the x direction (horizontal) was 22.75 and 187.5 Hz, whereas in the y direction (vertical) the natural frequency was 42 and 191.25 Hz. The clear change in phase at these frequencies can be observed from the phase measurements [see Fig. 2(ii)].

Mobility of the rotor system is plotted (Fig. 3) as a function of frequency at a speed of 7200 RPM (120 Hz) for checking the reciprocity theorem. The acceleration response at a bearing location was taken with a triaxial accelerometer (B&K 4321), which was integrated in a conditioning amplifier to get the velocity response and force response at the other bearing was measured with an impedance head (B&K 8001). In Fig. 3(a), mobility is defined as the ratio of velocity

response at bearing number 2 to the force response at bearing number 1 in the horizontal direction. Whereas mobility of the rotor system in Fig. 3(b) is defined as the ratio of velocity response at bearing number 1 to the force response at bearing
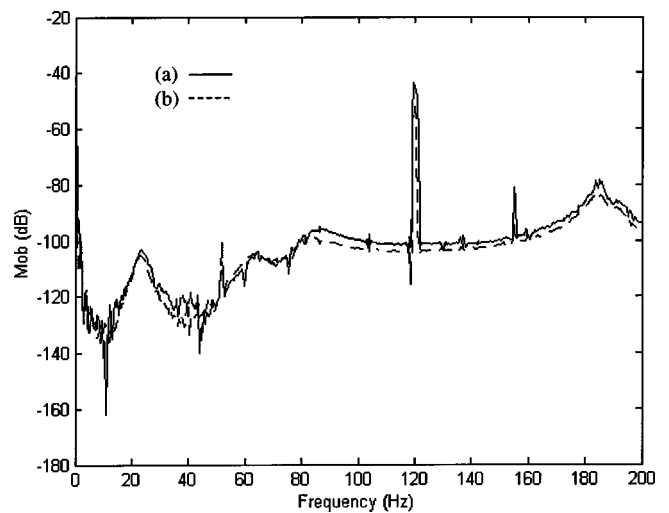
FIG. 3. Mobility measurements at 7200 RPM of the rotor-bearing system. (a) The force at bearing #1 and velocity at bearing #2. (b) Force at bearing #2 and velocity at bearing #1.
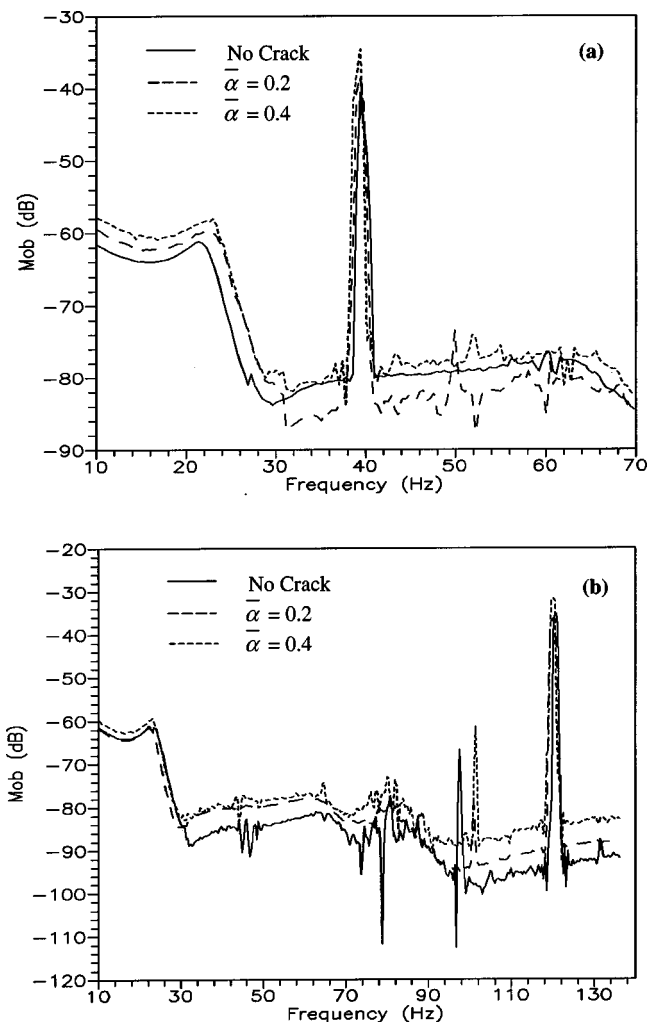
Prabhakar *et al.*: Crack detection by impedance measurement   2827

FIG. 4. The variation of mobility with frequency for different crack depths; mobility measurements at bearing number two in the horizontal direction. (a) Rotor speed, 2400 RPM; (b) rotor speed, 7200 RPM.

FIG. 5. The variation of mobility with frequency for different crack depths; mobility measurements at bearing number two in the vertical direction. (a) Rotor speed, 3600 RPM; (b) rotor speed, 7200 RPM.

number 2 in the horizonal direction. From the figure, it was observed that both the mobility plots were more or less the same and thus satisfy the reciprocity theorem that ensures that the experimental measurements are carried out properly.

Figure 4 shows the measured change of mobility of the rotor-bearing system with frequency for different crack depths. The mobility measurements were taken at bearing number 2 in the horizontal direction. Mobility measurements were taken at two different rotor speeds one at 2400 RPM (40 Hz) and the other at 7200 RPM (120 Hz), as shown in Figs. 4(a) and (b). The results show that the mobility changes substantially due the presence of crack. It is noticed from the figures that the mobility is sensitive at two significant frequencies. One is at the natural frequency of the rotor system in the x direction (22.75 Hz) and the other is at the running frequency. For example, in Fig. 4(a) two significant peaks at 22.75 and 40 Hz are observed.

Mobility measurements were also made in the vertical direction with and without the presence of crack in the shaft. These were taken at two different speeds of 3600 RPM (60 Hz) and 7200 RPM (120 Hz) and were shown in Fig. 5. Similar crack behavior with mobility was observed in this case also when compared with horizontal mobility measure-

ments. The significant frequencies in this case are 42 Hz (natural frequency in the y direction) and 60 or 120 Hz according to running speed [see Figs. 5(a) and (b)].

Further, the sensitivity of mobility with crack can be seen clearly from Figs. 6 and 7. The normalized mobility (M_c/M_0) can be defined as the ratio of mobility of the rotor system with crack (M_c) to that of without crack (M_0). The variation of normalized mobility in the horizontal direction of the rotor system with normalized crack depth $(\bar{\alpha}=\alpha/D)$ at the two significant frequencies in shown in Fig. 6. As expected, the mobility increases with the increase of crack depth. And for the given force, the rate of change of mobility is more at the running frequency. However, the rate of change of mobility with crack depth at the running frequency of 40 Hz was higher as compared to that of at 120 Hz speed [see Figs. 6(a) and (b)]. This is because 40 Hz speed is near the natural frequency.

Figure 7 shows the variation of normalized mobility of the rotor system in the vertical direction for different crack depths and speeds. Similar crack behavior with mobility was observed in this case also when compared with horizontal measurements. However, the rate of change of mobility with crack depth is more in the vertical direction as compared to the horizontal direction (see Fig. 6).

Prabhakar *et al.*: Crack detection by impedance measurement
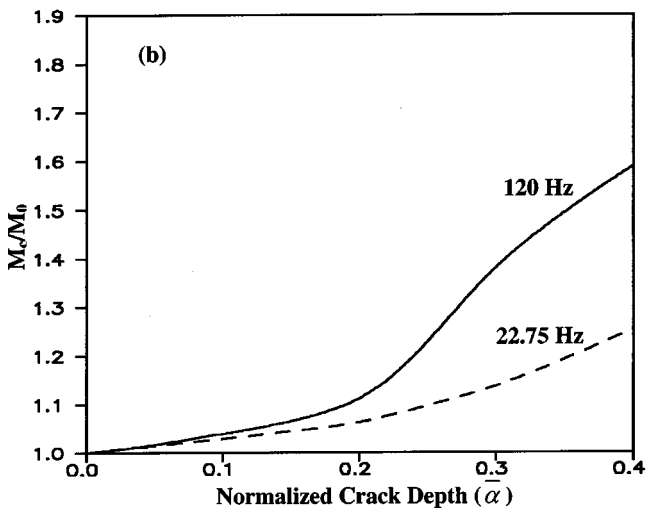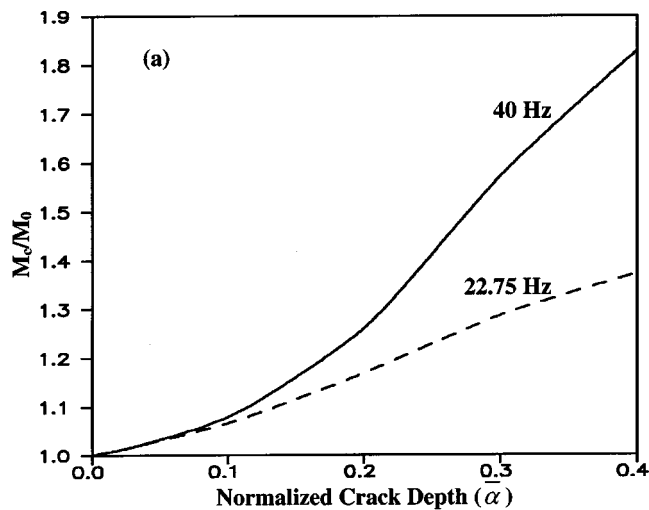
FIG. 6. The variation of normalized mobility with normalized crack depth at significant frequencies; mobility measurements at bearing number two in the horizontal direction. (a) Rotor speed, 2400 RPM; (b) rotor speed, 7200 RPM.

FIG. 7. The variation of normalized mobilty with normalized crack depth at significant frequencies; mobility measurements at bearing number two in vertical direction. (a) Rotor speed, 3600 RPM; (b) rotor speed, 7200 RPM.

In Ref. 14, the authors presented the numerical simulations using the finite element method (FEM) for mechanical impedance of the rotor with and without cracks. Mechanical impedance of the rotor system was suggested for crack detection and monitoring. Proceeding in a similar way as given in Ref. 14, numerical simulations were performed for the test rig data with and without the presence of crack. Figure 8 shows the comparison of numerically simulated mobility with experimental mobility measurements. Mobility plots at bearing number 2 in the horizontal direction with and without the presence of cracks are shown in Figs. 8(a) and (b), respectively. Since the crack is saw cut and also weight of the rotor is not dominating, the experimental results are compared with the open crack FEM results. In the open crack case, only two significant frequencies in the mobility plot can be observed, namely, running frequency and natural frequencies of the system unlike in the breathing crack case (where the significant frequencies are natural frequencies and multiples of running frequencies). In Fig. 8, a big peak at running frequency (120 Hz) and the other peak at natural frequency (22.75 Hz) of the rotor system can be seen. Also,

a significant increase in mobility with the presence of crack can be observed in Fig. 8. It is noticed that the experimental results are well matching with numerical simulations. From the experimental results, it is felt that mechanical impedance or mobility can be used for detecting cracks in a rotor system.

IV. CONCLUSIONS

Experimental studies were performed on the rotor-bearing test rig for detecting transverse crack. The mobility changes substantially with the presence of crack exhibiting definite trends depending upon the depth of crack and the direction of force application.

The mobility of the rotor system increases as the crack depth increases at the significant frequencies. The rate of change of mobility with crack depth is more in the vertical direction as compared to the horizontal direction. Good agreement between the experimental results and numerical simulations was found. The results suggest that the measurements of mobility can be used for crack detection and monitoring in a rotor-bearing system.
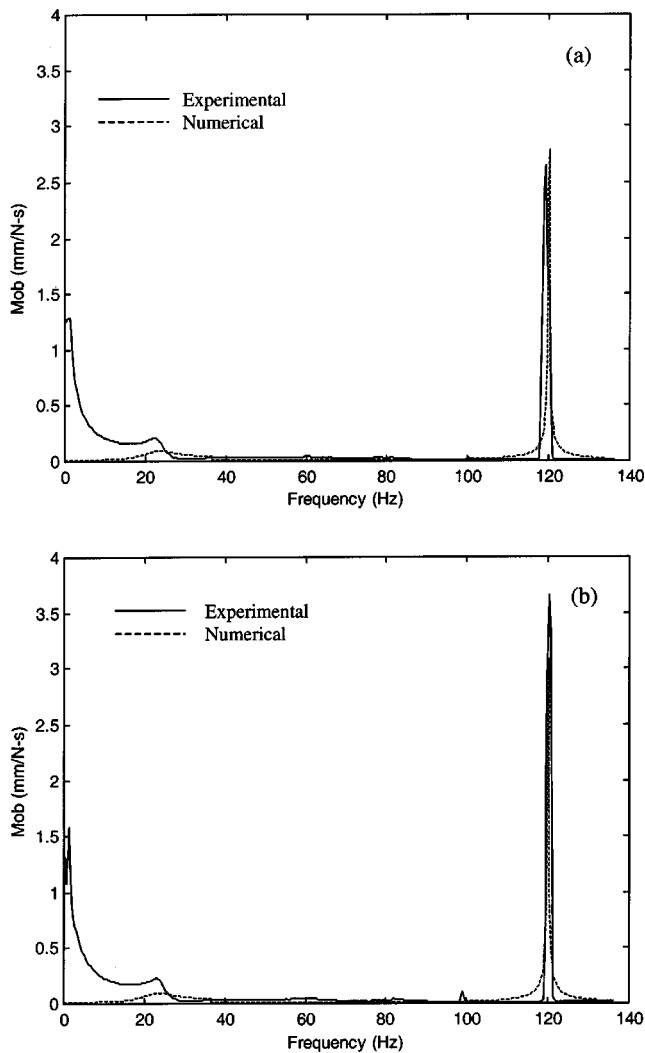
FIG. 8. A comparison of numerically simulated mobility with experimental mobility measurement, rotor speed 7200 RPM. (a) No crack; (b) $\bar{\alpha}=0.4$.

In contrast to detection methods based on the change of eigenfrequencies and modes, a method using impedance or-

mobility measurements is better suitable: the change in the mobility for small cracks increases linearly with an increasing crack depth so that crack detection based on this has some potential.

[1] A. D. Dimarogonas and S. A. Paipetis, *Analytical Methods in Rotor Dynamics* (Applied Science, London, 1983), pp. 144–193.

[2] J. Wauer, "Dynamics of cracked rotors, literature Survey," Appl. Mech. Rev. **43**, 13–17 (1990).

[3] R. Gaush, "A survey of the dynamic behavior of simple rotating shaft with a transverse crack," J. Sound Vib. **160**, 313–332 (1993).

[4] A. D. Dimarogonas, "Vibration of cracked structures: A state of the art review," Eng. Frac. Mech. **55**, 831–857 (1996).

[5] P. F. Rizos, N. Aspragathos, and A. D. Dimarogonas, "Identification of crack location and magnitude in a cantilever beam from vibration modes," J. Sound Vib. **138**, 381–388 (1990).

[6] A. K. Panday, M. Biswas, and M. M. Samman, "Damage detection from changes in curvature mode shapes," J. Sound Vib. **145**, 321–332 (1991).

[7] M. A. Mannan and M. H. Richardson, "Detection and location of structural cracks using FRF measurements," *Proceedings of the 8th International Model Analysis Conference*, 1990, Vol. 1, pp. 652–657.

[8] I. Imam, S. H. Azzaro, R. J. Bankert, and J. Scheibel, "Development of on-line rotor crack detection and monitoring system," ASME J. Vib., Acoust., Stress Reliab. Des. **111**, 241–250 (1989).

[9] T. G. Chondros, A. D. Dimarogonas, and J. Yao, "A continuous cracked beam vibration theory," J. Sound Vib. **215**, 17–34 (1998).

[10] I. Ballo, "Nonlinear effects of vibration of a continuous transverse cracked slender shaft," J. Sound Vib. **217**, 321–333 (1998).

[11] J. Brandon, "Nonlinear vibration of cracked structures: perspectives and horizons," Shock Vib. Dig. **32**, 273–280 (2000).

[12] K. Nezu and H. Kodoguchi, "A new damage detection method by mechanical impedance measurements," Bull. JSME **23**, 2125–2131 (1980).

[13] G. Bamnios and A. Trochidis, "Mechanical impedance of a cracked cantilever beam," J. Acoust. Soc. Am. **97**, 3625–3635 (1995).

[14] S. Prabhakar, A. S. Sekhar, and A. R. Mohanty, "Detection and monitoring of cracks using mechanical impedance of rotor-bearing system," J. Acoust. Soc. Am. **110**, 2351–2359 (2001).

[15] D. J. Ewins, *Modal Testing: Theory, Practice and Application*, 2nd ed. (Research Studies Press Ltd., Hertfordshire, 1999).

2830   J. Acoust. Soc. Am., Vol. 112, No. 6, December 2002

Prabhakar *et al.*: Crack detection by impedance measurement

Three-dimensional vibration analysis of a torus with circular cross section

D. Zhou
*Department of Mechanics and Engineering Science, Nanjing University of Science and Technology,
Nanjing 210014, People's Republic of China*

F. T. K. Au, S. H. Lo, and Y. K. Cheung[a)]
Department of Civil Engineering, The University of Hong Kong, Hong Kong, People's Republic of China

The free vibration characteristics of a torus with a circular cross section are studied by using the three-dimensional, small-strain, elasticity theory. A set of three-dimensional orthogonal coordinates system, comprising the polar coordinate (r, θ) at each circular cross section and the circumferential coordinate φ around the ring, is developed. Each of the displacement components u_r, ν_θ, and w_φ in the r, θ, and φ directions, respectively, is taken as a product of the Chebyshev polynomials in the r direction and the trigonometric functions in the θ and φ directions. Eigenfrequencies and vibration mode shapes have been obtained via a three-dimensional displacement-based extremum energy principle. Upper bound convergence of the first seven eigenfrequencies accurate to at least six significant figures is obtained by using only a few terms of the admissible functions. The eigenfrequency responses due to variation of the ratio of the radius of the ring centroidal axis to the cross-sectional radius are investigated in detail. Very accurate eigenfrequencies and deformed mode shapes of the three-dimensional vibration are presented. All major modes such as flexural thickness-shear modes, in-plane stretching modes, and torsional modes are included in the analysis. The results may serve as a benchmark reference for validating other computational techniques for the problem. © *2002 Acoustical Society of America.* [DOI: 10.1121/1.1509429]

PACS numbers: 43.40.−r, 43.40.Cw, 43.40.At [ANN]

I. INTRODUCTION

A torus (circular ring beam with circular cross section) as basic structural element can find its applications in civil, mechanical, aircraft, and marine engineering like gyroscopes, springs, stiffeners and tires, etc. In some cases, the torus has to bear dynamic loads, and therefore to understand its dynamic behavior is very important for designers. One-dimensional mathematical models about rings have been available for more than a century.[1,2] Considering the ring as a curved beam or rod, the vibration of a ring can be classified as in-plane, out-of-plane, and circumferential modes. Based on the classical theory (i.e., the hypothesis of a straight normal line), three uncoupled differential equations can be developed for these three modes and solved easily if the extension of the centerline of the ring is negligible. In order to improve the classical solutions, some investigators[3–6] have studied the effect of extension, transverse shear, and rotary inertia.

The existing research work shows that for rings with a circular cross section, the error of the one-dimensional models increases with the decrease of the ratio of ring centroidal-axis radius to cross-sectional radius. Similar conclusions can also be drawn for rings with a cross section of any shape. In addition to the one-dimensional models, sometimes investigators also applied two-dimensional plate[7,8] and shell[9,10] models to analyze the mechanical behavior of a torus. According to a recent literature survey,[11] most of the published papers are about rings with a rectangular cross section. For rings with a circular cross section, only the one-dimensional models have been developed. It is well known that these mathematical models have serious limitations in their scope of applications, which are only suitable for slender or thin structural elements. As a result, the three-dimensional analysis of structural elements has long been a goal of those who work in the field. In the recent two decades, with the development of digital computers and computational techniques, it has now become possible to obtain accurate eigenfrequencies and vibration mode shapes for some structural elements. Exact, closed-form three-dimensional elasticity solutions can be obtained only for a few cases, such as the axisymmetric vibration of annular plates,[12] and the vibration of rectangular plates with four simply supported edges.[13] Using a series expansion method, accurate solutions for the free vibration of circular plates and cylinders have been derived by Hutchinson.[14–18] In recent years, the Ritz method has been extensively applied to the three-dimensional vibration analysis of some typical structural elements, such as beams with a circular cross section,[19] circular plates[20,21] and cylindrical shells,[22,23] rectangular and trapezoidal plates,[24,25] prismatic columns,[26] shell panels,[27,28] triangular plates,[29,30] and rings with isosceles trapezoidal and triangular cross sections,[31] etc. In these references, high accuracy, a small computational cost, and easy coding preparation have been shown if suitable admissible functions are selected.

In the present work, the Ritz method is applied to the free vibration analysis of a torus with a circular cross section

---

[a)]Author to whom correspondence should be addressed. Electronic mail: hreccyk@hkucc.hku.hk
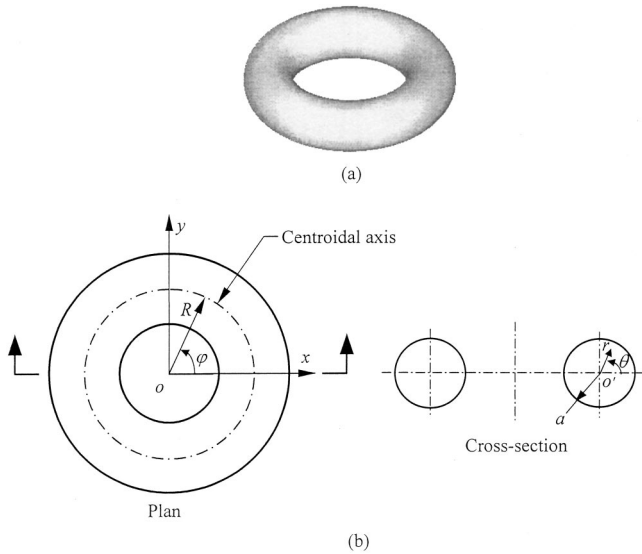
FIG. 1. A torus with a circular cross section: (a) three-dimensional view; (b) coordinate system.

based on the three-dimensional elasticity theory. Although the method itself does not guarantee us to provide exact solutions, high accuracy and quick convergence may be achieved if one selects the displacement functions properly. In this paper, a combination of the polar coordinate (r, θ) at each circular cross section and the circumferential coordinate φ around the ring, is developed to describe the strain and stress distributions in the torus. The corresponding displacement components are taken to be u_r, ν_θ, and w_φ in the r, θ, and φ directions, respectively. Each displacement component is expressed as a product of three separable coordinate functions: a series of Chebyshev polynomials in the r coordinate and a series of trigonometric functions in the θ and φ coordinates. It is obvious that each displacement function is composed of orthogonal and complete series in the region because each component function is orthogonal and complete. Therefore, the eigenfrequencies presented in this work are very accurate and often accurate to at least six significant figures. They can therefore serve as a benchmark solution for the one-dimensional ring theory and future computational techniques for the problem.

II. THEORETICAL FORMULATION

Consider a torus with a circular cross section, as shown in Fig. 1. The cross-sectional radius of the ring is a and the centroidal-axis radius of the ring is R ($R > a$). A combination of the polar coordinate (r, θ) at each cross section and the circumferential coordinate φ around the ring is chosen to describe the strain and stress in the torus. The polar coordinate with an origin at the centroidal axis of the ring is used to describe the stress and strain at the cross section. The circumferential coordinate with an origin at the center of the torus is used to describe those quantities along the direction normal to the cross section. It is obvious that the three coordinates (r, θ, φ) in this set of curved coordinate system are orthogonal to each other. The transformation relations between the Cartesian coordinates and the present curved coordinates are given as follows:

$$x = (R + r \cos \theta) \cos \varphi; \quad y = (R + r \cos \theta) \sin \varphi;$$
$$z = r \sin \theta. \tag{1}$$

Let u, ν, and w, respectively, be the displacements in r, θ, and φ directions. The relations between three-dimensional tensorial strains and displacement components in the orthogonal curved coordinate system are given by

$$\epsilon_r = \frac{\partial u}{\partial r}; \quad \epsilon_\theta = \frac{1}{r} \frac{\partial \nu}{\partial \theta} + \frac{u}{r};$$

$$\epsilon_\varphi = \frac{1}{R + r \cos \theta} \frac{\partial w}{\partial \varphi} + \frac{\cos \theta}{R + r \cos \theta} u - \frac{\sin \theta}{R + r \cos \theta} \nu;$$

$$\gamma_{r\theta} = \frac{\partial \nu}{\partial r} - \frac{\nu}{r} + \frac{1}{r} \frac{\partial u}{\partial \theta}; \tag{2}$$

$$\gamma_{\theta\varphi} = \frac{1}{r} \frac{\partial w}{\partial \theta} + \frac{\sin \theta}{R + r \cos \theta} w + \frac{1}{R + r \cos \theta} \frac{\partial \nu}{\partial \varphi};$$

$$\gamma_{\varphi r} = \frac{1}{R + r \cos \theta} \frac{\partial u}{\partial \varphi} + \frac{\partial w}{\partial r} - \frac{\cos \theta}{R + r \cos \theta} w.$$

From Eq. (1), the determinant of the Jacobian matrix of the coordinate system is given by

$$|J| = r(R + r \cos \theta). \tag{3}$$

Therefore, the strain energy V and the kinetic energy T of the torus undergoing free vibration are

$$V = (1/2) \int_0^{2\pi} \int_0^{2\pi} \int_0^a [(\lambda + 2G) \epsilon_r^2 + 2\lambda \epsilon_r \epsilon_\theta + 2\lambda \epsilon_r \epsilon_\varphi$$
$$+ (\lambda + 2G) \epsilon_\theta^2 + 2\lambda \epsilon_\theta \epsilon_\varphi + (\lambda + 2G) \epsilon_\varphi^2$$
$$+ G(\gamma_{r\theta}^2 + \gamma_{\theta\varphi}^2 + \gamma_{\varphi r}^2)] |J| \, dr \, d\theta \, d\varphi; \tag{4}$$

$$T = (\rho/2) \int_0^{2\pi} \int_0^{2\pi} \int_0^a (\dot{u} + \dot{\nu} + \dot{w}) |J| \, dr \, d\theta \, d\varphi,$$

where ρ is the constant mass per unit volume; $\dot{u}$, $\dot{\nu}$, and $\dot{w}$ are the velocity components. The parameters λ and G are the Lamé constants for a homogeneous and isotropic material, which are expressed in terms of Young's modulus E and the Poisson's ratio ν by

$$\lambda = \nu E / [(1 + \nu)(1 - 2\nu)]; \quad G = E / [2(1 + \nu)]. \tag{5}$$

In free vibrations, the displacement components may be expressed as

$$u = U(r, \theta, \varphi) e^{i\omega t}; \quad \nu = V(r, \theta, \varphi) e^{i\omega t};$$
$$w = W(r, \theta, \varphi) e^{i\omega t}, \tag{6}$$

where ω is the circular eigenfrequency of the torus and $i = \sqrt{-1}$.

Considering the circumferential symmetry of the torus about the coordinate φ, the displacement functions can be expressed as

$$U(r,\theta,\varphi)=\bar{U}(r,\theta)\cos(n\varphi);$$

$$V(r,\theta,\varphi)=\bar{V}(r,\theta)\cos(n\varphi); \qquad (7)$$

$$W(r,\theta,\varphi)=\bar{W}(r,\theta)\sin(n\varphi),$$

where n is the circumferential wave number that should be an integer, i.e., $n=0,1,2,3,...,\infty$ to ensure periodicity. It is obvious that $n=0$ denotes the axisymmetric modes. Rotating the axes of symmetry, another set of free vibration modes can be obtained, which corresponds to an interchange of $\cos(n\varphi)$ and $\sin(n\varphi)$ in Eq. (7). However, in such a case, $n=0$ means $U(r,\theta,\varphi)=0$, $V(r,\theta,\varphi)=0$ and $W(r,\theta,\varphi)=\bar{W}(r,\theta)$, which corresponds to the torsional modes.

Defining the following dimensionless coordinates:

$$\bar{R}=R/a; \quad \bar{r}=r/a, \qquad (8)$$

and then substituting Eqs. (6) and (7) into Eq. (4), gives

$$V_{\max}=(Ga/2)\int_0^{2\pi}\int_0^1[(\bar{\lambda}+2)\bar{\epsilon}_r^2+2\bar{\lambda}\bar{\epsilon}_r\bar{\epsilon}_\theta+2\bar{\lambda}\bar{\epsilon}_r\bar{\epsilon}_\varphi$$

$$+(\bar{\lambda}+2)\bar{\epsilon}_\theta^2+2\bar{\lambda}\bar{\epsilon}_\theta\bar{\epsilon}_\varphi+(\bar{\lambda}+2)\bar{\epsilon}_\varphi^2+\bar{\gamma}_{r\theta}^2+\bar{\gamma}_{\theta\varphi}^2$$

$$+\bar{\gamma}_{\varphi r}^2]\bar{r}(\bar{R}+\bar{r}\cos\theta)d\bar{r}\,d\theta;$$

$$ \qquad (9)$$

$$T_{\max}=(\rho a^3\omega^2/2)\int_0^{2\pi}\int_0^1(\Gamma_1\bar{U}^2+\Gamma_1\bar{V}^2+\Gamma_2\bar{W}^2)$$

$$\times\bar{r}(\bar{R}+\bar{r}\cos\theta)d\bar{r}\,d\theta,$$

in which

$$\bar{\lambda}=\frac{2\nu}{1-2\nu}; \quad \bar{\epsilon}_r^2=\Gamma_1\left(\frac{\partial\bar{U}}{\partial\bar{r}}\right)^2;$$

$$\bar{\epsilon}_\theta^2=\frac{\Gamma_1}{\bar{r}^2}\left[\left(\frac{\partial\bar{V}}{\partial\theta}\right)^2+2\bar{U}\frac{\partial\bar{V}}{\partial\theta}+\bar{U}^2\right];$$

$$\bar{\epsilon}_\varphi^2=\frac{\Gamma_1}{(\bar{R}+\bar{r}\cos\theta)^2}[n^2\bar{W}^2+2n\cos\theta\bar{U}\bar{W}-2n\sin\theta\bar{V}\bar{W}$$

$$+\cos^2\theta\bar{U}^2-\sin(2\theta)\bar{U}\bar{V}+\sin^2\theta\bar{V}^2];$$

$$\bar{\epsilon}_r\bar{\epsilon}_\theta=\frac{\Gamma_1}{\bar{r}}\left(\frac{\partial\bar{U}}{\partial\bar{r}}\frac{\partial\bar{V}}{\partial\theta}+\bar{U}\frac{\partial\bar{U}}{\partial\bar{r}}\right);$$

$$\bar{\epsilon}_\theta\bar{\epsilon}_\varphi=\frac{\Gamma_1}{\bar{r}(\bar{R}+\bar{r}\cos\theta)}\left[n\left(\frac{\partial\bar{V}}{\partial\theta}\bar{W}+\bar{U}\bar{W}\right)\right.$$

$$\left.+\cos\theta\left(\bar{U}\frac{\partial\bar{V}}{\partial\theta}+\bar{U}^2\right)-\sin\theta\left(\bar{V}\frac{\partial\bar{V}}{\partial\theta}+\bar{U}\bar{V}\right)\right];$$

$$ \qquad (10)$$

$$\bar{\epsilon}_\varphi\bar{\epsilon}_r=\frac{\Gamma_1}{\bar{R}+\bar{r}\cos\theta}\left[n\frac{\partial\bar{U}}{\partial\bar{r}}\bar{W}+\cos\theta\bar{U}\frac{\partial\bar{U}}{\partial\bar{r}}-\sin\theta\frac{\partial\bar{U}}{\partial\bar{r}}\bar{V}\right];$$

$$\bar{\gamma}_{r\theta}^2=\Gamma_1\left[\left(\frac{\partial\bar{V}}{\partial\bar{r}}\right)^2-\frac{2}{\bar{r}}\bar{V}\frac{\partial\bar{V}}{\partial\bar{r}}+\frac{2}{\bar{r}}\frac{\partial\bar{U}}{\partial\theta}\frac{\partial\bar{V}}{\partial\bar{r}}+\frac{1}{\bar{r}^2}\bar{V}^2\right.$$

$$\left.-\frac{2}{\bar{r}^2}\frac{\partial\bar{U}}{\partial\theta}\bar{V}+\frac{1}{\bar{r}^2}\left(\frac{\partial\bar{U}}{\partial\theta}\right)^2\right];$$

$$\bar{\gamma}_{\theta\varphi}^2=\Gamma_2\left[\frac{1}{\bar{r}^2}\left(\frac{\partial\bar{W}}{\partial\theta}\right)^2+\frac{2}{\bar{r}(\bar{R}+\bar{r}\cos\theta)}\right.$$

$$\times\left(\sin\theta\bar{W}\frac{\partial\bar{W}}{\partial\theta}-n\bar{V}\frac{\partial\bar{W}}{\partial\theta}\right)+\frac{1}{(\bar{R}+\bar{r}\cos\theta)^2}$$

$$\left.\times(\sin^2\theta\bar{W}^2-2n\sin\theta\bar{V}\bar{W}+n^2\bar{V}^2)\right];$$

$$\bar{\gamma}_{\varphi r}^2=\Gamma_2\left[\left(\frac{\partial\bar{W}}{\partial\bar{r}}\right)^2-\frac{2}{(\bar{R}+\bar{r}\cos\theta)}\right.$$

$$\times\left(\cos\theta\bar{W}\frac{\partial\bar{W}}{\partial\bar{r}}+n\bar{U}\frac{\partial\bar{W}}{\partial\bar{r}}\right)+\frac{1}{(\bar{R}+\bar{r}\cos\theta)^2}$$

$$\left.\times(n^2\bar{U}^2+2n\cos\theta\bar{U}\bar{W}+\cos^2\theta\bar{W}^2)\right],$$

where

$$\Gamma_1=\int_0^{2\pi}\cos^2 n\varphi\,d\varphi=\begin{cases}2\pi, & \text{if } n=0,\\ \pi, & \text{if } n\geq 1,\end{cases}$$

$$ \qquad (11)$$

$$\Gamma_2=\int_0^{2\pi}\sin^2 n\varphi\,d\varphi=\begin{cases}0, & \text{if } n=0,\\ \pi, & \text{if } n\geq 1.\end{cases}$$

The Lagrangian energy functional Π is given as

$$\Pi=T_{\max}-V_{\max}. \qquad (12)$$

The displacement functions $\bar{U}(\bar{r},\theta)$, $\bar{V}(\bar{r},\theta)$, and $\bar{W}(\bar{r},\theta)$ are approximately expressed in terms of a finite series as

$$\bar{U}(\bar{r},\theta)=\sum_{i=1}^I\sum_{j=1}^J A_{ij}F_i(\bar{r})G_j(\theta);$$

$$\bar{V}(\bar{r},\theta)=\sum_{l=1}^L\sum_{m=1}^M B_{lm}F_l(\bar{r})\bar{G}_m(\theta); \qquad (13)$$

$$\bar{W}(\bar{r},\theta)=\sum_{p=1}^P\sum_{q=1}^Q C_{pq}F_p(\bar{r})G_q(\theta),$$

where A_{ij}, B_{lm}, and C_{pq} are undetermined coefficients and I, J, L, M, P, and Q are the truncated orders of their corresponding series. It is obvious that if $F_i(\bar{r})$ $(i=1,2,3,...,\infty)$, $G_j(\theta)$ $(j=1,2,3,...,\infty)$ and $\bar{G}_m(\theta)$ $(m=1,2,3,...,\infty)$ are all sets of mathematically complete series, then these three sets are capable of describing any three-dimensional motion of the torus. Therefore, as sufficient terms are taken, the results will approach the exact solutions as closely as desired.

TABLE I. Convergence of eigenfrequencies of a torus with a circular cross section when $\bar{R}=1.5$ and $n=1$.

Terms	Ω_1	Ω_2	Ω_3	Ω_4	Ω_5	Ω_6	Ω_7
			Symmetric modes about the centroidal-axis plane				
4×4	1.185 76	2.334 75	2.753 63	3.049 33	3.508 54	3.732 38	3.837 33
5×5	**1.185 74**	2.334 06	2.753 26	3.048 28	3.503 98	3.729 11	3.831 64
6×6	1.185 74	**2.334 04**	**2.723 21**	3.048 15	3.503 39	3.728 47	3.831 07
7×7	1.185 74	2.334 04	2.753 21	**3.048 14**	3.503 38	**3.728 44**	**3.831 05**
8×8	1.185 74	2.334 04	2.753 21	3.048 14	**3.503 37**	3.728 44	3.831 05
9×9	1.185 74	2.334 04	2.753 21	3.048 14	3.503 37	3.728 44	3.831 05
			Antisymmetric modes about the centroidal-axis plane				
4×4	1.155 46	2.143 68	2.492 66	3.108 78	3.473 95	3.778 32	4.629 33
5×5	1.155 07	**2.143 37**	2.492 04	3.108 55	3.470 28	3.772 59	4.549 37
6×6	1.155 04	2.143 37	**2.492 03**	**3.108 41**	**3.469 83**	3.771 67	4.545 57
7×7	**1.155 03**	2.143 37	2.492 03	3.108 41	3.469 83	3.771 65	**4.545 42**
8×8	1.155 03	2.143 37	2.492 03	3.108 41	3.469 83	**3.771 64**	4.545 42
9×9	1.155 03	2.143 37	2.492 03	3.108 41	3.469 83	3.771 64	4.545 42

Substituting Eqs. (10) and (13) into Eq. (9) and minimizing the Lagrangian functional Π with respect to the undetermined coefficients A_{ij}, B_{lm}, and C_{pq}, i.e.,

$$\frac{\partial}{\partial A_{ij}}(V_{\max}-T_{\max})=0 \quad (i=1,2,3,...,I;j=1,2,3,...,J);$$

$$\frac{\partial}{\partial B_{lm}}(V_{\max}-T_{\max})=0 \quad (l=1,2,3,...,L;m=1,2,3,...,M);$$

(14)

$$\frac{\partial}{\partial C_{pq}}(V_{\max}-T_{\max})=0 \quad (p=1,2,3,...,P;q=1,2,3,...,Q),$$

a set of eigenvalue equations is derived, which can be written in matrix form as

$$\left\{ \begin{bmatrix} [K_{uu}] & [K_{uv}] & [K_{uw}] \\ & [K_{vv}] & [K_{vw}] \\ \text{symmetric} & & [K_{ww}] \end{bmatrix} -\Omega^2 \begin{bmatrix} [M_{uu}] & & \\ & [M_{vv}] & \\ & & [M_{ww}] \end{bmatrix} \right\} \begin{bmatrix} \{A\} \\ \{B\} \\ \{C\} \end{bmatrix} = \begin{bmatrix} \{0\} \\ \{0\} \\ \{0\} \end{bmatrix},$$

(15)

in which $\Omega=\omega a\sqrt{\rho/G}$, $[K_{ij}]$ and $[M_{ii}]$ $(i,j=u,v,w)$ are, respectively, the stiffness submatrices and the diagonal mass submatrices, $\{A\}$, $\{B\}$, and $\{C\}$ are the column vectors of the unknown coefficients, respectively, corresponding to A_{ij} $(i=1,2,3,...I;\ j=1,2,3,...,J)$, B_{lm} $(l=1,2,...,L;\ m=1,2,3,...,M)$ and C_{pq} $(p=1,2,3,...,P;\ q=1,2,3,...,Q)$. A nontrivial solution is obtained by setting the determinant of the coefficient matrix of Eq. (15) to zero. The roots of the determinant are the square of the dimensionless eigenfrequencies (eigenvalues). The mode shapes (eigenfunctions) are determined by backsubstitution of the eigenvalues, one by one, in the usual manner.

It is noted that in using the Ritz method, the stress boundary conditions of the structure need not be satisfied in advance, but the geometric boundary conditions should be satisfied exactly. For a torus, there is actually no restraint on the surface displacements. In the present work, the Chebyshev polynomial series defined in the interval $[0, 1]$ and the trigonometric series defined in the interval $[0, 2\pi]$ are used as the admissible functions of displacements in the r and θ directions, respectively. It is obvious that a torus with a circular cross section is symmetric about the centroidal-axis plane (i.e., the plane containing the centroidal axis of the ring). Therefore, the vibration modes of the torus can be

TABLE II. The convergence of eigenfrequencies of a torus with a circular cross section when $\bar{R}=1.5$ and $n=5$.

Terms	Ω_1	Ω_2	Ω_3	Ω_4	Ω_5	Ω_6	Ω_7
			Symmetric modes about the centroidal-axis plane				
5×5	2.461 38	3.189 81	3.709 52	4.298 67	4.409 67	4.871 47	5.242 81
6×6	2.461 26	3.189 71	3.708 74	4.298 22	4.407 66	4.865 66	5.236 25
7×7	**2.461 24**	3.189 71	3.709 63	4.298 19	4.407 47	4.864 89	5.235 40
8×8	2.461 24	**3.189 70**	**3.709 61**	**4.298 18**	**4.407 44**	4.864 76	5.235 24
9×9	2.461 24	3.189 70	3.709 61	4.298 18	4.407 44	**4.864 74**	**5.235 21**
10×10	2.461 24	3.189 70	3.709 61	4.298 18	4.407 44	4.864 74	5.235 21
			Antisymmetric modes about the centroidal-axis plane				
5×5	2.163 12	3.156 36	3.772 63	4.307 75	4.688 60	5.106 18	5.472 98
6×6	2.163 08	3.156 21	3.771 99	4.306 44	4.685 39	5.103 40	5.436 34
7×7	**2.163 07**	**3.156 19**	3.771 91	4.306 38	4.684 98	5.103 10	5.435 22
8×8	2.163 07	3.156 19	**3.771 90**	**4.306 37**	4.684 92	**5.103 07**	5.435 14
9×9	2.163 07	3.156 19	3.771 90	4.306 37	**4.684 91**	5.103 07	**5.435 13**
10×10	2.163 07	3.156 19	3.771 90	4.306 37	4.684 91	5.103 07	5.435 13

TABLE III. The convergence of eigenfrequencies of axisymmetric vibration for a torus with circular cross section when $\bar{R}=1.5$.

Terms	Ω_1	Ω_2	Ω_3	Ω_4	Ω_5	Ω_6	Ω_7
			Symmetric modes about the centroidal-axis plane				
5×5	1.176 85	2.614 42	2.879 30	3.799 87	4.116 45	4.504 47	4.898 72
6×6	**1.176 82**	2.614 28	2.879 06	3.797 26	4.115 71	4.502 95	4.884 95
7×7	1.176 82	**2.614 26**	**2.879 04**	3.797 06	4.115 65	4.502 83	4.883 42
8×8	1.176 82	2.614 26	2.879 04	**3.797 03**	**4.115 64**	**4.502 82**	4.883 18
9×9	1.176 82	2.614 26	2.879 04	3.797 03	4.115 64	4.502 82	**4.883 15**
10×10	1.176 82	2.614 26	2.879 04	3.797 03	4.115 64	4.502 82	4.883 15
			Antisymmetric modes about the centroidal-axis plane				
5×5	0.802 725	2.520 71	2.988 77	3.807 28	4.477 76	4.906 16	5.181 13
6×6	0.802 670	2.520 58	2.988 49	3.803 39	4.475 62	4.883 92	5.171 83
7×7	0.802 665	**2.520 56**	**2.988 47**	3.803 07	4.475 45	4.881 04	5.171 53
8×8	**0.802 664**	2.520 56	2.988 47	**3.803 03**	**4.475 44**	4.880 65	**5.171 51**
9×9	0.802 664	2.520 56	2.988 47	3.803 03	4.475 44	**4.880 60**	5.171 51
10×10	0.802 664	2.520 56	2.988 47	3.803 03	4.475 44	4.880 60	5.171 51

classified into two distinct categories: symmetric modes and antisymmetric modes about the centroidal-axis plane. If the angle θ is measured with respect to an axis within the centroidal-axis plane, then for the symmetric modes one has

$$F_s(\bar{r}) = \cos[(s-1)\arccos(2\bar{r}-1)];$$
$$G_s(\theta) = \cos[(s-1)\theta]; \qquad (16)$$
$$\bar{G}_s(\theta) = \sin(s\theta), \quad s=1,2,3,...,$$

and for the antisymmetric modes, one has

$$F_s(\bar{r}) = \cos[(s-1)\arccos(2\bar{r}-1)]; \quad G_s(\theta) = \sin(s\theta);$$
$$\bar{G}_s(\theta) = \cos[(s-1)\theta], \quad s=1,2,3,.... \qquad (17)$$

It can be seen that $F_s(\bar{r})$, $G_s(\theta)$, and $\bar{G}_s(\theta)$ in both Eqs. (16) and (17) are all orthogonal and complete series in the defined intervals.

Each of these two categories can be separately determined and thus it results in a smaller set of eigenvalue equations while maintaining the same level of accuracy.

III. CONVERGENCE STUDY

It is well known that eigenvalues provided by the Ritz method converge as upper bounds to the exact values. The solution of any accuracy can be obtained theoretically by using sufficient terms of admissible functions. However, there is a limit to the number of terms actually used in computation. Therefore, it is important to understand the convergence rate and the accuracy of the method. In the following convergence study, a thick torus with radius ratio $\bar{R}=R/a$ = 1.5 was used and in all the calculations, the Poisson's ratio $\nu=0.3$ was fixed. In most cases, optimal convergence could be obtained by using different number of terms in the component series of displacement functions. However, for simplicity, an equal number of terms in the Chebyshev polynomial series and the trigonometric series were used for every displacement function, i.e., $I=J=L=M=P=Q$, in the present analysis. Tables I and II show the convergence of the first seven eigenfrequency parameters $\Omega = \omega a \sqrt{\rho/G}$ for the circumferential wave number $n=1$ and $n=5$, respectively. Both the symmetric and antisymmetric modes were studied. Extensive convergence studies were also carried out for the axisymmetric vibration and the torsional vibration of the ring with the results shown in Table III and Table IV, respectively.

All the above computations were performed in double precision (16 significant figures) and piecewise Gaussian quadrature was used numerically to obtain the matrices in

TABLE IV. The convergence of eigenfrequencies of torsional vibration for a torus with circular cross section when $\bar{R}=1.5$.

Terms	Ω_1	Ω_2	Ω_3	Ω_4	Ω_5	Ω_6	Ω_7
			Symmetric modes about the centroidal-axis plane				
5×5	**2.260 99**	3.292 90	4.014 80	4.423 15	5.498 76	5.586 19	6.833 90
6×6	2.260 99	**3.292 68**	4.013 94	4.421 59	5.481 19	5.564 43	6.614 10
7×7	2.260 99	3.292 68	**4.013 94**	4.421 50	5.480 36	5.563 71	6.596 69
8×8	2.260 99	3.292 68	4.013 93	**4.421 49**	**5.480 32**	5.563 66	6.595 97
9×9	2.260 99	3.292 68	4.013 93	4.421 49	5.480 32	**5.563 65**	**6.595 92**
10×10	2.260 99	3.292 68	4.013 93	4.421 49	5.480 32	5.563 65	6.595 92
			Antisymmetric modes about the centroidal-axis plane				
5×5	**1.913 73**	3.266 34	4.410 64	5.411 69	5.525 28	6.617 86	6.837 02
6×6	1.913 73	**3.266 16**	4.409 75	5.397 88	5.523 02	6.597 85	6.829 73
7×7	1.913 73	3.266 16	**4.409 69**	5.397 56	5.522 41	6.596 06	6.818 01
8×8	1.913 73	3.266 16	4.409 69	**5.397 52**	5.522 40	6.595 91	6.817 95
9×9	1.913 73	3.266 16	4.409 69	5.397 52	**5.522 39**	**6.595 90**	**6.817 89**
10×10	1.913 73	3.266 16	4.409 69	5.397 52	5.522 39	6.595 90	6.817 89
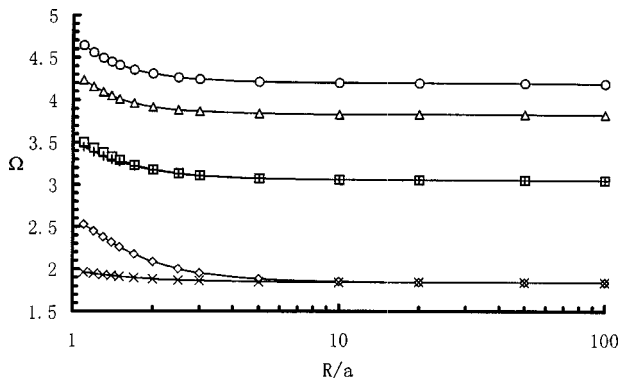
FIG. 2. The first six eigenfrequency parameters Ω of torsional vibration of a torus: $\diamond$, first symmetric mode; $\square$, second symmetric mode; $\triangle$, third symmetric mode; $\times$, first antisymmetric mode; $+$, second antisymmetric mode; $\bigcirc$, third antisymmetric mode.

Eq. (15). It is seen that the first seven eigenfrequencies have converged monotonically to six significant figures by using only a few terms. As both the Chebyshev polynomial series and the trigonometric series are complete, one can conclude that these eigenfrequencies are "exact values" to six digits. Values given in boldface type and underlined are the converged values for the smallest number of terms used. Comparing Tables I and II, one can find that the convergence rate is almost the same for $n=1$ and $n=5$. The first seven eigenfrequencies accurate to six significant figures have been obtained by using only nine terms of the admissible functions in each coordinate.

IV. EIGENFREQUENCIES AND MODE SHAPES

The results for a torus with circular cross section are presented in Figs. 2–6, where the parameter R/a is plotted along a logarithmic axis. The ratio of the centroidal-axis radius to the cross-sectional radius varies from 1.1 to 100. Figure 2 shows the first six eigenfrequency parameters $\Omega = \omega a \sqrt{\rho/G}$ for torsional vibration, comprising three symmetric modes and three antisymmetric modes. The third to eighth eigenfrequency parameters Ω of axisymmetric vibration are given in Fig. 3, and they include the second to fourth symmetric modes and the second to fourth antisymmetric modes. Figure 4 gives the third to eighth eigenfrequency
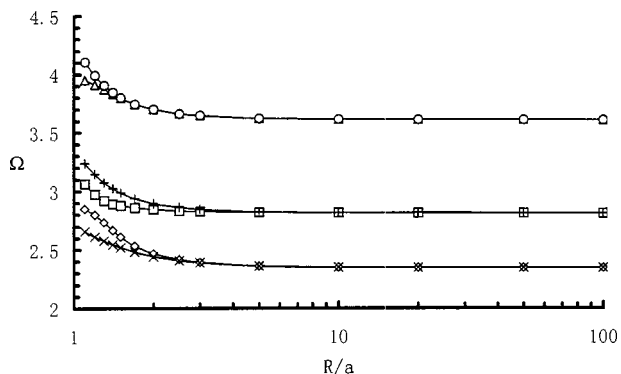
FIG. 3. The third to eighth eigenfrequency parameters Ω of axisymmetric vibration of a torus: $\diamond$, second symmetric mode; $\square$, third symmetric mode; $\triangle$, fourth symmetric mode; $\times$, second antisymmetric mode; $+$, third antisymmetric mode; $\bigcirc$, fourth antisymmetric mode.
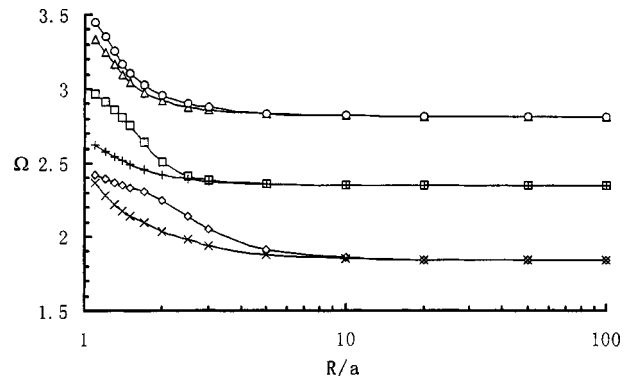
FIG. 4. The third to eighth eigenfrequency parameters Ω of a torus for circumferential wave number $n=1$: $\diamond$, second symmetric mode; $\square$, third symmetric mode; $\triangle$, fourth symmetric mode; $\times$, second antisymmetric mode; $+$, third antisymmetric mode; $\bigcirc$, fourth antisymmetric mode.

parameters Ω for the circumferential wave number $n=1$ that consist of the second to fourth symmetric modes and the second to fourth antisymmetric modes. From Figs. 2–4, it is seen that with the increase of the radius ratio R/a, the eigenfrequency parameters Ω of symmetric modes eventually coincide with those of antisymmetric modes. For a given cross-sectional radius a, the eigenfrequencies monotonically decrease with the increase of centroidal-axis radius R of the torus and approach certain constant values. In general, for $R/a > 10$, we may consider the eigenfrequency parameters Ω to be constant.

The first and second eigenfrequencies of axisymmetric vibration, which correspond to the fundamental antisymmetric mode and symmetric mode, respectively, are described by a new eigenfrequency parameter $\Gamma = (R/a)\Omega = \omega R \sqrt{\rho/G}$. It is clear that both the torsional vibration and the axisymmetric vibration are independent of the coordinate θ. Torsional vibration is related to the coordinates φ and r while axisymmetric vibration is only related to the coordinate φ. In Fig. 5, six eigenfrequency parameters are shown for the fundamental symmetric and antisymmetric modes for circumferential wave number $n=1$, the second symmetric and antisymmetric modes for circumferential wave number $n=2$, as well as the fundamental symmetric and antisymmetric modes of axisym-
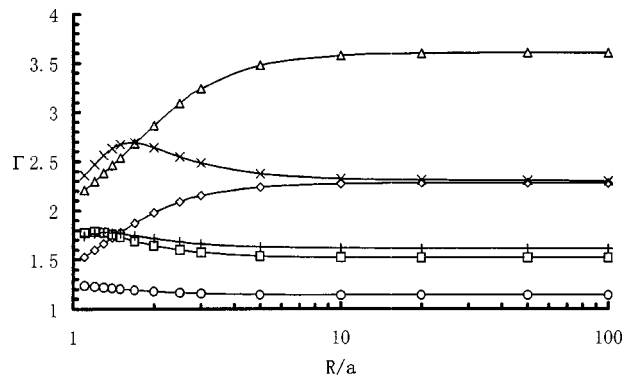
FIG. 5. Eigenfrequency parameters Γ of a torus for circumferential wave number $n \leqslant 2$ and for the axisymmetric vibration: $\diamond$, first symmetric mode for $n=1$; $\square$, first antisymmetric mode for $n=1$; $\triangle$, second symmetric mode for $n=2$; $\times$, second antisymmetric mode for $n=2$; $+$, first symmetric mode for axisymmetric vibration; $\bigcirc$, first antisymmetric mode for axisymmetric vibration.

Zhou *et al.*: Vibration analysis of a torus
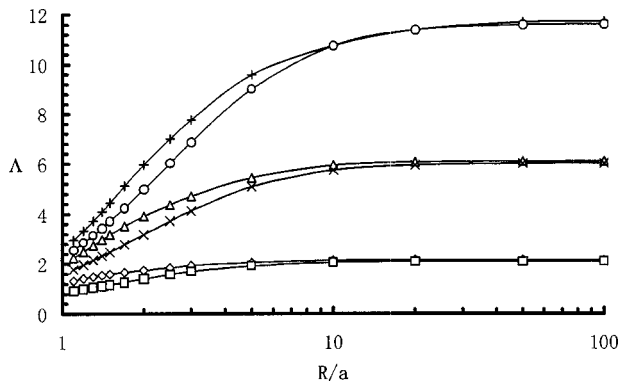
FIG. 6. The fundamental eigenfrequency parameters Λ of a torus for circumferential wave number $n \geq 2$: $\diamond$, first symmetric mode for $n=2$; $\square$, first antisymmetric mode for $n=2$; $\triangle$, first symmetric mode for $n=3$; $\times$, first antisymmetric mode for $n=3$; $+$, first symmetric mode for $n=4$; $\bigcirc$, first antisymmetric mode for $n=4$.

metric vibration. From the figure, one can find that the fundamental eigenfrequency parameter of symmetric modes for circumferential wave number $n=1$ and the second eigenfrequency parameter of symmetric modes for circumferential wave number $n=2$ monotonically increase with the increase of the radius ratio R/a. Among the rest, the eigenfrequency parameter of the first antisymmetric modes for axisymmetric vibration monotonically decreases with the increase of the radius ratio R/a. However, the others are not monotonic. In general, for $R/a > 10$, we may also consider the eigenfrequency parameters Γ to be constant. In Fig. 6, the dimensionless parameter $\Lambda = (R/a)^2 \Omega$ is used to describe the fundamental eigenfrequencies of a torus for circumferential wave number $n \geq 2$. In the figure, the fundamental eigenfrequency parameters of symmetric and antisymmetric modes for $n = 2, 3, 4$ are plotted against the radius ratio R/a. It is seen that all the eigenfrequency parameters monotonically increase, and approach certain constant values with the increase of the radius ratio R/a. Moreover, with the increase of the radius ratio R/a, the eigenfrequencies of symmetric modes become close to those of antisymmetric modes.

In the above analysis, three different dimensionless eigenfrequency parameters Ω, Γ, and Λ are introduced, which facilitate not only the trends of the variation of eigenfrequencies but also a comparison with other solutions. In the approximate one-dimensional theory, the in-plane vibration and out-of-plane vibration of a ring are separately investigated. In Fig. 6, the symmetric modes correspond to the in-plane vibration solutions of the one-dimensional theory while the antisymmetric modes correspond to the out-of-plane vibration solutions. For example, according to the clas-

sical one-dimensional ring theory,[1,2] the eigenfrequencies for in-plane vibration of a circular ring are given by

$$\Lambda_{s-1}^2 = 0.65 s^2 (s^2 - 1)^2 / (s^2 + 1), \quad s = 2, 3, 4, \ldots, \quad (18)$$

and the eigenfrequencies for out-of-plane vibration are given by

$$\Lambda_{s-1}^2 = 0.65 s^2 (s^2 - 1)^2 / (s^2 + 1 + \nu), \quad s = 2, 3, 4, \ldots. \quad (19)$$

A comparison of the present results with those obtained from the classical theory is given in Table V for a thin circular ring with the radius ratio $R/a = 50$. It is shown that for thin circular rings, the classical theory can predict the lower-order eigenfrequencies with good accuracy. However, like all kinds of approximate theories, it cannot provide a full vibration spectrum of the circular ring and the error increases with the decrease of the radius ratio R/a. Moreover, the classical theory does not include shear deformation or rotary inertia effects. Taking a torus with the radius ratio $R/a = 1.5$ as an example, the fundamental eigenfrequency parameter of in-plane vibration obtained by using the classical one-dimensional ring theory is $\Lambda_1 = 2.163\,33$. However, the corresponding eigenfrequency parameter obtained by using the present three-dimensional elasticity theory is $\Lambda_1 = 1.591\,17$. The error of the classical one-dimensional ring theory is up to about 36%! Considering the relations $\Lambda = (R/a)^2 \Omega$ and $\Gamma = (R/a)\Omega$, and noting that $R/a > 1$, one can find out from Figs. 2–6 by comparing Ω that for a torus, whether thin or thick, the lowest eigenfrequencies of both symmetric modes and antisymmetric modes are always those for $n = 2$. Although the lower eigenfrequencies of a torus with large radius ratio R/a are confined to some particular modes, as seen from Fig. 6, for a torus with small radius ratio R/a, the lower eigenfrequencies for a larger variety of modes tend to cluster together, as is evident from Figs. 2–6.

Corresponding to each eigenfrequency, the three-dimensional deformed mode shapes of the torus can be easily obtained from Eqs. (13) and (15). As an example, the first three antisymmetric mode shapes and symmetric mode shapes of torsional vibration for a torus with radius ratio $R/a = 1.5$ are given in Figs. 7 and 8 in contour form, respectively. It is known that for torsional vibration, the modes of the torus are the same at each cross section and only the deflection $W(r, \theta)$ in the circumferential direction φ exists. Therefore, only the mode shapes in a cross section need to be given.

TABLE V. A comparison of the eigenfrequency parameters Λ for a thin circular ring, $R/a = 50$.

Methods	Λ_1	Λ_2	Λ_3	Λ_4	Λ_5	Λ_6
			In-plane vibration			
Present	2.162 23	6.110 11	11.7002	18.8898	27.6539	37.9700
Classical	2.163 33	6.118 82	11.7323	18.7938	27.8340	38.3099
			Out-of-plane vibration			
Present	2.099 17	6.016 84	11.5907	18.7688	27.5231	37.8296
Classical	2.101 21	6.029 06	11.6301	18.8651	27.7218	38.1955

J. Acoust. Soc. Am., Vol. 112, No. 6, December 2002

Zhou *et al.*: Vibration analysis of a torus   2837
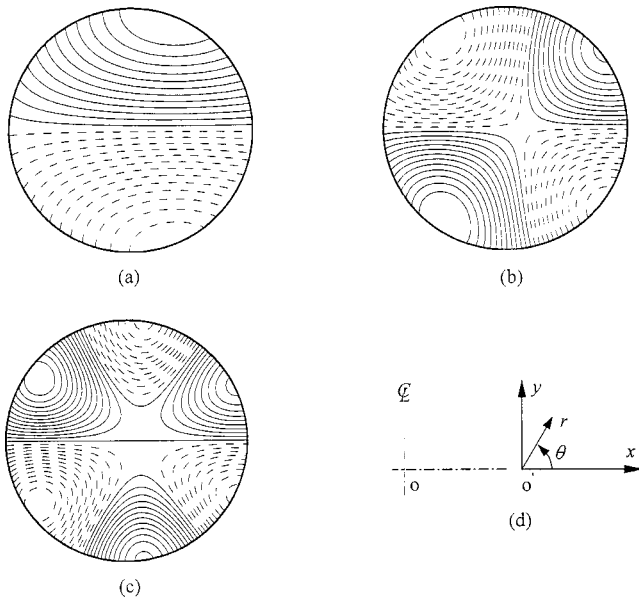
FIG. 7. The first three antisymmetric modes of torsional vibration when $R/a = 1.5$: (a) the first mode; (b) the second mode; (c) the third mode; (d) coordinate system for the cross section.

V. CONCLUSIONS

This paper describes the detailed development of a three-dimensional analysis method for the free vibration of a torus with a circular cross section. The spatial integrals for strain and kinetic energy components have been formulated by developing a set of orthogonal coordinate systems. An energy functional has been defined and its extremum determined to arrive at the governing eigenfrequency equation. A combination of Chebyshev polynomials and trigonometric series are used as the admissible functions of the displacement components. The vibration of a torus is classified into three distinct categories, namely, axisymmetric vibration,
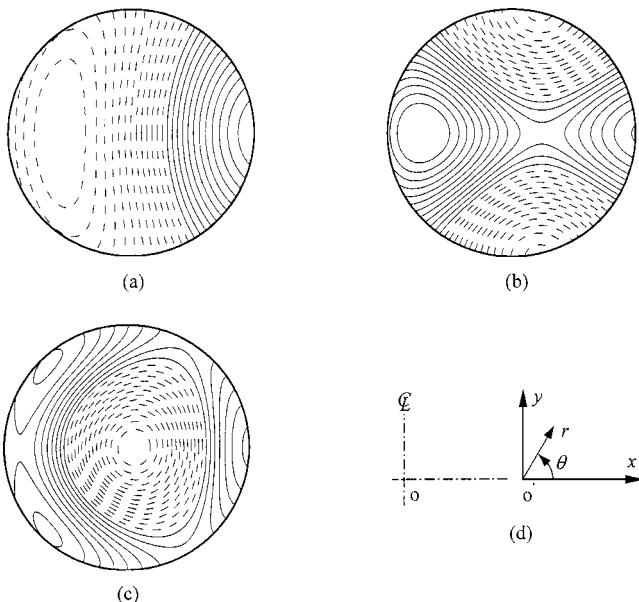
FIG. 8. The first three symmetric modes of torsional vibration when $R/a = 1.5$: (a) the first mode; (b) the second mode; (c) the third mode; (d) coordinate system for the cross section.

torsional vibration, and vibration related to the circumferential wave number n. By using the symmetry of the structure, the vibration modes of every category are divided into symmetric and antisymmetric ones. This greatly reduces the computational cost while maintaining the same level of accuracy.

The convergence of eigenfrequencies has been examined. It is shown that the first seven eigenfrequencies accurate to at least six significant figures for each vibration type can be obtained by using only nine terms of the admissible functions. Through the parametric studies, the variation of eigenfrequencies versus the radius ratio of the torus is found. Important lower eigenfrequencies corresponding to general cross-sectional motions, which can only be determined by the three-dimensional elasticity theory, have been obtained. The present method is capable of determining eigenfrequencies and mode shapes very accurately. The results may serve as valuable benchmark solutions for validating the one-dimensional ring theories and new computational techniques for the problem.

[1] A. E. H. Love, "On the vibrations of an elastic circular ring (abstract)," Proc. London Math. Soc. **24**, 118–120 (1892–1893).

[2] R. Hoppe, "The bending vibration of a circular ring," Crelle J. Math. **73**, 158–168 (1871).

[3] S. S. Rao and V. Sundararajan, "In-plane flexural vibrations of circular rings," J. Appl. Mech. **36**, 620–625 (1969).

[4] L. L. Philipson, "On the role of extension in the flexural vibration of ring," J. Appl. Mech. **23**, 364–366 (1956).

[5] J. Kirkhope, "Simple frequency expression of in-plane vibration of thick circular rings," J. Acoust. Soc. Am. **59**, 86–89 (1976).

[6] J. Kirkhope, "Out-plane vibration of thick circular ring," J. Eng. Mech. **102**, 239–247 (1976).

[7] J. S. Bakshi and W. R. Callahan, "Flexural vibrations of a circular ring when transverse shear and rotary inertia are considered," J. Acoust. Soc. Am. **40**, 372–375 (1966).

[8] C. S. Tang and C. W. Bert, "Out-of-plane vibrations of thick rings," Int. J. Solids Struct. **23**, 175–185 (1987).

[9] O. Taniguchi and M. Endo, "An approximate formula for the flexural vibration of a ring of rectangular cross section," Bull. JSME **14**, 348–354 (1971).

[10] A. W. Leissa, "Vibration of shells," NASA SP-288, U.S. Govt. Printing Office, Washington, DC, 1973.

[11] P. Chidamparam and A. W. Leissa, "Vibrations of planar curved beams, rings, and arches," Appl. Mech. Rev. **46**, 467–483 (1993).

[12] H. J. Ding and R. Q. Xu, "Free axisymmetric vibration of laminated transversely isotropic annular plates," J. Sound Vib. **230**, 1031–1044 (2000).

[13] S. Srinivas, C. V. Rao, and A. K. Rao, "An exact analysis for vibration of simply supported homogeneous and laminated thick rectangular plates," J. Sound Vib. **12**, 187–199 (1970).

[14] J. R. Hutchinson, "Axisymmetric vibrations of a free finite-length rod," J. Acoust. Soc. Am. **51**, 233–240 (1972).

[15] J. R. Hutchinson, "Vibration of solid cylinders," J. Appl. Mech. **47**, 901–907 (1980).

[16] J. R. Hutchinson, "Transverse vibration of beams, exact versus approximate solutions," J. Appl. Mech. **48**, 923–928 (1981).

[17] J. R. Hutchinson, "Vibrations of free hollow circular-cylinders," J. Appl. Mech. **53**, 641–646 (1986).

[18] J. R. Hutchinson, "Vibrations of thick free circular plates, exact versus approximate solutions," J. Appl. Mech. **51**, 581–585 (1984).

[19] A. W. Leissa and J. So, "Comparisons of vibration frequencies for rods and beams from one-dimensional and three-dimensional analysis," J. Acoust. Soc. Am. **98**, 2122–2135 (1995).

[20] J. So and A. W. Leissa, "Three-dimensional vibrations of thick circular and annular plates," J. Sound Vib. **209**, 15–41 (1998).

[21] J. H. Kang and A. W. Leissa, "Three-dimensional vibrations of thick, linearly tapered, annular plates," J. Sound Vib. **217**, 927–944 (1998).

[22] A. W. Leissa and J. H. Kang, "Three-dimensional vibration analysis of thick shells of revolution," J. Eng. Mech. **125**, 1365–1371 (1999).

[23] J. H. Kang and A. W. Leissa, "Three-dimensional vibrations of hollow cones and cylinders with linear thickness variations," J. Acoust. Soc. Am. **106**, 748–755 (1999).

[24] K. M. Liew, K. C. Hung, and M. K. Lim, "A continuum three-dimensional vibration analysis of thick rectangular plates," Int. J. Solids Struct. **30**, 3357–3379 (1993).

[25] K. M. Liew, K. C. Hung, and M. K. Lim, "Three-dimensional elasticity solutions to vibration of cantilevered skewed trapezoids," AIAA J. **32**, 2080–2089 (1994).

[26] K. M. Liew, K. C. Hung, and M. K. Lim, "Vibration of thick prismatic structures with three-dimensional flexibilities," J. Appl. Mech. **65**, 619–625 (1998).

[27] C. W. Lim, K. M. Liew, and S. Kitipornchai, "Vibration of open cylindrical shells: A three-dimensional elasticity approach," J. Acoust. Soc. Am. **104**, 1436–1443 (1998).

[28] K. M. Liew and Z. C. Feng, "Vibration characteristics of conical shell panels with three-dimensional flexibility," J. Appl. Mech. **67**, 314–320 (2000).

[29] O. G. McGee and G. T. Giaimo, "Three-dimensional vibrations of cantilevered right triangular plates," J. Sound Vib. **159**, 279–293 (1992).

[30] Y. K. Cheung and D. Zhou, "Three-dimensional vibration analysis of cantilevered and completely free isosceles triangular plates," Int. J. Solids Struct. **39**, 673–687 (2002).

[31] J. H. Kang and A. W. Leissa, "Three-dimensional vibrations of thick, circular rings with isosceles trapezoidal and triangular cross-section," J. Vibr. Acoust. **122**, 132–139 (2000).

Reduction of sound transmission into a circular cylindrical shell using distributed vibration absorbers and Helmholtz resonators

Simon J. Estève[a] and Marty E. Johnson
Vibration and Acoustics Laboratories, Department of Mechanical Engineering,
Virginia Polytechnic Institute and State University, Blacksburg, Virginia 24061

A modal expansion method is used to model a cylindrical enclosure excited by an external plane wave. A set of distributed vibration absorbers (DVAs) and Helmholtz resonators (HRs) are applied to the structure to control the interior acoustic levels. Using an impedance matching method, the structure, the acoustic cavity, and the noise reduction devices are fully coupled to yield an analytical formulation of the structural kinetic energy and acoustic potential energy of a treated cylindrical cavity. Lightweight DVAs and small HRs tuned to the natural frequencies of the targeted structural and acoustic modes, respectively, result in significant acoustic and structural attenuation when the devices are optimally damped. Simulations show that significant interior noise reduction can only be achieved by adding damping to both structural and acoustic modes, which are resonant in the frequency bandwidth of interest. In order to be independent of the azimuth angle of the excitation and to avoid unwanted modal interactions, the devices are distributed evenly around the cylinder in rings. This treatment can only achieve good performance if the structure and the acoustic cavity are lightly damped. © *2002 Acoustical Society of America.* [DOI: 10.1121/1.1514933]

PACS numbers: 43.40.Tm, 43.40.At, 43.40.Sk [ANN]

I. INTRODUCTION

Large cylindrical structures are common in the aerospace industry. The reduction of noise transmitted into such enclosures is particularly challenging due to the high excitation levels, the complex nature of the disturbance, and the severe mass and volume constraints imposed on the design of the treatments. The development of lightweight structures, made of composite materials, has lowered the acoustic transmission loss of such structures and therefore further increased the acoustic transmission problem.

The transmission of sound into an enclosed acoustic cavity can be simplified into four stages: (i) coupling between the external noise and the structure, (ii) structural vibration, (iii) coupling between the structural vibration and the interior fluid, and (iv) the sound in the interior. Control treatments can operate at some or all of these stages in order to achieve attenuation of the interior noise levels.

Control devices can be attached to the structure in order to directly reduce the vibration level [stage (ii)] and in order to reduce the structural acoustic coupling [stages (i) and (iii)]. For example, Huang and Fuller[1,2] used dynamic absorbers to reduce the interior sound level in an aircraft fuselage, at a single excitation frequency, by reducing the structural velocity. Guigou *et al.*[3] extended this work by detuning the absorbers in order to reduce the coupling between the structure and the interior sound field. For broadband applications it becomes difficult to reduce the structural acoustic coupling using lightweight treatment as decoupling at one frequency tends to increase coupling at another. Gardonio *et al.*[4] had some success achieving this using blocking masses placed on the structure but had to assume some knowledge of the angle of the incident noise field. Jolly and Sun[5] used vibration absorbers to reduce the radiation of broadband noise from a vibrating panel and Nagaya and Li[6] examined the optimization of an absorbers treatment applied to a radiating plate using neural network but neither considered radiation into a cavity.

The other approach to control the sound transmission is to directly treat the sound in the enclosure [stage (iv)]. Absorptive materials, such as acoustic blankets, perform well in the high-frequency range, but are unsuitable for low-frequency control due to the volume and mass constraints imposed in aerospace applications. However, acoustic attenuation can be obtained in the low-frequency range by the use of Helmholtz resonators (HR). Fahy and Schofield[7] investigated the interaction between a single optimally damped HR and an acoustic mode in an enclosure and Cummings[8] extended the analysis to a resonator array and its effect on the sound field in a cavity. Also, Doria[9] tried to broaden the functional frequency range of a HR by using a resonator with multiple natural frequencies. In all these studies, the acoustic disturbance is generated by an arbitrary source distribution inside the cavity and is not excited by a structure.

The contribution of this work lies in the simultaneous application of both structural and acoustic control devices to a fully coupled structural-acoustic system [stages (ii) and (iv)]. Multiple optimally damped distributed vibration absorbers (DVAs) and HRs are applied to control the sound transmission in a cylindrical enclosure over a broad frequency range containing many structural and acoustic resonances. A conventional modal expansion method[4] is used to describe the behavior of the cylindrical shell, excited by an external acoustic plane wave, and its acoustic cavity. The

---

[a]Electronic mail: sesteve@vt.edu
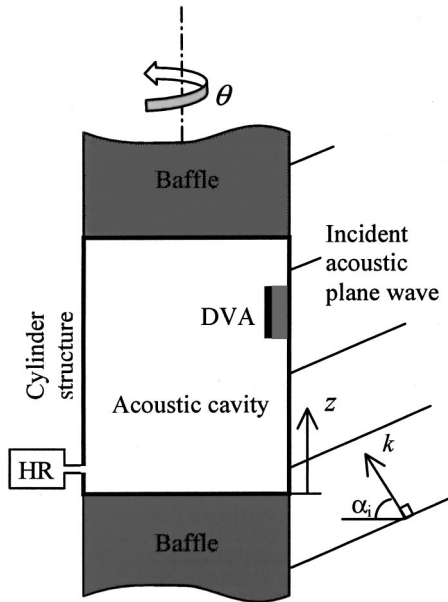
FIG. 1. Test cylinder mounted in an infinite baffle and excited by an external acoustic plane wave treated with HRs and DVAs.

optimization of the DVA treatment based on the studies by Johnson *et al.*[10,11] is extended by analogy to the HR treatment. All the elements are then fully coupled using an impedance matching method to compute the interior acoustic attenuation provided by the noise reduction devices.

II. THEORY

In this section the analytical formulation of the problem is introduced. The system being modeled is shown in Fig. 1. It is constituted of a simply supported cylinder embedded in an infinite rigid baffle excited by an acoustic plane wave. To control the vibration of the cylinder, DVAs can be attached anywhere on its surface except the top and bottom disks, which are not excited by the exterior acoustic field due to the presence of the baffle. HRs can be placed anywhere inside the cylinder, but in order to maintain a simple model for the acoustic cavity they are assumed to lie outside and to couple to the enclosed fluid at the circumference of the structure. The behavior of the structure and the acoustic cavity is described using a modal approach. The system is put in a matrix form, and using an impedance matching method is then fully coupled with the noise reduction devices. Once the necessary components of the model are defined, the expression for the vibration and interior acoustic response of the system is derived.

A. Cylinder structural model

The dynamic behavior of thin cylindrical shells has generated a multitude of theory based on different assumptions and approximations. The comparison of these different theories has also been subject to valuable studies, such as the work done by Leissa.[12] For the purpose of this work, the cylinder is assumed to be thin, isotropic, and made out of a homogeneous material whose mechanical properties are adjusted in order to match the behavior of an experimental composite prototype. Therefore within the framework of this

study, the standard Donnell–Mushtari theory, even though inaccurate for the low circumferential wave number, gives a sufficient first approximation of the resonant frequencies. The shape of the (n_s, m_s) structural mode shapes $\Psi^s_{n_s m_s}$ (the "s" superscript or subscript signifies that the variable refers to the structure) is given by

$$\Psi^s_{n_s m_s}(z, \theta) = \frac{1}{\sqrt{\Lambda_{n_s m_s}}} \sin\left(\frac{\pi n_s z}{L}\right) \begin{Bmatrix} \cos(m_s \theta) \\ \sin(m_s \theta) \end{Bmatrix}, \quad (1)$$

where the mode orders are $1 \leq n_s \leq n_{\max}$, $0 \leq m_s \leq m_{\max}$, L is the length of the cylinder, $\Lambda_{n_s m_s}$ is the normalization factor of the (n_s, m_s) mode, such that $\int\int_S (\Psi^s_{n_s m_s})^2 dS = S$, and S denotes the surface of the cylinder. Because of their symmetry, cylinders have circumferential modes whose orientation depends on the excitation location. Therefore, the cylinder is considered to have two orthogonal circumferential modes of the same order m_s: one sine and one cosine. These two modes are independent and although they have the same resonant frequency, the incident acoustic field excites them differently. This is equivalent to a single mode with an orientation angle that changes depending on the excitation. The out-of-plane velocity w can be described as a modal summation by

$$w(\theta, z, \omega) = \sum_{N_s} v_{n_s m_s}(\omega) \Psi^s_{n_s m_s}(\theta, z), \quad (2)$$

where $v_{n_s m_s}$ is the complex mode amplitude, and N_s is the total number of structural modes considered. Once the structural natural frequency $\omega_{n_s m_s}$ is obtained, the modal mobility of the cylinder $A^s_{n_s m_s}$ is derived using the second-order system equation:

$$A^s_{n_s m_s}(\omega) = \frac{i\omega}{M(\omega^2_{n_s m_s} - \omega^2 + 2\xi_{n_s m_s} i \omega_{n_s m_s} \omega)}, \quad (3)$$

where M is the mass of the cylinder, $\xi_{n_s m_s}$ the modal damping ratio, and $A^s_{n_s m_s}$ denotes a modal velocity over a modal force. In the simulations, the modal damping ratios are adjusted to be representative of the observable damping level in real composite cylinders. In the case of structures vibrating in dense fluid such as submarines, the effect of fluid loading (or radiation loading) on the structure dynamics must be taken into account. In the present case, the external radiation loading can be neglected because of the low density of air. The complex amplitude $v_{n_s m_s}$ of each structural mode is obtained by multiplying the mobility of the cylinder $A^s_{n_s m_s}$ by the total modal force $F_{n_s m_s}$ applied to the cylinder. Writing this in a matrix form yields

$$\mathbf{v} = \mathbf{A^s F}, \quad (4)$$

where $\mathbf{A^s}$ is an $N_s \times N_s$ diagonal matrix of modal mobilities obtained with Eq. (3), $\mathbf{F}$ is an $N_s \times 1$ vector of modal forces, and $\mathbf{v}$ is an $N_s \times 1$ vector of structural modal velocities.

Part of the force exerted on the cylinder is due to the incident acoustic plane wave. In order to calculate the external acoustic pressure acting on a cylinder, it is necessary to account for the scattering caused by the cylinder. The exter-

nal pressure at the cylinder surface P_{ext} is a function of the azimuth and elevation angles θ_i and α_i, respectively, and of the frequency ω of the wave, as shown in Fig. 1. Since the cylindrical baffle is assumed to be infinite, the scattering is only a function of angle θ. The simple phase dependence in the z direction can then be calculated from the axial wave number in air $k_z = k \sin \alpha_i$, where $k = \omega/c$, and c is the speed of sound in the fluid. From Morse and Ingard,[13] the pressure around the cylinder expressed in terms of cylindrical waves is the sum of the incident field pressure P_i and the scattered field pressure P_s:

$$P_{\text{ext}}(\theta,z,\omega,\theta_i,\alpha_i) = P_i(\theta,z,\omega,\theta_i,\alpha_i) + P_s(\theta,z,\omega,\theta_i,\alpha_i). \tag{5}$$

The amplitude of each scattered cylindrical wave is derived using a hard wall boundary condition. The pressure distribution P_{ext} on the surface of the cylinder due to an incident plane wave of amplitude P_0 is thus expressed as a summation of cylindrical waves of circumferential amplitude P_m,[13]

$$P_{\text{ext}}(\theta,z,\omega,\theta_i,\alpha_i)$$
$$= P_0 e^{i(k_z z - \omega t)} \sum_{m=0}^{\infty} P_m(\omega,\alpha_i) \cos(m(\theta - \theta_i)). \tag{6}$$

The exterior modal force $F_{n_s m_s}^{\text{ext}}$ that excites each mode is thus obtained by integrating the external pressure over the structural mode shape:

$$F_{n_s m_s}^{\text{ext}}(\omega,\alpha_i,\theta_i) = \int \int_S \Psi_{n_s m_s}^s P_{\text{ext}}(\theta,z,\omega,\alpha_i,\theta_i) dS, \tag{7}$$

where the structural mode shapes $\Psi_{n_s m_s}^s$ are given in Eq. (1). Note that any kind of force can be decomposed on the structural modal base using this method.

B. Structure–acoustic cavity coupling

In this section, the elements of the acoustic cavity model are derived using a similar approach as for the previously derived structural model, after which the coupling mechanisms between the two models are presented.

1. Cylinder acoustic model

Using Bessel functions[13] J_m, the acoustic mode shapes Ψ^a for a circular cylindrical enclosure of radius R are given by

$$\Psi_{nmp}^a(r,\theta,z) = \frac{1}{\sqrt{\Lambda_{nmp}}} J_m(k_{mp} r) \begin{Bmatrix} \cos(m\theta) \\ \sin(m\theta) \end{Bmatrix} \cos\left(\frac{\pi n z}{L}\right), \tag{8}$$

where Λ_{nmp} is the normalization factor such that $\int\int\int_V (\Psi_{nmp}^a)^2 dV = V$, V is the volume of the cavity, and the superscript "a" signifies that the variable refers to the acoustic cavity. The circumferential wave numbers k_{mp} are derived from the hard wall boundary condition $(\partial/\partial r) J_m(k_{mp} r)|_{r=R} = 0$. The resonant frequency of the (n,m,p) mode is thus given by $\omega_{nmp} = \sqrt{k_n^2 + k_{mp}^2}$, where $k_n = n\pi/L$ is the axial modal wave number. As with the structural modes, the cir-

cumferential orientation of an acoustic mode results from the combination of two independent orthogonal modes, one sine and one cosine, of the same order m. At any point (r,θ,z) inside the cylinder, the acoustic pressure $p(r,\theta,z,\omega)$ is approximated by the modal summation:

$$p(r,\theta,z,\omega) = \sum_{N_a} p_{nmp}(\omega) \Psi_{nmp}^a(r,\theta,z), \tag{9}$$

where p_{nmp} is the complex mode amplitude, and N_a the total number of acoustic modes considered. The acoustic modal impedance of the enclosed fluid A_{nmp}^a defined as a modal pressure over a modal acoustic source strength is given by

$$A_{nmp}^a(\omega) = \frac{\rho c^2 i \omega}{V(\omega_{nmp}^2 - \omega^2 + 2 i \xi_{nmp} \omega_{nmp} \omega)}, \tag{10}$$

where ρ is the air density and ξ_{nmp} the modal damping ratio. This damping is incorporated to account for the absorption of the acoustic treatment that is usually present in real applications but is typically very small at low frequencies. Once an $N_a \times 1$ vector of acoustic modal source strengths $\mathbf{u}$ is defined, the $N_a \times 1$ vector of acoustic modal pressures $\mathbf{p}$ can be expressed by

$$\mathbf{p} = \mathbf{A^a u}, \tag{11}$$

where $\mathbf{A^a}$ is the $N_a \times N_a$ diagonal matrix of modal acoustic impedances of the cylinder calculated from Eq. (10). Once the components of the structural and acoustic model are defined, the two models are coupled together, as described below.

2. Structural–acoustic spatial coupling

The coupling coefficient C between a structural and an acoustic mode is computed by integration of the product of their shapes over the cylinder surface at $r = R$,

$$C = \int_0^L \int_0^{2\pi} \Psi_{n_s m_s}^s(\theta,z) \Psi_{nmp}^a(R,\theta,z) R \, d\theta \, dz. \tag{12}$$

Due to the orthogonality of the sine and cosine function, the structural cosine circumferential mode couples only with the cosine circumferential acoustic modes and likewise with the sine modes. The coupling coefficients have the dimension of a surface (m²). These coefficients can thus form an $N_a \times N_s$ coupling matrix $\mathbf{C}$, whose elements are the result of the integral in Eq. (12),

$$C([n,m,p],[n_s,m_s])$$
$$= \frac{2RL J_m(Rk_{mp})}{\epsilon_m \sqrt{\Lambda_{n_s m_s} \Lambda_{nmp}}} \frac{n_s |(-1)^n - (-1)^{n_s}|}{(n_s^2 - n^2)} \delta_{m,m_s}, \tag{13}$$

where the Kronecker delta symbol δ_{m,m_s} is zero if $m \neq m_s$ and unity if $m = m_s$ and the Neumann symbol ϵ_m equals 1 if $m = 0$ and equals 2 if $m \neq 0$. Therefore, to obtain a coupling coefficient different than zero, the circumferential orders m_s and m of the structural and acoustic mode must be equal and the axial orders n_s and n, must define an odd–even or even–odd combination. Due to the $(n_s^2 - n^2)$ term in the denomi-
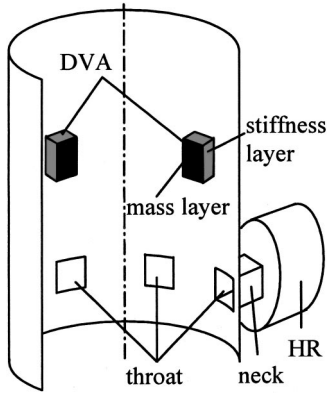
FIG. 2. Coupling between the cylinder and the noise reduction devices: HRs and DVAs.

nator of Eq. (13), modes with greatly different axial mode orders will be poorly coupled. As shown by Gardonio et al.,[4] the properties of the coupling coefficients C determine the number of modes required in the simulations. The number of acoustic modes can be reduced to those whose resonant frequencies lie inside a band slightly larger than the one of interest, however, the structural modes that are well coupled to the acoustic modes must be included, even though their resonant frequencies lie well outside the band of interest.

The matrix $\mathbf{C}$ represents the link between the structural and acoustic model. By means of its physical dimension (m^2), it converts the $N_s \times 1$ structural modal velocity vector $\mathbf{v}$ into an $N_a \times 1$ modal acoustic source strength vector $\mathbf{u}$, or, reciprocally, it converts the $N_a \times 1$ modal acoustic pressure vector $\mathbf{p}$ into an $N_s \times 1$ internal modal force vector $\mathbf{F^{int}}$:

$$\mathbf{u} = \mathbf{Cv}, \tag{14}$$

$$\mathbf{F^{int}} = -\mathbf{C^T p}; \tag{15}$$

$\mathbf{C^T}$ denotes the transpose of $\mathbf{C}$ and the minus sign used in Eq. (15) yields a positive $\mathbf{F^{int}}$ in the inward normal direction.

C. Coupling of the noise reduction devices

In this section we present the modeling of the noise reduction devices and their coupling to the structural and acoustic model.

1. DVA and HR modeling

As shown in Fig. 2, a DVA consists of a distributed spring typically made of acoustic polyurethane foam on which is placed a distributed mass. Therefore, a DVA can be considered as a vibration absorber acting over a surface area s_d. The reaction force of the DVA induced by the velocity of the structure represents the DVA impedance Z_d:

$$Z_d(\omega) = m_d \frac{i\omega\omega_d^2 + 2\zeta_d\omega^2\omega_d}{(\omega_d^2 - \omega^2) - 2i\zeta_d\omega\omega_d}, \tag{16}$$

where ω_d is the natural frequency, m_d the mass, and ζ_d the damping ratio of the DVA. The terms $Z_d(\omega)$ are grouped into an $N_d \times N_d$ diagonal DVA impedance matrix $\mathbf{Z_d}$, where N_d is the number of DVAs.

A HR consists of a rigid wall cavity of volume V_h and a neck of cross section area s_h and length l_h, as shown in Fig. 2. If all its dimensions are small compared to the acoustic wavelength, a HR can be modeled as an acoustic equivalent to a mechanical vibration absorber, where the air in the cavity acts like a spring, and the air in the neck like a lumped mass. The interior radiation mass effect is included by a correction factor[14] added to l_h, yielding an equivalent neck length l_e. The external radiation loading is accounted for by the summation of the N_a acoustic modes at the HR throat. Since this is a near-field effect, the convergence of the velocity amplitude at the throat of the HR with increasing N_a was checked. At resonance, the HR throat velocity converges quickly as only a 0.16 dB magnitude difference between $N_a = 76$ and $N_a = 273$ occurs. Thus, 76 is set as a lower bound for N_a. Using a second-order spring-mass system equation, the HR acoustic admittance, expressed as a volume velocity over a pressure, is given by

$$Y_h(\omega) = \frac{s_h i\omega}{\rho l_e[(\omega_h^2 - \omega^2) - 2i\zeta_h\omega\omega_h]}, \tag{17}$$

where $\omega_h = c\sqrt{s_h/V_h l_e}$ is the HR resonant frequency, and $l_e = l_h + 0.85\sqrt{s_h/\pi}$ for a square necked resonator. The admittance terms $Y_h(\omega)$ are grouped in an $N_h \times N_h$ diagonal HR admittance matrix $\mathbf{Y_h}$, where N_h is the number of HR.

In order to couple DVAs and HRs to the structural and acoustic model described in the previous sections, the velocity and pressure inputs to the impedance and admittance of the DVA and HR, respectively, are expressed using a modal summation at the location of the devices. This location on the surface of the cylinder with respect to a particular mode shape (node or antinode) defines a level of spatial coupling between the device and the different modes, as shown in the next section.

2. Structure–DVA and acoustic–HR spatial coupling

The coupling between a DVA and the cylinder is obtained by integrating each structural mode shape over the DVA rectangular surface of attachment $s_d = b \times a$ at its desired location (θ_0, z_0) on the cylinder. The contact surface between the cylinder and the DVA is assumed to be flat. Normalized by s_d, the dimensionless coupling coefficients $\varphi_{n_s m_s}^s$, are given by

$$\varphi_{n_s m_s}^s(\theta_0, z_0, s_d) = \frac{1}{s_d} \int_{z_0 - b/2}^{z_0 + b/2} \int_{\theta_0 - \Delta\theta}^{\theta_0 + \Delta\theta} \Psi_{n_s m_s}^s(\theta, z) R \, d\theta \, dz, \tag{18}$$

where $\Delta\theta = \sin^{-1}(a/2R)$. The structural modes in the mass layer of the DVA itself are not taken into account; it is assumed that the DVA applies a uniformly distributed normal force on the cylinder. The coefficients $\varphi_{n_s m_s}^s$ form $\mathbf{\Phi^s}$, a fully populated $N_d \times N_s$ matrix that couples N_d DVAs to N_s structural modes.

In a similar manner, the coupling between a HR and the enclosed fluid is computed by integrating each acoustic mode shape over the square area ($s_h = a \times a$) of the resonator throat at its desired location (r_0, θ_0, z_0) in the cylinder. In the simulations the resonators are assumed to lie outside the cyl-

inder and to couple at the circumference ($r_0 = R$). This is considered to be comparable to placing HRs inside the cavity, as long as the HR dimensions are small compared to the acoustic wavelength and have a small volume. By making this assumption, the mode shapes remain unchanged, and this simplifies the simulation considerably. As with the DVAs coupling, the HR throat is assumed flat over s_h,

$$\varphi_{nmp}^{a}(\theta_0, z_0, s_h) = \frac{1}{s_h} \int_{z_0 - a/2}^{z_0 + a/2} \int_{\theta_0 - \Delta\theta}^{\theta_0 + \Delta\theta} \Psi_{nmp}^{a}(R, \theta, z) R \, d\theta \, dz. \tag{19}$$

The coefficients φ_{nmp}^{a} form a fully populated $N_h \times N_a$ matrix, $\mathbf{\Phi^a}$, coupling N_h HRs to N_a acoustic modes. Using the different elements previously defined, the velocity and acoustic response of the fully coupled system is derived in the next section.

D. Matrix formulation of the coupled system

The coupling between all the components of the system is achieved using an impedance matching method. Therefore, the modal force $\mathbf{F^{DVA}}$ exerted on the structure by the DVAs is expressed as a function of the matrix $\mathbf{\Phi^s}$, its transpose $\mathbf{\Phi^{sT}}$, the diagonal matrix $\mathbf{Z_d}$, and the structural modal vibration vector $\mathbf{v}$:

$$\mathbf{F^{DVA}} = \mathbf{\Phi^{sT} Z_d \Phi^s v}. \tag{20}$$

Assuming the velocity distribution in the throat of the HR to be uniform over the surface s_h, HRs act as acoustic piston sources. Therefore, the total acoustic modal source strength

of the coupled system $\mathbf{u}$ is the sum of two quantities, $\mathbf{u^h}$ and $\mathbf{u^s}$. The modal source strength produced by the HR $\mathbf{u^h}$ is a function of the acoustic modal pressure $\mathbf{p}$, and the acoustic modal source strength due to the structure $\mathbf{u^s}$ given by Eq. (14) is a function of $\mathbf{v}$,

$$\mathbf{u} = \mathbf{u^h} + \mathbf{u^s} = \mathbf{\Phi^{aT} Y_h \Phi^a p} + \mathbf{Cv}. \tag{21}$$

Using Eq. (11), the acoustic modal pressure vector $\mathbf{p}$ due to the total acoustic source strength $\mathbf{u}$ becomes

$$\mathbf{p} = \mathbf{A^a}(\mathbf{\Phi^{aT} Y_h \Phi^a p} + \mathbf{Cv}). \tag{22}$$

The total force $\mathbf{F}$ exciting the cylinder is the sum of the external acoustic force $\mathbf{F^{ext}}$, the internal acoustic force $\mathbf{F^{int}}$ given by Eq. (15), and the reacting force of DVAs $\mathbf{F^{DVA}}$ given by Eq. (20). Expanding the vector $\mathbf{F}$ in Eq. (4) into these three components, the structural modal velocity vector $\mathbf{v}$ becomes

$$\mathbf{v} = \mathbf{A^s}(\mathbf{F^{ext}} - \mathbf{C^T p} + \mathbf{\Phi^{sT} Z_d \Phi^s v}). \tag{23}$$

Equations (22) and (23) are two coupled matrix equations defining the behavior of the fully coupled system. Solving this system of two equations yields $\mathbf{v}$ and $\mathbf{p}$ as a function of the external acoustic modal force $\mathbf{F^{ext}}$,

$$\mathbf{v} = \left[\mathbf{I} + \overbrace{\mathbf{A^s C^T}[\mathbf{I} - \mathbf{A^a \Phi^{aT} Y_h \Phi^a}]^{-1} \mathbf{A^a C}}^{\text{Coupling of acoustic space back onto structure}} - \mathbf{A^s \Phi^{sT} Z_d \Phi^s} \right]^{-1} \mathbf{A^s F^{ext}}$$

$$\underbrace{\phantom{\mathbf{I}}}_{\text{Exterior acoustic field}} \qquad \underbrace{\phantom{\mathbf{A^a C}}}_{\text{HRs}} \qquad \underbrace{\phantom{\mathbf{Z_d}}}_{\text{DVAs}} \tag{24}$$

$$\mathbf{p} = \underbrace{[\mathbf{I} - \mathbf{A^a \Phi^{aT} Y_h \Phi^a}]^{-1}}_{\text{HRs}} \mathbf{A^a C} \left\{ [\mathbf{I} + \mathbf{A^s C^T}[\mathbf{I} - \mathbf{A^a \Phi^{aT} Y_h \Phi^a}]^{-1} \mathbf{A^a C} - \mathbf{A^s \Phi^{sT} Z_d \Phi^s}]^{-1} \mathbf{A^s F^{ext}} \right\}. \tag{25}$$

$$\underbrace{\phantom{[\mathbf{I} + \mathbf{A^s C^T}]^{-1} \mathbf{A^s F^{ext}}}}_{\mathbf{v}}$$

Assuming the interior acoustic space to be relatively uncoupled from the structure, and so neglecting the internal acoustic force $\mathbf{F^{int}}$ in comparison to the external acoustic force $\mathbf{F^{ext}}$, the expression for $\mathbf{v}$ and $\mathbf{p}$ can be simplified to

$$\mathbf{v} = \left[\mathbf{I} - \overbrace{\mathbf{A^s \Phi^{sT} Z_d \Phi^s}}^{\text{DVAs}} \right]^{-1} \mathbf{A^s F^{ext}} \tag{26}$$

$$\mathbf{p} = \underbrace{[\mathbf{I} - \mathbf{A^a \Phi^{aT} Y_h \Phi^a}]^{-1}}_{\text{HRs}} \mathbf{A^a} \left[\mathbf{C} [\mathbf{I} - \underbrace{\mathbf{A^s \Phi^{sT} Z_d \Phi^s}}_{\text{DVAs}}]^{-1} \mathbf{A^s F^{ext}} \right]. \tag{27}$$

Several simulations using different damping ratios for the structure and the acoustic cavity, with different configurations of DVA and HR, have shown that the difference in the obtained noise reduction using Eqs. (26), (27) instead of Eqs. (24), (25), respectively, are negligible.

As is shown in the simplified equations (26) and (27), the vibration of the cylinder is only affected by the DVAs; however, the internal acoustic field represented by $\mathbf{p}$ is modi-

fied by both HRs and DVAs. In order to obtain an average sound pressure level independent of the location inside the cylinder, the total time average acoustic potential energy E_p is computed as

$$E_p(\omega) = \frac{1}{4c^2\rho} \int \int_V \int |p(\omega, r, \theta, z)|^2 \, dV. \tag{28}$$

If the modal expression for the pressure given by Eq. (9) is substituted into Eq. (28), the orthonormal properties of the modes allow the acoustic potential energy[15] to be computed using $\mathbf{p}$ and its Hermitian transpose $\mathbf{p^H}$:

$$E_p(\omega, \alpha_i, \theta_i) = \frac{V}{4\rho c^2} \sum_{N_s} |p_{nmp}(\omega, \alpha_i, \theta_i)|^2 = \frac{V}{4\rho c^2} \mathbf{p^H p}. \tag{29}$$

Similarly, the total structural kinetic energy is used as an indicator of the average vibration level of the cylindrical

TABLE I. Geometry and physical properties used in the numerical simulations.

Density of air ρ	1.19 kg m^{-3}
Speed of sound in air c	343 ms^{-1}
Density of structure ρ_s	380 kg m^{-3}
Young's Modulus E	3.5e Pa
Length of cylinder L	2.81 m
Radius of cylinder R	1.23 m
Thickness of cylinder	0.01 m

structure. Due to the orthogonality and normalization of the structural modes, the total structural kinetic energy E_k can be expressed by summing the square of the N_s structural modal velocities, which is equal to the product of $\mathbf{v}$ by its Hermitian transpose $\mathbf{v}^{\mathbf{H}}$,

$$E_k(\omega,\alpha_i,\theta_i) = \frac{1}{2} M \sum_{N_s} [v_{n_s m_s}(\omega,\alpha_i,\theta_i)]^2 = \frac{1}{2} M \mathbf{v}^{\mathbf{H}} \mathbf{v}. \quad (30)$$

III. NUMERICAL SIMULATION

The previously developed analytical formulation is applied to a cylinder whose geometry and physical properties are summarized in Table I. The incident acoustic wave excites the structure with an elevation angle $\alpha_i = 70°$ and an azimuth angle $\theta_i = 0°$. The structural and acoustic cavity damping ratios are set to 1% in order to be representative of the damping levels encountered below 200 Hz in a typical composite cylindrical enclosure.

A. Bare cylinder response to incident acoustic field

In this section we present the main sound transmission mechanisms in agreement with the detailed study by Gardonio et al.[4] The coupling between the external field and the structural modes characterizes the excitation of the cylinder. This external acoustic–structural coupling is represented by the external modal force $F_{n_s m_s}^{\text{ext}}$, which, after integration of Eq. (7), reduces to

$$F_{n_s m_s}^{\text{ext}}(\omega,\alpha_i) = P_0 \frac{2R\pi e^{-i\omega t}}{\sqrt{\Lambda_{n_s m_s}}} \frac{n_s \pi/L}{k_z^2 - (n_s \pi/L)^2}$$
$$\times [(-1)^{n_s} e^{ik_z L} - 1] P_{m_s}(\omega,\alpha_i). \quad (31)$$

The circumferential amplitude P_{m_s} denotes the scattering of the wave by the cylinder, and is plotted in Fig. 3(a) for different m_s as a function of frequency. This amplitude P_{m_s}, behaves like a "high-pass filter" whose cut-on frequency increases with the circumferential mode order m_s, except for the breathing mode $m_s = 0$, which has a maximum value at 0 Hz. The axial component represented by the term $\{n_s \pi/L/[k_z^2 - (n_s \pi/L)^2]\}[(-1)^{n_s} e^{ik_z L} - 1]$ is the Fourier wave number transform of the axial mode shape $\sin(n_s \pi/L)$. It represents the spatial coupling between the axial wave number in air $k_z = k \sin \alpha_i$ and the axial modal wave number $k_{n_s} = n_s \pi/L$ in the cylinder. This coupling is therefore characterized by a main lobe near the coincidence frequency between k_z and k_{n_s} and sidelobes of decaying amplitude. However, for $n_s = 1$, the axial modal wave number k_{n_s} represents
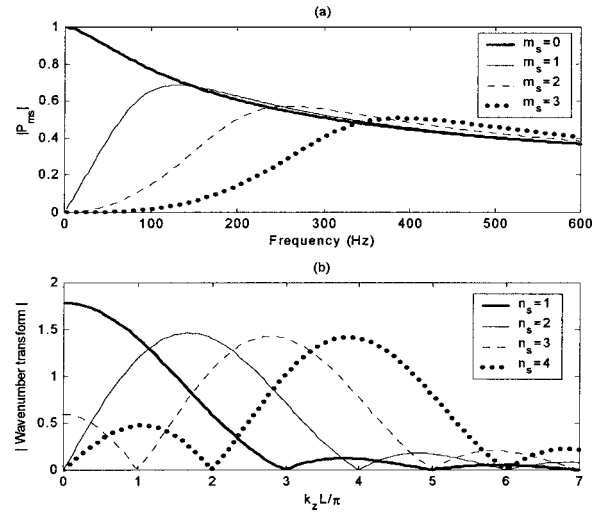
FIG. 3. (a) Magnitude of the circumferential amplitude P_{m_s} of $F_{n_s m_s}^{\text{ext}}$ due to an incident plane wave of 1 Pa. ($\alpha_i = 70°, \theta_i = 0°$) as a function of the excitation frequency for $m_s = 0,1,2,3$. (b) Magnitude of the Fourier wave number transform of $\sin(n_s \pi/L)$ as a function of the normalized axial wave number in air for $n_s = 1,2,3,4$.

only half of a wave along the length of the cylinder and so has its main lobe at $k_z = 0$. This axial component of $F_{n_s m_s}^{\text{ext}}$ is plotted in Fig. 3(b) as a function of the normalized axial wave number in air. Although 36 structural modes with circumferential order as high as 13 resonate below 200 Hz, Fig. 3 shows that only modes with circumferential order $m_s \leq 3$ and axial order $n_s \leq 5$ are well excited by the incident field. This is confirmed by Fig. 4, which shows that the structural kinetic energy of the bare cylinder, computed using all the modes resonating in the band, is dominated by only three lower-order modes. This filtering effect allows a reduction in the number of structural modes necessary to obtain convergence of the simulated results.

The internal acoustic response, plotted on top of the structural kinetic energy in Fig. 4 is composed of both acoustic resonances and structural resonances well excited by the incident acoustic field. The level of coupling between a structural and an acoustic mode is both spatial and frequency related. In Fig. 4, the (1,2) structural mode is well coupled to the (0,2,0) acoustic mode due to a maximum of the spatial
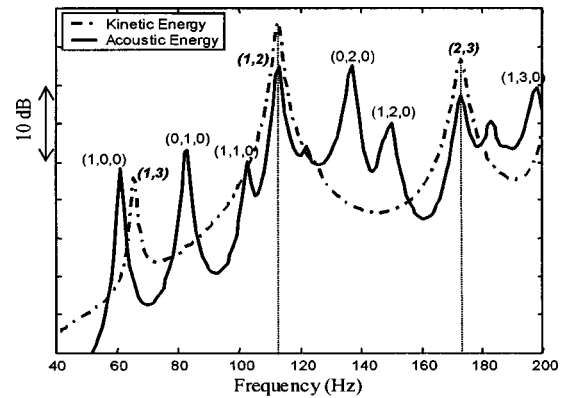
FIG. 4. Overlay of the structural kinetic and total acoustic potential energy curves due to an incident plane wave ($\alpha_i = 70°, \theta_i = 0°$), with structural mode order (bold italic) and acoustic mode order.

coupling coefficient $C([0,2,0],[1,2])$ given by Eq. (13), and also due to the proximity of the two resonances, 112 Hz for the (1,2) mode, and 137 Hz for the (0,2,0) mode. Therefore, the (0,2,0) acoustic mode is responsible for nearly all of the response in the 100–150 Hz range. Similarly, in the 160–200 Hz range, the coupling between the (2,3) structural and the (1,3,0) acoustic modes is responsible for the majority of the interior noise.

B. Noise reduction mechanisms

In this section we present the HRs' and DVAs' effects on the system and the strategies developed to optimize the noise attenuation. The mechanism of both HRs and DVAs is based on the dynamic vibration absorber system.[16] Consider a vibration absorber of mass m_d and natural frequency ω_d attached to a mass-spring system with mass m and natural frequency ω_n. Tuning the vibration absorber such that $\omega_d = \omega_n$ splits the resonance of the system into two new resonances of similar amplitude on either side of ω_n. The bigger the mass ratio, the farther apart the two resonances of the coupled system appear. By adding damping to the absorber (i.e., between the system and the absorber mass), both "new" resonances are well damped and significant broadband attenuation can be achieved. Depending on the type of excitation, several formulas for damping ratios[16,17] lead to optimal vibration reduction. For a wide band random excitation, the optimal damping ratio ζ_d^{opt} derived by Korenev and Reznikov[16] is expressed as

$$\zeta_d^{opt} = \sqrt{\frac{\nu(1+0.75\nu)}{4(1+\nu)^3}}, \quad (32)$$

where $\nu = m_d/m$. Once coupled to a continuous structure of mass M, the effective mass ratio ν is weighted by the normalized mode shape squared at the absorber location (θ_0, z_0),

$$\nu \simeq [\Psi_{n_s m_s}^s(\theta_0, z_0)]^2 \frac{m_d}{M}. \quad (33)$$

The coupling between a HR of volume V_h and an acoustic mode of an enclosure of volume V obeys the same mechanisms. By analogy with den Hartog's optimized dynamic absorber,[17] Fahy and Schofield[7] derive an optimal HR damping level ζ_h^{opt} as a solution of

$$\mu^2 \left(\frac{1}{2\zeta_h^{opt}}\right)^4 + \frac{4\mu}{\xi_{nmp}} \left(\frac{1}{2\zeta_h^{opt}}\right)^3 + \mu \left(\frac{1}{2\zeta_h^{opt}}\right)^2 - 1 = 0, \quad (34)$$

where ξ_{nmp} is the damping of the enclosure and μ the effective volume ratio, given by

$$\mu \simeq [\Psi_{nmp}^a(r_0, \theta_0, z_0)]^2 \frac{V_h}{V}. \quad (35)$$

In reality, the damping of the resonator is created by viscous losses of the air moving in the neck. Therefore the damping can be adjusted by placing small amounts of porous material in the HR throat. In a DVA, the damping is produced by structural losses in the acoustic foam as it compresses. Using different types of foam leads to different levels of damping for the DVAs. In both cases, the amount of vibration attenu-
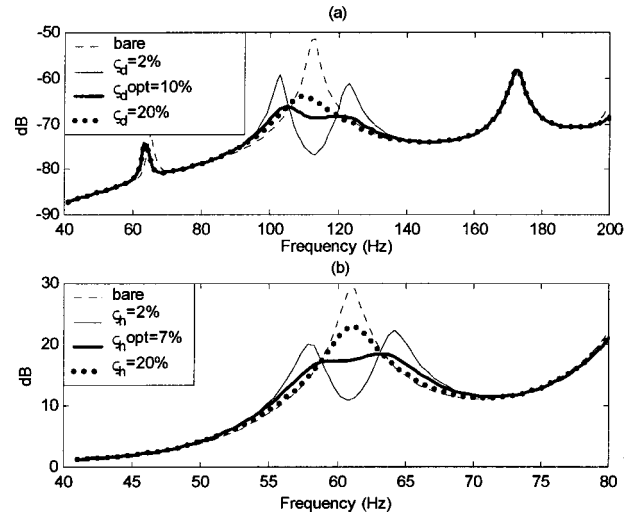
FIG. 5. (a) Influence of the damping ratio of the DVAs, ζ_d, on the structural kinetic energy of the cylinder, the optimal damping ratio ζ_d^{opt} is given by Eq. (32). (b) Influence of the damping ratio of the HRs, ζ_h, on the acoustic potential energy of the cylinder; the optimal damping ratio ζ_h^{opt} is given by Eq. (34).

ation is a weak function of the damping ratio, and thus a small variation about the optimal level only marginally degrades the performance of the HRs and DVAs.

To illustrate the mechanisms of the noise reduction devices, Fig. 5 shows the effect of the DVA and HR damping ratio on the structural kinetic energy (a) and the acoustic potential energy (b) response of the cylinder, respectively. With low damping, the two "new" modes are both fairly lightly damped and only small broadband noise reduction is achieved. Alternatively, if the damping is too high, the devices become uncoupled from the structural/acoustic mode and no longer dissipate energy.

In both cases the devices are split into several identical units distributed evenly around the circumference and tuned to the resonant frequency of the targeted mode: 112 Hz for the 13 DVAs and 61 Hz for the 5 HRs. Multiple devices are used for two reasons. First, using a symmetric ring of absorbers allows the treatment to be independent of the azimuth angle θ_i of the incident field that is assumed to be unknown. Consequently, only the axial mode shape component is used in the computation of the effective mass or volume ratio, which is weighed by $1/\epsilon_m$ since half the mass or volume of the devices is effectively acting on circumferential modes different than zero. Second, the devices act as discontinuities that can couple modes together by shifting energy from one circumferential mode to another. For instance, a

TABLE II. Amplitude of the (1,2) and (3,8) mode [normalized by the (1,2) mode amplitude of the bare cylinder] at 112 Hz for a 3 DVAs and 13 DVAs ring treatment tuned to 112.5 Hz.

Mode order (frequency)	Normalized mode amplitude at 112 Hz (dB)		
	Bare cylinder	Ring of 3 DVAs	Ring of 13 DVAs
1,2 (112.5 Hz)	0	−5.5	−18.5
3,8 (112.7 Hz)	−131	−8.5	−112

S. J. Estève and M. E. Johnson: Control of sound transmission into cylinder

TABLE III. Acoustic modes below 160 Hz.

Mode order (n,m,p)	Resonant frequency (Hz)
(1,0,0)	61
(0,1,0)	82.4
(1,1,0)	102.5
(2,0,0)	122
(0,2,0)	136.6
(2,1,0)	147
(1,2,0)	149.6

FIG. 6. Acoustic potential energy inside the cylinder excited by 1 Pa. Plane wave before and after treatment.

ring of N_d DVAs targeting a mode of circumferential order $m_s = i$ redistributes the energy to all $m_s = |i \pm q N_d|$ modes, where q is an integer. Thus, a DVA treatment is likely to excite structural modes that are not forced by the incident acoustic field. The closer the resonant frequency of the $m_s = |i \pm q N_d|$ mode is to the DVAs' tuning frequency, the higher the excitation. Therefore, a large number of DVAs per ring ensures a weak modal coupling since only modes with greatly different circumferential order, which in most cases implies greatly different resonant frequencies, can interact. As an example, Table II presents the performance on the targeted (1,2) structural mode of two different treatments, both weighing 2% of the total mass of the cylinder. A ring of 13 DVAs leads to an attenuation of 18 dB at the resonance, whereas a ring of 3 DVAs only reduces it by 5 dB and increases the amplitude of the (3,8) mode, which is barely excited by the external acoustic field.

C. Control of the 50–160 Hz band with DVAs and HRs

In this section we present an example of a treatment designed to control the interior acoustic level from 50 to 160 Hz. In this frequency band, the enclosure presents only seven acoustic modes listed in Table III. The first three are well separated and so are targeted individually by three independent rings of HR, whereas targeting two out of the last four modes ensures good reduction. Because the highest circumferential order below 230 Hz is $m = 3$, five HRs per ring is sufficient to obtain a negligible excitation of higher-order modes. A ring of 13 DVAs tuned to 112 Hz is used to target the structural (1,2) mode. Each ring of devices is placed on

an axial antinode of the targeted mode shape to maximize the effective volume ratio μ or mass ratio ν. The total volume of the HRs represents 6% of the cavity volume V, and the total mass of the DVAs 2% of the cylinder mass. The characteristics of this treatment are detailed in Table IV. Using sets of 76 acoustic modes and 36 structural modes, including the two orthogonal modes of the same circumferential order, the effect of the HRs and DVAs on the acoustic potential energy is plotted in Fig. 6. Although the optimally damped HRs reduce the acoustic resonances by more than 10 dB, almost half of the energy transmitted in the 50–160 Hz band is due to the (1,2) structural resonance, as shown in Fig. 6. The DVA treatment is therefore necessary to improve the noise reduction. Once the damping, the frequency, and the location of the devices are optimized, the performance of a treatment can only be improved by increasing both the total mass of DVAs and the total volume of HRs, as shown in Table V. Note that for each case, the damping is optimized with the new mass and volume ratios.

As explained previously, the DVA and HR noise reduction mechanism is based on adding damping to sharp structural and acoustic resonances responsible for the majority of the interior noise. Therefore, such treatment can be adapted to a different type of excitation by targeting in each different case the unfavorable resonances. However, the performance of these devices is directly related to the amount of damping initially present in the structure and in the acoustic cavity.

TABLE IV. Noise reduction device characteristics for the treatment used in Fig. 6.

	Ring of 13 DVAs total mass = 1.6 Kg					
Targeted mode	Tuning frequency (Hz)	Mass/M (%)	ν (%)	s_d (cm²)	ζ_d^{opt} (%)	z (m)
(1,2)	112.5	2	5	200	10	1.49

	Rings of 5 Hrs total volume = 0.8 m³					
Targeted mode	Tuning frequency (Hz)	Volume/V (%)	μ (%)	s_h (cm²)	ζ_h^{opt} (%)	z (m)
(1,0,0)	61	0.5	1	22	6.7	0.02
(0,1,0)	82.4	0.5	2	22	9.6	1.43
(1,1,0)	102.5	1	8.3	223	18.7	0.07
(0,2,0)	136.6	2	14.8	354	24.6	1.5
(1,2,0)	149.6	2	14.7	346	24.6	0.07

TABLE V. Attenuation in the 50–160 Hz band of the acoustic potential energy using the treatment described in Table IV for a different total mass of DVAs and total volume of HRs with optimal damping ratios computed accordingly.

50–160 Hz attenuation (dB)	Total volume of HRs (% of cavity volume)			
Total mass of DVA (% of cylinder mass)	3%	6%	9%	12%
1%	6.2	7.2	7.8	8.6
2%	6.7	7.7	8.3	9.1
4%	7.3	8.3	8.8	9.6

TABLE VI. HR-DVA treatment performance with different initial acoustic and structural damping ratios.

Acoustic and structural damping ratios (%)	Noise attenuation from 50–160 Hz (dB)
0.5	9.9
1	7.7
3	4.4
5	3.1
10	1.6
15	1.0

The higher the damping ratios of the system, the less reduction the treatment can provide. This is illustrated by Table VI, which displays the noise attenuation provided by the treatment described in Table IV over the 50–160 Hz band for different structural and acoustic initial damping ratios of the cylinder. When the structure and the acoustic cavity are lightly damped, i.e., structural and acoustic damping ratios below 3%, the DVAs and HRs can provide significant noise attenuation.

The performance of a combined HRs/DVAs treatment is also robust with respect to the elevation angle of the external acoustic plane wave. As an example, simulations show that the treatment detailed in Table IV, which is designed for an elevation angle of 70°, achieves attenuation between 6.2 and 8.2 dB in the 50–160 Hz band for different elevation angles between 30° and 80°. This is to be expected since the main mechanism of the control is damping and not modal restructuring, which is more sensitive to the primary excitation.

IV. CONCLUSIONS

This work evaluated the ability of a combined DVA/HR treatment to reduce the sound transmission in an enclosed cylindrical shell excited by an external plane wave. Using a modal expansion and an impedance matching method, the structure, the interior acoustic field, and the noise reduction devices were fully coupled, leading to the analytical formulation of the structural kinetic energy and the acoustic potential energy of a treated cylindrical cavity.

The analysis shows that at low frequencies, the structural vibration is only dominated by a few lower-order modes because of the coupling between the plane wave and the cylinder. The favorable coupling between these modes and the cavity generates an acoustic response composed of both acoustic and structural resonances. As a consequence, a significant reduction of the interior acoustic levels can only be achieved by using DVAs and HRs simultaneously.

As an example, an overall reduction of 7.7 dB in the 50–160 Hz band is obtained by using DVAs weighing only 2% of the cylinder mass and HRs representing 6% of its volume. This result was obtained by tuning the devices to the natural frequency of the targeted modes and by using optimal damping ratios for both DVAs and HRs. The devices were used in rings to avoid unfavorable modal interactions and to obtain a treatment independent of the azimuth angle of excitation. Such treatment is also robust to variations in the elevation angle of excitation as it is based on adding damping to sharp structural and acoustic resonances, and not on reducing the structural–acoustic coupling. In conclusion, this work has shown that lightweight DVA and small HR treatment can significantly reduce the sound transmission in an enclosure as long as the structure and the cavity are lightly damped, which is usually the case at low frequency in aerospace applications.

[1] Y. M. Huang and C. R. Fuller, "The effects of dynamic absorbers on the forced vibration of a cylindrical shell and its coupled interior sound field," J. Sound Vib. **200**, 401–418 (1997).

[2] Y. M. Huang and C. R. Fuller, "Vibration and noise control of the fuselage via dynamic absorbers," J. Vibr. Acoust. **120**, 496–502 (1998).

[3] C. Guigou, J. P. Maillard, and C. R. Fuller, "Study of globally detuned absorbers for controlling aircraft interior noise," *4th International Congress on Sound and Vibration*, St. Petersburg, Russia, June 1996.

[4] P. Gardonio, N. S. Fergusson, and F. J. Fahy, "A modal expansion analysis of the noise transmission through circular cylindrical shell structure with blocking masses," J. Sound Vib. **244**, 259–297 (2001).

[5] M. R. Jolly and J. Q. Sun, "Passive tuned vibration absorbers for sound radiation reduction from vibrating panels," J. Sound Vib. **191**, 577–583 (1996).

[6] K. Nagaya and L. Li, "Control of sound noise radiated from a plate using dynamic absorbers under the optimization by neural network," J. Sound Vib. **208**, 289–298 (1997).

[7] F. J. Fahy and C. Schofield, "Note on the interaction between a Helmholtz resonator and an acoustic mode of an enclosure," J. Sound Vib. **72**, 365–378 (1980).

[8] A. Cummings, "The effect of a resonator array on the sound field in a cavity," J. Sound Vib. **154**, 25–44 (1992).

[9] A. Doria, "Control of acoustic vibrations of an enclosure by means of multiple resonators," J. Sound Vib. **181**, 673–685 (1995).

[10] M. E. Johnson, C. R. Fuller, and P. Marcotte, "Optimization of distributed vibration absorber for sound transmission into a composite cylinder," *Proceedings of the 7th AIAA/CEAS Aeroacoustics Conference*, May 2001, p. 2232.

[11] H. Osman, M. E. Johnson, C. R. Fuller, and P. Marcotte, "Interior noise reduction of composite cylinders using distributed vibration absorbers," in Ref. 10, p. 2230.

[12] A. W. Leissa, "Vibration of shells," NASA-SP-288, 1973, Chap. 2, pp. 31–49.

[13] M. Morse and K. U. Ingard, *Theoretical Acoustics* (McGraw-Hill, New York, 1986), Chap. 8, p. 400; Chap. 9, p. 511.

[14] L. E. Kinsler, A. R. Frey, A. B. Coppens, and J. V. Sanders, *Fundamentals of Acoustics*, 4th ed. (Wiley, New York, 2000), Chap. 10, pp. 284–286.

[15] P. A. Nelson and S. J. Elliott, *Active Control of Sound* (Academic, New York, 1992), Chap. 10, pp. 319–322.

[16] B. G. Korenev and L. M. Reznikov, *Dynamic Vibration Absorbers* (Wiley, New York, 1993), Chap. 1, p. 62.

[17] J. P. den Hartog, *Mechanical Vibrations* (Dover, New York, 1985), Chap. 3, pp. 93–106.

Feasibility of a phased acoustic array for monitoring acoustic signatures from meshing gear teeth

Adrian A. Hood[a] and Darryll J. Pines

Alfred Gessow Rotorcraft Center, Department of Aerospace Engineering, University of Maryland,
College Park, Maryland 20742

This paper investigates the feasibility of sensing damage emanating from rotating drivetrain elements such as bearings, gear teeth, and drive shafts via airborne paths. A planar phased acoustic array is evaluated as a potential fault detection scheme for detecting spatially filtered acoustic signatures radiating from gearbox components. Specifically, the use of beam focusing and steering to monitor individual tooth mesh dynamics is analyzed taking into consideration the constraints of the array/gearbox geometry and the spectral content of typical gear noise. Experimental results for a linear array are presented to illustrate the concepts of adaptive beam steering and spatial acoustic filtering. This feasibility study indicates that the planar array can be used to track the acoustic signatures at higher harmonics of the gear mesh frequency. © *2002 Acoustical Society of America.* [DOI: 10.1121/1.1515790]

PACS numbers: 43.50.Cb, 43.50.Pn, 43.50.Yw [JHG]

I. INTRODUCTION

Acoustic noise in helicopter gearboxes arises from both structureborne and airborne sources as transmission elements mesh.[1–6] Characteristic frequencies commonly found in noise spectra tests typically appear at gearbox mesh frequencies and at harmonics of the mesh frequency.[7,8] During normal operation under loaded conditions, gearbox elements are subjected to damage due to gear tooth contact dynamics. Damage can manifest itself in a variety of forms, including pitting, scoring, spalling, and incipient cracks. While damage does effect system performance, many of these damage modes are the precursors to catastrophic failure. Thus numerous researchers have attempted to develop qualitative and quantitative fault detection methods using vibration measurements obtained from conventional accelerometers.[9–23] While the use of vibration measurements has led to the development of several fault indicators, such techniques are susceptible to coupled structureborne effects thus complicating the acceleration signal with coupled dynamics along the load path. These effects may obscure gearbox faults, especially for planetary systems. Fortunately, gearbox faults also appear via airborne paths as a result of tooth on tooth contact that occurs during meshing. Hence, sound radiating from gear contact may represent an alternative method for detecting incipient failure modes of individual teeth.

II. GEAR NOISE

Gear noise arises from several sources including structureborne noise due to transmission error, aerodynamic noise caused by the pumping action of the gears, impact noise due to meshing gears, and acoustic radiation caused by vibrating gear wheels and housing elements (Fig. 1). Transmission error is the difference between the actual position of an output gear and its ideal location based on the gear pair maintaining the same velocity ratio. Since the driving gear has to continuously accelerate and/or decelerate the teeth of the driven gear, a force is produced that excites the tooth and causes it to vibrate. These vibrations propagate throughout the gear drive system which includes the shafts, bearings, couplings, and housings and produces appreciable noise when it vibrates an efficient radiator like a panel. Some causes of transmission error include gear profile error, tooth and shaft deflection, runout error, and gear system dynamics. Airborne acoustics at the meshing location is also generated. Wang *et al.* modeled the airborne acoustics as the impact of two cylinders of variable radii of curvature and developed an analytical solution based on geometric parameters of the gear teeth and their duration of contact.[5] Houjoh investigated the aerodynamic noise caused by the expelling of trapped fluid caught in the root of meshing teeth. This fluid is expelled both axially and toward adjacent root spaces. The aerodynamic noise was modeled as a series of pumps with the teeth represented as pistons and the root spaces as cylinders.[3] The cylinder contains orifices to represent the axial and tangential acoustic paths. It was found that the aerodynamic noise originates as a point source from the middle of the facewidth in the mesh end region and also as a linear distribution of sources along the gear teeth in contact with a sine-like distribution of source strength. Sibe *et al.* modeled this aerodynamic noise as two out of phase sets of quadrupoles on the entrance and exit sides of the gear and determined the quadrupole parameters to fit the experimental data of Houjoh.[6] They deduced that the entrance side quadrupole dominates at low rotation speeds, and at high speeds the exit side quadrupole dominates. They also measured the directivity pattern of two spur gears and found that the tangential/radial power can be up to 30 dB more than in the axial direction. In their paper, they also modeled the gear wheel as a thick annular plate with boundary conditions such that the inner boundary is fixed to represent a rigid shaft and the outer is free except at the meshing location where a harmonic excitation force is

---

[a] Electronic mail: djpterp@aero.umd.edu
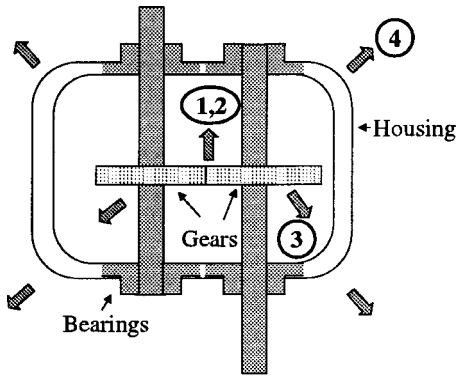
FIG. 1. Sources of gearbox noise: (1) transmission error, (2) pumping action of gears, (3) vibrating gear wheels, (4) vibrations of gearbox, shaft, couplings, etc.

assumed. They found that the pumping action dominates in the tangential direction and the acoustics from the bending modes of the gear wheel dominate axially. The resonance frequencies of the acoustic signatures appear at the natural frequencies of the gears plus integer multiples of the gear mesh frequency.

This paper attempts to develop the necessary framework for developing a microphone array for monitoring acoustic signatures for incipient failure modes associated with individual teeth by steering and focusing the array's main directivity lobe to track the element of interest. In this initial study, a planar array is proposed to filter out unwanted acoustic signatures from other elements. It is assumed that at the frequencies of interest, the radiation patterns are broad enough to be assumed omnidirectional.

III. THEORETICAL DEVELOPMENT

The inhomogeneous wave equation is described by

$$\nabla^2 P(t,\mathbf{r}) - \frac{1}{c^2}\frac{\partial^2 P(t,\mathbf{r})}{\partial t^2} = H(t,\mathbf{r}_s), \tag{1}$$

where $P(t,r)$ is the acoustic pressure at time t and position $\mathbf{r}$ as displayed in Fig. 2(a), c is the sonic velocity, and $H(t,\mathbf{r}_s)$ is a general time-dependent source term located at position $\mathbf{r}_s$.

A pulsating sphere of radius a located at $\mathbf{r}_0$ oscillating with multiple frequency content such that $k_{max}a \ll 1$, with $k_{max} = 2\pi f_{max}/c$ where f_{max} is the maximum frequency content of the acoustic pressure, can be represented as:

$$H(t,\mathbf{r}_0) = -4\pi \sum_{b=1}^{B} \Re\{C_b e^{j(\omega_b t + \Phi_b)}\}\delta(\mathbf{r}-\mathbf{r}_0), \tag{2}$$

for $C_b = (j\rho_0 c/4\pi)k_b Q_b$, where ρ_0 is the static density of air, Q_b, k_b, and Φ_b are the source strength, wave number, and relative phase of the bth frequency component, respectively, $\Re$ represents the real part, and B is the number of discrete frequencies. This results in an acoustic pressure given by

$$P(t,\mathbf{r}_0) = \sum_{b=1}^{B} \Re\left\{\frac{C_b}{|\mathbf{r}-\mathbf{r}_0|}e^{j(\omega_b t - k_b|\mathbf{r}-\mathbf{r}_0|+\Phi_b)}\right\}, \tag{3}$$

(a)

(b)
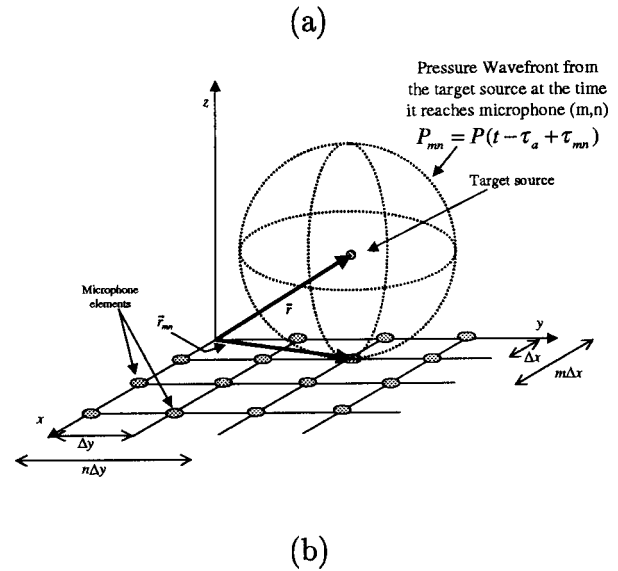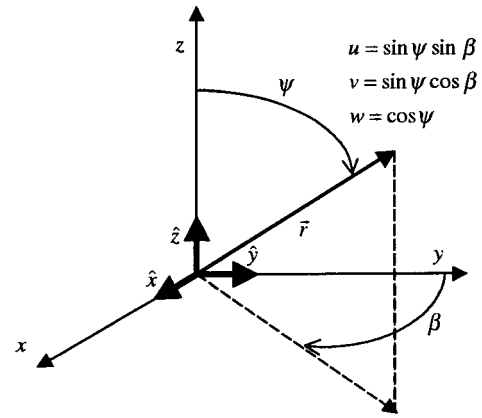
FIG. 2. (a) Direction cosines. (b) A spherical wave hitting the planar array at microphone (m,n).

where the role of source and sensor have been reversed, thus the source is located at $\mathbf{r}$ and the sensor is located at $\mathbf{r}_0$.

A. Discrete planar microphone array

The source is assumed to be an omnidirectional point source, therefore the pressure, described by Eq. (3), can be represented by a spherically diverging wave front. Figure 2(b) shows one quadrant of a distribution of omnidirectional microphones in the $x-y$ plane being acted upon by this wave front. The source is located at $\mathbf{r}=|\mathbf{r}|\hat{\mathbf{r}}$ for $\hat{\mathbf{r}}$ given by $\hat{\mathbf{r}}=u\hat{\mathbf{x}}+v\hat{\mathbf{y}}+w\hat{\mathbf{z}}$, where u, v, and w are the direction cosines of the source. The location of each microphone is described by

$$\mathbf{r}_0 = \mathbf{r}_{mn} = (m\Delta x)\hat{\mathbf{x}} + (n\Delta y)\hat{\mathbf{y}}, \tag{4}$$

where m and n are both integers and Δx and Δy are the uniform interelement spacing in x and y directions, respectively. The sphere, shown in Fig. 2(b), represents the acoustic pressure wave front at the time it reaches the microphone located at $\mathbf{r}_{mn}$, therefore it can be described by

$$P(t, \mathbf{r}_{mn}) = P(t - \tau_a + \tau_{mn}), \tag{5}$$

where $\tau_a = |\mathbf{r}|/c$ is the time it takes for the sound to reach the center of the array. The term, τ_{mn}, is the relative time delay between the center microphone and the microphone located at $\mathbf{r}_{mn}$ and is given by

$$\tau_{mn} = \frac{|\mathbf{r}| - R_{mn}}{c}, \tag{6}$$

where R_{mn} is the radius of the sphere and is given by $R_{mn} = |\mathbf{r} - \mathbf{r}_{mn}|$. Therefore,

$$R_{mn} = \sqrt{r^2 + r_m^2 + r_n^2 - 2r[ur_m + vr_n]}, \tag{7}$$

where $r_m = m\Delta x$ and $r_n = n\Delta y$.

The objective is to determine the frequency spectrum of the target source assuming that the direction cosines of the source are known a priori. The discrete sampled electrical response for a microphone located at position $\mathbf{r}_{mn}$ is

$$y(t, \mathbf{r}_{mn}) = \sum_{l=0}^{L-1} y(l\Delta t, \mathbf{r}_{rm}) \delta(t - l\Delta t), \tag{8}$$

where L is the number of time series data points. Taking the temporal Fourier transform of Eq. (8) and multiplying the individual frequency spectra of each microphone signal by a complex gain $c_{mn}(q) = \eta_{mn}(q) e^{j\theta_{mn}(q)}$ and then summing up each microphone produces

$$\mathbf{Y}(q) = \sum_{m=-M'}^{M'} \sum_{n=-N'}^{N'} c_{mn}(q) \sum_{l=0}^{L-1} y(l\Delta t, \mathbf{r}_{rm}) W_L^{-lq}, \tag{9}$$

where $W_L = e^{j2\pi/L}$. Equation (9) represents the weighted sum frequency spectrum of the acoustic source for $M' = (M-1)/2$ and $N' = (N-1)/2$, where M and N are both odd number of microphones in the x and y directions, respectively. As will be shown in Sec. III B, $c_{mn}(q)$ is used to control the array's sensitivity for acoustic sources coming from different directions.

If each microphone has a flat frequency response given by $\bar{\alpha}_{mn}$, then $P(l\Delta t, \mathbf{r}_m) = \bar{\alpha}_{mn} y(l\Delta t, \mathbf{r}_{rm})$. Substituting this result into Eq. (9) and using Eq. (5), yield

$$\mathbf{Y}(q) = \sum_{m=-M'}^{M'} \sum_{n=-N'}^{N'} \bar{\sigma}_{mn} \sum_{l=0}^{L-1} P(l\Delta t - \tau_a + \tau_{mn}) W_L^{-lq}, \tag{10}$$

where $\bar{\sigma}_{mn} = c_{mn}(q)/\alpha_{mn}$. The Fourier coefficients for the pressure without the time delay is given by

$$\bar{P}_q = \frac{1}{L} \sum_{l=0}^{L-1} P(l\Delta t) W_L^{-lq} \tag{11}$$

and the Fourier coefficients of the shifted signal, $P(t - \tau_a + \tau_{mn})$, is $\bar{P}_q e^{j2\pi q\Delta f(\tau_{mn} - \tau_a)}$. Therefore,

$$\sum_{l=0}^{L-1} P(l\Delta t - \tau_a + \tau_{mn}) W_L^{-lq} = L\bar{P}_q e^{j2\pi q\Delta f(\tau_{mn} - \tau_a)}. \tag{12}$$

Substituting this result into Eq. (10) generates the following relationship:

$$\mathbf{Y}(q) = \underbrace{L\tilde{P}_q e^{-j2\pi q\Delta f\tau_a}}_{DFT\{P(t-\tau_a)\}} \underbrace{\sum_{m=M'}^{M'} \sum_{n=-N'}^{N'} \frac{c_{mn}(q)}{\bar{\alpha}_{mn}} e^{j2\pi q\Delta f\tau_{mn}}}_{\bar{D}(q, \psi, \beta)},$$
$$\tag{13}$$

where the first term is the Fourier coefficient at $f = q\Delta f$ of the pressure at the middle microphone and $\bar{D}(q, \psi, \beta)$ is the un-normalized directivity function at a given frequency, $f = q\Delta f$. The terms ψ and β are included in the argument of $\bar{D}(q, \psi, \beta)$ to show how the directivity function is an explicit function of the target's direction cosines. The discrete Fourier coefficient at $f = q\Delta f$ is adjusted in magnitude and phase before summing. As shown in subsequent sections, the spot diameter is a function of the target frequency, hence there is a different spot diameter for each frequency component. Thus, the energy from the higher frequency component is heard from a narrower region of the acoustic field. The spot diameter dependence on frequency can be countered by the frequency-dependent weighting $\eta_{mn}(q)$. A method that divides the microphone array into clusters and selects the weights based on the cluster is discussed in Brooks et al.[24]

B. Beam steering and focusing

Let us define c_{mn} as

$$c_{mn}(q) = \eta_{mn}(q) e^{-j2\pi q\Delta f\tau'_{mn}}, \tag{14}$$

where $\eta_{mn}(q)$ is the frequency-dependent array aperture window function that describes the relative amplitude weighting of each microphone in the array and is used to modify the shape of the directivity pattern, and $\tau'_{mn} = (r - R'_{mn}/c)$, where

$$R'_{mn} = \sqrt{r^2 + r_m^2 + r_n^2 - 2r[u'r_m + v'r_n]} \tag{15}$$

is used to steer and focus the array to a direction corresponding to the direction cosines: $u' = \sin\psi' \sin\beta'$ and $v' = \sin\psi' \cos\beta'$, where ψ' and β' are the angles corresponding to the target source. For the present discussion, $\eta_{mn}(q)$ is assumed to be frequency independent. Substituting Eq. (14) into Eq. (13) and dividing by the number of microphones yields the following normalized spectrum:

$$\bar{\mathbf{Y}}(q) = \bar{H} \sum_{m=-M'}^{M'} \sum_{n=-N'}^{N'} \frac{\eta_{mn}}{\bar{\alpha}_{mn}} e^{-j2\pi q\Delta f(\tau'_{mn} - \tau_{mn})}, \tag{16}$$

where $\bar{H} = L\bar{P}_c e^{-j2\pi q\Delta f\tau_a}/MN$. Equation (16) will have its greatest response when $\tau'_m = \tau_m$, i.e., the array is steered and focused to the target.

Therefore, computing

$$\bar{\mathbf{Y}}(q) = \frac{1}{MN} \sum_{m=-M'}^{M'} \sum_{n=-N'}^{N'} \frac{\eta_{mn} e^{-j2\pi \Delta f\tau'_{mn}}}{\bar{\alpha}_{mn}} P_{mn}(q), \tag{17}$$

where P_{mn} is the spectrum of the pressure at $\mathbf{r}_{mn}$, corresponds to the spatially filtered response of Eq. (16).

C. Array aperture window functions

In this section, the effect of the array aperture window, η_{mn}, on the shape of the array's directivity function will be

(a)

(b)
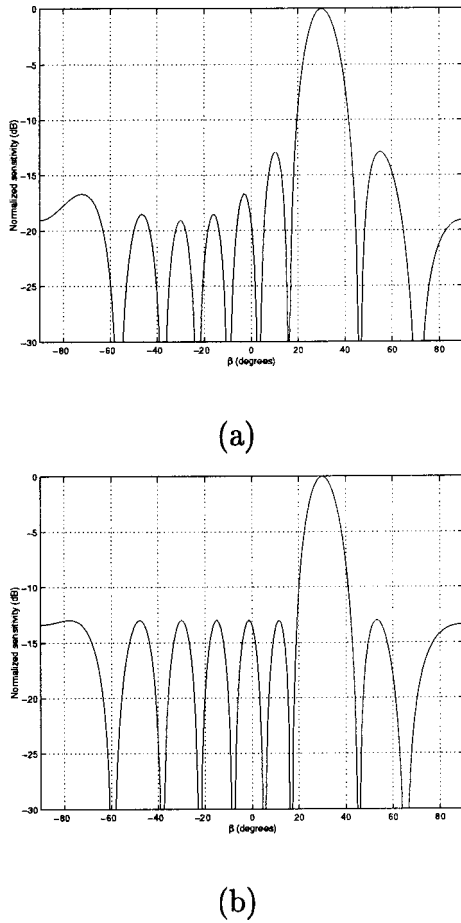
FIG. 3. Directivity functions steered to 30°, $(k\Delta x = \pi)$: (a) rectangular aperture window, $\eta_m = 1$, (b) Dolph–Chebyshev aperture window (-13 dB).

discussed. If the microphones are assumed omnidirectional and all have the same sensitivity, then $\bar{\alpha}_{mn} = \bar{\alpha}$, where $\bar{\alpha}$ is the sensitivity constant that can be set to unity without any loss in generality.

The normalized directivity pattern, $D(q, \psi', \beta') = (1/MN)\bar{D}(q, \psi', \beta')$, is given by

$$D(q, \psi', \beta') = \frac{1}{MN} \sum_{m=-M'}^{M'} \sum_{n=-N'}^{N'} \eta_{mn} e^{j2\pi q \Delta f(\tau'_{mn} - \tau_{mn})}.$$
(18)

A linear array is used with the understanding that the insight gained is directly applicable to the two-dimensional case projected onto the X–Y plane ($\psi' = \pi/2$). For the case in which the array is properly focused and steered to β':

$$D\left(f, \frac{\pi}{2}, \beta'\right) = \frac{1}{M} \sum_{m=-M'}^{M'} \eta_m e^{jk(R_m - R'_m)},$$
(19)

where the relationships $f = q\Delta f$, $k = 2\pi f$, are used. Also, Eqs. (7) and (15) reduce to

$$R_m = \sqrt{r^2 + r_m^2 - 2rr_m \sin \beta},$$
(20)

$$R'_m = \sqrt{r^2 + r_m^2 - 2rr_m \sin \beta'},$$
(21)

for $r_m = m\Delta x$.

For the case of a rectangular aperture window, $\eta_m = 1$, the response using 9 microphones is shown in Fig. 3(a) for

$k\Delta x = \pi$. The beamwidth, measured by the angle between the -3 dB points, is about 11.3° and the next sidelobe level is -13 dB. Notice also that the main sensitivity lobe was properly shifted to 30°.

Other aperture window functions can be used to modify the shape of the directivity function, but the trend is that the smoother the aperture window function approaches zero, the smaller the sidelobe levels, but at a cost of wider beamwidths.[25] An exception is the proper choice of Dolph–Chebyshev weights which allows, for a given sidelobe level, the narrowest beamwidth.[25] This method involves shaping the directivity pattern to take the form of a $(M-1)$th-order Chebyshev polynomial with predetermined sidelobe levels and computing the appropriate microphone weights. The trend is still the same in that the smaller the sidelobe level, the wider the beamwidth, however, it is possible to get a narrower beamwidth than that given by using a rectangular aperture window. Figure 3(b) shows a normalized plot using the Dolph–Chebyshev weighted aperture window and the sidelobe level set to -13 dB to directly compare it with the rectangular aperture window case. The maximum response is shown to be -2.6 dB less. Although, at -13 dB, the Dolph–Chebyshev aperture window produces a smaller beamwidth, its only narrower by 2.5%. Also shown is the fact that the use of Dolph–Chebyshev weights have the undesirable feature of constant sidelobe levels that do not drop off with increased angle like the case for the rectangular aperture window. Because it is desired to have a sidelobe level that drops off with the increased angle, at least -13 dB sidelobe attenuation, and because there is no significant benefit in using the Dolph–Chebyshev weights to achieve a significantly narrower beamwidth, this feasibility study is based on using a rectangular aperture window function.

D. Interelement spacing

To avoid grating lobes due to aliasing, the distance between microphones must satisfy the Nyquist condition: $\Delta x \leq \lambda_{min}/2$ where λ_{min} is the minimum wavelength component it the signal. Figure 4(a) shows how the beamwidth varies with the interelement distance, Δx, for a target frequency of 2 kHz where Δx is given as a percentage of the Nyquist distance, $\lambda_{min}/2$. Different plots are made for varying number of microphones. Figure 4 shows that as $\Delta x \mapsto \lambda_{min}/2$, the beamwidth gets narrower. Also, the beamwidth narrows as the number of elements increase. This suggests that the larger the array, the narrower the beamwidth. Of course, there is a practical limit to the size of the array and this is discussed in subsequent sections. Since the beamwidth decreases as the interelement spacing approaches the Nyquist distance, the desired microphone spacing is $\Delta x = \lambda_{min}/2$.

A target with multiple frequencies will have a different directivity pattern for each frequency component. Hence, if the microphone spacing is fixed, then the spacing would have to be less than half the smallest wavelength in the signal to avoid grating lobes. Figure 4(b) shows a plot of the beamwidth versus $f^* = f/f_{max}$ for 5 different numbers of microphones where f is the frequency component of interest. This figure shows that the beamwidth for frequencies less than the maximum frequency will be wider. As an example,

A. A. Hood and D. J. Pines: Acoustic array for monitoring meshing gears
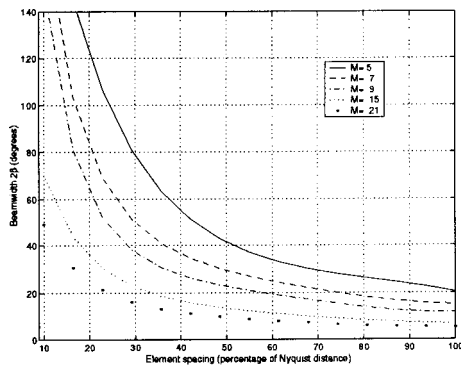
(a)
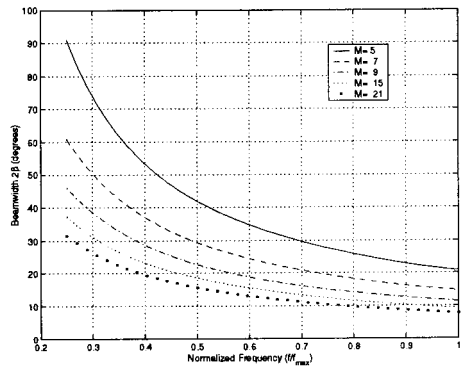
(b)

FIG. 4. (a) Beamwidth versus interelement spacing (2 kHz). (b) Beamwidth, 2β, in degrees.

for a 9 element array with a pressure signal containing two harmonics at 4 and 6 kHz, the beamwidth for the 6 kHz signal ($f^*=1$) is 11.3° and the beamwidth for the 4 kHz signal ($f^*=2/3$) would increase to about 17°. Figure 4 also shows that as the number of sensors increase, the beamwidth decrease for the same f^*. The desire is to get the smallest beamwidth possible, which would favor higher frequencies, larger interelement spacing, and larger arrays.

IV. MICROPHONE ARRAY TO MONITOR GEAR MESHING DYNAMICS

This section will discuss the feasibility of using a discrete planar acoustic array to monitor the gear meshing dynamics of a planetary gear transmission system.

Figure 5(a) shows the relative geometry of the profile of a discrete circular planar array with maximum radius of R_a sensing the acoustics from a planetary gear system with 6 meshing locations. The goal is to create a beamwidth that will achieve a spot diameter of $2a_d$ meters. The gears are located at a perpendicular distance d_g from the array. The necessary spot angle (2β) is found to be

$$2\beta = 2\tan^{-1}\frac{a_d}{d_g}. \tag{22}$$

Because a discrete planar circular array can be thought of as a linear array swept about an axis perpendicular to the plane
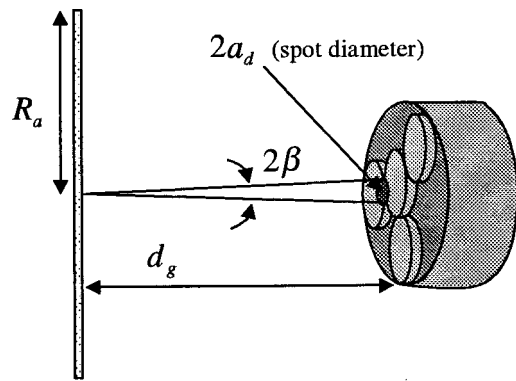
(a)
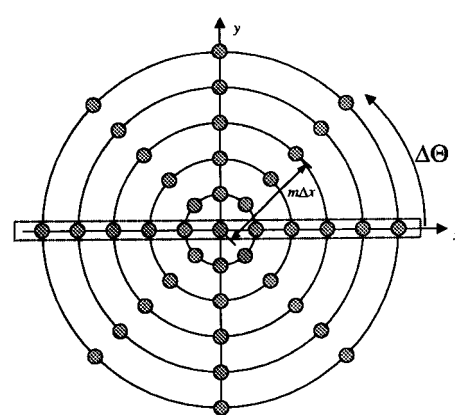
(b)

FIG. 5. (a) Illustration with profile of planar array. (b) Swept linear array geometry.

of the array and through the middle element [Fig. 5(b)], the directivity pattern it produces will follow suit. Therefore, the beamwidth of the resulting directivity pattern for the discrete linear array will match that for the discrete concentric circular array. Whereas the beam pattern for a linear array can be swept about the axis parallel to the linear array, the planar array is required to create a spot diameter. For this reason, the linear array will be analyzed with the beamwidth results being understood to also correspond to the beamwidth of a concentric circular array with the same radial microphone spacing.

Equation (17) is based on a rectangular grid of microphones, therefore a minor modification is required for a discrete concentric circular grid. Let $\Delta\Theta$ be the discrete angle with respect to the x axis and $r_m = m\Delta x$ be the radial distance from the center of the array to microphone (m,n)- [Fig. 5(b)]. Therefore, $\mathbf{r}_{mn}$ can now be described by

$$\mathbf{r}_{mn} = m\Delta x\,\cos(n\Delta\Theta)\hat{\mathbf{x}} + m\Delta x\,\sin(n\Delta\Theta)\hat{\mathbf{y}}, \tag{23}$$

where now m ranges from 1 to M'' and n ranges from 1 to (N''), where M'' is the number of microphones in the radial direction and $N'' = 2\pi/\Delta\Theta$ is the number of discrete angles ($\mathbf{r}_{00}=0$). Equation (6) is still used to evaluate τ_{mn}, however, R_{mn} is now evaluated using
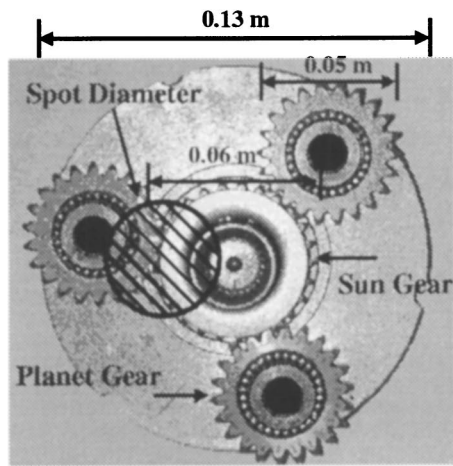
(a)
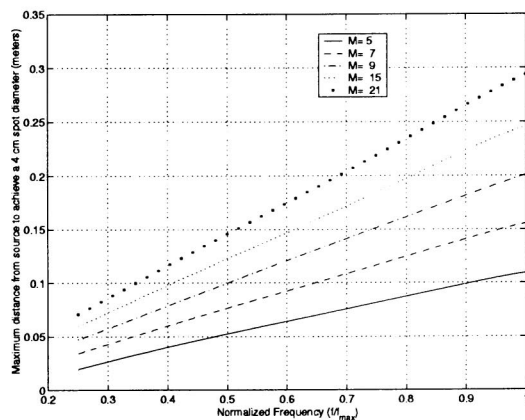
(b)

FIG. 6. (a) Testbed planetary gear. (b) Maximum distance to achieve a 0.04 m spot diameter.

$$R_{mn} = |\mathbf{r} - \mathbf{r}_{mn}| = \sqrt{r^2 + r_m^2 - 2rr_m\overline{\Omega}} \qquad (24)$$

for $r_m = m\Delta x$ and $\overline{\Omega} = u\,\cos(n\Delta\Theta) + v\,\sin(n\Delta\Theta)$. Equation (17) now can be rewritten as

$$\overline{\mathbf{Y}}(q) = \overline{V}\left\{ \frac{c_0}{\overline{\alpha}_0} P_0(q) \right.$$
$$\left. + \sum_{m=1}^{M''} \sum_{n=1}^{N''} \frac{\eta_{mn} e^{-j2\pi q\Delta f\tau'_{mm}}}{\overline{\alpha}_{mn}} P_{mn}(q) \right\}, \qquad (25)$$

where c_0 and $\overline{\alpha}_0$ are the complex gain and sensitivity of the middle microphone, respectively, $P_0(q)$ is the Fourier coefficient of the middle microphone at $f = q\Delta f$, and $\overline{V} = 1[(M''-1)N''+1]$.

The dimensions of the testbed planetary gear system are shown in Fig. 6(a). The sun gear has 25 teeth, each planet gear has 22 teeth, and the ring gear—not shown—has 71 teeth producing a mesh frequency of 431 Hz. The ultimate goal is to be able to isolate the planet/ring meshing and planet/sun meshing at different meshing locations. The target spot diameter, shown in Fig. 6(a), is 4 cm. From Eq. (22), the
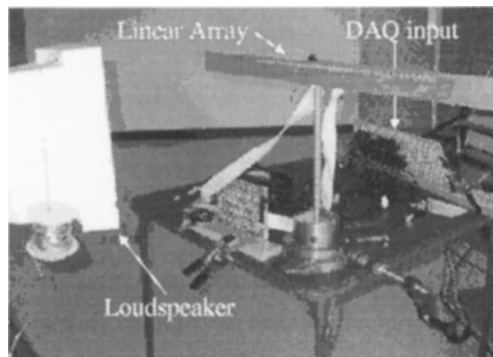
FIG. 7. Experimental setup.

maximum distance the array can be from the source in order to achieve the correct spot diameter for a given frequency is

$$d_g(f) \leqslant \frac{a_d}{\tan(\beta(f))}, \qquad (26)$$

where the f in the arguments of d_g and β are to show the explicit dependence of these terms on the frequency. Using the results, $\beta(f^*)$, from Fig. 4(b) for the rectangular array aperture window, Fig. 6(b) is generated.

Figure 6 shows that the maximum distance the microphone array can be from the gear increases linearly with frequency. Suppose the array consists of 9 microphone elements and the maximum frequency of interest is 3 kHz. The array length would be 0.44 m with an interelement spacing of 0.06 m. Also suppose the array is placed 0.1 m away from the gears. Then the minimum frequency ratio, f^*, at which a 0.04 m spot diameter is possible is $f^* = 0.5$, which puts f_{min} at 1.5 kHz. This range would correspond to the fourth through seventh harmonics of the mesh frequency of the planetary gear test bed. Figure 6(b) would suggest that by choosing the interelement spacing to be the Nyquist distance of the highest frequency content, the narrowest bandwidth is possible using the rectangular aperture function. However, the smaller the maximum frequency, the larger the distance between microphone elements will be, thus the size of the array will be larger. Not only is there a practical limit as to how far the array can be from the gears, but there is also a practical limit as to how large the array can be.

V. EXPERIMENTAL VALIDATION

A. Directivity pattern

To validate the analysis of the previous sections, a 0.6 m linear acoustic array consisting of 39, 9.8 mm omnidirectional microphones was constructed with a microphone spacing of 15.2 cm. A photograph of the experimental setup is shown in Fig. 7. The individual frequency response of each microphone was experimentally measured and calibrated against a calibrated 1/4 in. condenser microphone. The middle microphone was used as the reference and had a sensitivity of 1.2 mV/Pa for a 4.5 V excitation and the SPL of the speaker at the reference microphone was measured to be 102 dB re 20 μPa at 2 kHz. The source consisted of a loudspeaker placed 0.5 m away and excited at 2 kHz. The

A. A. Hood and D. J. Pines: Acoustic array for monitoring meshing gears
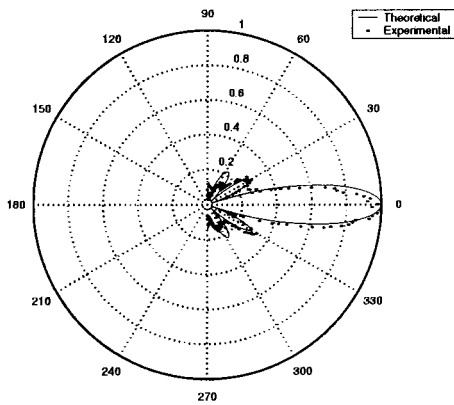
(a)
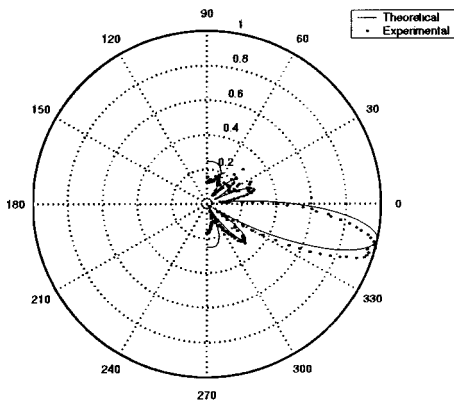
(b)

FIG. 8. Comparison with theory using 7 microphones. (a) Unsteered. (b) Steered to 45°.

speaker stayed fixed and the array was rotated from $\beta = -\pi/2$ to $\beta = \pi/2$. For each angle, the time history of each microphone was simultaneously collected at a sampling rate of 200 ks/s. For each angle, the fast Fourier transform of each microphone signal was computed and the resulting Fourier coefficients were multiplied by its appropriate gain as determined by Eq. (14) and then summed and recorded for that angle. Since this is done for a single frequency, the summed signal has the same frequency as the target frequency, thus the magnitude of the wave form was enough to characterize the resulting signal. Every 5th microphone (5th, 10th, 15th, 20th, 25th, 30th, and 35th), was used so that the spacing approached the Nyquist distance of 85.5 cm as much as possible with this fixed array configuration. The results are shown along with theoretical results obtained using simulated microphone time series in Fig. 8. In Fig. 8(a), the array was only focused. In Fig. 8(a), the array was focused and steered to −45°. The shift in the experimental case appears to be slightly off, which would suggest that during testing, the loudspeaker was slightly off-center. Nevertheless, the theory compares quite well with experiment.
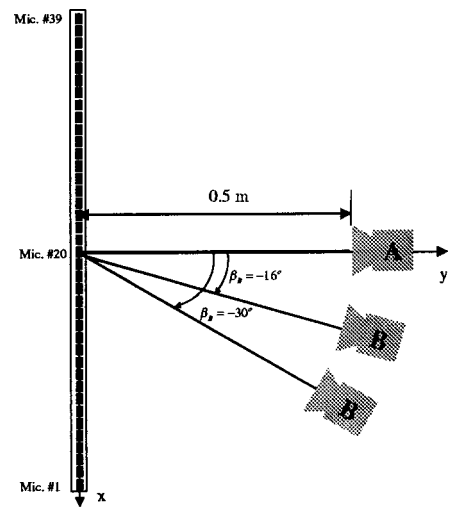
FIG. 9. Spatial filtering experimental setup.

B. Justification for treating microphones as omnidirectional

It is important to determine if these individual microphone elements have their own directionality. Suppose the individual elements do not act as omnidirectional point elements but instead have a continuous circular elemental aperture function $\eta(x,z) = \mathrm{circ}(r_a/a)$ where a is the radius of the microphone, and

$$\mathrm{circ}\left(\frac{r_a}{a}\right) = \begin{cases} 1 & r_a \leq a \\ 0 & r_a > a \end{cases} \tag{27}$$

for $r_a = \sqrt{x^2 + z^2}$. Since the microphone's membrane is continuous, its directivity pattern can be approximated by the far-field spatial Fourier transform of the microphone's aperture function. (This can be shown by using a similar analysis to that done for the discrete case. The far field is described by $kr > 10$, where r is the radial distance from the individual microphone.) The far field spatial Fourier transform of Eq. (27) becomes[25]

$$D(f,\psi,\beta) = a \frac{J_1((2\pi a/\lambda)\sin\psi)}{(\sin\psi/\lambda)}. \tag{28}$$

If we assume $J_1(2\gamma) \approx \gamma$, then the relative error is less than 10% if $\gamma < 0.4$. Therefore taking $\gamma = \pi a \sin\psi/\lambda < 0.4$ and setting $\sin\psi = 1$ to extremize the condition results in

$$\frac{\pi a}{\lambda_{min}} < 0.4 \mapsto a < \frac{0.4c}{f_{max}\tau} \mapsto a < \frac{43.7}{f_{max}}, \tag{29}$$

TABLE I. Spatial filtering results.

Speaker A Signal type (kHz)	Speaker B Signal type (kHz)	β_b	β'	Attenuation (dB)
2	3	−30°	0°	14
2	3	−30°	−30°	11
BL:20	2	−30°	−30°	15
2	BL:10	−16°	0°	20
10	2	−16°	−16°	47
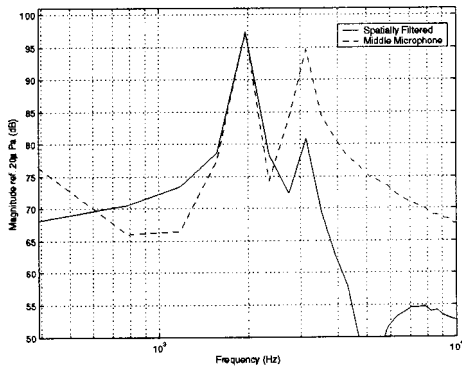
(a)
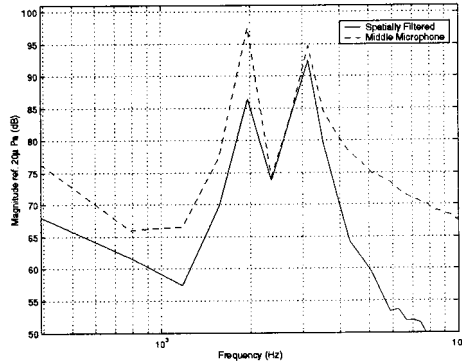
(b)

FIG. 10. Spatial filtering: (a) 2 kHz target at 0° with 3 kHz noise at −30, (b) 3 kHz target at −30° with 2 kHz noise at 0°.

where $\lambda_{\min}$ and $f_{\max}$ are the minimum source wavelength and maximum source frequency, respectively. In this case, the directivity function for each element is

$$D(f,\psi,\beta)\approx a\,\frac{\pi a/\lambda\ \sin\ \psi}{\sin\ \psi/\lambda}=\pi a^2. \qquad (30)$$

This shows that if Eq. (29) is satisfied, an elemental circular aperture function has the same space independent directivity function as that of an omnidirectional point element, just scaled by the area of the element, πa^2. For the current microphones, $a=4.6$ mm and the maximum source frequency for the microphones to be considered omnidirectional is $f_{\max}=9.3$ kHz.

C. Spatial filtering

In this setup, 2 loudspeakers were used, speaker A and speaker B. Speaker A was located at $\beta_A=0°$ while speaker B was located at $\beta_B=0°$, $\beta_B=-16°$ or $\beta_B=-30°$ (Fig. 9). The SPL at the reference microphone was 97.5 dB *re* 20 μPa at 2 kHz. Each loudspeaker was independently excited using various signals. The signal types and results are presented in Table I and figures of the spatially filtered spectrum plotted along with the spectrum of the reference microphone are given in Figs. 10–12.

The random signals were band limited to the frequency specified. Both speakers were located 0.5 m from the array
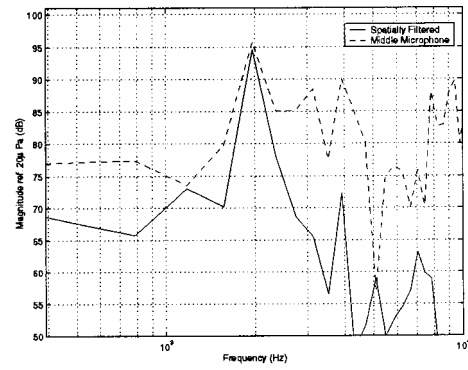
(a)
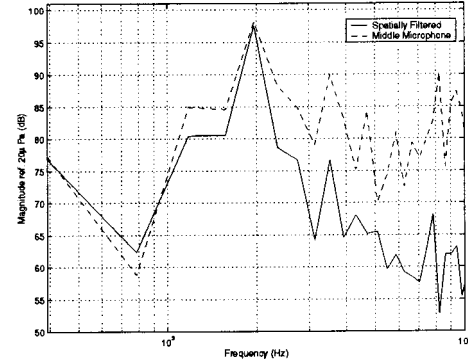
(b)

FIG. 11. Spatial filtering: (a) 2 kHz target at 0° with 20 kHz bandlimited white noise at −30°, (b) 2 kHz target at 0° with 10 kHz bandlimited white noise at −16°.

center. Each channel was simultaneously sampled at 200 ks/s using 512 points creating a frequency resolution of 390 Hz. Figure 10(a) shows the case for when the target is located at 0° and excited with a 2 kHz signal and the noise source is at −30° and excited at 3 kHz. A 14 dB attenuation at 3 kHz is obtained in this case. When the array is steered to the 3 kHz source, an 11 dB attenuation of the 2 kHz signal is obtained [Fig. 10(b)].

Figure 11(a) shows the case when the noise source is located at 0° and is excited with white noise band limited to 20 kHz. The target source is at −30°. The level of attenuation of the noise source was determined by averaging the difference between the filtered spectrum and the spectrum of the middle microphone up to 10 kHz. For this case, an average attenuation of 15 dB is obtained.

Figure 11(b) uses a white noise source band limited to 10 kHz and located closer to the target, 16°. A 20 dB average attenuation in the range up to 10 kHz is obtained.

Figure 12(a) is another case in which the separation is 16°. The level of attenuation of the 10 kHz signal is 47 dB. Figure 12(b) shows a time domain comparison between the signal at the middle microphone and the spatially filtered signal for the last case.

VI. CONCLUSIONS

The feasibility of using a phased planar acoustic array to monitor the gear meshing of a planetary gear transmission
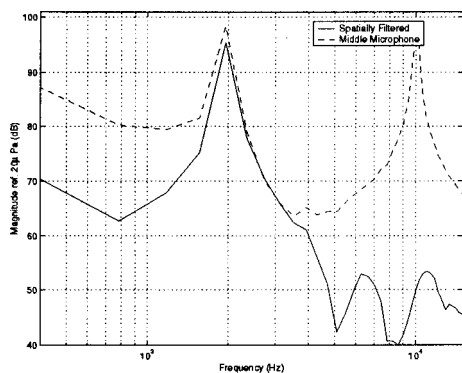
(a)
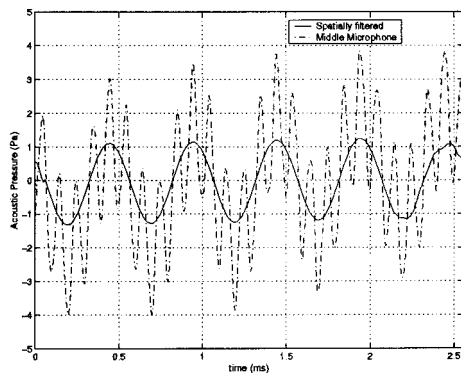
(b)

FIG. 12. Spatial filtering: (a) 2 kHz target at $-16°$ with 10 kHz noise at $0°$, (b) comparison between the signal at the middle microphone and the spatially filtered signal.

system has been investigated. The algorithm for beamshaping, steering, and focusing to achieve a narrow beamwidth was discussed and validated experimentally. The relationship between the array's proximity to the gears, array size, and the frequency range of interest was developed for a concentric circular array using uniform weights. It was found that source frequencies higher than the mesh frequency of our planetary gear testbed are required in order to obtain a spot diameter that can isolate different tooth meshing locations. In order to maintain a practical distance between the gear system and the microphone array of 0.1 m, the source frequency will have to be at least 1.5 kHz (Nyquist distance based on 3 kHz) in order to achieve a spot diameter of 4 cm. For this reason, it may be required that the higher harmonics of the acoustic signature be analyzed. The array's dimensions required for helicopter application are feasible in terms of the order of magnitude but are very dependent on the helicopter's size.

[1] J. Smith, *Gear Noise and Vibration* (Dekker, New York, 1999).
[2] F. B. Oswald, J. J. Zakrajsed, D. P. Townsend, W. Atherton, and H. H. Lin, "Effect of operating conditions on gearbox noise," Int. Power Transmission Gearing Conference **2**, 669–674 (1992).
[3] H. Honjoh, "Radiation mechanism for the aerodynamic sound of gears (an explanation for the radiation process by air flow observation)," JSME Int. J. **35**, 623–632 (1992).
[4] D. Houser, "The root of gear noise: Transmission error," Power Transmission Design, pp. 27–30 (1986).
[5] Y.-F. Wang and Z.-F. Tong, "Influence of gear errors on acceleration noise from spur gears," J. Acoust. Soc. Am. **99**, 2922–2929 (1996).
[6] A. Sibe and J. Sabot, "Gearbox noise: Description and modelling of the two main internal acoustic sources," Acta Acustica **85**, 850–858 (1996).
[7] M. Hayduk, E. Jacobs, and C. Lowenstein, "Recent advances in main transmission noise reduction for the sikorsky s-76 helicopter," *International Technical Specification Meeting*, October 1991, pp. 1–8.
[8] F. H. Schmitz and Y. H. Yu, "Helicopter impulsive noise: Theoretical and experimental status," J. Sound Vib. **109**, 361–422 (1986).
[9] R. Stewart, "Some useful analysis techniques for gearbox diagnostics," *Report No. MHM/R/10/77, Machine Health Monitoring Group, Institute of Sound and Vibration Research, University of Southampton*, July 1997.
[10] J. Zakrajsek, "A review of transmission diagnostics research at NASA Lewis research center," NASA Tech. Memo. **106746**, ARL-TR-599 (1994).
[11] J. Zakrajsek, D. Townsend, and H. Decker, "An analysis of gear fault detection methods as applied to pitting fatigue failure data," NASA Tech. Memo. **TM-105950**, AVSCOM TR-92-C-035 (1993).
[12] H. Decker, R. Handschuh, and J. Zakrajsek, "An enhancement to the na4 gear vibration diagnostic parameter," NASA Tech. Memo. **106553**, ARL-TR-389 (1994).
[13] F. Choy, S. Huang, J. Zakrajsek, R. Handschuh, and D. Townsend, "Vibration signature analysis of a faulted gear transmission system," NASA Tech. Memo. **106623** (1994).
[14] H. Chin, K. Danai, and D. Lewicki, "Efficient fault diagnosis of helicopter gearbox transmission," NASA Tech. Memo. **106253**, TR-93-C-034 (1992).
[15] H. Chin, K. Danai, and D. Lewicki, "Fault detection of helicopter gear boxes using the multi-valued influence matrix method," NASA Tech. Memo. **106100**, AVSCOM TR-92-C-015 (1992).
[16] V. Jammu, K. Danei, and D. Lewicki, "Unsupervised connectionist network for fault diagnosis of helicopter gearboxes," *Proceedings of the AHS 53rd Forum, Virginia Beach, VA*, 29 April–1 May 1997, pp. 1297–1307.
[17] P. McFadden, "Detecting fatigue cracks in gears by amplitude and phase demodulation of the meshing vibration," J. Vib., Acoust. Stress, and Reliability in Design **108**, 165–170 (1986).
[18] M. Brennan, M. Chen, and A. Reynolds, "Use of vibration measurements to detect local tooth defects in gears," Sound Vib. **31**, 12–17 (1997).
[19] B. Larder, "An analysis of hums vibration diagnostic capabilities," *Proceedings of the AHS 53rd Forum, Virginia Beach, VA*, 29 April–1 May 1997, pp. 1308–1315.
[20] B. Forrester, "Analysis of gear vibration in the time-frequency domain," *44th Meeting of the Mechanical Failure Prevention Group*, February 1990.
[21] P. McFadden and W. Wang, "Time-frequency domain analysis of vibration signal for machinery diagnostics (ii) the weighted Wigner-Ville distribution," *Report OUEL 1891 University of Oxford*, 1991.
[22] P. D. Samuel, D. J. Pines, and D. G. Lewicki, "A comparison of stationary and non-stationary metrics for detecting faults in helicopter gearboxes," J. Am. Helicopter Soc. (1998).
[23] P. D. Samuel and D. J. Pines, "Classifying helicopter gearbox faults using a normalized energy metric," Smart Mater. Struct. **9** (2000).
[24] T. Brooks, M. A. Marcolini, and D. S. Pope, "A directional array approach for the measurement of rotor noise source distribution with controlled spatial resolution," J. Sound Vib. **112**, 192–197 (1987).
[25] L. Ziomek, *Fundamentals of Acoustic Field Theory and Space-Time Signal Processing* (CRC Press, Boca Raton, FL, 1995).

Temperature dependence of acoustic impedance for specific fluorocarbon liquids

Jon N. Marsh,[a) Christopher S. Hall, Samuel A. Wickline, and Gregory M. Lanza
Washington University School of Medicine, Cardiovascular Division, 216 South Kingshighway, St. Louis, Missouri 63110

Recent studies by our group have demonstrated the efficacy of perfluorocarbon liquid nanoparticles for enhancing the reflectivity of tissuelike surfaces to which they are bound. The magnitude of this enhancement depends in large part on the difference in impedances of the perfluorocarbon, the bound substrate, and the propagating medium. The impedance varies directly with temperature because both the speed of sound and the mass density of perfluorocarbon liquids are highly temperature dependent. However, there are relatively little data in the literature pertaining to the temperature dependence of the acoustic impedance of these compounds. In this study, the speed of sound and density of seven different fluorocarbon liquids were measured at specific temperatures between 20 °C and 45 °C. All of the samples demonstrated negative, linear dependencies on temperature for both speed of sound and density and, consequently, for the acoustic impedance. The slope of sound speed was greatest for perfluorohexane (-278 ± 1.5 cm/s-°C) and lowest for perfluorodichlorooctane (-222 ± 0.9 cm/s-°C). Of the compounds measured, perfluorohexane exhibited the lowest acoustic impedance at all temperatures, and perfluorodecalin the highest at all temperatures. Computations from a simple transmission-line model used to predict reflectivity enhancement from surface-bound nanoparticles are discussed in light of these results. © *2002 Acoustical Society of America.* [DOI: 10.1121/1.1517251]

PACS numbers: 43.58.Bh, 43.64.Jb, 43.64.Kc [SLE]

I. INTRODUCTION

Ultrasound applications for fluorocarbon liquids hold interest because of these substances' unusual physical properties, such as their acoustic impedances. The wide range of values for longitudinal speed of sound exhibited by different fluorocarbon liquids has permitted their use in applications such as couplants for acoustic microscopy,[1] acoustic lenses for improving Bragg diffraction images,[2] signal storage in optical computing,[3] and as filling fluids for sonar targets and acoustic lenses.[4] More recently, fluorocarbon liquid emulsions have been adopted for use as principal components in ultrasound contrast agents[5–13] because of their stability, safety, and low acoustic impedance relative to that of soft tissue. Our laboratory has developed a fluorocarbon nanoparticle emulsion for targeted binding and molecular imaging that exhibits a long half-life *in vivo* and the ability to enhance the acoustic reflectivity of specifically targeted surfaces both *in vitro* and *in vivo*.[8–13] We have also shown that the extent of enhancement of a surface targeted with the fluorocarbon nanoparticles depends on both the type of encapsulated fluorocarbon[14] and on the temperature of the system.[15]

In a recent study by Hall *et al.*,[15] targeted nanoparticles containing perfluorooctane (C_8F_{18}) exhibited increasing acoustic reflectivity with increasing temperature, presumably due to changes in the acoustic impedance of perfluorooctane with temperature. Previous measurements performed on certain freons and other fluorocarbon liquids have shown that the speed of sound and mass density of these substances decrease as a function of temperature.[16,17] However, data pertaining to thermo-acoustic properties of perfluorinated liquids are relatively sparse in the literature. Furthermore, mass density data relating to perfluorooctane used in the previous study by Hall were not available at the time of publication. Accordingly, we now report the temperature dependence of speed of sound and density for not only perfluorooctane, but also for several other potentially useful fluorocarbon liquids that span a wide range of acoustic impedances. The results are useful for further refining a simple transmission-line mathematical model that we have employed to describe the source and magnitude of site-targeted ultrasonic enhancement.[11,15] Additionally, the data presented here for seven different liquid types may be useful for deriving other thermodynamic quantities for these compounds, and for determination of the nonlinear parameter B/A.[16,18]

II. METHODS

A. Fluorocarbon liquids

Seven types of fluorocarbon liquids were investigated in this study. Four of the samples were obtained from 3M Specialty Materials (St. Paul, MN): FC-72 (perfluorohexanes, C_6F_{14}), FC-75 (perfluoro-1-butyltetrahydrofuran, $C_8F_{16}O$), PF-5080 (perfluorooctanes, C_8F_{18}), and PF-5070 (perfluoroheptanes, C_7F_{16}). Perfluorodichlorooctane ($C_8F_{16}Cl_2$, abbreviated "PFDCO") and perfluorooctyl bromide ($C_8F_{17}Br$, abbreviated "PFOB") were obtained from Hemagen/PFC (St. Louis, MO); perfluorodecalin ($C_{10}F_{18}$, abbreviated "PFD") was obtained from Aldrich (Milwaukee, WI). Molecular weights for these liquids are listed in Table I.

a)Electronic mail: jnm@cvu.wustl.edu

TABLE I. List of physical properties of fluorocarbon liquids investigated in this study. Fluorocarbon speed of sound and mass density as functions of temperature can be obtained using the constants in the table and the formulas $c(T) = c_0 + c_1 T$ and $\rho(T) = \rho_0 + \rho_1 T$, respectively. Error values are uncertainties in the linear regression coefficients.

Fluorocarbon	Formula	Molecular weight	c_0 (cm/s)	c_1 (cm/s-°C)	ρ_0 (g/mL)	ρ_1 (g/mL-°C)
PFD	$C_{10}F_{18}$	462.1	$74\,440 \pm 50$	-242.4 ± 1.3	1.990 ± 0.001	$-0.002\,320 \pm 0.000\,032$
PFDCO	$C_8F_{16}Cl_2$	471.0	$73\,020 \pm 30$	-222.4 ± 0.9	1.843 ± 0.001	$-0.002\,188 \pm 0.000\,031$
PFOB	$C_8F_{17}Br$	499.0	$67\,950 \pm 30$	-222.9 ± 0.8	1.978 ± 0.001	$-0.002\,400 \pm 0.000\,031$
PF-5080	C_8F_{18}	438.1	$64\,630 \pm 40$	-262.5 ± 1.2	1.824 ± 0.001	$-0.002\,600 \pm 0.000\,013$
FC-75	$C_8F_{16}O$	416.1	$64\,030 \pm 70$	-255.9 ± 1.9	1.825 ± 0.001	$-0.002\,623 \pm 0.000\,029$
PF-5070	C_7F_{16}	388.0	$61\,060 \pm 30$	-268.3 ± 0.8	1.796 ± 0.001	$-0.002\,817 \pm 0.000\,022$
FC-72	C_6F_{14}	338.0	$57\,940 \pm 50$	-277.8 ± 1.5	1.759 ± 0.001	$-0.003\,087 \pm 0.000\,035$

B. Ultrasound specimen chamber

Measurements of longitudinal speed of sound in the various fluorocarbon liquids were performed with a custom-designed specimen chamber. The chamber comprised an assembly of three pieces that were clamped together when performing measurements (see Fig. 1 for details). The transducer was encased in a block of Delrin® with a rectangular well milled out at one end. A 0.5-in.-diam, 10-MHz center frequency PZT contact transducer (Panametrics model V111, Waltham, MA) was placed facing outward from the center of the well. A coaxial cable was fed through a borehole drilled from one end of the block into the well, and provided electrical connection to the transducer. The entire well was then filled with a silicone rubber compound (RTV 615, General Electric Silicones, Waterford, NY) to the level of the block's surface and allowed to cure, completely sealing the transducer and coaxial connector. This particular type of silicone was selected for its relatively low longitudinal-wave attenuation coefficient. The exposed surface of the cured silicone was flat and parallel to the transducer face and to the opposite wall. The second major part of the chamber assembly consisted of a "U"-shaped steel bracket with edge channels for O-ring seals. The last component of the assembly was a flat piece of plate glass. To assemble the specimen chamber, the transducer block and cover plate were clamped on opposite sides of the gasket frame, forming a thin, water-tight cavity sealed on the bottom and sides. The liquid fluorocarbon samples were slowly poured into this space before measurements. Because of the very low surface tension of the fluorocarbon liquids, no air bubbles were observed within the sample or adhering to the sides of the chamber. The propagation path length between the silicone and glass surfaces was approximately 7.2 mm. The top of the chamber was open to allow for pressure equalization at all temperatures. The entire specimen chamber assembly was immersed in a temperature-controlled waterbath with 0.1 °C accuracy (RTE-111, NESLAB Instruments Inc., Newington, NH) to a level just above the level of the enclosed fluorocarbon sample for the duration of the measurements. All samples were maintained at ambient atmospheric pressure; no attempt was made to control for the amount of dissolved air in the samples in this study.
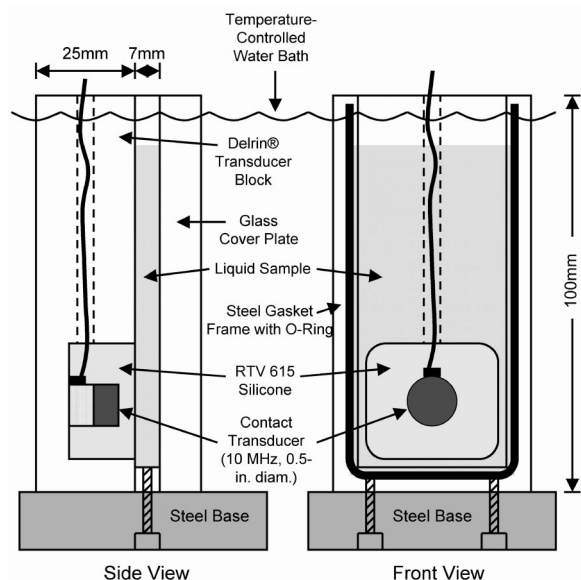
FIG. 1. Schematic showing side and front views of specimen chamber used for determining longitudinal speed of sound of fluorocarbon liquids as a function of temperature. The chamber was immersed in a temperature-controlled waterbath to a level near the top. Not shown are clamps used to hold the three parts of the chamber together during use.

C. Data acquisition and analysis

The transducer was excited using a Panametrics 5900 pulser. The first returned echoes from the silicone/fluorocarbon and fluorocarbon/glass interfaces were digitized (Tektronix 2430A, Beaverton, OR) at 100 MHz and stored to disk. Measurements were performed over a temperature range of 25 °C to 45 °C at 2.5 °C increments. The specimen chamber with fluorocarbon sample was allowed to equilibrate at each temperature for 15 min before acquisition. Subsequent to the measurements for each fluorocarbon liquid, a reference measurement was performed using distilled water in the chamber. The reference data allowed determination of the acoustic path length through the chamber by using established values for the temperature-dependent speed of sound in water.[19] Prior measurements obtained using distilled water demonstrated that there was no significant change in the chamber's dimensions for the temperature range investigated here, so a single value for the round-trip distance through the chamber was used for each fluorocarbon data run. Group velocity was measured rather than phase velocity, because previous work with fluorocarbon liquids has demonstrated that these substances exhibit negligible velocity dispersion in
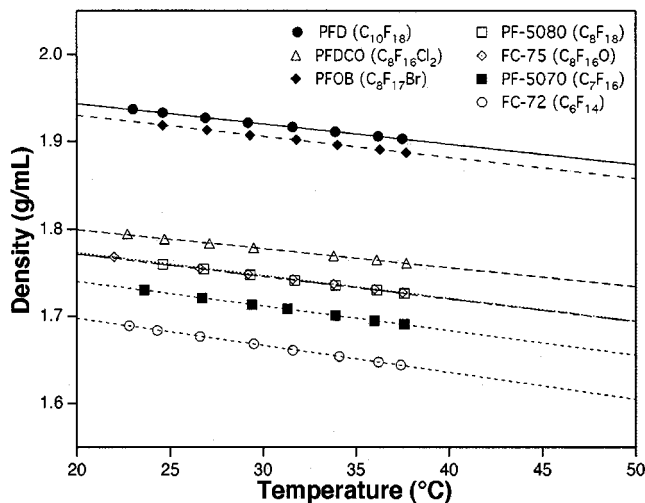
FIG. 2. Experimentally determined mass density for fluorocarbon liquids as a function of temperature. Linear fits are shown overlaying the data points.

FIG. 3. Experimentally determined longitudinal speed of sound for fluorocarbon liquids as a function of temperature. Linear fits are shown overlaying the data points.

the frequency range between 1 and 22 MHz,[4,20] well beyond the range used in this study. The fluorocarbon speed of sound was determined by dividing the difference of the front- and rear-wall echo arrival times by the round-trip distance through the chamber. Echo arrival times were determined using the envelope peaks of the rf data. There were only minimal apparent changes to the shape and magnitude of the echo waveform at different temperatures, so that this method of extracting timing information was relatively consistent over the range of temperatures used.

The density of each fluorocarbon was measured as a function of temperature using an electronic balance (PB303, Mettler-Toledo, Inc., Columbus, OH) and a 10-mL glass pycnometer (Kimble Glass Inc., Vineland, NJ). The pycnometer was heated in a temperature-controlled waterbath. Densities were measured over a temperature range of approximately 22 °C to 38 °C (the upper temperature limit was determined by the supplied mercury thermometer). The precision of the temperature readings was estimated at ±0.1 °C.

III. RESULTS

Each of the seven fluorocarbon liquids exhibited speed of sound and density that decreased in a linear fashion with increasing temperature. Results for the temperature-dependent density and speed of sound are shown in Figs. 2 and 3, respectively. Experimentally determined values are plotted as data points with a linear fit overlaying the data. The values of slope and intercept for the best-fit lines [of the form $\rho(T) = \rho_0 + \rho_1 T$ for density and $c(T) = c_0 + c_1 T$ for sound speed] are shown in Table I. The values for the slope of density and speed of sound were somewhat similar among all the samples tested in the study. The predicted temperature-dependent acoustic impedance, given by $z(T) = \rho(T)c(T)$, is plotted in Fig. 4.

IV. DISCUSSION

The fluorocarbon liquids examined in this study spanned a wide range of acoustic impedances, all of which are lower than that of water at similar temperatures. At 25 °C, PFD
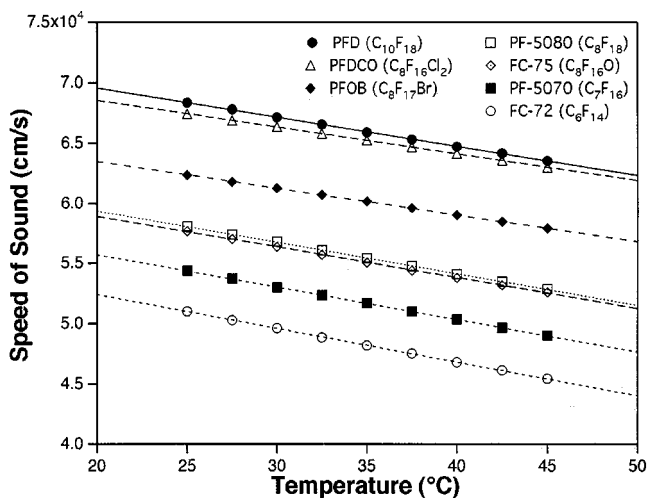
exhibited the higher impedance (132 100 g/cm^2-s), while FC-72 was the lower (85 800 g/cm^2-s). Both density and speed of sound decreased linearly as functions of temperature, with the rate of density change ranging from $-0.002\,188$ g/mL-°C (PFDCO) to $-0.003\,087$ g/mL-°C (FC-72), and the rate of velocity change ranging from -222 (PFDCO) to -278 cm/s-°C (FC-72). The velocity slope was a larger contributor than was the density slope to the nearly linear change in acoustic impedance with temperature, by a factor of approximately 3 to 1.

Although relatively few reports exist in the literature regarding the specific fluorocarbon liquids tested here, some comparisons can be made. Temperature-dependent speed of sound data from several authors[1,3,4,16,17,20,21] are graphed in Fig. 5 for five of the perfluorocarbons, alongside the data reported above. Each graph represents results for a specific perfluorocarbon liquid, and the liquids are labeled by their chemical formulas rather than their trade names. The
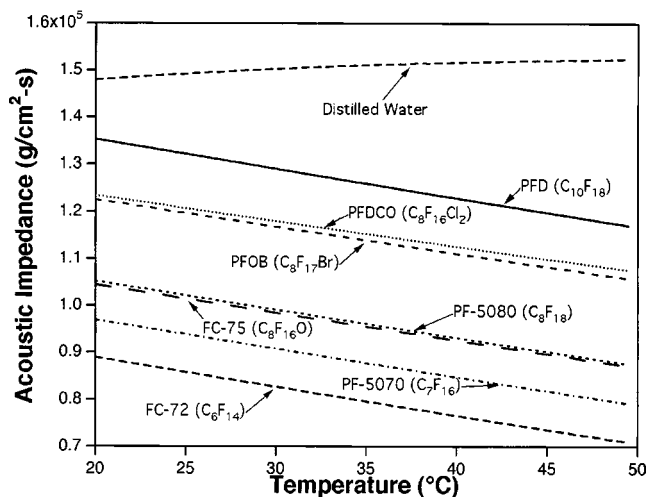
FIG. 4. Acoustic impedance $z(T) = \rho(T)c(T)$ of fluorocarbon liquids and distilled water as a function of temperature. Curves were generated from linear fits to measured data for temperature-dependent mass density and speed of sound.
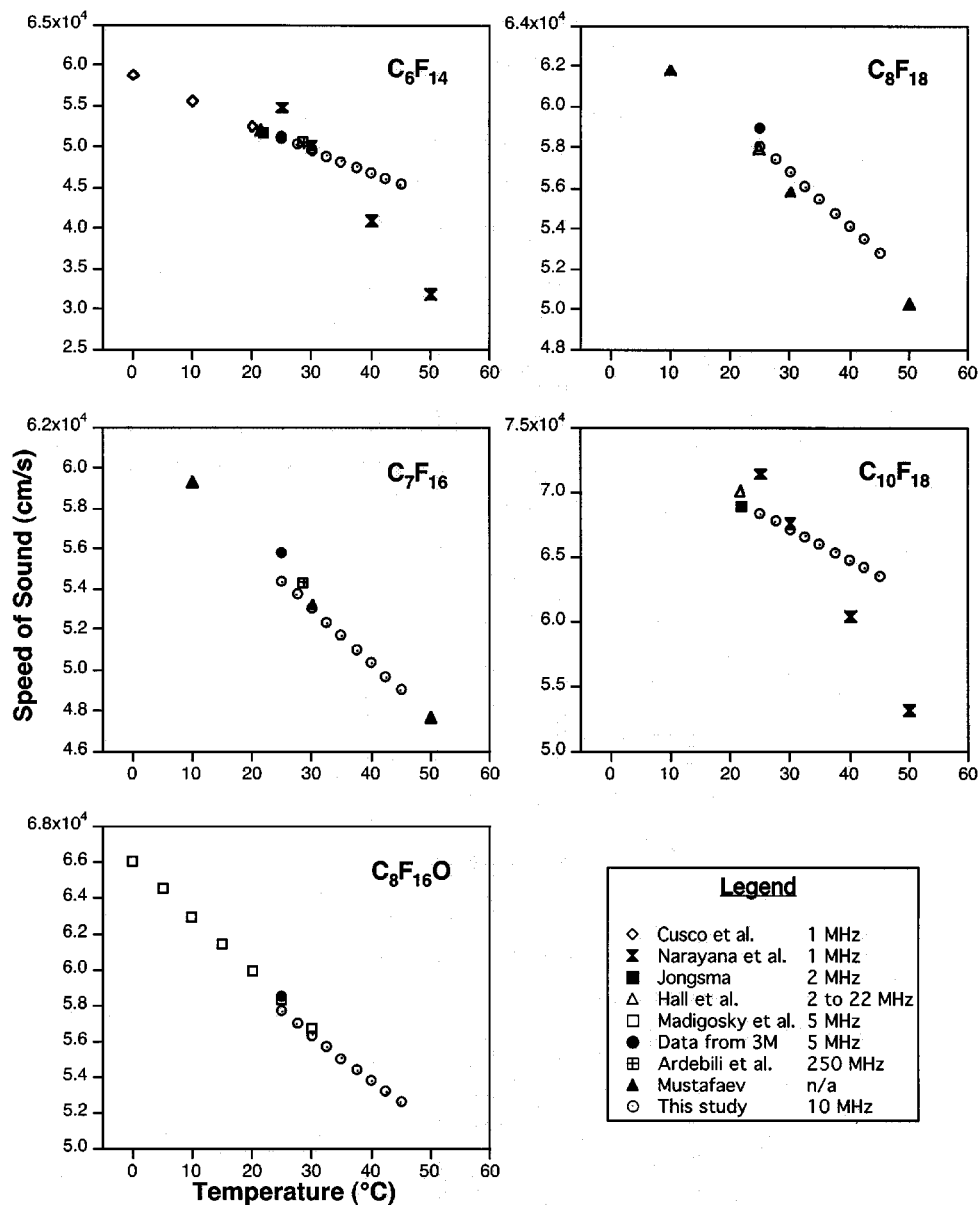
FIG. 5. Comparison of speed of sound as a function of temperature with previously reported results for specific perfluorocarbon liquids at ambient pressure. The perfluorocarbon liquids are labeled by chemical formula rather than trade name. Vertical axes represent speed of sound in cm/s, and horizontal axes represent temperature in °C. List of authors and frequencies at which the measurements were made is given in the legend at lower right of figure.

author list and frequencies at which the measurements were made are given in the legend. Overall, there is good agreement in both absolute value and slope of the sound speed for each perfluorocarbon, in spite of the wide range of techniques and frequencies used to obtain the measurements. The only exceptions appear to be the results of Narayana and Swamy for perfluorohexane and perfluorodecalin; in both cases, the slope of the temperature-dependent speed of sound is significantly more negative than reported by any of the other authors. The reason for this apparent discrepancy is unknown, although their reported values near room temperature appear to follow the general trends more closely. On the other hand, Narayana and Swamy's results for the temperature dependence of the density of these liquids exhibit good agreement with the results presented here. Likewise, the density behavior of FC-75, PF-5070, and FC-72 reported here agree with results given by Madigosky et al.,[16] and with the

formulas supplied by 3M for calculating density as a function of temperature.

We recently demonstrated that increases in temperature could be used to augment the magnitude of reflectivity imparted by targeted perfluorooctane nanoparticles, thereby permitting further differentiation of contrast-enhanced sites from surrounding, untargeted material.[15] As demonstrated in that study, the trend of increasing reflectivity with temperature was corroborated by predictions from a simple transmission-line model used to describe the magnitude of the reflected acoustic wave from the bound nanoparticle/substrate layer. At the time of the study, however, no data were available for the temperature-dependent density of perfluorooctane and a constant value was used for input to the model. The results presented here can now be used to further refine modeling of the targeted system by providing a more complete description of the temperature-dependent behavior
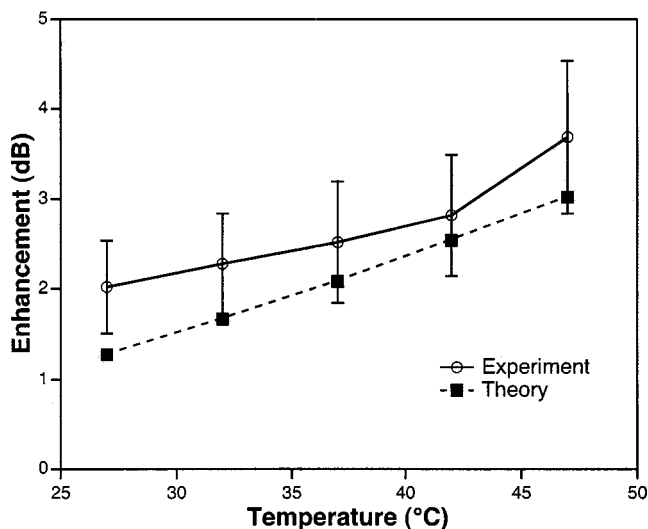
FIG. 6. Experimental measurements of reflectivity enhancement of nitrocellulose membrane targeted with perfluorooctane nanoparticles compared with predictions from simple transmission-line model. Temperature-dependent density and speed of sound data for PF-5080 were used as input to the model. Experimental measurements excerpted from Hall *et al.*[15]

of many useful perfluorocarbons. In Fig. 6, we compare the experimentally measured reflectivity enhancement of nitrocellulose membrane at specific temperatures when bound with a 250-nm thick layer of perfluorooctane nanoparticles (results are excerpted from Hall *et al.*[15]) with predictions from the transmission-line model using the temperature-dependent inputs for PF-5080 shown in Table I. The temperature dependence of sound speed[19] and mass density[22] of the surrounding distilled water medium are now also incorporated into the theoretical results. Although the magnitude of enhancement predicted by the model underestimates the measured values somewhat, the trend of increased reflectivity of the targeted surface with increasing temperature is consistent between theory and experiment. The greater than predicted enhancement encountered in practice with nitrocellulose membrane (and other substrates such as plasma thrombi[15]) points to the need for a more sophisticated mathematical description of the targeted contrast system, which will be facilitated with the measurements presented here.

[1] V. S. Ardebili, A. N. Sinclair, and J. K. Spelt, "Ultrasonic couplants for acoustic microscopy of low speed materials," IEEE Trans. Ultrason. Ferroelectr. Freq. Control **44**, 102–107 (1997).

[2] G. Wade, "Acoustic lenses and low velocity fluids for improving Bragg diffraction images," Acoust. Hologr. **6**, 345–362 (1975).

[3] F. H. M. Jongsma, "Liquids with a very low ultrasound propagation velocity," Ultrasonics **17**, 233 (1979).

[4] L. Cuscó and J. P. M. Trusler, "Identification of environmentally acceptable low-sound speed liquids," Int. J. Thermophys. **16**, 675–685 (1995).

[5] M. André, T. Nelson, and R. Mattrey, "Physical and acoustical properties of perfluorooctylbromide, an ultrasound contrast agent," Invest. Radiol. **25**, 983–987 (1990).

[6] R. Satterfield, V. M. Tarter, D. J. Schumacher, P. Tran, and R. F. Mattrey, "Comparison of different perfluorocarbons as ultrasound contrast agents," Invest. Radiol. **28**, 325–331 (1993).

[7] R. F. Mattrey, "The potential role of perfluorochemicals (PFCs) in diagnostic imaging," Artif. Cells Blood Substit. Immobil. Biotechnol. **22**, 295–313 (1994).

[8] G. M. Lanza, K. D. Wallace, M. J. Scott, W. P. Cacheris, D. R. Abendschein, D. H. Christy, A. M. Sharkey, J. G. Miller, P. J. Gaffney, and S. A. Wickline, "A novel site-targeted ultrasonic contrast agent with broad biomedical application," Circulation **94**, 3334–3340 (1996).

[9] G. M. Lanza, K. D. Wallace, S. E. Fischer, D. H. Christy, M. J. Scott, R. L. Trousil, W. P. Cacheris, J. G. Miller, P. J. Gaffney, and S. A. Wickline, "High-frequency ultrasonic detection of thrombi with a targeted contrast system," Ultrasound Med. Biol. **23**, 863–870 (1997).

[10] G. M. Lanza, R. L. Trousil, K. D. Wallace, D. R. Abendschein, M. J. Scott, J. G. Miller, P. J. Gaffney, and S. A. Wickline, "In vivo efficacy of fibrin targeted perfluorocarbon contrast system following intravenous injection reflects prolonged systemic half-life and persistent acoustic contrast effect," Circulation **95**, I-457 (1997).

[11] G. M. Lanza, R. L. Trousil, K. D. Wallace, J. H. Rose, C. S. Hall, M. J. Scott, J. G. Miller, P. R. Eisenberg, P. J. Gaffney, and S. A. Wickline, "In vitro characterization of a novel, tissue-targeted ultrasonic contrast system with acoustic microscopy," J. Acoust. Soc. Am. **104**, 3665–3672 (1998).

[12] G. M. Lanza, C. H. Lorenz, S. E. Fischer, M. J. Scott, W. P. Cacheris, R. J. Kaufmann, P. J. Gaffney, and S. A. Wickline, "Enhanced detection of thrombi with a novel fibrin-targeted magnetic resonance imaging agent," Acad. Radiol. **5** (Suppl. 1), S173-6; discussion S183-4 (1998).

[13] G. M. Lanza, D. R. Abendschein, C. S. Hall, J. N. Marsh, M. J. Scott, D. E. Scherrer, and S. A. Wickline, "Molecular imaging of stretch-induced tissue factor expression in carotid arteries with intravascular ultrasound," Invest. Radiol. **35**, 227–234 (2000).

[14] J. N. Marsh, C. S. Hall, M. J. Scott, R. W. Fuhrhop, P. J. Gaffney, S. A. Wickline, and G. M. Lanza, "Improvements in the ultrasonic contrast of targeted perfluorocarbon nanoparticles using an acoustic transmission-line model," IEEE Trans. Ultrason. Ferroelectr. Freq. Control **49**, 29–38 (2002).

[15] C. S. Hall, J. N. Marsh, M. J. Scott, P. J. Gaffney, S. A. Wickline, and G. M. Lanza, "Temperature dependence of ultrasonic enhancement with a site-targeted contrast agent," J. Acoust. Soc. Am. **110**, 1677–1684 (2001).

[16] W. M. Madigosky, I. Rosenbaum, and R. Lucas, "Sound velocities and B/A in fluorocarbon fluids and in several low density solids," J. Acoust. Soc. Am. **69**, 1639–1643 (1981).

[17] K. L. Narayana and K. M. Swamy, "Temperature variation of ultrasonic velocity in some low velocity fluorocarbon liquids," Acoust. Lett. **9**, 137–143 (1986).

[18] J. Tong, Y. Dong, and T. Tong, "Expressions of acoustic parameters in organic liquid derived from Schaaff's theory," J. Acoust. Soc. Am. **93**, 291–294 (1993).

[19] V. A. Del Grosso and C. W. Mader, "Speed of sound in pure water," J. Acoust. Soc. Am. **52**, 1442–1446 (1972).

[20] C. S. Hall, G. M. Lanza, J. H. Rose, R. J. Kaufmann, R. W. Fuhrhop, S. H. Handley, K. R. Waters, J. G. Miller, and S. A. Wickline, "Experimental determination of phase velocity of perfluorocarbons: Applications to targeted contrast agents," IEEE Trans. Ultrason. Ferroelectr. Freq. Control **47**, 75–84 (2000).

[21] M. R. Mustafaev, "The sound velocity in some perfluorocarbons in a wide range of parameters of state," High Temp. **35**, 214–219 (1997).

[22] R. C. Weast, ed., *Handbook of Chemistry and Physics*, Vol. 1, Student Ed. (CRC, Boca Raton, FL, 1988).

Sound power flux measurements in strongly exited ducts with flow

Keith R. Holland[a] and Peter O. A. L. Davies
Institute of Sound and Vibration Research, University of Southampton, Southampton SO17 1BJ, United Kingdom

Danie C. van der Walt
Bosal Afrika, P.O. Box 1652, Pretoria 0001, South Africa

This contribution describes new robust procedures for the measurement of sound power flux at appropriate axial positions along a duct with flow, using pairs of flush wall mounted microphones, or pressure transducers. The technology includes the application of selective averaging, order tracking, and optimized sampling rate methods to identify the small fraction of the total fluctuating wave energy that is being propagated along the flow path in a reverberent, or highly reactive duct system. Such measurements can also be used to quantify the local acoustic characteristics that govern the generation, transfer, and propagation of wave energy in the system. Illustrative examples include the determination of the acoustic characteristics of individual silencing elements installed in IC engine intakes and exhausts both on the flow bench and during controlled acceleration or run down on a test bed, where the wave component spectral levels approached 170 dB. © *2002 Acoustical Society of America.* [DOI: 10.1121/1.1509434]

PACS numbers: 43.58.Fm, 43.20.Mv, 43.20.Ye, 43.28.Ra [SLE]

LIST OF SYMBOLS

a	duct radius
c	speed of sound
d	pipe internal diameter
f	cyclic frequency
$\hat{G}_{12}$	cross-power spectrum $\hat{p}_1^* \hat{p}_2$
G_{11}	autospectrum $\hat{p}_1^* \hat{p}_1$
$\hat{H}_{12}$	transfer function $\hat{p}_2 / \hat{p}_1$
I	acoustic intensity
k	wave number ω_0 / c
l	transducer spacing
M	Mach number u_0 / c_0
p	pressure
$\hat{p}$	spectral pressure component, complex amplitude
$\hat{p}^+, \hat{p}^-$	positively and negatively travelling acoustic component wave amplitudes
R	pressure reflection coefficient $\hat{p}^- / \hat{p}^+$
t	time
S	surface, cross-section area
s	fluctuating entropy
u	velocity
u_i	acoustic velocity component
U_i	time averaged flow velocity component
v_i	fluctuating solenoidal velocity component
W	acoustic power flux
α	viscothermal attenuation coefficient
ρ	fluid density
ω	radian frequency $2\pi f$

Subscripts

a	acoustic, isentropic
0	ambient value
s	solenoidal

I. INTRODUCTION

Compliance with legislation and other directives restricting the permissible levels of sound emission is normally demonstrated by performing appropriate sound power measurements.[1] The major contribution to traffic noise by both engine intake and exhaust is widely recognized, while similar flow generated noise often contributes significantly to emissions from industrial plant, domestic equipment, or other activities. The development and validation of appropriate noise control strategies also requires appropriate sound power measurements, while such measurements are also featured widely in methodologies[2] for the acoustic design and refinement of quality products. This includes the assessment of the acoustic properties of the individual components with their contribution to the overall performance of the system under operational conditions. The techniques described here assume one-dimensional acoustic wave propagation and have already been experimentally validated[1] with periodic excitation up to a sound pressure level (SPL) of around 130 dB. The measurements described here concern fluctuating pressure levels from one to two orders of magnitude in excess of this value, thus extending their successful application to conditions commonly experienced in practice.

[a]Electronic mail: krh@isvr.soton.ac.uk

In an ideal acoustic medium at rest, the sound power crossing any closed surface S is defined[3] as

$$W = \int_s I_i dS_i, \tag{1}$$

where $I_i = \langle p_a u_i \rangle$, $i = 1,2,3$, are the components of the time averaged acoustic intensity vector, p_a is the fluctuating acoustic pressure and u_i the corresponding acoustic velocity components in the isentropic irrotational fluid motion associated with the acoustic wave. In a moving acoustic medium, Morfey[3] showed that the corresponding components of the acoustic energy flux per unit area are expressed by

$$I_i = \langle p_a u_i \rangle + \frac{U_i}{\rho_0 c_0^2} \langle p_a^2 \rangle + \frac{U_i U_j}{c_0^2} \langle p_a u_j \rangle + \rho_0 U_j \langle u_i u_j \rangle, \tag{2}$$

where U_i, U_j are the time averaged components of the flow velocity and ρ_0, c_0 are, respectively, the ambient density and sound speed.

Sound power flux in flow ducts. Flow duct geometry is normally complex and consists of lengths of uniform pipe connecting other system components such as expansions, contractions, resonators, branches, and junctions. Flow duct acoustic behavior is usually highly reactive, while wave reflection at the junctions between elements,[4–6] with interference between the resulting incident and reflected waves, results in an acoustic field consisting of both standing and progressive waves. As well as isentropic acoustic disturbances propagating at the speed of sound, the fluid motion generally includes other solenoidal disturbances convecting with the flow. These represent turbulent and vortical motion generated at the duct boundaries or shed[4,6] with separating shear layers and wakes. They include fluctuating velocity components v_i and entropy s with their associated pressure and density fluctuations p_s and ρ_s. Thus, for example, sound power measurements require appropriate experimental procedures[4–6] that isolate or identify the acoustic contribution $p_a(t)$ in the observed pressure time history $p'(t) = p_a(t) + p_s(t)$. Furthermore, as well as such contamination, the systematic axial distribution of acoustic pressure and velocity amplitude associated with the standing waves may result in adverse signal to noise ratios for sequences of specific frequencies, at one or more axial positions along each pipe.

Sets of examples are presented here describing the application of robust procedures yielding reliable estimates of the net sound power flux associated with one-dimensional wave motion under strongly reactive conditions in ducts with flow. These show that appropriate cross-power spectral analysis of the signals acquired simultaneously from a sequence of pairs of flush wall mounted pressure transducers can be processed[1,4–7] to establish the acoustic characteristics of each system element of interest. From these one can calculate the small proportion of the total fluctuating wave energy that is being propagated through it. The appropriate procedures differed somewhat with each application, which included strong acoustic excitation by an acoustic driver,[1] aeroacoustic excitation produced by the flow alone,[8] and finally by the exhaust process of a petrol engine[9] accelerating on a test bed. A common representative geometry, consisting of an expansion chamber with its inlet and outlet pipes, was chosen for each case.

Acoustic energy propagation is restricted to one-dimensional wave motion below the cutoff frequency at which higher order modes decay exponentially. In a pipe with radius a this corresponds[5] to a Helmholtz number $ka = 1.84(1 - M^2)^{0.5}$, where M is the mean flow Mach number u_0/c_0. This limit corresponds to 2000 Hz in a 100-mm-diam pipe at room temperature. Provided the frequency range of interest lies below such limits, this restriction to plane wave motion offers a considerable simplification to both measurement procedures and to their subsequent analysis. For example, the measurement[10] of the acoustic characteristics of the first two propagating circumferential modes in a 300-mm-diam duct just above "cut on" at frequencies of 646 and 1072 Hz, respectively, required an array of eight pairs of flush wall mounted microphones.

II. SOUND POWER FLUX MEASUREMENTS IN FLOW DUCTS

With one-dimensional acoustic wave motion (plane waves) traveling along a uniform pipe the amplitude of each spectral component of the acoustic pressure p_a and velocity u_a is related to the corresponding amplitude of the incident $\hat{p}^+$ and reflected $\hat{p}^-$ component waves,[5] at a mean flow Mach number M by

$$\hat{p}_a = \hat{p}^+ + \hat{p}^-, \tag{3a}$$

$$\rho_0 c_0 \hat{u}_a = \hat{p}^+ - \hat{p}^-, \tag{3b}$$

where Eq. (3a) is always true and Eq. (3b) remains a close approximation for $M > 0$,[5] so long as the influence of viscothermal attenuation remains sufficiently small. After substitution from Eq. (3), Eq. (2)—describing the acoustic intensity—simplifies[4,5] to

$$I = I^+ - I^- = [|\hat{p}^+|^2 (1 + M)^2 - |\hat{p}^-|^2 (1 - M)^2] / \rho_0 c_0, \tag{4}$$

where I^+ and I^- are, respectively, the incident and reflected components of the spectral acoustic intensity I.

A. Extraction of the $\hat{p}^+, \hat{p}^-$ spectra from the transducer signals

Consider the two pressure time histories measured by transducers at positions 1 and 2 an axial distance l apart. The corresponding acoustic contributions to the pressure spectra derived from the signals recorded at the two positions are related by[1,4–7]

$$\hat{p}_1(\omega) = \hat{p}_1^+(\omega) + \hat{p}_1^-(\omega), \tag{5a}$$

$$\hat{p}_2(\omega) = \hat{p}_1^+ \exp(-jk^+ l) + \hat{p}_1^- \exp(jk^- l), \tag{5b}$$

where $k^\pm$ are the corresponding wave numbers given by $(\omega/c + \alpha(1 - j))/(1 \pm M)$ respectively and α is the viscothermal attenuation coefficient.[1,5] If the cross-spectrum estimated from the pressure-time histories at positions 1 and 2 is $\hat{G}_{12}$, while G_{11} and G_{22} are the corresponding autospectra, one can show that the acoustic pressure reflection coefficient

2864   J. Acoust. Soc. Am., Vol. 112, No. 6, December 2002

Holland *et al.*: Sound power measurements in ducts
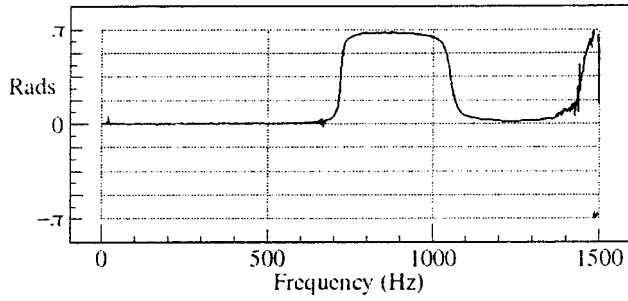
FIG. 1. Phase of cross spectrum in exhaust tailpipe.

FIG. 2. Single shot sample spectrum—only highlighted lines contribute to averaging—signal to noise ratio 0 dB.

spectrum $\hat{R}_1$ defined as the ratio $\hat{p}_1^-/\hat{p}_1^+$ is also[1] expressed by

$$\hat{R}_1 = -[\hat{G}_{12} - G_{11}\exp(-jk^+l)]/$$
$$[\hat{G}_{12} - G_{11}\exp(jk^-l)], \tag{6}$$

assuming that the influence of other than acoustic pressure fluctuations on the spectral estimates can be neglected. From this,

$$|p_1^+| = (G_{11})^{0.5}/|1 + \hat{R}_1|, \tag{7a}$$

$$p_1^- = \hat{R}_1 \hat{p}_1^+, \tag{7b}$$

when the signal from transducer 1 is also chosen as a reference.

One should note that the effectiveness of the decomposition into $\hat{p}^{\pm}$ depends on the extent to which the spectral estimates G_{11}, $\hat{G}_{12}$, and G_{22} are contaminated by flow-induced pressure fluctuations p_s and any other signal acquisition or processing "noise." The method also relies on the differences between the acoustic pressure signals at positions 1 and 2. In a standing wave field the two signals are almost identical [Eqs. (5a), (5b)], when $kl = n\pi$, with n any integer, so poor results can be expected when the spacing l is close to multiples of a half wavelength. On the other hand, due to the different propagation velocities, any influence of p_s on the spectral estimates of $\hat{G}_{12}$ will decrease as the distance l increases. Similarly, since p_s is generally random and uncorrelated with p_a, all three spectral estimates will more closely reflect the acoustic behavior as the number of averages increases. A similar improvement occurs as the spectral analysis bandwidth is reduced. Clearly the most appropriate strategy will vary to some extent with application, depending on the spectral characteristics and strength of the acoustic field with its associated isentropic irrotational motion compared with that associated with the remaining disturbances convecting with the flow.

B. Pressure transducer calibration

It turns out[1,7] that the net power flux is almost proportional to the magnitude of the imaginary part of $\hat{G}_{12}$. As shown in Fig. 1, this may be close to zero over substantial ranges of the frequency spectrum, where adequate precision for the measurements of phase, among other factors, depends on the relative calibration of each transducer pair. If the measured transfer function $\hat{p}_2/\hat{p}_1$ measured between two transducers (1, 2) at positions 1 and 2 is $\hat{H}_A$, while after they
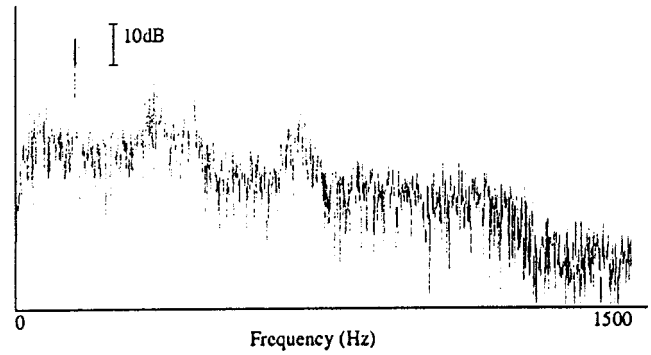
were interchanged, including all signal path elements, the measurement yields $\hat{H}_B$, the required calibration independent transfer function[1,7] is then $H = \hat{H}_A^{0.5}\hat{H}_B^{0.5}$. This procedure can be repeated for each transducer pair in turn yielding relative transducer calibration data for the whole set. An absolute calibration of one of the sets is required when absolute sound pressure levels are required.

C. Experimental procedures

Laboratory tests at Southampton and bench tests at Bosal Afrika were mainly concerned with the development of robust procedures yielding reliable estimates of the net power flux[1] and coherent power flux,[8] leading to the identification[8] of flow noise sources. The acceleration tests at Bosal Afrika[9] concerned the application of order tracking and optimized sampling rate methods[9] to evaluate the acoustic properties of a system element in an industrial environment. As an approximation to the cyclic excitation during an acceleration test[1] a digitally generated slow sine sweep signal recorded on one channel of a digital tape recorder was used to excite the laboratory system at Southampton. Ten minutes of data was recorded synchronously on the remaining seven channels for each run, and analyzed with 1 Hz resolution with Hanning windowing and 50% overlap giving rise to 1200 process averages after analog filtering with cut-off set to 1350 Hz. A representative individual record showing the analysis of 1 s of data appears in Fig. 2, where the coherent acoustic signal stands some 20 dB above the background pressure fluctuations, although the corresponding signal to noise ratio of the signal records was 0 dB. Since the excitation frequency is known at any particular time, it is possible to exclude from the averaging process all frequencies except those within a narrow band centered on the excitation.

The potential advantage of such selective averaging for identifying coherent acoustic signals $p_a(f,t)$ buried in other local flow induced random turbulent pressure fluctuations $p_s(t)$ is demonstrated in the comparison between the results with swept sine and with more conventional random excitation set out in Fig. 3. So long as the spectral level of any acoustic signal remains significantly above that of $p_s(t)$, the two transfer functions $\hat{H}_{12} = \hat{p}_2/\hat{p}_1$ in Figs. 3(a1) and (b1) are very similar. However, swept sine signals $p_a(f,t)$ remain

J. Acoust. Soc. Am., Vol. 112, No. 6, December 2002

Holland *et al.*: Sound power measurements in ducts   2865
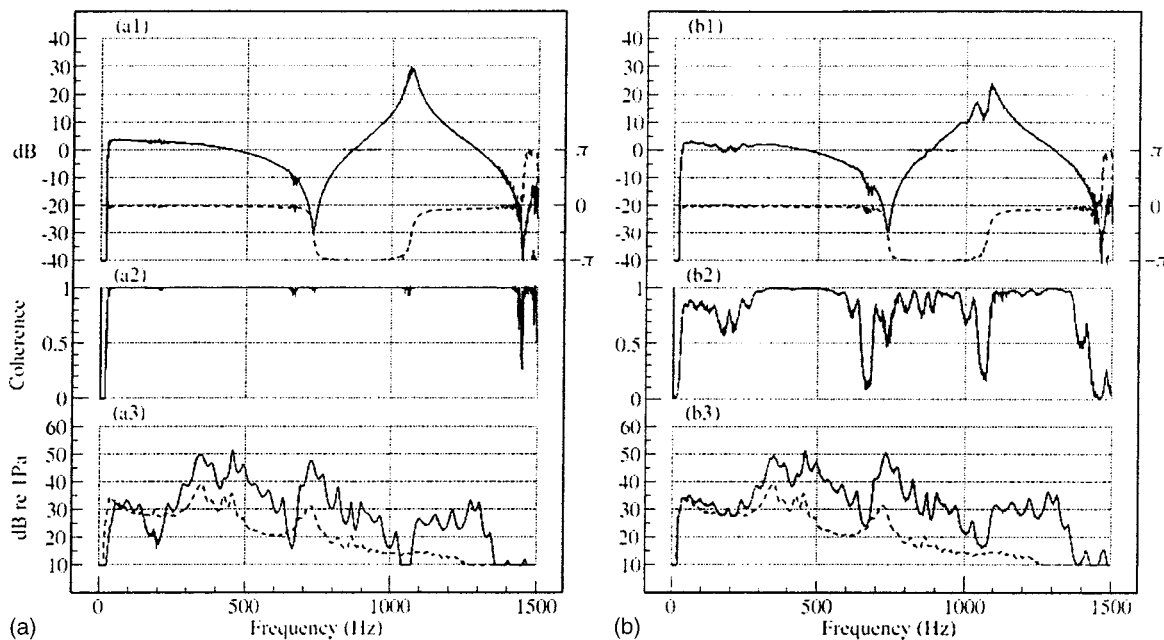
FIG. 3. Comparison of measurements with flow Mach number 0.1: (a) with swept sine excitation and selective averaging; (b) with White noise excitation. (1) Transfer function $\hat{H}_{12}$, (—)mod, (---) phase; (2) coherence; (3) autospectrum at microphone 1, (—) with acoustic excitation, (---) flow only.

highly correlated over the transducer separation path, while the corresponding narrow band spectral components of the relatively slowly moving turbulent pressure functions become sufficiently incoherent to cancel on average. Thus the corresponding coherences are very different, which also explains the clear difference in the autospectra around 200, 770, and 1050 Hz, in Figs. 3(a3) and (b3), where elsewhere they remain similar. These results demonstrate that selective averaging provides a clear identification of the more coherent acoustic fluctuations even when their spectral level lies well below that of local turbulent pressure fluctuations generated by the flow as indicated in Fig. 3(a3).

The transfer function $\hat{p}_2/\hat{p}_1$ may be calculated with the $\hat{H}_1$ estimator, $\hat{G}_{12}/\hat{G}_{11}=\hat{p}_1^*\hat{p}_2/\hat{p}_1^*p_1$, where an asterisk indicates the complex conjugate, or alternatively with the $\hat{H}_2$ estimator, $G_{22}/\hat{G}_{12}^*=\hat{p}_2^*\hat{p}_2/\hat{p}_2^*\hat{p}_1$. With high coherence, both estimates should be closely similar. However, near standing wave minima, the corresponding signal to noise ratio of $\hat{p}_2$ may, for example, be significantly higher than that of $\hat{p}_1$. Substitution of the $\hat{H}_2$ estimator for the corresponding ratio $\hat{G}_{12}/\hat{G}_{11}$ in Eq. (6) should then yield a "best" estimate for the reflection coefficient $\hat{R}_1$ at that frequency.

D. Experimental procedures with controlled engine acceleration

Currently, tailpipe orifice noise emissions spectra are measured during controlled acceleration or deceleration of the engine on a dynamometer to evaluate and then refine the exhaust system acoustic performance. The results are normally displayed as engine order spectra against engine rpm, which are harmonically related to the firing frequency. With a four cylinder four stroke engine, the firing frequency occurs at $2E$ or twice the engine rotational frequency, while with six cylinders this is $3E$ and so on. With two stroke

engines these values are doubled. Measurement of the individual contribution of each system element to the overall system acoustic performance clearly has a beneficial influence on the rate at which significant improvements are obtained during system refinement. Although the underlying principles are similar, the engine acceleration rather than the acoustic excitation is now the controlled variable, which requires[9] appropriate changes to the experimental and data processing procedures. The engine cyclic frequency, the mass flow, and temperature all change systematically in time at some sweep rate that is never quite stationary and is also restricted by operating conditions, such as engine overheating. Standard order tracking[9] was adopted where the sampling frequency was synchronized with the instantaneous engine rotational speed and the time records and spectra represented, respectively, in revolutions and orders. Each record length contained an integer number of periods with the power of each harmonic component concentrated in an individual line. Special analogous procedures[9] were also developed to estimate the signal to noise ratios at each order in the pressure signal records, so as to obtain similar improvements in the identification of acoustic behavior to those indicated in Fig. 3.

E. Signal measurement

Electret microphones modified to operate up to sound pressure levels of 165 dB (Knowles, CA-8374) were used for the pressure measurements at Southampton, while water cooled Kistler type 701A quartz pressure transducers were used at Bosal Afrika. Measurements of flow temperature mean pressure and mass flow were also required to define the corresponding sound speed, and flow Mach number required for the calculations. The experimental layout and measured flow conditions during engine run up are illustrated in Fig. 4. A similar arrangement was adopted at Southampton with a
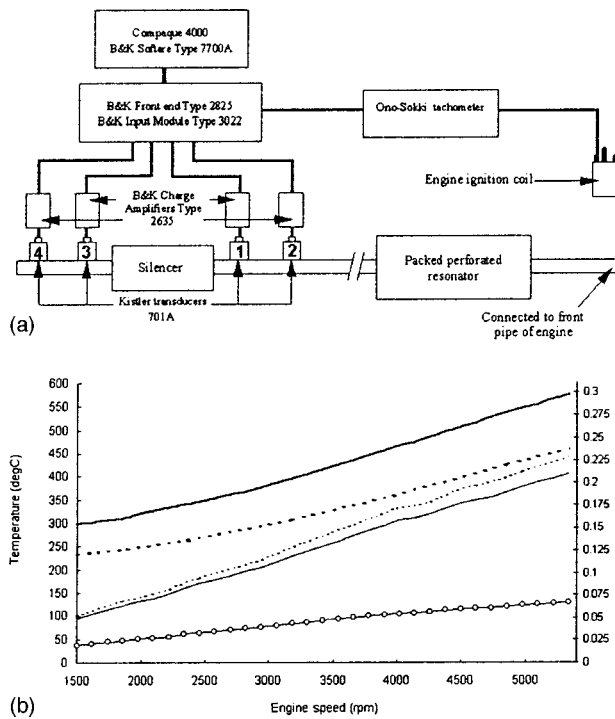
FIG. 4. (a) Experimental setup used for the measurements on the vehicle. Mass flow (circles), inlet temperature (thick solid line), outlet temperature (thick dashed line), inlet Mach number (thin dashed line), and outlet Mach number (thin solid line) recorded for the Honda 1.5 l during a full throttle run up on the chassis dynamometer.

FIG. 5. Normalized acoustic power flux in the tailpipe at Mach number $M = 0.2$, (a) low flow noise system, (b) high flow noise system; (—) measured; (- - -) predicted.

further pair of electrets mounted on the expansion chamber, with an additional one in free field near the open termination.

III. DETERMINATION OF FLOW DUCT ACOUSTIC PROPERTIES

Some acoustic characteristics of flow ducts, such as reflection coefficients, impedance, and sound power flux spectra, can all be evaluated at some specific location[5] with the corresponding values of the incident and reflected component wave spectra $\hat{p}_n^{\pm}$. These relate to the axial reference position of say the transducer labeled n of the local pair.[1] However, when the required behavior concerns acoustic transfer across a duct element or section linking two lengths of pipe, such as in Fig. 4, one also needs to establish the relative phase of the signals from the two pairs of transducers on the corresponding pipes. This can be determined[1] by calculating either the cross-spectrum $\hat{G}_{1n}$, or transfer function $\hat{H}_{1n}$ between the reference transducer n of one pair and say 1 of the other. Then one can establish the required $\hat{p}_{n(\text{ref})}^{\pm}$ from

$$\hat{p}_{n(\text{ref})}^{\pm} = \hat{p}_n^{\pm} \frac{\hat{G}_{1n}}{(\hat{p}_1^+ + \hat{p}_1^-)^*(\hat{p}_n^+ + \hat{p}_n^-)} = \hat{p}_n^{\pm} \hat{H}_{1n} \frac{(\hat{p}_1^+ + \hat{p}_1^-)}{(\hat{p}_n^+ + \hat{p}_n^-)}. \quad (8)$$

Computer codes exist for predicting wave propagation along flow ducts, but it seems that they all rely to some extent on measurement to quantify acoustic sources, and aeroacoustic sources in particular,[11,12] when seeking to predict sound power emissions. However measurement of source independent properties, such as transfer functions, impedances, and appropriately normalized sound power flux, can all be com-

pared directly with predictions by appropriate existing codes.[1] One such experimentally validated linear acoustic code, APEX, developed by the second author (P.O.A.L.D.),[11,12] proved suitable for this purpose.

A. Sound power measurements in strongly excited ducts

Sound pressure levels within industrial ducts with flow may commonly exceed 160 dB, so that arguably, the assumption of linear acoustic behavior ceases to be realistic. To investigate this, initial laboratory measurements were undertaken at corresponding sound pressure levels. First, this was with a simple expansion chamber ten-pipe-diameters long with an area-expansion ratio of 7.8, as shown in Fig. 1 of Ref. 1. These proportions were chosen[4] to ensure that any contributions from aeroacoustic sources remained relatively small. The observed sound power flux in the exit pipe (or tailpipe) normalized by the incident power in the inlet (or downpipe)[1] is compared with predictions obtained with APEX in Fig. 5(a). A sequence of such measurements gave similar results. Here the peaks in power flux at 360, 720, 1100, and 1460 Hz correspond to tailpipe acoustic resonances while those at 450, 900, and 1350 Hz correspond to chamber resonances. Reference to the autospectra in Fig. 3(a3) indicates that the raggedness of the plots from 100 to 300 Hz and around 900 or 1000 Hz corresponds to relatively low acoustic signal levels at microphone 1, so this is probably an artifact of the experimental conditions. Similar comments apply to the comparisons in Fig. 6(a) between observed radiated power and that predicted from the similarly contaminated measured tailpipe power flux. Elsewhere, in Figs. 5 and 6, the generally close agreement to within 1 or 2 dB between observed and predicted spectra suggests that any experimen-
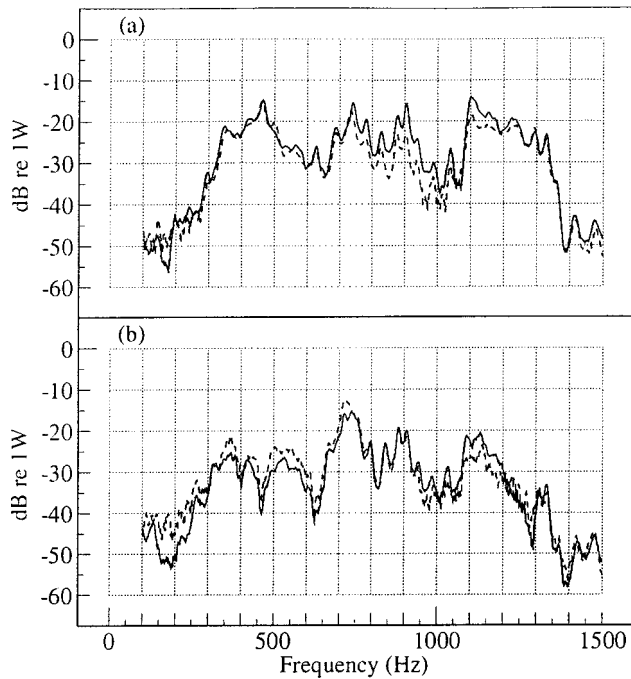
FIG. 6. Radiated acoustic power at Mach number $M=0.2$, (a) low flow noise system, (b) high flow noise system; (—) measured; (---) predicted from tailpipe power flux.

tal or modeling errors are no greater than this, in agreement with earlier observations.[1] However, there is also a shortfall of some 3–5 dB in the measured tailpipe power flux in Fig. 5(a) between 800 and 1000 Hz. As expected this is also reproduced in the predictions in Fig. 6(a) and corresponds to rather lower levels of acoustic excitation of the system over this frequency band.

Similar comparisons in Figs. 5(b) and 6(b) were obtained after the chamber had been modified by halving the length of the internal flow path to 5 diameters, resulting in a 20-fold increase[4] in the strength of excitation by aeroacoustic sources associated with vortex shedding in the expansion chamber. This was accomplished by inserting the tailpipe halfway into the chamber, as shown in Fig. 2(b) of Ref. 8, to form an annular sidebranch[2,5] at its outlet end. The new geometry produced reductions in sound power flux in excess of 10 dB centered at 400 and 1200 Hz corresponding, respectively, to the first two sidebranch resonances and these are clearly indicated in both observed and predicted results. Furthermore, the results in Fig. 6(b) show that measurements of the radiated power are generally in good agreement with predictions calculated[1] from the measured tailpipe flux. This is a result that was consistent with all those from several similar sets of experiments. Combined with existing experimental evidence,[4,6,8,12] this strongly suggests that the discrepancies between predictions and measurements between 400 and 700 Hz in Fig. 5(b) arise from nonlinear transfers between flow energy and sound energy by aeroacoustic mechanisms.[8] These are directly associated with acoustically synchronized vortex shedding at an area expansion,[4,8,12] leading to frequency-dependent reverberant amplification or attenuation[4] of an incident sound field, thus giving rise to the observations recorded in Fig. 5(b). It is well known[2,4] that
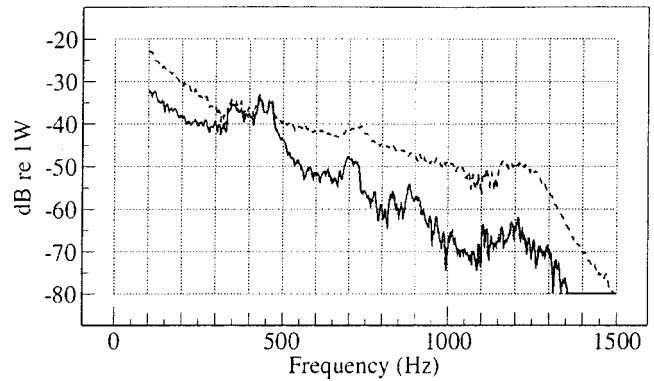
FIG. 7. Measured power flux in tailpipe at $M=0.1$, sound sources switched off; (—) coherent; (---) total.

such behavior can be effectively eliminated by bridging between the inlet and outlet pipes of an expansion chamber with an acoustically transparent perforated pipe,[4] since its presence then suppresses periodic vortex formation. Such aeroacoustic mechanisms and their control is a topic of active research, but any representation of their acoustic influence is not currently included in the APEX code.

The experimental evidence also demonstrates that the assumption of one-dimensional linear acoustic wave motion during the reduction of the experimental data was justified in the present context, at least for sound power measurements based on signals acquired from closely spaced transducer pairs. To show this, one notes first, that the wave motion in an intake/exhaust duct with flow represents a periodically excited, highly reverberent field, where propagating wave energy normally remains a small fraction of the total fluctuating energy. Second, that the peak to trough pressure ratio corresponding to a SPL of 165 dB is around 1.07, and that this pressure change is not a step, but is spread over a distance of some 0.5 m at the relatively modest frequencies of interest. Also that this predominately standing wave motion exists in relatively short runs of uniform pipe, typically less than 1 or 2 m long, bridging between area discontinuities. It is not surprising that the combined influence of all these relevant factors remains too small[11–14] for any significant wave steepening to occur within each pipe or system element. Finally the observed radiated power spectrum that is not subject to such nonlinearities corresponded closely to the
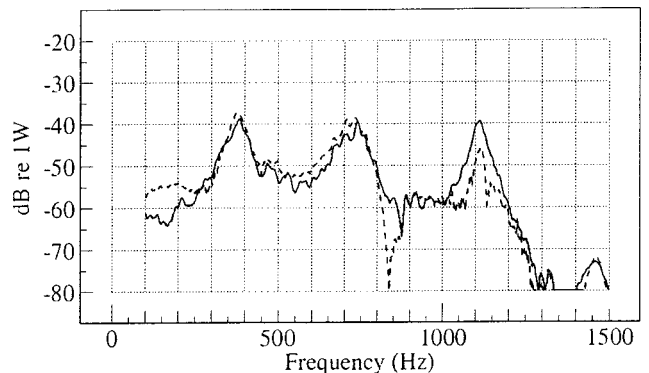
FIG. 8. Radiated coherent power; with "noisy" chamber at $M=0.2$; (—) measured in free field; (---) predicted from tailpipe power flux.

Holland *et al.*: Sound power measurements in ducts
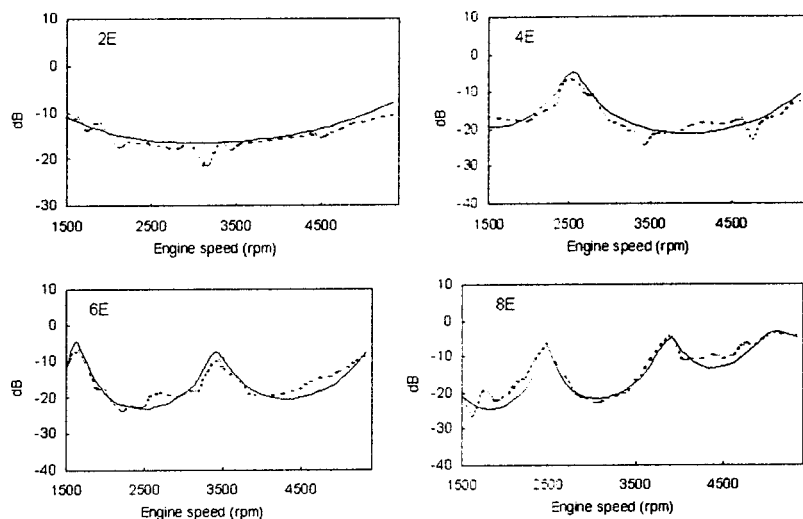
FIG. 9. Measured (thin dash line) and predicted (solid line) normalized acoustic power flux in the outlet pipe for a full throttle run up of the Honda 1.5 l.

measured power flux spectrum in the tailpipe. In such circumstances, it seems a reasonable assumption that acoustic models of wave propagation can still provide an adequate representation, even though, as one reviewer pointed out, many of the results compare measurements based on linear assumptions to computational results from a linear code.

Furthermore, other existing experimental evidence[15] suggests that acoustic models still provide a fair approximation to observed behavior with continuous periodic excitation at pressure amplitudes that are at least an order of magnitude higher than those recorded in the sequence of experiments described here. Such facts leads one to speculate whether some discrepancies reported in the literature between observations and predicted flow duct acoustic behavior, calculated with acoustic models, arise-from inadequacies in the assumptions adopted in the acoustic modeling,[2,11,12] rather than from wave steepening or similar physical factors. Among such,[11–14] one can include the neglect of the existence of aeroacoustic sources or sinks[4–6,8] at appropriate sites along the flow path, such as those whose influence is recorded in Fig. 5(b).

B. Flow excited sound fields

The measurements were repeated with the sound source switched off to identify the contributions from the aeroacoustic sources which were clearly audible. All the experimental evidence just described indicated that the coherent power flux represented the acoustic contribution[8] to the total power flux. The total and coherent power flux measured in the tailpipe of the simple chamber are compared in Fig. 7. Comparisons with Fig. 5(a) reveal that the tailpipe resonances at 360, 720, and 1100 Hz are clearly present as are the chamber resonances at 450 and 900 Hz. Clearer indications of these appear in the coherent power measurements indicating that the total power flux includes significant contributions from the pressure fluctuations convected with the flow. Such contributions are not evident with the excitation switched on, since the corresponding acoustic power was then increased by 30–40 dB, while both measured total and coherent power flux spectra are then closely similar, doubtless due to the selective averaging.

Similar comparisons shown in Fig. 8 were made for the "noisy" chamber. Here, the measured coherent radiated power is seen to be in close agreement with that predicted with the measured coherent tailpipe power flux[8] above 10^{-5} W and in fair agreement otherwise. This result also implies that the coherent power flux measured in the tailpipe arises predominately from the acoustic pressure field. Furthermore, such measurements provide a useful procedure for identifying the acoustic contributions in a fluctuating pressure field with direct application to isolating and quantifying aeroacoustic sources. Comparison of the results in Fig. 8 with the corresponding observations with excitation in Fig. 6(b) reveals that the contributions to the radiated power spectrum arising from reverberant amplification of the incident sound fields are absent from Fig. 8 as one would expect. See, for example, the reverberant increase of 10 dB between 500 and 600 Hz clearly present in both Figs. 5(b) and 6(b) but not in Fig. 8. Otherwise they indicate that there was now a relative drop in radiated sound power from 15 to 25 dB rather than 30 to 40 dB when the excitation is switched off, showing that the strength of the flow generated sources has been increased by 15 dB by halving the length of the free flow path in the expansion. This result is in fair agreement with previous observations.[4,8]

C. Vehicle measurements and predictions

The exhaust measurements[9] were performed at constant acceleration on a vehicle dynomometer at a controlled sweep
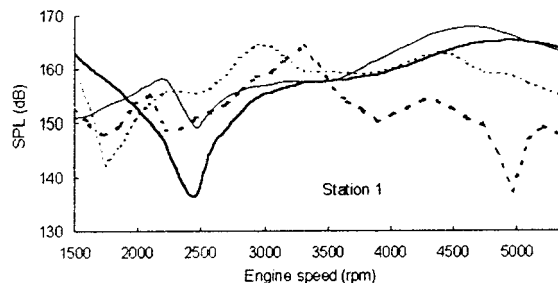
FIG. 10. Sound pressure orders measured at station 1 for the Honda 1.5 l during a full throttle run up on the chassis dynamometer, $2E$ (thick solid), $4E$ (thin solid), $6E$ (thin dash), $8E$ (thick dash).
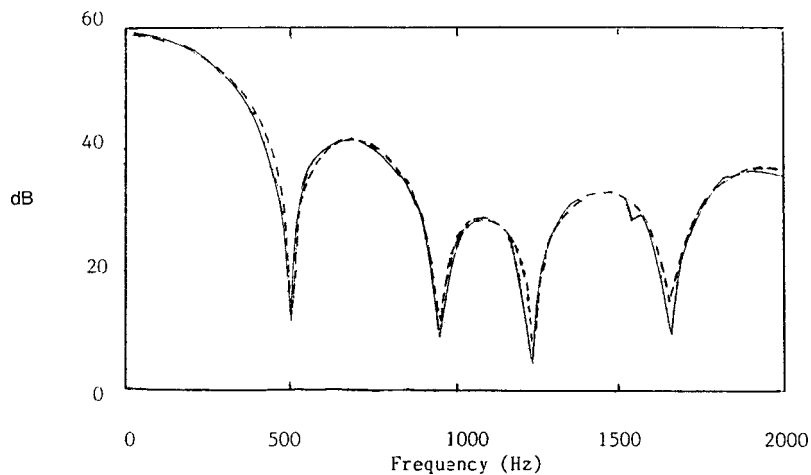
FIG. 11. Comparison between predicted transfer functions, (—) MOC and FDM (Ref. 16), (---) APEX.

rate of 30 rpm/s. The relevant signal processing used 0.025 order resolution, 75% overlap with a Hanning window, providing five averages over the measurement interval for each record. The order tracking was synchronized with the tachometer and the corresponding measured flow conditions [Fig. 4(b)] were employed for the power flux and other acoustic calculations with each record. Special precautions were taken when possible to avoid positioning the transducers at or near standing wave minima, particularly in the tailpipe. Appropriate additions and adjustments were also made to the APEX prediction code, to equip it for following the changing flow conditions during acceleration. A typical set of sound power flux measurements for the first four orders,[9] normalized by the incident power flux at transducer 2 in Fig. 4(a) is compared with the corresponding predictions in Fig. 9. Thus they represent the relative reductions in sound power flux associated with the expansion chamber. The results show close agreement between measured and predicted power flux at the resonant peaks. These spectral regions are obviously of the greatest practical significance for noise emission predictions. Similar agreement was found with comparisons[9] between the measured normalized radiated power and the predictions, and also between the corresponding pressure transfer functions at each of the four orders. One also notes that there is no evidence in these observations of any systematic energy transfer toward the higher harmonics that should be present in the spectral amplitude distributions if significant nonlinearities were present in the wave propagation.

The rather localized discrepancies elsewhere in the spectra in Fig. 9 often seem to be correlated[9] with low signal to noise ratios at one or more of the pressure transducers. The sound pressure levels for each of the first four orders recorded at transducer 1 during run up are plotted in Fig. 10. These exhibit systematic fluctuations of 20–30 dB, a feature presumably associated with wave interference and the resulting standing wave maxima and minima. Similar fluctuations in level were present[9] at the other transducer positions. Other measured characteristics,[9] such as acoustic attenuation spectra, showed better agreement with prediction as one might expect, since signal contamination by flow disturbances[1] then tends to cancel.

IV. DISCUSSION

The results summarized in this paper demonstrate several of the problems associated with the estimation of sound power flux in flow duct systems, such as those arising from poor signal to noise ratios associated with the existence of turbulent pressure fluctuations in combination with acoustic standing waves. The consequences of their presence may be tolerable when considering global system properties, such as pressure transfer functions, but further processing of the data records to yield robust estimates of acoustic power flux reveals the need for techniques providing greater experimental precision for these measurements. The success of swept-sine[1] or swept periodic excitation[9] combined with appropriate selective averaging in reducing such problems is demonstrated by the material presented here. With uncontrolled excitation, such as that induced by the flow, it has also been shown that coherent power flux measurements[8] can be closely identified with the acoustic contribution to the total power flux and thus assist in the evaluation of aeroacoustic sources.[8] In both cyclically and flow excited situations the results confirm that the assumptions involved in the derivation of Eqs. (6) and (7) remain appropriate even when boundary layer and other flow-induced pressure fluctuations are present.

The experimental evidence presented here also demonstrates that, in appropriate circumstances, data reduction, based on the one-dimensional linear acoustic models, can provide realistic descriptions of the acoustic characteristics of cyclicly excited flow duct systems and their elements, up to sound pressure levels in excess of 165 dB! With flow excited systems the maximum sound pressure levels recorded were around 20 dB lower than this, although the corresponding overall fluctuating pressure levels were still close to 160 dB. Acoustic characteristics calculated with linear acoustic models[1,8,9] were also found to be in good agreement with the measurements, indicating that wave steepening is not a significant factor at the conditions of these experiments.

One reviewer expressed some disagreement with these conclusions suggesting comparisons should also be made with predictions from a fully nonlinear computation. Such calculations of the pressure transfer function spectra between system input and the radiated field[16] by the method of char-

Holland *et al.*: Sound power measurements in ducts

acteristics and by second-order finite difference schemes provide an appropriate sequence of five examples where leading geometric dimensions are given, but not the flow temperatures. Calculations with APEX providing linear predictions for the first system, where the geometry was fully defined, for a best-fit temperature of 18 °C are compared with the results[16] of nonlinear calculations in Fig. 11. Similar comparisons for the four more complex systems normally gave similarly good agreement up to 1000–1400 Hz, but there were some local spectral discrepancies at higher frequencies, probably where the missing geometric detail and the neglect of three-dimensional effects[16] had a significant influence.

ACKNOWLEDGMENTS

[1] K. R. Holland and P. O. A. L. Davies, "The measurement of sound power flux in flow ducts," J. Sound Vib. **230**, 915–932 (2000).

[2] P. O. A. L. Davies, "Piston engine intake and exhaust system design," J. Sound Vib. **190**, 677–712 (1996).

[3] C. L. Morfey, "Acoustic energy in non-uniform flows," J. Sound Vib. **14**, 159–170 (1971).

[4] P. O. A. L. Davies, "Flow-acoustic coupling in ducts," J. Sound Vib. **77**, 191–209 (1981).

[5] P. O. A. L. Davies, "Practical flow duct acoustics," J. Sound Vib. **124**, 91–115 (1988).

[6] P. O. A. L. Davies, "Aeroacoustics and time varying systems," J. Sound Vib. **190**, 345–362 (1996).

[7] J. V. Chung and D. A. Blaser, "Transfer function method of measuring acoustic intensity in a duct system with flow," J. Acoust. Soc. Am. **68**, 1570–1579 (1980).

[8] P. O. A. L. Davies and K. R. Holland, "The observed aeroacoustic behavior of some flow-excited expansion chambers," J. Sound Vib. **239**, 695–708 (2001).

[9] D. C. van der Walt, "Measurement technique to assess the acoustic properties of a silencer component for transient engine conditions," J. Sound Vib. **243**, 797–821 (2001).

[10] R. Ramakrishnan, "A note on the reflection coefficients of higher duct modes," J. Sound Vib. **72**, 554–558 (1980).

[11] P. O. A. L. Davies and M. F. Harrison, "Predictive acoustic modeling applied to the control of intake/exhaust noise of internal combustion engines," J. Sound Vib. **202**, 249–274 (1997).

[12] P. O. A. L. Davies and K. R. Holland, "IC engine intake and exhaust noise assessment," J. Sound Vib. **223**, 425–444 (1999).

[13] R. J. Alfredson and P. O. A. L. Davies, "The radiation of sound from an engine exhaust," J. Sound Vib. **13**, 389–408 (1970).

[14] R. J. Alfredson and P. O. A. L. Davies, "The performance of exhaust silencer components," J. Sound Vib. **15**, 175–196 (1971).

[15] E. A. A. Yaseen and P. O. A. L. Davies, "Finite interfering waves in continuously excited open pipes," J. Sound Vib. **124**, 586–59 (1988).

[16] A. Onerati, "Nonlinear fluid dynamic modeling of reactive silencers involving extended inlet/outlet and perforated ducts," Noise Control Eng. J. **45**, 35–51 (1997).

Adaptive beamforming for nonstationary arrays

Michael V. Greening[a]

Defence Science and Technology Organisation, Edinburgh Site, MOD Building 79, P.O. Box 1500, Edinburgh, S.A., 5111, Australia

Jane E. Perkins

Defence Science and Technology Organisation, HMAS Stirling Site, MOD Building A51, Rockingham, W.A., 6958, Australia

Adaptive beamformers automatically adjust to the input data on the sensors in an attempt to maximize the bearing resolution of a signal and minimize the effects of noise or interfering signals. To the author's knowledge, all adaptive beamformers currently available in the literature assume that the sensors are stationary over the time required to collect the data. This assumption is invalid on arrays of sensors mounted on nonstationary platforms, and results in poor beamforming performance. In this paper we present an adaptive beamformer that has been designed to operate on nonstationary arrays. The beamformer directly incorporates any changes in array shape or heading that may occur during the time required to collect the data. The output of the adaptive beamformer is shown for both synthetic data and for real data collected on a towed array. Results show that signal detection, bearing accuracy, bearing resolution, and interference suppression all increase when the array shape and track are incorporated into the beamformer if the sensor platform is not stationary. © *2002 Acoustical Society of America.* [DOI: 10.1121/1.1514931]

PACS numbers: 43.60.Gk, 43.30.Wi [JCB]

I. INTRODUCTION

Beamforming techniques determine the direction of incoming signals by applying weights and phase changes to the sensor inputs, and summing the results to match the phase changes across the array that would occur for a signal arriving from a given direction. Conventional beamforming techniques use a fixed set of weights that do not change with the sensor inputs or the direction examined. Adaptive beamformers automatically adjust the weights depending on both the sensor inputs and the direction.[1–3] This is done to maximize the array gain and bearing resolution while minimizing the effects of noise or interfering signals.

One problem with most adaptive beamformers is that the input data must be averaged over time to form an estimate of the noise and to decorrelate different signals.[4–6] Without data averaging, different signals appear correlated and signal cancellation occurs. The amount of time averaging required can be decreased by dividing the array into subarrays and performing spatial smoothing.[7,8] A second problem with most adaptive beamformers is that they are sensitive to errors or perturbations in the system response, the propagating medium, or the signal field.[9–12] The sensitivity of adaptive beamformers can be partially controlled by applying different forms of constraints to the minimization.[13,14]

The combination of sensitivity to array errors such as errors in sensor positions, along with the requirement to average data means that adaptive beamformers are sensitive to array movement.[15] Most adaptive beamformers assume that the array is stationary over the time required to collect the data. This assumption results in poor performance on nonsta-

tionary arrays. In the context of this paper, a nonstationary array is an array that is moving in a manner such that the relative phase changes measured across the array from an infinitely distant source change as a function of time. This includes arrays that change shape or heading. In this paper we present an adaptive beamformer that has been designed to operate on nonstationary arrays by directly incorporating any changes in array shape and heading that may occur during the time required to collect the data.

The output of the adaptive beamformer is shown for both synthetic data and real data on moving arrays. The real data were collected on a towed array that performed a 60° turn. The array shape and path were estimated by incorporating a compass on the array to determine the track of the compass and array. Results show that signal detection, bearing accuracy, bearing resolution, and interference suppression all increase when the array shape and track are incorporated into the beamformer if the sensor platform is moving.

II. THEORY

In this section we give a mathematical review of the minimum variance distortionless response (MVDR) adaptive beamformer for stationary arrays, and also give the theory of the adaptive beamformer designed for nonstationary arrays. Although the theory of the MVDR beamformer is available in the literature,[1–3] it will be outlined here to help set the stage for the derivation of the adaptive beamformer for nonstationary arrays.

A. Adaptive beamforming on stationary arrays

Consider a stationary array of N sensors with the axis defined as pointing in the direction from the Nth to the first sensor. Which end is defined as having the first or Nth sensor

[a]Electronic mail: mike.greening@dsto.defence.gov.au
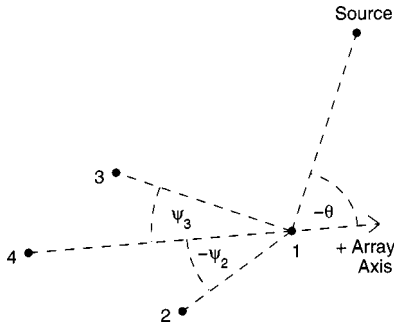
FIG. 1. A four-sensor stationary array showing the positive array axis, the sensor angles ψ_2 and ψ_3 ($\psi_1 = \psi_4 = 0$), and the arrival angle for a source at bearing $-\theta$ relative to the array axis. The array axis is defined as pointing from the fourth to the first sensor as used in Eq. (1).

is arbitrary, but for the purposes of towed arrays it is convenient to define the first sensor as that closest to the towship. For a plane wave source arriving at angle θ, the time delay τ_n between the first and nth sensor is given as

$$\tau_n(\theta) = (d_n/v)\cos(\theta - \psi_n), \tag{1}$$

where d_n is the distance from the first to nth sensor, v is the speed of propagation of the wave, $v = f\lambda$, f is the frequency, λ is the wavelength, and ψ_n is the angular separation of the nth sensor from the axis of the array, as shown in Fig. 1. The source angle θ is defined as the angle between the source, the first sensor of the array, and the positive axis of the array, with positive source angles in a clockwise direction relative to the positive axis of the array. The sensor angle ψ_n is defined as the angle between the nth sensor, the first sensor, and the negative axis of the array, with positive sensor angles in a clockwise direction relative to the negative axis of the array. For straight arrays, $\psi_n = 0$. Beamforming then determines the bearing of the source by summing the weighted and delayed outputs of the sensors to form a beam $y(t, \theta)$ as

$$y(t, \theta) = \sum_{n=1}^{N} z_n x_n(t + \tau_n(\theta)), \tag{2}$$

where $x_n(t)$ is the output of the nth sensor at time t, and z_n and τ_n are the complex weight and time delay or phase lag applied to the nth sensor. Weightings are applied to increase resolution or minimize sidelobes while phase lags are used to steer the beam in a particular direction. Again, considering a plane wave source arriving at angle θ relative to the axis of the array, the beam $y(t, \theta)$ will have a maximum when the time delays applied at each sensor match those predicted from Eq. (1) for a source at that angle.

A particular frequency can then be examined by taking the Fourier transform of Eq. (2) to get

$$
\begin{aligned}
Y(f, \theta) &= \sum_{n=1}^{N} z_n \exp(2\pi i f \tau_n(\theta)) X_n(f) \\
&= \sum_{n=1}^{N} z_n \exp\left(2\pi i f \frac{d_n}{v}\cos(\theta - \psi_n)\right) X_n(f) \\
&= \sum_{n=1}^{N} z_n s_n(f, \theta) X_n(f), \tag{3}
\end{aligned}
$$

where $s_n(f, \theta)$ is defined as the steering vector and contains the phase lags used to steer the beam in the direction θ. The conventional beamformer is then defined as

$$B(f, \theta) = |Y(f, \theta)|^2. \tag{4}$$

In the conventional beamformer, the weights z_n are independent of the input $X_n(f)$, or the look direction angle θ. To help reduce the effects of noise, time averaging is often performed to give

$$B(f, \theta) = \langle |Y(f, \theta)|^2 \rangle, \tag{5}$$

where $\langle \rangle$ denotes the expected value or time average. For a stationary array, the steering vector term, $s_n(f, \theta)$, is independent of time and can be taken outside of the expectation. In matrix notation, Eq. (5) can then be transformed into

$$B(f, \theta) = \vec{w}^*(f, \theta)\underline{R}(f)\vec{w}(f, \theta), \tag{6}$$

where $\underline{R}(f)$ is an $N \times N$ covariance matrix $\underline{R}(f) = \langle \vec{X}(f)\vec{X}^*(f) \rangle$, $\rightarrow$ denotes a column vector, $*$ denotes the complex conjugate transpose, $\vec{w}(f, \theta)$ is a weighted steering vector combining both the sensor weights and phase changes with components $w_n = z_n^* s_n^*$. Note that z_n and s_n are sometimes redefined as their complex conjugates in Eq. (3) so that w_n can be written as $w_n = z_n s_n$.

The MVDR beamformer is an adaptive beamformer that adjusts the weights applied to the array depending on both the input $\vec{X}(f)$ and the look direction angle θ. This is done to increase the bearing resolution and decrease the contribution of sidelobes. The technique works by minimizing the total received power while keeping the response in the look direction equal to that of the conventional beamformer. Thus, the idea is to minimize $B(f, \theta) = \vec{w}^*(f, \theta)\underline{R}(f)\vec{w}(f, \theta)$ subject to the constraint $\vec{s}^*(f, \theta)\vec{w}(f, \theta) = N$ where $\vec{s}(f, \theta)$ is the steering vector with components s_n and represents an ideal plane wave arriving at angle θ. This is solved by the method of Lagrange multipliers which turns the constrained minimization into an unconstrained minimization by minimizing the function

$$F = \vec{w}^*(f, \theta)\underline{R}(f)\vec{w}(f, \theta) + \lambda(\vec{s}^*(f, \theta)\vec{w}(f, \theta) - N), \tag{7}$$

where λ is the Lagrange multiplier (not the wavelength of the acoustic plane wave as previously). The minimization is solved by setting the derivatives $\partial F/\partial \vec{w} = 0$ and $\partial F/\partial \lambda = 0$. This results in

$$\vec{w}(f, \theta) = \frac{N\underline{R}^{-1}(f)\vec{s}(f, \theta)}{\vec{s}^*(f, \theta)\underline{R}^{-1}(f)\vec{s}(f, \theta)}, \tag{8}$$

which in turn leads to:

$$B(f, \theta) = \frac{N^2}{\vec{s}^*(f, \theta)\underline{R}^{-1}(f)\vec{s}(f, \theta)}. \tag{9}$$

It should be noted that for the conventional beamformer, time averaging is not necessary for the mathematical derivation and either Eq. (4) or (5) can be used. This allows continuous beamforming using Eq. (4) or a slower but less noise sensitive beamforming using Eq. (5). The MVDR beamformer however, requires averaging for the mathematical derivation. This is because the inverse of the covariance matrix $\underline{R}$ is used. A necessary condition for $\underline{R}$ to be nonsingular

is that averaging is performed over more samples than the number of sensors. Another potential problem with MVDR beamforming that can be solved by time averaging relates to how the method responds to coherent signals. If two signals arriving from different angles remain perfectly coherent over the averaging time, then minimizing $B(f,\theta)$ will cancel both of these signals so that they will not be seen.[4–6] Fortunately, the real world contains moving sources, time-varying sound speed profiles, etc., which all cause slight phase and amplitude fluctuations in arriving signals as a function of time and, thus, signals do not remain perfectly coherent over time. The amount of time averaging required to ensure incoherent signals depends on several properties such as sea state, frequency, and target speed. In practice, to reduce the effects of coherent signals, and make $\underline{R}$ well conditioned, averaging is often performed over twice as many samples as the number of sensors. An alternate method of ensuring the nonsingularity of $\underline{R}$ is to prewhiten it by adding a scalar multiple of the identity matrix.[16] This is often performed in beamforming techniques[17] and in matched field processing.[18] If the data is broadband, then steered covariance matrices can also be used to make $\underline{R}$ well conditioned.[19]

B. Adaptive beamforming on nonstationary arrays

For nonstationary arrays, the time delay or phase change given by Eq. (1) must be modified to be

$$\tau_n(\theta,t)=(d_n(t)/v)\cos(\theta-\psi_n(t)),\tag{10}$$

where $d_n(t)$, $\psi_n(t)$, and $\tau_n(\theta,t)$ are now functions of time t. A question that now arises is how to define the axis of the array. If the axis is still defined as pointing from the Nth to the first sensor and the array is not following a straight path, the axis will change directions with every time step. The beamformed output, which is determined relative to the axis of the array, will then show the direction to a stationary source changing over time as the array axis changes. Time averaging would spread the measured source direction over a bearing spread equal to the array axis change. A better choice for array axis is one in which a distant, stationary source remains at a fixed direction. Thus, the array axis will be defined as the line passing through the first sensor and pointing north, as shown in Fig. 2.

A beam steered in direction θ is then given as

$$Y(f,\theta,t)=\sum_{n=1}^{N} z_n \exp(2\pi i f \tau_n(\theta,t))X_n(f,t)$$

$$=\sum_{n=1}^{N} z_n \exp\left(2\pi i f \frac{d_n(t)}{v}\cos(\theta-\psi_n(t))\right)X_n(f,t)$$

$$=\sum_{n=1}^{N} z_n s_n(f,\theta,t)X_n(f,t),\tag{11}$$

where the steering vector term s_n now depends on time and therefore cannot be taken outside the expectation when time averaging is performed. Note also that X_n is now explicitly written as a function of time because the response of a stationary signal will change with time as the array changes with time. In practice, the time series is divided into short
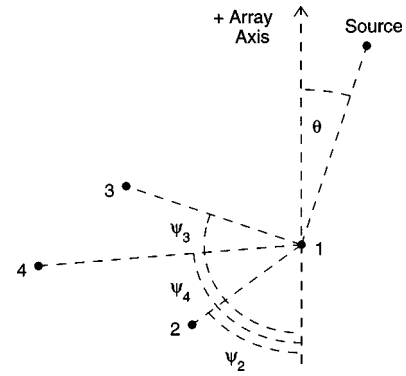
FIG. 2. A four-sensor nonstationary array for one time step, showing the positive array axis, the sensor angles ψ_2, ψ_3, and ψ_4 ($\psi_1=0$), and the arrival angle for a source at bearing θ relative to the array axis. The array axis is defined as passing through the first sensor and pointing north, as used in Eq. (10).

sections of data, each of which is used to obtain an X_n at time t. The array is then assumed to be stationary over the time span of individual sections of data but may be nonstationary between sections. Note that Eq. (11) does not include the Doppler effect that can be important in some applications. The significance of the Doppler effect will be examined in Sec. III A.

The fact that s_n cannot be taken outside the expectation means that Eq. (6) cannot be used for beamforming on a nonstationary array. This is a problem for adaptive beamforming since this is usually the starting point for its derivation.[2,3] However, if Eq. (5) is used as the starting point, then beamforming can be written as

$$B(f,\theta)=\langle|Y(f,\theta,t)|^2\rangle$$

$$=\langle\vec{z}^*\underline{S}^*(f,\theta,t)\vec{X}(f,t)\vec{X}^*(f,t)\underline{S}(f,\theta,t)\vec{z}\rangle$$

$$=\vec{z}^*\langle\underline{S}^*(f,\theta,t)\vec{X}(f,t)\vec{X}^*(f,t)\underline{S}(f,\theta,t)\rangle\vec{z}$$

$$=\vec{z}^*\underline{P}(f,\theta)\vec{z},\tag{12}$$

where z_n has been redefined as its complex conjugate and $\underline{S}$ is a diagonal matrix (steering matrix), with the diagonal elements given by

$$S_{n,n}=s_n^*=\exp\left(-2\pi i f \frac{d_n(t)}{v}\cos(\theta-\psi_n(t))\right).\tag{13}$$

The difference between Eqs. (12) and (6) is that in Eq. (6) the weighting vector $\vec{z}$ and steering vector $\vec{s}$ have been combined to form a weighted steering vector $\vec{w}$ with components $w_n=z_n s_n$, which is removed from the expectation, while in Eq. (12) the weighting vector and steering matrix have been left separate and only the weighting vector is removed from the expectation. The matrix $\underline{P}(f,\theta)$ is a steered covariance matrix similar to that used by Krolik and Swingler.[19] In their work, only stationary arrays were considered so that the steering matrix $\underline{S}$ remained time independent but was used to produce a more stable adaptive beamformer by averaging over frequency for broadband signals. In this work, nonstationary arrays are considered by including the time dependence of the array shape in the steering matrix $\underline{S}$.

M. V. Greening and J. E. Perkins: Beamforming for nonstationary arrays

As in the MVDR beamformer for linear, stationary arrays, the power is minimized under the constraint that the response in the look direction equals that of the conventional beamformer. Using Eq. (12), the constraint is $\vec{c}^*\vec{z}=N$ where $\vec{c}$ is a unit column vector. Then, using the method of Lagrange multipliers, the unconstrained minimization problem is to minimize the function

$$F=\vec{z}^*\underline{P}(f,\theta)\vec{z}+\lambda(\vec{c}^*\vec{z}-N), \tag{14}$$

by setting the derivatives $\partial F/\partial\vec{z}=0$ and $\partial F/\partial\lambda=0$. This results in

$$\vec{z}=\frac{N\underline{P}^{-1}(f,\theta)\vec{c}}{\vec{c}^*\underline{P}^{-1}(f,\theta)\vec{c}}, \tag{15}$$

which in turn leads to

$$B(f,\theta)=\frac{N^2}{\vec{c}^*\underline{P}^{-1}(f,\theta)\vec{c}}. \tag{16}$$

Note that the adaptive beamformer for a nonstationary array requires calculating and inverting a separate $\underline{P}(f,\theta)$ for every look direction, θ, desired. This may take significant computational time for large numbers of sensors. The computational time may be significantly reduced by implementing the problem in beam space rather than element space.[20,21] It should be noted that if the array is stationary, Eq. (16) reduces to Eq. (9).

III. RESULTS

In this section we show some results of the nonstationary array adaptive beamformer on both synthetic data and real data. The synthetic data study shows the improvement in beamforming performance on moving arrays when the array motion is incorporated into the beamformer. It also shows the interference suppression available on the nonstationary array adaptive beamformer, along with the effects of coherent signals on the beamformer. The real data shows results from a towed array that performed a 60° turn.

A. Incoherent synthetic sources

For the first part of the synthetic data study, all signals are assumed to be completely incoherent, even if measured over only a single time sample. Thus, the covariance matrix $\underline{R}$ and steered covariance matrix $\underline{P}$ for K sources and T time steps can be estimated according to

$$\underline{R}(f)=\frac{1}{T}\sum_{t=1}^{T}\left[\sum_{k=1}^{K}[\vec{X}_k(f,t)\vec{X}_k^*(f,t)]+\sigma^2I\right]$$

$$=\frac{1}{T}\sum_{t=1}^{T}\underline{R}_{\text{inc}}(f,t), \tag{17}$$

$$\underline{P}(f,\theta)=\frac{1}{T}\sum_{t=1}^{T}[\underline{S}^*(f,\theta,t)\underline{R}_{\text{inc}}(f,t)\underline{S}(f,\theta,t)], \tag{18}$$

where σ^2 is a white noise intensity level, and I is the identity matrix. Although the assumption of completely incoherent sources measured over only a single time sample is invalid, it allows an estimation of absolute beamforming levels when array motion is included, without the requirement to model

FIG. 3. Conventional (dashed) and adaptive (solid) beamformed output for synthetic data averaged over a maneuver. The towship heading starts due north and turns 40° to the east. The array starts straight, bends so that the deviation from linear is 2.5 acoustic wavelengths in the middle of the turn, and then straightens again to be straight by the end of the turn. A single target occurs due east. Beamforming is performed assuming the array is linear, stationary (top), or assuming both the array curvature and track are known (bottom). Output strength is in dB and bearings are given relative to towship heading (top) or relative to the north (bottom).

the effects of data averaging or coherent signals. These effects will be examined in Sec. III B.

Figure 3 shows the beamformed output of both the conventional and adaptive beamformers for synthetic data when the data are generated and averaged over 100 time steps during which the array is undergoing a maneuver. The array contains 24 hydrophones spaced at 0.5 acoustic wavelengths and the input consists of white noise of intensity level 0.1 and a single source of received intensity level 1.0 as measured on a single sensor. Thus, the beamformed level in the source direction should be $24^2\times1.0+24\times0.1=578.4=27.6$ dB while the background noise level should be $24\times0.1=2.4=3.8$ dB. At the start of the simulation, the array is straight, and the towship and array are traveling due north with the source due east. The array then undergoes a 40° turn east toward the source with a constant rate bearing change of 0.4° per time step. During the turn, the array shape is modeled as half a period of a sinusoid with an amplitude that starts at zero (straight array) for the first time step, increases by 0.05 acoustic wavelengths per time step for the first 50 time steps (to a maximum of 2.5 acoustic wavelengths), and decreases by 0.05 acoustic wavelengths per time step for the remaining time steps.

When beamforming is performed, assuming the array is linear and stationary (Fig. 3, top), neither the conventional nor the adaptive beamformers can distinguish between the left and right sides. Both the conventional and adaptive beamformers return broad peaks approximately 40° wide centered at ±70° with a received level of approximately 20 dB for the conventional beamformer and 16 dB for the adaptive beamformer. If beamforming is performed using the known array shape and track (Fig. 3, bottom), then both the conventional and adaptive beamformers improve, showing the target with the correct signal strength of 27.6 dB at 90°. On the east side (0° to 180°), the conventional beamformer shows a wide main beam and sidelobe structure while the
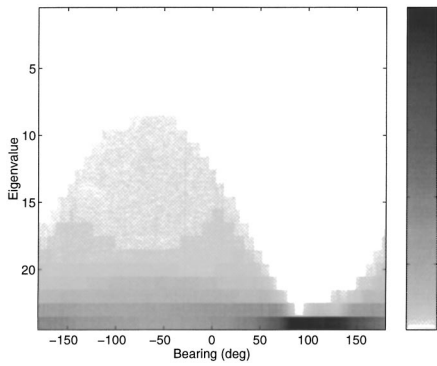
FIG. 4. Eigenvalues of $\underline{P}$ for the array and input data used to generate Fig. 3.

FIG. 5. Conventional (dashed) and adaptive (solid) beamformed output for synthetic data averaged over a maneuver. The towship heading starts due north and turns 40° to the east in only 5 time steps for which the array is always linear but changes heading by 10° in each time step. A single target occurs due east. Beamforming is performed on a linear array assuming the array is stationary (top), or assuming the array track is known (bottom). Output strength is in dB and bearings are given relative to towship heading (top) or relative to the north (bottom).

adaptive beamformer shows a narrow beam with a nearly flat background at the noise level of 3.8 dB. On the west side, however, both the conventional and adaptive beamformers perform poorly, showing a broad peak approximately 80° wide centered at −50°. The reason for this broad peak is due to the left/right ambiguity of straight arrays and will be explained in more detail later.

An examination of the eigenvalues of $\underline{R}$ shows that the smallest 10 eigenvalues are the noise level of 0.1, while the next 14 eigenvalues increase in size to a maximum of approximately 8. If the data were generated on a linear, stationary array, then the largest eigenvalue would be 24 while the remaining 23 eigenvalues would be 0.1. The smearing of the largest eigenvalue into other eigenvalues is caused by the array motion, which is not considered when calculating $\underline{R}$. An examination of the eigenvalues of $\underline{P}$ shows that at 90°, the largest eigenvalue is 24 while the remaining eigenvalues are 0.1. For all other bearings, there is some smearing of the eigenvalues of $\underline{P}$, as shown in Fig. 4. If the data were generated and beamformed on a linear, stationary array, then the largest eigenvalue of $\underline{P}$ would be 24 while the remaining eigenvalues would be 0.1, independent of bearing.

Figure 5 shows the beamformed output for synthetic data when the data are generated and averaged over only five time steps during which time the array remains straight but undergoes a 40° maneuver in steps of 10° for each time step. Note that by generating the synthetic data according to Eqs. (17) and (18), the covariance matrix $\underline{R}$ and steered covariance matrix $\underline{P}$ are invertible even though the number of time samples used is less than the number of sensors. When beamforming is performed assuming a stationary array (Fig. 5, top), both the conventional and adaptive beamformers return signals at ±50°, ±60°, ±70°, ±80° and ±90°, with no left/right distinction. The beamformed level of each of the ten signals is $\frac{1}{5}(24^2 \times 1.0) + 24 \times 0.1 = 117.6 = 20.7$ dB. If beamforming is performed using the known array track (Fig. 5, bottom), then both the conventional and adaptive beamformers show the target with the correct signal strength of 27.6 dB at 90°. Both beamformers also show 5 ambiguous signals on the west side at −10°, −30°, −50°, −70° and −90° with beamformed levels of 20.7 dB. The ambiguous signals occur because the array remains straight for every time step, and thus, each time step has an exact left/right ambiguity that cannot be resolved by one time step alone.

The difference between east and west occurs in this example because the known array heading allows all five time samples to be summed at the correct bearing on the east, but shifted by twice the heading change on the west. In general, Fig. 5 shows that errors in array heading for a given time step cause the signal to be estimated at an incorrect bearing for that time step.

When the array changes from linear, the left/right ambiguity begins to disappear, as seen in Fig. 6. The amount of left/right resolution for both the conventional and adaptive beamformers is shown in Fig. 7 as a function of the array curvature. As in Figs. 3, 5, and 6, the array is modeled as half a period of a sinusoid with the amplitude of the sinusoid given as the array curvature. Figure 7 is generated for a source at broadside to the array. As the source moves closer toward endfire, the left/right resolution decreases. If the scenario used for Fig. 3 started with an array curvature of 1.5 acoustic wavelengths, increased to 2.5 acoustic wavelengths,
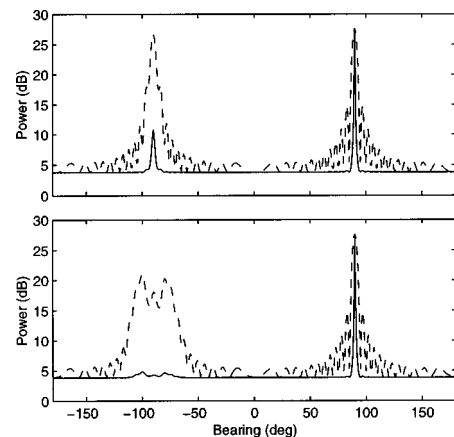
FIG. 6. Conventional (dashed) and adaptive (solid) beamformed output for synthetic data gathered on a stationary array with the towship heading due north and a single target due east. The array shape is half a period of a sinusoid with an amplitude of 0.1 acoustic wavelengths (top) and 0.5 acoustic wavelengths (bottom).
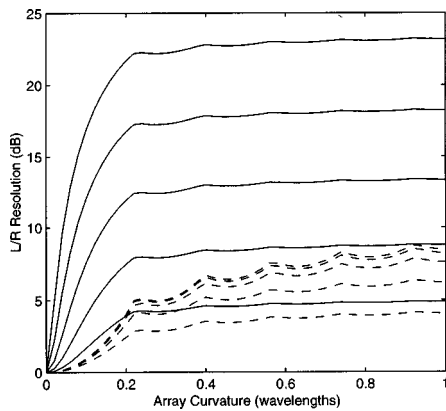
FIG. 7. Left/right resolution of the conventional (dashed) and adaptive (solid) beamformers for a curved array of 24 sensors with intersensor spacing of 0.5 acoustic wavelengths. The array shape is half a period of a sinusoid with an amplitude given as the array curvature measured in acoustic wavelengths. The left/right resolution is shown for sources at broadside with a SNR of +10, +5, 0, −5 and −10 dB as measured on a single sensor. The left/right resolution increases with increasing SNR.

and then decreased back to 1.5 acoustic wavelengths so that the array was never straight, then the suppression of the ambiguous side (west) improves, as shown in Fig. 8.

The left/right ambiguity resolution shown in Fig. 7 is closely related to the beamformers sensitivity to errors in the sensor positions. The left/right resolution shown in Fig. 7 as a function of array curvature is the same as the power loss associated with an error in the measured array curvature of twice the true curvature (i.e., the ambiguous side has an error in array shape of twice the true curvature of the array). The power loss in beamformed output of a signal for random sensor location errors is shown in Fig. 9. The loss shown in Fig. 9 is valid for both the stationary and non-stationary array beamformers if there is no error in the array headings. The large loss in power of the adaptive beamformer caused by errors in the estimated sensor locations emphasizes the

FIG. 8. Conventional (dashed) and adaptive (solid) beamformed output for synthetic data averaged over a maneuver. The towship heading starts due north and turns 40° to the east. The array shape starts with a curvature of 1.5 acoustic wavelengths, increases to 2.5 acoustic wavelengths, and decreases back to 1.5 acoustic wavelengths by the end of the turn. A single target occurs due east. Beamforming is performed assuming the array is linear, stationary (top), or assuming both the array curvature and track are known (bottom). Output strength is in dB and bearings are given relative to towship heading (top) or relative to the north (bottom).
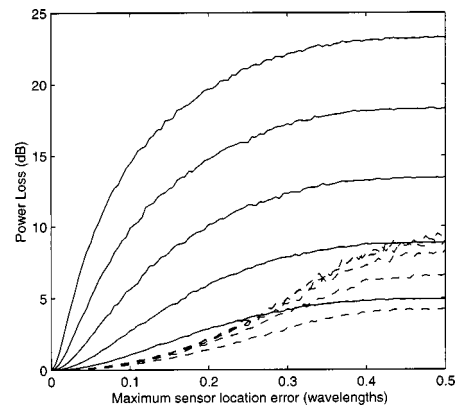
FIG. 9. Power loss of the conventional (dashed) and adaptive (solid) beamformers for an array of 24 sensors with intersensor spacing of 0.5 acoustic wavelengths when each array sensor location (both the x and y coordinate) is incorrectly estimated on a uniform distribution within $\pm$ maximum error indicated. The power loss is shown for sources with a SNR of +10, +5, 0, −5, and −10 dB, as measured on a single sensor. The power loss increases with increasing SNR. Each data point represents an average of 100 realizations of randomly incorrect array estimations.

need for nonstationary array adaptive beamforming when the array is changing shape.

Errors caused by an incorrect array shape are also related to errors caused by an incorrect frequency estimation created by the Doppler shift of a moving array. Consider an array initially traveling away from a signal at a speed of $v = 10$ m/s, and then performing a maneuver of $\theta = 60°$. The received signal after the maneuver will contain a frequency shift of

$$f_1 = f_0 \left(1 + \frac{v \cos \theta}{c} \right) = 1.0033 f_0, \quad (19)$$

where f_1 is the received frequency after the maneuver, f_0 is the received frequency before the maneuver, and c is the sound speed. For a broadband, flat spectrum signal, this will have no effect on the beamforming results. However, for a narrow band signal, there can be two effects on the beamformer: one caused by spreading of the signal into adjacent frequency bins, and a second caused by frequency shifts within a frequency bin. Consider an infinitesimally narrowband signal with an initial received frequency of 2000 Hz measured on a system with a processing resolution of 1 Hz. After the maneuver, the received frequency will be 2006.6 Hz. If the data is averaged over the entire maneuver, the signal will be spread over eight frequency bins and each frequency bin will contain approximately $\frac{1}{8}$ of the received signal level. Within each frequency bin, the signal will shift by 1 Hz over time while the processing assumes a constant frequency equal to the center frequency of the bin. The effect on beamforming of this frequency shift within the bin is equivalent to a stretching of the array by a ratio of $(1 + 1/2000) = 1.0005$. Thus, for a 24 element array at $\lambda/2$ spacing, the array has an effective stretch from 11.5 λ to 11.506λ. Figure 9 shows that an error in array shape estimation of 0.006λ has an insignificant effect on conventional or adaptive beamforming. Thus, the frequency shift within a bin has little effect on the beamforming for this example. If the signal had an initial received frequency of 200 Hz, then the
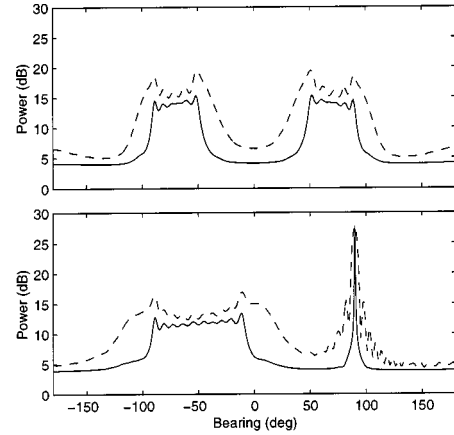
FIG. 10. Conventional (dashed) and adaptive (solid) beamformed output for synthetic data averaged over a maneuver. The towship heading starts due north and turns 40° to the east. The array starts straight, bends so that the deviation from linear is 2.5 acoustic wavelengths in the middle of the turn, and then straightens again to be straight by the end of the turn. The known array shape and track is always used in the beamformer. Input consists of a single target of intensity 100 at 90° (top), two targets each of intensity 100 at 90° and 92.5° (middle), and two targets of intensity 100 at 90° and intensity 1 at 92.5° (bottom).

FIG. 11. Conventional (dashed) and adaptive (solid) beamformed output for synthetic data gathered on a linear, stationary array with a heading due north. Input consists of a single target of intensity 100 at 90° (top), two targets each of intensity 100 at 90° and 92.5° (middle), and two targets of intensity 100 at 90° and intensity 1 at 92.5° (bottom).

received frequency after the maneuver is 200.66 Hz for a frequency shift of 0.66 Hz, which is contained within one frequency bin (assuming a center frequency of 200.5 Hz). In this case, the effective array stretch is by a factor of 1.0033 from 11.5λ to 11.538λ. Figure 9 shows that an error in length of 0.038λ can cause a 7 dB loss in adaptive beamforming output for a 10 dB SNR signal. Thus, for narrow band signals, the Doppler effect can cause the beamformed output to be spread over adjacent frequency bins or can cause a loss in performance within a frequency bin.

Two important issues with adaptive beamformers are the signal resolution and interference suppression available. Figure 10 shows the beamformed output of the nonstationary conventional and adaptive beamfo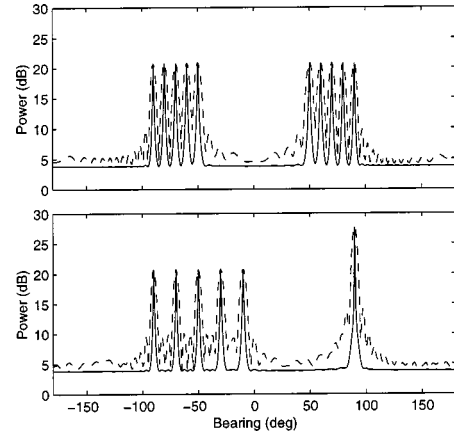rmers using the same array scenario as for Fig. 3, but with different input signals. The top figure has a white noise intensity level of 0.1 along with a single source at 90° with a received intensity level of 100 as measured on a single sensor. The middle and bottom figures have an additional signal at 92.5° with received intensity level 100 in the middle figure and received intensity level 1.0 for the bottom figure. The signal at 92.5° is well within the main lobe of the conventional beamformer and is only half the Rayleigh angle resolution limit of 2/(24-1) ≈0.087 rad≈5.0° away from the signal at 90°. The nonstationary array adaptive beamformer easily resolves the two signals when they are of equal strength and even gives an indication of the weaker signal at 92.5° when the signal at 90° is 20 dB stronger.

For comparison, Fig. 11 shows the results using the same input signals, but when the data are generated and beamformed on a stationary array that remains linear and is heading north. It can be seen that the interference suppression of the data collected and beamformed on a linear, sta-

tionary array is better than that collected and beamformed on a nonlinear, nonstationary array. However, Figs. 3, 5, and 8 showed that the stationary array adaptive beamformer breaks down if the array is changing shape or traveling along a nonlinear path. For the linear, stationary case shown in Fig. 11, the smallest 22 eigenvalues of both $\underline{R}$ and $\underline{P}$ are 0.1 while the largest two eigenvalues sum to 4800.0 (middle figure) and 2424.0 (bottom figure). For the nonlinear, nonstationary case shown in Fig. 10, the largest two eigenvalues of $\underline{P}$ at 90° and 92.5° have smeared into the smaller eigenvalues so that for the middle figure, eigenvalues 21 and 22 are approximately 0.22 and 2.6, respectively; while for the bottom figure, eigenvalue 22 is approximately 0.14.
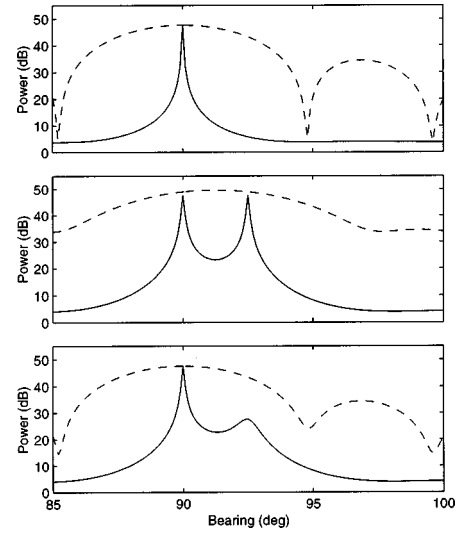
B. Coherent synthetic sources

The previous section generated synthetic data assuming signals were always perfectly incoherent. This is an invalid assumption when the data are averaged over a finite number of time samples, or when the signals are multipath arrivals from the same source. To model finite time samples or coherent sources, the complex output of the nth sensor for K plane wave arrivals at time t is given as

$$X_n(f,t) = \sum_{k=1}^{K} X_{nk}(f,t)$$

$$= \sum_{k=1}^{K} \sigma_k \exp\left[2\pi i \left(f \frac{d_n(t)}{v} \cos(\theta_k - \psi_n(t)) \right. \right.$$

$$\left. \left. + \phi_k(t) \right) \right], \tag{20}$$

where σ_k is the received pressure level of source k (σ_k^2 is the received intensity level), θ_k is the bearing of source k relative to the array axis, and $\phi_k(t)$ is the phase of the signal as measured at the first receiver at time t. The degree of coherence between two different signals is determined by the dif-
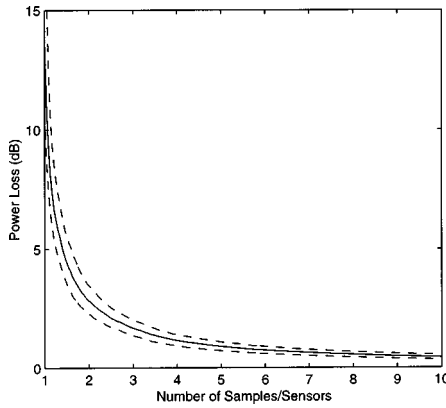
FIG. 12. Power loss of the adaptive beamformer when averaging over a finite number of data samples. The average power loss (solid) and standard deviation (dashed) is shown for 100 realizations at each number of data samples.

FIG. 13. Power loss of the adaptive beamformer as a function of the magnitude squared coherence of two signals. The number of data samples averaged was ten times the number of sensors.

ferences between the phases $2\pi(\phi_1(t) - \phi_2(t))$ as a function of time. For perfectly coherent signals, $2\pi(\phi_1(t) - \phi_2(t))$ is a constant, while incoherent signals are modeled by allowing $2\pi(\phi_1(t) - \phi_2(t))$ to be randomly chosen over a full 2π radians for each time sample. Intermediate levels of coherence are modeled by allowing the phase difference term to be randomly chosen from a smaller angular spread. For a stationary array, d_n and ψ_n are independent of time. Remember that the array axis is chosen as the line passing through the first sensor and pointing north so that the bearing of a distant source relative to the array axis is also independent of time.

The covariance matrix $\underline{R}$ and steered covariance matrix $\underline{P}$ for K sources and T time steps are now estimated as

$$\underline{R}(f) = \frac{1}{T}\sum_{t=1}^{T}\left[\left(\vec{\sigma}(t) + \sum_{k=1}^{K}\vec{X}_k(f,t)\right)\right.$$
$$\left.\times\left(\vec{\sigma}^*(t) + \sum_{k=1}^{K}\vec{X}_k^*(f,t)\right)\right]$$
$$= \frac{1}{T}\sum_{t=1}^{T}\underline{R}_{\mathrm{coh}}(f,t), \tag{21}$$

$$\underline{P}(f,\theta) = \frac{1}{T}\sum_{t=1}^{T}\left[\underline{S}^*(f,\theta,t)\underline{R}_{\mathrm{coh}}(f,t)\underline{S}(f,\theta,t)\right], \tag{22}$$

where $\vec{\sigma}(t)$ is the noise pressure level, which has a random level and phase for each sensor at every time step. For this study, the noise pressure level at each sensor was randomly picked from a Gaussian distribution centered on a desired noise pressure level with a standard deviation of $\frac{1}{4}$ the desired noise pressure level. Using Eqs. (21) and (22) to generate data, the number of time samples T must be at least as large as the number of sensors N for $\underline{R}$ and $\underline{P}$ to be invertible.

Using Eqs. (20)–(22), a finite averaging time results in all sources being measured with some degree of coherence, and adaptive beamforming will try to cancel the signals. Figure 12 shows the amount of power loss of each signal as a function of the number of data samples averaged, when adaptive beamforming is performed on a 24 element array. Figure 12 was produced using a desired noise pressure level

of 1.0 along with two signals of equal pressure level 1.0 at 60° and 90° with the phase difference term $2\pi(\phi_1(t) - \phi_2(t))$ being randomly chosen over a full 2π radians. The results show the average and standard deviation from 100 realizations for each number of data samples averaged. For a different number of sensors N, the power loss starts at $10\log N$ when the number of data samples equals the number of sensors, decreases to approximately 3 dB when the number of data samples is double the number of sensors, and decreases further to approximately 0.5 dB when the number of data samples is ten times the number of sensors. This is true using Eq. (21) for a stationary array, and also using Eq. (22) for a nonstationary array.

The effect of coherent signals on the stationary and non-stationary adaptive beamformers can be examined by changing the allowed angular spread in the difference in phases $2\pi(\phi_1(t) - \phi_2(t))$. Figure 13 shows the power loss of adaptive beamforming for each signal as a function of the magnitude squared coherence of the two signals. The magnitude squared coherence is estimated as

$$|\gamma|^2 = \frac{|\Sigma_{t=1}^{T}\vec{X}_1(f,t)\vec{X}_2^*(f,t)|^2}{(\Sigma_{t=1}^{T}|\vec{X}_1(f,t)|^2)(\Sigma_{t=1}^{T}|\vec{X}_2(f,t)|^2)}. \tag{23}$$

Figure 13 was produced using a desired noise pressure level of 0.001 along with two signals of equal pressure level 1.0 at 60° and 90°. All covariance matrices $\underline{R}$ and steered covariance matrices $\underline{P}$ were generated by averaging over 240 time samples (10 times the number of sensors). It should be noted that the power loss as a function of the signal coherence is the same for the stationary and nonstationary adaptive beamformers.

To help demonstrate the effects of time averaging, Fig. 3 was reproduced as Fig. 14 using Eqs. (20)–(22) to generate the data by averaging over 100 time samples with the phase difference term of the signals randomly chosen over a full 2π radians. The time averaging causes the background noise to be more random instead of flat, and results in the adaptive beamformer returning a signal level of only 26.8 dB at 90° instead of 27.6 dB. The signal loss of 0.8 dB for the adaptive beamformer agrees with that predicted from Fig. 12 when the number of data samples is approximately four times the
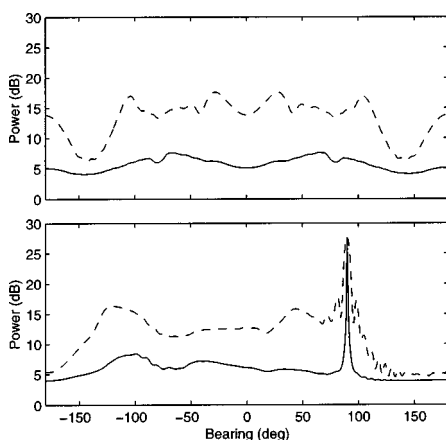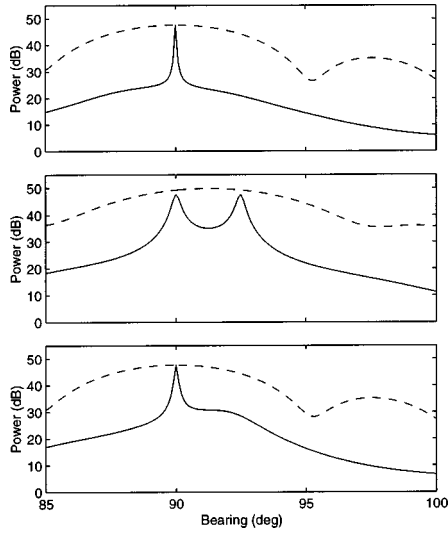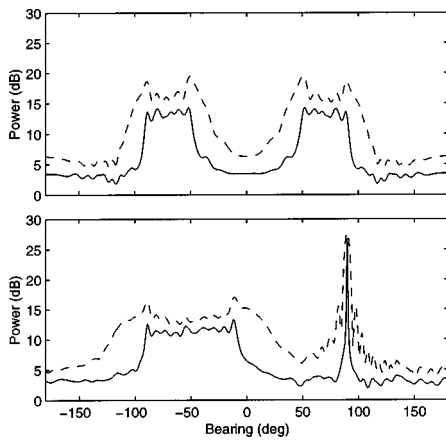
FIG. 14. Conventional (dashed) and adaptive (solid) beamformed output for synthetic data averaged over a maneuver. The towship heading starts due north and turns 40° to the east. The array starts straight, bends so that the deviation from linear is 2.5 acoustic wavelengths in the middle of the turn, and then straightens again to be straight by the end of the turn. A single target occurs due east. Beamforming is performed assuming the array is linear, stationary (top), or assuming both the array curvature and track are known (bottom). Output strength is in dB and bearings are given relative to towship heading (top) or relative to the north (bottom). Data is generated and averaged for 100 time steps on a 24-sensor array.

number of sensors. For the closely spaced signals in Figs. 10 and 11, if the data are produced using Eqs. (20)–(22), and averaged over 100 time samples, then the signals at 90° and 92.5° also suffer a loss of approximately 0.8 dB when adaptive beamforming is performed. This signal loss increases, as shown in Figs. 12 and 13, if the number of the data samples averaged is decreased, or the signals are made more coherent by restricting the angular spread of the phase difference term of the signals.

C. Real data

The nonstationary adaptive beamformer was also tested using real data. For the real data, both a towship towing an acoustic array and a target ship producing a tonal source were used. The target ship was approximately 60 km west, 20 km north of the towed array. The acoustic array contained 48 hydrophones with an interelement spacing of 0.66 acoustic wavelengths relative to the tonal source. The array contained a compass just past the last hydrophone to aid in estimating the array shape and track. Measurements of the towship speed and array heading were obtained every 4 s. Figure 15 shows the track of the compass in the array over a time sample of 200 s, during which the array has undergone a 60° maneuver. Positions are shown relative to the north and the compass position at a start time before the maneuver. The array is assumed to follow the track of the compass and the shape of the array is assumed to be a section of this track. The array shape and track could be determined more accurately using a fluid mechanical model along with measurements of the currents and mechanical properties of the array.[22,23] However, this was not performed here.

Figure 16 shows the beamformed output at times before, during, and after the towship maneuver. Before the maneuver (Fig. 16, bottom), the array heading is 15° and the target ship appears at −75° with a left/right ambiguity at 100°. The left/right ambiguity is unresolved because the array is trav-
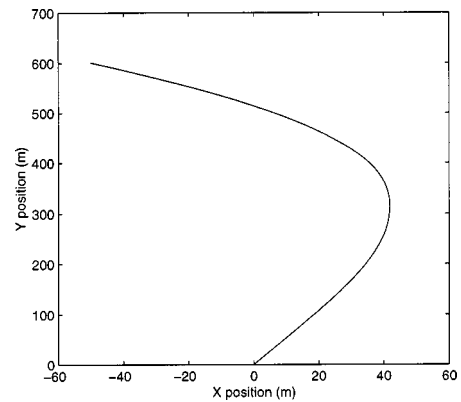
FIG. 15. The track of the compass in the array over a time sample of 200 s, during which the array has undergone a 60° maneuver. Positions are shown relative to the north and the compass position at a start time before the maneuver.

eling in a nominally straight line for this time. After the maneuver (Fig. 16, top), the array heading is −45° and the target ship again appears at −75° but the left/right ambiguity has shifted to −15°. The peaks at −175° and 85° are the aliases of the target ship and its left/right ambiguity. The aliases occur after the maneuver but not before because the target ship has moved from near broadside to near endfire. During the maneuver (Fig. 16, middle), the array undergoes a 60° turn and the array shape changes from linear to curved with a maximum deviation from linear of approximately two wavelengths, and back to linear again. It can be seen that even under such a maneuver, both the conventional and adaptive beamformers show the correct bearing for the target at −75° when the array shape and track are used. The array shape and track are estimated assuming the array follows the same path as the compass shown in Fig. 15.

IV. SUMMARY

An adaptive beamformer has been presented that allows the beamformer to be applied to nonstationary arrays. It does
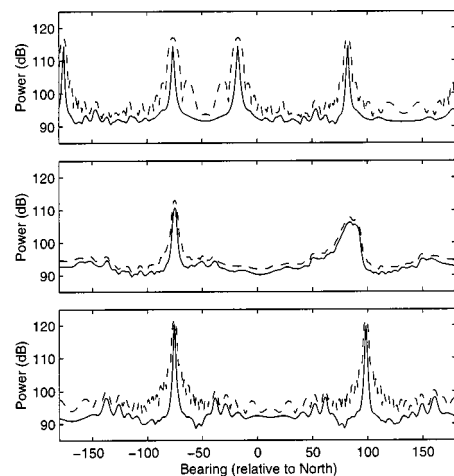
FIG. 16. Conventional (dashed) and adaptive (solid) beamformed output averaged over 3 mins prior to the towship maneuver shown in Fig. 15 (bottom), during the towship maneuver (middle), and after the towship maneuver (top). The true target always appears at −75°, even during the maneuver.

this by directly incorporating both changes in shape and heading that may occur in the array during the time required to collect data. Most adaptive beamforming applications assume the sensors are stationary and result in poor beamforming performance during a maneuver of the sensor platform. The technique presented has been applied to both synthetic data and real data from an acoustic towed array. Results show that the signal detection, bearing accuracy, and bearing resolution increase when an estimate of the array shape and track are incorporated into the beamformer if the sensor platform is not stationary.

ACKNOWLEDGMENTS

[1] J. Capon, "High-resolution frequency–wavenumber spectrum analysis," Proc. IEEE **57**, 1408–1419 (1969).

[2] D. H. Johnson, "The application of spectral estimation methods to bearing estimation problems," Proc. IEEE **70**, 1018–1028 (1982).

[3] A. O. Steinhardt and B. D. Van Veen, "Adaptive beamforming," Int. J. of Adaptive Control Sig. Proc. **3**, 253–281 (1989).

[4] D. M. Boroson, "Sample size considerations for adaptive arrays," IEEE Trans. Aerosp. Electron. Syst. **AES16**, 446–451 (1980).

[5] S. R. DeGraaf and D. H. Johnson, "Capability of array processing algorithms to estimate source bearings," IEEE Trans. Acoust., Speech, Signal Process. **ASSP33**, 1368–1379 (1985).

[6] D. E. Grant, J. H. Gross, and M. Z. Lawrence, "Cross-spectral matrix estimation effects on adaptive beamforming," J. Acoust. Soc. Am. **98**, 517–524 (1995).

[7] V. U. Reddy, A. Paulraj, and T. Kailath, "Performance analysis of the optimum beamformer in the presence of correlated sources and its behavior under spatial smoothing," IEEE Trans. Acoust., Speech, Signal Process. **ASSP35**, 927–936 (1987).

[8] M. E. Ali and F. Schreib, "Adaptive single snapshot beamforming: a new concept for the rejection of nonstationary and coherent interferers," IEEE Trans. Signal Process. **ASP40**, 3055–3058 (1992).

[9] R. N. McDonough, "Degraded performance of nonlinear array processors in the presence of data modeling errors," J. Acoust. Soc. Am. **51**, 1186–1193 (1972).

[10] H. Cox, "Resolving power and sensitivity to mismatch of optimum array processors," J. Acoust. Soc. Am. **54**, 771–785 (1973).

[11] A. M. Vural, "Effects of perturbations on the performance of optimum/adaptive arrays," IEEE Trans. Aerosp. Electron. Syst. **AES15**, 76–87 (1979).

[12] N. K. Jablon, "Adaptive beamforming with the generalized sidelobe cancellor in the presence of array imperfections," IEEE Trans. Antennas Propag. **AP34**, 996–1012 (1986).

[13] K. M. Ahmed and R. J. Evans, "An adaptive array processor with robustness and broad-band capabilities," IEEE Trans. Antennas Propag. **AP32**, 944–950 (1984).

[14] H. Cox, R. M. Zeskind, and M. M. Owen, "Robust adaptive beamforming," IEEE Trans. Acoust., Speech, Signal Process. **ASSP35**, 1365–1375 (1987).

[15] S. D. Hayward, "Effects of motion on adaptive arrays," IEE Proc.: Radar, Sonar Navigation **144**, 15–20 (1997).

[16] P. C. Hansen, "Rank-deficient prewhitening with quotient SVD and ULV decomposition," Bit **38**, 34–43 (1998).

[17] A. C. Barthelemy and P. K. Willet, "Volumetric array prewhitening," IEEE Trans. Signal Process. **46**, 281–293 (1998).

[18] C. A. Zala, J. M. Ozard, and M. J. Wilmut, "Prewhitening for improved detection by matched-field processing in ice-ridging correlated noise," J. Acoust. Soc. Am. **98**, 2726–2734 (1995).

[19] J. Krolik and D. Swingler, "Multiple broad-band source location using steered covariance matrices," IEEE Trans. Acoust., Speech, Signal Process. **ASSP37**, 1481–1494 (1989).

[20] D. A. Gray, "Formulation of the maximum signal-to-noise ratio array processor in beam space," J. Acoust. Soc. Am. **72**, 1195–1201 (1982).

[21] D. A. Gray, "Output statistics of the sample matrix inverse beamformer implemented in beam space," J. Acoust. Soc. Am. **80**, 1737–1739 (1986).

[22] M. P. Paidoussis, "Dynamics of flexible slender cylinder in axial flow; Part I theory," J. Fluid Mech. **26**, 717–736 (1966).

[23] M. P. Paidoussis, "Dynamics of flexible cylinders in axial flow; Part II experiment," J. Fluid Mech. **26**, 737–751 (1966).

Multiple internal reflections in the cochlea and their effect on DPOAE fine structure

Sumitrajit Dhar[a)]
Department of Speech and Hearing Sciences, Indiana University, Bloomington, Indiana 47405

Carrick L. Talmadge
National Center for Physical Acoustics, University of Mississippi, University, Mississippi 38677

Glenis R. Long
Graduate Center, City University of New York, New York, New York 10016

Arnold Tubis
Institute for Nonlinear Science, University of California–San Diego, La Jolla, California 92093

In recent years, evidence has accumulated in support of a two-source model of distortion product otoacoustic emissions (DPOAEs). According to such models DPOAEs recorded in the ear canal are associated with two separate sources of cochlear origin. It is the interference between the contributions from the two sources that gives rise to the DPOAE fine structure (a pseudoperiodic change in DPOAE level or group delay with frequency). Multiple internal reflections between the base of the cochlea (oval window) and the DP tonotopic place can add additional significant components for certain stimulus conditions and thus modify the DPOAE fine structure. DPOAEs, at frequency increments between 4 and 8 Hz, were recorded at fixed f_2/f_1 ratios of 1.053, 1.065, 1.08, 1.11, 1.14, 1.18, 1.22, 1.26, 1.30, 1.32, 1.34, and 1.36 from four subjects. The resulting patterns of DPOAE amplitude and group delay (the negative of the slope of phase) revealed several previously unreported patterns in addition to the commonly reported log sine variation with frequency. These observed "exotic" patterns are predicted in computational simulations when multiple internal reflections are included. An inverse FFT algorithm was used to convert DPOAE data from the frequency to the "time" domain. Comparison of data in the time and frequency domains confirmed the occurrence of these "exotic" patterns in conjunction with the presence of multiple internal reflections. Multiple internal reflections were observed more commonly for high primary ratios ($f_2/f_1 \geq 1.3$). These results indicate that a full interpretation of the DPOAE level and phase (group delay) must include not only the two generation sources, but also multiple internal reflections. © 2002 Acoustical Society of America. [DOI: 10.1121/1.1516757]

PACS numbers: 43.64.Bt, 43.64.Ha, 43.64.Jb [BLM]

I. INTRODUCTION

Distortion product otoacoustic emissions (DPOAEs) are signals generated in the cochlea in response to simultaneous stimulation by two pure tones (Kemp, 1978). The two stimulus tones, at frequencies f_1 and f_2 ($f_2 > f_1$), commonly referred to as primaries, generate distortion products at several frequencies (f_{dp}) that are mathematically related to the frequencies of the primaries. In the currently accepted model of apical DPOAEs ($f_{dp} < f_1$), the initial DP energy is generated by the nonlinear interaction between the primaries at their overlap region near the tonotopic location of the higher frequency primary (see Kummer *et al.*, 1995, for review). This energy at the distortion product frequency then travels both apically and basally. The apically traveling energy reaches the region of the DP characteristic place and is reflected back due to localized random inhomogeneities on the basilar membrane, while the fraction of the energy traveling basally from the generation region reaches the ear canal directly. The theory of reflections on the basilar membrane from randomly

distributed inhomogeneities was formalized by Zweig and Shera (1995) and later incorporated in a comprehensive model of otoacoustic emissions by Talmadge *et al.* (1998). The DPOAE signal recorded in the ear canal is a combination of the "overlap" or "generator" and "reflection" components (Talmadge *et al.*, 1998, 1999; Mauermann *et al.*, 1999b; Knight and Kemp, 2000; Dreisbach, 1999; Kalluri and Shera, 2001; Konrad-Martin *et al.*, 2001). The fundamental distinction between the two components is expressed primarily as a difference in their phase behaviors as functions of the DPOAE frequency (Talmadge *et al.*, 1998, 1999; Shera and Guinan, 1999). The approximate scaling symmetry of the cochlea implies that the phase of the generator component due to cochlear nonlinearities is very nearly independent of f_{dp} for fixed primary ratios (Shera *et al.*, 2000). However, the phase of the reflection component varies rapidly with f_{dp} because the inhomogeneities responsible for the reflections are fixed in location on the basilar membrane (Shera and Zweig, 1993; Zweig and Shera, 1995). The DPOAE level recorded in the ear canal is a result of the interference between the two components that generates a pseudoperiodic variation in level as a function of frequency

---

[a)]Electronic mail: sumit@indiana.edu
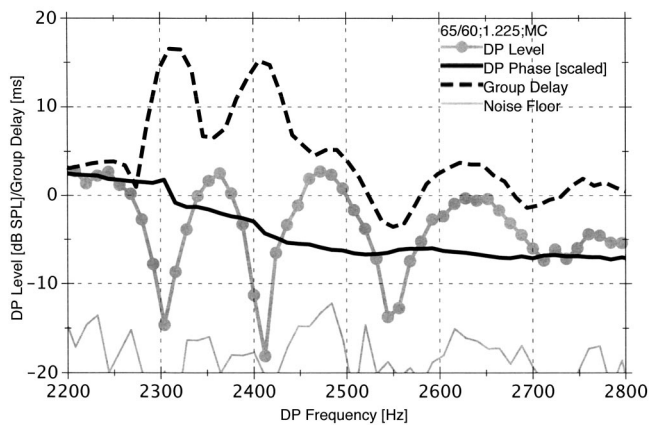
FIG. 1. DP level, phase, and group-delay fine structure from a normal-hearing ear recorded with primary levels of 65 and 60 dB SPL and a frequency ratio of 1.225. Group delay is calculated as the negative of the slope of the phase divided by 2π. The DPOAE phase changes rapidly between the frequencies of 2300 and 2450 Hz, indicating dominance of the reflection component. The slow variation in phase with frequency above 2450 Hz indicates dominance of the generator component. The level and group delay fine structures are negatively and positively correlated below and above 2450 Hz, respectively.

known as fine structure. Typical fine-structure data from a normal-hearing ear is displayed in Fig. 1. Note the pseudo-periodic variation (fine structure) observed for both level and group delay. Group delay is calculated as the $1/2\pi$ times the negative of the slope of the phase. The steep slope of the phase curve below 2450 Hz reflects a dominant reflection component. On the other hand, the relatively slow phase variation above 2450 Hz is indicative that the generator component is dominant. Note that the relationship between the level and group-delay fine structures is a direct consequence of the phase behavior at the fine structure minima. The two fine structures are negatively and positively correlated below and above 2450 Hz, respectively.

Computational models proposed by several researchers give theoretical support for the two-source model (Zweig and Shera, 1995; Talmadge et al., 1998, 1999; Mauermann et al., 1999b) and convincing evidence for such models has been presented using several experimental paradigms by various research groups (e.g., Talmadge et al., 1999; Mauermann et al., 1999a; Konrad-Martin et al., 2001; Kalluri and Shera, 2001). Specific experimental paradigms include suppression of the "reflection" component (e.g., Heitmann et al., 1988; Talmadge et al., 1999; Kalluri and Shera, 2001; Konrad-Martin et al., 2001) or indirect isolation of the "generator" component by computing a moving average of the overall amplitude and phase (Brown et al., 1996). The two components have also been isolated using inverse-FFT analysis (Stover et al., 1996; Fahey and Allen, 1997; Kalluri and Shera, 2001; Knight and Kemp, 2001). Additionally, results from novel experimental designs such as using pulsed primaries (Talmadge et al., 1999) or placing the DP characteristic place in a region of hearing loss (Mauermann et al., 1999a) have also provided support for these models. Talmadge et al. (1999) exploited the temporal differences in the generation of the two components, when one of the primaries is pulsed on and off, to visualize them in the time domain. The generator component is present alone for a brief period

after the onset of the pulsed primary, while the reflection component is present alone for a brief period after its offset. Mauermann et al. (1999a) used the pattern of DPOAE fine structure in individuals with notched hearing losses to show that the presence of fine structure depended on a region of normal hearing at the DP frequencies.

Along with this convincing body of evidence in support of a two-source model of DPOAEs, preliminary evidence has also been presented to indicate that a simple two-source model might not encapusulate the full complexity of the process of DPOAE generation (Stover et al., 1996; Talmadge et al., 1999; Konrad-Martin et al., 2001). This evidence points towards the contribution of additional cochlear reflection components to the signal recorded in the ear canal. Stover et al. (1996) observed multiple peaks in "time domain" data derived from frequency-domain DPOAE data using an inverse FFT algorithm. In discussing the possible source of the multiple peaks, the authors considered the presence of (i) multiple sources in the cochlea, (ii) "one (or two) sources and multiple reflections between them," and (iii) a single source responsible for all the observed peaks. After careful consideration of all three possibilities, Stover et al. (1996) concluded that

> ... the most parsimonious explanation, at this time, may be that there are multiple sources for the acoustic distortion that is measured in the ear canal... .

However, advances in the theory of DPOAE generation and supporting experimental evidence obtained since 1996 have led the same group to attribute the presence of multiple peaks in IFFT data to multiple reflections in the cochlea (Konrad-Martin et al., 2001). The most direct evidence for multiple internal reflections to date has perhaps come from direct time domain measurements of Talmadge et al. (1999) in which additional "peaks" of energy were observed after the offset of the pulsed primary. While the reflection component forms the first "peak" after stimulus offset, multiple internal reflections would be responsible for any additional peaks. It should be noted that the above results were merely casual observations made during examination of the properties of the generator and reflection components and the specifics of the phenomenon of multiple internal reflections have not yet been reported in the literature.

Although experimental work regarding multiple internal reflections has been limited, the theoretical foundation of this phenomenon has already been explored in considerable detail. The basis for multiple internal reflections is tied to the presence of an impedance mismatch at the base of the cochlea (oval window), resulting in a basal reflectance. Any basal-moving wave from the generator region or the DP characteristic region will encounter this reflectance and a portion of this wave will be reflected back towards the cochlear apex. This phenomenon of reflection of retrograde waves at the stapes has been formalized in detail by Shera and Zweig (1991). The presence of the two reflectances, an apical reflectance at the DP tonotopic location and a basal reflectance at the base of the cochlea, results in multiple reflections inside the cochlea. Some of the specific details of
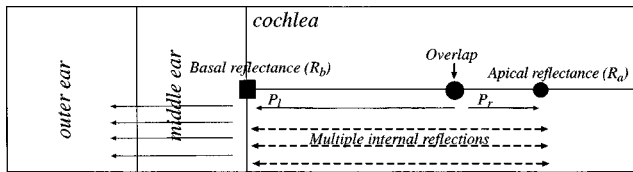
FIG. 2. Schematic representation of the mechanisms involved in the two-source model. The two sources are associated with the "generator" region and the "reflection" region. P_l represents the initial basally traveling DP wave; P_r represents the initial apically traveling DP wave. R_a is the apical reflectance due to reflection sources in the $2f_1-f_2$ tonotopic region, while R_b is the basal reflectance at the stapes.

multiple-internal-reflection models (e.g., Talmadge *et al.*, 1998, 1999) are discussed in a later section.

In this paper we examine the phenomenon of multiple internal reflections and their effects on DPOAE fine structure. We begin by discussing the relevant aspects of the two-source model. The emphasis here is in highlighting the factors that influence the generation of multiple internal reflections. It is shown that internal reflections have a profound effect on level and group-delay fine structures. Several terms are introduced to help describe and categorize the varied fine structure shapes that are predicted by the model. Finally, the programmatically determined predictions of the level and group-delay fine structure shapes are presented and shown to be supported by observations of different fine-structure shapes in normal-hearing adult human ears. These observations were made from a data base of high-resolution DPOAE recordings from four subjects under a broad range of primary levels and frequency ratios. The implications of these findings and their impact on the currently established model of DPOAEs are discussed to conclude the paper.

II. MODEL SUMMARY

The analytic aspects critical to the presence of multiple internal reflections presented here are based on the comprehensive model of DPOAEs proposed by Talmadge *et al.* (1997, 1998, 1999). This model falls in the general class of two-source interference models and shares basic features with other published analytic models (e.g., Zweig and Shera, 1995; Mauermann *et al.*, 1999b).

The process of DPOAE generation, incorporated in the above model, is comprised of three separate stages, as illustrated in Fig. 2. In the first stage the two primary traveling waves propagate to their characteristic places on the basilar membrane and reach peaks in their activity patterns. DP energy is generated in the region of overlap between the activity patterns of the two primaries (near the f_2 tonotopic place) due to cochlear nonlinearities. If the two primary stimuli are considered to be of angular frequencies ω_1 and ω_2 ($\omega_2 > \omega_1$), DP energy at the frequencies $\omega_{dp}=(n+1)\omega_1-n\omega_2$ ($n=1,2,3...$) are generated in the cochlea. Note that this relationship describes (apical) DPOAEs that are lower in frequency than the primaries (tonotopic site of DP apical to those of the primaries, $\omega_{dp}<\omega_1<\omega_2$). Although only the DPOAE at the frequency $2f_1-f_2$ is considered in this paper, the theoretical implications of the findings should be applicable to all other apical DPOAEs. A fraction of the DP

energy generated in this overlap region travels basally towards the middle ear, while another fraction travels apically towards its characteristic place on the basilar membrane. Based on the typical picture of the basilar membrane with the base to the left and the apex to the right, we will refer to the energy traveling basally as associated with the initially left moving component (P_l), and the energy traveling towards the $2f_1-f_2$ region with the initially right moving component (P_r).

In the second stage of the generation process, the initial apically traveling DP wave reaches the region of its characteristic place and achieves a tall and broad activity pattern. A fraction of this wave is reflected basally due to coherent reflections from random inhomogeneities on the basilar membrane. [The reader is directed to Shera and Zweig (1993) and Zweig and Shera (1995) for technical details on the mechanism of coherent reflections.] This mechanism is characterized by the apical reflectance (R_a). At this stage there are two separate DP waves at the angular frequency ω_{dp} traveling basally. Both of these waves are partially transmitted to the ear canal through the middle ear.

In the third and final stage, the basally traveling DP waves encounter a basal reflectance (R_b) at the stapes due to the impedance mismatch between the middle ear and the cochlea. Both of these waves are reflected back towards the cochlear apex. Thus two reflectances, at the DP tonotopic place (R_a) and the stapes (R_b), are set up and result in DP waves that are reflected back and forth. These multiple internal reflections produce an "internal resonance" factor in the expression for the DP ear canal signal (Talmadge *et al.*, 1998). In summary, the DPOAE recorded in the ear canal is a result of all three of the following elements:

(i)   initial basal- and apical-moving DP waves generated at the generator region on the basilar membrane,
(ii) reflected DP wave from the DP tonotopic region, and
(iii) internal resonance components due to multiple reflections of cochlear DP waves between the stapes and the DP tonotopic region.

The main observable difference between the generator and reflection components is in their phase behaviors, which are reflective of the putative mechanisms responsible for them. When recorded using a fixed (f_2/f_1) ratio paradigm, the phase of the generator component is almost independent of frequency (f_{dp}) due to the approximate scaling symmetry in the cochlea (Shera *et al.*, 2000). The phase of the reflection component(s), on the other hand, varies rapidly with frequency since the source of these reflections is fixed in location on the basilar membrane (Talmadge *et al.*, 1999; Shera and Guinan, 1999). This distinction is essentially the same as that made between "wave" and "place-fixed" emissions (see Knight and Kemp, 2000, for review). As was discussed in the previous section, the fine structure observed in the ear-canal signal is a consequence of the interaction between the components of DPOAE. The complex amplitude of the DPOAE recorded in the ear canal has been analytically derived by Talmadge *et al.* (1998):

$$P_e(\omega_2, r, \omega_{\mathrm{dp}}) = \left[\frac{1}{1 - R_a(\omega_{\mathrm{dp}}) R_b(\omega_{\mathrm{dp}})} \right] [P_l(\omega_2, r, \omega_{\mathrm{dp}})$$

$$+ R_a(\omega_{\mathrm{dp}}) P_r(\omega_2, r, \omega_{\mathrm{dp}})], \tag{1}$$

where ω_1 and ω_2 are the angular frequencies of the primary stimuli and $r = \omega_2 / \omega_1$, and ω_{dp} is the angular DPOAE frequency. R_a is the apical reflectance due to random inhomogeneities around the DP tonotopic site, R_b is the basal reflectance at the junction between the cochlea and stapes (oval window), and P_l and P_r are measures respectively of the initially basal-moving and apical-moving DP wave components. In the absence of basal reflectance, the component from the $2f_1 - f_2$ tonotopic region is determined by the total energy generated in the generator region, the ratio between the apical and basal DP wave energy from the generator region, and the reflectance R_a. R_b determines the proportion of basally traveling energy that is reflected towards the cochlear apex at the junction of the cochlea with the stapes. In the limit of $R_a = 1$ and negligible multiple internal reflections ($R_a R_b \ll 1$), the DPOAE ear canal pressure signal would be $P_l + P_r$. Talmadge *et al.* (1998) parameterize the ratio between the initial apical and basal DP waves as $R_d(\omega_{\mathrm{dp}}) = P_r(\omega_{\mathrm{dp}}) / P_l(\omega_{\mathrm{dp}})$.

If the dependence of various quantities on ω_1 and ω_2 are suppressed, the full fine-structure equation [Eq. (1)] can be re-written as follows:

$$P_e(\omega_{\mathrm{dp}}) = \frac{P_l(\omega_{\mathrm{dp}}) + R_a(\omega_{\mathrm{dp}}) P_r(\omega_{\mathrm{dp}})}{1 - R_a(\omega_{\mathrm{dp}}) R_b(\omega_{\mathrm{dp}})}. \tag{2}$$

Equation (2) can be simplified in appearance as:

$$P_e(\omega_{\mathrm{dp}}) = P_l(\omega_{\mathrm{dp}}) \frac{1 + R_a(\omega_{\mathrm{dp}})[P_r(\omega_{\mathrm{dp}})/P_l(\omega_{\mathrm{dp}})]}{1 - R_a(\omega_{\mathrm{dp}}) R_b(\omega_{\mathrm{dp}})}$$

$$\equiv P_l(\omega_{\mathrm{dp}}) \frac{1 + R_a(\omega_{\mathrm{dp}}) R_d(\omega_{\mathrm{dp}})}{1 - R_a(\omega_{\mathrm{dp}}) R_b(\omega_{\mathrm{dp}})}$$

$$\equiv P_l(\omega_{\mathrm{dp}}) \frac{1 + R_1}{1 - R_2}, \tag{3}$$

where $R_d = P_r / P_l$, $R_1 = R_a R_d$, and $R_2 = R_a R_b$.

The fraction involving the terms R_1 and R_2 in Eq. (3) modulates P_l. R_1 is the contribution of the reflection from the DP tonotopic region to the DPOAE in the absence of any reflections from the stapes. The $1/(1 - R_2)$ term represents the contributions of the resonance created inside the cochlea due to multiple internal reflections between the stapes and the DP region on the basilar membrane. Since only the term $R_a(\omega_{\mathrm{dp}})$ is expected to have rapid phase dependence on ω_{dp}, a new term $\mathcal{F}_{\mathrm{dp}}(\omega_{\mathrm{dp}})$ is introduced to characterize fine structure:

$$\mathcal{F}_{\mathrm{dp}}(\omega_{\mathrm{dp}}) = \frac{1 + R_1}{1 - R_2}. \tag{4}$$

The relevant characteristics of this function are

$$\mathcal{L}_{\mathrm{dp}}(\omega_{\mathrm{dp}}) = \log|\mathcal{F}_{\mathrm{dp}}(\omega)|,$$

$$\varphi_{\mathrm{dp}}(\omega_{\mathrm{dp}}) = \arg[\mathcal{F}_{\mathrm{dp}}(\omega)], \tag{5}$$
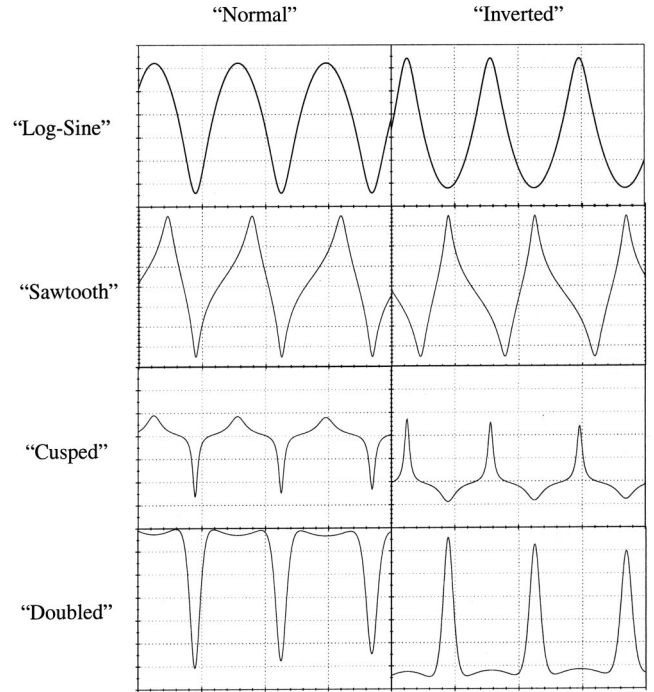
FIG. 3. Full model prediction of DPOAE fine-structure taxonomy. The "doubled" shape is not expected in level fine structure; all shapes should be observed in group-delay fine structure.

$$\tau_{\mathrm{dp}}(\omega_{\mathrm{dp}}) = -\varphi'_{\mathrm{dp}}(\omega_{\mathrm{dp}}).$$

$\mathcal{L}_{\mathrm{dp}}$, φ_{dp}, and τ_{dp} represent the level, total phase, and group-delay fine structure functions, respectively. Note that $\mathcal{L}_{\mathrm{dp}}$ is given by

$$\mathcal{L}_{\mathrm{dp}}(\omega_{\mathrm{dp}}) = \frac{1}{2} \log \left[\frac{1 + |R_1|^2 + 2|R_1| \cos \varphi_1}{1 + |R_2|^2 - 2|R_2| \cos \varphi_2} \right], \tag{6}$$

where $\varphi_{1,2} = \arg[R_{1,2}]$. Thus, the terms on the left-hand side of Eqs. (4)–(6) represent the combined contribution of all components from the DP tonotopic region and their salient characteristics, namely, level, phase, and group delay. Under most stimulus conditions the only significant contribution to the ear canal signal comes from the first reflection. However, additional reflections can contribute significantly to the ear canal signal under specific stimulus conditions. The combined levels and phases of all significant reflections from the DP tonotopic region determine the exact characteristics of the final fine structure.

III. FINE-STRUCTURE SHAPE

A. Effect of resonance

The relationship between level and group-delay fine structures is determined by the relative dominance of the generator and reflection components of the DPOAE measured in the ear canal. The predicted pattern for DPOAE level fine structure, when just the two components are taken into account ($R_2 = 0$), is limited to "normal log-sine" for all values of R_1 (top-left panel in Fig. 3). This pattern is classified as "log-sine" as this would be the pattern if a sine wave plus a constant ($1 + b \cos \omega t$) were plotted on a log scale. This fine-structure pattern is further classified as "normal"
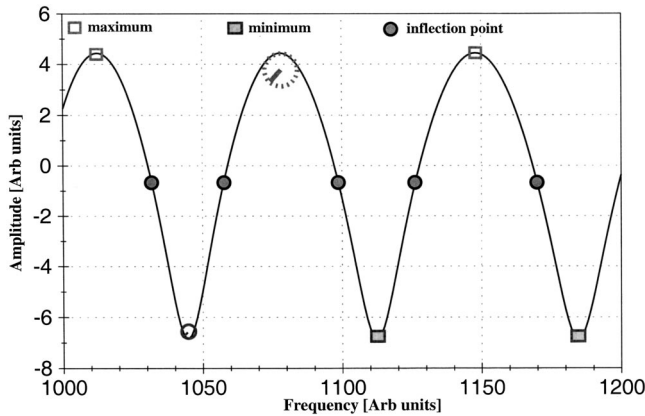
FIG. 4. Schematic representation of fine-structure extrema. The open and filled squares represent maxima and minima, respectively. The closed circles represent inflection points. The hatched circles are used to define curvature at maxima and minima.

(maxima broader than minima) since this is the most commonly observed form. Group-delay fine structure is predicted to be either normal log-sine (top-right panel of Fig. 3) or "inverted" (minima broader than maxima—top-left panel of Fig. 3) for $|R_1| < 1$ or $|R_1| > 1$, respectively. This limited model, incorporating the generator and the initial reflection components, also predicts that only group-delay fine structure can be inverted. While both level and group-delay fine structures are normal when the generator component is larger in magnitude than the reflection component, group-delay fine structure is inverted when the reflection component is larger in magnitude than the generator component (Talmadge *et al.*, 1999). This combination of normal level fine structure and inverted group-delay fine structure has been reported previously by Talmadge *et al.* (1999), and the reader is directed to that publication for further details.

When the full model with all terms including multiple internal reflections is examined, a more complex family of fine-structure shapes is predicted. The predicted set of fine-structure patterns is depicted in Fig. 3.

B. Determining fine structure shape

Upon inclusion of the effects of multiple internal reflections, several novel fine-structure shapes, that have not been published previously, are predicted (see Fig. 3). Here we present an objective system of classification of these "exotic" shapes using a quantitative protocol for identification of magnitude extrema and inflection points and subsequently using the number of inflection points between adjacent maxima and minima to identify different fine-structure patterns. Two fundamental types of extrema are defined in Fig. 4. Magnitude-extrema are defined as the values of ω_{dp} at which a given function, DP-level or group delay, is at a local maximum or minimum. These are represented by open and filled squares in Fig. 4, and correspond to locations where the slope of a given function is equal to zero.

Inflection-extrema or inflection points are values of ω_{dp} for which the slope of a given function is at a maximum or minimum. These are represented by the solid circles in Fig. 4. The open tangent circles are used to illustrate the concept

of curvature. Curvature magnitude is defined as the reciprocal of the radius of the tangent circle. The curvature of a function can also be expressed as a positive factor times the second derivative of the function at that point. Thus, since the radius of the hatched circle at the maximum is greater than that of the solid-line circle at the minimum, the magnitude of curvature at the minimum is greater than that at the maximum. The second derivative of the function is positive at the minimum, and negative at the maximum. Since the curvatures at maxima and minima have opposite signs, there has to be an odd number of inflection points (where the value of curvature becomes zero and curvature changes sign) between adjacent maxima and minima.

The number and type of extrema can be used to objectively categorize the type of fine structure observed in a given experimental measurement, as is discussed below. They can also be used in the analysis of the behavior of Eq. (3) to determine the type of fine structure expected for different values of R_1 and R_2.

C. Shape function

A quantity termed the "shape function" was introduced to objectively differentiate between normal and inverted fine-structure. Shape function (S) is defined as

$$S(\omega_{dp}) = -f''(\omega_{dp})|_{max} / f''(\omega_{dp})|_{min}, \tag{7}$$

where $f''(\omega_{dp})|_{max,min}$ are the second derivatives of the function evaluated at the maximum and minimum, respectively.

Figure 4 is a schematic representation of normal level fine structure. Note that the curvature magnitudes at minima are greater than those at maxima. By definition, the value of S is limited between 0 and ∞. In Fig. 4, $S \le 1$, which is the case for "normal" fine structure. Fine structure is categorized as "inverted" when $1 \le S \le \infty$.

D. Asymmetry factor

Asymmetry factor is another quantity used in the objective categorization of fine-structure shape. Normal fine structure has equally spaced minima and maxima when plotted against basilar membrane position, where "normal" is defined as log-sinusoidal structure with the minima having maximum curvature magnitude. However, the two-source interference model predicts unequal spacing between maxima and minima in some cases (Fig. 5).

To define the asymmetry factor (A), the limits of a fine structure period (D) are defined by two consecutive magnitude extrema (maxima or minima) with the greatest curvature. The distance between the first of these extrema and the intermediate extreme is called d. A is quantified as $2d/D - 1$. By definition the range of possible values for A is between -1 and 1. $A = 0$ when fine structure is symmetric. Since asymmetry is measured relative to absolute maxima or minima with the largest curvature, it is not influenced by inversion of fine structure.

E. Classification of fine-structure shape

The shape function (S), asymmetry factor (A), and the number of inflection points between adjacent maxima and
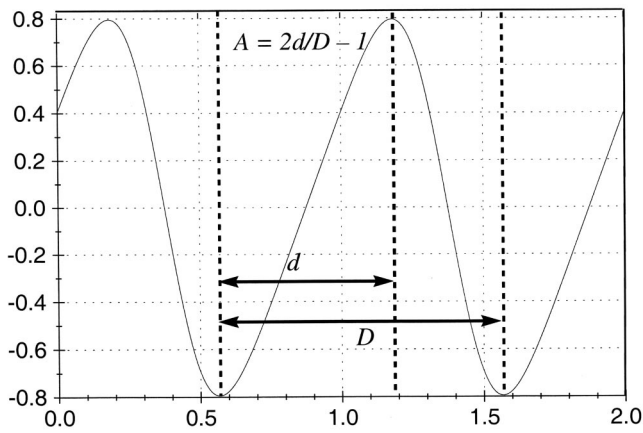
FIG. 5. Definition of asymmetry factor. Both axes represent arbitrary units.

minima were used to classify fine structure as normal or inverted, and to categorize fine-structure shape into four possible categories. This classification scheme is represented in Table I. Both log-sine and doubled fine structure have one inflection point between adjacent magnitude extrema. These two categories were differentiated based on the number of magnitude extrema in a given frequency range. Fine-structure shape was classified as "cusped" in case of three inflection points between adjacent magnitude extrema. Sawtooth fine structure was characterized by unequal number of inflection points in adjacent half-periods. There is one inflection point in the half-period between maxima and minima, but there are three inflection points in the following half-period between minima and maxima in case of normal sawtooth fine structure. The number of inflection points in each half period is reversed in case of inverted sawtooth fine structure. The value of S was used to differentiate between normal and inverted fine structure with equal number of inflection points in adjacent half periods. Fine structure was classified as "normal" when $S \leq 1$ and "inverted" when $1 \leq S \leq \infty$.

F. Analysis results

The criteria listed above were coded into a computer program. This was used to develop "maps" of the fine-structure shapes expected for different values of $|R_1|$ and $|R_2|$ and $\varphi_0 = \varphi_1 - \varphi_2$, as illustrated in Fig. 6.

The commonly observed and usually reported shape is termed "normal log-sine." This shape and its inverted counterpart are presented in the top panel of Fig. 3. The remain-

TABLE I. Classification system for fine-structure shape. Note that doubled and log-sine fine structures are differentiated on the basis of frequency of fine-structure magnitude extrema.

| Shape | No. of inflection points | | | |
| | Normal ($S \leq 1$) | | Inverted ($1 \leq S \leq \infty$) | |
	min to max	max to min	min to max	max to min
Log-sine	1	1	1	1
Sawtooth	3	1	1	3
Cusped	3	3	3	3
Doubled	1	1	1	1

ing panels represent "exotic" shapes that are predicted by the models that incorporate multiple internal reflections ($|R_b| > 0$). "Doubled" patterns are predicted for group delay alone while "normal" and "inverted" forms of all other shapes are predicted for both level and group-delay fine structure.

The two-source interference model incorporating multiple internal reflections predicts that these various fine-structure shapes vary as the values of $|R_1|$, $|R_2|$, and φ_0 are varied. Several maps of fine-structure behavior for a wide range of values for $|R_1|$ and $|R_2|$ for specific choices of φ_0 are presented in Fig. 6.

Certain patterns become clear when comparing the level and group delay fine structures that are summarized in Fig. 7. Additionally, distinctions between values of $|R1|$ and $|R2|$ resulting in "normal" and "inverted" patterns can be made more easily in Fig. 7. The different classes of level fine structure behavior are demarcated by the lines $|R_1| = |R_2|$ and $|R_1||R_2| = 1$, whereas the different classes for group delay are demarcated by $|R_1| = |R_2|$, $|R_1| = 1$, and $|R_2| = 1$.

Note that neither inverted group delay nor inverted level fine structure in themselves are direct evidence for a net co-chlear gain (e.g., $|R_a| > 1$). However, the experimental observation of inverted fine structure in both level and group delay or the departure of fine-structure shape from the more common log-sine pattern is direct evidence of an interference between two sources and for a direct role of cochlear resonance (i.e., multiple internal reflections).

It is also the case that these exotic interference patterns will only be observed when either $|R_1|$ or $|R_2|$ (or both) approach unity. In the classic two-source model, it is expected that $|R_1| \ll 1$. When $|R_1| \gg 1$, the behavior returns to log-sine even though the value of $|R_1|$ is well outside the classic range. This observation provides an explanation for why DPOAE fine structure can deepen when the DPOAE reflection component is suppressed by an external tone (e.g., Talmadge et al., 1999).

An interesting result of this numerical analysis (together with analytic studies) is that only the group delay fine structure function is expected to exhibit a doubled fine structure. In general, the group delay fine structure behaves more "wildly" as $|R_1|$ and $|R_2|$ approach unity. This has interesting implications for the expected changes in level and group-delay fine structure, when these measurements are obtained in the presence of a suppressor tone.

G. Effect of scale-invariance violations

If $a(x, \omega)$ is the amplitude of motion of the basilar membrane at position x (measured from the base) relative to the motion of the stapes in response to an external tone, and if $a(x, \omega) = a(\omega / \hat{\omega}(x))$, where $\hat{\omega}(x)$ is the place angular frequency for position x, then the cochlea is said to be *scale invariant*. The function $a(x, \omega)$ is often described as the *transfer function* from the stapes to the basilar membrane. If $P_e(\omega_{dp}, \omega_1, \omega_2)$ is the DPOAE ear canal pressure due to the two primaries of angular frequencies ω_1 and ω_2, then if $P_e(\omega_{dp}, \omega_1, \omega_2) = P_e(\omega_2 / \omega_1)$, an even more general type of scale invariance is exhibited (Shera et al., 2000).
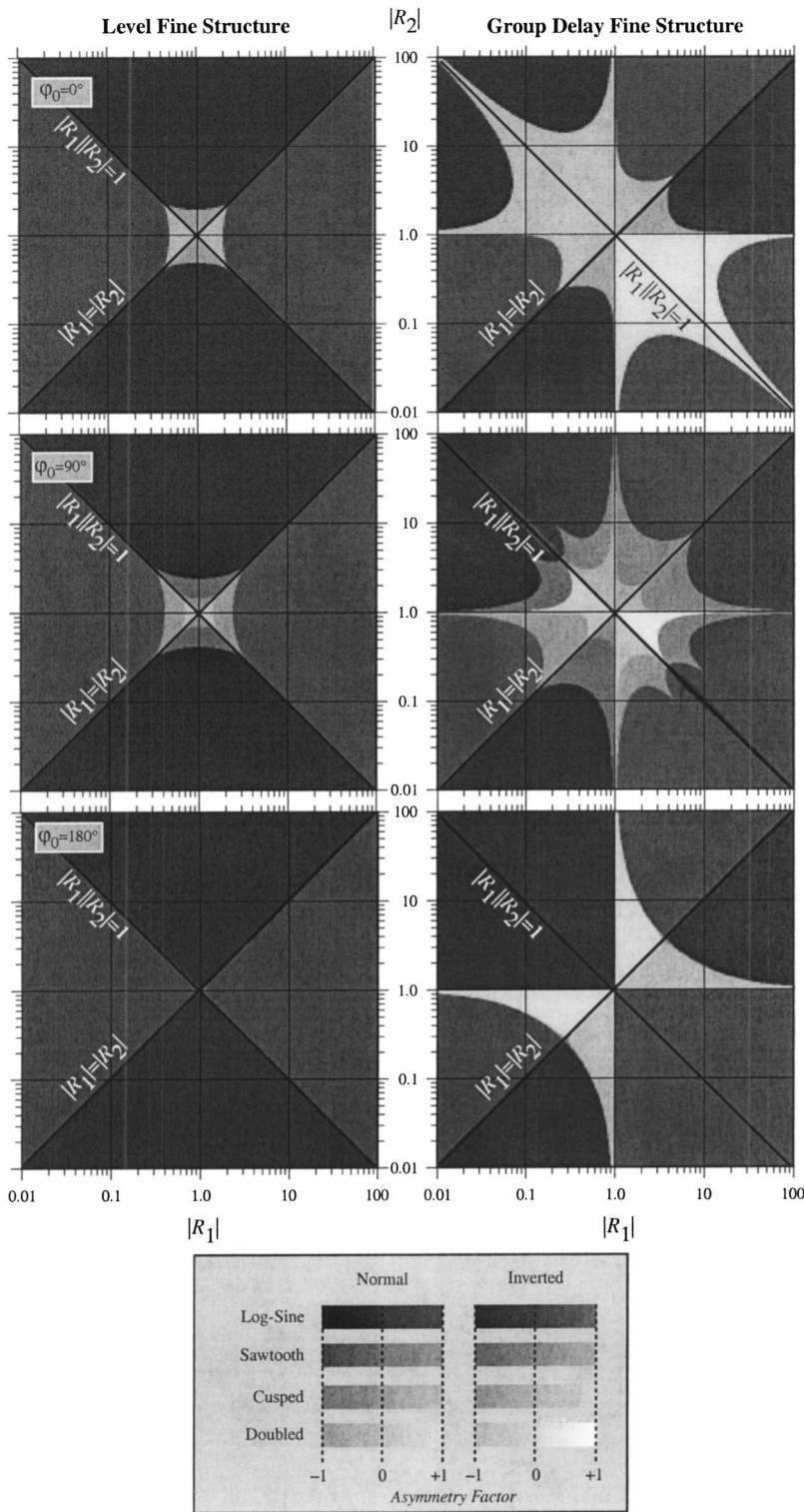
FIG. 6. Density plots of different fine-structure shapes for different values of R_1 and R_2 at specific values of $\varphi_0 (\varphi_0 = \varphi_1 - \varphi_2)$. Variations in the maps with φ_0 notwithstanding, "exotic" patterns are predicted more frequently for group-delay fine structure. These patterns are also predicted for values of $|R_1|$ and/or $|R_2| \approx 1$. Fine-structure patterns interestingly return to normal log-sine for values of $|R_1|$ and $|R_2| \gg 1$. These maps are also summarized in Fig. 7 where different shapes are collapsed into normal versus inverted patterns only.

Scale invariance violations for measurements in the ear canal result from a number of different sources, including (i) the presence of the middle/outer ear, (ii) the high-frequency cut-off of the basilar membrane, (iii) the variation in the sharpness of tuning of the basilar membrane from base to apex, and (iv) the presence of roughness on the basilar membrane.

From the perspective of DPOAE measurements, the principal effect of (ii) is to introduce a fine structure in the measured DPOAE level and group delay. The magnitude of this fine structure varies from base to apex due to fluctuations in the magnitude of the apical reflectance induced by this basilar membrane roughness. The effect of (iii) is to produce a variation in the relative spacing between fine structure maxima; $\Delta\omega/\omega$ (see, e.g., Zweig and Shera, 1995), as a function of the DPOAE frequency ω. It also influences the amount of DP energy generated in the overlap region of the two primaries.

The main effect of (i) and (ii) is to cause a variation in the ratio of the driving pressure in the ear canal to the motion

Dhar *et al.*: Multiple reflections and DP fine structure
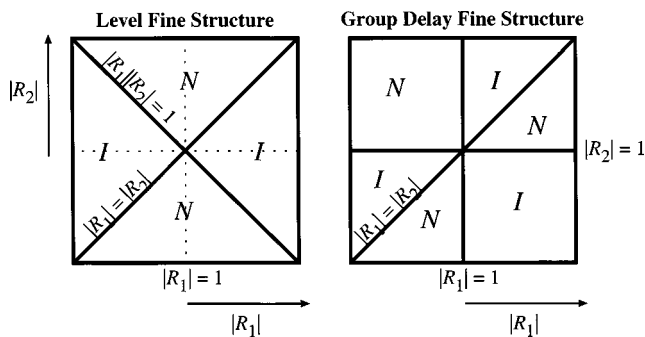
FIG. 7. Summary of numerical studies showing regions where the level and group delay fine structures are normal (N) versus inverted (I).

on the basilar membrane from base to apex. This will affect the amount of overall nonlinear interaction generated at fixed primary levels (in the ear canal) as the frequency of the primaries is varied.

Because of (i) and (ii) the magnitudes of the activity patterns associated with the primaries for mid-range frequencies (1000–2000 Hz in humans) can be significantly higher than they are for lower or higher frequency regions. This problem can be partly addressed by fixing the level of the primaries relative to the threshold of hearing, such that the primaries are set to a fixed pressure level in dB HL rather than dB SPL. Because of variations in the cochlear parameters from base to apex, there is reason to believe that the cochlea exhibits more gain at its base (60 dB) than at its apex. Hence, even fixing the stimulus to the hearing level of the subject will *not* remove the variation in the amount of nonlinear interaction generated by the primaries with stimulus frequency.

In spite of these complications, the assumption of "ear-canal scale invariance" is usually adequate as long as the frequency region being considered is not too large. If ear-canal scale invariance were exact, the phase of the DPOAE (generator component) would be expected to be constant with respect to DP frequency for fixed-f_2/f_1 data. In fixed-ratio DPOAE measurements in humans (Talmadge *et al.*, 1999) and in guinea pigs (Shera *et al.*, 2000), the slow DPOAE phase dependence with DPOAE frequency indicates that the assumption of ear-canal scale invariance holds reasonably well over a fairly large range of frequencies.

The principal effect of fine structure is to produce a quasiperiodic variation of the phase with frequency about an approximately constant value, as long as the generator site is dominant. In regions where the reflection site is dominant, a quasiperiodic variation about a rapidly varying monotonic behavior of the phase with frequency is observed (Piskorski, 1997; Talmadge *et al.*, 1999).

IV. METHODS

A. General methods

The methods used were similar to those reported earlier by our group. The reader is directed to Talmadge *et al.* (1999) for details. In brief, the signals were generated on a NeXT computer and passed through a set of TDT PA4 attenuators and HB6 headphone buffer before being fed to a

pair of ER2 tubephones. The tubephones were coupled to the subjects ear using an ER10B microphone probe assembly and a size-matched immittance (GSI) probe tip. The signal picked up in the ear canal by the ER10B low-noise microphone was filtered and amplified by a battery-operated Stanford Research SR560 filter/low-noise amplifier before being digitized by a Singular Solutions AD64x analog to digital converter. The digital signal was then recorded on the hard drive of the NeXT computer for offline analysis. An analysis technique using least squares fit (LSF) filters was used to estimate the level and phase of several orders of DPOAEs as well as the level of the noise floor (Long and Talmadge, 1997).

DPOAE recordings were obtained from a total of four subjects recruited from the Purdue University community. Subject selection was done via a series of screening tests involving audiological history, otoscopy, multifrequency tympanometry, tracking audiometry, spontaneous, and distortion product otoacoustic emissions. Subjects selected for the experiments had no family history of hearing loss, no recent middle or outer ear infections, had normal, type A tympanograms, and had hearing thresholds better than 10 dB HL at half-octave frequencies between 250 and 8000 Hz. The selected subjects exhibited DPOAE signal-to-noise ratio of 20 dB or better at stimulus levels of 65 dB SPL and a primary ratio of 1.225. The subjects also had distinct amplitude fine structure of DPOAEs in the frequency regions of interest. Presence or absence of spontaneous otoacoustic emissions was not used to determine subject eligibility, but the frequencies of spontaneous emissions, when present, were taken into account when analyzing DPOAE fine structure data. The subjects were seated comfortably in a double-walled EAC sound chamber during the experimental sessions which lasted approximately 2 h each.

Fine-resolution DPOAEs were recorded from each subject using several primary level combinations and frequency ratios with a frequency resolution approximating 0.025-mm tonotopic spacing on the basilar membrane. This spacing resulted in a variable frequency resolution with DPOAE frequency but each fine-structure period was always sampled by approximately 16 data points. The resultant frequency spacing was approximately 4 Hz around 1500 Hz and 8 Hz around 2500 Hz. The primary frequency ratio (f_2/f_1) was varied between 1.053 and 1.36 in approximate steps of 0.04 between 1.14 and 1.30. The step size was reduced at narrower and wider ratios outside of the limits of $1.14 \leqslant f_2/f_1 \leqslant 1.30$. The nominal ratios used were 1.053, 1.065, 1.08, 1.11, 1.14, 1.18, 1.22, 1.26, 1.30, 1.32, 1.34, and 1.36. Three equal level primary combinations ($L_1 = L_2 = 45, 65, 75$ dB SPL) were used to record data. Additionally, several L_2 levels (45, 50, 55, and 60 dB SPL) were used in conjunction with an L_1 of 65 dB SPL.

The initial analysis of the data was accomplished using automated programs that have been developed in our laboratory to implement the LSF analysis technique. Upon completion of the initial analysis an automated three-stage procedure was employed to "clean up" the data. In the first step all data points with a noise floor higher than a preset level, determined based on the average noise floor observed

in our laboratory, were rejected. At the next stage, a three-point, overlapping, median filter based on the noise floor estimate was applied to the data set. Data points with a signal-to-noise ratio less than a preset value, based on the data for the given subject and stimulus condition, were rejected. The data set generated after the first two steps was saved in a subdirectory for the last stage of analysis. In this stage the phase data were unwrapped using an automated algorithm, the results of which were cross checked manually in every case and additional unwrappings were performed where necessary.

Once the phase was completely unwrapped and visually inspected to be smoothly varying, the data were used to calculate group delay. Group delay was calculated by fitting the unwrapped DP phase with a straight line in five-point intervals. The group delay is given by $-m_\varphi/2\pi$, where m_φ is the slope of the straight line.

B. Inverse FFT

A customized algorithm was developed in the laboratory to implement an inverse fast Fourier transform (IFFT) procedure on DPOAE frequency-domain data. The goal of the IFFT procedure was to resolve DPOAE components with different latencies. Simply stated, a FFT converts signals from the time domain to the frequency domain; an IFFT works in the reverse direction, converting signals from the frequency to the time domain. IFFT protocols have previously been used to convert frequency-domain DPOAE data to the time domain (e.g., Stover *et al.*, 1996; Knight and Kemp, 2001; Kalluri and Shera, 2001; Konrad-Martin *et al.*, 2001). In the present application of the IFFT protocol, the real and imaginary parts of the complex DPOAE amplitude were used as input for the IFFT algorithm (FFT filter size = 1024) following interpolation of data points to ensure equal spacing. The result was a reverse transformation of the data into the time domain. A rectangular and a Welch window were used in the time and frequency domains, respectively. These windows were chosen after careful experimentation with several other window types in both time and frequency domains. The chosen window combination resulted in the lowest maximum error (in dB) when frequency-domain fine structures reconstructed from the IFFT output were compared with original data. This combination also produced the least amount of peak-broadening without elevating the noise floor in the absence of a signal.

The IFFT protocol was also used to reduce the noise in the data by time-domain filtering. Once the DPOAE components were identified and the time window containing the maximum energy for all components was established, a filter to remove noise outside of the time window was applied. This removed noise-related fluctuations in the amplitude spectra and allowed visualization of minute alterations in fine-structure shape. The efficacy of the objective shape-determination analysis described in the next section improved as a result of time-domain filtering. The effects of filtering were most noticeable at high ratios ($f_2/f_1 > 1.30$) with poor separation between the signal and noise.

C. Determining fine-structure shape

It was expected that natural variance in DPOAE data would make determination of fine-structure shape difficult. An objective method of fine-structure shape determination, that was tolerant of experimental error, was developed so as to eliminate observer bias. This method was based on the classification system decribed in Sec. III.

Level and group delay fine structures were filtered in the time domain using an IFFT analysis and then restored to the frequency domain. The first and second derivatives of the level and group delay were calculated and used to determine maxima, minima, and inflection points. Data points at which the first derivative equaled zero were identified as magnitude extrema. Thus, a maximum was defined as a data point where the first derivative equaled zero and the value of the second derivative was less than zero. A minimum was defined as a data point where the first data point equaled zero and the value of the second derivative was greater than zero. Finally, data points where the second derivative equaled zero were designated as inflection points.

D. Classification of fine-structure shapes of measured results

In order to strengthen the objectivity of the procedure described previously for classifying the fine-structure shape, a set of objective criteria was developed to determine data points where the first and second derivative curves crossed zero. An error range of two standard deviations was calculated for derivatives of both orders. Zero crossings were identified when either the data or the error bar crossed zero. In cases of multiple consecutive zero crossings of error bars only, the first and the last of the series were considered to be actual zero crossings.

Interpolated data were used for shape determination unless there were gaps of 20 Hz or more between adjacent data points in the original data. These gaps were a result of elimination of several contiguous data points due to low signal-to-noise ratio. Interpolation in these cases rendered the data unreliable in terms of the location of magnitude extrema and inflection points.

E. Relating fine-structure shape to stimulus parameters

The application of statistical methods to evaluate the relationship between different fine-structure shapes and stimulus parameters was complicated due to the variety of variable types. The explanatory or independent variables in this data set were primary levels and primary ratios. While these can be treated as interval variables, the dependent variable, fine-structure shape is purely nominal or categorical.

Given the nominal nature of the dependent variable, a generalized polytomous logistic regression model was deemed appropriate in this case. Generalized logit models, like ordinary regression models, can contain continuous or discrete explanatory variables (Agresti, 1990; Hosmer and Lemeshow, 1989). Moreover, the dependent variable can lack any form of ordering. A generalized logit model is stated as follows:
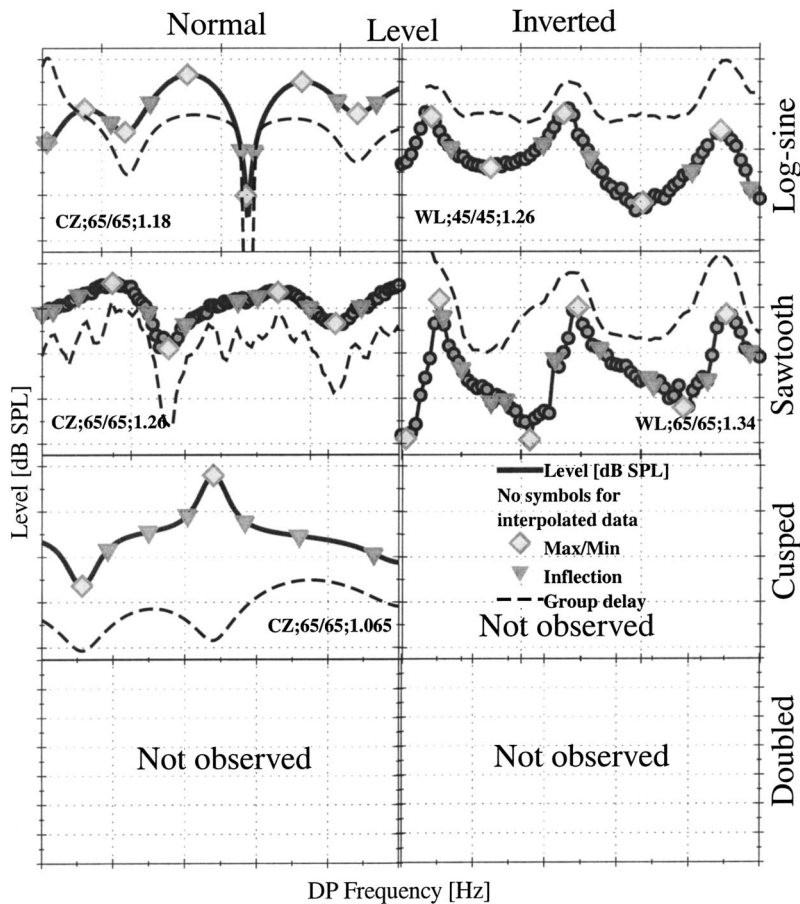
FIG. 8. Examples of different fine-structure shapes for DPOAE level. DPOAE level is presented with maxima, minima, and inflection points marked by diamonds and inverted triangles, respectively. The dashed line represents group delay under the same stimulus conditions. Subject and stimulus condition information is included in each panel. Symbols are not used in panels where interpolated data are presented. Abscissa and ordinate ranges are different for each panel.

$$\pi_j(x_i) = \frac{\exp(\beta'_j x_i)}{\sum_{h=1}^{J} \exp(\beta'_h x_i)}, \tag{8}$$

where $\pi_j(x_i)$ denotes the probability of response ($j = 1,...,J$) at the ith setting of values of k explanatory variables, $x_i = (1, x_{i1},...,x_{ik})$. The eight predicted fine-structure shapes (four patterns each for normal and inverted) are associated with values of $j = 1,...,8$. k equals 2 in this data set as there are two explanatory variables—primary ratio and level. The first explanatory variable (primary ratio) has 12 settings, while primary level has 7 settings. The CATMOD procedure of the statistical software package, SAS, was used to obtain maximum likelihood estimates for the occurrence of different fine-structure shapes for different stimulus parameters. Primary level, ratio, and an interaction term involving level and ratio were included in the CATMOD model. The output of this procedure contained an ANOVA table which was used to establish statistical significance. Note that the dependent variable categories were designed to be divided into two groups with $j \leq 4$ and $j \geq 5$ signifying normal and inverted fine-structure shapes, respectively. This allowed estimation of maximum likelihood of normal versus inverted fine structure for different stimulus parameters.

The above model was used to analyze level and group delay fine-structure shapes independently. In a parallel analysis, the dependent variable was altered to reflect a combination of level and group delay fine-structure shapes. Combination of level and group delay shapes resulted in 64 categories.

Fine-structure periods in the frequency range of interest were assigned nominal center-frequency values in 50-Hz increments. Thus, frequency was treated as an observational variable. In order to avoid the contaminating effects of windowing, the three central fine-structure periods within the test-frequency range for each subject were considered.

V. RESULTS

Different fine-structure shapes observed in level and group-delay data are presented in Figs. 8 and 9. Log-sine, sawtooth, cusped, and doubled shapes in both normal and inverted forms were observed for group-delay fine structure, and all shapes except doubled and inverted-cusped were observed in level fine structure. Each panel in Figs. 8 and 9 represents data from different subjects and stimulus conditions. The line with circular symbols represents either level (Fig. 8) or group delay (Fig. 9). The diamond symbols represent maxima and minima while the inverted triangles represent inflection points. Lines without symbols are used when interpolated data are presented.

There were several instances of different fine-structure shapes for the same stimulus condition for a given subject. One such example is displayed in Fig. 10. Group delay data are presented for subject KT for primary levels of 45 dB SPL and primary ratio of 1.22. Three different fine-structure shapes (cusped, log-sine, and doubled—from left to right) are observed. All three shapes are of the normal form in this case. However, observations of switching between normal
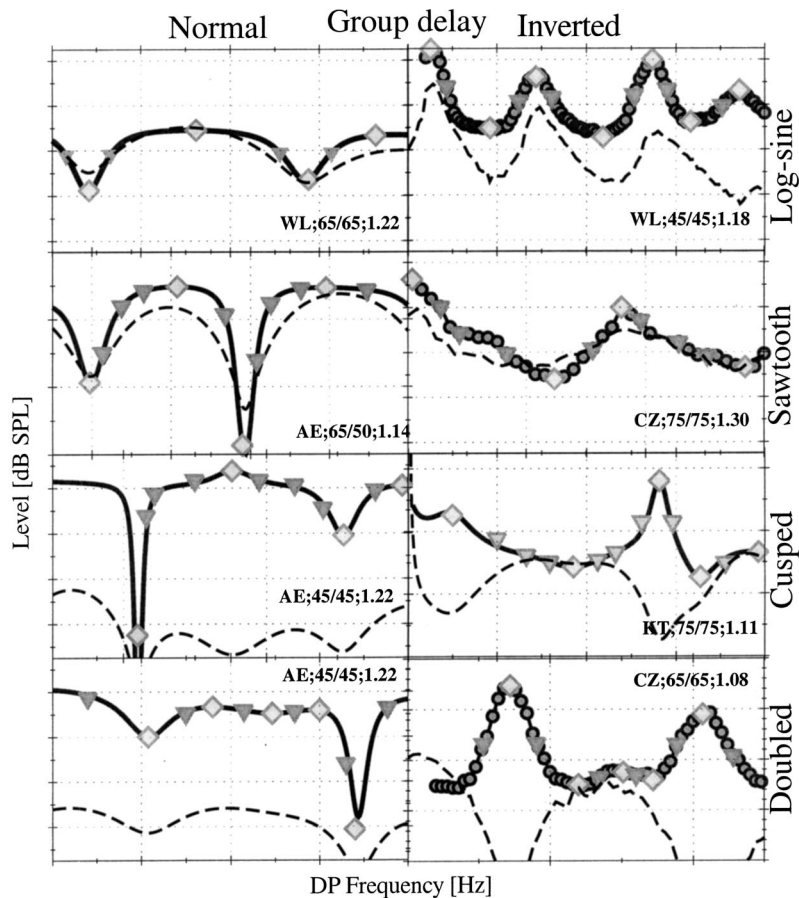
FIG. 9. Examples of different fine-structure shapes for DPOAE group delay. Group delay is presented with maxima, minima, and inflection points marked by diamonds and inverted triangles, respectively. The dashed line represents DPOAE level under the same stimulus conditions. Subject and stimulus condition information is included in each panel. Symbols are not used in panels where interpolated data is presented. Abscissa and ordinate ranges are different for each panel.

and inverted forms were also made within the same stimulus condition. No systematic patterns of shape combinations or stimulus conditions were observable.

The shapes of three central fine-structure periods in a 500-Hz frequency range (1500 to 2000: CZ; 1750 to 2250: KT; 2000 to 2500: AE) were determined for statistical analyses. Generalized logistic regression models were developed to look at distributions of eight categories of level and group-delay fine-structure shapes. In addition, the 64 combinations of level and group-delay fine-structure shape were similarly investigated. A full model was fit with subject, level, and

FIG. 10. Example of different fine-structure shapes generated by the same stimulus condition in a subject. Interpolated group delay data are presented from subject KT for primary levels of 45 dB SPL and primary ratio of 1.22. Normal cusped, log-sine, and doubled fine-structure shapes are observed from left to right.

ratio as dependent variables along with an interaction term involving level and ratio. The results of a CATMOD (SAS Inc., 1999) analysis indicated only level and ratio to be significant ($p < 0.05$). A reduced model was fit using these two dependent variables and a maximum likelihood analysis of variance was performed. Primary ratio was the only significant main effect for both level and group delay fine-structure shapes. Ratio had a Wald chi-square value of 12.05 ($p < 0.05$) for level fine-structure and a Wald chi-square value of 39.33 ($p < 0.0001$) for group-delay fine structure. Neither ratio nor primary level had a significant main effect on combination fine-structure shapes.

Response frequencies for different fine-structure shapes for level and group delay out of a total of 660 evaluated fine-structure periods are presented in Fig. 11. The top panels display frequency of occurrence of different fine-structure shapes for different primary levels. Data for level fine structure are displayed in the left panel, while those for group-delay fine structure are in the right panel. Similar information for different primary ratios is displayed in the bottom panels. The most prevalent shape in all four panels is normal log-sine. The discrepancy between this and other shapes is greater for level fine structure. As was noted in Figs. 8 and 9, the diversity of patterns is greater for group delay fine structure. The difference in prevalence between normal log-sine and other patterns for group delay fine structure are reduced at narrow f_2/f_1 ratios.

Given the dominance of the normal log-sine shape, a subsequent maximum likelihood analysis of variance was
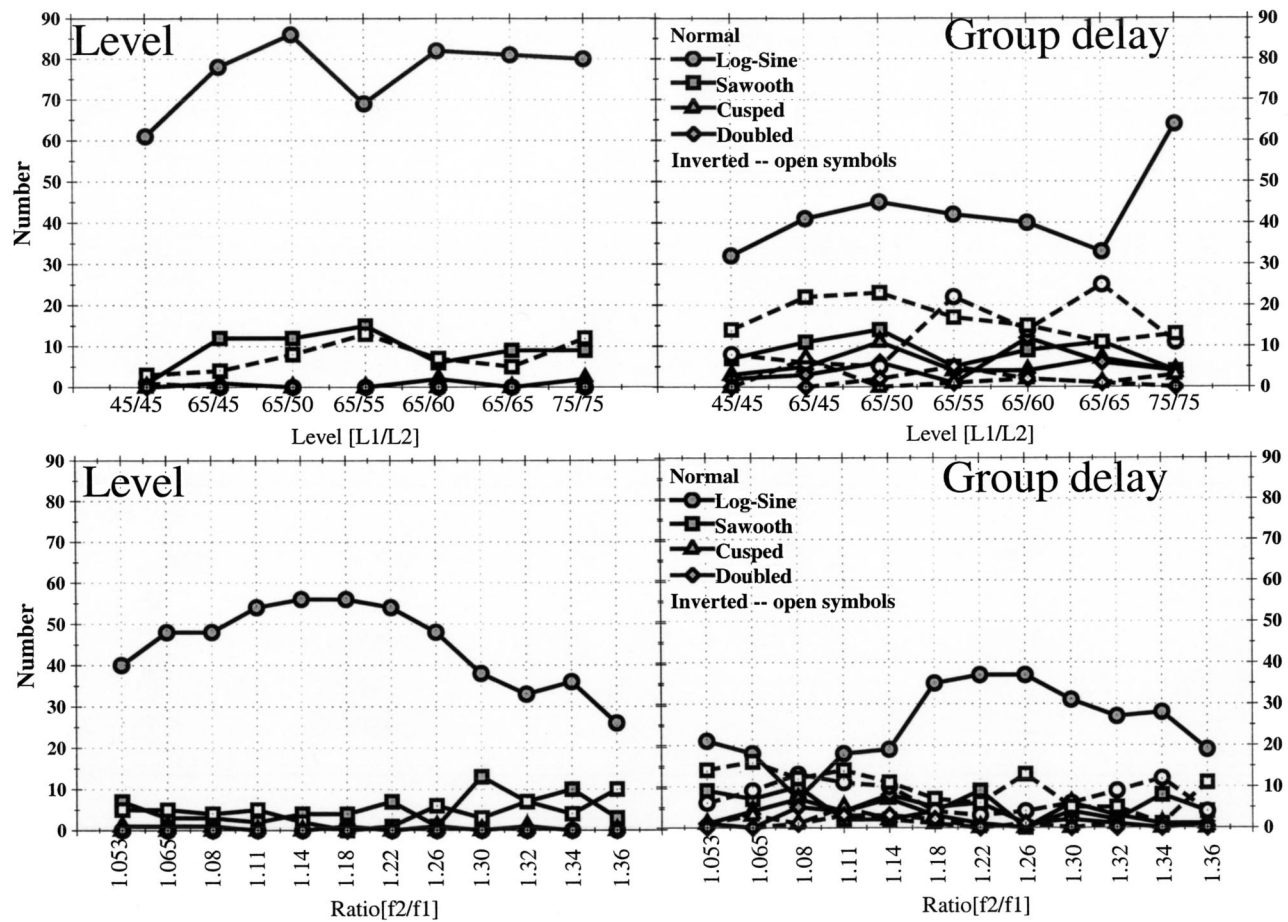
FIG. 11. Number of occurrences of different fine-structure shapes out of a total of 660 fine-structure periods evaluated. The upper panels display the number of occurrences for level and group-delay fine structure for different primary levels. The lower panels display similar information for different primary ratios. Normal and inverted shapes are represented by filled and open symbols, respectively. Inverted-cusped and doubled fine-structure shapes were not observed for DPOAE level.

performed on a reduced data set not containing normal log-sine shapes. The goal was to detect significant effects of primary ratio or level on fine-structure shapes that were not normal log-sine. However, the results of this analysis showed no significant effects of either primary level or ratio on group-delay or level fine structure.

A count of different fine-structure shapes showed greater diversity in group-delay fine structure as compared to level fine structure. Approximately 80% of all level-fine-structure shapes were log-sine of which only 0.9% were inverted. The majority of the remaining level shapes were sawtooth. However, approximately 50% of sawtooth level patterns were inverted. Only 7 cusped level patterns were observed out of a total of 660 fine-structure periods evaluated. No doubled patterns were observed for level fine structure. Group-delay shape distribution was in sharp contrast with that observed for level. Patterns were more evenly distributed with only approximately 50% being long-sine. The proportion of normal and inverted patterns varied between shape categories and no consistent pattern was observed.

The use of 64 categories in the combined shape analysis made it rather complex. However, since no main effects for either primary level or ratio was observed when all 64 categories were used in the analysis, the combinations were reduced to four broad categories. The four combination cat-

egories were level-normal–group-delay-normal, level-normal–group-delay-inverted, level-inverted–group-delay normal, and level-inverted–group-delay inverted. A maximum likelihood analysis of variance revealed ratio to have a significant main effect (Wald chi-square value of 27.75, $p < 0.0001$). The response frequencies for this analysis are displayed in Fig. 12. Results for different primary levels are displayed in the left panel, those for different primary ratios are displayed in the right panel. The two combinations involving normal level fine structure were the most common, with the combination of normal level and group delay being the most common. The only exception was at small ratios ($f_2/f_1 \leqslant 1.14$) where the combination of normal level and inverted group delay had similar prevalence. The two combinations involving inverted level fine structure were rarely observed.

A. Exotic shapes and multiple reflections

In order to verify the model prediction relating the "exotic" fine-structure shapes and multiple reflections in the cochlea, a comparative analysis between time- and frequency-domain results was done. Results of the IFFT analysis were used as time-domain representations of the frequency domain data. A comparison of time-domain results and the cor-
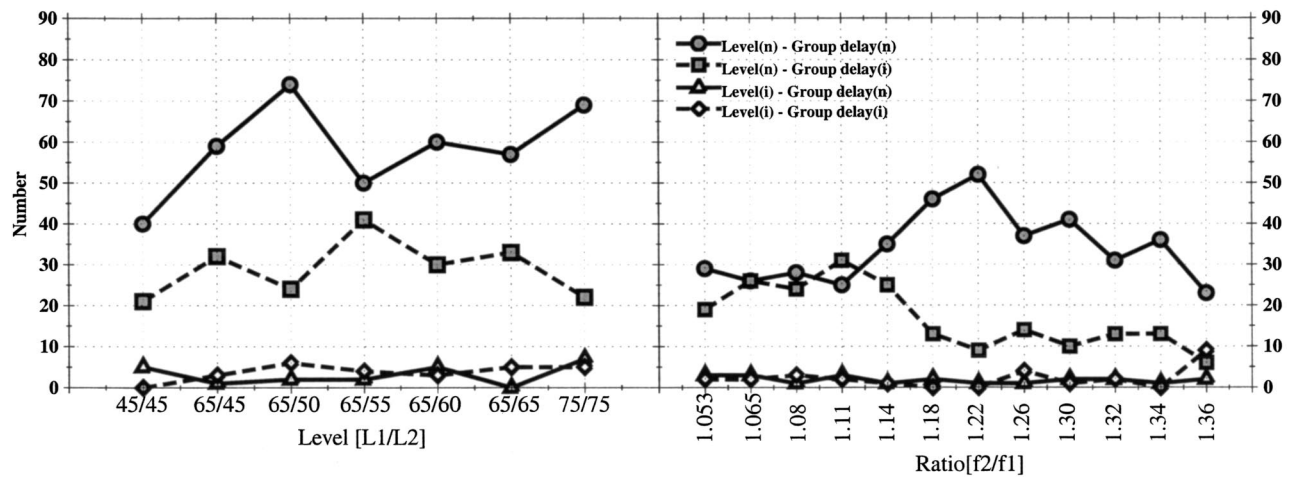
FIG. 12. Number of occurrences of fine-structure-shape combinations for level and group-delay fine structure. Four groups of combinations were formed based on normal or inverted shapes of level and group-delay fine structure. Data for different primary levels and ratios are displayed in the left and right panels, respectively.

responding level or group delay fine structure in the frequency domain for subject WL under different stimulus conditions is displayed in Fig. 13.

The first two major peaks in the left column of Fig. 13 represent the component from the overlap region and the initial reflected component from the $2f_1 - f_2$ tonotopic region, respectively. These are the major peaks observed in the top two rows. The corresponding level and group-delay fine structures are displayed in the right column. Both level and group delay fine structures are classified as normal log-sine in the top row ($L_1 = L_2 = 65$ dB SPL; $f_2/f_1 = 1.22$). While both level and group delay fine structures are again classified as log-sine in the second row ($L_1 = L_2 = 65$ dB SPL; $f_2/f_1 = 1.11$), level fine structure is normal and group-delay fine structure is inverted in this case. Note that, in the time domain results, the reflection component is larger in this case and no additional peaks are observed in time. Both level and group-delay fine structures are inverted log-sine in the third row ($L_1 = L_2 = 45$ dB SPL; $f_2/f_1 = 1.18$). Additional peaks occurring after the generator and initial reflection components can be observed in this case. Finally, both level and group-delay fine structures are inverted and the shape of level fine structure is classified as sawtooth in the last row ($L_1 = L_2 = 65$ dB SPL; $f_2/f_1 = 1.34$). Additional peaks in the time domain are observed in this case as well. Note the correspondence between the observation of longer-latency peaks (>15 ms) and "exotic" fine-structure shapes.

B. Summary

In our analysis of 660 fine-structure periods, predicted "exotic" patterns in both normal and inverted forms were observed. Level fine structure was predominantly log-sine, while group delay fine structure exhibited more varied patterns. While all predicted shapes were observed in group delay fine structure, doubled and inverted-cusped shapes were not observed in level fine structure. Primary ratio had a significant main effect on fine-structure shape. However, this effect was not significant when normal log-sine shapes were excluded from the data set. The combination of normal level

and group delay fine structure constituted the majority of fine structure shapes at most ratios. However, the combination of normal level and inverted group delay fine structure was equally prevalent at low f_2/f_1 ratios. Finally, simultaneous examination of time and frequency domain results revealed a correspondence between the occurrence of multiple peaks and exotic fine-structure shapes.

VI. DISCUSSION

Several "exotic" and previously unreported fine-structure patterns for DPOAE level and group delay are predicted when multiple internal reflections are incorporated into a classic two-source interference model of DPOAEs. All but one of the predicted fine-structure patterns were observed in our analysis of 660 fine-structure periods recorded from four subjects. The fine-structure pattern classified as "normal log-sine" here has been the only one reported in published literature. The shapes observed in this data set deviate from those in previous reports with respect to inversion and existence of "sawtooth," "doubled," and "cusped" shapes. Inversion of group delay fine structure in the context of log-sine shape is discussed first, and is followed by a detailed treatment of other shapes and their inverted forms.

Inversion of log-sine group-delay fine structure is predicted when $|R_1| > 1$. Recall that R_1 is the product of R_d and R_a. $|R_d|$ is predicted to be greater than 1 at narrow f_2/f_1 ratios (<1.11) (Talmadge $et\ al.$, 1998; Knight and Kemp, 1999), thereby increasing the likelihood of $|R_1|$ being greater than 1 at these ratios. In physical terms, R_d can be related to the ratio of energy moving apically versus basally from the overlap region on the basilar membrane. Thus, a value of $|R_d| > 1$ simply implies that the fraction of DPOAE energy traveling apically is greater than that propagating basally from the overlap region. R_a refers to the apical reflectance that is responsible for reflecting the apical-moving energy towards the base of the cochlea. Thus, the magnitude of the initial reflection component is determined by the product of R_d and R_a. When $|R_d|$ is greater than 1 at narrow f_2/f_1 ratios it increases the likelihood of the reflection component

Dhar $et\ al.$: Multiple reflections and DP fine structure
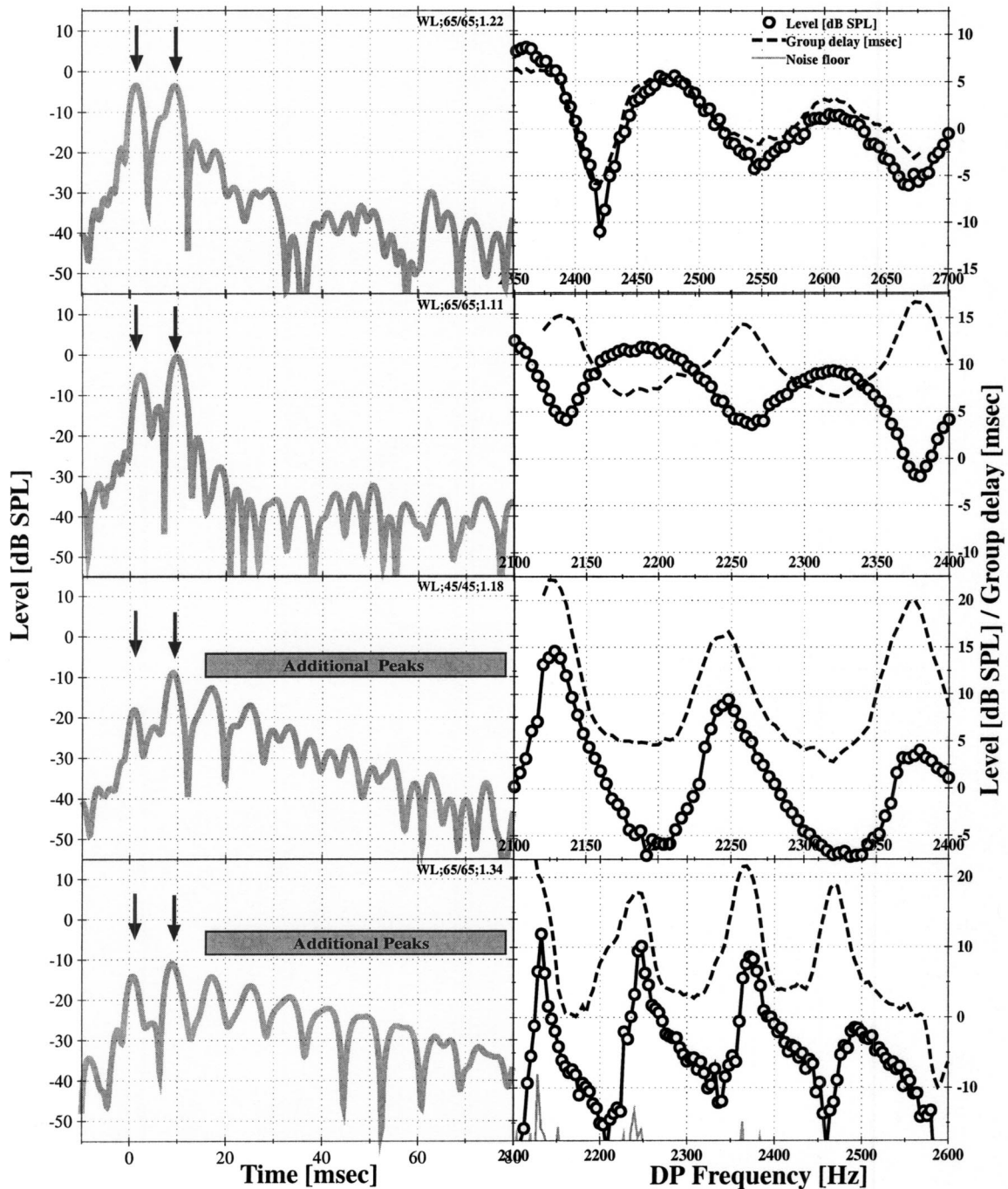
FIG. 13. Comparison of results in times and frequency domains for different stimulus conditions from one subject. Time domain results are displayed in the left column. Level (solid line) and group-delay (broken line) fine structures are displayed in the right column. While two principal peaks in time, presumably from the generator and the initial reflected components (marked by arrows), are seen in the two top rows, additional peaks beyond 15 ms are observed in the bottom two rows. Note the changes in fine-structure shape in the right column of the bottom two rows.

being larger than the generator component as recorded in the ear canal. Group-delay fine structure is expected to be inverted when the reflection component is larger than the generator component (Talmadge *et al.*, 1999). Indeed, this combination of inverted group-delay and normal level fine structure is observed more often at f_2/f_1 ratios lower than approximately 1.14 (see Fig. 12). This fact is in consonance with the previously published observation that the reflection component is larger than the generator component at low f_2/f_1 ratios (Talmadge *et al.*, 1999; Knight and Kemp, 1999,

2000, 2001). Note that multiple internal reflections are not needed for the occurrence of this pattern. This is evident in the second row of Fig. 13 where group-delay fine structure is inverted and the reflection component is larger than the generator component (as seen in the time-domain data). Multiple reflections in the form of additional peaks in the time domain are not observed in this case.

Given the above results, one would predict that this pattern should be observed at high f_2/f_1 ratios as well since $|R_a|$ may be large and $R_d \approx 1$ at these ratios. The magnitude

of the apical reflectance $|R_a|$ is expected to tend to be high for high f_2/f_1 ratios as the $2f_1-f_2$ tonotopic place moves further away from the peak regions of the excitation patterns of the primaries and the suppressive effects of the primaries on R_a are reduced. However, as $|R_a|$ becomes larger, so must $|R_2|$ since it is the product of $|R_a|$ and $|R_b|$ (recall that R_b is the basal reflectance). High $|R_2|$ can be produced by large values of either $|R_a|$ or $|R_b|$, or both. $|R_b|$, the magnitude of the basal reflectance at the junction of the cochlea and the middle ear, is independent of the primary frequency ratio or levels, but depends on f_{dp}. Simply stated, $|R_b|$ is at its lowest at DP frequencies most conducive to reverse transmission of energy from the cochlea through the middle ear. Our current two-source interference model incorporates a simple model of the middle ear where the tympanic membrane is treated as a single piston with a fixed incudo-stapedial joint. Given these simplifications, Talmadge et al. (1998) have derived the behavior of R_b with respect to frequency. The model predicts $|R_b|$ to be minimum at middle ear resonance which turns out to be between 1000 and 1500 Hz. It should be noted that the low-frequency slope of $|R_b|$ is steeper and perhaps more importantly the value of $|R_b|$ can be quite large $[0.92 \leqslant |R_b| \leqslant 1$ over all frequencies for the mode of Talmadge et al. (1998)]. Such values of $|R_b|$ would result in a majority of the basal energy in the cochlea being reflected back towards the apex and a small portion being transmitted to the ear canal. This is consistent with observations that the level of the $2f_1-f_2$ DPOAE is approximately 30 dB higher in the cochlea than in the ear canal (Zwicker and Harris, 1990; Puria and Rosowski, 1996).

The predictions for $|R_b|$ in the simplified middle ear model used in our model of DPOAEs are consistent with reports of reverse middle ear transmission in humans. Although reverse transmission of the middle ear is more difficult to study and consequently not as frequently studied as forward transmission, Puria and Rosowski (1996) found a peak around middle ear resonance (≈ 1000 Hz) and a low-pass function between 1000 and 4000 Hz. Thus, it can be argued that larger variations of $|R_2|$ would have to be due to variations of $|R_a|$ which is expected to vary with frequency (Talmadge et al., 1998; Talmadge et al., 2000).

Since $|R_a|$ tends to be high at wide f_2/f_1 ratios and low primary levels, $|R_2|$ is expected to be high also. In physical terms, high values of $|R_2|$ imply high values of both apical and basal reflectances resulting in multiple internal reflections. Such additional components are observed at large f_2/f_1 ratios with latencies greater than that of the initial reflection component (see two bottom panels of Fig. 13). Although significant correlation between stimulus parameters and these multiple reflections could not be established, they were observed at high f_2/f_1 ratios and low primary levels. The lack of significant correlation between stimulus parameters and occurrence of "exotic" fine-structure patterns (and multiple reflections by deduction) could be due to the relative paucity of such observations in the data set. Several conditions have to be met for these multiple reflections to occur and all these conditions were obviously not frequently present in the current data set.

The presence of such additional components has been postulated in cochlear models (Zweig and Shera, 1995; Talmadge et al., 1998). These internal reflections are also necessary for the generation of spontaneous otoacoustic emissions, fine structure in transient and stimulus frequency emissions, and threshold microstructure (Talmadge et al., 1998). Evidence for them has also been seen in time domain measurements of DPOAEs (Talmadge et al., 1999). Stover et al. (1996) observed multiple peaks in the time domain when they applied an inverse FFT to their fixed-f_2 data. Consistent with observations made in this data set, higher latency peaks emerged for lower stimulus levels. Stover et al. (1996) proposed the presence of "one (or two) sources and multiple reflections between this (these) and the boundaries of the cochlea" as one of three possible mechanisms responsible for the generation of these additional peaks. After a detailed analysis of the three mechanisms, they proposed that the presence of multiple sources inside the cochlea was the most likely causative agent. The lack of a constant temporal relationship between the additional peaks was one of the reasons for rejecting multiple internal reflections as a probable mechanism. The lack of a constant temporal relationship between peaks could be a result of their use of a fixed-f_2 paradigm. As one primary is fixed and the other varied in frequency, the distance between the generator and the $2f_1-f_2$ tonotopic regions, and that between the $2f_1-f_2$ region and the base of the cochlea, are altered simultaneously. This negates the approximate phase constancy of the generator component, thereby making the interpretation of IFFT data more ambiguous. These latency relationships are easier to interpret in a fixed-ratio paradigm. Another issue that confounded Stover et al. (1996) was "why progressively later occurring reflections become dominant as (stimulus) level is decreased." It can be argued that as stimulus level decreases, $|R_a|$ becomes larger as there is less suppression from the primaries. Additionally the gain of the cochlear amplifier around the DP tonotopic region could also be higher as the magnitude of the apical-moving energy reaching the DP tonotopic region is reduced. A higher value of $|R_a|$ would result in increased magnitude of the reflection component for a given $|R_d|$. Although we did not observe any instances where the amplitudes of secondary reflection components were larger than the generation or initial reflection component, such an observation would only point towards the inherent complexity of the DPOAE generation process. A detailed understanding of the dependence of $|R_a|$ on stimulus level needs to be developed in order to fully appreciate the complexity of multiple internal reflections in the cochlea. It should be noted that in a later publication by the same group, the multiple peaks from an IFFT analysis were attributed to multiple internal reflections (Konrad-Martin et al., 2001).

The presence of non-log-sine fine structures lends credence to the presence of multiple internal reflections as their observation demonstrates the significance of the contribution of these reflections to the signal in the frequency domain. Again, this is not unique to DPOAEs. Alterations in frequency-domain waveforms are seen when a broadband noise is added to itself after a specific time delay. The spe-

cific shape of the waveform is heavily dependent on the number of iterations of the original noise source added to the final signal. Such a signal is referred to as ''iterated ripple noise'' (Yost, 1996; Yost *et al.*, 1998) and exhibits a shape much like the inverted log-sine fine structure observed here.

Our model correctly predicts the occurrence of different fine-structure shapes for both group delay and level fine structures. The inverted cusped shape for level fine structure is the only shape-category predicted by the model that was not observed in the data set. Finally, we demonstrated a correspondence between the occurrence of these ''exotic'' patterns and the presence of multiple internal reflections using an IFFT analysis. These results show that a detailed model of DPOAEs should indeed include multiple internal reflections. The complexity of the predictions of such a model is also apparent from these data. While we have presented convincing evidence in support of the presence of multiple reflections, this phenomenon still needs to be investigated directly in the time domain.

ACKNOWLEDGMENTS

Agresti, A. (**1990**). *Categorical Data Analysis* (Wiley, New York).

Brown, A. M., Harris, F. P., and Beveridge, H. A. (**1996**). ''Two sources of acoustic distortion products from the human cochlea,'' J. Acoust. Soc. Am. **100**, 3260–3267.

Dreisbach, L. (**1999**). ''Characterizing the $2f_1 - f_2$ distortion-product otoacoustic emission and its generators measured from 2 to 20 khz in humans'', unpublished doctoral dissertation, Northwestern University.

Fahey, P. F., and Allen, J. B. (**1997**). ''Measurement of distortion product phase in the ear canal of the cat,'' J. Acoust. Soc. Am. **102**, 2880–2891.

Heitmann, J., Waldmann, B., Schnitzler, H. U., Plinkert, P. K., and Zenner, H. P. (**1998**). ''Suppression of distortion product otoacoustic emissions (DPOAE) near $2f_1 - f_2$ removes DP-gram fine structure—evidence for a secondary generator,'' J. Acoust. Soc. Am. **103**, 1527–1531.

Hosmer, D. W., and Lemeshow, S. (**1989**). *Applied Logistic Regression* (Wiley, New York).

Kalluri, R., and Shera, C. A. (**2001**). ''Distortion-product source unmixing: A test of the two-mechanism model for dpoae generation,'' J. Acoust. Soc. Am. **109**, 622–637.

Kemp, D. T. (**1978**). ''Stimulated acoustic emissions from within the human auditory system,'' J. Acoust. Soc. Am. **64**, 1386–1391.

Knight, R. D., and Kemp, D. T. (**1999**). ''Relationship between dpoae and teoae characteristics,'' J. Acoust. Soc. Am. **106**, 1420–1435.

Knight, R. D., and Kemp, D. T. (**2000**). ''Indications of different distortion product otoacoustic emission mechanisms from a detailed f_1, f_2 area study,'' J. Acoust. Soc. Am. **107**, 457–473.

Knight, R. D., and Kemp, D. T. (**2001**). ''Wave and place fixed dpoae maps of the human ear,'' J. Acoust. Soc. Am. **109**, 1513–1525.

Konrad-Martin, D., Neely, S. T., Keefe, D. H., Dorn, P. A., and Gorga, M. P. (**2001**). ''Sources of distortion product otoacoustic emissions revealed by suppression experiments and inverse fast Fourier transforms in normal ears,'' J. Acoust. Soc. Am. **109**, 2862–2879.

Kummer, P., Janssen, T., and Arnold, W. (**1995**). ''Suppression tuning characteristics of the $2f_1 - f_2$ distortion product otoacoustic emission in humans,'' J. Acoust. Soc. Am. **98**, 197–210.

Long, G. R., and Talmadge, C. L. (**1997**). ''Spontaneous otoacoustic emission frequency is modulated by heartbeat,'' J. Acoust. Soc. Am. **102**, 2831–2848.

Mauermann, M., Uppenkamp, S., van Hengel, P. W. J., and Kollmeier, B. (**1999a**). ''Evidence for the distortion product frequency place as a source of distortion product otoacoustic emission (DPOAE) fine structure in humans. II. Fine structure for different shapes of cochlear hearing loss,'' J. Acoust. Soc. Am. **106**, 3484–3491.

Mauermann, M., Uppenkamp, S., van Hengel, P. W. J., and Kollmeier, B. (**1999b**). ''Evidence for the distortion product frequency place as a source of distortion product otoacoustic emission (DPOAE) fine structure in humans. I. Fine structure and higher-order DPOAE as a function of the frequency ratio $f2/f1$,'' J. Acoust. Soc. Am. **106**, 3473–3483.

Piskorski, P. (**1997**). ''The origin of the distortion product otoacoustic emission fine structure,'' unpublished doctoral dissertation, Purdue University.

Puria, S., and Rosowski, J. J. (**1996**). ''Measurements of reverse transmission in the human middle ear: Preliminary results,'' in *Diversity in Auditory Mechanics*, edited by E. R. Lewis, G. R. Long, R. F. Lyon, P. M. Narins, C. R. Steele, and E. Hecht-Poinar (World Scientific, Singapore), pp. 151–157.

SAS Inc. (**1999**). *SAS/STAT User's Guide* (SAS Institute, Inc., Cary, NC).

Shera, C. A., and Zweig, G. (**1991**). ''Reflection of retrograde waves within the cochlea and at the stapes,'' J. Acoust. Soc. Am. **89**, 1290–1305.

Shera, C. A., and Zweig, G. (**1993**). ''Dynamic symmetry creation: The origin of spectral periodicity in evoked otoacoustic emissions,'' in *Biophysics of Hair Cell Sensory Systems*, edited by H. Duifhuis, J. W. Horst, P. van Dijk, and S. M. van Netten (World Scientific, Singapore), pp. 54–63.

Shera, C. A., and Guinan, J. J. (**1999**). ''Evoked otoacoustic emissions arise by two fundamentally different mechanisms: A taxonomy for mammalian OAEs,'' J. Acoust. Soc. Am. **105**, 782–798.

Shera, C. A., Talmadge, C. L., and Tubis, A. (**2000**). ''Interrelations among distortion-product phase-gradient delays: their connection to scaling symmetry and its breaking,'' J. Acoust. Soc. Am. **108**, 2933–2948.

Stover, L. J., Neely, S. T., and Gorga, M. P. (**1996**). ''Latency and multiple sources of distortion product emissions,'' J. Acoust. Soc. Am. **99**, 1016–1024.

Talmadge, C. L., Long, G. R., Tubis, A., and Dhar, S. (**1999**). ''Experimental confirmation of the two-source interference model for the fine structure of distortion product otoacoustic emissions,'' J. Acoust. Soc. Am. **105**, 275–292.

Talmadge, C. L., Tubis, A., Long, G. R., and Piskorski, P. (**1998**). ''Modeling otoacoustic emission and hearing threshold fine structures in humans,'' J. Acoust. Soc. Am. **104**, 1517–1543.

Talmadge, C. L., Tubis, A., Long, G. R., and Tong, C. (**2000**). ''Modeling the combined effects of basilar membrane nonlinearity and roughness on stimulus frequency otoacoustic emission fine structure,'' J. Acoust. Soc. Am. **108**, 2911–2932.

Talmadge, C. L., Tubis, A., Piskorski, P., and Long, G. R. (**1997**). ''Modeling otoacoustic emission fine structure,'' in *Diversity in Auditory Mechanics*, edited by E. R. Lewis, G. R. Long, R. F. Lyon, P. M. Narins, C. R. Steele, and E. Hecht-Poinar (World Scientific, Singapore), pp. 462–471.

Yost, W. A. (**1996**). ''Pitch of iterated ripple noise,'' J. Acoust. Soc. Am. **100**, 511–518.

Yost, W. A., Patterson, R., and Sheft, S. (**1998**). ''The role of the envelope in processing iterated rippled noise,'' J. Acoust. Soc. Am. **104**, 2349–2361.

Zweig, G., and Shera, C. A. (**1995**). ''The origins of periodicity in the spectrum of evoked otoacoustic emissions,'' J. Acoust. Soc. Am. **98**, 2018–2047.

Zwicker, E., and Harris, F. P. (**1990**). ''Psychoacoustical and ear canal cancellation of $2f_1 - f_2$-distortion products,'' J. Acoust. Soc. Am. **87**, 2583–2591.

Characterizing cochlear mechano-electric transduction with a nonlinear system identification technique: The influence of the middle ear

Chul-Hee Choi,[a] Mark E. Chertoff, and Xing Yi
Hearing and Speech Department, University of Kansas Medical Center, Kansas City, Kansas 66160

Previously a third-order polynomial equation characterizing mechano-electric transduction was obtained from a nonlinear system identification procedure applied to an ear canal acoustic signal and cochlear microphonic (CM/AC). In this paper, we examine the influence of the linearity and frequency response of the intervening middle ear on the nonlinearity, frequency response, and coherence of the third-order polynomial model of mechano-electric transduction (MET). Ear canal sound pressure (AC), cochlear microphonics (CM), and stapes velocity (SV) were simultaneously recorded from Mongolian gerbils. Linear and nonlinear transfer and coherence functions relating stapes velocity to the acoustic signal (SV/AC), CM to the acoustic signal (CM/AC), and CM to the stapes velocity (CM/SV) were computed. The results showed that SV/AC was linear while CM/AC and CM/SV were not, indicating that the nonlinearity of CM/AC was not due to nonlinearity of the middle ear. The frequency response of the linear term of CM/AC was similar to that of ST/AC but differed from that of CM/SV while the cubic term of CM/AC was similar to that of CM/SV. This indicates that the frequency dependence of CM/AC was due to both the middle ear and frequency dependence of the inner ear. Finally the fit of the polynomial model of MET without the middle ear (CM/SV) did not improve from the fit including the middle ear (CM/AC). A cochlear model of the CM indicated that the lack of improvement was due to the limitations of a third-order polynomial equation characterizing the hair cell transducer function. © *2002 Acoustical Society of America.* [DOI: 10.1121/1.1514936]

PACS numbers: 43.64.Bt, 43.64.Ha, 43.64.Ld [LHC]

I. INTRODUCTION

Mechano-electric transduction (MET) in the cochlea is a nonlinear process in which mechanical movement of the cochlear partition is changed into electrical signals via deflection of the hair-cell stereocilia and opening and closing ion channels located within or in the vicinity of the stereocilia (Hudspeth, 1982). A functional description of MET can be obtained *in vivo* from the cochlear microphonic (CM), a far-field electric potential generated from the spatial summation of the hair cell receptor currents, recorded at the round window using pure tones (Patuzzi *et al.*, 1989; Patuzzi, 1987; Dallos, 1985; Dallos *et al.*, 1972; Nieder and Nieder, 1971), or from an engineering-based nonlinear systems identification technique (Chertoff *et al.*, 2000, 1997, 1996). The nonlinear systems identification (NLID) procedure provides a third-order polynomial model of MET. Physiologic indices including slope, root or operating point, maxima, minima, and saturation sound pressure levels at maxima (SPL_{max}) and minima (SPL_{min}) can be derived from mathematical manipulation of the model. These indices are sensitive and specific to changes in cochlear transduction due to cochlear pathology (Bian and Chertoff, 2001, 1998).

In the previous studies characterizing MET, the parameters of the third-order polynomial equation were obtained from the relation between the input acoustic sound pressure (AC) measured at the tympanic membrane and CM measured at the round window. The results showed that the polynomial coefficients were frequency dependent and accounted for approximately 90% of the CM to AC input–output relation. Previously, it was unknown whether the frequency dependence of the coefficients and the fit of the polynomial were due to the middle ear (ME) that intervenes between the acoustic and CM measurement location, or inner ear mechanisms. Moreover, the NLID procedure used to obtain the polynomial equation assumed a system organized as a nonlinear system followed by a linear system (nonlinear–linear system) (Bendat and Piersal, 1993; Bendat and Palo, 1990).

Many studies of the middle ear show that the middle ear, on the whole, acts as a band-pass filter, although the filter's parameters such as cutoff frequency and slope differ among species (Teoh *et al.*, 1997; Rosowski, 1994; Price and Kalb, 1991; Pickles, 1988; Zwislocki, 1975; Nuttall, 1974; Price 1974; Dallos, 1973; Guinan *et al.*, 1967). Without the activation of the middle ear muscles, it has been shown that the middle ear behaves as a linear system (Guinan *et al.*, 1967) and therefore the middle ear and cochlea together are assumed to act as a linear system followed by a nonlinear system (linear–nonlinear system). Thus the nonlinear–linear system assumed in the NLID procedure characterizing MET does not truly represent the anatomic linear–nonlinear system and may have lead to inaccuracies of the polynomial model and limited fit of the equation (Bian and Chertoff, 2001, 1998; Chertoff *et al.*, 1997, 1996). This possibility is illustrated in the following simulation of a linear system fol-
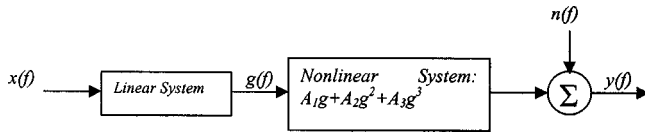
FIG. 1. Diagram of a linear–nonlinear system with a linear filter followed by a nonlinear system where $x(f)$ is an input acoustic signal, $g(f)$ is an output of a linear filter, $y(f)$ is an output of the nonlinear system, and $n(f)$ is an extraneous noise uncorrelated with $g(f)$ and $y(f)$.

lowed by a nonlinear system. Figure 1 represents a diagram of the linear–nonlinear system where $x(f)$ is the input, $g(f)$ is the output of a linear filter, $y(f)$ is the output of the nonlinear system, and $n(f)$ is an extraneous noise uncorrelated with $g(f)$ and $y(f)$. The linear filter is modeled as two band-pass filters and the nonlinear system is represented by a polynomial equation. The input is Gaussian noise with a standard deviation of 1 and mean of 0. The two band-pass filter linear system is a band-pass filter between 100 Hz–4 kHz and 4 kHz–10 kHz for simulating the CM/AC transfer function of gerbils with the bulla open shown in the previous study (Chertoff *et al.*, 1997). The output of the filter is sent to a third-order polynomial nonlinearity with arbitrary coefficients ($A_1 = 0.5$, $A_2 = 0.02$, and $A_3 = 0.35$) to produce the output $y(f)$. Application of the NLSI technique to data measured at $x(f)$, $g(f)$, and $y(f)$ yields the predicted A coefficients of the polynomial equation.

Panels (A), (B), and (C) of Fig. 2 show the estimates of the coefficients based on the NLID analysis relating the input signal, x, to the nonlinear output, y (y/x, solid lines) as well as relating the output of the linear filter, g, to the nonlinear output, y (y/g, dotted lines). The coefficients estimating the nonlinearity were not correct in y/x (including the linear filter). The A coefficients computed from y/x were very different from the coefficients ($A_1 = 0.5$, $A_2 = 0.02$, and $A_3 = 0.35$) used to produce the output whereas the A coefficients computed from y/g (excluding the linear filter) were correct. Furthermore, the A coefficient, especially, A_1 of y/x was dependent on frequency whereas the A_1 coefficient computed from y/g was not dependent on frequency. The frequency dependence of y/x was due to the linear filter and not due to any inherent frequency dependence in the polynomial equation. Panel (D) of Fig. 2 shows the total coherence. The total coherence, the sum of linear, quadratic, and cubic coherence functions, provides a measure of "goodness of fit" of the third-order polynomial equation as a function of frequency (Chertoff *et al.*, 1996). The total coherence of y/g was one whereas that of y/x ranged 0.7 to 0.92. When the linear filter was excluded, the total coherence was significantly improved.

The results of this simulation suggest that it is necessary to determine the influence of the ME on both the fit and frequency dependence of the polynomial model of MET de-
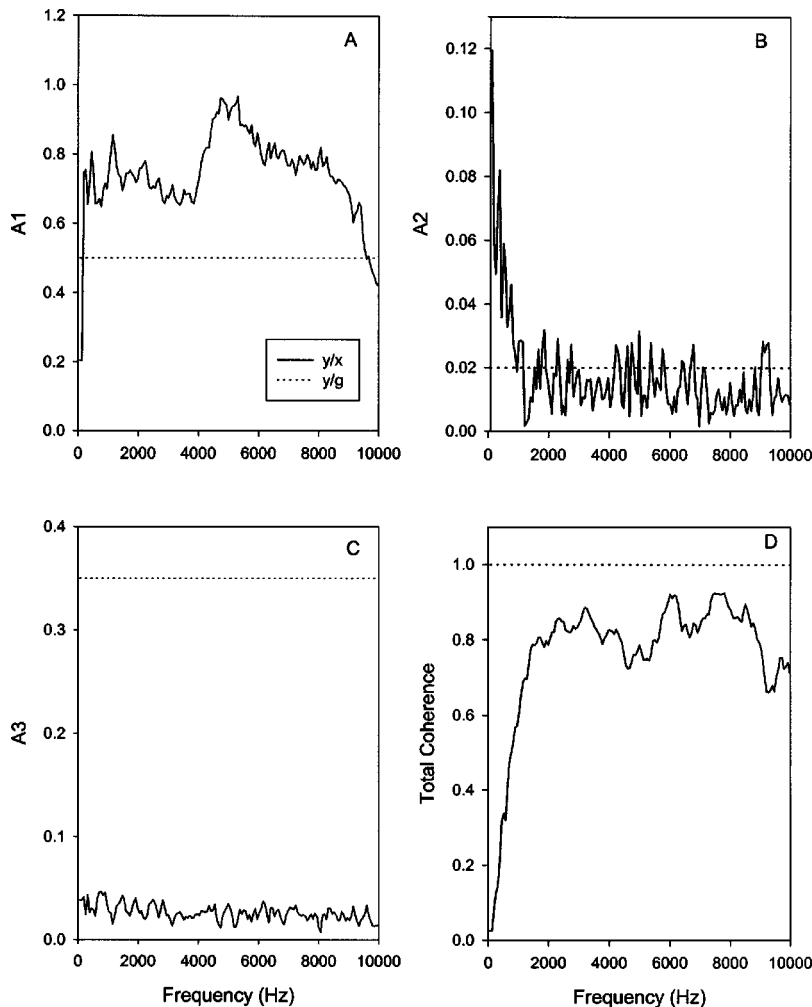
FIG. 2. Comparison of the linear (A_1) and nonlinear (A_2, A_3) coefficients of a polynomial equation and total coherence function computed from the acoustic signal to the CM (y/x, solid lines) and from the output of the ME filter to the CM (y/g, dotted lines). Panel (A) shows the linear coefficient (A_1) between y/x and y/g. Panel (B) shows the quadratic coefficient (A_2) between y/x and y/g. Panel (C) shows the cubic coefficient between y/x and y/g. Panel (D) shows the total coherence function between y/x and y/g.

scribed earlier by Chertoff *et al.* (1997, 1996). This study has three distinctive purposes. The first purpose was to determine if the nonlinear terms characterizing MET in the previous studies was due to the ME or the inner ear. The second purpose was to determine if the frequency dependence of the linear and nonlinear terms was due to the frequency response of the middle ear. The final purpose was to determine whether the total coherence of the polynomial model of MET was improved when the ME was excluded as in the simulation.

II. METHODS

A. Animal preparation

Animal preparation and experimental procedure were very similar to those presented previously by Chertoff *et al.* (1997) and Bian and Chertoff (1998) except using a laser for the measurement of the stapes vibration. Mongolian gerbils were used as subjects because of the ease of surgical approach to the cochlea, similar low frequency hearing thresholds to humans, and a huge normative data base in the lab. Weights of 10 gerbils used in the experiment ranged from 48 to 61 grams. The experimental procedures were approved by the Institutional Animal Care and Use Committee of the University of Kansas Medical Center.

The gerbils were initially sedated with pentobarbital (64 mg/kg) and subsequently maintained with injections of 1/3 of the initial dose given every hour. Under pentobarbital anesthesia the middle ear reflex is inactive, rendering the middle ear to be linear (Schmiedt and Zwislocki, 1977). A rectal thermometer was used to monitor the body temperature of the gerbils, which remained constant at 37 °C with a heating pad (Harvard). With removal of the left pinna and the surrounding skin and muscle, the postauricular aspect of the bulla was surgically opened and remained opened during the entire experiment. A ball-tip silver wire electrode insulated by #31 polymide tubing (Micro ML) was placed on the round window and glued (cyanoacrylate ester) to the surrounding bone. In addition, a cotton wick was used to absorb the fluid condensation at the round window niche. Compound action potential (CAP) thresholds elicited by 1, 2, 4, 8, and 16 kHz tone bursts were obtained with visual detection of N_1 on a digital storage oscilloscope (Hitachi VC-6045A). The CAP thresholds for the gerbils were within the normal range of hearing, below 25 dB SPL across the whole frequency range, with the exception of one gerbil excluded in the data analysis because of the abnormal hearing threshold (above 25 dB SPL).

B. Signal delivery

Tone bursts and Gaussian noises were created in an array processor (AP2, Tucker-Davis Technology) and converted from digital to analog with a sampling frequency of 65,536 Hz (DA2, Tucker-Davis Technology). Through a headphone buffer (HB6, Tucker-Davis Technology) which was coupled to a tube sealed to the bony external ear canal, the analog signals were passed to a μ-metal incased headphone (Etymotic ER-2) designed to reduce electromagnetic artifact. A calibrated probe microphone (Etymotic ER-7C)

sealed at the end of the tube was placed approximately 5 mm from the umbo of the tympanic membrane in order to monitor signal level and spectrum.

Tone bursts were 2 ms in duration and windowed with a 1-ms $\cos^2$ ramp to elicit CAP. Gaussian noise was 250 ms in duration and windowed with a 5-ms $\cos^2$ ramp to evoke CM responses. Tone bursts were attenuated in 5 dB steps until a CAP threshold (50% visually detectable level) was found. Gaussian noise was presented at 78, 88, and 98 dB SPL in random order and equalized with a bandwidth from 0.1 to 10.24 kHz using an inverse filter method developed by Chertoff *et al.* (1996).

C. Data acquisition

The ear canal sound pressure, the CM, and stapes velocity were recorded simultaneously. The acoustic signal was band-pass filtered between 3 Hz–30 kHz (12 dB/octave) and amplified 100, 50, and 10 times for three signal levels of 78, 88, and 98 dB SPL, respectively, through one channel of a low-noise preamplifier (Stanford SR560). The CM responses were recorded from an electrode placed on the round window and a needle electrode inserted into the neck as ground. The signals initially were band-pass filtered between 3 Hz–30 kHz, amplified 500 times through a preamplifier (Stanford SR560), and subsequently low-pass filtered at 16 kHz (54 dB/octave) through one channel of a dual filter and amplified 10 times (Stewart VBF 10M). Stapes velocity was measured with a laser Doppler vibrometer (LDV, Polytec HLV 1000) focused on the stapes footplate. Silver ink was used to mark the stapes footplate during the experiment. The output of LDV was low-pass filtered at 30 kHz and set to an output range of 25 mm/s/V. The signal was low-pass filtered at 16 kHz through another channel of the dual filter and amplified 100 times (Stewart VBF 10M). Finally, all signals were digitalized at sampling frequency of 65,536 Hz (AD2, Tucker-Davis Technology).

D. Data analysis

The microphone output in the ear canal, and the CM and stapes responses were simultaneously recorded and saved to disk. Input and output responses were obtained for twenty Gaussian noise sequences. Auto and cross spectra were computed on 1024 point segments from a time-history record of 8192 points that were windowed with a Hanning window, with 50% overlapping to recover the energy leakage in the spectrum (Bendat and Piersol, 1986). The magnitude of the linear system transfer functions resulted from the ratio of the cross-spectral density to the input autospectral density functions. Spectral estimates were obtained by averaging the spectra across 8 subrecords per record resulting in a total of 160 averages. In this study, the different combinations of input and output signals resulted in the following transfer functions: the frequency response function of the middle ear (SV/AC transfer function), computed from the ratio of the cross-spectral density of the stapes velocity (SV) and the acoustic signal (AC) to the input auto-spectral density, the frequency response function of the CM including the middle ear effect (CM/AC transfer function), obtained from the ratio
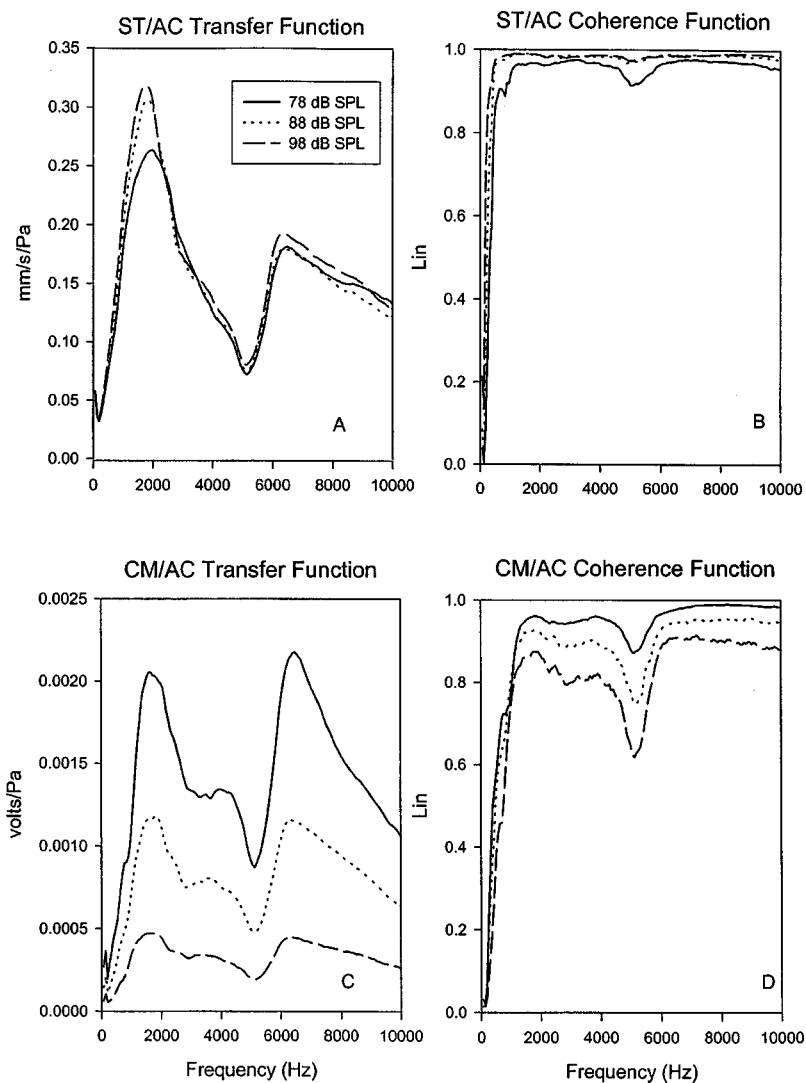
FIG. 3. Panel (A) shows the SV/AC transfer function at three signal levels (78, 88, and 98 dB SPL) and panel (B) is the SV/AC linear coherence function. Panel (C) shows the CM/AC transfer function at three signal levels (78, 88, and 98 dB SPL). Panel (D) is the CM/AC linear coherence function.

of the cross-spectral density of the CM and the acoustic signal to the input auto-spectral density, and the frequency response function of the CM excluding the ME effect (CM/SV transfer function), computed from the ratio of the cross-spectral density of the CM and the stapes velocity to the input auto-spectral density. The CM/AC and CM/SV transfer functions represent the optimal linear description of MET with and without including the ME, respectively. The non-linear frequency response functions representing the polynomial model of MET (A_1, A_2, and A_3) and coherence function were obtained from the uncorrelated cross- and input auto-spectral density functions (Bendat, 1990; Bendat and Palo, 1990; Bendat and Piersol, 1993, 1986).

E. Statistics

The amplitude of the SV/AC, CM/AC, and CM/SV transfer functions was statistically analyzed across signal levels. Significant differences between means of the transfer functions in signal level were tested by a within group repeated measure analysis of variance (ANOVA) (SPSS 11.0 for Windows). Statistical significance was determined by the probability of less than 0.05. When a level main effect was shown, a *post hoc* test (Scheffe test) was performed to deter-

mine significant differences among each means of the three signal levels. Stepwise regression, a statistical method to determine what independent variables should be included in the regression equation based on the highest partial correlation, was fitted to the CM/SV transfer function to determine the frequency dependency of the CM/SV function (Norusis, 1990).

III. RESULTS

A. The ME transfer function

The system transfer functions and the corresponding linear coherence functions for the different Gaussian noise levels of 78 dB, 88 dB, and 98 dB SPL are shown in Fig. 3. These mean data were obtained from ten animals. The magnitude of the SV/AC transfer function [panel (A)] reaches a maximum at approximately 2 kHz followed by a minimum at around 5.5 kHz, and slowly rolls off above 6.7 kHz. The magnitude varies from 0.05 mm/s/Pa to 0.32 mm/s/Pa according to frequency. Even though a slight difference is noticeable at approximately 2 kHz, it is not significant in the SV/AC transfer function between the signal levels. In panel (B), the linear coherence of SV/AC is close to 1.00 except for frequencies below 500 Hz indicating linearity of the
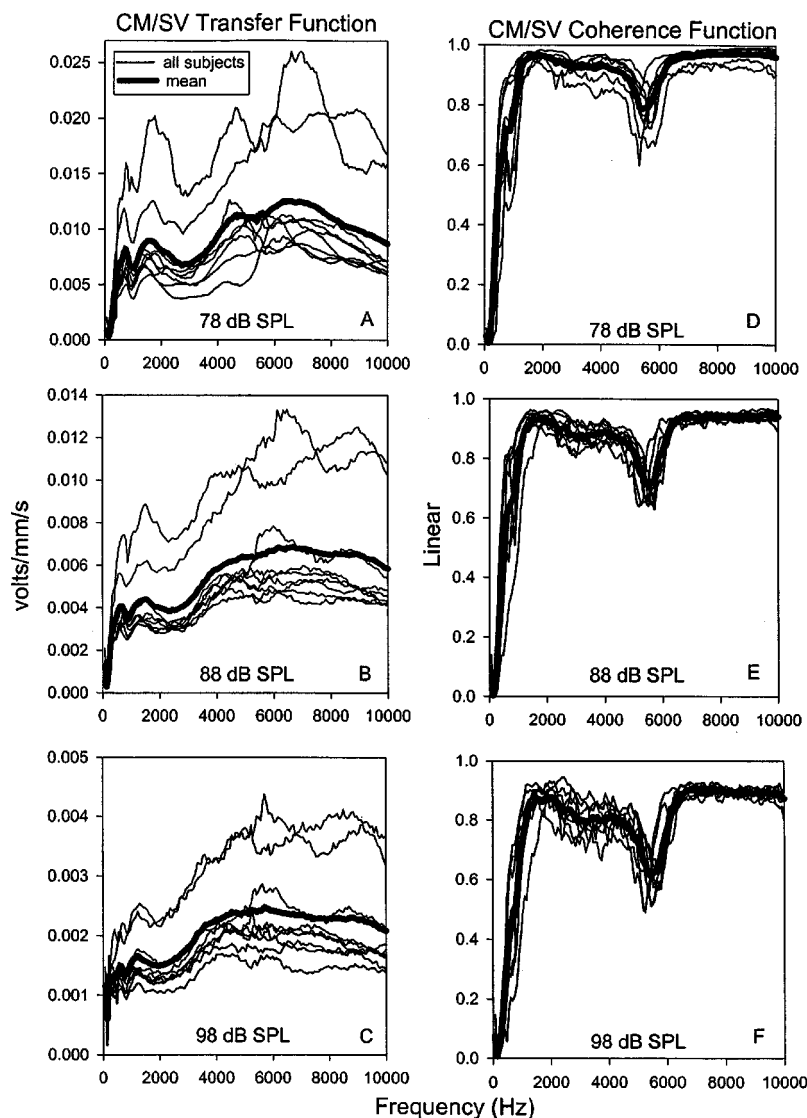
FIG. 4. All subjects and mean data of the CM/SV transfer function at 78 dB SPL [panel (A)], 88 dB SPL [panel (B)], and 98 dB SPL [panel (C)]. All subjects and mean data of the CM/SV linear coherence function at 78 dB SPL [panel (D)], 88 dB SPL [panel (E)], and 98 dB SPL [panel (F)].

middle ear transfer function. The linear coherence for 78 dB is approximately 0.95 and the values for 88 and 98 dB SPL, ranged from 0.97 to 0.98, slightly higher than that of 78 dB SPL. There are no significant differences between the linear coherences across signal level and frequency.

B. Linear characterization of MET (CM/AC and CM/SV)

The shape of the CM/AC transfer function [panel (C)] is very similar to the SV/AC transfer function. For all signal levels, the shape of the transfer function displays a maximum at around 2 kHz, followed by a minimum at 5.5 kHz, and a roll off above 6.7 kHz. There is a significant difference between the mean gain across the signal levels ($p < 0.01$) indicating the transfer function was dependent upon signal level. *Post hoc* analysis indicates that the magnitudes are significantly reduced as the signal level increases. In panel (D), the linear coherence of CM/AC varies with signal level and frequency with a notch at around 5.5 kHz appearing for the higher levels. The average linear coherence across frequency is largest for 78 dB SPL, followed by 88 dB SPL and 98 dB SPL, respectively.

Panels (A), (B), and (C) of Fig. 4 shows the CM/SV transfer function for all animals and the mean data at each level. The magnitude of the CM/SV transfer function varies among gerbils, but the shape of the transfer function has a similar pattern. The shape is "bandpass" with notches at 1 kHz and 2.5 kHz at 78 dB SPL. Stepwise regressions were used to fit polynomial equations to the CM/SV transfer function data for each subject to determine frequency dependence of the CM/SV function. The stepwise regression analysis showed a significant improvement in the change in r^2 for each subject when quadratic and cubic terms were added to the regression model. The increased r^2 with the increased terms of the polynomial equation strongly indicates that the CM/SV transfer function is frequency dependent even though the ME frequency response is removed. As the signal level increases, the frequency responses become flatter. The average gain collapsed across frequency significantly differs among signal levels ($p < 0.01$) and *post hoc* analysis indicates that when signal level increases, the amplitude of the transfer function decreases.

The intersubject variability and the mean of the linear coherence of CM/SV are shown in panels (D), (E), and (F) of Fig. 4. The linear CM/SV coherence function is similar to

Choi *et al.*: Middle ear's influence on mechano-electric transduction
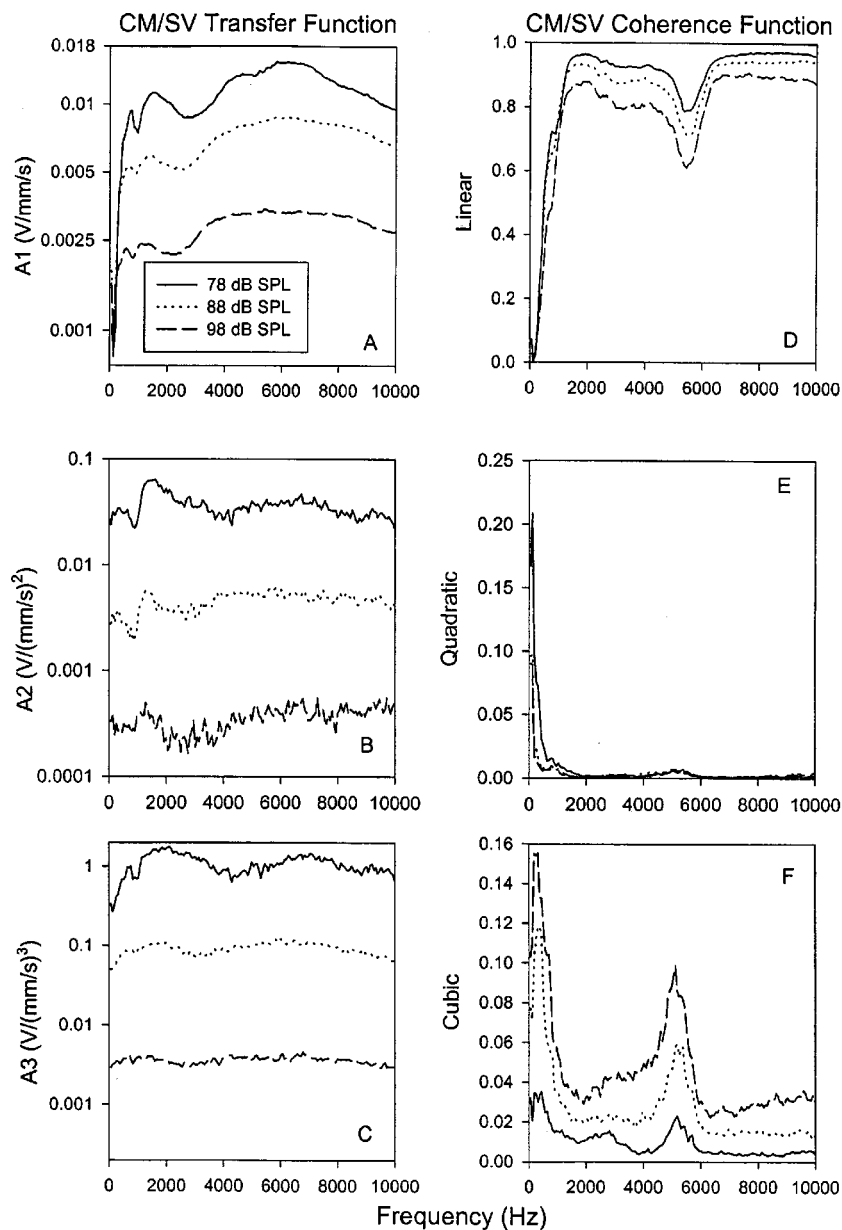
FIG. 5. Magnitude of the linear [A_1, panel (A)], quadratic [A_2, panel (B)], and cubic [A_3, panel (C)] terms and the coherence of the linear [panel (D)], quadratic [panel (E)], and cubic [panel (F)] terms of the CM/SV transfer function for three signal levels.

that of the CM/AC showing a decreasing trend in linearity with increasing signal level. This indicates that with increasing signal level the optimal linear transfer function (CM/AC and CM/SV) becomes poor in describing MET.

C. Polynomial characterization of MET (*A* coefficients)

The "*A*" coefficients, the parameters of the third-order polynomial equation describing cochlear MET, were derived from the NLID procedure for the three signal levels (Chertoff *et al.*, 1996). Figure 5 illustrates the magnitudes of the "*A*" coefficients characterizing MET using stapes velocity as the input and the CM as the output. The A_1, A_2, and A_3 coefficients are largest at 78 dB SPL, followed by 88 dB SPL and 98 dB SPL, respectively, across frequency.

The average linear, quadratic, and cubic coherence functions of the CM/SV for three signal levels are displayed as a function of frequency in panels (D), (E), and (F) of Fig. 5. These functions indicate the contribution of each term of the third-order polynomial function characterizing cochlear

MET. The linear coherence function [panel (D)] explained approximately 80% to 90% of the third-order polynomial function at the three signal levels. The quadratic coherence function [panel (E)] accounted for less than 1% of the polynomial function at the three signal levels across frequency, except in the low frequency where it accounted for 3% to 20% of the output. Panel (F) illustrates the cubic coherence function of three signal levels. The cubic coherence values reach to 9%, 6%, and 2% for 98, 88, 78 dB SPL, respectively, indicating that adding the cubic term in describing MET is more important for higher signal levels. Table I shows the averages (mean computed across frequency and animal) and the standard deviations of the three coherences and total coherence for the three signal levels. Relative to the mean of the coherence, the variability of the linear coherence is smallest followed by the cubic coherence and the variability of quadratic coherence is largest.

The *A* coefficients, especially, A_1 and A_3, of each animal for the three signal levels were compared between

TABLE I. Average and standard deviation of the linear, quadratic, cubic, and total coherence functions.

Levels	Linear		Quadratic		Cubic		Total	
	Mean	STD	Mean	STD	Mean	STD	Mean	STD
78 dB	0.8619	0.1517	0.0096	0.0411	0.0069	0.0063	0.8784	0.1172
88 dB	0.8431	0.1496	0.0052	0.0185	0.0238	0.016	0.872	0.1235
98 dB	0.7725	0.1602	0.0025	0.0035	0.0488	0.0294	0.8239	0.1308

CM/AC and CM/SV to determine if the frequency dependency of the coefficients changed after eliminating the ME. Because of the low coherence, the quadratic term (A_2) was not meaningful in characterizing MET and therefore A_2 was not included. Figure 6 shows the comparison of the A_1 and A_3 coefficients. The coefficients were standardized (Z score) by subtracting the mean magnitude computed across frequency from the magnitude at each frequency and dividing by the standard deviation across frequency. Standardization was required because of the different scales of the A_1 and A_3 terms. The figure illustrates that although the shape of the A_1 of CM/AC differs from CM/SV, it is still frequency dependent [panels (A), (B), and (C)]. The A_3 coefficients [panels (D), (E), and (F)] from CM/SV are also frequency dependent

FIG. 6. Comparison in the A_1 between CM/AC and CM/SV for each subject for 78 dB SPL [panel (A)], 88 dB SPL [panel (B)], and 98 dB SPL [panel (C)], respectively, and the A_3 between CM/AC and CM/SV for 78 dB SPL [panel (D)], 88 dB SPL [panel (E)], and 98 dB SPL [panel (F)], respectively.

but in contrast to the A_1 coefficient, their frequency dependence is similar to A_3 from CM/AC.

IV. DISCUSSION

A. The middle ear transfer function

The first purpose of this study was to determine if the polynomial terms required to characterize MET in previous studies were due to the middle ear (SV/AC). The similarity of the SV/AC transfer function across signal level indicates that stapes velocity is linearly related to sound pressure at the tympanic membrane. The linearity of the middle ear was affirmed by the linear coherence function ranging to 0.98 at 98 dB SPL. This indicates that no additional nonlinear terms are required to characterize the ME. These results are similar to those of others who showed linearity of the middle ear transfer function with the acoustic reflex inactivated over a large range of signal levels in various animals (Lynch *et al.*, 1994; Wilson and Johnstone, 1975; Guinan and Peake, 1967; Møller, 1963). The linearity of the SV/AC transfer function indicates that the polynomial terms characterizing MET in previous work are not due to the ME.

The average magnitude (0.02 to 0.3 mm/s/Pa) of the middle ear transfer function in our study is very similar to that (0.01 to 0.3 mm/s/Pa) estimated visually from the graph shown by Rosowski *et al.* (1999). In addition, the frequency dependence found in our study is very similar to their work. A slight difference in location of the resonant and antiresonant frequencies between the two studies exists but this may be due to the size of the hole in the bulla used for recording and reflective beads on the footplate of the stapes in the Rosowski *et al.* study. The average magnitude and frequency dependence of the middle ear transfer function found in our study are not consistent with the work by Overstreet III and Ruggero (2002) who reported a mean stapes velocity of 0.34 mm/s/Pa which was approximately constant in the 1–40 kHz frequency range. The inconsistent results may be due to the stimulus and the frequency resolution used in each study. Our study used Gaussian noise and a frequency resolution of 64 Hz in the 1–10 kHz frequency range while Overstreet III and Ruggero (2002) used tones and a frequency resolution of 500 or 1000 Hz in the 1–40 kHz range.

B. Level dependence of the polynomial coefficients

The magnitude of the polynomial terms changed as a function of signal level. When signal level increased, the magnitude of the terms decreased. These results are consistent with the previous studies investigating the relation between CM amplitude and sound pressure at the TM (Bian and Chertoff, 1998; Chertoff *et al.*, 1997, 1996; Kohllöffel,
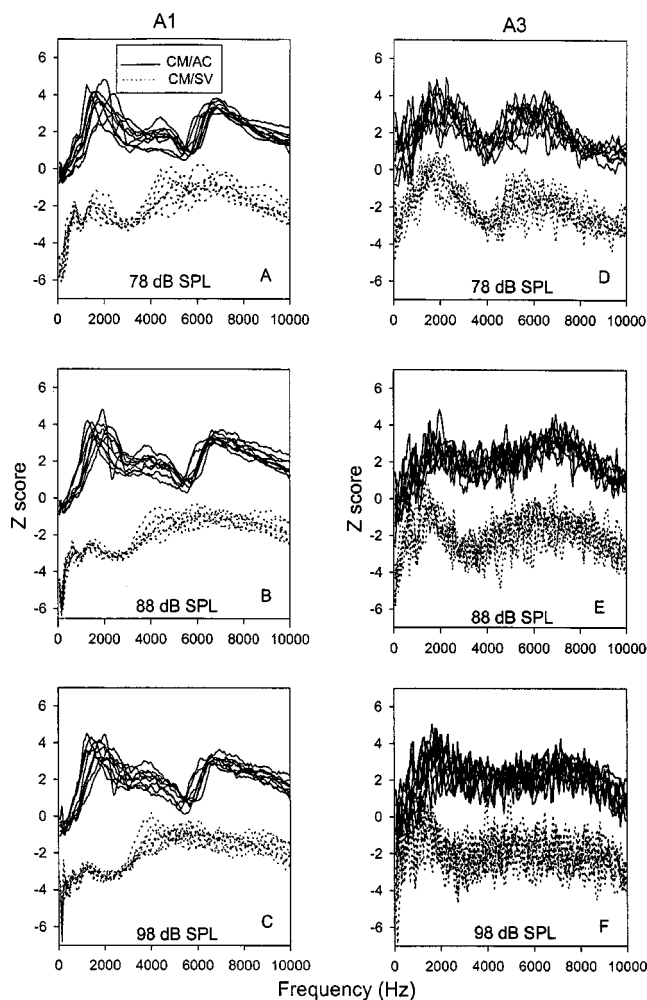
Choi *et al.*: Middle ear's influence on mechano-electric transduction

1971) and may reflect the saturation of hair cell receptor currents during hair-cell transduction (Chertoff *et al.*, 1996; Patuzzi, 1995). Basically, acoustical signals result in the displacement of the cochlear partition, which in turn moves stereocilia, opening hair cell transduction channels and producing hair cell current. When stereocilia displacement increases, more hair-cell channels are opened, producing an increase in the current flow until a maximum is reached. As signal level increases further no additional current is produced. Therefore, even though the input increases the output does not increase proportionally, causing the ratio of CM to stapes velocity and the polynomial coefficients to decrease.

Saturation is also shown by the coherence of each of the polynomial terms. The coherence quantifies the contribution of each term of the model of MET relative to the total output. If the coherence of a term changes, then the contribution of that term to describing the output changes independent of the size of the coefficient. In this study the linear coherence decreased and the cubic coherence increased as signal level increased. This indicates that the linear term contributes less to explaining the input–output relation whereas the cubic term contributes more at high signal levels. As shown by Chertoff *et al.* (1996) the cubic term of a third-order polynomial with a sign opposite to the linear term, creates a sigmoidal MET function that reaches a maximum and a minimum. The maximum and minimum points of the function represent the saturation of hair-cell currents when ion channels are fully open or completely closed. At low signal levels, the input is within the linear operating range of the hair cell and consequently the linear coherence is large and the cubic coherence is small. At high signal levels, the currents produced by the hair cell begin to saturate. Therefore, because the cubic term is necessary for creating a sigmodal function its contribution to the polynomial model of MET increases to account for the saturation of hair cell receptor currents.

It is interesting to note that the cubic coherence increased with signal level whereas the quadratic coherence did not. These results indicate that the odd order term is more important than the even-order term in characterizing MET. This suggests that MET (as recorded by a round window electrode) is symmetrical with respect to the direction of the basilar membrane displacement. That is, hair-cell receptor currents are modified equally when basilar membrane displaces toward scala vestibuli or scala tympani. This is consistent with outer hair cells in the base whose input–output function recorded *in vivo* tends to be symmetric (Russell *et al.*, 1986).

C. Frequency dependence of the polynomial coefficients

The second purpose of this study was to determine if the frequency dependence of the linear and nonlinear terms characterizing MET was due to the ME. After excluding the ME transfer function, A_1 from CM/SV was still frequency dependent and differed from A_1 of CM/AC. The frequency dependence as represented in A_1 from CM/SV may be due to the cochlear input impedance. Several studies report that the CM is associated with a difference in pressure between scala vestibuli and scala tympani at specific frequencies (Lynch III

et al., 1982; Nedzelnitsky, 1980; Dallos, 1970). If $P = \mu * Z$ where Z is the cochlear input impedance, μ is volume velocity of the stapes, P is the pressure in the cochlea, and the CM is proportional to the pressure in the cochlea, then the CM/SV transfer function reflects the cochlear input impedance. The CM/SV transfer function at low frequencies (below approximately 1 kHz) may result from the helicotrema that behaves as an acoustic resistance (Nedzelnitsky, 1980). For frequency between 3–6 kHz, the raise in the CM/SV transfer function may reflect a mass component that contributes to the cochlear impedance. The mass effect may result from the mass of the perilymph in scala tympani.

The result that A_1 from CM/SV is frequency dependent differs from Weiss *et al.* (1971) who revealed that the CM/SV responses are approximately constant in the frequency range of 100 Hz to 10 kHz and at signal levels ranging from 40 to 90 dB SPL in cats. In their study, they used a ± 9 dB criteria allowing for large variation in the transfer function. Using the same criteria for our data would also suggest that CM/SV is constant across frequency. However, our regression method of determining frequency dependence may be more sensitive than using the ± 9 dB criteria. The work by Weiss *et al.* may be limited because they used a general stapes velocity to compute CM/SV and not the actual one from each animal, which could contribute to the variability.

After excluding the ME transfer function the cubic coefficient (A_3) from CM/SV was still frequency dependent. The frequency dependence was similar to A_3 from CM/AC at low signal levels and changed slightly as signal level increased. This suggests that there may be a frequency dependent nonlinearity inherent in the MET process. Although the source of this frequency dependence is not known, the A_3 coefficient may reflect the saturation of hair cell currents (as mentioned previously). It is possible that a frequency dependent nonlinearity may be present in the drive to stereocilia and the hair cell transduction channels (Jaramillo *et al.*, 1993).

V. A COCHLEAR MODEL OF THE CM

The third purpose of this study was to investigate if the total coherence of the polynomial model of MET computed from CM/SV improved from the model computed from CM/AC. As illustrated in the simulation in the introduction, the y/g measurement relating the output of a linear filter (g) to the output of the nonlinear system (y) did improve the accuracy and fit of a polynomial model. The improvement was clearly shown in the total coherence of y/g compared to that of y/x [panel (D) of Fig. 2]. However, this improvement did not occur in our measured data. Figure 7 illustrates the comparison of total coherences between CM/SV and CM/AC at each signal level. There was a significant difference between average total coherences of CM/SV and CM/AC at 78 dB SPL across frequency ($p < 0.05$). The total coherence of the CM/SV was smaller than that of the CM/AC. However, at both 88 and 98 dB SPL, the total coherences of the CM/AC and CM/SV did not significantly differ. In other words, the total coherence of CM/SV did not significantly improve from
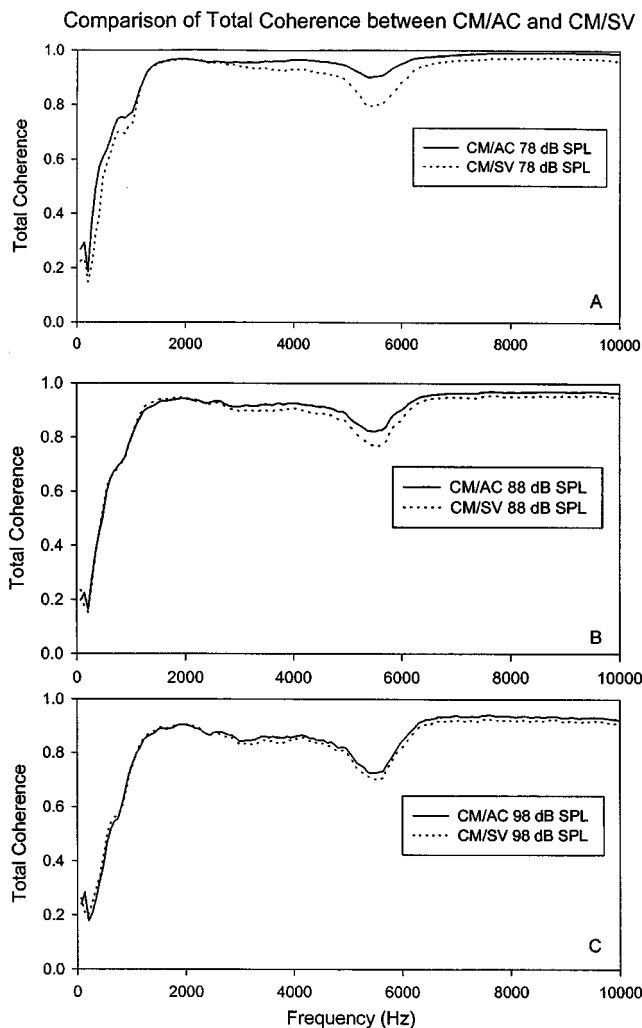
FIG. 7. Comparison of the total coherence functions for the CM/AC and CM/SV at 78 dB SPL [panel (A)], 88 dB SPL [panel (B)], and 98 dB SPL [panel (C)].

the total coherence of CM/AC. Therefore, we developed a model CM to explore why the coherence of CM/SV did not improve compared to that of CM/AC. Our initial goal was to determine the influence of vector summation of hair-cell receptor currents as the reason for the lack of model improvement. It has been known that the CM is spatially localized in the same way as the traveling wave of the basilar membrane and hence vector summation is a major concern when interpreting the CM recorded from the round window.

A. Methods

The model consisted of three components: the response of the basilar membrane (BM), the outer hair-cell receptor currents, and the weighted electrode response decay along the cochlear partition. It was assumed that the CM is generated from hair-cell receptor currents produced by vibration of the tail of the basilar membrane traveling wave. The vibration of the tail is approximately linear (Rhode, 1978) and there is no active feedback from the outer hair cells. The BM was divided into 80 BM segments ranging 62, 828 Hz to 725 Hz. The BM filters were obtained from an all-pole gammatone filter (APGF) with adjusted Q values and tip to tail
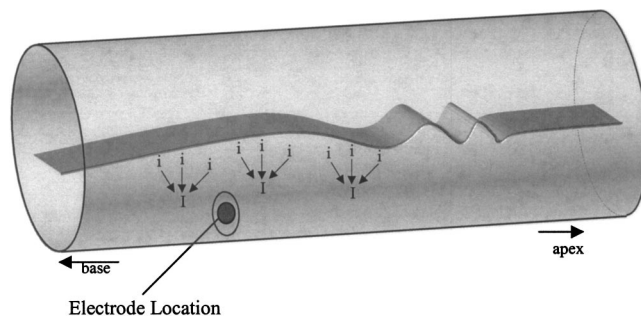
FIG. 8. Conceptualization of cochlear model producing the CM. I is the current in the scala tympanic and i is the current from each cochlear segment. The black circle inside on oval indicates the electrode location.

ratios in order to emulate the physiologic state (Lyon, 1997). The BM vibration at each location was obtained by convolving stapes velocity data from an individual animal with each BM impulse response. The peak BM displacement was scaled to 95 nm for a 98 dB SPL noise. This value was chosen from the maximal sound pressure at 3 standard deviations of Gaussian noise and a BM displacement of 40 nm at 100 dB SPL at CF estimated from data personally provided by Nigel Cooper. BM segments with CFs below 10 kHz were scaled at ± 0.25 dB/dB whereas the BM segments with CFs above 10 kHz were scaled at ± 1 dB/dB to reflect the compressive growth of the BM at CF.

Subsequently, basilar membrane displacement was given as input to a hair-cell function to produce hair-cell receptor currents at each BM segment. The hair-cell function was expressed as follows:

$$I = \frac{1}{1 + 10^{(x - x_0)/a}}, \tag{1}$$

where I is the hair-cell receptor current, x is the input (BM displacement), x_0 is the operating point, and a is the sensitivity, or slope of the function. The operating point was assigned 2.5 to reflect an asymmetric hair-cell function whereas the sensitivity was set to 20 to produce half-saturated hair-cell currents at 10 nm displacement (Patuzzi, 1998). The hair-cell responses were filtered using a first-order Butterworth filter between 3 kHz and 9 kHz. As illustrated in Fig. 8, the electric current measured at a given location (I) in scala tympani was the weighted summation of currents (i) from surrounding locations where the weight is given as follows:

$$W = \exp(-|x - \text{center}|/a), \tag{2}$$

where x is BM position in mm, center is a given cochlear place, and a is a space constant (1 mm) from Weiss et al. (1971). The hair-cell receptor currents (I) were weighted [Eq. (2)] with a decay function centered at 2.5 mm from the base to simulate a decrease in voltage as a function of electrode distance from the round window. The CM was obtained by summing the weighted hair-cell receptor currents (I) across the BM segments. The cochlear place-frequency map of Müeller (1996) was used to describe the relation between frequency and cochlear place along the average BM length of gerbils (12 mm) as follows:

$$CF = A * (10^{ax} - k), \tag{3}$$

Choi *et al.*: Middle ear's influence on mechano-electric transduction
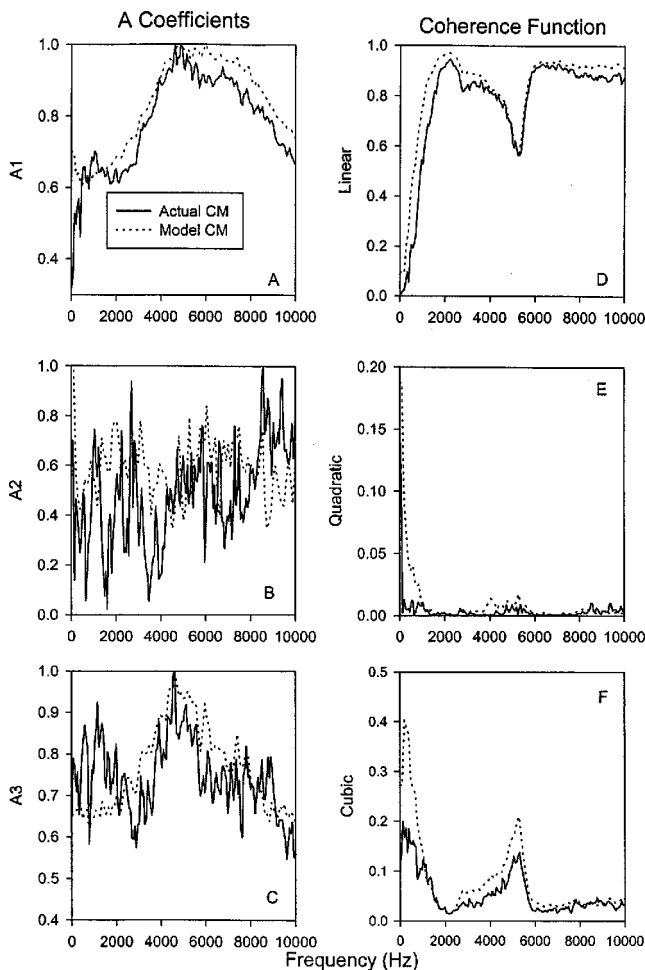
FIG. 9. Comparison of the polynomial coefficients (A_1, A_2, and A_3) of the CM/SV transfer function for the model CM (dotted) and actual CM (solid line). Panels (A), (B), and (C) show the linear, quadratic, and cubic coefficient, respectively. Comparison of the linear and nonlinear coherence functions between the model CM and the actual CM data. Panels (D), (E), and (F) illustrate the linear, quadratic, and cubic coherence, respectively.

where A is 0.398, a is 0.022, k is 0.631, and x is $100 - ($BM length$*100/12)$.

Stapes velocity from one animal was used as input to this model. The CM was obtained as output in response to the input Gaussian noise of 98 dB SPL. Bendat's NLID procedure was applied to the input/output records to obtain a third-order polynomial equation estimating MET. The CM/SV transfer function and its coherence function obtained from the model were compared to the data obtained from experiment.

B. Comparison between the actual CM and model CM

Figure 9 illustrates the "A" coefficients and the corresponding coherence functions from the model CM (dotted line) and the actual CM (line) as a function of frequency. The coefficients were normalized to unity by dividing each coefficient by its maximum value. Although there are slight differences between the model CM and actual CM, the model CM was well fitted to the actual CM. The linear (A_1), quadratic (A_2), cubic (A_3) coefficients in the model CM were similar to the shape of the actual CM across frequency [pan-

els (A), (B), and (C) of Fig. 9]. However, the model CM did not show small peaks present in the actual CM.

Similarity and differences between the model CM and actual CM were reflected in the corresponding coherence functions [panels (D), (E), and (F) of Fig. 9]. Although the value of the linear coherence for the model CM was slightly higher than that for the actual CM at low (below 0.5 kHz) and high frequencies (above 7 kHz), the model CM showed the shape matched exactly to the notch at around 5.5 kHz present in the actual CM. The quadratic coherence for the model CM was larger than that for the actual CM at frequencies below 1 kHz, and between 4 and 6 kHz [panel (E) of Fig. 9]. For the cubic coherence function, the model CM was similar to the actual CM although it was larger at low frequencies [panel (F) of Fig. 9].

To explore why the coherence did not improve when we accounted for the linear ME system as suggested by the simulation in Fig. 1, the contribution of vector summation and the mathematical function used for the hair cell in the CM model were evaluated. The number of segments producing the CM was varied to simulate the vector summation of the hair-cell receptor currents. The total coherence of the model was obtained for the CM produced by the accumulation of 10, 20, 30, 40, 50, and 60 segments. The average total coherences across frequencies were 0.946, 0.937, 0.927, 0.924, 0.923, and 0.923. When the number of segments increased, the total coherence function slightly decreased. In other words, a change in the vector summation results in a small change in the total coherence function. Finally, the hair-cell function used in the CM model was replaced with a third-order polynomial equation obtained from the best polynomial fit to Eq. (1) (Boltzmann function). With the third-order polynomial equation as the hair-cell function, the total coherence function increased from approximately 93% to 97% across frequency (Fig. 10). This indicates that the third-order polynomial function is the limiting factor in modeling MET. The CM model showed that if the hair-cell transducer could be modeled as a third-order polynomial, the NLID procedure would have accurately identified the hair-cell transducer function. To determine if the number of terms of the polynomial equation influenced our results, we analyzed the CM/SV using a higher order polynomials. However, this did not improve the fit. This suggests that although the polynomial is a fair description of MET, it may not completely characterize the hair-cell transducer function.

VI. SUMMARY AND CONCLUSIONS

By adding a laser Doppler vibrometer focused on the footplate of the stapes, the intervention of the ME on CM/AC was measured in this study. The ME transfer function (SV/AC transfer function) was independent of signal level and the linear coherence was close to 1.0, suggesting linearity. Both the CM/AC and CM/SV transfer function were nonlinear and frequency dependent. This indicates that the nonlinearity of the CM/AC transfer function is not due to the ME but due to inner ear mechanisms. The frequency response of the linear term of the CM/SV transfer function differed from that of the response of the CM/AC transfer

Comparison of Boltzmann and Polynomial Hair-Cell Functions
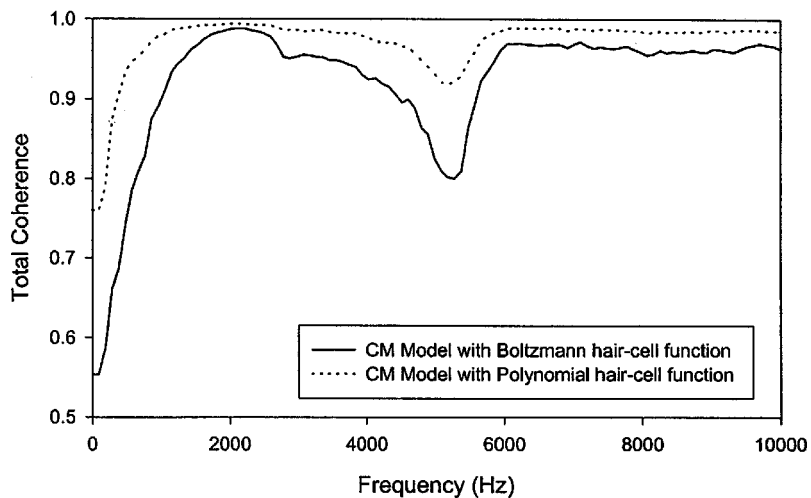
FIG. 10. Comparison of total coherence between the model CM with a Boltzmann hair-cell function and the model CM with a third-order polynomial hair-cell function. The model CM with the third-order polynomial equation was obtained from the best polynomial fit to the Boltzmann function [Eq. (1)].

function while the cubic nonlinear term of the CM/ST transfer function was similar to that of the CM/AC transfer function. Finally, the total coherence of CM/SV did not improve as predicted by a simulation of a linear–nonlinear system. We developed a CM model to explain the reason of lack of improvement in the total coherence of the CM/SV transfer function. The lack of improvement was shown to be minimally influenced by vector summation. A more likely contributor was the limitations of a third-order polynomial equation to model the hair-cell transducer function.

Bendat, J. S. (**1990**). *Nonlinear System Analysis and Identification from Random Data* (Wiley, New York).

Bendat, J. S., and Palo, P. A. (**1990**). "Practical techniques for nonlinear system analysis/identification," Sound Vib. **24**, 21–26.

Bendat, J. S., and Piersol, A. G. (**1993**). *Engineering Applications of Correlation and Spectral Analysis* (Wiley, New York).

Bendat, J. S., and Piersol, A. G. (**1986**). *Random Data: Analysis and Measurement Procedures*, 2nd ed. (Wiley, New York).

Bian, L., and Chertoff, M. E. (**1998**). "Differentiation of cochlear pathophysiology in ears damaged by salicylate or a pure tone using a nonlinear systems identification technique," J. Acoust. Soc. Am. **104**, 2261–2271.

Bian, L., and Chertoff, M. E. (**2001**). "Distinguishing cochlear pathophysiology in 4-aminopyridine and furosemide treated ears using a nonlinear systems identification technique," J. Acoust. Soc. Am. **109**, 671–685.

Chertoff, M. E., Lerner, D., Amani-Taleshi, D., and Nagai, Y. (**2000**). "Characterizing non-linearity in the cochlear microphonic using the instantaneous frequency," Hear. Res. **145**, 190–202.

Chertoff, M. E., Steele, T. C., Ator, G. A., and Bian, L. (**1996**). "Characterizing cochlear mechano-electric transduction using a nonlinear systems identification procedure," J. Acoust. Soc. Am. **100**, 3741–3753.

Chertoff, M. E., Steele, T. C., and Bian, L. (**1997**). "Characterizing cochlear mechano-electric transduction in ears damaged with pure tones," J. Acoust. Soc. Am. **102**, 441–450.

Dallos, P. (**1970**). "Low-frequency auditory characteristics: Species dependence," J. Acoust. Soc. Am. **48**, 489–499.

Dallos, P. (**1973**). *The Auditory Periphery: Biophysics and Physiology* (Academic, New York).

Dallos, P. (**1985**). "Response characteristics of Mammalian cochlear hair cell," J. Neurosci. **5**, 1591–1608.

Dallos, P., Billone, M. C., Durrant, J. D., Wang, C. Y., and Raynor, S. (**1972**). "Cochlear inner and outer hair cells: Functional differences," Science **177**, 356–358.

Guinan, J. J., and Peake, W. T. (**1967**). "Middle ear characteristics of anesthetized cats," J. Acoust. Soc. Am. **41**, 1237–1261.

Hudspeth, A. J. (**1982**). "Extracellular current flow and the site of transduction by vertebrate hair cells," J. Neurosci. **2**, 1–10.

Jaramillo, F., Markin, V. S., and Hudspeth, A. J. (**1993**). "Auditory illusions and the single hair cell," Nature (London) **364**, 527–529.

Kohllöffel, L. U. E. (**1971**). "Studies of the distribution of cochlear potentials along the basilar membrane," Acta Oto-Laryngol., Suppl. **288**, 1–66.

Lynch, T. J. III, Nedzelnitsky, V., and Peake, W. T. (**1982**). "Input impedance of the cochlea in cat," J. Acoust. Soc. Am. **72**, 108–130.

Lynch, T. J. III, Peake, W. T., and Rosowski, J. J. (**1994**). "Measurements of the acoustic input impedance of cat ears: 10 Hz to 20 kHz," J. Acoust. Soc. Am. **96**, 2184–2209.

Lyon, R. F. (**1997**). "All-pole models of auditory filtering," in *Diversity in Auditory Mechanics*, edited by X. Lewis *et al.* (World Scientific, Singapore), pp. 205–211.

Møller, A. R. (**1963**). "Transfer function of the middle ear," J. Acoust. Soc. Am. **35**, 1526–1534.

Müeller, M. (**1996**). "The cochlear place-frequency map of the adult and developing Mongolian gerbil," Hear. Res. **94**, 148–156.

Nedzelnitsky, V. (**1980**). "Sound pressures in the basal turn of the cat cochlea," J. Acoust. Soc. Am. **68**, 1676–1689.

Nieder, P., and Nieder, I. (**1971**). "Determination of microphonic generator transfer characteristic from modulation data," J. Acoust. Soc. Am. **49**, 478–492.

Norusis, M. J. (**1990**). *SPSS Base System User's Guide* (SPSS Inc., Chicago).

Nuttall, A. L. (**1974**). "Measurements of the guinea-pig middle ear transfer characteristic," J. Acoust. Soc. Am. **56**, 1231–1238.

Overstreet, E. O. III, and Ruggero, M. A. (**2002**). "Development of wideband middle ear transmission in the Mongolian gerbil," J. Acoust. Soc. Am. **111**, 261–270.

Patuzzi, R. B. (**1987**). "A model of the generation of the cochlear microphonic with nonlinear hair cell transduction and nonlinear basilar membrane mechanics," Hear. Res. **30**, 73–82.

Patuzzi, R. B. (**1998**). "The Goldman-Hodgkin-Katz equation and graphical 'load-line' analysis of ionic flow through outer hair cells," Hear. Res. **125**, 71–97.

Patuzzi, R. B. (**1995**). "Monitoring cochlear homeostasis with automatic analysis of the low-frequency cochlear microphonic," in *Active Hearing*, edited by A. Flock, D. Ottoson, and M. Ulfendahl (Elsevier, New York), pp. 141–153.

Patuzzi, R. B., Yates, G. K., and Johnstone, B. M. (**1989**). ''Outer hair cell current and sensorineural hearing loss,'' Hear. Res. **42**, 47–72.

Pickles, J. O. (**1988**). *An Introduction to the Physiology of Hearing*, 2nd ed. (Academic, London).

Price, G. R. (**1974**). ''Upper limit to stapes displacement: implications for hearing loss,'' J. Acoust. Soc. Am. **56**, 195–197.

Price, G. R., and Kalb, J. T. (**1991**). ''Insights into hazard from intense impulses from a mathematical model of the ear,'' J. Acoust. Soc. Am. **90**, 219–226.

Rhode, W. (**1978**). ''Some observation on cochlear mechanics,'' J. Acoust. Soc. Am. **64**, 158–176.

Rosowski, J. J. (**1994**). ''Outer and middle ears,'' in *Handbook of Auditory Research, Volume IV: Comparative Hearing: Mammals*, edited by A. N. Popper and R. R. Fay (Springer-Verlag, New York), pp. 172–248.

Rosowski, J. J., Ravicz, M. E., Teoh, S. W., and Flandermeyer, D. (**1999**). ''Measurements of middle-ear functions in the Mongolian Gerbil, a specialized Mammalian ear,'' Audiol. Neuro-Otol. **4**, 129–136.

Russell, I. J., Cody, A. R., and Richardson, G. P. (**1986**). ''The responses of inner and outer hair cells in the basal turn of the guinea-pig cochlea and in the mouse cochlea grown in vitro,'' Hear. Res. **22**, 199–216.

Schmiedt, R. A., and Zwislocki, J. J. (**1977**). ''Comparison of sound-transmission and cochlear-microphonic characteristics in Mongolian gerbil and guinea pig,'' J. Acoust. Soc. Am. **61**, 133–149.

Teoh, S. W., Flandermeter, D. T., and Rosowski, J. J. (**1997**). ''Effects of pars flaccida on sound condition in ears of Mongolian gerbil: acoustic and anatomical measurements,'' Hear. Res. **106**, 39–65.

Weiss, T. F., Peake, W. T., and Sohmer, H. S. (**1971**). ''Introcochlear potential recorded with micropipets. III. Relation of cochlear microphonic potential to stapes velocity,'' J. Acoust. Soc. Am. **50**, 602–615.

Wilson, J. P., and Johnstone, J. R. (**1975**). ''Basilar membrane and middle-ear vibration in guinea pig measured by capacitive probe,'' J. Acoust. Soc. Am. **57**, 705–723.

Zwislocki, J. J. (**1975**). ''The role of the external and middle ear in sound transmission,'' Nerv. Syst. **3**, 45–55.

Evidence of upward spread of suppression in DPOAE measurements

Michael P. Gorga,[a] Stephen T. Neely, Patricia A. Dorn, Darcia Dierking, and Emily Cyr

Boys Town National Research Hospital, 555 North 30th Street, Omaha, Nebraska 68131

Measurements of DPOAE level in the presence of a suppressor were used to describe a pattern that is qualitatively similar to population studies in the auditory nerve and to behavioral studies of upward spread of masking. DPOAEs were measured in the presence of a suppressor (f_3) fixed at either 2.1 or 4.2 kHz, and set to each of seven levels (L_3) from 20 to 80 dB SPL. In the presence of a fixed f_3 and L_3 combination, f_2 was varied from about 1 oct below to at least $\frac{1}{2}$ oct above f_3, while L_2 was set to each of 6 values (20–70 dB SPL). L_1 was set according to the equation $L_1 = 0.4L_2 + 39$ [Janssen *et al.*, J. Acoust. Soc. Am. **103**, 3418–3430 (1998)]. At each L_2, L_1 combination, DPOAE level was measured in a control condition in which no suppressor was presented. Data were converted into decrements (the amount of suppression, in dB) by subtracting the DPOAE level in the presence of each suppressor from the DPOAE level in the corresponding control condition. Plots of DPOAE decrements as a function of f_2 showed maximum suppression when $f_2 \approx f_3$. As L_3 increased, the suppressive effect spread more towards higher f_2 frequencies, with less spread towards lower frequencies relative to f_3. DPOAE decrement versus L_3 functions had steeper slopes when $f_2 > f_3$, compared to the slopes when $f_2 < f_3$. These data are consistent with other findings that have shown that response growth for a characteristic place (CP) or frequency (CF) depends on the relation between CP or CF and driver frequency, with steeper slopes when driver frequency is less than CF and shallower slopes when driver frequency is greater than CF. For a fixed amount of suppression (3 dB), L_3 and L_2 varied nearly linearly for conditions in which $f_3 \approx f_2$, but grew more rapidly for conditions in which $f_3 < f_2$, reflecting the basal spread of excitation to the suppressor. The present data are similar in form to the results observed in population studies from the auditory nerve of lower animals and in behavioral masking studies in humans. © *2002 Acoustical Society of America.* [DOI: 10.1121/1.1513366]

PACS numbers: 43.64.Ha, 43.64.Jb [BLM]

I. INTRODUCTION

Single-unit tuning curves or frequency-threshold curves (FTCs) are plots of threshold as a function of frequency for an auditory neuron innervating a single inner hair cell (IHC). Because of this, they can be viewed as measures of the frequency response of a single place along the cochlea. A large literature exists describing FTCs in both normal and impaired ears of lower animals (e.g., Kiang *et al.*, 1965; Kiang and Moxon, 1974; Kiang *et al.*, 1976; Liberman and Kiang, 1978; Dallos and Harris, 1978; Liberman, 1978; Liberman and Dodds, 1984). In the normal case, these curves are characterized by a best or characteristic frequency (CF), for which threshold is lowest (i.e., most sensitive). As the stimulus frequency moves away from CF, the level necessary to elicit a response from the fiber increases. This increase in threshold, however, is asymmetrical. On both the high- and low-frequency sides relative to CF, the slope of the function relating threshold to frequency increases rapidly. On the high-frequency side, this increase in threshold apparently continues indefinitely, at least up to the limits of typical stimulus-generation systems. In contrast, thresholds for lower frequencies relative to CF increase rapidly, but this threshold increase does not continue indefinitely. Rather, as the frequency moves to between $\frac{1}{2}$ and 1 oct below CF, thresholds either increase slowly or achieve a relatively constant level as frequency decreases further.

Direct measurements of low-level, basilar-membrane responses at a specific site also show a CF, and that as driver frequency moves away from this CF, displacement or velocity thresholds increase. (See Robles and Ruggero, 2001 for a comprehensive review of basilar-membrane mechanics.) Thus, both the frequency-dependent response properties of auditory neurons and the mechanical response of the basilar membrane share similar frequency-response characteristics. Indeed, comparative studies have led to the conclusion that the cochlear mechanical action caused by sounds differing in frequency is reflected in the frequency-dependent thresholds of neural FTCs (e.g., Sellick *et al.*, 1982; Ruggero *et al.*, 1992, 1997, 2000). That is, FTCs reflect the basilar-membrane frequency resolution in the vicinity of the IHC innervated by the neuron. At high levels, the mechanical response to low-frequency stimuli (at a fixed cochlear place) can be as large or even larger than the response to a frequency that was the BF at low levels of stimulation (Ruggero and Rich, 1991; Ruggero *et al.*, 1992; Rhode and Recio, 2000). Thus, upward (or basal) spread of excitation is evident in both mechanical responses and in neural responses from the auditory periphery.

In the above examples, the ability of low-frequency

---

stimuli to excite higher frequency regions was evaluated by measuring the response properties at a single cochlear place while stimulus frequency was manipulated. Frequency-dependent spread of excitation has also been evaluated by examining response properties of many auditory neurons to a single tone that was varied in level (Pfeiffer and Kim, 1975; Kim and Molnar, 1979; Kim, 1983; Kim *et al.*, 1990). These experiments are sometimes referred to as population studies because the responses from a large number of auditory-nerve fibers are studied to a fixed stimulus. At low stimulus levels, discharge rate is largest for nerve fibers whose CFs are close to stimulus frequency. As level increases, discharge rate increases primarily for fibers whose CFs approximate stimulus frequency; however, fibers innervating cochlear places slightly different from CF also start to respond. Thus, there is a spread of excitation as level increases. The spread of excitation, however, is asymmetrical, especially for high stimulation levels. Fibers with CFs at and above the stimulus frequency are more likely to respond, compared to fibers with CFs lower than stimulus frequency. Thus, evidence exists in neural population responses that the spread of cochlear excitation with increases in level is towards basal, high-frequency cochlear regions. The spread of excitation is less towards apical, low-frequency regions relative to stimulus frequency. Although basilar-membrane measurements have been reported for several sites in the same animal (Rhode and Recio, 2000), the measurements do not cover the same cochlear range as the single-unit recordings, presumably because of the difficulty in placing sources at distant locations within the same cochlea.

In humans, direct measurements of frequency selectivity at one cochlear place or spread of excitation across the cochlea are not possible. However, similar response patterns have been observed indirectly, based on ''masking'' measurements. For example, data have been collected in masking experiments in which a probe stimulus (fixed in level and frequency) was presented, and the response to that probe was ''masked'' by the presentation of a masker. Plots of the masker level necessary to achieve a ''threshold'' amount of masking as a function of masker frequency provide indirect estimates of frequency selectivity that are similar in many ways to direct measurements from the basilar membrane and from individual auditory neurons. These indirect measurements have been obtained behaviorally (psychophysical tuning curves), electrophysiologically (with gross potentials such as the whole-nerve action potential and auditory brainstem response), and acoustically (otoacoustic emission suppression tuning curves). These ''masking'' tuning curves, obtained both in lower animals and in humans, show frequency relationships that are similar to those observed in more direct studies from lower animals (e.g., Abdala, 1998, 2001; Abdala *et al.*, 1996; Gorga *et al.*, 2002; Harris *et al.*, 1992; Kemp and Brown, 1983; Kummer *et al.*, 1995; Martin *et al.*, 1987, 1999; Eggermont, 1977; Smoorenburg and van Heusden, 1979; Dallos and Cheatham, 1976; Harris, 1979; Florentine *et al.*, 1980; Abbas and Gorga, 1981; Gorga and Abbas, 1981; Harrison *et al.*, 1981; Nelson and Turner, 1980; Wightman *et al.*, 1977; Ryan *et al.*, 1979; Gorga *et al.*, 1983). In these experiments, the goal was to describe the frequency

selectivity for a specific place along the cochlea. Plots relating masker level and frequency have been taken as an indirect estimate of the representation of different frequencies at the probe-frequency place in the cochlea. Similar to single-unit and basilar-membrane data, basal spread of excitation is evident in these masking studies in that low-frequency maskers or suppressors were able to affect the responses of high-frequency signals.

Behavioral evidence of the spread of excitation from a single tone also has been explored in humans using masking paradigms. High-level, low-frequency stimuli have been shown to cause masking for distant, high-frequency regions, but not for frequencies on the low-frequency side of the masker (Wegel and Lane, 1924; Egan and Hake, 1950; Oxenham and Plack, 1998). This asymmetrical effect has been called upward spread of masking. Presumably, it is a result of the same cochlear mechanics and traveling-wave dynamics that are responsible for the frequency dependence of single-unit FTCs, the pattern seen in neural population responses to a single tone, and the level and frequency dependence of basilar-membrane motion.

Psychophysical studies typically require time-intensive measurements, thus generally limiting their application to adult, cooperative subjects. In addition, psychophysical masking might reflect processes at several levels along the auditory pathway, including the cochlea, the auditory nerve, and perhaps even more central auditory centers. For example, the ''central detector'' during psychophysical masking studies could ''optimize'' performance by evaluating response properties from fibers innervating cochlear regions whose ''best frequencies'' are not exactly equal to the probe or signal frequency (off-frequency listening). Both basilar-membrane and single-unit studies describe only peripheral processes because there is no opportunity for a central detector to optimize the region over which the response is examined. Furthermore, both behavioral masking and single-unit responses might involve short-term, neural adaptation (Smith and Zwislocki, 1977; Smith, 1979; Harris and Dallos, 1979), which is thought to be due to processes localized to the synapse between the IHC and the nerve fiber (e.g., Furukawa and Matsuura, 1978; Furukawa *et al.*, 1978). Synaptic events occur central to the frequency resolution imposed by cochlear mechanical responses. For these reasons, perhaps one should not expect a one-to-one correspondence between behavioral data, obtained in humans, and direct measurements of frequency resolution based on basilar-membrane measurements in lower animals.

Distortion product otoacoustic emission (DPOAE) measurements have been used to describe the frequency response of the cochlea of humans (e.g., Brown and Kemp, 1984; Martin *et al.*, 1987; Harris *et al.*, 1992; Kummer *et al.*, 1995; Abdala *et al.*, 1996; Gorga *et al.*, 2002). These measurements require less time than psychophysical measurements and reflect only cochlear response properties. In this latter respect, they may more closely approximate the conditions from more direct basilar membrane measurements in lower animals. In DPOAE tuning-curve studies, the eliciting stimulus, a pair of primary tones, typically is held constant in frequency and level. This ''probe'' is used to elicit a re-

J. Acoust. Soc. Am., Vol. 112, No. 6, December 2002

Gorga *et al.*: Suppression in DPOAE measurements 2911

sponse, whose level is then suppressed by another tone that is varied in frequency and level. Plots of suppressor level as a function of suppressor frequency necessary to reduce the probe-elicited DPOAE level by a ''threshold'' amount have been called DPOAE suppression tuning curves. These tuning curves resemble other similar measurements that use a masking paradigm to derive an estimate of frequency selectivity for a fixed cochlear place. The procedures for measuring a DPOAE suppression tuning curve can be completed in relatively short periods of time and, because they are noninvasive and do not require a behavioral response, they can be performed in subjects of any age or developmental level (e.g., Abdala, 1998, 2001).

It also may be possible to use DPOAEs to measure cochlear spread of excitation to a single tone in humans, providing data that are similar in form to population studies at the level of the auditory nerve or behavioral studies of masking patterns. The purpose of the present study was to evaluate the extent to which DPOAE measurements in a suppression paradigm can be used to provide an indirect estimate of the representation of a single tone along the basilar membrane. Suppressor frequency and level were fixed and the amount of suppression was measured as a function of probe frequency, where probe frequency was defined as the higher frequency (f_2) in the primary-frequency pair (f_1, f_2). Data were obtained for two different suppressor frequencies, several suppressor levels, many probe frequencies and several probe levels. The amount of suppression produced by the suppressor as a function of probe frequency was taken as an indirect estimate of the representation of the suppressor at different places along the cochlea.

II. METHODS

A. Subjects

A total of 17 adult subjects with normal hearing participated in this study. Our goal was to make measurements in 10 subjects for each set of stimulus conditions (see below). Due to time constraints, however, some subjects were unable to participate in studies at both suppressor frequencies, thus necessitating the recruitment of 17 subjects in order to assure that measurements were made in 10 subjects per condition. Each subject had pure-tone audiometric thresholds of 15 dB HL or better (*re*: ANSI, 1996) for octave and half-octave frequencies from 250 to 8000 Hz. In addition, each subject had normal middle-ear function each day on which DPOAE measurements were made. Tympanometric patterns for a 226-Hz probe tone were used to assess middle-ear status.

B. Stimuli

All stimuli were generated by custom-designed software (EMAV, Neely and Liu, 1994) that controlled a soundcard (CardDeluxe, Digital Audio Labs), which was housed in a PC. Primary frequencies $(f_1, f_2, f_2/f_1 \approx 1.22)$ were produced by separate channels of the soundcard. The channel producing f_2 also produced the suppressor tone (f_3). The signals generated on each channel were delivered to separate loudspeakers in a probe-microphone system (Etymotic Research,

ER-10C) and mixed acoustically in the ear canal. The probe-microphone system was modified to remove 20 dB of attenuation from each sound-delivery channel.

Suppressor frequencies (f_3) were set either to 2.1 or 4.2 kHz. Suppressor levels (L_3) were varied from 20 to 80 dB SPL in 10-dB steps. The primary tones eliciting the DPOAE were viewed as probes, similar to the way signals are viewed in psychophysical or behavioral masking experiments. These DPOAE probes consisted of primary pairs (f_2, f_1), with f_2 ranging in frequency from at least $\frac{1}{2}$ oct below f_3 to between $\frac{1}{2}$ and $1\frac{1}{2}$ oct above f_3, depending on f_3 and on an interaction between L_2 and L_3. There were approximately 25 primary pairs for each f_3. The level of the higher-frequency primary in each primary pair (L_2) was varied from 20 to 70 dB SPL in 10-dB steps. The level of the lower frequency primary (L_1) was adjusted according to the formula, $L_1 = 0.4L_2 + 39$ dB (Janssen *et al.*, 1998). This level relationship, sometimes referred to as the ''scissor paradigm,'' results in the largest DPOAEs for subjects having normal hearing. More recent work indicates that this level paradigm applies across a wide range of frequencies, exceeding the range of f_2 frequencies studied in the present experiment (Kummer *et al.*, 2000). All stimulus levels were calibrated in the ear canal by the probe system's recording microphone.

In all cases, the probe-microphone system was used to calibrate stimulus level in the ear canal. As has been shown previously (Siegel, 1994, 2002), such procedures may result in errors in estimating stimulus level, due to standing-wave problems in the ear canal. An alternative calibration procedure is to measure level in a standard cavity, and use those values in all subjects. This approach avoids standing wave problems, but is not without problems, in that some decision must be made in determining what constitutes a ''standard'' cavity, and values in individual ears will vary widely. A calibration procedure based on measurements of acoustic intensity in individual ears circumvent all of these problems. Unfortunately, these calibration procedures have not yet been implemented in a way that can be easily used in individual subjects. We recognize that calibration problems may exist for real-ear pressure measurements at the plane of the probe microphone; the approach we have taken is in common use, but its limitations are recognized.

C. Procedures

Data collection was initiated with an unsuppressed condition, in which DPOAE levels were measured in the absence of a suppressor, L_2 was fixed at one of six L_2 levels, and f_2 was varied (i.e., a ''DPgram''), while f_2/f_1 was held constant at approximately 1.22. Next, the same DPgram was recorded in the presence of a suppressor tone (fixed at either 2.1 or 4.2 kHz) set at each of seven L_3 levels (20 to 80 dB SPL). The level produced with the suppressor present was subtracted from the level produced in the unsuppressed (control) condition, converting the data into decrements, or amount of suppression, in dB. This process was continued until DPOAE levels were measured at all f_2 frequencies for each of seven L_3 levels. The entire process was repeated for each of six values of L_2. In addition to estimating the amount of suppression, decrements have the additional ad-

vantages of providing data in a form that may be compared to other measures of cochlear spread of excitation. Normalizing data to the unsuppressed condition also partially takes into account individual differences in absolute DPOAE level (Gorga *et al.*, 2002). With these procedures, the amount of suppression was measured over its entire range, from 0 dB of suppression until the response was either completely suppressed (i.e., SNR=0 dB) or up to the limits of the suppressor level. For some f_2, L_2 combinations, the maximum suppressor level ($L_3=80$ dB SPL) did not result in a completely suppressed response.

Measurement-based stopping rules were used, such that data collection continued until the noise floor was ≤ -25 dB SPL or until 32 s of artifact-free data-collection time had expired, whichever occurred first. The noise-floor stopping rule was chosen for two reasons. With a maximum primary level (L_2) of 70 dB SPL, system distortion did not exceed -25 dB SPL (Dorn *et al.*, 2001). Furthermore, it provided a wide dynamic range for the DPOAE measurements. As a result, decrements could be reliably measured, even for primary levels (L_2's) as low as 20 dB SPL. The absolute time limit was included in the stopping rule to prevent averaging from continuing indefinitely. This time constraint was necessary, given the large number of stimulus conditions per subject. Total data-collection time per subject, including audiometric, tympanometric, all DPOAE measurements, and periodic breaks, was approximately 12–14 h.

III. RESULTS

A. Iso-suppressor contours

Figure 1 plots mean DPOAE decrements (amount of suppression, in dB) as a function of f_2. In this form, these plots were viewed as iso-suppressor contours, in which the suppressor level was held constant and the decrement (or amount of suppression) produced by the suppressor was plotted for different f_2 frequencies. Data are shown for the conditions in which $f_3=2.1$ kHz (left column) and when $f_3=4.2$ kHz (right column). A vertical dotted line is drawn at f_3 in each panel. Each panel represents data for a different L_2, with L_2 increasing down each column. Within each panel, the parameter is L_3, with decreasing line weights used to signify increasing L_3 level. A moving, three-point smoothing function, in which equal weight was given to every data point, was applied to each curve. Notably, only five of ten subjects when $L_2=20$ dB SPL and nine of ten subjects when $L_2=30$ produced DPOAEs with sufficient signal-to-noise ratios (SNR) over a sufficiently wide range of frequencies to allow for reliable measurements of suppression when $f_3=2.1$ kHz. For f_2 frequencies around and below 2.1 kHz, the SNR was not sufficient to measure decrements in other subjects. Thus, fewer data were available for these stimulus conditions. For other L_2 levels, the SNR was large enough that the amount of suppression could be measured reliably. When the suppressor frequency was 4.2 kHz, six of ten subjects produced large enough SNRs to permit measurements when $L_2=20$ dB SPL. At higher L_2 levels, reliable measurements were possible in all ten subjects because they produced large SNRs for all f_2 frequencies surrounding an $f_3=4.2$ kHz.
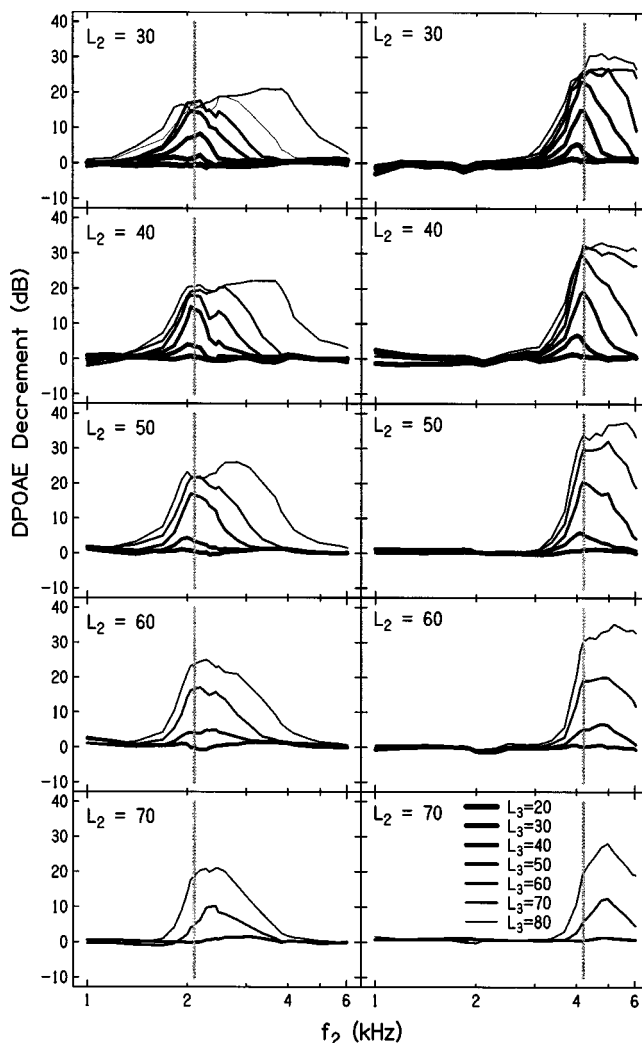
FIG. 1. DPOAE decrement (in dB) as a function of f_2 frequency (in kHz). Left column: $f_3=2.1$ kHz; right column: $f_3=4.2$ kHz. Vertical dotted lines are drawn at the f_3 frequency. Each panel shows data for a different L_2. The parameter within each panel is suppressor level (L_3).

Several trends were evident for both suppressor frequencies. At low suppressor levels, suppression was first evident for f_2 frequencies close to f_3. As L_3 increased, the decrement (i.e., the amount of suppression) increased; however, the increase was not uniformly centered at f_3. Rather, the suppressive effect of f_3 spread more towards the high-frequency side of these suppression patterns, compared to the suppression that was measured at low frequencies relative to f_3. The range of frequencies over which the suppressor had an effect and the amount of suppression decreased as L_2 increased. For example, note the more narrow range of suppressed f_2 frequencies when $L_2=60$ and 70 dB SPL, compared to when $L_2=30$ or 40 dB SPL. Still, the asymmetry in the spread of suppression was evident at all L_2 levels. When $L_2=20$ dB SPL at both f_3 frequencies, the spread of suppression was observed for frequencies less than f_3, although not nearly as much as was observed on the high-frequency side of f_3. There also was less suppression for f_2 frequencies less than f_3 when L_2 was 50, 60, or 70 dB SPL, especially when $f_3=4.2$ kHz, and the upward spread of suppression was not as extensive, compared to when L_2 was set to lower levels. This

J. Acoust. Soc. Am., Vol. 112, No. 6, December 2002

Gorga *et al.*: Suppression in DPOAE measurements   2913
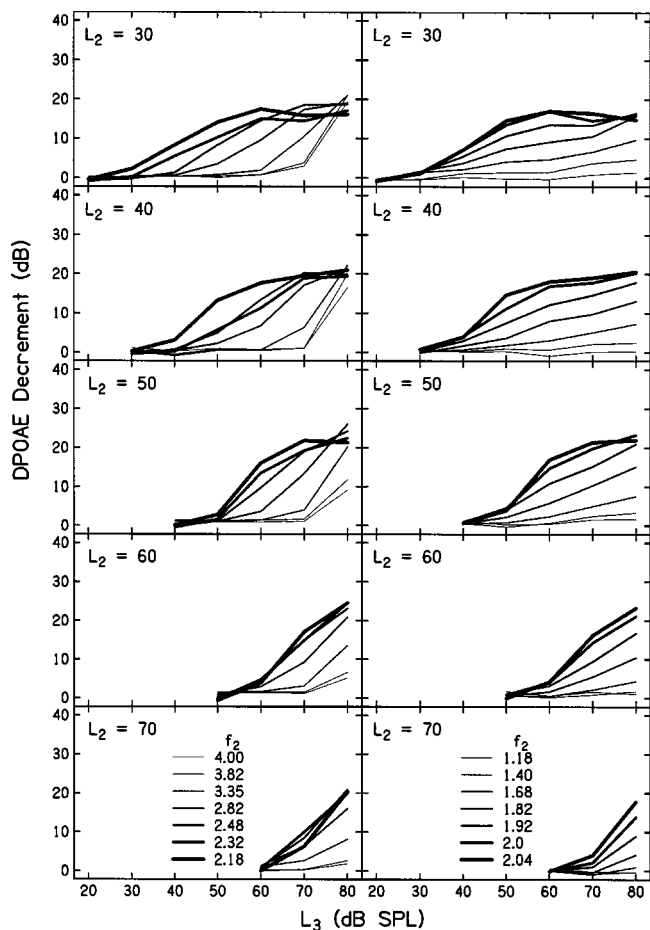
FIG. 2. DPOAE decrement (in dB) as a function of suppressor level, L_3 (in dB SPL) when $f_3 = 2.1$ kHz. Left column: $f_2 > f_3$; right column: $f_2 < f_3$. Each panel shows data for a different L_2. The parameter within each panel is f_2, as indicated.

FIG. 3. DPOAE decrement (in dB) as a function of suppressor level, f_3 (in dB SPL) when $f_3 = 4.2$ kHz. Left column: $f_2 > f_3$; right column: $f_2 < f_3$. Each panel shows data for a different L_2. The parameter within each panel is f_2, as indicated.

may reflect an interaction between signal and suppressor levels. That is, suppression was observed only for the case in which L_3 was at least as high as L_2. For example, when $L_2 = 60$ dB SPL, L_3 levels of 60, 70, and 80 dB SPL were needed in order for suppression to occur at any frequency, including f_2 frequencies close to f_3.

B. Growth of suppression

Figures 2 and 3 show DPOAE decrement as a function of suppressor level for suppressor frequencies of 2.1 and 4.2 kHz, respectively. These figures were generated by taking vertical slices through the iso-suppressor patterns shown in Fig. 1. In both figures, each panel shows data for a different L_2. Within each panel, the parameter is f_2, with $f_2 > f_3$ shown in the left column and $f_2 < f_3$ shown in the right column. Line weights are used to designate different f_2 frequencies, with the heaviest weight for the f_2 closest to f_3, and thinning lines representing data for progressively more distant frequencies. In the interest of clarity, data are shown only for a subset of the 25 f_2 frequencies. Data are presented for both suppressor frequencies, but only Fig. 2 will be discussed because the trends were similar at 2.1 and 4.2 kHz.

As expected, suppression occurred at the lowest L_3 levels with f_2 frequencies closest to the suppressor frequency.

As f_2 moved away from f_3, the lowest level at which a decrement was first observed increased. This was generally true across L_2 levels, although some exceptions were noted. That is, the lowest threshold was not always observed for the condition in which f_2 was closest to f_3. When $L_2 = 70$ dB SPL, more suppression was observed at f_2 frequencies slightly higher than f_3 (see the lower left panel in Fig. 2). Finally, for $f_2 > f_3$, decrement-versus-L_3 functions grew more rapidly, compared to conditions in which $f_2 < f_3$ (contrast the left and right columns of Fig. 2), with intermediate slopes when $f_2 \approx f_3$.

Several decrement functions "saturated," such that increases in L_3 did not result in further increases in the decrement (i.e., the amount of suppression). Saturated values reflect the fact that the response has been decremented into the noise floor. Thus, the maximum decrements represent the dynamic range of the measurements. For example, when $f_2 = 2.18$ kHz and $L_2 = 30$ dB SPL (Fig. 2, left column, second row, heaviest line), the maximum decrement or amount of suppression that could be measured was slightly less than 20 dB, which was achieved when $L_3 = 50$–60 dB SPL. This means that the average DPOAE for this condition was about 20 dB above the noise floor, and that changes in DPOAE level could be measured only over this 20-dB range. This effect was more obvious when lower L_2 levels were used.
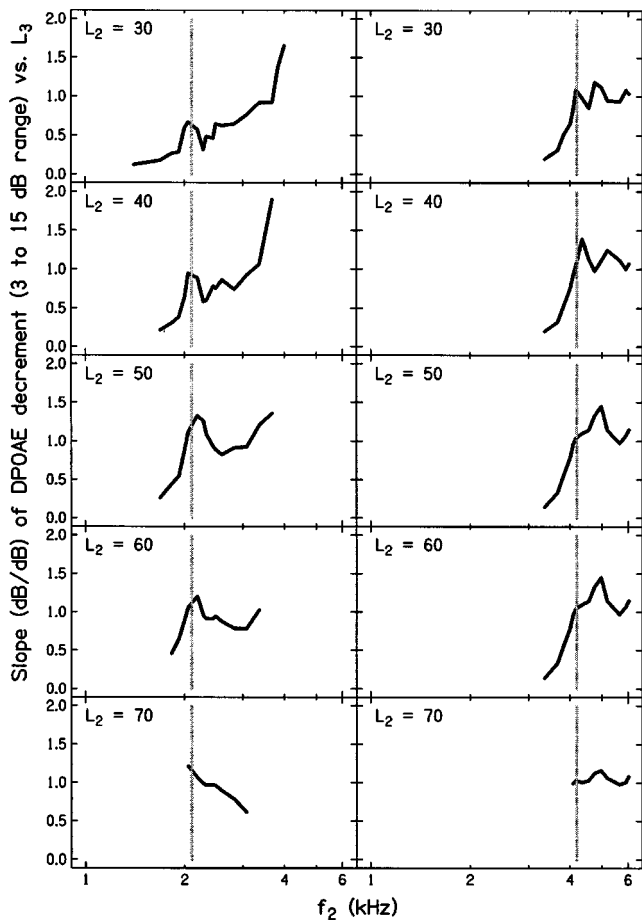
FIG. 4. Slope (dB/dB) of the decrement versus L_3 functions as a function of f_2. Left column: $f_3 = 2.1$ kHz; right column: $f_3 = 4.2$ kHz. Vertical dotted lines are drawn at the f_3 frequency. Each panel shows data for a different L_2. Slopes estimates were based on linear regressions of 3- to 15-dB decrements onto L_3.

Under these conditions, DPOAE levels (in the unsuppressed condition) were smaller, and, thus, it was possible to suppress these smaller responses into the noise floor. At higher L_2 levels, the response was larger and frequently was not suppressed into the noise floor, even for the highest suppressor level ($L_3 = 80$ dB SPL). The relation between L_3 and L_2 in order for suppression to occur is evident in the migration of these decrement versus L_3 functions towards the right side as one progresses down each column. Notably, suppression was observed only if L_3 was at least equal to L_2; if L_3 was just 10 dB lower than L_2, suppression was not evident. This was true regardless of the relationship between f_3 and f_2. Essentially all of the trends that were evident when $f_3 = 2.1$ kHz (Fig. 2) were evident when $f_3 = 4.2$ kHz (Fig. 3).

Figure 4 provides a summary of decrement versus L_3 functions, showing slopes of linear fits to the data shown in Figs. 2 and 3. The left and right columns provide estimates when $f_3 = 2.1$ and 4.2 kHz, respectively. Vertical dotted lines are drawn at these two frequencies in order to provide a point of reference. Fits were restricted to the range of decrements between 3 and 15 dB, and to cases for which at least two points were available. To obtain the two limiting values (i.e., decrements of 3 and 15 dB), it was necessary to interpolate between two points in order to estimate L_3. In general, this

was not a problem because of the wide dynamic range of decrements (see maximum decrements in Figs. 2 and 3). However, slope was not estimated when decrements were observed for only one level (the highest L_3, 80 dB SPL). Although uncommon, this event was more likely to occur when f_2 was distant from f_3 on both the high- and low-frequency side.

It was sometimes the case that the decrement was 0 dB at one level (10 dB below L_2) and between 1 and 12 dB at the next level (when $L_3 = L_2$). Simple linear regression was used to estimate L_3 at a decrement of 3 dB. Such an approach, however, introduced error in this estimated value because of differences in the "origin" (and therefore, the slope) of the linear regressions across f_2 frequencies. In any case, all points falling between 3 and 15 dB (even though the limiting values were derived through interpolation) were included in the linear fits to the data.

As a general rule, slopes of 1 or greater were observed when $f_2 > f_3$, and slopes less than 1 were observed when $f_2 < f_3$. Stated differently, the response to the suppressor grew more rapidly when it (f_3) was lower in frequency relative to the signal frequency (f_2). The extent to which this rule applied varied with L_2. At the highest L_2 (70 dB SPL), the slope variation with f_2 decreased, although not universally. At least part of this effect was due to absence of data when $f_2 < f_3$ for L_2 conditions at 70 dB SPL (see bottom row of panels). At this level, therefore, slope could not be estimated for conditions in which f_2 was much lower in frequency than f_3.

There were, however, differences across f_3 frequency. For example, at the lowest L_2 levels (20 and 30 dB SPL) when $f_3 = 2.1$ kHz, the slope was less than 1 when $f_2 \approx f_3$. The slope increased to values greater than 1 as f_2 frequency increased above f_3, at least for L_2 levels of 40 dB SPL and less. At 4.2 kHz, the slope was close to unity when $f_2 \approx f_3$ for all L_2 conditions, which also was close to the maximum value when $f_2 > f_3$. Some of the differences across f_3 frequencies at low levels may reflect differences in the reliability of DPOAE measurements across frequency. As a general rule, noise levels were higher for f_2 frequencies surrounding 2.1 kHz, compared to the measurements surrounding 4.2 kHz. However, this explanation is inadequate when $f_2 > f_3$, because the noise levels under these circumstances were low at the f_2 frequencies used for both suppressor frequencies. Part of the difference on the high-frequency side also could reflect differences in the range of f_2 frequencies that were used at each f_3. When $f_3 = 2.1$ kHz measurements were made at f_2 frequencies that were 1 to $1\frac{1}{2}$ octaves higher. The highest f_2 frequency was about $\frac{1}{2}$ oct above f_3 in frequency when $f_3 = 4.2$ kHz. Perhaps steeper slopes would have been observed when $f_3 = 4.2$ kHz if measurements were extended to higher f_2 frequencies.

C. Iso-suppression contours

Figure 1 represented the amount of suppression as L_3 increased for a range of f_2 frequencies and L_2 levels. These data may be converted into iso-suppression contours by finding the suppressor levels necessary for a fixed decrement. By holding the decrement constant, presumably the response to
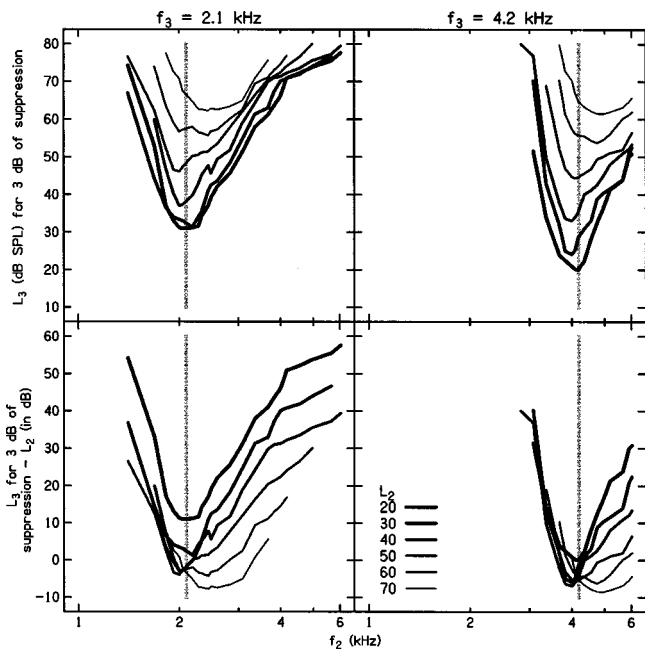
FIG. 5. Top row: Suppressor level (L_3, in dB SPL) required for 3 dB of suppression as a function of f_2. Bottom row: The dB difference between L_3 of 3 dB of suppression and L_2 as a function of f_2. Left column: $f_3 = 2.1$ kHz; right column: $f_3 = 4.2$ kHz. Vertical dotted lines are drawn at the f_3 frequency. Within each panel, the parameter is L_2.

the suppressor is held constant at each f_2 frequency, and by extension at the places at which the DPOAE is generated. Thus, plots of suppressor level for a fixed decrement represent (to a first approximation) the level necessary for a fixed-frequency suppressor (f_3) to cause the same response over a range of cochlear places (represented by the range of f_2 frequencies).

Figure 5 represents DPOAE data when the decrement was held constant at 3 dB. The right and left columns show data when $f_3 = 2.1$ and 4.2 kHz, respectively. Vertical dotted lines are drawn at the suppressor frequency in both columns. Within each of the four panels, the parameter is L_2, with decreasing line weights reflecting increases in L_2. In the top row, the level of the suppressor (L_3) that was required to produce a "threshold" decrement, defined as 3 dB, is plotted as a function of f_2. These plots demonstrate that iso-suppression patterns have the lowest threshold for f_2 frequencies approximately equal to f_3. Higher suppressor levels were required as f_2 moved away from f_3 in either direction. As L_2 increased, higher L_3 levels were required to maintain a constant 3-dB decrement. When $f_2 \approx f_3$, a 10-dB increase in L_3 for every 10-dB increase in L_2 was required in order to maintain a constant response to the suppressor, although some exceptions were noted (consider the shift between $L_2 = 20$ and $L_2 = 30$ when $f_3 \approx f_2$ and $f_3 = 2.1$ kHz). In contrast, L_3 increased at a slower rate relative to L_2 when $f_2 > f_3$, which is evident in the relatively close spacing of the functions when f_2 was between $\frac{1}{2}$ and 1 oct higher than f_3. This means that the response to f_3 grew more rapidly when f_2 was higher than f_3, compared to the rate of growth when $f_2 \approx f_3$. Although less pronounced, the reverse was true when $f_2 < f_3$, in that the response to the suppressor with L_2 grew at a rate that was less than or equal to the rate when $f_2 \approx f_3$.

The bottom row of Fig. 5 presents the same data, only here, L_3 necessary for 3 dB of suppression minus L_2 is plotted as a function of f_2. This operation normalizes suppression threshold to L_2. The extent to which L_2 and L_3 approximate each other and grow at the same rate is estimated by the deviation from zero (0) in these differences. For differences close to zero, the probe and suppressor level were equal and it was necessary to increase L_3 by 10 dB for every 10-dB increase in L_2. Deviations from zero reflect the dB differences between suppressor and probe levels, and changes in these differences with L_2 reflect differences in growth of suppression at different f_2 frequencies (assumed to represent different places along the cochlea).

Differences less than zero dB mean that L_3 for 3 dB of suppression was less than L_2. While the absolute magnitude of these negative differences should be viewed cautiously because the value had to be estimated using interpolation, there is little doubt that there were conditions in which L_3 was less than L_2. We know this was the case because there were conditions in which more than 3 dB of suppression was observed when $L_3 = L_2$ (see Figs. 1–3). Uncertainty exists only in the estimate of the magnitude of the negative deviation from zero.

Returning to the bottom row of Fig. 5, differences between L_3 and L_2 approximating zero were more likely to occur when f_2 was close to f_3. When $f_3 = 4.2$ kHz, the range of these difference was about 8 dB for a 50-dB range of L_2 levels (20 to 70 dB SPL) for f_2 frequencies close to f_3. Similarly, when $f_3 = 2.1$ kHz, the total difference was about 15 dB for the same 50-dB range of L_2 levels when $f_2 \approx f_3$. Much of the total difference for $f_3 = 2.1$ kHz occurred when L_2 was 20 dB SPL, a condition marked by greater variability and fewer data, compared to other L_2 conditions. Excluding this condition, the total difference when f_2 approximated f_3 was about 5 dB for a 40-dB range in L_2 when $f_3 = 2.1$ kHz. This means that for both suppressor frequencies, 3-dB decrements were achieved when L_3 and L_2 were nearly equal, and this rule held over a 40- to 50-dB range in L_2.

When f_2 was greater than f_3, the differences between L_3 (for a 3-dB decrement) and L_2 were large when L_2 was low. For example, at an L_2 of 20 dB SPL, "threshold" suppressor levels were between 32 and 57 dB greater than L_2 (depending on f_3) when f_2 was between $\frac{1}{2}$ and 1 oct higher in frequency than f_3. The highest f_2 frequency, 6.03 kHz, was only slightly more than $\frac{1}{2}$ oct above f_3 when $f_3 = 4.2$ kHz. Perhaps larger differences would have been observed between on-frequency ($f_2 \approx f_3$) and high-frequency ($f_2 > f_3$) conditions if higher f_2 frequencies had been tested. As L_2 increased, the difference between L_3 (for a 3-dB decrement) and L_2 decreased. This means that the response to the lower frequency suppressor grew rapidly at the f_2 place for frequencies greater than f_3, compared to how the response grew to tones at their characteristic place (i.e., when $f_2 \approx f_3$). At the highest L_2 (70 dB SPL), the difference between L_3 (for 3-dB decrements) and L_2 approximated zero or was negative for a wider range of frequencies, compared to the case when L_2 was at low levels. These trends were apparent at both f_3 frequencies. The observation that the differences at higher f_2 frequencies decreased as level increased indicates that up-

Gorga *et al.*: Suppression in DPOAE measurements

ward spread of suppression increased with level. Finally, the superimposition of these iso-suppression contours, as shown in the bottom row of panels, results in the impression that there may be two modes to these patterns, one peaked when $f_2 \approx f_3$ at low levels, and the other peaked at $f_2 > f_3$ at higher levels.

IV. DISCUSSION

The goal of this experiment was to determine if upward spread of suppression is evident in DPOAE measurements. Previous DPOAE suppression experiments have demonstrated that this is the case, although the measurement paradigm used in those previous studies differed from the one used presently. In all of these indirect experiments (especially those involving human subjects), it is assumed that stimulus frequency roughly equates with place. This assumption does not hold in an absolute sense, and the extent to which this assumption is violated depends on level. On the other hand, only more direct measurements more full assess the extent to which these assumptions hold, and those direct measurements are not possible in humans. Given this fact, our approach was to evaluate suppressive effects for two suppressor frequencies for a wide range of suppressor levels. These effects were assessed for a wide range of probe frequencies presented at a wide range of probe levels. Thus, changes in the representation of the suppressor were evaluated for a wide range of suppressor and probe levels.

An additional concern in DPOAE suppression studies relates to the complex set of stimuli that are used during these measurements. The probe consists of two pure tones and suppression measurements involve the presentation of a third tone. While it is assumed that the interaction of f_2 and f_1 (presumably near the place where f_2 is represented) produces the DPOAE and this response is suppressed by f_3, opportunities exist for the generation of additional distortion products, due to interactions between the suppressor and either one of the primary frequencies, or perhaps due to interactions between the DPOAEs and one of the external tones.

In spite of these problems, the general trends observed in the present study are consistent with other physiological and behavioral evidence of upward spread of excitation. Upward spread of suppression was evident at both suppressor frequencies ($f_3 = 2.1$ or 4.2 kHz) and increased systematically with suppressor level. The present results also are consistent with population studies in the auditory nerve, in which the stimulus frequency was held constant, its level was varied, and the responses of neurons with different CFs were sampled (Pfeiffer and Kim, 1975; Kim and Molnar, 1979; Kim, 1983; Kim et al., 1990). In these single-unit studies, initial increases in stimulus level resulted in an increase in discharge rate for fibers with CFs close to the stimulus frequency. At higher levels, the discharge rate increased for fibers with CFs more distant from the stimulus frequency. Although this spread of excitation was observed in fibers with CFs both above and below the stimulus frequency, the spread of excitation was greater for fibers on the high-frequency side of the stimulus. A similar pattern was observed in the classical behavioral-masking data (Wegel and Lane, 1924; Egan and Hake, 1950). Using simultaneous masking techniques, these previous studies showed that psychoacoustical thresholds increased first at frequencies close to masker frequency. However, as masker level increased, the masking effect spread asymmetrically, with greater effect at higher frequencies than at lower frequencies relative to masker frequency. These same trends were evident in the present data (Fig. 1). The present results, however, presumably are unaffected by synaptic events (such as short-term adaptation and recovery) or neural events (such as "line-busy" effects), which might contribute to the behavioral measurements (Delgutte, 1996), and possibly to single-unit measurements. Furthermore, off-frequency listening might play a role in behavioral-masking experiments, but is unlikely to contribute to the DPOAE suppression measurements. The present results, therefore, are viewed as reflective of peripheral "masking" mechanisms restricted to the cochlear mechanical response. This is not to suggest that the DPOAE is generated at a point source, but only suggests that a combination of DPOAE suppression data and behavioral masking data might provide insights into the role played by central mechanisms.

There are other DPOAE data with which the present results may appear to disagree. For example, Martin et al. (1999) found that suppressor tones one octave or more above f_2 and as much as 40 dB lower than L_2 could suppress or enhance the $2f_1 - f_2$ DPOAE, an effect that was somewhat more pronounced at primary levels of 55 dB SPL and higher, and perhaps more evident for equal-level primaries. Suppression of low-frequency regions by suppressors one octave higher in frequency was not observed in the present study. In addition, suppression was not observed when L_2 was greater than suppressor level. The reasons for these differences are not obvious, but could be due to factors related to the stimuli (i.e., differences in the range of f_2 frequencies and the way L_1 was set relative to L_2) and perhaps species differences (Martin et al. made their measurements primarily in rabbits whereas the present work involved only humans).

Growth of suppression was more rapid when the suppressor was lower in frequency than the signal frequency (f_2), a pattern that has been observed in other studies of DPOAE suppression (e.g., Kemp and Brown, 1983; Kummer et al., 1995; Abdala, 1998, 2001; Gorga et al., 2002) and is consistent with more direct physiological measurements of response growth (Sachs and Abbas, 1974; Delgutte, 1990; Ruggero and Rich, 1991; Ruggero et al., 1997). Similar trends were evident in behavioral masking data as well (Wegel and Lane, 1924; Egan and Hake, 1950; Oxenham and Plack, 1998).

In the present study, a near-linear growth in suppressor threshold (defined as the L_3 necessary to produce 3 dB of suppression) with probe level (L_2) was observed when $f_3 \approx f_2$. A linear pattern under conditions of simultaneous masking is to be expected, even though the response of the basilar membrane at a specific place is nonlinear for best-frequency tones, because both the masker and the signal are being processed through the same nonlinearity (Oxenham and Plack, 1998; Plack and Oxenham, 1998). In fact, nonlinear processing in suppression or masking studies is revealed when signal level (at some defined threshold) is measured as

a function of suppressor (or masker) frequency for suppressor frequencies below signal frequency (e.g., Oxenham and Plack, 1998; Gorga *et al.*, 2002). This occurs because the response to the signal (f_2 in the present study) is nonlinear at its characteristic place, but the response to a lower frequency tone (f_3) at the same place is more linear. The summary provided in Fig. 5 is consistent with this view.

The present results also suggest a possible means for separating factors that contribute to behavioral masking. These measurements evaluated suppressive effects on DPOAE level. It is generally thought that suppression is a memoryless phenomenon, in that both signal and suppressor must be on simultaneously in order to observe an effect. Unlike the behavioral-masking data, the present measurements reflect only cochlear mechanical processes, devoid of neural effects (excluding effects from the olivocochlear system). On the other hand, it is possible that other factors, beside basic cochlear response properties, play a role in behavioral-masking measurements. As stated above, neural short-term adaptation, "line-busy" phenomena, and/or off-frequency listening potentially could contribute to behavioral-threshold data. Such factors, however, are unlikely to play a role in DPOAE suppression measurements. Thus, the present data provide an estimate of cochlear contributions to simultaneous masking independent of other factors that might play a role during psychoacoustical experiments. Therefore, the use of DPOAE suppression measurements, in combination with behavioral studies of simultaneous masking, might provide insights into how different factors contribute to psychophysical data. Future work will explore this directly by measuring DPOAE suppression and behavioral masking in the same group of subjects using similar paradigms for both measurements.

The bimodal pattern that was observed when iso-suppression contours were normalized to L^2 (bottom row of panels, Fig. 5) would be consistent with an active, highly tuned mechanism at low levels and a passive, more broadly tuned mechanism operating at high levels: In this interpretation, the active, low-level mechanism is evident when $f_2 \approx f_3$.

Additionally, it might be possible to apply these techniques with patients having mild hearing loss in order to describe any changes in upward spread of suppression as a consequence of cochlear damage. One would predict an increase in upward spread of suppression in ears with hearing loss if these measures reflect underlying cochlear frequency selectivity, given the well-documented changes to FTCs as a consequence of hair cell damage (e.g., Kiang *et al.*, 1976; Dallos and Harris, 1978; Liberman and Dodds, 1984). While the present results showed that spread of suppression increased with level in normal ears, greater spread might be observed in ears for which frequency selectivity is further reduced by hearing loss. Furthermore, it may be the case that ears with hearing loss do not produce two modes, depending on level, which was evident in the present data from subjects with normal hearing. Rather, one might expect to observe only the broad pattern that was observed at high levels in normal-hearing ears. Of course, all of these measurements likely will be restricted to individuals with mild hearing loss,

given the reliance on DPOAE measurements, which are absent in most ears with moderate or greater hearing loss.

In contrast to these predictions is the work that has suggested that DPOAE data and other physiological results do not agree when reversible damage exists (e.g., Rubsamen *et al.*, 1995; Martin *et al.*, 1998; Howard *et al.*, 2002). In these studies, it was not uncommon to find normal DPOAE suppression tuning curves following cochlear insult with such agents as noise or furosemide. These results are surprising in light of what is known regarding changes in cochlear tuning with damage to the cochlear mechanisms responsible for nonlinear behavior. They suggest that DPOAE measurements and other physiological measures are not describing similar underlying behaviors. Alternatively, perhaps more agreement would have been observed between DPOAE and other estimates of tuning if more permanent lesions were induced. This explanation is not entirely satisfying, since there are studies demonstrating changes in other physiological responses following reversible insult. In either case, there would be value in exploring DPOAE estimates of tuning (whether suppression tuning curves or upward spread of masking) in humans with hearing loss to determine the extent to which these measures depend on sensitivity.

ACKNOWLEDGMENTS

Abbas, P. J., and Gorga, M. P. (**1981**). "AP responses in forward-masking paradigms and their relationship to responses of auditory-nerve fibers," J. Acoust. Soc. Am. **69**, 492–499.

Abdala, C. (**1998**). "A developmental study of distortion product otoacoustic emission ($2f_1 - f_2$) suppression in humans," Hear. Res. **121**, 125–138.

Abdala, C. (**2001**). "Maturation of the human cochlear amplifier: Distortion product otoacoustic emission suppression tuning curves recorded at low and high primary levels," J. Acoust. Soc. Am. **110**, 1465–1476.

Abdala, C., Sininger, Y. S., Ekelid, M., and Zeng, F-G. (**1996**). "Distortion product otoacoustic emission suppression tuning curves in human adults and neonates," Hear. Res. **98**, 38–53.

American National Standards Institute (**1996**). "Specifications for Audiometers," ANSI S3.6, American Institute of Physics.

Brown, A. M., and Kemp, D. T. (**1984**). "Suppressibility of the $2f_1 - f_2$ stimulated acoustic emission is gerbil and man," Hear. Res. **13**, 29–37.

Dallos, P. J., and Cheatham, M. A. (**1976**). "Compound action potential (AP) tuning curves," J. Acoust. Soc. Am. **59**, 591–597.

Dallos, P. J., and Harris, D. M. (**1978**). "Properties of auditory-nerve responses in the absence of outer hair cells," J. Neurophysiol. **41**, 365–383.

Delgutte, B. (**1990**). "Two-tone rate suppression in auditory-nerve fibers: Dependence on suppressor frequency and level," Hear. Res. **49**, 225–246.

Delgutte, B. (**1996**). "Physiological basis for basic auditory percepts," in *Auditory Computation*, edited by H. L. Hawkins, T. A. McMullan, A. N. Popper, and R. R. Fay (Springer-Verlag, New York), pp. 157–220.

Dorn, P. A., Konrad-Martin, D., Neely, S. T., Keefe, D. H., Cyr, E., and Gorga, M. P. (**2001**). "Distortion product otoacoustic emission input/output functions in normal-hearing and hearing-impaired ears," J. Acoust. Soc. Am. **110**, 3119–3131.

Egan, J. P., and Hake, H. W. (**1950**). "On the masking pattern of a simple auditory stimulus," J. Acoust. Soc. Am. **22**, 622–630.

2918   J. Acoust. Soc. Am., Vol. 112, No. 6, December 2002

Gorga *et al.*: Suppression in DPOAE measurements

Eggermont, J. J. (**1977**). "Compound action potential tuning curves in normal and pathological human ears," J. Acoust. Soc. Am. **62**, 1247–1251.

Florentine, M., Buus, S., Scharf, B., and Zwicker, E. (**1980**). "Frequency selectivity in normally-hearing and hearing-impaired observers," J. Speech Hear. Res. **23**, 646–669.

Furukawa, T., and Matsuura, S. (**1978**). "Adaptive rundown of excitatory post-synaptic potentials at synapses between hair cells and eight-nerve fibers in the goldfish," J. Physiol **276**, 193–210.

Furukawa, T., Hayashida, Y., and Matsuura, S. (**1978**). "Quantal analysis of the size of excitatory post-synaptic potentials at synapses between hair cells and afferent nerve fibers in foldfish," J. Physiol. **276**, 211–226.

Gorga, M. P., and Abbas, P. J. (**1981**). "Forward-masking AP tuning curves in normal and in acoustically traumatized ears," J. Acoust. Soc. Am. **70**, 1322–1330.

Gorga, M. P., Neely, S. T., Dorn, P. A., and Konrad-Martin, D. (**2002**). "The use of distortion product otoacoustic emission suppression as an estimate of response growth," J. Acoust. Soc. Am. **111**, 271–284.

Gorga, M. P., McGee, J., Walsh, E. J., Javel, E., and Farley, G. R. (**1983**). "ABR measurements in the cat using a forward-masking paradigm," J. Acoust. Soc. Am. **73**, 256–261.

Harris, D. M. (**1979**). "Action potential suppression, tuning curves, and threshold: Comparison with single fiber data," Hear. Res. **1**, 133–154.

Harris, D. M., and Dallos, P. J. (**1979**). "Forward masking of auditory nerve fiber responses," J. Neurophysiol. **42**, 1083–1107.

Harris, F. P., Probst, R., and Xu, L. (**1992**). "Suppression of the $2f_1-f_2$ otoacoustic emission in humans," Hear. Res. **64**, 133–141.

Harrison, R. U., Aran, J.-M., and Erre, J.-P. (**1981**). "AP tuning curves from normal and pathological human and guinea pig cochleas," J. Acoust. Soc. Am. **69**, 1374–1385.

Howard, M. A., Stagner, B. B., Lonsbur-Martin, B. L., and Martin, G. K. (**2002**). "Effects of reversible noise exposure on the suppression tuning of rabbit distortion-product otoacoustic emissions," J. Acoust. Soc. Am. **111**, 285–296.

Janssen, T., Kummer, P., and Arnold, W. (**1998**). "Growth behavior of the $2f_1-f_2$ distortion product otoacoustic emission in tinnitus," J. Acoust. Soc. Am. **103**, 3418–3430.

Kemp, D. T., and Brown, A. M. (**1983**). "A comparison of mechanical nonlinearities in the cochleae of man and gerbil from ear canal measurements," in *Hearing: Physiological Basis and Psychophysics*, edited by R. Klinke and R. Hartman (Springer-Verlag, Berlin), pp. 82–88.

Kiang, N. Y.-S., and Moxon, E. C. (**1974**). "Tails of tuning curves of auditory-nerve fibers," J. Acoust. Soc. Am. **55**, 620–630.

Kiang, N. Y.-S., Liberman, M. C., and Levine, R. A. (**1976**). "Auditory-nerve activity in cats exposed to ototoxic drugs and high-intensity sounds," Ann. Otol. Rhinol. Laryngol. **85**, 752–768.

Kiang, N. Y.-S., Watanabe, T., Thomas, E. C., and Clark, L. F. (**1965**). "Discharge patterns of single fibers in the cat's auditory nerve," MIT Res. Monogr. No. 35.

Kim, D. O. (**1983**). "Spatiotemporal resonse patterns in populations of cochlear nerve fibers: Single- and two-tone studies," Ann. N.Y. Acad. Sci. **405**, 68–78.

Kim, D. O., and Molnar, C. E. (**1979**). "A population study of cochlear nerve fibers: Comparison of spatial distributions of average-rate and phase-locking measures of responses to single tones," J. Neurophysiol. **42**, 16–30.

Kim, D. O., Chang, S. O., and Sirianni, J. G. (**1990**). "A population study of auditory-nerve fivers in unanesthetized decerebrate cats: Response to pure tones," J. Acoust. Soc. Am. **87**, 1648–1655.

Kummer, P., Janssen, T., and Arnold, W. (**1995**). "Suppression tuning characteristics of the $2f_1-f_2$ distortion-product otoacoustic emission in humans," J. Acoust. Soc. Am. **98**, 197–210.

Kummer, P., Janssen, T., and Arnold, W. (**1998**). "The level and growth behavior of the $2f_1-f_2$ distortion product otoacoustic emission and its relationship to auditory sensitivity in normal hearing and cochlear hearing loss," J. Acoust. Soc. Am. **103**, 3431–3444.

Kummer, P., Janssen, T., Hulin, P., and Arnold, W. (**2000**). "Optimal L_1-L_2 primary tone level separation remains independent of test frequency in humans," Hear. Res. **146**, 47–56.

Liberman, M. C. (**1978**). "Auditory-nerve responses from cats raised in a low-noise chamber," J. Acoust. Soc. Am. **63**, 442–455.

Liberman, M. C., and Kiang, N. Y. S. (**1978**). "Acoustic trauma in cats: Cochlear pathology and auditory-nerve activity," Acta Oto-Laryngol., Suppl. **358**, 1–63.

Liberman, M. C., and Dodds, L. W. (**1984**). "Single-unit labeling and chronic cochlear pathology. III. Stereocilia damage and alterations of threshold tuning curves," Hear. Res. **16**, 55–74.

Martin, G. K., Lonsbury-Martin, B. L., Probst, R., Scheinin, S. A., and Coats, A. C. (**1987**). "Acoustic distortion products in rabbit ear canal. II. Sites of origin revealed by suppression contours and pure-tone exposures," Hear. Res. **28**, 191–208.

Martin, G. K., Jassir, D., Stagner, B. B., and Lonsbury-Martin, B. L. (**1998**). "Effects of loop diuretics on the suppression tuning of distortion-product otoacoustic emissions in rabbits," J. Acoust. Soc. Am. **104**, 972–983.

Martin, G. K., Stagner, B. B., Jassir, D., Telischi, F. F., and Lonsbury-Martin, B. L. (**1999**). "Suppression and enhancement of distortion-product otoacoustic emissions by interference tones above f_2. I. Basic findings in rabbits," Hear. Res. **136**, 105–123.

Neely, S. T., and Liu, Z. (**1994**). "EMAV: Otoacoustic emission averager," Tech. Memo No. 17 (Boys Town National Research Hospital, Omaha, NE).

Nelson, D. A., and Turner, C. W. (**1980**). "Decay of masking and frequency resolution in sensorineural hearing-impaired listeners," in *Psychophysical, Physiological, and Behavioral Studies of Hearing*, edited by G. van den Brink and F. A. Bilsen (Delft U.P., The Netherlands), pp. 175–182.

Oxenham, A. J., and Plack, C. J. (**1998**). "Suppression and the upward spread of masking," J. Acoust. Soc. Am. **104**, 3500–3510.

Pfeiffer, R. R., and Kim, D. O. (**1975**). "Cochlear nerve fiber responses: Distributions along the cochlear partition," J. Acoust. Soc. Am. **58**, 867–869.

Plack, C. J., and Oxenham, A. J. (**1998**). "Basilar-membrane nonlinearity and the growth of forward masking," J. Acoust. Soc. Am. **103**, 1598–1608.

Rhode, W. S., and Recio, A. (**2000**). "Study of mechanical motions in the basal region of the chinchilla cochlea," J. Acoust. Soc. Am. **107**, 3317–3332.

Robles, L., and Ruggero, M. A. (**2001**). "Mechanics of the mammalian cochlea," Physiol. Rev. **81**, 1305–1352.

Rubsamen, R., Mills, D. M., and Rubel, E. W. (**1995**). "Effects of furosemide on distortion product otoacoustic emissions and on neuronal responses in the anteroventral cochlear nucleus," J. Neurophysiol. **74**, 1628–1638.

Ruggero, M. A., and Rich, N. C. (**1991**). "Furosemide alters organ of cortin mechanics: Evidence for feedback of outer hair cells upon the basilar membrane," J. Neurol. **11**, 1057–1067.

Ruggero, M. A., Robles, L., and Rich, N. C. (**1992**). "Two-tone suppression in the basilar membrane of the cochlea: Mechanical basis of auditory-nerve rate suppression," J. Neurophysiol. **68**, 1087–1099.

Ruggero, M. A., Rich, N. C., Recio, A., Narayan, S. S., and Robles, L. (**1997**). "Basilar-membrane responses to tones at the base of the chinchilla cochlea," J. Acoust. Soc. Am. **101**, 2151–2163.

Ruggero, M. A., Narayan, S. S., Temchin, A. N., and Recio, A. (**2000**). "Mechanical bases of frequency tuning and neural excitation at the base of the cochlea: Comparison of basilar-membrane vibrations and auditory-nerve-fiber responses in chinchilla," Proc. Natl. Acad. Sci. U.S.A. **97**, 11744–11750.

Ryan, A., Dallos, P., and McGee, T. (**1979**). "Psychophysical tuning curves and auditory thresholds after hair cell damage in the chinchilla," J. Acoust. Soc. Am. **66**, 370–378.

Sachs, M. B., and Abbas, P. J. (**1974**). "Rate versus level functions for auditory-nerve fibers in cats: Tone-burst responses," J. Acoust. Soc. Am. **56**, 1835–1847.

Sellick, P. M., Patuzzi, R., and Johnstone, B. M. (**1982**). "Measurement of basilar membrane motion in the guinea pig using the Mossbauer technique," J. Acoust. Soc. Am. **72**, 131–141.

Siegel, J. H. (**1994**). "Ear-canal standing waves and high-frequency sound calibration using otoacoustic emission probes," J. Acoust. Soc. Am. **95**, 2589–2597.

Siegel, J. H. (**2002**). "Calibrating otoacoustic emission probes," in *Otoacoustic Emissions: Clinical Applications*, 2nd ed., edited by M. S. Robinette and T. J. Glattke (Thieme Medical, New York), pp. 416–441.

Smith, R. L. (**1977**). "Short-term adaptation in single auditory-nerve fibers: Some postimulatory effects," J. Neurophysiol. **40**, 1098–1112.

Smith, R. L. (**1979**). ''Adaptation, saturation and physiological masking in single auditory-nerve fibers,'' J. Acoust. Soc. Am. **65**, 166–178.

Smoorenburg, G. F., and van Heusden, E. (**1979**). ''Effects of acute noise traumata on whole-nerve and single-unit activity,'' Arch. Oto-Rhino-Laryngol. **224**, 117–124.

Wegel, R. L., and Lane, C. E. (**1924**). ''The auditory masking of one pure tone by another and its probable relation to the dynamics of the inner ear,'' Phys. Rev. **23**, 266–285.

Wightman, F., McGee, T., and Kramer, M. (**1977**). ''Factors influencing frequency selectivity in normal and hearing-impaired listeners,'' in *Psychophysics and Physiology of Hearing*, edited by E. F. Evans and J. P. Wilson (Academic, London), pp. 295–306.

Spectro-temporal processing in the envelope-frequency domain

Stephan D. Ewert,[a] Jesko L. Verhey,[b] and Torsten Dau[c]
Carl von Ossietzky Universität Oldenburg, Medizinische Physik, D-26111 Oldenburg, Germany

The frequency selectivity for amplitude modulation applied to tonal carriers and the role of beats between modulators in modulation masking were studied. Beats between the masker and signal modulation as well as intrinsic envelope fluctuations of narrow-band-noise modulators are characterized by fluctuations in the ''second-order'' envelope (referred to as the ''venelope'' in the following). In experiment 1, masked threshold patterns (MTPs), representing signal modulation threshold as a function of masker-modulation frequency, were obtained for signal-modulation frequencies of 4, 16, and 64 Hz in the presence of a narrow-band-noise masker modulation, both applied to the same sinusoidal carrier. Carrier frequencies of 1.4, 2.8, and 5.5 kHz were used. The shape and relative bandwidth of the MTPs were found to be independent of the signal-modulation frequency and the carrier frequency. Experiment 2 investigated the extent to which the detection of beats between signal and masker modulation is involved in tone-in-noise (TN), noise-in-tone (NT), and tone-in-tone (TT) modulation masking, whereby the TN condition was similar to the one used in the first experiment. A signal-modulation frequency of 64 Hz, applied to a 2.8-kHz carrier, was tested. Thresholds in the NT condition were always lower than in the TN condition, analogous to the masking effects known from corresponding experiments in the audio-frequency domain. TT masking conditions generally produced the lowest thresholds and were strongly influenced by the detection of beats between the signal and the masker modulation. In experiment 3, TT masked-threshold patterns were obtained in the presence of an additional sinusoidal masker at the beat frequency. Signal-modulation frequencies of 32, 64, and 128 Hz, applied to a 2.8-kHz carrier, were used. It was found that the presence of an additional modulation at the beat frequency hampered the subject's ability to detect the envelope beats and raised thresholds up to a level comparable to that found in the TN condition. The results of the current study suggest that (i) venelope fluctuations play a similar role in modulation masking as envelope fluctuations do in spectral masking, and (ii) envelope and venelope fluctuations are processed by a common mechanism. To interpret the empirical findings, a general model structure for the processing of envelope and venelope fluctuations is proposed. © *2002 Acoustical Society of America.* [DOI: 10.1121/1.1515735]

I. INTRODUCTION

The temporal envelope of a stimulus is known to play an important role for the perception of everyday-life sounds. Even in psychoacoustic experiments that are primarily related to the *spectral* resolution of the auditory system, such as masking patterns, the information of the temporal envelope often cannot be ignored. Masking patterns have long been used to illustrate the frequency selectivity of the auditory system and have been used as a tool for estimating the spread of excitation of the masker within the cochlea (e.g., Wegel and Lane, 1924; Fletcher and Munson, 1937; Zwicker, 1956). They are typically obtained by measuring threshold for a signal as a function of the signal frequency in the presence of a masker with fixed frequency and level. The masking patterns of narrow-band sounds, either sinusoids or bands of noise, have been measured in many experiments. It became apparent that the masking patterns showed complex features that could not be readily explained in terms of spread of excitation. In particular, temporal envelope fluctuations (modulations) were shown to strongly influence the ''spectral masking'' data in some conditions. For example, if the masking of a tonal signal by a tonal masker (tone-in-tone masking) is measured, the beats between the masker and the signal provide an important cue if the spectral separation between the signal and the masker is small (Wegel and Lane, 1924; Fletcher and Munson, 1937; Egan and Hake, 1950; Ehmer, 1959). Interestingly, beats appear to be less salient if a narrow-band noise is used instead of a tone as the masker (e.g., tone-in-noise masking). In such a condition, it is assumed that the intrinsic envelope fluctuations of the noise at least partly mask the beat cue. On the other hand, these inherent fluctuations of the noise can also provide a detection cue if the role of the signal and the masker is reversed, i.e., if a narrow-band noise acts as the signal and is masked by a tone (noise-in-tone masking). In such a reversed condition, much lower thresholds are generally observed (Hall, 1997).

The role of temporal cues, such as beats and intrinsic envelope fluctuations, in spectral masking has recently been investigated quantitatively by Derleth and Dau (2000) and

Verhey (2002). Predictions from the modulation-filterbank model by Dau *et al.* (1997a, b), which performs a combined spectro-temporal signal analysis, were compared to experimental data from Hall (1997). The model could generally describe the masking data reasonably well, whereas predictions from a version of the model that acts like an energy detector failed in some conditions. Within the framework of the processing model, the modulation filterbank concept allowed for the explanation of both the detection of beats as well as the masking of beats when inherent envelope fluctuations of similar spectral content as the beats are present at the same time.

Several recent studies of amplitude-modulation detection with two- or multicomponent modulators have revealed that beats between the components may become a salient cue in modulation masking experiments (e.g., Fassel, 1994; Strickland and Viemeister, 1996; Sheft and Yost, 1997; Ewert and Dau, 2000). Furthermore, Moore *et al.* (1999) demonstrated that the threshold for 5-Hz signal modulation was affected by the presence of a two-component masker modulator beating at a 5-Hz rate. The threshold was dependent on the phase of the signal modulation relative to the beat cycle of the masker modulators. In two recent studies, Lorenzi *et al.* (2001a, b) measured detection thresholds for slow sinusoidal variations of the modulation depth of a ''carrier'' amplitude modulation applied to noise and pure-tone carriers. It was shown that in some conditions the resulting ''second-order'' modulation detection thresholds were close to those for ''first-order'' modulations. The above findings suggest that these slow fluctuations, not present in the envelope spectrum of the stimuli, are perceptually relevant in several experimental conditions.

Second-order modulations and beats between modulators can be mathematically well described in terms of the second-order envelope for arbitrary stimuli (see the Appendix). Throughout the present paper, the new term ''venelope'' is used to describe the envelope of the ac-coupled envelope. Figure 1 illustrates the relation between envelope and venelope. The upper left panel shows the temporal waveform of a sinusoidal carrier that is modulated at two frequencies (64 and 80 Hz). The lower left panel shows the envelope of the stimulus (solid line). The envelope spectrum is given in the upper right panel of the figure. While the envelope spectrum shows two peaks at the frequencies of the primary components, the temporal waveform also contains a slow variation of the modulation depth, with a periodicity equal to the difference frequency of the two primary components. The venelope is indicated as the dashed line in the lower left panel of Fig. 1. The lower right panel shows the spectrum of the venelope. In the given example, the venelope is a rectified sinusoid and the venelope spectrum consists of equally spaced components with a fundamental at the beat frequency and harmonics that decrease in amplitude with increasing frequency.

The present study investigates if the venelope can produce similar effects in masking experiments in the envelope-frequency domain as were found for the envelope in the audio-frequency domain. In analogy to the spectral masking experiments in the audio-frequency domain, tones and
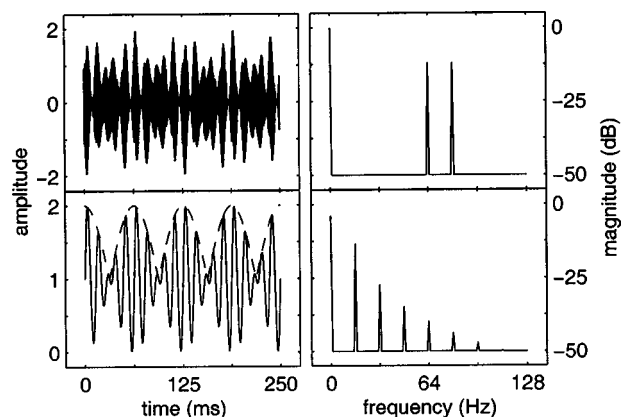
FIG. 1. Sample representation of the stimuli used in the present study. The upper left panel shows the waveform of a 2.8-kHz tone modulated by the sum of two sinusoids at 64 and 80 Hz, respectively. Its Hilbert envelope (solid curve) and venelope (dashed curve) are shown in the lower left panel. The upper right panel displays the envelope-power spectrum of the stimulus. The lower right panel the venelope-power spectrum.

narrow-band noises were used as the signal and the masker modulation. In order to avoid the possibility that inherent fluctuations of the carrier influence the results, sinusoidal carriers were used in the present study. Experiment 1 investigates modulation masking using carrier frequencies of 1.4, 2.8, and 5.5 kHz. These frequencies were chosen to cover the midfrequency audio range from earlier modulation-masking studies with broadband noise carriers (Bacon and Grantham, 1989; Houtgast, 1989; Ewert and Dau, 2000). The goal was to obtain information on modulation processing in the three separate frequency regions. The modulation masking paradigm was the same as described earlier in Ewert and Dau (2000): A masked threshold pattern (MTP) was obtained for a fixed signal-modulation frequency in the presence of a narrow-band-noise masker modulation. The spectral position of the masker modulation was shifted relative to the signal modulation. The experiment served as a reference for experiments 2 and 3, described below. The fixed signal frequency approach was also used by Takahashi and Bacon (1992) and Lorenzi *et al.* (1997). This paradigm is particularly suitable for the derivation of modulation filters. In contrast, masking patterns where a fixed masker and a variable signal frequency is used (e.g., Houtgast, 1989; Bacon and Grantham, 1989), would reflect a ''modulation excitation pattern'' evoked by the masker modulation, analogous to the excitation patterns commonly described in the audio-frequency domain (e.g., Zwicker and Feldtkeller, 1967; Moore and Glasberg, 1986). Hence, the shape of the masking pattern for a particular masker would not directly reflect the shape of a specific modulation filter.

In experiment 2, masking patterns with different stimulus types for the signal and the masker are investigated. Narrow-band noises or tones were used for the signal and the masker modulation and several signal–masker combinations were considered. The experiment is focused on a set of parameters where beats between the signal and masker modulation might have played a role in experiment 1. The experiment examines whether beats between modulations play the same role in tone-in-noise, noise-in-tone, and tone-in-tone

masking in the envelope-frequency domain, as they do in comparable masking experiments in the audio-frequency domain.

Experiment 3 addresses the question whether envelope fluctuations and venelope fluctuations (the beats between the modulator components) can interact when they lie in a similar range of frequencies. A masking effect might be expected from the results of Moore *et al.* (1999), who showed an interference when the task was to detect an amplitude modulation in the presence of a venelope component at the same frequency. However, Lorenzi *et al.* (2001b) showed that the detection of envelope beat cues cannot be abolished when using a narrow-band noise carrier. In this case, the inherent envelope fluctuations of the carrier showed only a small effect on the detectability of venelope fluctuations in the same frequency range. Experiment 3 investigates whether the detection of beats between a sinusoidal signal modulation and a sinusoidal masker modulation is influenced by an additional sinusoidal masker modulation at the beat frequency.

Based on the experimental findings, a general model structure for the processing of the envelope and the venelope is proposed.

II. EXPERIMENT 1: ENVELOPE-FREQUENCY SELECTIVITY USING SINUSOIDAL CARRIERS

A. Method

1. Subjects

Three normal-hearing subjects participated in the study. Their age ranged from 26 to 29 years. All subjects had experience in other psychoacoustic experiments. One of the subjects (S3) was author SE; the other subjects were paid an hourly wage for their participation.

2. Apparatus and stimuli

Subjects listened diotically via Sennheiser HD 25 headphones while seated in a sound-attenuating booth. Signal generation and presentation during the experiments were computer controlled using the signal-processing software package SI developed at the Drittes Physikalisches Institut at the University of Göttingen. The stimuli were digitally generated on a Silicon Graphics workstation at a sampling rate of 32 kHz and converted to analog signals by an onboard two-channel 16-bit DAC including reconstruction filtering. A sinusoidal signal modulation and a narrow-band Gaussian-noise masker modulation were applied to a pure-tone carrier. Sinusoidal carriers at 1.4, 2.8, and 5.5 kHz were used. The duration of the carrier was 600 ms, including 50-ms $\cos^2$ onset and offset ramps. The modulation started 50 ms after carrier onset, ended 50 ms before carrier offset, and was gated with 50-ms $\cos^2$ ramps. The signal modulation frequency was 4, 16, or 64 Hz. For each signal frequency, the spectral position of the masker modulation was varied in the range from -2 to $+2$ octaves relative to the signal frequency, using a step size of 2/3 octaves. In order to avoid spectral cues because of partly resolved spectral components, the maximum masker-modulation frequency was chosen in proportion to the carrier frequency. It was 64, 128, and 256 Hz for the carrier frequencies 1.4, 2.8, and 5.5 kHz, respec-

tively. The bandwidth of the masker modulation was fixed at 1.4, 5.6, and 22.3 Hz for the signal frequencies of 4, 16, and 64 Hz, respectively. For the masker centered at the signal frequency (on-frequency condition) this corresponded to a 1/2-octave bandwidth. The root-mean-square (rms) modulation depth of the masker was -10 dB in all conditions. The signal modulation started at a positive-going zero crossing. A masker realization of 2^{16} samples (approximately 2 seconds) was generated before each threshold run. In each presentation interval during the experimental run, the masker waveform $m_m(t)$ was cut randomly from the long realization. The stimuli are as follows:

$$s(t) = a\{\sin(2\pi f_c t)[1 + m\sin(2\pi f_s t)][1 + bm_m(t)]\},$$
(1)

where f_c is the carrier frequency, m is the signal modulation depth and f_s represents the signal-modulation frequency. Setting b to zero eliminates the masker modulation, as used to determine the (unmasked) reference threshold. This multiplicative approach of combining signal and masker modulation was also used in Houtgast (1989) and Ewert and Dau (2000). To avoid possible level cues due to the presence of the signal modulation, the stimuli were adjusted to have equal energy in each interval of the forced-choice trial. The overall presentation level was 65 dB SPL.

3. Procedure

A three-interval, three-alternative forced-choice paradigm was used to measure modulation-detection thresholds. The psychophysical task was to identify the one randomly chosen interval containing the signal modulation. The two other intervals contained either no modulation or only the masker modulation. The modulation depth of the signal was varied in dB ($20\log m$) using a one-up, two-down procedure, estimating the 70.7%-correct point of the psychometric function (Levitt, 1971). The three observation intervals were separated by 500 ms. The step size in each run was initially 4 dB and was divided by 2 after every second reversal until it reached 1 dB. At this step size, eight reversals were obtained and the threshold estimate was calculated as the mean value of $20\log m$ at these reversals. Each threshold reported represents the mean of the estimates from at least three runs. On the rare occasions when the standard deviation of the three estimates exceeded 3 dB, an additional estimate was obtained and the first estimate was discarded.

B. Results

The pattern of results was similar for the three subjects, so the mean data and standard deviations are shown in Fig. 2. The three panels show data for the different carrier frequencies of 5.5 kHz (top panel), 2.8 kHz (middle panel), and 1.4 kHz (bottom panel). Masked thresholds (solid lines) are shown for the signal frequencies 4 Hz (circles), 16 Hz (squares), and 64 Hz (diamonds). In addition, each panel shows the "absolute" thresholds where no masker modulation was presented (dashed line). For the different signal frequencies, these thresholds are indicated by the corresponding

J. Acoust. Soc. Am., Vol. 112, No. 6, December 2002

Ewert *et al.*: Spectro-temporal envelope processing   2923
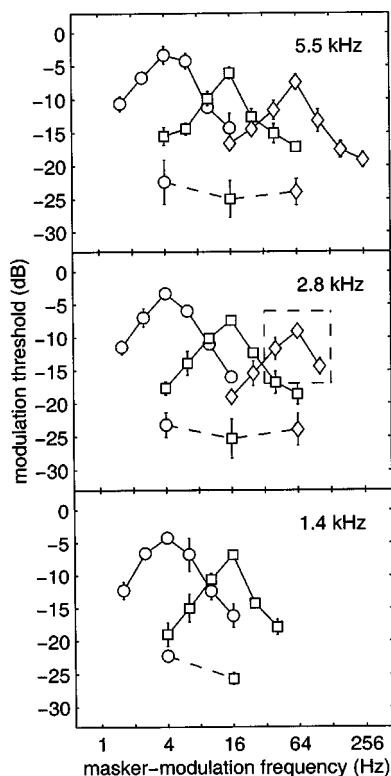
FIG. 2. Average masked-threshold patterns for signal frequencies of 4 Hz (circles), 16 Hz (squares), 64 Hz (diamonds) and carrier frequencies of 5.5 kHz (upper panel), 2.8 kHz (middle panel), and 1.4 kHz (bottom panel). The signal-modulation depth at threshold is plotted as a function of the masker frequency. The masker level was always −10 dB. In each on-frequency condition, the noise masker was one-half-octave wide. The absolute band-width was held constant when the masker was shifted in the range from −2 to +2 octaves relative to the signal frequency (see the text). The dashed curve represents the "reference" thresholds without modulation masker. The dashed box refers to the focus of the second experiment.

TABLE I. Best-fitting Q values for the second-order bandpass filters at center frequency cf as assumed within the framework of the EPSM. The value was fitted to the masked-threshold patterns from Fig. 2. A least-square fitting procedure was used. Corresponding −3-dB bandwidths of the filters are given in parentheses. The bar denotes a condition where no empirical date were obtained.

	Carrier frequency		
cf (Hz)	1.4 kHz	2.8 kHz	5.5 kHz
4	1.29 (3.1)	1.24 (3.2)	1.10 (3.6)
16	1.82 (8.8)	1.16 (13.8)	1.03 (15.5)
64	—	1.15 (55.5)	1.25 (51.4)

tion filter centered at the signal-modulation frequency. A second-order bandpass filter was chosen for the modulation filter. The bandwidth of the filter is easily described with a single variable, the Q value. Its transfer function provides the required symmetry on a logarithmic frequency scale, as observed in the data. In order to account for the increasing asymmetry of the filter shape observed for the higher masker center frequencies (>64), a first-order low-pass filter with a cutoff frequency of 150 Hz was combined with the bandpass filter tuned to the signal frequency. The low-pass filter function also resembles a general loss in sensitivity to high-frequency amplitude modulations according to the data described in Kohlrausch et al. (2000). Table I shows the best fitting Q values and −3-dB bandwidths in Hz (in parentheses) for each of the patterns in Fig. 2.

The Q values range from 1 (for the 16-Hz signal and the 5.5-kHz carrier) to 1.8 (for the 16-Hz signal and the 1.4-kHz carrier). The average Q value across all eight patterns is 1.26(±0.23). Except for the 16-Hz signal at 1.4 kHz (Q =1.8), all estimates lie very close to the average value. Thus, the envelope-frequency selectivity can be characterized well by an estimated Q value of about 1.25. Filter shape and Q value do not depend systematically on either the signal-modulation frequency or the carrier frequency for the range of parameters tested here. The results are in qualitative agreement with the findings in Ewert and Dau (2000). They estimated the modulation-filter shape and bandwidth using the same experimental paradigm for broadband noise carriers, and found an average Q value of about 1. However, their estimates showed somewhat more variability across the conditions. The present data are also consistent with the modulation masking data by Houtgast (1989) and Bacon and Grantham (1989) obtained with a different experimental paradigm than that used in the present study. Both studies used a noise carrier and fixed the masker (center) frequency while the signal frequency was varied. The present data are also in agreement with the results of Lorenzi et al. (2001a) using a different paradigm (see Sec. V).

III. EXPERIMENT 2: THE ROLE OF ENVELOPE BEATS IN MODULATION MASKING

A. Rationale

This experiment investigates modulation masking obtained with different stimulus type combinations of the signal and the masker. While experiment 1 examined tone-in-noise (TN) masking, the current experiment also investigates

symbols connected by the dashed line. Note that for the lowest carrier frequency (1.4 kHz, bottom panel) the 64-Hz signal pattern was not obtained since spectrally resolved side-bands most likely would have influenced the results. The results are very similar across carrier frequency. All patterns show a peak when the masker center frequency was equal to the signal frequency. In general, the patterns are roughly symmetric and invariant in width on a relative (logarithmic) frequency scale.

The patterns for the 4-Hz signal seem to be slightly broader compared to the patterns for the higher frequencies. The 4-Hz patterns also exhibit the highest overall thresholds, with a maximum threshold of −3.6 dB, averaged across all carrier frequencies. For 16 and 64 Hz the maximum average threshold is at −6.8 and −8.2 dB, respectively.

In order to obtain a more quantitative estimate of envelope-frequency selectivity, the transfer function of a second-order bandpass filter combined with a first-order low-pass filter was fitted to the empirical data. The same method and underlying envelope power spectrum model (EPSM) as proposed in Ewert and Dau (2000) were used. This model is conceptually related to the power spectrum model of masking (Fletcher, 1940; Patterson and Moore, 1986) in the audio-frequency domain. It is assumed that thresholds are related to the integrated envelope power in the passband of a modula-

noise-in-tone (NT) as well as tone-in-tone (TT) masking. The question is whether effects similar to those found in the audio-frequency domain, as described in the introduction, can be observed in the envelope-frequency domain.

B. Method

1. Subjects

Three subjects participated in the experiment. Two of the subjects (S1 and S3) also participated in experiment 1. The third subject (S4) was the second author (JV). All subjects had clinically normal hearing and had experience in other psychoacoustic experiments. Their age ranged from 27 to 32 years. Subject S1 was paid for his participation on an hourly basis.

2. Apparatus, stimuli, and procedure

The stimuli were presented diotically via AKG K501 headphones. Subjects were seated in a sound-attenuating booth. The stimuli were generated digitally at a sampling rate of 48 kHz and converted to analog signals by a two-channel 24-bit DAC including reconstruction filtering (SEKD ADSP 2496). Signal generation and presentation during the experiments were computer controlled using the AFC (alternative forced choice) software package for MATLAB, developed at the University of Oldenburg. Modulation detection thresholds were obtained using a sinusoidal carrier of 2.8 kHz. The stimuli had a duration of 500 ms including 50-ms $\cos^2$ ramps. Signal and masker modulation were either a tone or a narrow-band noise with a bandwidth of 22.3 Hz. Several signal–masker combinations were considered: (i) tone-in-noise masking (TN), where a sinusoidal signal modulation was masked by a noise; (ii) tone-in-tone masking (TT), where a sinusoidal signal was masked by a sinusoidal masker; and (iii) noise-in-tone masking (NT), where a noise signal was masked by a tone. The signal modulation was always centered at 64 Hz. Thus, as in experiment 1, the noise had a bandwidth of 1/2 octave in the on-frequency condition where the center frequency of the masker was equal to the signal frequency. The masker was centered at -2, $-2/3$, $-1/3$, 0, 1/3, 2/3 octaves relative to the signal. The masker rms level was set to -12 dB. In one additional experiment with a tonal signal and a tonal masker modulation (TTr), the masker level was roved by ±3 dB. The roving of the modulation depth introduces a random power fluctuation to the pure-tone masker across the presentation intervals. This is more comparable to the narrow-band-noise masker condition, while in contrast to the noise masker, the pure-tone masker still exhibits no inherent fluctuations. In contrast to experiment 1, where a multiplicative approach was used, the sum of the masker and signal modulation was applied to the carrier. This results in the following equation for the stimuli:

$$s(t)=a\{\sin(2\pi f_c t)[1+mm_s(t)+bm_m(t)]\}, \qquad (2)$$

where f_c is the carrier frequency, a is the amplitude of the stimulus, m indicates the signal-modulation depth, and $m_s(t)$ represents the signal-modulation waveform. b is the masker modulation depth and $m_m(t)$ the masker modulation wave-
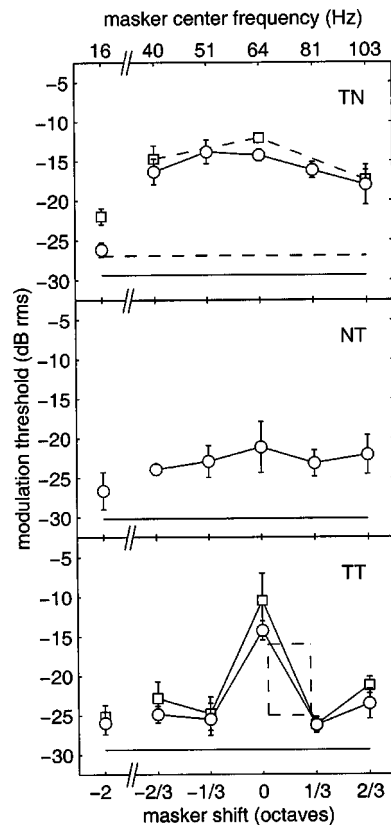
FIG. 3. Average masked-threshold patterns for a 64-Hz signal modulation as a function of the spectral position of the masker modulation. Panels show data for the tone-in-noise condition (TN, upper panel), noise-in-tone (NT, middle panel), and tone-in-tone (TT, lower panel). The lower panel shows also data for the TT condition with a 3-dB modulation-depth roving applied to the masker tone (indicated by the squares). Unmasked ("reference") thresholds for the 64-Hz signal are represented by the horizontal line in all panels. The data points connected by the dashed lines and the horizontal dashed line in the upper panel are replotted from Fig. 2. The dashed box indicates the focus of the third experiment.

form. Setting b to zero eliminates the masker modulation, as used to determine the unmasked "reference" threshold. The sinusoidal signal modulation in the TN, TT, and TTr condition as well as the sinusoidal masker modulation in the NT condition always started in sine phase. In the two tone-in-tone conditions (TT and TTr), the phase of the masker modulation was randomized. The overall presentation level was 65 dB SPL. The increase in level due to the presence of the signal and/or masker modulation was not compensated for.[1] As in experiment 1, a three-interval, three-alternative forced-choice paradigm in combination with a one-up, two-down tracking procedure was used to obtain threshold estimates.

C. Results

The results were similar across subjects, so only the mean data are presented here. The upper panel of Fig. 3 shows results for the TN condition (circles) together with the data from experiment 1 (replotted from Fig. 2), indicated as squares connected by the dashed lines. Masked thresholds are shown as a function of the masker shift (in octaves) relative to the signal (center) frequency (64 Hz). Values are given in dB rms of the modulator waveform in contrast to

J. Acoust. Soc. Am., Vol. 112, No. 6, December 2002

Ewert *et al.*: Spectro-temporal envelope processing   2925

experiment 1, where the modulation depth, m, in dB was given. This was done since m is well defined only for a sinusoidal modulation.[2] In this experiment, a smaller stepsize (1/3 octave instead of 2/3 octave) and a smaller spectral range of masker positions than in experiment 1 was used (as indicated by the dashed box in the middle panel of Fig. 2). The solid horizontal line indicates the threshold in the absence of the masker modulation (unmasked threshold). The highest masked threshold can be observed for a masker frequency slightly lower than the signal frequency ($-1/3$ octave). Masking, defined as the difference between masked and unmasked threshold, amounts to 15.5 dB in this condition. Within the range from $-2/3$ to $+2/3$ octave, masking is smallest (11.3 dB) for the $+2/3$-octave condition. For the masker presented two octaves below the signal tone, masking is further reduced to 3.2 dB.

The middle panel of Fig. 3 displays the results for the NT masking condition. While the unmasked threshold for the noise (horizontal line) is only 0.8 dB lower than that for the tone (solid horizontal line in the upper panel), the masked thresholds (circles) are considerably lower than in the TN condition shown in the upper panel. The amount of masking reaches a maximum of 9 dB for the on-frequency masker, i.e., about 6 dB less than in the TN condition. Thresholds show less variation with masker frequency than in the TN condition. For masker frequencies in the range from $-2/3$ to $+2/3$ octave relative to the signal frequency, thresholds are only 3–5 dB higher than for the masker position at -2 octaves.

Finally, the lower panel of Fig. 3 shows the data for a sinusoidal signal modulation in the presence of a sinusoidal masker modulation. Data for two different masker conditions are shown: the circles indicate thresholds for a fixed masker level (TT) while the squares represent thresholds where the masker level was roved (TTr). The two masking patterns are very similar and do not differ by more than 2 dB from each other, except for the on-frequency condition where the difference is 3.8 dB. For all masker frequencies below and above the signal frequency, thresholds are roughly independent of the masker position. A substantial increase in threshold (of about 17 dB) is only observed for the on-frequency condition where the masker frequency equals the signal frequency. In this case no beating between masker and signal modulation can occur and the only cue for the presence of the signal modulation is a variation in the overall modulation depth at the signal frequency. Since signal and masker modulation are added in random phase, the sum will result in an increase or a decrease of the overall modulation depth, depending on the phase relation between the two. This effect leads to the elevated threshold in the on-frequency condition. The level roving in the TTr condition further increases the on-frequency threshold.

IV. EXPERIMENT 3: INTERFERENCE OF ENVELOPE AND VENELOPE PROCESSING IN TONE-IN-TONE MASKING

A. Rationale

The previous experiment showed that thresholds in the tone-in-tone (TT) masking conditions are considerably lower than in the tone-in-noise (TN) masking conditions. In the TT conditions, the subjects probably use beats between the signal and the masker as an additional detection cue. Experiment 3 examines this hypothesis by adding a sinusoidal modulation component with a period equal to the beat period between signal and masker in the TT condition. If the detection of beats was responsible for the threshold difference between the TT and TN condition, the additional component should influence the results.

B. Method

Subjects, apparatus, and procedure were the same as in experiment 2. Thresholds for signal modulations of 32, 64, and 128 Hz were obtained in two masking conditions. The first one was the TT condition of experiment 2, i.e., the masker was a pure tone with an rms level of -12 dB. However, only spectral masker positions *above* the signal frequency were used (as indicated by the dashed box in the lower panel of Fig. 3 for the 64-Hz signal modulation). For a signal frequency of 128 Hz, the difference between the signal and the masker frequency was 2, 4, 8, 16, or 32 Hz, respectively. For signal frequencies of 32 and 64 Hz, the masker–signal separation was restricted to 2 to 8 and 2 to 16 Hz, respectively. In the second condition (TTm), the masker consisted of two components. The primary component was the same as used in the first condition. In addition, a second component was presented at the difference frequency between the signal and the masker. The level of this second component was roved within $-\infty$ dB (absence) and -12 dB (uniform distribution on a linear scale) in order to prevent the subjects from using any reliable information based on the absence or presence of a temporal fluctuation at the masker–signal difference (beat) frequency. The equation for the stimuli in the two conditions was

$$s(t) = a\{\sin(2\pi f_c t)[1 + m m_s(t) + b m_m(t) + r m_i(t)]\},$$
(3)

where r is the modulation depth of the random-phase interfering tone $m_i(t)$ at the difference frequency. The other abbreviations are the same as used in Eq. (2). For the first condition (TT), r was equal to zero. For the second condition (TTm), r was chosen randomly in each realization.

C. Results

Figure 4 shows average masked thresholds as a function of the spectral separation between (primary) masker and signal modulation. The three panels display results for signal frequencies of 128 Hz (top), 64 Hz (mid), and 32 Hz (bottom). The circles represent the thresholds for the TT condition. The squares indicate the thresholds obtained in the presence of the additional interferer at the difference frequency (TTm). The position of the masker was shifted in certain steps above the signal frequency, e.g., for the 128-Hz signal frequency (top panel), the resulting masker frequencies were 130, 132, 136, 144, and 160 Hz, respectively. The middle panel additionally shows the unmasked threshold for the 64-Hz signal as a horizontal line. The triangle indicates the threshold when only the interferer tone at 16 Hz was pre-
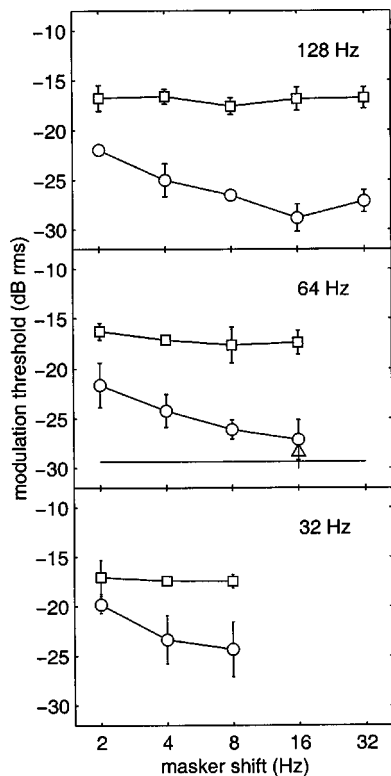
FIG. 4. Average masked-threshold patterns (circles) for signal-modulation frequencies of 128 Hz (upper panel), 64 Hz (middle panel), and 32 Hz (lower panel). The masker was always higher in frequency. The frequency difference between masker and signal is indicated at the bottom and ranged up to a quarter of the signal frequency in all conditions. The squares represent masked thresholds in presence of an additional masker modulation at the beat frequency of the signal and primary masker. The horizontal line in the middle panel indicates the unmasked threshold for the 64-Hz signal modulation.

sented. As shown in Kohlrausch *et al.* (2000), very similar unmasked thresholds can be expected for the other two signal frequencies.

The threshold patterns are similar for the three signal frequencies. In the TT conditions (circles), masked threshold decreases with increasing masker shift, except for the highest masker shift (32 Hz) for the 128-Hz signal frequency, where threshold is slightly increased (by about 2 dB) compared to the 16-Hz shift. For a masker shift of 16 Hz, threshold almost reaches the unmasked threshold for 64- and 128-Hz signal frequency. For all three signal frequencies the shape of the threshold pattern strongly changes when the interfering modulation at the masker–signal difference frequency (beat rate) is presented in addition to the signal and the (primary) masker modulation (indicated by the squares). A threshold of about −17 dB is obtained for all masker positions and all signal frequencies. This threshold is only 2.8 dB below the masked threshold obtained in the TN condition for the on-frequency masker (see Fig. 3). The average threshold difference between the two curves amounts to about 9 dB for 8-Hz masker shift and signal frequencies of 64 and 128 Hz and to about 7 dB for 32-Hz signal frequency. The maximum difference of 12 dB between the thresholds in the two conditions is observed for a masker shift of 16 Hz. The threshold increase cannot be explained by the masking effect caused by the interferer alone since the threshold for the 64-Hz sig-

nal frequency in the presence of a 16-Hz tonal interferer alone, indicated by the triangle, is only slightly higher than the unmasked threshold.

V. DISCUSSION

The primary purpose of the present study was to examine the extent to which the detection of envelope beats, or venelope fluctuations, influences modulation detection. The question was whether the detection of venelope fluctuations plays a similar role in modulation masking as does the detection of envelope fluctuations in spectral masking. While the envelope of a stimulus is extracted by the halfwave-rectifying properties of the inner hair cells, it is unclear which process may cause a "demodulation" of the venelope to the envelope domain. In the following, first the experimental results of the present study are discussed in the context of recent literature data. In the second part, a general modeling structure for the processing of the envelope and the venelope in the auditory system is proposed.

A. Experimental results

Experiment 1 examined envelope-frequency selectivity using pure-tone carriers and served as a reference for the subsequent experiments. Masked threshold patterns for three different signal-modulation frequencies (4, 16, and 64 Hz) were obtained for three carrier frequencies. The similarity of the Q values of the filters fitted to the data suggest that modulation masking can be accounted for very well by assuming an *invariant* array of modulation filters at the output of each critical band. Alternatively, the results may, in principle, also support the hypothesis that envelope information is first integrated over a wide range of audio frequencies and is then subjected to a *common* modulation filterbank. Neither of the two possible processing schemes can be excluded from the experimental findings. However, experiments on modulation detection interference (MDI) showed that results cannot easily be modeled in terms of "hard-wired" modulation cross talk across peripheral frequency channels (Hall and Grose, 1991; Oxenham and Dau, 2001). The analysis of across-frequency information seems to take place only after some degree of perceptual grouping has occurred, suggesting that information is integrated at some more central stage of processing. It therefore seems plausible to assume that envelope information is first processed separately (at different carrier frequencies) in terms of a modulation filterbank analysis, and is later combined across frequency in a way depending on the specific acoustical context of the stimuli. The assumption of an invariant modulation filterbank mechanism whose parameters do not change with carrier frequency was already made in the first model implementation described in Dau *et al.* (1997a, b).

Experiment 2 investigated modulation masking patterns obtained for one of the signal-modulation frequencies (64 Hz) and one of the carrier frequencies (2.8 kHz) used in experiment 1, whereby only spectral masker positions *close* to the signal frequency were considered. In these conditions, the low-frequency beats between the signal and the masker provided a strong detection cue depending on the stimulus type of the signal and the masker. The masking patterns ob-

J. Acoust. Soc. Am., Vol. 112, No. 6, December 2002

Ewert *et al.*: Spectro-temporal envelope processing   2927

tained for TN, NT, and TT masking conditions showed the same general characteristics as masking patterns obtained in the audio-frequency domain: A narrow-band noise is more effective in masking a tonal signal (TN) than vice versa (NT). Also, if a tonal signal is used, a narrow-band noise (TN) is a more effective masker than a tone (TT). The results are especially striking in the TT condition, where only little masking is observed, except for the on-frequency condition. However, the on-frequency condition of the TT masking pattern is comparable to a modulation-depth discrimination experiment and thus does not provide any information on modulation masking. In the framework of a model that is restricted to only the mean envelope power passing the modulation filter tuned to the signal frequency (EPSM, Ewert and Dau, 2000), the same pattern of results would be expected for all masking conditions. Such a model would not include effects of temporal venelope fluctuations originating from beats between the components of the signal and masker modulation. A masking pattern as expected from the EPSM is empirically observed only for the TN condition. This suggests that, in contrast to the TN condition, the venelope provides additional detection cues in the TT and the NT condition, similar to the envelope in the audio-frequency domain. However, it is important to realize that in the audio-frequency domain, envelope fluctuations (reflecting beats between the spectral components) and resolved spectral components have a completely different perceptual quality while in the modulation domain, venelope fluctuations (reflecting beats between envelope components) and ''resolved'' envelope components are of the *same* perceptual quality. In the latter case both evoke a temporal impression. Thus, there are two independent ''dimensions'' (perceptually and neurally) represented in the periphery, the frequency and envelope frequency axes, while there is no further independent dimension available for the coding of venelope fluctuations.

This was further supported by the results from experiment 3, where an additional modulation component at the difference frequency between the (primary) masker and the signal was imposed in a tone-in-tone masking configuration. The substantial threshold elevation observed in the presence of such an ''interferer'' clearly demonstrated that beats must have been the prominent detection cue in the TT masking condition (without the additional component). As demonstrated for the 64-Hz signal and a 16-Hz interferer, the masking effect caused by the interferer alone cannot account for the threshold increase. This should hold especially for the larger spectral separations between the signal and the interferer. Since the Q value of the modulation filters is independent of filter center frequency, the same is expected for signal frequencies of 32 and 128 Hz. The data clearly showed that the detection of a modulation strongly interferes with the beating modulators fluctuating at the same rate. This experiment differs from the experimental paradigm in Moore *et al.* (1999), since a low-frequency component was introduced in order to mask the beat cue produced by two higher frequency components while Moore *et al.*'s study investigated masking of a low-frequency component by introducing two higher frequency beating components. Nevertheless, the underlying mechanisms are probably the same in the two studies. In
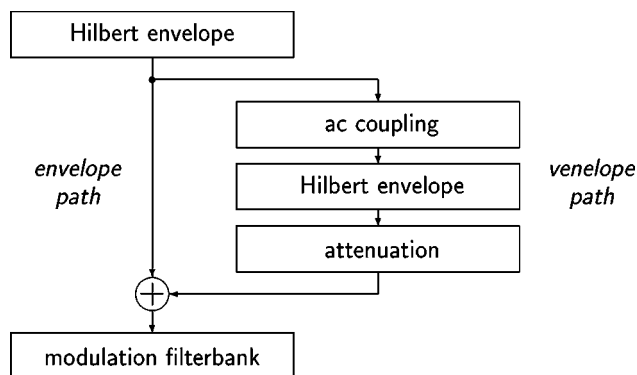
FIG. 5. General processing scheme to account for the empirical results from the present study. In parallel to the envelope path, a second path extracts the venelope (second-order envelope) of the stimulus. After attenuation (free parameter in this scheme) the venelope is added to the envelope. The resulting ''envelope'' is then subjected to a modulation filterbank.

addition, the findings in experiment 3 suggest that beats become less prominent at low rates (2 Hz) than at higher rates (8 to 16 Hz). This is probably caused by the reduced number of beat cycles available during the stimulus presentation of 500 ms.

Lorenzi *et al.* (2001b) suggested that the detection of venelope fluctuations might *not entirely* be based on the detection of the physical envelope component(s) introduced by some nonlinear process. They measured ''second-order'' modulation detection thresholds with pure-tone and 2-Hz-wide narrow-band noise carriers. In contrast to the pure-tone carrier, the narrow-band noise carrier exhibits low-frequency intrinsic envelope fluctuations (Lawson and Uhlenbeck, 1950; Dau *et al.*, 1997a, b). If venelope detection was entirely based on the detection of energy in the envelope domain, thresholds for low-frequency venelopes should be considerably higher in case of a narrow-band noise carrier than in case of a pure-tone carrier. Even though some masking was observed in that study, the amount of masking was only relatively weak compared to that observed for first-order modulations. The authors suggested that a second ''unknown'' process might be involved in the detection of the venelope, suggesting that the venelope maybe represented ''independently'' at some intermediate stage of processing.

Overall, the findings from the present study clearly suggest that (i) the venelope is extracted by the auditory system at some stage of processing and that (ii) envelope and venelope fluctuations evoke the same (temporal) perception. This suggests a common encoding scheme for the processing of the envelope and the venelope of the stimulus.

B. Possible model structures

Figure 5 shows a general processing scheme that can in principle account for the empirical results from the present study. In parallel to the envelope path, a second path extracts the venelope of the stimulus. The mathematical definition of the venelope is given in the Appendix. After some amount of attenuation (which is a free parameter in this scheme) the venelope is added to the envelope path. The resulting activity is then subjected to a modulation filterbank. Thus, it is as-
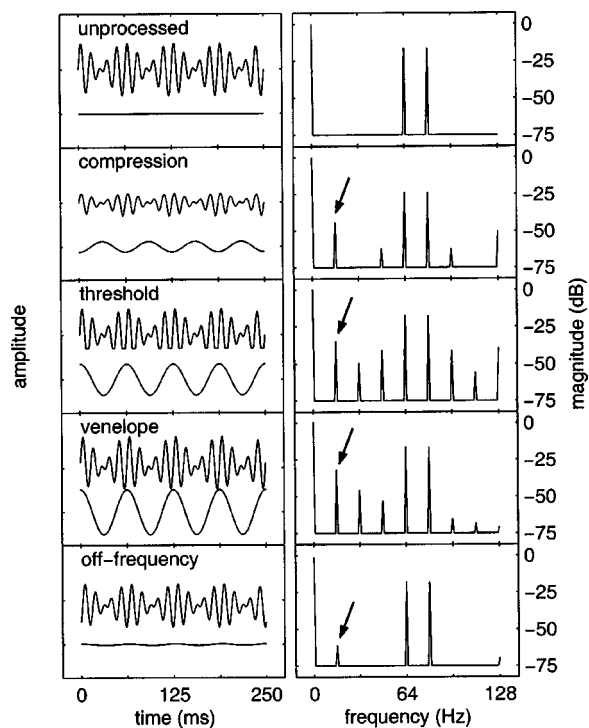
FIG. 6. Each panel of the left-hand column shows the envelope waveform (upper graph) resulting from the sum of two sinusoidal amplitude modulations at 64 and 80 Hz. The lower graph in each of the panels is the 16-Hz component of the envelope multiplied by a factor of 10. The right-hand column shows the corresponding envelope spectra. Different transformations were applied to the envelope in each row, as indicated in the left-hand panels.

sumed that the extraction of the venelope and the combination of envelope and venelope occur at a processing stage prior to the bandpass filtering process. This processing scheme represents a very simple and straightforward way to realize *functionally* an internal representation that contains envelope and venelope in the same ''dimension.'' Such a scheme is also compatible with recent data from Lorenzi *et al.* (2001a) on second-order modulation detection. Lorenzi *et al.* (2001a) concluded from their data that, if modulation filters do exist, they have to be broadly tuned (Q value less than 2) in order to avoid the detection of spectrally resolved envelope frequencies in different modulation filters. The current filters have a Q value of about 1.

Physiological mechanisms that may generate neural activity at frequencies corresponding to the venelope frequency have been discussed recently in the literature. For example, Shofner *et al.* (1996) measured responses of neurons in the chinchilla cochlear nucleus to carriers at the characteristic frequency that were amplitude modulated by two-component modulators. The study revealed evidence for a distortion component at the beat rate of the modulators. In the following, some possible mechanisms for the generation of such a component are compared to the venelope concept.

The top panels of Fig. 6 show the temporal envelope of a two-tone modulator with components of 64 and 80 Hz (left; compare to Fig. 1) and the corresponding envelope spectrum (right). There is no energy at the beat rate of 16 Hz in the stimulus envelope. The remaining panels show corresponding stimuli and spectra obtained with different transfor-

mations, all of which introduce energy at the beat rate. In addition to the envelope waveforms, the left panels also show the waveform of the component at the difference frequency. Since the energy of this component is rather small compared to that of the primary components, the waveform was multiplied by a factor of 10 for illustration. The panels in the second row show the effect of a *compressive* nonlinearity as suggested in some studies (Shofner *et al.*, 1996; Sheft and Yost, 1997; Moore *et al.*, 1999). In this case, a power-law function with an exponent of 0.4 was assumed. In the third row, the stimulus envelope was clipped at a certain threshold level, as suggested by Shofner *et al.* (1996). The fourth row displays the waveform and the spectrum at the output of the venelope model as proposed in the present study, assuming an arbitrary attenuation factor of 0.2. Finally, the bottom panel shows the envelope calculated at the output of a critical band filter tuned ''off-frequency'' to the lowest sideband originating from the modulation. All processing schemes clearly generate a physical envelope component at the beat frequency. The size of this distortion component depends on the transformation. For all transformations except the off-frequency filter scheme (bottom panel), the size of the component at the difference frequency scales with the parameters given above, i.e., the exponent, the threshold value, or the attenuation factor. The off-frequency filter scheme produces a much weaker component compared to the nonlinear transformations. Probably more importantly, the phase of the introduced component relative to the phase of the beat differs for the different transformations. A compressive nonlinearity results in a 180-degree phase shift relative to the phase of the venelope. In contrast, all other transformations produce a component in phase with the venelope, as an expansive nonlinearity (not shown) in the processing path would do. The off-frequency calculation nicely shows that it is not necessarily a nonlinear mechanism that is needed to demodulate the beat component to the envelope domain. Since the data of the present study do not depend on the relative phase between the different modulator components, they do not allow one to distinguish between the different model realizations. Critical experiments that are focused on these phase effects are described in a companion paper (Verhey *et al.*, 2002). Their results suggest that a compressive nonlinearity, such as that introduced by the input–output function of the basilar membrane (Sellick *et al.*, 1982; Ruggero *et al.*, 1997; Moore and Oxenham, 1998), does not account for their modulation beating data. This agrees with results from a recent study by Tandetnik *et al.* (2001), where it was found that second-order modulation detection thresholds were very similar in sensorineural hearing-impaired listeners and in normal-hearing listeners. Cochlear damage results in a reduction or loss of the compressive nonlinearity in the input–output function of the basilar membrane (see Moore, 1995, for a review). This suggests that the detection of venelope fluctuations is not related to nonlinear processing on the basilar membrane.

While the above-mentioned modeling schemes assumed the introduction of spectral energy at the envelope beat rate *prior* to the modulation bandpass filtering process, it is in principle also possible that low-frequency envelope beat cues

appear in the temporal pattern at the output of modulation filters tuned to the (higher) signal and masker modulation rates. Theoretically, such envelope beat cues should then not be affected by the presentation of an interfering modulator at the beat rate if the signal/masker modulation rates and the beat rates are sufficiently separated from each other. Thus, in order to predict a masking effect as observed in the data, some integration/interference mechanism across envelope frequencies would have to be assumed *after* the modulation filtering process. Such processing certainly reflects a possible alternative modeling scheme within a more complex model that preserves and analyzes the temporal structure of the output of modulation filters (unlike the EPSM). The envelope/ venelope processing scheme proposed in the present study may be considered as the most straightforward and functional model which is consistent with the experimental data from the present study. Although the envelope and venelope path are combined in order to account for the empirical data, one main feature of the venelope extraction scheme is the parallel representation of the envelope and venelope at some stage of the model, in contrast to pure ''in-line'' schemes such as the compression model by Moore *et al.* (1999). Future investigations will show how useful this approach is for the description of the internal representation(s) of the stimuli in simple and complex stimulus configurations.

VI. SUMMARY AND CONCLUSIONS

The results of this study provide further evidence that linear spectral analysis of the (first-order) envelope is not sufficient to describe all temporal properties of nonstationary stimuli that are relevant for our perception. As the ''synthetic'' stimuli used in psychoacoustical experiments, most natural sounds are not limited to a single component in the envelope spectrum. Indeed, typical everyday-life sounds like speech (Plomp, 1988; Drullman *et al.*, 1994; Greenberg and Arai, 1998) and noise-like sounds (e.g., Lawson and Uhlenbeck, 1950) exhibit a number of components in the envelope spectrum. Since the auditory system most likely processes the envelope nonlinearly, distortion components are introduced to the internal representation of the stimuli. These components were demonstrated to be perceptually highly relevant in specific modulation masking experiments. The main results of the study are as follows:

(i) Peaked masked threshold patterns (MTPs) were obtained for signal-modulation frequencies in the range from 4 to 64 Hz and a half-octave-wide noise masker, using pure-tone carriers (experiment 1). The shape of the MTPs did not depend on the carrier frequency. The estimated Q value of the filters was about 1.2. This is in good agreement with the Q value of 1 found in a previous study with broadband noise carriers (Ewert and Dau, 2000) using the same envelope power spectrum model and the same fitting procedure.

(ii) Masked threshold patterns showed large threshold variations for different combinations of sinusoidal and narrow-band noise masker and signal modulators (experiment 2). Thresholds in noise-in-tone (NT) masking conditions were always lower than in tone-

in-noise (TN) masking, similar to corresponding experiments in the audio-frequency domain. In the NT conditions, subjects use beats between the noise signal and the tone masker as a detection cue, while in the TN conditions, the beats are masked by the inherent fluctuations of the noise masker.

(iii) In tone-in-tone (TT) masking conditions, thresholds were close to the ''absolute'' threshold for spectral separations ≥4 Hz since the beats produced by the signal and the masker provided a strong detection cue. By adding an additional sinusoidal modulation at the difference frequency, the salience of the beats was strongly reduced and thresholds were raised up to 12 dB.

(iv) The venelope defined as the Hilbert envelope of the ac-coupled (first-order) Hilbert envelope provides an analytical tool for describing the interactions between the different envelope components for arbitrary multicomponent waveforms. A model structure that combines the envelope and the venelope of a stimulus was proposed to qualitatively account for the data presented here. The venelope concept is only one possible ''mechanism'' that produces distortion. A set of physiologically plausible nonlinearities were discussed. A critical test of these is undertaken in an accompanying study (Verhey *et al.*, 2002).

APPENDIX: VENELOPE

Envelope fluctuations are a feature of all waveforms except for pure tones or frequency-modulated tones. In many processing models of the auditory periphery, the envelope is derived from demodulation, realized by (half-wave) rectification followed by low-pass-filtering in order to remove the fine structure of the waveform. The (Hilbert) envelope is less physiologically motivated and reflects a mathematical description. Consider the real waveform $s(t)$: The envelope $he(t)$ of s(t) is defined as the absolute value of the corresponding analytical signal $\hat{s}(t) = s(t) + i\tilde{s}(t)$:

$$he(t) = \sqrt{s^2(t) + \tilde{s}^2(t)}. \tag{A1}$$

The imaginary part of the analytical signal is the Hilbert transform of its real part

$$\tilde{s}(t) = \mathcal{H}(s(t)) = -\frac{1}{\pi} \int_{-\infty}^{+\infty} \frac{s(t')}{t'-t} dt'. \tag{A2}$$

Following this notation, the nth-order (Hilbert) envelope $he_n(t)$ can be defined recursively by

$$he_n(t) = \sqrt{(he_{n-1}(t) - \langle he_{n-1}(t) \rangle_t)^2 + \mathcal{H}((he_{n-1}(t) - \langle he_{n-1}(t) \rangle_t)^2)} \quad n \geq 2, \tag{A3}$$

with $he_{n-1}(t) - \langle he_{n-1}(t) \rangle_t$ representing the ac-coupled $(n-1)$th-order envelope, where $\langle \rangle_t$ denotes the temporal long-term average. The second-order envelope $(n=2)$ is referred to as the venelope throughout this study. As a consequence of the diminishing power of higher-order envelopes, the second-order envelope might be the only perceptually salient one for acoustic stimuli.

[1]By the stochastic nature of the narrow-band noise signal and masker modulation, the individual noise samples in the different intervals may vary in their rms level, with a long-term average equal to -12 dB. This introduces slight level variations to the stimuli when applied to the fixed level pure-tone carrier. In order to avoid changes to the stimulus statistics, this increase in level due to the presence of the signal and/or masker modulation was not compensated for. It is, however, unlikely that the change in level caused by the signal modulation (<0.25 dB) was used as the detection cue.

[2]Note that, for the sinusoidal signal modulation, the values in dB rms are 3 dB lower than the values expressed as modulation depth, m, in dB.

Bacon, S. P., and Grantham, D. W. (**1989**). "Modulation masking: Effects of modulation frequency, depth, and phase," J. Acoust. Soc. Am. **85**, 2575–2580.

Dau, T., Kollmeier, B., and Kohlrausch, A. (**1997a**). "Modeling auditory processing of amplitude modulation. I. Modulation detection and masking with narrow-band carriers," J. Acoust. Soc. Am. **102**, 2892–2905.

Dau, T., Kollmeier, B., and Kohlrausch, A. (**1997b**). "Modeling auditory processing of amplitude modulation. II. Spectral and temporal integration in modulation detection," J. Acoust. Soc. Am. **102**, 2906–2919.

Derleth, R. P., and Dau, T. (**2000**). "On the role of envelope fluctuation processing in spectral masking," J. Acoust. Soc. Am. **108**, 285–296.

Drullman, R., Festen, J. M., and Plomp, R. (**1994**). "Effect of temporal envelope smearing on speech reception," J. Acoust. Soc. Am. **95**, 1053–1064.

Egan, J. P., and Hake, H. W. (**1950**). "On the masking pattern of a simple auditory stimulus," J. Acoust. Soc. Am. **22**, 622–630.

Ehmer, R. H. (**1959**). "Masking patterns of tones," J. Acoust. Soc. Am. **31**, 1115–1120.

Ewert, S. D., and Dau, T. (**2000**). "Characterizing frequency selectivity for envelope fluctuations," J. Acoust. Soc. Am. **108**, 1181–1196.

Fassel, R. (**1994**). "Experimente und Simulationsrechnungen zur Wahrnehmung von Amplitudenmodulationen im menschlichen Gehör," Doctoral thesis, Universität Göttingen.

Fletcher, H. (**1940**). "Auditory patterns," Rev. Mod. Phys. **12**, 47–65.

Fletcher, H., and Munson, W. A. (**1937**). "Relation between loudness and masking," J. Acoust. Soc. Am. **9**, 1–10.

Greenberg, S., and Arai, T. (**1998**). "Speech intelligibility is highly tolerant of cross-channel spectral asynchrony," J. Acoust. Soc. Am. **103**, 3057.

Hall, J. L. (**1997**). "Asymmetry of masking revisited: Generalization of masker and signal bandwidth," J. Acoust. Soc. Am. **101**, 1023–1033.

Hall, J. W., and Grose, J. H. (**1991**). "Some effects of auditory grouping factors on modulation detection interference (MDI)," J. Acoust. Soc. Am. **90**, 3028–3035.

Houtgast, T. (**1989**). "Frequency selectivity in amplitude-modulation detection," J. Acoust. Soc. Am. **85**, 1676–1680.

Kohlrausch, A., Fassel, R., and Dau, T. (**2000**). "The influence of carrier level and frequency on modulation and beat-detection thresholds for sinusoidal carriers," J. Acoust. Soc. Am. **108**, 723–734.

Lawson, J. L., and Uhlenbeck, G. E. (**1950**). *Threshold Signals*, Radiation Laboratory Series Vol. 24 (McGraw-Hill, New York).

Levitt, H. (**1971**). "Transformed up–down procedures in psychoacoustics," J. Acoust. Soc. Am. **49**, 467–477.

Lorenzi, C., Micheyl, C., Berthommier, F., and Portalier, S. (**1997**). "Modulation masking with sensorineural hearing loss," J. Speech Lang. Hear. Res. **40**(1), 200–207.

Lorenzi, C., Soares, C., and Vonner, T. (**2001a**). "Second-order temporal modulation transfer functions," J. Acoust. Soc. Am. **110**, 1030–1038.

Lorenzi, C., Simpson, M. I. G., Millman, R. E., Griffiths, T. D., Woods, W. P., Rees, A., and Green, G. G. R. (**2001b**). "Second-order modulation detection thresholds for pure-tone and narrow-band noise carriers," J. Acoust. Soc. Am. **110**, 2470–2478.

Moore, B. C. J. (**1995**). *Perceptual Consequences of Cochlear Damage* (Oxford University Press, Oxford).

Moore, B. C. J., and Oxenham, A. J. (**1998**). "Psychoacoustic consequences of compression in the peripheral auditory system," Psychol. Rev. **105**, 108–124.

Moore, B. C. J., and Glasberg, B. R. (**1986**). "The role of frequency selectivity in the perception of loudness, pitch and time," in *Frequency Selectivity in Hearing*, edited by B. C. J. Moore (Academic, London), 251–308.

Moore, B. C. J., Sek, A., and Glasberg, B. R. (**1999**). "Modulation masking produced by beating modulators," J. Acoust. Soc. Am. **106**, 938–945.

Oxenham, A., and Dau, T. (**2001**). "Modulation detection interference: Effects of concurrent and sequential stream segregation," J. Acoust. Soc. Am. **110**, 402–408.

Patterson, R. D., and Moore, B. C. J. (**1986**). "Auditory filters and excitation patterns as representations of frequency resolution," in *Frequency Selectivity in Hearing*, edited by B. C. J. Moore (Academic, London).

Plomp, R. (**1988**). "The negative effect of amplitude compression in multi-channel hearing aids in the light of the modulation-transfer function," J. Acoust. Soc. Am. **83**, 2322–2327.

Ruggero, M. A., Rich, N. C., Recio, A., Narayan, S. S., and Robles, L. (**1997**). "Basilar-membrane responses to tones at the base of the chinchilla cochlea," J. Acoust. Soc. Am. **101**, 2151–2163.

Sellick, P. M., Patuzzi, R., and Johnstone, B. M. (**1982**). "Measurement of basilar-membrane motion in the guinea pig using the Mössbauer technique," J. Acoust. Soc. Am. **72**, 131–141.

Sheft, S., and Yost, W. A. (**1997**). "Modulation detection interference with two-component masker modulators," J. Acoust. Soc. Am. **102**, 1106–1112.

Shofner, W. P., Sheft, S., and Guzman, S. J. (**1996**). "Responses of ventral cochlear nucleus units in the chinchilla to amplitude modulation by low-frequency, two-tone complexes," J. Acoust. Soc. Am. **99**, 3592–3605.

Strickland, E. A., and Viemeister, N. F. (**1996**). "Cues for discrimination of envelopes," J. Acoust. Soc. Am. **99**, 3638–3646.

Takahashi, G. A., and Bacon, S. P. (**1992**). "Modulation detection, modulation masking, and speech understanding in noise in the elderly," J. Speech Lang. Hear. Res. **35**(6), 1410–1421.

Tandetnik, S., Garnier, S., and Lorenzi, C. (**2001**). "Measurement of first- and second-order modulation detection thresholds in listeners with cochlear hearing loss," Br. J. Audiol. **35**, 355–364.

Verhey, J. L. (**2002**). "Modeling the influence of inherent envelope fluctuations in simultaneous masking experiments," J. Acoust. Soc. Am. **111**, 1018–1025.

Verhey, J. L., Ewert, S. D., and Dau, T. (**2002**). "Modulation masking produced by complex tone modulators," J. Acoust. Soc. Am. (submitted).

Wegel, R. L., and Lane, C. E. (**1924**). "The auditory masking of one sound by another and its probable relation to the dynamics of the inner ear," Phys. Rev. **23**, 266–285.

Zwicker, E. (**1956**). "Die elementaren Grundlagen zur Bestimmung der Informationskapazität des Gehörs," Acustica **6**, 356–381.

Zwicker, E., and Feldtkeller, R. (**1967**). *Das Ohr als Nachrichtenempfänger* (Hirzel Verlag, Stuttgart).

Psychophysical recovery from pulse-train forward masking in electric hearing

David A. Nelson[a] and Gail S. Donaldson
Clinical Psychoacoustics Laboratory, University of Minnesota, MMC396, Minneapolis, Minnesota 55455

Psychophysical pulse-train forward-masking (PTFM) recovery functions were measured in fifteen subjects with the Nucleus mini-22 cochlear implant and six subjects with the Clarion cochlear implant. Masker and probe stimuli were 500-Hz trains of 200- or 77-μs/phase biphasic current pulses. Electrode configurations were bipolar for Nucleus subjects and monopolar for Clarion subjects. Masker duration was 320 ms. Probe duration was either 10 ms or 30 ms. Recovery functions were measured for a high-level masker on a middle electrode in all 21 subjects, on apical and basal electrodes in 7 of the Nucleus and 3 of the Clarion subjects, and for multiple masker levels on the middle electrode in 8 Nucleus subjects and 6 Clarion subjects. Recovery functions were described by an exponential process in which threshold shift (in μA) decreased exponentially with increasing time delay between the offset of the masker pulse train and the offset of the probe pulse train. All but 3 of the 21 subjects demonstrated recovery time constants on a middle electrode that were less than 95 ms. The mean time constant for these 18 subjects was 54 ms (s.d. 17 ms). Three other subjects tested on three electrodes exhibited time constants larger than 95 ms from an apical electrode only. Growth-of-masking slopes depended upon time delay, as expected from an exponential recovery process, i.e., progressively shallower slopes were observed at time delays of 10 ms and 50 ms. Recovery of threshold shift (in μA) for PTFM in electrical hearing behaves in the same way as recovery of threshold shift (in dB) for pure-tone forward masking in acoustic hearing. This supports the concept that linear microamps are the electrical equivalent of acoustic decibels. Recovery from PTFM was not related to speech recognition in a simple manner. Three subjects with prolonged PTFM recovery demonstrated poor speech scores. The remaining subjects with apparently normal PTFM recovery demonstrated speech scores ranging from poor to excellent. Findings suggest that normal PTFM recovery is only one of several factors associated with good speech recognition in cochlear-implant listeners. Comparisons of recovery curves for 10- and 30-ms probe durations in two subjects showed little or no temporal integration at time delays less than 95 ms where recovery functions have steep slopes. The same subjects exhibited large amounts of temporal integration at longer time delays where recovery slopes are more gradual. This suggests that probe detection depends primarily on detection of the final pulses in the probe stimulus and supports the use of offset-to-offset time delays for characterizing PTFM recovery in electric hearing. © *2002 Acoustical Society of America.* [DOI: 10.1121/1.1514935]

PACS numbers: 43.66.Dc, 43.66.Mk, 43.66.Ts [NFV]

I. INTRODUCTION

This paper describes psychophysical forward-masking recovery functions obtained in cochlear implant listeners using a stimulus paradigm in which both masker and probe stimuli are trains of biphasic current pulses. We refer to this paradigm as "pulse-train forward masking" (PTFM). PTFM recovery functions are of interest because they are thought to reflect neural adaptation or persistence mechanisms located in neural pathways central to the cochlea (Shannon, 1990a, 1990b) and may affect the ability of cochlear-implant listeners to discriminate temporal envelope characteristics of the electrical stimulus. Such envelope cues are particularly important for discriminating speech through a cochlear implant, especially when minimal spectral cues are available (Van Tasell *et al.*, 1992; Shannon *et al.*, 1995). Individual differences in recovery rates from forward masking may be one of the factors underlying individual differences in cochlear implant users' speech recognition abilities.

It is important to distinguish PTFM from single-pulse forward masking (SPFM), which uses single electric pulses as masker and probe signals, since the two paradigms yield recovery functions with quite different recovery rates (Donaldson and Nelson, 1999). Although differences between PTFM and SPFM are not well understood, it is likely that the rapid recovery of SPFM provides a direct measure of short-term recovery processes in surviving auditory nerve fibers (Nelson and Donaldson, 2001), whereas PTFM may reflect more central temporal processes that could affect envelope resolution and temporal pattern recognition (Blamey and Dooley, 1993).

Psychophysical PTFM recovery functions for electrical stimulation have been studied by previous investigators (Shannon, 1983, 1986, 1990a; Chatterjee and Shannon, 1998; Chatterjee, 1999). Shannon's earlier work (Shannon,

---

TABLE I. **Subjects**. Subject identifying code (N-Nucleus; C-Clarion), gender, age when tested for the present study, etiology of deafness in implanted ear (and electrode type for Clarion subjects), duration of bilateral severe-to-profound hearing loss prior to implantation, depth of electrode array insertion (mm from the round window, with 25 mm representing complete insertion), duration of implant use prior of the study, and percent-correct score on the NU-6 monosyllabic word test in quiet.

Subject code	m/f	Age	Etiology of deafness (EL type)	Dur. (yrs)	Depth (mm)	CI use (yrs)	NU 6 (% C)
N09	m	66	Meniere's disease	1	22	10	24
N13	m	61	progressive SNHL	4	24	9	70
N14	m	56	hereditary; progressive SNHL	1	25	7	68
N24	m	55	skull fracture; progressive SNHL	24	20	12	32
N28	m	59	meningitis	<1	25	2	28
N30	f	59	otosclerosis	10	25	1	40
N31	m	79	noise exposure; progressive SNHL	25	20	8	6
N32	m	31	maternal rubella; progressive SNHL	<1	23	2	70
N34	f	54	mumps; progressive SNHL	9	22	10	0
N35	m	49	measles, age 2	37	20	10	8
N36	f	73	hereditary; progressive SNHL	??	19	10	2
N37	f	70	hereditary, unknown	4	25	5	10
N38	f	65	measles, otosclerosis, prog SNHL	10	10	6	4
N39	f	79	hereditary; progressive SNHL	14	25	6	32
N41	f	66	hereditary; progressive SNHL	19	21.5	6	14
C05	m	48	unknown; sudden SNHL (1.2E)	1	25	4	52
C12	f	50	otosclerosis, progressive (1.2E)	13	25	2	
C13	m	81	noise-induced progressive (1.2E)	6	25	3	50
C14	m	66	hereditary, unknown (HFP)	48	25	2	76
C15	f	42	unknown progressive SNHL (HFP)	7	25	2	68
C16	f	49	hereditary; progressive SNHL (HF)	18	25	1	80

1983, 1986, 1990a) showed that PTFM recovery in electric hearing is similar to that seen in normal acoustic hearing (Plomp, 1964; Duifhuis, 1973; Jesteadt *et al.*, 1982; Nelson and Freyman, 1987; Nelson and Pavlov, 1989) once intensity is scaled appropriately to account for nonlinear cochlear processing. This similarity suggests that the same physiological mechanisms are responsible for acoustic and electric forward-masking recovery, and that those mechanisms must reside beyond the auditory nerve. As yet, there has been no rigorous examination of PTFM recovery characteristics at different stimulation levels and in different electrode regions; thus, it is not clear whether an acoustic recovery model describes recovery in electrical hearing. If a single model can accurately describe the characteristics of forward masking in both acoustic and electric hearing, then it seems likely that they share common physiological mechanisms.

Because Shannon's cochlear-implant listeners all had similar recovery functions but exhibited a wide range of speech recognition abilities, he reasoned that PTFM was unrelated to speech recognition. Later work (Chatterjee and Shannon, 1998; Chatterjee, 1999) confirmed that PTFM recovery rates in most cochlear implant listeners are similar to those in acoustic listeners, but also identified some implant listeners with very fast recovery and poor speech recognition. This association between fast PTFM recovery and poor speech recognition is counterintuitive, and is contrary to recent SPFM results which found listeners with the slowest recovery rates to have the poorest speech recognition (Brown *et al.*, 1990; Brown *et al.*, 1996; Nelson and Donaldson, 2001). Thus, the existing literature is inconclusive as to the relationship between PTFM and speech recognition in cochlear-implant listeners.

The present study was designed to examine characteris-

tics of psychophysical PTFM recovery functions in a relatively large group of implant listeners, including the general form of the PTFM recovery function, the dependence of recovery-function shape and amount of masking on masker level, and the extent to which recovery characteristics vary across cochlear implant listeners and regions of the implanted array. Recovery functions were obtained for subjects with two different device types, for electrodes in different regions of the cochlea, for a range of masker levels, and for different probe durations. They were analyzed using an exponential model of recovery that is commonly used to describe recovery from acoustic stimulation. Recovery was characterized by recovery time constants and amounts of masking at specific time delays following masker offset. Possible relations between these PTFM measures and speech recognition were examined with the goal of clarifying earlier findings.

II. METHODS

A. Subjects

Subjects were 21 post-lingually deafened adults, 15 implanted with a Nucleus mini-22 device (Patrick and Clark, 1991), and 6 implanted with a Clarion C-I device (Schindler and Kessler, 1993). The Nucleus users were implanted with a 22-electrode straight array. The Clarion users were implanted with a 16-electrode Spiral array (1.2E), a 16-electrode HiFocus array (HF) or a 16-electrode HiFocus array with an electrode positioning system (HFP). Table I displays relevant information for each subject, including age, etiology of deafness, electrode type for Clarion users, duration of hear-
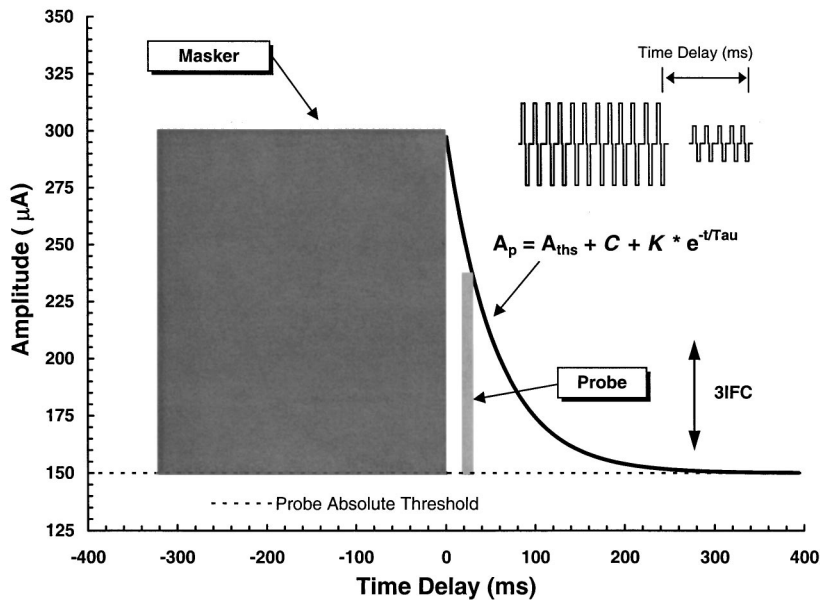
FIG. 1. Schematic diagram of the stimulus protocol used to measure pulse-train forward-masking recovery functions.

The figure shows: Amplitude (μA) on the y-axis ranging from 125 to 350, and Time Delay (ms) on the x-axis from -400 to 400. Labels include "Masker", "Probe", "Time Delay (ms)", "3IFC", "Probe Absolute Threshold", and the equation:

$$A_p = A_{ths} + C + K * e^{-t/Tau}$$

ing loss prior to implantation, insertion depth, duration of implant use prior to participation in the study, and score on the NU-6 monosyllabic word test in quiet.

For each of the 21 subjects, a psychophysical recovery function was obtained from an electrode near the middle of the array using a masker level above 70% of the masker dynamic range (DR) in decibels. For 8 Nucleus subjects and 6 Clarion subjects, recovery functions for the middle electrode were measured at additional masker levels (20% to 80% DR). For 7 Nucleus subjects and 3 Clarion subjects, recovery functions for a high-level masker (>70% DR) were measured for an apical electrode and a basal electrode in addition to the middle electrode.[1]

All Nucleus subjects were stimulated in bipolar mode, using an electrode separation of 1.5 mm (BP+1) or the narrowest separation greater than 1.5 mm that would allow maximum acceptable loudness to be achieved at realizable current amplitudes. Nucleus electrodes were numbered sequentially from 1–22, beginning with the most apical electrode. All Clarion subjects were stimulated in a monopolar mode. The Clarion Spiral electrode array (1.2E) incorporates 8 pairs of lateral and medial electrodes. Electrodes were numbered sequentially from 1–16, beginning with the most apical electrode, thus all odd-numbered electrodes were lateral electrodes and all even-numbered electrodes were medial electrodes. Electrodes in the Clarion HiFocus array were numbered 1–16, beginning with the most apical electrode.

B. Stimuli and procedures

1. PTFM recovery functions

Experiments were controlled by a computer connected through a parallel port to a specialized cochlear implant interface (Shannon *et al.*, 1990) for the Nucleus users, and through a special-purpose micro-processor that controlled the speech processor for the Clarion users (Clarion C-I Research Interface). For the Nucleus users, stimuli were trains of 500-Hz biphasic current pulses, with a per-phase duration of 200 μs and a delay between phases of 44 μs. Stimulus

amplitudes were specified in integer *current step units* (CSUs), which are uneven amplitude steps that vary between 0.07 and 0.30 dB for the range of current amplitudes used here. CSUs were converted to calibrated current amplitudes using user-specific tables provided by Cochlear Corporation. For the Clarion users, stimuli were trains of 500-Hz biphasic current pulses, with a per-phase duration of 77 μs and no delay between phases. Stimulus amplitudes were specified in integer *stimulus units* (SUs), which are logarithmic amplitudes steps of 0.15 to 0.30 dB. SU values were translated to calibrated amplitudes using a set of look-up tables developed in our laboratory. These tables compensate for nonlinearities in the current source that depend upon elecrode impedance and pulse rate. Electrode impedances for Clarion subjects were measured at the beginning and end of each data collection session using the SCLIN for Windows clinical software running on a IBM Think Pad computer. Calibrated amplitudes for a given electrode were calculated using the average of all beginning and ending impedance values for data collection sessions in which that electrode was tested.

Figure 1 illustrates the stimulation protocol used to obtain PTFM recovery functions. As shown in the figure, a 320-ms ''masker'' pulse train was presented first, followed at some time delay by a 10- or 30-ms ''probe'' pulse train. The current amplitude of the masker pulse train was fixed and the amplitude of the probe pulse train was varied adaptively to determine masked threshold. By varying the time delay between masker and probe pulse trains in different adaptive tracks, a recovery function was defined. In this report, time delay (ms) is specified as the time between the offset of the masker pulse train and the offset of the probe pulse train (Fig. 1 inset). This differs from previous reports which measured time delay between the offset of the masker pulse train and the *onset* of the probe pulse train (Shannon, 1990a; Chatterjee, 1999). Our specification of time delay was based on a comparison of recovery functions for 10- and 30-ms probe pulse trains in two cochlear implant listeners (see Appendix A), which indicated that earlier pulses in the 30-ms pulse train did not contribute substantially to detection of the probe

during recovery from forward masking. Masker and probe amplitudes were specified in microamperes (μA) of current, and masked thresholds for the probe were specified in terms of threshold shift (TS) in μA, i.e., the amplitude difference between the masked threshold of the probe (A_p) and the unmasked threshold of the probe in quiet (A_{0p}). This is similar to the normalized level scale used by Shannon (1990a), except that masked thresholds are not normalized to masker sensation level (in μA). Loudness balances between an acoustic stimulus in one ear and an electric stimulus in the other ear (Eddington *et al.*, 1978; Zeng and Shannon, 1992) indicate that equal ratio changes in acoustic intensity are balanced by equal linear amplitude changes in electrical current. This suggests that threshold shift in μA in electric hearing is equivalent to threshold shift in dB in acoustic hearing. Thus, if PTFM is a retrocochlear phenomenon, then the recovery process examined here should be similar to that seen in acoustic hearing.

2. Absolute thresholds and maximum acceptable loudness levels

Prior to obtaining recovery functions for a particular electrode, absolute detection threshold (THS) and maximum acceptable loudness level (MAL) were determined for both the 320-ms masker pulse train and for a 10- or 30-ms probe pulse train. THS was measured with a three-interval forced choice (3IFC) adaptive procedure similar to that used for measuring masked thresholds (described below). MAL was measured with an ascending method of limits procedure in which pulse trains, presented at a rate of 2/s, were slowly increased in amplitude until the subject indicated that loudness had reached a ''maximum acceptable'' level. Estimates for two consecutive ascending runs were averaged to obtain a single measure of MAL. THS and MAL were measured at the start of each test session for the particular electrode to be evaluated in that session, and THS was measured again at the end of each test session. Values of THS and MAL reported here represent the average of all measures obtained across sessions.

3. Masked thresholds

Forward-masked thresholds were obtained using a 3IFC adaptive procedure. The masker pulse train was presented in each of three listening intervals. The probe pulse train was presented in one of the three intervals, chosen randomly from trial to trial, at some fixed time delay following the masker. The subject's task was to choose the ''different'' interval by pressing the appropriate button on a three-button computer mouse. Stimulus intervals were cued on a video monitor, and correct-answer feedback was provided after each trial. The amplitude of the probe pulse train was initially set to a level 2 dB to 4 dB (depending on the probe dynamic range of the test electrode) above the anticipated masked threshold. For the first four reversals, probe level was altered according to a 1-down, 1-up stepping rule, with step size equal to 1 dB. In a few subjects with very small dynamic ranges, the initial step size was 0.5 dB. These initial reversals quickly moved the adaptive procedure into the target region for masked threshold. After the fourth reversal,

step size was reduced, typically to one-fourth of the initial step size, and a 3-down, 1-up stepping rule was assumed. This stepping rule estimates the stimulus level corresponding to 79.4% correct discrimination (Levitt, 1971). Step size was constant for all remaining trials. Trials continued until a total of 12 reversals occurred. The mean of the final eight reversals was taken as the masked threshold estimate.

Masked thresholds were determined in this manner for nine time delays between 11 ms and 300 or 500 ms, in equal ratio steps, to define a complete forward-masking recovery function. Each point on the recovery function was based on the average of three to five forward-masked threshold estimates. Data were obtained in sets, where a single set included one adaptive track at each time delay. Three to five sets were obtained, with the order of time delays alternated for consecutive sets (short-to-long time delays alternated with long-to-short). This allowed any learning effects to be distributed across time delays. Most recovery functions were completed within a single test session. At the end of a session, absolute threshold for the probe pulse train was remeasured. Threshold shift was based on the average of thresholds measured before and after each session.

When masker level effects were investigated in the Nucleus subjects, a recovery curve for the highest masker level was obtained first, followed by recovery functions for the two lower masker levels. The complete recovery curve for the highest masker level was then repeated on the Nucleus subjects to demonstrate the reliability of our procedure. High-level recovery curves were not repeated for Clarion subjects. When recovery functions were obtained from apical, middle, and basal electrodes, data were obtained first on the middle electrode and then on the remaining two electrodes. The order of testing basal and apical electrodes varied across subjects.

4. Exponential fits to PTFM functions

Least-squares regression procedures were used to fit individual recovery functions with the equation

$$(A_p - A_{0p} - C) = K \cdot e^{-t/tau}, \tag{1}$$

where A_p is the forward-masked threshold of the probe (μA), A_{0p} is the unmasked probe threshold (μA), t is the masker-probe time delay (ms), tau is the time constant of recovery from forward masking (ms), and K and C are constants. Values of tau and K were determined using standard least-squares fitting procedures on threshold shift minus a C constant [left-hand side of Eq. (1)]. This was repeated for different values of C until the residual squared error between the fitted and the actual recovery curve was minimized. Equation (1) is the same equation used previously to characterize SPFM recovery functions (Nelson and Donaldson, 2001). The constant C was included in Eq. (1) to accommodate residual masking (incomplete recovery) observed in some recovery functions at moderate or long masker-probe delays. Such residual masking is commonly observed in acoustic forward-masking experiments (Abbas and Gorga, 1981; Markman, 1989; Oxenham and Moore, 1995), but is not well understood.

5. Speech recognition tests

All subjects were tested with three different sets of speech materials: medial vowels in /hVd/ context, medial consonants in /aCa/ context, and NU-6 monosyllabic words. Speech stimuli were presented through loudspeakers in a sound insulated room with the frequent speech peaks set to 60 dB SPL_A at the microphone of the speech processor.

Vowel and consonant recognition. Vowel and consonant recognition were assessed using a standard phoneme–confusion procedure. Vowel stimuli were 11 /hVd/ monosyllables spoken by three male talkers,[2] taken from the database of Hillenbrand *et al.* (1995). Vowels tested were /æ, ɑ, ɛ, e, ɚ, ɪ, i, o, ʊ, ʌ, u/ as in "had, hod, head, hayed, heard, hid, heed, hoed, hood, hud, and who'd." Consonant stimuli were 19 /aCa/ disyllables spoken by three male and three female talkers, taken from the stimulus set of Van Tasell *et al.* (1992). Consonants tested were /p, t, k, b, d, g, f, θ, s, ʃ, v, ð, z, ʒ, m, n, r, l, j/. Digitized speech tokens were played out from computer memory, low-pass filtered at half the digitization rate, amplified and presented through the speakers. The stimulus was presented once on each trial, and the subject used a computer mouse to select his or her response from a list of possible alternatives displayed on a video screen. Correct-answer feedback was provided immediately after each stimulus presentation.

Vowel and consonant recognition data were obtained in separate test sessions. For each stimulus type, one practice block and five standard blocks of data were obtained. Practice blocks were comprised of two trials per vowel phoneme (33 trials) or three trials per consonant phoneme (38 trials). Standard blocks were comprised of six trials per phoneme (66 vowels or 114 consonants) presented in random sequence. A merged confusion matrix was created from the five standard blocks of data for a particular subject. Each merged

matrix represented 30 observations (5 blocks×6 tokens) per stimulus. Merged confusion matrices were analyzed using sequential information analysis (SINFA) to obtain relative transmitted information (RTI) measures for overall vowel and consonant recognition, and for specific vowel and consonant features (Wang, 1976; Van Tasell *et al.*, 1992; Donaldson and Allen, 2002).

NU-6 words. A single list of 50 words was presented using tape-recorded stimuli spoken by a single male talker. Subjects provided written responses, which were scored in terms of percent phonemes as well as percent words identified correctly.

Subjects used their own speech processors for all testing. Nucleus subjects had a Spectra speech processor programmed in the SPEAK strategy. Clarion subjects had a v1.2 or S-series speech processor programmed in the CIS strategy. Nucleus subjects adjusted the sensitivity controls on their processors to achieve comfortable loudness for the test stimuli. Clarion subjects adjusted the volume control, leaving the sensitivity control set to a level at which AGC compression would not be activated for the stimulus levels used ("10:30" for the v1.2 processor; "11:00" for the S-series processor).

III. RESULTS

A. Characteristics of individual PTFM recovery functions

PTFM recovery functions obtained from the middle electrodes of three Nucleus subjects (N14r12, N32r12, and N13r11) are shown in Fig. 2. Each panel shows the data for one electrode at several masker levels. Four recovery curves are shown in panels (A) and (B): one for each of three different masker levels (at approximately 25%, 50%, and 75%
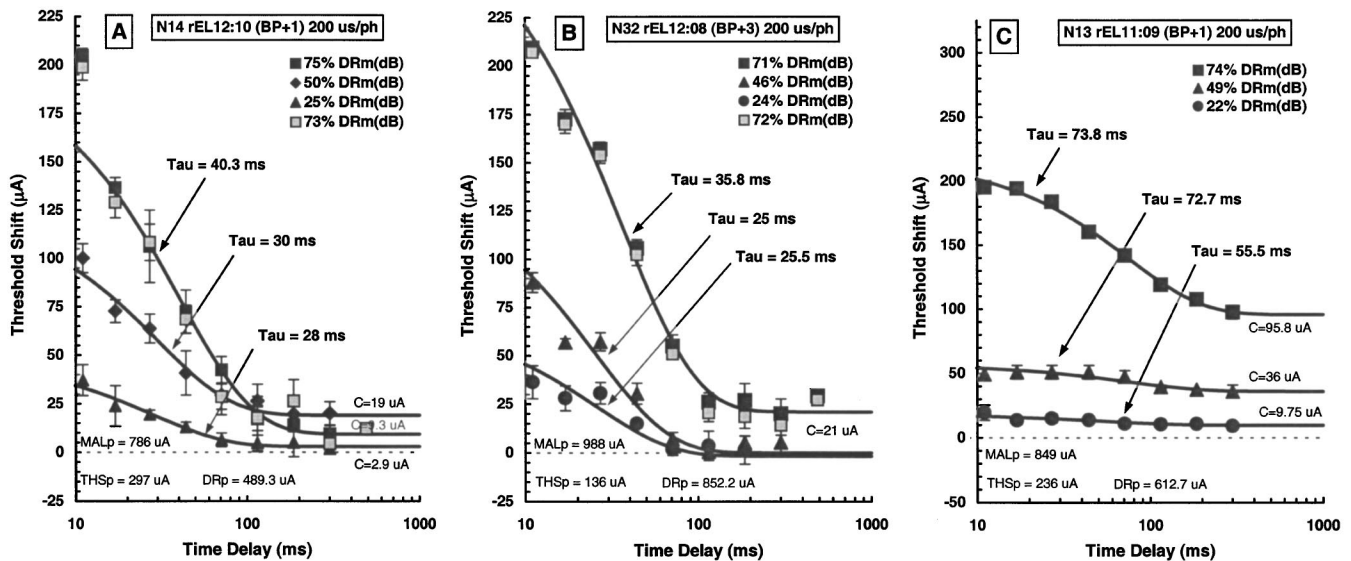
FIG. 2. Pulse-train forward-masking recovery functions are plotted in terms of threshold shift (TS) in microamps, as a function of the time delay between masker offset and probe offset. Data are from Nucleus subjects N14, N32, and N13, all with N-22 electrodes. These subjects demonstrated short time constants for the recovery process ($tau<40$ ms) and high speech recognition scores. Each panel contains recovery functions for a single electrode in the middle of the electrode array. Error bars indicate 1 standard deviation from the mean. The parameter is masker level, expressed as a percentage of the dynamic range of the masker pulse train that was available on each electrode. Threshold (THSp), maximum acceptable loudness level (MALp) and dynamic range (DRp) for the probe pulse train are given within each panel. Time constants for each recovery function are indicated by tau; residual constants are indicated by C (μA TS).

David A. Nelson and Gail S. Donaldson: Pulse-train forward masking
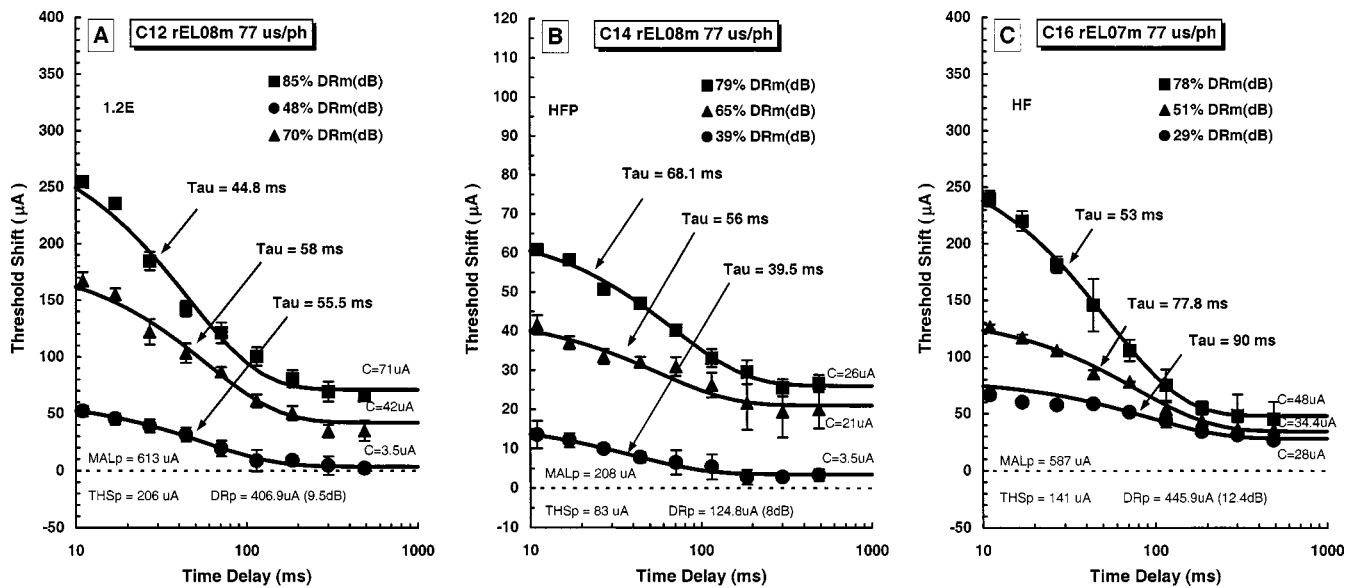
FIG. 3. Pulse train forward-masking recovery functions from a middle electrode in Clarion subjects C12, C14, and C16. C12 has a spiral electrode (1.2E). C14 has a high-focus electrode with a positioner (HFP). C16 has a high-focus electrode without a positioner. Each panel contains recovery functions for a single electrode in the middle of the electrode array. Error bars indicate 1 standard deviation from the mean. The parameter is masker level, expressed in the legend as a percentage of the dynamic range of the masker pulse train that was available on each electrode. Dynamic range (DRp in μA) for the probe pulse train is indicated by the hatched horizontal line at the top of the graphs, and is listed within each panel in μA and dB μA. Time constants for each recovery function are indicated by Tau; residual constants are indicated by C (TS in uA).

of DR in dB), and a retest for the highest masker level (Lm>70% of DR in dB). Only three recovery curves are shown in panel (C) because N13r11 was not retested at the highest masker level. The shapes of these functions are typical of recovery functions obtained from other Nucleus subjects. Recovery time constants [tau in Eq. (1)] are indicated next to each curve. Recovery rates for the two electrodes represented in panels (A) and (B) were among the fastest observed, with time constants ranging from 25 to 40 ms. The electrode in panel (C) had slightly longer time constants (55–74 ms). All three of the subjects represented in Fig. 2 scored high on speech recognition tests.

The PTFM recovery functions in Fig. 2 illustrate several

characteristics common to the functions measured in other subjects. First, PTFM recovery curves were well fit by the exponential recovery process given by Eq. (1). Second, most of the recovery curves exhibited a residual threshold shift specified by the constant C. Third, recovery curves at the highest masker level exhibited good test-retest reliability, with repeat masked thresholds that were not significantly different from the original ones [e.g., shaded vs solid squares in Figs. 2(A) and (B)].

One atypical characteristic sometimes seen in PFTM recovery functions is illustrated in Fig. 2(A). At the shortest time delay (11 ms), when the probe pulse train immediately follows the masker pulse train, a large amount of threshold
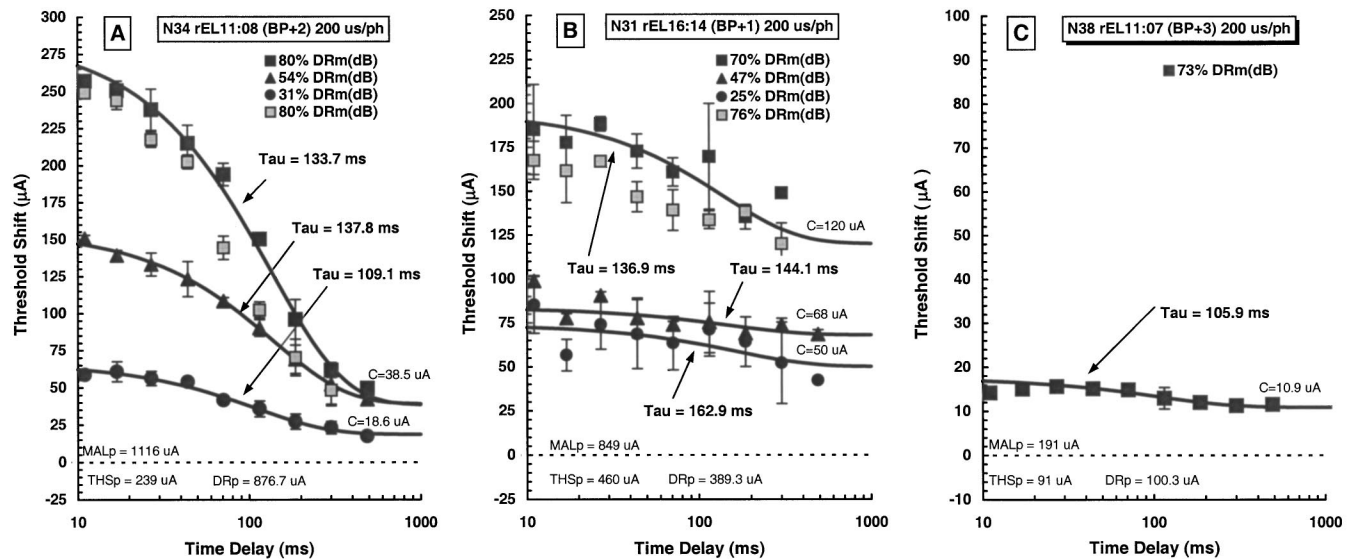
FIG. 4. Pulse-train forward-masking recovery functions from subjects N34, N31, and N38, who demonstrated long time constants for the recovery process ($tau > 100$ ms) and low speech recognition scores. Legend as in Fig. 2.

shift is evident. This threshold shift greatly exceeds that predicted by the exponential recovery curve that describes masked thresholds at longer time delays. Excessive masking at 11 ms was observed for only one (middle) electrode in two subjects (N14r12 and C05r08), and then only at the highest of three masker levels.

PTFM recovery functions obtained from the middle electrodes of three Clarion subjects (C12r08, C14r08, and C16r07) are shown in Fig. 3. Each of the subjects has a different type of electrode array: C12 has a Spiral electrode (1.2E), C14 has a HiFocus electrode with a positioner, and C16 has a HiFocus electrode without a positioner. Qualita-

TABLE II. Recovery function parameters obtained from 8 Nucleus and 6 Clarion subjects at multiple masker levels on a middle electrode: subject code, research electrode number, and electrode type (Subj/Elect); stimulation mode (Mode); threshold (THS), maximum acceptable loudness level (MAL) expressed in μAmps of current; dynamic range (DR) for probe and masker stimuli (expressed in dB); masker level (Lm) expressed as percent dynamic range of the masker in dB (%DRm); time constant (tau); residual constant (C); goodness of fit (R^2). Average parameter values are shown in bold for each subject/electrode.

Subj/Elect	Mode	THSp (uA)	MALp (uA)	DRp (dB)	THSm (uA)	MALm (uA)	DRm (dB)	Lm (%DRm)	Tau (ms)	C (uA)	R^2
N09 rEL15:13	BP+1	139	459	10.4	124	310	7.9	75.9%	44.2	25.4	0.990
NUC	BP+1	143	437	9.7	120	305	8.1	53.5%	46.8	22.8	0.848
	BP+1	128	425	10.4	104	305	9.4	25.9%	45.3	10.0	0.849
		136.6	**440.4**	**10.2**	**116.1**	**306.8**	**8.4**				**0.896**
N13 rEL11:09	BP+1	233	845	11.2	157	591	11.5	74.2%	73.8	95.8	0.986
NUC	BP+1	238	855	11.1	146	542	11.4	49.0%	72.7	36.0	0.926
	BP+1	237	845	11.1	151	566	11.4	22.2%	55.5	9.8	0.360
		235.8	**848.5**	**11.1**	**151.6**	**566.3**	**11.4**				**0.757**
N14 rEL12:10	BP+1	301	780	8.3	171	647	11.5	75.0%	40.3	9.3	0.999
NuC	BP+1	290	789	8.7	166	662	12.0	49.8%	30.0	19.0	0.985
	BP+1	299	789	8.4	167	652	11.8	25.2%	28.0	2.9	0.985
		296.7	**786.0**	**8.5**	**168.3**	**653.4**	**11.8**				**0.990**
N28 rEL12:10	BP+1	157	396	8.0	126	305	7.7	79.3%	36.8	59.0	0.995
NUC	BP+1	155	385	7.9	129	303	7.4	52.9%	39.8	39.0	0.964
	BP+1	156	380	7.7	132	296	7.0	24.6%	59.9	13.5	0.839
		155.8	**386.9**	**7.9**	**129.2**	**301.4**	**7.4**				**0.933**
N30 rEL17:15	BP+1	174	557	10.1	126	432	10.7	75.6%	65.2	32.4	0.963
NUC	BP+1	177	565	10.1	130	423	10.2	51.6%	80.5	28.0	0.982
	BP+1	175	544	9.8	129	405	10.0	28.3%	33.3	5.7	0.978
		175.1	**555.2**	**10.0**	**128.4**	**419.7**	**10.3**				**0.974**
N32 rEL12:08	BP+3	131	1019	17.8	65	644	19.9	71.5%	35.8	21.0	0.985
NUC	BP+3	139	1039	17.5	65	636	19.8	46.2%	25.0	0.0	0.959
	BP+3	137	911	16.5	65	679	20.4	24.4%	25.5	−1.8	0.926
		135.8	**989.6**	**17.3**	**64.8**	**653.1**	**20.1**				**0.957**
N31 rEL16:14	BP+1	458	838	5.3	341	686	6.1	70.3%	136.9	120.0	0.824
NUC	BP+1	459	855	5.4	345	673	5.8	46.6%	144.1	68.0	0.698
	BP+1	463	855	5.3	340	682	6.0	24.6%	162.9	50.0	0.505
		460.1	**849.4**	**5.3**	**341.7**	**680.1**	**6.0**				**0.676**
N34 rEL11:08	BP+2	236	1103	13.4	195	609	9.9	80.1%	133.7	38.5	0.988
NUC	BP+2	238	1098	13.3	199	609	9.7	54.0%	137.8	39.1	0.998
	BP+2	243	1147	13.5	197	609	9.8	30.5%	109.1	18.6	0.988
		238.9	**1115.8**	**13.4**	**197.1**	**608.8**	**9.8**				**0.991**
C05 rEL08m	mono	104	400	11.7	52	330	16.1	87.0%	60.2	42.0	0.986
1.2E	mono	104	380	11.3	53	319	15.6	71.0%	60.5	16.0	0.979
	mono	98	361	11.3	42	319	17.5	50.4%	60.7	0.6	0.964
		101.9	**380.3**	**11.4**	**49.0**	**322.5**	**16.4**				**0.976**
C12 rEL08m	mono	199	572	9.2	106	574	14.7	85.5%	44.8	71.0	0.962
1.2E	mono	198	610	9.8	101	635	16.0	69.6%	58.0	42.0	0.957
	mono	221	659	9.5	102	642	15.9	48.3%	55.5	3.5	0.993
		205.9	**613.7**	**9.5**	**103.2**	**616.8**	**15.5**				**0.971**
C13 rEL08m	mono	131	348	8.5	69	351	14.1	87.0%	76.8	41.5	0.991
1.2E	mono	136	388	9.1	67	353	14.5	70.3%	78.8	22.5	0.933
		133.5	**367.7**	**8.8**	**67.7**	**352.0**	**14.3**				**0.962**
C14 rEL08m	mono	82	205	8.0	55	178	10.2	79.2%	68.1	26.0	0.983
HFP	mono	82	212	8.2	55	175	10.1	65.4%	56.0	21.0	0.868
	mono	84	206	7.8	57	164	9.1	39.1%	39.5	3.5	0.997
		82.7	**207.5**	**8.0**	**55.7**	**172.6**	**9.8**				**0.949**
C15 rEL08m	mono	69	116	4.5	32	61	5.8	71.2%	48.2	2.0	0.885
HFP	mono	68	117	4.7	33	77	7.4	43.8%	63.3	3.5	0.967
		68.6	**116.6**	**4.6**	**32.3**	**69.3**	**6.6**				**0.926**
C16 rEL07m	mono	147	632	12.7	149	495	10.5	78.2%	53.0	48.0	0.998
HF	mono	134	524	11.8	138	453	10.3	51.2%	77.8	34.4	0.945
	mono	144	612	12.6	141	507	11.1	28.8%	90.0	28.0	0.992
		141.5	**589.3**	**12.4**	**142.5**	**484.9**	**10.6**				**0.978**

David A. Nelson and Gail S. Donaldson: Pulse-train forward masking

tively, recovery curves from Clarion subjects are similar to those observed in Nucleus subjects, regardless of electrode type. These curves are well fit by exponential curves with time constants (tau) and residual constants (*C*) within the same range as seen in Nucleus subjects. All three of these subjects also performed well on the speech tests.

PTFM recovery functions from a middle electrode in three Nucleus subjects (N34r11, N31r16, and N38r11) are shown in Fig. 4. Two of these subjects (N34r11 and N31r16) exhibited extended PTFM recovery with long time constants at all three levels, and the third subject (N38r11) exhibited a long time constant for the one high-level masker that was tested. For N31r16 [Fig. 4(B)], residual masking was exceptionally high, with *C* constants between 50 and 120 μA. For N38r11 [Fig. 4(C)], the THS and MAL values were unusually low and only a small amount of threshold shift was produced by the PTFM masker. The three subjects represented in Fig. 4 also exhibited low speech scores. Comparison of time constants and speech scores for the subjects in Fig. 2 and Fig. 4 suggests that PTFM time constants are inversely related to speech recognition scores. As will be shown later, a simple inverse relationship does not exist. Rather, prolonged PTFM recovery appears to predict poor speech recognition, whereas apparently normal PTFM recovery may be observed in subjects with all levels of speech recognition.

B. Group tendencies in PTFM recovery functions

1. Masker level effects

The effect of masker level on PTFM recovery curves was examined for the middle electrodes of 8 Nucleus and 6 Clarion subjects. Parameters of the exponential fits obtained at different masker levels are given in Table II. For each test electrode (denoted by research electrode number, rEL), THS, MAL, and DR for the probe and masker stimuli are shown, together with fitting parameters *tau* and *C* for the exponential

recovery process. Excellent exponential fits to the data were obtained at the highest masker level, as evidenced by coefficients of determination (R^2) that were typically above 0.98. Fits were less good at lower masker levels, but still provided an adequate characterization of the data.

Time constants for the recovery process (*tau*) were largely independent of masker level. As shown in Fig. 5(A), values for *tau* on the middle electrode varied considerably across subjects, from 25 ms to 163 ms, but did not vary systematically with masker level for most of the 8 Nucleus or 6 Clarion subjects tested at multiple levels. Thus, the PTFM recover process appears to be adequately described by an exponential recovery model [Eq. (1)] that produces level-independent time constants. As indicated in Fig. 5, two subjects (N31 and N34) demonstrated time constants greater than 95 ms, the upper 99% confidence limit of the mean (dashed line in Fig. 5).

Probe dynamic ranges for subjects' middle electrodes varied from 4.5 to 17.8 dB (47 to 904 μA). Figure 5(B) shows time constants plotted as a function of dynamic range for the probe pulse train, expressed in μA. There was no simple relationship between tau and DR. Subjects with shorter time constants (filled symbols) exhibited dynamic ranges from small to very large.

2. Growth of masking

If an exponential model with a level-independent time constant is truly appropriate for describing the PTFM recovery process, then the model should accurately predict the rate at which forward masking grows with masker level at all time delays. To evaluate characteristics of growth of masking (GOM), parameter *K* in Eq. (1) was expressed as a linear function of masker sensation level ($A_m - A_{0m}$), as follows:

$$K = b + n \cdot (A_m - A_{0m}). \tag{2}$$

Substituting Eq. (2) for *K* in Eq. (1) yields the following:
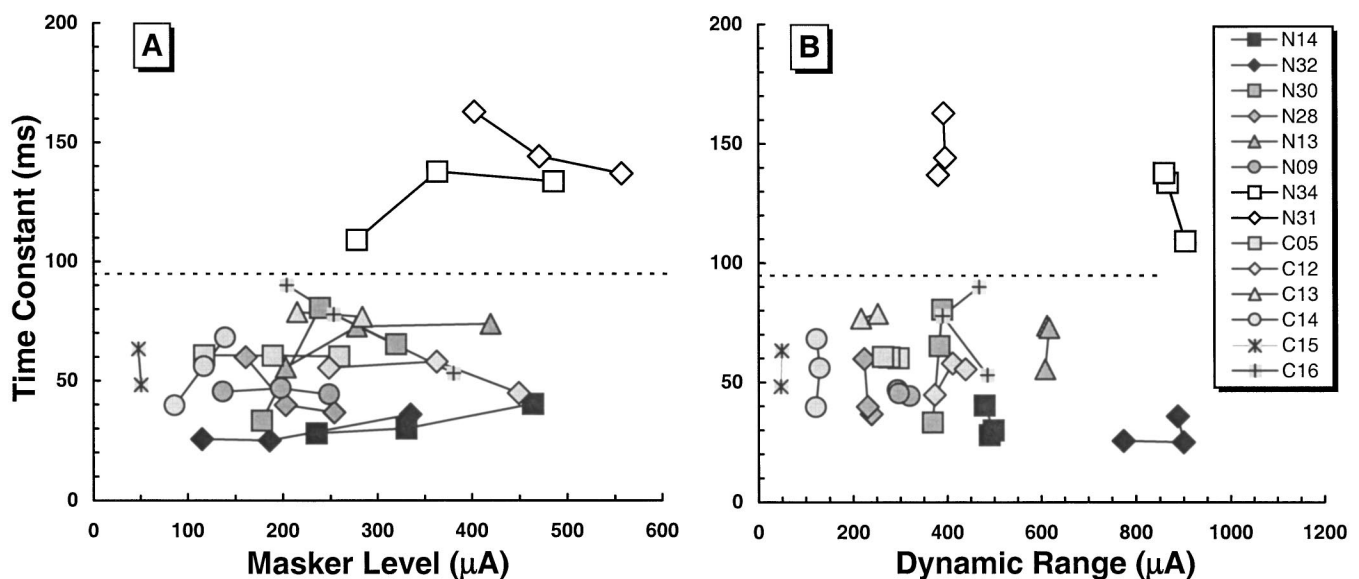
FIG. 5. Time constants for the recovery process on middle electrodes, from 8 Nucleus and 6 Clarion subjects, as a function of masker level [panel (A)] and as a function of dynamic range for the probe pulse train [panel (B)]. Time constants were obtained from exponential fits to the pulse-train forward-masking recovery functions. The dashed line indicates 99% confidence limits above the mean; time constants above this line are identified by unfilled symbols.
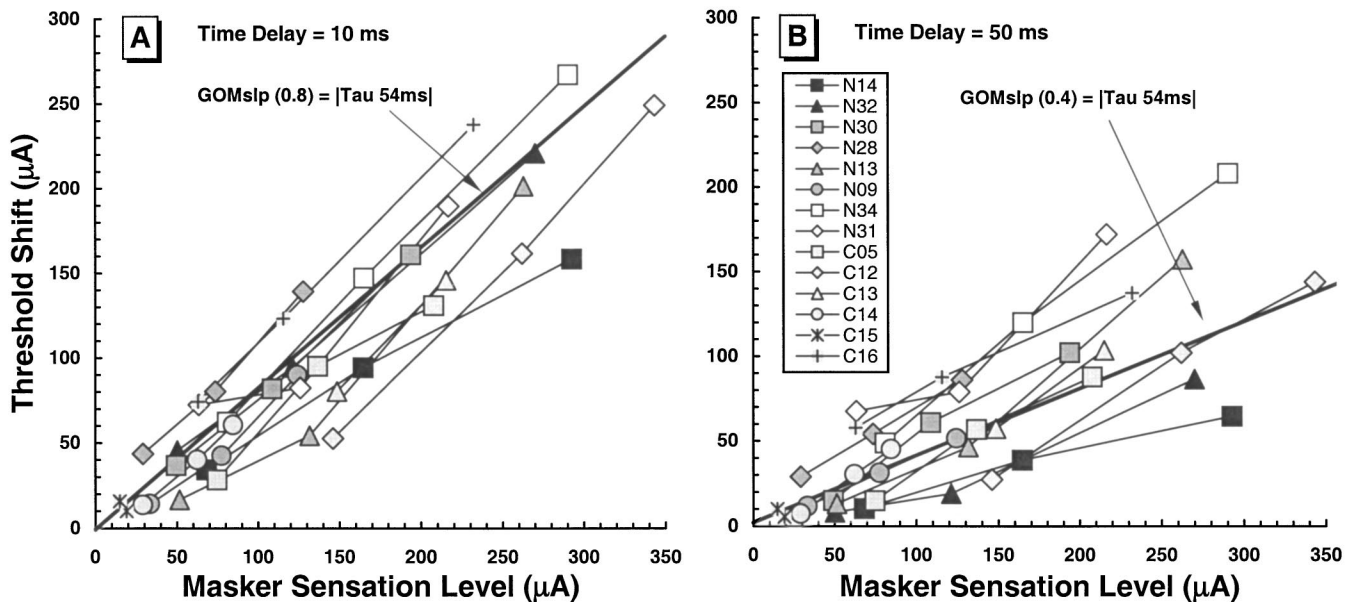
FIG. 6. Amount of masking as a function of masker sensation level, calculated for time delays of 10 ms [panel (A)] and 50 ms [panel (B)]. The growth of masking functions predicted by Eq. (3) for a time constant of 54 ms are shown by the solid lines, which have slopes of 0.8 and 0.4 for the 10- and 50-ms time delays, respectively.

$$(\mathbf{A}_p - \mathbf{A}_{0p} - C) = [b + n(\mathbf{A}_m - \mathbf{A}_{0m})] \cdot e^{-t/tau}. \qquad (3)$$

This shows that for a time delay of $t = 0$ ms, the growth rate of masking is equal to n, and the sensitivity to masking is equal to b. For other values of t, Eq. (3) shows that the rate of growth of masking is inversely related to *tau*. Growth of masking slopes were evaluated for several values of t in order to determine if the expected dependence of growth rate on *tau* was actually reflected in the data.

Figures 6(A) and (B) show GOM functions for time delays of 10 and 50 ms, respectively. In each graph, threshold shifts calculated from the fitted recovery curves at time delays of 10 or 50 ms are plotted as a function of masker sensation level. The GOM functions at 50 ms exhibit lower slopes than those at 10 ms, which is consistent with Eq. (3). For comparison, the GOM functions predicted from Eq. (3) using a time constant of 54 ms are shown by solid lines in Figs. 6(A) and (B). Recall that 54 ms was the average time constant for 18 subjects with apparently normal rates of recovery on a middle electrode. For both 10- and 50-ms time delays, the general trend of the slopes of the GOM functions are well described by the solid line. A linear fit across all electrodes to the amount of masking at a 10-ms delay as a function of masker sensation level indicates that, on average, forward masking at a 10-ms delay begins when the masker is slightly above its detection threshold (0.9 μA SL). These results suggest that, for most subjects, effective masking due to a pulse-train masker tends to grow monotonically with the sensation level of the masker (in μA), and that forward masking begins when masker amplitude is at absolute threshold. This outcome adds further support to the validity of an exponential model for describing recovery from PTFM in electric hearing.

3. Effects of electrode location

Parameters for recovery curves obtained from three regions of the same electrode array (apical, middle, and basal) at a single masker level ($>70\%$ DR) in 7 Nucleus and 3 Clarion subjects, are given in Table III. Parameters for recovery curves obtained on a middle electrode at a single masker level ($>70\%$ DR) in an additional 8 Nucleus and 3 Clarion subjects are also listed. To examine whether recovery function parameters differed significantly for electrodes located in the apical, middle, or basal regions of the electrode array, single factor repeated-measures ANOVAs were performed on the measures of *tau* and threshold shift at $t = 10$ ms or $t = 50$ ms. None of the resulting F-ratios approached statistical significance for either group. This indicates that neither the recovery from PTFM nor the amount of threshold shift at a 10- or 50-ms time delay varied consistently with electrode region. Repeated-measures ANOVAs similarly showed that neither absolute threshold nor probe dynamic range varied systematically with electrode location.

Figure 7 shows the time constants obtained from different electrode regions, plotted as a function of masker level. In addition to subjects N31 and N34, one additional subject (N38) who was tested only on a middle electrode exhibited a long time constant. Thus, out of 15 Nucleus and 6 Clarion subjects tested on a middle electrode, only three exhibited time constants longer than 95 ms. As shown in Fig. 7, two of the subjects with long time constants on a middle electrode (N31 and N34) also exhibited long time constants on a basal electrode. One of those subjects (N34) exhibited long time constants on all three electrodes. In addition, three subjects (N13, N30, C14) exhibited long time constants on an apical electrode only, with normal time constants on a middle and basal electrode.

David A. Nelson and Gail S. Donaldson: Pulse-train forward masking

TABLE III. Recovery function parameters obtained from apical, middle or basal electrodes at the highest masker level (Lm>70% DR) in 21 subjects. Column 1 shows the subject code and electrode pair stimulated (m=monopolar). Rows 1–21: 7 Nucleus subjects tested on apical, middle and basal electrodes. Rows 22–29: 8 additional Nucleus subjects tested on a middle electrode. Row 30–38: 3 Clarion subjects tested on apical, middle and basal electrodes. Rows 39–41: 3 additional Clarion subjects tested on a middle electrode.

Subj/Elect	Mode	THSp (uA)	MALp (uA)	DRp (dB)	THSm (uA)	MALm (uA)	DRm (dB)	Lm (%DRm)	Tau (ms)	C (uA)	R^2	TS(10 ms)/ DRp(uA)	TS(50 ms)/ DRp(uA)
N13 rEL07:02	BP+4	239	525	6.8	169	491	9.3	70.6%	112.6	65.5	0.919	0.44	0.38
N13 rEL11:09	BP+1	233	845	11.2	157	591	11.5	74.2%	73.8	95.8	0.986	0.33	0.26
N13 rEL16:11	BP+4	273	767	9.0	180	581	10.2	75.7%	52.8	91.2	0.976	0.36	0.27
N14 rEL06:04	BP+1	412	833	6.1	246	796	10.2	75.1%	25.0	5.8	0.935	0.56	0.12
N14 rEL12:10	BP+1	301	780	8.3	171	647	11.5	75.0%	40.3	9.3	0.999	0.33	0.13
N14 rEL20:18	BP+1	411	809	5.9	229	730	10.1	74.0%	21.7	19.0	0.980	0.49	0.12
N28 rEL05:03	BP+1	339	550	4.2	156	410	8.4	75.0%	58.8	6.4	0.909	0.23	0.13
N28 rEL12:10	BP+1	157	396	8.0	126	305	7.7	79.3%	36.8	59.0	0.995	0.58	0.36
N28 rEL20:18	BP+1	410	811	5.9	193	571	9.4	77.9%	42.7	6.4	0.987	0.28	0.12
N30 rEL04:02	BP+1	329	1088	10.4	178	892	14.0	73.2%	127.6	68.9	0.994	0.34	0.27
N30 rEL17:15	BP+1	174	557	10.1	126	432	10.7	75.6%	65.2	32.4	0.963	0.42	0.27
N30 rEL21:19	BP+1	299	1388	13.3	226	850	11.5	78.4%	53.6	108.3	0.997	0.34	0.21
N31 rEL12:10	BP+1	643	1029	4.1	438	869	6.0	76.1%	71.1	107.8	0.994	0.41	0.35
N31 rEL16:14	BP+1	458	838	5.3	341	686	6.1	70.3%	136.9	120.0	0.824	0.50	0.45
N31 rEL21:19	BP+1	688	1083	3.9	443	897	6.1	79.0%	107.4	80.0	0.990	0.40	0.34
N32 rEL05:01	BP+3	140	1738	21.9	71	699	19.9	77.7%	41.0	51.3	0.996	0.18	0.09
N32 rEL12:08	BP+3	131	1019	17.8	65	644	19.9	71.5%	35.8	21.0	0.985	0.25	0.10
N32 rEL19:15	BP+3	88	724	18.3	44	565	22.3	73.4%	48.9	31.8	0.995	0.33	0.17
N34 rEL06:02	BP+3	294	1283	12.8	221	717	10.2	82.2%	107.6	67.5	0.976	0.31	0.23
N34 rEL11:08	BP+2	236	1103	13.4	195	609	9.9	80.1%	133.7	38.5	0.988	0.31	0.24
N34 rEL17:13	BP+3	241	608	8.0	173	523	9.6	74.8%	110.9	52.0	0.963	0.45	0.36
N09 rEL15:13	BP+1	139	459	10.4	124	310	7.9	75.9%	44.2	25.4	0.990	0.28	0.16
N24 rEL11:08	BP+2	368	1038	9.0	218	791	11.2	74.4%	33.9	50.0	0.990	0.35	0.16
N35 rEL12:07	BP+4	225	1656	17.3	229	1221	14.5	88.8%	22.2	85.0	0.997	0.64	0.15
N36 rEL11:08	BP+2	262	981	11.5	217	801	11.3	79.9%	60.9	145.0	0.983	0.54	0.38
N37 rEL11:09	BP+1	505	933	5.3	282	703	7.9	74.2%	18.2	42.0	0.997	0.18	0.11
N38 rEL11:07	BP+3	91	191	6.5	53	122	7.2	73.2%	105.9	10.9	0.973	0.17	0.15
N39 rEL12:10	BP+1	217	641	9.4	146	694	13.6	75.4%	75.3	71.0	0.996	0.64	0.44
N41 rEL12:10	BP+1	360	852	7.5	246	649	8.4	78.1%	85.5	65.0	0.976	0.36	0.28
C05 rEL02m	mono	102	341	10.5	51	273	14.6	82.3%	50.2	25.0	0.980	0.42	0.25
C05 rEL08m	mono	104	400	11.7	52	330	16.1	87.0%	60.2	42.0	0.986	0.44	0.30
C05 rEL14m	mono	72	314	12.8	42	250	15.6	83.6%	67.7	30.3	0.951	0.45	0.31
C12 rEL02m	mono	242	663	8.8	118	694	15.4	85.0%	33.8	70.0	0.985	0.72	0.34
C12 rEL08m	mono	199	572	9.2	106	574	14.7	85.5%	44.8	71.0	0.962	0.67	0.39
C12 rEL14m	mono	232	646	8.9	110	711	16.2	82.8%	37.7	73.5	0.995	0.72	0.36
C14 rEL02m	mono	75	120	4.1	51	98	5.7	78.8%	99.4	4.3	0.877	0.35	0.27
C14 rEL08m	mono	82	205	8.0	55	178	10.2	79.2%	68.1	26.0	0.983	0.49	0.37
C14 rEL14m	mono	83	153	5.3	43	110	8.1	78.4%	48.4	5.0	0.924	0.30	0.17
C13 rEL08m	mono	131	348	8.5	69	351	14.1	87.0%	76.8	41.5	0.991	0.67	0.48
C15 rEL08m	mono	69	116	4.5	32	61	5.8	71.2%	48.2	2.0	0.885	0.21	0.12
C16 rEL07m	mono	147	632	12.7	149	495	10.5	78.2%	53.0	48.0	0.998	0.49	0.28

4. Comparisons across electrode types

An examination of recovery curves from subjects with different types of implanted electrodes did not reveal any systematic differences in recovery characteristics. Earlier (Fig. 3), recovery curves were shown for subjects with each of the three types of Clarion electrodes. The recovery curve parameters fit to these curves fall within the range shown earlier for Nucleus subjects. The only obvious difference is that dynamic ranges (in μA) are smaller for subject C14 [panel (B)] than for the other subjects. C14 has a HiFocus electrode and a positioner (HFP), which presumably resides closer to the modiolar wall than the Spiral electrode (1.2E) or the HiFocus electrode without the positioner (HF). Recovery curve parameters for the two Clarion subjects with HFP electrodes, C14 and C15 (see Table III) were not different from those of other subjects, even though their THS and MAL values were noticeably smaller. Because Clarion subjects were stimulated in monopolar mode and Nucleus subjects were stimulated in bipolar mode, our findings suggest that electrode coupling (bipolar versus monopolar) has no major effect on PTFM recovery.

C. Correlations with speech recognition scores

Table IV shows correlation coefficients between word and phoneme recognition scores and PTFM time constants or threshold shifts at 10- and 50-ms time delays. All of the coefficients for tau vs speech scores are negative, indicating that higher speech scores are associated with smaller time constants. However, the coefficients are all small in magnitude, ranging from -0.13 to -0.38; none account for more than 14% of the variance. The coefficients for threshold shift
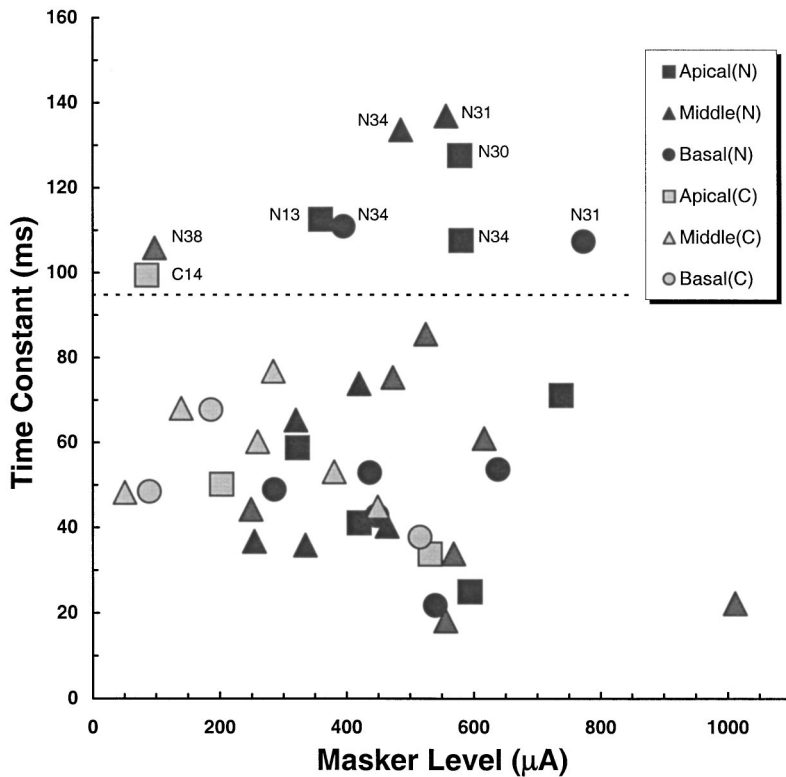
FIG. 7. Time constants for the recovery process at the highest masker level (>70% DRdB) on apical (squares), middle (triangles), and basal (circles) electrodes, plotted as a function of masker level. The dashed line indicates the 99% confidence limit. Time constants above this line are identified by their subject codes.

at 10 or 50 ms vs speech scores are even smaller. These results indicate that measures of PTFM are unable to explain the variance observed in speech recognition scores.

Figure 8 shows scattergrams of some the relationships summarized in Table IV. The relationships between recovery time constants and speech scores are shown in Figs. 8(A), (B), and (C). Subjects with time constants in the "normal" range (<100 ms) exhibit speech scores ranging from poor to excellent. Among these subjects, two subjects with very short time constants (N35 and N37) exhibit very poor speech scores, similar to a subject (N3) identified by Chatterjee (1999). On the other hand, the three subjects with prolonged time constants on a middle electrode (N31, N34, and N38) all exhibit poor speech scores. These results suggest that normal recovery from PTFM is a necessary but not sufficient requirement for good speech recognition. That is, prolonged

PTFM recovery in itself may eliminate the possibility of good speech recognition, but other factors such as poor spatial resolution must be responsible for the low speech scores observed in some subjects with normal PTFM recovery rates.

Figure 8(D) shows threshold shift at a time delay of 50 ms plotted against percent transmitted information for the consonant envelope feature (Van Tasell *et al.*, 1992). Threshold shift is expressed as a percentage of the dynamic range (μA) of the probe pulse train. If extended forward masking were preventing the detection of a consonant following an intense vowel, this correlation would be expected to be strongly negative. As indicated in Fig. 8(D), there is no relationship between the two variables. Table IV shows that small correlation coefficients are obtained for threshold shifts at 10 ms as well.

TABLE IV. Correlations between pulse-train time constants (tau), threshold shift (TS in μA) at 10-ms or 50-ms time delays (all from a middle electrode), and various speech recognition scores (15 Nucleus and 6 Clarion subjects).

		Pulse train tau	TS (10 ms)	TS (50 ms)
/aCa/ consonants				
	Stimulus (RTI)	−0.29	−0.07	−0.07
	Envelope (RTI)	−0.23	−0.07	−0.11
	Place (RTI)	−0.30	−0.08	−0.07
NU-6 words				
	Phonemes (%C)	−0.38	0.04	0.01
	Words (%C)	−0.32	−0.02	−0.09
Hillenbrand vowels				
	Stimulus (RTI)	−0.23	0.00	0.00
	$F1$ Frequency (RTI)	−0.22	−0.08	−0.05
	$F2$ Frequency (RTI)	−0.31	0.08	0.00
	Duration (RTI)	−0.13	−0.06	−0.05
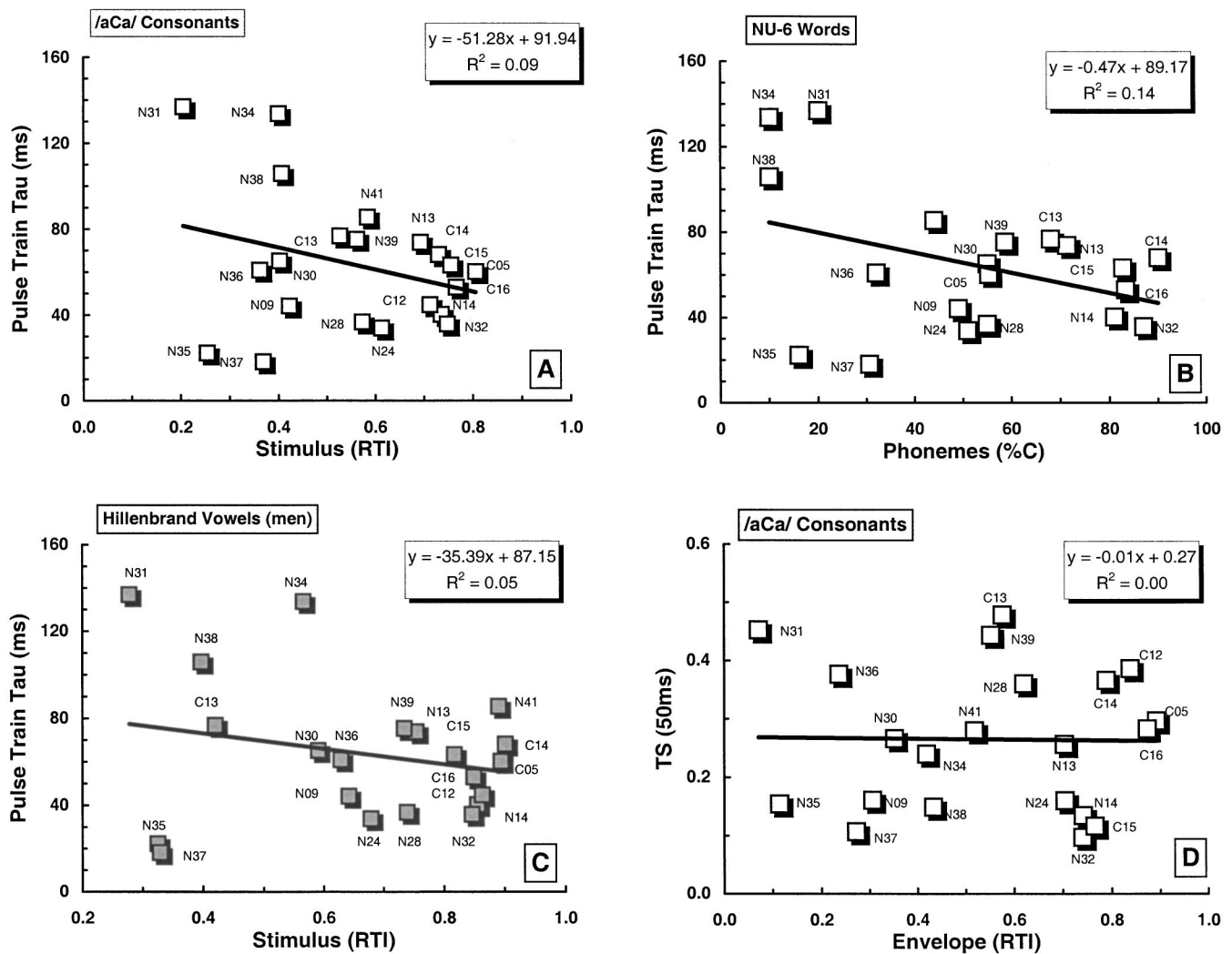
FIG. 8. Scattergrams of time constants (tau), or threshold shifts (TS in %DRuA) at a time delay of 50 ms, and different speech recognition scores. Time constants and threshold shifts are for pulse-train forward-masking recovery functions obtained from a middle electrode with a masker level above 70% DRdB. Speech scores are given as percent correct (%C) phoneme scores or relative transmitted information (RTI).

IV. DISCUSSION

A. Exponential recovery process

An important finding of this study is that recovery from psychophysical pulse-train forward masking can be accurately described by a recovery process in which the amount of threshold shift produced by a masker pulse train recovers exponentially in time. The recovery process requires only a single time constant to account for PTFM data obtained over a wide range of masker amplitudes. In this study, the average recovery time constant for 18 subjects with apparently normal PTFM recovery was 54 ms, with a standard deviation of 17 ms. This means that approximately 99% of subjects in a similar cochlear implant population would be expected to demonstrate forward-masking time constants shorter than 95 ms.

Previous measures of pulse-train forward masking in electric hearing have found that recovery occurs over the same period of time as seen in the current study (Shannon, 1990a, 1990b; Chatterjee and Shannon, 1998; Chatterjee, 1999). Shannon specified recovery with a slightly different model (dB of threshold shift versus log delay time), which is

another model used to describe recovery in acoustic hearing (Plomp, 1964; Jesteadt *et al.*, 1982). Nelson and Freyman (1987) showed that both models describe the recovery process in acoustic hearing equally well. We have evaluated some of Shannon's (1990a) data using the same exponential coordinates as in the present study, and using offset-to-offset rather than offset-to-onset time delays. Shannon's recovery curves do not differ qualitatively from those seen here, and the time constants are within the range of time constants seen here. Similarly, Chatterjee's (1999) published recovery curves, evaluated using offset-to-offset time delays, reveal time constants within the range of those seen here, except for one subject (N3) with a time constant of 11 ms (using our coordinates). For this subject, the recovery curves were well fit with two recovery processes, the faster one with an 11-ms time constant and the longer one with a 79-ms time constant.

A recent study of single-pulse forward masking (SPFM) from our laboratory (Nelson and Donaldson, 2001) used the same exponential recovery process to describe SPFM recovery curves, except that two time constants were evident, one a fast-recovery time constant under 10 ms and the other a

long time constant in the same range as those seen here for PTFM. Because the fast time constants were in the same range as those obtained from electrophysiologic measures of recovery in the whole-nerve action potential (Brown *et al.*, 1990; Brown *et al.*, 1996), it is likely that the fast SPFM time constant reflects refractory characteristics at the level of the auditory nerve and that the long time constant reflects recovery characteristics of more central processes. For SPFM, the fast-recovery time constant was also level independent and GOM slopes were determined by the fast time constant. In both of these studies, forward masking was specified as a threshold shift measured in terms of microamperes of current, i.e., recovery was described by an exponential decline in the difference between masked threshold and absolute threshold over time.

The traditional approach in acoustic hearing specifies forward masking as a threshold shift measured as a ratio of masked threshold to absolute threshold, i.e., recovery was described by an exponential decline in the ratio between masked threshold and absolute threshold over time, expressed in decibels (Duifhuis, 1973; Nelson and Freyman, 1987; Nelson and Pavlov, 1989). Almost all of the forward-masking recovery functions reported in studies of acoustic hearing have time constants shorter than 95 ms, except those obtained from hearing-impaired ears (Nelson and Freyman, 1987). Earlier studies in hearing-impaired subjects did not account for the fact that cochlear nonlinearities are present in normal-hearing ears and absent in hearing-impaired ears. Recent evidence indicates that forward-masking recovery time constants from normal-hearing and hearing-impaired ears are similar if non-linearities in normal-hearing ears are taken into account (Nelson and Schroder, 2001). Thus, recovery from forward masking is similar for normal and impaired acoustic hearing, and as we see here, it is also similar for acoustic and electric hearing.

In the acoustic case, stimulus amplitude must be transformed compressively by a decibel-like conversion process (a compressive nonlinearity within the cochlea), and then the compressed amplitude produces a neural effect that recovers exponentially with time. In the electric case, stimulus amplitude produces a direct neural effect (without any compression) that then recovers exponentially with time. It appears that the neural responses produced by either acoustic or electric stimulation are subjected to the same post-stimulatory recovery processes. This suggests that neural recovery is mediated by adaptation or persistence processes that occur at, or central to, the eighth nerve.

These observations suggest that linear units of electrical stimulation are comparable to logarithmic units of acoustic stimulation. In fact, loudness matches obtained in listeners with acoustic hearing in one ear and electric hearing in the opposite ear indicate that linear changes in μAmps of current are proportional to decibels of acoustic sound pressure (Eddington *et al.*, 1978; Zeng and Shannon, 1992). Thus, the use of linear μAmps of current as the input to a neural adaptation or persistence mechanism in electric hearing is consistent with the use of decibels as the input to the same mechanism in acoustic hearing.

In summary, both the form of the recovery curve de-

scribed by Eq. (3) and the range of time constants obtained across subjects and electrodes in the present study, are consistent with data from previous psychophysical studies of forward masking in both acoustic hearing and electric hearing. These results support the notion that PTFM in electric hearing and pure-tone forward masking in acoustic hearing are mediated by the same physiological mechanisms.

B. Relationship to speech recognition

Our findings suggest that "normal" recovery from PTFM (i.e., tau <95 ms) does not, by itself, predict good speech recognition through a cochlear implant. Among our 21 subjects, the 18 with normal time constants on a middle electrode varied widely in their speech recognition abilities. Two of these subjects had very fast PTFM recovery yet exhibited poor speech recognition. This outcome was also seen in one subject (N3) tested by Chatterjee and Shannon (1998). In our data set, prolonged recovery from PTFM (>95 ms) on both middle and basal electrodes predicted poor speech recognition but prolonged recovery on only an apical electrode did not. This suggests that adequate PTFM recovery may be more important in middle and basal regions of the cochlea where consonant envelope cues are transmitted and less important in apical regions that primarily code vowel formant information. These finding suggest a model wherein PTFM recovery is only one of several psychophysical "requirements" for good speech recognition. It seems certain that another requirement would be adequate spatial resolution, since it has been repeatedly shown that some degree of spectral resolution is critical for speech recognition through a cochlear implant (Nelson *et al.*, 1995; Hanekom and Shannon, 1996; Collins *et al.*, 1997; Donaldson and Nelson, 2000; Henry *et al.*, 2000).

Shannon (1990a) measured PTFM recovery rates similar to the "normal" recovery rates shown here (i.e., <95 ms) in a group of cochlear implant subjects with disparate speech recognition scores. He concluded that recovery from forward masking was unrelated to speech perception. Whereas this appears to be true for the majority of implant users with PTFM time constants <95 ms, Shannon may not have sampled the small proportion of implant users with prolonged forward masking. This group included 3 of 21 subjects tested in our study, suggesting that a small proportion of the implant population may fall into this category.

It is possible that the small segment of cochlear implant listeners with prolonged PTFM time constants have widespread deficiencies in auditory processing rather than a specific deficit in forward-masking recovery. This might be expected if prolonged PTFM recovery is a reflection of widespread or severe auditory degeneration. If so, then subjects with prolonged PTFM time constants may also have poor spatial resolution, further limiting their potential for speech recognition.

V. CONCLUSIONS

Recovery from psychophysical pulse-train forward masking can be described by an exponential recovery pro-
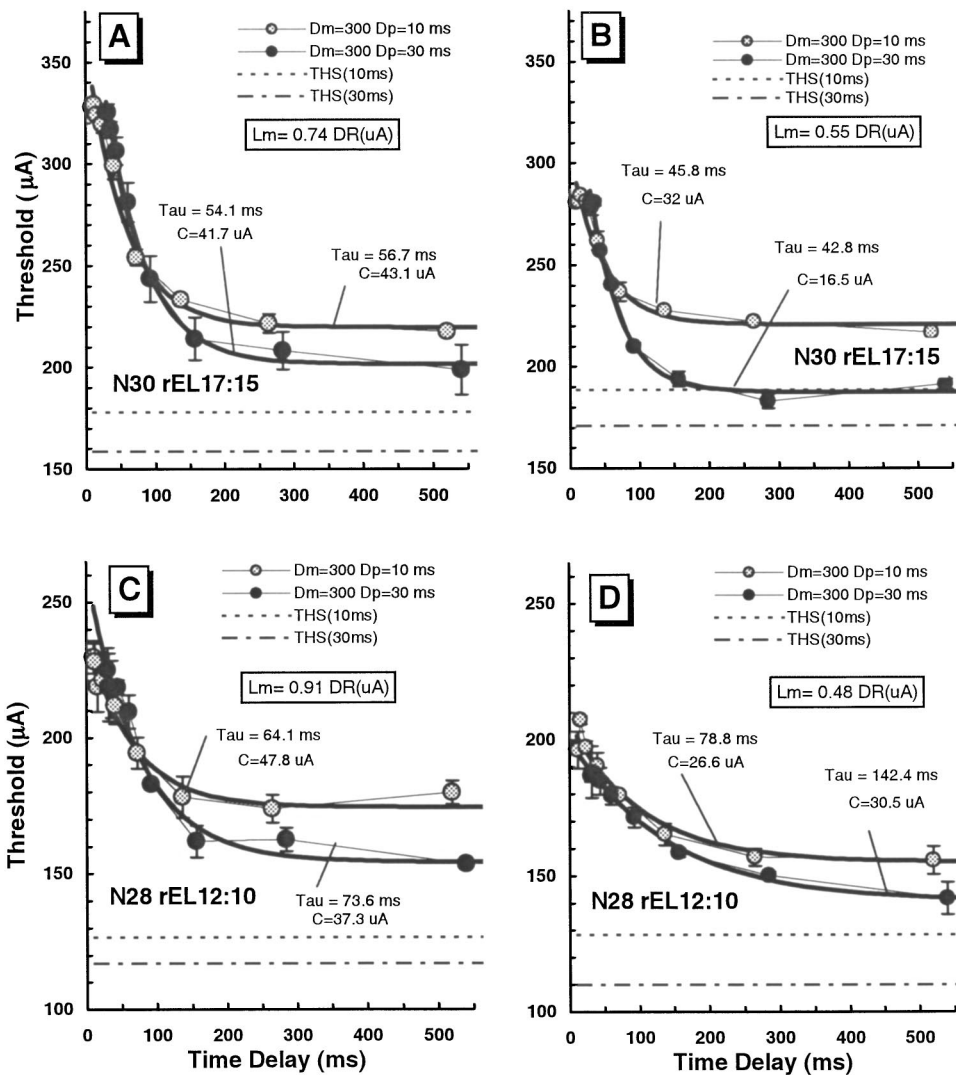
FIG. 9. Pulse-train forward masking functions from two subjects for probe durations of 10 and 30 ms, at two masker levels throughout the masker dynamic range (DR). Threshold of the probe (μA) is plotted against the time delay in ms between masker and probe offsets (note the linear scale on the x axis).

cess in which the amount of threshold shift (in μA) for a pulse-train signal recovers exponentially in time. Time constants for 18 subjects with "normal" PTFM recovery averaged 54 ms with a standard deviation of 17 ms. Time constants are independent of masker level and do not vary systematically with electrode location.

Response to the masker grows monotonically with masker level (in μA). Growth rates at longer time delays are less than 1.0, and are determined by the level-independent time constant. This behavior is consistent with an exponential recovery process.

The addition of a constant residual threshold shift improves the exponential fit to most PTFM recovery curves, consistent with the existence of cumulative fatigue during the experiment or a distraction component.

The PTFM recovery process is similar to that seen with acoustic stimulation. The same recovery model describes acoustic stimulation, the range of time constants is similar for acoustic stimulation, and similar residual constants are needed to obtain good fits for acoustic stimulation. Essentially, recovery of threshold shift (in microamps) in electric hearing is equivalent to recovery of threshold shift (in decibels) in acoustic hearing. The primary difference is in the input of the recovery model; acoustic stimulation requires an

additional compressive transform before the recovery process. These findings are consistent with the idea that linear microamps of electrical stimulation to the auditory nerve are equivalent to acoustic decibels, as suggested by loudness balancing experiments that show a log-linear relationship between acoustic and electrical stimuli.

PTFM recovery parameters obtained from Clarion users were not significantly different than those obtained from Nucleus users, even though maximum acceptable loudness levels and dynamic ranges were significantly smaller in those Clarion users with a HiFocus electrode and electrode positioning system.

Small negative correlations between PTFM time constants and speech recognition scores did not approach statistical significance. Long time constants were associated with poor speech scores; however, short time constants were not strictly associated with good speech scores. Instead, subjects with short time constants demonstrated a wide range of speech recognition performance. This suggests that normal PTFM recovery is only one of several psychophysical abilities needed for good speech recognition in cochlear implant subjects. Adequate spatial resolution is almost certainly another critical factor.

APPENDIX: PTFM RECOVERY FOR 10- AND 30-ms PROBE DURATIONS

If recovery from PTFM is governed by neural adaptation or persistence that recovers or decays gradually following masker offset, then the earlier pulses in the probe must be subjected to more adaptation or persistence than the later pulses. Assuming that detection involves integration of probe excitation over time (temporal integration), then it follows that responses to earlier pulses would contribute less to probe detection than responses to later pulses. This reasoning suggests that when large amounts of adaptation or persistence exist, and recovery or decay is occurring rapidly, the end of the probe pulse train determines detection threshold. If so, then it is most appropriate to specify the time delay between masker and probe pulse trains as the time between masker and probe offsets (rather than the time between masker offset and probe onset).

To examine this issue more closely, PTFM recovery functions were obtained from two subjects (N30 and N28) for two different probe durations. In one case the probe duration was 10 ms, consisting of five biphasic pulses separated by 2 ms (as in the main experiment, above). In the other case the probe duration was 30 ms, consisting of 15 biphasic pulses separated by 2 ms. All other conditions were the same as those described above for the main experiment. The data were actually collected using the same offset-to-onset delays between masker and probe for the 10- and 30-ms conditions, but the recovery curves were displayed and fitted using the corresponding offset-to-offset time delays. Use of the 10-ms probe allowed examination of shorter (offset-to-offset) time delays than was possible with the 30-ms probe.

The PTFM recovery curves obtained at two masker levels and two probe durations are shown in Fig. 9. For both subjects, masked thresholds at time delays shorter than about 100 ms were the same for the 10- and 30-ms probe durations. This means that the extra 10 pulses in the 30-ms probe did not contribute to detection, i.e., little or no temporal integration was observed during the steep recovery portion of the recovery function. In contrast, masked thresholds at time delays longer than 100 ms were considerably lower for the 30-ms probe duration than the 10-ms probe duration. The same was true for quiet thresholds for the probe pulse trains (dashed lines in Fig. 9). At these longer time delays, recovery from adaptation was very gradual, such that responses to early and late portions of the probe were similar. Responses to the additional 10 pulses in the 30-ms probe contributed significantly to detection, therby reducing the probe level at masked (or quiet) threshold.

These results strongly support the specification of PTFM time delay as the time between masker offset and probe offset, since the later pulses in the probe determine detection at time delays less than 100 ms. However, these findings do not resolve the question of whether PTFM is due to adaptation that recovers over time or to neural persistence that decays over time (Oxenham, 2001). In either case, earlier pulses would contribute less to detection than later pulses, due to reduced sensitivity or due to greater persistence at the beginning of the probe train.

---

[1]Facial nerve stimulation restricted electrode selection in two subjects (N31 and N30). For these subjects, test electrodes were distributed across the range of stimulable electrodes.

[2]Only male talkers were used for vowel testing because female talkers exhibit wide, sometimes overlapping, ranges of formant frequencies for a given vowel. This prevents categorization of formant frequencies for purposes of information transmission analyses.

Abbas, P. J., and Gorga, M. P. (**1981**). "AP responses in forward-masking paradigms and their relationship to responses of auditory-nerve fibers," J. Acoust. Soc. Am. **69**, 492–499.

Blamey, P. J., and Dooley, G. J. (**1993**). "Pattern recognition and masking in cochlear implant patients," in *Progress in Brain Research*, edited by J. H. J. Allison, D. J. Allison-Mecklenburg, F. P. Harris, and R. Probst (Elsevier Science, New York), Vol. 97, pp. 271–278.

Brown, C. J., Abbas, P. J., Borland, J., and Bertschy, M. R. (**1996**). "Electrically evoked whole nerve action potentials in Ineraid cochlear implant users: Responses to different stimulating electrode configurations and comparison to psychophysical responses," J. Speech Hear. Res. **39**, 453–467.

Brown, C. J., Abbas, P. J., and Gantz, B. J. (**1990**). "Electrically evoked whole-nerve action potentials: data from human cochlear implant users," J. Acoust. Soc. Am. **88**, 1385–1391.

Chatterjee, M. (**1999**). "Temporal mechanisms underlying recovery from forward masking in multielectrode implant listeners," J. Acoust. Soc. Am. **105**, 1853–1863.

Chatterjee, M., and Shannon, R. V. (**1998**). "Forward masked excitation patterns in multielectrode electrical stimulation," J. Acoust. Soc. Am. **103**, 2565–2572.

Collins, L. M., Zwolan, T. A., and Wakefield, G. H. (**1997**). "Comparison of electrode discrimination, pitch ranking, and pitch scaling data in postlingually deafened adult cochlear implant subjects," J. Acoust. Soc. Am. **101**, 440–455.

Donaldson, G. S., and Allen, S. L. (**2002**). "Effects of presentation level on phoneme and sentence recognition in quiet by cochlear implant listeners," Ear Hear. (submitted).

Donaldson, G. S., and Nelson, D. A. (**1999**). "Single-pulse and pulse-train forward masking functions: Do they reflect different neural recovery processes," Abstracts of 1999 Conference on Implantable Auditory Prostheses (Pacific Grove, California), p. 30.

Donaldson, G. S., and Nelson, D. A. (**2000**). "Place-pitch sensitivity and its relation to consonant recognition by cochlear implant listeners using the MPEAK and SPEAK speech processing strategies," J. Acoust. Soc. Am. **107**, 1645–1658.

Duifhuis, H. (**1973**). "Consequences of peripheral frequency selectivity for nonsimultaneous masking," J. Acoust. Soc. Am. **54**, 1471–1488.

Eddington, D. K., Doebelle, W. H., Brackmann, D. E., Mladejovsky, M. G., and Parkin, J. L. (**1978**). "Auditory prostheses research with multiple channel intracochlear stimulation in man," Ann. Otol. Rhinol. Laryngol. **87**, 5–39.

Hanekom, J. J., and Shannon, R. V. (**1996**). ''Place pitch discrimination and speech recognition in cochlear implant users,'' S Afr. J. Commun. Disord. **43**, 27–40.

Henry, B. A., McKay, C. M., McDermott, H. J., and Clark, G. M. (**2000**). ''The relationship between speech perception and electrode discrimination in cochlear implantees,'' J. Acoust. Soc. Am. **108**, 1269–1280.

Hillenbrand, J., Getty, L. A., Clark, M. J., and Wheeler, K. (**1995**). ''Acoustic characteristics of American English Vowels,'' J. Acoust. Soc. Am. **97**, 3099–3111.

Jesteadt, W., Bacon, S. P., and Lehman, J. R. (**1982**). ''Forward masking as a function of frequency, masker level, and signal delay,'' J. Acoust. Soc. Am. **71**, 950–962.

Levitt, H. (**1971**). ''Transformed up-down methods in psychoacoustics,'' J. Acoust. Soc. Am. **49**, 467–477.

Markman, N. D. (**1989**). ''Recovery from forward masking in listeners with normal hearing, sensorineural hearing loss, and simulated hearing loss,'' Masters thesis, University of Minnesota.

Nelson, D. A., and Donaldson, G. S. (**2001**). ''Psychophysical recovery from single-pulse forward masking in electric hearing,'' J. Acoust. Soc. Am. **109**, 2921–2933.

Nelson, D. A., and Freyman, R. L. (**1987**). ''Temporal resolution in sensorineural hearing-impaired listeners,'' J. Acoust. Soc. Am. **81**, 709–720.

Nelson, D. A., and Pavlov, R. (**1989**). ''Auditory time constants for off-frequency forward masking in normal-hearing and hearing-impaired listeners,'' J. Speech Hear. Res. **32**, 298–306.

Nelson, D. A., and Schroder, A. C. (**2001**). ''A new procedure for estimating peripheral compression in normal-hearing and hearing-impaired ears,'' J. Acoust. Soc. Am. **110**, 2045–2064.

Nelson, D. A., Van Tasell, D. J., Schroder, A. C., Soli, S., and Levine, S. (**1995**). ''Electrode ranking of ''place pitch'' and speech recognition in electrical hearing,'' J. Acoust. Soc. Am. **98**, 1987–1999.

Oxenham, A. J. (**2001**). ''Forward masking: Adaptation or integration?,'' J. Acoust. Soc. Am. **109**, 732–741.

Oxenham, A. J., and Moore, B. C. J. (**1995**). ''Additivity of masking in normally hearing and hearing-impaired subjects,'' J. Acoust. Soc. Am. **98**, 1921–1934.

Patrick, J. F., and Clark, G. M. (**1991**). ''The Nucleus 22-channel cochlear implant system,'' Ear Hear. **12**, 3S–9S.

Plomp, R. (**1964**). ''Rate of decay of auditory sensation,'' J. Acoust. Soc. Am. **36**, 277–282.

Schindler, R. A., and Kessler, D. K. (**1993**). ''Clarion cochlear implant: phase I investigation results,'' Am. J. Otol. **14**, 263–272.

Shannon, R., Zeng, F.-G., Kamath, V., Wygonski, J., and Ekelid, M. (**1995**). ''Speech recognition with primarily temporal cues,'' Science **270**, 303–304.

Shannon, R. V. (**1983**). ''Multichannel electrical stimulation of the auditory nerve in man. I. Basic psychophysics,'' Hear. Res. **11**, 157–189.

Shannon, R. V. (**1986**). ''Temporal processing in cochlear implants,'' in *Sensorineural Hearing Loss: Mechanisms, Diagnosis and Treatment—The Reger Conference*, edited by M. J. Collins, T. J. Glattke, and L. A. Harker, pp. 349–367.

Shannon, R. V. (**1990a**). ''Forward masking in patients with cochlear implants,'' J. Acoust. Soc. Am. **88**, 741–744.

Shannon, R. V. (**1990b**). ''A model of temporal integration and forward masking for electrical stimulation of the auditory nerve,'' in *Cochlear Implants: Models of the Electrically Stimulated Ear*, edited by J. M. Miller and F. A. Spelman (Springer-Verlag, New York), pp. 187–205.

Shannon, R. V., Adams, D. D., Ferrel, R. L., Palumbo, R. L., and Grandgenett, M. (**1990**). ''A computer interface for psychophysical and speech research with the Nucleus cochlear implant,'' J. Acoust. Soc. Am. **87**, 905–907.

Van Tasell, D. J., Greenfield, D. G., Logeman, J. L., and Nelson, D. A. (**1992**). ''Temporal cues for consonant recognition: training, talker generalization, and the use in evaluation of cochlear implants,'' J. Acoust. Soc. Am. **92**, 1247–1257.

Wang, M. D. (**1976**). ''SINFA: Multivariate uncertainty analysis for confusion matrices,'' Behav. Res. Methods Instrum. **8**, 471–472.

Zeng, F. G., and Shannon, R. V. (**1992**). ''Loudness balance between electric and acoustic stimulation,'' Hear. Res. **60**, 231–235.

Susceptibility to acoustic trauma in young and aged gerbils

Flint A. Boettcher[a]

*Department of Otolaryngology—Head & Neck Surgery, Medical University of South Carolina,
39 Sabin Street, Room 608, P.O. Box 250150, Charleston, South Carolina 29425*

The effect of age on susceptibility to noise-induced hearing loss (NIHL), the effect of gender on the interaction of age-related hearing loss (ARHL) and NIHL, and the relative contributions of ARHL and NIHL to total hearing loss are poorly understood. The issues are difficult to resolve empirically in human subjects because of lack of control over extrinsic variables and for ethical reasons. Accordingly, these issues were examined in a well-studied animal model of both ARHL and NIHL, the Mongolian gerbil. Animals were exposed to an intense tone (3.5 kHz, 113 dB SPL, 1 h) either as young adults (6–8 months) or near the end of the average lifespan of the species (34–38 months). Hearing thresholds were determined with the auditory brainstem response (ABR). ARHL was approximately 5–10 dB, with slightly more observed in males at 16 kHz ($p < 0.05$). NIHL of approximately 15–20 dB was similar for the young and old groups, suggesting no differences in susceptibility as a function of age. There were no gender differences in NIHL. The relative contributions of ARHL and NIHL to total hearing loss in aged, noise-exposed gerbils were predicted by an addition of ARHL and NIHL in dB, similar to an international standard on hearing loss allocation, ISO-1999 [Determination of Occupational Noise Exposure and Estimation of Noise-Induced Hearing Impairment (1990)]. Previous evaluations of ISO-1999 using the gerbil animal model concluded that addition of ARHL and NIHL in dB overpredicts total hearing loss. However, in these studies, ARHL was large and nearly equal to NIHL. In the current study, where ARHL was much less than NIHL, addition of the two factors in dB, as recommended by ISO-1999, results in fairly accurate predictions of total hearing loss. © *2002 Acoustical Society of America.*
[DOI: 10.1121/1.1513364]

PACS numbers: 43.66.Ed, 43.66.Sr [MRL]

I. INTRODUCTION

Age-related hearing loss (presbyacusis or ARHL) and noise-induced hearing loss (NIHL) are the two most common types of sensorineural hearing loss. Three issues regarding ARHL and NIHL are not well understood: (a) the effect of ARHL on susceptibility to NIHL; (b) the effect of gender on the interaction of ARHL and NIHL; and (c) the relative contributions of ARHL and NIHL to hearing loss in the older, noise-exposed individual. The issues of susceptibility to noise as a function of age and the contributions of ARHL and NIHL to the hearing loss in an older individual are necessary for determining the need for age-correction factors for occupational health standards and medical-legal issues (Dobie, 1993).

Occupational hearing standards, or the laws that govern the allowable noise exposures in a working environment, do not incorporate age correction factors. Whereas the current noise standard for most workers in the United States, the Occupational Safety and Health Act (OSHA, 1971, 1981), states that a worker may be exposed to a time-weighted average of 90 dBA with a 5-dB trading ratio without protection (thus, 8 h per day at 90 dBA, 4 h at 95 dBA, etc.), there are no corrections for the age of the individual. If an older individual has a different susceptibility to NIHL than a young worker, standards should reflect these age-related differences in susceptibility to NIHL.

A. Age and susceptibility

Little is known regarding the effects of ARHL on susceptibility to subsequent NIHL in human subjects. Welleshick and Raber (1978, described in Dobie, 1993) reported that persons with preexisting ARHL incurred further hearing loss due to occupational noise exposure, although Novotny (1975) did not find such an effect in persons entering noisy occupations late in life. Results from animal studies regarding the influence of ARHL on susceptibility to NIHL are contradictory. Whereas Sun *et al.* (1994) reported that aged chinchillas incurred similar amounts of hair cell loss from noise as young chinchillas, McFadden *et al.* (1997) reported that older chinchillas had more hair cell loss, but not hearing loss, than young chinchillas following noise exposure. Miller *et al.* (1998) exposed young and aged CBA/J mice with similar preexposure thresholds to noise and reported that aged animals were more susceptible to both threshold shifts (as measured with ABRs) and hair cell loss.

B. Gender effects

It is generally accepted that older males have more high-frequency hearing loss than females. Epidemiologic databases show as much as 12–20 dB more hearing loss in males than females at 4 kHz at ages 55 years and over (Gallo and Glorig, 1964; Glorig and Roberts, 1965; Milne and Lauder, 1975; Milne, 1977; Robinson and Sutton, 1979; Møller, 1981; Moscicki *et al.*, 1985; Robinson, 1988; Pedersen *et al.*, 1989; Gates *et al.*, 1990).

[a]Electronic mail: boettcfa@musc.edu

Data regarding gender effects on NIHL vary. Several studies suggest that males may be more susceptible to NIHL than females (Gallo and Glorig, 1964; Ward, 1966; Berger *et al.*, 1978) whereas others do not necessarily support such a conclusion (Baughn, 1973). The data of Baughn, redrawn in Berger *et al.* (1978), show minimal gender differences in hearing loss at 4 kHz. Similarly, a replotting of data of Burns and Robinson (1970) by Berger *et al.* show losses of approximately 5 dB in both males and females after 10 years of exposure, although Burns and Robinson suggested a 1.5-dB correction factor (i.e., that males were slightly more susceptible to noise). In contrast, Berger *et al.* (1978) reported that females working in a factory with A-weighted L_{eqs} of approximately 89 dB incurred only about 5 dB of NIHL at 4 kHz compared to approximately 15 dB in males. They used corrections for age from a control group, but neither the control nor experimental groups were screened for nonoccupational noise. Welleschick and Körpert (1980; described in Ward, 1995) reported that NIHL grew at the same rate in males and females exposed to similar noise. Similarly, Müller and Richartz (1989; described in Ward, 1995) reported no differences in occupational hearing loss in a group of 65 males and 65 females. In some of the few animal studies examining the issue of gender and susceptibility to noise, McFadden and colleagues reported that male chinchillas incur more high-frequency NIHL from exposure to impulse noise than females, but that the opposite is true at low frequencies (McFadden *et al.*, 1999, 2000).

C. ISO-1999

A great deal of controversy has been generated regarding the most accurate method for assessing the relative contributions of ARHL and NIHL in an individual. A current international standard used for workers' compensation assumes that ARHL and NIHL add in dB to produce a total hearing loss. The standard is termed ISO-1999 and is cited as ISO (1990) or ISO-1999. The formula is in the form

$$ HL = ARHL + NIHL - \frac{(ARHL)(NIHL)}{120}, \qquad (1) $$

with the latter portion a compression factor used for hearing losses over 40 dB. ARHL is predicted from Database A of ISO-1999 [based primarily on an analysis of several data bases by Passchier-Vermeer (1977) and Johnson (1978)] which consists of hearing thresholds (dB HL) as a function of age. NIHL is also predicted based on data from ISO-1999 (based largely on a summary of Johnson, 1978) which show thresholds as a function of duration of noise exposure. A series of curves is available based on the intensity of the noise. Data are available for both ARHL and NIHL for the median as well as most and least susceptible individuals. To allocate hearing loss in an individual, ARHL is taken from Database A based on the age of the individual and HL is measured empirically. NIHL is then determined by subtracting ARHL from HL (with the compression factor used if necessary). What cannot be determined empirically in an individual are the ARHL or NIHL components of the loss.

The ISO-1999 formula has been supported by studies with human subjects (Macrae, 1971, 1991b; Johnson, 1978; Robinson, 1991) and gerbils when external controls were used (Mills, 1992). In the latter, gerbils were raised in 85 dBA noise for 720 days and hearing losses were predicted by the addition of NIHL and ARHL in dB. The age-only controls were gerbils raised in a quiet animal colony. Thus, this experiment was performed with a procedure similar to that used in ISO-1999; NIHL could only be extrapolated by using a nonexposed group.

In contrast, Mills *et al.* (1997, 1998) reported that when internal controls were used, ARHL and NIHL combined to produce hearing loss equal to the sum of the intensities of the losses. In the latter experiment, gerbils aged approximately 18 months were exposed monaurally to an intense tone (113 dB SPL, 3.5 kHz, 1 h) under anesthesia, similar to that used in the present experiment. Subjects incurred a mean NIHL of 20–25 dB in the exposed ear at 4–8 kHz and little or no NIHL in the contralateral ear. The animals were allowed to age to 36 months and retested. The thresholds (in dB SPL) in the unexposed ears at 36 months defined the ARHL, the thresholds (in dB SPL) in the exposed ears at 20 months defined the NIHL, and the thresholds (in dB SPL) in the exposed ears at 36 months defined the HL. Addition of ARHL and NIHL in dB, as described in ISO-1999, resulted in significantly larger hearing losses than observed empirically. A modified power-law model closely predicted the observed loss (Mills *et al.*, 1997, 1998). Similarly, Corso (1976) and Bies and Hansen (1990) have suggested that hearing loss interacts in a manner reflecting addition in sound intensity rather than in dB and Humes and Jesteadt (1991) proposed a power-law formula as a fit to empirical data.

Despite questions regarding its accuracy, ISO-1999 is straightforward and easy to implement in clinical and medical-legal situations and remains the most common method for allocation of ARHL and NIHL. Furthermore, several authors have extended ISO-1999 for use following exposures of different characteristics (Dobie, 1993; Lutman, 1996). Empirical evaluation of ARHL and NIHL is difficult in human subjects because of lack of control over extrinsic variables (i.e., nonoccupational noise exposure, otologic disease, and exposure to ototoxic drugs) as well as ethical considerations (i.e., human subjects cannot be exposed to noise which causes NIHL and workers showing NIHL must receive hearing protection or be removed from a work environment).

Limitations in human studies as well as earlier equivocal results suggest that empirical evaluation of occupational noise standards, gender effects on ARHL and NIHL, and allocation models of hearing loss require an animal model. The Mongolian gerbil is a well-studied model of both ARHL (e.g., Mills *et al.*, 1990; Schulte and Schmiedt, 1992; Keithley *et al.*, 1989; Boettcher *et al.*, 1993a, b; Gratton and Schulte, 1995; Thomopoulos *et al.*, 1997) and NIHL (e.g., Schmiedt *et al.*, 1990; Boettcher, 1993; Boettcher and Schmiedt, 1995; White *et al.*, 1998). Accordingly, the gerbils are particularly good species for studying the interaction of these two forms of hearing loss. The present study examines

the interaction in a different experimental paradigm than that used by Mills *et al.* (1997, 1998) and allows for empirical examination of allocation models of hearing loss.

II. METHODS

A. Subjects

Mongolian gerbils (*Meriones unguiculatus*), aged either 6–8 months ($n = 17$) or 34–38 months ($n = 17$), were used as subjects. Young animals were excluded from the study if they had preexposure thresholds at any frequency greater than one standard deviation above the mean as previously described for young gerbils (Mills *et al.*, 1990). Each gerbil was born and raised in a sound-shielded vivarium with average A-weighted sound levels of 35–40 dB. Subjects had normal presentation upon otoscopic examination, had no history of otologic disease, and received no ototoxic drugs. Procedures utilized in the project were approved by the Institutional Animal Care and Use Committee of the Medical University of South Carolina.

B. Stimuli

Stimuli were 1.8 ms tone pips (0.7 ms rise–fall times; octave intervals from 1 to 16 kHz) presented at a rate of 11/s, at levels of 10–80 dB SPL in 5- or 10-dB steps (see below). Spectra of the signals have been previously published in Dolan *et al.* (1985) and Mills *et al.* (1990). The stimuli were generated digitally (16-bit D/A, Tucker-Davis Technology© [TDT], 200-kHz sampling rate), attenuated, and presented freefield through a Beyer DT-48 earphone placed approximately 5 mm from the pinna of a subject. The earphone was calibrated for each subject using a Knowles microphone located in a customized probe tube. The probe microphone system, calibrated with a B&K sound level meter, was clipped to the pinna of a subject with the opening of the tube at the opening of the ear canal.

C. Data collection

Each subject was anesthetized with a mixture of ketamine (35 mg/kg) and xylazine (8 mg/kg) and placed on an automated heating pad which maintained body temperature at a stable 37.5 °C, normal for the Mongolian gerbil. Customized needle electrodes were placed at vertex (positive) and behind each mastoid (reference for each test ear). A bite bar served as the ground. Neurological activity was routed from the electrode to a Grass Model 12 Neurodata system where it was amplified (100 000×), and filtered (0.3–3.0 kHz, 6 dB/oct filter slopes), and routed to a TDT A/D convertor (25-kHz sampling rate).

Thresholds were chosen as the mid-point between two levels, where a response was clearly observed in any of the three prominent ABR waves at the higher level but absent at the lower level. The exception to this was if a response was observed near a criterion of 0.25 μV (peak-to-trough); in this case, the level at which this criterion was observed was chosen as threshold. This technique has been successfully used to measure gerbil ABR thresholds for many years with little
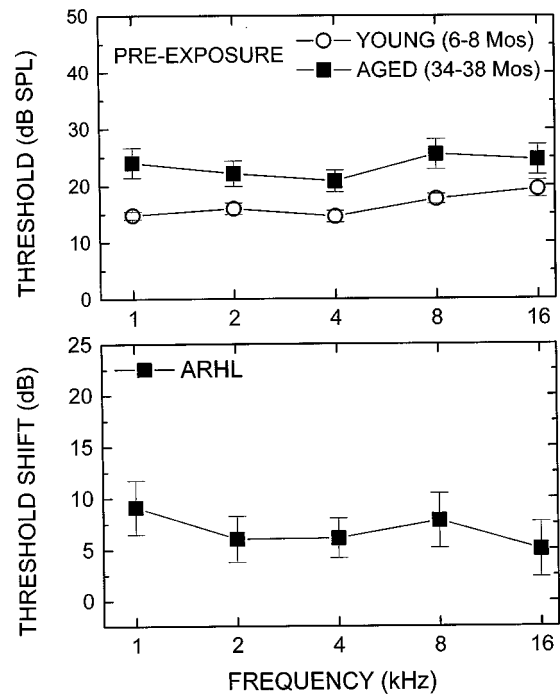
FIG. 1. Upper panel: Mean (± 1 SE) preexposure thresholds in dB SPL for 17 young (6–8 months) and 17 aged (34–38 months) Mongolian gerbils. Values are the average of two preexposure tests in each subject. Lower panel: Mean ARHL for aged gerbils, defined as preexposure thresholds for aged gerbils *minus* preexposure thresholds for young gerbils.

interexperimenter variability in threshold judgment (see Mills *et al.*, 1990; Boettcher *et al.*, 1993a, b).

Thresholds were determined 10 days prior to exposure (using 10-dB steps in threshold measurement) and again immediately prior to exposure (using 5-dB steps). These two preexposure tests were averaged as the preexposure threshold. Thresholds were measured again in 5-dB steps approximately 30 days following exposure.

D. Exposure

Each animal was exposed monaurally to a 3.5-kHz tone at a level of 113 dB SPL for one hour. The exposure was performed under anesthesia (identical to that for threshold testing). The exposure stimulus was generated digitally (TDT Waveform Generator), amplified (Crown Amplifier Model D60), and presented freefield through a Beyer DT-48 earphone fitted with an otoscope speculum. The speculum was placed near the entrance to the ear canal of the subject. The level of the exposure was calibrated in a manner similar to that described for calibration of signals used in threshold testing. The contralateral ear of each subject was plugged; the average level at the entrance to the contralateral ear was 91 dB SPL at 3.5 kHz. Thresholds were tested in a subset of unexposed (contralateral) ears and average shifts were less than 5 dB one-month following exposure.

III. RESULTS

A. Preexposure sensitivity and age-related hearing loss

Figure 1 (upper panel) shows the preexposure thresholds in dB SPL for the two groups. The mean preexposure thresh-

FIG. 2. Upper panel: Mean (±1 SE) thresholds in dB SPL in young and aged gerbils, recorded approximately 4 weeks after exposure to a 3.5-kHz tone at 113 dB SPL for 1 h. Lower panel: Mean (±1 SE) noise-induced hearing loss (NIHL) in dB in young and aged gerbils, recorded approximately 4 weeks after exposure to a 3.5-kHz tone at 113 dB SPL for 1 h. NIHL is the threshold measured 4 weeks after exposure *minus* the preexposure threshold.

FIG. 3. Upper panel: Mean (±1 SE) age-related hearing loss (ARHL) in dB in six male and nine female gerbils aged 34–38 months. ARHL equals the preexposure thresholds for aged subjects *minus* the preexposure thresholds for young subjects of the same gender. Lower panel: Mean (±1 SE) noise-induced hearing loss (NIHL) in dB in aged subjects. NIHL equals the postexposure thresholds for the aged male and female subjects *minus* the preexposure thresholds for the same subjects.

olds for the young animals ranged from approximately 15 to 19 dB SPL, within the range of normal for young gerbils as described by Mills *et al.* (1990). The mean preexposure thresholds for the aged subjects ranged from approximately 22 dB SPL at 4 kHz to 27 dB SPL at 8 kHz. The lower panel of Fig. 1 shows the ARHL, or the difference in the preexposure thresholds between the groups, plotted in terms of dB threshold shift. The ARHL ranged from 5 to 9 dB and was statistically significant at 1–8 kHz (two-tailed *t*-tests, assuming unequal variance [based on an *F*-test], $p < 0.05$), but not at 16 kHz. The ARHL was fairly uniform across frequency and relatively small compared to the average ARHL reported by Mills *et al.* (1990).
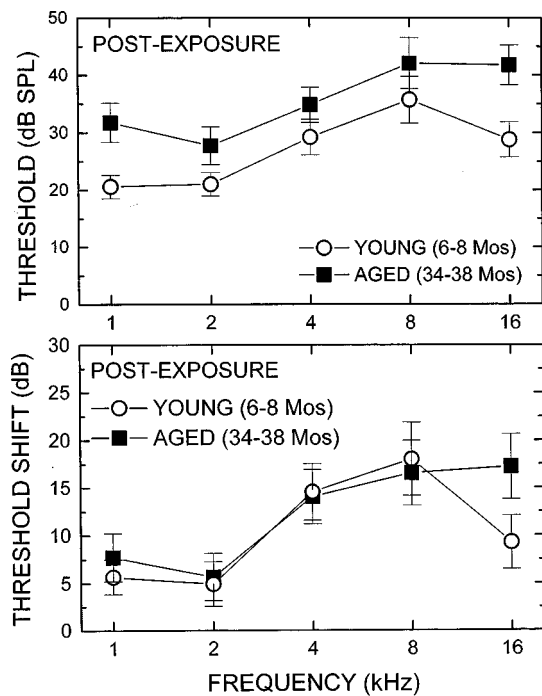
B. Postexposure thresholds and noise-induced hearing loss

Figure 2 (upper panel) shows the mean postexposure thresholds in dB SPL for the two groups. The postexposure thresholds for the young subjects ranged from approximately 20 dB SPL at 1 kHz to 36 dB SPL at 8 kHz. Postexposure thresholds for the aged subjects ranged from approximately 27 dB SPL at 2 kHz to 42 dB SPL at 8 and 16 kHz. The differences in postexposure thresholds between young and aged subjects were statistically significant at 1 and 16 kHz (*t*-tests, $p < 0.05$). The lower panel of Fig. 2 shows the NIHL in dB (postexposure thresholds *minus* preexposure thresholds) for the two groups. The NIHL was minimal at 1 and 2 kHz (6 dB or less) as would be expected given the spectrum

of the exposure. The NIHL ranged from 15 to 18 dB at 4 and 8 kHz for the two groups; at 16 kHz the shift was approximately 9.3 dB for the young subjects and 17 dB for the aged subjects. Differences in NIHL between groups were not significant at 1–8 kHz, whereas NIHL was significantly larger in the aged subjects than in young subjects at 16 kHz ($p < 0.05$).

C. Gender effects

Figure 3 (upper panel) shows ARHL in dB for seven male and ten female gerbils aged 34–38 months. Here, ARHL refers to the mean preexposure thresholds for males and for females *minus* the mean preexposure thresholds for young gerbils of the same gender. ARHL ranged from approximately 0 to 8 dB for females and 8 to 12 dB for males. Although there was a trend for males to have more ARHL than females, the difference was statistically significant only at 16 kHz ($p < 0.05$).

The lower panel of Fig. 3 shows NIHL for aged males and females. Here, NIHL refers to the postexposure thresholds for males and for females *minus* preexposure thresholds in the same subjects. NIHL ranged from approximately 5 to 20 dB in the females and 6 to 16 dB in the males. There were no significant differences in NIHL between the two groups at any frequency ($p > 0.05$). There were too few young males to make a meaningful comparison between genders regarding susceptibility to NIHL in young gerbils.
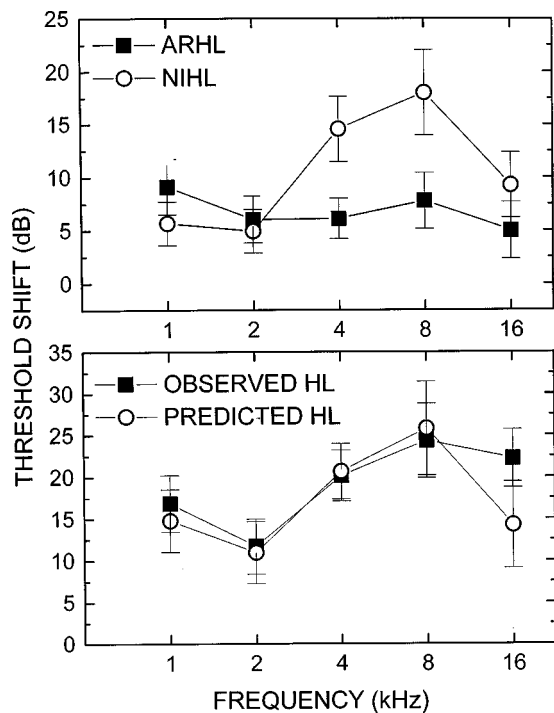
FIG. 4. Upper panel: Mean (±1 SE) NIHL used in testing the ISO-1999 allocation formula. Lower panel: Observed HL in aged subjects compared to predicted threshold shift in the aged subjects according to ISO-1999.

D. Evaluation of ISO-1999

An international standard (ISO-1999) states that ARHL and NIHL add in dB, such that total hearing loss in an older, noise-exposed individual equals ARHL+NIHL −(ARHL*NIHL/120) [see Eq. (1) above]. In humans, HL is an empirically measured threshold or threshold shift, ARHL is estimated from the age of the subject (based on Database A of ISO-1999), and NIHL may be derived through subtraction of ARHL from HL. These values are specified as shifted thresholds; i.e., ARHL is the threshold change in an older subject compared to younger subjects. In this study, the evaluation of ISO-1999 was made as follows:

ARHL=(preexposure thresholds for aged gerbils *minus* preexposure thresholds for young gerbils);

NIHL=(postexposure thresholds for young gerbils *minus* preexposure thresholds for young gerbils);

HL=postexposure thresholds for aged gerbils *minus* preexposure thresholds for young gerbils).

Figure 4 (upper panel) shows the mean (±1 SE) values for ARHL and NIHL used to evaluate ISO-1999. Figure 4 (lower panel) shows the predicted values of HL using ISO-1999 compared to observed values of HL. Thus, in this experiment, predictions used in the ISO formula were similar to the observed threshold shifts in noise-exposed older gerbils, except at 16 kHz.

IV. DISCUSSION

A. Effects of age on susceptibility to noise

The results demonstrate that aged gerbils with mild ARHL are equally susceptible to intense noise exposure as young gerbils with normal thresholds. An exception was at 16 kHz where aged subjects had slightly more NIHL than young subjects. Although gerbils hear at frequencies above 16 kHz, the frequency range of interest in this experiment was that of human hearing.

However, it is possible that the interaction of ARHL and NIHL differs in the apical and basal regions of the cochlea. Thus, histopathological studies are being performed on the animals described in this study to determine if cochlear damage from noise differs between young and aged subjects.

As previously described, OSHA standards require hearing protection for any worker exposed to a time-weighted average of 90 dBA (OSHA, 1971, 1981), but such standards do not incorporate corrections for the age or prior hearing loss of the individual. The data from the present study do not necessarily support the need for age-correction factors in occupational standards. The data also suggest that a person with a strictly age-related hearing loss is not more susceptible to additional hearing loss from amplification than a younger person.

There are several *caveats* that must be considered regarding the present results. First, the data were collected in nonhuman subjects. The exposure was a short-duration, intense tone which is not typical of occupational noise exposure. Finally, there is some evidence that the ABR may overestimate threshold shift in aged subjects as compared to behavioral thresholds (Mills *et al.*, 2001). The latter would suggest that ARHL may have been overestimated, but results nevertheless do not support the assumption that older individuals will incur greater hearing loss from noise than young subjects.

Mouse models have also been used to examine susceptibility to NIHL as a function of age. Some mouse strains (such as the CBA) show age-related hearing loss which follows a pattern similar to most species, i.e., a very gradual loss as a function of age, whereas others (e.g., the C57BL/6 and BALB/c) demonstrate a rapidly progressive hearing loss which starts much earlier in the lifespan of the species than does the age-related loss observed in other species. The C57BL/6 mouse, which carries the *Ahl* mutation for age-related hearing loss (Erway *et al.*, 1993, 1996) is more susceptible to NIHL than CBA mice (Shone *et al.*, 1991; Li, 1992; Erway *et al.*, 1996). Recently, Ohlemiller *et al.* (2000) reported that a wideband noise (4–45 kHz, 110–113 dB SPL, 1–63 minute duration) caused more NIHL and hair cell loss in 5–7-month-old C57BL/6 and BALB/c than in CBA mice. The studies using C57BL/6, BALB/c, and other mice with early-onset hearing loss are difficult to interpret due to differences in age-related histopathology of the auditory system of these strains compared with humans and most laboratory mammals. Mice with early-onset hearing loss, such as the C57BL/6, lose hair cells early in life (Willott and Mortenson, 1991; Willott *et al.*, 1998; Spongr *et al.*, 1997). In contrast, humans and laboratory species such as the gerbil and chinchilla with minimal exposure to noise maintain a relatively normal complement of hair cells. Indeed, most studies show that sensory cell losses are limited to the extreme basal and apical ends of the cochlea (Tarnowski *et al.*, 1991; Bohne *et al.*, 1990; Sun *et al.*, 1994) and are likely to

be the least important cause of ARHL in the human (Schuknecht and Gacek, 1993). Instead, ARHL is associated with degeneration of the lateral wall of the cochlea (Schulte and Schmiedt, 1992; Schuknecht and Gacek, 1993) and primary degeneration of the spiral ganglion (Keithley *et al.*, 1989; Felder *et al.*, 1995, 1997). Although commonly used as a model of human presbyacusis, the time course of the hearing loss as well as the histopathologic mechanism of hearing loss in the C57BL/6 and related mouse strains are not consistent with ARHL in humans or other laboratory species. Thus, the gerbil, chinchilla, or CBA mouse may be more appropriate models of the influence of age on susceptibility to NIHL than the C57BL/6 or BALB/c mouse.

B. Gender effects on the interaction of ARHL and NIHL

Although the sample sizes for the two gender groups were small, the results suggest that older female and male gerbils incur similar amounts of NIHL, but that male gerbils have slightly more ARHL than females at very high frequencies. As all subjects were exposed at the time of existing ARHL, the data further suggest no gender effects on the interaction of ARHL and NIHL. Extrapolation of these results would suggest that in a group of well-screened older subjects, older males might be expected to have slightly poorer high-frequency thresholds than females. These data are consistent with epidemiologic studies of older individuals (e.g., ISO-1999, 1990; Gates *et al.*, 1990; Pearson *et al.*, 1995) that have shown that males have greater high-frequency hearing loss than females.

The results from the present study suggest no gender effects on susceptibility to NIHL in older subjects. Several human studies (Gallo and Glorig, 1964; Ward, 1966; Burns and Robinson, 1970; Berger *et al.*, 1978) have suggested that males may be more susceptible than females to NIHL, although age of the subject at the time of exposure has not always been controlled. As described previously, a reanalysis of Baughn (1973) by Berger *et al.* (1978), as well as data from Welleschick and Körpert (1980) and Müller and Richartz (1989) do not demonstrate a significant gender effect in susceptibility to noise and thus data from the present study are consistent with such results. In some of the few animal studies examining the issue of gender, data from chinchillas (McFadden *et al.*, 1999, 2000) suggest that females may be more susceptible to NIHL at low frequencies than males with the converse true at higher frequencies. Several possibilities exist for the differences in results across studies. First, the data from the present study come from animals raised in a well-controlled environment so that all extrinsic sources of hearing loss could be ruled out, which is not the case in epidemiologic studies in humans. Furthermore, McFadden *et al.* (1999, 2000) used an impulse noise in the chinchilla, which may cause immediate mechanical damage to the cochlea (i.e., see Hamernik *et al.*, 1986) compared to more gradual damage in the noise used in the present study. In summary, further data are required to definitively address the relationship of gender and ARHL, NIHL, and the interaction of the two.

C. Evaluation of predictions using ISO-1999 and the intensity rule

ISO-1999 is a current international standard used to determine the age-related and noise-induced components of a hearing loss in an older, noise-exposed individual. The formula, described previously, purports accurate prediction of total hearing loss if ARHL and NIHL are added in dB. The results of this experiment suggest that predictions using the ISO-1999 formula were accurate at 1–8 kHz in estimating the total hearing loss caused by exposure to a narrow-band signal. Mills *et al.* (1997, 1998), using a similar signal, concluded that addition of ARHL and NIHL in dB overpredicts the total hearing loss in aged, exposed ears. Instead, these authors showed that adding the losses due to age and noise in intensity units predicted their data more successfully. The difference in outcomes between the present study and Mills *et al.* (1997, 1998) may be explained as follows. In this study, ARHL was small, and was much smaller than NIHL at some frequencies. Therefore, differences in prediction using addition in dB and addition in intensity would be negligible. This was not the case in the earlier studies of Mills, where ARHL and NIHL were larger and approximately equal at some frequencies, which would result in larger differences in predictions between the ISO-1999 prediction and the intensity-rule prediction.

In summary, if ARHL and NIHL are large and similar, ISO-1999 overpredicts the total hearing loss but is accurate when the two are small or very unequal. For example, if ARHL is 20 dB and NIHL is 20 dB, ISO-1999 predicts a total loss of 40 dB whereas the intensity rule predicts a loss of 23 dB, a value similar to that observed in previous laboratory studies. In contrast, if ARHL is 5 dB and NIHL is 20 dB, ISO-1999 would predict a total loss of 25 dB, whereas the intensity rule would predict a value of 20–21 dB, suggesting that both formulas are valid if ARHL and NIHL are small or very different.

V. SUMMARY AND CONCLUSIONS

The results of this experiment demonstrate that (a) aged gerbils are not more susceptible than young adult gerbils to threshold elevation caused by exposure to an intense tone (3.5 kHz, 113 dB SPL, 1 h); (b) male and female gerbils incur similar degrees of noise-induced hearing loss but males incur slightly more high-frequency age-related hearing loss; and (c) if either the age-related or noise-induced component of a hearing loss is relatively small compared to the other component, an international standard for allocation of hearing loss, ISO-1999, is fairly accurate at predicting the total hearing loss in an older, noise-exposed individual. The experiments do not suggest a need for correction factors for age in rules regarding allowed exposure to occupational noise. Furthermore, they support evidence that males have more high-frequency hearing loss than females, including in conditions where no extrinsic effects on the auditory system occur, thus suggesting that greater high-frequency loss in males is not simply due to noise exposure. Previous studies with gerbils (Mills *et al.*, 1997, 1998) suggest that ISO-1999 is not accurate in predicting hearing loss when the age-related

J. Acoust. Soc. Am., Vol. 112, No. 6, December 2002

Flint A. Boettcher: Susceptibility to acoustic trauma 2953

and noise-induced components of a loss are fairly equal, whereas the present study suggests ISO-1999 is accurate if the losses are unequal. Further laboratory studies, with control over extrinsic factors affecting hearing, are warranted to better define the boundaries of hearing loss in which ISO-1999 is accurate.

Baughn, W. L. (**1973**). "Relation between daily noise exposure and hearing loss based on the evaluation for 6, 835 industrial exposure cases," Aerosp. Med. Res. Lab, Wright-Patterson AFB, OH, Rep. No. AMRL-TR-73-53.

Berger, E. H., Royster, L. R., and Thomas, W. G. (**1978**). "Presumed noise-induced permanent threshold shift resulting from exposure to an A-weighted Leq of 89 dB," J. Acoust. Soc. Am. **64**, 192–197.

Bies, D. A., and Hansen, C. H. (**1990**). "An alternative mathematical description of the relationship between noise exposure and hearing loss," J. Acoust. Soc. Am. **88**, 2743–2754.

Boettcher, F. A. (**1993**). "Auditory brain-stem response correlates of resistance to noise-induced hearing loss in the Mongolian gerbil," J. Acoust. Soc. Am. **94**, 3207–3214.

Boettcher, F. A., and Schmiedt, R. A. (**1995**). "Distortion-product otoacoustic emissions in Mongolian gerbils with resistance to noise-induced hearing loss," J. Acoust. Soc. Am. **98**, 3215–3222.

Boettcher, F. A., Mills, J. H., and Norton, B. L. (**1993a**). "Age-related changes in auditory evoked potentials of gerbils. I. Response amplitudes," Hear. Res. **71**, 137–145.

Boettcher, F. A., Mills, J. H., Norton, B. L., and Schmiedt, R. A. (**1993b**). "Age-related changes in auditory evoked-potentials of gerbils. II. Response latencies," Hear. Res. **71**, 146–156.

Bohne, B. A., Gruner, M. M., and Harding, G. W. (**1990**). "Morphological correlates of aging in the chinchilla cochlea," Hear. Res. **48**, 79–92.

Burns, W., and Robinson, D. W. (**1970**). Hearing and Noise in Industry (Her Majesty's Stationary Office, London).

Corso, J. F. (**1976**). "Presbyacusis as a complicating factor in evaluating noise-induced hearing loss," in Effects of Noise on Hearing, edited by D. Henderson, R. P. Hamernik, D. S. Dosanjh, and J. H. Mills (Raven, New York), pp. 497–524.

Dobie, R. A. (**1993**). Medical-Legal Evaluation of Hearing Loss (Van Nostrand Reinhold, New York).

Dolan, T. G., and Maurer, J. F. (**1996**). "Noise exposure associated with hearing aid use in industry," J. Speech Hear. Res. **39**, 251–260.

Dolan, T. G., Mills, J. H., and Schmiedt, R. A. (**1985**). "Brainstem, whole-nerve AP and single-fiber suppression in the gerbil: normative data," Hear. Res. **18**, 203–210.

Erway, L. C., Willott, J. F., Arch, J. R., and Harrison, D. E. (**1993**). "Genetics of age-related hearing loss in mice: I. Inbred and F1 hybrid strains," Hear. Res. **65**, 125–132.

Erway, L. C., Shiau, Y.-W., Davis, R. R., and Kreig, E. F. (**1996**). "Genetics of age-related hearing loss in mice. III. Susceptibility of inbred and F1 hybrid strains to noise-induced hearing loss," Hear. Res. **93**, 181–187.

Felder, E., and Schrott-Fischer, A. (**1995**). "Quantitative evaluation of myelinated nerve fibers and hair cells in cochleae of humans with age-related high-tone hearing loss," Hear. Res. **91**, 19–32.

Felder, E., Kanonier, G., Scholtz, A., Rask-Anderson, H., and Schrott-Fischer, A. (**1997**). "Quantitative evaluation of cochlear neurons and computer-aided three dimensional reconstruction of spiral ganglion cells in humans with a peripheral loss of nerve fibers," Hear. Res. **105**, 183–190.

Gallo, R., and Glorig, A. (**1964**). "Permanent threshold shift changes produced by noise exposure and aging," Am. Ind. Hyg. Assoc. J. **25**, 237–245.

Gates, G. A., Cooper, J. C., Kannel, W. B., and Miller, N. J. (**1990**). "Hearing in the elderly: The Framingham cohort, 1983–1985," Ear Hear. **11**, 247–256.

Glorig, A., and Roberts, J. (**1965**). Hearing Levels of Adults by Age and Sex: United States—1960–1962, Vital and Health Statistics Survey, Public Health Service, Washington, DC, Publication 1000, Series 11, No. 11.

Gratton, M. A., and Schulte, B. A. (**1995**). "Alterations in microvasculature are associated with atrophy of the stria vascularis in quiet-aged gerbils," Hear. Res. **82**, 44–52.

Hamernik, R. P., Ahroon, W. A., and Hsueh, K. D. (**1986**). "Impulse noise: Critical review," J. Acoust. Soc. Am. **80**, 569–584.

Humes, L. E., and Jesteadt, W. (**1991**). "Modeling the interaction between noise exposure and other variables," J. Acoust. Soc. Am. **90**, 182–188.

International Organization for Standards: Acoustics (**1990**). Determination of Occupational Noise Exposure and Estimation of Noise-Induced Hearing Impairment, ISO-1999, Geneva.

Johnson, D. L. (**1978**). "Derivation of presbycusis and noise induced permanent threshold shift (NIPTS) to be used for the basis of a standard on the effects of noise on hearing," AMRL-TR-78-128. Aerospace Medical Research Laboratory, Wright-Patterson AFB, OH.

Keithley, E. M., Ryan, A. F., and Woolf, N. K. (**1989**). "Spiral ganglion cell density in young and old gerbils," Hear. Res. **38**, 125–134.

Li, H. S. (**1992**). "Influence of genotype and age on acute acoustic trauma and recovery in CBA/Ca and C57BL/6J mice," Acta Oto-Laryngol. **112**, 956–967.

Lutman, M. E. (**1996**). "Estimation of noise-induced hearing impairment for compound noise exposures based on ISO 1999," J. Audiol. Med. **5**, 1–7.

Macrae, J. H. (**1971**). "Noise-induced hearing loss and presbyacusis," Audiology **10**, 323–333.

Macrae, J. H. (**1991a**). "Presbycusis and noise-induced permanent threshold shift," J. Acoust. Soc. Am. **90**, 2513–2516.

Macrae, J. H. (**1991b**). "Permanent threshold shift associated with overamplification by hearing aids," J. Speech Hear. Res. **34**, 403–414.

McFadden, S. L., Henselman, L. W., and Zhang, X. Y. (**1999**). "Sex differences in auditory sensitivity of chinchilla before and after exposure to impulse noise," Ear Hear. **20**, 164–174.

McFadden, S. L., Zhang, X. Y., and Ding, D.-L. (**2000**). "Conditioning-induced protection from impulse noise in female and male chinchillas," J. Acoust. Soc. Am. **107**, 2162–2168.

McFadden, S. L., Campo, P., Quaranta, N., and Henderson, D. (**1997**). "Age-related decline of auditory function in the chinchilla (Chinchilla laniger)," Hear. Res. **111**, 114–126.

Miller, J. M., Dolan, D. F., Raphael, Y., and Altschuler, R. A. (**1998**). "Interactive effects of aging with noise induced hearing loss," Scand. Audiol. Suppl. **48**, 53–61.

Mills, J. H. (**1992**). "Noise-induced hearing loss: Effects of age and existing hearing loss," in Noise Induced Hearing Loss, edited by A. Dancer, D. Henderson, R. Salvi, and R. Hamernik (Mosby Year Book, St. Louis).

Mills, J. H., Schmiedt, R. A., and Kulish, L. F. (**1990**). "Age related changes in auditory potentials of Mongolian gerbils," Hear. Res. **46**, 201–210.

Mills, J. H., Boettcher, F. A., and Dubno, J. R. (**1997**). "Interaction of noise-induced permanent threshold shift and age-related threshold shift," J. Acoust. Soc. Am. **101**, 1681–1686.

Mills, J. H., Dubno, J. R., and Boettcher, F. A. (**1998**). "Interaction of noise-induced hearing loss and presbyacusis," Scand. Audiol. **27**, 117–122.

Mills, J. H., Dubno, J. R., Boettcher, F. A., Matthews, L. J., and Ahlstrom, J. B. (**2001**). "Deriving estimates of auditory sensitivity in quiet-aged domestic gerbils," Assoc. Res. Otolaryngol. **24**, 82–83.

Milne, J. (**1977**). "A longitudinal study of hearing loss in older people," Br. J. Audiol. **11**, 7–14.

Milne, J. S., and Lauder, I. J. (**1975**). "Pure tone audiometry in older people," Br. J. Audiol. **9**, 50–58.

Møller, M. (**1981**). "Hearing in 70 and 75 year old people: Results from a cross section and longitudinal population study," Am. J. Otolaryngol. **2**, 22–29.

Moscicki, E., Elkins, E., Baum, H., and McNamera, P. (**1985**). "Hearing loss in the elderly: An epidemiologic study of the Framingham Heart Study Cohort," Ear Hear. **6**, 184–190.

Müller, W., and Richartz, G. (**1989**). "Ist die These von der höheren Lärm-

resistenz berufstätiger Frauen aufrechthaltbar?'' Z. Gesamte Hyg. **35**, 505–507.

Novotny, Z. (**1975**). ''Development of occupational deafness after entering a noisy employment in older age,'' Cesk Otolaryngol. **24**, 151–154.

Occupational Safety and Health Administration (**1971**). ''Occupational Safety and Health Standards, National Consensus Standards and Established Federal Standards,'' Federal Register 36 (105; May 29, 1971): 10518.

Occupational Safety and Health Administration (**1981**). ''Occupational Noise Exposure: Hearing Conservation Amendment,'' Federal Register 46 (11; January 16, 1981): 4078–4179.

Ohlemiller, K. K., Wright, J. S., and Heidbreder, A. F. (**2000**). ''Vulnerability to noise-induced hearing loss in 'middle-aged' and young adult mice: a dose-response approach in CBA, C57BL, and BALB inbred strains,'' Hear. Res. **149**, 239–247.

Passchier-Vermeer, W. (**1977**). ''Hearing levels of non-noise-exposed subjects and of subject exposed to constant noise during working hours. Report B37,'' Research Institute for Environmental Hygiene, Delft, The Netherlands.

Pearson, J. D., Morrell, C. H., Gordon-Salant, S., Brant, L. J., Metter, E. J., Klein, L. L., and Fozard, J. L. (**1995**). ''Gender differences in a longitudinal study of age-associated hearing loss,'' J. Acoust. Soc. Am. **97**, 1196–1205.

Pedersen, K. E., Rossenhall, U., and Møller, M. (**1989**). ''Changes in pure-tone thresholds in individuals aged 70–81: Results from a longitudinal study,'' Audiology **28**, 194–204.

Robinson, D. W. (**1988**). ''Threshold of hearing as a function of age and sex for the typical unscreened population,'' Br. J. Audiol. **22**, 5–20.

Robinson, D. W. (**1991**). ''Relation between hearing threshold level and its component parts,'' Br. J. Audiol. **25**, 93–103.

Robinson, D. W., and Sutton, G. J. (**1979**). ''Age effect in hearing: A comparative analysis of published threshold data,'' Audiology **18**, 320–334.

Schmiedt, R. A., Mills, J. H., and Adams, J. C. (**1990**). ''Tuning and suppression in auditory nerve fibers of aged gerbils raised in quiet or noise,'' Hear. Res. **45**, 221–236.

Schulte, B. A., and Schmiedt, R. A. (**1992**). ''Na-K-ATPase and endocochlear potentials decline in quiet-aged gerbils,'' Hear. Res. **61**, 35–46.

Schuknecht, H. F., and Gacek, M. R. (**1993**). ''Cochlear pathology in presbyacusis,'' Ann. Otol. Rhinol. Laryngol. **102**, 1–16.

Shone, G., Altschuler, R. A., Miller, J. M., and Nuttall, A. L. (**1991**). ''The effect of noise exposure on the aging ear,'' Hear. Res. **134**, 39–47.

Spongr, V. P., Flood, D. G., Frisina, R. D., and Salvi, R. J. (**1997**). ''Quantitative measures of hair cell loss in CBA and C57BL/6 mice throughout their life spans,'' J. Acoust. Soc. Am. **101**, 3546–3553.

Sun, J. C., Bohne, B. A., and Harding, G. W. (**1994**). ''Is the older ear more susceptible to noise?'' Laryngoscope **104**, 1251–1258.

Tarnowski, B. I., Schmiedt, R. A., Hellstrom, L. I., Lee, F. S., and Adams, J. C. (**1991**). ''Age-related changes in cochleas of Mongolian gerbils,'' Hear. Res. **54**, 123–154.

Thomopoulos, G. N., Spicer, S. S., Gratton, M. A., and Schulte, B. A. (**1997**). ''Age-related thickening of basement membrane in stria vascularis capillaries,'' Hear. Res. **111**, 31–41.

Ward, W. D. (**1966**). ''Temporary threshold shift in males and females,'' J. Acoust. Soc. Am. **40**, 478–485.

Ward, W. D. (**1995**). ''Endogenous factors related to susceptibility to damage from noise,'' Occup. Med. **10**, 561–575.

Welleshick, B., and Raber, A. (**1978**). ''Einfluss von expositionszeit und alter auf den iarmbedingten horverlust [Influence of exposure time and age on noise-induced hearing loss: Observations of 25,544 industrial workers (translation by authors, cited in Dobie, 1993)],'' Laryngol. Rhinol. Otol. (Stuttg) **57**, 1037–1048.

Welleshick, B., and Körpert, K. (**1980**). ''Ist das Lärschwerhörigkeitsrisiko für Männer grösser als für Frauen?'' Laryngol. Rhinol. Otol. (Stuttg) **59**, 681–689.

White, D. R., Boettcher, F. A., Miles, L. R., and Gratton, M. A. (**1998**). ''Effectiveness of intermittent and continuous acoustic stimulation in preventing noise-induced hearing I and hair cell loss,'' J. Acoust. Soc. Am. **103**, 566–1572.

Willott, J. F., and Mortenson, V. (**1991**). ''Age-related cochlear histopathology in C57BL/6J and CBA/J mice,'' Assoc. Res. Otolaryngol. Abstracts. **14**, 16.

Willott, J. F., Turner, J. G., Carlson, S., Ding, D., Bross, L. S., and Falls, W. A. (**1998**). ''The BALB/c mouse as an animal model for progressive sensorineural hearing loss,'' Hear. Res. **115**, 162–174.

Virtual pitch integration for asynchronous harmonics

John H. Grose,[a] Joseph W. Hall III, and Emily Buss
Department of Otolaryngology/Head & Neck Surgery, University of North Carolina at Chapel Hill,
Chapel Hill, North Carolina 27599-7070

This experiment examined the generation of virtual pitch for harmonically related tones that do not overlap in time. The interval between successive tones was systematically varied in order to gauge the integration period for virtual pitch. A pitch discrimination task was employed, and both harmonic and nonharmonic tone series were tested. The results confirmed that a virtual pitch can be generated by a series of brief, harmonically related tones that are separated in time. Robust virtual pitch information can be derived for intervals between successive 40-ms tones of up to about 45 ms, consistent with a minimum estimate of integration period of about 210 ms. Beyond intertone intervals of 45 ms, performance becomes more variable and approaches an upper limit where discrimination of tone sequences can be undertaken on the basis of the individual frequency components. The individual differences observed in this experiment suggest that the ability to derive a salient virtual pitch varies across listeners. © *2002 Acoustical Society of America.*
[DOI: 10.1121/1.1514934]

PACS numbers: 43.66.Hg, 43.66.Mk [NFV]

I. INTRODUCTION

Several lines of evidence point to the existence of an integration window for virtual pitch extraction. First, the virtual pitch extracted from harmonic complexes can be influenced by surrounding, temporally nonoverlapping, complexes (Carlyon, 1996; Micheyl and Carlyon, 1998). A parsimonious account for this finding is that an integration window centered on the signal complex includes information from the surrounding fringe complexes, and this ''overintegration'' affects the virtual pitch estimation of the signal. Second, the virtual pitch generated by a given harmonic complex can be influenced by a single tone that does not overlap the harmonic complex in time (Ciocca and Darwin, 1999). When a resolvable harmonic is missing from the harmonic complex, a separate tone can affect the pitch of the complex as long as the frequency of the tone differs by less than about 8% from that of the missing harmonic. Ciocca and Darwin showed that this influence could extend over silent intervals between the two 90-ms stimuli (tone and complex) of up to 160 ms, but failed to occur if the duration of the synchronous harmonic complex was sufficiently long (e.g., 410 ms). They interpreted this finding in terms of a pitch integration period having a duration of about 200–300 ms. A third line of evidence comes from parametric studies of fundamental frequency (f_0) discrimination that manipulate the number, duration, and frequency content of harmonic complexes. The duration of an integration window for pitch appears to depend on the harmonic content of the stimulus, being longer for unresolved harmonics than for resolved harmonics (White and Plack, 1998; Plack and White, 2001). In addition, the pitch integrator can be ''reset'' by level discontinuities in the stimuli, such as temporal gaps (Plack and White, 2000; Plack and White, 2001). A final line of evi-

dence for a pitch integration window is the finding that virtual pitch can be extracted from a set of harmonics even when those harmonics do not overlap in time. Hall and Peters (1981) demonstrated that a sequence of three successive low-order harmonics, each 40 ms in duration and separated from each other by 10 ms, could generate a virtual pitch provided they were presented against a broadband noise background. A virtual pitch was not generated when the harmonic sequence was presented in quiet. Using a similar timing sequence, Houtsma (1984) found that some listeners could extract a virtual pitch from nonsynchronous harmonics even in quiet. However, he also found that the majority of listeners in his study could not reliably express melodic intervals using virtual pitches extracted from nonoverlapping harmonics.

The primary purpose of this study was to test the notion of a pitch integration period using a procedure similar to that used by Hall and Peters (1981). The approach was to present sequences of brief tones that either did or did not form low-order harmonic sequences, and to systematically vary the interval between successive tones. An f_0 discrimination task was used to determine whether a virtual pitch was generated by the tone sequences. Such a task can probe pitch in terms of differential scaling on a high/low dimension, but it cannot assess pitch in the musical sense of recognizing specific frequency ratios. The hypothesis to be tested here is that virtual pitch discrimination is feasible only for harmonically related tones whose intertone intervals (ITIs) allow them to fall within the pitch integration period. Once the ITI exceeds this criterion, no virtual pitch is perceived and the task can no longer be performed on the basis of virtual pitch. By the same token, a discrimination task based on the perception of virtual pitch is also not feasible for tone sequences that are not harmonically related.
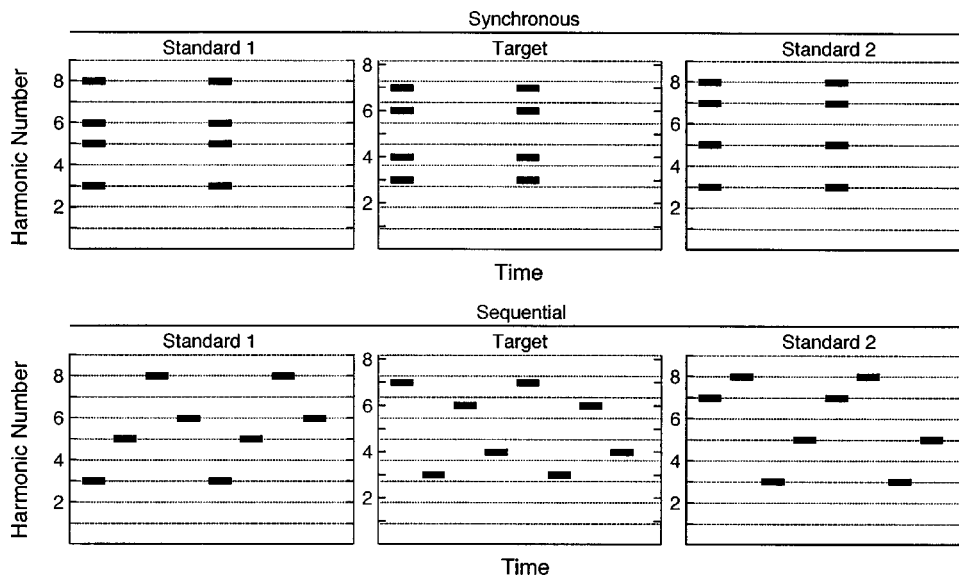
FIG. 1. Stimulus schematic showing a typical 3AFC trial for synchronous presentation of harmonic tones (upper panel) and sequential presentation of harmonic tones (lower panel). Within a trial, selection of the four tones is random for each observation interval, allowing for different tone complexes in the two standard intervals. Within an interval, the four tones are presented twice. Horizontal dashed lines across intervals are isofrequency lines for reference.

II. METHOD

A. Subjects

Five listeners with normal hearing participated in this experiment. They ranged in age from 19 to 42 years (mean = 25 years), and all had audiometric thresholds less than 20 dB HL across the octave frequencies 250–8000 Hz (ANSI, 1996). None of the listeners had extensive musical training, although informal questioning indicated that at least three had some degree of musical experience: observers 1 and 5 played instruments, and observer 4 sang in a choir. All received a regimen of familiarization and training with the task as described below.

B. Stimuli

The stimuli for the virtual pitch discrimination task were four-component tone complexes. In the main experiment using harmonic complexes, each component was 40 ms in duration, including a 10-ms $\cos^2$ rise/fall ramp, and the individual components were presented either synchronously or sequentially. Figure 1 shows a schematic of the stimuli in each of the observation intervals in a typical three-alternative forced-choice (3AFC) trial. For both synchronous and sequential configurations, two replications of the complete stimulus were presented within each observation interval, resulting in either two complex tone bursts or a stream of eight individual tone bursts per interval. For each observation interval, the four components were selected randomly from among the third to tenth harmonics of a given f_0. Across trials, the nominal f_0 of the standard was 200 Hz, and the nominal f_0 of the signal was varied adaptively relative to this standard by a factor of 1.26. A virtual pitch region of 200 Hz was selected because this region has been extensively studied (e.g., Plomp, 1976). The direction of f_0 shift of the signal was always to a higher frequency. However, from trial to trial, the actual f_0 of the standard stimuli varied randomly by ±20% of 200 Hz, and the actual f_0 of the signal maintained proportionality to this actual standard f_0 within a trial. The randomization of actual f_0 from trial to trial, coupled with the random selection of harmonics from interval to interval

within a trial, was implemented to undermine the cue effectiveness of monitoring individual components within the harmonic complexes to perform the task. Nevertheless, as the frequency separation between the standard and signal f_0's increased, the probability of the signal complex containing higher frequency components than the standard complex increased. Consequently, the task could well be undertaken by monitoring just the higher frequency components. To test for this limit, stimulus configurations were also constructed using logarithmically spaced tones. No virtual pitch cue would be expected for these stimuli, so discrimination performance was assumed to reflect the effectiveness of monitoring individual component tones. In these configurations, stimulus components were randomly drawn in each observation interval from a series of eight tones that were equally spaced on a log scale between the nominal frequencies of 333 and 1995 Hz. Again, from trial to trial the actual frequencies in this series varied by ±20%.

The main independent variable was the intertone interval (ITI) between successive components when presented sequentially. This ITI was defined as the interval between the zero-voltage point at the offset of one component and the zero-voltage point at the onset of the next component. The ITIs ranged in 15-ms steps from 0 to 90 ms. The choice of ITI determined the overall duration of the eight-tone sequence in each observation interval of a 3AFC trial (Fig. 1, panel B). To maintain a complementary temporal pattern for the synchronous conditions (Fig. 1, panel A), the interval between the two complex tone bursts also varied systematically with the choice of ITI. The relation between the repetition interval for the complex tone bursts in the synchronous conditions and the ITI in the sequential conditions was 4(40+ITI). Thus, for example, an ITI of 15 ms between successive tones in the sequential condition corresponded to a repetition interval of 220 ms for the complex tone bursts in the complementary synchronous condition.

Although most of the test stimuli were composed of 40-ms tones that were presented twice within each observation interval, two other longer-duration stimulus configurations were also included. Both of these were comprised of

320-ms synchronous complex tones which were presented only once in each observation interval. In one configuration the tones were harmonically related, and in the other the tones were logarithmically spaced. The rules for random draws within an observation interval and jitter of root frequency across trials were the same as those described for the synchronous conditions above.

Each component within the four-component complex was presented at a level of 60 dB SPL. This level was chosen because pilot listening found it to be a comfortable level that generated a clear virtual pitch. The complexes were generated digitally from trial to trial at a sampling rate of 10 kHz (TDT AP2), output via a 16-bit DAC (TDT PD1), antialias filtered at 4000 Hz (Kemo VBF8), attenuated (TDT PA4), and presented monaurally to the left ear using a Sennheiser HD580 headphone. A continuous broadband background noise (0–8000 Hz) was always present at an overall level of 52 dB SPL.

C. Procedure

Prior to the experiment, each listener undertook a familiarization/training regimen. In the first phase of this regimen, the listener was presented with 320-ms harmonic complexes that alternated between harmonics 3–12 of 200 Hz and harmonics 3–12 of 225 Hz. The purpose of this phase was to familiarize the listener with virtual pitch using a perceptually salient example. The alternating sequence was discontinued by the listener once s/he felt comfortable with the perception of an alternating pitch. The second phase of the regimen was similar except that the complex with the virtual pitch of 200 Hz was comprised of harmonics 4–13, whereas the complex with the virtual pitch of 225 Hz was comprised of harmonics 2–11. Here, the complex with the lower virtual pitch contained the highest absolute frequency component. The final phase of the regimen again consisted of alternating 200-Hz and 225-Hz virtual pitch complexes, but now the 200-Hz complex was comprised of harmonics 7–10, whereas the 225-Hz complex was comprised of harmonics 3–6. In this configuration, the entire frequency content of the complex with the higher virtual pitch was lower than the frequency content of the complex with the lower virtual pitch. This three-phase regimen familiarized the listener with virtual pitch using complexes that increasingly diverged in their frequency content and number of components. None of the listeners experienced difficulty extracting an alternating virtual pitch in the three training phases, and all completed the training within 15–30 min.

In the experiment proper, an adaptive stepping rule was incorporated into the 3AFC procedure to converge on the 79.4% correct point of the psychometric function. The signal, consisting of the upward-shifted frequency set, occurred in one of the three observation intervals at random. Following three correct responses in a row, the frequency separation between the standard and signal f_0's was reduced by a factor of 1.26; following one incorrect response, the frequency separation was increased by the same factor. A threshold track was terminated after 12 reversals in direction of frequency separation, and the geometric mean of the frequency differences at the final eight reversal points was taken as the

estimate of threshold for that track. For each condition, at least four threshold estimates were collected and the geometric mean of the estimates was taken as threshold for that condition.

All listeners began with the synchronous 320-ms harmonic stimulus condition. This was the condition anticipated to provide the most salient perception of virtual pitch, and the condition was repeated until systematic improvements in threshold no longer occurred. At this point data collection began and at least four further replications were undertaken. Following this condition, all listeners then received the conditions incorporating synchronous 40-ms harmonic tone bursts. Recall that in these conditions, each observation interval contained two tone bursts (see Fig. 1) which were separated in time by an interval that corresponded to the sequence repetition time associated with the complementary sequential presentation of the individual components. All listeners were tested first in the synchronous condition that had a repetition interval of 160 ms ($\cong$0-ms ITI). Each listener was also tested in a synchronous condition corresponding to at least one other ITI; the selection of this condition varied from listener to listener. Conditions involving sequences of harmonically related tone bursts were tested next. The order of ITIs was not random; rather, each listener began with the 0-ms ITI condition and progressed on to successively longer ITIs until performance declined markedly. The final set of three conditions involved the logarithmically spaced tones. These included the 40-ms tones presented sequentially at an ITI of 0 ms, the complementary synchronous presentation of the 40-ms tones, and the synchronous 320-ms tones.

III. RESULTS

The results of the experiment are displayed in Fig. 2. Because there was some individual variability in performance, the individual results are displayed separately in the five panels. Each panel plots pitch discrimination against a measure of temporal interval appropriate for given conditions (repetition interval for the synchronous conditions, ITI for the sequential conditions). Points to the left of the abscissa break refer to the conditions involving 320-ms tones where a measure of temporal interval is not applicable. Symbols in each graph indicate stimulus type as defined in the figure legend. For each listener, the boundaries of performance are usefully described by the thresholds for the 320-ms tone conditions. For 320-ms harmonic complexes (open circles), virtual pitch discrimination thresholds ranged from about 2 Hz to about 11 Hz across listeners. Because it was assumed that the 320-ms harmonic complexes would provide the listeners with the best opportunity to derive a virtual pitch, these thresholds represent the lower limit of performance for the task. For log-spaced complexes (solid circles), discrimination thresholds ranged between about 65 Hz to about 173 Hz across listeners. The inharmonic log-spaced tones were unlikely to generate a virtual pitch and so these thresholds represent the upper bound of performance wherein the discrimination task is reduced to identifying the interval containing the highest individual frequency(ies). In each panel, horizontal dashed lines extend from these reference thresholds across the remaining conditions.
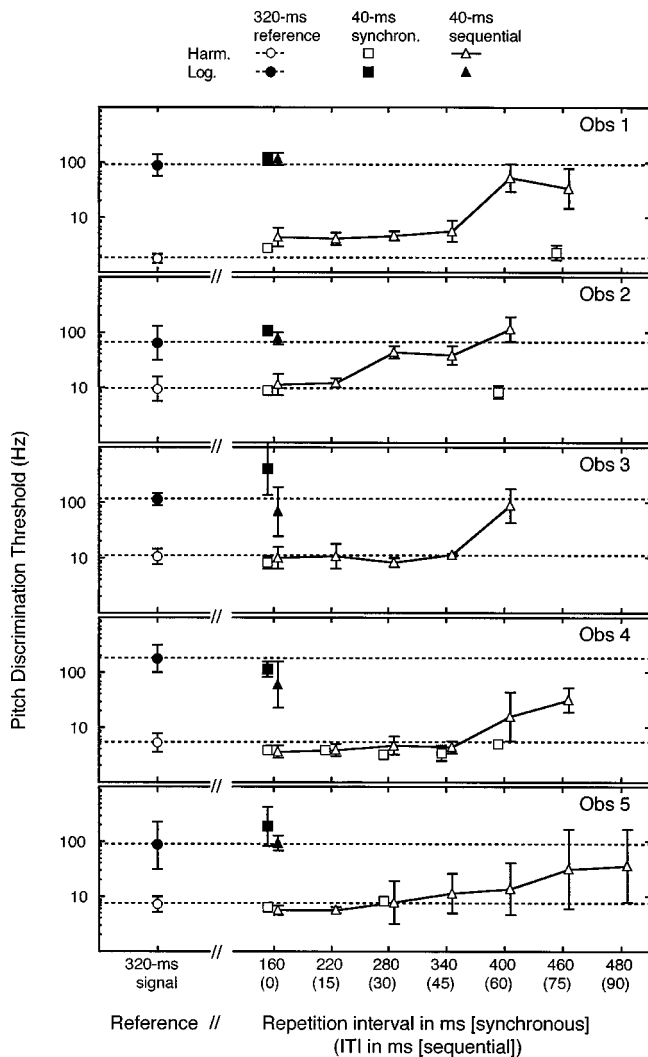
FIG. 2. Individual results plotting discrimination threshold against a measure of temporal interval. For synchronous conditions (squares) this was repetition interval; for sequential conditions (triangles) this was ITI. Each panel shows the mean results of one listener. Error bars indicate ±1 standard deviation computed in the log-transform domain. Open circle: 320-ms synchronous harmonic complex; Solid circle: 320-ms synchronous log-spaced complex; Open squares: 40-ms synchronous harmonic complexes; Solid square: 40-ms synchronous log-spaced complex; Open triangles: 40-ms sequential harmonic tones; Solid triangle: 40-ms sequential log-spaced tones. Horizontal dashed lines in each panel are reference lines associated with the 320-ms stimulus thresholds.

The performance bounds set by the long-duration stimulus configurations provide a context in which to assess the results of the 40-ms tone burst conditions. When the brief tone bursts were logarithmically spaced, performance remained poor whether the tones were presented synchronously (solid squares) or sequentially (solid triangles). A repeated-measures analysis of variance (ANOVA) on the log-transformed thresholds from all three logarithmically spaced conditions indicated no significant difference between conditions ($F_{2,8}=3.3$; $p=0.09$). This is consistent with the assumption that a monitoring of absolute frequency content rather than a derived virtual pitch underlies performance for logarithmically spaced tones. The grand average discrimination threshold across all listeners for these three conditions was about 108 Hz.

For the 40-ms synchronous harmonic tone bursts (open squares), performance was generally on a par with the synchronous 320-ms duration harmonic stimulus (open circle) independent of the overall repetition interval of the tone burst complexes within each observation interval. It can be seen from Fig. 2 that the number of synchronous tone burst conditions and the choice of tone burst repetition intervals varied across listeners, although all received the condition having a repetition interval of 160 ms ($\cong 0$-ms ITI). Nevertheless, for each listener where multiple conditions were run, thresholds remained relatively constant. To assess this apparent equivalence, log-transformed thresholds for three synchronous harmonic conditions were submitted to a repeated-measures ANOVA. These three conditions were: (1) the 320-ms condition; (2) the 40-ms condition having a repetition interval of 160 ms ($\cong 0$-ms ITI); and (3) the remaining 40-ms synchronous condition yielding the *highest* threshold for an individual. (For Obs. 3, no remaining ITI conditions were tested; therefore, a univariate analysis was undertaken to accommodate the missing data point.) The analysis indicated that these thresholds did not differ across conditions ($F_{2,7}=0.24$; $p=0.79$). This suggests that the virtual pitch derived from a single 40-ms tonal complex was sufficiently salient to perform the virtual pitch discrimination task, and that increasing the duration of the stimulus complex to 320 ms, or providing a repetition of the 40-ms complex within an observation interval added no further benefit. This suggestion is reminiscent of White and Plack (1998), who found little change in d' for f_0 discrimination for resolved harmonic complexes once the signal duration exceeded 40 ms. Furthermore, they found little effect of gap duration between two brief harmonic complexes on f_0 discrimination.

The primary interest of this experiment was in the conditions where the 40-ms harmonically related tone bursts were presented sequentially, shown as triangles in Fig. 2. For all listeners, discrimination performance was at or near the lower limits for ITIs close to 0 ms, but approached the upper bounds of performance for longer ITIs. It is apparent that the ITI at which performance began to depart from the lower limit differed across listeners, although performance had clearly declined in most listeners by an ITI of 60 ms. Moreover, for some listeners the departure from baseline performance was relatively abrupt (e.g., Obs. 1), whereas for others it was more gradual (e.g., Obs. 5). To provide an efficient test of this data pattern, log-transformed thresholds from three conditions were submitted to a repeated-measures ANOVA. The three conditions were: (1) synchronous harmonic complexes corresponding to an ITI of 0 ms (repetition interval = 160 ms); (2) sequences of harmonically related tones having an ITI of 45 ms; and (3) sequences of harmonically related tones having an ITI of 60 ms. Comparison of (1) and (2) would indicate whether performance with an ITI of 45 ms was still as good as for simultaneously presented components. Comparison of (2) and (3) would indicate whether performance had, on average, declined at an ITI of 60 ms. The results of the analysis indicated that there was a significant effect of stimulus condition across these three conditions ($F_{2,8}=18.315$; $p=0.001$). The first of the two planned comparisons described above indicated that thresholds for

the tone sequence with an ITI of 45 ms did not differ reliably from thresholds for the synchronous harmonic complex corresponding to an ITI of 0 ms ($p = 0.09$). This conservative comparison indicates that pitch discrimination for harmonic tone sequences presented with ITIs of 45 ms was still at the lower bounds of performance, suggesting that the task was still being done on the basis of virtual pitch. The second of the two planned comparisons indicated that thresholds for the tone sequence with an ITI of 60 ms were significantly different from thresholds for an ITI of 45 ms ($p = 0.004$). This finding indicates that, on average, the breakpoint in performance between baseline (good) performance and a significant decline in performance occurred for intertone intervals between 45 and 60 ms.

IV. DISCUSSION

The purpose of this experiment was to test the notion of an integration period for virtual pitch using a paradigm of sequentially presented harmonic tones. A parsimonious interpretation of the results is that a virtual pitch can be generated by sequences of 40-ms tones presented against a noise background for intervals between the tones of up to about 45 ms. For ITIs longer than about 60 ms, performance declines and becomes more variable, suggesting that a reliable virtual pitch is no longer being generated. The relation between these ITIs and an integration period for virtual pitch is not entirely straightforward. Because of the random selection of harmonic numbers from interval to interval within a 3AFC trial and the random order of presentation of these harmonics, the generation of a virtual pitch from just two successive components in the tone sequence would be an unreliable cue because the pitch could vary randomly across even the standard intervals. That is, two successive tones from the random sequence presented in standard interval 1 might be compatible with one virtual pitch (e.g., 600 and 800 Hz generating an f_0 of 200 Hz), whereas two successive tones from the random sequence presented in standard interval 2 might be compatible with another virtual pitch (e.g., 800 and 1600 Hz generating an f_0 of 800 Hz). Given this, it seems reasonable that any pitch integration period must cover at least three of the tones in the sequence.[1] Thus, a virtual pitch integration period must be at least 210 ms long (three 40-ms tones separated by ITIs of 45 ms). By the same reasoning, an interval of 240 ms would extend beyond the integration period (three 40-ms tones separated by ITIs of 60 ms). Integration periods in the region of 200 ms are compatible with the results of Hall and Peters (1981), whose three-tone sequences covered at interval of 140 ms, as well as those of Ciocca and Darwin (1999), whose data suggest that the pitch integration period continues for 170–250 ms following the onset of a complex tone.

Although the data of this experiment are discussed in the context of an integration period for virtual pitch, one trend in the data suggests that an alternative interpretation might deserve consideration. It is evident from Fig. 2 that for at least two of the listeners (Obs. 1 and 5) the deterioration in performance appeared to plateau below the upper bound indicated by thresholds for the logarithmically spaced tones. It was argued that this upper bound represented the point at which the task was undertaken on the basis of discrimination of individual frequencies rather than discrimination of virtual pitch. A plateau in performance below this point might suggest that some (nonsalient) virtual pitch information can be gleaned from the tone sequences, even for relatively long ITIs. One strategy with which this might be accomplished is to view the tone sequences as arpeggios where the listener internally constructs the f_0 that is the best fit to a given arpeggio. The discrimination task therefore becomes one of identifying the observation interval where the tone sequence represents an arpeggio of an f_0 that is different from the other two observation intervals. Here, the limitation in performance is the duration over which the harmonic relation between successive tones can be remembered accurately.

The ability to integrate frequency components that do not overlap in time into a single percept, in this instance virtual pitch, is concordant with other manifestations of perceptual integration. In particular, the perception of multifrequency-channel speech exhibits analogous integrative features. Greenberg and Arai (1998) have shown that the perception of speech that is filtered into multiple narrow bands can tolerate misalignments of up to 140 ms across bands. If temporal misalignments between filtered speech bands can be viewed as a special case of temporally nonoverlapping frequencies, then the resilience of speech perception to this manipulation is congruent with a process of spectral integration over time. Our own work on amplitude modulation of multiple narrow bands of speech has shown that speech perception is unaffected by the relative phase of 10-Hz modulation across bands (Buss *et al.*, 2001). In other words, speech perception is not sensitive to whether adjacent bands are modulated in phase or 2π radians out of phase. The latter case can be thought of as yielding frequency regions whose energy contents do not overlap in time.

In summary, this experiment has confirmed that a virtual pitch can be generated by a series of brief harmonically related tones that are separated over time. Robust virtual pitch information can be derived for intervals between successive 40-ms tones of up to about 45 ms, consistent with a minimum estimate of integration period of about 210 ms. Beyond ITIs of 45 ms, performance becomes more variable and approaches the upper limit of performance where discrimination of tone sequences can be undertaken on the basis of the individual frequency components. The individual differences observed in this experiment suggest that the ability to derive a salient virtual pitch varies across listeners.

---

[1]A simulation incorporating the random sequencing of harmonic tones used in this experiment indicated that a three-tone sequence compatible with a virtual pitch of only 200 Hz (in contrast to, for example, 200 or 600 Hz) occurred about 90% of the time.

ANSI (**1996**). ANSI S3.6-1996, ''American National Standard Specification for Audiometers'' (American National Standards Institute, New York).

Buss, E., Hall, J. W., III, and Grose, J. H. (**2002**). ''Effect of masker amplitude modulation modulation coherence for speech signals filtered into narrow bands,'' J. Acoust. Soc. Am. (in press).

Carlyon, R. P. (**1996**). ''Masker asynchrony impairs the fundamental-frequency discrimination of unresolved harmonics,'' J. Acoust. Soc. Am. **99**, 525–533.

Ciocca, V., and Darwin, C. J. (**1999**). ''The integration of nonsimultaneous frequency components into a single virtual pitch,'' J. Acoust. Soc. Am. **105**, 2421–2430.

Greenberg, S., and Arai, T. (**1998**). ''Speech intelligibility is highly tolerant of cross-channel spectral asynchrony,'' J. Acoust. Soc. Am **103** (Pt. 2), 3057.

Hall, J. W., and Peters, R. W. (**1981**). ''Pitch for nonsimultaneous successive harmonics in quiet and noise,'' J. Acoust. Soc. Am. **69**, 509–513.

Houtsma, A. J. M. (**1984**). ''Pitch salience of various complex sounds,'' Music Percept. **1**, 296–307.

Micheyl, C., and Carlyon, R. P. (**1998**). ''Effects of temporal fringes on fundamental-frequency discrimination,'' J. Acoust. Soc. Am. **104**, 3006–3018.

Plack, C. J., and White, L. J. (**2000**). ''Perceived continuity and pitch perception,'' J. Acoust. Soc. Am. **108**, 1162–1169.

Plack, C. J., and White, L. J. (**2001**). ''Temporal integration in pitch perception,'' in *Proceedings of the 12th International Symposium on Hearing. Physiological and Psychophysical Bases of Auditory Function*, edited by D. J. Breebaart, A. J. M. Houtsma, A. Kohlrausch, V. F. Prijs, and R. Schoonhoven (Shaker, Mierlo, The Netherlands).

Plomp, R. (**1976**). *Aspects of Tone Sensation* (Academic, London).

White, L. J., and Plack, C. J. (**1998**). ''Temporal processing of the pitch of complex tones,'' J. Acoust. Soc. Am. **103**, 2051–2063.

Auditory processing efficiency deficits in children with developmental language impairments[a]

Douglas E. H. Hartley and David R. Moore[b]

University Laboratory of Physiology, University of Oxford, Parks Road, Oxford OX1 3PT, United Kingdom

The ''temporal processing hypothesis'' suggests that individuals with specific language impairments (SLIs) and dyslexia have severe deficits in processing rapidly presented or brief sensory information, both within the auditory and visual domains. This hypothesis has been supported through evidence that language-impaired individuals have excess auditory backward masking. This paper presents an analysis of masking results from several studies in terms of a model of temporal resolution. Results from this modeling suggest that the masking results can be better explained by an ''auditory efficiency'' hypothesis. If impaired or immature listeners have a normal temporal window, but require a higher signal-to-noise level (poor processing efficiency), this hypothesis predicts the observed small deficits in the simultaneous masking task, and the much larger deficits in backward and forward masking tasks amongst those listeners. The difference in performance on these masking tasks is predictable from the compressive nonlinearity of the basilar membrane. The model also correctly predicts that backward masking (i) is more prone to training effects, (ii) has greater inter- and intrasubject variability, and (iii) increases less with masker level than do other masking tasks. These findings provide a new perspective on the mechanisms underlying communication disorders and auditory masking. © 2002 Acoustical Society of America.
[DOI: 10.1121/1.1512701]

I. INTRODUCTION

About 10% of children who are otherwise unimpaired fail to develop language or reading skills, or both, at the normal rate (US Department of Education, 1985). Claims have been made that children with these conditions, known respectively as specific language impairment (SLI) and specific reading impairment (SRI, ''dyslexia''), have particular difficulty separating rapidly presented or brief sounds, degrading their ability to perceive transient elements of speech (Tallal *et al.*, 1993; Merzenich *et al.*, 1996). These claims, known as the ''temporal processing hypothesis'' (Merzenich *et al.*, 1996), are supported by demonstrations that impaired individuals (Wright *et al.*, 1997, 2001) have profound and particular difficulty detecting a brief tone presented before a masking noise (backward masking). Thus, language and reading impairments have been associated with poor temporal resolution (Moore, 1995). In this paper, we present data and a hypothesis suggesting that poor processing efficiency, rather than poor temporal resolution, accounts for deficits in auditory masking among impaired and immature listeners.

Although many studies have investigated backward masking, this basic aspect of auditory processing produces anomalous results and remains poorly understood (Moore,

1995). For example, backward masking yields more variable results than simultaneous masking, especially in unpracticed subjects (Zwicker and Fastl, 1999), and practice leads to unusually large improvements (Wright *et al.*, 1996; Wright, 1998). In contrast, only small effects of practice are seen in simultaneous masking (Wright, 1998). During childhood, backward masking thresholds improve over a comparatively protracted period (Hartley *et al.*, 2000) (Fig. 1). Individuals with SLI and SRI have abnormally enhanced backward masking, but perform nearly as well as controls on simultaneous masking (Fig. 1) (Wright *et al.*, 2001). In addition to supporting the temporal processing hypothesis, the latter result has been interpreted as suggesting that temporal resolution deficits may *cause* language and reading impairments (Tallal *et al.*, 1993; Wright *et al.*, 1997). However, we propose here that these and other results can be explained more completely by poor processing efficiency.

Processing efficiency refers to all the factors, aside from temporal and spectral resolution, that affect the ability to detect acoustic signals in noise. Efficiency is measured by the threshold signal-to-noise ratio. It may be influenced by neural events intrinsic to the auditory system, as well as by cognitive factors including attention, memory, and learning (Patterson *et al.*, 1982; Werner and Bargones, 1991).

II. TEMPORAL PROCESSING MODEL

Performance of adult listeners on backward and forward masking tasks, has been described by a model (Moore *et al.*, 1988; Moore, 1995) [Fig. 2(a)]. The first part of the model is a bandpass filter, one of a bank of filters in the auditory periphery. The output of the filter leads to a compressive
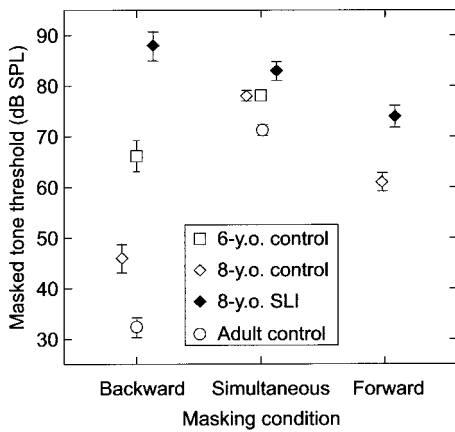

FIG. 1. Mean thresholds for a brief tone in three masking conditions for normal-hearing adults ($n=10$) and for 6-year-old ($n=16$) and 8-year-old children ($n=8$). Thresholds are also plotted for 8-year-old children with SLI ($n=8$). Stimuli: A 1-kHz, 20-ms duration tone (10-ms rise–fall) was presented immediately before (backward masking), during (simultaneous masking) or after (forward masking) a band-pass masking noise (0.6–1.2 kHz, 300-ms duration, 10-ms rise–fall, 40 dB/Hz). Error bars show ±1 standard error. Adult and 6-year-old control data from Hartley *et al.* (2000); 8-year-old SLI and control data from Wright *et al.* (1997).

nonlinear device simulating the input–output function of the basilar membrane (BM; Yates, 1990) [Fig. 2(b)]. For low (<45 dB SPL) and high (>80 dB SPL) input levels, the response of the BM is roughly linear, at least for low-frequency stimuli.[1] In contrast, for moderate (45–80 dB SPL) input levels, the response is highly compressive (about 6.25:1 compression) (Yates, 1990; Ruggero, 1992; Murugasu and Russell, 1995) [Fig. 2(b)]. It is widely believed that the BM compression depends on an "active physiological mechanism" mediated by the outer hair cells (Moore and Oxenham, 1998). A sliding temporal integrator or "temporal window" follows the nonlinear device (Moore *et al.*, 1988; Plack and Moore, 1990) [Fig. 2(c)]. It has been hypothesized

that the temporal window occurs at some point after the auditory nerve and that it probably reflects more "central" auditory processing (Plack and Moore, 1990).

The output of the temporal window takes some time to build up and decay. Critically, the build up is steeper than the decay [Fig. 2(c)], accounting for the rapid decay of backward masking, relative to forward masking, when the delay between the signal and masker is increased (Oxenham and Moore, 1994). Finally, a decision device follows the temporal window. It is assumed that the threshold for detecting a brief signal is reached when the peak of the internal effect of the signal (E_s) is a constant proportion of the internal effect of the masker [E_m; Fig. 2(a)]. The model has been previously used to explain the shallow growth of forward masking with increasing masker level (Moore and Oxenham, 1998) and excess masking produced when forward and backward maskers are combined (Oxenham and Moore, 1994).

III. GROWTH OF MASKING

To investigate some properties of backward masking, we began by measuring "growth of masking functions" (Fig. 3).

A. Methods

Normal-hearing adult listeners (three males and three females, aged 20.3–20.8 years, with audiometric pure-tone thresholds <15 dB HL at 0.125–8 kHz) were recruited from the undergraduate community of Oxford University.

A 1-kHz, 20-ms tone (5-ms cosine-squared rise–fall times) was gated on at −20 ms (backward masking), 200 ms (simultaneous masking), or 300 ms (forward masking), relative to the onset of a 0.6–1.4-kHz, 300-ms noise (10-ms cosine-squared rise–fall times) at five levels from 0 to 40 dB/Hz. All stimuli were digitally generated using Tucker-Davis Technologies (TDT, Gainesville, FL) System II hardware controlled by locally written and TDT software.
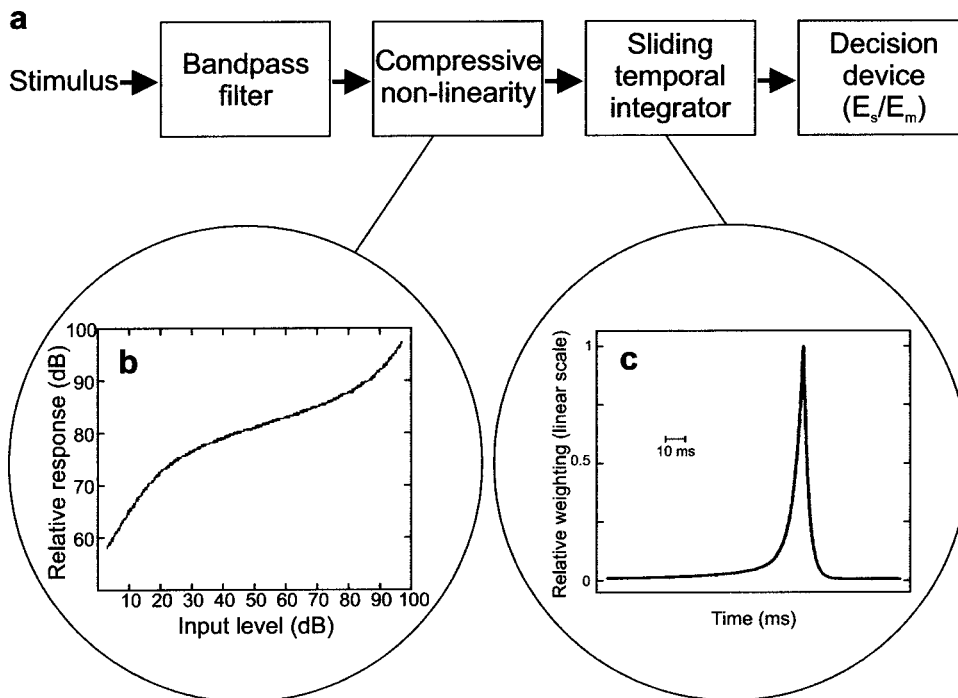
FIG. 2. (a) A block diagram of the model proposed by Moore *et al.* (1988) to describe auditory temporal resolution. (b) A schematic representation of the compressive input–output function of the basilar membrane to a pure-tone stimulus. The relative response is arbitrarily scaled so that an input of 100 dB gives an output of 100 dB. (c) The shape of the sliding temporal integrator or "temporal window" (Plack and Moore, 1990). Note the asymmetry of the rising and falling phases of the function.
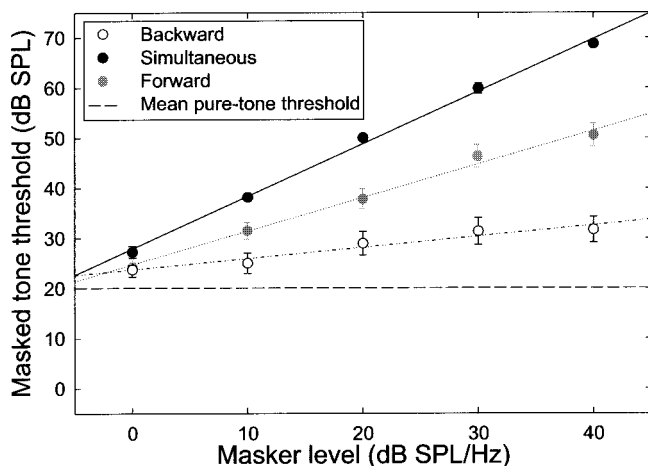
FIG. 3. Growth of masking functions. Mean tone thresholds for six normal-hearing listeners are plotted as a function of masker (noise) level, with best fitting linear regressions, for each masking condition. Mean pure-tone threshold (at 1 kHz, unmasked) is also shown. See Fig. 1 for details of masking conditions.

A two-interval, forced-choice, maximum-likelihood (Green, 1990) procedure was used to estimate the tone level for 94% correct detection. The final threshold was derived from the mean of two threshold estimates, consisting of 30 trials per estimate. Participants were tested in a locally designed, sound-attenuated room, and all stimuli were presented to the right ear only, using calibrated Sennheiser HD-414 headphones. A visual display marked the observation intervals, and gave feedback to participants. All participants were paid.

B. Results and discussion

Tone thresholds in each masking condition increased linearly with masker level. Consistent with previous data (Moore and Oxenham, 1998), the slopes of the growth of masking function for simultaneous and forward masking were approximately 1 and 0.7, respectively. However, the slope of the function for the backward condition (0.2) was considerably shallower.

The model is consistent with these results. At the highest masker level (40 dB/Hz), thresholds for forward masking were about 19 dB greater than those for backward masking. At the lowest masker level (0 dB/Hz), thresholds were just 1 dB higher for forward masking. Let us assume that, at the time the internal effect of the signal (E_s) reaches a maximum, the internal effect of the masker will be E_{mf} for forward masking and E_{mb} for backward masking. Data (Oxenham and Moore, 1994) show that E_{mf} is greater than E_{mb} by about 2.5 dB. If the masker is intense (e.g., 40 dB/Hz), signal thresholds will fall within the range where the input–output function on the BM is highly compressive [Fig. 2(b)]. The signal threshold will then be about 16 dB higher in forward compared with backward masking, to change its internal effect by 2.5 dB. If the masker level is low (e.g., 0 dB/Hz), tone thresholds are in the linear part of the input–output function on the BM [Fig. 2(b)]. Here, the signal intensity needs to change by only 2.5 dB to change its internal effect by 2.5 dB, in keeping with the current findings.

IV. OTHER MASKING DATA

The hypothesis proposed here, incorporating a fixed temporal window and variable efficiency, also fits other properties of masking. For simultaneous masking (Fig. 1), tone thresholds are generally high, around 80 dB SPL for 8-year-old children. However, they are only slightly (by 6 dB) higher for 8-year-old SLI children than for 8-year-old control children (data from Wright *et al.*, 1997). Above 80 dB SPL, there is little BM compression [Fig. 2(b)] and, for simultaneous masking, both signal and noise are subject to the same compression. In contrast, for backward masking, tone thresholds average 47 dB SPL for control children. At this level, the BM is highly compressive. Moreover, the compression is fast acting (Yates, 1990) and it has been suggested that the signal and masker will be compressed independently, even when they are presented close in time (Moore and Oxenham, 1998). Assuming a typical amount of mid-level compression (6.25:1; Yates, 1990; Ruggero, 1992; Murugasu and Russell, 1995), and a constant signal-to-noise ratio of E_s/E_m at threshold across tasks, the signal intensity needs to be increased by nearly 40 dB to change its internal effect by 6 dB. Thus, if we assume that, compared with controls, children with SLI have poor processing efficiency and require the internal effect of the signal (E_s) to be 6 dB higher at threshold, the model correctly predicts that the signal level at threshold would be about 40 dB higher for children with SLI, compared with controls. Poor processing efficiency, which does not invoke any change in cochlear function or in the width of the temporal window, nevertheless largely accounts for the excess backward masking in individuals with SLI (Fig. 1; data from Wright *et al.*, 1997) and SRI (Wright *et al.*, 2001).

A similar argument can be used to explain excess forward masking in children with SLI (Fig. 1). Tone thresholds for forward masking in control children are higher than for backward masking and, consequently, lie in a region of the input–output function on the BM that is less compressive [Fig. 2(b); see also footnote 1]. Thus, children with SLI have larger deficits in backward masking than in forward masking (Fig. 1).

The efficiency hypothesis can account for the excess backward masking found in young, normal-hearing children (Hartley *et al.*, 2000). Six year olds have backward masking thresholds that are 34 dB higher than those of adults (Fig. 1; data from Hartley *et al.*, 2000). The model successfully predicts that the children should have only about 5–6 dB higher simultaneous masking thresholds (Fig. 1).

The unusually large variability and practice effects associated with backward masking may, finally, also be explained in terms of processing efficiency. If we assume that E_s/E_m varies over a range of 1–2 dB between successive threshold estimates, then, for simultaneous masking, the signal level at threshold will vary over a 1–2-dB range. However, for backward masking, because tone thresholds lie within a highly compressive response region on the BM, signal levels at threshold will vary over a 6.25–12.5-dB range. Similarly, if we assume that processing efficiency improves with practice by 1–2 dB, thresholds in practiced listeners will be just 1–2 dB lower for simultaneous masking, but 6.25–12.5 dB lower

D. E. Hartley and D. R. Moore: Auditory efficiency deficits in children

for backward masking. These predictions are, again, consistent with the experimental data (Wright, 1998). Compared with simultaneous masking, backward masking thus magnifies changes in processing efficiency.

Temporal resolution has also been assessed in young children (Hall and Grose, 1994) and dyslexic adults (Mennell et al., 1999) using amplitude modulation detection. The depth of modulation at threshold was found to be greater in these groups than in older or unimpaired listeners. However, changes in threshold with frequency of modulation were the same for all ages and reading abilities, suggesting that younger children and individuals with reading impairments have poor processing efficiency. Hall and Grose (1991) also showed that differences in criterion signal-to-noise ratio, and thus processing efficiency, can lead to apparent differences in frequency resolution in adults and children using the "notched-noise" method. These results, like the analysis of masking data presented here, support the suggestion that younger children and individuals with language and reading impairments have deficits in processing efficiency. Together these studies suggest that intervention strategies should be focused on improving efficiency rather than on temporal processing.

Whether the auditory processing inefficiency discussed here is symptomatic of a broader, cross-modal problem involving the visual and other systems is presently difficult to assess, since tasks differ across modalities, and other systems appear not to use the term "efficiency" in this way. However, Wright and colleagues (2001) have reported elevated visual masking in dyslexic adults under conditions that closely resemble the auditory tasks used in their study and in others reported here. In addition, there have been reports and discussions in the visual literature of the relation between efficiencylike constructs and measures of resolution that suggest a common problem. For example, Stuart and colleagues (2001) recently modeled the contrast sensitivity functions of SRI participants from several studies. They showed that much of the data previously interpreted as supporting a specific temporal deficit (the "magnocellular hypothesis") could be well modeled by inattention, a factor that is known to be comorbid with SRI. In the contrast sensitivity task, the effect of "inefficiency" was to reduce sensitivity by a constant proportion across a range of spatial frequencies. This result may be analogous to the constant loss of efficiency found across the various masking tasks presented here, once the amplifying effect of the basilar membrane was eliminated.

ACKNOWLEDGMENTS

[1]There is some controversy about the linearity of the input–output function at high sound levels (Ruggero et al., 1997). However, significant compression at high levels seems only to occur for high-frequency stimuli in the basal end of the cochlea (Rhode and Cooper, 1996; Nelson et al., 2001).

Green, D. M. (**1990**). "Stimulus selection in adaptive psychophysical procedures," J. Acoust. Soc. Am. **87**, 2662–2674.

Hall, J. W., and Grose, J. H. (**1991**). "Notched-noise measures of frequency selectivity in adults and children using fixed-masker-level and fixed-signal-level presentation," J. Speech Hear. Res. **34**, 651–660.

Hall, J. W., and Grose, J. H. (**1994**). "Development of temporal resolution in children as measured by the temporal modulation transfer function," J. Acoust. Soc. Am. **96**, 150–154.

Hartley, D. E. H., Hogan, S. C., Hardiman, M. J., Wright, B. A., and Moore, D. R. (**2000**). "Age-related improvements in auditory backward and simultaneous masking in 6 to 10 year old children," J. Speech Lang. Hear. Res. **43**, 1402–1415.

Menell, P., McAnally, K. I., and Stein, J. F. (**1999**). "Psychophysical sensitivity and physiological response to amplitude modulation in adult dyslexic readers," J. Speech Lang. Hear. Res. **42**, 797–803.

Merzenich, M. M., Jenkins, W. M., Johnston, P., Schreiner, C., Miller, S. L., and Tallal, P. (**1996**). "Temporal processing deficits of language-learning impaired children ameliorated by training," Science **271**, 77–81.

Moore, B. C. J. (**1995**). "Frequency analysis and masking," in Hearing: Handbook of Perception and Cognition, 2nd ed., edited by B. C. J. Moore (Academic, London, U.K.), pp. 61–205.

Moore, B. C. J., and Oxenham, A. J. (**1998**). "Psychoacoustic consequences of compression in the peripheral auditory system," Psychol. Rev. **105**, 108–124.

Moore, B. C. J., Glasberg, B. R., Plack, C. J., and Biswass, A. K. (**1988**). "The shape of the ear's temporal window," J. Acoust. Soc. Am. **83**, 1102–1116.

Murugasu, E., and Russell, I. J. (**1995**). "Salicylate ototoxicity: The effects on basilar membrane displacement, cochlear microphonics, and neural responses in the basal turn of the guinea pig cochlea," Aud. Neurosci. **1**, 139–150.

Nelson, D. A., Schroder, A. C., and Wojtczak, M. (**2001**). "A new procedure for measuring peripheral compression in normal-hearing and hearing-impaired listeners," J. Acoust. Soc. Am. **110**, 2045–2064.

Oxenham, A. J., and Moore, B. C. J. (**1994**). "Modeling the additivity of nonsimultaneous masking," Hear. Res. **80**, 105–118.

Patterson, R. D., Nimmo-Smith, I., Weber, D. L., and Milroy, R. (**1982**). "The deterioration of hearing with age: frequency selectivity, the critical ratio, the audiogram, and speech threshold," J. Acoust. Soc. Am. **72**, 1788–1803.

Plack, C. J., and Moore, B. C. J. (**1990**). "Temporal window shape as a function of frequency and level," J. Acoust. Soc. Am. **87**, 2178–2187.

Rhode, W. S., and Cooper, N. P. (**1996**). "Nonlinear mechanics in the apical turn of the chinchilla cochlea in vivo," Aud. Neurosci. **3**, 101–121.

Ruggero, M. A. (**1992**). "Responses to sound of the basilar membrane of the mammalian cochlea," Curr. Opin. Neurobiol. **2**, 449–456.

Ruggero, M. A., Rich, N. C., Recio, A., Narayan, S. S., and Robles, L. (**1997**). "Basilar-membrane responses to tones at the base of the chinchilla cochlea," J. Acoust. Soc. Am. **101**, 2151–2163.

Stuart, G. W., McAnally, K. I., and Castles, A. (**2001**). "Can contrast sensitivity functions in dyslexia be explained by inattention rather than a magnocellular deficit?" Vision Res. **41**, 3205–3211.

Tallal, P., Miller, S., and Fitch, R. H. (**1993**). "Neurobiological basis of speech: A case for the preeminence of temporal processing," Ann. N.Y. Acad. Sci. **682**, 27–47.

U.S. Department of Education (**1985**). "Seventh Annual Report to Congress on the Implementation of Public Law 94-142: the Education for All Handicapped Children Act."

Werner, L. A., and Bargones, J. Y. (**1991**). "Sources of auditory masking in infants: distraction effects," Percept. Psychophys. **50**, 405–412.

Wright, B. A. (**1998**). "Specific language impairment: abnormal auditory masking and the potential for its remediation through training," in Psychophysical and Physiological Advances in Hearing, edited by A. R. Palmer, A. Rees, A. Q. Summerfield, and R. Meddis (Whurr, London, U.K.), pp. 604–610.

Wright, B. A. (**2001**). "Deficits in frequency resolution and processing efficiency for short tones in children with language or listening impairments," ARO Abstracts **24**, 172.

Wright, B. A., Johnston, P. A., and Reid, M. D. (**1996**). "Learning and generalization in auditory backward masking," J. Acoust. Soc. Am. **100**, 2818(A).

Wright, B. A., Lombardino, L. J., King, W. M., Puranik, C. S., Leonard, C. M., and Merzenich, M. M. (**1997**). "Deficits in auditory temporal and spectral resolution in language-impaired children," Nature (London) **387**, 176–178.

Wright, B. A., Zecker, S. G., and Bowen, R. W. (**2001**). "Abnormal auditory and visual masking associated with reading and language disorders," abstract presented at "Sensory Bases of Reading and Language Disorders" meeting, Department of Psychology, University of Essex, May 27–30th May 2001.

Yates, G. K. (**1990**). "Basilar-membrane nonlinearity and its influence on auditory nerve rate-intensity functions," Hear. Res. **45**, 203–220.

Zwicker, E., and Fastl, H. (**1999**). *Psychoacoustics: Facts and Models*, 2nd ed. (Springer-Verlag, New York), pp. 61–110.

D. E. Hartley and D. R. Moore: Auditory efficiency deficits in children

Humans detect gaps in broadband noise according to effective gap duration without additional cues from abrupt envelope changes

Paul D. Allen,[a] Tracy M. Virag, and James R. Ison
Department of Brain and Cognitive Sciences, Meliora Hall, University of Rochester, Rochester, New York 14627

Previous studies of behavior and IC single units in the mouse support theoretical expectations that gaps with ramped trailing markers have reduced detectability compared to equivalent gaps with ramped leading markers. In experiment 1, detection probability and response speeds of humans listening for gaps in broadband noise were investigated by independently varying either leading marker fall-time (FT) or trailing marker rise-time (RT). Gaps with silent duration of 1, 4, or 12 ms were presented 2 s into a 3-s noise burst, with either abrupt marker onsets and offsets or linearly ramped RT/FT of 2, 4, or 8 ms durations. Addition of a nonzero RT or FT to the gap silent period increased detectability and also increased reaction speed on trials with "Yes" response, but there was no difference in detectability or response speeds between RT and FT conditions. Experiment 2 extended this finding to gaps having two, one, or no abrupt marker edges. These findings suggest that human listeners do not make use of abrupt onset or offset information to enhance gap detection, but seem to rely on the effective sound level reduction associated with the gap for detection. © *2002 Acoustical Society of America.* [DOI: 10.1121/1.1518697]

PACS numbers: 43.66.Mk, 43.66.Dc [MRL]

I. INTRODUCTION

The detection of gaps in broadband noise has been studied using a variety of physiological and psychophysical techniques, which have provided similar measures of temporal acuity. These studies range from single unit recordings of auditory nerve fibers in the chinchilla (Zhang *et al.*, 1990), inferior colliculus (IC) neurons in the mouse (Walton *et al.*, 1997; Barsz *et al.*, 1998), and primary auditory cortex neurons in the cat (Eggermont, 2000), to behavioral techniques such as prepulse inhibition in the rat (Ison, 1982; Leitner *et al.*, 1993) and the mouse (Ison *et al.*, 1998; Ison *et al.*, 2002) as well as psychophysical perceptual measures in humans (e.g., Plomp, 1964; Green, 1985; Green and Forrest, 1989; Snell, 1997; He *et al.*, 1999; Florentine *et al.*, 1999). In addition to these applications, gap detection has also assumed significance owing to the importance of temporal acuity for human speech perception (Tyler *et al.*, 1982, 1989; Gordon-Salant and Fitzgibbons, 1993; Busby and Clark, 1999; Phillips *et al.*, 2000; Snell and Frisina, 2000).

Plomp (1964) established much of the theoretical framework that underpins research on auditory temporal acuity. He found that the threshold for gap detection depends on the sound levels of pre- and postgap noise burst markers and suggested that below some minimum gap threshold (MGT) a finite rate of decay of auditory sensation masks the presence of gaps that occur within this decay envelope. This masking also determines the magnitude of the onset response to the trailing noise burst marker. The MGT for simple rectangular gaps in broadband noise is typically between 2 and 3 ms (Plomp, 1964; Irwin and Purdy, 1982; Forrest and Green,

1987; Green and Forrest, 1989; He *et al.*, 1999) and the psychometric function for gap detection is very steep, with a range of approximately 2 ms between 0% and 100% detectability (Green and Forrest, 1989; Moore *et al.*, 1992; He *et al.*, 1999). Computational models of gap detection have generally assumed that detection occurs on the basis of short-term fluctuations within single-channel detectors (Buunen and van Valkenberg, 1979; Buus and Florentine, 1985; Forrest and Green, 1987) or within multiple-channel detectors (Heinz *et al.*, 1996). Florentine *et al.* (1999) have recently suggested that discrepancies between their empirical data and a loudness detector model might arise from additional detection cues being provided by the onset response to the trailing marker of the gap. If so, then altering the onset information of the trailing marker should affect gap detection.

Previous studies in the mouse suggest that ramped marker onsets and offsets do impair gap detection. Barsz and colleagues (1998) covaried the leading marker fall-time (FT) and trailing marker rise-time (RT) of gap envelopes and examined the effect of this manipulation on the encoding of gaps by mouse IC single units. They found that symmetric gaps (RT=FT) with RT/FT greater than 4 ms showed increased detection thresholds, requiring longer gap durations to produce a significant difference in firing rate from the no-gap control. Increasing RT produced longer first spike latencies for phasic units, and slowed the rate of recovery of their asymptotic firing rate response. In contrast, increasing FT reduced the decay of excitation during the gap for tonic units. Ison and colleagues (2002) found, using prepulse inhibition in the mouse, that adding RT and FT to small gaps increased their detectability owing to increased effective gap duration, consistent with energy detector models. They found additionally that the salience of longer gaps was reduced for

RT ramps compared with FT ramps, supporting the importance of onset information for gap detection.

These mouse studies indicate that onset information is important for gap detection, and that ramped gap envelopes may have reduced psychophysical salience compared with gaps having abrupt marker offsets and onsets. Accordingly, the object of this investigation was to test in humans the effect on gap detectability of ramped marker edges.

II. GENERAL METHODS

Two experiments were conducted to test the effect of ramped marker edges on gap detection. In experiment 1, the effects on detectability and response speeds were investigated of varying the ramp duration at one gap edge (either the leading or trailing marker) while keeping the other edge abrupt. In experiment 2, the effects of having a single abrupt edge versus two or no abrupt edges on gap detection were investigated.

A. Subjects

Fourteen volunteers (nine men and five women) aged between 19 and 65, with a median age of 21 years, participated in this study. All had normal audiograms for their age. The University of Rochester Research Subject Review Board approved the experimental procedure and participants were reimbursed for their participation.

B. Stimuli

The carrier for the gaps consisted of 3 s of broadband noise (16 Hz to 20 kHz, 60 dB A) generated and controlled via a digital signal processing platform (Tucker-Davis AP2) and custom software on a 486 personal computer. The noise bursts were created with a flat frequency spectrum using a sampling rate of 50 kHz. They were presented binaurally using Beyer headphones (DT 48). The noise bursts were separated by a silent postresponse intertrial interval of 2 s. Variously shaped gaps (described for the two experiments below) were located 2 s into the noise burst.

C. Procedures

Throughout the experiment, participants were seated in a sound-attenuating chamber and asked to listen for the presence or absence of a gap in the noise bursts. A "Yes"/"No" single-interval procedure was used. Participants were instructed to respond as quickly and accurately as possible on hearing a gap by pressing the right-hand button on a response box, and if no gap was detected to press the left-hand button.

The latency between the 2-s point of the stimuli, where gaps were presented except on control trials, and the subject's response was collected. For "Yes" responses, if the response latency was greater than 170 ms, but less then 2500 ms, this latency was converted to a reaction speed (speed=1/latency) in order to reduce the skewing effects of occasional long reaction time latencies, and mean response speeds for each gap were calculated. Subjects used various response strategies for trials during which they did not hear a gap. The most common strategy was to respond "No" after the cessa-
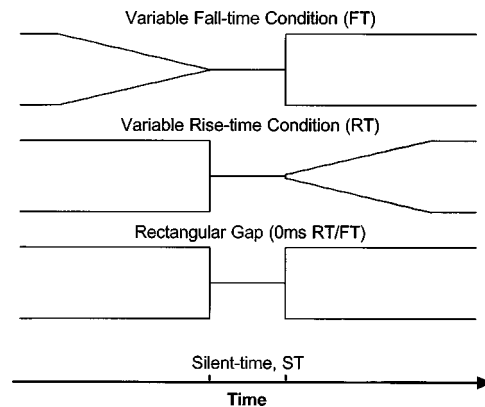
FIG. 1. Schematic representation of temporal gap stimuli used in experiment 1.

tion of the 3-s noise burst, at considerably longer latency than for trials during which they responded "Yes". In experiment 1 asymptotic values for reaction speed were determined using a 12-ms gap with abrupt edges.

III. EXPERIMENT 1: EFFECT ON GAP DETECTION OF A SINGLE RAMPED EDGE

A. Methods

There were seven participants in experiment 1 (four men and three women) aged between 19 and 65, with a median age of 22 years. Participants were tested over two days, and on each day were presented with six blocks of trials. Within a single block, participants were presented with either variable-RT or variable-FT trials (described below), and each block contained eight presentations of each of the eight stimulus types and a no-gap control trial, so that each condition was presented 48 times. On each day three variable-FT and three variable-RT blocks were randomly presented. Each trial block lasted approximately 7 min and participants were given the opportunity to take a short rest between blocks.

The gap stimuli in this experiment are shown schematized in Fig. 1, and were chosen to correspond directly with those used in a prepulse inhibition study of mice by Ison *et al.* (2002). The nominal gap duration is the silent time of the gap, to which ramped marker onsets and offsets are added. On each trial, except for control trials on which there was no gap in the noise, a gap with a silent-time, ST, of 1-, 4-, or 12-ms duration was presented 2 s after the onset of the noise burst. Gaps with 1- and 4-ms ST were either preceded by a 0, 2, 4, or 8 ms fall-time of the leading marker and followed by an abrupt onset of the trailing marker (Variable-FT Condition), or had an abrupt leading marker offset and a rise-time of the trailing marker of 0, 2, 4, or 8 ms (Variable-RT Condition). The 12-ms ST gap had abrupt marker edges.

The detection probability and response speed data were each subjected to a three-way within-subject repeated measures factorial analysis of variance (ANOVA). The data entered into the ANOVA were the mean values across blocks of trials for each subject for each condition. The three factors were (1) gap silent time, here using only the 1- and 4-ms durations, (2) rising versus falling ramps, and (3) ramp du-

FIG. 2. Percent detection functions for individual subjects. Increasing gap fall- and rise-time (FT and RT) conditions are plotted together, illustrating that there is little difference between them. The data are presented in age order, demonstrating also that there is no systematic age effect.

FIG. 3. Group average percent detection functions against gap FT (left panel) and RT (right panel) for three gap silent times. Error bars denote standard errors of the mean, while the within-subject standard error is 3.6% for the RT condition and 3.4% for the FT condition. The false alarm rate (FA) for both experimental conditions was <5%. Both 1-ms silent time data sets are shown with a logistic function described by Eq. (1) obtained by fitting to the FT data.

ration. The number of levels in each factor were, respectively, 2, 2, and 3. The interpretation of the statistical significance of the resulting F-values used the Huynh–Feldt correction (Huynh and Feldt, 1976) for violations of compound symmetry in repeated measures designs.
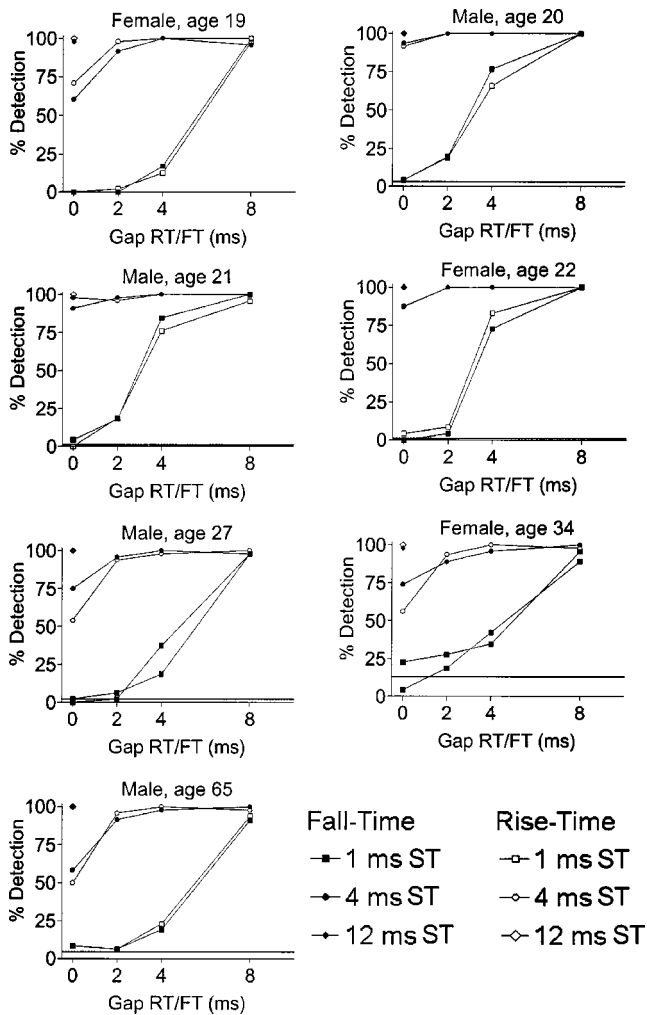
B. Results

Individual subject psychometric functions for gap detection are shown in Fig. 2. Gap detectability increased uniformly with the silent duration of the gap, ST, and with both increasing RT and FT, with no systematic difference in detectability apparent between these two types of gaps across subjects. These data also demonstrate the uniformity in psychometric functions across participants, who are presented in age order, showing also that there is no apparent age dependence for the effects of this RT/FT manipulation on gap detection.

Mean gap detection probabilities across participants were calculated and are shown in Fig. 3. Detection of gaps increased with increasing ST and also with increasing gap FT and RT. The ANOVA shows that there was no significant difference in detectability between the FT and RT conditions

for equal gap silent time $[F(1,6)=1.1, p>0.3]$. Gaps with 1-ms silent time and 0-ms RT/FT were infrequently detected. These gaps had a mean detectability and standard error of $4.5(\pm1.6)\%$. Detectability increased equally with increasing RT and FT, with 50% detectability near 4 ms for both, and approached 100% for the 8-ms RT/FT. The logistic function is commonly used to descriptively model psychometric detection functions (e.g., Green, 1993; Florentine *et al.*, 1999; He *et al.*, 1999) and takes the form

$$\text{Detection}(\%) = \alpha + \frac{100 - \alpha}{1 + e^{-k(t-m)}}, \tag{1}$$

where α is the false alarm rate, m is the midpoint of the psychometric function, and k describes the slope of the function (Green, 1993). The 1-ms FT and RT data of Fig. 3 are shown with a function of this form, calculated by least-squares fitting to the FT data. The function describes these data well, with $R^2=0.9997$, and additionally the same function describes the RT data with $R^2=0.9963$, further highlighting the similarity of these two data sets.

The detectability of all the 4-ms silent-time gaps was above 50% and their detectability increased rapidly from the 0-ms RT/FT gap, $74.9(\pm4.5)\%$ detection, with little difference between variable-RT and FT condition, and approached 100% for longer RT/FT. These data cannot be fit reliably with a logistic function because they are clustered at high values of this function, but are shown in Fig. 3 with a logistic function fitted to the FT data to illustrate the similar trends in detectability for the two gap-types.

The 12-ms abrupt-edged gap was almost always detectable (means for RT and FT conditions were 100% and 99.0% detection, respectively). The false alarm rate was $4.0(\pm2.0)\%$ for the variable-FT condition and $3.1(\pm1.6)\%$ for the variable-RT condition. The within-subject standard error terms obtained from the ANOVA, which exclude variance arising between subjects (Loftus and Masson, 1994), are 3.6% for the RT condition and 3.4% for the FT condition.

The individual participant data for response speeds are shown in Fig. 4, calculated from the response latencies on trials with "Yes" responses. Across subjects, speeds increased with silent duration and with RT/FT and again showed uniformity between the RT and FT conditions, although response speed appears more variable among subjects

J. Acoust. Soc. Am., Vol. 112, No. 6, December 2002

Allen *et al.*: Effect on detection of ramped gap markers   2969

FIG. 4. Individual subject response speeds (1/Latency) shown with increasing gap RT and FT for each of the three gap silent times.

than does detectability. Mean response speeds across subjects are shown in Fig. 5, and were again nearly identical for both the variable-RT and variable-FT conditions. The ANOVA shows that there was no significant difference in detectability between the FT and RT conditions for equal gap silent time $[F(1,6)<1, p>0.75]$. The data for both FT and RT condi-
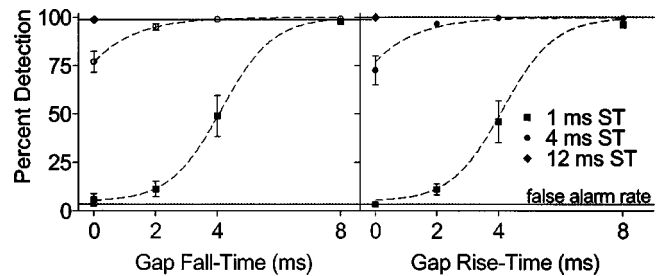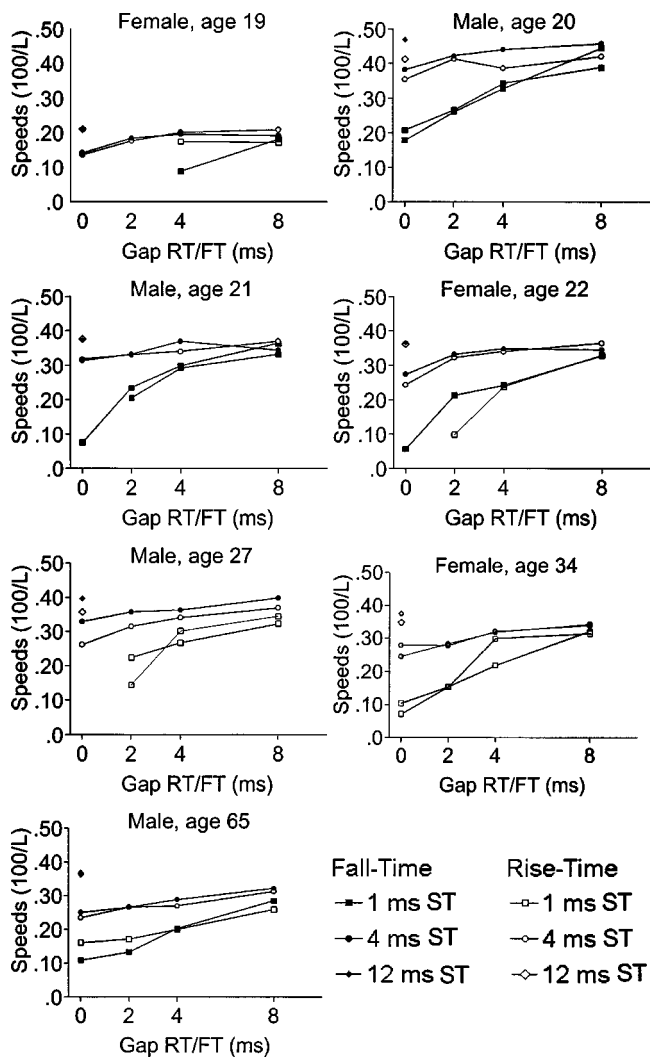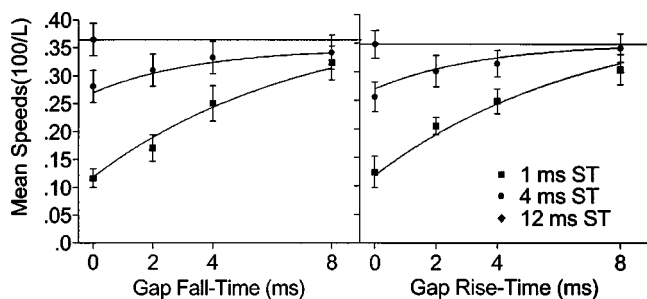

FIG. 5. Mean response speeds for gap FT (left panel) and RT (right panel). Error bars denote standard errors of the mean, while the within-subject standard error is 0.012 for the RT condition and 0.013 for the FT condition. The data are well described by two exponential functions fitted to the mean of the aggregated RT and FT data for each of the 1- and 4-ms silent time conditions. The 12-ms speed is shown with a dashed line to indicate the asymptotic response speed.

tions are shown with exponential functions of the form

$$RS = RS_{Max} - A \exp(-t/\tau), \qquad (2)$$

so that response speed, RS, approaches the asymptotic maximum response speed, RS_{Max}, with a time constant, τ, and free fitting parameter, A. The curves were obtained by fitting to the mean of the RT and FT data for each of the 1- and 4-ms silent-time conditions. The exponential fits describe the data well, with $R^2 = 0.9971$ and 0.9990 for the 1- and 4-ms silent-time conditions, respectively. These curves illustrate that the response speed has a more gradual approach to asymptote than does the detection data and highlights the similarity of the RT and FT data. The 12-ms gap response speed is shown on each graph in Fig. 5 with a dashed line to indicate the asymptotic response speed, which the other curves approach with increasing gap RT/FT.

C. Discussion

This experiment examined the effects on detection and response speed for gaps in noise having ramped offsets or onsets. Detection of gaps was not impaired by ramped onset of the trailing marker: for a given gap silent period, adding a ramped edge to either the leading or the trailing marker improved gap detectability and response speed, and this improvement was the same regardless of which marker possessed the ramp. This result in humans stands in contrast to the finding of Ison *et al.* (2002) in mice using the same ramped-edge gap stimuli, that ramped edges on the trailing marker impair gap detection relative to ramps on the leading marker. However, the result here is consistent, at least qualitatively, with energy or loudness detector models of gap detection (e.g., Florentine *et al.*, 1999). Examination of Figs. 3 and 5 suggests that the detectability and response speed data for different silent durations in both the variable-RT and FT conditions would superimpose if they were appropriately shifted or rescaled on the time-axis. If gap detection relies on detecting energy fluctuations of the sound envelope, then the addition of RT and FT serves to increase the effective duration of gaps. Rescaling the gap duration in terms of the silent gap plus the appropriately weighted ramp duration provides an effective gap duration,

$$t_{eff} = ST + m \, RT \ (or \ FT). \qquad (3)$$

Previous studies of the detectability of partially filled gaps in broadband noise indicate that decrements of 35% to 50% of the carrier all produce MGTs of 2–3 ms (Forrest and Green, 1987) and that sound level within the gap has little effect on gap thresholds as long as the decrease in the carrier is at least 5 to 10 dB below the initial sound level (Penner, 1975; Irwin and Purdy, 1982). These studies suggest that MGT and t_{eff} are determined by the time that the envelope remains below some minimum decrement.

The weighting factor, m, in Eq. (3) reflects how much the ramp time contributes to t_{eff}. Large values of m indicate that most of the ramp contributes, and that small decrements are sufficient to enhance t_{eff}. Conversely, if large decrements in the carrier are needed in order to increase t_{eff}, then the

Allen *et al.*: Effect on detection of ramped gap markers
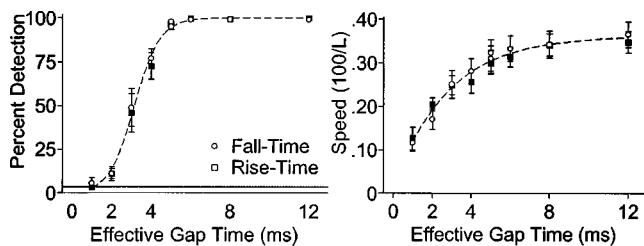
FIG. 6. Group mean detectability and response speed data with standard errors of the mean plotted against effective gap duration, $t_{eff} = ST + 0.5RT$ (or FT). Rescaling yields simple curves that collapse all the experimental data irrespective of silent gap duration or RT/FT condition.

contribution of ramps will be less and the value of m will be smaller. For linear ramps, if this minimum decrement is X in dB, then

$$m = 10^{-X/20}. \tag{4}$$

The range of m expected from these previous studies is 0.32 to 0.63 for 10- to 4-dB decrements, respectively. For $m = 0.5$, t_{eff} corresponds to the time between the 50% amplitude, or -6 dB points of the gap envelope. Figure 6 shows the detectability and response speed data of Figs. 3 and 5 replotted against this effective gap duration, using $m = 0.5$. The three different silent time data sets for both variable-RT and variable-FT conditions rescale onto a single logistic and exponential curve for the detectability and response speed data, respectively. These functions have characteristic time constants, m and τ, which have 95% confidence intervals of 2.93–3.36 ms and 2.25–3.29 ms, respectively. The rescaling yields similar characteristic time constants for the two experimental measures, supporting the conclusion that subjects were responding to effective gap duration owing to an energy detector like mechanism, and not differentially to particular features of the gap envelope. It is notable that the rescaling may not be unique. The detectability data can be rescaled with m between 0.3 and 0.55 (corresponding to decrements of 4 to 7 dB) to also produce satisfactory rescaling, such that a single sigmoidal function describes all the detection data with $R^2 > 0.990$. However, R^2 decreases rapidly for $m > 0.5$, so this value was used above for simplicity.

In this experiment reaction speeds were measured and showed a slower approach to asymptote than did the detectability data, but also demonstrated significant systematic differences among the readily detectable gaps. This is noteworthy since the method of constant stimuli usually leads to psychometric functions that are very steep around an operational threshold. While these gaps had near 100% detectability, responses to them showed differential latencies, with faster speeds for longer gaps. This increase in response speed is continuous with the process of detection, as subthreshold gaps, when detected, are responded to more slowly than the more readily detectable stimuli. Consequently, reaction speeds appear to provide a useful measure of the perceptual equivalence and salience of stimuli that are above the detection threshold, consistent with previous findings (e.g., Kohfeld et al., 1981a, b).

The stimuli used in this experiment were selected to test in humans the effect seen in mouse IC single units, and also

behaviorally via prepulse inhibition, that ramped edges on the trailing gap marker led to decreased gap detectability. These mouse data depend on brainstem processing, and there is the possibility that in psychophysical experiments humans make use of cues that are not strongly coded in the brainstem, but which are perhaps more important in cortical processing. Gaps in the current experiment had at least one abrupt edge, raising the possibility that listeners made equally good use of abrupt marker offset or onset information to assist detection. Experiment 2 was designed to test the hypothesis that gaps having either a single abrupt edge or two abrupt edges have higher detectability than those with two ramped edges.

IV. EXPERIMENT 2: EFFECTS OF ZERO, ONE, OR TWO RAMPED EDGES

A. Methods

The results of experiment 1 suggest that humans do not make special use of onset information to detect brief gaps in noise with ramped edges, but rather do so by detecting overall energy fluctuations. In experiment 2, gap stimuli were constructed to compare differential detectability among gaps that should have the same detectability according to one such energy detector model, but which have zero, one, or two ramped edges.

There were seven participants in experiment 2 (five men and two women) aged between 19 and 22, with a median age of 19 years. Participants were each tested on a single day and were presented with four blocks of trials. Each block contained ten presentations of each gap type (described below) and the no-gap control so that each condition was presented a total of 40 times. Each trial block lasted approximately 9 mins and participants were given the opportunity to take a short rest between blocks.

Gaps in the noise carrier were presented on each trial, except for control trials on which there was no gap in the noise. Gaps were constructed with various combinations of ramped and abrupt edges to have equal effective gap duration, t_{eff}, using $m = 0.5$. There were two series of gaps, the "2-ms series" and "3-ms series" with t_{eff} of 2 or 3 ms, respectively. Each series consisted of five gap-types: (1) an abrupt edged gap ("square"), (2) a gap with an abrupt leading marker offset and 2-ms ramped trailing marker onset ("rising"), (3) a gap with a 2-ms ramped leading marker offset and abrupt trailing marker onset ("falling"), (4) a gap with two 1-ms ramped edges ("fast"), and (5) a gap with two 2-ms ramped edges ("slow"). To illustrate these stimuli, Fig. 7 shows the 2-ms series of gaps; the 3-ms series has the same shaped edges, but the total gap durations are 1 ms longer by extending the duration of the silent portion of the gap.

The percent detection and response speed data were each subjected to a two-way within-subject repeated measures factorial ANOVA. The two factors were (1) effective gap duration and (2) gap type, and the number of levels in each factor were, respectively, 2 and 5. Otherwise, the treatment of these data followed the pattern used in experiment 1.
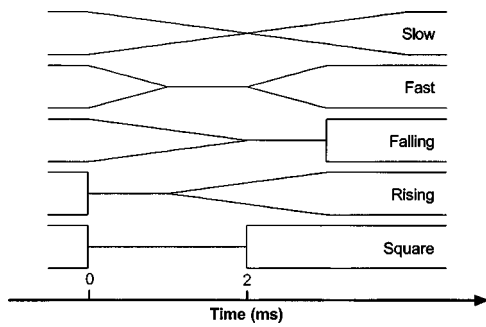
FIG. 7. Schematic representation of temporal gap stimuli used in experiment 2. All five gaps have $t_{eff}=2$ ms, according to Eq. (3) with $m=0.5$.

FIG. 9. Group average detectability and standard errors of the mean, for the "2-ms" and "3-ms" effective gap duration series. The within-subject standard errors are 2.7% for the 2-ms series, and 2.6% for the 3-ms series.

B. Results

Individual subject data for gap detection are shown in Fig. 8. Gap detectability increased with increasing gap duration between the 2- and 3-ms series of gaps and within series seem to show increasing detectability between the "square" and the "slow" gaps. The variability among subjects appears greater than in experiment 1. This might reflect an increase in the subjects' decision uncertainty as the stimuli were deliberately chosen to lie on the steepest region of the psychometric function.

Mean gap detection probabilities across participants

FIG. 8. Individual subject gap detection data shown for the "2-ms" (open squares) and "3-ms" (filled circles) effective gap duration series consisting of gap types "square," "falling," "rising," "fast," and "slow" depicted in Fig. 7. Data show means and standard deviations across four sessions.

were calculated and are shown in Fig. 9. The ANOVA reveals a strong effect of gap duration between the two series, $F(1,6)=59.2$, $p<0.001$, and of gap type within the series, $F(4,24)=27.15$, $p<0.001$, but no interaction, $F(4,24)<1$, $p>0.97$. In order to identify the source of these differences, subsequent ANOVA were performed with particular conditions. There was a significant difference between the "square" and "falling" gaps, $F(1,6)=50.73$, $p<0.001$, and between the "fast" and "slow" gaps, $F(1,6)=8.63$, $p<0.05$. There was no significant difference among the "falling," "rising," and "fast" gaps, $F(2,12)<1$, $p>0.84$. Statistical power analysis indicates that this experiment had a 70% chance of detecting a difference in detectability of 5% with 95% confidence, and in fact the mean detectabilities of these three types of gap vary by less than 2%.

Response speeds (not shown) were again calculated from latencies of trials with "Yes" responses. Compared with experiment 1, speeds were more variable among subjects, but the ANOVA demonstrated significant effects of gap duration, $F(1,6)=22.99$, $p<0.01$, and gap type, $F(4,24)=3.66$, $p<0.05$, with no interaction, $F(4,24)=1.48$, $p>0.2$.

C. Discussion

In this experiment, detectability and response speeds were measured for gaps that have one, two, or no abrupt edges. Two series of gaps were designed to have the same equivalent gap duration based on Eq. (3) with $m=0.5$. While the results of experiment 2 suggest that a different value of m would be more appropriate, they confirm the findings of experiment 1, namely that human listeners (1) make use of FT and RT to increase effective gap duration and (2) do not make use of information from abrupt changes in the acoustic envelope to assist detection.

In experiment 2, differential detectability was seen between "square" and "slow" gaps, and between these and the intermediate series of "rising," "falling," and "fast" gaps, which were themselves not detected differently from each other. These data suggest that effective gap duration does determine detectability, but this constructed measure should not be calculated from the 50% amplitude points of the gap envelope, as chosen for simplicity in the rescaling of the data from experiment 1. A better estimate of the contribution of ramps to increased effective gap duration can be made from

Allen *et al.*: Effect on detection of ramped gap markers

the data of experiment 2 by noting that the addition of 1 ms of silence between the 2- and 3-ms "square" gaps increases detectability by 40%. In the 2-ms gap series, the "rising," "falling," and "fast" gaps have an average increase in detectability of 11.9% compared to the "square" gap, while the "slow" gap has an increase in detectability of 20.4%. Assuming that these gaps lie on a linear section of the psychometric function, then the extra time added to the effective gap duration by the ramps is 0.29 and 0.51 ms, for a total t_{eff} of 2.29 and 2.51 ms, respectively. Working backwards through Eq. (3), the "rising," "falling," and "fast" gaps each have ST=1 ms and RT (or FT, or RT+FT)=2 ms leading to a value of m of 0.645. The "slow" gap has ST=0 ms and RT+FT=4 ms, leading to a value of m of 0.628. Hence a better estimate of the effective gap duration is obtained by calculating the time between the 63%–65% amplitude points of the gap envelope, or for linear ramps $t_{\text{eff}} \approx \text{ST} + 0.64\,\text{RT (or FT)}$. This new approximation is not inconsistent with the data from experiment 1, and corresponds to decrements in the gap envelope of 4 dB, which as noted also rescaled the data detectability data of experiment 1 with $R^2 > 0.990$.

Statistical power analysis of the data indicates that it is reasonable to accept the null-hypothesis, that "rising," "falling," and "fast" gaps are not different in their detectability. This implies that gap detection by human listeners is not assisted by abrupt edge detection cues, because the "fast" gap does not have abrupt edges, but rather has the single ramped edge of the "rising" and "falling" gaps distributed evenly on both markers. A possible situation in which this conclusion would not be valid is if the auditory system had insufficient temporal resolution to resolve envelope changes of 0-, 1-, or 2-ms duration. However, the data from the two experiments reported here show differential detection when gap features are manipulated on this time scale, indicating that the human auditory system can, in fact, resolve these ramps.

V. GENERAL DISCUSSION AND CONCLUSIONS

The experiments reported here indicate that brief gaps in noise with ramped edges are detected by human listeners according to an effective gap duration, consistent at a qualitative level with energy or loudness detector models (Florentine *et al.*, 1999). Detection is not sensitive to particular envelope features, such as abruptness of onset or offset, beyond the capacity of such features to extend the effective duration of the gap. Consequently, these data do not support the expectation that abrupt changes in envelope, specifically onset information, provide additional cues for detection beyond the energy fluctuation in the carrier associated with the gap. This finding is surprising in light of results from mouse behavior (Ison *et al.*, 2002) and IC single units (Barsz *et al.*, 1998), and also from theoretical expectations. The loudness detector model of Florentine *et al.* (1999) provides good estimates of gap detection in bandpass noise based on stationary transformation of the output of an auditory filter, with discrepancies between model and data arising for low-frequency bands. To account for this discrepancy these authors drew on extant physiological data suggesting the importance for gap encoding of onset responses (Zhang *et al.*, 1990), and concluded that onset information may provide additional cues to gap detection. The two experiments reported here do not support this possibility, at least for gaps in broadband noise, and for onset information with time scales of 1 to 12 ms, which are the conditions under which onset sensitive gap detection was observed in the mouse studies.

The data here suggest that there are interesting differences between the gap detection mechanisms apparently used by human listeners compared with those reported for mouse IC neurons and for acoustic startle inhibition, which seem to depend in part on features of the gap envelope. The neural mechanisms underlying the different gap detection strategies apparently employed by mice and humans are not immediately apparent. It is possible that methods for assessing gap detection that are sensitive to brainstem processing, such as prepulse inhibition, might produce a result in human listeners that would be more like that reported for mice. It is also possible that mouse IC neurons encode effective gap duration in some way that is not yet understood, but which might have implications for the general understanding of temporal acuity in the mammalian auditory system. Certainly, the importance of timing for human speech perception, as shown, for example, in voicing onset information (e.g., Kewley-Port *et al.*, 1988), indicates that humans utilize temporal information of signal envelopes, but the results of these experiments suggest that these features might be more important for discrimination rather than for detection *per se*.

Barsz, K., Benson, P. K., and Walton, J. P. (**1998**). "Gap encoding by inferior collicular neurons is altered by minimal changes in signal envelope," Hear. Res. **115**, 13–26.

Busby, P. A., and Clark, G. M. (**1999**). "Gap detection by early-deafened cochlear-implant subjects," J. Acoust. Soc. Am. **105**, 1841–1852.

Buunen, T. J., and van Valkenberg, D. A. (**1979**). "Auditory detection of a single gap in noise," J. Acoust. Soc. Am. **65**, 534–536.

Buus, S., and Florentine, M. (**1985**). "Gap detection in normal and inpaired listeners: The effect of level and frequency," in *Time Resolution in Auditory Systems*, edited by A. Michelsen (Springer-Verlag, London), pp. 159–179.

Eggermont, J. J. (**2000**). "Neural responses in primary auditory cortex mimic psychophysical, across-frequency-channel, gap-detection thresholds," J. Neurophysiol. **84**, 1453–1463.

Forrest, T. G., and Green, D. M. (**1987**). "Detection of partially filled gaps in noise and the temporal modulation transfer function," J. Acoust. Soc. Am. **82**, 1933–1943.

Florentine, M., Buus, S., and Geng, W. (**1999**). "Psychometric functions for gap detection in a yes-no procedure," J. Acoust. Soc. Am. **106**, 3512–3520.

Gordon-Salant, S., and Fitzgibbons, P. J. (**1993**). "Temporal factors and speech recognition performance in young and elderly listeners," J. Speech Hear. Res. **36**, 1276–1285.

Green, D. M. (**1985**). ''Temporal factors in psychoacoustics,'' in *Time Resolution in Auditory Systems*, edited by A. Michelsen (Springer, London), pp. 122–140.

Green, D. M. (**1993**). ''A maximum-likelihood method for estimating thresholds in a yes-no task,'' J. Acoust. Soc. Am. **93**, 2096–2105.

Green, D. M., and Forrest, T. G. (**1989**). ''Temporal gaps in noise and sinusoids,'' J. Acoust. Soc. Am. **86**, 961–970.

He, N. J., Horwitz, A. R., Dubno, J. R., and Mills, J. H. (**1999**). ''Psychometric functions for gap detection in noise measured from young and aged subjects,'' J. Acoust. Soc. Am. **106**, 966–978.

Heinz, M. G., Goldstein, M. H., and Formby, C. (**1996**). ''Temporal gap detection in sinusoidal markers simulated with a multi-channel, multi-resolution model of the auditory periphery,'' Aud. Neurosci. **3**, 35–56.

Huynh, H., and Feldt, L. S. (**1976**). ''Estimation of the Box correction for degrees of freedom from sample data in the randomized block and split-plot designs.'' J. Educat. Statist. **1**, 964–973.

Irwin, R. J., and Purdy, S. C. (**1982**). ''The minimum detectable duration of auditory signals for normal and hearing-impaired listeners,'' J. Acoust. Soc. Am. **71**, 967–974.

Ison, J. R. (**1982**). ''Temporal acuity in auditory function in the rat: reflex inhibition by brief gaps in noise,'' J. Comp. Physiol. Psychol. **96**, 945–954.

Ison, J. R., Agrawal, P., Pak, J., and Vaughn, W. J. (**1998**). ''Changes in temporal acuity with age and with hearing impairment in the mouse: A study of the acoustic startle reflex and its inhibition by brief decrements in noise level,'' J. Acoust. Soc. Am. **104**, 1696–1704.

Ison, J. R., Castro, J., Allen, P. D., Virag, T. M., and Walton, J. P. (**2002**). ''The relative detectability for mice of gaps having different ramp durations at their onset and offset boundaries,'' J. Acoust. Soc. Am. **112**, 740–747.

Kewley-Port, D., Watson, C. S., and Foyle, D. C. (**1988**). ''Auditory temporal acuity in relation to category boundaries; speech and nonspeech stimuli,'' J. Acoust. Soc. Am. **83**, 1133–1145.

Kohfeld, D. L., Santee, J. L., and Wallace, N. D. (**1981a**). ''Loudness and reaction time: I,'' Percept. Psychophys. **29**, 535–549.

Kohfeld, D. L., Santee, J. L., and Wallace, N. D. (**1981b**). ''Loudness and reaction time: II. Identification of detection components at different intensities and frequencies,'' Percept. Psychophys. **29**, 550–562.

Leitner, D. S., Hammond, G. R., Springer, C. P., Ingham, K. M., Mekilo, A. M., Bodison, P. R., Aranda, M. T., and Shawaryn, M. A. (**1993**). ''Parameters affecting gap detection in the rat,'' Percept. Psychophys. **54**, 395–405.

Loftus, G. R., and Masson, M. E. J. (**1994**). ''Using confidence intervals in within-subject designs,'' Psychonom. Bull. Rev. **1**, 476–490.

Moore, B. C., Peters, R. W., and Glasberg, B. R. (**1992**). ''Detection of temporal gaps in sinusoids by elderly subjects with and without hearing loss,'' J. Acoust. Soc. Am. **92**, 1923–1932.

Penner, M. J. (**1975**). ''Persistence and integration: Two consequences of a sliding integrator,'' Percept. Psychophys. **18**, 114–120.

Phillips, S. L., Gordon-Salant, S., Fitzgibbons, P. J., and Yeni-Komshian, G. (**2000**). ''Frequency and temporal resolution in elderly listeners with good and poor word recognition,'' J. Speech Lang. Hear. Res. **43**, 217–228.

Plomp, R. (**1964**). ''Rate of decay of auditory sensation,'' J. Acoust. Soc. Am. **36**, 277–282.

Snell, K. B. (**1997**). ''Age-related changes in temporal gap detection,'' J. Acoust. Soc. Am. **101**, 2214–2220.

Snell, K. B., and Frisina, D. R. (**2000**). ''Relationships among age-related differences in gap detection and word recognition,'' J. Acoust. Soc. Am. **107**, 1615–1626.

Tyler, R. S., Moore, B. C., and Kuk, F. K. (**1989**). ''Performance of some of the better cochlear-implant patients,'' J. Speech Hear. Res. **32**, 887–911.

Tyler, R. S., Summerfield, Q., Wood, E. J., and Fernandes, M. (**1982**). ''Psychoacoustic and phonetic temporal processing in normal and hearing-impaired listeners,'' J. Acoust. Soc. Am. **72**, 740–752.

Walton, J. P., Frisina, R. D., Ison, J. R., and O'Neill, W. E. (**1997**). ''Neural correlates of behavioral gap detection in the inferior colliculus of the young CBA mouse,'' J. Comp. Physiol., A **181**, 161–176.

Zhang, W., Salvi, R. J., and Saunders, S. S. (**1990**). ''Neural correlates of gap detection in auditory nerve fibers of the chinchilla,'' Hear. Res. **46**, 181–200.

Effect of modulator asynchrony of sinusoidal and noise modulators on frequency and amplitude modulation detection interference

Hedwig Gockel[a)]
CNBH, Department of Physiology, University of Cambridge, Downing Street, Cambridge CB2 3EG, United Kingdom

Robert P. Carlyon and John M. Deeks
MRC Cognition and Brain Sciences Unit, 15 Chaucer Road, Cambridge CB2 2EF, United Kingdom

The effect on modulation detection interference (MDI) of timing of gating of the modulation of target and interferer, with synchronously gated carriers, was investigated in three experiments. In a two-interval, two-alternative forced choice adaptive procedure, listeners had to detect 15 Hz sinusoidal amplitude modulation (AM) or frequency modulation (FM) imposed for 200 ms in the temporal center of a 600 ms target sinusoidal carrier. In the first experiment, 15 Hz sinusoidal FM was imposed in phase on both target and interferer carriers. Thresholds were lower for nonoverlapping than for synchronous modulation of target and interferer, but MDI still occurred for the former. Thresholds were significantly higher when the modulators were gated synchronously than when the interferer modulator was gated on before and off after that of the target. This contrasts with the findings of Oxenham and Dau [J. Acoust. Soc. Am. **110**, 402–408 (2001)], who reported no effect of modulation asynchrony on AM detection thresholds, using a narrowband noise modulator. Using FM, experiment 2 showed that for temporally overlapping modulation of target and interferer, modulator asynchrony had no significant effect when the interferer was modulated by a narrowband noise. Experiment 3 showed that, for AM, synchronous gating of modulation of the target and interferer produced *lower* thresholds than asynchronous gating, especially for sinusoidal modulation of the interferer. Results are discussed in terms of specific cues available for periodic modulation, and differences between perceptual grouping on the basis of common AM and FM. © *2002 Acoustical Society of America.* [DOI: 10.1121/1.1512291]

PACS numbers: 43.66.Mk, 43.66.Dc, 43.66.Ba [MRL]

I. INTRODUCTION

The ability to detect modulation of a target carrier can be strongly impaired in the presence of another modulated carrier spectrally remote from the target. This effect has been called modulation detection interference (MDI), and has been reported for amplitude modulation ("AMDI") and frequency modulation ("FMDI") of the target and interferer. Most studies have focused on AMDI (Yost and Sheft, 1989; Yost *et al.*, 1989; Yost and Sheft, 1990; Hall and Grose, 1991; Moore *et al.*, 1991; Moore and Jorasz, 1992; Moore and Shailer, 1992; Bacon and Konrad, 1993; Bacon and Moore, 1993; Bacon and Opie, 1994; Bacon *et al.*, 1995; Mendoza *et al.*, 1995b; Verhey and Dau, 2000; Oxenham and Dau, 2001) while only a few have investigated FMDI (Wilson *et al.*, 1990; Moore *et al.*, 1991; Carlyon, 1994; Lyzenga and Carlyon, 1999; Gockel and Carlyon, 2000). To the knowledge of the authors, so far, no marked differences between AMDI and FMDI have been reported in the literature. It is quite conceivable that AMDI and FMDI reflect similar processes, as frequency modulation (FM) is converted to amplitude modulation (AM) at the outputs of individual auditory filters, and FM interferes with AM detection and vice versa (Moore *et al.*, 1991).

One well-established and important feature of MDI is that asynchronous gating of target and interferer decreases MDI substantially relative to that observed for synchronous gating (Hall and Grose, 1991; Moore and Jorasz, 1992; Moore and Shailer, 1992; Mendoza *et al.*, 1995b; Gockel and Carlyon, 2000). Generally, this has been interpreted as evidence that at least part of MDI is caused by a difficulty in perceptual segregation of the target and interferer. Recently, Oxenham and Dau (2001) investigated the effect of asynchronous gating of the modulation of the target and the interferer. The targets were sinusoidally amplitude modulated (SAM) and the interferers were modulated in amplitude by a narrowband noise. No effect of modulation asynchrony was found, either with synchronous carriers or with asynchronous carriers. On the other hand, asynchronous gating of the *carriers* led to the usually observed significant reduction in MDI (Hall and Grose, 1991; Moore and Jorasz, 1992; Moore and Shailer, 1992; Mendoza *et al.*, 1995b; Gockel and Carlyon, 2000). The results were explained in terms of perceptual segregation of the carriers. Carrier asynchrony was thought to be effective in achieving this segregation, whereas modulator asynchrony was not.

Here we present three experiments intended to investigate further the effects of asynchronous gating of the modulation of target and interferer. Knowledge about these effects and their possible interactions with characteristics of the

_____
[a)]Electronic mail: hedwig.gockel@mrc-cbu.cam.ac.uk

stimuli seems essential in order to evaluate possible mechanisms underlying MDI. In our first experiment, the main interest was in the effect of interferer modulation which does not overlap in time with the modulation of the target. In an earlier study, Gockel and Carlyon (2000) showed that FM interferers presented *nonsimultaneously* with a FM target produced a significant amount of FMDI. This is an important finding, as we are not aware of any model of MDI which predicts the existence of MDI for nonsimultaneous modulation. In the study of Gockel and Carlyon (2000), the modulators and carriers were always gated together, and the amount of FMDI with nonsimultaneous FM was significant, but much smaller than for simultaneous and synchronously gated modulated carriers. The recent finding of Oxenham and Dau (2001), that carrier but not modulator asynchrony affected AMDI (with temporally overlapping modulation of target and interferer), raised the interesting possibility that the amount of FMDI with nonsimultaneous modulation of target and interferer might be much bigger if the carriers were gated synchronously instead of asynchronously as in Gockel and Carlyon (2000). If this were to be confirmed, it would present even stronger evidence against current models of MDI based on simultaneously present modulation.

The first experiment investigated whether synchronous gating of the target and interferer carriers would indeed substantially increase FMDI with nonsimultaneous modulation of target and interferer. The results showed that it did not. FMDI with nonsimultaneous modulation was not larger when the carriers were gated synchronously (present experiment) than when they were gated asynchronously (Gockel and Carlyon, 2000). In both studies, FMDI with nonsimultaneous modulation of target and interferer was always considerably smaller than when the interferer modulation was gated synchronously with that of the target. This indicates that a considerable proportion of the FMDI effect was due to the *modulation* of interferer and target being gated simultaneously. The present results also showed that, for temporally overlapping modulation of target and interferer, thresholds were higher for synchronously gated modulation than for asynchronously gated modulation, even though the carriers were gated synchronously in all cases. This differed from the finding of Oxenham and Dau (2001), that carrier but not modulator asynchrony affected AMDI. In the second and third experiments possible reasons for this discrepancy were investigated.

II. EXPERIMENT 1: SINUSOIDAL FREQUENCY MODULATION - ASYNCHRONOUS MODULATION OF SYNCHRONOUS CARRIERS

Stimuli were similar to the ones used by Gockel and Carlyon (2000). The main difference was that, in the present study, the carriers of the target and interferer were always gated synchronously. In addition, the interferer was modulated at several different time periods during its presentation to investigate the effects of various relative timings of interferer and target modulation on FMDI.
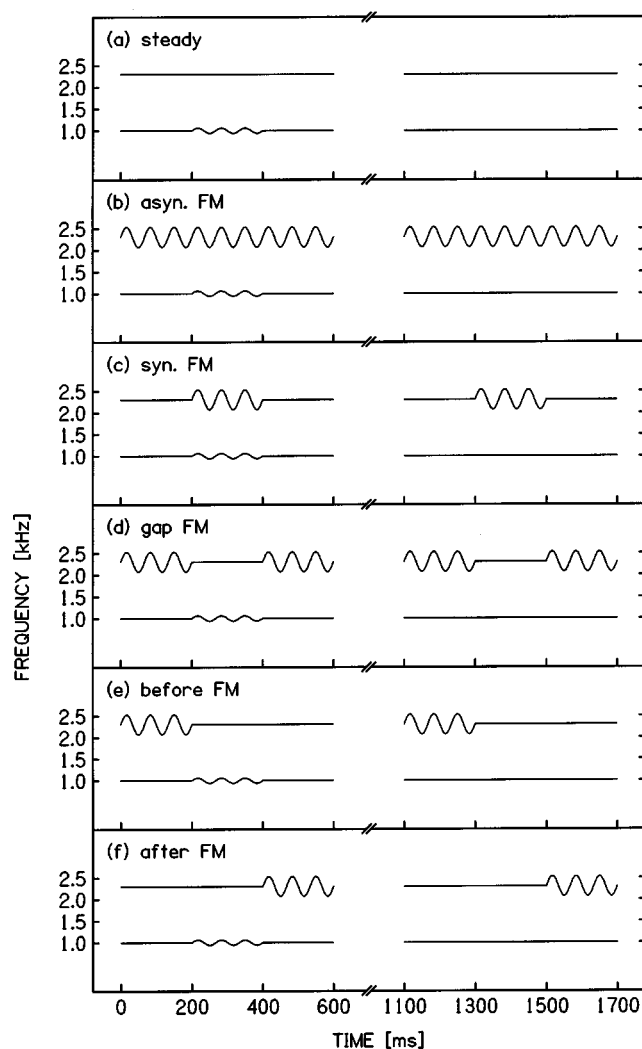
FIG. 1. Schematic spectrograms of stimuli presented over the course of one 2AFC trial in the different conditions of experiment 1: (a) steady; (b) asynchronous FM; (c) synchronous FM; (d) gap FM; (e) before FM; (f) after FM. Note that, for illustrative purposes only, (i) an extreme FM depth has been chosen for the target and (ii) the signal interval is always the first interval.

A. Stimuli

Listeners had to detect sinusoidal FM with a modulation frequency (f_m) of 15 Hz, imposed for 200 ms (temporally centered) on a 600 ms target with a carrier frequency (f_c) of 1 kHz. The target was accompanied by a synchronous 600 ms interferer with a carrier frequency of 2.3 kHz. The interferer was either unmodulated or sinusoidally modulated at various times with f_m of 15 Hz, with a FM depth of 10% of the carrier frequency (resulting in a peak deviation from f_c of 230 Hz).

Schematic spectrograms of the stimuli are shown in Fig. 1. Condition "steady," with the unmodulated interferer [Fig. 1(a)], provided the baseline against which thresholds in the other conditions were compared. In condition "asyn. FM" [Fig. 1(b)], the interferer was modulated throughout its duration. In condition "syn. FM" [Fig. 1(c)], the interferer was modulated only synchronously with the target's modulation. Comparison of thresholds in this condition with those in condition asyn. FM would indicate the effect of asynchronous

gating of modulation *per se*. In condition "gap FM" [Fig. 1(d)], the interferer was modulated for 200 ms immediately before and for 200 ms immediately after the target's modulation. Comparison of thresholds in this condition with those in condition asyn. FM would indicate the contribution to FMDI of the part of the interferer modulation present simultaneously with the target's modulation. In condition "before FM" [Fig. 1(e)], the interferer was modulated for 200 ms before the target's modulation started and was steady thereafter. In condition "after FM" [Fig. 1(f)], the interferer was modulated for the last 200 ms, after the target's modulation stopped. Comparison of thresholds in the last two conditions would indicate the relative contribution to FMDI of modulation of the interferer before and after modulation of the target.

The starting phase of the modulator was always 0° (sine phase). In conditions where the target and interferer modulators overlapped in time [Figs. 1(b) and (c)], they were in phase. When they did not overlap in time [Figs. 1(d)–(f)], the target's modulator started in the same phase at which the first part of the interferer's modulator stopped, and/or the second part of the interferer modulation started at the same phase as the target modulation stopped. Over a modulation duration of 200 ms, three complete modulation cycles were presented. The target and interferer carriers each had a level of 50 dB SPL, and were gated with 10 ms raised-cosine onset and offset ramps.

All stimuli were generated digitally, played out of a 16 bit digital-to-analog converter (CED 1401 plus) at a sampling rate of 20 kHz, and passed through an anti-aliasing filter (Kemo 21C30) with a cutoff frequency of 8.6 kHz (slope of 100 dB/oct). Stimuli were presented monaurally, using Sennheiser HD250 headphones. Subjects were seated individually in an IAC double-walled sound-attenuating booth.

B. Procedure

A two-interval two-alternative forced-choice task was used. The target and interferer carriers were presented in both intervals in each trial. The subjects were required to indicate the interval with the modulated target. Feedback was provided following each response. The modulation depth (expressed as a percentage of f_c) of the target in the signal interval was adjusted using a two-down one-up adaptive tracking rule (Levitt, 1971), tracking 71% correct responses. At the beginning of each threshold measurement, the target was modulated with a FM depth of 10%, which made the task easy in all conditions. Initially, the FM depth was divided or multiplied by a factor of $\sqrt{2}$. Following four reversals, the factor was reduced to $\sqrt[4]{2}$ and 10 further reversals were obtained. The threshold estimate was defined as the geometric mean of the FM depths at the last 10 reversals. The time interval between the two signals in a trial was fixed at 500 ms. Each interval was marked by a light.

The total duration of a single session was about 2 h, including rest times. Six threshold estimates were obtained for each of the six conditions from each subject. Six subjects ran through the six conditions in a Latin-square design order
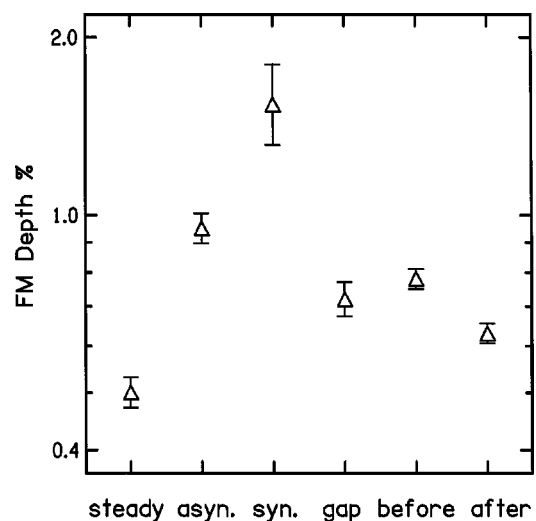
FIG. 2. The geometric mean FM detection thresholds, and the associated geometric standard errors (across subjects) obtained in experiment 1.

(one threshold was obtained for each condition in turn, before additional measurements were obtained in any other condition). The reported thresholds correspond to the geometric mean of these six thresholds for each condition and subject. To familiarize subjects with the procedure and equipment, they participated in one threshold track in each condition, before data collection was started.

C. Subjects

Six subjects participated in all six conditions. Their ages ranged from 20 to 34 years, and they all had normal hearing at audiometric frequencies between 500 and 4000 Hz.

D. Results and discussion

Figure 2 shows the geometric mean data and the associated geometrical standard errors[1] for the six conditions. The ordinate shows FM detection thresholds expressed as percentage of f_c. Thresholds were highest when the modulation of the interferer and target was gated synchronously. They were lowest when the target was accompanied by a steady interferer. Thresholds were intermediate for all other conditions.

To examine the statistical significance of differences between thresholds, a one-way repeated measures ANOVA (on the logarithms of the geometric mean thresholds of each subject) was calculated. Throughout the paper, if appropriate, the Huynh–Feldt correction was applied to the degrees of freedom (see, e.g., Howell, 1997). The main effect of condition was highly significant [$F(5,25) = 19.0$, $p < 0.001$]. *Post hoc* paired comparisons based on Fisher's least significant difference procedure were made across all six conditions. Thresholds in condition "steady" were significantly lower than thresholds in all other conditions ($p < 0.01$ in all cases). Also, thresholds in condition "syn. FM" were significantly higher than those in all other conditions ($p < 0.01$ in all cases, except for "asyn. FM" where $p < 0.05$). Thresholds in condition "before FM" were significantly higher than in "after FM" ($p < 0.01$). However, this difference was small.

Thresholds in conditions "before FM" and "after FM" did not differ significantly from those in condition "gap FM," indicating that the effects of interferer modulation before and after the target modulation did not sum. Thresholds in condition "asyn. FM" were significantly higher than in conditions "gap FM" and "after FM" but not significantly higher than in condition "before FM."

The results give support to our earlier finding that non-simultaneous modulation of an interferer, with no overlap in time between modulation of the target and that of the interferer, can lead to significant FMDI. However, the amount of FMDI due to nonsimultaneous modulation was not substantially greater when the carriers were gated synchronously (as in present study) than when they were asynchronous (as in Gockel and Carlyon, 2000). Also, in both studies, thresholds in condition "gap FM" were significantly lower than for synchronously gated FM even though, here, the carriers were gated synchronously. Thus, a considerable proportion of the FMDI effect must be due to the *modulation* of interferer and target being gated simultaneously.

Interestingly, a significant reduction in FMDI was obtained by gating the temporally overlapping modulation of the target and interferer asynchronously (condition "asyn. FM" vs "syn. FM"). This contrasts with the results of Oxenham and Dau (2001), who reported no effect of modulation asynchrony. There were two main differences between the two studies which might be responsible for the opposing findings: (i) They used AM sounds while we used FM sounds. (ii) They used a narrowband noise to modulate the interferer while we used sinusoidal modulation. The first difference was considered unlikely to be responsible. As mentioned in Sec. I, we were not aware of any evidence of divergent findings for AMDI and FMDI. The second difference seemed to be more relevant. The effect of modulator asynchrony may depend on whether the interferer modulator is periodic or not. For periodic modulation, the asynchronous part of the modulator might be perceived as a stable pattern of modulation. The additional target modulation might be easier to detect when added to this stable modulation pattern than when gated synchronously with the onset of modulation of the interferer. A noise modulator would not provide a stable temporal pattern and therefore asynchronous modulator gating would give no advantage over synchronous gating. Note that, in both studies, the target was modulated sinusoidally. The second experiment investigated whether the reduction in FMDI for asynchronously modulated carriers would be absent if the interferer were frequency modulated by a narrowband noise.

III. EXPERIMENT 2: SINUSOIDAL VS NOISE MODULATION OF INTERFERER—FMDI

A. Stimuli

As in experiment 1, listeners had to detect sinusoidal FM ($f_m = 15$ Hz) imposed on the central 200 ms of a 600 ms target ($f_c = 1$ kHz). The first three conditions, "asyn. periodic," "syn. periodic," and "gap periodic" [see Figs. 3(a), (b), and (c)], were nearly identical to the conditions "asyn.

FM," "syn. FM," and "gap FM," respectively, run in experiment 1. The only difference was that the modulator had 20 ms raised-cosine onset and offset ramps.

The next three conditions were similar to the first three with respect to the onset and offset timing of the interferer's modulation. However, instead of a sinusoidal modulator, a narrow band of noise was used to modulate the interferer in frequency [see Figs. 3(d), (e), and (f)]. Equation (1) specifies the time waveform of the interferer when it was frequency modulated:

$$x(t) = \sin 2\pi \left(f_c t + \int_0^t n(\lambda) d\lambda \right), \tag{1}$$

where f_c is the carrier frequency of the interferer (2300 Hz), t is time in seconds, λ is the integration variable, and $n(t)$ is the time waveform of the noise.

The noise had a bandwidth of 15 Hz and was centered at 15.5 Hz. It was digitally synthesized by summing sinusoids ranging in frequency from 8 to 23 Hz, spaced at 1 Hz intervals. The amplitudes were drawn from a Rayleigh distribution, and the phases from a uniform distribution in the range of 0–360°. The noise had a rms value of 162.6 (i.e., $230/\sqrt{2}$) and had 20 ms onset and offset ramps. Thus, the rms FM depth of the interferer (in those parts where it was modulated) corresponded to the rms FM depth of the sinusoidally modulated interferer which had a peak deviation from f_c of 230 Hz. In condition "asyn. noise" [see Fig. 3(d)], the interferer was modulated throughout its 600 ms duration by a narrow band noise. In condition "syn. noise" the interferer was modulated for 200 ms in its temporal center [see Fig. 3(e)], and in condition "gap noise" the interferer was modulated for the first and last 200 ms [see Fig. 3(f)].

All stimuli were generated digitally in advance. For each noise FM interferer, ten different realizations of the random FM were produced. In the "gap noise" condition, independent realizations of noise were used for the first and the last part of the interferer. For each stimulus presentation, one out of the ten realizations was picked at random.

The target and interferer carriers each had a level of 50 dB SPL, and were gated with 10 ms raised-cosine onset and offset ramps. All stimuli were generated digitally, at a sampling rate of 40 kHz, and passed through an anti-aliasing filter (Kemo 21C30) with a cutoff frequency of 8.6 kHz (slope of 100 dB/oct). The procedure and experimental design were the same as in experiment 1.

B. Subjects

Six new subjects participated in all six conditions. Their ages ranged from 23 to 36 years, and they all had normal hearing at audiometric frequencies between 500 and 4000 Hz.

C. Results and discussion

Figure 4 shows the geometric mean data and the associated geometric standard errors[1] for the six conditions in experiment 2. The open and closed triangles show thresholds obtained with the sinusoidal and the narrowband noise FM interferers, respectively. Consider first the effect of the sinu-
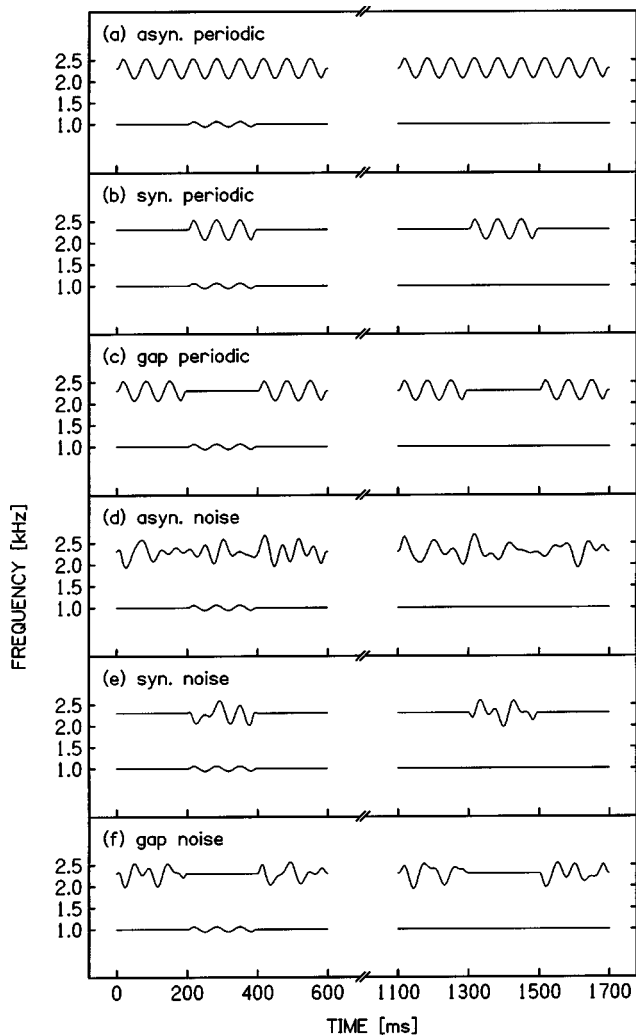
FIG. 3. Schematic spectrograms of stimuli presented over the course of one 2AFC trial in the different conditions of experiment 2: (a) asynchronous periodic; (b) synchronous periodic (c) gap periodic; (d) asynchronous noise; (e) synchronous noise; (f) gap noise. Note that, for illustrative purposes only, (i) an extreme FM depth has been chosen for the target and (ii) the signal interval is always the first interval.

FIG. 4. The geometric mean FM detection thresholds, and the associated geometric standard errors (across subjects) obtained in experiment 2. The abscissa indicates the three types of gating of the interferer's modulation relative to that of the target. The open and the closed symbols show the results when the interferer was FM by a sinusoidal and by a narrowband noise modulator, respectively.

soidal modulation (open triangles). Thresholds were overall a little higher than in the corresponding conditions of experiment 1, probably due to differences between subjects. However, in general, the same pattern was observed. Thresholds were highest when the modulation of interferer and target was gated synchronously. They were clearly lower and very similar to each other in conditions "asyn. periodic" and "gap periodic." Consider next the conditions with the noise modulated interferers (closed triangles). Here the pattern of results is different. Thresholds with synchronous and with "gapped" noise modulation were similar to those with periodic modulation. However, when asynchronous modulation was used, thresholds with the noise modulator were substantially higher than with periodic modulation, and were similar to those seen when the target and interferer modulations were gated synchronously.

A two-way repeated measures ANOVA (gating of modulation [3]×regularity of modulator [2]) showed a significant main effect of gating of modulation [$F(2,10) = 13.3$, $p < 0.01$], a significant main effect of regularity of modulator

[$F(1,5) = 35.2$, $p < 0.01$], and, more importantly here, a significant interaction between gating and regularity [$F(2,10) = 5.4$, $p < 0.05$], reflecting that the effects of gating were different with the sinusoidal and with the narrowband noise modulator. *Post hoc* contrasts showed that this interaction was due to thresholds being significantly higher in condition "asyn. noise" than in "asyn. periodic" ($p < 0.01$); in no other gating condition did thresholds with the sinusoidal modulator and with the narrowband noise modulator differ significantly. Also, thresholds in condition "asyn. noise" did not differ significantly from those in conditions "syn. noise" and "syn. periodic."

The present findings with FM sounds agree with those of Oxenham and Dau (2001), employing AM sounds, in that asynchronous gating of modulation alone did not reduce MDI for noise modulated interferers. However, our results also showed that asynchronous gating of modulation alone did reduce FMDI when sinusoidally modulated interferers were used. Thus, the effect of modulator asynchrony did indeed depend on whether the modulator was periodic or not.

This is a finding which, *a priori*, might not have been expected, since randomly amplitude modulated (RAM) and SAM stimuli generally produce the same pattern of results in AMDI. For example, Mendoza *et al.* (1995a) found that AMDI as a function of modulation depth showed the same behavior for RAM and SAM stimuli, i.e., AMDI increased with increased modulation depth of the interferer. They also were the first to show that, as in earlier studies with SAM stimuli (Hall and Grose, 1991; Moore and Shailer, 1992; Mendoza *et al.*, 1995b), asynchronous gating of RAM target and RAM interferer decreased AMDI relative to that found for synchronous gating. Employing RAM targets and SAM interferers, Moore *et al.* (1995) showed that AMDI is broadly tuned to modulation rate of the interferer, similar to the tuning reported earlier with SAM targets (Yost *et al.*, 1989; Moore *et al.*, 1991; Bacon and Opie, 1994). Relative

phase of target and masker modulation did not affect AMDI with either RAM or SAM stimuli (Mendoza *et al.*, 1995a; Moore *et al.*, 1995). Thus, overall, the same pattern of AMDI was observed with SAM and with RAM stimuli with respect to such factors as effect of modulation depth, relative gating of target and interferer, broad tuning for modulation rate, and lack of influence of modulation phase.

There was, however, one difference between RAM and SAM stimuli, reported by Mendoza *et al.* (1995a). They compared the effectiveness of SAM interferers presented together with SAM targets and RAM interferers presented together with RAM targets. They found that, for equal rms modulation depths of the RAM and SAM interferers, AMDI was greater for RAM stimuli than for SAM stimuli. In the present study, thresholds with the noise modulator were not significantly higher than those with the periodic modulator when gated synchronously. Thus, the differential effect of modulator asynchrony cannot be explained by a general difference between the degree of difficulty with sinusoidal and noise modulated interferers. Note, however, that even if thresholds with the noise modulator had been higher than with the periodic modulator, it is not obvious how this could explain the different pattern of results for asynchronous modulators, since the use of an adaptive procedure with a given up and down rule ensures measurement at the same level of performance, i.e., degree of difficulty, in each condition.

A possible explanation of the different effect of modulator asynchrony for SAM and RAM interferers is that asynchronous gating of periodic modulation provides an additional cue. The asynchronous periodic modulator provides a stable modulation pattern in which a change—the additional target modulation—may be detected more easily than when the target modulation is gated together with the larger interferer modulation. In the former, the change in the temporal pattern caused by the additional target modulation is immediately preceded by the stable temporal pattern caused by the interferer modulation on its own; discrimination in this case might be easier than in the latter condition where discrimination would be based on comparison across two intervals. The noise modulator would not provide such a stable modulation pattern, and thus no advantage would result from asynchronous over synchronous modulator gating.

One might speculate whether a deterministic noise modulator would lead to the same reduction of FMDI with asynchronous gating of modulation as the periodic modulator used here. Under the assumption that the advantage in the asynchronous onset condition results from the within-interval information which in turn is due to the stable (periodic) temporal pattern, as was described previously, one would not expect a deterministic noise modulator to produce the same reduction in FMDI when gated asynchronously. Whether this speculation is correct, remains to be tested.

In condition "gap noise," thresholds were considerably lower than in condition "syn. noise;" this is the same pattern of results as observed for the SAM interferer. Probably, the unmodulated part of the interferer, which coincides with the modulation of the target in the gap condition, makes it much easier to detect the target's modulation; this seems to be in-

dependent of the form of the interferer modulation. Hall and Grose (1991) reported that listeners had difficulty in deciding which carrier in a two-carrier complex sound was modulated, even if they could detect the presence of modulation. This finding is compatible with the idea of modulation filters whose output is combined in some way across carrier frequency (Dau and Verhey, 1999). Thus, detection of probe modulation in the presence of interferer modulation would amount to detection of an increase in overall amount of modulation. The finding that interferer modulation which is temporally nonoverlapping with the target modulation produce some interference (even for temporally nonoverlapping carriers) is inconsistent with models in which only *simultaneous* modulation is summed across channels (Yost and Sheft, 1989). It may be possible to account for this finding by assuming that *all* modulation is combined in some way across channels, unless the carriers are perceptually segregated. In these terms, the task with gapped modulators can be described as discriminating between two sounds, one containing modulation—of variable degree—throughout its duration (the signal interval), and the second having a pause or gap in its modulation (the standard interval). If this interpretation in terms of "gap detection" in overall modulation is correct, then the same pattern of thresholds should result when a single carrier is modulated by a function that is identical to the overall modulation of interferer and target. This remains to be tested.

The main finding of experiment 2 was that FMDI was independent of the gating of the modulators when the interferer was modulated with a narrowband noise function, but dependent on modulator gating when it was sinusoidally modulated. Thus, the difference in the modulator functions seemed to explain the contrasting findings of Oxenham and Dau (2001) and the present study, concerning the absence/presence of effect of modulator gating. In the third experiment we assessed whether similar effects of modulator asynchrony would be observed for AMDI. The hypothesis was that the effects would be similar to those for FMDI, since, as mentioned previously, to the knowledge of the authors so far no essential differences between AMDI and FMDI have been reported in the literature.

IV. EXPERIMENT 3: SINUSOIDAL VERSUS NOISE MODULATION OF INTERFERER—AMDI

The stimuli in the third experiment were chosen to be similar to the ones used by Oxenham and Dau (2001) with respect to the carrier frequencies and levels of target and interferer. However, we were concerned about possible level effects due to the increase in power resulting from AM (see Viemeister, 1979). In order to eliminate within-interval level cues introduced by the transition from unmodulated to amplitude modulated carrier, we applied the modulation to the intensity of each carrier instead of applying it to its amplitude. Intensity modulation does not change the rms level of the stimulus. In the case of sinusoidal modulation, this means that the carrier is sinusoidally modulated in intensity, but that the amplitude is modulated with a function corresponding to the square root of a sinusoid.

A. Stimuli

Listeners had to detect sinusoidal intensity modulation with a rate of 15 Hz imposed for 200 ms (temporally centered) on a 600 ms target with a carrier frequency of 4.3 kHz. The target was either presented alone (condition "none") or was accompanied by a synchronous 600 ms interferer with a carrier frequency of 1 kHz. The interferer was either unmodulated (condition "steady") or modulated. When it was modulated, it was either modulated throughout its duration, i.e., asynchronously gated with the target modulation (conditions "Asy"), or temporally centered for 200 ms, i.e., synchronously gated with the target modulation (conditions "Syn"). The interferer was either sinusoidally modulated with a rate of 15 Hz (conditions "Sin") or narrowband noise modulated (conditions "Noi") in intensity. The narrowband noise modulator was generated in the same way as in experiment 2, with a bandwidth of 15 Hz and centered around 15.5 Hz.

Equation (2) specifies the time waveform of the interferer for sinusoidal intensity modulation, i.e., square-root sinusoidal amplitude modulation:

$$x(t) = \sqrt{(1 + m \sin 2\pi f_m t)} \sin 2\pi f_c t, \qquad (2)$$

where f_c is the carrier frequency of the interferer (1 kHz), f_m is the modulation rate (15 Hz), and t is time in seconds. The modulation index m was set to 0.588. For "classical" amplitude modulation, $m = 0.588$ corresponds to -4.6 dB (re unity). Here, $m = 0.588$ corresponds to about -10.2 dB classical amplitude modulation and -4.6 dB in intensity modulation; these two modulators have the same power, i.e., identical rms values. When the modulator was a narrowband noise, it was scaled to have the same rms value as the sinusoidal modulator. Note, that the -10.2 dB modulation depth used here is almost identical to the -10 dB rms level used by Oxenham and Dau (2001) for their narrowband noise modulator. In order to facilitate comparisons across studies, when presenting the results we will specify modulation depth in dB, referring to a classical amplitude modulator with rms value identical to that of the intensity modulator.

The modulators had 20 ms raised-cosine onset and offset ramps. All stimuli were generated digitally in advance. For each noise modulated interferer, ten different realizations of random AM were produced. For each stimulus presentation, one out of the ten realizations was picked at random. The target and interferer each had a level of 65 dB SPL, and were gated with 10 ms raised-cosine onset and offset ramps. All stimuli were generated digitally, at a sampling rate of 12.5 kHz, and passed through an anti-aliasing filter (Kemo 21C30) with a cutoff frequency of 5.38 kHz (slope of 100 dB/oct).

B. Procedure

The procedure was similar to that of experiment 1, except for the following points. At the beginning of each threshold measurement, the target modulation depth was set to -4 dB. The initial step size was 3 dB, which was reduced to 2 dB after two reversals. Following four reversals, the step size was reduced to 1 dB and 10 further reversals were ob-
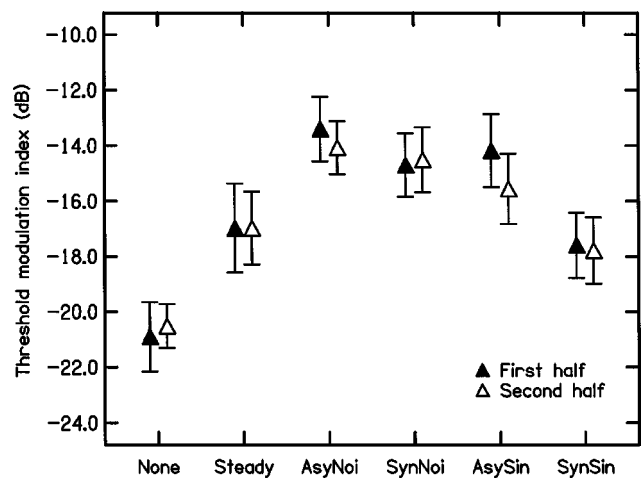
FIG. 5. The mean AM detection thresholds, and the associated standard errors (across subjects) obtained in experiment 3. The six different conditions are indicated on the abscissa: (i) None—no interferer present; (ii) Steady—unmodulated interferer present; (iii) AsyNoi—interferer modulated by a narrowband noise with asynchronously gated modulator relative to that of the target; (iv) SynNoi as AsyNoi but with synchronous gating of interferer and target modulation; (v) AsySin—sinusoidally modulated interferer with asynchronously gated modulation relative to that of the target; (vi) SynSin as AsySin but with synchronous gating of interferer and target modulation. The open and the closed triangles show the mean of the first and second half (about 10 each) of the thresholds obtained.

tained. The threshold estimate was defined as the mean of the levels at the last 10 reversals. When subjects responded several times incorrectly at the beginning of a run, theoretically requiring a level of modulation above 0 dB, it was set to 0 dB and otherwise continued as normal, if this happened before they reached the final step size; if they had reached the final step size already, the run was discarded. This was done to allow subjects to get used to the specific condition.

The duration of the experiment was 8 h for each subject. Each subject did between 20 and 25 runs in each condition. As some of the runs were discarded for some subjects, the number of threshold estimates obtained varies somewhat between subjects and conditions, being typically about 20 (the minimum was 14, the maximum was 25). As before, subjects participated in one threshold track in each condition, before data collection was started. Also, each 2 h session was started with one run in the condition without the interferer.

C. Subjects

Six new subjects participated in all six conditions, all of whom had prior experience in other listening tasks. Their ages ranged from 21 to 40 years, and they all had normal hearing at audiometric frequencies between 500 and 4000 Hz.

D. Results and discussion

Figure 5 shows the mean data and the associated standard errors for the six conditions in experiment 3. The closed and open triangles correspond to the first and second half of the about 20 thresholds obtained overall. Thresholds were lowest without any interferer (condition "none"). Mean thresholds here are about -21 dB compared to about -26 dB reported by Oxenham and Dau (2001). The presence of

an unmodulated interferer (condition "steady") increased thresholds by about 4 dB; a 3 dB increase was observed by Oxenham and Dau. The next two pairs of triangles give thresholds in the presence of the narrowband noise AM interferers. Here thresholds are increased by about 3 dB relative to those for the steady interferer; they are somewhat *higher* for asynchronous onset (condition "AsyNoi") than for synchronous onset (condition "SynNoi") of target and interferer modulation, a trend which could also be seen in Oxenham and Dau's (2001) results. The two rightmost pairs of triangles give thresholds for the interferer modulated sinusoidally in intensity. For asynchronous onset of modulation (condition "AsySin") thresholds are 2–3 dB higher than for the steady interferer; in this condition improvement with practice was largest (about 1.4 dB). Surprisingly, for synchronous onset (condition "Synsin") thresholds are clearly lower than in condition "AsySin," and almost equal to those observed for the steady interferer.

A two-way repeated measures ANOVA using all conditions (practice [2]×condition [6]) showed a significant main effect of condition [$F(5,25) = 18.3$, $p < 0.001$], but no effect of practice and no interaction. *Post hoc* contrasts based on Fisher's least significant difference procedure showed that thresholds without the interferer were significantly lower than thresholds in all other conditions ($p < 0.01$ in all cases, except for condition "SynSin," where $p < 0.05$). Also, thresholds with the steady interferer were significantly lower than thresholds with modulated interferers ($p < 0.05$) except in condition "SynSin;" here no AMDI was observed.

To assess differences between conditions with modulated interferers only, a two-way repeated measures ANOVA restricted to those four conditions with modulated interferers (practice [2]×condition [4]) was conducted. The results showed a significant main effect of condition [$F(3,15) = 7.1$, $p < 0.01$], but no effect of practice or interaction. *Post hoc* contrasts showed that thresholds in condition "SynSin" were significantly lower than thresholds in all other conditions ($p < 0.05$ in all cases); they did not differ significantly between the other conditions. When a three-way repeated measures ANOVA (practice [2]×gating of modulation [2]×regularity of modulator [2]) was used to assess the effects of modulator asynchrony and periodicity of the interferer modulator, a slightly different outcome was observed. The results showed a significant main effect of regularity of modulator [$F(1,5) = 10.0$, $p < 0.05$], indicating that sinusoidal modulation resulted in lower thresholds than noise modulation. Furthermore, the main effect of gating was significant [$F(1,5) = 9.6$, $p < 0.05$], indicating *higher* thresholds for asynchronous gating of the modulators than for synchronous. There was a significant interaction between practice and regularity of the modulator [$F(1,5) = 8.4$, $p < 0.05$], indicating more improvement with practice for the sinusoidal than for the noise modulator. The interaction between gating and regularity of the modulators was *not* significant, indicating that for the noise modulators too, asynchronous gating produced *slightly* higher thresholds than synchronous gating. However, as mentioned previously, the *post hoc* comparison between "AsyNoi" and "SynNoi" did not show a significant difference.

Overall thresholds in the present study were somewhat higher than those observed by Oxenham and Dau (2001) for the corresponding conditions. This is probably due to the difference in duration of the target modulation (200 ms here compared to 500 ms in their study) and/or to differences between the two groups of subjects. Also, the elimination of a possible within-interval level cue due to the use of intensity modulation, i.e., square-root amplitude modulation, might have increased thresholds somewhat. The surprising and new finding is that, mainly for the sinusoidal modulator, asynchronous gating of the modulation of target and interferer results in *larger* AMDI than synchronous gating. A trend in the same direction was observed for the noise modulator, not only in the present experiment but also in the data of Oxenham and Dau (2001).

For FM, in experiment 2, FMDI for asynchronous gating of sinusoidal modulators was less than for synchronous gating. The same pattern of results was expected for AM. However, the findings clearly show the opposite pattern. As mentioned in Sec. I, the authors are not aware of any essential differences between AMDI and FMDI being reported in the literature. For sinusoidal AM, relative phase of target and masker modulation has generally been found to have little or no effect on AMDI (Yost and Sheft, 1989; Moore *et al.*, 1991; Bacon and Konrad, 1993), although in some cases small effects have been found (Yost and Sheft, 1989; Moore and Shailer, 1992). For narrowband noise modulators, AMDI has been found to be independent of similarity in the moment-by-moment fluctuations in the envelopes of target and interferer (Mendoza *et al.*, 1995a; Moore *et al.*, 1995). Similarly, for sinusoidal FM, relative phase of modulators did not affect FMDI provided that aurally generated combination tones were not audible (Moore *et al.*, 1991; Carlyon, 1994). A broad tuning to modulation rate has been observed for both AMDI (Yost *et al.*, 1989; Moore *et al.*, 1991; Bacon and Opie, 1994; Moore *et al.*, 1995) and FMDI (Wilson *et al.*, 1990; Moore *et al.*, 1991). Thus, there was no obvious reason why the factor "gating of a periodic modulator" should produce contrasting results for FMDI and AMDI.

A "*post hoc*" explanation might be provided by the following considerations. In the case of sinusoidal AM, it has been suggested that carriers which are amplitude modulated in phase tend to be perceived as more strongly fused than carriers which are modulated at different rates or with different phases (McAdams, 1984; Bregman *et al.*, 1985; Bregman *et al.*, 1990; Moore *et al.*, 1990; Carrell and Opie, 1992). In condition "SynSin" of experiment 3 (AMDI), this might lead to subjects hearing the carriers of the target and interferer as one sound in the signal interval. In the nonsignal interval, the carriers would be less likely to fuse, as only the interferer is modulated; the target carrier is more likely to be heard as a steady tone. Subjects could then choose the interval in which they did not hear a steady tone. Thus, the "breakdown" of fusion in the nonsignal interval would provide an additional cue. The cue would not be available for asynchronously gated modulators, as here fusion of the carriers would be weaker in both intervals, due to the asynchrony in the gating of the modulators. This reasoning also can explain why a similar tendency has been observed in the

results for the narrowband noise modulator. Here modulation of target and interferer would not be in phase, but would be close in rate for most of the time; the fusion due to AM with similar rate in the signal interval would be present but weaker. Note, that a similar mechanism would not be expected to work for FM sounds, as there has been no evidence showing that common FM rate and phase enhances the fusion of two sounds. Indeed, listeners are not able to discriminate between in-phase and out-of-phase FM of inharmonic carriers (Carlyon, 1991).

V. GENERAL DISCUSSION

The experiments described here and elsewhere may shed some light on the relationship between MDI and auditory grouping. One useful distinction between two possible components of MDI was described by Moore and Shailer (1992). They suggested that part of MDI may be caused by a failure to perceptually segregate the target from the interferer, and hence to selectively process any modulation imposed on it. They argued that this "carrier specific" component should be highly sensitive to grouping cues. In contrast, a "modulation specific" component resulted from some form of interference from the modulation imposed on the interferer, even when it was not perceptually fused with the target.

The fact that MDI occurs even when the interferer and target are presented nonsimultaneously (Gockel and Carlyon, 2000) provides strong evidence that MDI can occur between frequency components that are not perceptually fused into a single auditory event, even though, as Oxenham and Dau (2001) have pointed out, it may be necessary for them to form part of the same perceptual stream. MDI between nonsimultaneous partials may be related to Moore and Shailer's "modulation specific" form of the effect, and has been recently demonstrated to also occur for suprathreshold tasks (Cusack and Carlyon, 2000). In contrast, there is evidence that MDI can be modified by grouping factors such as temporal asynchrony (Hall and Grose, 1991; Moore and Jorasz, 1992; Moore and Shailer, 1992; Mendoza *et al.*, 1995b; Gockel and Carlyon, 2000) and, for harmonic complex carriers, differences in $F0$ (Lyzenga and Carlyon, 1999). This component of MDI may be related to Moore and Shailer's (1992) "carrier specific" effect, in which the subject attempts to segregate the target modulation from that of interfering sounds. According to this idea, onset asynchronies and $F0$ differences reduce MDI by making the target component easier to "hear out." Our explanation for one of the results of experiment 3, i.e., thresholds being lower for synchronously than for asynchronously gated sinusoidal AM, suggests that grouping cues can modify MDI in a quite different way: when the target and interferer AM start and stop at the same time, the fact that the modulated interferer may fuse with the signal (modulated target carrier) but not with the standard (unmodulated target carrier) may *reduce* thresholds, which then increase when a modulator asynchrony is introduced. It is also worth stressing that the absence of such an effect for *FMDI* reflects a difference in the types of grouping cue available for the two types of modulation, while remaining consistent with the idea that the mechanism responsible for the

"modulation specific" *interference* does not distinguish between AM and FM (Moore *et al.*, 1991).

VI. SUMMARY

(1) Experiment 1 measured FMDI for 15 Hz sinusoidal FM imposed in phase on synchronously gated target and interferer carriers. Thresholds were lower for nonoverlapping than for synchronous modulation of target and interferer, but FMDI still occurred for the former. Modulation of the interferer before the target modulation increased thresholds more than modulation after. FMDI was significantly larger when the modulators were gated synchronously than when the interferer modulator was gated on before and off after that of the target.

(2) Experiment 2 showed that, when the interferer was frequency modulated with a narrowband noise, asynchronous gating of the modulation of target and interferer did not reduce FMDI relative to synchronous gating of the modulation. This finding with FMDI extends earlier observations of the absence of an effect of modulator gating with noise modulators on AMDI.

(3) Experiment 3 showed that, for sinusoidal intensity modulation, synchronous gating of the target and interferer modulation produced less AMDI than asynchronous gating.

We conclude that the effect of modulation asynchrony depends on the regularity of the modulation function applied and differs between AMDI and FMDI, reflecting differences in the grouping cues available for the two types of modulation.

[1]Standard errors were derived after dividing each subjects' geometric mean threshold in each condition by the geometric mean threshold for that subject across all conditions. This "normalized" standard error was calculated to give an indication of the variability that remained after compensating for differences in the overall level of performance across subjects.

Bacon, S. P., and Konrad, D. L. (**1993**). "Modulation detection interference under conditions favoring within- or across-channel processing," J. Acoust. Soc. Am. **93**, 1012–1022.

Bacon, S. P., and Moore, B. C. J. (**1993**). "Modulation detection interference: Some spectral effects," J. Acoust. Soc. Am. **93**, 3442–3453.

Bacon, S. P., Moore, B. C. J., Shailer, M. J., and Jorasz, U. (**1995**). "Effects of combining maskers in modulation detection interference," J. Acoust. Soc. Am. **97**, 1847–1853.

Bacon, S. P., and Opie, J. M. (**1994**). "Monotic and dichotic modulation detection interference in practiced and unpracticed subjects," J. Acoust. Soc. Am. **95**, 2637–2641.

Bregman, A. S., Abramson, J., Doehring, P., and Darwin, C. J. (**1985**). "Spectral integration based on common amplitude modulation," Percept. Psychophys. **37**, 483–493.

Bregman, A. S., Levitan, R., and Liao, C. (**1990**). "Fusion of auditory components: Effects of the frequency of amplitude modulation," Percept. Psychophys. **47**, 68–73.

Carlyon, R. P. (**1991**). "Discriminating between coherent and incoherent frequency modulation of complex tones," J. Acoust. Soc. Am. **89**, 329–340.

Carlyon, R. P. (**1994**). ''Further evidence against an across-frequency mechanism specific to the detection of frequency modulation (FM) incoherence between resolved frequency components,'' J. Acoust. Soc. Am. **95**, 949–961.

Carrell, T. D., and Opie, J. M. (**1992**). ''The effect of amplitude comodulation on auditory object formation in sentence perception,'' Percept. Psychophys. **52**, 437–445.

Cusack, R., and Carlyon, R. P. (**2000**). ''Auditory pop-out: Perceptual asymmetries in sequences of sounds,'' Br. J. Audiol. **34.2**, 112.

Dau, T., and Verhey, J. L. (**1999**). ''Modeling across-frequency processing of amplitude modulation,'' in *Psychophysics, Physiology and Models of Hearing*, edited by V. Hohmann, B. Kollmeier, and T. Dau (World Scientific, Singapore).

Gockel, H., and Carlyon, R. P. (**2000**). ''Frequency modulation detection interference produced by asynchronous and nonsimultaneous interferers,'' J. Acoust. Soc. Am. **108**, 2329–2336.

Hall, J. W., and Grose, J. H. (**1991**). ''Some effects of auditory grouping factors on modulation detection interference (MDI),'' J. Acoust. Soc. Am. **90**, 3028–3035.

Howell, D. C. (**1997**). *Statistical Methods for Psychology* (Duxbury, Belmont, CA).

Levitt, H. (**1971**). ''Transformed up-down methods in psychoacoustics,'' J. Acoust. Soc. Am. **49**, 467–477.

Lyzenga, J., and Carlyon, R. P. (**1999**). ''Center frequency modulation detection for harmonic complexes resembling vowel formants and its interference by off-frequency maskers,'' J. Acoust. Soc. Am. **105**, 2792–2806.

McAdams, S. (**1984**). ''Spectral fusion, spectral parsing and the formation of the auditory image,'' Ph.D. thesis, Stanford.

Mendoza, L., Hall, J. W., and Grose, J. H. (**1995a**). ''Modulation detection interference using random and sinusoidal amplitude modulation,'' J. Acoust. Soc. Am. **97**, 2487–2492.

Mendoza, L., Hall, J. W., and Grose, J. H. (**1995b**). ''Within- and across-channel processes in modulation detection interference,'' J. Acoust. Soc. Am. **97**, 3072–3079.

Moore, B. C. J., Glasberg, B. R., Gaunt, T., and Child, T. (**1991**). ''Across-channel masking of changes in modulation depth for amplitude- and frequency-modulated signals,'' Q. J. Exp. Psychol. **43A**, 327–347.

Moore, B. C. J., Glasberg, B. R., and Schooneveldt, G. P. (**1990**). ''Across-channel masking and comodulation masking release,'' J. Acoust. Soc. Am. **87**, 1683–1694.

Moore, B. C. J., and Jorasz, U. (**1992**). ''Detection of changes in modulation depth of a target sound in the presence of other modulated sounds,'' J. Acoust. Soc. Am. **91**, 1051–1061.

Moore, B. C. J., Sek, A., and Shailer, M. J. (**1995**). ''Modulation discrimination interference for narrow-band noise modulators,'' J. Acoust. Soc. Am. **97**, 2493–2497.

Moore, B. C. J., and Shailer, M. J. (**1992**). ''Modulation discrimination interference and auditory grouping,'' Philos. Trans. R. Soc. London, Ser. B **336**, 339–346.

Oxenham, A. J., and Dau, T. (**2001**). ''Modulation detection interference: Effects of concurrent and sequential streaming,'' J. Acoust. Soc. Am. **110**, 402–408.

Verhey, J., and Dau, T. (**2000**). ''Modulation detection interference with narrow-band noise interferers,'' J. Acoust. Soc. Am. **107**, 2915.

Viemeister, N. F. (**1979**). ''Temporal modulation transfer functions based on modulation thresholds,'' J. Acoust. Soc. Am. **66**, 1364–1380.

Wilson, A. S., Hall, J. W., and Grose, J. H. (**1990**). ''Detection of frequency modulation (FM) in the presence of a second FM tone,'' J. Acoust. Soc. Am. **88**, 1333–1338.

Yost, W. A., and Sheft, S. (**1989**). ''Across-critical-band processing of amplitude-modulated tones,'' J. Acoust. Soc. Am. **85**, 848–857.

Yost, W. A., and Sheft, S. (**1990**). ''A comparison among three measures of cross-spectral processing of amplitude modulation with tonal signals,'' J. Acoust. Soc. Am. **87**, 897–900.

Yost, W. A., Sheft, S., and Opie, J. (**1989**). ''Modulation interference in detection and discrimination of amplitude modulation,'' J. Acoust. Soc. Am. **86**, 2138–2147.

Within-ear and across-ear interference in a cocktail-party listening task

Douglas S. Brungart[a)]
Air Force Research Laboratory, Wright–Patterson Air Force Base, Ohio 45433-7901

Brian D. Simpson
Veridian, Dayton, Ohio

Although many researchers have shown that listeners are able to selectively attend to a target speech signal when a masking talker is present in the same ear as the target speech or when a masking talker is present in a different ear than the target speech, little is known about selective auditory attention in tasks with a target talker in one ear and independent masking talkers in both ears at the same time. In this series of experiments, listeners were asked to respond to a target speech signal spoken by one of two competing talkers in their right (target) ear while ignoring a simultaneous masking sound in their left (unattended) ear. When the masking sound in the unattended ear was noise, listeners were able to segregate the competing talkers in the target ear nearly as well as they could with no sound in the unattended ear. When the masking sound in the unattended ear was speech, however, speech segregation in the target ear was substantially worse than with no sound in the unattended ear. When the masking sound in the unattended ear was time-reversed speech, speech segregation was degraded only when the target speech was presented at a lower level than the masking speech in the target ear. These results show that within-ear and across-ear speech segregation are closely related processes that cannot be performed simultaneously when the interfering sound in the unattended ear is qualitatively similar to speech. © *2002 Acoustical Society of America.*
[DOI: 10.1121/1.1512703]

PACS numbers: 43.66.Pn, 43.66.Rq, 43.71.Gv [LRB]

I. INTRODUCTION

One of the classic listening tasks in the study of auditory attention is the ''cocktail-party'' task, in which a listener is asked to extract information from a target speech signal that is masked by one or more simultaneous interfering talkers. Over the past 50 years, researchers have examined a number of different variations of the cocktail-party task [see Bronkhorst (2000) or Ericson and McKinley (1997) for recent reviews of this literature]. One common implementation of the cocktail-party experiment is the monaural listening configuration illustrated in the left panel of Fig. 1. In this configuration, the speech waveform from the target talker (T) is mixed together electronically with the speech waveform from the masking talker (M) and the combined signal is presented to the listener via headphones.

Previous experiments have shown that two distinct kinds of masking contribute to interference in the monaural cocktail-party task (Kidd *et al.*, 1998; Freyman *et al.*, 2001, 1999; Brungart, 2001b). ''Energetic masking'' occurs when the competing speech signals overlap in time and frequency in such a way that the listener is unable to detect some of the acoustic information contained in the target speech. ''Informational masking'' occurs when the competing speech signals are similar and the listener is unable to segregate the acoustically detectable elements of the target speech from the acoustically detectable elements of the masking speech. Despite the effects of these two kinds of masking, listeners are generally able to perform well in monaural speech segregation tasks with two competing talkers. This segregation is apparently achieved by taking advantage of differences in the characteristics of the competing voices ($F0$, vocal tract length, prosody, overall level, etc.) (Brungart, 2001b; Darwin and Hukin, 2000; Bregman, 1994; Brokx and Nooteboom, 1982) and by exploiting differences in the envelopes of the two speech signals by listening to the target speech ''in the gaps'' of the envelope of the masking speech (Festen and Plomp, 1990; Bronkhorst and Plomp, 1992).

A second common implementation of the cocktail-party listening task is the ''dichotic'' listening configuration illustrated in the middle panel of Fig. 1. In this configuration, stereo headphones are used to present the target talker T and the masking talker M to different ears. Because each ear receives an unaltered speech signal, the effects of energetic masking are negligible in the dichotic listening configuration. The effects of informational masking are also greatly reduced because differences in the apparent spatial locations of the talkers can be used to help segregate the competing speech signals (Freyman *et al.*, 2001). Because the effects of energetic and informational masking are greatly reduced in the dichotic listening configuration, performance in the dichotic cocktail-party listening task is generally much better than performance in the monaural cocktail-party listening task. Previous experiments have shown that, under most stimulus conditions, listeners in the dichotic cocktail-party task are able to attend to the signal in the target ear without any measurable interference from masking sounds in the unattended ear. Cherry (1953) found that a listener's ability to

---
[a)]Electronic mail: douglas.brungart@he.wpafb.af.mil

FIG. 1. Three configurations of the cocktail-party effect that isolate the effects of within-ear and across-ear interference. The left panel shows a monaural version of the cocktail-party task that produces only within-ear interference between the target talker T and the masking talker M. The middle panel shows a dichotic version of the cocktail-party task that produces only across-ear interference between talkers T and M. The right panel shows a hybrid version of the cocktail-party task that produces within-ear interference between T and M1 and across-ear interference between T and M2.

shadow an ongoing speech signal presented to one ear was unaffected by the presence of unrelated speech in the unattended ear. Moreover, other researchers have shown that the ability to selectively attend to a single ear extends to the case where multiple talkers are presented in the unattended ear (Drullman and Bronkhorst, 2000) and to dichotic tone detection tasks with a target tone in one ear and a random-frequency "informational" masker in the unattended ear (Neff, 1995; Kidd *et al.*, 1995). There are, however, a few situations where across-ear interference does occur in dichotic listening. When the semantic content of the speech signal in the unattended ear is surprising and unexpected, such as an unexpected occurrence of the listener's first name (Moray, 1959; Wood and Cowan, 1995; Conway *et al.*, 2001), or related in some way to the signal in the target ear, such as a mid-sentence swap between the signals in the target and unattended ears (Triesman, 1960), errors often occur in the target-ear listening task. The dependence of across-ear interference on the semantic content of the interfering speech suggests that listeners perform some semantic processing on the acoustic signal in the unattended ear. This processing allows listeners to recall general physical characteristics of the speech signal in the unattended ear (such as the sex of the talker) after the completion of a dichotic speech segregation task (Cherry, 1953), but, under most circumstances, it does not result in any appreciable amount of across-ear interference.

One cocktail-party listening configuration that has thus far received relatively little attention is the hybrid configuration shown in the right panel of Fig. 1. In this configuration, a target talker (T) is presented to the listener's right ear, a masking talker (M1) is presented in the same ear as the target speech, and a second masking talker (M2) is presented in the ear opposite the target speech. This allows a direct examination of any possible interactions between the informational and energetic "within-ear" interference that occurs from a masking talker in the same ear as the target speech and the primarily informational "across-ear" interference that occurs from a masking talker in the ear opposite the target talker. The remainder of this paper describes a series of experiments that were conducted with this hybrid monaural-dichotic cocktail-party listening task.

II. EXPERIMENT 1: A HYBRID MONAURAL-DICHOTIC COCKTAIL-PARTY TASK

A. Methods

The experiments described in this paper employed the coordinate response measure (CRM), a call-sign-based intelligibility test that has been shown to produce a substantial amount of informational masking in diotic listening tests with two or more simultaneous talkers (Brungart, 2001a, b). The CRM phrases were taken from the publicly available CRM speech corpus for multitalker communications research (Bolia *et al.*, 2000), which contains phrases of the form "Ready (call sign) go to (color) (number) now," spoken by four male and four female talkers with all possible combinations of eight call signs ("Arrow," "Baron," "Charlie," "Eagle," "Hopper," "Laker," "Ringo," "Tiger"); four colors ("blue," "green," "red," "white"); and eight numbers (1–8).

In experiment 1, the signal presented to the right (target) ear always consisted of a mixture of two simultaneous phrases from the corpus: a target phrase, which was randomly selected from the phrases containing the call sign "Baron" and a masking phrase, which was randomly selected from all the phrases with a different call sign, color, and number than the target phrase. The level of the target phrase was scaled relative to the masking phrase to produce one of five different randomly selected signal-to-noise ratios (−8, −4, 0, 4, or 8 dB).

The signal presented to the left (unattended) ear consisted of one of three different masking sounds:

(1) Speech-shaped noise that was filtered to match the average long-term spectrum of all of the phrases in the CRM corpus (Brungart, 2001b) and presented at a rms level 20 dB higher than the rms level of the masking phrase in the target ear.[1]
(2) A randomly selected CRM phrase with a different call sign, color, and number than the phrases used in the target ear, presented at the same rms level as the masking phrase in the target ear.
(3) A randomly selected CRM phrase with a different call sign, color, and number than either of the phrases used in the target ear, presented at a rms level 15 dB lower than the rms level of the masking phrase in the target ear.

In addition to these three experimental conditions, two control conditions were tested. The first control condition was a purely monaural listening condition, with two competing talkers in the target ear and no signal in the unattended ear. The second control condition was a purely dichotic listening condition, with only the target talker in the target ear and a single masking talker in the unattended ear.

These five conditions were tested separately for two different target talkers: a male talker (talker 0 from the corpus) and a female talker (talker 5 from the corpus). In each case, the masking talkers were randomly selected from the remaining three talkers in the corpus who were the same sex as the target talker.[2] Thus, the talkers in any given stimulus presentation were always either all males or all females.

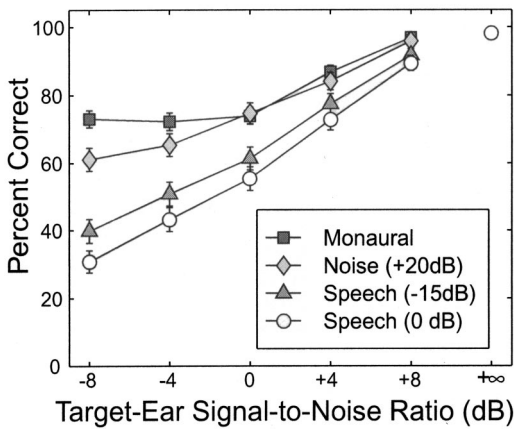A total of eight paid volunteer listeners with normal

FIG. 2. Color and number identification performance in experiment 1, a dichotic listening experiment with one target talker and one masking talker in the target ear and an interfering speech or noise masker in the unattended ear. Each of the four curves shows performance for a different masking condition in the unattended ear (see legend), and the curves are all plotted as a function of signal-to-noise ratio (SNR) in the target ear. The error bars show the 95% confidence intervals for each data point (±1.96 standard errors).

hearing (three male, five female) participated in the experiment. All had previous experience in experiments using the CRM. These listeners were seated at a control computer in a sound-treated listening booth and they were instructed to listen in their right ear for the target phrase containing the call sign ''Baron'' and respond by selecting the color–number combination contained in the target phrase from a matrix of colored numbers displayed on the CRT of the control computer. They were also instructed to ignore any signals occurring in their left ear.

The listeners first participated in a block of 120 practice trials in which they heard only the male target talker's voice in the right ear and no masker in either ear. This allowed them to become familiar with the voice characteristics of the male target talker. Then they participated in two blocks of 120 trials for each stimulus condition in a randomly assigned order that was counterbalanced across the listeners with a latin square design. Finally, they participated in two blocks of 120 trials in the dichotic control condition. The procedure was then repeated using the female target talker. Thus, each of the eight listeners in the experiment participated in a total of 480 trials in each of the five experimental and control conditions tested in the experiment.

B. Results

The curves in Fig. 2 show the percentage of trials in which the listeners correctly identified both the color and the number in the target phrase as a function of the SNR in the target ear for each of the contralateral-ear masking configurations tested in experiment 1. In the dichotic control condition (shown by the open circle at a target-ear SNR of ∞) the listeners responded correctly in nearly 100% of the trials. This result is consistent with the results of other experiments that have shown listeners have no difficulty segregating competing speech signals that are presented to different ears

(Cherry, 1953; Drullman and Bronkhorst, 2000). It also provides a performance baseline for a condition that involves only across-ear interference.

In the monaural condition, where there was no signal in the contralateral ear, performance decreased as the target-ear SNR decreased from 8 to 0 dB, but leveled off at SNR values less than 0 dB (filled squares in Fig. 2). This performance curve closely matches the results of an earlier diotic experiment that used the CRM corpus to measure the effects of SNR on two-talker speech segregation with same-sex talkers (Brungart, 2001b). The only difference is that performance at negative SNRs plateaued at roughly 70% correct responses in this experiment and at roughly 60% correct responses in the previous experiment. This difference probably occurred because the listeners were provided with *a priori* information about the target voice that they did not receive in the earlier experiment. The results of this monaural condition provide a performance baseline for a condition that involves only within-ear interference.

The addition of the +20 dB speech-shaped noise to the unattended ear had relatively little impact on overall performance (diamonds in Fig. 2). When the SNR in the target ear was 0 dB or higher, the noise had no effect on performance. When the SNR in the target ear was less than 0 dB, the noise produced only a slight (less than 10 percentage point) decrease in overall performance (relative to the monaural control condition). Thus it appears that even a relatively high-level contralateral noise masker produces only a small amount of across-ear interference in the two-talker target-ear segregation task.

When an interfering speech signal was added to the contralateral ear, however, performance was much worse than in the monaural control condition (open circles in Fig. 2). This reduction in performance was particularly large at negative target-ear SNR values: whereas performance in the monaural condition plateaued at negative target-ear SNR values, performance in the contralateral speech condition decreased monotonically at negative target-ear SNR values. This resulted in a net decrease in performance as large as 40 percentage points in the contralateral-speech condition when the target-ear SNR was −8 dB. When the target-ear SNR was greater than 0 dB, the contralateral speech masker produced a more modest 10 percentage point decrease in performance relative to the monaural control condition. The level of the contralateral speech signal had relatively little impact on overall performance: attenuating the masking talker in the contralateral ear by 15 dB improved performance by less than 10 percentage points across the range of SNRs tested (triangles in Fig. 2). Thus, it does not appear that the overall level of the signal in the unattended ear has much impact on the amount of across-ear interference it produces.

These results clearly show that within-ear and across-ear speech segregation are not independent processes. Listeners are extremely good at segregating a target speech signal from an interfering talker in the opposite ear. Listeners are also relatively good at segregating a target speech signal from an interfering talker in the same ear. But listeners have a great deal of difficulty segregating a target speech signal from an

interfering talker in the same ear when an interfering talker is simultaneously presented to the opposite ear.

There are at least two possible ways to view this interaction between within-ear interference and across-ear interference. One possibility is that the presence of the masking talker in the same ear as the target speech degrades the listener's ability to ignore the interfering signal in the unattended ear. The other possibility is that the presence of the masking speech signal in the unattended ear degrades the listener's ability to segregate the two talkers in the target ear. By looking at the distribution of incorrect responses in the experiment, it is possible to distinguish between these two possibilities. Figure 3 shows how the color and number responses were distributed at each target-ear SNR in the experimental condition with the 0-dB masking talker in the unattended ear. The responses are divided into four categories: (1) responses that matched the color or number in the target phrase; (2) responses that matched the color or number in the masking phrase presented in the target ear; (3) responses that matched the color or number spoken in the masking phrase presented in the unattended ear; and (4) responses that did not match any of the colors or numbers presented in the stimulus. These results show that an overwhelming majority of the incorrect responses contained color and number coordinates that were presented in the target ear. Only a small portion contained the color–number coordinates presented in the unattended ear. This result suggests that listeners' performance was degraded in the contralateral masking condition because the presence of the masking talker in the unattended ear interfered with their ability to segregate the two talkers in the target ear, and not because the presence of the masking talker in the target ear impaired their ability to ignore the signal in the unattended ear.

The distribution of errors in Fig. 3 further suggests that this inability to segregate the talkers in the target ear was due to an increase in within-ear informational masking rather than an increase in within-ear energetic masking. The vast majority of the incorrect responses included the color or number words present in the target-ear masking phrase, and almost none included a color or number that was not spoken by any of the talkers in the stimulus. This result indicates that the errors occurred because the listeners were unable to distinguish between the target and masking talkers in the target ear (informational masking), and not because they were unable to detect the acoustic elements of the two speech signals in the target ear (energetic masking). Thus it appears that the decrease in performance that occurred in the contralateral speech-masking conditions of experiment 1 occurred primarily because of a marked increase in the informational masking component of the within-ear interference in the target ear.

III. EXPERIMENT 2: THE IMPACT OF ACROSS-EAR INTERFERENCE ON ENERGETIC MASKING IN THE TARGET EAR

The results of the first experiment show that the presence of a speech signal in the unattended ear produces a substantial increase in the amount of informational masking in the two-talker within-ear segregation task in the target ear. However, because previous experiments have shown that
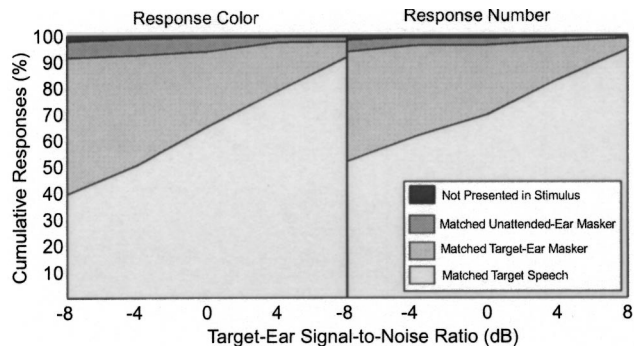

FIG. 3. Cumulative distributions of the responses in experiment 1 in the stimulus condition with two talkers in the target ear and a 0 dB masking talker in the unattended ear. The responses are divided according to their relation with the color and number words used in the target and masking phrases of the stimulus. The results are shown separately for the color responses (left panel) and the number responses (right panel) to simplify the display of data from situations where the color response and the number response did not match the same talker. See text for details.

two-talker within-ear segregation with the CRM is almost completely dominated by informational masking (Brungart, 2001b), it is difficult to determine from these results whether there is also an interaction between the presence of an interfering talker in the unattended ear and the amount of energetic masking that occurs in the target ear. In order to isolate the effects of speech in the unattended ear on the energetic portion of within-ear interference in the target ear, a second experiment was conducted in which the masking talker in the target ear was replaced by a speech-shaped noise masker.

A. Methods

The procedure used in the second experiment was the same as the procedure used in the first experiment, except that the CRM masking phrase in the right (target) ear was replaced with speech-shaped noise that was filtered to match the average long-term spectrum of all of the phrases in the CRM corpus (Brungart, 2001b). This noise was scaled relative to the rms power of the target speech to produce one of five different target-ear SNR values (-16, -12, -8, -4, or 0 dB). Only two of the five unattended-ear masking conditions in experiment 1 were reproduced in experiment 2: the monaural control condition with no signal in the unattended ear and the 0-dB contralateral speech condition with a CRM phrase in the unattended ear.

Eight paid volunteer listeners participated in the experiment, four of whom were also participants in the first experiment. Each of the listeners first participated in a total of four blocks of 120 trials: one block with the male talker and one block with the female talker in each of the two unattended-ear masking conditions. A preliminary analysis of the data from these four blocks indicated that it would be useful to collect additional data at a higher target-ear SNRs value, so each listener was asked to participate in four additional blocks of 48 trials with the target-ear SNR fixed at $+4$ dB. Thus, each of the eight listeners participated in a total of 672 trials.
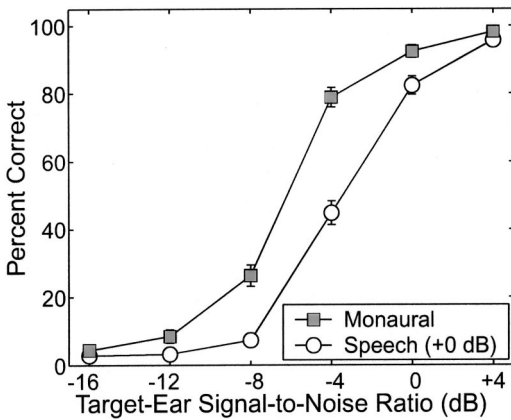
FIG. 4. Color and number identification performance in experiment 2, a dichotic listening experiment with a target talker and an interfering noise masker in the target ear and either an interfering speech signal (open circles) or no signal (filled squares) in the unattended ear. The curves are plotted as a function of SNR in the target ear. The error bars show the 95% confidence intervals for each data point (± 1.96 standard errors).

B. Results and discussion

Figure 4 shows the percentage of correct color and number identifications in experiment 2 as a function of the SNR in the target ear. In the condition with no interfering signal in the unattended ear (filled squares), the results were consistent with previous experiments that have used the CRM to measure performance as a function of SNR with a speech-shaped noise masker (Brungart, 2001a, b): identification performance was near 100% when the SNR was greater than 0 dB and dropped off rapidly as the SNR was reduced below 0 dB. When the masking speech was added to the unattended ear, overall performance decreased substantially: the performance curve was shifted to the right by roughly 2–4 dB. This result shows that the addition of a speech masker to the unattended ear produced a decrease in performance that was roughly equivalent to a 2–4-dB decrease in the SNR in that ear. Thus, it is either the case that the interfering talker in the unattended ear increased the amount of energetic masking in the target ear or that the noise in the target ear increased the amount of informational masking from the talker in the unattended ear. An analysis of the incorrect responses in the experiment provides at least partial support for the latter hypothesis. When the SNR in the target ear was −16 dB, 38% of the color responses and 25% of the number responses contained the color or number spoken by the masking talker in the unattended ear. This suggests that an increase in across-ear informational masking may have contributed to the overall decrease in performance in the contralateral-speech conditions of experiment 2. Because an interfering speech signal produces both informational and energetic masking, it is likely that energetic masking in the target ear also had some effect on the amount of informational masking caused by the contralateral speech masker in experiment 1. However, the fact that the vast majority of the incorrect responses in experiment 1 matched the color and number spoken by the masking talker in the target ear (see Fig. 3) suggests that informational masking from the interfering talker

in the target ear played a larger role than energetic masking from the interfering talker in the unattended ear in that experiment.

IV. EXPERIMENT 3: ACROSS-EAR INTERFERENCE WITH A NOISE-MASKED SPEECH SIGNAL IN THE UNATTENDED EAR

The results of the first experiment show that a speech masker in the unattended ear produces substantially more across-ear interference in the hybrid monaural-dichotic cocktail-party task than a noise masker in the unattended ear. It therefore follows that the amount of across-ear interference may be reduced when the speech signal in the unattended ear is masked by noise. Experiment 3 was conducted to examine the change in across-ear interference that occurs as noise is added to the speech signal in the unattended ear.

A. Methods

The experimental procedure was generally similar to the procedures used in experiments 1 and 2. The signal presented to the listener's right (target) ear always consisted of two simultaneous phrases from the CRM corpus: a target phrase containing the call sign "Baron," and a randomly selected masking phrase with a different call sign, color, and number than the target phrase. The rms level of the target signal was scaled relative to the masker to produce a fixed target-ear SNR value of −4 dB.[3] The signal presented to the listener's left (unattended) ear was a mixture of a randomly selected phrase from the CRM corpus and speech-shaped noise that was filtered to match the average long-term spectrum of all of the phrases in the CRM corpus (Brungart, 2001b). The contralateral speech signal was always presented at the same level as the masking speech in the target ear, and the level of the contralateral noise was adjusted relative to the speech signal to produce one of seven different SNR values in the unattended ear (−20, −12, −4, 4, 12, 20, and 28 dB). Note that this method of adding noise to a fixed-level speech masker caused the total energy in the unattended-ear stimulus to increase when the SNR in the contralateral ear decreased. When the SNR in the unattended ear was −20 dB, the combined speech and noise masker was approximately 20 dB more intense than the masking talker in the target ear (similar to the +20 dB contralateral noise condition of experiment 1). When the SNR in the unattended ear was +28 dB, the combined speech and noise masker in the unattended ear was presented at approximately the same level as the masking talker in the target ear (similar to the +0 dB contralateral speech condition of experiment 1).

The same eight listeners who participated in experiment 1 also participated in experiment 3. Each listener participated in a total of four blocks of 84 trials. Note that only the female target talker was tested in experiment 3: the target talker was always talker 5, and the masking talkers were randomly selected from the other female talkers in the corpus.
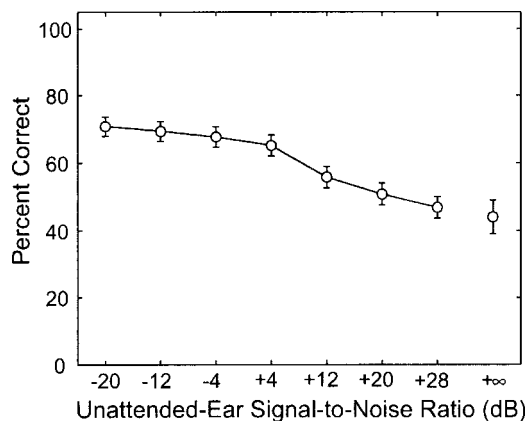
FIG. 5. Percentage of correct color and number responses in experiment 3, a dichotic listening experiment with one target talker and one masking talker in the target ear and a noise-masked speech signal in the unattended ear. The results are shown as a function of the SNR in the unattended ear; the SNR in the target ear was fixed at −4 dB. The point at +∞ shows the results from experiment 1 with a pure speech signal in the unattended ear. The error bars represent 95% confidence intervals (±1.96 standard errors).

B. Results and discussion

Figure 5 shows the percentage of correct color and number responses in experiment 3 as a function of the SNR in the unattended ear. When the SNR value was +28 dB and the signal in the unattended ear was primarily speech, performance was similar to the contralateral speech condition of experiment 1 (shown by the data point at +∞ dB); when the SNR value was −20 dB and the signal in the unattended ear was primarily noise, performance was similar to the contralateral noise masking condition of experiment 1. Between these two extremes, overall performance decreased monotonically with increasing SNR in the unattended ear. The only notable feature of this transition was the particularly steep decrease in performance between the SNR values of +4 and +12 dB.

The contralateral-ear SNR values in experiment 3 can also be used to estimate how intelligible the unattended-ear signal would be if listeners were instructed to attend to it rather than the target speech. The results from experiment 2 (Fig. 5) showed that performance with a speech-shaped noise masker in the target ear was near 100% when the target-ear SNR was +4 dB, and that it dropped to near 0% when the target-ear SNR was −12 dB. Thus all of the change in intelligibility caused by the addition of speech-shaped noise to a phrase from the CRM corpus occurs in the range of target-ear SNRs from −12 to +4 dB. In contrast, the results from experiment 3 (Fig. 5) show that less than a quarter of the 25 percentage point change in performance caused by the addition of noise to the CRM phrase in the unattended ear occurs in the range of SNRs from −12 to +4 dB. Viewed another way, the results show that a speech-shaped noise masker that had no effect on performance in experiment 2 when it was added to the CRM phrase in the target ear at an SNR of +4 dB produced a roughly 20 percentage point increase in performance in experiment 3 when it was added to the CRM phrase in the unattended ear at an SNR of +4 dB. Based on these results, it does not appear that the release from across-ear interference that occurs when the interfering speech sig-

nal in the unattended ear is masked by noise can be explained by a reduction in the intelligibility of the interfering speech. One possible alternative explanation is that the addition of noise to the unattended ear adds a distinguishing characteristic to the masking talker in that ear ("noisiness") that makes it easier to segregate from the target speech. Another possibility is that the masking noise makes the interfering talker less "speechlike" and more "noiselike" in some other dimension that causes it to produce less across-ear interference than clean speech. Either of these alternatives could help explain why even very low levels of noise in the unattended ear (at SNRs of +12 dB or more) reduced the amount of across-ear interference in the hybrid monaural-dichotic cocktail-party task.

V. EXPERIMENT 4: ACROSS-EAR INTERFERENCE WITH MULTIPLE TALKERS IN THE UNATTENDED EAR

The results of experiment 3 show that the amount of across-ear interference in the hybrid monaural-dichotic cocktail-party task can be reduced by adding noise to the speech signal in the unattended ear. As mentioned previously, one possible explanation for this result is that the noise makes the interfering speech less "speechlike" and more "noiselike," and thus easier to distinguish from the target speech. Another possible way to make a speech signal less "speechlike" and more "noiselike" is to increase the number of talkers in the signal; each additional talker fills in some of the "gaps" in the overall envelope of the signal. In the limit, a signal with an infinite number of simultaneous talkers with random onsets will be indistinguishable from speech-shaped noise (Bronkhorst and Plomp, 1992). Thus one might expect that a release from masking could be obtained by adding additional talkers to the unattended ear. A fourth experiment was conducted to test this hypothesis.

A. Methods

The experimental procedures used in experiment 4 were similar to those used in the earlier experiments. In most of the conditions, the speech signal in the right (target) ear consisted of a mixture of two CRM phrases: a target phrase containing the call sign "Baron," and a randomly selected masking phrase that was scaled to produce a target-ear SNR of either +4 or −4 dB. The signal in the unattended ear in these conditions consisted of zero, one, two, three, or four randomly selected masking phrases from the CRM corpus, each presented at the same level as the masking speech in the target ear. These conditions are denoted by TM, TM-M, TM-MM, TM-MMM, and TM-MMMM, respectively. Two additional configurations were also tested. In the TMM condition, the signal in the target ear consisted of the target phrase mixed with two randomly selected CRM masking phrases. The masking phrases were combined and then scaled relative to the target phrase to make the overall target-ear SNR −4 dB. In the T-MM condition, only the target phrase was presented to the target ear and two randomly selected masking phrases were presented to the unattended ear at the same level.

Each of these conditions was tested in two different modes. In the standard onset mode, which was also used in experiments 1–3, all of the target and masking CRM phrases started simultaneously. In the random onset mode, each of the masking phrases started at a randomly selected point (uniformly distributed over the length of the utterance), played to the end of the waveform, and then wrapped around to play from the beginning of the waveform to the randomly selected starting point. This randomization varied the temporal positions of the call signs, colors, and numbers in the masking phrases without changing the overall lengths of the utterances. The conditions with random-onset maskers are denoted in the same way as the conditions with the standard onset maskers, but the M associated with the randomized masker is replaced by an R. Thus, the TM-RR condition consisted of a target phrase and a standard-onset masking phrase in the target ear and two random-onset masking phrases in the masking ear. The eight random-onset conditions are TM-R, TM-RR, TM-RRR, TM-RRRR, T-RR, TR, TRR, and TMR.

As in the first two experiments, experiment 4 was conducted separately with two different masking talkers: one male talker (talker 0) and one female talker (talker 5). Six listeners participated in the experiment, including five who also participated in experiment 1. In the first phase of the experiment, where the target-ear SNR was always fixed at −4 dB, each listener first participated in four blocks of 120 trials (two with a male talker, two with a female talker) in each of the seven standard-onset conditions (conducted in random order). They then participated in four blocks of 120 trials in each of the eight random-onset conditions. In the second phase of the experiment, where the target-ear SNR was always fixed at +4 dB, the six listeners each participated in four blocks of 120 trials (two with a male talker, two with a female talker) in five of the 15 listening configurations tested in the first phase of the experiment (TM, TM-M, TM-R, TM-MMMM, and TM-RRRR). Thus, each listener participated in a total of 8640 trials in the two phases of experiment 4.

B. Results and discussion

The left panel of Fig. 6 shows the percentages of correct color and number identifications in the conditions from the first phase of experiment 4 with two competing talkers in the target ear and a target-ear SNR of −4 dB. When no competing talkers were present in the unattended ear (the TM condition), the listeners correctly identified the color and number in approximately 75% of the trials. When the first talker was added to the unattended ear, the percentage of correct identifications dropped to about 50%. There was not, however, any additional degradation in performance with the addition of the second, third, or fourth masking talkers in the unattended ear. Randomizing the onsets of the talkers significantly improved performance in the conditions with three or four competing talkers in the unattended ear, but performance in these random-onset conditions was still much worse than in the TM condition with no masking talker in the unattended ear. These results suggest that the amount of across-ear interference in the hybrid monaural-dichotic lis-
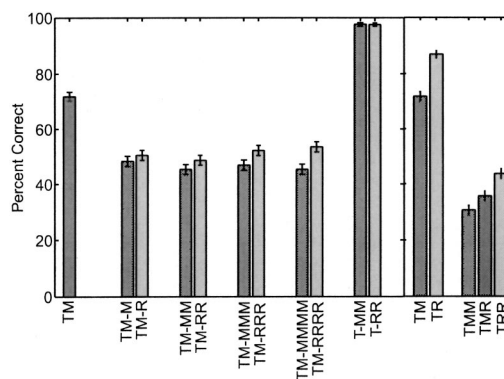

FIG. 6. Color and number identification performance in the first phase of experiment 4, a dichotic listening experiment with zero to four interfering talkers in the unattended ear, one or two interfering talkers in the target ear, and a target-ear SNR value of −4 dB. The conditions are labeled in the form TA-B, where T represents the target phrase, A represents the masking phrases in the same ear as the target phrase, and B represents the masking phrases in the unattended ear. In each case, an M stands for a standard-onset masker, and an R stands for a random-onset masker (see text for details). Note that the TM condition is plotted twice (once in the left panel and once in the right panel) to allow an easier comparison across conditions. The error bars represent 95% confidence intervals (±1.96 standard errors).

tening task is relatively insensitive to the characteristics of the speech signal in the unattended ear: the amount of interference is roughly the same with a single standard-onset CRM phrase that starts at the same time as the target phrase as it is with a four-talker random-onset signal.

The right panel of Fig. 6 shows the effects that randomizing the onsets of the masking speech signals had on the amount of within-ear interference in the monaural cocktail-party task when there were no interfering talkers in the unattended ear and the target-ear SNR was fixed at −4 dB. In the two-talker monaural listening task (TM), randomizing the onset of the masking phrase (TR) produced a 15 percentage point increase in overall performance. In the three-talker monaural listening task, performance was worst when neither interfering talker was randomized (TMM), slightly better when one interfering talker was randomized (TMR), and best when both interfering talkers were randomized (TRR). Thus it appears that onset randomization substantially reduced the amount of within-ear interference in the multi-talker listening task. This was true even in the TRR condition, where a reduction in the number of opportunities to listen to the target talker in the "gaps" of the two-talker random-onset masker should have increased the amount of energetic masking in the stimulus. The most likely explanation for this result was a release in informational masking that occurred because the color and number coordinates in the masking phrases were much less likely to overlap with the color and number coordinates in the target phrase in the random-onset conditions of the experiment.

Figure 7 compares performance in each of the five listening conditions tested in the second phase of experiment 4 where the target-ear SNR was +4 dB (right panel) to performance in the same five conditions in the first phase of experiment 4 where the target-ear SNR was fixed at −4 dB (left panel). As would be expected, overall performance was substantially better at the higher target-ear SNR value. Be-
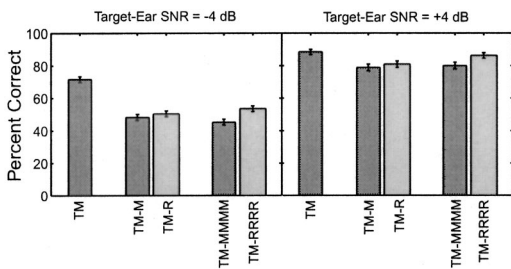
FIG. 7. Comparison of color and number identification performance in the first and second phases of experiment 4. The left panel shows performance in five of the listening configurations from the first phase of experiment 4 where the target-ear SNR was fixed at −4 dB. The right panel shows performance in the same listening configurations from the second phase of experiment 4 where the target-ear SNR was fixed at +4 dB. See text for details. The error bars represent 95% confidence intervals (±1.96 standard errors).

cause the listeners were performing well in all the conditions, the range of performance across the different listening conditions was smaller when the target-ear SNR was +4 dB than when it was −4 dB. There was, however, a significant performance improvement of approximately 7 percentage points between the TM-M and TM-RRRR conditions of the experiment ($p < 0.001$, one-tailed t-test). Thus it appears that the qualitative differences between a single-talker standard-onset masker in the unattended ear and a four-talker random-onset masker in the unattended ear led to a decrease in across-ear interference in the TM-RRRR configuration even in the relatively easy conditions where the target-ear SNR was fixed at +4 dB.

Note, however, that the results of experiment 4 do not provide much evidence to support the hypothesis that the "noiselike" contralateral signal that results from the presence of multiple interfering talkers in the unattended ear will produce less across-ear interference than a "speechlike" contralateral signal generated from a single interfering talker in the unattended ear. At both positive and negative target-ear SNRs, performance with four talkers in the unattended ear was roughly the same as performance with a single talker in the unattended ear. Thus, although there are many reasons to believe a four-talker signal is more "noiselike" than a single-talker signal, four-talker speech is much more similar to single-talker speech than it is to speech-shaped noise in terms of the amount of across-channel interference it produces in a dichotic cocktail-party listening task. It appears that substantially more than four talkers are necessary to produce a multitalker speech signal that generates the same amount of across-ear interference as speech-shaped noise.

The results of experiments 2–4 also indicate that the amount of across-ear interference in the hybrid monaural-dichotic cocktail-party task cannot be predicted from the intelligibility of the individual CRM phrases in the unattended ear. Low-level noise that had no effect on the intelligibility of the CRM phrase when it was added to the signal in the target ear in experiment 2 was found to substantially improve performance when it was added to the unattended ear in experiment 3. Increasing the number of masking talkers has been shown to substantially reduce the intelligibility of the target phrase in a monaural CRM listening task (Brungart

et al., 2001), and randomizing the onsets of the masking speech signals produced large changes in the intelligibility of the target phrase in the monaural conditions of experiment 4, but these manipulations had little or no effect on overall performance when they were applied to the masking speech signals in the unattended ear. Thus, it appears that the amount of across-ear interference that occurs in the hybrid monaural-dichotic task cannot be predicted from the intelligibility of any one of the interfering speech signals in the unattended ear. Indeed, all signals that contain at least one speech signal and are free of noise seem to produce roughly the same amount of across-ear interference in the cocktail-party listening task.

VI. EXPERIMENT 5: ACROSS-EAR INTERFERENCE WITH A TIME-REVERSED TALKER IN THE UNATTENDED EAR

The results of experiment 4 show that the amount of across-ear interference is roughly constant for a wide range of different unattended-ear speech signals. A single-talker speech signal produces the same amount of interference as a four-talker speech signal, and a random-onset speech signal produces only slightly less interference than a standard-onset speech signal. These results suggest that the amount of across-ear interference caused by a speech signal in the unattended ear has more to do with its qualitative similarity to the target speech than with its semantic similarity to the target phrase. However, it is difficult to test this hypothesis directly with the phrases of the CRM corpus, which are all semantically similar. One manipulation that is capable of removing semantic content from a speech signal without eliminating its "speechlike" characteristics is time reversal, which produces a meaningless signal with the same temporal and spectral characteristics as normal speech (Duquesnoy, 1983; Hygge et al., 1992). Experiment 5 was conducted to determine what effect time reversal has on the amount of across-ear interference caused by a speech signal in the unattended ear.

A. Methods

Experiment 5 was conducted concurrently with experiment 1 and used essentially the same methodology. That is, a target talker and masking talker were presented to the target ear, and a masking speech signal was presented in the unattended ear at the same level as the masking phrase in the target ear. The only difference was that the masking phrase in the unattended ear was played backward rather than forward. The same eight listeners who participated in experiment 1 also participated in experiment 5, and the four blocks of 120 trials collected from each listener were intermixed with the other experimental conditions collected in experiment 1.

B. Results

Figure 8 compares the results of experiment 5 to two of the experimental conditions from experiment 1: the monaural control condition with no signal in the unattended ear, and the 0-dB contralateral-speech condition with a nonreversed talker in the unattended ear. This comparison shows that the

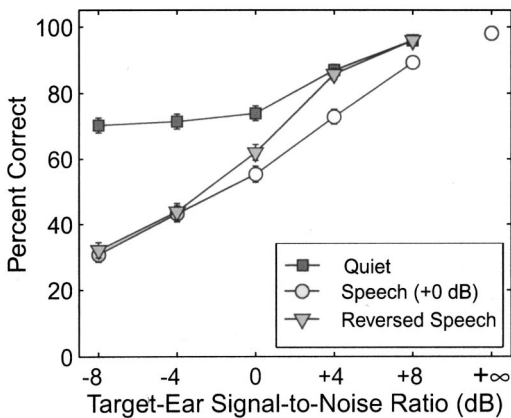D. S. Brungart and B. D. Simpson: Dichotic speech perception

FIG. 8. Color and number identification performance in experiment 5, a dichotic listening experiment with one target talker and one masking talker in the target ear and a time-reversed speech signal in the unattended ear. The triangles show data in the condition with a time-reversed speech signal in the unattended ear. For comparison, results are also shown for the conditions of experiment 1 with no signal in the unattended ear (squares) and with an unattenuated speech signal in the unattended ear (circles). The error bars show the 95% confidence intervals for each data point (± 1.96 standard errors).

amount of across-ear interference generated by the time-reversed speech in the unattended ear varied systematically with the SNR in the target ear: when the target-ear SNR was less than 0 dB, the time-reversed speech condition (triangles) was no different than the non-reversed condition from experiment 1 (circles); when the target-ear SNR was greater than 0 dB, the time-reversed condition was no different than the monaural condition of experiment 1 (squares); and when the target-ear SNR was 0 dB, performance with the time-reversed signal fell in between the other two conditions.

The strong relation between the target-ear SNR and the amount of across-ear interference caused by a time-reversed contralateral speech signal suggests that a listener's ability to ignore a masker in the contralateral ear is directly related to the difficulty of the within-ear segregation task in the target ear. At positive target-ear SNRs, where the within-ear segregation process is relatively easy, listeners may be able to take advantage of the semantic differences between forward and reversed speech in the unattended ear. At negative target-ear SNRs, where the within-ear segregation process is relatively difficult, listeners do not appear to be able to take advantage of these semantic differences.

VII. GENERAL DISCUSSION

A. Comparison with results of previous experiments

At this point, we are aware of only one previous study that has systematically examined performance in hybrid monaural-dichotic cocktail party tasks similar to the ones examined in these experiments. In a recent study on cocktail party listening, Drullman and Bronkhorst (2000) examined a total of three different hybrid configurations: a TM-M condition with a target talker in one ear and one interfering talker in each ear, a TMM-M condition with two interfering talkers in the target ear and one in the unattended ear, and a TMM-MM condition with two interfering talkers in each ear. In general, the results Drullman and Bronkhorst reported for these hybrid listening configurations were much different than the results of the experiments reported in this paper. Specifically, Drullman and Bronkhorst found no difference in performance between the hybrid monaural-dichotic listening configurations and the corresponding monaural listening configurations with the same number of masking talkers in the target ear. In other words, they found that the addition of a masking talker in the unattended ear had no effect on the listener's ability to segregate competing talkers in the target ear.

The most likely explanation for this discrepancy with our results is a difference in the vocal characteristics of the masking voices used in the cocktail-party listening tasks. In our experiments, all of the configurations were tested with same-sex target and masking talkers. In the Drullman and Bronkhorst study, the TM configuration was tested with male target and masking talkers, but the TM-M configuration was tested with a male target talker, a male masking talker in the unattended ear, and a *female* masking talker in the target ear. Thus, in evaluating the effect of a masking talker in the unattended ear, our study compared performance with a same-sex masker in the target ear to performance with same-sex talkers in both ears, while the Drullman and Bronkhorst study compared performance with a same-sex masker in the target ear to performance with a same-sex masker in the unattended ear and a *different-sex* masker in the target ear. Previous studies have shown that monaural speech segregation is substantially easier with a different-sex masker than with a same-sex masker. Brungart (2001b), for example, found performance in the monaural CRM task improved from about 60% correct identifications to approximately 85% correct identifications when a same-sex masking talker was replaced with a different-sex masking talker at a 0-dB SNR. Thus, it is likely that Drullman and Bronkhorst did not find any degradation in performance when a masking talker was added to the unattended ear because the additional interference caused by that talker was offset by the improvement in performance that occurred when the same-sex masking talker in the target ear was replaced by a different-sex masking talker. The TMM-M and TMM-MM configurations tested by Drullman and Bronkhorst do not have any direct parallels in our experiments, so it is difficult to say whether we would have encountered the same results with our CRM task. However, the poor overall level of performance in these configurations ($\approx$20% correct responses with words and near 0% correct with sentences) suggests that the amount of across-ear interference caused by adding an interfering talker to the unattended ear may be limited when more than one masking talker is present in the target ear.

B. A shared-resource model of within-ear and across-ear speech segregation

The results of these five experiments show that there are substantial interactions between the within-ear and across-ear segregation processes that occur in the hybrid monaural-dichotic cocktail-party task. Although these interactions are complicated, many of their important features are consistent with a shared-resource model of attention (Wickens, 1984, 1980; Hirst and Kalmar, 1987) where speech segregation

ability is constrained by a limited pool of shared attentional resources that listeners must choose to allocate either to within-ear speech segregation or to across-ear speech segregation. Such a model could explain the main results of these experiments simply by assuming that the shared pool contains enough attentional resources to do either across-ear segregation or within-ear segregation, but not enough resources to perform both segregation tasks at the same time. A shared-resource model could also explain why the amount of interference caused by the masking sound in the unattended ear systematically increases with the difficulty of the selective attention task in the target ear: when the segregation task in the target ear is relatively easy (i.e., when the target-ear SNR is greater than 0 dB), relatively few attentional resources are required by the within-ear segregation task and enough resources are left over to effectively segregate the target from the signal in the unattended ear; when the segregation task in the target ear is more difficult (i.e., when the listener has to concentrate on the quieter of two talkers in the target ear), fewer resources are available for across-ear segregation and listeners are more susceptible to interference from a contralateral masking sound. This would explain why the presence of a forward or reversed talker in the unattended ear had a much larger effect on performance when the target-ear SNR was negative than when the target-ear SNR was positive.

A shared-resource model of attention could also explain why some kinds of masking sounds in the unattended ear (like speech and reversed speech) cause more across-ear interference than other kinds of sounds (like noise). In general, the results of these experiments indicate that listeners are much more susceptible to across-ear interference from sounds that are qualitatively similar in some way to speech (such as reversed speech or multitalker speech) than from sounds that are qualitatively different than speech (i.e., noise). A shared-resource model could explain this effect by assuming that more resources are required for across-ear segregation for a speechlike signal and that this additional resource requirement either leaves the listener with fewer resources available for the within-ear segregation task or with insufficient resources to perform the across-ear segregation task.

Unfortunately, substantially more research is needed before this shared-resource model of attention can progress beyond the conceptual stage. One major question that still needs to be addressed is what kind of properties determine the amount of across-ear interference caused by a contralateral masking sound. Time-reversed speech and multitalker speech are qualitatively much different (and much less intelligible) than normal speech, but they appear to generate almost as much across-ear interference as a normal speech signal. However, the results of experiment 3 show that a "noisy" speech signal produces much less across-ear interference than a time-reversed speech signal even at an SNR of +4 dB, where the intelligibility of the noisy speech would be near 100%. Only when the parameters that determine the amount of interference caused by a contralateral masker are better understood will it be possible to begin developing a quantitative model of within-ear and across-ear speech segregation.

VIII. SUMMARY AND CONCLUSIONS

This series of experiments has examined the interactions that occur between within-ear speech segregation and across-ear speech segregation in a hybrid monaural-dichotic cocktail-party task. The results have shown that listeners are not generally able to perform both of these segregation tasks simultaneously: they can segregate a target speech signal that is masked by a single interfering talker in the target ear, or one that is masked by an interfering speech signal in the unattended ear, but not one that is masked by interfering speech signals in both ears at the same time. In general, the amount of across-ear interference generated by a signal in the unattended ear depends on the SNR of the two talkers in the target ear. When the target-ear SNR is positive, only a speech signal in the unattended ear seems to produce any appreciable degradation in performance. When the target-ear SNR is negative, noise signals in the unattended ear produce a slight degradation in performance, and "speechlike" signals produce a dramatic degradation in performance. This degradation occurs even when the speech signal in the unattended ear is distorted by time reversal or onset randomization. Taken together, these results suggest that within-ear segregation and across-ear segregation are closely related processes that may draw from a single shared pool of attentional resources.

In conclusion, it seems appropriate to comment briefly on the relation between the results of these experiments and those of previous experiments in auditory attention. Many experiments have replicated Cherry's original finding that listeners are able to easily segregate unrelated speech signals that are presented to different ears (Moray, 1959; Triesman, 1964; Egan *et al.*, 1954; Drullman and Bronkhorst, 2000), and some have extended this result to show that listeners can ignore more than one talker in the unattended ear (Drullman and Bronkhorst, 2000; Triesman, 1964). However, we know of no experiments that have shown that listeners are unable to ignore a speech signal in the unattended ear when more than one talker is presented in the target ear. Indeed, the only experiments that have found any effects of contralateral masking on speech perception in the target ear have used unattended ear signals that either contained key words that were highly relevant to the listener [such as the listener's name (Moray, 1959)] or were contextually related to the target speech signal [such as a speech signal that was switched between the two ears in mid sentence (Triesman, 1960)]. While one might argue that the similar call sign, color, and number structures of the CRM phrases might cause context-related across-ear intrusions in the contralateral speech conditions of experiment 1, such a context-related argument could not explain why nearly all of the incorrect responses in experiment 1 contained the color or number spoken by the interfering talker in the target ear, or why the relatively unintelligible four-talker stimuli from experiment 4 and the completely unintelligible reversed speech stimuli from experiment 5 caused nearly as much across-ear interference at negative target-ear SNRs as a single-talker speech signal.

Thus, although most of the classic models of auditory attention assume that listeners are able to extract some information from the signal in the unattended ear (Triesman, 1964; Deutsch and Deutsch, 1963), none would expect an irrelevant or unintelligible sound in the unattended ear to severely degrade a listener's ability to attend to a two-talker stimulus in the target ear. Future models of auditory attention will have to account for this result.

ACKNOWLEDGMENTS

[1]The +20 dB noise level was used because preliminary experiments showed that +0 dB noise had little effect in the unattended ear and we wanted to explore the upper limits of across-ear interference for a noise source. One concern of having such a strong contralateral noise masker is the possibility of acoustic crosstalk between the noise in the unattended ear and the signal in the target ear. In order to ensure that no crosstalk was occurring, we listened to unmasked CRM speech signals in the target ear that were as much as 50 dB quieter than the noise in the unattended ear and found that we were still able to respond correctly more than 90% of the time. Thus there did not appear to be any evidence that acoustic crosstalk was occurring with the +20 dB noise signal in the unattended ear.

[2]Because the selection was random, $\frac{1}{9}$ of the contralateral speech trials used the same masking talker in both ears. An analysis of the results revealed that these trials generated the same overall pattern of performance as the trials with different masking talkers in the two ears.

[3]The −4 dB value was chosen to ensure a reasonably large difference between performance in the contralateral-speech and contralateral-noise conditions of the experiment.

Bolia, R., Nelson, W., Ericson, M., and Simpson, B. (**2000**). "A speech corpus for multitalker communications research," J. Acoust. Soc. Am. **107**, 1065–1066.

Bregman, A. S. (**1994**). *Auditory Scene Analysis* (MIT, Cambridge).

Brokx, J., and Nooteboom, S. (**1982**). "Intonation and the perceptual separation of simultaneous voices," J. Phonetics **10**, 23–36.

Bronkhorst, A. (**2000**). "The Cocktail Party Phenomenon: A Review of Research on Speech Intelligibility in Multiple-Talker Conditions," Acustica **86**, 117–128.

Bronkhorst, A., and Plomp, R. (**1992**). "Effects of multiple speechlike maskers on binaural speech recognition in normal and impaired listening," J. Acoust. Soc. Am. **92**, 3132–3139.

Brungart, D. (**2001a**). "Evaluation of speech intelligibility with the coordinate response measure," J. Acoust. Soc. Am. **109**, 2276–2279.

Brungart, D. (**2001b**). "Informational and energetic masking effects in the perception of two simultaneous talkers," J. Acoust. Soc. Am. **109**, 1101–1109.

Brungart, D., Simpson, B., Ericson, M., and Scott, K. (**2001**). "Informational and energetic masking effects in the perception of multiple simultaneous talkers," J. Acoust. Soc. Am. **110**, 2527–2538.

Cherry, E. (**1953**). "Some experiments on the recognition of speech, with one and two ears," J. Acoust. Soc. Am. **25**, 975–979.

Conway, R. A., Cowan, N., and Bunting, M. (**2001**). "The cocktail party phenomenon revisited: The importance of working memory capacity," Psychonomic Bulletin and Review **8**, 331–335.

Darwin, C., and Hukin, R. (**2000**). "Effectiveness of spatial cues, prosody, and talker characteristics in selective attention," J. Acoust. Soc. Am. **107**, 970–977.

Deutsch, J., and Deutsch, D. (**1963**). "Attention: some theoretical considerations," Psychol. Rev. **70**, 80–90.

Drullman, R., and Bronkhorst, A. (**2000**). "Multichannel speech intelligibility and talker recognition using monaural, binaural, and three-dimensional auditory presentation," J. Acoust. Soc. Am. **107**, 2224–2235.

Duquesnoy, A. (**1983**). "Effect of a single interfering noise or speech source on the binaural sentence intelligibility of aged persons," J. Acoust. Soc. Am. **74**, 739–943.

Egan, J., Carterette, E., and Thwing, E. (**1954**). "Factors affecting multichannel listening," J. Acoust. Soc. Am. **26**, 774–782.

Ericson, M., and McKinley, R. (**1997**). "The intelligibility of multiple talkers spatially separated in noise," in *Binaural and Spatial Hearing in Real and Virtual Environments*, edited by R. H. Gilkey and T. R. Anderson (Erlbaum, Hillsdale, NJ), pp. 701–724.

Festen, J., and Plomp, R. (**1990**). "Effects of fluctuating noise and interfering speech on the speech reception threshold for impaired and normal hearing," J. Acoust. Soc. Am. **88**, 1725–1736.

Freyman, R., Balakrishnan, U., and Helfer, K. (**2001**). "Spatial release from informational masking in speech recognition," J. Acoust. Soc. Am. **109**, 2112–2122.

Freyman, R., Helfer, K., McCall, D., and Clifton, R. (**1999**). "The role of perceived spatial separation in the unmasking of speech," J. Acoust. Soc. Am. **106**, 3578–3587.

Hirst, W., and Kalmar, D. (**1987**). "Characterizing Attentional Resources," J. Exp. Psychol. Gen. **116**, 68–81.

Hygge, S., Ronnberg, J., Larsby, B., and Arlinger, S. (**1992**). "Normal-hearing and hearing-impaired subjects' ability to just follow conversation in competing speech, reversed speech, and noise backgrounds," J. Speech Hear. Res. **35**, 208–215.

Kidd, G. J., Mason, C., and Rohtla, T. (**1995**). "Binaural advantage for sound pattern identification," J. Acoust. Soc. Am. **98**, 1977–1986.

Kidd, G. J., Mason, C., Rohtla, T., and Deliwala, P. (**1998**). "Release from informational masking due to the spatial separation of sources in the identification of nonspeech auditory patterns," J. Acoust. Soc. Am. **104**, 422–431.

Moray, N. (**1959**). "Attention in dichotic listening: affective cues and the influence of instructions," Q. J. Exp. Psychol. **9**, 56–60.

Neff, D. (**1995**). "Signal properties that reduce masking by simultaneous random-frequency maskers," J. Acoust. Soc. Am. **98**, 1909–1921.

Triesman, A. (**1960**). "Contextual cues in selective listening," Q. J. Exp. Psychol. **12**, 242–248.

Triesman, A. (**1964**). "The effect of irrelevant material on the efficiency of dichotic listening," Am. J. Psychol. **77**, 533–546.

Wickens, C. D. (**1980**). "The structure of attentional processes," in *Attention and Performance VIII*, edited R. Nickerson (Erlbaum, Hillsdale, NJ), pp. 239–258.

Wickens, C. D. (**1984**). "The structure of attentional processes," in *Varieties of Attention*, edited by R. Parasuraman and D. Davies (Academic, Orlando).

Wood, N., and Cowan, N. (**1995**). "The Cocktail Party Phenomenon Revisited: Attention and Memory in the Classic Selective Listening Procedure of Cherry," J. Exp. Psychol. **124**, 243–262.

Pressure and velocity profiles in a static mechanical hemilarynx model

Fariborz Alipour[a)]
*Department of Speech Pathology and Audiology, The University of Iowa, 334 WJSHC, Iowa City,
Iowa 52242*

Ronald C. Scherer
*Department of Speech Pathology and Audiology, The University of Iowa, Iowa City, Iowa 52242
and Department of Communication Disorders, Bowling Green State University, Bowling Green, Ohio 43403*

This study examined pressure and velocity profiles in a hemilarynx mechanical model of phonation. The glottal section had parallel walls and was fabricated from hard plastic. Twelve pressure taps were created in the vocal fold surface and connected to a differential pressure transducer through a pressure switch. The glottal gap was measured with feeler gauges and the uniform glottal duct was verified by use of a laser system. Eight pressure transducers were placed in the flat wall opposite the vocal fold. Hot-wire anemometry was used to obtain velocity profiles upstream and downstream of the glottis. The results indicate that the pressure distribution on the vocal fold surface was consistent with pressure change along a parallel duct, whereas the pressures on the opposite flat wall typically were lower (by 8%–40% of the transglottal pressure just past mid-glottis). The upstream velocity profiles were symmetric regardless of the constriction shape and size. The jet flow downstream of the glottis was turbulent even for laminar upstream conditions. The front of the jet was consistently approximately 1.5 mm from the flat wall for glottal gaps of 0.4, 0.8 and 1.2 mm. The turbulence intensity also remained approximately at the same location of about 4 mm from the flat wall for the two larger gaps. © *2002 Acoustical Society of America.* [DOI: 10.1121/1.1519540]

PACS numbers: 43.70.Aj, 43.70.Bk [AL]

I. INTRODUCTION

Hemilarynx studies are providing new insights into the aerodynamics and acoustics of phonation. These studies, mostly performed on canine excised larynges, have the advantages of access to the oscillating glottis from the midsagittal plane, visual inspection of the vertical motion of vocal folds, and measurement of pressure and velocity distributions in the glottis (Jiang and Titze, 1993, 1994; Berry and Montequin, 1998; Alipour and Scherer, 2000; Alipour *et al.*, 2001). These studies were limited by the possible damage to the sensitive pressure and velocity sensors in the vicinity of vibrating tissues.

Alipour and Scherer (2000), as well as Alipour *et al.* (2001), reported dynamic pressure distributions in both the vertical and horizontal direction using a hemilarynx canine vocal fold model. The pressure taps in those studies were placed in the flat wall opposite the vocal fold. Although the dynamic (phonatory) configurations of the glottis were not reported, it may be inferred from the pressure waveforms that the pressures at the moment when the most uniform glottis would occur appeared to correspond to pressures that decreased monotonically from the subglottal region through the glottis (entrance to exit). This is consistent with the usual steady-flow notion of reduced pressure along ducts with parallel sides. However, the number of pressure taps in the flow direction was not sufficient to quantify pressure distribution

accurately, and the equality of pressures on both sides of the glottis could not be tested.

Scherer *et al.* (2001) reported detailed pressure distributions for a symmetric glottis with constant volume flows in a scaled-up model. They found that for smaller diameters the glottal pressures along the uniform (parallel walled) glottis decreased in an expected manner (due to viscous effects), but for larger glottal diameters, the pressures tended to be relatively flat (for diameters of 0.08 and 0.16 cm) or even rise from entrance to exit (0.32 cm). In addition, the pressures were slightly different on the two sides despite being geometrically symmetrical. A computational package (FLUENT) supported the empirical data for laminar glottal flow.

The aforementioned studies intended to model glottal pressures and flows for the purpose of phonation. Whether measurements were made on a full larynx or a hemilarynx, on a canine or a physical model, it is the pressure and velocity information in the laryngeal model that helps to improve our understanding of phonation and test the calculation of aerodynamic forces on the vocal folds during computer simulations of speech. Differences in pressure across the glottal duct need to be shown empirically, and velocity profiles can help to explain the relation between volume flow and duct geometry.

This report is our second study using a mechanical hemilarynx model. The first study (Alipour and Scherer, 2001) examined the mean transglottal pressure and mean volume flow for a range of glottal diameters, glottal amplitudes, and oscillation frequencies. That study suggested a
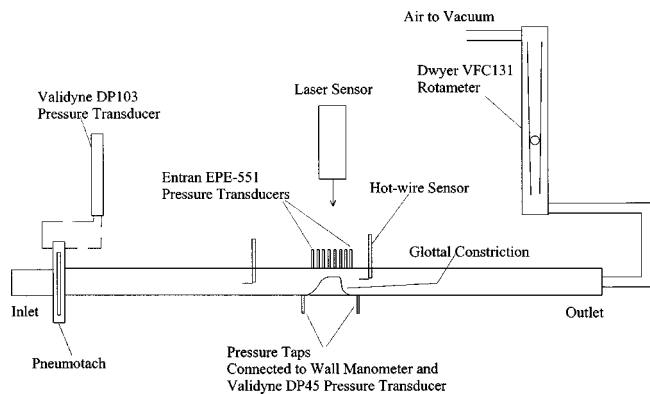
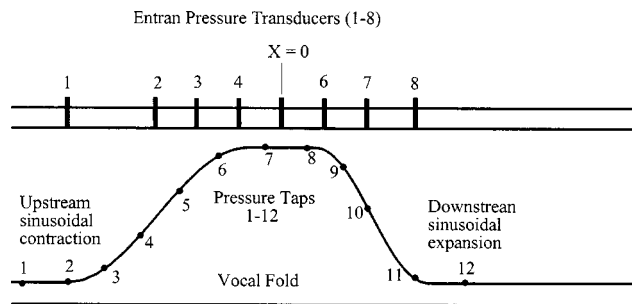FIG. 1. Schematic of the mechanical hemilarynx model and experimental setup.

FIG. 2. Schematic of the glottis with vocal fold pressure taps and pressure transducers in the flat wall. The locations of the pressure taps and transducers are approximate.

nondimensional equation interrelating those variables and concluded that flow resistance was not significantly affected by the frequency of oscillation. This study presents measured pressure distributions on the flat plate opposite the single vocal fold, as well as on the vocal fold itself. Also included are velocity profiles upstream and downstream of the glottis. The glottal diameters and flows were held constant.

The model of this study was similar to that used by Ikeda *et al.* (1994). Their model incorporated a single piston-like vocal fold (10 mm long in the flow direction) that could oscillate near a flat wall with pressure taps. The position of their six pressure taps spanned the glottis, with one pressure tap in the mid-glottal region. They reported pressures for a variety of constant glottal diameters and flows.

The purpose of this study was to quantify pressure distributions and velocity profiles in a hemilarynx mechanical model to better understand the aerodynamics of this model. Because the design of this model is a hemilarynx, the results also may help to better understand phonatory function in the hemilaryngectomized patient, provide data for validation of computational models of larynges with a single vocal fold, and give insight into asymmetric phonatory function in general.

II. METHODS

The Plexiglas model was designed with three sections, an inlet tunnel, the glottis, and an outlet tunnel (Fig. 1). The inlet section was 80 cm long and rectangular (25 mm wide, 20 mm high). Straws were placed at the entrance of the inlet section to smooth the flow. The outlet section was rectangular with the same cross section and 60 cm long. The end was connected to a flowmeter (Dwyer Model VFC131) by means of 40 cm of flexible tubing with 2.5 cm inside diameter. A vacuum source with variable speed drew the air through the model.

The vocal fold of the model (Fig. 2) was fabricated out of hard plastic and included a sinusoidal convergence from the tunnel wall up to the entrance of the glottis. The exit was also sinusoidal in shape with a steeper descent to the tunnel wall. The medial surface of the vocal fold and the opposite Plexiglas wall formed a rectangular (parallel-walled) glottal duct 8 mm long and 25 mm wide.

The glottal gap was measured with feeler gauges as the gap was adjusted to the desired values by raising the vocal fold model in its compartment. To measure the glottal angle, a laser beam shone perpendicular to the upper flat plate and reflected off the straight section of the vocal fold (using a reflective tape). The angle was then measured from the reflected spot on a screen positioned 50 cm above the vocal fold with an accuracy of better that half a degree.

The mean airflow was measured with a Rudolph 4700B pneumotach and a Validyne DP103 pressure transducer calibrated against a midrange flowmeter (Gilmont model J197) and a high range flow meter (Dwyer model VFC131). The pneumotach was placed at the entrance to the inlet tunnel (Fig. 1). A well-type manometer (Dwyer) measured the mean pressure drop across the glottis from pressure taps 30 mm upstream of the vocal fold section and 23 mm downstream of the vocal fold section. These transglottal pressure taps were located on the bottom of the channel. A Validyne DP45 pressure transducer measured the transglottal pressures.

Velocity measures were obtained by using a constant-temperature hot-wire probe (Dantec 55P14). There were two traverse locations, one 165 mm upstream of the vocal fold, and another 48.3 mm downstream of the vocal fold. The velocity profiles obtained were from the upper to lower sides of the wind tunnel, which is medial-to-lateral across the physiological flow axis. For the downstream location, therefore, the profile would show the faster velocities near the upper wall where the airflow exited the glottis, and slower velocities near the lower wall. The hot wire probe was placed no closer than 0.5 mm from either wall so as not to break the wire. The hot wire system was calibrated against a pitot tube placed over the center of an air jet exiting a 0.6 cm-diam nozzle, with accuracy of ±4% in the experimental range (Alipour *et al.*, 1995).

To measure pressures along the Plexiglas wall of the tunnel opposite the vocal fold, eight holes were made through the wall (Figs. 2 and 3). The holes were approximately 2.4 mm in diameter, ending with a smaller diameter of approximately 1.0 mm facing the glottal duct. The eight Entran EPE-551 transducers fit snugly into the pressure holes, and were positioned 1.5 to 2.5 mm away from the channel end of the holes. The distance between the centers of each pressure tap was 5.4 mm. Tap 5 was positioned at mid-glottis. Tap 4 was positioned just upstream of the rectangular section. Tap 6 was likewise placed just downstream of the

FIG. 3. Photograph of the glottis with positions of pressure taps on the vocal fold and eight pressure transducers within the flat upper wall.

rectangular section. The eight pressure transducers were calibrated together via a calibration chamber attached to a wall manometer. The chamber pressure was varied by applying flow through the chamber under high flow resistance at the end of the tunnel. The accuracy of pressure readings in the experimental range was estimated to be within 2% (the linear calibration of pressure transducers had correlation coefficients of 0.999 or better).

A Validyne DP45 pressure transducer was connected to the pressure taps of the vocal fold through a wafer-type pressure switch (Scanivalve Corp.) used to measure the pressures sequentially. Once the flow rate was stabilized, the pressure readings of the vocal fold taps were recorded on a computer using a 12-bit Dataq Instruments serial A/D device recording at 120 samples/s for 2 min (10 s per tap). The upper-wall pressure signals were recorded on another computer simultaneously using a 14-bit Dataq Instruments A/D board at 2000 samples/s for 10 s. The recorded data were later processed and averaged using MATLAB software.

The hot-wire signals were digitized with the Dataq Instruments A/D device and recorded on the computer at 10 000 samples/s for 10 s and later time-averaged. This averaging filtered out the rapid changes due to any presence of turbulence. The Reynolds number was defined as Re $=VD/\nu$, where V was the upstream channel mean velocity, D was the channel height, and ν was the air kinematic viscosity.

III. RESULTS

A. Pressure distributions

Figures 4(a)–(c) show the glottal wall pressures for three diameters, 0.4, 0.8, and 1.6 mm, respectively. The x axis represents the axial distance and the symbols represent measured pressure drops from the subglottal reference pressure. Pressures are 10-s time-averaged values of the individual pressure-tap readings. The empty symbols represent pressures on the vocal fold, and the filled symbols the pressures on the opposite flat wall.
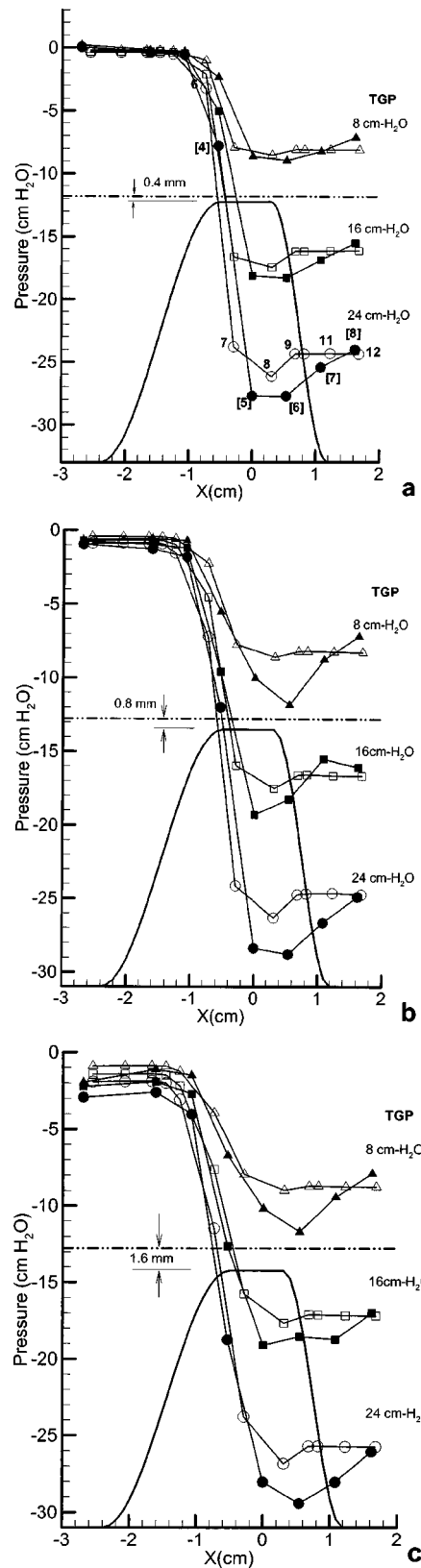
FIG. 4. Pressure distributions on the vocal fold (open symbols) and on the flat upper wall above the vocal fold (filled symbols) for glottal diameters of (a) 0.4 mm, (b) 0.8 mm, and (c) 1.6 mm. The taps are numbered relative to Fig. 2. The value of zero on the x axis represents the center of the vocal fold. For orientation, the vocal fold surface and opposite flat wall are also shown. Transglottal pressure (TGP) is the parameter (8, 16, 24 cm H_2O).

The most obvious observation is that the pressures in the glottis were consistently lower on the flat wall opposite the vocal fold than on the vocal fold itself. This held for all diameters and transglottal pressures. Across the diameters and transglottal pressures, the pressure differences in the glottis at the tap 8 location ranged from about 8%–40% of the transglottal pressure. The lower pressures on the flat wall opposite the vocal fold would be consistent with faster airflow along that wall.

Because the glottal channel forms parallel sides (the uniform case), the expected pressure change within the duct is to have the pressures fall between taps 7 and 8 due primarily to viscous pressure losses. This pressure drop was evident for all conditions on the vocal fold side. Just past tap 8 on the vocal fold side, the pressure recovered (increased) consistently to tap 9 just downstream of the glottis. This would be due to the area increase at that location. Thereafter the pressures remain essentially constant on the vocal fold due to the relatively large cross sectional areas and relatively low velocities on that side of the duct.

The pressure distributions also show a pressure recovery on the flat wall, but not immediately past the uniform glottis section; the pressure at tap 6 downstream of the mid-glottal tap shows various behaviors. For the smallest diameter, 0.4 mm, the pressures at taps 5 and 6 are approximately equal. For the 0.8- and 1.6-mm cases, the pressure varied from less than, to greater than, and then less than the center pressure as the transglottal pressure increased. One might expect, then, to see a complicated flow structure in these cases as the transglottal pressure (and Reynolds number) increases. A full-field examination of the velocities was beyond the scope of this study. The pressure rise at the next to last pressure tap on the flat wall (tap 7) typically was still less than the pressure on the vocal fold side and less than the pressure at the last tap; this would be consistent with decelerating velocities as the cross sectional area increased but with the glottal jet still remaining near the upper flat wall. There was an exception for the 0.8-mm, 16-cm H_2O condition where the pressure was greater than at the last pressure.

B. Velocity profiles

Velocity profiles were obtained 165 mm upstream of the glottis for various glottal gaps and flow rates. To investigate whether these velocity profiles are affected by the glottal gap, the peak of this velocity of the profiles was obtained for a wide range of Reynolds number and plotted in Fig. 5. This graph indicates that the velocity profiles are independent of glottal diameters. The figure also shows that there are two distinct regions that appear to correspond to two flow regimes, laminar for the lower left values, and turbulent for the upper right. The lower left curve follows the assumption of laminar flow, and the linear fit follows the assumption of turbulent flow (White, 1974). The turbulent region shows a good linear correlation between peak velocity and Reynolds number. These results suggest that the upstream flow was laminar up to a Reynolds number of about 1500, and turbulent flow was present starting at about 1600.

Figure 6 gives upstream axial velocity profiles for a glottal gap of 0.5 mm. Five transglottal pressures were used and
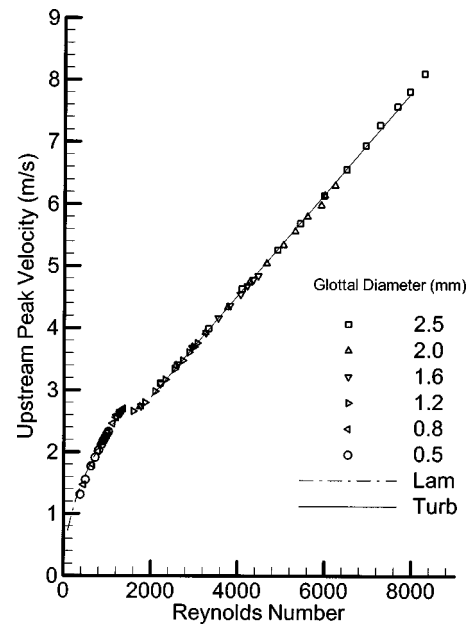
FIG. 5. Maximum velocity versus Reynolds number for flows at a location 165 mm upstream of the glottis. Two flow regimes are suggested (laminar, lower left, and turbulent, the linear portion).

the corresponding Reynolds numbers are shown in the figure. The profiles indicate time-averaged values of the velocity for 5-s intervals (50 000 samples). The symmetry of the profiles indicates that the asymmetric and eccentric (off-center) glottis was too far away to have any distortion effect on the upstream velocities. These velocity profiles are similar to those found for steady and pulsatile flow using other laryngeal models (Alipour et al., 1996, 1995).

Figure 7 illustrates the instantaneous turbulent velocities at the downstream hot-wire probe for 10 cm H_2O transglottal pressure and for the three glottal diameters of 0.4, 0.8, and 1.2 mm, respectively. Each velocity signal shows a random
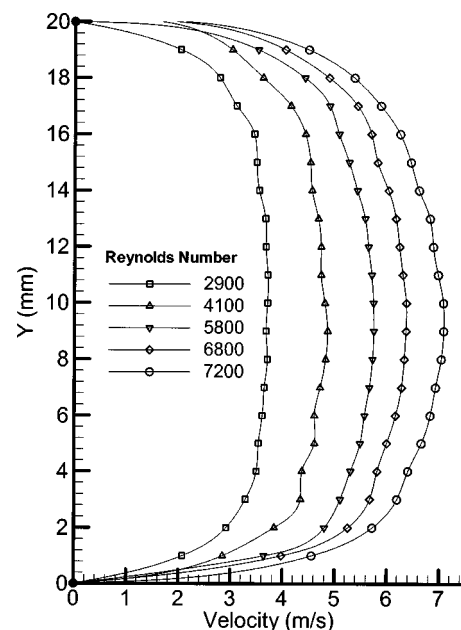
FIG. 6. Velocity profiles at a location of 165 mm upstream of the glottis for five transglottal pressures and corresponding Reynolds numbers.
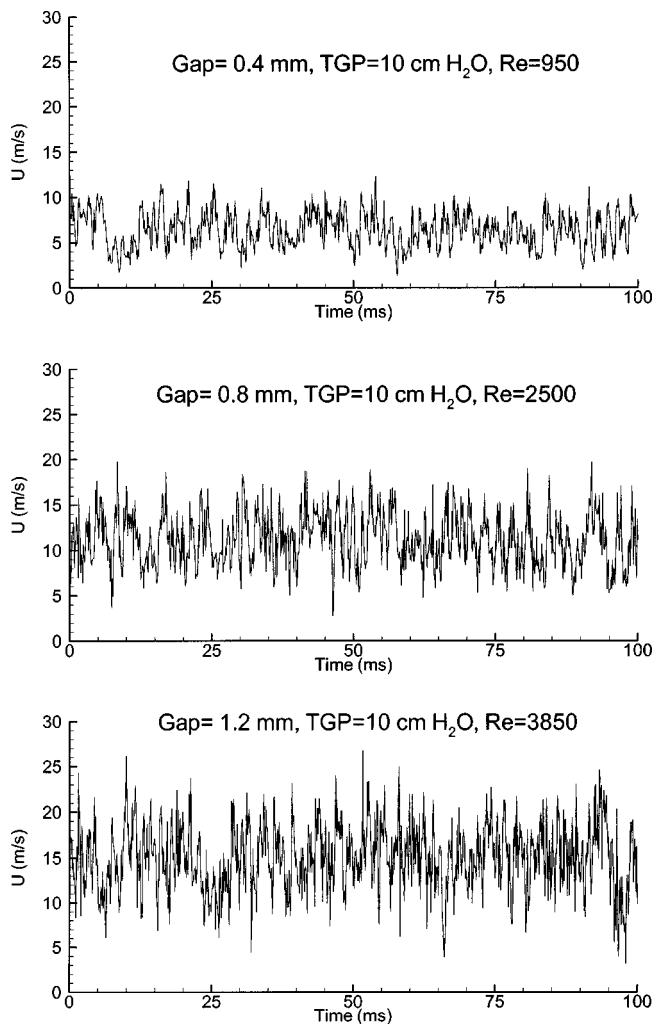
FIG. 7. Instantaneous velocities measured 48.3 mm downstream of the glottis for transglottal pressure of 10 cm H$_2$O and glottal diameters of 0.4, 0.8, and 1.2 mm.

noise (u) that fluctuates around an average velocity ($\bar{U}$). We can write an expression for the instantaneous velocity as

$$U = \bar{U} + u, \tag{1}$$

where the over bar symbol indicates the time averaging. The intensity of the turbulence is defined as the root-mean-square of the fluctuations (Hinze, 1975)

$$u' = \sqrt{\bar{u^2}}. \tag{2}$$

Thus, we need to time-average the velocity signals of Fig. 7 for a long period of time to obtain both mean velocity and turbulent intensity. Theoretically this period should be infinite. However, for practical purposes we need to choose a period that is long enough such that there is little variation in the time-averaged velocity.

Figure 8 shows the time-averaged velocities of Fig. 7 as a function of averaging time. The instantaneous velocity was averaged for the periods of 0.1 to 10 s, incremented by 0.1 s at a time. The ratios of the time-averaged velocities at the end to the previous time-averaged values were 1.0003,
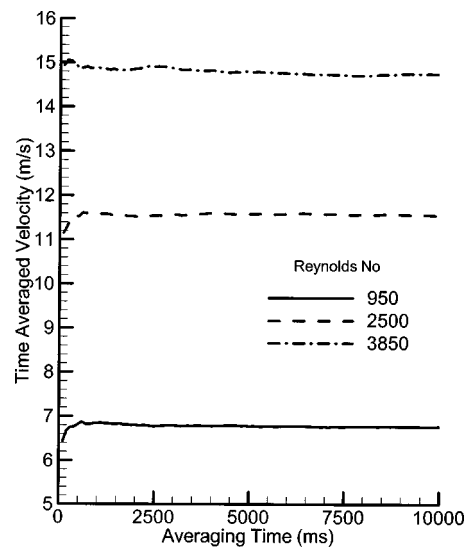
FIG. 8. Time-averaged velocities of Fig. 7 as a function of averaging time.

0.9999, and 1.0005, respectively. Thus, the 10-s averaging period appears to be sufficient for the range of Reynolds number used in this study.

Figures 9(a)–(c) show jet velocity profiles 48.3 mm downstream of the glottis for various transglottal pressures (TGP) for a glottal gap of 0.4, 0.8, and 1.2 mm, respectively. The profiles were obtained by time averaging the jet velocities for 10-s durations (sampled at 10 000 samples/s). The mean peak velocities increased as transglottal pressure increased and as the gap size increased. The peak velocities were consistently near the 18.5-mm location, despite the various gap sizes.

The absolute turbulence intensities are shown in Figs. 10(a)–(c) for the glottal gaps of 0.4, 0.8, and 1.2 mm, respectively. The turbulence intensity (also) increased as transglottal pressure and gap size increased. The location of the maximum turbulence intensity was further away from the upper flat wall than the maximum velocities (Fig. 9), becoming established at approximately 4 mm from the wall for the two larger gaps, well on the "skirt" of the velocity profiles.

IV. DISCUSSION

One convenience of the single vocal fold model presented here is that pressures were easily obtained on the flat wall opposite the vocal fold as well as on the vocal fold itself. The pressures can be obtained for a wide range of glottal diameters and airflow rates; other glottal angles than the one used here can also be incorporated. Also, the mechanical model is similar to the human larynx for a hemilaryngectomy in that there is one relatively normal vocal fold that would vibrate against a reconstructed nonvibrating opposite side (Hirano *et al.*, 1987; Leeper *et al.*, 1990).

A relatively direct application of the results of this model is in the consideration of dynamic hemilarynx models. For example, the studies using hemilarynx canine models (Jiang and Titze, 1993, 1994; Alipour and Scherer, 2000; Alipour *et al.*, 2001) measure pressures on the flat wall opposite the vibrating tissue. One might assume that the pressures on the flat wall are equal to those on the vocal fold
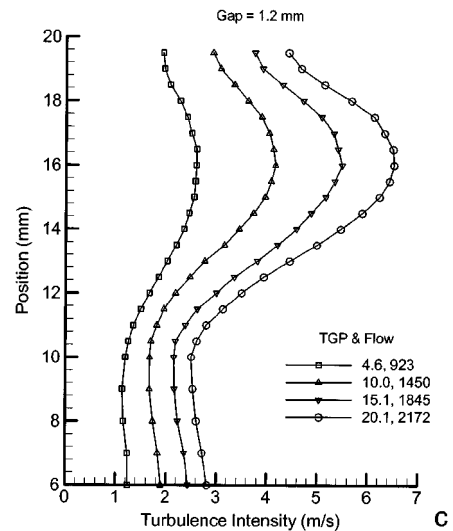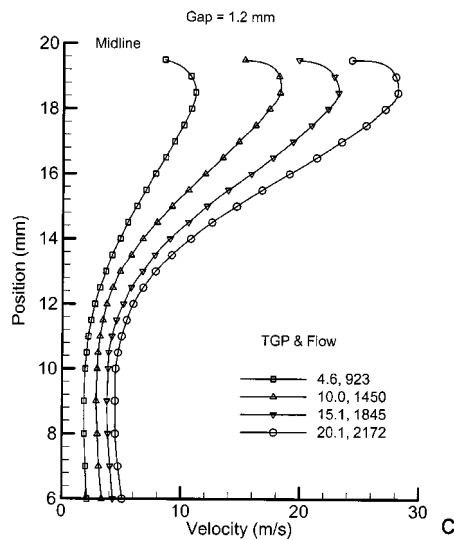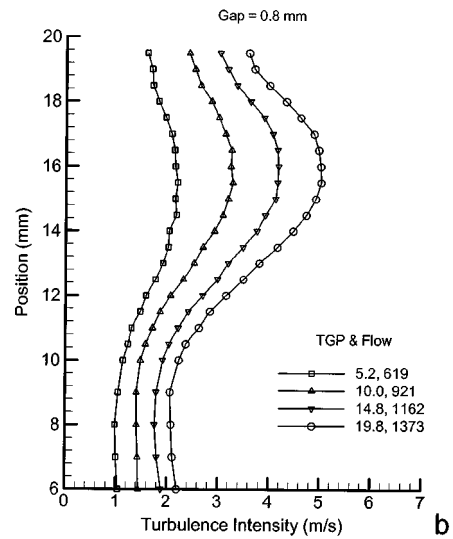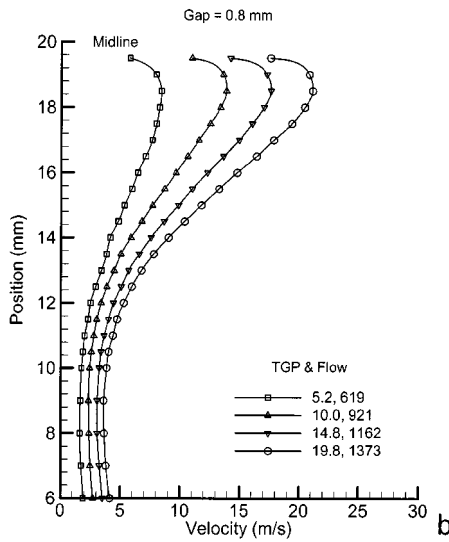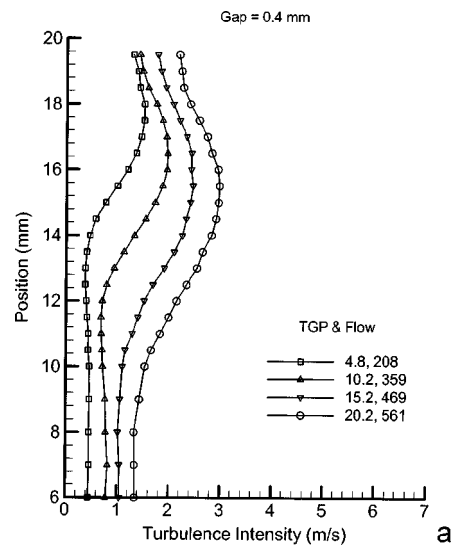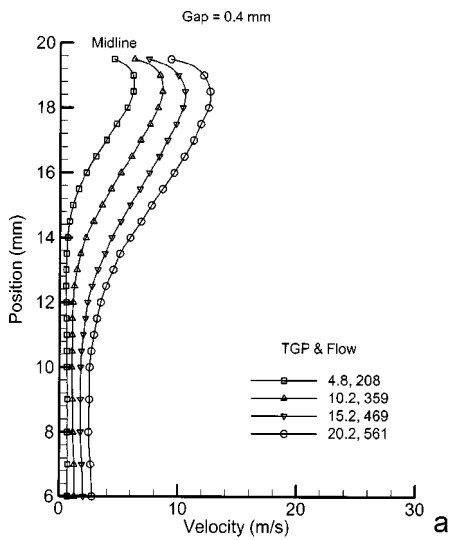
FIG. 9. Jet velocity profiles 48.3 mm downstream of the glottis, time averaged for 10 s, for various values of transglottal pressure and glottal diameters of (a) 0.4 mm, (b) 0.8 mm, and (c) 1.2 mm.

FIG. 10. Turbulence intensity obtained from the velocities measured 48.3 mm downstream of the glottis for glottal diameters of (a) 0.4 mm, (b) 0.8 mm, and (c) 1.2 mm.

surface. However, this study suggests that those pressures may differ when the oscillation creates a relatively uniform glottis, with higher pressures on the vocal fold than on the opposite wall.

A. Pressure

The pressures presented in Figs. 4(a)–(c) are graphed having negative values due to drawing the air using down-

J. Acoust. Soc. Am., Vol. 112, No. 6, December 2002

F. Alipour and R. C. Scherer: Mechanical hemilarynx   3001

stream suction. If the data were shown by letting the last pressures equal zero (atmospheric pressure), (1) the pressure values upstream of the glottis would be positive; (2) the pressures in the glottis on the vocal fold side typically would be positive for the first pressure tap near glottal entry (tap 7) and then negative for the second tap near glottal exit (tap 8), and the pressures further downstream approximately zero; and (3) the pressures on the flat wall opposite the vocal fold would be negative in the glottis (taps 5 and 6) and typically also beyond the glottis for the next pressure tap (7). These observations and the finding that the flat wall pressures were lower in the glottis suggest that (1) the pressures are lower in the glottis on the flat wall side and thus the flat wall would receive more "pull" inward than applied to the vocal fold (an asymmetric intraglottal pressure condition), and (2) there is less pressure on the flat wall side even downstream of the glottis. The negative intraglottal pressures would most likely aid in creating and sustaining phonation in the real larynx if the glottis were to take on the uniform configuration. From a surgical point of view, if these pressure findings were to hold, and the side opposite the good vocal fold were to be made flat, that side would be placed under negative air pressures, and thus the stiffness of that side would need to be taken into consideration—it also would move if not stiff enough.

B. Velocity

Figure 5, a plot of the maximum velocity of the velocity profile upstream of the glottis versus the Reynolds number of the flow, has two sections of data. The first in the lower left-hand corner has a curvilinear fit to approximately Re =1500, given approximately by $V = a(\text{Re})^{0.5}$, consistent with laminar flow. The second portion of Fig. 5 is linear and represents turbulent velocity profiles which can be approximated by an analytic equation (White, 1974), viz.,

$$\frac{u}{U_m} \approx 1 - 0.33\eta^2 - 0.67\eta^{32}, \tag{3}$$

where the term on the left side is the ratio of the local velocity (u) to the peak velocity (U_m), and η is the ratio of the distance to the centerline and the half channel height. The mean velocity normalized to the peak velocity based on this formula is about 0.8697. The peak velocity in m/s can be estimated from this formula and the Reynolds number to be

$$U_m = \frac{\text{Re}}{1160}. \tag{4}$$

The linear regression on the data of Fig. 5 provides a slope of $\frac{1}{1218}$, which is close to the analytical value of $\frac{1}{1160}$. One can therefore crudely estimate the upstream peak velocity by dividing the Reynolds number by 1000. People with a hemilaryngectomy often have higher flow rates than those with normal larynges (Hirano et al., 1987; Leeper et al., 1990; Andrews et al., 1997). Thus, for example, if the Reynolds number in the trachea reaches 3000, the peak velocity may be approximately 3 m/s, approximately ten times less than expected peak glottal velocities [see Fig. 9(c)]. These results suggest that the flow becomes turbulent in the trachea for

Reynolds numbers greater than about 2000, and the peak velocities are approximately an order of magnitude less than the glottal peak velocities.

The jet front exiting the glottis stayed within 1.5 mm of the upper flat wall at a distance of 48 mm from the glottal exit, suggesting that the peak velocities were not moving out into the airway. This is similar to the wall jet data reported by Fujisawa and Shirai (1989), in which the longitudinal jet velocity profiles were preserved for a distance of up to 150 times the jet-exit diameter. For the smallest gap of 0.4 mm, it appeared that the jet stayed close to the wall for a distance of at least 75 mm, much farther than the hot wire sensor. The maximum turbulence intensity was positioned on the skirt of the jet in a location consistent with jet behavior (Fujisawa and Shirai, 1989) at which the strong axial velocities are reduced and mixing. The jet regime is shown to be turbulent even at low Reynolds number. This creates a challenge for the CFD community whereby the inlet part of the flow should be simulated with a laminar code but the glottal jet flow with a turbulent code. Models of turbulent flow rely on the turbulence intensity distribution and the information here may help in that area.

V. CONCLUSION

It is important to explore various models of phonation to learn what each may reveal. The hemilarynx model studied here (one vocal fold and a long flat wall opposite, forming a uniform or rectangular glottis region) is one of a variety of possible hemilarynx models, and permits acquisition of static or dynamic pressures, as well as velocity profiles. In this study, static pressures, velocity profiles, and turbulence intensity were presented. The results are pertinent to the aerodynamics of phonation wherein one side of the glottis is an extended flat wall, either for bench experiments or for computational modeling. The results are also pertinent to the general area of asymmetric intraglottal pressures. Of particular importance is the challenge these results make to computational studies in which one portion of the flow field (upstream of the glottis) can have laminar flow, while simultaneously another portion (downstream of the glottis) has turbulent flow. The results of this study suggest the following:

(1) The pressures were asymmetric in the glottis for this asymmetric (hemilarynx) geometry; the pressures on the vocal fold were typically higher than on the opposite flat wall. The asymmetric pressures across the duct continued up to the last pressure tap approximately 13 mm downstream of the glottal exit.

(2) The pressures decreased along the vocal fold, consistent with viscous pressure losses in a duct with parallel sides. The pressure upstream in the glottis typically was higher than the supraglottal pressure, and the pressure downstream in the glottis was lower than the supraglottal pressure.

(3) The pressure recovery just downstream of the glottis was significant, and greater than found in other recent laryngeal models, which tend to find negligible recovery. The

F. Alipour and R. C. Scherer: Mechanical hemilarynx

continuation of the flat opposite wall as well as less abrupt area change would be consistent with this finding.

(4) The glottal jet maintained the location of the peak velocity for gaps of 0.4, 0.8, and 1.2 mm at approximately 1.5 mm from the upper flat wall, and the maximum turbulence intensity also remained at the same location (for the two larger gaps) at approximately 4 mm below the upper wall.

ACKNOWLEDGMENTS

Alipour, F., and Scherer, R. C. (**2000**). "Dynamic Glottal Pressures in an Excised Hemilarynx Model," J. Voice **14**, 443–454.

Alipour, F., and Scherer, R. C. (**2001**). "Effects of oscillation of a mechanical hemilarynx model on mean transglottal pressures and flows," J. Acoust. Soc. Am. **110**, 1562–1569.

Alipour, F., Montequin, D., and Tayama, N. (**2001**). "Aerodynamic profiles of a hemilarynx with a vocal tract," Ann. Otol. Rhinol. Laryngol. **110**, 550–555.

Alipour, F., Scherer, R. C., and Knowles, J. (**1996**). "Velocity Distributions in Glottal Models," J. Voice **10**(1), 50–58.

Alipour, F., Scherer, R. C., and Patel, V. C. (**1995**). "An Experimental Study of Pulsatile Flow in Canine Larynges," J. Fluids Eng. **117**, 577–581.

Andrews, R. J., Sercarz, J. A., Ye, M., Calcaterra, T. C., Kreiman, J., and Berke, G. S. (**1997**). "Vocal function following vertical hemilaryngectomy: comparison of four reconstruction techniques in the canine," Ann. Otol. Rhinol. Laryngol. **106**, 261–270.

Berry, D. A., and Montequin, D. W. (**1998**). "Contrasting chest and falsetto-like vibration pattern of the vocal folds," Proc. Int. Congn. Acoust. **4**, 2667–2668.

Fujisava, N., and Shirai, H. (**1989**). "Mean flow and turbulence characteristics of three-dimensional wall jet along plane surface" Trans. Jpn. Soc. Aeronaut. Space Sci. **32**(95), 35–46.

Hinze, J. O. (**1975**). *Turbulence*, Second Ed. (McGraw–Hill, New York).

Hirano, M., Kurita, S., and Matsuoka, H. (**1987**). "Vocal function following Hemilaryngectomy," Ann. Otol. Rhinol. Laryngol. **96**, 586–589.

Ikeda, T., Matsuzaki, Y., and Sasaki, T. (**1994**). "Separated flow in a channel with an oscillating constriction (Numerical analysis and experiment)," JSME (Japanese) **93**, 28–35.

Jiang, J. J., and Titze, I. R. (**1993**). "A methodological study of hemilaryngeal phonation," Laryngoscope **103**, 872–882.

Jiang, J. J., and Titze, I. R. (**1994**). "Measurement of vocal fold intraglottal pressure and impact stress-Review," J. Voice **8**, 132–144.

Leeper, H. A., Heeneman, H., and Reynolds, C. (**1990**). "Vocal function following vertical hemilaryngectomy: a preliminary investigation," J. Otolaryngol. **19**, 62–67.

Scherer, R. C., De Witt, K. J., and Kucinschi, B. R. (**2001**). "Intraglottal pressures for large glottal diameters," J. Acoust. Soc. Am. **110**, 2762(A).

White, F. M. (**1974**). *Viscous Fluid Flow* (McGraw–Hill, New York).

Quantifying the intelligibility of speech in noise for non-native talkers

Sander J. van Wijngaarden,[a] Herman J. M. Steeneken, and Tammo Houtgast
TNO Human Factors, P.O. Box 23, 3769 ZG Soesterberg, The Netherlands

The intelligibility of speech pronounced by non-native talkers is generally lower than speech pronounced by native talkers, especially under adverse conditions, such as high levels of background noise. The effect of foreign accent on speech intelligibility was investigated quantitatively through a series of experiments involving voices of 15 talkers, differing in language background, age of second-language (L2) acquisition and experience with the target language (Dutch). Overall speech intelligibility of L2 talkers in noise is predicted with a reasonable accuracy from accent ratings by native listeners, as well as from the self-ratings for proficiency of L2 talkers. For non-native speech, unlike native speech, the intelligibility of short messages (sentences) cannot be fully predicted by phoneme-based intelligibility tests. Although incorrect recognition of specific phonemes certainly occurs as a result of foreign accent, the effect of reduced phoneme recognition on the intelligibility of sentences may range from severe to virtually absent, depending on (for instance) the speech-to-noise ratio. Objective acoustic-phonetic analyses of accented speech were also carried out, but satisfactory overall predictions of speech intelligibility could not be obtained with relatively simple acoustic-phonetic measures. © *2002 Acoustical Society of America.* [DOI: 10.1121/1.1512289]

I. INTRODUCTION

The intelligibility of a speech utterance depends on many factors, among which the individual characteristics of the talker. Differences between the intelligibility of individual talkers are caused by, among other things, differences in articulatory precision (Bradlow *et al.*, 1996), speaking rate (Sommers *et al.*, 1994), and speaking style (Picheny *et al.*, 1985; Bradlow and Pisoni, 1999). A special class of talker characteristics stems from being raised in another language than the language that is being spoken. These characteristics cause listeners to perceive the speech as foreign accented; moreover, they may reduce the intelligibility of the speech.

The effect of non-nativeness on speech intelligibility sometimes complicates communication with non-native talkers significantly. Especially under adverse conditions, such as background noise and bandwidth limiting, non-native talkers tend to be less intelligible (e.g. Lane, 1963; van Wijngaarden, 2001a).

Knowing the extent to which the intelligibility of non-native talkers is reduced can be very useful. Predictions of speech intelligibility are widely used in systems design and engineering; for instance, for the design of telecommunication equipment and in room acoustics. When the influence of having a non-native talker on speech intelligibility can be quantified, design criteria can be adjusted.

Of course, having a foreign accent will not affect speech intelligibility equally for all non-native talkers. Experienced second language talkers, and talkers who started learning their second language at a relatively early age, are likely to suffer a smaller decrease in speech intelligibility (e.g., Flege

et al., 1997). By conducting speech intelligibility experiments for closely defined populations of talkers (in terms of all relevant factors, including L2 experience and age of acquisition) it should be possible to quantify intelligibility effects of non-nativeness for these populations. Preferably, one would like to be able to predict speech intelligibility effects from talker characteristics that are easily observed.

In order to properly quantify speech intelligibility effects, it is essential that out of many ''standard'' methods to measure intelligibility, a method is chosen that is suitable for quantifying effects of non-nativeness (van Wijngaarden, 2001b). In principle, segmental as well as supra-segmental influences can be expected. There has traditionally been much attention to effects found at the phoneme level. Researchers find more or less consistent patterns of phoneme confusions, largely depending on the relation between the language background of talkers and listeners (e.g., Peterson and Barney, 1952; Singh, 1966). Although the occurrence of these confusions will surely reduce the overall intelligibility, it is unclear *to what degree*. The presence of context will enable listeners to correctly interpret many nonauthentic speech sounds, despite the talker's poor production.

It seems reasonable to expect that the overall effect of non-nativeness on speech intelligibility is closely related to the degree of perceived foreign accent. Not unlike the degree of perceived accent, the overall effect on speech intelligibility results from several characteristics of non-native speech production. Without examining all of these characteristics in detail, one would expect that the degree of foreign accent would predict the effect on speech intelligibility, and vice versa. This hypothesis can be tested by examining speech intelligibility and foreign accent for talkers, differing in L2 proficiency.

[a]Electronic mail: vanWijngaarden@tm.tno.nl

TABLE I. Measures related to the foreign accent of 15 speakers of the Dutch language. The mean proficiency self-rating is the mean across four different self-ratings (speaking, listening, reading, and writing). The pairwise comparison rating is derived from an experiment in which 19 native listeners compared all combinations of the 15 talkers presented in this table, in a total of 39 sessions.

Talker	Native language	Age of first acquisition	Experience with Dutch (years)	Self-rating for speaking	Mean self-rating	Pairwise comparison rating (overall foreign accent)
DM-1	Dutch	⋯	⋯	5	5	−1.80
DM-2	Dutch	⋯	⋯	5	5	−1.61
DF-3	Dutch	⋯	⋯	5	5	−1.50
GM-4	German	23	3	4	4.25	−0.05
GM-5	German	28	0.5	2	3	1.01
GF-6	German	19	11	4	4	−1.07
EF-7	Am. English	23	6	3	3.25	0.02
EM-8	Am. English	19	28	5	4.75	−0.78
EM-9	Am. English	27	2.5	2	3.25	0.99
PM-10	Polish	24	2	3	2.5	0.65
PF-11	Polish	26	2	2	2.5	1.36
PF-12	Polish	26	1.5	2	2.5	0.72
CF-13	Chinese	20	21	4	3.5	−0.59
CF-14	Chinese	23	0.25	2	2	1.22
CF-15	Chinese	27	20	2	2	1.44

The objective of this study is to find a way to quantify the effects of a non-native talker on speech intelligibility. The relative importance of low-level (phoneme) and high-level (sentence) effects of non-native speech production on intelligibility is examined. Furthermore, the relationship between accent and speech intelligibility is investigated, hoping to establish a method to predict speech intelligibility from accent strength. The reliability of non-native talkers' self-ratings for their second language proficiency is also determined.

Under perfect listening conditions, even subjects with a strong accent can be perfectly intelligible. As communication conditions become more adverse (due to speech degrading factors such as additive noise, bandwidth limiting, or reverberation) the effects of foreign accent on speech intelligibility can be expected to increase. For this reason, the experiments in this study are all concerned with speech in the presence of *noise*. The influence of noise can be seen as representative for many speech degrading conditions.

II. DEGREE OF PERCEIVED FOREIGN ACCENT

A. Methods

Inexperienced second language (L2) talkers are often recognized as being non-native because their L2 speech production incorporates typical traits of their native language. The resulting foreign accent is usually perceived holistically, despite the fact that certain specific deviations from native speech production can be pointed out (e.g., Magen, 1998; Flege, 1984). The components that constitute a foreign accent are both segmental (such as deviations from expected voice onset times, effects of poorly developed L2 phonetic categories) and supra-segmental (less authentic intonation, unnatural pauses, effects on speaking rate). Upon being presented with non-native speech fragments of sufficient length, native listeners should be able to produce foreign accent ratings that include influences of all relevant cues.

One could reason that non-native talkers can hardly be reliable judges of their own accent. The reasons why non-native talkers exhibit a certain accent are certain limitations of their L2 speech production. These limitations may perhaps also be expected to affect (or even originate from) speech perception, rendering them "deaf" to certain aspects of their own accent.

However, this does not mean that non-native talkers' self-ratings for their second language proficiency are useless. Our main interest in the degree of foreign accent comes from the hypothesis that this may predict the extent to which speech intelligibility is affected. Proficiency self-ratings by non-native talkers may serve the same purpose, even if these talkers are not sensitive to their own accent. It seems reasonable to assume that non-native talkers are aware of their own proficiency in producing second-language speech, because of the fact that they are repeatedly confronted with the effects of their accent. Especially non-native talkers that are submerged in an L2 environment should be able to assess the strength of their own accent, if only by its apparent effect on native listeners.

1. Subjects, method for obtaining self-ratings

Speech recordings were made for a total of 15 talkers. Three of the talkers were native Dutch, the other 12 were learners of the Dutch language from four different language backgrounds (German, English, Polish, and Chinese; three talkers for each language background). The talkers also differed with respect to gender, age of acquisition, time since the first contact and average frequency of use of the Dutch language (Table I).

All talkers were asked to rate their Dutch proficiency on a five-point scale, assigning separate ratings for their oral and written skills, both passive (reading/listening) and active (speaking/writing).

All self-ratings were registered just before the start of a speech recording session. The talkers were given the oppor-

tunity to revise their self-ratings after the recording session, but none of the talkers chose to do so.

2. Method for obtaining accent ratings from pairwise comparisons

In order to obtain accurate accent ratings with a relatively limited number of native listeners, a pairwise comparison experiment was carried out. The listeners compared each voice out of the set of 15 talkers to every other voice, always indicating which of the two showed the strongest foreign accent. Computer-stored speech samples of at least 15 s in length were presented to the listeners through headphones, by means of a high-quality sound device. The listeners were allowed to repeat speech samples of the pair of talkers as often as they liked, switching back and forth between the voices as they wished. They could indicate which of the two had the strongest accent by pressing buttons on a computer keyboard.

Upon completion of the experiment by a listener, a preference matrix was compiled from the results. By adding such matrices across multiple subjects, an average preference matrix (representing the preferences of the listener group as a whole) was composed. To extract accent ratings from the preference matrix, this matrix was converted to a probability matrix and subjected to a Z-transform. By then adding all elements in each column (or row) of the matrix a rating of the subjective accent strength was obtained (Torgerson, 1958).

The sentences used in the experiment were taken from the speech reception threshold (SRT) corpus (Plomp and Mimpen, 1979), and recorded using the procedure designed for creating a multi-lingual SRT database (van Wijngaarden, 2001b). The same sentences were used for both voices in each pair.

A total of 19 native listeners participated; ten of these listeners repeated the experiment three times with different speech material. Hence, all ratings are based on 39 sets of comparisons between all talkers. All listeners were between 17 and 31 years of age, and tested for having normal hearing.

B. Results

In Table I, relevant information regarding the 15 talkers is given, together with proficiency self-ratings and accent ratings from the pairwise comparison experiment.

As can be seen in Table I, the L2 talkers differ with respect to their experience with the Dutch language. All first started learning Dutch as an adult. Hence, the experimental results obtained with these talkers apply to clearly postlingual second language learners.

One would expect a decrease of the degree of foreign accent with L2 experience. Such a relationship is already informally observed in Table I, and further established by Fig. 1, which shows the foreign accent rating by native listeners as a function of the number of years of experience with the Dutch language. Talker CF-15 takes an exceptional position. This talker reported 20 years of L2 experience, but was also the only talker to indicate a very low frequency of use of the Dutch language; she was also the only talker without written Dutch skills.
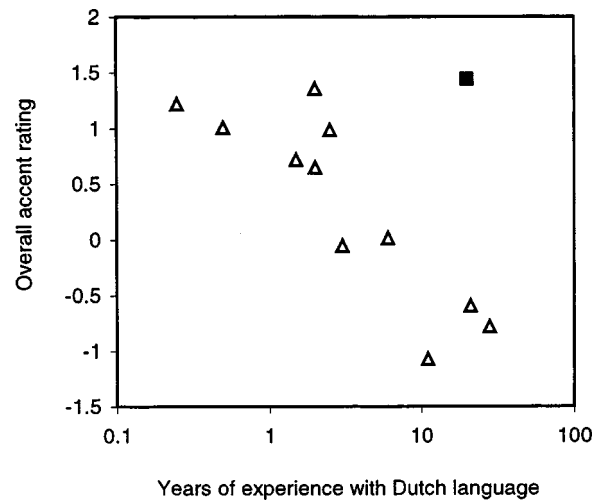
FIG. 1. Relation between foreign accent ratings and years of experience with the Dutch language, for the 12 L2 talkers. With the exception of talker CF-15 (indicated by a black square) the accent rating correlates well with the logarithm of the number of years of experience ($R^2 = 0.74$, without CF-15).

Please note the logarithmic scale in Fig. 1. The degree of foreign accent decreases with experience, but this decrease slows down as a function of time.

To investigate the correlation between self-ratings for speaking proficiency and foreign accent rating by native listeners, these measures are plotted against each other in Fig. 2.

The correlation between self-ratings and foreign accent is relatively strong; 91% of the total variance in foreign accent strength can be accounted for from self-ratings only.

We are mostly interested in the degree of foreign accent for its effect on speech intelligibility. In this light, a limitation of the accent ratings from Figs. 1 and 2 is that, since the subjects rated accent holistically, various speech characteristics may have attributed to the ratings. For example, a fluent
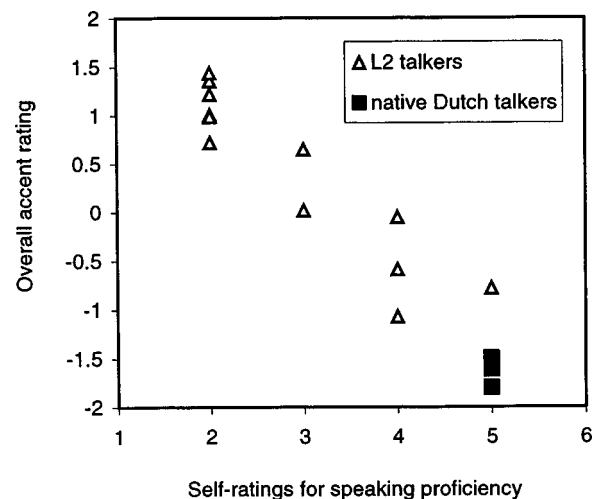
FIG. 2. Relation between self-ratings for speaking proficiency and foreign accent ratings from pairwise comparisons by native Dutch listeners ($R^2 = 0.91$).

van Wijngaarden *et al.*: Speech intelligibility for non-native speakers
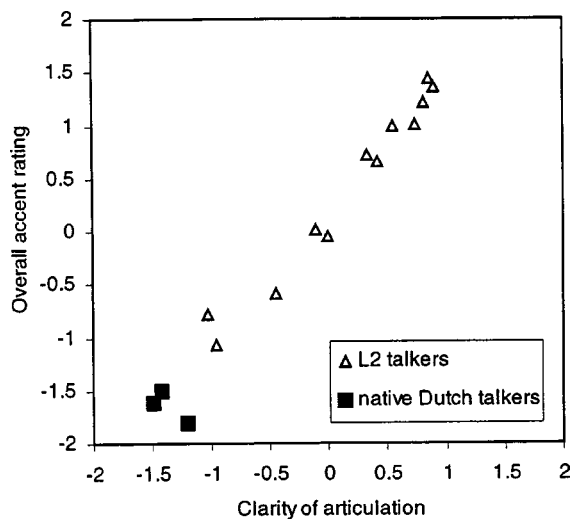
FIG. 3. Relation between pairwise comparison ratings for "clarity of articulation" and overall foreign accent ($R^2 = 0.97$).

FIG. 4. Relation between pairwise comparison ratings for "fluency" and overall foreign accent ($R^2 = 0.89$).

talker who is unable to produce certain speech sounds may be judged to have the same degree of accent as a talker with near-perfect articulation, who however speaks very dysfluently. Yet, it is reasonable to expect differences in speech intelligibility between these two talkers.

To find out if the overall accent ratings can be separated into two dimensions ("clarity of articulation" and "fluency"), the pairwise comparison experiment was repeated with ten listeners. The subjects were first exposed to all talkers and asked to give overall accent ratings. After this, they were asked on which criteria they based their decision. All ten subjects mentioned (in their own words) clarity and fluency. A short discussion about the difference between these dimensions was held to verify the subjects' proper understanding of the difference. Next, the subjects were explicitly asked to compare the pairs of talkers, based on only one of these two dimensions at a time.

The same ten listeners compared all pairs of talkers twice on both dimensions, in consecutive experiments. In the break between these two sessions, the difference between clarity and fluency was again discussed. The relation between the scores from these experiments and the overall accent ratings from the original pairwise comparison experiment is given in Figs. 3 and 4.

Clearly, the holistically perceived foreign accent is related to clarity of articulation as well as fluency. The very high correlation between the overall ratings and the ratings for clarity of articulation indicate that clarity of articulation is the most important factor for the perception of overall accent strength.

Some of the 15 talkers are relatively similar in terms of the severity of their foreign accent. The data is arranged more conveniently by grouping the talkers into categories of accent strength. The 15 talkers were divided into four categories of accent strength based on the pairwise comparison ratings. This division into categories is given in Table II.
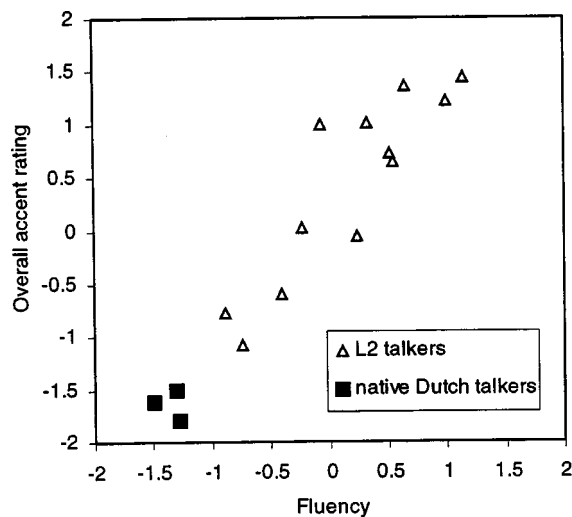
III. INTELLIGIBILITY OF SPEECH IN NOISE FOR NON-NATIVE TALKERS

A. Methods

We expect non-native speech production to be influenced by factors at segmental *and* supra-segmental level. When we wish to include all possible supra-segmental effects in our quantification of speech intelligibility, we must apply a type of speech intelligibility test that uses speech tokens consisting of multiple words. A suitable test method for this purpose is the speech reception threshold, or SRT (Plomp and Mimpen, 1979). Although developed as an audiological screening tool, the SRT method has proven to be useful for multi-lingual and cross-language speech communication research (van Wijngaarden, 2001b). Speech intelligibility can be thought of as the success that a talker and a listener have in transmitting linguistic information. By measuring the "success rate" (intelligibility) at the receiving end of the channel (the listener), the performance of the whole chain from talker to listener is measured. To evaluate the difference in intelligibility when L2 talkers are introduced, results are compared the results of baseline (L1) experiments.

A suitable method for investigating speech intelligibility at the phoneme level is the semi-open response consonant-vowel-consonant test (van Wijngaarden, 2001a).

1. Subjects

The same 15 talkers were used as in the accent rating experiment. A group of 20 Dutch university students of various disciplines (not including languages or phonetics), aged 17–26, were recruited as listeners.

2. Speech reception threshold (SRT) method

The SRT test gives a robust measure for sentence intelligibility in noise, corresponding to the speech-to-noise ratio that gives 50% correct responses for short redundant sentences.

TABLE II. Separation of talkers into four different categories of foreign accent strength, according to pairwise comparison ratings r.

Accent strength	Category I	Category II	Category III	Category IV
Accent rating r	$r \leqslant -1$	$-1 < r \leqslant 0$	$0 < r \leqslant 1$	$r > 1$
Talkers	DM-1	EM-8	EF-7	GM-5
	DM-2	CF-13	PM-10	CF-14
	DF-3	GM-4	PF-12	PF-11
	GF-6		EM-9	CF-15

In the SRT testing procedure, masking noise is added to test sentences in order to obtain speech at a known speech-to-noise ratio. The masking noise spectrum is equal to the long-term average spectrum of the test sentences. After presentation of each sentence, the subject responds by orally repeating the sentence to an experimenter. The experimenter compares the response with the actual sentence, and decides whether the response is correct.

The first sentence of each list of 13 sentences is initially presented at such a low SNR that is very likely to be unintelligible to the listener. This same sentence is repeated until it is responded correctly, the SNR going up in 4-dB steps. This is done to quickly converge to the 50% intelligibility threshold. The remaining 12 sentences are only presented once. If every word in the responded sentence is correct, the noise level for the next sentence is increased by 2 dB; after an incorrect response, the noise level is decreased by 2 dB. By taking the average speech-to-noise ratio over the last ten sentences (ignoring the first sentences of the list to eliminate initialization effects), the 50% sentence intelligibility threshold (SRT) is obtained.

3. Measuring the slope of the psychometric function for sentence recognition in noise

SRT scores characterize the psychometric function of sentence intelligibility by a single value: the SNR for which 50% sentence recognition occurs. Since sentence intelligibility as a function of SNR is known to be a steep function, the 50% point gives sufficient information for many applications. However, most speech communication in real life takes place at speech-to-noise ratios corresponding to other intelligibility levels than 50%. We would therefore like to know the full psychometric function, so that we can predict the SNR necessary to meet *any* intelligibility criterion.

By modeling the psychometric function as a cumulative normal distribution (e.g., Versfeld *et al.*, 2000), we can fully describe it with two parameters: the mean (which is the SRT) and the standard deviation (or, equivalently, the slope around the mean). These two parameters were determined by first measuring the SRT (50% point) following the standard procedure, and next measuring percentages of correct responses for SNR values 2 and 4 dB above and below the SRT value (using five sentence lists altogether). The mean and the slope of the psychometric function (in % per dB) around the 50% point were estimated by fitting a cumulative normal distribution through these points (Gauss–Newton nonlinear fit).

Before the actual SRT tests and slope measurement tests, all conditions were verified to yield 85% to 100% sentence recognition in the *absence* of noise (i.e., the psychometric function was tested for showing ceiling effects). This is a necessary requirement for the distribution-fitting procedure to yield meaningful results.

4. Semi-open response consonant-vowel-consonant method

A semi-open-response CVC (consonant-vowel-consonant) intelligibility test, specifically developed for the purpose of testing phoneme intelligibility with non-native subjects, was used for measuring speech intelligibility at the phoneme level (van Wijngaarden, 2001a). Using nonsense consonant-vowel-consonant words, the recognition of 17 initial consonants and 15 vowels was systematically measured with 16 native listeners.

Because of the time-consuming nature of the test, only the three Polish talkers (PM-10, PF-11, and PF-12) were included, as well as a single native Dutch talker (DM-2) to serve as a native baseline. To measure the effect of noise on phoneme recognition, the experiments were carried out at four speech-to-noise ratios (-9, -3, $+3$, and $+9$ dB). The masking noise used in this experiment had a long-term spectrum equal to that of speech by the tested talker.

B. Results and discussion

1. SRT scores of non-native talkers

Speech reception thresholds for each of the 12 L2 talkers, as measured with 20 native listeners, were all equal to or higher than for the three native talkers. This means that the intelligibility of the L2 talkers is, as expected, equal or lower, compared to native speakers of the Dutch language. The mean SRT score for each talker is given in Table III.

The relation between perceived foreign accent and speech intelligibility is shown in Fig. 5.

Although there is a relatively high correlation ($R^2 = 0.70$), there is some residual variance in SRT scores that cannot be explained from foreign accent strength. This is partly normal inter speaker variability, which is also ob-

TABLE III. Mean SRT scores and associated standard errors ($N = 20$).

Talker	Native language	Mean SRT	Standard error
DM-1	Dutch	-0.22	0.29
DM-2	Dutch	-1.28	0.25
DF-3	Dutch	-1.12	0.26
GM-4	German	2.5	0.39
GM-5	German	2.7	0.32
GF-6	German	-0.46	0.26
EF-7	Am. English	0.8	0.32
EM-8	Am. English	0.38	0.24
EM-9	Am. English	1.86	0.38
PM-10	Polish	1.96	0.46
PF-11	Polish	3.6	0.45
PF-12	Polish	1.9	0.41
CF-13	Chinese	0.68	0.46
CF-14	Chinese	1.9	0.46
CF-15	Chinese	0.82	0.30

3008   J. Acoust. Soc. Am., Vol. 112, No. 6, December 2002

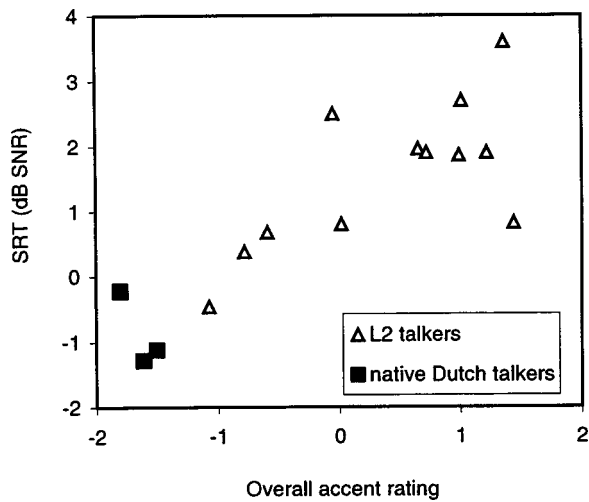van Wijngaarden *et al.*: Speech intelligibility for non-native speakers

FIG. 5. Relation between foreign accent ratings and SRT scores for speech intelligibility. Accent strength is significantly correlated with speech intelligibility ($R^2 = 0.70$).

TABLE IV. Mean (SRT) and slope of the psychometric function for sentence recognition in noise. Means and standard errors across five listeners are given.

Talker	Accent category	Native language	50%-point (dB)	s.e. 50%-point	Slope around 50% (%/dB)	s.e. slope
DM-1	I	Dutch	0.2	0.3	12.2	1.0
DM-2	I	Dutch	−1.0	0.4	13.4	1.4
DF-3	I	Dutch	−0.7	0.4	12.2	1.2
CF-13	II	Chinese	0.7	0.4	10.5	0.9
PM-10	III	Polish	1.8	0.4	8.9	0.8
PF-11	IV	Polish	3.6	1.1	8.3	1.5

Table IV shows that, as proficiency increases, the mean of the psychometric function shifts, but the curve becomes steeper as well. This is further indicated by Fig. 6, which shows the full psychometric functions according to the data in Table IV, assuming that these follow a cumulative normal distribution.

Figure 6 clearly shows that the reduction of intelligibility of non-native speech depends both on the proficiency of the talker and the speech-to-noise ratio. It is interesting to observe that the psychometric functions coincide near 0%, at a speech-to-noise ratio that is more or less the same for native and non-native talkers. Only as the speech-to-noise ratio rises, do differences between the talkers become apparent.

3. Phoneme recognition

So far, all presented speech intelligibility data was based on complete sentences. In all cases, near-perfect intelligibility of these sentences was found to occur in the absence of noise. Such good performance, despite the influence of foreign accents, is largely possible because of context effects. The recognition of individual speech sounds is much aided by word and sentence context.

A complication arises when comparing the influences of different foreign accents—the relation between the native language of the talker and the language that is spoken is likely to have an important influence on the patterns of phoneme confusions that occur. To prevent confounding of this

served for the native talkers. There is also a somewhat lower, but still significant, correlation between self-reported proficiency and SRT ($R^2 = 0.59$). This means that accent ratings from pairwise comparison experiments (Fig. 5) as well as self-ratings hold a predictive value for speech intelligibility.

When comparing Table III and Fig. 5 to similar data for non-native *listeners* instead of talkers (e.g., van Wijngaarden *et al.*, 2002), it appears that the effect of non-native speech production on intelligibility tends to be smaller than that of non-native perception. The worst-case SRT deficit for an L2 talker is around 5 dB in this experiment, compared to 7 dB for non-native listener of roughly comparable proficiency. In a within-subjects study comparing effects of L2 production versus L2 perception, perception was also found to be of greater influence (van Wijngaarden, 2001a).

2. Slope of the psychometric function for sentence reception

Because of the large number of test sentences needed per condition, the slope of the psychometric function for sentence recognition was not measured for all talkers, but only for one talker out of each category given in Table II. Since perceived accent strength and intelligibility correlate well, it can be assumed that the division into accent strength categories holds as a division in categories for intelligibility effects. The selected talkers are the ones closest to the mean of their category in terms of foreign accent rating.

An exception was made for native talkers; these were all three included, in order to be able to get an impression of the regular (native) interspeaker variability. The mean of the psychometric function and the slope around the 50%-point are given in Table IV.

Please note that the 50%-point of the psychometric function as reported in Table IV is essentially the same measure as the SRT reported in Table III, but determined with another paradigm. The correspondence between these values for the same talkers is good; the difference is smaller than 0.4 dB for any talker.
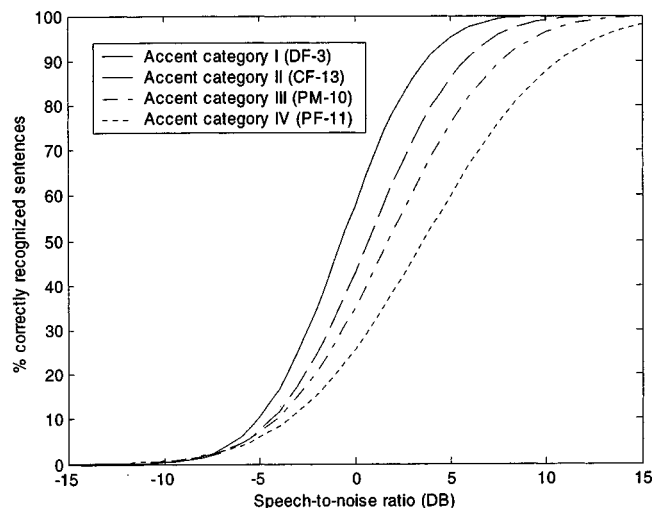

FIG. 6. Average psychometric functions for the recognition of sentences by four talkers, differing in accent strength.
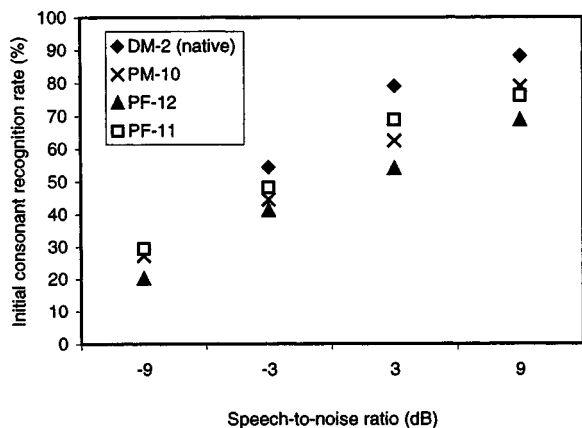
FIG. 7. Percentage of correctly recognized initial consonants in CVC words for three Polish and one Dutch talker speaking Dutch, as a function of speech-to-noise ratio (mean values across 16 native listeners; standard errors are in the range of 2–4.5 percent points).

effect with the effect of talker proficiency, only Polish talkers are compared to a (baseline) Dutch talker (see Figs. 7 and 8).

There is a clear (and statistically significant) overall effect of foreign accent on initial consonant recognition (Fig. 7), but the lowest-scoring talker is not the talker with the accent that was rated to be the strongest. At the highest speech-to-noise ratio (+9 dB), the ceiling for initial consonant recognition is not yet reached.

The recognition of individual vowels (Fig. 8) appears to be explainable by means of foreign accent strength: the stronger the perceived foreign accent, the lower the "ceiling" to which the percentage of correctly recognized vowels rises as the noise level decreases. This suggests that the L2 talkers consistently mispronounce some vowels. Since the talkers are from the same language background, one might expect that they all have difficulties pronouncing the same vowels. The Polish vowel system has eight vowels, of which six (/Iieaou/) also occur in Dutch, and are included in the CVC test. Individual realizations of these vowels differs between Dutch and Polish, depending on context; specifically, vowel duration is used differently in Dutch than in Polish. Hence, these six vowels are in practice not always the *same*
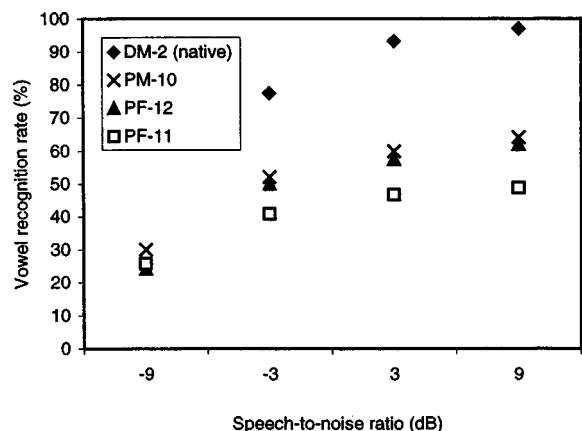

FIG. 8. Percentage of correctly recognized vowels in CVC words for three Polish and one Dutch talker speaking Dutch, as a function of speech-to-noise ratio (mean values across 16 native listeners; standard errors are in the range of 2.2–5.3 percent points).

TABLE V. Values of R^2 (explained variance) from an analysis of the correlation between specific vowel recognition errors for individual talkers. High values of R^2 indicate that the recognition errors of the 15 individual vowels follow the same patterns for each of the individual talkers. None of the correlations is statistically significant.

R^2	DM-1	PM-10	PF-12	PF-11
DM-1	⋯	0.17	0.03	0.01
PM-10	0.17	⋯	0.06	0.07
PF-12	0.03	0.06	⋯	0.01
PF-11	0.01	0.07	0.01	⋯

in both languages, but are always at least *similar*. The other nine vowels included in the Dutch CVC test (including three diphthongs) do not occur in Polish at all.

To see if the patterns of vowel confusions are consistent across talkers, the percentage of correct recognition is calculated separately for each of the 15 tested vowels. The correlation between these specific vowel recognition scores indicates whether or not the vowel confusion patterns are consistent between L2 talkers. As Table V shows, there seems to be no consistency, despite the common language background of the L2 talkers. This was also informally observed by inspecting vowel confusion matrices for the individual talkers. The lack of consistency in auditory judgments of L2 speech sounds is a known phenomenon (Leather, 1983). When testing hypotheses regarding the L2 speech learning process, this inconsistency is experienced as a practical problem. However, when quantifying the intelligibility of cross-language speech communication, it reflects the situation that occurs in practice: poorly pronounced speech sounds are less likely to be correctly heard, but what they *will* sound like to the listener is unpredictable.

The speech learning model (SLM; Flege, 1992, 1995) predicts that late L2 learners, such as the Polish talkers in our experiments, are able to master *completely new* L2 sounds to perfection, if provided with sufficient phonetic input. Speech sounds that are *similar* to sounds that occur in L1 are never completely learned; these sounds are "mapped" onto L1 categories in L2 perception and production. For our CVC experiment, this implies that we may expect different relations between overall proficiency and recognition of the nine new versus the six similar vowels. In Fig. 9, the scores for "new" and "similar" vowels are given for the different talkers.

The recognition of new vowels does not differ significantly between the L2 talkers, despite differences in proficiency and overall intelligibility. The recognition of similar vowels *does* differ between L2 talkers: the lowest-proficiency talker shows the lowest overall recognition percentage of vowels that are similar to Polish vowels. For this talker (PF-11), new vowels are recognized better than similar vowels, while for talker PF-12 the opposite is true. When regarding the proficiency difference between PF-11 and PF-12, the difference in vowel recognition patterns is as predicted from Flege's SLM (Flege, 1995).

4. Relation between phoneme and sentence intelligibility

The overall recognition of sentences (Fig. 6), although fundamentally based on phoneme recognition, follows a

3010   J. Acoust. Soc. Am., Vol. 112, No. 6, December 2002

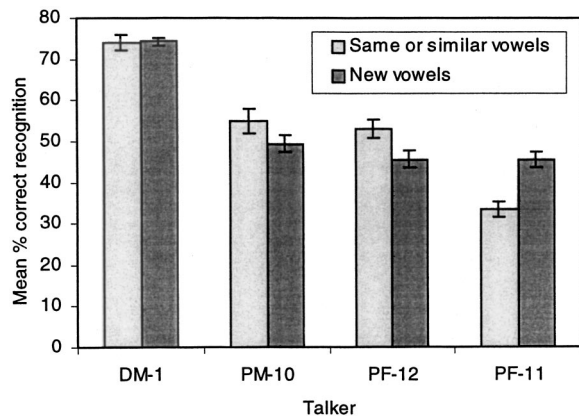van Wijngaarden *et al.*: Speech intelligibility for non-native speakers

FIG. 9. Percentage of correctly recognized vowels for two sets of vowels: Dutch vowels that are the same (or similar) in Polish, and Dutch vowels that are new to Polish learners of the Dutch language. The error bars indicate the standard error ($N = 16$; mean percentages taken per listener).
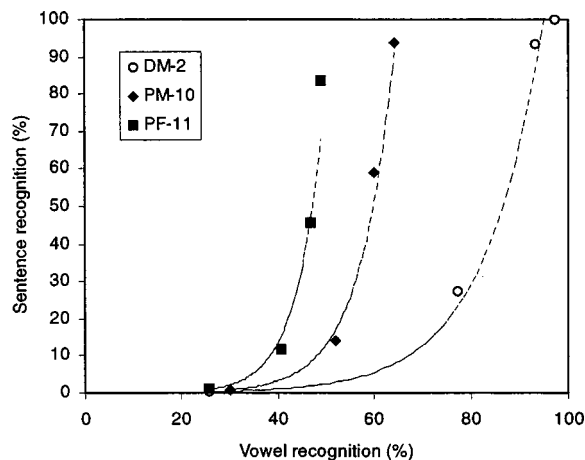

FIG. 10. Sentence recognition as a function of vowel recognition for three talkers: one native, two non-native) at four different speech-to-noise ratios (-9, -3, 3, and 9 dB). To guide the eye, and exponential curve is fit to the data of each talker.

somewhat different pattern than the recognition of individual phonemes (Figs. 7 and 8). The difference that is perhaps noted first is that ceiling effects as observed for vowel recognition appear absent from sentence recognition results.[1] When no noise is present, the sentences are sufficiently redundant to allow native listeners to make up for the faulty recognition of individual phonemes by making use of sentence context.

For native speech, when assessing speech intelligibility in rooms, or speech transmission quality of communication channels, the applied methods mostly make use of phoneme-level stimuli. Although one is invariably interested in transmission of complete messages rather than individual phonemes, there are good reasons to use a phoneme-based method. An advantage over sentence-based tests is that phoneme tests do not have such a steep transition around 50%, giving a better coverage of the range from excellent to very poor conditions. As long as a one-to-one relation between phoneme and sentence intelligibility is observed, phoneme intelligibility can be used as a predictor for the intelligibility of entire messages. Ceiling effects do, in this case, occur for vowels (Fig. 8), and perhaps also for consonants. This means that this condition is apparently not always met for non-native speech; hence, phoneme-based results can not always be relied upon as a predictor for the intelligibility of messages. This is further illustrated by Fig. 10, which combines data from Figs. 6 and 8.

Because of the ceiling effects in the vowel recognition scores, the (nearly) one-to-one relation between sentence and vowel intelligibility observed for the native talker is not realized for the non-native talkers. This does not mean that the intelligibility of non-native speech can *never* be predicted from phoneme level results. In this case, for instance, initial consonant recognition can be used to predict sentence intelligibility much better than vowel recognition. However, the current results indicate that phoneme-based measures that are known to predict sentence intelligibility in native speech require validation before applying those measures to non-native speech.

IV. RELATION BETWEEN SPEECH INTELLIGIBILITY AND ACOUSTIC-PHONETIC MEASURES

A. Global acoustic measures

The effects of specific talker-related influences on speech intelligibility are clearly present in the speech signal, since these are related to the source of this speech: the non-native talker. It is thus conceivable that an acoustic-phonetic analysis of foreign accented speech could yield objective predictions of the effect of foreign accent on intelligibility. The potentials of having such objective predictions, if sufficiently reliable, are great. Instead of needing a talker's self-ratings for foreign accent, or some other measure that may be difficult to obtain, intelligibility can then be predicted from physical measurements. Within the scope of this article, only relatively simple acoustic-phonetic measures were considered, because methods that are complex or require great annotation effort will probably have limited applicability.

Bradlow *et al.* (1996) distinguish "global" and "fine-grained" talker characteristics in predicting the influence of acoustic talker characteristics on speech intelligibility. Typical global characteristics are measures related to pitch and speaking rate; typical fine-grained characteristics include phoneme categorization and segmental timing relations.

To investigate the relation between speaking rate and intelligibility for non-native talkers, the results from the SRT experiments (Table III) were used. The SRT sentence recordings had been paced by means of a visual time indicator, allowing the talkers up to a maximum of 2.6 s for each SRT sentence. The talkers had been instructed to maintain a constant speaking rate across all sentences, trying to use as much of the 2.6-s "recording window" as possible. Despite the use of this pacing method, small (and in some cases statistically significant) differences in talking rate were observed between talkers (0.40–0.65 sentences per second). An analysis of the relation between talking rate and SRT revealed, however, no significant correlations. Mean $F0$ and $F0$ range (mean difference between highest and lowest $F0$ in a sentence) were found to vary across talkers, to the same degree for native as well as non-native talkers. The latter indicates

TABLE VI. Percentage of vowels (ten vowels, three realizations each) correctly classified according to the vowel regions by Pols *et al.* (1973).

Talker	Accent category	Correctly classified (%)
DM-1 (native)	I	83.3
DM-2 (native)	I	86.7
GM-4	II	60.0
EM-8	II	70.0
EM-9	III	63.3
PM-10	III	63.3
GM-5	IV	73.3

that pitch variations are applied by native *and* non-native talkers. However, $F0$ and $F0$ range did not correlate significantly with SRT or CVC results, meaning that these measures can not be used as predictors of speech intelligibility.

B. Fine-grained acoustic measures

A more fine-grained talker characteristic that is known, at least for native talkers, to correlate with speech intelligibility, is vowel space size (e.g., Bradlow *et al.*, 1996). Larger vowel spaces tend to lead to more intelligible speech in native talkers.

Of each of the 15 talkers, mid-vowel formant frequencies were calculated for 3 stressed instances of 11 different Dutch vowels. First, the overall variance in $F1$ and $F2$, for all 33 vowels of each talker, was considered, as a broad estimate of vowel space size. This variance did not correlate with SRT results ($R^2 = 0.03$, across 15 talkers), nor with CVC vowel recognition scores ($R^2 = 0.07$, across 4 talkers). This means that the size of the vowel space does not predict intelligibility differences between non-native talkers.

The ratio between within-vowel variance and overall variance was also determined. In this way, essentially by comparing the statistical spread of different instances of the same vowel to the spread of *all* vowels, a coarse indication of "discriminability" in the $F1$-$F2$ plane is obtained. However, this variance ratio does not correlate significantly with non-native CVC or SRT results either.

For non-native talkers, one could expect the decreased intelligibility to result from a distorted rather than just a reduced vowel space. Distortion, in this context, is not as easy to measure as reduction, since it requires a priori knowledge of how the vowel space should be organized to be perceptually acceptable. Such a priori knowledge can in some cases be taken from vowel space studies, such as reported by Pols *et al.* (1973) for Dutch vowels of 50 male talkers. Pols *et al.* defined vowel categories in the $F1$-$F2$ plane as maximum-likelihood regions, indicating clear borders between categories. The same $F1$-$F2$ data as used for calculation of the variance ratios was applied to determine which percentage of the vowels are correctly categorized according to the regions by Pols *et al.* (only for the male talkers). The results are given in Table VI.

The scores for the two male native talkers are higher than for the non-native talkers. The mean percentages of correct classification per vowel, for all of the talkers in Table VI,

were subjected to a two-way ANOVA (the two factors being native/non-native and vowel category). A significant ($P < 0.01$) main effect of native versus non-native was found. The percentage correct classification was also found to correlate significantly with accent ratings ($R^2 = 0.57$) and SRT ($R^2 = 0.67$). This means that of the acoustic-phonetic measures that were considered in this study, this is the only one that was found capable of predicting intelligibility effects of non-native speech. Unfortunately, it is also the measure that is the most difficult to obtain. It requires detailed and reliable a priori knowledge of the native $F1$-$F2$ plane, and hand-labeling of suitable stressed vowels for each talker.

V. GENERAL DISCUSSION AND CONCLUSIONS

Foreign accented speech tends to be less intelligible than native speech. The results presented in this article confirm that L2 experience is an important determining factor for the intelligibility of a non-native talker.

The overall effect on speech intelligibility is proportional to the degree of foreign accent ($R^2 = 0.70$). Hence, by estimating the severity of a talker's accent, a first impression of the intelligibility effects is obtained. Moreover, a talker's own opinion of his L2 proficiency can also be used as a predictor of speech intelligibility ($R^2 = 0.59$).

For non-native speech, the recognition of individual phonemes may sometimes be impaired even in the absence of noise. In the case of the Polish subjects who participated in this study, this was found to be the case for a large fraction of the Dutch vowels. Nevertheless, sentence intelligibility could still reach 100%. This shows the powerful effect of contextual information in human speech recognition. The practical implication for quantifying the overall effects of foreign accent on speech intelligibility is that sentence-based methods seem to be more suitable than phoneme-level methods. Before using any phoneme-level test result to predict the intelligibility of non-native speech, the existence of a reversible one-to-one relation needs to be established.

Objective phonetic-acoustic measurements are not easily applied to predict effects of foreign accent on intelligibility. Of several global and fine-grained acoustic phonetic measures, the only one found to correlate significantly with intelligibility was a measure that quantifies the deviations between a talker's own (non-native) vowel realizations to the native $F1$-$F2$ plane. However, this measure is not particularly suitable for intelligibility predictions. The fact that the process of obtaining this measure is laborious, and requires detailed knowledge of the native $F1$-$F2$ plane, was already mentioned. Moreover, the measure is only concerned with vowels. The relation between vowel recognition and sentence intelligibility was shown *not* to be a one-to-one relation for non-native speech; any measure related to vowel space should be expected to suffer the same limitations.

As a final note, it is important to realize that all experiments described in this article were concerned with the intelligibility of *recorded* non-native speech. In real conversations, non-native talkers have the ability to respond to listeners' apparent comprehension of their speech. They are also less likely to use words or grammatical constructions

they are not familiar with, which may very well lead to a better overall speech intelligibility.

ACKNOWLEDGMENTS

[1]One could argue that the psychometric functions of Fig. 6 are the result of modeling the psychometric function as a cumulative normal distribution, and will therefore always go up to 100%. However, the individual responses on which the calculation of the psychometric function is based show that saturation at 100% (or very close to 100%) is in fact observed for native as well as non-native speech.

Bradlow, A. R., and Pisoni, D. B. (**1999**). ''Recognition of spoken words by native and non-native listeners: talker-, listener- and item-related factors,'' J. Acoust. Soc. Am. **106**, 2074–2085.

Bradlow, A. R., Toretta, G. M., and Pisoni, D. B. (**1996**). ''Intelligibility of normal speech I: Global and fine-grained acoustic-phonetic talker characteristics,'' Speech Commun. **20**, 255–272.

Flege, J. E. (**1984**). ''The detection of French accent by American listeners,'' J. Acoust. Soc. Am. **76**, 692–707.

Flege, J. E. (**1992**). ''The intelligibility of English vowels spoken by British and Dutch talkers,'' in *Intelligibility in Speech Disorders*, edited by R. D. Kent (Benjamins, Amsterdam).

Flege, J. E. (**1995**). ''Second-language speech learning: theory, findings, and problems,'' in *Speech Perception and Linguistic Experience*, edited by W. Strange (York, Baltimore).

Flege, J. E., Bohn, O-S., and Jang, S. (**1997**). ''Effects of experience on non-native speakers' production and perception of English vowels,'' J. Phonetics **25**, 437–470.

Lane, H. (**1963**). ''Foreign accent and speech distortion,'' J. Acoust. Soc. Am. **35**, 451–453.

Leather, J. (**1983**). ''Second-language pronunciation learning and teaching,'' Language Teach. **16**, 198–219.

Magen, H. S. (**1998**). ''The perception of foreign accented speech,'' J. Phonetics **26**, 381–400.

Peterson, G. E., and Barney, H. L. (**1952**). ''Control methods used in a study of the vowels,'' J. Acoust. Soc. Am. **24**, 175–184.

Picheny, M. A., Durlach, N. I., and Braida, L. D. (**1985**). ''Speaking clearly for the hard of hearing I: Intelligibility differences between clear and conversational speech,'' J. Speech Hear. Res. **28**, 96–103.

Plomp, R., and Mimpen, A. M. (**1979**). ''Improving the reliability of testing the speech reception threshold for sentences,'' Audiology **18**, 43–52.

Pols, L. C. W., Tromp, H. C. R., and Plomp, R. (**1973**). ''Frequency analysis of Dutch vowels from 50 male speakers,'' J. Acoust. Soc. Am. **53**, 1093–1101.

Singh, S. (**1966**). ''Crosslanguage study of perceptual confusion of plosive phonemes in two conditions of distortion,'' J. Acoust. Soc. Am. **40**, 635–656.

Sommers, M. S., Nygaard, L. C., and Pisoni, D. B. (**1994**). ''Stimulus variability and spoken word recognition. I. Effects of variability in speaking rate and overall amplitude,'' J. Acoust. Soc. Am. **96**, 1314–1324.

Torgerson, W. S. (**1958**). *Theory and Methods of Scaling* (Wiley, New York).

van Wijngaarden, S. J. (**2001a**). ''The intelligibility of Non-native Dutch speech,'' Speech Commun. **35**, 103–113.

van Wijngaarden, S. J. (**2001b**). ''Methods and models for the assessment of cross-language speech intelligibility,'' Workshop on Multi-lingual Speech and Language Processing, Aalborg, Denmark, 8 September.

van Wijngaarden, S. J., Steeneken, H. J. M., and Houtgast, T. (**2002**). ''Quantifying the intelligibility of speech in noise for non-native listeners,'' J. Acoust. Soc. Am. **111**, 1906–1916.

Versfeld, N. J., Daalder, J., Festen, J. M., and Houtgast, T. (**2000**). ''Method for the selection of sentence materials for efficient measurement of the speech reception threshold,'' J. Acoust. Soc. Am. **107**, 1671–1684.

Direct magnitude estimation and interval scaling of pleasantness and severity in dysphonic and normal speakers

Tanya L. Eadie[a) and Philip C. Doyle
Voice Production and Perception Laboratory, School of Communication Sciences and Disorders, Elborn College, University of Western Ontario, London, Ontario N6G 1H1, Canada

The purpose of this study was to determine the validity of voice pleasantness and overall voice severity ratings of dysphonic and normal speakers using direct magnitude estimation (DME) and equal-appearing interval (EAI) auditory-perceptual scaling procedures. Twelve naive listeners perceptually evaluated voice pleasantness and severity from connected speech samples produced by 24 adult dysphonic speakers and 6 normal adult speakers. A statistical comparison of the two auditory-perceptual scales yielded a linear relationship representative of a metathetic continuum for voice pleasantness. A statistical relationship that is consistent with a prothetic continuum was revealed for ratings of voice severity. These data provide support for the use of either DME or EAI scales when making auditory-perceptual judgments of pleasantness, but only DME scales when judging overall voice severity for dysphonic speakers. These results suggest further psychophysical study of perceptual dimensions of voice and speech must be undertaken in order to avoid the inappropriate and invalid use of EAI scales used in the auditory-perceptual evaluation of the normal and dysphonic voice. © *2002 Acoustical Society of America.* [DOI: 10.1121/1.1518983]

I. INTRODUCTION

In recent years, the use of auditory-perceptual judgments of speech and voice has been shown to provide a means of classifying and describing a variety of communication disorders (Metz, Schiavetti, and Sacco, 1990; Southwood and Weismer, 1993). Further, auditory-perceptual methods may assist in evaluating the outcome of a given intervention program. In some instances, such judgments may represent the final validation in clinical decision making, as well as providing a standard against which other so-called "objective" methods are evaluated for many speech and voice disorders (Kent, 1996). Although auditory-perceptual methods carry advantages of "...convenience, economy, and robustness" (Kent, 1996, p. 7), potential sources of listener error and bias such as a common understanding of perceptual labels, consistent use of descriptors and associated scale values, and concerns pertaining to intra- and inter-rater reliability (Kearns and Simmons, 1988), etc., must also be considered. Because of these concerns, auditory-perceptual methods represent one approach to providing valid measurement of attributes inherent to a given voice and speech disorder (see Kent, 1996). Yet, several concerns about the validity of traditional protocols for rating vocal quality have been raised in the literature (Gerratt and Kreiman, 2001; Kreiman and Gerratt, 2000; Kreiman and Gerratt, 1998; Kreiman and Gerratt, 1996).

Specifically, Kreiman and Gerratt (2000) have suggested that difficulties arise when listeners are asked to discriminate single perceptual dimensions of complex stimuli. For example, listeners have difficulty agreeing not only on the *kind* of voice quality (e.g., breathiness, roughness) (Gelfer, 1988; Kreiman and Gerratt, 1998; Kreiman, Gerratt, and Berke, 1994), but also on *how much* of that dimension is present in a given voice. This led Gerratt and Kreiman (2001) to pursue preliminary investigation into the use of an alternative method of measuring voice quality, one that was designed to control for sources of measurement error. In their study, Gerratt and Kreiman varied speech synthesis parameters to create an auditory match to a natural voice stimulus. In this case, listeners were able to vary the signal-to-noise ratio (SNR) because it had previously been found to be important in describing voice quality (e.g., Hirano *et al.*, 1988; Klingholz, 1990; Qi, Hillman, and Milstein, 1999). These researchers found that listener agreement was significantly greater for the synthesis task than for a traditional rating task. Their findings also indicate that listeners do in fact agree in their perceptual assessments of pathological voice quality, and that tools can be devised to reliably measure perceptual judgments.

Despite the promise of the new technique evaluated by Gerratt and Kreiman (analysis-by-synthesis), traditional rating procedures including the use of visual analog (VA), equal-appearing interval (EAI), and direct magnitude estimation (DME) scales remain popular today (Gerratt *et al.*, 1991). An alternative source of voice quality measurement error and subsequent difficulties in listener reliability includes the improper use of these rating scales (i.e., VA, EAI, DME). As such, the validity of measuring specific perceptual dimensions or attributes using such traditional scales needs further investigation. The current work sought to further clarify the source of error of listener disagreement by identifying the improper use of rating scales for particular dimensions. Therefore, the purpose of the present investigation fo-

a)Electronic mail: teadie@uwo.ca

cused on empirical investigation of the construct validity related to use of EAI and DME scales for measuring auditory-perceptual dimensions of voice quality.

A. Common approaches to the measurement of voice quality

Despite a long history, the DME procedure (Stevens, 1975) was not used for voice judgments until relatively recently (Toner and Emanuel, 1989; Whitehill, Lee, and Chun, 2002; Zraick and Liss, 2000). One type of DME scale allows listeners to make perceptual judgments relative to a "standard" that represents the approximate midpoint of any given perceptual continuum (Schiavetti, 1984). This standard, termed a modulus, is usually given an arbitrary value of "100." For example, in an auditory-perceptual task, listeners are asked to rate a specific perceptual attribute (e.g., roughness, breathiness) for the voice/speech samples from a given population (e.g., individuals with dysphonia, dysarthria, etc.). With DME, samples are judged relative to the modulus and a numerical rating is given. Hence, this rating represents the relative magnitude of the perceptual attribute in question. Individual samples with voice or speech attributes perceived as twice as good when compared to the modulus are assigned a value of "200;" samples with an attribute perceived as half as good relative to the modulus are assigned a value of "50." As such, the endpoints of the DME continua are unspecified since perceptual phenomena are scaled relative to the modulus and its assigned value.

In contrast, EAI scales require listeners to provide perceptual ratings based on a fixed, predefined scale suggestive of implied "equality" in perceptual distance, weight, or magnitude between numeric components. In the voice and speech literature, most EAI scales are 7 points (1–7), plus or minus 2 points (i.e., 5 pt-EAI or 9 pt-EAI scales) (Kreiman *et al.*, 1993). For example, when using a 7-pt EAI scale, "1" may represent one end of the scale (e.g., normal) and "7" may represent the other extreme (e.g., severely impaired). Unlike DME scales, the endpoints for EAI scales are fixed and scaling is performed using whole numbers (i.e., any whole number between "1" and "*n*").

Stevens (1975) suggested that there are two types of perceptual continua that can be scaled: *prothetic* and *metathetic*. A prothetic continuum is additive, and *quantitative* in nature. It is best scaled with DME because observers cannot subdivide a prothetic continuum into equal intervals. The prototypical example of a prothetic continuum is loudness. In contrast, a metathetic continuum is a substitutive, *qualitative* continuum that can be scaled with either DME or EAI scaling procedures. Pitch best exemplifies a metathetic continuum. Stevens (1975) outlined a method for determining whether a given dimension falls along a metathetic or prothetic continuum. In Stevens' procedure, the arithmetic means of EAI scale ratings are plotted against the geometric means of the scaled DME ratings. If the relationship is linear then the scale is considered metathetic in nature, implying equal perceptual space between the intervals of the scale. Metathetic dimensions, therefore, may be scaled using either DME or EAI scales. If, however, the relationship between

the EAI scores and DME scores is nonlinear, it is suggestive of a prothetic continuum for which only the DME method is appropriate.

Researchers in communication sciences and disorders have tested a variety of psychophysical attributes of speech and voice relative to Stevens' (1975) procedure. Perceptual dimensions commonly scaled in voice and speech often have revealed prothetic continua, suggesting that for these dimensions, DME rating scales are most appropriate. Using the methodology of Stevens (1975), speech intelligibility of hearing-impaired speakers (Schiavetti, Metz, and Sitler, 1981), stuttering severity (Schiavetti *et al.*, 1983), judgments of roughness in sustained vowels (Toner and Emanuel, 1989), and ratings of nasality in synthesized vowels (Zraick and Liss, 2000) have been found to be prothetic. Recently, Whitehill, Lee, and Chun (2002) found that ratings of nasality from connected speech samples of individuals with repaired cleft palate and hypernasality were also prothetic in nature. However, in examining the acoustic and psychophysical dimensions of perceived speech naturalness of nonstutterers and post-treatment stutterers, Metz, Schiavetti, and Sacco (1990) found that speech naturalness behaves like a metathetic continuum. Similarly, Sewall *et al.* (1999) found that the ratings of breathiness in normal speakers also are metathetic. Because EAI scales abound in the auditory-perceptual literature (cf. Kreiman *et al.*, 1993), it is critical that the nature (i.e., prothetic vs metathetic) of perceptual attributes is determined so that valid scales are used. The validity of such auditory-perceptual scales has widespread implications for all empirical efforts addressing auditory-perceptual phenomena associated with voice and speech (Kent, 1996).

B. Consideration of perceptual dimensions

Kreiman and Gerratt (1998, 2000) have suggested that one factor that may add to listener disagreement found in auditory-perceptual studies relates to the finding that listeners are unable to selectively attend to individual elements or dimensions inherent in a multidimensional signal. This skill is traditionally required in most voice evaluation paradigms (e.g., rating of "pitch," "roughness," "breathiness"). As such, the dimensions chosen for the present study included judgments of voice pleasantness and severity. These dimensions were chosen so that listeners could use the whole signal as a basis for their overall judgment of the voice signal under study. Second, scales used to measure voice pleasantness and overall voice severity require direct investigation because they have been used in the speech and voice literature for evaluation of pathological voices and related correspondence to acoustic measures of voice (e.g., Eskenazi, Childers, and Hicks, 1990; Reich and Lerman, 1978; Wolfe and Martin, 1997). Consequently, the purpose of the present study was: (1) to determine the psychophysical nature of voice pleasantness and severity in normal and dysphonic speakers using Stevens' (1975) methods, and (2) to determine the construct validity of rating scales used for these two perceptual dimensions in this population of speakers.

TABLE I. Summary of subject information for participant speakers in the voice disordered group.

Subject	Age	Sex	Medical diagnosis/Description
1 (Mod)	34	M	Incoordination of VF
2	39	F	Clear larynx, hyperfunctional
3	54	M	Small, soft nodule
4	57	M	Polypoidal change, bilateral
5	48	F	Clear larynx, hyperfunctional
6	32	F	Small nodule
7	38	F	Large polyps
8	51	M	Clear larynx, hyperfunctional
9	37	F	Small nodule, verux
10	23	F	Clear larynx, hyperfunctional
11	60	M	Possible cancer VF
12	50	M	Clear larynx, hyperfunctional
13	36	F	Small nodule, cyst
14 (Mod)	25	F	Papilloma
15	32	M	VF cyst
16	44	F	Vocal hyperfunction
17	38	M	Polypoid change; mass lesion
18	39	M	Papilloma
19	43	F	Clear larynx, hyperfunctional
20	41	M	Papilloma
21	57	F	VF edema
22	42	M	Contact granuloma; Reinke's edema
23	41	M	Granuloma
24	64	F	Clear larynx, hyperfunctional

Age and gender information for participant speakers in the normal group.

1	26	F	
2	28	M	
3	47	F	
4	41	M	
5	55	F	
6	56	M	

II. METHOD

A. Stimuli

The voices of 12 male and 12 female adult speakers with vocal pathology were selected from a large library of samples recorded under identical conditions as part of a phonatory function analysis. Voice samples included individuals who ranged in age from 20 to 65 years (mean age = 42 years), with roughly equal numbers of diagnostic categories, a range of voice quality severities (mildly to severely dysphonic), including those who presented without visible laryngeal pathology (i.e., physiologic disturbances without anatomic change) and those who exhibited benign mass lesions of the vocal fold(s). A range of voice quality severities was chosen in order to scale results of each perceptual dimension along the breadth of its psychophysical continuum (Stevens, 1975). The speakers' ages, gender, and medical diagnoses are presented in Table I.

In addition to the 24 speakers who exhibited dysphonic voice samples, six normal speech samples (3 males and 3 females) were included, with one male and one female chosen from each of the following age ranges: 20–35 years, 36–50 years, and 51–65 years. These age ranges were arbitrarily selected in an effort to control for general age effects on voice quality, as they were representative of the range of

ages for the dysphonic speakers who provided the experimental stimuli.

All speaker samples were recorded using a unidirectional microphone (AKG-451-E) and a research-quality digital audiotape (DAT) player/recorder (Sony DTC-57ES) routed to an audio mixer (Tascam 112). All speakers had bilateral pure-tone hearing within normal limits (<30 dB) for the octave frequencies 250–2000 Hz (ANSI, 1989), and all were native English speakers.

B. Listening tapes

The second sentence of the "Rainbow Passage" ("The rainbow is a division of white light into many beautiful colors") was extracted and used for scaling judgments (Fairbanks, 1960). Sentence stimuli were used in lieu of sustained vowels because: (a) connected speech contains important voicing onset and offset information needed for multidimensional judgments such as "pleasantness" (Qi, Hillman, and Milstein, 1999); (b) sentence stimuli offer a more representative sample of voice quality relative to static stimuli such as vowels; (c) the Rainbow Passage is a commonly employed assessment of voice, and (d) listeners are able to judge connected speech stimuli as reliably as vowel stimuli (Hillebrand and Houde, 1996; Klingholz, 1990). The modulus was chosen from the 24 dysphonic speaker samples by a consensus between a highly experienced clinician and a clinician with less than 5 years clinical experience. The modulus was selected as the voice sample that represented the approximate midpoint for pleasantness and severity among the 24 dysphonic speaker samples.

Listening tapes (Sony DTC-57ES) (DAT) were constructed for pleasantness, scaled with EAI (pl-EAI), pleasantness, scaled with DME (pl-DME) and for voice severity, scaled with EAI (s-EAI) and voice severity, scaled with DME (s-DME). Presentation order was randomized and there was a 5-s interstimulus interval. Six of the 24 speech samples were presented two times for each condition (pl-EAI, pl-DME, s-EAI, s-DME) to allow for assessment of intrarater reliability of auditory-perceptual judgments.

C. Listeners

Twelve graduate students in speech-language pathology served as listeners (age range, 21–26 years). All listeners were considered to be naive to voice pathology issues (i.e., listeners had no prior educational experience with or exposure to voice disorders). Naive listeners were selected for the present study because experience with pathological voices can lead to decreased interjudge reliability (Kent, 1996; Kreiman et al., 1993) and we believed that naive listeners would be more representative of the general population at large relative to highly trained, experienced listeners. None of the listeners reported any history of hearing, speech, voice, or language difficulties.

D. Rating scale task

Listeners were required to evaluate the dimensions of pleasantness and severity from the taped voice samples of the 24 dysphonic and 6 normal speakers using both EAI and

DME scaling procedures. Pleasantness was defined as "a dimension that relates to how 'pleasant' you find the speaker's voice as a listener." The rating was to be made exclusive of "speech intelligibility, dialectical variation, and/or accent" (adapted from Doyle *et al.*, 1995). Voice severity was defined as "a comprehensive measure of how 'good' or 'poor' the voice sample is judged to be by the listener." This judgment was based on "multiple factors which ultimately range from profoundly impaired to normal on a continuum (e.g., profound, severe-to-profound, severe, moderate-to-severe, moderate, mild-to-moderate, mild, nearly normal, and normal)."

To obtain ratings with the DME procedure, listeners were first familiarized with the modulus sample and informed that it arbitrarily represented a value of "100" on the DME scale. All other judgments were made relative to the modulus. DME scales with or without a modulus (the so-called "free-modulus procedure") have been shown to be both valid and reliable measures of voice (Whitehill, Lee, and Chun, 2002). Use of a modulus was chosen in the present study because of two specific disadvantages of the free-modulus procedure. First, listeners are often uncomfortable using a free-modulus scale in which they must assign inherent values to a stimulus and, second, the free-modulus technique requires use of a sophisticated normalization procedure to equate judgments between listeners (Weismer and Laures, 2002). Listeners were instructed to scale taped samples that were twice as pleasant or twice as good at a value of "200;" speaker samples judged to be half as pleasant or half as good were to be given a value of "50." The modulus was repeated after every sixth stimulus item to maintain referential value of the modulus, thereby reducing the potential for a shift in the listeners' internal standard for the judgments in question (Kreiman *et al.*, 1993). Studies that have used DME with a modulus in speech research have varied in how frequently the modulus sample was repeated, ranging from only once at the beginning of the task (Prather, 1960) to every sample (McHenry, 1999), with others repeating the modulus after every 10 stimuli (Zraick and Liss, 2000). The decision to repeat the modulus after every sixth stimulus item in the current study was somewhat arbitrary, but was made because (a) it was approximately in the middle of this range, and (b) Prather (1960) reported that the results of repetition after every six samples "do not appear to differ in any substantial way" (p. 391) from playing the modulus sample only at the beginning of the task. Listeners followed this procedure for their ratings of both pleasantness and severity.

Severity and pleasantness ratings also were obtained using 9-point EAI scales (Metz *et al.*, 1990). For voice severity, listeners were asked to scale each sample according to the definition provided with a rating of "1" representing the most severe sample and a rating of "9" representing a normal voice. For pleasantness ratings, 1 represented "very unpleasant" and 9 indicated a "very pleasant" voice sample. Listeners were randomly divided into two groups of 6 each. Order of task presentation was randomized across listeners and rating sessions were separated by 48 h to control for possible learning effects.

TABLE II. Individual and group intraclass correlations (ICCs) for direct magnitude estimation (DME) and equal-appearing interval (EAI) scale judgments of voice pleasantness and severity for dysphonic and normal speakers.

	pl-DME	s-DME	pl-EAI	s-EAI
Group reliability	0.969	0.971	0.964	0.984
Individual reliability	0.724	0.736	0.692	0.839

E. Data analysis

Stevens' (1975) psychophysical method of comparing DME and EAI ratings was used. Arithmetic means of the EAI scale values were plotted as a function of the geometric means of the DME values for all speech samples. This procedure was duplicated for both the pleasantness and severity ratings. A linear relationship between the two sets of scaled judgments would indicate a metathetic continuum, whereas a downward-bowed, negatively accelerating curvilinear function would indicate a prothetic continuum.

III. RESULTS

A. Intrarater reliability

Six speech samples (25%) were rerated by all listeners for reliability purposes. This proportion of repeated samples is commonly reported for voice perception studies (cf. Kreiman *et al.*, 1993). Intrarater reliability was calculated using Pearson's correlation coefficients for DME conditions. Intrarater reliability values ranged from $r=0.682-0.992$ for pleasantness ratings, and from $r=0.493-0.968$ for the severity ratings. For EAI ratings, values assigned by each rater were compared to values assigned to the repeated speaker samples. The percent agreement was calculated by counting the number of comparisons in which the assigned scale value did not differ by more than ± 1 scale value, dividing this number by 6 for each speaker, and multiplying by 100. The mean intrarater reliability was also calculated for each condition by dividing the number of matches by 72 (6 repeated samples $\times$ 12 raters) and multiplying by 100. Intrarater agreement ± 1 scale value for the pl-EAI condition ranged from 67% ($n=4$) to 100% ($n=7$) (mean$=88\%$). Intrarater agreement ± 1 scale value for the s-EAI condition ranged from 67% ($n=2$) to 100% ($n=7$) (mean$=90\%$). Thus, intrarater reliability values were high relative to a 9-pt scale, suggesting that each rater maintained internal consistency in making judgments of both voice pleasantness and severity.

B. Interrater reliability

The interrater reliability of the ratings was analyzed with the intraclass correlation (ICC), model 2 (Shrout and Fleiss, 1979). The reliability coefficients for the group and individual ratings are shown in Table II, and are consistent with previously reported ratings for other variables such as stuttering severity and speech naturalness (Martin *et al.*, 1984; Metz *et al.*, 1990; Schiavetti *et al.*, 1983). Group reliability coefficients were highly acceptable (i.e., >0.90) for all conditions. Individual rater reliability coefficients were somewhat lower, but moderately acceptable (range$=0.69-0.84$). However, since scaled data such as that for voice pleasant-
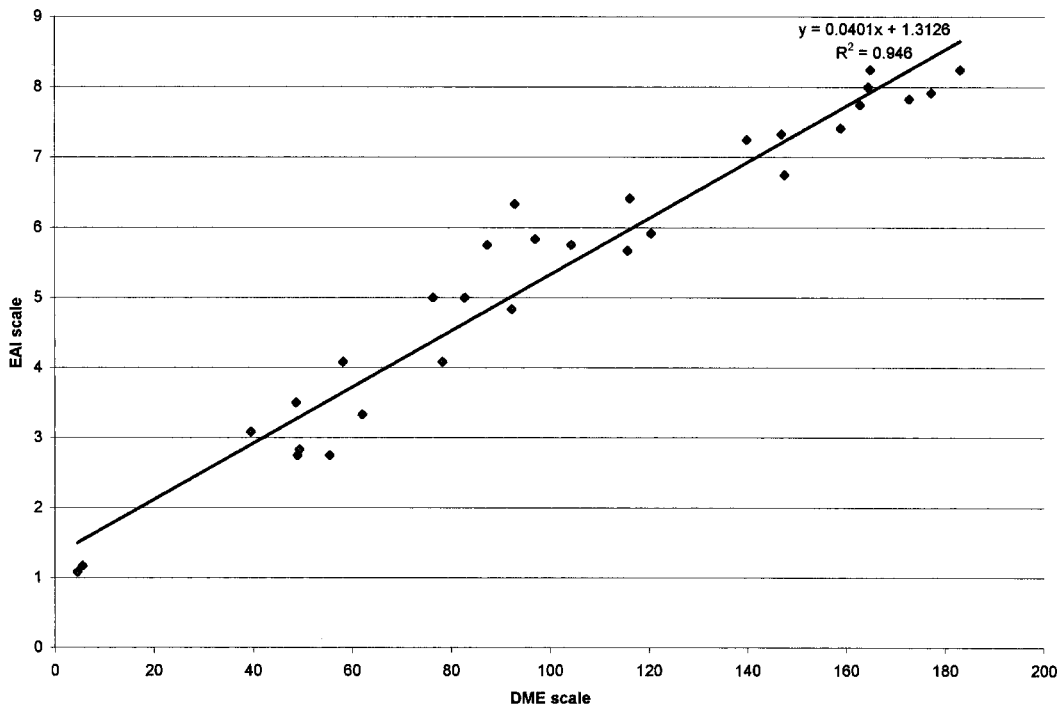
FIG. 1. Mean interval scale values of voice pleasantness plotted as a function of geometric mean DME estimates of voice pleasantness for dysphonic and normal speakers.

ness and severity are usually employed as group mean ratings for research purposes, the group reliability coefficients are more descriptive of the reliability of actual data used to determine pleasantness and severity in this study.

C. Rating scale comparisons

1. Pleasantness

EAI means were plotted as a function of the DME geometric means for the voice pleasantness ratings of dysphonic and normal speakers (see Fig. 1). Results indicated that the relationship was significantly predicted with the best-fit linear equation ($y = 0.0401x + 1.313$) for EAI pleasantness values from the listeners' DME estimates [$r^2 = 0.946$, $F(1,22) = 328.496$, $p < 0.001$]. A test for curvilinearity revealed no significant improvement in the variance accounted for by any of the curvilinear models over the linear model. Visual inspection of the data presented in Fig. 1 also revealed a good approximation to the raw data by the linear regression, with no apparent downward bowing.

2. Severity

For severity ratings, EAI means plotted as a function of the DME geometric means revealed a statistically significant result [$r^2 = 0.953$, $F(2,27) = 274.280$, $p < 0.001$] for a second-order polynomial as shown in Fig. 2 (line of best fit: $y = -0.0001x^2 + 0.0673x + 0.217$). This indicates that the curvilinear model accounted for a statistically significant amount of the variance observed, above and beyond that accounted for by a simple linear model. Visual inspection of the model revealed a downward bowing and a ceiling effect towards the end of the curve, a finding that is in agreement with other data for prothetic continua reported in the literature (Schiavetti *et al.*, 1981, 1983; Whitehill *et al.*, 2002).

IV. DISCUSSION

The significant linear relationship between the EAI and DME ratings of voice pleasantness in the listeners' ratings for the present voice samples indicates that a metathetic continuum best represents perceived pleasantness of the dysphonic and normal speakers' voices used in this investigation. The results indicate that either EAI or DME scales can validly measure the dimension of voice pleasantness in this dysphonic population. Nevertheless, further investigation is required to determine whether the present results are generalizable to other populations such as dysarthric speakers, alaryngeal speakers, and speakers with neurologically based voice disorders. A comparison of reliability as a function of severity for a multidimensional attribute such as pleasantness also is warranted. Kreiman and Gerratt (2000) have suggested that this is a weakness of traditionally used rating scales. However, this suggestion has only been identified for unidimensional attributes and in those studies where EAI scales have been used without anchor stimuli.

In contrast to the findings for pleasantness, a significant curvilinear relationship was found between the EAI and DME voice severity ratings. These data indicate that a prothetic continuum best represents the severity dimension of the dysphonic samples assessed in the present study. This result suggests that the "severity" of dysphonia, like stuttering severity, must be measured with DME scales to avoid the linear partitioning assumed when EAI scales are employed. Using EAI scales to rate the severity of a dysphonic speaker's voice introduces a bias as listeners attempt to partition their perception of severity into equal intervals. Stevens (1974) indicated that with prothetic dimensions, listeners do not perceive intervals equally along different locations of the rating scale. That is, the implied difference between a sever-
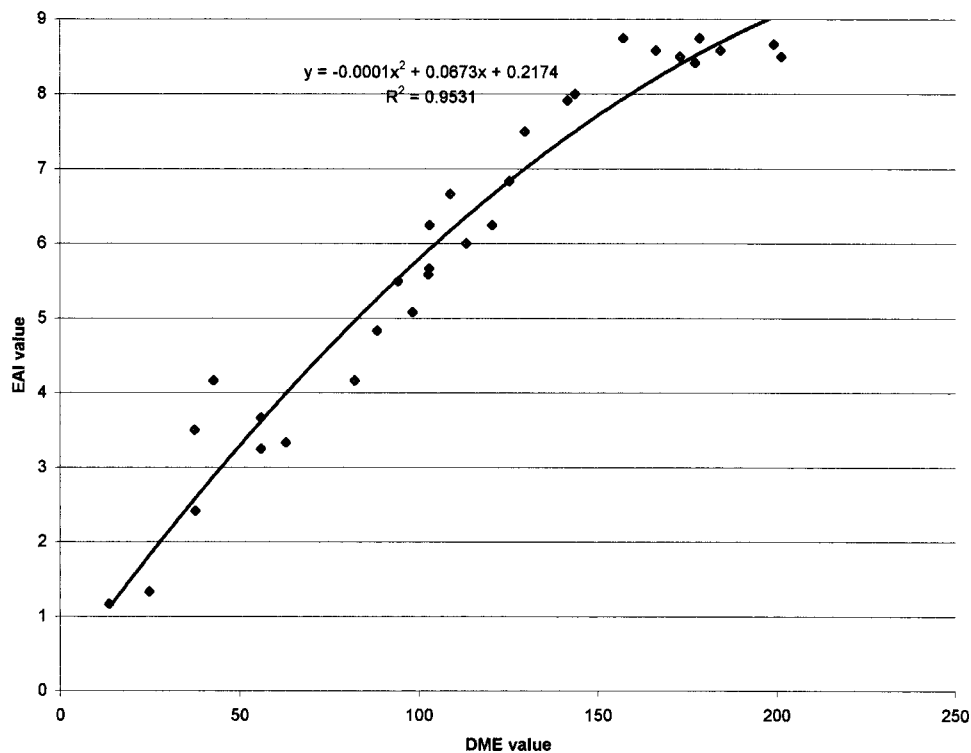
FIG. 2. Mean interval scale values of voice severity plotted as a function of the geometric mean DME estimations of voice severity for dysphonic and normal speakers.

ity rating of "1" and "2" may not be the same magnitude of difference as that which exists between a rating of "2" and "3," "8" and "9," etc. This difference has several clinical implications. For example, using an EAI scale to quantify intervention outcomes relative to the dimension of severity is inappropriate since it is difficult to interpret relative differences between scale values pre- and postintervention (i.e., a change from 1 to 2 may mean something different than a change from a 8 to 9).

Over the past decade, perceptual evaluation of voice and voice disorders has gained considerable attention in the empirical literature (cf. Kent, 1996; Kreiman et al., 1993). In fact, the importance of the ear to the evaluative process has made it the primary tool when evaluating voice and speech disturbances (Gerratt et al., 1991), as well as serving a variety of empirical perceptual endeavors (cf. Colton and Estill, 1981; Kent, 1996). Much of the recent work addressing voice perception has indicated that numerous factors must be considered relative to interpreting data obtained. Factors such as listener experience, definitions of the feature under assessment, scale resolution, interactions between the task and the listener and many others, are all elements to consider when perceptual questions are critically addressed (Kreiman et al., 1993). Of course, when considering all of these factors, one must also assume that the scale used is valid.

Kreiman et al. (1993) compared listeners' ratings of vocal roughness using an equal appearing interval (EAI) scale and a visual analog (VA) scale. Listeners rated the same voices ($n = 22$) twice, and since there were a large number of normal or near-normal speaker samples, rough voices were judged as "rougher" when heard a second time. This phenomenon occurred for listeners' ratings using the EAI scale, but not for the VA ratings (Kreiman et al., 1993). Likewise, Gerratt et al. (1993) found that after a time, listeners using a

5-pt EAI scale rated moderately rough voice stimuli as even rougher after they had heard a large number of normal and mildly rough voice samples. Yet, when listeners were provided with explicitly anchored stimuli for each scale point, a "drift" in ratings did not occur. These results led the authors to conclude that the "variability in voice quality ratings might be reduced by replacing listeners' idiosyncratic, unstable, internal standards with fixed external standards for 'reference voices' for different vocal qualities" (Gerratt et al., 1993, p. 33) (Kreiman et al., 1992). Gerratt et al. (1993) also found that ratings gathered using the anchored scale were significantly more reliable than those gathered using an unanchored EAI scale (i.e., both intra- and interrater reliability were significantly better for the anchored paradigm). Further, Gerratt et al. (1993) and Kreiman et al. (1993) found that although listeners frequently agreed about what constituted normal or severe voice quality, they disagreed about the character of mildly-to-moderately dysphonic voices. Thus, offering a standard, referent voice(s) (i.e., a modulus sample) may dramatically increase the reliability of auditory-perceptual ratings. These findings have obvious implications for the auditory-perceptual assessment of voice quality, especially when listeners are asked to rate voices (or speech characteristics) with which they have little formal experience (i.e., dysphonic). Previous data also suggest that DME scales and the use of modulus voices may help replace variable internal representations with more stable external representations of an attribute. By doing so, reliability may be improved substantially and the use of a modulus may provide a standard from which repeated evaluations of the same set of stimuli may be achieved, thus permitting an opportunity for experimental replications of such psychophysical evaluations. However, Kreiman and Gerratt (2000) also suggest that listeners still might exhibit difficulty for rating

values found in between "anchor" stimuli. Because of these concerns, this line of research is in need of further investigation.

Multidimensional factors inherent in the voice/speech signal must be considered of primary importance from the standpoint of evaluating voice change over time. For example, the ultimate arbiter of voice/speech "success" likely finds some component in the realm of how much the individual speaker is not noticed as being "different" or "abnormal" or from the listeners' normal expectation (Van Riper, 1978). These considerations extend beyond unidimensional measures/features inherent to the voice signal (e.g., pitch, loudness, and rate). A clear indicator of comprehensive perception is found in the multidimensional feature potentially represented by one's judgment of the "pleasantness" or "severity" for a given voice relative to a given standard. Thus, it is vital that more global auditory-perceptual judgments of voice are validly scaled since they could potentially serve as meaningful indicators of voice change over time. When this consideration is coupled with that related to the experience level of listeners, it would seem that more global evaluations of voice may permit the use of naive listeners provided definitions and standards are provided *a priori*. The results of the present study suggest further investigation of voice dimensions using Stevens' (1975) procedures in an attempt to better understand the perceptual correlates of voice beyond unidimensional aspects of the signal. More broadly, the nature of each perceptual dimension assessed (e.g., pleasantness, severity, acceptability, etc.) must be investigated to insure that auditory-perceptual scales are valid.

V. CONCLUSIONS

This investigation assessed the validity of pleasantness and severity ratings of dysphonic and normal speakers using direct magnitude estimation (DME) and equal-appearing interval (EAI) scales. Based on a comparison of the two scales, voice pleasantness was found to be consistent with a metathetic continuum and voice severity was prothetic in nature. These data provide support for the use of either DME or EAI scales when making auditory-perceptual judgments of pleasantness, but only DME scales when judging overall voice severity for dysphonic speakers.

Implications for future research suggest development of a clinical scale that uses a DME measurement procedure in order to avoid applying the incorrect type of scale for attributes such as pleasantness and severity (Schiavetti, 1984). This is especially important since many attributes of speech and voice are known to be prothetic (Schiavetti *et al.*, 1981, 1983; Toner and Emanuel, 1989; Whitehill *et al.*, 2002; Zraick and Liss, 2000). The present results also suggest that a method for comparing across listeners and scales is necessary since DME is not currently useful in applied applications (Schiavetti, 1984). Thus, results of past studies using EAI scales to measure severity must be interpreted with caution. Studies that attempt to establish relationships between perceptual dimensions and acoustic correlates also should employ valid perceptual scaling options. Further study of dimensions such as voice pleasantness and severity need to be compared with data from multidimensional scaling (e.g.,

Kreiman, Gerratt, and Berke, 1994). New investigations such as "analysis-by-synthesis" also may offer alternatives to traditional rating scales as a way of controlling error effects (Gerratt and Kreiman, 2001). For now, possibilities for the development of applied applications of DME methods also remain a valuable area for future investigations and findings from such work hold promise in helping to further define the nature of auditory-perceptual phenomena.

ANSI (**1989**). S3.6-1989, "Specifications for audiometers" (American National Standards Institute, New York).

Colton, R. H., and Estill, J. A. (**1981**). "Elements of voice quality: Perceptual, acoustic, and physiologic aspects," in *Speech and Language: Advances in Basic Research and Practice*, edited by N. J. Lass (Academic, New York), Vol. 5, pp. 311–403.

Doyle, P. C., Leeper, H. A., Houghton-Jones, C., Heeneman, H., and Martin, G. F. (**1995**). "Perceptual characteristics of hemilaryngectomized and near-total laryngectomized male speakers," J. Med. Speech-Lang. Path. **3**, 131–143.

Eskenazi, L., Childers, D. C., and Hicks, D. M. (**1990**). "Acoustic correlates of vocal quality," J. Speech Hear. Res. **33**, 298–306.

Fairbanks, G. (**1960**). *Voice and Articulation Drillbook*, 2nd ed. (Harper, New York).

Gelfer, M. P. (**1988**). "Perceptual attributes of voice: Development and use of rating scales," J. Voice **2**, 320–326.

Gerratt, B. R., and Kreiman, J. (**2001**). "Measuring vocal quality with speech synthesis," J. Acoust. Soc. Am. **110**, 2560–2566.

Gerratt, B. R., Kreiman, J., Antonanzas-Barroso, N., and Berke, G. S. (**1993**). "Comparing internal and external standards in voice quality judgments," J. Speech Hear. Res. **36**, 14–20.

Gerratt, B. R., Till, J., Rosenbek, J. C., Wertz, R. T., and Boysen, A. E. (**1991**). "Use and perceived value of perceptual and instrumental measures in dysarthria management," in *Dysarthria and Apraxia of Speech*, edited by C. A. Moore, K. M. Yorkston, and D. R. Beukelman (Brookes, Baltimore), pp. 77–93.

Hillebrand, J., and Houde, R. A. (**1996**). "Acoustic correlates of breathy vocal quality: Dysphonic voices and continuous speech," J. Speech Hear. Res. **39**, 311–321.

Hirano, M., Hibi, S., Yoshida, T., Hirade, Y., Kasuya, Ha., and Kikuchi, Y. (**1988**). "Acoustic analysis of pathological voice," Acta Oto-Laryngol. **105**, 432–438.

Kearns, K. P., and Simmons, N. N. (**1988**). "Interobserver reliability and perceptual ratings: More than meets the ear," J. Speech Hear. Res. **31**, 131–136.

Kent, R. (**1996**). "Hearing and believing: Some limits to the auditory perceptual assessment of speech and voice disorders," Am. J. Speech-Lang. Path. **5**, 7–23.

Klingholz, F. (**1990**). "Acoustic recognition of voice disorders: A comparative study of running speech versus sustained vowels," J. Acoust. Soc. Am. **87**, 2218–2224.

Kreiman, J., and Gerratt, B. R. (**2000**). "Sources of listener disagreement in voice quality assessment," J. Acoust. Soc. Am. **108**, 1867–1876.

Kreiman, J., and Gerratt, B. R. (**1998**). "Validity of rating scale measures of voice quality," J. Acoust. Soc. Am. **104**, 1598–1608.

Kreiman, J., and Gerratt, B. R. (**1996**). "The perceptual structure of pathologic voice quality," J. Acoust. Soc. Am. **100**, 1787–1795.

Kreiman, J., Gerratt, B. R., and Berke, G. S. (**1994**). "The multidimensional nature of pathologic vocal quality," J. Acoust. Soc. Am. **96**, 1291–1302.

Kreiman, J., Gerratt, B. R., Kempster, G. B., Erman, A., and Berke, G. S. (**1993**). "Perceptual evaluation of voice quality: Review, tutorial, and a framework for future research," J. Speech Hear. Res. **36**, 21–40.

Kreiman, J., Gerratt, B. R., Precoda, K., and Berke, G. (**1992**). "Individual differences in voice quality perception," J. Speech Hear. Res. **35**, 512–520.

Martin, R. R., Haroldson, S. K., and Triden, K. A. (**1984**). "Stuttering and speech naturalness," J. Speech Hear Disord. **49**, 53–58.

McHenry, M. A. (**1999**). "Aerodynamic, acoustic, and perceptual measures of nasality following traumatic brain injury," Brain Inj. **13**, 281–290.

Metz, D. E., Schiavetti, N., and Sacco, P. R. (**1990**). "Acoustic and psychosocial dimensions of the perceived speech naturalness of nonstutterers and posttreatment stutterers," J. Speech Hear Disord. **55**, 516–525.

Prather, E. M. (**1960**). "Scaling defectiveness of articulation by direct magnitude-estimation," J. Speech Hear. Res. **3**, 380–392.

Qi, Y., Hillman, R. E., and Milstein, C. (**1999**). "The estimation of signal-to-noise ratio in continuous speech for disordered voices," J. Acoust. Soc. Am. **105**, 2532–2535.

Reich, A. R., and Lerman, J. W. (**1978**). "Teflon laryngoplasty: An acoustical and perceptual study," J. Speech Hear Disord. **153**, 496–505.

Schiavetti, N. (**1984**). "Scaling procedures for quantification of speech, language and hearing variables," in *Articulation Assessment and Treatment Issues*, edited by R. G. Daniloff (College-Hill, San Diego), pp. 237–253.

Schiavetti, N., Metz, D. E., and Sitler, R. W. (**1981**). "Construct validity of direct magnitude estimation and interval scaling: Evidence from a study of the hearing-impaired," J. Speech Hear. Res. **24**, 441–445.

Schiavetti, N., Sacco, P. R., Metz, D. E., and Sitler, R. W. (**1983**). "Direct magnitude estimation and interval scaling of stuttering severity," J. Speech Hear. Res. **26**, 568–573.

Sewall, A., Weglarski, A., Metz, D. E., Schiavetti, N., and Whitehead, R. L. (**1999**). "A methodological control study of scaled vocal breathiness measurements," Cont. Issues Comm. Sci. Dis. **26**, 168–172.

Shrout, P. E., and Fleiss, J. L. (**1979**). "Intraclass correlations: Uses in assessing rater reliability," Psychol. Bull. **86**, 420–428.

Southwood, H. M., and Weismer, G. (**1993**). "Listener judgments of the bizarreness, acceptability, naturalness, and normalcy of the dysarthria associated with amyotrophic lateral sclerosis," J. Med. Speech-Lang. Path. **1**, 151–161.

Stevens, S. S. (**1974**). "Perceptual magnitude and its measurement," in *Handbook of Perception*, edited by E. C. Caterette and M. P. Friedman (Academic, New York), Vol. 2, pp. 22–40.

Stevens, S. S. (**1975**). *Psychophysics: Introduction to its Perceptual, Neural and Social Prospects* (Wiley, New York).

Toner, M. A., and Emanuel, F. W. (**1989**). "Direct magnitude estimation and equal appearing interval scaling of vowel roughness," J. Speech Hear. Res. **32**, 78–82.

Van Riper, C. (**1978**). *Speech Correction: Principles and Methods* (Prentice Hall, Englewood Cliffs, NJ).

Weismer, G., and Laures, J. S. (**2002**). "Direct magnitude estimates of speech intelligibility in dysarthria: Effects of a chosen standard," J. Speech Lang. Hear. Res. **45**, 421–433.

Whitehill, T. L., Lee, A. S. Y., and Chun, J. C. (**2002**). "Direct magnitude estimation and interval scaling of hypernasality," J. Speech Lang. Hear. Res. **45**, 80–88.

Wolfe, V., and Martin, D. (**1997**). "Acoustic correlates of dysphonia: Type and severity," J. Commun. Disord. **30**, 403–416.

Zraick, R. I., and Liss, J. M. (**2000**). "A comparison of equal-appearing interval scaling and direct magnitude estimation of nasal voice quality," J. Speech Lang. Hear. Res. **43**, 979–988.

The effects of familiarization on intelligibility and lexical segmentation in hypokinetic and ataxic dysarthria

Julie M. Liss[a) and Stephanie M. Spitzer
Motor Speech Disorders Laboratory, Arizona State University, Box 871908, Tempe, Arizona 85281

John N. Caviness and Charles Adler
Department of Neurology, Mayo Clinic–Scottsdale, Scottsdale, Arizona 85259

This study is the third in a series that has explored the source of intelligibility decrement in dysarthria by jointly considering signal characteristics and the cognitive–perceptual processes employed by listeners. A paradigm of lexical boundary error analysis was used to examine this interface by manipulating listener constraints with a brief familiarization procedure. If familiarization allows listeners to extract relevant segmental and suprasegmental information from dysarthric speech, they should obtain higher intelligibility scores than nonfamiliarized listeners, and their lexical boundary error patterns should approximate those obtained in misperceptions of normal speech. Listeners transcribed phrases produced by speakers with either hypokinetic or ataxic dysarthria after being familiarized with other phrases produced by these speakers. Data were compared to those of nonfamiliarized listeners [Liss *et al.*, J. Acoust. Soc. Am. **107**, 3415–3424 (2000)]. The familiarized groups obtained higher intelligibility scores than nonfamiliarized groups, and the effects were greater when the dysarthria type of the familiarization procedure matched the dysarthria type of the transcription task. Remarkably, no differences in lexical boundary error patterns were discovered between the familiarized and nonfamiliarized groups. Transcribers of the ataxic speech appeared to have difficulty distinguishing strong and weak syllables in spite of the familiarization. Results suggest that intelligibility decrements arise from the perceptual challenges posed by the degraded segmental and suprasegmental aspects of the signal, but that this type of familiarization process may differentially facilitate mapping segmental information onto existing phonological categories. © *2002 Acoustical Society of America.* [DOI: 10.1121/1.1515793]

PACS numbers: 43.71.Bp, 43.71.Gv, 43.70.Dn, 43.70.Fq [DOS]

I. INTRODUCTION

With great facility, we are able to extract spoken words from a continuous acoustic stream that contains virtually no reliable and consistent word boundary cues (Lehiste, 1972; Nakatani and Schaffer, 1978). We easily negotiate the spoken messages of friends and strangers; men, women, and children; fast and slow talkers; synthetic speech; and the messages of speakers whose first language or dialect is not our own. Even in suboptimal listening conditions, such as noisy rooms or poor phone connections, we execute the task of lexical segmentation with surprising accuracy. This ability to be successful in the face of variable acoustic manifestations of words has proven problematic for theories of speech perception (see McQueen and Cutler, 2001). Learning, adaptation, and normalization appear to be highly operative processes that underlie the plasticity of our speech perception capabilities.

But these perceptual capabilities have limits, and cognitive effort increases and accuracy decreases as the acoustic information becomes degraded or unreliable (Munro and Derwing, 1995; Pisoni *et al.*, 1987). This is precisely the case with the perception of dysarthric speech. Although reductions in speech intelligibility secondary to dysarthria are well documented, we know very little about the cognitive–

perceptual source of these decrements. That is to say, we do not understand how the nature of the degraded speech signal affects our ability to process it. The study of the perception of dysarthric speech has not only clinical implications, but offers a test case for theories and models of normal speech perception processes.

The current report is the third in a series of studies that has attempted to identify part of the source of intelligibility decrements in connected dysarthric speech by examining the mistakes listeners make in lexical segmentation. The Metrical Segmentation Strategy (MSS) proposed by Cutler and Norris (1988) was selected as a framework for these investigations because of its ability to jointly represent signal characteristics (i.e., the dysarthric speech patterns) and listener constraints (as evidenced by lexical boundary error patterns). Furthermore, its predictions based on prosodic patterns can be applied directly to the prosodic disruptions that are common in dysarthria. The MSS posits that listeners capitalize on the rhythmic structures of language to identify the location of word boundaries. In English, listeners will be highly successful in their lexical segmentation if they attend to strong syllables as potential word-onsets (Cutler and Carter, 1987). Dysarthric speech, particularly the types targeted in the current series of studies, is characterized in part by disruptions in prosody or rhythm. It was assumed that if listeners rely on syllabic stress information for identification of word boundaries, then their patterns of lexical boundary

errors (LBE) should reveal difficulties in applying this strategy when the prosodic structure is disturbed. As reported previously, this was found to be the case (Liss *et al.*, 1998; Liss *et al.*, 2000). The data were consistent with the idea that the degraded prosodic pattern made it more difficult to identify word boundaries from stress for some forms of dysarthria than others (Liss *et al.*, 2000). Hypokinetic dysarthria, characterized by a perceptually rapid rate and monotonicity, generated a large number of lexical boundary errors whose patterns generally conformed to the predictions based on normal degraded speech, particularly at higher levels of intelligibility. However, ataxic dysarthria characterized by a slow rate of speech with equal and even syllabic stress, elicited LBE patterns that did not conform to predictions. Erroneous insertions and deletions of lexical boundaries occurred equally often before strong and weak syllables. It appeared that the type of prosodic degradation associated with ataxic dysarthria made it particularly difficult for listeners to use stress cues for lexical segmentation. This distinction between LBE patterns elicited by these hypokinetic and ataxic dysarthric speech samples is of particular note because the two samples were of equivalent intelligibility. These studies shed light on how the nature of the speech signal contributes to the efficiency with which normal cognitive–perceptual processes can be applied.

In contrast to our two previous reports on the perception of dysarthric speech, the current study focused on the manipulation of listener constraints. We wondered whether listeners could learn something about the degraded signal that would assist them in applying the metrical segmentation strategy, and whether this would be evident in their pattern of LBEs. Our previous studies suggested a reduced ability to distinguish strong and weak syllables in dysarthric speech, particularly in ataxic dysarthric speech. If listeners can acquire information that facilitates the distinction of strong and weak syllables, their LBE patterns should align more closely with predicted patterns. A process of brief familiarization was selected to examine this issue.

The construct of familiarization encompasses a broad array of methodological and conceptual categories, including exposure, training, adaptation, and experience. Each of these categories can vary along a number of continua, including amount of exposure, duration of exposure, type of information presented, and the quality and quantity of performance feedback provided. Irrespective of these methodological variations, experience with a degraded speech signal has been shown to facilitate subsequent processing of that signal in many studies. Benefits have been demonstrated as improved intelligibility of synthetic or electronically modified speech signals (Dupoux and Green, 1997; Greenspan *et al.*, 1988; Rosen *et al.*, 1999; Sebastián-Gallés *et al.*, 2000; Schwab *et al.*, 1985), disordered speech (Dagenais *et al.*, 1999; DePaul and Kent, 2000; Flipsen, 1995; Robinson and Summerfield, 1996; Tjaden and Liss, 1995; although see Yorkston and Beukelman, 1983, for evidence to the contrary), and non-native speech (e.g., Logan *et al.*, 1991; Tremblay *et al.*, 1997). Although the precise cognitive–perceptual mechanisms underlying the benefits of familiarization have not been discovered, it is hypothesized that it promotes the normalization process and the mapping of speech stimulus features onto existing phonological representations (Dupoux and Green, 1997; Guenther *et al.*, 1999; Schwab *et al.*, 1985).

The purpose of the present study was to examine the effects of modifying listener constraints through the process of a brief prior exposure to either hypokinetic or ataxic dysarthric speech. The following questions were addressed: (1) Do listeners who are familiarized with dysarthric speech in general obtain higher intelligibility scores than those who have had no prior exposure; (2) Is there a dysarthria-specific effect of familiarization on intelligibility, in which exposure to hypokinetic or ataxic speech improves intelligibility of hypokinetic or ataxic speech, respectively; (3) Do lexical boundary error patterns provide evidence that listeners learn about prosodic form from the familiarization procedure? Evidence for the final question would be found in the distribution of lexical boundary errors relative to strong and weak syllables. Specifically, do the patterns of LBEs produced by the listeners who were familiarized with the dysarthric speech adhere more strongly to the predicted patterns than those elicited from nonfamiliarized listeners?

II. METHOD

A. Study overview

A between-group design was selected for the present study to more closely control the familiarization effects than a within-group design would permit. By its nature, the phenomenon of familiarization is cumulative and irreversible within the context of a circumscribed investigation. Although a within-subjects design is preferable for a variety of reasons, we believed it was necessary first to establish the magnitude of any effect in separate groups.

Two groups of listeners were familiarized with either hypokinetic or ataxic speech and then they transcribed a series of phrases produced by speakers with the corresponding type of dysarthria. Appended to the 60 phrase series was a subset of 20 low-intelligibility phrases produced by speakers with the other type of dysarthria. Thus, one listener group was familiarized with hypokinetic speech. They transcribed 60 hypokinetic phrases (hypokinetic familiarized), then they transcribed 20 low intelligibility ataxic phrases (familiarized with other). The second listener group was familiarized with ataxic speech. They transcribed 60 ataxic phrases (ataxic familiarized), then they transcribed 20 low intelligibility hypokinetic phrases (familiarized with other). Results for the 60-phrases and 20-phrases were compared with the corresponding data from a third and fourth group (reported previously in Liss *et al.*, 2000) who transcribed the phrases without prior exposure to any dysarthric speech, and were therefore considered the control groups (hypokinetic control and ataxic control) for this investigation. The comparisons of interest are summarized in Table I.

B. Listeners

Data from two groups of 40 listeners were collected for this investigation. These data were compared with those of two control groups of 20 listeners that did not receive expo-

TABLE I. Comparisons of interest.

60 phrases (between-group): 　Hypokinetic control versus hypokinetic familiarized 　Ataxic control versus ataxic familiarized
20 phrases (between-group): 　Hypokinetic control versus hypokinetic familiarized versus familiarized 　　with other 　Ataxic control versus ataxic familiarized versus familiarized with other

sure to dysarthric speech prior to the transcription task[1] (Liss *et al.*, 2000). Each of the four listener groups contained equal numbers of men and women whose ages ranged from 18 to 50 years old. Most were undergraduate students at Arizona State University, and all were compensated for their participation in this study. All listeners self-reported normal hearing, were native speakers of Standard American English, and reported having little or no experience listening to dysarthric speech.

C. Speech stimuli

Construction of the stimulus tapes has been described in detail in our previous reports (Liss *et al.*, 1998, 2000). Briefly, three audiotapes of phrases were produced by three groups of speakers: six speakers with hypokinetic dysarthria, six with ataxic dysarthria, and six neurologically normal control speakers (whose tape was not used in the present investigation). All of the phrases on the hypokinetic and ataxic tapes complied with our operational definitions, which were derived from the Mayo Classification System (Darley *et al.*, 1969; Duffy, 1995). All of the hypokinetic phrases were characterized by a perceptually rapid speaking rate with monopitch and monoloudness; little use of variation in pitch or loudness to achieve differential syllabic stress; imprecise articulation that gives the impression of a blurring of phonemes and syllables; and a breathy and perhaps hoarse/harsh voice. The ataxic phrases were characterized by a perceptually slow speaking rate with a tendency toward equal and even syllable duration (scanning speech); excessive loudness variation; and irregular articulatory breakdown.

These perceptual impressions of reduced syllabic strength (see Fear *et al.*, 1995) were corroborated by acoustic measures of phrase duration, strong-to-weak vowel duration calculations, vowel formant frequencies and point-vowel quadrilateral areas, and fundamental frequency and amplitude variation (see Liss *et al.*, 2000, Tables I and II). Briefly, the hypokinetic phrases were significantly shorter in duration than those of the ataxic or neurologically normal speakers; they had a significantly smaller range of fundamental frequency variation; and their vowel quadrilateral areas were 50% smaller than those of the normal speakers. This coincided with the perception of rapid and monotonous speech. The ataxic phrases were significantly longer in duration than those of the hypokinetic or neurologically normal speakers; their adjacent strong and weak vowel durations were of similar durations; and their vowel quadrilateral areas also were 50% smaller than those of the control speakers. This corroborated the perception of slow, equal, and even speech.

By design, the phrases on the two dysarthria tapes were of equivalent intelligibility. As reported in Liss *et al.* (2000), the mean words-correct score for the ataxic tape was 43.2% and the mean for the hypokinetic tape was 41.8%. This allowed differences in the dependent variables to be interpreted as arising from differences in speech production characteristics, specifically syllabic strength contrasts.

The phrases, modeled after Cutler and Butterfield (1992), were designed to permit the interpretation of LBE patterns. The phrases themselves were of low interword predictability to reduce the contribution of semantic information to word perception. They consisted of six syllables that alternated in phrasal stress patterns. Half of the phrases alternated strong–weak (SWSWSW), and the other half alternated weak–strong (WSWSWS). The majority of the strong and weak syllables contained full and reduced vowels, respectively. The phrases ranged in length from 3 to 5 words and no word contained more than two syllables. None of the words in the phrases was repeated except articles and auxiliary verbs; all English phonemes except /zh/ were represented.[2]

The stimulus audiotapes consisted of phrases produced by dysarthric speakers, each preceded by a neurologically normal female saying the phrase number, and followed by 12 seconds of silence in which to transcribe what had been heard. Each tape contained one production of the 60 phrases, 10 phrases per each of the six speakers in each group.

In addition to the data from the 60 core phrases, we wished to obtain information upon which to compare the effects of specific versus general familiarization with dysarthric speech. The 60 phrases provided data for specific familiarization effects, or benefits to the perception of hypokinetic or ataxic speech after being familiarized with hypokinetic or ataxic speech, respectively. To obtain a measure of more general effects, 20 phrases from the other dysarthria type were appended to the end of each 60-phrase tape. The 60 phrases of the hypokinetic speakers were followed by 20 phrases from the ataxic speakers; the 60 ataxic phrases were followed by 20 phrases from the hypokinetic speakers. Because the 20 phrases were a subset of the 60 phrases, it was necessary to minimize the possibility that listeners would recognize the phrases, thereby improving transcription performance. Thus, 20 low-intelligibility phrases were selected from the two dysarthria tapes. The 20 phrases were selected based on phrase-level intelligibility data acquired from Liss *et al.* (2000). The mean words-correct intelligibility scores of the 20 phrases were 18.0% and 18.2% for the hypokinetic and ataxic phrases, respectively.

In addition to the stimulus tapes, two familiarization tapes were constructed. Each of the hypokinetic and ataxic familiarization tapes contained 18 novel phrases, three from each of the six speakers. The familiarization phrases were identical to the test phrases in their syllabic strength alternation, low interword predictability, phoneme representation, and general composition. However, there was no phrase overlap between the stimulus and familiarization phrases.

TABLE II. Examples of coding lexical boundary errors from the listeners' transcriptions.[a]

Target phase	Listener response	Error type(s)
Younger rusty viewers	Younger rest if you are	IW, IW
The rally found some light	The real effects of light	IW, DS
Soon the men were asking	Cinnamon were asking	DW, DS
His display collects it	Hands did spray collected	IS, DW
Friendly slogans catch it	Fred eats slow with ketchup	IW, IW, DW
Govern proper landings	Car and prop for landings	IW, IW
Call a random voter	Coming from the motor	DW, IW
A term arranged inside	A turmoil raged inside	DW, IS
Convince the council here	In winds the cows will here	IS, IW
She describes a nuisance	Strangers cause a nuisance	DW, IS

[a]IS refers to insertion of a lexical boundary before a strong syllable; IW refers to insertion before a weak syllable. DS and DW refer to deletions of lexical boundaries before strong and weak syllables, respectively. The first five examples are from transcripts from the ataxic familiarized transcripts, and the second five are from hypokinetic familiarized transcripts.

D. Procedures

The listeners were seated in individual cubicles. The audiotapes were presented via the Tandberg Educational sound system in the ASU Language Laboratory over high quality Tandberg supra-aural headphones. Equivalent sound pressure levels across headphones were verified with a headphone coupler sound level meter (Quest 215 Sound Level Meter). Listeners were instructed to adjust the volume to a comfortable listening level (in 4 dB increments up or down) during the preliminary instructions. They were directed not to alter the volume once the stimulus phrases had begun. The listeners transcribed three practice phrases, which were read by a neurologically normal female speaker. Listeners who made more than one word-transcription error in the practice phrases would not be eligible for the study. No listeners were excluded by this criterion.

Prior to the transcription task, listeners in the two familiarization groups were given a list of the 18 familiarization phrases. They were asked to follow along carefully as the various speakers read the phrases. The listeners then received instructions for the transcription task. They were asked to listen to each phrase and to write down exactly what they heard. They were told that all phrases consisted of real words in the English language produced by several different male and female speakers. They were told that some of the phrases may be difficult to understand, but that they should guess if they did not know what the speaker was saying. They were told that if they could not venture a guess, they were to use a slash to indicate that part of the phrase they could not understand.

E. Analysis

The familiarization corpus consisted of 6400 phrase transcriptions (80 listeners×80 phrases). A words-correct score was calculated for each phrase as an index of intelligibility. A word was counted as correct when it exactly matched the target, or when it differed only by tense (-ed) or plural (-s) and did not add another syllable. Substitutions between "a" and "the" were also regarded as correct.[3] The percentages of words-correct were calculated for each listener and averaged within listening groups as indices of intelligibility. Intelligibility scores for the 60 phrases and the subset of 20 phrases were calculated separately.

Two trained judges (the first two authors) independently coded the listener transcripts for the presence and type of LBEs to obtain a corpus of errors identified and/or agreed upon by both judges. Lexical boundary violations were defined as erroneous insertions or deletions of lexical boundaries. These insertions or deletions were coded as occurring either before strong or before weak syllables (as determined by the target phrasal stress pattern of the phrase, SWSWSW or WSWSWS). Thus, four error types were possible: Insert boundary before a strong syllable (IS); insert boundary before a weak syllable (IW); delete boundary before a strong syllable (DS); and delete boundary before a weak syllable (DW). Each phrase had the possibility of containing more than one LBE.[4] Examples from the actual transcripts are provided in Table II.

Analyses of variance and post-hoc pairwise multiple comparisons were conducted to detect differences in mean intelligibility scores between and among groups (see Table I for comparisons of interest). Because 40 listeners were included in the familiarization groups as compared to the twenty listeners in the control groups, a conservative alpha of 0.001 was selected. This was intended to minimize the potential for an overpowered study, in which small between-group differences may attain statistical significance without being clinically (or perceptually) relevant. Chi-square procedures were conducted to determine the relationship between the variables of insert/delete and strong/weak for 10 sets of lexical boundary error data: 60-phrase control and familiarized; 20-phrase control, familiarized, and familiarized with other, for both sets of dysarthric speech.

In addition to the LBE proportion comparisons in the contingency tables, IS/IW and DW/DS ratios were calculated for all 10 sets of LBE data. These ratios permitted a comparison with previously published data regarding strength of adherence to predicted error patterns. Specifically, if listeners use the strategy of attending to syllabic strength to mark
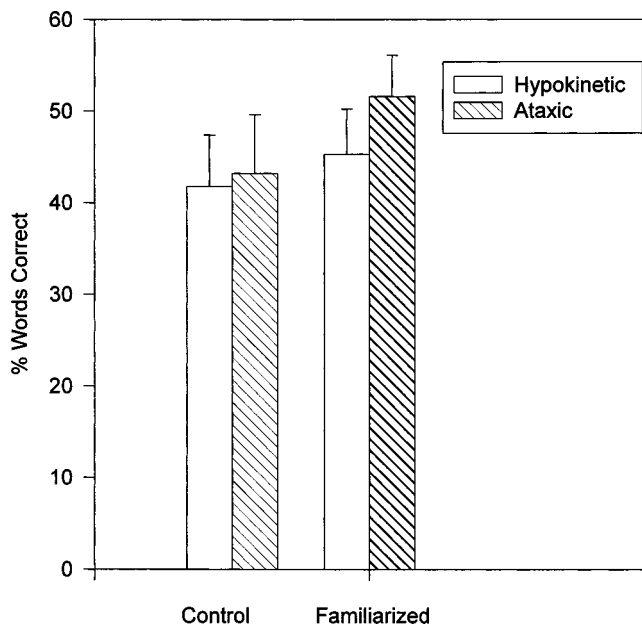
FIG. 1. Intelligibility scores for the 60 phrases. The first two bars show the mean (+1 standard deviation) for the control groups, and the second bars show the same values for the familiarized groups. Means of the hypokinetic familiarized and ataxic familiarized were significantly higher than their respective control group ($P<0.05$).

FIG. 2. Intelligibility scores for the 20-phrase subset. The first three bars show the mean (+1 standard deviation) for the control, familiarized, and familiarized with other conditions for the hypokinetic tape. The second three bars show the same information for the ataxic tape. For each tape, significant differences were found among all three conditions ($P<0.05$).

word boundaries in the connected acoustic stream, they will most likely erroneously insert lexical boundaries before strong syllables (IS), and delete them most often before weak syllables (DW). Ratio values of 1 indicate that insertions and deletions occur equally as often before strong and weak syllables. Therefore, the greater the positive distance from "1," the greater the strength of adherence to the predicted pattern. Between-group differences in median values among conditions were assessed by nonparametric Kruskal–Wallis one-way analysis of variance on ranks procedures.

III. RESULTS

A. Intelligibility

Figure 1 shows the mean percent words-correct intelligibility scores for each of the groups on the 60 phrases. A one-way analysis of variance showed significant differences among the means of the familiarized and nonfamiliarized listener groups [$F(3,116)=22.1$, $P<0.0001$]. The student–Newman–Keuls procedure indicated that both familiarized groups significantly outperformed the corresponding nonfamiliarized groups ($P<0.05$). The mean of the ataxic familiarized group was 51.6% (s.d.$=4.48$), which was significantly greater than that of the ataxic control group ($\underline{M}=43.2$, s.d.$=6.41$). The hypokinetic familiarized group mean was 45.3% (s.d.$=4.91$), which was significantly greater than that of the hypokinetic Control group ($\underline{M}=41.8$, s.d.$=5.58$).

The 20-phrase subset intelligibility means and standard deviations are shown Fig. 2. Three different values are presented for each of the two dysarthria tapes. The first bars for each dysarthria type correspond with the intelligibility score achieved by the control subjects from Liss *et al.* (2000). The second values correspond with the scores derived from the
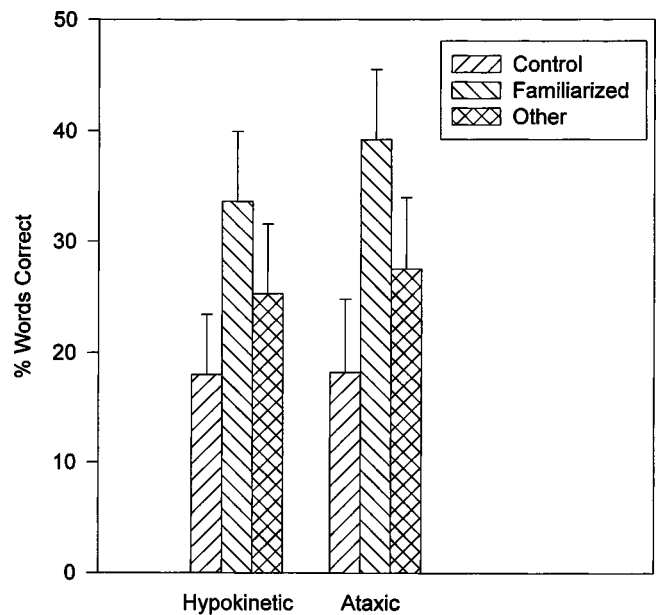
familiarization condition (familiarization). This is the percentage of words-correct for these 20 phrases (taken from the set of 60) when the listener had been familiarized with that particular dysarthria type. The third bars represent the percentage of words-correct on these 20 phrases when the listener had been familiarized with the *other* dysarthria type (other). Analyses of variance were significant at $P<0.001$ for both groups [$F(2,97)=45.899$ for hypokinetic; $F(2,97)=76.795$ for ataxic]. Post-hoc analysis showed significant differences ($p<0.05$) for all pairwise comparisons within both hypokinetic and ataxic groups. Thus, for both types of dysarthric speech, the specific familiarization condition resulted in the highest score, followed by the general familiarization condition, followed by the no-familiarization condition.

B. Lexical boundary error pattern

Table III contains the total LBEs, the LBE category proportions thereof,[5] and the median IS/IW and DW/DS ratios

TABLE III. LBE totals, category proportions expressed in percentages, and median ratio values for each of the four listener groups for the 60 phrases.

	Total LBEs	%IS	%IW	%DS	%DW	Median IS/IW	Median DW/DS
Hypokinetic control ($N=20$)	820	47.1	27.4	9.0	16.5	1.75	1.83
Hypokinetic familiarized ($N=40$)	1633	44.9	27.1	10.3	17.6	1.56	1.75
Ataxic control ($N=20$)	610	40.5	34.4	12.3	12.8	1.18	0.90
Ataxic familiarized ($N=40$)	1266	36.0	34.0	14.5	15.4	1.04	1.00

TABLE IV. LBE totals, category proportions expressed in percentages, and median ratio values for the 20-phrase subset for the hypokinetic tapes.

	Total LBEs	%IS	%IW	%DS	%DW	Median IS/IW	Median DW/DS
Control (N=20)	434	47.0	22.1	9.0	21.9	1.81	1.72
Familiarized (N=40)	710	39.1	30.0	12.7	18.2	1.56	1.75
Familiarized with other (N=40)	883	44.8	21.4	12.5	21.3	2.00	1.63

TABLE V. LBE totals, category proportions expressed in percentages, and median ratio values for the 20-phrase subset for the ataxic tapes.

	Total LBEs	%IS	%IW	%DW	%DS	Median IS/IW	Median DW/DS
Control (N=20)	284	39.1	34.5	12.3	14.1	1.05	1.08
Familiarized (N=40)	585	35.7	32.9	15.7	15.7	1.04	1.00
Familiarized with other (N=40)	744	35.9	35.6	12.6	15.9	1.00	1.00

for each of the four groups for the 60 phrases. Contingency tables were constructed for the LBEs for each of the familiarized listener groups to determine whether the variables of lexical boundary error type (i.e., insertion/deletion) and lexical boundary error location (i.e., before strong/weak syllable) were significantly related. Consistent with our previous report on the hypokinetic control (Liss *et al.*, 2000), chi-square results were significant for the data derived from the hypokinetic speech samples [hypokinetic familiarized, $\chi^2(1,N=4)=83.5$, $P<0.0001$]. That is, there was a significant relationship between LBE type and the locations in which the errors occurred. Erroneous lexical boundary insertions occurred more often before strong than before weak syllables, and erroneous lexical boundary deletions occurred more often before weak than before strong syllables. This was not the case for LBE pattern for the ataxic data. Consistent with our previous report on ataxic control, there was no statistically significant relationship between LBE type and location among the ataxic familiarization data [$\chi^2(1,N=4)=0.759$, $P=0.3838$].

The IS/IW and DW/DS ratios echo the chi-square findings, and offer a source of examining the strength of adherence to the predicted pattern of results both between and within dysarthria type. Because the ratio data were not normally distributed, Kruskal–Wallis ANOVA on Ranks procedures were performed on the two sets of ratio data. The median IS/IW ratios for the hypokinetic control and hypokinetic familiarization groups were significantly greater than those for the ataxic control and ataxic familiarization groups [$H(3)=40.4$, $P<0.0001$]. Similarly the median DW/DS ratios for the two hypokinetic groups were significantly greater than those for the two ataxic groups [$H(3)=19.9$, $P=0.0002$]. However, there were no significant differences between the median values of either the hypokinetic control and familiarization groups, or of the ataxic control and familiarization groups, according to Dunn's method of all pairwise multiple comparisons ($P<0.05$). Thus, both hypokinetic tapes elicited significantly higher strength of adherence values than did either of the two ataxic tapes.

Tables IV and V contain the LBE information for the 20-phrase subset taken from the control condition, the familiarized condition, and the familiarized with other condition. As with the data from the 60 phrases, significant relationships between LBE type and location were found for all data derived from the hypokinetic tapes as shown in Table IV [hypokinetic control, $\chi^2(1,N=4)=55.3$, $P<0.0001$; hypokinetic familiarized, $\chi^2(1,N=4)=14.0$, $P=0.0002$; famil-

iarized with other, $\chi^2(1,N=4)=75.2$; $P<0.0001$], but not for the LBE proportions derived from the ataxic tapes as shown in Table V [ataxic control, $\chi^2(1,N=4)=0.678$, $P=0.4104$; ataxic familiarized, $\chi^2(1,N=4)=0.15$, $P=0.6986$; familiarized with other, $\chi^2(1,N=4)=1.85$, $P=0.174$].

Kruskal–Wallis ANOVAs on ranks were conducted on ratio values within each of the dysarthria categories to identify specific versus general effects of familiarization in the subset of 20 phrases. No significant differences were found among control, familiarized, and familiarized with other for any of the ataxic data [IS/IW,$H(2)=2.45,P=0.029\,43$;DW/DS,$H(2)=2.05,P=0.3586$], nor for the hypokinetic data [$H(2)=6.33,P=0.0422$]. Thus, IS/IW and DW/DS ratios were similar and consistent within dysarthria subtype across all three conditions.

IV. DISCUSSION

The results of the present study demonstrate perceptual benefits of familiarization with dysarthric speech. However, these benefits were apparent only in intelligibility scores, and not in lexical boundary error patterns. In fact, the LBE results were remarkably consistent with the data from nonfamiliarized listeners, in which it appears that different patterns of dysarthria may differentially affect listeners' abilities to apply the MSS. If listeners had gleaned information about distinguishing strong and weak syllables in the two dysarthric speech patterns, LBE results should have reflected this. Although knowledge about prosodic patterns and syllabic stress manifestations may have benefited intelligibility, the absence of LBE differences suggests the familiarization procedure did not improve strong/weak syllable identification, but rather improved performance at some other (perhaps segmental) level.

The question of general and specific familiarization effects on intelligibility scores in dysarthria has significant clinical and theoretical implications. The familiarization procedure of the present investigation was very brief, just three phrases each from the six speakers with dysarthria who provided the stimulus phrases. It also required little active participation by the listeners. They simply were instructed to follow along with a written transcript of the 18 familiarization phrases as they listened. They were not instructed to listen for certain features or characteristics, nor were they even told the purpose of the procedure. Nonetheless, this brief and relatively passive experience resulted in significantly higher intelligibility scores for the familiarized groups

than those obtained by nonfamiliarized listeners. When the dysarthria of the familiarization procedure matched the dysarthria of the transcription task, the benefits were even greater.

Although the data cannot provide a definitive source for the intelligibility benefit, they do offer a number of clues. First, familiarization effects were not of the same magnitude for the two dysarthria subtypes. Transcriptions of both the hypokinetic and ataxic phrases evidenced familiarization effects, however the effects were greater for the ataxic speech. This is particularly compelling because the two dysarthria tapes were constructed to ensure equivalent intelligibility, and to ensure that each phrase was perceptually representative of the operational definitions of the respective dysarthria (Liss *et al.*, 2000). Thus, the 8.4% advantage for the ataxic tape can be compared directly to the clinically less impressive 3.5% advantage for the hypokinetic tape. Listeners who heard then transcribed ataxic speech benefited more from their exposure than did listeners who heard and then transcribed hypokinetic speech.

This pattern is even more robust in the subset of data from the 20 low-intelligibility phrases for which the familiarization procedure produced greater gains. The ataxic familiarized listeners who transcribed the ataxic phrases enjoyed a 21% advantage over those who were not familiarized, while the hypokinetic familiarized realized a 15.6% gain over those who transcribed the hypokinetic phrases without prior exposure to that particular dysarthria. In both of these cases, the benefit of being familiarized with the specific dysarthria was roughly double the intelligibility gain for the familiarized with other condition. Thus, the *general* benefit of exposure to dysarthric speech was of the same magnitude for transcribers of both dysarthric tapes, but the *specific* benefits were substantially higher for the ataxic familiarization group than for the hypokinetic familiarization group.

If only the intelligibility data were considered, it could only be concluded that *something* about exposure to the ataxic speech was disproportionately beneficial to listeners who transcribed the ataxic phrases. However, the second clue of LBE patterns allows us to speculate that the cognitive–perceptual source of benefit may not lie in the mapping of suprasegmental patterning. The LBE patterns elicited by the hypokinetic familiarized and ataxic familiarized conditions were nearly identical to those of the hypokinetic control and ataxic control, respectively. This finding is quite unexpected because it suggests that the phenomenon underlying the LBE patterns must be extraordinarily robust to persist across different listener groups and listening circumstances (see Cutler *et al.*, 1997). If the assumption is correct that LBE analysis offers a window to lexical segmentation strategies relative to syllabic strength, it must be concluded that this particular familiarization procedure did not facilitate recognition of syllabic strength contrasts. As in the previous study, listeners in the current study appeared to have less success applying this strategy to the ataxic speech than to the hypokinetic speech.

This points toward the possibility that the familiarization procedure allowed the listeners to map aspects of the degraded acoustic signal onto pre-existing phonological templates. This hypothesis has been explicated in the psycholinguistic literature (e.g., Dupoux and Green, 1997; Dupoux *et al.*, 2001; Francis *et al.*, 2000; Greenspan *et al.*, 1988) but empirical data from motor speech disorders are limited. Tjaden and Liss (1995) attempted to tease out the relative contributions of segmental and suprasegmental information in the familiarization process. Using the speech of a Korean woman with moderate–severe spastic–ataxic dysarthria secondary to cerebral palsy, they created two familiarization tapes. The first contained a paragraph, consisting of 12 six-word sentences, read by the woman. The second consisted of a list of all 72 words contained in the paragraph, but arranged in a random order and read as a word list. Thus the content of the two tapes was identical, but the paragraph tape provided listeners with sentence level prosodic and interword coarticulatory information not found in the word list. The task consisted of transcribing 48 six-word sentences produced by the woman. It was expected that the Paragraph group would obtain higher words-correct intelligibility scores than the other two groups because they would have received the most information relevant to the transcription task (see Greenspan *et al.*, 1988). However, the results demonstrated that although the two familiarized groups outperformed the control group, there was no significant performance difference between the Paragraph and Word groups. Although the high degree of variability in listener scores may have masked actual differences, perhaps the segmental information gleaned from both familiarization tapes accounted for the majority of familiarization benefit.

This possibility has some support in the psycholinguistic literature. The construct of perceptual adaptation is related to the process of familiarization in the present study, and has been the subject of a number of investigations with time-compressed speech. As listeners are exposed to a time-compressed speech signal, their ability to understand that signal improves to a point. This improvement is taken as evidence of perceptual adaptation to the distorted signal. Sebastián-Gallés and colleagues (2000) examined language-specific rhythmical, lexical, and phonological factors in perceptual adaptation to time-compressed speech. Their Spanish-speaking listeners transcribed time-compressed Spanish sentences after exposure to time-compressed speech of different languages. These listeners showed perceptual benefits only from prior exposure to time-compressed Spanish, and from Italian and French, which are rhythmically (syllable-timed) and phonologically similar to Spanish. The listeners did not demonstrate significant gains in intelligibility with exposure to the dissimilar languages of English (a stress-timed language) or Japanese (a mora-timed language). Moreover, a second experiment with time-compressed Greek (a syllable-timed but not a Romance language) revealed the effect was not simply one of lexical overlap or similarity between Spanish and Italian. They suggested that perceptual adaptation benefits derive not only from the similarity of language rhythm, but also from phonetic and phonologic similarity. This conclusion coincides with the work of Dupoux and Green (1997) who found robust and relatively long-term perceptual adaptation effects for time-compressed speech. They also concluded that the adaptation mechanism

Liss *et al.*: Familiarization and lexical segmentation in dysarthria

must contain a component of phonetic-to-phonological mapping.

Consistent with Sebastián-Gallés *et al.* (2000), the current data support the notion that the intelligibility decrement derives from both difficulty in decoding the rhythmic structure of the signal, and mapping the degraded acoustic phonetic information onto existing phonologic templates. In the current study, intelligibility was most improved when the prosodic and segmental features of the familiarization stimulus matched those of the transcription task. However, the LBE analysis indicates that the improvement cannot be attributed predominantly to knowledge about prosodic form, so a segmental explanation must be entertained. The data of the present report were not collected in a way to confirm a phonetic-to-phonologic adaptation mechanism, but some preliminary support is offered in a methodological paper from our laboratory that evaluated word substitution errors in a subset of these transcribed phrases. Spitzer *et al.* (2000) proposed an analysis method by which to capture evidence of the segmental benefits of the familiarization procedure. Twenty phrases transcribed by 34 listeners were analyzed for the presence of word substitution errors. Word substitutions were defined as whole words that did not violate the lexical boundaries or the syllabic constitution of the intended target words. The goal was to develop a classification scheme that would quantify phonemic preservation of either vowels or consonants within these word substitutions. It was hypothesized that if the familiarization procedure facilitates mapping of the degraded segmental information onto stored representations for phonemes, word substitutions should bear phonemic resemblance to the target word. The results from this preliminary analysis were encouraging. In this subset of phrases, more word substitutions from the familiarized groups bore phonemic resemblance to the target than did those word substitutions from the nonfamiliarized groups. Additionally, a dysarthria-specific difference was discovered. The word substitutions taken from transcriptions of the ataxic speech had significantly more phonetically related than nonphonetically related word substitutions. This difference was not found in the word substitutions elicited by the hypokinetic speech. Because such a small proportion of the full data set was examined in this methodological paper, the inconclusive findings for the hypokinetic speech are not particularly interpretable. However, the patterns of phoneme preservation elicited by the ataxic speech are consistent with the idea that familiarization improves the perceptual process of phonetic–phonologic mapping.

V. CONCLUSION

The present report offers additional evidence for the bidirectional relationship between the nature of the degraded signal and the cognitive–perceptual processes brought to bear on that signal (Lindblom, 1990). The LBE data suggest three important conclusions. First, consistent with our previous reports, it appears that syllabic strength contrasts are a source of information to listeners as they attempt to segment these types of dysarthric speech. Were this not the case, the LBE patterns would have been more closely aligned with chance, based on the number of opportunities to commit certain errors (in the case of this phrase set, deletions >insertions, IW>IS, and DS>DW). Second, the data are consistent with the notion that the form of the prosodic disturbance offers differential challenge to the application of the MSS. As in our previous report, there was no difference between error location for either erroneous insertions or deletions for the ataxic speech (IS=IW;DW=DS). Third, the level and type of familiarization provided herein did not convey sufficient knowledge about syllabic strength contrastivity to facilitate the application of a metrical segmentation type of strategy. Nonetheless, the familiarized listeners obtained higher intelligibility scores than those who did not receive familiarization, and a dysarthria-specific effect was evident. Thus, it can be hypothesized that intelligibility decrements may arise from inefficient processing of the degraded segmental and suprasegmental aspects of the signal, but this familiarization process differentially facilitates the cognitive–perceptual process of mapping the degraded segmental information onto existing phonological categories.

The study of naturally degraded speech offers ecological validity, but is replete with its own set of limitations. Although the two dysarthria tapes were of equivalent intelligibility and each phrase was representative of the corresponding dysarthria, the specific articulatory deficits varied across speakers both between and within groups. Some speakers may have had more consistent articulatory errors than others, making it conceivably easier to "break the code" during the brief familiarization procedure. It is not possible with these natural speech samples to control for critical acoustic features that would allow us to draw firm conclusions about the cognitive mechanisms underlying the perception of dysarthric speech. However, the data are a springboard for constructing controlled experiments with (re)synthesized samples, perhaps emulating the various syllabic contrastivity differences between the two dysarthria subtypes.

There are several aspects of the study design that call for caution in the interpretation of the data. The 20 phrases of the familiarization with other condition were not novel, as the listeners had transcribed them as part of the 60 phrase familiarization list. Because listeners understood very little of the phrases in the original exposure (18% of words), we expected that perceptual benefits would be minimal. Our design did not permit us to ascertain the relative contributions of this prior exposure to the phrases and exposure to the dysarthric speech. However, the pattern of data does support our interpretation of a dysarthria-specific benefit to perception. Rather than a uniform benefit that might be predicted from prior exposure to phrases that were 18% intelligible, a differential benefit to the ataxic phrases was discovered. Future experiments may control for such possible confounds by ensuring that phrases across conditions do not overlap, or overlap in controlled and systematic ways.

Interpretive power would be additionally strengthened by including a more extensive nondysarthric familiarization procedure for the control group. These listeners did hear a three-phrase practice series recorded by a neurologically normal speaker, which consisted of low-predictability phrases similar to the stimulus phrases. However, they did not hear 18 phrases, as did the familiarization groups. This step would

have permitted us to identify any perceptual improvements afforded by simply learning more about the nature of the phrases, separate from the influences of exposure to dysarthric speech.

Finally, the familiarization procedure of the present study was brief and relatively passive. It is likely that more impressive gains in intelligibility, and perhaps evidence of more efficient application of the MSS, can be realized with more extensive familiarization procedures (Francis *et al.*, 2000). A paradigm in which different types of information are offered may shed light on the dysarthria-specific findings of the present (and previous) studies. In addition, the 15–20 % intelligibility advantage evidenced in the low intelligibility phrases strongly supports the integration of familiarization procedures in motor speech disorders clinical practice.

ACKNOWLEDGMENTS

[1]To ensure a sufficient number of errors for the LBE analyses of the 20-phrase subset, 40 listeners were recruited for the familiarization groups (as compared to 20 for the groups from the previous investigations).

[2]A list of the phrases is available electronically from the first author.

[3]The same criteria for words-correct were applied in all published studies related to the larger investigation (Liss *et al.*, 1998; Liss *et al.*, 2000; Spitzer *et al.*, 2000).

[4]The opportunities for producing the different types of LBEs were not equal, however are representative of the opportunities generally available in the English language (Cutler and Carter, 1987). Please refer to Liss *et al.* (2000) for a breakdown of the possible error sites in this set of phrases.

[5]The data from the two control conditions were reported in Liss *et al.* (2000) and are provided here for ease of comparison.

Cutler, A., and Butterfield, S. (**1992**). ''Rhythmic cues to speech segmentation: Evidence from juncture misperception,'' J. Mem. Lang. **31**, 218–236.

Cutler, A., and Carter, D. M. (**1987**). ''The predominance of strong syllables in the English vocabulary,'' Comput. Speech Lang. **2**, 133–142.

Cutler, A., Dahan, D., and van Donselaar, W. (**1997**). ''Prosody in the comprehension of spoken language: A literature review,'' Lang. Speech **40**, 141–201.

Cutler, A., and Norris, D. (**1988**). ''The role of strong syllables in segmentation for lexical access,'' J. Exp. Psychol. Hum. Percept. Perform. **14**, 113–121.

Dagenais, P. A., Watts, C. R., Tarnage, L. M., and Kennedy, S. (**1999**). ''Intelligibility—acceptability of moderately dysarthric speech by three types of listeners,'' J. Med. Speech-Lang. Path. **7**, 91–96.

Darley, F., Aronson, A., and Brown, J. (**1969**). ''Differential diagnostic patterns of dysarthria,'' J. Speech Hear. Res. **12**, 246–269.

DePaul, R., and Kent, R. D. (**2000**). ''A longitudinal case study of ALS: Effects of listener familiarity and proficiency on intelligibility judgements,'' Am J. Speech-Lang. Path **9**, 230–240.

Duffy, J. R. (**1995**). *Motor Speech Disorders* (Mosby, St. Louis).

Dupoux, E., and Green, K. (**1997**). ''Perceptual adjustments to highly compressed speech: Effects of talker and rate changes,'' J. Exp. Psychol. Hum. Percept. Perform. **23**, 914–927.

Dupoux, E., Pallier, C., Kakehi, K., and Mehler, J. (**2001**). ''New evidence for prelexical phonological processing in word recognition,'' Language Cognitive Processes **16**, 491–505.

Fear, B. D., Cutler, A., and Butterfield, S. (**1995**). ''The strong/weak syllable distinction in English,'' J. Acoust. Soc. Am. **97**, 1893–1904.

Flipsen, P. J. (**1995**). ''Speaker-listener familiarity: Parents as judges of delayed speech intelligibility,'' J. Commun. Dis. **28**, 3–19.

Francis, A. L., Baldwin, K., and Nusbaum, H. C. (**2000**). ''Effects of training on attention to acoustic cues,'' Percept. Psychophys. **62**, 1668–1680.

Greenspan, S. L., Nusbaum, H. C., and Pisoni, D. B. (**1988**). ''Perceptual learning of synthetic speech produced by rule,'' J. Exp. Psychol. Learn. Mem. Cogn. **14**, 421–433.

Guenther, F. H., Husain, F. T., Cohen, M. A., and Shinn-Cunningham, B. G. (**1999**). ''Effects of categorization and discrimination training on auditory perceptual space,'' J. Acoust. Soc. Am. **106**, 2900–2912.

Lehiste, I. (**1972**). ''The timing of utterances and linguistic boundaries,'' J. Acoust. Soc. Am. **51**, 2018–2024.

Lindblom, B. (**1990**). ''Explaining phonetic variation: A sketch of the H and H theory,'' in *Speech Production and Speech Modeling*, edited by W. J. Hardcastle and A. Marchal (Kluwer Academic, The Netherlands), pp. 403–439.

Liss, J. M., Spitzer, S. M., Caviness, J. N., Adler, C., and Edwards, B. (**1998**). ''Syllabic strength and lexical boundary decisions in the perception of hypokinetic dysarthric speech,'' J. Acoust. Soc. Am. **104**, 2457–2466.

Liss, J. M., Spitzer, S. M., Caviness, J. N., and Adler, C. A. (**2000**). ''Lexical boundary decisions in the perception of hypokinetic and ataxic dysarthric speech,'' J. Acoust. Soc. Am. **107**, 3415–3424.

Logan, J. S., Lively, S. E., and Pisoni, D. B. (**1991**). ''Training Japanese listeners to identify English /r/ and /l/: A first report,'' J. Acoust. Soc. Am. **82**, 874–885.

McQueen, J. M., and Cutler, A. (**2001**). ''Spoken word access processes: An introduction,'' Language Cognitive Processes **16**, 469–490.

Munro, M. J., and Derwing, T. M. (**1995**). ''Processing time, accent, and comprehensibility in the perception of native and foreign-accented speech,'' Lang. Speech **38**, 289–306.

Nakatani, L. H., and Schaffer, J. A. (**1978**). ''Hearing ''words'' without words: Prosodic cues for word perception,'' J. Acoust. Soc. Am. **63**, 234–245.

Pisoni, D. B., Manous, L. M., and Dedina, M. J. (**1987**). ''Comprehension of natural and synthetic speech: effects of predictability on the verification of sentences controlled for intelligibility,'' Comput. Speech Lang. **2**, 303–320.

Robinson, K., and Summerfield, A. Q. (**1996**). ''Adult auditory learning and training,'' Ear Hear. **17**, 51S–65S.

Rosen, S., Faulkner, A., and Wilkinson, L. (**1999**). ''Adaptation by normal listeners to upward spectral shifts of speech: Implications for cochlear implants,'' J. Acoust. Soc. Am. **106**, 3629–3636.

Schwab, E. C., Nusbaum, H. C., and Pisoni, D. B. (**1985**). ''Some effects of training on the perception of synthetic speech,'' Hum. Factors **27**, 395–4081.

Sebastián-Gallés, N., Dupoux, E., Costa, A., and Mehler, J. (**2000**). ''Adaptation to time-compressed speech: Phonological determinants,'' Percept. Psychophys. **62**, 834–842.

Spitzer, S. M., Liss, J. M., Caviness, J. N., and Adler, C. (**2000**). ''An exploration of familiarization effects in the perception of hypokinetic and ataxic dysarthric speech,'' J. Med. Speech-Lang. Path **8**, 285–293.

Tjaden, K. K., and Liss, J. M. (**1995**). ''The role of listener familiarity in the perception of dysarthric speech,'' Clin. Ling. Phon. **9**, 139–154.

Tremblay, K., Kraus, N., Carrell, T. D., and McGee, T. (**1997**). ''Central auditory system plasticity: Generalization to novel stimuli following listening training,'' J. Acoust. Soc. Am. **102**, 3762–3773.

Yorkston, K. M., and Beukelman, D. R. (**1983**). ''The influence of judge familiarization with the speaker on dysarthric speech intelligibility,'' in *Clinical Dysarthria*, edited by W. Berry (College-Hill Press, San Diego, CA), pp. 155–164.

An alternative to the traveling-wave approach for use in two-port descriptions of acoustic bores

Eric Ducasse[a)]

École Nationale Supérieure d'Arts et Métiers, C.E.R. de Bordeaux-Talence, 33405 Talence Cedex, France

For more than a decade, the digital waveguide model for musical instruments has been improved through the simulation of cylindrical and conical bores. But several difficulties remain, such as instabilities due to growing exponentials which appear when two conical bores are connected with decreasing taper. In this paper, an alternative overcoming these difficulties is proposed and can be extended to shapes other than cylinders, cones, and hyperbolic horns. A two-port model with more general state variables than usual traveling waves works efficiently for any shape without discontinuities in cross section. The equations for connecting separate elements at discontinuities make this two-port model appropriate for use in time domain simulation of the physical behavior of the wind instrument and its interactions with the player. The potential of this new approach is illustrated by several detailed examples. © *2002 Acoustical Society of America.*
[DOI: 10.1121/1.1515734]

PACS numbers: 43.75.Ef, 43.60.Gk [NHF]

I. INTRODUCTION

Two decades ago, sound synthesis by physical modeling of musical instruments was at an embryonic stage,[1,2] though already raising high expectations. Since the end of the 1980s,[3,4] this method of sound synthesis has improved steadily, computers have become faster and faster, and nowadays, commercial products based on this technology are available. In 1996, Smith[5] summed up the situation in this domain of research and pointed out several difficulties. To create a physical model of a wind instrument, a suitable model of a bore with varying cross section needs to be implemented. In this context, previous descriptions of wind instruments are briefly reviewed, separated into two groups.

The first approach considers a wind instrument to be composed of a nonlinear excitation mechanism (the mouthpiece) and of a resonator (the body) which is a linear element. The resonator is completely characterized by either its reflection function or its input impedance.[6–12] This *lumped* approach, which gives precise results and a good match between experiments and theory for a given note, has a disadvantage: the properties of the resonator are fixed. Thus, simulations close to real playing situations, including realistic transients between several notes, are difficult to obtain. For instance, the dynamic closing of tone-holes by fingers or keys, or the motion of a trombone slide, are not simulated.

For sound synthesis, the relationship between the player and the instrument needs to be taken into account,[4,13–17] including the actions of lips, tongue, blown air, and fingers. A *distributed* approach is generally used. Because modularity is a key to this second approach—a wind instrument is composed of a mouthpiece, tubes, tone-holes, a slide, a bell, etc.—a tube has to be modeled as an element which can be connected at both ends to other elements. In this approach, piecewise element modeling techniques are generally employed for acoustic bores with varying cross section. Each element is a two-port which can be seen as a *waveguide* provided it is either a cylinder, a truncated cone, or a hyperbolic horn. It has been shown that in a cylindrical bore, the acoustical pressure wave is the sum of two traveling plane waves which propagate in opposite directions; the same holds for a conical bore with two traveling spherical waves.[6,8] Further, previous works show[18] that in cylindrical and hyperbolic bores, "*flow waves propagate without dispersion.*" Thus, "*A convenient model of a waveguide* [can also be built] *using piecewise hyperbolic elements.*"[18] In the context of a step by step calculation in discrete time domain, this approach gives the *digital waveguide*[4] model which is used by almost all the authors.[4,13–23] This method is efficient due to its very low computational load.

The digital waveguide model was first conceived for a cylindrical bore without losses.[4] It has been progressively improved by the addition of fractional delays,[24,23,25] viscothermal losses, and conical bores.[13–23] Nevertheless, difficulties are encountered as soon as the bore is noncylindrical.[9] The connecting equations with separate elements are indeed rather complicated, showing integral terms that may generate growing exponentials, for instance in the case of two conical bores connected with "*a decreasing taper.*"[10] From another point of view,[18] these instability phenomena correspond to the existence of "*trapped modes*" in addition to normal "*traveling modes.*"

In this paper, Sec. II summarizes the traveling-wave approach and points out the sources of instabilities in models using piecewise element techniques for waveguides. Section III presents a new stable two-port which is usable not only for cylinders, truncated cones, and hyperbolic horns but also for tubes of arbitrarily varying cross section. Finally, detailed examples illustrating the potential of this model are given in Sec. IV.

a)Electronic mail: eric.ducasse@bordeaux.ensam.fr

II. INSTABILITIES IN WAVEGUIDE MODELING

A. Traveling signals in lossless bores

1. Pressure waves in cylindrical and conical bores

In a bore with varying cross section, a commonly used model for lossless propagation is based on the following equation, usually named the "*Horn Equation*:" [26–30]

$$\frac{\partial^2 p}{\partial x^2} - \frac{1}{c^2}\frac{\partial^2 p}{\partial t^2} = \frac{-S'(x)}{S(x)}\frac{\partial p}{\partial x}, \tag{1}$$

where p is the mean acoustic pressure in a cross-section S of the bore, depending on abscissa x and time t, and c the sound speed (usually 340 m s^{-1}). It is assumed that the wave fronts are planar and that the bore is relatively wide.

After the transformation $p(x,t) = [S(x)]^{-1/2} \psi(x,t)$, Eq. (1) becomes

$$\frac{\partial^2 \psi}{\partial x^2} - \frac{1}{c^2}\frac{\partial^2 \psi}{\partial t^2} = \frac{1}{\sqrt{S(x)}}\frac{\partial^2 \sqrt{S(x)}}{\partial x^2}\psi. \tag{2}$$

When the second term of Eq. (2) is zero, mainly in the case of either a cylinder or a truncated cone, Eq. (2) becomes the standard wave equation, the solution of which is the sum of two traveling waves, giving

$$p(x,t) = \frac{\psi^+(x-c\,t)}{\sqrt{S(x)}} + \frac{\psi^-(x+c\,t)}{\sqrt{S(x)}}. \tag{3}$$

Using a common approximation for the Euler equation, where u is the acoustic volume velocity through cross-section $S(x)$, and ρ_0 the air mean density (usually 1.21 kg m^{-3}):

$$\rho_0 \frac{\partial u}{\partial t} + S(x)\frac{\partial p}{\partial x} = 0. \tag{4}$$

Equations (3) and (4) now give the volume velocity u:

$$u(x,t) = \frac{S(x)}{\rho_0 c}\left[\frac{\psi^+(x-c\,t) - \psi^-(x+c\,t)}{\sqrt{S(x)}}\right.$$
$$\left. + \frac{c\,S'(x)}{2\,S(x)}\int_{-\infty}^{t} p(x,\sigma)\,d\sigma\right]. \tag{5}$$

2. Volume velocity waves in cylindrical and hyperbolic bores

Similarly, a "*Horn Equation for volume velocity*" can be given [Ref. 18, Eq. (3.126)]:

$$\frac{\partial^2 u}{\partial x^2} - \frac{1}{c^2}\frac{\partial^2 u}{\partial t^2} = \frac{S'(x)}{S(x)}\frac{\partial u}{\partial x}. \tag{6}$$

After the transformation $u(x,t) = \sqrt{S(x)}\,\phi(x,t)$, Eq. (6) becomes [Ref. 18, Eq. (3.137)]

$$\frac{\partial^2 \phi}{\partial x^2} - \frac{1}{c^2}\frac{\partial^2 \phi}{\partial t^2} = \sqrt{S(x)}\frac{\partial^2 [S(x)^{-1/2}]}{\partial x^2}\phi. \tag{7}$$

In the case of either a cylinder or a hyperbolic horn, the solution of Eq. (7) is the sum of two traveling waves which gives

$$u(x,t) = \sqrt{S(x)}\,\phi^+(x-c\,t) + \sqrt{S(x)}\,\phi^-(x+c\,t). \tag{8}$$

The mass conservation law being

$$S(x)\frac{\partial p}{\partial t} + c^2\rho_0\frac{\partial u}{\partial x} = 0, \tag{9}$$

the acoustic pressure can be deduced:

$$p(x,t) = \frac{\rho_0 c}{S(x)}\left(\sqrt{S(x)}\,(\phi^+(x-c\,t) - \phi^-(x+c\,t))\right.$$
$$\left. - \frac{c\,S'(x)}{2\,S(x)}\int_{-\infty}^{t} u(x,\sigma)\,d\sigma\right). \tag{10}$$

A numerical model using digital waveguides in conjunction with a decomposition into a pair of traveling waves is deduced from Eqs. (3) and (5) when the air column is cylindrical or conical, or from Eqs. (8) and (10) when the air column is hyperbolic.

B. Description of the waveguide model

Consider both ends ($x=0$ and $x=L$) of a conical bore. Substituting $q^+(x,t)$ and $q^-(x,t)$ for $[S(x)^{-1/2}]\psi^+(x-c\,t)$ and $[S(x)^{-1/2}]\psi^-(x+c\,t)$, respectively, Eqs. (3) and (5) become

$$q^+(L,t) = \frac{1}{\zeta}q^+(0,t-\tau),$$

$$q^-(0,t) = \zeta\,q^-(L,t-\tau),$$

$$p(0,t) = q^+(0,t) + q^-(0,t),$$

$$u(0,t) = \frac{S(0)}{\rho_0 c}\left[q^+(0,t) - q^-(0,t)\right.$$

$$\left. + \frac{c\,S'(0)}{2\,S(0)}\int_{-\infty}^{t} p(0,\sigma)\,d\sigma\right],$$

$$p(L,t) = q^+(L,t) + q^-(L,t),$$

$$u(L,t) = \frac{S(L)}{\rho_0 c}\left[q^+(L,t) - q^-(L,t)\right.$$

$$\left. + \frac{c\,S'(L)}{2\,S(L)}\int_{-\infty}^{t} p(L,\sigma)\,d\sigma\right], \tag{11}$$

where L is the length of the tube, $\tau = L/c$ the propagation delay between the extremities, and $\zeta = [S(L)/S(0)]^{1/2}$ the radii ratio.

The first two equations of system (11) define a waveguide filter including a double delay line and radius correctors.[31] These equations constitute the uniform transmission-line and transformer components of Fig. 1. Visco-thermal losses can be lumped in additional filters. The transfer function of these filters is $G(s) = \exp(-\beta L \sqrt{s}/r)$ for cylindrical tubes,[32,33,20] where s is the complex variable of the Laplace transformation, $r = \sqrt{S/\pi}$ the radius, $\beta = [\sqrt{l_v} + (\gamma-1)\sqrt{l_t}]/\sqrt{c}$ (usually 1.6×10^{-5} s$^{1/2}$) a constant representing the visco-thermal effects, γ the ratio of specific heats, l_v and l_t the characteristic lengths of the viscous and thermal effects, e.g., Refs. 7, 34, 35, 33, and 11. It
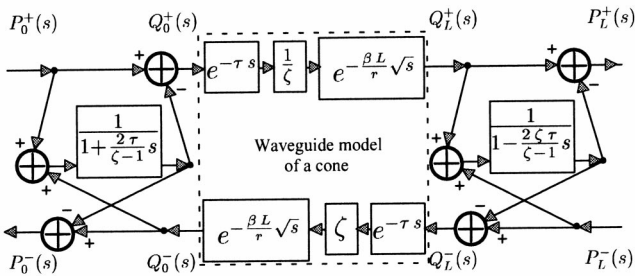
FIG. 1. Block diagram of a conical bore where both the usual waveguide state variables q^+, q^- and the new state variables p^+, p^- can be observed.

can be extended to truncated cones by taking r as an equivalent radius {e.g.,[14] $r = (r_L - r_0) [\log(r_L/r_0)]^{-1}$ where r_0 and r_L are the radii at the two ends}.

The integral terms[36,14] in system (11) explain the instabilities encountered in the case of conical bores, as detailed in Sec. II C.

Similarly, a waveguide model of a hyperbolic bore can be defined by substituting $q^+(x,t)$ and $q^-(x,t)$, respectively, for $\sqrt{S(x)}\,\phi^+(x - c\,t)$ and $\sqrt{S(x)}\,\phi^-(x + c\,t)$. Integral terms appear in this case also.

C. Instabilities in a junction of two conical tubes

The instability phenomena associated with conical bores have been demonstrated through various approaches.[5,10,21,18,37] In the case of two conical tubes connected with a continuous radius (cf. Fig. 2), continuity of mean pressure, conservation of volume velocity, and system (11) give after a Laplace transform:

$$Q_{\text{left}}^+(s) + Q_{\text{left}}^-(s) = Q_{\text{right}}^+(s) + Q_{\text{right}}^-(s) = P_J(s),$$

$$Q_{\text{left}}^+(s) - Q_{\text{left}}^-(s) + \frac{c\,r_{\text{left}}'}{r_J\,s} P(s)$$
$$= Q_{\text{right}}^+(s) - Q_{\text{right}}^-(s) + \frac{c\,r_{\text{right}}'}{r_J\,s} P_J(s), \tag{12}$$

where $p_J(t)$ is the mean pressure at the junction, r' the taper (derivative of r with respect to x), and the following convention is adopted: if w is a signal or a vector of signals, $W = \mathcal{L}(w)$ is its Laplace transform defined for all s by $W(s) = \int_{-\infty}^{+\infty} w(t)\,e^{-s\,t}\,dt$. The other quantities are defined in Fig. 2.

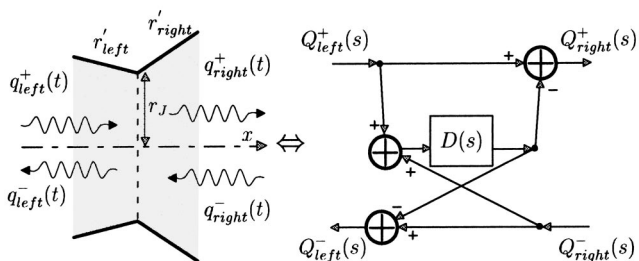If the taper is not continuous, Eq. (12) becomes

FIG. 2. A junction of two conical tubes with radius continuity and its block diagram. $D(s) = \{1 + 2\,r_J\,s/[c\,(r_{\text{right}}' - r_{\text{left}}')]\}^{-1}$ is the transmittance of a first-order filter which is unstable provided $r_{\text{right}}' < r_{\text{left}}'$.
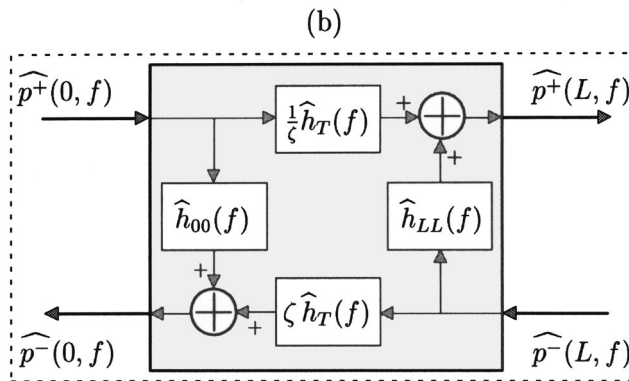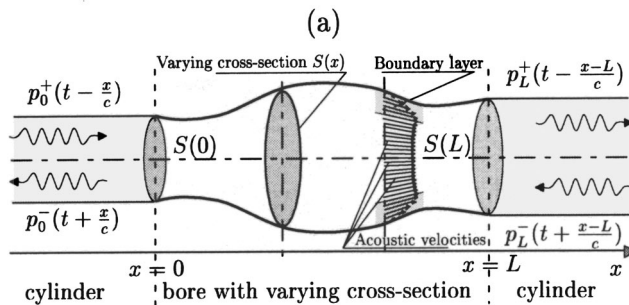

FIG. 3. (a) A bore with varying cross section. Both extremities of this bore are connected to cylinders without cross-section discontinuities. Each cylinder has an anechoic termination at its unconnected end. p_0^+, p_0^-, p_L^+, and p_L^- are traveling waves. The typical boundary layer in the air column is shown with the acoustic velocity distribution. (b) Block diagram of a two-port modeling the air column inside the main bore, with the inputs $p^+(0,t) = p_0^+(t)$ and $p^-(L,t) = p_L^-(t)$, and the outputs $p^-(0,t) = p_0^-(t)$ and $p^+(L,t) = p_L^+(t)$.

$$Q_{\text{left}}^-(s) = Q_{\text{right}}^-(s) - \left[1 + \frac{2\,r_J}{c\,(r_{\text{right}}' - r_{\text{left}}')}s\right]^{-1}$$
$$\times [Q_{\text{left}}^+(s) + Q_{\text{right}}^-(s)],$$

$$Q_{\text{right}}^+(s) = Q_{\text{left}}^+(s) - \left[1 + \frac{2\,r_J}{c\,(r_{\text{right}}' - r_{\text{left}}')}s\right]^{-1}$$
$$\times [Q_{\text{left}}^+(s) + Q_{\text{right}}^-(s)]. \tag{13}$$

Equation (13) can be translated into the block diagram of Fig. 2, containing a first-order filter.[21] This filter is stable for increasing taper ($r_{\text{right}}' > r_{\text{left}}'$) and unstable for decreasing taper ($r_{\text{right}}' < r_{\text{left}}'$), as shown in previous work.[10] Even if visco-thermal losses are introduced, instabilities remain.

Section III presents an alternative to the usual traveling-waves approach. This approach suppresses instabilities.

III. A TWO-PORT WITH PHYSICALLY OBTAINABLE TRAVELING WAVES AS INPUTS AND OUTPUTS

In this approach, traveling waves are not formulated inside the modeled bore. Instead they are formulated outside it, in cylinders which are connected to it so that the cross section is continuous [see Fig. 3(a)]. This lumped approach has already been used in the "*reflection function*" characterization of a resonator given by Schumacher:[1] when a cylinder with an anechoic termination at one end is connected to the
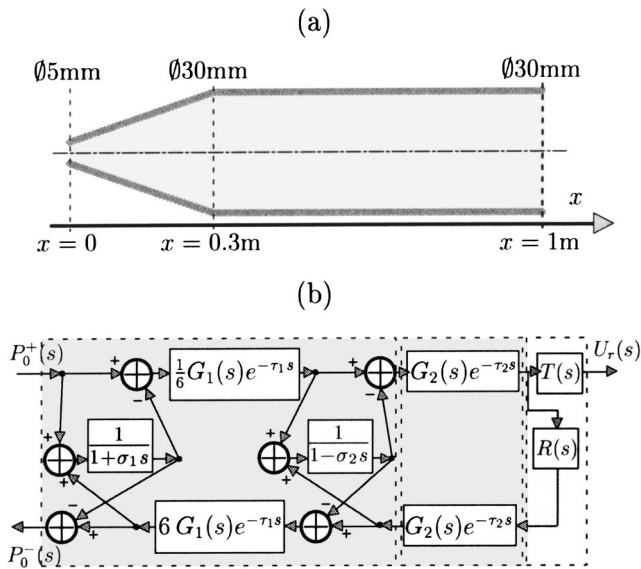
FIG. 4. (a) A bore built with a truncated cone and a cylinder (from Agulló *et al.*—Ref. 9, Fig. 10, p. 1611) and (b) its block diagram including the bell radiation.

input of the resonator with continuity of cross section, the reflection function corresponds to a reflected traveling wave which is the response of the resonator to an incoming impulse wave. This approach differs from the usual piecewise element modeling techniques. It has been already mentioned in Scavone[23] (pp. 119–123 and Fig. 3.25) to solve an example problem of instability. Since incoming and outgoing waves are physically obtainable in cylinders, with anechoic terminations at unconnected ends in this case, the modeled bore is necessarily seen as a passive two-port [see Fig. 3(b)] without any stability problem. It should be noticed that, in the "*traveling and trapped modes*" approach (Berners,[18] Sec. 3.1.3), trapped modes disappear as soon as the bore has cylindrical terminations at both ends.

A. Hypotheses

The following hypotheses are made:[11] the bore section is quasicircular; its area $S(x)$, which is not too small[33] ($\alpha = \beta c/(2\sqrt{S}\sqrt{f}) \ll 1$, where f is the frequency) or too large, is a continuous function with moderate variations [$S'(x)$ is defined almost everywhere and bounded]. The tube is also quasirectilinear or has only very smooth bends. Subject to these conditions we can adopt the plane wave approximation: the acoustic pressure p and velocity v are considered uniform over the section $S(x)$ as well as functions of abscissa x and time t. This is in fact the mean over the bore [cf. Fig. 3(a)] obtained by integration over the boundary layer.

B. Equations

The following system is adopted in accordance with Polack [Ref. 11, Eq. (41)]: the first equation is the mass conservation law where ρ is the acoustic density, the second one is an extended approximation of the Euler equation, and the last one is the equation of state for the air,

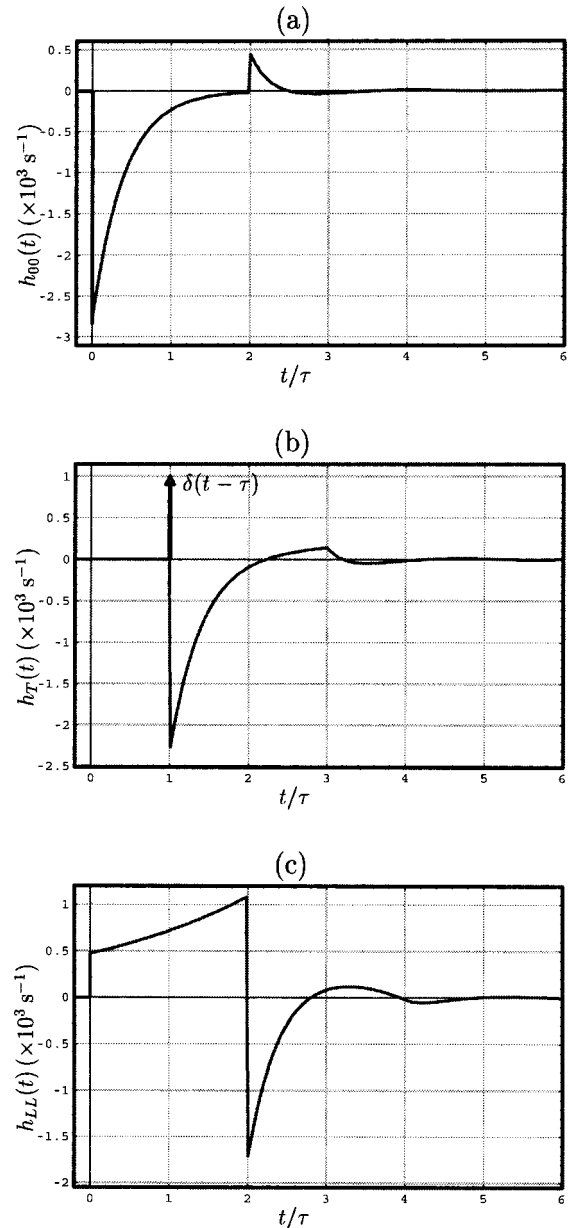$$S(x)\frac{\partial \rho}{\partial t} + \rho_0 \frac{\partial u}{\partial x} = 0,$$

FIG. 5. Continuous-time impulse responses [the calculation is made in Sec. III D, Eq. (30)] for the conical part of the bore which is given in Fig. 4. $\tau \approx 0.88$ ms and $\zeta = 6$.

$$\rho_0 \frac{\partial u}{\partial t} + 2\rho_0 c \sqrt{\frac{\pi}{S(x)}}\beta \frac{\partial^{1/2} u}{\partial t^{1/2}} + S(x)\frac{\partial p}{\partial x} = 0, \qquad (14)$$

$$p = c^2 \rho.$$

Two state variables are chosen to determine a numerical solution in the discrete time-domain. These state variables may differ from the ones used in traveling-wave approaches.

C. Choosing the suitable state variables

The choice of state variables, including input and output signals, is fundamental to a convenient description of a physical phenomenon. The following example shows how the effect of such a choice can explain phenomena like non-

causality or growing exponentials, as pointed out in previous studies.[9,18,37,38] Suitable state variables are then given for a bore with varying cross section.

1. Preliminary

Let a physical system be described by the following differential equation:

$$\frac{d\,w(t)}{dt} - 500\,w(t) = \frac{d\,v(t)}{dt} + 1500\,v(t)$$

$$\text{for all } t < 0, \quad v(t) = 0, \quad w(t) = 0. \tag{15}$$

Its input and output can *a priori* supposedly be chosen freely.

If v and w are, respectively, selected as input and output, the system is unstable because its impulse response h_1 contains a growing exponential:

$$h_1(t) = \delta(t) + 2000\,\epsilon(t)\,e^{+500t}, \tag{16}$$

where δ is the Dirac impulse pseudofunction[39] and ϵ the Heaviside step function.

On the contrary, if w is the input and v the output, the system is stable because its impulse response is

$$h_2(t) = \delta(t) - 2000\,\epsilon(t)\,e^{-1500t}. \tag{17}$$

It is also possible to take the input as $s_{\text{in}} = w + v$ and the output as $s_{\text{out}} = w - v$. Equation (15) becomes

$$\frac{d\,s_{\text{out}}(t)}{dt} + 500\,s_{\text{out}}(t) = 1000\,s_{\text{in}}(t)$$

$$\text{for all } t < 0, \quad s_{\text{in}}(t) = 0, \quad s_{\text{out}}(t) = 0. \tag{18}$$

In this third case, the physical phenomenon is modeled as a stable first-order system and its impulse response contains neither growing exponentials nor pseudofunctions. It can be noticed that in any case for a given input e_{in} and a given output s_1 and for any number a, the output modification $s_2(t) = s_1(t) + a\,e_{\text{in}}(t)$ changes neither the stability nor the characteristic time of the model.

This example emphasizes that stability is not intrinsic to a given physical phenomenon but notably depends on the choice of the input, which has to be physically obtainable. Pseudofunctions can generally be eliminated in the impulse response by modifying the output.

2. From the reflection function to a two-port model

The reflection function[1] h_r of a woodwind resonator verifies $p_0^- = h_r \star p_0^+$, where p_0^+ and p_0^- are traveling pressure waves in a lossless cylinder connected to the entrance of the resonator, with continuity of cross section [cf. the left half of Fig. 3(a)], and the operator $\star$ is the convolution (for all t, $(h_r \star p_0^+)(t) = \int_{-\infty}^{+\infty} h_r(t-\xi)\,p_0^+(\xi)\,d\xi$). The reflection function is necessarily stable for physical reasons (the resonator is a passive system and the input is physically obtainable) and can be considered as causal if the following hypothesis is laid down: we can neglect the thickness ε of the air slice between $x = -\varepsilon$ and $x = 0$ (in the cylinder, just before the entrance of the resonator) which is directly influenced by the resonator shape.

Following this idea, the state vector $P = \binom{p^+}{p^-}$ is chosen to describe the acoustic state of the air column, the signals p^+ and p^- being defined as follows:

$$p^+(x,t) = \frac{1}{2}\left[p(x,t) + \frac{\rho_0 c}{S(x)}\,u(x,t)\right],$$

$$p^-(x,t) = \frac{1}{2}\left[p(x,t) - \frac{\rho_0 c}{S(x)}\,u(x,t)\right], \tag{19}$$

$$p(x,t) = p^+(x,t) + p^-(x,t),$$

$$u(x,t) = \frac{S(x)}{\rho_0 c}\,[p^+(x,t) - p^-(x,t)]. \tag{20}$$

These signals are traveling waves only in the model of a cylindrical bore without losses, i.e., $p^+(x,t)$ can be written $p^+(x - c\,t)$ and $p^-(x,t)$, $p^-(x + c\,t)$. In any other case, p^+ and p^- are not traveling on the whole air column but can be qualified as "*locally traveling*" (in a slice of air of area S and infinitesimal thickness). The connecting equations of the bore with any other element of the instrument remain elementary (continuity of mean pressure and flow conservation) because of Eq. (20), similar to the last four equations of system (11) but without any integral term. Above all, the main advantage is that any piece of bore with a varying cross section can be modeled as a single two-port [cf. Fig. 3(b)], which is necessarily stable and causal for reasons similar to the reflection function case [cf. Fig. 3(a)].

After a Fourier transform, systems (14) and (20) give the following nonlinear differential system:

$$\frac{\partial}{\partial x}\hat{P}(x,f) = A[S(x),S'(x),f]\,\hat{P}(x,f), \tag{21}$$

where $\hat{P}(x,f)$ is the Fourier transform of the state vector P at the frequency f:

$$\hat{P}(x,f) = \begin{bmatrix} \widehat{p^+}(x,f) \\ \widehat{p^-}(x,f) \end{bmatrix} = \begin{bmatrix} \int_{-\infty}^{+\infty} p^+(x,t)\,e^{-2i\pi ft}\,dt \\ \int_{-\infty}^{+\infty} p^-(x,t)\,e^{-2i\pi ft}\,dt \end{bmatrix} \tag{22}$$

and

$$A(S,S',f) = \begin{bmatrix} \dfrac{-2i\pi f}{c} - \dfrac{(1+i)\,\beta\,\pi\,\sqrt{f}}{\sqrt{S}} - \dfrac{S'}{2S} & \dfrac{(1+i)\,\beta\,\pi\,\sqrt{f}}{\sqrt{S}} + \dfrac{S'}{2S} \\[3mm] \dfrac{-(1+i)\,\beta\,\pi\,\sqrt{f}}{\sqrt{S}} + \dfrac{S'}{2S} & \dfrac{2i\pi f}{c} + \dfrac{(1+i)\,\beta\,\pi\,\sqrt{f}}{\sqrt{S}} - \dfrac{S'}{2S} \end{bmatrix}. \tag{23}$$

Systems like Eq. (21) are generally solved by numerical techniques. The transfer matrix $T(f)=\begin{bmatrix} T_{11} & T_{12} \\ T_{21} & T_{22} \end{bmatrix}$ of the locally traveling waves, from the end at $x=0$ to that at $x=L$, verifies $\hat{P}(L,f)=T(f)\,\hat{P}(0,f)$ and can be deduced from Eqs. (21)–(23).

The scattering matrix $H(f)$ verifying $\begin{bmatrix} \widehat{p^-}(0,f) \\ \widehat{p^+}(L,f) \end{bmatrix}=H(f)\times\begin{bmatrix} \widehat{p^+}(0,f) \\ \widehat{p^-}(L,f) \end{bmatrix}$ is then deduced from the transfer matrix:

$$
H(f)=\begin{bmatrix} \hat{h}_{00}(f) & \hat{h}_{L0}(f) \\ \hat{h}_{0L}(f) & \hat{h}_{LL}(f) \end{bmatrix}
$$

$$
=\frac{1}{T_{22}}\begin{bmatrix} -T_{21} & 1 \\ T_{11}T_{22}-T_{12}T_{21} & T_{12} \end{bmatrix}, \tag{24}
$$

where h_{jk} is the impulse response from the end at $x=j$ to the end at $x=k$, $\hat{h}_{jk}$ its Fourier transform, and H_{jk} its Laplace transform.

In the scattering matrix, reciprocity implies the existence of a single transfer function $\hat{h}_T(f)$:

$$
\hat{h}_T(f)=\zeta\,\hat{h}_{0L}(f)=\frac{1}{\zeta}\hat{h}_{L0}(f). \tag{25}
$$

It has to be noticed that, in all simulated cases (see, e.g., Fig. 5), the four transmittances in the scattering matrix correspond to causal stable filters with fast-decreasing impulse responses, contrary to other methods.[9,37,38] Accordingly, the present method is promising for time-domain simulations, all the more so as usual techniques of transfer matrix calculation[7] can be used for complex resonators including discontinuities, side-holes, or higher modes.

In the case of a conical bore, it can be observed in Sec. III D that these new state variables suppress the instabilities pointed out previously.

D. How instabilities vanish in the waveguide model of a conical bore

The block diagram of a conical tube in the waveguide approach is only the middle element of the block diagram drawn in Fig. 1. In the present approach, the whole block diagram includes junctions with virtual external cylinders at both ends. On the left-hand side, $r_J=r_0$, $r'_{\text{left}}=0$, $r'_{\text{right}}=(\zeta-1)\,r_0/L$, and $D(s)=[1+2\,\tau s/(\zeta-1)]^{-1}$. On the right-hand side, $r_J=r_L$, $r'_{\text{left}}=(\zeta-1)\,r_L/(\zeta L)$, $r'_{\text{right}}=0$, and $D(s)=[1-2\,\zeta\,\tau s/(\zeta-1)]^{-1}$.

The scattering matrix of the conical tube is deduced from Fig. 1:

$$
H_{00}(s)
$$

$$
=\frac{(\zeta-1)\,[\,\zeta-1-2\zeta\,\tau s+(2\,\tau s-\zeta+1)G(s)^2\,e^{-2\tau s}]}{(2\zeta\,\tau s-\zeta+1)\,(2\,\tau s+\zeta-1)+(\zeta-1)^2 G(s)^2\,e^{-2\tau s}},
$$

$$
H_T(s)
$$

$$
=\frac{\zeta\,(2\tau s)^2\,G(s)\,e^{-\tau s}}{(2\zeta\,\tau s-\zeta+1)\,(2\,\tau s+\zeta-1)+(\zeta-1)^2 G(s)^2\,e^{-2\tau s}}, \tag{26}
$$

$$
H_{LL}(s)
$$

$$
=\frac{(\zeta-1)\,[2\,\tau s+\zeta-1-(2\zeta\,\tau s+\zeta-1)G(s)^2\,e^{-2\tau s}]}{(2\zeta\,\tau s-\zeta+1)\,(2\,\tau s+\zeta-1)+(\zeta-1)^2 G(s)^2\,e^{-2\tau s}}.
$$

If losses are ignored (i.e., $G(s)=1$), H_{00}, H_T, and H_{LL} are functions continuous at $s=0$: $H_{00}(0)=(1-\zeta^2)/(1+\zeta^2)$, $H_T(0)=2\zeta/(1+\zeta^2)$, and $H_{LL}(0)=(\zeta^2-1)/(1+\zeta^2)$. Each pole $(a+i\,b)/\tau$ $(a\neq0$ or $b\neq0)$ of H_{00}, H_T, or H_{LL} verifies

$$
(2\zeta a-\zeta+1+i\,2\zeta b)\,(2a+\zeta-1+i\,2b)
$$

$$
+(\zeta-1)^2\,e^{-2(a+i\,b)}=0, \tag{27}
$$

which implies

$$
\frac{\sin(2b)}{2b}=e^{2a}\left[1+\frac{4a\zeta}{(\zeta-1)^2}\right]. \tag{28}
$$

Consequently, $a<0$ and thus H_{00}, H_T, and H_{LL} are transmittances of stable filters. System (26) can be written:

$$
H_{00}(s)=\frac{\zeta-1}{1-\zeta-2\,\tau s}-4(\tau s)^2
$$

$$
\times\sum_{n=1}^{+\infty}\frac{(\zeta-1)^{2n-1}}{(\zeta-1+2\,\tau s)^{n+1}(s-1-2s\,\tau s)^n}\,e^{-2n\,\tau s},
$$

$$
H_T(s)=-4\zeta\,(\tau s)^2
$$

$$
\times\sum_{n=0}^{+\infty}\frac{(\zeta-1)^{2n}}{(\zeta-1+2\,\tau s)^{n+1}(s-1-2s\,\tau s)^{n+1}}
$$

$$
\times e^{-(2n+1)\,\tau s}, \tag{29}
$$

$$
H_{LL}(s)=\frac{1-\zeta}{\zeta-1-2\zeta\,\tau s}-4\zeta^2(\tau s)^2
$$

$$
\times\sum_{n=1}^{+\infty}\frac{(\zeta-1)^{2n-1}}{(\zeta-1+2\,\tau s)^n(s-1-2s\,\tau s)^{n+1}}\,e^{-2n\,\tau s}.
$$

The initial parts of the three causal impulse responses are deduced from Eq. (29) as follows:

$$
h_{00}(t)=\frac{1-\zeta}{2\tau}\exp\left[\frac{1-\zeta}{2\tau}t\right],\quad 0\leq t<2\tau
$$

$$
=\frac{\zeta-1}{4e\,\tau(1+\zeta)^2}\left\{2[e^\zeta(1+\zeta+\zeta^2)-e(1+\zeta)^2]\right.
$$

$$
-e^\zeta(\zeta^2-1)\frac{t}{\tau}\right\}\exp\left[\frac{1-\zeta}{2\tau}t\right]
$$

$$
+\frac{e^{(1-\zeta)/\zeta}(\zeta-1)}{2\tau\zeta(1+\zeta)^2}\exp\left[\frac{\zeta-1}{2\zeta\tau}t\right],
$$

$$
2\tau\leq t<4\tau\ldots\text{etc.,}
$$

$$
h_T(t)-\delta(t-\tau)=0,\quad 0\leq t<\tau
$$

$$
=\frac{e^{(\zeta-1)/2}\zeta\,(1-\zeta)}{2\tau\,(\zeta+1)}\exp\left[\frac{1-\zeta}{2\tau}t\right]
$$

$$
+\frac{e^{(1-\zeta)/(2\zeta)}(\zeta-1)}{2\tau\,\zeta\,(\zeta+1)}\exp\left[\frac{\zeta-1}{2\zeta\tau}t\right],
$$

$$
\tau\leq t<3\tau\ldots\text{etc.,} \tag{30}
$$

$$h_{LL}(t) = \frac{\zeta-1}{2\zeta\tau}\exp\left[\frac{\zeta-1}{2\zeta\tau}t\right], \quad 0 \leq t < 2\tau$$

$$= \frac{1-\zeta}{4e\,\zeta\,\tau(1+\zeta)^2}\left\{2[e^{1/\zeta}(1+\zeta+\zeta^2) - e(1+\zeta)^2]\right.$$

$$\left. + e^{1/\zeta}(\zeta^2-1)\frac{t}{\tau}\right\}\exp\left[\frac{\zeta-1}{2\zeta\tau}t\right]$$

$$+ \frac{e^{\zeta-1}\zeta^2(1-\zeta)}{2\tau(1+\zeta)^2}\exp\left[\frac{1-\zeta}{2\tau}t\right],$$

$$2\tau \leq t < 4\tau\ldots\text{etc.}$$

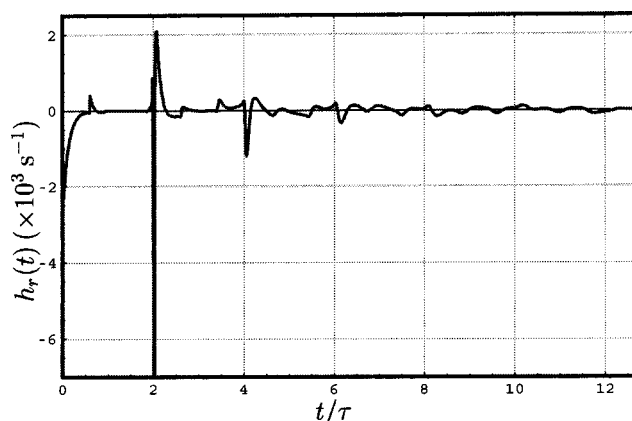A numerical example is given in the following.

FIG. 6. h_r, the reflection function of the bore (cf. Fig. 4) at its small end, with a reflection, at the other end, which is calculated by using the Levine and Schwinger formulas (Ref. 43). This function is completely calculated in the discrete time domain with causal digital finite impulse response filters which model the conical part of the bore, the cylindrical one and the radiation. The propagation delay between both ends is $\tau \approx 2.94$ ms.

IV. EXAMPLES

Three cases are chosen to show the potential of this improved two-port model: the first one, taken from Agulló et al.,[9] produces some instability effects using the traveling-wave approach[5] and includes cylindrical and conical tubes; the textbook case of the exponential horn follows; and finally, a complex profile of a trumpet bore taken from van Walstijn and Smith[17] is treated.

For a noncylindrical bore, the numerical determination of the transfer matrix at frequencies lying between 0 and $f_s/2$ (f_s is the sampling frequency) is made by the *fourth-order Runge–Kutta algorithm* with an auto-adaptive step[40] applied to Eqs. (21) and (23). This numerical method is computationally rather expensive but calculation has to be performed only once for a given bore. Exact and numerical calculations of the scattering matrix are compared in the following for both a conical bore and an exponential horn.

Digital filter design methods are numerous and generally pay great attention to the frequency response magnitude but do not take into account the phase which is very important in acoustic looped systems. As written in van Walstijn and Smith,[17] "*there is a need for more effective digital filter techniques in this context.*" Thus, basic weighted least-squares design for *finite impulse response* (FIR) digital filters[41–46] is used in these examples to obtain time domain responses. It is obvious that other efficient methods[17] of digital filter design can be used.

Reflection function calculation is performed entirely in the discrete time-domain, using the Levine and Schwinger formulas[47] to design a FIR digital filter for bell radiation[14] [cf. Fig. 4(b)].

A. Discrete time calculation of the reflection function of a cone–cylinder combination

As mentioned in Sec. I and shown in Sec. II C, when several bores are connected with "*decreasing widening rate*"[9] as in Fig. 4 taken from Agulló et al.[9] (Fig. 10), stability problems with growing exponentials appear in the usual models. With the improved two-port model, these stability artifacts vanish. The impulse responses h_{00}, h_T, and h_{LL} [cf. Eq. (30)] of the conical part of the bore are drawn in Fig. 5. The reflection function of the bore at its small end is drawn in Fig. 6.

Several observations can be made in Fig. 5 about the conical part. For a noncylindrical bore, it is qualitatively possible to consider, in an air slice of infinitesimal thickness dx, that every traveling wave has an infinitesimal reflection which is proportional to $-dS/S$. At the smaller end, the beginning of the impulse response h_{00} (reflection) is negative and increasing with t because $-dS/S$ is negative and increasing with x. For similar reasons, at the larger end, h_{LL} is positive and increasing between 0 ms and 2τ. Concerning the transmission impulse response after the τ-delayed perfect impulse δ, which is obtained in waveguide models without losses, an additional effect of the taper can be observed after τ. In frequency domain, good agreement appears in Fig. 7 between the waveguide and numerical techniques. Nevertheless, it seems that the equivalent radius technique[14] in the waveguide approach of conical bores overestimates the visco-thermal losses in both transmission and reflection at the larger end.

B. The exponential horn

Let an exponential horn be defined by the radius formulas $r(x) = r_0 \exp(\Lambda x/L)$ where $\Lambda = \log(\zeta)$. In this classical case, Eqs. (21) and (23) admit exact solutions, provided loss terms are neglected, and give the following transmittances in the scattering matrix:

$$H_{LL}(s) = -H_{00}(s) = \frac{\Lambda\left[1 - e^{-2\sqrt{(\tau s)^2 + \Lambda^2}}\right]}{\sqrt{(\tau s)^2 + \Lambda^2}\left[1 + e^{-2\sqrt{(\tau s)^2 + \Lambda^2}}\right] + \tau s\left[1 - e^{-2\sqrt{(\tau s)^2 + \Lambda^2}}\right]},$$

$$\text{(31)}$$

$$H_T(s) = \frac{2\sqrt{(\tau s)^2 + \Lambda^2}\, e^{-\sqrt{(\tau s)^2 + \Lambda^2}}}{\sqrt{(\tau s)^2 + \Lambda^2}\left[1 + e^{-2\sqrt{(\tau s)^2 + \Lambda^2}}\right] + \tau s\left[1 - e^{-2\sqrt{(\tau s)^2 + \Lambda^2}}\right]}.$$

A comparison between numerical calculation with losses and Eq. (31) is made in Fig. 8 for a horn of 68 cm length, 3
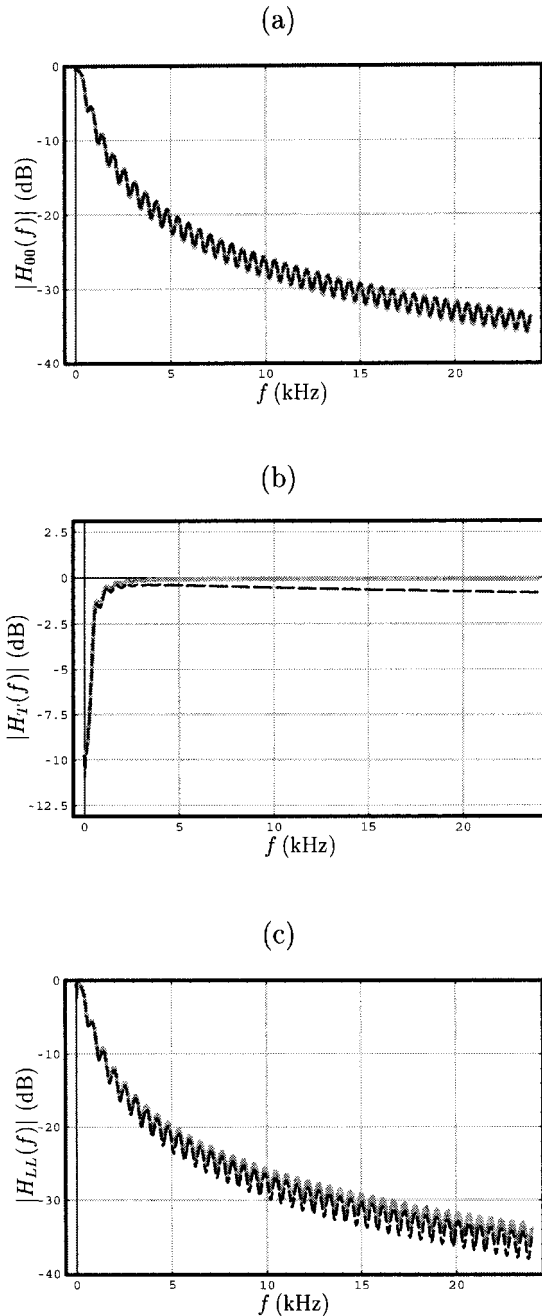
(a)

(b)

(c)

FIG. 7. Moduli of transmittance for the conical part of the bore shown in Fig. 4, according to the waveguide approach [cf. Sec. III D, Eq. (26), dashed line] and the numerically calculated one from Eqs. (21) and (23) (unbroken line).

mm and 3 cm radii ($\zeta = 10$ and $\tau = 2$ ms), with a good agreement. The observed cutoff frequency agrees with the expected value $f_c = \Lambda/(2\pi\tau) \approx 183.2$ Hz. In the time domain, the impulse responses can be given using the following property: the function defined for all s by $\left[(\sqrt{s^2 + \Lambda^2} - s)/\Lambda\right]^n$ is the Laplace transform of the signal $\mathcal{K}_n$ defined for all t by $\mathcal{K}_n(t) = (n/t)\, J_n(\Lambda t)\, \epsilon(t)$ provided n is a positive integer, where J_n is the Bessel function of the first kind.[48]

After the substitution of

$$\sum_{n=0}^{+\infty} \frac{(-1)^n \left[\sqrt{(\tau s)^2 + \Lambda^2} - \tau s\right]^{2n+1}}{\Lambda^{2n+2}}$$

$$\times e^{-2n\left[\sqrt{(\tau s)^2 + \Lambda^2} - \tau s\right]}\, e^{-2n\tau s}$$

$$\text{(32)}$$

for

$$\left\{\sqrt{(\tau s)^2 + \Lambda^2}\left[1 + e^{-2\sqrt{(\tau s)^2 + \Lambda^2}}\right]\right.$$

$$\left. + \tau s\left[1 - e^{-2\sqrt{(\tau s)^2 + \Lambda^2}}\right]\right\}^{-1},$$
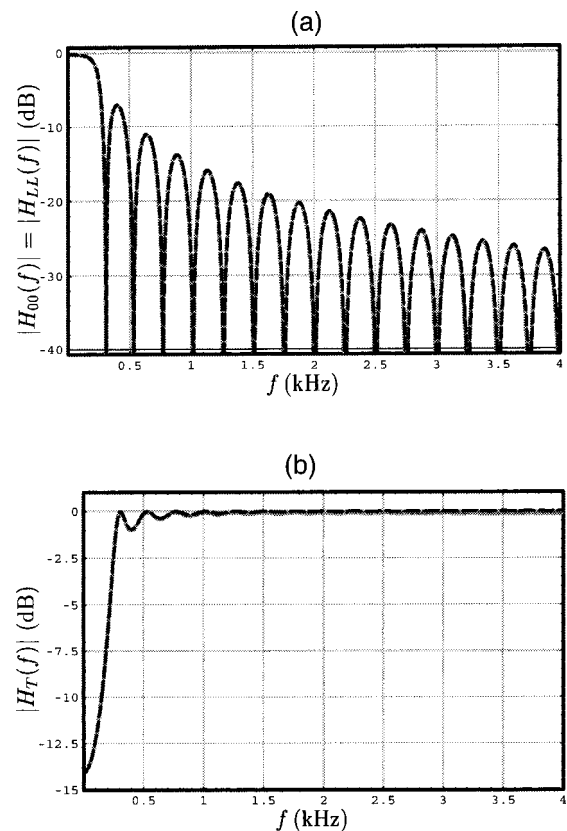
(a)

(b)

FIG. 8. Transmittance modulus of an exponential horn of 68 cm length, 3 mm and 3 cm radii ($\zeta = 10$ and $\tau = 2$ ms). Comparison between exact (without losses, dashed line) and numerical (unbroken line) calculations.
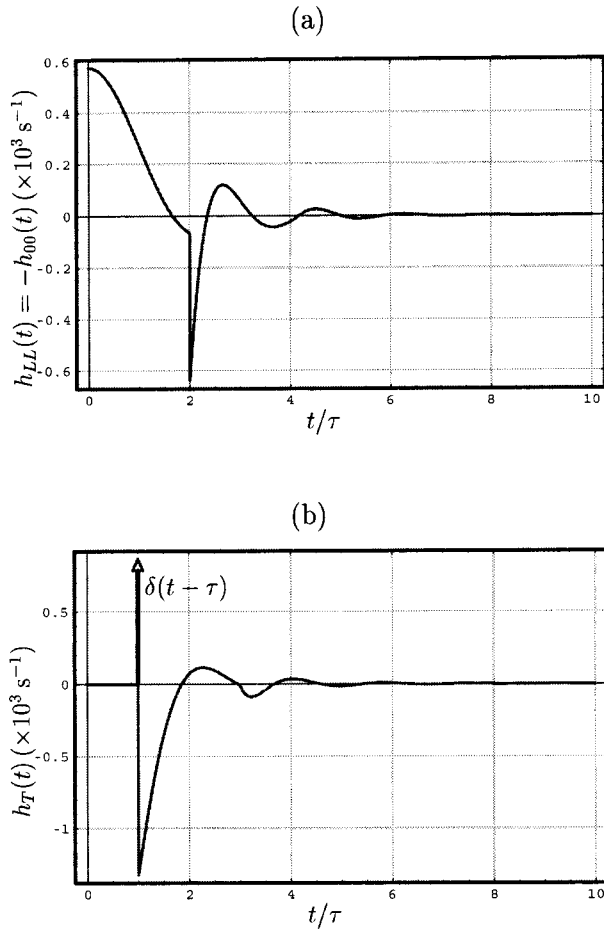
Eric Ducasse: Two-port descriptions of acoustic bores

(a)

(b)

FIG. 9. Continuous-time impulse responses of an exponential horn of 68 cm length, 3 mm and 3 cm radii ($\zeta = 10$ and $\tau = 2$ ms).

Eq. (31) becomes

$$H_{LL}(s) = -H_{00}(s)$$

$$= \frac{1}{\Lambda}(\sqrt{(\tau s)^2 + \Lambda^2} - \tau s) + 2 \sum_{n=1}^{+\infty} (-1)^n \mathcal{B}_{2n} \, e^{-2n\tau s}, \tag{33}$$

$$H_T(s) = 2 \sum_{n=0}^{+\infty} (-1)^n \mathcal{B}_{2n+1} \, e^{-(2n+1)\tau s},$$

where

$$\mathcal{B}_m = \frac{1}{\Lambda^{m+1}} \sum_{k=0}^{+\infty} \frac{(-m)^k}{k!} \{ \Lambda^2 [\sqrt{(\tau s)^2 + \Lambda^2} - \tau s]^{m+k-1}$$

$$- \tau s [\sqrt{(\tau s)^2 + \Lambda^2} - \tau s]^{m+k} \}. \tag{34}$$

After an inverse Laplace transform, Eqs. (33) and (34) give with the convention $\mathcal{K}_0 = 0$:

$$h_{LL}(t) = -h_{00}(t) = \frac{1}{\tau} \mathcal{K}_1\left(\frac{t}{\tau}\right) + \frac{2}{\tau} \sum_{n=1}^{+\infty} (-1)^n$$

$$\times b_{2n}(t - 2n\,\tau), \tag{35}$$

$$h_T(t) = \delta(t - \tau) + \frac{2}{\tau} \sum_{n=0}^{+\infty} (-1)^n b_{2n+1}[t - (2n+1)\tau],$$

where

(a)

(b)

(c)
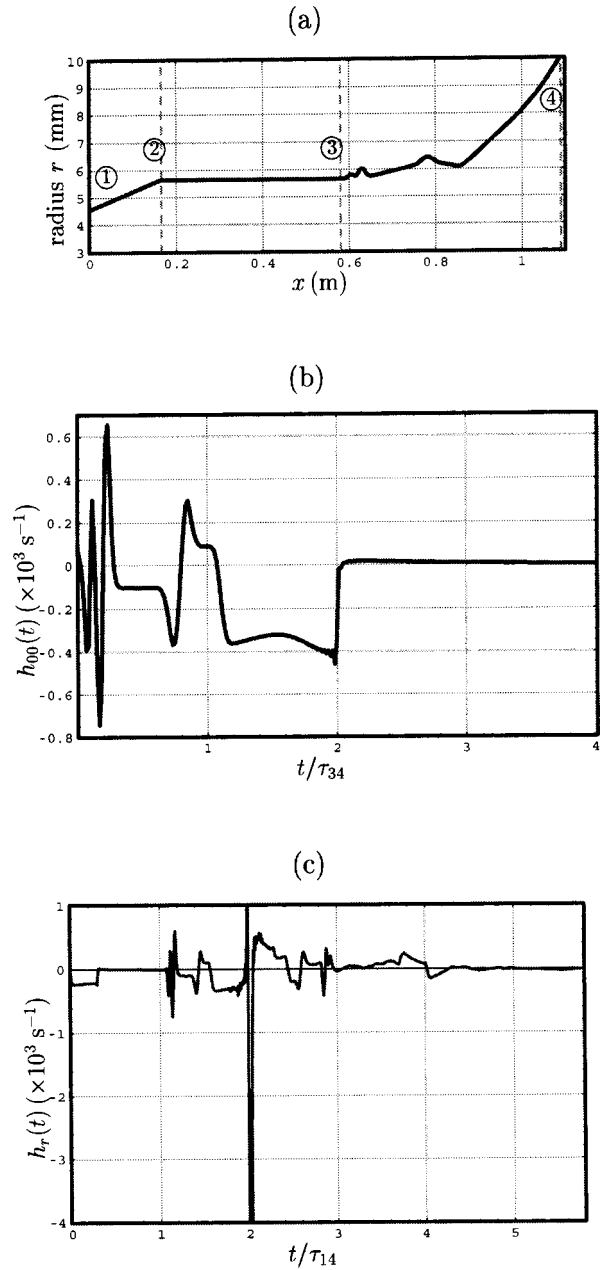
FIG. 10. (a) Profile of a trumpet bore (from Fig. 3 in van Walstijn and Smith—Ref. 17). The resonator is divided into three parts, from left to right: the "*mouthpipe*" (from ① to ②) is a conical bore of 165 mm length, 4.54 and 5.65 mm radii; the "*main bore*" (from ② to ③) is a cylindrical bore, of 415 mm length and 5.65 mm radius; the third part (from ③ to ④) is the beginning, which radius is less than 10 mm, of the "*flared bell*;" the length of this truncated flared bell is 510 mm. (b) Reflection impulse response h_{00} of the flared bell at its small end ③ ($\tau_{34} = 1.5$ ms). (c) Reflection function of the whole trumpet bore at the entrance of the mouthpipe ① ($\tau_{14} \approx 3.2$ ms).

$$b_m(t) = \sum_{k=0}^{+\infty} \frac{(-m\Lambda)^k}{k!} \left[\mathcal{K}_{m+k-1}\left(\frac{t}{\tau}\right) - \frac{1}{\Lambda} \mathcal{K}'_{m+k}\left(\frac{t}{\tau}\right) \right]. \tag{36}$$

The continuous-time impulse responses are drawn in Fig. 9. They are similar to discrete-time ones which are numerically obtained by inverse discrete Fourier transform.

C. A complex bore profile

The two-port model can also be used for an arbitrarily varying bore: the profile of a truncated trumpet bore, taken from van Walstijn and Smith[17] (Fig. 3), is given in Fig. 10(a). The impulse response h_{00} (reflection) of the truncated flared bell at its small end (mark ③), is given in Fig. 10(b). Because "*trajectories*" with a single reflection are predominant, the profile of the bore can almost be followed on the curve of h_{00} by converting length into time (coefficient $2/c$). The propagation delay between both ends is $\tau_{34}=1.5$ ms. It can be observed that each small profile irregularity produces a significant effect on the h_{00} curve.

The reflection function of the whole truncated trumpet bore at the entrance of the mouthpipe (mark ①) is drawn in Fig. 10(c). The total propagation delay between both ends is $\tau_{14}\approx 3.21$ ms. Between 0 and 0.3 τ_{14}, the negative reflection inside the mouthpipe (divergent cone) is perceptible. Between 0.3 τ_{14} and 1.06 τ_{14}, reflections are negligible (cylindrical part). Between 1.06 τ_{14} and about 2 τ_{14}, the reflection impulse response h_{00} of the truncated flared bell is recognizable. The negative peak, which appears at 2 τ_{14} and reaches a magnitude of about 1.5×10^4 s^{-1}, results from the reflection at the opening end (mark ④). After about 2 τ_{14}, multiple reflections inside the tube are superimposed, the effects of the three parts of the bore are more difficult to differentiate, even if a kind of $(2\,\tau_{14},0)$-centered symmetry can be observed and qualitatively explained by the predominance of trajectories containing three reflections.

V. CONCLUDING REMARKS

This new two-port model is promising for accurate time-domain simulation of musical wind instruments with an arbitrary bore shape. The present approach based on locally traveling plane waves may be seen as an alternative to waveguide filter approaches which include piecewise element modeling.

This approach improves time-domain modeling of bores with varying cross section but it is only an element of a complete physical model. This global model could lead to an implementation of a tool for instrument makers, which may enable them to listen to an instrument before it is manufactured. However, improvements are still necessary in the physical modeling of other elements of wind instruments, including their interactions with the player.

[1] R. T. Schumacher, "*Ab initio* calculations of the oscillations of a clarinet," Acustica **48**, 71–85 (1981).

[2] M. E. McIntyre, R. T. Schumacher, and J. Woodhouse, "On the oscillations of musical instruments," J. Acoust. Soc. Am. **74**, 1325–1345 (1983).

[3] J.-M. Adrien and E. Ducasse, "Dynamic modeling of instruments for sound synthesis," in Proceedings of the International Conference on Acoustics, Belgrade, 1989, Vol. 3, pp. 105–108.

[4] J. O. Smith, "Efficient simulation of the reed-bore and bow-string mechanisms," in Proceedings of the International Music Conference, The Hague, 1986, pp. 275–280.

[5] J. O. Smith, "Physical modeling synthesis update," Comput. Music J. **20**, 44–56 (1996).

[6] G. R. Plitnik and W. J. Strong, "Numerical method for calculating input impedances of the oboe," J. Acoust. Soc. Am. **65**, 816–825 (1979).

[7] R. Caussé, J. Kergomard, and X. Lurton, "Input impedance of brass musical instruments. Comparison between experiment and numerical models," J. Acoust. Soc. Am. **75**, 241–254 (1984).

[8] R. D. Ayers, L. J. Eliason, and D. Mahgerefteh, "The conical bore in musical acoustics," Am. J. Phys. **53**, 528–537 (1985).

[9] J. Agulló, A. Barjau, and J. Martínez, "Alternatives to the impulse response $h(t)$ to describe the acoustical behavior of conical ducts," J. Acoust. Soc. Am. **84**, 1606–1612 (1988).

[10] J. Martínez and J. Agulló, "Conical bores. I. Reflection functions associated with discontinuities," J. Acoust. Soc. Am. **84**, 1613–1619 (1988).

[11] J.-D. Polack, "Time domain solution of Kirchhoff's Equation for sound propagation in viscothermal gases: A diffusion process," J. Acoust. **4**, 47–67 (1991).

[12] B. Gazengel, J. Gilbert, and N. Amir, "Time domain simulation of single reed wind instrument. From the measured input impedance to the synthesis signal. Where are the traps?," Acta Acustica **3**, 445–472 (1995).

[13] J. O. Smith, "Waveguide simulation of non-cylindrical acoustic tubes," in Proceedings of the International Computer Music Conference, Montreal, 1991, pp. 304–307.

[14] E. Ducasse, "Modélisation d'instruments de musique pour la synthèse sonore: Application aux instruments à vent (Physical modeling synthesis of wind instruments)," Colloque de Physique (Sup.), Lyon, France, 1990, Vol. 52, pp. 837–840.

[15] V. Välimäki, T. I. Laakso, M. Karjalainen, and U. K. Laine, "A new computational model for the clarinet," in Proceedings of the International Computer Music Conference, San Jose, CA, 1992.

[16] M. van Walstijn, J. S. Cullen, and D. M. Campbell, "Modeling viscothermal wave propagation in wind instrument air columns," in Proceedings of the International Symposium on Musical Acoustics, Edinburgh, 1997, Vol. 19, pp. 413–418.

[17] M. van Walstijn and J. O. Smith, "Use of truncated infinite impulse response (TIIR) filters in implementing efficient digital waveguide models of flared horns and piecewise conical bores with unstable one-pole filter elements," in Proceedings of the Symposium on Musical Acoustics, Leavenworth, WA, 1998, pp. 309–314.

[18] D. P. Berners, "Acoustics and signal processing techniques for physical modeling of brass instruments," Ph.D. thesis, Stanford University, 1999.

[19] J. Martínez, J. Agulló, and S. Cardona, "Conical bores. II. Multiconvolution," J. Acoust. Soc. Am. **84**, 1620–1627 (1988).

[20] D. Matignon, "Représentation en variables d'état de modèles de guides d'ondes avec dérivation fractionnaire (State variables representation of waveguides including fractional derivation)," Thèse de l'Université Paris XI, Orsay, France, 1994.

[21] V. Välimäki and M. Karjalainen, "Digital waveguide modeling of wind instrument bores constructed of truncated cones," in Proceedings of the International Computer Music Conference, Aarhus, Denmark, 1994, pp. 423–430.

[22] N. Amir, U. Shimony, and G. Rosenhouse, "A discrete model for tubular acoustic systems with varying cross section—the direct and inverse problems. 1. Theory," Acustica **81**, 450–462 (1995).

[23] G. P. Scavone, "An acoustic analysis of single-reed woodwind instruments with an emphasis on design and performance issues and digital waveguide modeling techniques," Ph.D. thesis, Stanford University, 1997.

[24] T. I. Laakso, V. Välimäki, M. Karjalainen, and U. K. Laine, "Splitting the unit delay—tools for fractional delay filter design," IEEE Signal Process. Mag. **13**, 30–60 (1996).

[25] S. Tassart and P. Depalle, "Analytical approximations of fractional delays: Lagrange interpolators and allpass filters," in Proceedings IEEE ICASSP 97, Munich, Germany, 1997, pp. 455–458.

[26] A. G. Webster, "Acoustical impedance, and the theory of horns and of the phonograph," Proc. Natl. Acad. Sci. U.S.A. **5**, 275–282 (1919).

[27] V. Salmon, "Generalizes plane wave horn theory," J. Acoust. Soc. Am. **17**, 199–211 (1946).

[28] A. F. Stevenson, "Exact and approximate equations for wave propagation in acoustic horns," J. Appl. Phys. **22**, 1461–1463 (1951).

[29] A. H. Benade and E. V. Jansson, "On plane and spherical waves in horns with nonuniform flare," Acustica **31**, 79–98 (1974); **31**, 185–202 (1974).

[30] N. H. Fletcher and T. D. Rossing, *The Physics of Musical Instruments*, 2nd ed. (Springer, New York, 1998).

[31] A. H. Benade, "Equivalent circuits for conical waveguides," J. Acoust. Soc. Am. **83**, 1764–1769 (1988).

[32] C. J. Nederveen, *Acoustical Aspects of Woodwind Instruments*, revised ed. (Northern Illinois University Press, DeKalb, IL, 1998).

[33] J. Kergomard, J.-D. Polack, and J. Gilbert, "Vitesse de propagation d'une onde plane impulsionnelle dans un tuyau sonore (Propagation speed of an impulsional plane wave in a sound pipe)," J. Acoust. **4**, 467–483 (1991).

[34] A. M. Bruneau, M. Bruneau, Ph. Herzog, and J. Kergomard, "Boundary layer attenuation of higher order modes in waveguides," J. Sound Vib. **119**, 15–27 (1987).

[35] J. D. Polack, X. Meynial, J. Kergomard, C. Cosnard, and M. Bruneau, "Reflection function of a plane sound wave in a cylindrical tube," Rev. Phys. Appl. **22**, 331–337 (1987).

[36] X. Meynial, "Systèmes micro-intervalles pour instruments à trous latéraux (Micro-intervals systems for wind instruments with tone holes)," thèse de Docteur-Ingénieur, Université du Maine, Le Mans, France, 1987.

[37] J. Gilbert, J. Kergomard, and J.-D. Polack, "On the reflection functions associated with discontinuities in conical bores," J. Acoust. Soc. Am. **87**, 1773–1780 (1990).

[38] J. Agulló, A. Barjau, and J. Martínez, "On the time-domain description of conical bores," J. Acoust. Soc. Am. **91**, 1099–1105 (1992).

[39] L. Schwartz, *Théorie des Distributions* (Theory of Distributions), 2nd ed. (Hermann, Paris, 1966).

[40] W. H. Press, S. A. Teukolsky, W. T. Vetterling, and B. Flannery, "Integration of ordinary differential equations," in *Numerical Recipes in C. The Art of Scientific Computing*, 2nd ed. (Cambridge University Press, New York, 1992), Chap. 16, pp. 707–752.

[41] L. R. Rabiner, J. H. McClellan, and T. W. Parks, "FIR digital filter design techniques using weighted-Chebyshev approximation," Proc. IEEE **63**, 595–610 (1975).

[42] A. Antoniou, "New improved method for the design of weighted-Chebyshev, nonrecursive, digital filters," IEEE Trans. Circuits Syst. **30**, 740–750 (1983).

[43] J. W. Adams, "FIR digital filters with least-squares stopbands subject to peak-gain constraints," IEEE Trans. Circuits Syst. **38**, 376–388 (1991).

[44] C. S. Burrus, J. A. Barreto, and I. W. Selesnick, "Iterative reweighted design of FIR filters," IEEE Trans. Signal Process. **42**, 2926–2936 (1994).

[45] R. A. Vargas and C. S. Burrus, "Adaptive iterative reweighted least squares design of L_p FIR filters," *Proceedings ICCASSP 99*, Signal Processing, Theory and Methods, Vol. 3 (1999), pp. 1129–1132.

[46] W.-S. Lu and T.-B. Deng, "An improved weighted least-squares design for variable fractional delay FIR filters," IEEE Trans. Signal Process. **46**, 1035–1040 (1999).

[47] H. Levine and J. Schwinger, "On the radiation of sound from an unflanged circular pipe," Phys. Rev. **73**, 383–406 (1948).

[48] M. Abramowitz and I. Stegun, *Handbook of Mathematical Functions*, National Bureau of Standards Appl. Math. Series, No. 55 (USGPO, Washington, DC, 1964).

Short sound decay of ancient Chinese music bells[a]

Jie Pan[b]

Department of Mechanical and Materials Engineering, The University of Western Australia,
35 Stirling Highway, Crawley, WA 6009, Australia

Xiaodong Li and Jing Tian

Institute of Acoustics, Chinese Academy of Sciences, P.O. Box 2712, Beijing 100080,
People's Republic of China

Tanran Lin

Department of Mechanical and Materials Engineering, The University of Western Australia,
35 Stirling Highway, Crawley, WA 6009, Australia

Ancient Chinese music bells, which have oval-like cross sections, possess the unique feature of a short sound-decay time that is especially suitable for music with fast tempo. Although recorded in the literature nearly 1000 years ago, this feature has never been truly understood. Recent damping measurement of oval pipes with different axial ratios suggested a challenging task for acousticians as the increase of the modal damping with the pipe's axial ratio is significant only when the pipe response is measured in air but not in vacuum. In this paper, the decrease of sound-decay time of oval pipes with the increased cross-section ovality is investigated. This is the first time that such short sound-decay feature is explained in terms of the rich sound radiation characteristics of the symmetric modes of music bells and the oval pipes. Finite element and boundary element methods are employed to explain how axial ratio significantly affects the normal velocity distribution, radiation efficiency, and directivity of acoustic modes. © *2002 Acoustical Society of America.*
[DOI: 10.1121/1.1518985]

PACS numbers: 43.75.Kk [NHF]

I. INTRODUCTION

The history of Chinese bells can be traced back to the Shang dynasty (1600–1100 B.C.).[1] Ancient Chinese music bells (Bian Zhong) differ from Western bells in having oval cross sections as shown in Fig. 1. Musicologists believe that it took five people to play the set of 65 bells hanging in three rows on the elaborately carved L-shaped frame shown in Fig. 2. The unique acoustical features of ancient Chinese music bells include two different strike notes, and a short sound-decay time which is suitable for music with fast tempo. The interval between the two strike notes is often found to be a major or minor third.

The two-tone property of the bells has been studied and mechanisms are understood.[2] The natural frequencies of the degenerated modes of a bell become split as the cross section changes from circular to oval. Two different natural frequencies corresponding to the same modal indices but with symmetric and antisymmetric mode shapes (with respect to the major axis) are thus possible. Depending upon whether the bell is struck at the normal- or at the side-strike position, the symmetric or antisymmetric mode is excited and the corresponding tone generated.

Around 1090, Sheng Kuo documented the short decay time of music bells by comparing it with the long decay time of bells with circular cross sections;[3] however, the mechanism of short sound decay was never understood. Significant progress was made towards such understanding by the experimental work of Wang *et al.*[4] in 1991. In their experiment, four identical steel pipes (144 mm long, 4 mm thick, and 105 mm in external diameter) with circular cross section were used to simulate the vibration of the music bells. Three of the four pipes were flattened to different axial ratios ($\alpha = a/b$, where a and b are, respectively, the major and minor axes of the symmetric oval). The time decay of the structural vibration of these pipes was measured in vacuum and in air after initial impact excitation at the normal strike position. The measured damping constants are summarized in Table I. Here, the damping constant β_i of a mode describes the decay of the mode amplitude ϕ_i [$\phi_i(t) = \phi_i(0) e^{-\beta_i t}$]. It was concluded that material damping is not related to pipe axial ratio; however, air damping increases with axial ratio.

II. SOUND RADIATION FROM SYMMETRICAL OVAL PIPES

Vibrating pipes lose their energy in air through sound radiation. The analysis of radiation characteristics will shed light on the air damping of oval pipes and the mechanism of short decay time of ancient Chinese music bells. Although the cross section of the bell has a slope discontinuity at each of the narrow ends (referred to as "almond shaped"), a comparison using the finite element analysis showed that the conclusions obtained for pipes with oval cross sections also apply to that with almond-shaped cross sections.
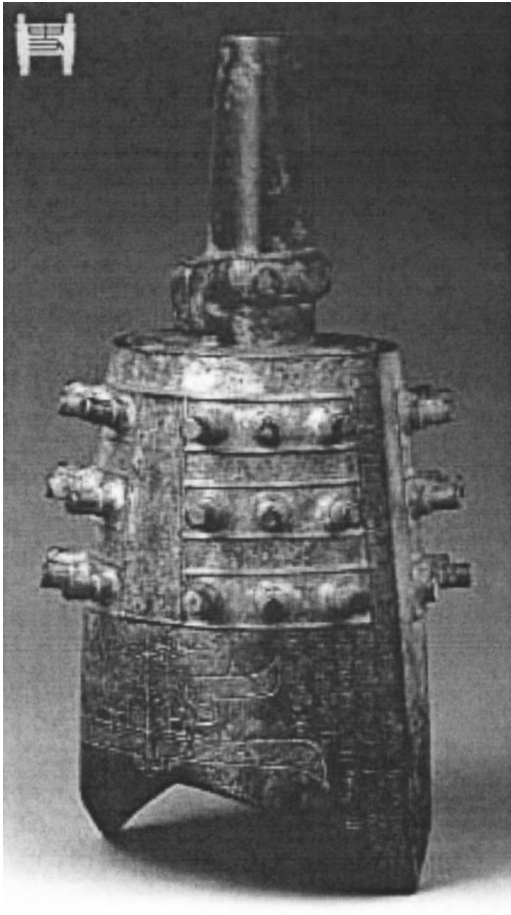
FIG. 1. The Chinese music bell (Bian Zhong).

Knowing the length, thickness, and circumference, we can calculate the resonance frequencies, mode shapes, and modal radiation efficiencies of oval steel pipes as a function of the pipe axial ratio. In this analysis, pipe dimensions are 144 mm in pipe length, 4-mm thickness, and 330-mm external circumference and both ends are free on. The coordinates of oval pipes are defined in Fig. 3. Finite element analysis of the pipe vibration gives rise to the resonance frequencies and mode shapes. Then, the boundary element method is used to calculate the radiated sound-pressure distribution of the first two pipe modes in the far field. The calculation was undertaken in SYSNOISE environment.[5]

A. Structural mode shapes

The first nonrigid mode pair of the free–free pipe has modal index $(n,m)=(2,0)$ representing 2 complete nodal
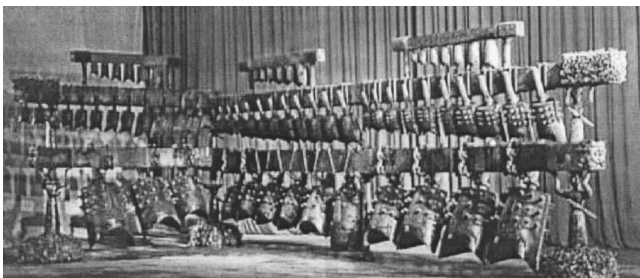
FIG. 2. Sixty-five music bells hanging in three rows on an elaborately carved L-shaped frame.

TABLE I. Damping constants of four pipes measured in vacuum and in air (Ref. 4).

$\alpha=a/b$	1	1.177	1.333	1.639
β_v (Vacuum)	0.601	0.746	0.933	0.705
β_a (Air)	0.710	1.285	2.631	4.817

meridians (4 antinodes in the circumferential direction) and rigid body translation in the axial direction. As the pipe axial ratio increases, the resonance frequency of the symmetric mode (with a node at the spine) $(2,0)_S$ decreases, while that of the antisymmetric mode $(2,0)_A$ increases, as shown in Fig. 4.

The normal displacement of the symmetric mode $(2,0)_S$ around the circumference is shown in Fig. 5, where l/L is the circumference position. As α increases, the amplitude and area of the in-phase vibration on the normal-strike surfaces increase. We observe a significant increase in comoving adjacent areas and a change from a symmetrical quadrupole vibration pattern to a predominantly monopole character. So, an increased efficiency of sound radiation is expected. On the other hand, the normal displacement of the antisymmetric mode $(2,0)_A$ remains unchanged as α increases. The variation of the energy loss of this antisymmetric mode due to sound radiation with α is only indirectly related to the pipe axial ratio due to the corresponding increase of the natural frequency.

B. Sound radiation efficiency

The energy loss of the ith pipe mode due to sound radiation is described in terms of radiation efficiency defined as[6]

$$\sigma_i = \frac{\int_S \mathrm{Re}(pv^*)ds}{\rho c \int_S v^2 \, ds},\qquad(1)$$

where p and v are, respectively, the sound pressure and normal velocity on the vibrating surface. * represents the complex conjugate and ρc is the characteristic impedance of the air. The damping constant of the mode β_i is related to the loss factor η_i of the mode by $\beta_i = \eta_i/2$. On the other hand, the time derivative of the modal energy in air is determined by the power radiated into air and dissipated in the material as

$$\frac{dE_i}{dt} = -\frac{\sigma_i \rho c}{h}E_i - 2\beta_M E_i,\qquad(2)$$

where $E_i = \hat{\rho} h \int_S v^2 \, ds$ is the modal energy. $\hat{\rho}$ and h are the mass density and thickness of the pipe wall, respectively. β_M
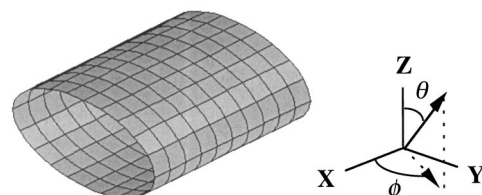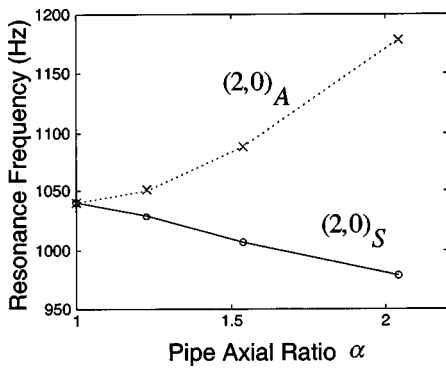

FIG. 3. Coordinates of the oval pipe.

FIG. 4. Resonance frequencies of the symmetric mode $(2,0)_S$ and antisymmetric mode $(2,0)_A$.

FIG. 6. Radiation efficiencies of the symmetric mode $(2,0)_S$ and the antisymmetric mode $(2,0)_A$.

is the material damping constant. As a result, the damping constant of the mode in air is obtained

$$\beta_i = (\sigma_i \rho c / 2\hat{\rho} h) + \beta_M. \tag{3}$$

The radiation efficiencies of the symmetric $(2,0)_S$ and antisymmetric $(2,0)_A$ modes (Fig. 6) increase with the increase of the pipe's axial ratio. The significant increase in the radiation efficiency of mode $(2,0)_S$ is due to the dramatic change of the mode shape, while the small increase in σ of mode $(2,0)_A$ is due to increase of resonance frequency. The observation indicates that the decay time of $(2,0)_A$ is reduced only slightly with increasing axial ratio. Our experiment has confirmed this. Detailed experiment on real music bells will reveal if the antisymmetrical mode of the bell also has a longer decay time than that of the symmetrical mode.

The damping constant of mode $(2,0)_S$ as a function of α is predicted using Eq. (3), and an average experimental value for the material-damping constant $\eta_{(2,0)_A} = 0.762$ is based on Table I. Figure 7 indicates reasonable agreement between predicted and measured damping constants [the symmetric $(2,0)_S$ mode] and leads to the conclusion that the decrease of decay time of an oval pipe is caused by the increase of the radiation efficiency of the symmetric mode $(2,0)_S$ when the pipe axial ratio is increased. However, such significant decrease of decay time only occurs to those modes with a significant increase in volume velocities. For example, the damping constant of $(2,0)_A$ mode is not affected significantly by the pipe axial ratio because a small increase of radiation efficiency is involved in this case.
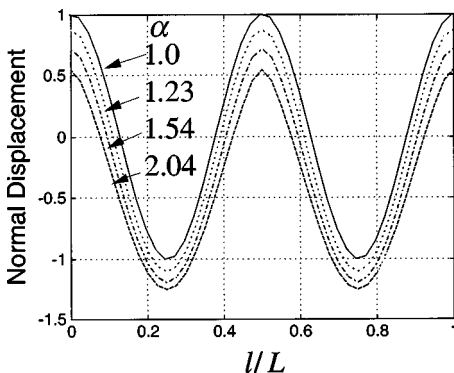
C. Model radiation of sound

The significant change of $(2,0)_S$ mode shape with α (Fig. 5) gives rise to a dramatic change in the sound radiation efficiency (Fig. 6) and in the directivity of the mode. The plot of radiation directivity of mode $(2,0)_S$ against α (Fig. 8) explains the mechanism associated with the increase of the modal radiation efficiency. At its resonance frequency, the $(2,0)_S$ mode of the circular pipe ($\alpha=1$) radiates sound as a lateral quadrupole with lobes oriented along the major and minor axes.

The directivity of the radiated sound pressure becomes dumbbell-shaped for $\alpha=1.23$. The distributed phase shown in Fig. 9 indicates that the two lobes of the radiated sound have the same phase, which is expected based on the symmetry of the corresponding mode shape.

As α further increases ($\alpha=2.04$), the distribution of modal sound radiation can be approximated as doughnut-shaped.

The area with large sound-pressure amplitude increases when the sound source transforms from a quadrupole to a source with the shape of a doughnut. This clearly corresponds to the increase of the radiated sound power and supports the claimed increase in energy loss through sound radiation with increased α.

III. CONCLUSIONS

Among the many acoustical innovations in Chinese history, the short decay time feature of music bells stands out as
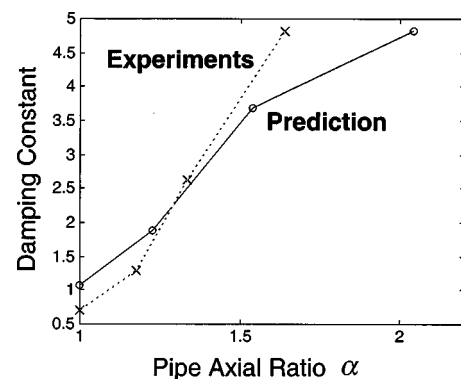

FIG. 5. Normal displacement of the symmetric mode $(2,0)_S$ along the circumferential direction.

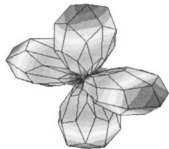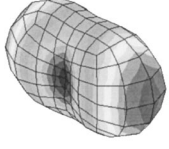FIG. 7. Damping constant of the symmetric mode $(2,0)_S$.

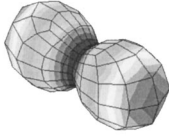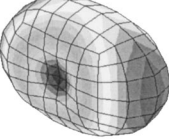| Pipe Axial Ratio	Radiation Directivity (2,0)$_S$ Mode	Pipe Axial Ratio	Radiation Directivity (2,0)$_S$ Mode
$\alpha = 1$		$\alpha = 1.54$	
$\alpha = 1.23$		$\alpha = 2.04$	

FIG. 8. Sound radiation directivity of mode $(2,0)_S$ as a function of α.

a fine example of ancient wisdom and technology; however, the underlying physics has remained unexplained for nearly 1000 years since the time of Sheng Kuo. This paper satisfactorily explains the behavior through the analysis of sound radiation characteristics of the first two modes in oval pipes.

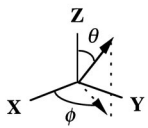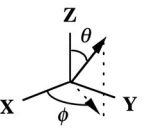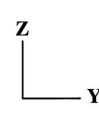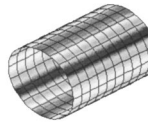As the axial ratio of a pipe increases, the resonance fre-
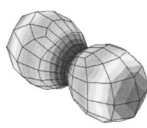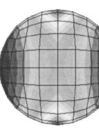
Pipe Axial Ratio	Mode Shape	Radiation Directivity	Radiation Phase
$\alpha = 1.23$			

FIG. 9. Mode shape, sound radiation directivity, and phase of mode $(2,0)_S$ for $\alpha = 1.23$.

quencies and mode shapes of the originally degenerate modes change significantly. The splitting of the degeneracy of the resonance frequencies between the symmetric and antisymmetric modes is responsible for the two-tone quality of the music bells. The dramatic change of the corresponding mode shapes is the reason for short modal decay time. However, only the symmetric mode $(2,0)_S$ out of the first couple of modes experiences the significant change in mode shape and hence increases in radiation efficiency. An evolution of the sound radiation directivity of this mode was observed as the axial ratio of a pipe increases. Starting as a quadrupole sound source for $\alpha=1$, the directivity gradually changes into a dumbbell and eventually into a doughnut shape as α increases. In summary, the short sound-decay time of ancient Chinese music bells can be explained with reference to the sound radiation of an oval pipe: the symmetric mode $(2,0)_S$ changes from a weak to a strong sound radiator as the axial ratio of the bell/pipe increases.

ACKNOWLEDGMENTS

[1] N. H. Fletcher and T. D. Rossing, *The Physics of Musical Instruments* (Springer, Berlin, 1990).
[2] T. D. Rossing, D. S. Hampton, B. E. Richardson, H. J. Sathoff, and A. Lehr, "Vibrational modes of Chinese two-tone bells," J. Acoust. Soc. Am. **76**, 1263–1267 (1988).
[3] K. Sheng, "Notes in Men Xi" (in Chinese) (1090).
[4] D. J. Wang, "The research on mechanical properties of ancient Chinese cultural relics," in *Proceedings of the 2nd Conference on History of Science and Technique* (Chinese University of Science and Technology Press, 1991), pp. 51–56.
[5] SYSNOISE Rev 5.3 User's manual, LMS Numerical Technologies.
[6] M. P. Norton and J. Pan, "Noise, noise radiated from baffled plates," *Encyclopedia of Vibration* (Academic, New York, 2001), Vol. 2, pp. 887–898.

Probability density functions for hyperbolic and isodiachronic locations

John L. Spiesberger
*Department of Earth and Environmental Science, 240 South 33rd Street, University of Pennsylvania,
Philadelphia, Pennsylvania 19104-6316*

Magnus Wahlberg
*Department of Zoophysiology, Aarhus University, Building 131, C. F. Moellers Alle, DK-8000 Aarhus C,
Denmark*

Animal locations are sometimes estimated with hyperbolic techniques by estimating the difference in distances of their sounds between pairs of receivers. Each pair specifies the animal's location to a hyperboloid because the speed of sound is assumed to be spatially homogeneous. Sufficient numbers of intersecting hyperboloids specify the location. A nonlinear method is developed for computing probability density functions for location. The method incorporates *a priori* probability density functions for the receiver locations, the speed of sound, winds, and the errors in the differences in travel time. The traditional linear approximation method overestimates bounds for probability density functions by one or two orders of magnitude compared with the more accurate nonlinear method. The nonlinear method incorporates a generalization of hyperbolic methods because the average speed of sound is allowed to vary between different receivers and the source. The resulting ''isodiachronic'' surface is the locus of points on which the difference in travel time is constant. Isodiachronic locations yield correct location errors in situations where hyperbolic methods yield incorrect results, particularly when the speed of propagation varies significantly between a source and different receivers. © *2002 Acoustical Society of America.*
[DOI: 10.1121/1.1513648]

I. INTRODUCTION

Hyperbolic locations are derived by intersecting hyperboloids from estimates of the differences in distances between pairs of receivers. There may not be a published method in the bioacoustics literature for computing probability density functions for hyperbolic locations without making the linear approximation between the data and the locations. Furthermore, hyperbolic location methods for locating calling animals are restricted to the case where the speed of sound is constant throughout space, in which case the difference in distance is estimated from the difference in arrival time of the sound. A nonlinear method is developed here for estimating probability density functions for location without requiring that the speed of sound be constant. Because the average speed is different between the source and each receiver, one no longer has hyperbolic geometries that are second order polynomials in the Cartesian coordinates. Instead, a new geometrical surface, called an ''isodiachron,'' is defined that depends on the Cartesian coordinates through a fourth order polynomial. The word isodiachron is derived from the Greek words ''iso,'' for same, ''dia,'' for difference, and ''chron,'' for time. The surface is one along which the locus of points has the same difference in travel time between two points in space. This reduces to a hyperboloid only if the speed of sound is spatially homogeneous.

The approach is not as complicated nor accurate as can be obtained by doing a joint tomographic inversion for the sound speed and wind fields and for the locations of the imperfectly known locations of the receivers and the source. But the method described here may give an answer with more computational efficiency. The density functions are derived using the nonlinear relationship between the differences in travel time and the unknown quantities such as the sound speed field, wind field, and the locations of the animal and the receivers. In many practical situations, the probability density functions reveal that locations can be made with one or more orders of magnitude more accuracy than those found with the linear approximation.

The problem with linear error analysis[1–7] alone is that source location is not a linear function of the travel time differences, speed of sound, and receiver locations. One expects linear analysis of errors to yield reasonable estimates when the source is near intersecting hyperboloids that are well approximated by planes. But this is often not the case, and the curvature of the hyperboloids near a source may be significant over the region that linear error analysis prescribes. In these cases a complete nonlinear analysis of errors is warranted. As we will see, the nonlinear analysis yields much smaller errors for location than linear analysis in many cases of interest because locations will be confined to be on the curved hyperbolic surfaces.

There appears to be another technical difficulty in estimating location errors even when one accounts for the fact that the linear approximation is invalid. When one has more than the minimum number of receivers required to locate an object, the method for assessing errors does not appear to have been dealt with in the literature in a satisfying method.

Schmidt's interesting paper[8] uses Monte Carlo simulations to estimate errors in source location. Suppose for the moment that a mathematically unambiguous location can be achieved with three receivers for a two-dimensional geometry. Schmidt jiggles ideal travel time differences and receiver coordinates within their expected errors to see how much a location changes with respect to the correct location. Errors are obtained by taking the largest misfit between the jiggled and correct estimate of location. When there are more than three receivers, say $\mathcal{R}$ receivers, he suggests using this procedure for each combination of three receivers giving,

$$\binom{\mathcal{R}}{3} = \frac{\mathcal{R}!}{(\mathcal{R}-3)!3!},$$

total combinations. Each combination is referred to as a "constellation" here. Schmidt suggests using a least squares procedure to find a final estimate of error from the results of the largest misfit from each constellation. He does not prove this least-squares procedure is optimal, and indeeds states that he is not sure of any advantages in using a least-squares procedure in this situation.

Instead of least-squares, a Monte Carlo technique is used to estimate a probability density function of source location from each receiver constellation. For a constellation, the sound speed, winds, and receiver locations are treated as random variables with some probability density function. The probability density function can be obtained from theory, data, or a guess. When guessing, it may be advantageous to let the probability density function have the largest possible bounds with the most ignorance so as to not overestimate the accuracy of a location. For example, suppose one believes the x location of a receiver is at 10 m with an error of two centimeters. Then the associated probability density function for this parameter can be taken to be a uniformly distributed random variable in the interval [9.8, 10.2] m. With the *a priori* probability density function, the various values of the sound speed, winds, and receiver locations yield possible source locations that occupy a cloud in three-dimensional space. The actual source must lie within the intersection of the clouds from different constellations. The final probability function for the source location is estimated from the distributions within the intersection. The density function has the benefit of being able to yield many useful values such as an average location, maximum likelihood location, and any desired confidence limit.

II. LOCATING SOUNDS USING FOUR OR FIVE RECEIVERS WITH INHOMOGENEOUS SOUND SPEED FIELD

Watkins and Schevill's[9] method for locating sounds using four receivers is imitated, but instead of letting the speed of sound be constant, it is allowed to have a different average speed between the source and each receiver. Although five receivers are required in general to locate a source in three dimensions in a homogeneous sound speed field, there are spatial regions where only four are required.[8,10,11] When ambiguous solutions occur with four receivers, the ambiguity is

resolved with the travel time difference between the first and fifth receiver.[11] The presentation below thus starts with a minimum constellation of four receivers.

The distance between the ith receiver at $\mathbf{r}_i$ and a source at $\mathbf{s}$ is $\|\mathbf{r}_i - \mathbf{s}\|$ so we have $\|\mathbf{r}_i - \mathbf{s}\|^2 = c_i^2 t_i^2 = c_i^2(\tau_{i1} + t_1)^2$. The average speed and travel time of sound between the source and receiver i are c_i and t_i respectively. $\tau_{i1} \equiv t_i - t_1$ and $\mathbf{s}$ is a column vector with Cartesian coordinates $(s_x, s_y, s_z)^T$ where T denotes transpose. Putting the first receiver at the origin of the coordinate system, one subtracts the equation for $i = 1$ from $i = 2, 3$, and 4 to get,

$$\|\mathbf{r}_i\|^2 - 2\mathbf{r}_i^T \mathbf{s} = c_i^2 \tau_{i1}^2 + 2c_i^2 \tau_{i1} t_1 + t_1^2(c_i^2 - c_1^2).$$

This simplifies to,

$$\mathbf{Rs} = \tfrac{1}{2}\mathbf{b} - t_1 \mathbf{f} - t_1^2 \mathbf{g}, \tag{1}$$

where,

$$\mathbf{R} \equiv \begin{pmatrix} r_2(x) & r_2(y) & r_2(z) \\ r_3(x) & r_3(y) & r_3(z) \\ r_4(x) & r_4(y) & r_4(z) \end{pmatrix};$$

$$\mathbf{b} \equiv \begin{pmatrix} \|\mathbf{r}_2\|^2 - c_2^2 \tau_{21}^2 \\ \|\mathbf{r}_3\|^2 - c_3^2 \tau_{31}^2 \\ \|\mathbf{r}_4\|^2 - c_4^2 \tau_{41}^2 \end{pmatrix}; \quad \mathbf{f} \equiv \begin{pmatrix} c_2^2 \tau_{21} \\ c_3^2 \tau_{31} \\ c_4^2 \tau_{41} \end{pmatrix}, \tag{2}$$

and,

$$\mathbf{g} \equiv \frac{1}{2}\begin{pmatrix} c_2^2 - c_1^2 \\ c_3^2 - c_1^2 \\ c_4^2 - c_1^2 \end{pmatrix}, \tag{3}$$

and where the Cartesian coordinate of $\mathbf{r}_i$ is $(r_i(x), r_i(y), r_i(z))$. Equation (1) simplifies to

$$\mathbf{s} = \mathbf{R}^{-1}\frac{\mathbf{b}}{2} - \mathbf{R}^{-1}\mathbf{f}t_1 - \mathbf{R}^{-1}\mathbf{g}t_1^2, \tag{4}$$

that can be squared to yield,

$$\mathbf{s}^T\mathbf{s} = \|\mathbf{s}\|^2 = \frac{a_1}{4} - a_2 t_1 + (a_3 - a_4)t_1^2 + 2a_5 t_1^3 + a_6 t_1^4, \tag{5}$$

where

$$a_1 \equiv (\mathbf{R}^{-1}\mathbf{b})^T(\mathbf{R}^{-1}\mathbf{b}), \quad a_2 \equiv (\mathbf{R}^{-1}\mathbf{b})^T(\mathbf{R}^{-1}\mathbf{f}),$$
$$a_3 \equiv (\mathbf{R}^{-1}\mathbf{f})^T(\mathbf{R}^{-1}\mathbf{f}), \quad a_4 \equiv (\mathbf{R}^{-1}\mathbf{b})^T(\mathbf{R}^{-1}\mathbf{g}), \tag{6}$$
$$a_5 \equiv (\mathbf{R}^{-1}\mathbf{f})^T(\mathbf{R}^{-1}\mathbf{g}), \quad a_6 \equiv (\mathbf{R}^{-1}\mathbf{g})^T(\mathbf{R}^{-1}\mathbf{g}),$$

and $\mathbf{R}^{-1}$ is the inverse of $\mathbf{R}$. A solution for t_1 is obtained by substituting,

$$\|\mathbf{s}\|^2 = c_1^2 t_1^2, \tag{7}$$

for $\|\mathbf{s}\|^2$ in Eq. (5) to yield a quartic equation in t_1,

$$a_6 t_1^4 + 2a_5 t_1^3 + (a_3 - a_4 - c_1^2)t_1^2 - a_2 t_1 + \frac{a_1}{4} = 0, \tag{8}$$

that can be solved analytically, as discovered by Lodovico Ferrari in 1540 (Ref. 12), or numerically with a root finder. Valid roots from Eq. (8) are finally used to estimate the location of the source using Eq. (4). Note that if the sound

speed is spatially homogeneous, i.e., $c_i = c_1 \; \forall \; i$, then the cubic and quartic terms vanish and the resulting quadratic equation is that found before for hyperbolic location.[9]

Ambiguous solutions occur for a spatially homogeneous sound speed field when there are two positive roots to the quadratic equation. For each ambiguous source location, one can generate a model for τ_{51} and choose the root for t_1 that yields a model for τ_{51} that is closest to that measured. In the cases investigated in this paper, the quartic equation (8) can yield four distinct positive values for t_1. This can only happen because the speed of propagation is spatially inhomogeneous. Because the values of c_i are similar in this paper, the four distinct roots yield two pairs of source locations, one pair of which is relatively close to the receivers and the other pair of which is located very far from the receivers. The distant pair is due to the fact that locations are not exactly determined by intersecting hyperboloids for a spatially inhomogeneous speed of propagation. The actual three-dimensional locus of points specified by a travel time difference is thus not quite a hyperboloid. More precisely, the hyperboloid is the locus of points $\mathbf{s}$ satisfying,

$$\|\mathbf{r}_i - \mathbf{s}\| - \|\mathbf{r}_j - \mathbf{s}\| = c \, \tau_{ij}, \tag{9}$$

where the spatially homogeneous speed of propagation is c. Letting the speed be different along each section yields the definition of the isodiachron which is the locus of points satisfying,

$$\frac{\|\mathbf{r}_i - \mathbf{s}\|}{c_i} - \frac{\|\mathbf{r}_j - \mathbf{s}\|}{c_j} = \tau_{ij}, \tag{10}$$

which turns out to depend on the Cartesian coordinates through a fourth order polynomial. The values of c_i can incorporate spatially inhomogeneous effects such as winds as well as wave speeds. The coefficients of the third and fourth powers in x, y, and z and their combinations become very small compared to the coefficients in the second, first, and zero powers as the various c_i approach the same value c (not shown).

III. PROBABILITY DENSITY FUNCTIONS FOR SOURCE LOCATION FROM RECEIVER CONSTELLATIONS

When $\mathbf{r}_i$, τ_{ij}, and c_i are random variables, then t_1 and $\mathbf{s}$ are random variables because of Eqs. (4), (8). For later convenience in comparing to linear theories, consider the situation where $(r_i(x), r_i(y), r_i(z))$, τ_{ij}, and c_i are mutually uncorrelated Gaussian random variables with given means and variances.

A computer generates a single random configuration of variables for a constellation of four receivers. Each configuration consists of the set $\{r_i(x), r_i(y), r_i(z), \tau_{ij}, c_i\}$ for some $i, j \in 1, 2, 3, \cdots, \mathcal{R}$ and $i > j$. Then for each constellation, of which there are a total of,

$$N \equiv \binom{\mathcal{R}}{4} = \frac{\mathcal{R}!}{(\mathcal{R}-4)! \, 4!}, \tag{11}$$

a source location is computed from Eq. (4) if that equation yields a unique location. If any constellation yields more than one location from this equation, a location is chosen to be that yielding the closest difference in travel time to a randomly chosen fifth receiver and receiver number one.

A valid configuration from a receiver constellation is one in which the source location lies within some predetermined spatial limits. For example, one would know that sounds from snapping shrimp occur below the surface of the water. If a receiver constellation yields a location above the surface, then that particular configuration of random variables could not have occurred in reality, and that source location is discarded.

Valid configurations from a receiver constellation define a cloud of source locations. Accurate probability density functions of location require a sufficient number of valid configurations. A sufficient number is generated for each of the N constellations.

Some constellations give better locations of the source than others. This happens for several reasons, and is usually due to the geometrical arrangement of the receivers. For example, suppose the source is near the geometric center of a pyramid and one constellation consists of four receivers on the vertices of the pyramid. That constellation would be able to locate the source rather well. Then consider another constellation of four receivers located close to a line at a great distance from the source. This constellation would not be able to locate the source as well.

The only physically possible locations for the source lie within the intersections of the clouds. The other source locations are invalid. In this paper, the upper and lower bounds of the intersected region, $(\hat{X}, \check{X})$, $(\hat{Y}, \check{Y})$, and $(\hat{Z}, \check{Z})$, are estimated along the Cartesian axes. If $(\hat{x}_c, \check{x}_c)$, $(\hat{y}_c, \check{y}_c)$, and $(\hat{z}_c, \check{z}_c)$ denote the maximum and minimum values of x, y, and z for cloud c, then the region of intersection is,

$$\hat{X} = \min(\hat{x}_1, \hat{x}_2, \hat{x}_3, \cdots \hat{x}_N)$$

$$\check{X} = \max(\check{x}_1, \check{x}_2, \check{x}_3, \cdots \check{x}_N)$$

$$\hat{Y} = \min(\hat{y}_1, \hat{y}_2, \hat{y}_3, \cdots \hat{y}_N)$$

$$\check{Y} = \max(\check{y}_1, \check{y}_2, \check{y}_3, \cdots \check{y}_N) \tag{12}$$

$$\hat{Z} = \min(\hat{z}_1, \hat{z}_2, \hat{z}_3, \cdots \hat{z}_N)$$

$$\check{Z} = \max(\check{z}_1, \check{z}_2, \check{z}_3, \cdots \check{z}_N).$$

For each cloud c, locations outside of the bounds in Eqs. (12) are discarded. New probability density functions are formed from the remaining locations in each cloud for the x, y, and z values separately. It is not expected that the new probability density functions would asymptotically approach one another because each constellation will be able to locate the source with a different quality.

The probability density functions for the source in its x, y, and z coordinates are dependent distributions. This can be accommodated by forming the joint probability density function of location for each cloud if desired. This is not done here.

P percent confidence limits are estimated by finding the P percent confidence limits for each cloud separately using its probability density functions in x, y, and z. The Cartesian

	x (m)	y (m)	z (m)
	Array 1		
R1	0 ± 0	0 ± 0	0 ± 0
R2	1000 ± 2	0 ± 0	0 ± 1
R3	1000 ± 2	1000 ± 2	0 ± 1
R4	0 ± 2	1000 ± 2	0 ± 1
R5	0 ± 5	0 ± 5	-100 ± 5
SOURCE	551	451	-100
	Array 2		
R1	0 ± 0	0 ± 0	0 ± 0
R2	1414 ± 2	0 ± 0	0 ± 1
R3	534 ± 2	400 ± 2	0 ± 1
R4	1459 ± 5	-1052 ± 5	-25 ± 5
R5	1459 ± 20	-1052 ± 20	-95 ∓ 20
R6	0 ± 20	0 ± 20	-100 ± 20
R7	1414 ± 20	0 ± 20	-100 ± 20
SOURCE	860	47	-5

FIG. 1. The receiver and source locations for arrays one and two.

upper and lower bounds for a specified confidence limit for constellation c are denoted $[\hat{P}_c(x), \check{P}_c(x)]$, $[\hat{P}_c(y), \check{P}_c(y)]$, and $[\hat{P}_c(z), \check{P}_c(z)]$. The final bounds for the source are chosen from the smallest bound for x, y, and z from each constellation. For example, suppose constellation p has the smallest value of $\hat{P}(x) - \check{P}(x)$ for all values of c, constellation q has the smallest value of $\hat{P}(y) - \check{P}(y)$ for all values of c, and constellation r has the smallest value of $\hat{P}(z) - \check{P}(z)$ for all values of c. Then the final confidence limits for the source are $[\hat{P}_p(x), \check{P}_p(x)]$, $[\hat{P}_q(y), \check{P}_q(y)]$, and $[\hat{P}_r(z), \check{P}_r(z)]$.

IV. EXAMPLES

Examples below utilize 2000 valid configurations of random variables to estimate probability density functions for each cloud.

A. Hyperbolic location

Because error bars derived from linearized hyperbolic location techniques[1–7] assume the speed of sound or light is spatially homogeneous, comparison with a linear theory is done using a spatially homogeneous value of 1475 m/s. The travel time differences are computed for this speed. In the error analysis, the sound speed is assumed to be a Gaussian random variable with mean 1475 m/s and standard deviation of 10 m/s. This standard deviation is realistic if one considers paths emitted from a shallow source to receivers at perhaps 3 m and 100 m depth because the surface region can be very warm compared with temperatures below. Travel time differences are assumed to be mutually uncorrelated Gaussian random variables with means given by true values and standard deviations of 0.000 141 4 s. Receiver locations are assumed to be mutually uncorrelated Gaussian random variables with means given by their true values and standard deviations as shown in Table I.
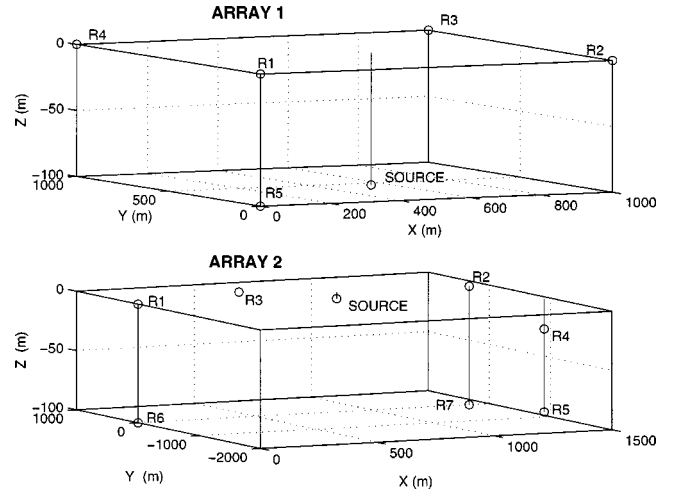
The errors in the travel time differences and receiver locations may not be mutually uncorrelated as assumed above. For example, errors in τ_{i1} may be correlated with τ_{j1} because both involve t_1. Also, for example, the errors in the location of receiver 3 are not necessarily uncorrelated between two constellations that both contain receiver 3. Linear error analysis can accommodate correlations between random variables,[7] as can the nonlinear analysis in this paper. However, incorporating these correlations leads to larger computational times in the nonlinear analysis, so they are not implemented. Error models that follow are done assuming that random variables are mutually uncorrelated for both the linear and nonlinear analysis. We found that the results were identical for the linear analysis[7] when the random variables were correlated.

To mimic marine examples, array one has five receivers separated by O(1000) m horizontally and up to 100 m vertically (Fig. 1, Table I). The five receiver constellations [Eq. (11)], one through five, are {1,2,3,4}, {1,2,3,5}, {1,2,4,5}, {1,3,4,5}, and {2,3,4,5}, respectively. The 100% confidence limits for the source are computed from Eq. (12) for increasing numbers of constellations where N is set to 1, 2, 3, 4, and 5 respectively in this equation for Fig. 2. As more clouds are intersected, the limits for the source decrease monotonically, with the biggest improvement occurring with the addition of constellation two with one. Constellation one only uses the receivers at z equal zero. Constellation two is the first one that includes the receiver at $z = -100$ m. This deeper receiver not only helps in locating the source's vertical coordinate, but significantly helps locate the horizontal coordinates as well. The probability density functions for the source location come from constellations two and four (Fig. 3). These density functions appear to be approximately Gaussian. The 68% confidence limits span only a few meters in the horizontal coordinates and are about 50 m in the vertical coordinate (Table II). The confidence limits from the nonlinear analysis are about a factor of ten less than those from the standard linear analysis of errors in the horizontal coordinates. The nonlinear analysis has smaller limits because the hyperboloids are not well approximated by planes in the horizontal directions as required by the linear analysis. Non-
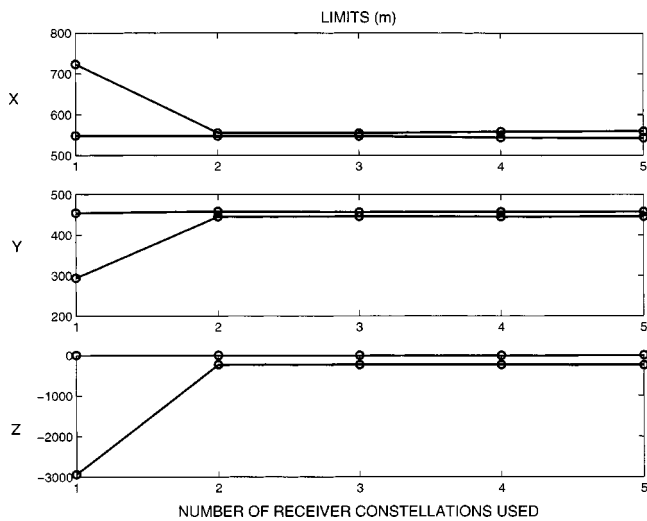
FIG. 2. 100% confidence limits for source location as a function of the number of receiver constellations used from array one (Fig. 1). There are five ways of choosing four receivers from five total without replacement. A receiver constellation consists of one of the choices of four receivers. As more constellations are used to locate the source, the bounds for the source's location decrease monotonically. The lines join results from different numbers of constellations.

linear analysis yields somewhat larger limits in z than linear analysis (Table II). Similarity of results in z indicates that the hyperboloids are fairly well approximated as planes in the vertical coordinate in the vicinity of the source.

Array two has seven receivers with the largest horizontal and vertical separations being about 1400 and 100 m, respectively (Fig. 1). There are 35 receiver constellations [Eq. (11)] of which the first four provide most of the accuracy for locating the source at the 100% confidence limits (Fig. 4). These constellations are the first of the 35 that include all the deeper receivers. There are modest increases in accuracy from other constellations, most notably 29 and 33. The probability density functions in the x-y-z coordinates come from constellations 7, 4, and 26, respectively (Fig. 5). The distributions in x and y do not look very Gaussian, while the
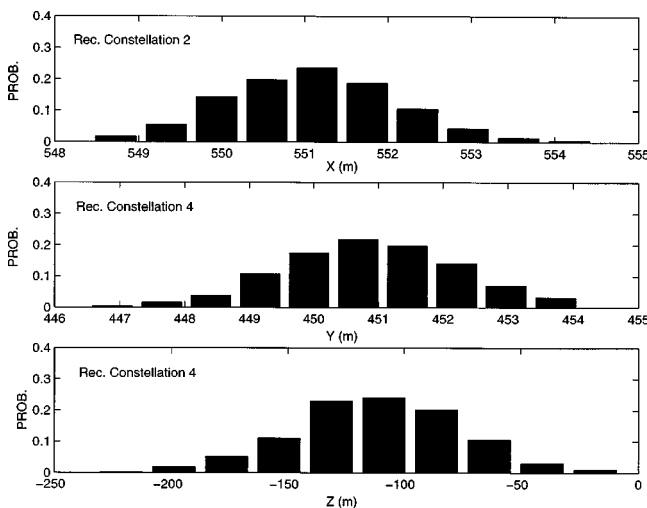

FIG. 3. Probability density functions for source location from array one (Fig. 1, top), calculated from the nonlinear method in this paper. Receiver constellation 2 is receivers 1, 2, 3, and 5 (Fig. 1, top). Receiver constellation 4 is receivers 1, 3, 4, and 5.

TABLE II. 68% confidence limits for source location corresponding to arrays one and two for the nonlinear and linear analyses.

Cartesian coordinate	68% Confidence limits (m)	
	Nonlinear	Linear
Array 1		
x	550 to 552	530 to 573
y	450 to 452	432 to 471
z	-145 to -77	-121 to -80
Array 2		
x	860 to 865	236 to 1486
y	46 to 62	-1890 to 1988
z	-138 to 65	-163 to 153

distribution in z looks more Gaussian-like. These departures from Gaussian distributions are quite different than the Gaussian distributions usually assumed from linear analyses. This time, the 68% confidence limits from the nonlinear analyses are two orders of magnitude smaller than those from standard linear analysis in x and y (Table II). The linear and nonlinear confidence limits are similar for the vertical coordinate.

B. Isodiachronic location

It appears there are two extreme situations in which isodiachronic locations are useful.

The first is one where the speed of sound is similar, but not exactly the same between each source and receiver. Consider an atmospheric example for locating a sound at Cartesian coordinate (20,100,7) m from five receivers at (0,0,0), (25,0,3), (50,3,5), (30,40,9), and (1,30,6) m, respectively. The speed of sound is a typical 330 m/s. The speed of propagation is made to be inhomogeneous by introducing a wind of 10 m/s in the positive y direction. Next, simulated values of the travel time differences are computed using these values. The source is located using hyperbolic and isodiachronic location. It will be seen that only isodiachronic location yields a correct solution.
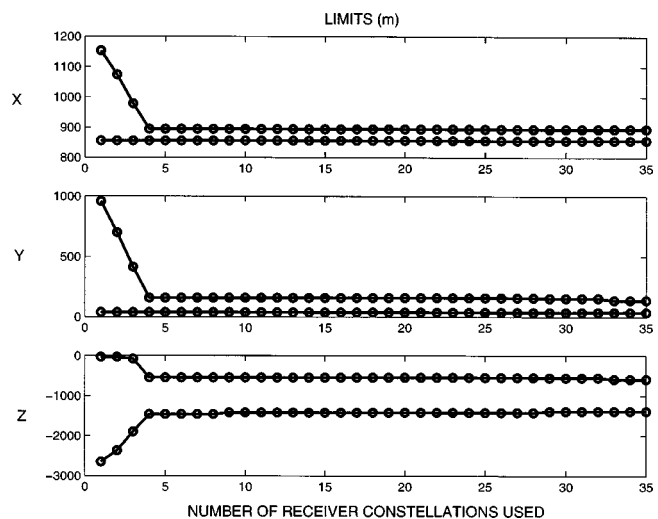

FIG. 4. Same as Fig. 2 except for array two in Fig. 1 and there are 35 ways of choosing 4 receivers from a total of 7 without replacement.
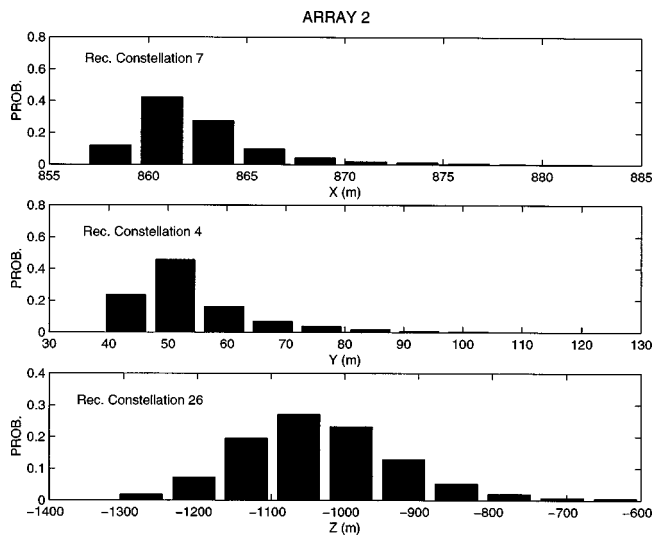
FIG. 5. Probability density functions for source location from array two (Fig. 1, bottom) using the nonlinear method of this paper. Receiver constellations 7, 4, and 26 are composed from receivers {1,2,4,7}, {1,2,3,7}, and {2,3,6,7}, respectively.

All Gaussian random variables in this simulation are truncated to have a maximum of two standard deviations for the following two reasons. First, many experimental situations are inaccurately represented by assuming that random variations differ from an estimate by say ten standard deviations. Instead, it is more realistic to truncate the variations. Second, it is important to note that a realistic truncation is easy to impose with the models developed here but is difficult to implement with analytical and linear approximations for error.

The standard deviation for receiver locations is 0.02 m. The variations are zero for the x, y, and z coordinates of receiver 1, the y and z coordinates of receiver 2, and the z coordinate of receiver 3. The coordinates with zero variations merely define the origin and orientation of the coordinate system. The x and z components of the winds are modeled to have a value of 0 m/s. For hyperbolic location, the speed of acoustic propagation must be spatially homogeneous. The mean and standard deviation for sound speed are 330 m/s and 10 m/s, respectively. For isodiachronic location, the speed of propagation is inhomogeneous. The speed of sound is taken to be 330 m/s. The *a priori* value of the wind in the y direction has mean 0 and standard deviation 10 m/s. Values of the speed of acoustic propagation, c_i, between receiver i and the source are unknown because the location of the source is initially unknown. Therefore, it is impossible to precompute the component of the wind vector along the direction from the source to each receiver. Instead, the value for each c_i is computed using a direction chosen at random through the simulated field of sound speed and wind. The error in travel time due to the straight path approximation is typically less than a microsecond at these ranges.[6] The travel time differences are derived with ideal values for means and from a standard deviation of 16 μs. The 16 μs value is derived from Eq. 41 in Ref. 6 using an rms bandwidth of 1000 Hz and a peak signal-to-noise ratio of 20 dB in the cross-correlation function of the signals between receivers.

Incorrect locations are obtained using the hyperbolic method. For example, the source's 100% confidence limits for x are 19.02 to 19.05 m, but its actual x location is 20 m. Similarly, the 100% confidence limits for y are 103 to 105 m, but the actual value is 100 m. So given *a priori* variations of receiver locations, travel time differences, and environmental variations, the hyperbolic method always yields incorrect answers.

With isodiachronic location, 95% confidence limits for the source are x: 19.5 to 23.7 m, y: 92.6 to 106 m, z: -26 to 13 m. These are correct. Other confidence limits could be given but they are not shown because the point is that isodiachronic location yields a correct answer at a stringent confidence of 95%.

The second case where isodiachronic location would be useful is one where the speed of sound is quite different between the source and each receiver. In this case, hyperbolic locations would be inappropriate to use because the speed of sound is not nearly constant in space. For example suppose low frequency sources such as Finback whales are located. Suppose some receivers close to the source pick up only the first acoustic path through the sea, while other distant receivers pick up only the acoustic path that propagates below the sea-floor[13] because the paths through the water are blocked by seamounts. The speed of propagation along the water and solid-Earth paths can differ by more than a factor of 2.[13] In other scientific fields, sounds can propagate to receivers along paths with different speeds of sound, such as from vehicles where paths propagate through the air and ground.

V. CONCLUSION

A method is developed for computing probability density functions for hyperbolic locations without relying on any linear approximation between travel time differences at pairs of receivers and the location of the source. In cases of practical interest, the confidence limits for location can be one or two orders of magnitude smaller with the nonlinear analysis than the linear one. The method for computing probability density functions includes *a priori* information about the probability density functions of the receiver locations, the speed of sound, and the errors in the differences in travel time.

It appears to be useful to relax the traditional assumption that the speed of acoustic propagation be spatially homogeneous for hyperbolic locations. Instead, one can allow the average speed to be different between each receiver and the source. This leads to a new geometrical surface, called an isodiachron, that approaches a hyperboloid when the speed of propagation is spatially homogeneous.

The ideas in this paper need to be tried with data.

ACKNOWLEDGMENTS

[1] N. Marchand, "Error distributions of best estimate position from multiple time difference hyperbolic networks," Aerosp. Navigational Electron. **11**, 96–100 (1964).

[2] W. H. Foy, "Position-location solutions by Taylor-series estimation," IEEE Trans. Aerosp. Electron. Syst. **AES-12**, 187–194 (1976).

[3] H. B. Lee, "A novel procedure for assessing the accuracy of hyperbolic multilateration systems," IEEE Trans. Aerosp. Electron. Syst. **AES-11**, 2–15 (1975).

[4] H. B. Lee, "Accuracy limitations of hyperbolic multilateration systems," IEEE Trans. Aerosp. Electron. Syst. **AES-11**, 16–29 (1975).

[5] J. M. Delosme, M. Morf, and B. Friedlander, "Source location from time differences of arrival: Identifiability and estimation," IEEE International Conference on Acoustics, pp. 818–824 (1980).

[6] J. L. Spiesberger and K. M. Fristrup, "Passive localization of calling animals and sensing of their acoustic environment using acoustic tomography," Am. Nat. **135**, 107–153, (1990).

[7] M. Wahlberg, B. Mohl, and P. T. Madsen, "Estimating source position accuracy of a large-aperture hydrophone array for bioacoustics," J. Acoust. Soc. Am. **109**, 397–406 (2001).

[8] R. O. Schmidt, "A new approach to geometry of range difference location," IEEE Trans. Aerosp. Electron. Syst. **AES-8**, 821–835 (1972).

[9] W. A. Watkins and W. E. Schevill, "Four hydrophone array for acoustic three-dimensional location," Woods Hole Oceanographic Technical Report 71–60 (1971).

[10] W. A. Tyrrell, "Design of acoustic systems," in *Marine Bioacoustics*, edited by W. N. Tavolga (Pergamon, Oxford, 1964), pp. 65–86.

[11] J. L. Spiesberger, "Hyperbolic location errors due to insufficient numbers of receivers," J. Acoust. Soc. Am. **109**, 3076–3079 (2001).

[12] G. Cardano, *Hieronymi Cardani Artis magn, sive, De regulis algebraicis lib. unus: qui & totius operis de arithmetica, quod opus perfectum inscripsit, est in ordine decimus* (Norimberg, Petreium excusum, 1545).

[13] V. Premus and J. L. Spiesberger, "Can acoustic multipath explain finback *B. physalus* 20-Hz doublets in shallow water?" J. Acoust. Soc. Am. **101**, 1127–1138 (1997).

Method of improved scatterer size estimation and application to parametric imaging using ultrasound

Michael L. Oelze[a) and William D. O'Brien, Jr.
Bioacoustic Research Laboratory, Department of Electrical and Computer Engineering,
University of Illinois, 405 North Mathews, Urbana, Illinois 61801

The frequency dependence of RF signals backscattered from random media (tissues) has been used to describe the microstructure of the media. The frequency dependence of the backscattered RF signal is seen in the power spectrum. Estimates of scatterer properties (average scatterer size) from an interrogated medium are made by minimizing the average squared deviation (MASD) between the measured power spectrum and a theoretical power spectrum over an analysis bandwidth. Estimates of the scatterer properties become increasingly inaccurate as the average signal to noise ratio (SNR) over the analysis bandwidth becomes smaller. Some frequency components in the analysis bandwidth of the measured power spectrum will have smaller SNR than other frequency components. The accuracy of estimates can be improved by weighting the frequency components that have the smallest SNR less than the frequencies with the largest SNR in the MASD. A weighting function is devised that minimizes the noise effects on the estimates of the average scatterer sizes. Simulations and phantom experiments are conducted that show the weighting function gives improved estimates in an attenuating medium. The weighting function is applied to parametric images using scatterer size estimates of a rat that had developed a spontaneous mammary tumor. © *2002 Acoustical Society of America.* [DOI: 10.1121/1.1517064]

PACS numbers: 43.80.Qf, 43.80.Vj [FD]

I. INTRODUCTION

Conventional B-mode images using ultrasound can resolve structures from hundreds of micrometers to centimeters in scale (structures greater than the acoustic wavelength). A conventional B-mode image is made up of several parallel or consecutively spaced axial RF time signals. Each RF time signal is a series of echoes backscattered from structures in the interrogated medium. In a conventional B-mode image, the frequency-dependent information in the RF time signals is not utilized. Instead, the conventional B-mode image relates the envelope of a backscattered RF time signal to a gray-scale image.

The frequency-dependent information in the RF time signal is related to the tissue microstructure (structures less than the acoustic wavelength).[1–13] Parametrizing the microstructure of tissues has been accomplished by modeling the frequency-dependent scattering from tissues. Several researchers have used parameter information about the shape of the spectrum of sound scattered from tissues to classify tissue microstructure and identify disease.[2,9,11–14] Other researchers have been able to estimate the size, shape and internal make-up of scatterers in tissues from models.[3,5–7,9–11]

Parametric images, which combine the estimated parameters or scatterer properties with conventional B-mode images, have been used to assist with clinical diagnosis and classification of tissue state.[6,9,12,13,15–18] Parametric images that utilize the slope and intercept parameters to describe the scattered power spectrum have been used by Feleppa *et al.*[12]

and Lizzi *et al.*[13] Insana *et al.* created parametric images using estimates of the average scatterer size to describe tissue microstructure.[9]

The advantage in using estimates of the scatterer properties, like the average scatterer size, is that the estimated property may be related to physical microstructures of the tissues. By relating estimated scatterer properties to physical structures, it may be possible to verify the models. Furthermore, if the estimated scatterer properties can be related to real physical structures in tissues, then a new clinical capability presents itself to diagnose tissue disease. If data processing strategies are found that improve the accuracy of estimations, then the utility of parametric imaging for diagnosis of diseased tissues is increased. A few authors have looked at techniques to improve estimates of scatterer properties from backscatter.[19,20] More accurate estimates of scatterer properties have been obtained through optimization of the backscatter measurements and estimation routines. In the work reported herein, a new optimization technique is introduced that increases the accuracy of scatterer property estimations from an attenuating medium. The technique extends the work of previous researchers to increase the accuracy of scatterer property estimations.[20] The new technique uses prior knowledge about the expected SNR of the frequency components in the scattered power spectrum to increase the accuracy of estimation schemes.

Section II explains the theoretical basis for the enhanced estimation technique. The enhanced estimation technique is based on weighting different frequency components used in the estimation according to their expected SNR. Section III discusses simulations and an experiment from a phantom with glass beads. The simulations were constructed to model

---

[a)]Author to whom correspondence should be addressed. Electronic mail: oelze@brl.uiuc.edu

scattering from glass beads and Gaussian scatterers embedded in a tissue-like medium. The phantom experiment was conducted to verify the simulations and the use of the enhanced estimation technique. Section IV applies the enhanced estimation technique to parametric B-mode images of a rat that had developed a spontaneous mammary tumor. The last section includes some concluding remarks about improvement in scattering property estimates achieved by the enhanced estimation technique.

II. THEORETICAL DESCRIPTION

Average effective scatterer sizes and acoustic concentrations from tissues or other media can be estimated from backscattered RF signals.[3,5,6,21–23] The estimates of scatterer sizes from backscattered RF signals are attractive because they allow the resolving of subwavelength structure in a statistical sense. The methods of estimation assume single scatter theory (no multiple scattering) and examine cases where the scatter is incoherent, i.e., no periodic structures. Relating the frequency-dependent RF signal to models of the tissue microstructure leads to estimates of the scatterer properties. The models describe the scattering through the magnitude and shape of the theoretical power spectrum. A method commonly used to estimate scatterer properties is to minimize the average squared deviation (MASD) between the theoretical power spectrum and the measured power spectrum. The best estimate of the desired scatterer property is the value of the scatterer property that minimizes the squared difference[5,6]

$$MASD = \min\left\{ \frac{1}{B} \sum_{i=1}^{B} (M_i - T_i)^2 \right\}, \tag{1}$$

where B is the number of samples in the analysis bandwidth and M_i and T_i are the logarithms of the measured and theoretical power spectra of the scattered RF signal expressed in dB, respectively. Trial and error could be used to find the scatterer properties that give the MASD or more elegant methods like the steepest descent could be used.[24]

Assuming the theory correctly describes the scattering phenomena, then as the SNR increases, the estimation of scattering properties through the MASD is increasingly accurate. As the SNR decreases, the MASD gives less accurate estimates of the scattering properties.[20] Particular frequency components in the analysis bandwidth will have a larger SNR than other frequency components.

Several factors introduce more noise into the measurement thereby decreasing the SNR for particular frequency components. Two factors that determine lower SNR at particular frequencies are the bandwidth and amplitude of the excitation-pulse power spectral shape.[20] The scattered power is proportional to the spectral power of the initial excitation pulse. Less power in the excitation pulse means smaller SNR in the scattered signal, especially at frequency components with little magnitude in the excitation-pulse power spectrum (−6 dB bandwidth edges assuming a Gaussian spectrum). Attenuation has a dramatic effect on the estimation of scattering properties by reducing signal and decreasing the SNR in the measurement. Typically, attenuation increases with increasing frequency so that the attenuation reduces the SNR at
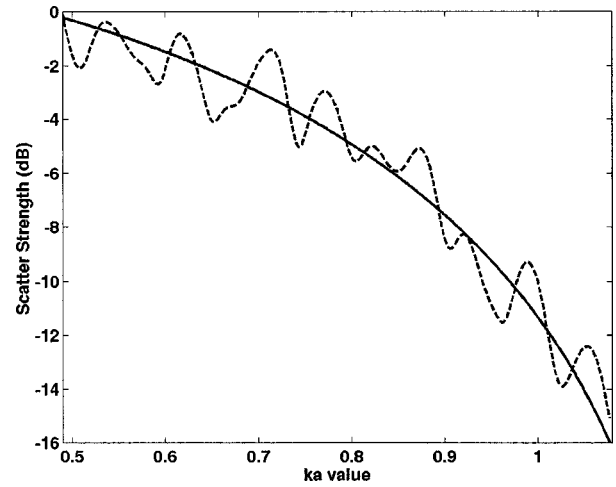

FIG. 1. Comparison of the theoretical and measured backscatter spectra (form factor) from a collection of randomly spaced glass beads of diameter 80 μm; —, theoretical form factor; ---, measured form factor.

higher frequencies more than at lower frequencies. A third factor that causes low SNR is the magnitude of the scattering power itself. Particular frequencies in the scattered power spectrum are scattered with different magnitudes according to the size, shape and makeup of the scattering particles.[3,5,6] Frequencies that are scattered with a low magnitude contribute to smaller SNR than frequencies scattered with large magnitude. Figure 1 compares a theoretical and measured scattered power spectrum (form factor) from a collection of randomly spaced glass beads of known size versus different ka values for a signal with minimal attenuation losses.[5] The ka value represents the acoustic wave number, k, times the average glass bead radius, a. The spectra show that different frequency components (ka values) scatter with different magnitudes. Inherent in the measured spectrum is a level of noise. A comparison of the two spectra shows that the ratio of noise to scattering magnitude is greater for certain frequencies than others, namely the larger frequencies.

The ability of the MASD to estimate scatterer properties is related to the SNR of the backscattered signals. The more noise there is in the backscattered signal (measured power spectrum) the less accurate the estimates of scatterer properties. Because particular frequency components have different SNRs, those frequency components with larger SNR increase the accuracy of the estimates while the frequency components with smaller SNR decrease the accuracy of scatterer property estimates. By weighting the frequency components in the analysis bandwidth that have larger SNR more than the frequency components that have smaller SNR, improved accuracy in scatterer property estimations can be obtained.[20]

Consider a backscattered RF time signal gated from a region of randomly spaced scatterers

$$x(t) = p(t) * s(t) + n(t), \tag{2}$$

where $p(t)$ is the impulse response of the system (including effects of diffraction and attenuation), $s(t)$ describes the tissue scattering, and $n(t)$ represents the random noise. The noise, $n(t)$, is modeled as a zero-mean Gaussian white noise coming from electronic noise in the system. The measured power spectrum is given by

M. L. Oelze and W. D. O'Brien, Jr.: Improved scatterer size estimation

$$W'_{\text{meas}}(f) = |X(f)|^2 = |P(f)|^2|S(f)|^2 + |N'(f)|^2, \qquad (3)$$

where $|S(f)|^2$ is the power spectrum of the scatterers determined by the size and shape of the scatterers in the medium,[10] $|P(f)|^2$ is the power spectrum of the impulse response, and $|N'(f)|^2$ is the noise contribution to the power spectrum from the electronic noise in the system and from noise related to the random scatterer spacings.[25] If measurements are taken in the depth of focus of the transducer then the power spectrum of the impulse response can be approximated as

$$|P(f)|^2 \approx W_{\text{ref}}(f)A^{-1}(f), \qquad (4)$$

where $W_{\text{ref}}(f)$ represents the power spectrum of the excitation pulse and $A^{-1}(f)$ represents the frequency-dependent attenuation loss over the gated length. The function $A(f)$ would represent an attenuation–compensation function. The power spectrum of the excitation pulse is approximated by a calibration (reference) spectrum that is found by measuring the pulse from a planar reflector of known reflectivity located at the same distance from the source to the gated signal.[5,6,26,27] Because the measurements are taken in the depth of focus of the transducer, diffraction effects are considered minimal.

The normalized power spectrum is found by dividing by $W_{\text{ref}}(f)$ and correcting for the attenuation losses with the attenuation–compensation function[6]

$$W_{\text{meas}}(f) = W'_{\text{meas}}(f)\frac{A(f)}{W_{\text{ref}}(f)} \qquad (5)$$

giving

$$W_{\text{meas}}(f) = |S(f)|^2 + \frac{|N'(f)|^2}{W_{\text{ref}}(f)}A(f) = |S(f)|^2 + |N''(f)|^2. \quad (6)$$

Letting

$$M(f_i) = 10\log W_{\text{meas}}(f_i) \qquad (7)$$

and

$$T(f_i) = 10\log|S_T(f_i)|^2 \qquad (8)$$

according to Eq. (1) where $S_T(f_i)$ is the theoretical power spectrum, then

$$\text{MASD} = \min\left\{\frac{1}{B}\sum_{i=1}^{B}(10\log[|S(f_i)|^2 + |N''(f_i)|^2]\right.$$
$$\left. -10\log|S_T(f_i)|^2)^2\right\}. \qquad (9)$$

If the theory correctly describes the scatter then

$$|S_T(f_i)|^2 = |S(f_i)|^2. \qquad (10)$$

Insertion of Eq. (10) into Eq. (9) yields

$$\text{MASD} = \min\left\{\frac{1}{B}\sum_{i=1}^{B}(10\log[|S_T(f_i)|^2 + |N''(f_i)|^2]\right.$$
$$\left. -10\log|S_T(f_i)|^2)^2\right\}. \qquad (11)$$

Simplifying Eq. (11) and using the notation $|S_T(f_i)|^2 = S_i$ and $|N''(f_i)|^2 = N''_i$ gives

$$\text{MASD} = \min\left\{\frac{1}{B}\sum_{i=1}^{B}\left(10\log\left[1+\frac{N''_i}{S_i}\right]\right)^2\right\}. \qquad (12)$$

Equation (12) is minimized and the best estimates are made when Eq. (10) holds and the noise is zero (MASD=0). The smallest possible value for the MASD occurs when the summation over the entire analysis bandwidth is zero. When the noise is not zero, another value for $S_T(f_i)$ may exist that does not yield the most accurate estimates of the true scatterer properties but minimizes the average squared deviation. In any real situation, the noise is not zero and the accuracy of the estimates is reduced by the level of noise. In order to get the best estimates from the MASD, Eq. (10) must hold and the noise effects seen in Eq. (12) must be minimized.

To a limited degree, weighting different frequency components based on their expected SNR will reduce the noise effects on the estimates. Defining the SNR according to[19]

$$\text{SNR} = 10\log\frac{|S(f_i)|^2}{|N''(f_i)|^2} \qquad (13)$$

then as long as the SNR$\geq$0, $N''_i/S_i\leq 1$ and the term in parenthesis in Eq. (12) can be expanded into a series as

$$\text{MASD} = \min\left\{\frac{1}{B}\sum_{i=1}^{B}\left(\left[\frac{N''_i}{S_i} - \frac{1}{2}\left(\frac{N''_i}{S_i}\right)^2\right.\right.\right.$$
$$\left.\left.\left. +\frac{1}{3}\left(\frac{N''_i}{S_i}\right)^3 - \cdots\right]10\log e\right)^2\right\}. \qquad (14)$$

If the $N''_i/S_i\leq 1$, then the first term contributes most to the MASD and

$$\text{MASD} \approx \frac{18.8}{B}\sum_{i=1}^{B}\left(\frac{N''_i}{S_i}\right)^2(1-\epsilon)^2, \qquad (15)$$

where ϵ represents some small value. If the frequency dependence of N''_i/S_i can be deduced, then a weighting function can be constructed that reduces the effect of the first term on the estimation scheme.

Let H_i^2 be the weighting function that minimizes the effect of the noise on the estimation of scatterer properties through the MASD. The weighting function is implemented into the MASD by

$$\text{MASD} \approx \frac{18.8}{B}\sum_{i=1}^{B}\left(\frac{N''_i}{S_i}\right)^2(1-\epsilon)^2 H_i^2. \qquad (16)$$

The form of H_i^2 depends on the frequency dependence of the ratio N''_i/S_i. From the definition of N''_i in Eq. (6)

$$N''_i = N'_i\frac{A(f_i)}{W_{\text{ref}}(f_i)}. \qquad (17)$$

Equation (17) shows that the noise function, N''_i, and hence N''_i/S_i increases as the attenuation coefficient and propagation distance increases, i.e., $A(f)$ gets larger. Furthermore, dividing the noise by the calibration spectrum, $W_{\text{ref}}(f_i)$, increases the overall magnitude of N''_i/S_i at the edges of the excitation pulse bandwidth, assuming a typical Gaussian-

type bandwidth. At frequency components where the scattering power, S_i, is smaller, N_i''/S_i will also be larger. The attenuation–compensation function and calibration spectrum are known and the scattering power can be approximated. Defining

$$\Omega_i = \frac{A(f_i)}{S_i \cdot W_{\text{ref}}(f_i)}, \tag{18}$$

then

$$\text{MASD} \approx \frac{18.8}{B} \sum_{i=1}^{B} N_i'^2 \Omega_i^2 (1-\epsilon)^2 H_i^2. \tag{19}$$

The factor Ω_i can be defined for each frequency component but the noise factor N_i' and the value of ϵ cannot be explicitly determined. The factor Ω_i acts to amplify the noise differently at different frequency components. By defining the weighting function as

$$H_i^2 = \frac{1}{\Omega_i^2} \tag{20}$$

the noise frequency components most amplified by the Ω_i factor are given less weight in the estimation process. The weighting scheme can be compared to placing a Wiener filter on the original measured spectrum except that the filtering is done on the squared difference between the logarithm of the actual measured spectrum and the theoretical spectrum. No matter what shape the original noise spectrum, N_i', the weighting scheme will give improvement to the accuracy of estimates because the weighting function cancels the amplification of noise by the Ω_i factor. The solution for H_i^2 weights the MASD according to the known attenuation losses, the shape of the excitation pulse and the approximated scattered power spectrum.

III. SIMULATIONS AND PHANTOM EXPERIMENT

To test the effectiveness of the SNR weighting, simulations were constructed to model scattering from a random, lossy medium. The simulations used different kinds of scatterers of various sizes in media with different attenuation coefficients to examine the ability of the SNR weighting scheme to improve estimation of scatterer properties under different conditions. The attenuation in each of the simulations was chosen to represent what is commonly found in biological tissues. An experiment was performed using backscatter data collected from a real phantom[28] with random scatterers. These data were used to verify the effectiveness of the SNR weighting and the accuracy of the simulations. Estimates of the average scatterer diameter were made from simulations and the phantom measurement with and without the SNR weighting and compared.

Each simulation was constructed by creating a volume matrix with scatterers placed randomly in the matrix. A certain volume of the scatterers corresponding to the beam of the transducer was excited by an acoustic pulse. A wavetrain of backscattered pulses was then created by summing the scattered excitation pulses from each scatterer back at the source aperture. The effects of the medium attenuation were incorporated in propagation of the pulse to and from each

scatterer back to the source. Electronic noise was simulated by adding zero-mean Gaussian white noise with standard deviation of -40 dB the amplitude of the calibration pulse at the focus. All scattering in the simulations were constructed to take place in the depth of focus of the transducer.

Estimates were made from the backscattered echoes, simulated and measured from the phantom. The ultrasonic bandwidth used for the estimates ranged from 5 to 11 MHz with a center frequency of 8 MHz for the simulations and 8.3 MHz for the phantom experiment. The transducer used in the measurements had an aperture diameter of 12 mm and a focal length of 58 mm. The simulated and measured backscattered RF echoes were digitally sampled at 50 MHz. Each scanned A-line was gated into 4-mm sections using a sliding Hanning window (75% overlap). The average normalized power spectrum was measured for each 4-mm section[6,26,27]

$$W_{\text{meas}}(f) = \frac{R^2}{4M} A(f,L) \sum_{n=1}^{M} \frac{W_n(f)}{W_{\text{ref}}(f)}, \tag{21}$$

where $W_n(f)$ is the measured power spectrum from a single A-line, A is an attenuation–compensation function,[29] L is the gate length (4 mm in the simulations and phantom experiments) and R is the reflection coefficient of the planar reflector used to obtain the reference spectrum, $W_{\text{ref}}(f)$. The average normalized power spectrum is the average of M power spectra from consecutive gated RF time series (A-lines) over a lateral length of 4 mm. The average normalized power spectrum represents the scattering properties from a 4 mm×4 mm box. In a particular box or region of interest (ROI), each consecutive RF time series is assumed to have similar statistical properties so that the average of the spectra reduces noise and anomalous artifacts that may exist in any spectrum measured from a single RF time series. The M power spectra averaged together represent the ensemble of scatterers in the ROI.

The first simulations were modeled as glass beads in agar and the phantom was made from glass beads embedded in agar. The theoretical power spectrum of scattering from glass beads was described using the form factor models.[5,6] The form factor model for glass beads gives a theoretical power spectrum

$$W_{\text{theor}}(f) = C(a_{\text{eff}}, n_z) f^4 F(f, a_{\text{eff}}), \tag{22}$$

where C is a constant with frequency and a function of the average effective radius, a_{eff}, of the scatterers and the average acoustic concentration, n_z, of scatterers. The acoustic concentration is defined as the product of the volumetric concentration of scatterers and the average fractional impedance change between the scatterers and surrounding tissues. $F(f, a_{\text{eff}})$ is the form factor describing the frequency dependence of the scattering based on the size, shape and impedance distribution of the average scatterer.[10] Insana and Hall[5] showed that the form factor for spherical shells closely approximated the form factor for glass beads as calculated using the theory of Faran.[21] The form factor for spherical shells (approximating the glass bead form factor) is given by[5]

$$F_{\text{glass}}(f,a) = \left[j_0 \left(\frac{4\pi fa}{c} \right) \right]^2, \tag{23}$$

M. L. Oelze and W. D. O'Brien, Jr.: Improved scatterer size estimation

where j_0 represents the spherical Bessel function of order zero and of the first kind, c is the speed of sound in the medium (1540 m/s) and a is the average radius of the glass beads. The form factor for the spherical shell was used to approximate the form factor for glass beads because it has a closed form solution that did not require numerical calculation using the theory of Faran for each trial diameter.[21]

Estimates of the average scatterer size were found through the MASD between the average normalized power spectrum and the theoretical power spectrum. From Eq. (1)

$$\text{MASD} = \min\left(\frac{1}{B} \sum_{i=1}^{B} \left[10 \log W_{\text{meas}}(f_i) \right. \right.$$

$$\left. \left. - 10 \log |C(a_{\text{eff}}, n_z) f_i^4 F(a_{\text{eff}}, f_i)|\right]^2 \right). \qquad (24)$$

Letting

$$X_i = 10 \log[W_{\text{meas}}(f_i)/F(a_{\text{eff}}, f_i) f_i^4] \qquad (25)$$

and using the fact that the constant C is not a function of frequency and can be seen as an intercept to define

$$\bar{X} = \langle 10 \log C(a_{\text{eff}}, n_z) \rangle_B$$

$$= \langle 10 \log[W_{\text{meas}}(f)/F(a_{\text{eff}}, f) f^4] \rangle_B \qquad (26)$$

yields for the MASD[5,6]

$$\text{MASD} = \min\left(\frac{1}{B} \sum_{i=1}^{B} [X_i - \bar{X}]^2 \right). \qquad (27)$$

The estimate of the average scatterer radius (diameter) is the argument that minimizes Eq. (27).

Implementation of the SNR weighting is given by

$$\text{MASD} = \min\left(\frac{1}{B} \sum_{i=1}^{B} (X_i - \bar{X})^2 H_i^2 \right), \qquad (28)$$

where H_i^2 is given by Eq. (20). The weighting function, H_i^2, is known only if the approximate scattered power spectrum, S_i, is known. The scattered power spectrum is assumed from measurements of the scattering properties in previous ROIs.

In the scattering medium, different regions of interest (ROIs) were selected to examine their scattering properties. In the measurements of the simulations and phantom experiments, the ROIs were selected to be 4 mm×4 mm boxes. The boxes represented gated backscattered signals in the axial direction averaged over a 4 mm length in the lateral direction. The boxes represented 10 half beamwidths (~0.4 mm) in the lateral direction and 20 wavelengths at the center frequency (8 MHz) in the axial direction. Figure 2 gives a representation of the ROI selection in a scattering medium. Each box had a 75% overlap (sliding Hanning window) of the previous ROI box in the axial and lateral directions. Where the boxes overlapped, estimates of scatterer properties were averaged to give regions of 1 mm×1 mm with distinct estimates. The total length of one scan was 1.5 cm in the lateral direction.

Scatterer estimates from regions of shallow propagation depth were assumed to have the best accuracy because less signal loss was introduced by attenuation. The approximate
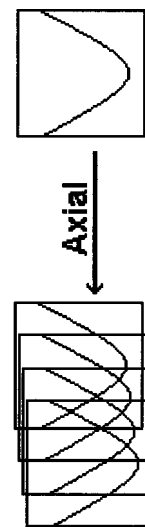

FIG. 2. Representation of the Hanning windowed regions of interest with 75% overlap between regions.

scattered power spectrum, S_i, used in the weighting function came from the scattered power spectrum estimated in the previous axial ROI. In the initial ROI of a particular axial line, no weighting with the approximate scattered power spectrum was used because it was assumed that the noise effects were minimal at the shallowest measured depth. By overlapping each ROI with a 75% overlap, the scattering properties from one ROI to the next was assumed to be slowly changing so that the scattered power spectrum used in the weighting function was approximately true.

Figures 3–9 show the estimates of scatterer sizes from simulations and the phantom experiment as the depth increases incrementally by 1 mm (distance between consecutive ROIs) in the scattering media. Figures 3 and 4 show the average estimated scatterer diameters from computer simulations of glass beads in agar. In the simulation for Fig. 3 the sizes of the glass beads are 80 μm in diameter while the sizes of the glass beads in the simulation for Fig. 4 are 40 μm in diameter. Both figures show that the estimates made using the SNR weighting provided better estimates of the true scat-

FIG. 3. Estimation of average scatterer diameter from backscattered echoes simulated from an attenuating medium (0.7 dB/MHz/cm) with randomly spaced glass bead scatterers of diameter 80 μm; □, estimates from simple MASD; ◇, estimates from MASD with SNR weighting. Each estimate is the average 10 estimates from 10 ROIs at the same depth with error bars representing one standard deviation about the average of the 10 estimates.

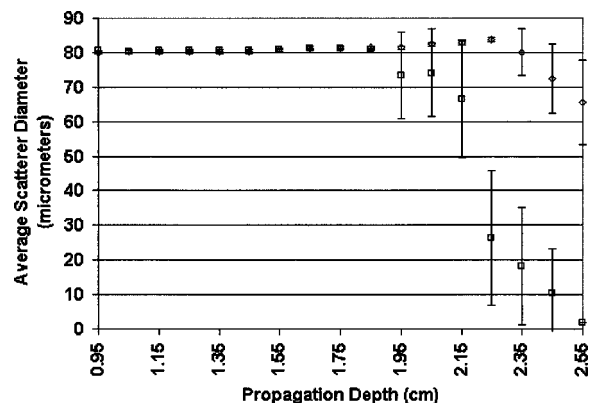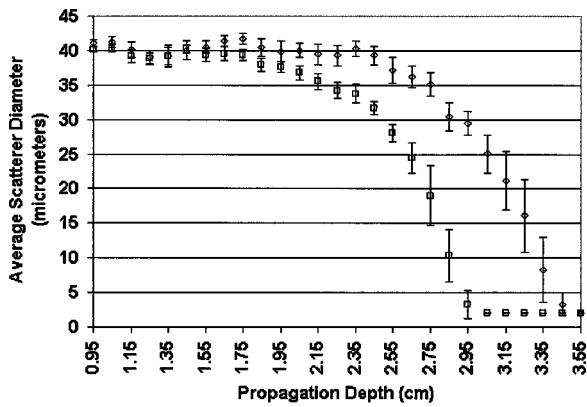M. L. Oelze and W. D. O'Brien, Jr.: Improved scatterer size estimation

FIG. 4. Estimation of average scatterer diameter from backscattered echoes simulated from an attenuating medium (0.7 dB/MHz/cm) with randomly spaced glass bead scatterers of diameter 40 μm; $\square$, estimates from simple MASD; $\diamond$, estimates from MASD with SNR weighting. Each estimate is the average 10 estimates from 10 ROIs at the same depth with error bars representing one standard deviation about the average of the 10 estimates.

FIG. 6. Estimation of average scatterer diameter from backscattered echoes measured from an agar phantom with attenuation 0.49 dB/MHz/cm and randomly spaced glass bead scatterers of diameter 48±2.5 μm; $\square$, estimates from simple MASD; $\diamond$, estimates from MASD with SNR weighting. Each estimate is the average 10 estimates from 10 ROIs at the same depth with error bars representing one standard deviation about the average of the 10 estimates.

terer sizes than estimates made without the SNR weighting. Particularly for the larger scatterer sizes (80 μm) of Fig. 3, the SNR-weighted measurements gave better results. The estimates made with the SNR weighting yielded more accurate results when the total attenuation was larger (SNR was smaller) and appeared to extend the ability to make estimates to a greater propagation depth. For example, in Fig. 3 the ability to estimate the average scatterer diameter within 10% of the actual value from the MASD was extended a half-centimeter in propagation depth using the SNR weighting. In Fig. 4 accurate estimates were extended by more than a half-centimeter in depth using the SNR weighting.

Estimates of scatterer sizes from a phantom embedded with randomly spaced scatterers were also compared with estimates from a simulation. The phantom contained glass beads with diameters of 48±2.5 μm embedded in agar.[28] The attenuation coefficient of the material was controlled by a concentration of graphite powder and was measured at around 0.49 dB MHz^{-1} cm^{-1}.

A single-element weakly focused transducer was used to

scan laterally across the phantom surface. The transducer was moved laterally across the phantom surface by a micropositioning system with step size of 100 μm between each A-line scan. The transducer had an aperture diameter of 12 mm and a focal length measured at 58 mm from a planar reflector. The center frequency of the transducer was 8.3 MHz with a −6-dB pulse-echo frequency bandwidth of 6 MHz. The analysis bandwidth ranged from 5 to 11 MHz. Figure 10 shows the calibration spectrum measured near the focus of the transducer from a planar surface and the backscattered spectrum from the phantom at the focus. Estimates of scatterer properties were made in the −6-dB pulse-echo depth of focus of the transducer, which ranged from 4.45 cm to 7.45 cm from measurements off a planar reflector.

The transducer was operated in pulse-echo mode through a Panametrics 5800 pulser/receiver (Waltham, MA). The signals were recorded and digitized on an oscilloscope (Lecroy 9354 TM; Chestnut Ridge, NY) that had a dynamic
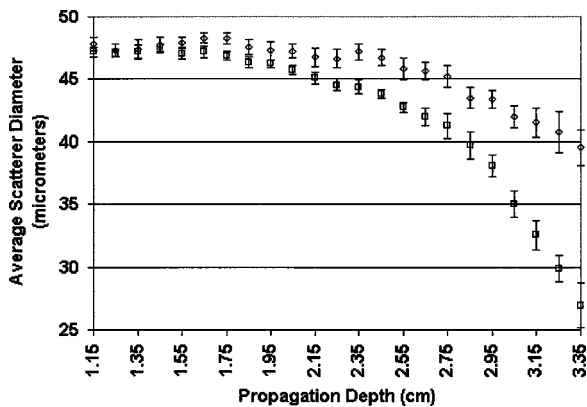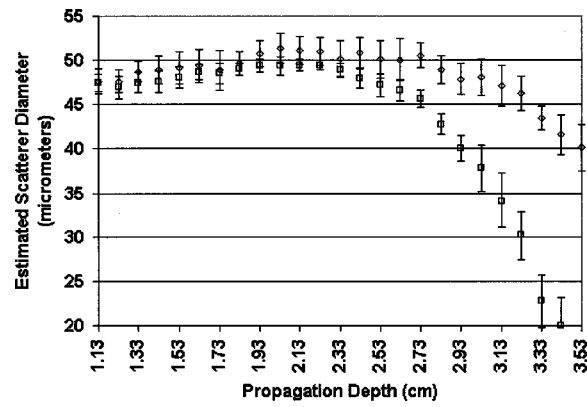

FIG. 5. Estimation of average scatterer diameter from backscattered echoes simulated from an attenuating medium (0.49 dB/MHz/cm) with randomly spaced glass bead scatterers of diameter 48 μm; $\square$, estimates from simple MASD; $\diamond$, estimates from MASD with SNR weighting. Each estimate is the average 10 estimates from 10 ROIs at the same depth with error bars representing one standard deviation about the average of the 10 estimates.

FIG. 7. Estimation of average, effective scatterer diameter from backscattered echoes simulated from an attenuating medium (0.7 dB/MHz/cm) with randomly spaced Gaussian scatterers of effective diameter 60 μm; $\square$, estimates from simple MASD; $\diamond$, estimates from MASD with SNR weighting. Each estimate is the average 10 estimates from 10 ROIs at the same depth with error bars representing one standard deviation about the average of the 10 estimates.

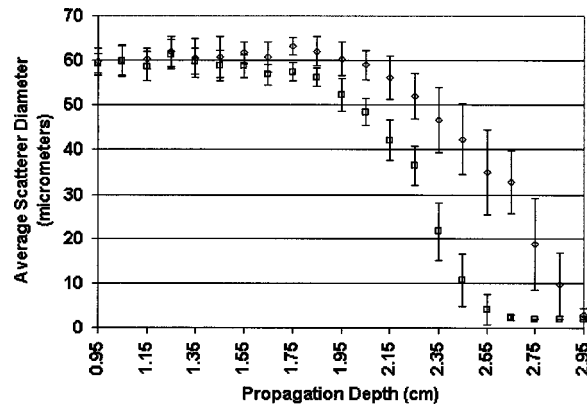M. L. Oelze and W. D. O'Brien, Jr.: Improved scatterer size estimation

FIG. 8. Estimation of average, effective scatterer diameter from backscattered echoes simulated from an attenuating medium (0.7 dB/MHz/cm) with randomly spaced Gaussian scatterers of effective diameter 60 ± 20 μm with a Gaussian distribution of scatterer sizes; $\square$, estimates from simple MASD; $\diamond$, estimates from MASD with SNR weighting. Each estimate is the average 10 estimates from 10 ROIs at the same depth with error bars representing one standard deviation about the average of the 10 estimates.
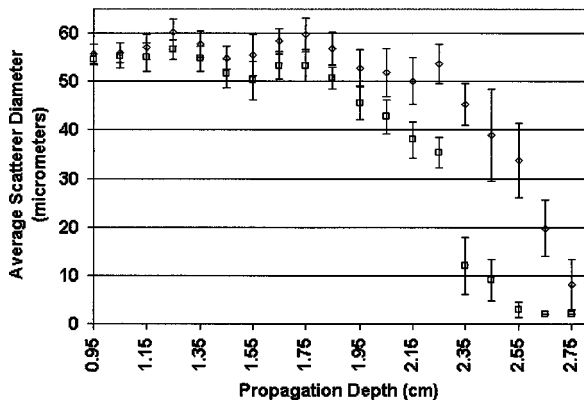
range of 48 dB and downloaded to a PC computer for post-processing. The sampling rate was 50 MHz.

A simulation was also constructed with glass bead scatterers of the same size and concentration and with the same attenuation coefficient as the phantom. Figures 5 and 6 show the results of estimates of the scatterer sizes from the simulation and the phantom measurements, respectively. Comparison of Figs. 5 and 6 shows that the simulation predicted well the improvement achieved using the SNR weighting function in the phantom estimates. Examination of the phantom results and the simulation showed that the ability to estimate the scatterer diameters accurately was increased by almost one centimeter using the SNR weighting for the particular attenuation and glass bead size. In addition, estimates from populations of scatterers with diameters of 40, 48, and 80 μm were examined to show that SNR weighting gave improvements for estimates of different scatterers sizes relative to acoustic wavelength.
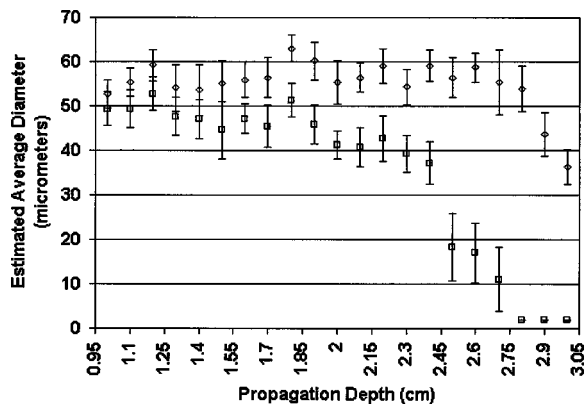

FIG. 9. Estimation of average, effective scatterer diameter from backscattered echoes simulated from an attenuating medium (0.7 dB/MHz/cm) with randomly spaced Gaussian scatterers of average effective diameter 60 μm with a uniform distribution of scatterer sizes between 40 and 80 μm; $\square$, estimates from simple MASD; $\diamond$, estimates from MASD with SNR weighting. Each estimate is the average 10 estimates from 10 ROIs at the same depth with error bars representing one standard deviation about the average of the 10 estimates.

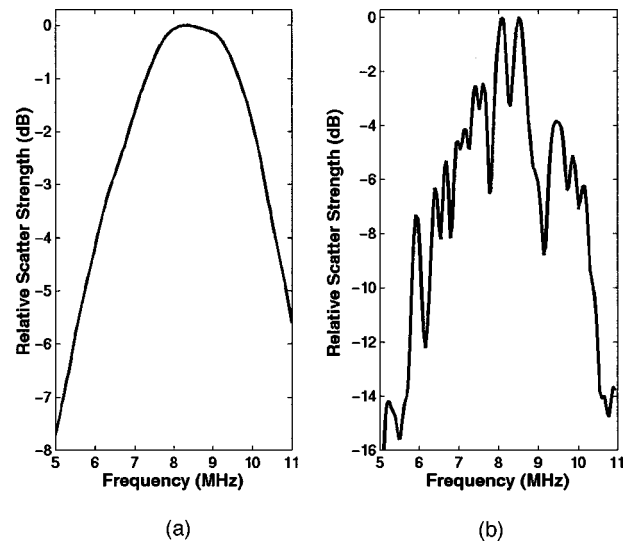(a)   (b)

FIG. 10. (a) Example of the calibration spectrum of the ultrasound pulse used in the phantom measurements reflected from a planar surface located near the transducer focus. (b) Example of the measured power spectrum backscattered from the transducer focus in a tissue-mimicking phantom.

A simulation was also constructed using Gaussian scatterers instead of glass beads. Gaussian scatterers are similar to glass beads because they represent spherical particles. Unlike the glass bead, however, the Gaussian scatterer represents an impedance change that varies continuously with the surrounding medium. A glass sphere has an abrupt change in impedance between the surrounding medium and the particle and, hence, a definite diameter. Instead of having a definite diameter, the Gaussian scatterer has an effective diameter. The effective diameter represents the width of the -6-dB edge of the Gaussian function describing the impedance distribution of the scatterer.[3]

Gaussian scatterers are described by the form factor[5]

$$F_{\text{Gauss}}(f) = e^{-0.75(2\pi f/c)^2 a_{\text{eff}}^2}, \qquad (29)$$

where the constant in the exponential is used to normalize the effective radius to the -6-dB edge of the Gaussian function. Gaussian scatterers have been used to describe the scattering from many soft tissues.[1,3–6,10] For the theoretical power spectrum using the Gaussian form factor, the MASD can be simplified. Inserting Eq. (29) into Eq. (22) gives for the theoretical log power spectrum of Eq. (8),[30]

$$T(f_i) = 10 \log f_i^4 + m(a_{\text{eff}})f_i^2 + b(a_{\text{eff}}, n_z), \qquad (30)$$

where f_i is a particular frequency component in the analysis bandwidth. The last two terms can be thought of as a line ($y = mx + b$) where $x = f_i^2$. The slope parameter, m, is a function of the average effective scatterer radius (diameter) and the intercept parameter is a function of the average effective scatterer diameter and acoustic concentration. The MASD, Eq. (1), is then given by

$$\text{MASD} = \min \left\{ \frac{1}{B} \sum_{i=1}^{B} (10 \log W_{\text{meas}}(f_i) - 10 \log f_i^4 \right.$$

$$\left. - m(a_{\text{eff}})f^2 - b(a_{\text{eff}}, n_z))^2 \right\}. \qquad (31)$$

Letting

$$X_i = 10 \log[W_{\text{meas}}(f_i)/f_i^4] - m(a_{\text{eff}})f_i^2 = y_i - m(a_{\text{eff}})f_i^2 \quad (32)$$

and calculating the average intercept

$$\bar{X} = \langle b(a_{\text{eff}}, n_z) \rangle_B = \frac{1}{B} \sum_{i=1}^{B} y_i - m(a_{\text{eff}})f_i^2 \quad (33)$$

then the MASD with the SNR weighting is given by Eq. (28). The MASD is determined when the diameter or the slope parameter, m, is found that minimizes the squared difference of Eq. (28). Lizzi *et al.* have estimated scatterer parameters from the measured power spectrum by fitting a line to the measured log power spectrum with $x = f$.[13] Equation (30) shows that the theoretical log power spectrum and, therefore, the measured log power spectrum is not linear. By subtracting $10 \log f^4$ from the measured log power spectrum according to Eq. (30) and fitting a line with $x = f^2$, a better fit to the measured log power spectrum can be made.[30]

When using the Gaussian form factor to model the scattering, the slope, m, that minimizes the average squared dif-

ference of Eq. (28) can be found by taking the derivative of Eq. (28) with respect to m and setting it equal to zero

$$\frac{\partial}{\partial m} \left(\frac{1}{B} \sum_{i=1}^{B} (X_i - \bar{X})^2 H_i^2 \right) = 0. \quad (34)$$

Evaluation of Eq. (34) gives

$$\frac{1}{B} \sum_{i=1}^{B} (X_i - \bar{X}) H_i^2 \left(\frac{\partial X_i}{\partial m} - \frac{\partial \bar{X}}{\partial m} \right) = 0, \quad (35)$$

where

$$\frac{\partial X_i}{\partial m} = -f_i^2 \quad \text{and} \quad \frac{\partial \bar{X}}{\partial m} = -\frac{1}{B} \sum_{i=1}^{B} f_i^2 = -\overline{f^2}. \quad (36)$$

Simplifying Eq. (35) yields

$$\sum_{i=1}^{B} (y_i - mf_i^2 - \bar{y} + m\overline{f^2}) H_i^2 (-f_i^2 + \overline{f^2}) = 0. \quad (37)$$

Solving for the slope, m, gives

$$m(a_{\text{eff}}) = \frac{\sum_{i=1}^{B} y_i f_i^2 H_i^2 - \bar{y} \sum_{i=1}^{B} f_i^2 H_i^2 - \overline{f^2} \sum_{i=1}^{B} y_i H_i^2 + \bar{y} \overline{f^2} \sum_{i=1}^{B} H_i^2}{\sum_{i=1}^{B} (f_i^2 - \overline{f^2})^2 H_i^2}. \quad (38)$$

The slope value determined by Eq. (38) is the value of the slope that minimizes the squared deviation between the logarithm of the measured and theoretical power spectra. Once the best-fit slope parameter is found, the estimated average scatterer diameter, D, is determined by[30]

$$m(a_{\text{eff}}) \approx -60a_{\text{eff}}^2 = -15D^2. \quad (39)$$

A simulation was constructed as with the glass bead simulations except that the backscattered echoes came from a collection of randomly spaced particles that scattered according to the Gaussian form factor. Comparisons were made of average scatterer size estimates with and without the SNR weighting. Figure 7 shows the estimates of average scatterer size with and without the SNR weighting. The estimates of the average effective size of the Gaussian scatterer were more accurate at larger propagation depth with the SNR weighting. Figure 7 shows that using the SNR weighting in the estimation technique improved the accuracy of the scatterer size estimates and extended the depth at which accurate estimates of scatterer size could be made.

Simulations were also run using Gaussian scatterers with a distribution of sizes about some mean size. Figure 7 represents estimates of scatterer sizes from a collection of randomly spaced scatterers of a single size, 60 μm. Figures 8 and 9 represent estimates of scatterer sizes from populations of scatterers with a distribution of sizes. Figure 8 shows estimates made from scatterers with a mean size of 60 μm and a Gaussian distribution of sizes about the mean with standard deviation of 20 μm. Figure 9 shows estimates made from

scatterers with a mean size of 60 μm and a uniform distribution of scatterers between 40 and 80 μm.

In Figs. 8 and 9 the overall scattering strength (intercept value) for all scatterers was modeled to be the same regardless of size. If the relative impedance difference between the scattering particles and the surrounding tissues were the same for smaller and larger sized particles, the smaller particles would scatter more weakly than the larger sized particles. By forcing the intercept value for scatterers of each size to be equal, the relative impedance difference is increased for the smaller particles and the relative contribution from scatterers of all sizes were equivalent.

Comparison of Figs. 7, 8, and 9 shows that the distributions of scatterers did not detrimentally effect the SNR weighting scheme. The SNR weighting still increased the depth to which accurate estimates could be made. Figure 9 shows an even larger depth increase than for the single sized population of scatterers in Fig. 7. Error bars are similar for Figs. 7 and 8, but error bars from Fig. 9 tend to be slightly larger for both the SNR weighted estimates and unweighted estimates. The larger error bars are expected from the larger number of scatterers with sizes farther from the mean.

In Figs. 3–9 it is observed that as estimates of scatterer sizes are made from increased depth, a larger and larger underestimation of the scatterer sizes is found with and without the MASD. The reason for the underestimation may be due to the shape of the spherical form factors, the noise and attenuation compensation. Figure 11 shows an example of the Gaussian form factor for three different effective diameters. The more negative the slope of the form factor the
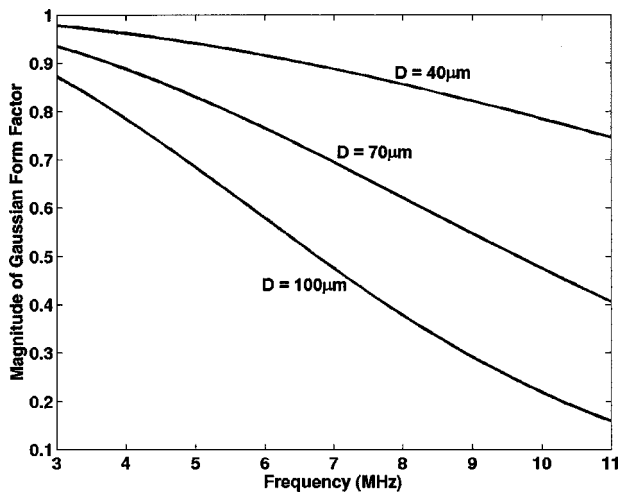
FIG. 11. The magnitude of the Gaussian form factor for spherical scatterers with three different effective diameters, D, versus frequency.

larger the scatterer diameter. When the scattered signal is attenuated, the overall SNR is reduced typically more for the higher frequencies than the lower frequencies in the analysis bandwidth. Therefore, when the frequency-dependent attenuation is compensated, the higher frequencies are amplified more than the lower frequencies. The effect of amplifying the noise more at the higher frequencies than the lower frequencies is to make the overall slope appear less negative with frequency. The less negative slope causes the underestimation of the scatterer sizes. To a degree, the SNR weighting scheme accounts for the underestimation effect. However, if the noise is too large relative to the signal, no amount of weighting can draw out the information.

Figures 3–9 also show that as the propagation depth increases and the signal is more attenuated, the error bars on the estimates increase. In the case of the estimates made without the SNR weighting, the error bars increase because the lower SNR decreases the accuracy of the estimates. Similarly, with the SNR weighting, the error bars also increase with increased propagation depth. The error bars are increased because of the lowering of SNR with depth, however, some of the noise effects are mitigated by the SNR weighting scheme. Some of the increase in the error bars with the SNR weighting may also be due to the effective decrease in the analysis bandwidth. If smaller and smaller frequency bandwidth is used to make estimates of the scatterer properties, the variance in the measurements will increase.[19] The SNR weighting scheme will effectively decrease the analysis bandwidth by weighting some frequency components much larger than other components. In comparing the error bars from estimates made with and without the SNR weighting, a significant difference in the size of the error bars with depth was not seen.

IV. APPLICATION TO PARAMETRIC IMAGING

The SNR weighting was applied to parametric image formation of a solid tumor in a rat.[30] The average scatterer sizes were estimated from the RF signals used to construct parametric B-mode images of the rat and tumor. The experimental protocol was approved by the campus Laboratory Animal Care Advisory Committee and satisfied all campus and National Institutes of Health rules for the humane use of laboratory animals. A Sprague-Dawley rat (Harlan, Indianapolis, IN) that had developed a spontaneous mammary tumor was evaluated. The rat was euthanized with CO_2 and the tumor and surrounding area was shaved and depilated. The rat was then placed on a holder in a tank of degassed water at 37 °C for scanning with an ultrasonic transducer.

A single-element weakly focused transducer was used to scan laterally across the tumors and surrounding tissues. The transducer was moved laterally across the chest and tumor by a micropositioning system with step size of 100 μm between each A-line scan. The transducer had an aperture diameter of 12 mm and a focal length of 58 mm measured from a planar reflector. The center frequency of the transducer was 8.3 MHz with a −6-dB pulse-echo frequency bandwidth of 6 MHz. The analysis bandwidth ranged from 5 to 11 MHz. The same transducer was used for the tumor measurement as the phantom measurement. The spectrum of Fig. 10(a) shows the calibration spectrum from the phantom measurement that was also used in the tumor measurement. Estimates of scatterer properties were made in or near the −6-dB pulse-echo depth of focus of the transducer.

The transducer was operated in pulse-echo mode through a Panametrics 5800 pulser/receiver (Waltham, MA). The signals were recorded and digitized on an oscilloscope (Lecroy 9354 TM; Chestnut Ridge, NY) that had a dynamic range of 48 dB and downloaded to a PC computer for post-processing. The sampling rate was 50 MHz. The assumed attenuation coefficient in the rat tissues was 0.9 dB MHz^{-1} cm^{-1}. The large attenuation coefficient value was based on reports of attenuation measurements in the chest walls of rats and mice.[31]

A two-dimensional B-mode image was constructed from the ultrasonic scan lines from the rat. The length of each gated scan line was approximately 3.5 cm. From the 2D B-mode image, ROIs were divided into regions inside and outside the tumor where the B-mode image appeared to be homogeneous (no interfaces or large echoes). The regions scanned and analyzed outside the tumor were intercostal tissues. The tumor was diagnosed as a fibroadenoma following histopathologic evaluation.

Scatterer estimates were made for each ROI using the best-fit line estimation scheme for the Gaussian form factor model, Eq. (38). The backscattered RF signal was gated from each ROI using a sliding Hanning window and the measured power spectrum was calculated according to Eq. (21). The average effective scatterer diameter was estimated from the measured power spectrum for each ROI. The ROIs were 4 mm×4 mm sections from the B-mode image. Each ROI had a 75% overlap (sliding Hanning window) of the previous ROI. By overlapping each ROI by 75% pixels of 1 mm×1 mm were constructed having distinct values for the scatterer size estimate. Each 1 mm×1 mm pixel represented the average scatterer size estimates from one or more overlapping ROIs.

Figure 12 shows a conventional gray-scale B-mode image of the tumor and surrounding tissues in the rat. In Fig. 12, the transducer was located above the image facing down-
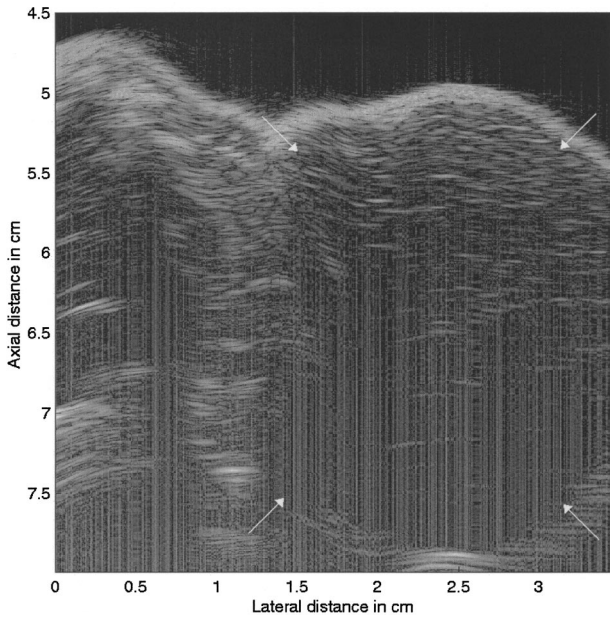
FIG. 12. Conventional, gray-scale B-mode image of rat chest wall and mammary tumor. The tumor is located on the right side of the picture with the white arrows indicating the boundaries of the tumor. Surrounding tissues to the first half-centimeter of depth are intercostal tissues.

wards. The transducer was scanned laterally across the chest from the left to the right side.

Parametric B-mode images of the rat were constructed using the Gaussian form factor and the MASD estimation technique with and without SNR weighting. Figure 13 shows the two parametric images of the rat with tumor. The image on the left shows the parametric image of the rat tissues from size estimates made without the SNR weighting and the image on the right shows the parametric image using the SNR weighting scheme.

A comparison of the two images shows that there exist similarities and important differences between the two images. In the first centimeter of tissue depth, the two images show identical-sized structures. On the left-hand side of each parametric image (axial distance of 5.5 cm and lateral distance of 0 cm) a small area contains estimates of scatterers with very small sizes. The area may represent coherent reflections from some structure in the rat below the chest wall.

As the tissue depth increases, the two images start to show differences. At an axial distance of about 6.5 cm, the

parametric image constructed from MASD without SNR weighting begins to give smaller scatterer size estimates within the tumor. At an axial depth of 7 to 7.1 cm, estimates can no longer be made in the tumor (less than the assumed cutoff value of 20 μm). The parametric image constructed with MASD and the SNR weighting obtains estimates out to bottom edge of the tumor (around 7.7 cm). More of the structure of the tumor and surrounding tissues is seen at a greater propagation depth in the enhanced parametric image than from the image made without SNR weighting. However, it is important to note that in the tumor at 7 cm depth, certain sections appear to give increasingly smaller estimates.

The smaller scatterer size estimates may indicate structure or it may indicate that the MASD with the SNR weighting is beginning to give inaccurate estimates. A limit exists to the gains that can be achieved using the SNR weighting. When the signal is completely lost in the noise, it is impossible to obtain any estimates no matter how the frequency components are weighted.

The parametric images of Fig. 13 show that the overall improvement of the SNR weighting is to extend the ability to make estimates to one-half centimeter and more in propagation depth of the imaged tumor. Determination of the accuracy of the estimates becomes difficult with biological materials since they cannot be characterized in the same detail as phantoms. Furthermore, the exact mechanisms of scattering are not always clearly known. The average effective radius may not be a true average of the scatterer sizes in the tissues but may be a combination of several sized scatterers weighted by the strength of the individual scatterers, i.e., the tissue may hypothetically be made of small scatterers that scatterer strongly and large scatterers that scatterer weakly.

V. CONCLUSION

A new technique was introduced that gives improved accuracy to estimates of scatterer properties from backscatter echoes in an attenuating media. Previous estimation routines did not take into account the decreased SNR for particular frequency components of the scattered spectrum when the signal propagated through an attenuating medium. The new technique enhanced existing estimation schemes by weighting less the contribution of frequency components that were expected to have smaller SNR than frequency components that were expected to have the largest SNR. Both the simu-
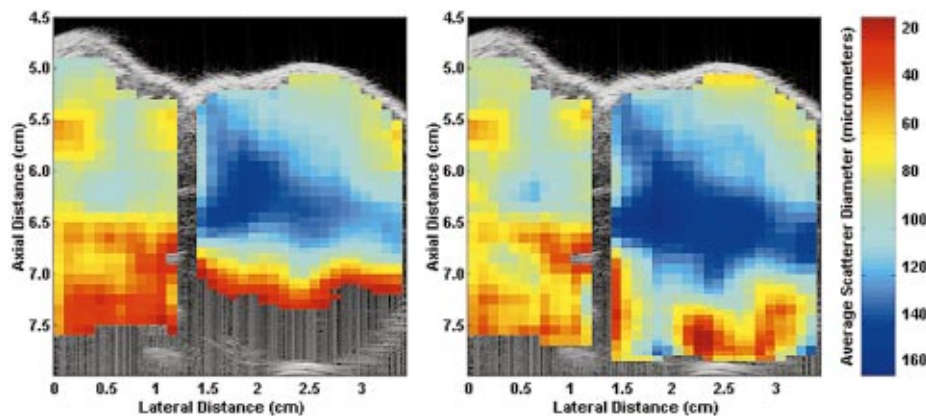

FIG. 13. Parametric B-mode image of rat chest wall and mammary tumor enhanced by average scatterer size estimations using a Gaussian form factor model and MASD without (left) SNR weighting and with (right) SNR weighting.

lations and the phantom experiment showed that the SNR weighting improved the accuracy of scatterer size estimates and extended the ability to obtain estimates to a greater propagation depth. The frequency weighting technique was applied to different kinds of scatterers that are encountered in biological tissues (hard spheres and Gaussian-type scatterers).

The frequency weighting technique was successfully applied to parametric images of spontaneous mammary tumors in rats. The parametric images showed that the SNR weighting technique extended the ability to obtain estimates at a greater propagation depth in the tissues. Furthermore, structure that was not seen without the SNR weighting could be seen with the SNR weighted images. The improvement seen in the parametric images of the rat chest wall and mammary tumor showed that the estimation schemes enhanced with the SNR weighting could aid in increasing the utility of parametric imaging for medical purposes.

[1] D. Nicholas, "Evaluation of backscattering coefficients for excised human tissues: results, interpretation and associated measurements," Ultrasound Med. Biol. **8**, 17–28 (1982).

[2] E. J. Feleppa, F. L. Lizzi, D. J. Coleman, and M. M. Yaremko, "Diagnostic spectrum analysis in ophthalmology: a physical perspective," Ultrasound Med. Biol. **12**, 623–631 (1986).

[3] F. L. Lizzi, M. Ostromogilsky, E. J. Feleppa, M. C. Rorke, and M. M. Yaremko, "Relationship of ultrasonic spectral parameters to features of tissue microstructure," IEEE Trans. Ultrason. Ferroelectr. Freq. Control **33**, 319–329 (1986).

[4] D. K. Nassiri and C. R. Hill, "The use of angular scattering measurements to estimate structural parameters of human and animal tissues," J. Acoust. Soc. Am. **87**, 179–192 (1990).

[5] M. F. Insana, R. F. Wagner, D. G. Brown, and T. J. Hall, "Describing small-scale structure in random media using pulse-echo ultrasound," J. Acoust. Soc. Am. **87**, 179–192 (1990).

[6] M. F. Insana and T. J. Hall, "Parametric ultrasound imaging from backscatter coefficient measurements: image formation and interpretation," Ultrason. Imaging **12**, 245–267 (1990).

[7] M. F. Insana, J. G. Wood, and T. J. Hall, "Identifying acoustic scattering sources in normal renal parenchyma from the anisotropy in acoustic properties," Ultrasound Med. Biol. **18**, 587–599 (1992).

[8] K. K. Shung and G. A. Thieme, *Ultrasonic Scattering in Biological Tissues* (CRC Press, Boca Raton, FL, 1993).

[9] M. F. Insana, T. J. Hall, J. G. Wood, and Z-Y. Yan, "Renal ultrasound using parametric imaging techniques to detect changes in microstructure and function," Invest. Radiol. **28**, 720–725 (1993).

[10] M. F. Insana, "Modeling acoustic backscatter from kidney microstructure using an anisotropic correlation function," J. Acoust. Soc. Am. **97**, 649–655 (1995).

[11] T. J. Hall, M. F. Insana, L. A. Harrison, and G. G. Cox, "Ultrasonic measurement of glomerular diameters in normal adult humans," Ultrasound Med. Biol. **22**, 987–997 (1996).

[12] E. J. Feleppa, T. Liu, A. Kalisz, M. C. Shao, N. Fleshner, and V. Reuter, "Ultrasonic spectral-parameter imaging of the prostate," Int. J. Imaging Syst. Technol. **8**, 11–25 (1997).

[13] F. L. Lizzi, M. Astor, T. Liu, C. Deng, D. J. Coleman, and R. H. Silverman, "Ultrasonic spectrum analysis for tissue assays and therapy evaluation," Int. J. Imaging Syst. Technol. **8**, 3–10 (1997).

[14] R. M. Golub, R. E. Parsons, B. Sigel, E. J. Feleppa, H. A. Zaren, M. Rorke, J. Sokil-Melgar, and H. Kimitsuki, "Differentiation of breast tumors by ultrasonic tissue characterization," J. Ultrasound Med. **12**, 601–608 (1993).

[15] K. A. Topp, J. F. Zachary, and W. D. O'Brien, Jr., "Quantifying B-mode images of *in vivo* rat mammary tumor with frequency dependence of backscatter," J. Ultrasound Med. **20**, 605–612 (2001).

[16] S. L. Bridal, P. Fornes, P. Bruneval, and G. Berger, "Parametric (integrated backscatter and attenuation) images constructed using backscattered radio frequency signals (25–56 MHz) from human aortae *in vitro*," Ultrasound Med. Biol. **23**, 215–229 (1997).

[17] J. A. Zagzebski, Z. F. Lu, and L. X. Yao, "Quantitative ultrasound imaging: *in vitro* results in normal liver," Ultrason. Imaging **15**, 335–351 (1983).

[18] R. H. Silverman, R. Folberg, H. C. Boldt, H. O. Lloyd, M. J. Rondeau, M. G. Mehaffey, F. L. Lizzi, and D. J. Coleman, "Correlation of ultrasound parameter imaging with microcirculatory patterns in uveal melanomas," Ultrasound Med. Biol. **23**, 573–581 (1997).

[19] P. Chaturvedi and M. F. Insana, "Error bounds on ultrasonic scatterer size estimates," J. Acoust. Soc. Am. **100**, 392–399 (1996).

[20] P. Chaturvedi and M. F. Insana, "Bayesian and least squares approaches to ultrasonic scatterer size image formation," IEEE Trans. Ultrason. Ferroelectr. Freq. Control **44**, 152–160 (1997).

[21] J. J. Faran, Jr., "Sound scattering by solid cylinders and spheres," J. Acoust. Soc. Am. **23**, 405–418 (1951).

[22] P. M. Morse and K. U. Ingard, *Theoretical Acoustics* (McGraw-Hill, New York, 1968).

[23] A. Ishimaru, *Wave Propagation and Scattering in Random Media* (Academic, New York, 1978).

[24] J. D. Faires and R. L. Burden, *Numerical Methods* (PWS Publishing, Boston, MA, 1993).

[25] K. A. Wear, R. F. Wagner, M. F. Insana, and T. J. Hall, "Application of autoregressive spectral analysis to cepstral estimation of mean scatterer spacing," IEEE Trans. Ultrason. Ferroelectr. Freq. Control **40**, 50–58 (1993).

[26] F. L. Lizzi, M. Greenbaum, E. J. Feleppa, and M. Elbaum, "Theoretical framework for spectrum analysis in ultrasonic characterization," J. Acoust. Soc. Am. **73**, 1366–1373 (1983).

[27] R. A. Sigelmann and J. M. Reid, "Analysis and measurement of ultrasound backscattering from an ensemble of scatterers excited by sine-wave bursts," J. Acoust. Soc. Am. **53**, 1351–1355 (1973).

[28] E. L. Madsen, F. Dong, G. R. Frank, B. S. Garra, K. A. Wear, T. Wislon, J. A. Zagzebski, H. L. Miller, K. Shung, S. H. Wang, E. J. Feleppa, T. Liu, W. D. O'Brien, Jr., K. A. Topp, N. T. Sanghvi, A. V. Zaitsev, T. J. Hall, J. B. Fowlkes, O. D. Kripfgans, and J. G. Miller, "Interlaboratory comparison of ultrasonic backscatter, attenuation, and speed measurements," J. Ultrasound Med. **18**, 615–631 (1999).

[29] M. L. Oelze and W. D. O'Brien, Jr., "Comparisons of frequency-dependent attenuation-compensation functions for ultrasonic signals backscattered from random media," J. Acoust. Soc. Am. **111**, 2308–2319 (2002).

[30] M. L. Oelze, J. F. Zachary, and W. D. O'Brien, Jr., "Characterization of tissue microstructure using ultrasonic backscatter: Theory and technique optimization using a Gaussian form factor," J. Acoust. Soc. Am. **112**, 1202–1211 (2002).

[31] G. A. Teotica, R. J. Miller, L. A. Frizzell, J. F. Zachary, and W. D. O'Brien, Jr., "Attenuation coefficient estimates of mouse and rat chest wall," IEEE Trans. Ultrason. Ferroelectr. Freq. Control **48**, 593–600 (2001).

The whistles of Hawaiian spinner dolphins

Carmen Bazúa-Durán[a)]
Department of Oceanography, SOEST, University of Hawaii, 1000 Pope Road MSB, Honolulu, Hawaii 96822

Whitlow W. L. Au
Hawaii Institute of Marine Biology, University of Hawaii, P.O. Box 1106, Kailua, Hawaii 96734

The characteristics of the whistles of Hawaiian spinner dolphins (*Stenella longirostris*) are considered by examining concurrently the whistle repertoire (whistle types) and the frequency of occurrence of each whistle type (whistle usage). Whistles were recorded off six islands in the Hawaiian Archipelago. In this study Hawaiian spinner dolphins emitted frequency modulated whistles that often sweep up in frequency (47% of the whistles were upsweeps). The frequency span of the fundamental component was mainly between 2 and 22 kHz (about 94% of the whistles) with an average mid-frequency of 12.9 kHz. The duration of spinner whistles was relatively short, mainly within a span of 0.05 to 1.28 s (about 94% of the whistles) with an average value of 0.49 s. The average maximum frequency of 15.9 kHz obtained by this study is consistent with the body length versus maximum frequency relationship obtained by Wang *et al.* (1995a) when using spinner dolphin adult body length measurements. When comparing the average values of whistle parameters obtained by this and other studies in the Island of Hawaii, statistically significant differences were found between studies. The reasons for these differences are not obvious. Some possibilities include differences in the upper frequency limit of the recording systems, different spinner groups being recorded, and observer differences in viewing spectrograms. Standardization in recording and analysis procedure is clearly needed. © *2002 Acoustical Society of America.*
[DOI: 10.1121/1.1508785]

I. INTRODUCTION

Hawaiian spinner dolphins (*Stenella longirostris*) are island-associated dolphins. This association with islands is a behavior that occurs widely throughout the tropical Pacific Ocean [e.g., French Polynesia in the South Pacific (Poole, 1995), around the Philippines in the western Pacific Ocean (Perrin *et al.*, 1999), and Kwajalein Atoll in the Marshall Islands (Norris and Dohl, 1980a)]. Although spinner dolphins are more abundant in oceanic waters [e.g., Eastern Tropical Pacific (Smith, 1983; Wade, 1993)], nearly all records of spinner dolphins are related to inshore waters, islands or banks [e.g., Gulf of Aden in the Indian Ocean (Robineau and Rose, 1983) and Archipelago of Fernando de Noronha off Brazil in the Atlantic Ocean (Secchi and Siciliano, 1995)].

Spinner dolphin acoustic emissions or phonations[1] can be classified into two general categories: (a) tonal whistles and (b) pulsed sounds or clicks. Dolphin whistles have typically been characterized in terms of their instantaneous frequency as a function of time (spectrograms), which is also referred to as "whistle contour" (Dreher, 1961). Spinner whistles are frequency-modulated sounds with a fundamental component usually below 23 kHz and harmonics up to 62 kHz (Au *et al.*, 1999). In this paper only the fundamental

component is considered. Duration of whistles usually varies between 0.1 and 1.5 s, although most cluster between 0.2 and 0.7 s (Steiner, 1981; Norris *et al.*, 1994). Whistles are believed to be important in regulating group organization and cohesion (Norris and Dohl, 1980b; Norris *et al.*, 1994).

Whistle contours are normally considered as independent units that follow one another (e.g., Dreher and Evans, 1964; Caldwell *et al.*, 1990; McCowan and Reiss, 1995; Rendell *et al.*, 1999). Dolphins seem to produce and share a large number of different whistle contours that, all together, comprise the whistle repertoire of a given species and/or population (McCowan and Reiss, 1995; Janik and Slater, 1998). Some researchers have studied whistles by visually lumping whistle contours subjectively into qualitative categories (e.g., Dreher and Evans, 1964; Dreher, 1966; Tyack, 1986; Caldwell *et al.*, 1990; Sayigh *et al.*, 1995; Janik, 1999), while others have extracted frequency and time parameters from whistle contours and quantitatively determined their similarities (e.g., Steiner, 1981; Buck and Tyack, 1993; McCowan, 1995; Wang *et al.*, 1995a, b; Sturtivant and Datta, 1996; Rendell *et al.*, 1999; Janik, 1999).

There is very little published information on spinner dolphin whistles (e.g., Steiner, 1981), especially for Hawaiian spinner dolphins (e.g., Norris *et al.*, 1994; Wang *et al.*, 1995a). Steiner's (1981) research was performed with animals from the Caribbean Sea and the Norris *et al.* (1994) and Wang *et al.* (1995a) studies were performed only off the Island of Hawaii. In this paper the frequency and time characteristics and general contour shape of Hawaiian spinner dol-

[a)]Current address: Laboratorio de Acústica Aplicada, Centro de Ciencias Aplicadas y Desarrollo Tecnológico (CCADET), Universidad Nacional Autónoma de México (UNAM), Cd. Universitaria, 04510 México, D.F. México. Electronic mail: bazua@soest.hawaii.edu
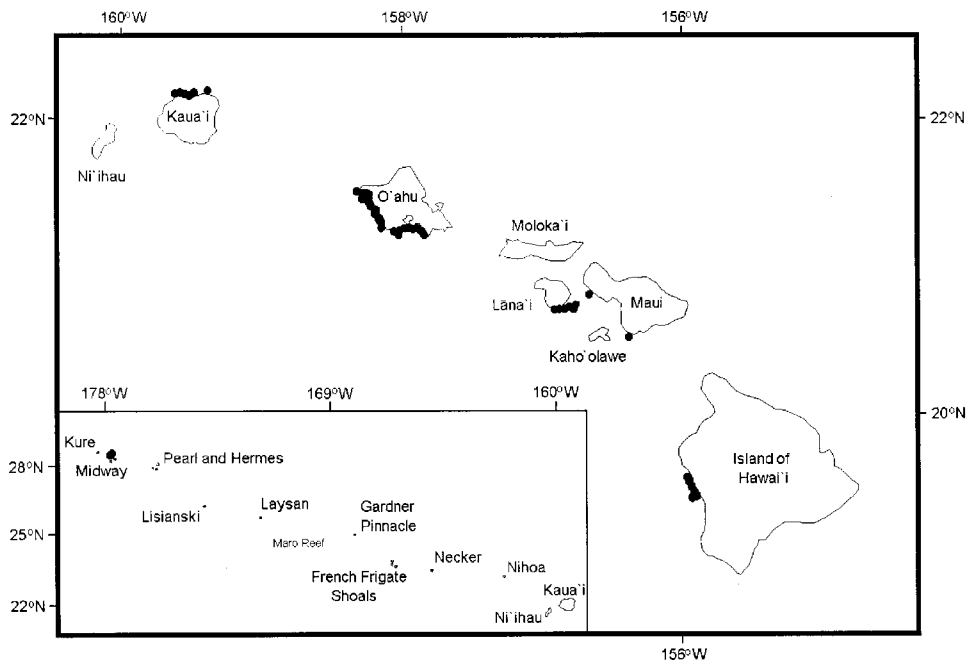
FIG. 1. Map showing the locations along the coasts of six Hawaiian Islands where spinner dolphin whistles were recorded.

phin whistles recorded off six islands in the Hawaiian Archipelago are discussed and compared to those measured by Wang *et al.* (1995a), Norris *et al.* (1994), and Driscoll (1995) in waters of the Island of Hawaii. It was expected that no significant differences would be found between studies performed in the same geographic region (e.g., Island of Hawaii).

II. METHODOLOGY

Field trips were conducted along the coastal waters of several Hawaiian Islands from 1998 to 2000, to measure spinner dolphin whistles. Small, outboard-driven motorboats that ranged from 4 to 10 m in length were used. Acoustic recordings were made in the coastal waters of Midway Atoll, Kauai, Oahu, Lanai, Maui, and the Island of Hawaii, as indicated by the solid circles in Fig. 1. A recording system consisting of an International Transducer Corporation (ITC) spherical hydrophone 1032 and a portable two-channel Sony® Digital Audio Tape (DAT) TCD-D8 recorder were used to record spinner dolphin whistles. The hydrophone is flat to about 35 kHz (± 3 dB) and the DAT has an upper frequency limit of 24 kHz (i.e., sampling rate of 48 kHz). Whistles were recorded on one channel of the DAT recorder with the boat engines turned off and the boat drifting. When the animals were too far away to be clearly seen, recording was stopped and the boat repositioned. The boat was usually positioned ahead or to the side of a group depending on the group behavior and the previous position of the boat with reference to the dolphin group. Unfortunately, we could not know if one or several dolphins were whistling, but such is the uncertainty often inherent in marine bioacoustics.

Additionally, a broadband system with an upper frequency limit of 140 kHz described in Au *et al.* (1999) was used to determine the frequency span of the fundamental component of spinner whistles. It was also used to determine if the DAT recorder was a suitable instrument to record spinner whistles. In the summer of 1998, recordings were made

in waters off the Islands of Hawaii and Lanai. The results indicated that 98% of the signals recorded (see Sec. III) were within the frequency span of the DAT.

The DAT recordings were redigitized with a sound card at a sample rate of 48 kHz at a 16-bit resolution using CoolEdit® 96. These files were stored as sound files (i.e., .wav format files) in the hard drive of a Windows based computer. A time-frequency spectral analysis by means of the fast Fourier Transform (FFT) with CoolEdit® (FFT size of 256 points and a Hamming window) was used to inspect the recordings and select the whistles suitable for detailed analysis. Whistles selected for analysis had the following properties:

(a) a good signal to noise ratio,
(b) clear in the overall contour shape, especially in their beginning and ending points,
(c) either nonoverlapping or overlapped with at most two other whistles, and
(d) not evidently cut by the upper frequency limit of the recording system.

When successive whistles (separated less than 1 s) were encountered, the following criteria were used to consider them individual whistles:

(a) a gap between them larger than 200 ms;
(b) a gap smaller than 200 ms, but larger than the duration of the whistles;
(c) a frequency difference between the ending-beginning frequency greater than 3 kHz; and
(d) a whistle twice as intense as the next one.

However, if there was any uncertainty as to whether successive whistles should be considered as different entities, the whistles were not considered at all. Therefore, from the pool of whistles recorded, about 80% were selected for analysis.[2] These selected whistles are representative of the spinner dol-
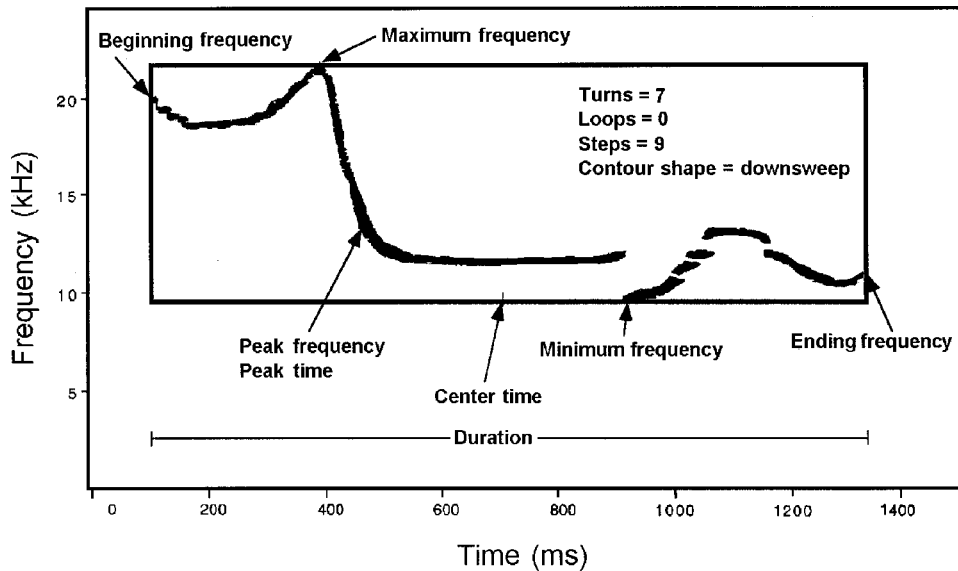
FIG. 2. The 11 parameters and 1 category measured with Canary® 1.2.4 for each whistle contour.

phin whistle repertoire (whistle types) and the frequency of occurrence of each whistle type (usage). Therefore, the different number of whistle types and their usage are described concurrently.

Whistle Recorder® 2.21 software was used to convert the sound files for a Windows based system created with CoolEdit® into aiff format files for a Macintosh based system. Aiff files were then used to generate the whistle contour of each whistle using Canary® 1.2.4 software with a FFT size of 1024 points, an overlap of 50%, and using a Hamming window. A frame length of 512 points (or 10.67 ms) was used for the analysis resolution, resulting in a filter bandwidth of 380.62 Hz and a time resolution of 5.33 ms.

From each whistle contour, the following 11 parameters (illustrated in Fig. 2) were extracted: (1) beginning frequency (BF), (2) ending frequency (EF), (3) peak frequency (PF), (4) maximum frequency (MaF), (5) minimum frequency (MiF), (6) duration, (7) peak time, (8) center time, (9) number of turns, (10) number of loops, and (11) number of steps. Parameters 1–8 were manually extracted using the measurement tool of Canary® software. Parameters 9–11 were calculated visually using quantitative limits (see description below). Each whistle contour was also ascribed to one of the six categories, illustrated in Fig. 3 and described in Table I, as upsweep, downsweep, concave, convex, constant frequency, and sine.

Peak frequency and time were taken within the whistle contour where the intensity was the highest. Center time was taken within the whistle contour where the collective intensity was half the total. A turn was defined as any point where there was more than a 50% change in the rate of ascent or descent of the contour slope, including all changes in the sign of the contour slope. The term turn differs from the term inflection point used by other authors (e.g., Wang *et al.*, 1995a; Norris *et al.*, 1994) because it considers changes in the slope rather than just sign changes in the contour slope. A loop is a generalization of the number of turns and was defined as the region where the whistle changed from mainly ascending to mainly descending, or vice versa, and the sum of the frequency span of the ascending and descending parts

must be at least 1.5 times the maximum frequency span of the whole whistle. For example, the concave and convex whistles in Fig. 3 have one loop and the sine whistles have two loops. Therefore, neither the number of turns nor the number of loops measured by this study are comparable to the number of inflection points measured by other authors (e.g., Wang *et al.*, 1995a; Norris *et al.*, 1994). A step was defined as a section of a whistle that had a sudden change in frequency with the next section of the whistle or where there was a break in the whistle contour. Both sections of the whistle that were separated were considered a step, therefore, the minimum number of steps in a whistle is two.

III. RESULTS AND DISCUSSION

Six spinner dolphin groups (three in both Lanai and the Island of Hawaii) were recorded with the broadband system. A total of 858 whistles were obtained from the recordings. The fundamental frequency had a maximum value of 32.4 kHz; however, whistles with fundamental components above 24 kHz occurred very infrequently (less than 2%). As shown in Table II, less than 3% of the whistles had fundamental MaFs between 22 and 24 kHz and approximately 95% of the whistles below 22 kHz. In addition, less than 1% of the whistles had MiFs below 2 kHz. A DAT recorder is therefore a suitable instrument to record the fundamental frequency of spinner dolphin whistles as more than 95% of the whistles emitted by spinner dolphins have fundamental components below 22 kHz.

A. Frequency and time characteristics of the fundamental component of whistles

In Table III is listed by island and date the 36 spinner dolphin groups that were recorded using the DAT system. From these recordings 8611 whistles were selected for analysis. The spinner dolphins recorded in this study produced high pitch frequency modulated whistles (see Table IV). The mid-frequency (MidF) between MiF and MaF averaged 12.9 ± 2.7 kHz ($N = 8611$). In addition, 94% of the whistles had MidFs between 7.8 and 17.7 kHz and 70% between of 10.5

C. Bazúa-Durán and W. W. Au: Hawaiian spinner dolphin whistles

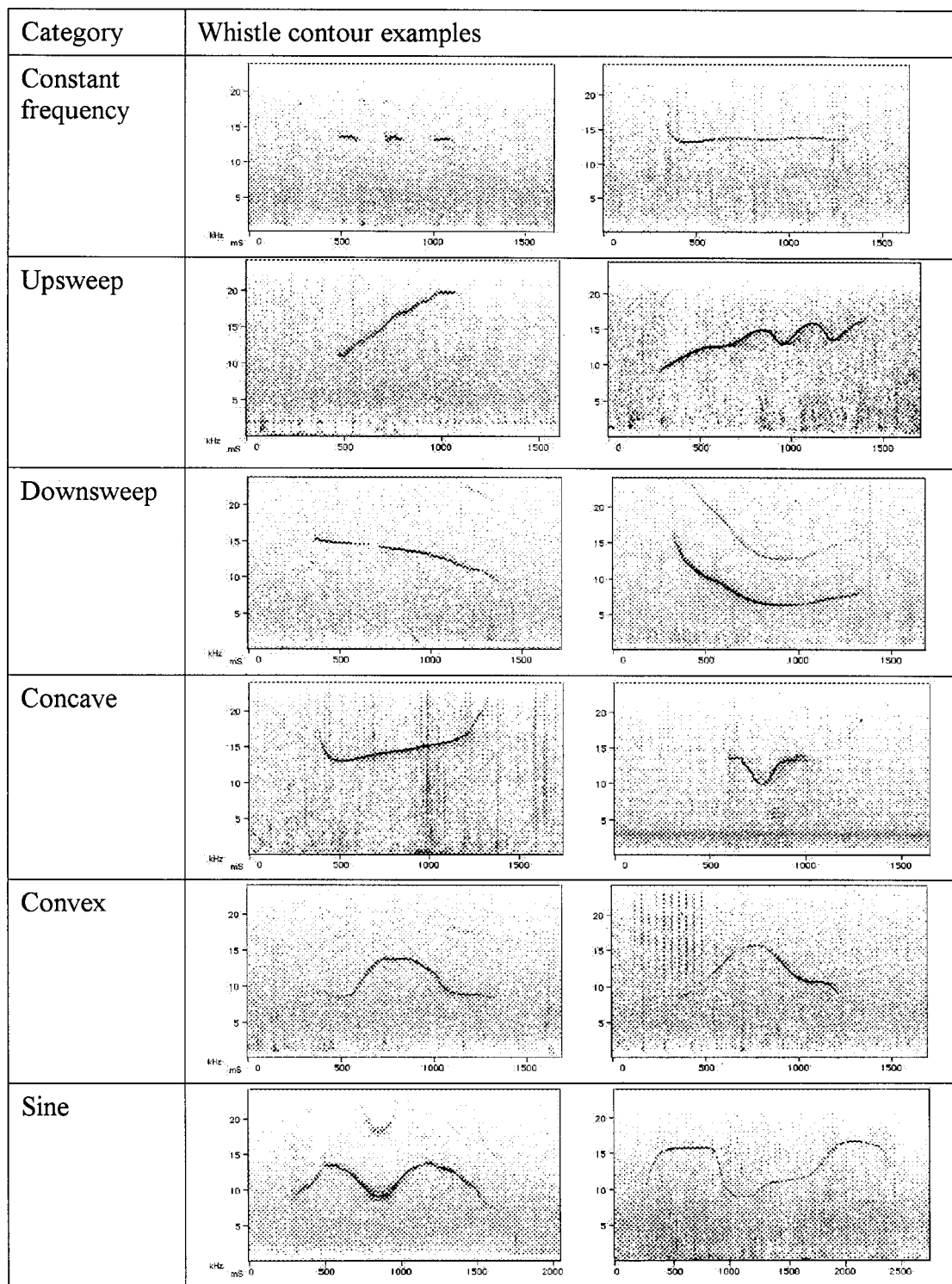| Category	Whistle contour examples

FIG. 3. The six general categories to which whistle contours were ascribed [adapted from Driscoll (1995) and Bazúa Durán (1997)]. Whistle contours are from spinners. X axis=time (ms), Y axis=frequency (kHz).

and 15.6 kHz (i.e., within the average duration $\pm$ the standard deviation). Whistles swept up in frequency, having a mean BF (11.4$\pm$3.7 kHz) lower than the mean EF (13.5$\pm$3.8 kHz) by 16%. The whistle durations were short, with an average of 0.49 $\pm$ 0.39 s (N=8611) and mainly within a span of 0.05 to 1.28 s (about 94% of the whistles). About 64% of the whistles were within the span of 0.11 to 0.88 s (i.e., within the average duration $\pm$ the standard deviation).

The values of the descriptive statistics for whistles re-corded in this study off the Kona coast of the Island of Hawaii were compared to those obtained by Driscoll (1995) and Wang et al. (1995a), also recorded off the Kona coast. Descriptive statistics are shown in Table IV and Fig. 4. Data from Norris et al. (1994) cannot be statistically compared to the other studies because they did not report standard deviations. Driscoll (1995) recordings were made from 1989 to 1991, and Wang et al. (1995a) recordings were made between 1980 and 1992.

TABLE I. Description of the six categories to which each whistle contour (fundamental component of the whistle) was ascribed [definitions adapted from Driscoll (1995) and Bazúa Durán (1997)].

Category	Description
Constant frequency	A contour where the frequency changes 1000 Hz or less during the duration of the whistle or whistles where the frequency span ("height") is less than one quarter of the duration ("length") of the whistle. The frequency rarely remains constant for the entire duration of the whistle.
Upsweep	A contour where the frequency is mainly ascending. If there are any inflection points, the descending frequency part comprises less than half of the frequency span of the whistle.
Downsweep	A contour where the frequency is mainly descending. If there are any inflection points, the ascending frequency part comprises less than half of the frequency span of the whistle.
Concave	A contour with at least one inflection point where the frequency is first mainly descending and then mainly ascending. The ascending and descending parts comprise more than half of the frequency span of the whistle.
Convex	A contour with at least one inflection point where the frequency is first mainly ascending and then mainly descending. The ascending and descending parts comprise more than half of the frequency span of the whistle.
Sine	A contour with at least two inflection points where the frequency is first mainly ascending, then mainly descending, and so forth, or vice versa. At least three of the ascending and descending parts comprise more than half of the frequency span of the whistle.

At first impression, the averages for the frequency and time parameters obtained by the three studies off the Island of Hawaii showed similar averages for all frequency and time parameters (see Fig. 4). The two-sided t test (Moore and McCabe, 1999, p. 541) was used to compare the means and standard deviation of the five parameters that could be compared between studies (BF, EF, MiF, MaF, and duration). The results of the t test are shown in Table V.

Significant differences in the mean values at the $p < 0.05$ level were obtained for all variables between Wang et al. (1995a) and this study and Driscoll (1995). Differences in the upper frequency limit of the recording system may be the main factor contributing to the differences in the frequency parameters of Wang et al. (1995a) and the other two studies [Driscoll (1995) also used a recording system with an upper frequency limit of 24 kHz]. Wang et al. (1995a) used a narrower frequency recording system, and his study reports

TABLE II. Percentage of whistle contours according to the maximum frequency (MaF) of the fundamental component ($N = 858$ whistles).

Maximum frequency	Percentage of whistles
<2 kHz	1
2 kHz<MaF<22 kHz	94
22 kHz<MaF<24 kHz	3
>24 kHz	2

TABLE III. Number of spinner dolphin groups recorded in each Hawaiian Island. Numbers in parentheses are the number of groups recorded on that date.

Hawaiian Island	No. of groups recorded	Date recorded
Midway	3	Nov 1999
Kauai	6	Aug 2000
Oahu	10	Aug 1998 (1), Mar 1999 (2), Jun–Jul 2000 (7)
Lanai	8	Aug 1998 (3), Jun 1999 (5)
Maui	2	Jun 1999 (1), Oct 2000 (1)
Island of Hawaii	6	Jun 1998 (2), Mar 1999 (4)

the lowest averages for all frequency parameters (see Table IV and Fig. 4).

Significant differences in the mean values at the $p < 0.05$ level were obtained for almost all variables between this study and Driscoll (1995) ($p < 0.01$). No significant differences were found for BF and MaF. Even though sample sizes were considerably larger in this and Driscoll's (1995) studies than those of Wang et al.'s (1995a), statistically significant differences were found between all studies. Different spinner dolphin groups sampled may be the main factor contributing to the differences found between this and Driscoll's (1995) studies. Bazúa Durán (2001) found that differences in the whistles of spinner groups did not depend on the year whistles were recorded and that differences within an island were greater than between Hawaiian Islands. However, Driscoll (1995) failed to mention details on how she selected whistles for analysis from the pool of whistles in her recordings. Differences in the selection of whistles for analysis (i.e., observer differences) and differences in the recording time from which whistles were selected (e.g., sampling time) are also factors that could explain these differences.

The differences found in whistle duration between all studies may be attributed to different group size and different general behavioral states. Bazúa Durán (2001) found that whistle duration was responsible for the differences found between spinner groups of different sizes engaging in either of three general behavioral states, social, travel or rest. Unfortunately, Driscoll (1995) and Wang et al. (1995a) failed to mention details on how they recorded and selected whistles for analysis, making it difficult to explain differences in our results.

Wang et al. (1995a) found that there is a linear relationship ($r^2 = 0.931$) between the maximum fundamental frequency of whistles and dolphin body length given by equation:

$$MaF = 21.452 - 3.2537 BL, \qquad (1)$$

where MaF is the maximum fundamental frequency in kHz and BL is the body length in m. Considering a minimum body length of 1.39 m and a maximum of 2.05 m for adult spinner dolphins (Perrin and Gilpatrick, 1994), a span for fundamental MaF of 17.3 to 14.8 kHz is obtained. The average fundamental MaF in this study was 15.9 ± 3.6 kHz, which is consistent with the formula of Wang et al. (1995a). Conversely, the equation of Wang et al. (1995a) may be used to estimate an average MaF for dolphins of known sizes.

C. Bazúa-Durán and W. W. Au: Hawaiian spinner dolphin whistles

TABLE IV. Comparison of the descriptive statistics (mean, standard deviation, and highest and lowest values) of 9 parameters of the fundamental component of Hawaiian spinner dolphin whistles from four different studies: this study, Driscoll (1995), Norris *et al.* (1994), and Wang *et al.* (1995a).

| Study | Descriptive Statistics | Frequency (kHz) | | | | | | Time (s) | | | Turns | No. of Loops | | N^b |
		Begin	End	Minimum	Maximum	Span	Peak	Peak	Center	Duration	Inflection points	Loops	Steps	
All	Mean	11.40	13.54	9.99	15.85	5.86	12.59	0.217	0.234	0.493	3.18	0.42	2.73	8611
Hawaiian Islands	s.d.	3.68	3.78	2.71	3.58	3.49	2.84	0.223	0.186	0.388	2.61	0.75	2.94	
(this study)	High	23.78	23.98	22.35	24.00	18.30	22.50	4.367	2.159	4.493	42	12	31	
	Low	1.38	1.07	0.85	1.71	0.22	1.22	0.000	0.003	0.013	0	0	0	
Island of	Mean	12.02	14.91	10.68	16.50	5.82	12.99	0.202	0.213	0.449	3.05	0.53	2.97	961
Hawaii	s.d.	3.66	3.80	2.68	3.54	3.67	2.47	0.223	0.179	0.372	3.05	0.95	3.32	
(this study)	High	22.90	24.00	18.34	24.00	16.93	19.92	1.658	1.115	2.256	29	8	24	
	Low	2.58	2.29	1.99	2.66	0.39	2.34	0.001	0.011	0.028	0	0	0	
	Mean	11.80	14.46	10.19	16.80	6.60	a	a	a	0.661	a	a	a	965
Driscoll	s.d.	3.66	3.91	2.40	3.17	a	a	a	a	0.334	a	a	a	
(1995)	High	21.44	23.04	21.22	23.04	a	a	a	a	1.870	a	a	a	
	Low	4.64	4.00	4.00	5.60	a	a	a	a	0.040	a	a	a	
Norris *et al.*	Mean	10.42	15.85	a	a	a	a	a	a	0.68	1.69		a	389
(1994)	s.d.	a	a	a	a	a	a	a	a	a	a		a	
	High	a	a	a	a	a	a	a	a	a	a			
	Low	a	a	a	a	a	a	a	a	a			a	
Wang *et al.*	Mean	10.61	14.05	9.03	15.20	6.17	a	a	a	0.75	1.07		a	271
(1995a)	s.d.	3.44	2.37	2.24	1.66	a	a	a	a	0.33	1.19		a	
	High	18.92	22.46	14.38	22.46	a	a	a	a	1.82	9		a	
	Low	3.91	7.19	3.91	8.75	a	a	a	a	0.10	0		a	

[a]Not reported by author(s).
[b]N=sample size.

B. Whistle contours

The number of whistles ascribed to each of the six contour categories for the six Hawaiian Islands combined are shown in Table VI. Hawaiian spinner dolphins recorded in this study emitted a great amount of upsweep whistles (47% of the whistles). Convex contours comprised 20% of the whistles and 13% were downsweep whistles, with percentages varying from 5 to 13 for the other three categories. The number of turns averaged 3.2±2.6 and the number of loops averaged 0.4±0.8, reflecting the high proportion of whistles (60%) without loops.

Driscoll (1995) classified whistles in seven categories, including the six used in this study plus a category defined as
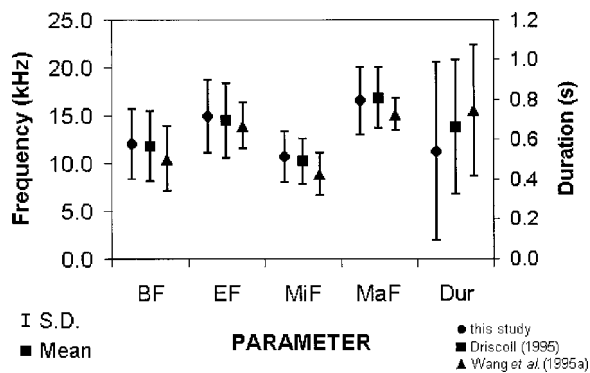

FIG. 4. Descriptive statistics (mean and standard deviation) of five parameters of spinner dolphin whistles collected in the Island of Hawaii by three different studies: this study, Driscoll (1995), and Wang *et al.* (1995a).

chirps, which were whistles with a duration of less than 300 ms. Although we felt that the chirp category of Driscoll (1995) was completely arbitrary without any biological or acoustical rationale, for comparison purposes, we included chirp as a category and obtained the results shown in Fig. 5 and Table VII for whistles recorded off the Island of Hawaii. Driscoll (1995) found that upsweep (37%), chirp (18%), and sine (18%) composed most of the spinner whistles, and our results show that chirp (44%), upsweep (27%), and sine (11%) contours also made up most of the whistles. Forty-nine percent of the chirps of this study were previously classified as upsweep contours (see Table VII). Chirps for all Hawaiian Islands combined comprised 40% of the whistles and had a mean duration of 0.14±0.07 s (median=0.12 s). The distribution of whistles in seven categories in this and Driscoll's (1995) study are statistically different ($X^2 = 181$, df=6; $p < 0.001$); however, both studies found that chirp, upsweep, and sine contours comprised more than 70% of the whistles selected for analysis.

The differences in the distributions of whistles in the seven categories between Driscoll (1995) and this study might be attributed to the choice of specific whistles analyzed. We obtained a higher proportion of chirps and a lower average duration (duration differed greatly between both studies, $p < 0.001$). Different spinners being recorded may also be a factor. In addition, observer differences in classifying whistles (e.g., Janik, 1999) may also be another reason for the statistical differences between this and Driscoll's (1995) study. Although the definition of the six categories of

TABLE V. Results of the two-sided *t*-test (Moore and McCabe 1999, p. 541) to compare five whistle parameters for spinner dolphin whistles in the Island of Hawaii reported by Driscoll (1995), Wang *et al.* (1995a), and this study.

| | This study vs | | | | | | Driscoll (1995) vs Wang *et al.* (1995a) | | |
| | Driscoll (1995) | | | Wang *et al.* (1995a) | | | | | |
Whistle parameter	*t*	df[a]	*p*	*t*	df[a]	*p*	*t*	df[a]	*p*
Beginning frequency	1.29	1000	0.20	5.87	300	0.01	4.97	300	0.01
Ending frequency	2.58	1000	0.01	4.56	300	0.03	2.14	300	0.03
Minimum frequency	4.21	1000	0.01	10.3	300	0.01	7.42	300	0.01
Maximum frequency	1.93	1000	0.056	8.53	300	0.01	11.1	300	0.01
Duration	13.1	1000	0.01	12.9	300	0.01	3.91	300	0.01

[a]df = degrees of freedom.

contour shapes is very similar, Driscoll (1995) did not use a rigorous limit to define the six categories as done in this study (see Table IV).

Bottlenose dolphin whistles comprise a graded rather than a discrete system (Herman and Tavolga, 1980).[3] Categorizing whistles in a definite number of mutually exclusive classes, such as the six or seven categories used in this and Driscoll's (1995) studies, is limited by the graded nature of dolphin whistles. It is sometimes difficult to ascribe a whistle contour to either the upsweep or downsweep category and the convex or concave categories. The border between an upsweep and a convex whistle can appear rather vague.

Recordings of whistles in the dolphin's natural environment consist of large opportunistic samples of unknown individuals in groups of varying composition and behavioral state. Norris *et al.* (1994) stated that if whistles have structures that are specific to individuals (i.e., signature whistles) and these structures are modulated according to the emotional state of the individual as suggested by Caldwell *et al.* (1990), large opportunistic samples of whistles quickly become "unclassifiable" if the classification system is based on slight differences in the whistle contour. For example, Bazúa Durán (1997) obtained 270 different whistle types out of 1320 whistles for Gulf of Mexico bottlenose dolphins; i.e., 80% of the whistles were repetitions of the 270 whistle types. Norris *et al.* (1994) mentioned that the classification system, therefore, should consist of broad categories so that differences in the whistle contour can be generalized and large samples of whistles can be allocated to specific categories. However, classifying whistles in a definite number of mutually exclusive categories as the six used in this study or categorizing whistles in an "indefinite" number of categories based on slight differences in the whistles' contour as those obtained by Bazúa Durán (1997) are equally limited by the graded nature of dolphin whistles. How many and which predetermined categories should be chosen? How much variation within the whistle contour should be considered as to say that two whistles are two different whistle types? The number of categories obtained depends on the "amount" of detail used when comparing whistle contours. Due to the graded nature of whistles, whistle categorization should not be used. Frequency and time measurements extracted from whistle contours can be used to compare different groups, populations, and species (e.g., Steiner, 1981; Wang *et al.*,

1995a, b; Rendell *et al.*, 1999; Bazúa Durán, 2001). However, whistle categorization is helpful in comparing studies and getting an overall view of the whistle repertoire. Therefore, if whistle categorization is to be performed, very specific limits should be used to define categories in order to reduce considerably observer differences. Furthermore, perception studies are needed to determine the real border between categories.
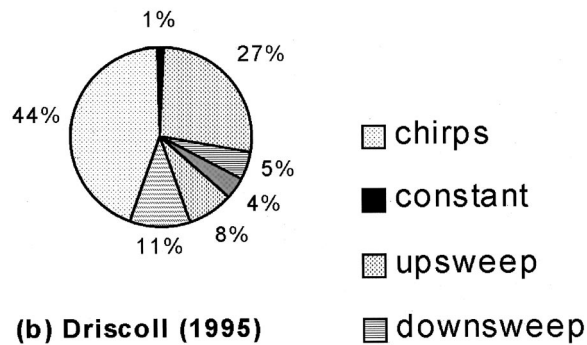
IV. CONCLUSIONS

Frequency and time parameters, as well as some other characteristics of whistle contours (e.g., number of turns, loops, and steps) have shown to be useful in describing dolphin whistles and in comparing the whistles of different dolphin groups. (e.g., Steiner, 1981; Wang *et al.*, 1995a, b; Rendell *et al.*, 1999; Bazúa Durán, 2001). However, care should be taken when selecting whistles for analysis if narrow band recordings are used. Whistles that appear to be chopped off or broken into pieces by the upper frequency limit of the recording system should not be considered (ideally, the recording system used should be chosen in accordance with the frequency span of the species under study). For example, Bazúa Durán (1997) obtained different results than Wang *et al.* (1995b) when analyzing the same recordings (tapes) from bottlenose dolphins from the northern Gulf of Mexico. Using Wang's data sheets, Bazúa Durán (1997) suggested that the difference in the results could be attributed to Wang *et al.* (1995b) considering two successive whistles as two individual whistles instead of a single whistle broken into pieces by the upper frequency limit of the recording system. Those whistles were not considered in the analysis of Bazúa Durán (1997). Furthermore, measurement of qualitative pa-

TABLE VI. Number of whistles ascribed to each of the six categories of whistle contours for all six Hawaiian Islands combined.

Whistle category	No. of whistles	Fraction
Constant	755	0.09
Upsweep	4010	0.47
Downsweep	1151	0.13
Concave	406	0.05
Convex	1765	0.20
Sine	524	0.06
N	8611	

C. Bazúa-Durán and W. W. Au: Hawaiian spinner dolphin whistles

(a) this study

- 1%
- 27%
- 44%
- 5%
- 4%
- 8%
- 11%

☐ chirps

■ constant

☐ upsweep

☰ downsweep

▨ concave

▨ convex

☐ sine

(b) Driscoll (1995)
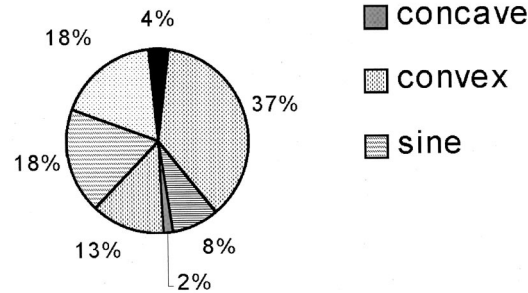

- 4%
- 18%
- 37%
- 18%
- 13%
- 8%
- 2%

FIG. 5. Comparison of the distribution of whistles ascribed to each of the seven categories of whistle contours of Driscoll (1995) for (a) this study in the Island of Hawaii and (b) Driscoll's (1995) study with data corrected from original that had numerical errors.

TABLE VII. Distribution of whistles ascribed to each of the seven whistle-contour categories of Driscoll (1995) for this and Driscoll's (1995)[a] studies on the Island of Hawaii.

Category	This study fraction		Driscoll (1995)[a] fraction
	All	Within chirp	
Chirp	**0.44**	⋯	0.18
Constant	0.01	0.12	0.04
Upsweep	0.27	**0.49**	**0.37**
Downsweep	0.05	0.14	0.08
Concave	0.04	0.12	0.02
Convex	0.08	0.12	0.13
Sine	0.11	0.01	0.18
N[b]	961	422	965

[a]Data corrected from original that had numerical errors.
[b]N = sample size.

rameters such as number of turns and steps should be as general as possible (Bazúa Durán, unpublished data) to avoid observer bias to a greater extent. The number of turns should measure most changes in the direction of the contour and not only the changes in the slope from positive to negative and vice versa (inflection points). Some spectrograms have step-wise appearance, therefore, the number of steps should include all breaks in the contour as well as sudden changes in frequency that do not include a break.

It was expected that no significant differences would be found in spinner dolphin whistles recorded by different studies performed in the Island of Hawaii. However, there was little agreement in the results of this and the previous studies of Wang et al. (1995a) and Driscoll (1995). The reasons for these differences are not clear. In order to eliminate possible observer differences while comparing different studies, standardization needs to be performed. The use of an automated method to select whistles from the recordings will eliminate completely observer differences in the selection. Unfortunately, the development of automated methods for dolphin recordings made in coastal waters has been highly limited by the considerable environmental noise existing in shallow waters. However, selection methods can be "standardized" if methodology is clearly stated. It is, therefore, very important to define all parameters taken into consideration when doing the analysis so that future studies can be "standardized" in procedure and the reasons of the differences can be more readily identified. Standardization and stricter limits are also needed if whistles are going to be classified into a definite number (either small, e.g., 6, or large, e.g., 200) of mutually exclusive categories.

Hawaiian spinner dolphins produced whistles with average frequencies of the fundamental component (BF, EF, MiF, and MaF) higher than those of larger odontocetes (see Wang et al., 1995a; Rendell et al., 1999; and Matthews et al., 1999). The average MaF is consistent with the body length of spinner dolphins according to Wang et al. (1995a) equation.

Hawaiian spinner dolphins also produced a great number of upsweep whistles (47%) that is reflected in a lower average BF than average EF (about 16% lower BF than EF). For Tursiops truncatus the relationship between average BF and EF varies (see Steiner, 1981; Wang et al., 1995b; and Bazúa Durán, 1997). Although Tursiops truncatus produced more sine whistles than spinner dolphins (more than 28% for T.t. versus less than 11% for S.l.), BF was lower than EF when there was a larger amount of upsweep whistles (e.g., 18% and 32% lower BF when there were 23% and 18% upsweeps and 4 and 35 times more upsweeps than downsweeps, respectively) (Bazúa Durán, 1997). For other dolphins and spinners in other oceans a lower average BF than average EF was also observed: Delphinus delphis showed 34% lower BF than EF, Lagenorhynchus albirostris 30% lower BF, Stenella longirostris from the Caribbean Sea 26% lower BF, Stenella plagiodon 26% lower BF, Stenella attenuata 24% lower BF, Sotalia fluviatis 25% lower BF, Stenella clymene 15% lower BF, Globicephala macrorhynchus 8% lower BF, Lagenodelphis hosei 9% lower BF, Stenella coeruleoalba 6% lower BF, and Stenella frontalis 5% lower BF (from Matthews et al., 1999). Therefore, it is possible that more than 18% of dolphin whistles are upsweeps when the average BF of their whistles is at least 15% lower than the average EF. Species such as Delphinus delphis, Lagenorhynchus albirostris, Stenella longirostris, Stenella plagiodon, Stenella attenuata, Sotalia fluviatis, and Stenella clymene share some of the characteristics of their whistles. Their whistle repertoire and usage may be similar.

The whistle repertoire of Hawaiian spinner dolphins seems to be large and varied. Although different whistle types were not characterized during the present study (for the reasons mentioned before about categorizing whistles), the number of turns was almost eight times larger than the number of loops and 80% of spinner whistles were ascribed to

three general contour shape categories. For a species that lives in large groups that coordinate behavior at all times of day (e.g., during foraging, travel, socializing, and rest) it is crucial to maintain communication between all members of the group. A large and varied whistle repertoire is therefore very important if whistles function as acoustic signals to regulate group organization and cohesion.

ACKNOWLEDGMENTS

[1]The term vocalization was not used because experimental evidence strongly suggests that dolphins use the monkey lips of their nasal system to produce sounds, not their vocal folds (Cranford *et al.*, 2000).

[2]This percentage does not take into account the sections of highly overlapped whistles or high-chorus whistling.

[3]A graded system is one that has slight changes from one "category" to the next, and when signals are in between two "categories" it is "nearly impossible" to ascribe one signal to one of the two categories.

Au, W. W. L., Lammers, M. O., and Aubauer, R. (**1999**). "A portable broadband data acquisition system for field studies in bioacoustics," Marine Mammal Sci. **15**(2), 526–531.

Bazúa Durán, M. C. (**1997**). "Comparisons of whistles among different populations of dolphins (*Tursiops truncatus*) from the Gulf of Mexico," Master's thesis, Universidad Nacional Autónoma de México, Mexico, DF Mexico.

Bazúa Durán, M. C. (**2001**). "The whistles of Hawaiian spinner dolphins (*Stenella longirostris*): Description and geographic variations," Doctoral Dissertation, University of Hawaii at Manoa, Honolulu.

Buck, J. R., and Tyack, P. L. (**1993**). "A quantitative measure of similarity for *Tursiops truncatus* signature whistles," J. Acoust. Soc. Am. **94**, 2497–2506.

Caldwell, M. C., Caldwell, D. K., and Tyack, P. L. (**1990**). "Review of the signature-whistle hypothesis for the Atlantic bottlenose dolphin," in *The Bottlenose Dolphin*, edited by S. Leatherwood and R. R. Reeves (Academic Press, San Diego, CA), pp. 199–234.

Cranford, T. W., Elsberry, W. R., Blackwood, D. J., Carr, J. A., Kamolnick, T., Todd, M., Van Bonn, W. G., Carder, D. A., Ridgway, S. H., Bozlinski, D. M., and Decker, E. C. (**2000**). "Two independent sonar signal generators in the bottlenose dolphin: Physiology evidence and implications," J. Acoust. Soc. Am. **108**(5), 2613.

Dreher, J. J. (**1961**). "Linguistic aspects of porpoise sounds," J. Acoust. Soc. Am. **33**, 1799–1800.

Dreher, J. J. (**1966**). "Cetacean communication: small group experiment," in *Whales, Dolphins and Porpoises*, edited by K. S. Norris (Univ. of California, Berkeley), pp. 529–543.

Dreher, J. J., and Evans, W. E. (**1964**). "Cetacean communication," in *Marine Bioacoustics*, edited by N. W. Tavolga (Pergamon Press, Oxford), Vol. 1, pp. 373–393.

Driscoll, A. D. (**1995**). "The whistles of Hawaiian spinner dolphins, *Stenella longirostris*," Master's thesis, University of California at Santa Cruz.

Herman, L. H., and Tavolga, W. N. (**1980**). "The communication system of cetaceans," in *Cetacean Behavior: Mechanisms and Functions*, edited by L. H. Herman (Wiley, New York), pp. 149–209.

Janik, V. M. (**1999**). "Pitfalls in the categorization of behaviour: A comparison of dolphin whistles classification methods," Anim. Behav. **57**(1), 133–143.

Janik, V. M., and Slater, P. J. B. (**1998**). "Context-specific use suggests that bottlenose dolphin signature whistles are cohesion calls," Anim. Behav. **56**(4), 829–838.

Matthews, J. N., Rendell, L. E., Gordon, J. C. D., and MacDonald, D. W. (**1999**). "A review of frequency and time parameters of cetacean tonal calls," Bioacoustics **10**(1), 47–71.

McCowan, B. (**1995**). "A new quantitative technique for categorizing whistle using simulated signals and whistles from captive bottlenose dolphins (Delphinidae, *tursiops truncatus*)" Ethology **100**(3), 177–193.

McCowan, B., and Reiss, D. (**1995**). "Quantitative comparison of whistle repertoires from captive adult bottlenose dolphins (Delphinidae, *Tursiops truncatus*): A re-evaluation of the signature whistle hypothesis," Ethology **100**(3), 194–209.

Moore, D. S., and McCabe, G. P. (**1999**). *Introduction to the Practice of Statistics*, 3rd ed. (Freeman, New York).

Norris, K. S., and Dohl, T. P. (**1980a**). "The structure and function of cetacean schools," in *Cetacean Behavior*, edited by L. M. Herman (Wiley, New York), pp. 211–261.

Norris, K. S., and Dohl, T. P. (**1980b**). "Behavior of the Hawaiian spinner dolphin, *Stenella longirostris*," Fish. Bull. **77**(4), 821–849.

Norris, B. S., Würsig, B., Wells, R. S., and Würsig, M. (**1994**). *The Hawaiian Spinner Dolphin* (Univ. of California, Berkeley, CA).

Perrin, W. F., and Gilpatrick Jr., J. W. (**1994**). "Spinner dolphin *Stenella longirostris* (Gray, 1828)," in *Handbook of Marine Mammals, Vol. 5*, edited by S. H. Ridgway and R. Harrison (Academic, London), pp. 99–128.

Perrin, W. F., Dolar, M. I., and Robineau, D. (**1999**). "Spinner dolphins (*Stenella longirostris*) of the western pacific and southeast Asia: Pelagaic and shallow-water forms," Marine Mammal Sci. **15**(4), 1029–1053.

Poole, M. (**1995**). "Aspects of the behavioral ecology of spinner dolphins (*Stenella longirostris*) in the nearshore waters of Mo'orea, French Polynesia," Doctoral dissertation, University of California at Santa Cruz.

Rendell, L. E., Matthews, J. N., Gill, A., Gordon, J. C. D., and Mcdonald, D. W. (**1999**). "Quantitative analysis of tonal calls from five odontocete species, examining interspecific and intraspecific variation," J. Zool. Lond. **249**(4), 403–410.

Robineau, D., and Robineau, J. M. (**1983**). "Note sur le *Stenella longirostris* du Golfe d'Aden," Mammalia **47**(2), 237–245.

Sayigh, L. S., Tyack, P. L., Wells, R. S., and Scott, M. D. (**1995**). "Sex difference in signature whistle production of free-ranging bottlenose dolphins, *Tursiops truncatus*," Behav. Ecol. Sociobiol. **36**(3), 171–177.

Secchi, E. R., and Siciliano, S. (**1995**). "Comments on the southern range of the spinner dolphin (*Stenella longirostris*) in the western south Atlantic," Aquat. Mamm. **21**(2), 105–108.

Smith, T. D. (**1983**). "Changes in size of three (*Stenella* spp) populations in the eastern tropical Pacific," Fish. Bull. U.S. **81**(1), 1–13.

Steiner, W. W. (**1981**). "Species-specific differences in pure tonal whistle vocalizations of five western north Atlantic dolphin species," Behav. Ecol. Sociobiol. **9**(4), 241–246.

Sturtivant, C., and Datta, S. (**1996**). "Classification of whistles from the common dolphin (*Delphinus delphis*)," Acoust. Lett. **20**(6), 129–133.

Tyack, P. L. (**1986**). "Whistle repertoires of two bottlenose dolphins, *Tursiops truncatus*: Mimicry of signature whistles?" Behav. Ecol. Sociobiol. **18**(4), 251–257.

Wade, P. R. (**1993**). "Estimation of historical population size of the eastern stock of spinner dolphin (*Stenella longirostris orientalis*)," Fish. Bull. U.S. **91**(4), 775–787.

Wang, D., Würsig, B., and Evans, W. (**1995a**). "Comparisons of whistles among seven odontocete species," in *Sensory Systems of Aquatic Mammals*, edited by R. A. Kastelein, J. A. Thomas, and P. E. Nachtigall (De Spil, Woerden, The Netherlands), pp. 299–323.

Wang, D., Würsig, B., and Evans, W. (**1995b**). "Whistles of bottlenose dolphins: Comparisons among populations," Aquat. Mamm. **21**(1), 65–77.

Empirical refinements applicable to the recording of fish sounds in small tanks

Tomonari Akamatsu[a]
Thomas H. Morgan School of Biological Sciences, University of Kentucky, Lexington, Kentucky 40506-0225

Tsuyoshi Okumura
National Research Institute of Fisheries Engineering, Hasaki, Kashima, Ibaraki 314-0421, Japan

Nicola Novarini and Hong Y. Yan
Thomas H. Morgan School of Biological Sciences, University of Kentucky, Lexington, Kentucky 40506-0225

Many underwater bioacoustical recording experiments (e.g., fish sound production during courtship or agonistic encounters) are usually conducted in a controlled laboratory environment of small-sized tanks. The effects of reverberation, resonance, and tank size on the characteristics of sound recorded inside small tanks have never been fully addressed, although these factors are known to influence the recordings. In this work, 5-cycle tone bursts of 1-kHz sound were used as a test signal to investigate the sound recorded in a 170-l rectangular glass tank at various depths and distances from a transducer. The dominant frequency, sound-pressure level, and power spectrum recorded in small tanks were significantly distorted compared to the original tone bursts. Due to resonance, the dominant frequency varied with water depth, and power spectrum level of the projected frequency decreased exponentially with increased distance between the hydrophone and the sound source; however, the resonant component was nearly uniform throughout the tank. Based on the empirical findings and theoretical calculation, a working protocol is presented that minimizes distortion in fish sound recordings in small tanks. To validate this approach, sounds produced by the croaking gourami (*Trichopsis vittata*) during staged agonistic encounters were recorded according to the proposed protocol in an 1800-l circular tank and in a 37-l rectangular tank to compare differences in acoustic characteristics associated with tank size and recording position. The findings underscore pitfalls associated with recording fish sounds in small tanks. Herein, an empirical solution to correct these distortions is provided. © *2002 Acoustical Society of America.* [DOI: 10.1121/1.1515799]

PACS numbers: 43.80.Ka, 43.20.Mv, 43.30.Gv [WAA]

I. INTRODUCTION

There is considerable diversity in fish sounds (Fish and Mowbray, 1970; Myrberg, 1981; Zerick *et al.*, 1999), and several mechanisms are involved in sound production (Tavolga, 1964). Sounds from many fish species have been recorded during agonistic interactions (Ballantyne and Colgan, 1978; Valinski and Rigley, 1981; Johnston and Johnson, 2000a, b), feeding (Colson *et al.*, 1998), and during courtship (Drewry, 1962; Gerald, 1971; Stout, 1975; Lobel, 1992; Lugli *et al.*, 1995, 1996, 1997; Mann and Lobel, 1998; Johnston and Johnson, 2000a). However, the role of sounds in the life history of sonic fishes is only poorly understood. With the availability of personal computers, a variety of acoustical signal analysis programs and low cost of hydrophones, lately the investigation of fish sounds has gained attention. This interest is reflected by the recent surge of publications analyzing the characteristics of fish sounds (e.g., Matsuno *et al.*, 1996; Bodnar and Bass, 1997; Crawford *et al.*, 1997; Fine *et al.*, 1997; Myrberg, 1997; Mann and Lobel, 1998; Ladich and Yan, 1998; Pruzsinszky and Ladich, 1998; Lugli and Torricelli, 1999; Johnston and Johnson,

2000a, b; Kaatz and Lobel, 2001; Lobel, 2001; Pedersen, 2001; Tolimieri *et al.*, 2001; Thorson and Fine, 2002a, b).

In order to understand the role of fish sounds in the overall behavioral repertoires of a species, accurate measurement of sound characteristics as well as concurrent behavioral observations are necessary. To minimize distortions due to reverberation, sound recordings should be conducted ideally in an open body of water with a depth and width exceeding the wavelength of the targeted sound. The open-water environment is readily available, although various experimental conditions (e.g., water temperature, ambient noise) are hard or impossible to control, and turbidity may render behavioral observations difficult.

Recording fish sounds in a small tank allows precise behavioral observation and better control of environmental factors than in the natural environment. However, due to physical limitations of small tanks, the true characteristics of sounds are hard to assess due to many physical constraints of small tanks (Parvalescu, 1964, 1967). For example, the duration of fish sounds usually exceeds 2 ms (Fish and Mowbray, 1970), during which the sound travels about 3 m, but most commonly used glass aquaria in a laboratory are rarely over 2 m in length. Therefore, even a short-duration sound could result in reverberation, defined as the persistence of sound in an enclosed space as a result of multiple reflections

---

after sound generation has stopped (Yost, 1994). Hence, it is impossible to separate the original sound from reflected sound in the time domain when the sounds are recorded in small tanks.

Tank resonance can cause an additional problem. In a closed-boundary system, standing waves persist after cessation of sound generation. Thus, the frequency recorded may be the resonant frequency of the standing wave due to its longer duration than the original fish sound. If the resonant frequency of the tank happens to be close to the frequency of the sounds produced by the fish, the original spectrum will be seriously distorted, thereby prohibiting an accurate characterization of the original sounds.

To reduce reverberation in a tank, various materials for sound absorption (horse hair, fibers, and sand) have been used (Tavolga, personal communication, 2002). In a series of elaborate field and laboratory recording and playback experiments, Myrberg (1972) and Myrberg and Spires (1972) found that the colonial male damselfish (*Eupomacentrus partitus*) are selecting a sound not for its familiarity but rather for its acoustic nature. It is suspected that this difference of choice between laboratory sound and field sound by male damselfish is due to artifacts from small tanks. However, the characteristics of sounds recorded from small tanks remain undefined. Because of this uncertainty, Myrberg later conducted all of his playback studies in the field and not in the laboratory (Myrberg, personal communication, 2002). Although the constraints of a small tank have been known for more than 30 years (Parvulescu, 1964, 1967), the acoustics of small tank has received very limited investigation and potential problems remain unaddressed in most studies analyzing fish sounds.

Against this background, our aim was to: (1) investigate sound distortion in small tanks using empirical approaches combined with theoretical calculations, and (2) offer guidelines as to how to obtain useful information from recordings of fish sound made in small tanks.

II. MATERIALS AND METHODS

Two types of tanks were used in this experiment. A 170-l glass-wall tank (88-cm length×43-cm width×45-cm, height) was used for calibration measurements and a large concrete tank (1000×1500×1000 cm) designed for acoustical experiments at the National Research Institute of Fisheries Engineering, Japan was used to simulate an open-water environment.

Many sounds produced by fish are pulsatile and have frequencies ranging from several tens to thousands of hertz (Fish and Mowbray, 1970). Thus, a 1-kHz, 5-cycle tone burst of 5-ms duration was chosen as a calibration signal within the frequency range of fish sounds. The tone bursts were generated every 200 ms with a personal computer (NEC PC-9821Nr15, Tokyo, Japan), which was connected to a piezo-film underwater sound transducer (diameter: 32 mm, thickness 9 mm). The sound projection and recording system were first tested in the large concrete tank to examine the characteristics of the transducer. The transducer was positioned at the center of the concrete tank at a depth of 1 m; a hydrophone (Brüel & Kjaer 8103, Naerum, Denmark; voltage sensitivity −211.8 dB *re*: 1 V/uPa, charge sensitivity 9.3×10^{-2} pC/Pa) was positioned 35 cm away from the transducer at the same depth. Tone bursts received by the hydrophone were fed into a charge amplifier (Brüel & Kjaer 2692 A0S2, with 10-kHz low-pass filter to eliminate electronic noise) and the signals were recorded with a digital audiotape recorder (SONY TCD-D8, Tokyo, Japan). The input volume of the TCD-D8 was set so that full range represented a 1-Vrms sinusoidal input. Hence, the power spectrum levels calculated were normalized. An analog/digital converter (Canopus, DA-Port USB and AD-Link, sampling frequency: 44.1 kHz) was used to digitize the signals from the tape. The total frequency response of the recording system was within ±1 dB up to 10 kHz.

The following sound analysis protocol was employed in the following three experiments. An analysis window of 50 ms was used because it included the entire waveform and permitted good frequency resolution. The power spectrum was averaged over 40 pulses. The dominant frequency was defined as the frequency at the highest peak of the power spectrum level. Data were analyzed on programs written with codes of MATLAB® (The Mathworks, Natick, MA) software.

The first experiment examined the effects of water depth on the power spectrum. The water level (depth) of the 170-l tank was changed from 10 to 40 cm at 5-cm increments. The transducer and the hydrophone were positioned at the center of the right and left halves of the tank, respectively [Fig. 1(A)] in the middle of the water column.

The second experiment examined the changes in the power spectrum as a function of the distance between the hydrophone and the transducer. The water depth of the tank was maintained at 40 cm, and the transducer was positioned at the center of the right half of the 170-l tank and at a depth of 20 cm. The hydrophone was first positioned 5 cm from the transducer [Fig. 1(B)] and moved horizontally at 5-cm intervals up to 60 cm away from the transducer.

The third experiment examined the changes in power spectrum level with both distance and frequency in the 170-l tank. Water depth was maintained at 40 cm. The transducer was positioned at the center of the right half of the 170-l tank and at a depth of 20 cm. The hydrophone was positioned 5 cm from the transducer and moved up to 60 cm holizontally. Projected frequency was changed from 1.0 to 2.6 kHz with 0.5-kHz increments between 1.0–2.0 kHz and 0.1-kHz increments from 2.0–2.6 kHz.

III. RESULTS

A. Playback experiment in the calibration tank

Waveforms of computer-generated 5-cycle tone bursts [Fig. 2(A)] and recordings of the sound [Fig. 2(C)] in the large concrete rectangular tank exhibited differences. Due to the inertia of the transducer, the first cycle of the recorded waveform was smaller than the next cycle, and surface reflections seemed to create two extra oscillations at the offset of the wave [as indicated by the arrows in Fig. 2(C)]. Both power spectra, however, peaked at 1.0 kHz [Figs. 2(B) and (D)].

3074   J. Acoust. Soc. Am., Vol. 112, No. 6, December 2002

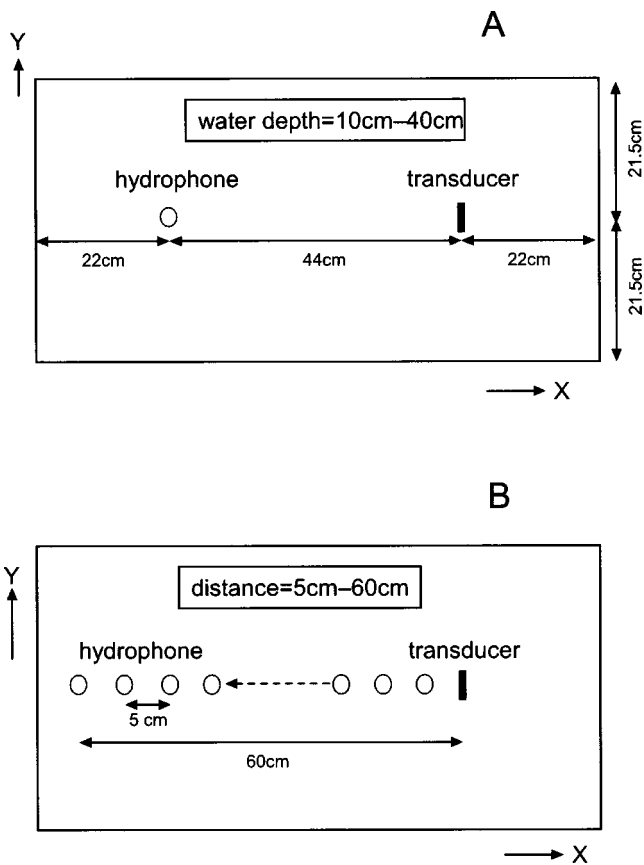Akamatsu *et al.*: Small tank acoustics

FIG. 1. Layout of the position of the transducer and the hydrophone used in a 170-l tank. For the first experiment (A), the distance between the hydrophone and the transducer was fixed at 44 cm and the water depth varied from 10 to 40 cm with 5-cm increments. For the second experiment (B), the water depth was 40 cm and the distance between the hydrophone and the transducer was changed from 5 to 60 cm with 5-cm steps (dashed arrow indicates the movement of hydrophone moving away from the transducer). The hydrophone and the transducer were always stationed in the middle depth of the water column.

The dominant frequency recorded in the 170-l tank varied as a function of water depth (solid black circles in Fig. 3). The sound spectra recorded in the 170-l tank were quite different from those recorded in the large concrete tank [cf. Fig. 2(D)]. For example, at 10-cm depth, no prominent peak could be found between 1 to 7.7 kHz and frequency peaked at 9.1 kHz (Fig. 3, upper inset), while at 40 cm depth, frequency peaked at 2.6 kHz (Fig. 3, lower inset).

The waveform recorded at 5 cm from the transducer in the 170-l tank [Fig. 4(A)] was similar to the original waveform [see Fig. 2(C)] and the power spectrum peaked at 1 kHz [Fig. 4(B)]. At 50 cm, the waveform exhibited multiple peaks of different amplitude with a dominant frequency of 2.6 kHz [Figs. 4(C), (D)].

In an open-water system, the power spectrum level of projected sound should attenuate following the inverse square law according to the distance between a sound source and a receiver. Instead, as shown in Fig. 4(E) (solid circles), inside the 170-l tank the power spectrum level of the projected frequency (1 kHz) decreased exponentially as the distance increased from the sound source. The first-order linear regression between the power spectrum level S (dB) of 1 kHz
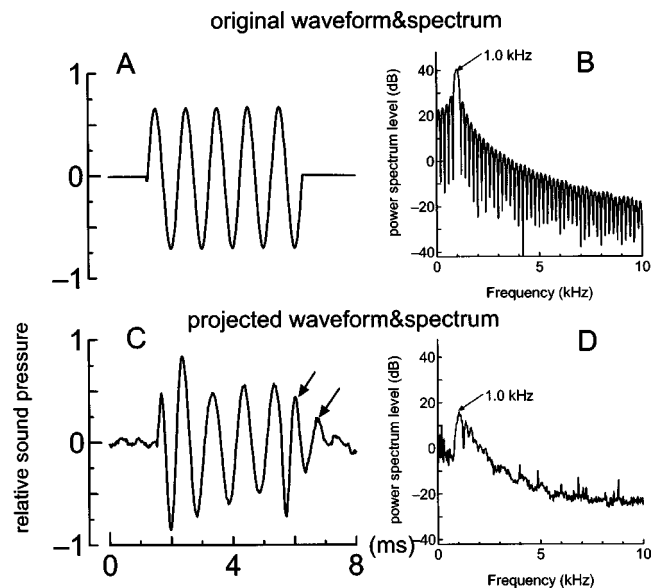

FIG. 2. The waveforms and power spectra of a playback experiment (1-kHz, 5-cycle tone burst) carried out in a semiopen-water environment, i.e., a 10-m×15-m×10-m concrete tank. (A) electronically generated waveform; (B) power spectrum of wave A with 50 ms analysis window. (C) recorded waveform. (D) power spectrum of wave C. Notice differences in waveform in C (indicated by arrows) due to surface reflections.

and the distance (X in cm) between the hydrophone and the transducer could be fitted with the following equation:

$$S = -20\frac{X}{D}. \tag{1}$$

Applying the least-square fit to the experimental data, coefficient D was determined as 23.0 cm. Here, we define D as the attenuation distance, meaning that the power spectrum level, at 1 kHz, was attenuated 20 dB for every change of D
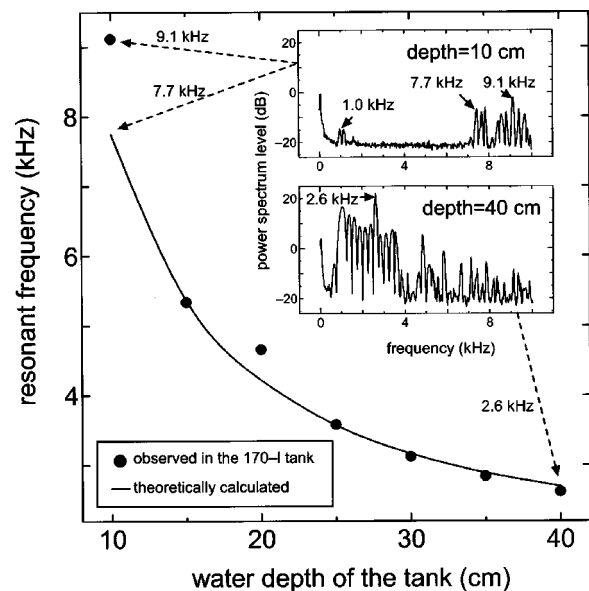

FIG. 3. Effects of water depth on changes of the empirically observed resonant frequencies (solid circles) recorded in a 170-l tank, where a 1-kHz 5-cycle tone burst was projected and recorded. Insets indicate the effect of water depth on the spectrum shape at 10 cm (upper inset) and 40 cm (lower inset), respectively. The theoretically calculated minimum resonant frequency is presented as a solid curved line.

J. Acoust. Soc. Am., Vol. 112, No. 6, December 2002

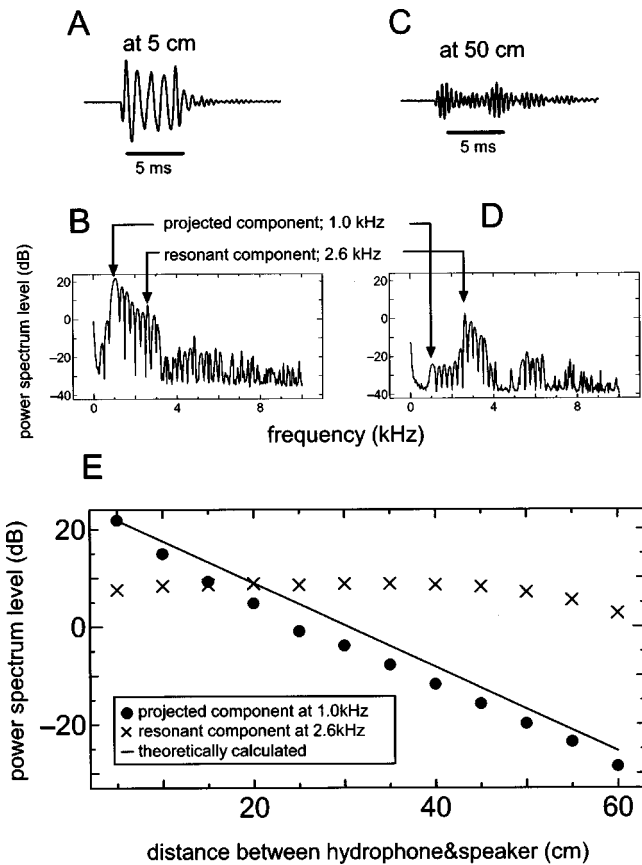Akamatsu *et al.*: Small tank acoustics   3075

FIG. 4. Waveforms and power spectra of a projected 1-kHz sound recorded 5 cm (A), (B) and 50 cm (C), (D) away from the sound source in a 170-l tank (E): The effect of distance between the hydrophone and the transducer on attenuation of the power spectrum level is depicted for a 1.0-kHz component (solid circles), 2.6-kHz resonant component (cross signs), and theoretically calculated value of a 1.0-kHz component (solid line).

cm further away from the sound source. In contrast, the power spectrum level at 2.6 kHz was nearly independent of the distance between the transducer and the hydrophone and did not attenuate significantly over this distance [Fig. 4(E), crosses].

In the third experiment, the attenuation distance for various frequencies (1.0, 1.5, 2.0, 2.1, 2.2, 2.3, 2.4, 2.5, and 2.6 kHz) was obtained experimentally and was nearly constant up to 2.0 kHz and thereafter increasing to 2.6 kHz (Fig. 5, solid circles). These results indicate that the attenuation distance increased as the frequency of the projected sound approaching the minimum resonant frequency of the 170-l tank.

B. Resonant frequency in a rectangular and a cylindrical tank

Multiple reflected waves in a closed boundary system can create standing waves whose frequency is called resonant frequency. The resonant frequency is given as the eigenfrequency of the eigenvalue equation with a specific boundary condition (Kinsler *et al.*, 2000). Glass or plastic walls of aquaria are easily bent by the sound pressure, and the particle movement exists even close to the wall. The sound-pressure
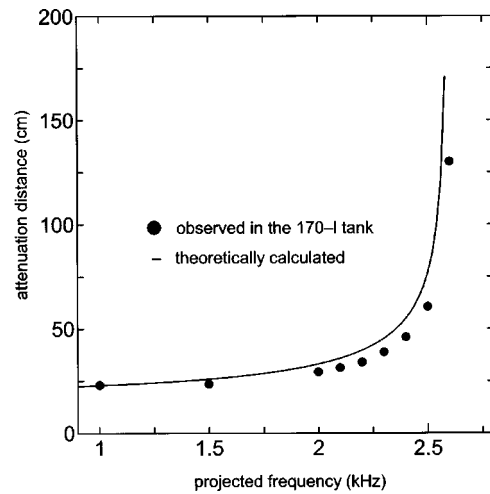
FIG. 5. The relationship between the projected frequency and the attenuation distance. Note that the attenuation distance remains almost constant for frequency less than 2.0 kHz and significantly rises as it approaches the minimum resonant frequency of the tank. The theoretical attenuation distance is depicted as a curved line.

level is adjusted to the air pressure at this interface site. Hence, a pressure-release boundary condition is assumed at the tank wall.

The calculated resonant frequencies of a rectangular glass tank with the dimension of L_x, L_y, and L_z (in centimeters) can be described by the following equation:

$$f_{lmn}^{\text{rectangular}} = \frac{c}{2} \sqrt{\left(\frac{l}{L_x}\right)^2 + \left(\frac{m}{L_y}\right)^2 + \left(\frac{n}{L_z}\right)^2}, \qquad (2)$$

where c is the sound velocity in the water approximately 1.5×10^5 cm/s, depending on water temperature and the salinity (Medwin, 1975). Each l, m, n represents an integer, and the combination of these parameters designates the "mode number" (Kinsler *et al.*, 2000). The minimum resonant frequency can be expressed as the mode (1, 1, 1). The waveform of mode (1, 1, 1) has a stable point of sound-pressure level called a node which exists only at the wall of the tank. For a wave with mode (2, 1, 1), in addition to a node at the wall, there is also another node at $L_x/2$ (see Fig. 6).
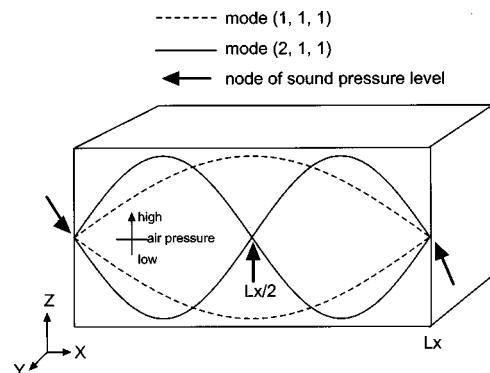

FIG. 6. Sound-pressure level along the X axis of mode (1, 1, 1) and mode (2, 1, 1) in a rectangular tank. The mode (1, 1, 1) represents the resonance wave of minimum frequency. The mode (2, 1, 1) represents one of the higher order of resonant component and has additional node of the sound-pressure level at the middle of the X axis, i.e., $L_x/2$.

With regard to a cylindrical-shape tank, the analytical solution of the eigenvalue equation is given as a linear combination of the Bessel functions of the first kind (see p. 249 of Kinsler *et al.*, 2000). The minimum resonant frequency is the minimum eigenvalue, and can be expressed by the following equation:

$$f_{minimum}^{circular} = \frac{c}{2}\sqrt{\left(\frac{2.405}{\pi a}\right)^2 + \left(\frac{1}{h}\right)^2}, \tag{3}$$

where a and h are the radius and the water depth of the circular tank, respectively. The value 2.405 is the first solution of the zeroth-order Bessel function of the first kind.

Based on the results obtained from the first experiment (Fig. 3), the observed resonant frequencies (solid circles) were in close agreement with the calculated minimum resonant frequencies (curve line) as described by Eq. (2), where $L_x = 88$ cm, $L_y = 43$ cm, $L_z = 10$ to 40 cm of mode (1, 1, 1) for 170-l tank.

C. Exponential attenuation of power spectrum level in a small tank: Analogy with a waveguide

Sound attenuation in the 170-l tank can best be explained by the waveguide model (Feynman *et al.*, 1989). Originally the waveguide was an electromagnetic feed line used in radio wave communications. Since the term L_x is relatively larger than the other dimension of the tank, it is assumed that the rectangular tank is an acoustical waveguide with a large L_x. The acoustical wave equation is expressed as follows:

$$\left(\frac{\partial^2}{\partial x^2} + \frac{\partial^2}{\partial y^2} + \frac{\partial^2}{\partial z^2}\right)p(x,y,z,t) = \frac{1}{c^2}\frac{\partial^2 p(x,y,z,t)}{\partial t^2}, \tag{4}$$

where c is the sound velocity and p is the sound-pressure level at time t, and the position (x,y,z) within the duct while (x,y,z) has the following limitations: $-\infty < x < \infty$ and $0 \leq y \leq L_y$ and $0 \leq z \leq L_z$. Assuming a pressure-release boundary condition exists, then the relative sound-pressure level compared with the air pressure at the boundary is zero.

$$p(x,0,z,t) = p(x,L_y,z,t) = p(x,y,0,t) = p(x,y,L_z,t) = 0. \tag{5}$$

If there is a fish that produces an f-Hz sinusoidal sound at the center of the duct, the sound pressure at the location of the fish can be expressed as

$$p\left(0,\frac{L_y}{2},\frac{L_z}{2},t\right) = P_0\exp(-i2\pi ft), \tag{6}$$

where P_0 is the source level of sound produced by the fish.

The low-frequency acoustic waves less than the cutoff frequency have imaginary wave number and are attenuated exponentially in the duct (Morse and Ingard, 1968). The cutoff frequency of the duct $f_{cutoff}^{rectangular}$ can be calculated as follows:

$$f_{cutoff}^{rectangular} = \frac{c}{2}\sqrt{\left(\frac{1}{L_y}\right)^2 + \left(\frac{1}{L_z}\right)^2}. \tag{7}$$

The solution of the wave equation satisfying the boundary condition (5) can be written as a linear combination of sinusoidal waves

$$p(x,y,z,t) = P_0\sum_{m=1}^{\infty}\sum_{n=1}^{\infty} C_{m,n}\exp(-k_{m,n}|x|)$$

$$\times \sin\left(\frac{\pi m}{L_y}y\right)\sin\left(\frac{\pi n}{L_z}z\right)\exp(-i2\pi ft), \tag{8}$$

$$k_{m,n} = \sqrt{\left(\frac{n\pi}{L_y}\right)^2 + \left(\frac{m\pi}{L_z}\right)^2 - \left(\frac{2\pi f}{c}\right)^2}, \tag{9}$$

where $C_{m,n}$ are the constants needed to agree with Eqs. (5) and (6) with integers m and n. $k_{m,n}$ can be determined using Eqs. (4) and (8).

When the sound frequency is less than the cutoff frequency, the $k_{1,1}$ is minimum among $k_{m,n}$ for any integers m and n, and corresponds to the smallest attenuation. Therefore, the acoustical wave of this mode can survive rather than other modes. When considering only this mode, then Eq. (8) can be simplified to the following expression:

$$p(x,y,z,t) \propto P_0 10^{-(x/2D^{rectangular})}\sin\left(\frac{\pi}{L_y}y\right)\sin\left(\frac{\pi}{L_z}z\right)$$

$$\times \exp(-i2\pi ft), \tag{10}$$

where $D^{rectangular}$ is the theoretically calculated attenuation distance, and can be expressed as the following equation:

$$D^{rectangular}(f) = (2\ln 10)\frac{c}{4\pi f_{cutoff}^{rectangular}}\frac{1}{\sqrt{1 - \left(\frac{f}{f_{cutoff}^{rectangular}}\right)^2}}$$

$$= \frac{550}{f_{cutoff}^{rectangular}\times\sqrt{1 - \left(\frac{f}{f_{cutoff}^{rectangular}}\right)^2}}. \tag{11}$$

This means that for every $D^{rectangular}$ apart from the sound source, the sound-pressure level at f Hz is decreased by 10 percent, which is equal to a 20-dB attenuation.

The observed and calculated attenuation distances D were 23.0 and 23.3 cm [solid line in Fig. 4(E) and Fig. 5], respectively, for 1-kHz tone bursts in the 170-l calibration tank with 40-cm water depth. Therefore, we have shown that the empirical and theoretical attenuation distances are in close agreement with each other.

Moreover, according to Eq. (11), the attenuation distance should increase as the projected frequency approaches the cutoff frequency of the waveguide, as shown in the curved line in Fig. 5, and closely fits the empirical results. The attenuation distance remained almost constant up to 2 kHz, but increased significantly from 2.1 to 2.6 kHz. Theoretically, the attenuation distance at the resonant frequency is infinite, which explains why the resonant frequency component is independent of the position of the hydrophone as observed in Fig. 4(E) (crosses).

A circular tank with a diameter larger than its depth is similar to a shallow-water system such as a flat-bottom pond

J. Acoust. Soc. Am., Vol. 112, No. 6, December 2002

Akamatsu *et al.*: Small tank acoustics   3077

or a creek, which is a natural habitat of many freshwater fish. Under this assumption, the attenuation distance and the cut-off frequency are represented as the following equations:

$$D^{\text{circular}}(f) = (2 \ln 10) \frac{c}{4 \pi f_{\text{cutoff}}^{\text{circular}}} \frac{1}{\sqrt{1 - \left(\dfrac{f}{f_{\text{cutoff}}^{\text{circular}}}\right)^2}}$$

$$= \frac{550}{f_{\text{curoff}}^{\text{circular}} \times \sqrt{1 - \left(\dfrac{f}{f_{\text{cutoff}}^{\text{circular}}}\right)^2}}, \qquad (12)$$

and

$$f_{\text{cutoff}}^{\text{circular}} = \frac{c}{2h}. \qquad (13)$$

IV. DISCUSSION

A. What happens in small tanks?

Data from the literature show that most fish sounds consist of pulse trains, and only a few are of a tonal nature (Winn, 1964; Fish and Mowbray, 1970). Pulsed sounds exhibit a broadband spectrum in comparison with tonal sounds. When a pulsed sound of a fish has a frequency component that is close to the minimum resonant frequency of the tank, then the resonant component will be overemphasized in recordings such shown as in Fig. 4(D).

A single-pulse sound [Fig. 4(A)] recorded 50 cm from the transducer exhibits a multipulsed waveform [Fig. 4(C)]. The first and second pulse appear to represent the response from onset and offset of the original pulse. The onset and offset of this wave have broadband spectra which enhance the resonant component.

The resonant component has a longer duration than the original wave. After 5 ms, which is the duration of the original wave, many small amplitudes of oscillations (characteristic of this resonance) appeared in our recordings [see Fig. 4(C) at tail ends].

If the original frequency is lower than the minimum resonant frequency, the signal-to-resonance ratio could be decreased when the hydrophone is placed beyond the attenuation distance from the sound source. In support of this viewpoint, when the hydrophone is placed only 30 cm from the sound source, in the 170-l tank, the resonant spectrum component is 10 dB greater than the projected spectrum component [Fig. 4(E); projected component vs resonant component]. This difference exists because the original signal frequency component is attenuated exponentially, whereas the resonant component remains almost uniform throughout the tank.

If a recording can be made within the attenuation distance and close to the sound sources, then the power spectrum of the projected signal would significantly exceed that of the resonant component [see Figs. 4(A) and (E) at 5 cm]. Therefore, recording a signal within the attenuation distance results in less distortion of the power spectrum.

The attenuation distance changes little for frequencies below 2 kHz (Fig. 5). This indicates that the observed power spectrum component within the frequency, which is lower than the cutoff frequency, is attenuated by a similar amount. Hence, the shape of the power spectrum is reliable for comparison purposes. Furthermore, since the power spectrum level attenuates exponentially within a short distance [Fig. 4(E)], the absolute value of the power spectrum level of each component will be unreliable, unless the position of the fish remains fixed.

B. Methods for acoustical measurements in a small tank

Based on the aforementioned measurements and theoretical calculations, we present a simple, yet practical procedure for correcting fish sound recording and measurement in small tanks. The general considerations are: (1) the targeted sound frequency, i.e., the sound produced by the fish should not be similar to the minimum resonant frequency of the tank; and (2) the hydrophone should be placed within the attenuation distance of the sound source to minimize possible distortion.

A useful working protocol for sound recordings in small tanks is discussed as follows.

(i) Measure the water depth, width, and length of a rectangular tank or diameter of a circular tank.

(ii) If the minimum dimension (either width, length, or diameter) of the tank is much larger than the distance that sound can travel during the pulse duration, then the tank can be considered as a semiopen-water system. Under such a condition, it may be possible to measure the original sound with less distortion because the direct and reflected waves will be separated from each other in the time domain except for the reflections from the water surface. If, however, the tank length is shorter than the distance that can be traveled by the pulse duration of the fish sound, then the following procedures should be taken:

(iii) Calculate the minimum resonant frequency (F_{min}) by using Eqs. (2) or (3). Subsequently, the attenuation distance (D) can be calculated by using Eqs. (11) or (12).

(iv) Record the fish sound within the attenuation distance in a small tank. Measure the dominant frequency of the original fish sound (F_{fish}).

(v) If either $F_{\text{min}} \ll F_{\text{fish}}$ or $F_{\text{min}} \gg F_{\text{fish}}$, the small tank may be used for recording fish sound. If $F_{\text{min}} = F_{\text{fish}}$, drain some water to reduce its level to increase F_{min}, then proceed to step (vi). If lowering water level causes behavioral changes in the fish, add water to decrease the F_{min} value; then proceed to step (vii).

(vi) In the case of $F_{\text{min}} \gg F_{\text{fish}}$, record the sound within the attenuation distance of the sound from the fish. As shown in Fig. 5, where the attenuation distance remains nearly constant, each frequency component should attenuate similarly for frequencies well below the minimum resonant frequency of the tank. Hence, the outline of the power spectrum shape is measurable

in this frequency range. However, since the sound-pressure level decreases exponentially under these circumstances, it is extremely difficult to have a precise measurement of the absolute sound-pressure level unless the fish is maintained in a fixed position.

(vii) For the case of $F_{min} \ll F_{fish}$, the attenuation distance is longer than for the case of $F_{min} \gg F_{fish}$ as mentioned in step (vi). In this situation, the measurable range between the fish and the hydrophone is proportionally increased and releases most restrictions on hydrophone position. However, the resonant components of higher modes may be closer to F_{fish}. If the power spectrum level of F_{fish} is independent of the distance between the sound source and the hydrophone (as measured outside of the attenuation distance), this component may be the result of the second or third modes of the resonant frequency.

(viii) Application of a frequency filter can be beneficial. If the recorded sound has an extra oscillation caused by the resonant wave, then a bandpass filter may be applied to eliminate the resonant component and other sources of unwanted noise. In the laboratory setting, low-frequency noises usually contaminate recorded sounds. Possible sources of such noises are building vibrations, human activities, ac-power current, etc. A bandpass filter that passes F_{fish} but excludes both F_{min} and noises should be selected. For example, application of such a bandpass filter to a recorded signal can be easily achieved by the use of a software-based, acoustical signal-analysis program (e.g., COOL EDIT 2000, Syntrillium Software Co.).

V. APPLICATION AND VALIDATION

A. Sound recording of croaking gourami (*Trichopsis vittata*)

Using the provisions outlined in the previous sections, sound recordings produced by croaking gourami in two different sizes of small tanks have been tested. Under staged agonistic conditions, the croaking gourami generates a train of double-pulse sounds with a pulse duration of several milliseconds (Ladich *et al.*, 1992). The croaking sounds are generated by two hypertrophied pectoral tendons rubbing against the fin rays (Kratochvil, 1978). The recording procedures of the croaking sounds used are outlined as follows.

(i) Two types of tanks were used for the recording: an 1800-l circular tank (diameter: 150 cm; height: 100 cm) with 42-cm water depth, and a 37-l rectangular glass tank ($50 \times 25 \times 30$ cm dimension; length $\times$width$\times$height) with 22-cm water depth.

(ii) The minimum dimension of both types of tanks was far shorter than the sound travel distance of a croaking pulse. Hence, serious distortion was expected.

(iii) The minimum resonant frequencies and attenuation distances were calculated using Eqs. (2), (3), (11), and (12) for each size tank, and the results are listed in Table I.

(iv) The sound of the croaking gourami had an approximate 1-kHz dominant frequency.

TABLE I. Theoretically calculated minimum resonant frequencies and attenuation distances of each type of experimental tanks.

	170-l tank	1800-l tank	37-l tank
Size (cm) (length$\times$width$\times$height)	$88 \times 43 \times 45$	Diameter; 150 Height; 100	$50 \times 25 \times 30$
Water depth (cm)	40	42	22
Minimum resonant frequency (kHz)	2.7	1.9	4.8
Attenuation distance (cm)	23.3	37.2	12.4

(v) F_{min} is larger than F_{fish} (1 kHz) and step (vi) is employed.

(vi) Three days prior to recording, two adult male croaking gouramis were each placed in two separate tanks. A minimal 3 days of separation guarantees the highest degree of display of agonistic behavior including croaking sound production when agonistic encounters are staged. At the time of recording, a fish was removed from its holding tank and introduced inside a plastic film cubic container where another fish was placed. The container (20 cm each side) was made of thin polyethylene plastic film (with a wooden stick frame) and soaked in the 1800-l tank. This container served as a cage to confine two fish and to guarantee the exhibition of agonistic encounter behavior. A Benthos AQ-18B hydrophone (sensitivity −171 dB *re*: 1 V/uPa) was positioned inside the container to ensure that even the maximum distance between the fish and the hydrophone was within the attenuation distance (termed test case A here). Since the wavelength ($\lambda = 150$ cm) of a 1-kHz sound was longer than the thickness of the film, and the density of polyethylene (0.93 to 0.97 g/cm^3) was similar to the water, sound could transmit through the film container without major distortion or attenuation.
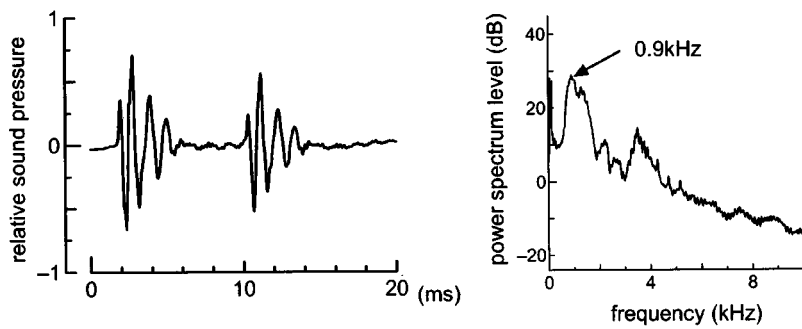
For purpose of comparison, the hydrophone was also placed outside the container (50 cm from the center of the container) at a depth of 20 cm in the 1800-l tank, but the fish remained inside the plastic film container (termed test case B here).

For recording in the small tank (37-l tank), the hydrophone was positioned in the right rear corner of the 37-l tank, 3 cm from both sides of the wall and 10 cm from the bottom of tank. The croaking sounds produced within 10 cm from the hydrophone were analyzed (termed test case C here).
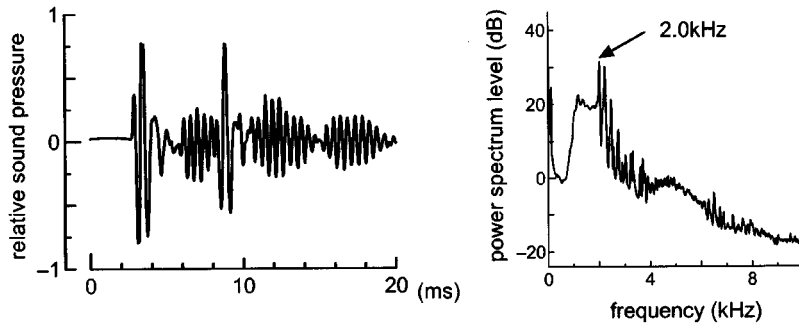
B. Validation

The typical waveforms and averaged power spectra ($n = 40$ each) of sounds produced by croaking gourami recorded in the test cases A, B, and C are shown in Fig. 7. The waveform recorded within the plastic-film container (test case A) in the 1800-l tank [Fig. 7(A), left panel] showed a typical double-pulse sound of a croaking gourami characterized by a dominant frequency of 0.9 kHz [Fig. 7(A) right panel]. However, for recordings made outside of the plastic film container (test case B), the waveforms revealed a series of several oscillations [Fig. 7(B), left panel] with a dominant

J. Acoust. Soc. Am., Vol. 112, No. 6, December 2002

Akamatsu *et al.*: Small tank acoustics   3079

A 1800–l tank within the fish container
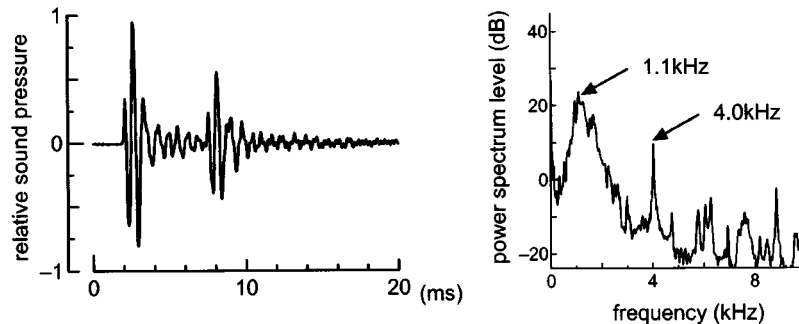

B 1800–l tank out of the fish container

FIG. 7. Recorded waveforms and spectra of double-pulse sounds produced by croaking gourami in a 1800-l tank (A), (B) and in a 37-l tank (C). The dominant frequency is 0.9 kHz for sound recorded inside a plastic film container, i.e., within the attenuation distance, located at the center of the tank (A). The dominant frequency changes to 2.0 kHz when recording is made at 50 cm (B), i.e., outside attenuation distance, away from the center of the tank where the fish is held inside a plastic film container. The dominant frequency was 1.1 kHz for croaking sound and the secondary peak frequency was 4.0 kHz for resonant component in a 37-l tank.

C 37–l tank

frequency of 2.0 kHz [Fig. 7(B), right panel], which was close to the calculated resonant frequency (1.9 kHz) of this tank. Recordings made inside the 37-l tank (test case C) revealed a series of decaying oscillations [Fig. 7(C), left panel] in the waveforms, and the power spectrum showed peaks at 1.1 and 4.0 kHz [Fig. 7(C), right panel] when the croaking gourami generated sounds close to the hydrophone. Only in case B was the hydrophone placed outside of the attenuation distance resulting in a power spectrum that was completely different from the original sound.

VI. CONCLUSION

As illustrated in this work when fish sound recordings were made inside small tanks, the characteristics of original signals could be greatly distorted. However, distortions can be avoided when certain features of the sounds are known and choices for the size of tanks are made to minimize resonance effects. For instance, the distance between a fish and a hydrophone should be within the "attenuation distance" to avoid distortion of the resonant component.

Some fishes produce low-frequency, continuous narrow-band sounds. If the dominant frequency of the fish sound is much less than the resonant frequency of the tank, an accurate measurement of a fish's sound in a small tank may be successful. Unlike those of pulse signals, the narrow-band sounds have less energy at the resonant frequencies of the tank. One would expect the signal-to-resonant component ratio to be higher than for the pulse sounds and therefore the spectral shape of a continuous signal would be similar to the spectrum of the original sound, with less distortion than for pulsed sounds.

Some sonic fishes (e.g., mormyrids, catfish, minnows, gouramis) possess ancillary auditory structures (i.e., otic gas-bladders of mormyrids, Weberian ossicles coupled with gas-bladder in catfish and minnows, suprabranchial chambers in gouramis) used to enhance hearing (von Frisch, 1938; Crawford et al., 1997; Yan, 1998; Johnston and Johnson, 2000a, b; Yan et al., 2000; Yan and Curtsinger, 2000). If a small tank is used for behavioral observations (e.g., agonistic encounter during sound production) on these sonic fish, it is imperative

to understand that not only could the sound-pressure level be significantly modified, but also the spectral characteristics impinging on the signal receivers are substantially altered from the original sound. These altered signals may be misinterpreted by the signal receivers and hence lead to the expression of unusual behavior (e.g., display of prolonged aggression). Therefore, caution should be taken when dealing with observations and interpretation of data of behavioral interactions among sonic fishes inside small tanks (also see Myrberg, 1972; Myrberg and Spires, 1972).

Ballantyne, P. K., and Colgan, P. W. (**1978**). "Sound production during agonistic and reproductive behavior in the pumpkinseed (*Lepomis gibbosus*), the bluegill (*L. macrochirus*), and their hybrid sunfish," 1. Context. Biology of Behavior **3**, 113–135.

Bodnar, D. A., and Bass, A. H. (**1997**). "Temporal coding of concurrent acoustic signals in the auditory midbrain," J. Neurosci. **17**, 7553–7564.

Colson, D. J., Patek, S. N., Brainerd, E. L., and Lewis, S. M. (**1998**). "Sound production during feeding in hippocampus seahorses (Syngnathidae)," Environmental Biology of Fishes **51**, 221–229.

Crawford, J. D., Jacob, P., and Bénech, V. (**1997**). "Sound production and reproductive ecology of a strongly acoustic fish in Africa: *Pollimyrus isidori*, Mormyridae," Behaviour **134**, 677–725.

Drewry, C. E. (**1962**). "Some observations of courtship behavior and sound production in five species of *Fundulus*," Master thesis, University of Texas at Austin.

Feynman, R. P., Leighton, R. B., and Sands, M. L. (**1989**). *The Feynman Lectures on Physics: Commemorative Issue*, Vol. 2 (Addison-Wesley, New York), Chap. 24, pp. 1–11.

Fine, M. L., Friel, J. P., McElroy, D., King, C. B., Loesser, K. E., and Newton, S. (**1997**). "Pectoral spine locking and sound production in the channel catfish *Lctalurus punctatus*," Copeia **1997**, 777–790.

Fish, M. P., and Mowbray, W. H. (**1970**). *Sounds of Western North Atlantic Fishes* (Johns Hopkins University Press, Baltimore).

Gerald, J. W. (**1971**). "Sound production during courtship in six species of sunfish (Centrarchidae,)" Evolution (Lawrence, Kans.) **25**, 75–87.

Johnston, C. E., and Johnson, D. L. (**2000a**). "Sound production during the spawning season in cavity-nesting darters of the subgenus *Cantonotus* (Percidae: *Etheostoma*)," Copeia **2000**, 475–481.

Johnston, C. E., and Johnson, D. L. (**2000b**). "Sound production in *Pimephales notatus* (Rafinesque)(Cyprinidae)," Copeia **2000**, 567–571.

Kaatz, I. M., and Lobel, P. S. (**2001**). "A comparison of sounds recorded from a catfish (*Orinocodoras eigenmanni*, Doradidae) in an aquarium and in the field," Biol. Bull. **201**, 278–280.

Kinsler, L. E., Frey, A. R., Coppens, A. B., and Sanders, J. V. (**2000**). *Fundamentals of Acoustics*, 4th ed. (Wiley, New York).

Kratochvil, H. (**1978**). "Structure of the sound producing organ of the croaking gourami (*Trichopsis vittatus* Cuvier and Valenciennes)(Anabantidae, Belontiidae)," Zoomorphologie **91**, 91–99.

Ladich, F., and Yan, H. Y. (**1998**). "Correlation between auditory sensitivity and vocalization in anabantoid fishes," J. Comp. Physiol., A **182**, 737–746.

Ladich, F., Bischof, C., Schleinzer, G., and Fuchs, A. (**1992**). "Intra- and interspecific differences in agonistic vocalization in croaking gouramis (Genus: Trichopsis, Anabantoidei. Teleostei)," Bioacoustics **4**, 131–141.

Lobel, P. S. (**1992**). "Sound produced by spawning fishes," Environmental Biology of Fishes **33**, 351–358.

Lobel, P. S. (**2001**). "Acoustic behavior of cichlid fishes," J. Aquacult. Aquat. Sci. **9**, 167–186.

Lugli, M., Pavan, G., Torricelli, P., and Bobbio, L. (**1995**). "Spawning vocalizations in male freshwater gobiids (Pisces, Gobiidae)," Environmental Biology of Fishes **43**, 219–231.

Lugli, M. G., Torricelli, P., Pavan, G., and Miller, P. J. (**1996**). "Breeding sounds of male *Pandogobius nigricans* with suggestions for further evolutionary study of vocal behavior in gobioid fishes," J. Fish Biol. **49**, 648–657.

Lugli, M. G., Torricelli, P., Pavan, G., and Mainardi, D. (**1997**). "Sound production during courtship and spawning among freshwater gobiids (Pisces, Gobiidae)," Marine and Freshwater Behavior and Physiology **29**, 109–126.

Lugli, M., and Torricelli, P. (**1999**). "Prespawning sound production in Mediterranean sand-gobies," J. Fish Biol. **54**, 691–694.

Mann, D. A., and Lobel, P. S. (**1998**). "Acoustic behavior of the damselfish *Dascyllus albisella*: Behavioral and geographic variation," Environmental Biology of Fishes **51**, 421–428.

Matsuno, Y., Hujieda, S., Yamanaka, Y., Kaparang, F. E., Yoichi, Y., and Kurihara, T. (**1996**). "Underwater sound production by amberjack, *Seriola dumerili*, in the net pen at the culture grounds in Sakurajima strait of Kagoshima," Bulletin of the Japanese Society of Fisheries Oceanography **60**, 122–129.

Medwin, H. (**1975**). "Speed of sound in water: A simple equation for realistic parameters," J. Acoust. Soc. Am. **58**, 1318–1319.

Morse, P. M., and Ingard, K. U. (**1968**). *Theoretical Acoustics* (Princeton University Press, Princeton, NJ), pp. 467–469.

Myrberg, Jr., A. A. (**1972**). "Ethology of the bicolor damselfish, *Eupomacentrus partitus* (Pisces: Pomacentridae): A comparative analysis of laboratory and field behavior," Animal Behavior Monographs **5**, Pt. 3, 199–283.

Myrberg, Jr., A. A., and Spires, J. A. (**1972**). "Sound discrimination by the bicolor damselfish, *Eupomacentrus partitus*," J. Exp. Biol. **57**, 727–735.

Myrberg, Jr., A. A. (**1981**). "Sound communication and interception in Fishes" in *Hearing and Sound Communication in Fishes*, edited by W. N. Tavolga, A. N. Popper, and R. R. Fay (Springer, New York), pp. 395–426.

Myrberg, Jr., A. A. (**1997**). "Sound production by a coral reef fish (*Pomacentrus partitus*): Evidence for a vocal, territorial 'keep-out' signal," Bull. Mar. Sci. **60**, 1017–1025.

Parvulescu, A. (**1964**). "Problems of propagation and processing," in *Marine Bio-Acoustics*, edited by W. N. Tavolga (Pergamon, Oxford), pp. 87–100.

Parvulescu, A. (**1967**). "The acoustics of small tanks," in *Marine Bio-Acoustics*, edited by W. N. Tavolga (Pergamon, Oxford), Vol. 2, pp. 7–13.

Pedersen, J. (**2001**). "Hydroacoustic measurement of swimming speed of North Sea saithe in the field," J. Fish Biol. **58**, 1073–1085.

Pruzsinszky, I., and Ladich, F. (**1998**). "Sound production and reproductive behavior of the armoured catfish *Corydoras paleatus* (Callichthyidae)," Environmental Biology of Fishes **53**, 183–191.

Stout, J. F. (**1975**). "Sound communication during the reproductive behavior of *Notropus analostanus* (Pisces: Cyprinidae)," American Midland Naturalists **94**, 296–325.

Tavolga, W. N. (**1964**). "Sonic characteristics and mechanisms in marine fishes," in *Marine Bio-Acoustics*, edited by W. N. Tavolga (Pergamon, Oxford), pp. 195–211.

Thorson, R. F., and Fine, M. L. (**2002a**). "Acoustic competition in the Gulf toadfish *Opsanus beta*: Acoustic tagging," J. Acoust. Soc. Am. **111**, 2302–2307.

Thorson, R. F., and Fine, M. L. (**2002b**). "Cresuscular changes in emission rate and parameters of the boatwhistle advertisement call of the Gulf toadfish, *Opsanus beta*," Environmental Biology of Fishes **63**, 321–331.

Tolimieri, N., Jeffs, A., and Montgomery, J. C. (**2001**). "Ambient sound as a cue for navigation by the pelagic larvae of reef fishes," Mar. Ecol. Prog. Ser. **207**, 219–224.

Valinski, B. W., and Rigley, L. (**1981**). "Function of sound production by the skunk loach *Botia horae* (Pisces, Cobitidae)," Z. Tierpsychol. **55**, 161–172.

von Frisch, K. (**1938**). "The sense of hearing in fish," Nature (London) **141**, 8–11.

Winn, H. E. (**1964**). "The biological significance of fish sounds," in *Marine Bio-Acoustics*, edited by W. N. Tavolga (Pergamon, Oxford), pp. 213–231.

Yan, H. Y. (**1998**). "Auditory role of the suprabranchial chamber in gourami fish," J. Comp. Physiol., A **183**, 313–324.

Yan, H. Y., Fine, M. L., Horn, N. S., and Colon, W. E. (**2000**). "Variability in the role of the gasbladder in fish audition," J. Comp. Physiol., A **186**, 435–445.

Yan, H. Y., and Curtsinger, W. S. (**2000**). "The otic gasbladder as an ancillary auditory structure in a mormyrid fish," J. Comp. Physiol., A **186**, 595–602.

Yost, W. A. (**1994**). *Fundamentals of Hearing: An Introduction*, 3rd ed. (Academic, San Diego).

Zerick, R., Mann, D. A., and Popper, A. N. (**1999**). "Acoustic communication in fishes and frogs," in *Comparative Hearing of Fish and Amphibians*, edited by R. R. Fay and A. N. Popper (Springer, New York), pp. 363–411.

Antimasking aspects of harp seal (*Pagophilus groenlandicus*) underwater vocalizations

Arturo Serrano[a] and John M. Terhune
Biology Department, University of New Brunswick, P.O. Box 5050, Saint John, New Brunswick E2L 4L5, Canada

Underwater sounds are very important in social communication of harp seals (*Pagophilus groenlandicus*) because they are the main means of long- and short-distance communication. Individual harp seals must try to avoid being masked and emit only those calls that will benefit them. Underwater vocalizations of harp seals were recorded during the breeding season. The physical characteristics associated with antimasking attributes of 16 call types were examined. Rising frequency or increasing amplitude within calls were not common. Most of the calls ended abruptly (range 145–966 dB/s), but call onset was more gradual. At high calling rates (95.1–135 calls/min) there were significantly more calls overlapping temporally than at medium (75.1–95 calls/min) or low (35–75 calls/min) calling rates, but even at the highest calling rates, 79.1% of the calls were not overlapped. When 2, 3, or 4 calls overlapped, there were significantly fewer frequency separations of less than 1/3 octave than would be expected by chance. This is important because sounds that are separated by less than 1/3 octave likely mask each other. When 2–4 calls are occurring simultaneously, only 4.5% to 14.2% are masked by virtue of being within 1/3 octave from their nearest neighbor. None of the overlappping calls was of the same type. This suggests that the seals are actively listening to each other's calls and are not randomly using the different call types. Harp seals use frequency and temporal separation in conjunction with a wide vocal repertoire to avoid masking each other. © *2002 Acoustical Society of America.* [DOI: 10.1121/1.1518987]

PACS numbers: 43.80.Lb, 43.80.Nd [WA]

I. INTRODUCTION

Several polygynous mammals use vocalizations for mate attraction and intrasexual competition (Smith, 1977; Vaughan, 1986; Chu, 1988; Bradbury and Vehrencamp, 1998; McElligot and Hayden, 1999). A variety of call characteristics such as duration, loudness, frequency (Hz), frequency changes, repetition, or calling rates carries the information. Information might be transmitted using a combination of these characteristics (Bradbury and Vehrencamp, 1998; McElligot and Hayden, 1999).

Vocal communication is strongly constrained by environmental factors. Vocalizations are subject to frequency-dependent attenuation, temporal degradation, and masking by environmental noise (Brenowitz, 1986; Mercado and Frazer, 1999). Thus, the level and the spectral and temporal characteristics of background noise are major determinants of the distance at which an acoustical signal is detectable (Wiley and Richards, 1982; Klump, 1996). Masking bands for marine mammals appear to be 1/6–1/3-octave wide. At low and very high frequencies, masking bands apparently widen (Richardson, 1995). Noises only mask adjacent frequencies. Thus pure tones separated by less than 1/3 octave likely mask each other (Richardson, 1995). These constraints are clearly reflected in the sound repertoires used by various species (Mercado and Frazer, 1999). An animal can avoid masking by calling at different times and using different fre-

quency bands (Ficken *et al.*, 1974). An animal must use appropriate signals that will distinguish its call from other animals' calling. It must try to avoid being masked and emit only those calls that will benefit itself (Smith, 1977).

Gourevitch (1987) has suggested that most species avoid masking by employing time differences, intensity differences, and high-frequency shifts. However, the mechanisms that animals use to avoid masking in order to communicate with each other have been rarely studied. Most of the work has been done on birds, and there are a few studies on marine mammals (Gourevitch, 1987).

Some marine mammals seem to be able to adjust the frequencies of their vocalizations, within limits, to avoid masking effects of background noise (Richardson and Malme, 1995). However, it is not known how much flexibility various marine mammals have in adjusting the frequencies of their calls. Most species either produce broadband calls or, at different times, produce narrow-band calls at specific frequencies (Richardson and Malme, 1995).

Masking studies on pinniped vocalizations are scarce. Terhune *et al.* (1994) proposed that Weddell seals (*Leptonychotes weddellii*) lengthen some calls presumably to enhance detectability of calls that were temporally masked. A harbor seal (*Phoca vitulina*) listening to repeated sounds at regular (predictable) rates had lower detection thresholds (relative to single sounds) in both masked and unmasked situations (Turnbull and Terhune, 1993).

High calling rates by harp seals (*Pagophilus groenlandicus*) produce a continuous broadband sound that might mask long-range vocalizations (Terhune and Ronald, 1986). Wat-
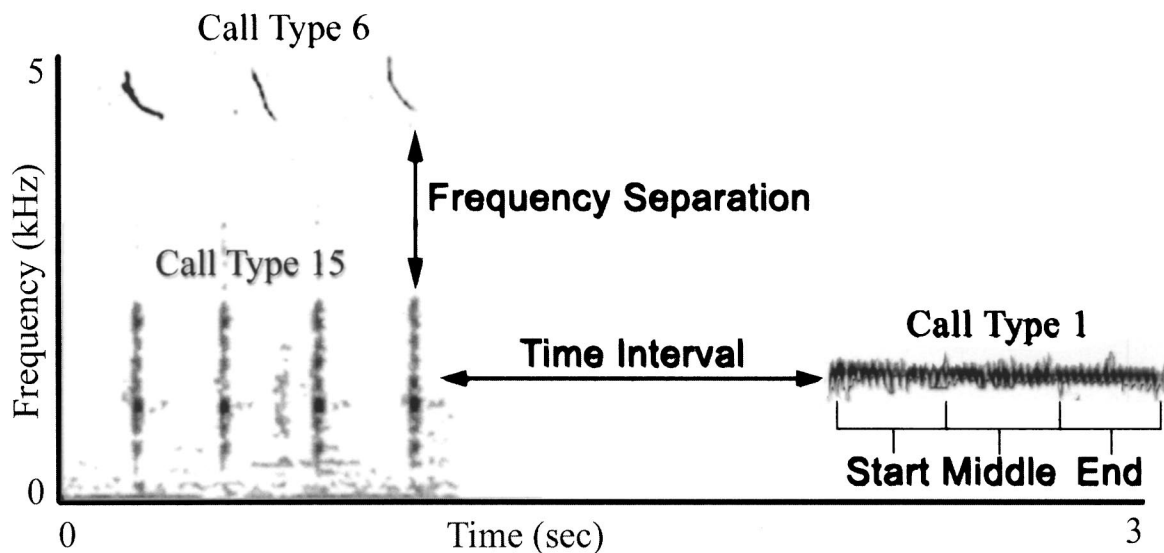
FIG. 1. Variables of underwater harp seal calls measured for this study. (a) Call names appear on top of each call and follow the nomenclature proposed by Møhl *et al.* (1975). The analyzing bandwidth was 31.5 Hz. (b) Amplitude measurements within calls. Vertical lines separate the call into thirds. The highest amplitude and highest frequency within each segment was recorded.

kins and Schevill (1979) reported that 75% of the underwater calls of harp seals were characterized by the following features: increasing within-call amplitude, increasing within-call frequency and/or pulse rates, and repetition of elements within the call. The redundancy of repetitive calling (in 94% of the calls), combined with spectral pattern shifts (in 75% of the calls) that contrast with ambient sound, provide a means of recognition of a herd at a distance and suggests that the sounds serve to advertise the whelping and breeding herd (Watkins and Schevill, 1979). These researchers concluded that harp seal call characteristics allow the seals to avoid masking, but they did not quantify all of the features they examined. Because harp seal calls contrast with environmental ambient noise they seem well suited for long-distance advertisements of various kinds (Watkins and Schevill, 1979), for example to promote herd formation or attract mates (Terhune and Ronald, 1986).

The purpose of this study was to quantify the physical characteristics of underwater harp seal calls that enhance call detection. For this purpose amplitude shifts, call onset/offset, frequency shifts, frequency separation between overlapping calls, and time intervals between calls were measured. Each of these aspects has features that can increase detectability of sounds.

II. MATERIALS AND METHODS

Recordings of harp seal underwater vocalizations were obtained during the breeding season (February–March, Sergeant, 1991) in the Gulf of St. Lawrence, near the Magdalen Islands, between 26 February–15 March 1999 and 1 March–15 March 2000.

Recordings were made from ice floes that were occupied by seals at 18 locations over the 2 years. Recording sessions were either in the morning or late afternoon and lasted from 1 to 5 h. Only harp seals were seen around the recording areas. Unfortunately, it was not possible to determine the location, sex, or age of the calling animals.

In 1999, recordings were made with a Brüel & Kjær 8100 hydrophone, a Brüel & Kjær 2635 charge preamplifier, and a Sony Digital Audio Tape (DAT) recorder (model TCD-D100). The frequency response of the system was ± 1.0 dB from 0.02 to 20 kHz. In 2000, recordings were made with a Vemco VHLF hydrophone and a Sony DAT recorder (model TCD-D100). The frequency response of this system was ± 4 dB from 0.02 to 20 kHz. The hydrophone was placed 5–10 m deep through breathing holes.

The underwater call characteristics analyzed were: amplitude and frequency shifts within calls, call onset and offset rates, frequency separation of overlapped calls, and the time interval between calls. These call features were measured because each of these aspects has features that can increase detectability of sounds (see Watkins and Schevill, 1979; Gourevitch, 1987; Terhune *et al.*, 1994; Richardson and Malme, 1995). Calls were classified using the nomenclature proposed by Møhl *et al.* (1975) and Terhune (1994). A call element is considered to be a single discrete sound within a call type. This sound has a clearly distinguishable beginning and end. Sound spectrograms were prepared using MULTI SPEECH model 3700 Version 2.2 (Kay Elemetrics Co., Pine Brook, NJ). Calls were digitized with a 10-bit A/D converter at a sampling rate of 44 kHz. Measurements were taken using an analyzing-filter bandwidth of 46 Hz (for frequency measurements) and 200 Hz (for time measurements) giving measurements accurate to ± 23 Hz and ± 2.2 ms.

Examples of the measurements taken are shown in Fig. 1. For all analyses only the first ten calls of each call type from each recording location were considered. This was done to minimize the problems caused by the possibility of analyzing calls produced by the same seal over and over again. Measurements were only made on calls that were clear enough to enable identical repeat measures of frequency or time to be made. The call type classification and number of overlapping calls were assessed by visual inspection of the sonograms at predetermined times. Calling rates were classi-

fied as low, medium, or high. The category of each recording was determined by averaging the number of calls per 30 s at ten randomly selected locations on the tape. The ranges selected for low, medium, and high categories were 35–75, 75.1–95, and 95.1–135 calls per min, respectively. Statistical tests were performed using SIGMA STAT Version 2.03 with an alpha level of 0.05.

A. Amplitude shifts

Amplitudes (dB) within calls were measured using the fast Fourier transform spectral slice of the sonograms. The first element of each call was divided into three segments based on time, and then the maximum amplitude within each segment (beginning, middle, and end of the element) was measured. The time scale of short-duration elements was expanded to enable these measurements to be made. The data were standardized by determining the maximum amplitude changes of the second and third segments relative to the first segment. Paired t-tests were used to compare the amplitude differences between the start and the middle, and between the start and the end of the element.

B. Call onset/offset rates

The call onset/offset rates (dB/s) were measured to establish if seals use abrupt changes in amplitude within calls. Amplitudes were measured at the start of the element, 10 ms later, 10 ms before the end of the element and at the end of the element. A Mann-Whitner test was used to compare the onset rate (dB/10 ms) and the offset rate (dB/10 ms) for each call type.

C. Temporal separation

The time interval (ms) between calls was measured to establish if seals use temporal separation to avoid masking each other. The time intervals between calls were measured from the end of one call to the beginning of the next call. The time interval for overlapping calls was considered to be zero. Consecutive pairs of calls per recording were analyzed independent of call type. Eighteen recording sites were analyzed. Time interval was compared against the three calling rates using a Kruskal–Wallis with a Dunn's pairwise multiple comparisons test.

D. Frequency shifts

Frequency shifts (in octaves) within the first element were analyzed. Measurements of the highest frequency with the most energy were taken from the first, middle, and last third of the call. The call frequencies were converted into an octave scale ($\log_2$ of the frequency) to allow for comparison in pitch separation. This was done because seals likely perceive frequency in terms of octaves (see Terhune, 1999). An analysis of variance (ANOVA) was used to compare the frequency differences between the start, middle, and end of the call. This analysis (frequency shifts) was taken one step further by comparing the maximum frequency of the call against the three calling rates. Therefore, frequency was used as a response variable, and calling rates as the explanatory

variable. For this analysis, a Kruskal–Wallis with a Dunn's pairwise multiple comparison test was used because the data did not present a normal distribution.

E. Frequency separation

The frequency separation and the number of overlapping calls of each recording were determined by measuring the frequency separation between overlapped calls at 20 randomly selected locations on each tape. Eighteen tapes were analyzed. Once again, the call frequencies were converted into $\log_2$ measures (an octave scale). A Kruskal–Wallis with a Dunn's pairwise multiple comparisons test was used to compare the frequency separation per number of overlapping calls at different calling rates.

The frequency separations of overlapping harp seal calls were compared to those of a random distribution. The distribution of expected frequency separations and the observed frequency separations were compared. To do this, random frequency distributions of frequency separations to match 2–4 simultaneous calls were generated for separations between 7.5 (185 Hz) and 12.5 (5.87 kHz) octaves. These values were selected because they were the minimum and maximum highest frequencies observed. Higher numbers of overlapped calls were not examined because they were not observed. A model was generated for each set of overlapping calls. A random number generator was used to determine the frequencies of simultaneous calls. The lowest frequency separation between a focal call and its nearest neighbors was determined. This process was repeated 40 000 times for each of 2, 3, and 4 overlapped calls to ensure that the results would be close to the true random distribution. The sample size from the expected distribution was at least 250 times larger than the observed frequency distributions. The Kolmogorov–Smirnov one-sample test was used to determine if the observed and the expected cumulative distributions of frequency separations in 1/3-octave increments were significantly different (Zar, 1996). A contingency table was used to determine if the observed and the expected cumulative distributions of frequency separations of less than 1/3 of an octave were significantly different.

III. RESULTS

Recordings were made at 18 sites over the 2 years. Call types 5, 16, or 19 were not detected in sufficient numbers to permit detailed analyses. Fewer than ten of these call types were recorded.

A. Amplitude shifts

Maximum amplitude in the last third of the calls was lower than that of the start and middle for all call types except 6 and 15 (Fig. 2). Call types 6 and 15 did not show a significant difference between the first portion and the middle or end of the call ($T=0.863$, $df=52$, $P=0.39$ and $T=1.646$, $df=42$, $P=0.107$, respectively; Fig. 2). A total of 603 calls was analyzed.
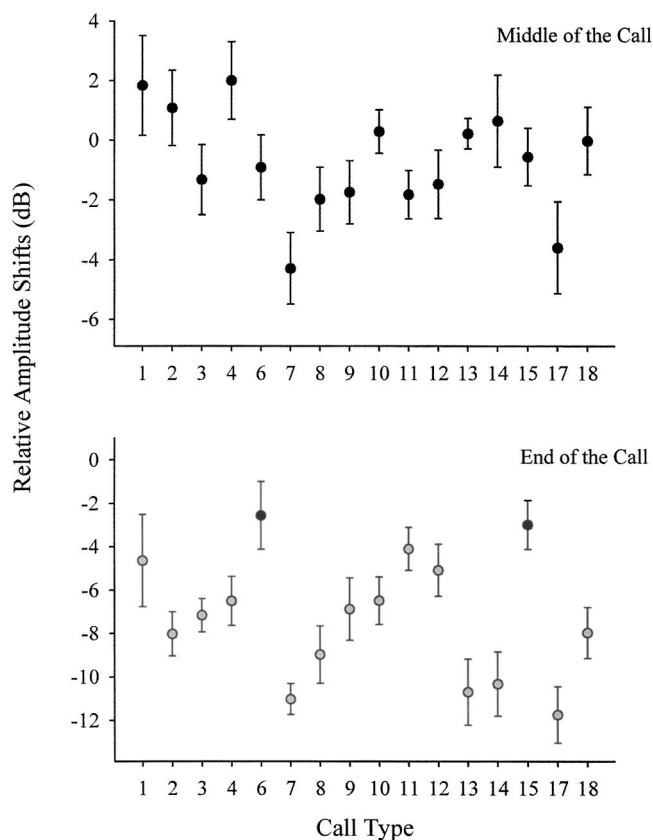
FIG. 2. Comparison of relative amplitude shifts (dB) between the start and middle or end of the call of harp seal underwater calls. Gray points denote significant differences.

B. Call onset/offset rates

Harp seal underwater calls increased or decreased in amplitude 10 ms after the start of the call (Table I). The offset rates were much higher and ranged from -1.45 to -9.66 dB/10 ms (145–966 dB/s). Twelve call types showed a significant difference between call onset rates and call offset rates (Table I).

TABLE I. Comparison of call onset and call offset rates (dB/10 ms) of harp seal underwater calls.

Call type	Onset	Offset	N	T	P
1	1.30	-2.42	34	526	0.205
2[a]	-1.35	-6.20	35	482	0.003
3[a]	1.39	-3.27	39	598	0.001
4[a]	1.11	-2.65	30	328	0.027
6	-1.04	-1.45	37	690	0.368
7[a]	-0.01	-8.04	41	623	0.001
8[a]	-0.24	-5.25	28	238	0.003
9[a]	-1.17	-4.83	35	525.5	0.031
10[a]	0.66	-2.93	37	617	0.031
11	-0.76	-3.44	32	424	0.098
12[a]	-1.19	-3.99	36	561	0.020
13[a]	-0.30	-6.15	28	253	0.012
14[a]	0.40	-6.38	40	645	0.001
15	-0.38	-2.36	32	459	0.40
17[a]	-0.82	-9.66	33	305	0.001
18[a]	0.56	-3.41	36	577	0.041

[a]Denotes a significant difference ($p < 0.05$).

TABLE II. Comparison of time intervals between harp seal underwater calls during low, medium, and high ambient calling rates. The percentages of overlapped calls at low, medium, high ambient calling rates are also listed.

Calling rates	Time intervals in ms (mean ± standard error)	Percentage of overlapped calls	N
Low	372.5 ± 19.53	12.69	588
Medium	350.0 ± 18.99	19.58	481
High	220.7 ± 10.50	20.63	744

C. Temporal separation

As expected, the time intervals between calls decreased as the calling rates increased. There was a significant difference between high calling rates and medium ($Q = 8.83$, $df = 2$, $P = 0.001$) and low ($Q = 7.41$, $df = 2$, $P = 0.001$) calling rates, but there was not a significant difference between low and medium ($Q = 0.87$, $df = 2$, $P = 0.356$; Table II). The percentage of calls overlapped (time $= 0$) was relatively low (Table II).

The frequency separation per number of overlapping calls was significantly different between high calling rates and medium calling rates ($Q = 3.26$, $df = 2$, $P = 0.02$) and between high and low calling rates ($Q = 4.18$, $df = 2$, $P = 0.01$). At low and medium calling rates there was not a significant difference ($Q = 0.55$, $df = 2$, $P = 0.50$). For overlapping calls only, the number of simultaneous calls at high calling rates was significantly higher than at either medium or low rates ($Q = 3.26$, $df = 2$, $P = 0.001$ and $Q = 4.18$, $df = 2$, $P = 0.050$, respectively; Table III). The number of simultaneous calls overlapping at low and medium calling rates was not significantly different ($Q = 0.55$, $df = 2$, $P = 0.550$; Table III).

D. Frequency shifts

A total of 645 calls was analyzed for this section. Only call type 12 showed a significant difference in the frequency with most energy between the start, middle, and the end of the call ($F = 5.403$, $df = 2$; $P = 0.006$; Fig. 3). All the other calls did not present a frequency difference along the call (Fig. 3). When this analysis was taken one step further, several calls presented a difference among the frequency (octaves) used at different calling rates. Nine call types exhibited a significant difference at low, medium, and/or high calling rates (Fig. 4). The call types that showed a significant difference were: 6 ($H = 9.580$, $df = 2$; $P = 0.008$); 7 ($H = 42.378$, $df = 2$; $P = 0.001$); 11 ($H = 30.012$, $df = 2$; $P = 0.001$); 12 ($H = 10.490$, $df = 2$; $P = 0.005$); 13 ($H = 24.273$, $df = 2$; $P = 0.001$); 14 ($H = 28.941$, $df = 2$; P

TABLE III. Number of simultaneous harp seal underwater calls that occur when calls overlap during low, medium, and high ambient calling rates. Calls that were not overlapped were excluded from this analysis.

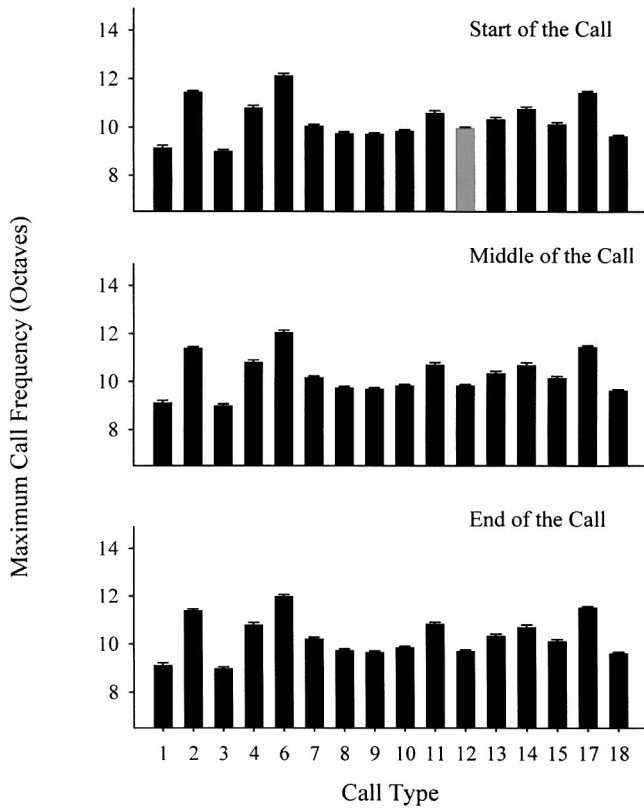| Calling rates	Simultaneous calls (mean ± standard error)	N
Low	2.62 ± 0.130	121
Medium	2.82 ± 0.140	115
High	3.48 ± 0.109	197

FIG. 3. Mean ($\pm$ s.e.) of maximum call frequency (octaves) of the start, middle, and end thirds of the call of harp seal underwater calls. Gray bar denotes a significant difference.

FIG. 4. Mean ($\pm$ s.e.) of maximum call frequency (octaves) at low, medium, and high calling rates of harp seal underwater calls. Bars with different colors denote significant differences.

$=0.001$); 15 ($H=47.038$, $df=2$; $P=0.001$); 17 ($H=11.482$, $df=2$; $P=0.003$); 18 ($H=25.537$, $df=2$; $P=0.001$).

E. Frequency separation

It is important to point out that none of the overlapping calls was of the same type. Of the 121, 115, or 197 occurrences of 2, 3, or 4 overlapping calls, there were no instances where two similar call types were involved.

The distributions of pitch separations between overlapping calls allowed us to assess the proportion of calls that was within a specified octave separation. The observed frequency separation between overlapped calls is greater than expected from a random distribution (Fig. 5). The cumulative frequency distributions of Fig. 5 indicate that there were fewer pitch separations that were lower than one octave than would be expected by chance. The Kolgomorov–Smirnov one-sample test showed a significant difference between the observed data and the expected data from a random distribution in all three comparisons (2 calls $n=112$, $D_{\mathrm{Max}}=0.23$, $D_{0.05,121}=0.12$; 3 calls $n=34$, $D_{\mathrm{Max}}=0.32$, $D_{0.05,115}=0.22$; 4 calls $n=20$, $D_{\mathrm{Max}}=0.52$, $D_{0.05,197}=0.29$). When two calls overlapped, the number of calls separated by less than 1/3 octave was 4.5%. A random distribution would be expected to yield 13.8% overlap. The observed (4.5%) and the expected (13.8%) were significantly different ($X^2=7.08$, $df=2$, $P=0.008$). When three calls overlapped, the number of calls separated by less than 1/3 octave was significantly different between the observed (5.8%) and the expected
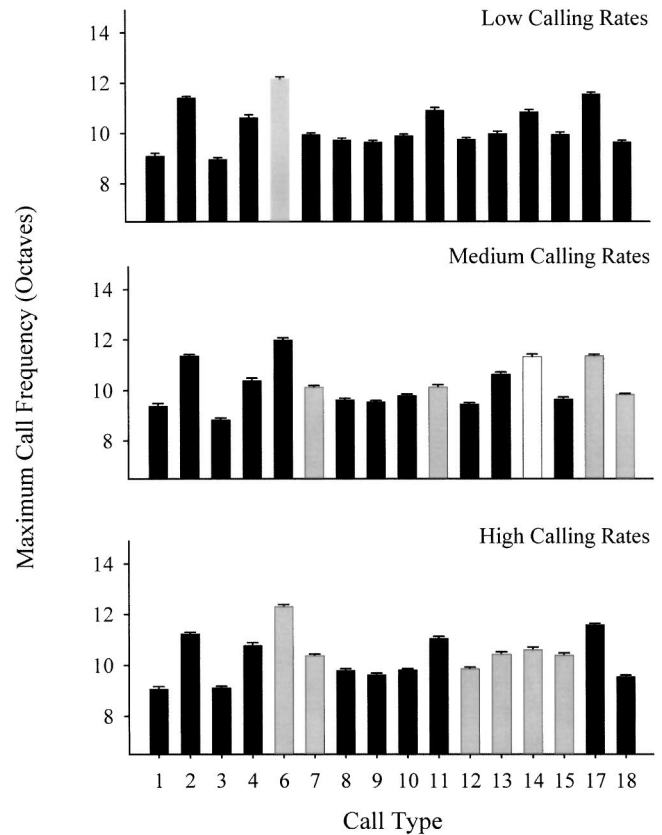
(19.5%; $X^2=10.59$, $df=2$, $P=0.001$). Finally, when four calls overlapped, the number of calls separated by less than 1/3 octave was significantly different between the observed (14.2%) and the expected (24.9%; $X^2=9.03$, $df=2$, $P=0.003$). That is, the observed frequency separations of 1/3 octave or less were all fewer than expected (Fig. 5).

IV. DISCUSSION

During the breeding season harp seals gather in groups of several thousands of animals (Sergeant, 1991) generating high underwater calling rates (Terhune and Ronald, 1986). Consequently, their vocal system has evolved under the pressure of a noisy environment. Some physical characteristics of the calls might have antimasking properties. Watkins and Schevill (1979) reported that 75% of the underwater calls of the harp seals were characterized by the following features: increasing within-call amplitude, increasing within-call frequency and/or pulse rates, and repetition in 94% of the calls. These researchers concluded that harp seals employ these characteristics to avoid masking by the abiotic background noise.

This study shows that increasing amplitude shifts were not evident along the call. These findings do not support Watkins and Schevill's (1979) observations or the hypothesis that increasing amplitudes within calls are used to enhance detection by being the opposite of this characteristic of abiotic noises.
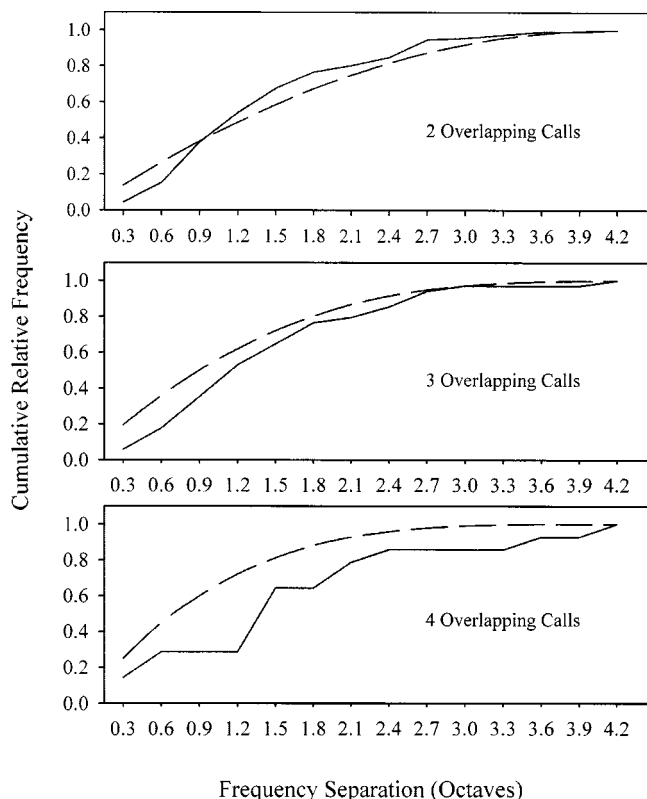
FIG. 5. Cumulative frequency distribution of frequency separation (octaves) of overlapping calls for the expected (dashed lines) and observed (solid lines) distributions of harp seal underwater calls.

It is generally accepted that an abrupt onset/offset of a call increases the call detectability (Watkins and Schevill, 1979; Wiley and Richards, 1982). Almost all the harp seal calls had an abrupt ending. Watkins and Schevill (1979) proposed that calls with abrupt endings are more detectable. The abrupt ending of the call is likely distinctive enough to serve as an antimasking strategy, because the background noise, especially abiotic noise, does not have this characteristic. This antimasking aspect is likely a relatively fixed characteristic associated with the structure of individual call types. The abrupt ending of the calls also provides an acoustic cue for localization (Terhune, 1974; Watkins and Schevill, 1979; Dooling, 1982). However, the seals did not exhibit a rapid onset of the calls. The results of this study differ slightly from those previously reported by Watkins and Schevill (1979). Watkins and Schevill (1979) only described the basic characteristics of the calls, and they reported rapid onsets and offsets for the calls but did not report any quantitative measurements. Today's technology allowed precise measures of the onset/offset rates of the calls.

The percentage of overlapping calls has its greatest change between low and medium calling rates, 12.7% to 19.6%, compared to an increase to only 20.6% at the high calling rate. All call changes in response to changing background calling rates become significant only at the high calling rate. This seems to be an indication that there is a threshold phenomenon that causes this increase. This observation is confounded by the use of ANOVA and the arbitrary limits of each calling rate category, however. As expected, the time intervals between calls decreased as the ambient calling rates increased. However, the percentage of overlapped calls was relatively low. This suggests that harp seals are actively avoiding temporal masking.

The mean durations of all single element harp seal calls are below 1.5 s and for multiple element calls, mean durations of the individual elements are all below 0.5 s (Serrano and Terhune, 2002). This contrasts with the mean durations of bearded seal trills which range from 31.5 to 2.1 s (Cleator et al., 1989). The short durations of the harp seal calls enable the low proportions of overlap even at high calling rates. Thus, the development of the harp seal repertoire of predominately short calls may have been a response to avoiding masking when calling rates were high.

Another mechanism to avoid being masked by overlapping conspecific vocalizations or irregular ambient noise is to lengthen the duration of the call. Weddell seals increase the number of elements in multiple element calls when overlapped by conspecific calls (Terhune et al., 1994). Harp seals increase the number of elements per call in seven call types when calling rates are high (Serrano and Terhune, 2001). King penguins (Aptenodytes patagonicus) increase the number of syllables per call as wind speed, and thus abiotic noise levels, increase (Aubin and Jouventin, 2002).

In many species in which animals produce advertisement signals in the form of vocalizations, the number of simultaneous callers is high enough to prevent signaling neighbors from perceiving one another (Greenfield, 1994). To prevent masking each other, animals need to adjust their signaling rhythms (Greenfield, 1994). For example, some bird species adjust the temporal pattern of their singing to avoid temporal overlap between songs of signaling neighbors (Ficken et al., 1974). Emperor penguins (Aptenodytes forsteri) within 7 m of each other appear to wait until the neighbor's call has finished before beginning their own call ("courtesy rule;" Aubin and Jouventin, 2002). Similarly, male African reed frogs (Hyperolius marmoratus) actively avoid overlapping their calls with those of their neighbors (Grafe, 1996). In other cases however, signalers actually try to mask each other. This is commonly observed in some species of anurans, where males try to mask each other in order to attract females (Greenfield, 1994). Evidently this is not the case for harp seals. One disadvantage of trying to temporally mask each other's calls is that the call becomes harder to pinpoint by the receiver of the signal (Greenfield, 1994). Therefore, for some species, such as the harp seal, where male competition is not intense (Le Boeuf, 1991), it may be more advantageous for the callers to actively avoid masking each other.

Clearly, harp seals are not using increasing frequency shifts to stand out from the abiotic noise patterns. Harp seal calls did not exhibit increasing frequency shifts within calls. Only call type 12 showed a significant difference (decrease in frequency) between the start and the end of the call. These observations do not support Watkins and Schevill's (1979) hypothesis that frequency increases at the end of the call.

Harp seals avoid masking each other by using frequency separation between overlapping calls. Most of the observed overlapping calls were separated by more than 1/3 octave. Using a 1/3-octave bandwidth distance is a conservative ap-

A. Serrano and J. M. Terhune: Antimasking harp seal calls

proach because the actual masking bandwidths may be smaller (Richardson, 1995). The observed cumulative frequency distributions for 2–4 overlapping calls showed that frequency separations of less than 1/3 octave occurred less frequently than expected by chance (Fig. 5). This, and the observation that similar call types were not made simultaneously, suggests that harp seals are choosing frequencies that are well separated from those of concurrent calls. This ability of harp seals to actively avoid masking each other is not unique to this species. Bearded seals (*Erignathus barbatus*) show a similar behavior. Bearded seal calls with a frequency separation of less than 1/3 octave occurred less often than expected from a random distribution (Terhune, 1999). The ability that harp and bearded seals have to space overlapping calls by more than 1/3 octave suggests that they are actively listening to nearby callers to avoid masking and also are not purposefully masking each other's calls.

Harp seal calls stand out sharply from the background noise as Watkins and Schevill (1979) noted. Thus, this contrast with ambient sound provides a means of herd recognition at a distance (Watkins and Schevill, 1979). Many physical characteristics of the harp seal underwater calls not only make the calls more distinctive from the abiotic background noise, but also allow the seals to avoid masking each other.

Some questions about seal vocal behavior can only be answered by comparisons across taxa. Bearded, Weddell, and harp seals are among the pinnipeds that have been better studied. During the breeding season, bearded seals remain widely separated. Males defend territories during this period (Burns, 1981). Adult male bearded seals produce six different types of trill vocalizations during the breeding season (Cleator *et al.*, 1989). Bearded seal calls are long (up to 176 s) and calling rates averaging 7.5 calls/min have been reported (Cleator *et al.*, 1989). These seals can avoid masking by means of frequency separation (Terhune, 1999). Probably the calls are used in male competition and courtship. Weddell seals form small aggregations during the breeding season. These seals probably have the largest vocal repertoire among pinnipeds with at least 34 different call types (Thomas and Kuechle, 1982). These seals use some long and some short calls. Many calls are made up of several short elements (Terhune *et al.*, 1994). Preliminary results indicate that Weddell seals are able to use frequency and temporal separation as an antimasking strategy (Terhune *et al.*, 1994; Galluchon, 1997). Probably Weddell seal males use their vocalizations to defend territories in the breeding areas and for courtship (Thomas and Kuechle, 1982). Harp seals form the largest aggregations with thousands of animals during the breeding season, and smaller groups during the nonbreeding season (Sergeant, 1991). Harp seals produce up to 26 different underwater calls (Serrano, 2001). Their calls are usually short in duration with several elements (Møhl *et al.*, 1975; Terhune, 1994). Harp seals are very vocal during the breeding season, producing calling rates of up to 135 calls/min. The short duration of individual calls, coupled with the frequency separation, makes these high calling rates possible. These seals avoid masking each other by using frequency and temporal separation. It is believed that the function of the harp seal calls is to help herd formation and courtship (Møhl

et al., 1975; Merdsoy *et al.*, 1978; Watkins and Schevill, 1979).

In summary, bearded seals avoid being masked by neighbors because the frequencies of overlapping calls are sufficiently different from each other (Terhune, 1999). Weddell seals likely use frequency and temporal separation to avoid masking each other. Harp seals use frequency and temporal separation in conjunction with a wide vocal repertoire to avoid masking each other. Probably one of the functions of the large vocal repertoire of this species is to provide the caller with a wide selection of calls to choose from to avoid being masked by a nearby seal. This idea implies that seals are actively listening to other seals and that they are not using the different call types randomly. This hypothesis is supported by the fact that the frequency separation between overlapping calls is larger than expected from a random distribution and by the fact that seals are using some call types more often than others (Serrano and Terhune, 2001).

Aubin, T., and Jouventin, P. (**2002**). ''How to vocally identify kin in a crowd: The penguin model,'' Adv. Study Behav. **31**, 243–277.

Bradbury, J. W., and Vehrencamp, S. L. (**1998**). *Principles of Animal Communication* (Sinauer, Sunderland, MA).

Brenowitz, E. A. (**1986**). ''Environmental influences on acoustic and electric animal communication,'' Brain Behav. Evol. **28**, 32–42.

Burns, J. J. (**1981**). ''Bearded seals,'' in *Handbook of Marine Mammals*, edited by S. H. Ridgway and R. J. Harrison (Academic, New York), Vol. 2, pp. 145–170.

Chu, K. C. (**1988**). ''Dive times and ventilation patterns of singing humpback whales (*Megaptera novaengliae*),'' Can. J. Zool. **66**, 1322–1327.

Cleator, H., Stirling, J. I., and Smith, T. G. (**1989**). ''Underwater vocalizations of the bearded seal (*Erignathus barbatus*),'' Can. J. Zool. **67**, 1900–1910.

Dooling, R. J. (**1982**). ''Auditory perception in birds,'' in *Acoustic Communication in Birds*, edited by D. E. Kroodsma and E. H. Miller (Academic, New York), pp. 95–130.

Ficken, R. W., Ficken, M. S., and Hailman, J. P. (**1974**). ''Temporal pattern shifts to avoid acoustic interference in singing birds,'' Science **183**, 762–763.

Galluchon, S. (**1997**). ''Proportion of masking in underwater vocalizations of the Weddell seal (*Leptonychotes weddellii*),'' B.Sc. Honours thesis, University of New Brunswick, Saint John, NB, Canada.

Gourevitch, G. (**1987**). ''Directional hearing in terrestrial mammals,'' in *Comparative Studies of Hearing in Vertebrates*, edited by A. N. Popper and R. R. Fay (Springer, New York), pp. 357–373.

Grafe, T. U. (**1996**). ''The function of call alternation in the African reed frog (*Hyperolius marmoratus*): Precise call timing prevents auditory masking,'' Behav. Ecol. Sociobiol. **38**, 149–158.

Greenfield, M. D. (**1994**). ''Cooperation and conflict in the evolution of signal interactions,'' Annu. Rev. Ecol. Syst. **25**, 97–126.

Klump, G. M. (**1996**). "Communication in the noisy world," in *Ecology and Evolution of Acoustic Communication in Birds*, edited by D. E. Kroodsma and E. H. Miller (Cornell University Press, Ithaca), pp. 321–338.

Le Boeuf, B. J. (**1991**). "Pinniped mating systems on land, ice and in the water: Emphasis on the Phocidae," in *The Behaviour of Pinnipeds*, edited by D. Renouf (Chapman and Hall, London), pp. 45–65.

McElligott, A. G., and Hayden, T. J. (**1999**). "Context-related vocalization rates of fallow bucks, *Dama dama*," Anim. Behav. **58**, 1095–1104.

Mercado, E., and Frazer, L. N. (**1999**). "Environmental constraints on sound transmission by humpback whales," J. Acoust. Soc. Am. **106**, 3004–3016.

Merdsoy, B. R., Curtsinger, W. R., and Renouf, D. (**1978**). "Preliminary underwater observations of the breeding behavior of the harp seal (*Pagophilus groenlandicus*)," J. Mammal. **59**, 181–185.

Møhl, B., Terhune, J. M., and Ronald, K. (**1975**). "Underwater calls of the harp seal, *Pagophilus groenlandicus*," Rapp. P.-V. Reun.-Cons. Int. Explor. Mer **169**, 533–543.

Richardson, W. J. (**1995**). "Marine mammal hearing," in *Marine Mammals and Noise*, edited by W. J. Richardson, C. R. Greene, C. I. Malme, and D. H. Thomson (Academic, San Diego), pp. 205–240.

Richardson, W. J., and Malme, C. I. (**1995**). "Zones of noise influence," in *Marine Mammals and Noise*, edited by W. J. Richardson, C. R. Greene, C. I. Malme, and D. H. Thomson (Academic, San Diego), pp. 325–386.

Serrano, A. (**2001**). "New underwater and aerial vocalizations of captive harp seals." Can. J. Zool. **79**, 75–81.

Serrano, A., and Terhune, J. M. (**2001**). "Within-call repetition may be an antimasking strategy in underwater calls of harp seals (*Pagophilus groenlandicus*)," Can. J. Zool. **79**, 1410–1413.

Serrano, A., and Terhune, J. M. (**2002**). "Stability of the underwater vocal repertoire of harp seals (*Pagophilus groenlandicus*)," Aquat. Mamm. **28**, 93–101.

Sergeant, D. E. (**1991**). "Harp seals, man and ice," Can. Spec. Publ. Fish. Aquat. Sci. **114**, 1–153.

Smith, W. J. (**1977**). *The Behaviour of Communication* (Harvard University Press, Cambridge).

Terhune, J. M. (**1974**). "Directional hearing of a harbor seal in air and water," J. Acoust. Soc. Am. **56**, 1862–1865.

Terhune, J. M. (**1994**). "Geographical variation of harp seal underwater vocalizations," Can. J. Zool. **72**, 892–897.

Terhune, J. M. (**1999**). "Pitch separation as a possible jamming-avoidance mechanism in underwater calls of bearded seals (*Erignathus barbatus*)," Can. J. Zool. **77**, 1025–1034.

Terhune, J. M., Grandmaitre, N. C., Burton, H. R., and Green, K. (**1994**). "Weddell seals lengthen many underwater calls in response to conspecific vocalizations," Bioacoustics **5**, 223–226.

Terhune, J. M., and Ronald, K. (**1986**). "Distant and near-range functions of harp seal underwater calls," Can. J. Zool. **64**, 1065–1070.

Thomas, J. A., and Kuechle, V. B. (**1982**). "Quantitative analysis of Weddell seal (*Leptonychotes weddelli*) underwater vocalizations at McMurdo Sound, Antarctica," J. Acoust. Soc. Am. **72**, 1730–1738.

Turnbull, S. D., and Terhune, J. M. (**1993**). "Repetition enhances hearing detection thresholds in a harbor seal (*Phoca vitulina*)," Can. J. Zool. **71**, 926–932.

Vaughan, T. A. (**1986**). *Mammalogy*, 3rd ed. (Saunders College Publishing, New York).

Watkins, W. A., and Schevill, W. E. (**1979**). "Distinctive characteristics of underwater calls of the harp seal, *Phoca groenlandica*, during the breeding season." J. Acoust. Soc. Am. **66**, 983–988.

Wiley, R. H., and Richards, D. G. (**1982**). "Adaptations for acoustic communication in birds: Sound transmission and signal detection," in *Acoustic Communication in Birds*, edited by D. E. Kroodsma and E. H. Miller (Academic, New York), pp. 131–181.

Zar, J. H. (**1996**). *Biostatistical Analysis*, 3rd ed. (Prentice-Hall, Englewood Cliffs, NJ).